*RaSiM 7(2009): Controlling Seismic Hazard and
Sustainable Development of Deep Mines,
C.A. Tang(ed), Rinton Press, 1-2*

KEYNOTE LECTURES

RaSiM 7(2009): Controlling Seismic Hazard and
Sustainable Development of Deep Mines,
C.A. Tang(ed), Rinton Press, 3-16

IMPORTANCE OF INHOMOGENEITY IN ROCK FRACTURING DEDUCED FROM DISTINCT ELEMENT SIMULATION AND IN-SITU DIRECT SHEAR TEST

TSUYOSHI ISHIDA, HIROYUKI SHIMIZU and SUMIHIKO MURATA

Dept. of Civil and Earth Resources Engineering, Kyoto University

Kyoto, 615-8540 JAPAN

TADASHI KANAGAWA

Nittoc Construction Co., Ltd,

Akashi-cho 13-18, Tokyo, 104-0044 Japan

Inhomogeneity is the important nature of rock fracturing including a rock burst. In this paper, the fact that inhomogeneity plays an important role in rock fracturing is elucidated by simulation of uniaxial compression test using our own code of the DEM (Distinct Element Method) and by comparison between AE (Acoustic Emission) source distribution and fracture plane observation of an in-situ direct shear test conducted in a survey tunnel for an underground powerhouse.

1 Introduction

Inhomogeneity is important in rock fracturing including a rock burst as suggested by Tang [1] and Chen et al. [2]. Since the magnitude of fracturing induced in inhomogeneous rock has wide variety from small to large as suggested by Mogi [3] and the fracturing location is usually unexpected, AE(Acoustic Emission)/MA (Microseismic Activity) monitoring is effective to detect the fracturing prior to macroscopic fracture like a rock burst and to predict it.

AE monitoring is also effective to study the fracturing process of inhomogeneous rock. Even at present, it is still difficult to measure all AE events generated during a laboratory experiment, due to the influence of noises and the limit of recording speed of a measuring device. In contrast, numerical methods, for examples, those based on FEM (Finite Element Method) [1, 2], BEM (Boundary Element Method) [4, 5], DEM (Distinct Element Method) [6, 7] and others, make it possible to simulate all micro-fracturing accompanying AE events too small to be measured in an actual fracturing experiment. Among them, the DEM seems to be the most appropriate numerical methods for the rock fracturing, because it can easily simulate inhomogeneous force transmission due to pre-existing cracks and flaws in a rock specimen by contact force transmission among individual particles in the model. We have programmed a DEM own cord and simulated a uniaxial compression test, and discussed the process in which microcracks are induced and results in a macroscopic fracture [8]. In this paper, at the first, we will introduce the results and the discussion as one of our fundamental researches for the inhomogeneous rock fracturing.

On the other hand, a rock burst and AE events prior to it strongly depend on geological condition, as many engineers usually encounter and, for an example, as reported by Milev and Spottiswood [9]. We have also similar experiences in AE monitoring of underground powerhouses [10, 11, 12], a rock slope [13, 14], hydraulic fracturing [15, 16, 17, 18] and a heater test [19]. The fact that geological inhomogeneity governs seismic energy release is accepted for earthquakes through establishment of the asperity model [20, 21], and is also elucidated by acoustic emission monitoring for a rock samples in laboratory [e.g. 22]. Thus, for successful engineering AE monitoring for a rock burst, it is important to clarify how and which kinds of the geological inhomogeneity govern locations of AE events and release of their seismic energy. With the background, we monitored AE events during an in-situ direct shear test conducted in a survey tunnel for an underground powerhouse [23, 24]. Since the test block included joints and a loosening seam, an AE clustering region was governed by them. In this paper, at the second, we will introduce the results and discuss the relation between located AE events and geological inhomogeneity by comparing the joints, the loosening seam, height distribution of the fracture plane and displacement of the test block.

2 DEM Analysis for Rock Fracturing under Uniaxial Compression

The DEM is a numerical technique for discontinuum, which was pioneered by Cundall [6]. In the two dimensional DEM, an intact rock is modelled as a dense packing of small rigid circular particles. Neighbouring particles are bonded together at their contact points and interact with each other. Bonds can break when load is applied, and microcracks are represented explicitly as broken bonds.

A rock specimen for a uniaxial compression test contains many pre-existing flaws such as pores, microcracks and grain boundaries. These micro-structures cause inhomogeneous force transmission with various orientations and magnitudes of micro-forces and micro-moments [25]. The DEM can represent these grain-scale micro-structural features directly by considering each grain as a DEM particle. The grain-scale discontinuities in the DEM model induce complex macroscopic behaviours without complicated constitutive laws [7]. This suggests that the DEM model may be more appropriate for the analysis of rock fracturing than other numerical techniques.

In this chapter, as a fundamental research of the rock fracturing, we simulated a uniaxial compression test using our own cord of the DEM and discuss the process in which microcracks are induced inside a rock specimen and result in a macroscopic fracture.

2.1 Simulation Methodology

(1) Formulation of bonds

In this section, only a summary of formulation for the mechanical behaviour of bonded particles will be given. More thorough details of the DEM are given in Reference [6] and [7].

The mechanical behaviour of the two bonded particles is represented with a set of three kinds of springs as shown in Figure 1. The normal force f_n, the tangential force f_s, and the moment f_θ are carried by these springs. The forces f_n, f_s and f_θ are produced by relative motion between the bonded particles, and are given by

$$\begin{aligned} \Delta f_n &= k_n\left(dn_j - dn_i\right) \\ \Delta f_s &= k_s\left(ds_j - ds_i - r_j d\theta_j - r_i d\theta_i\right) \\ \Delta f_\theta &= k_\theta\left(d\theta_j - d\theta_i\right) \end{aligned} \tag{1}$$

where k_x, k_y and k_θ are the spring stiffnesses of normal spring, shear spring, and rotation restriction spring, respectively; dn, ds and $d\theta$ are normal- and shear-directed displacements and rotation of each particles; r_i and r_j are the radii of the bonded particles.

A bond is depicted schematically as a gray rectangle in Figure 2, where D is a bond diameter. The normal stress σ and shear stress τ acting on the cross-section of the bond are calculated by

$$\sigma = \frac{f_n}{D}, \quad \tau = \frac{f_s}{D}, \quad D = \frac{4r_i r_j}{r_i + r_j} \tag{2}$$

If the normal stress σ exceeds the strength of normal spring S_t, or the shear stress τ exceeds the strength of shear spring S_s, then the bond breaks, and three springs are altogether removed from the model. A rotation restriction spring is used only for the force calculation, and the judgment of breakage is not applied to this spring.

(2) Correlation with AE

Each bond breakage is assumed to be a microcrack. A microcrack is generated at the contact point between two particles, and the direction of it is perpendicular to the line joining the two centres. When a microcrack is generated, the strain energy, which is stored in the normal and shear spring at the contact point shown in Figure 1, is released. So, in this simulation, the strain energy E given by the equation (3) is assumed to be the energy of AE.

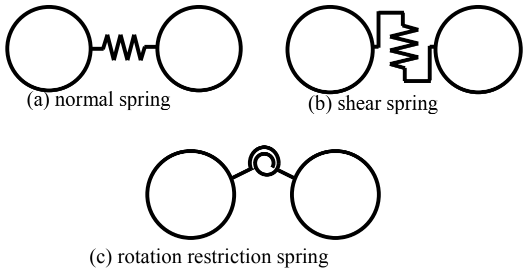

Figure 1 Connecting between particles with three kinds of springs.

When a bond breaks, both the normal stress σ and the shear stress τ are acting in almost all cases. Therefore, the crack modes are classified by shear-tensile stress ratio $|\tau/\sigma|$ as the equation (4).

$$E = \frac{1}{2}k_n\left(dn_j - dn_i\right)^2 + \frac{1}{2}k_s\left(ds_j - ds_i - r_j d\theta_j - r_i d\theta_i\right)^2 \tag{3}$$

$$\begin{cases} \sigma = \text{Compressive stress} \cdots\cdots \text{Shear Crack} \\ \begin{cases} \sigma = \text{Tensile stress} \\ |\tau/\sigma| > 1 \quad \cdots\cdots\cdots\cdots\cdots\cdots\cdots \text{Shear Crack} \\ |\tau/\sigma| \le 1 \quad \cdots\cdots\cdots\cdots\cdots\cdots\cdots \text{Tensile Crack} \end{cases} \end{cases} \tag{4}$$

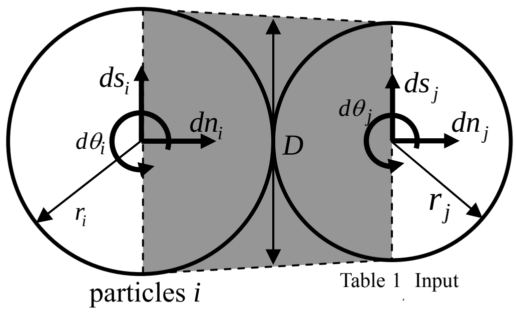

Figure 2 Bonded particles model.

2.2 Simulation Model

As shown in Figure 4, the rock model which is 10cm in width and 20cm in height was used. The rock model was expressed by the assembly of particles bonded with each other. Particles were irregularly arranged by using a random number. The particle radius was chosen to have a uniform distribution between the maximum radius and the minimum radius. The number of particles was 5033. The input parameter is shown in Table 1.

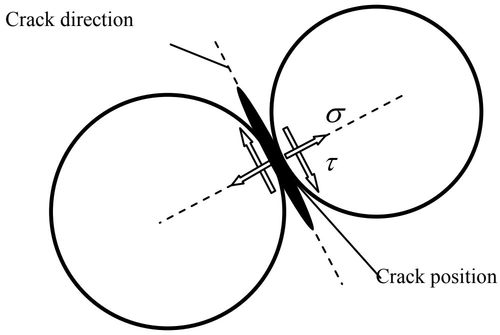

Figure 3 Crack position and direction.

The platen under the rock model was fixed and the upper loading platen was moved downward slowly to reproduce a uniaxial compression test. At this time, frictional force was acting between the rock model and the loading plate. The confining wall was not prepared in the side of the model. The axial stress applied to the rock model during compression test was calculated from width of the model and total force acted on the upper loading platen from particles.

2.3 Results

Figure 5 shows the relation between axial stress and the number of generated microcracks. The uniaxial strength that induced the macroscopic failure of the rock model was 38.2 (MPa). The closed and open bar graphs in the figure express the number of the tensile cracks and the shear cracks, respectively. This figure can be divided into three phases according to the tendency of microcracking. The crack generation tendencies in each phase are summarized in the following sections.

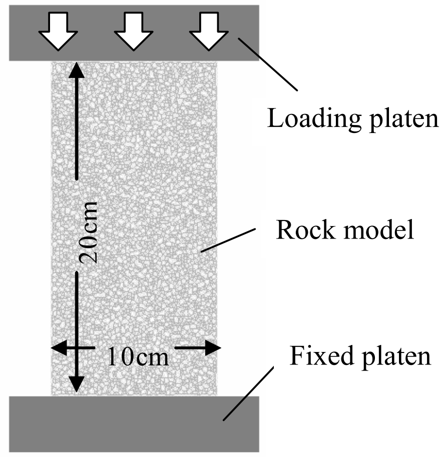

Figure 4 Simulation model

Table 1 Input parameters

Number of particles	:5033
Maximum radius	:1.2 (mm)
Minimum radius	:0.8 (mm)
Particle density	:2660 (kg/m3)
Friction coefficient of particle	:0.5
Friction coefficient of wall	:0.3
Young's modulus of particle	:50 (GPa)
Poisson's ratio of particle	:0.3
Young's modulus of bonding	:50 (GPa)
Poisson's ratio of bonding	:0.3
Shear strength of bonding	:60.0 (MPa)
Tensile strength of bonding	:5.0 (MPa)

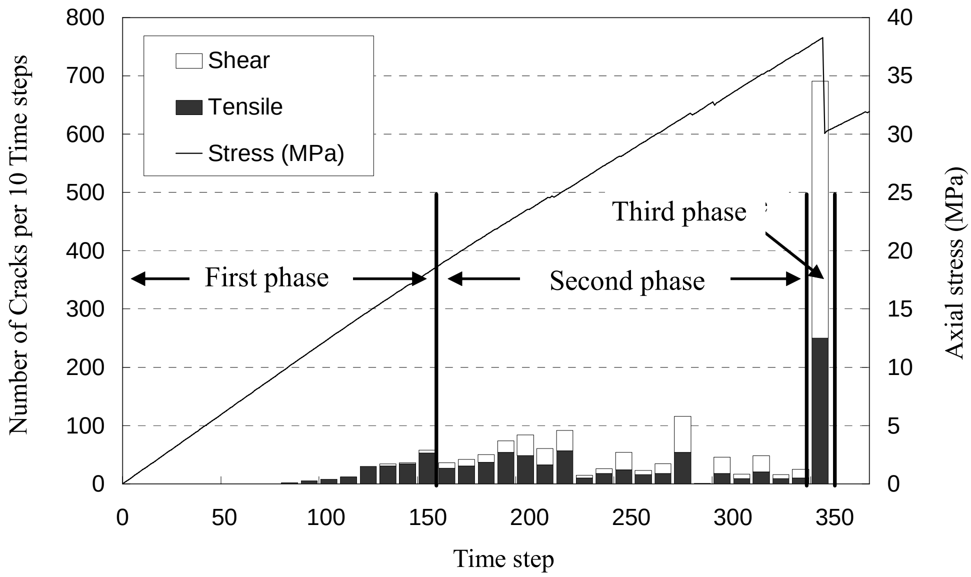

Figure 5 Relation between axial stress and number of cracks

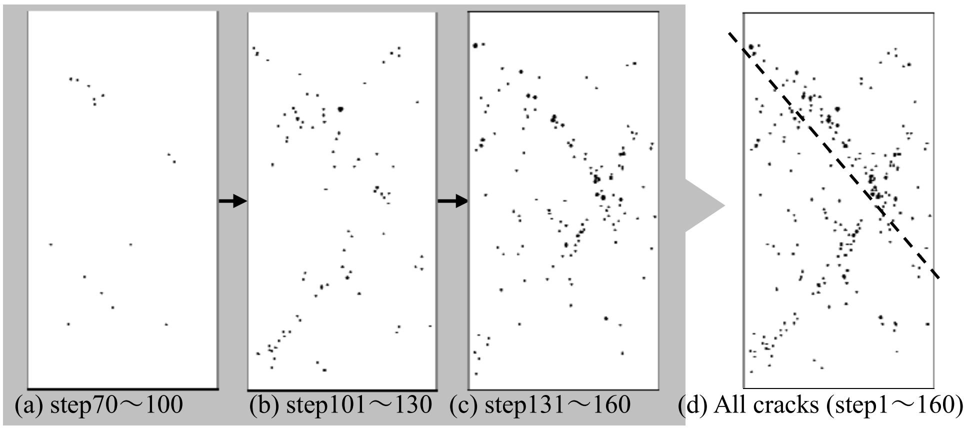

Figure 6 Spatial distribution of the cracks generated in the first phase. The diameter of the circle corresponds to each magnitude of energy. Cracks are initiated at step70. (a), (b), and (c) show cracks generated during every 30steps from step70. (d) shows distribution of all the cracks generated in the first phase.

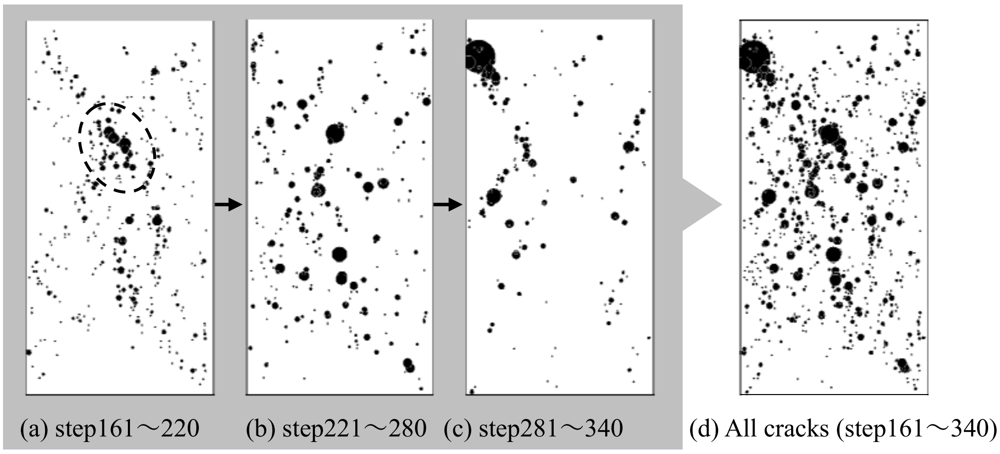

Figure 7 Spatial distribution of the cracks generated in the second phase. The diameter of the circle corresponds to each magnitude of energy. (a), (b), and (c) show cracks generated during every 60steps. (d) shows distribution of all the cracks generated in the second phase.

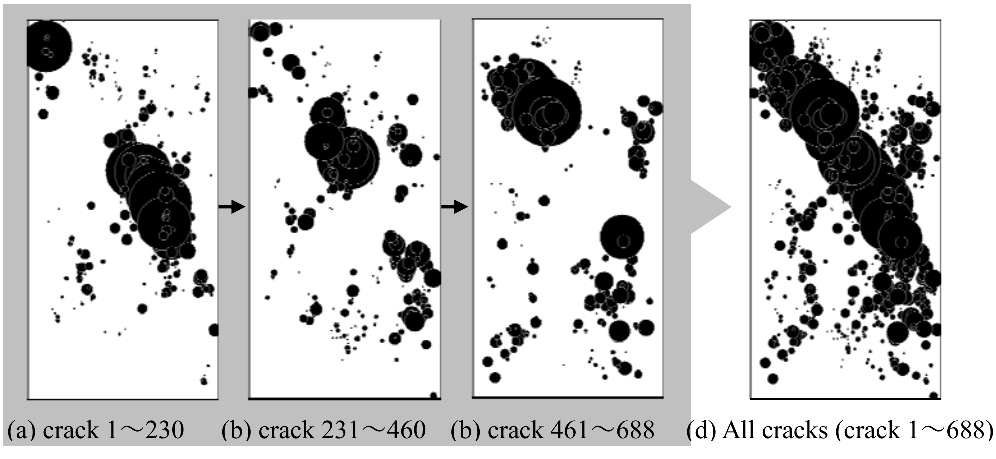

Figure 8 Spatial distribution of the crack generated in the third phase. The diameter of the circle corresponds to each magnitude of energy. In the third phase, 688 cracks are generated and these cracks were generated within a very short time. (a), (b), and (c) show cracks generated during every 230 steps. (d) shows distribution of all the cracks generated in the third phase.

(1) First phase

In the first phase, microcracks initiated at a stress level about 25% of the uniaxial strength. As shown in the bar graph of Figure 5, most of the microcracks generated in the low stress level were tensile cracks. Figure 6 shows distribution of microcracks generated in the first phase and each magnitude of the energy defined by equation (3). At first, microcracks were widely distributed over the whole model. As the axial stress increases, the number of microcracks increases gradually, and these microcracks align along the dotted line in Figure 6 (d). The macroscopic fracture was formed along this line as shown afterward.

(2) Second phase

Figure 7 shows distribution of the cracks generated in the second phase and each magnitude of the energy. In addition to tensile cracks, shear cracks began to be generated, in this phase. The number of microcracks increased further and microcracks that release comparatively large energy concentrated in the region surrounded by the dotted line in Figure 7(a). Such concentration of microcracks is called “clustering”. Comparing Figure 7(a) with Figure 6(a), (b) and (c), we can find that occurrence of microcracking have become active near the centre of the model in this phase. As shown in Figure 7(a), (b) and (c), the cluster which appeared near the centre of the model spread to the edge of the model gradually. Moreover, Figure 5 shows that the number of microcracks was decreasing temporarily, when the cluster migrated.

(3) Third phase

In the third phase, the number of microcracks increased rapidly. A macroscopic fracture has been formed in a very short time, and the model resulted in collapse. Distribution of the cracks generated in the third phase and the magnitude of the energy are shown in Figure 8. Microcracks concentrated near the centre of the model and they progressed to the upper left of the model. These microcracks that formed the macroscopic fracture released very large energy comparing with other microcracks. Most of the microcracks that released such large energy were shear cracks. This indicates that the macroscopic fracture was mainly formed of shear cracks.

2.4 Discussion

During the first phase, the tensile cracks were dominant and were widely distributed over the whole model. When the number of microcracks increases with increase of the axial stress, the interaction during cracks has become stronger gradually. This resulted that the tensile cracks concentrated and aligned along a line.

The simulation results in this phase are well in agreement with the experimental results. According to the experimental results, the major mechanism of microcracking at the lower stress level is the tensile cracks associated with some kind of initial rupture of pre-existing flaws. This is derived from the fact that the tensile strength of every microcrack is much lower than shear strength. Kranz [26] actually found under microscopic observation that tensile cracks are dominant rather shear cracks in a rock specimen subjected to uniaxial compressive stress. However, in contrast, in laboratory uniaxial compressive tests, AE events induced by shear cracks are rather dominant those by tensile [27]. Thus, the conflict is remained between microscopic observation and AE events. The simulation results in this phase suggest that the energy released from a tensile crack is very small comparing with that from a shear crack, due to the tensile strength much smaller than compressive strength. It is thought that such a small AE is easily buried in noises and hard to be measured in an experiment. Probably, this is a reason why shear AE events are dominantly observed in an actual AE monitoring experiment. The results, providing the new finding to solve the conflict, shows that the DEM can successfully represent the grain-scale microstructures such as pores, microcracks and grain boundaries directly by considering each grain as a DEM particle.

The typical feature of the second phase is initiation and migration of the cluster. The number of microcracks increases and dense microcracking intensifies the interaction between microcracks. Once the interaction has been strong enough within a certain region, resulting in an enhancement of the local stress concentration, then new microcracks are generated one after another in the region. Thus, a cluster can be formed. Meanwhile, cracking releases local stress. When stress has been sufficiently released in the previous region, migration of microcracking activity could proceed to new clustering regions. On the other hand, stress re-distribution decreases the local stress concentration during some moments. Therefore, the number of microcracking might have decreased temporarily as shown in Figure 5.

In the third phase, a catastrophic fracture was formed and the model resulted in collapse within a very short time. In this phase, the interaction during microcracks is so strong, and local stress concentration is very intense comparing with the previous two phases. In brief, this phase is very unstable. So, once a catastrophic fracture initiated at one key location, microcracks are connected again and again by sliding until the rock model is completely collapsed.

The catastrophic fracture in the third phase is located on the line along which the tensile cracks aligned in the first phase. This suggests that the formation of macroscopic fracture is guided by development of a process zone encompassing tensile cracks, while shear cracks are the dominant fracture mode in this phase.

3 AE Monitoring during In-situ Direct Shear Test of Rock

The AE monitoring during in-situ direct shear test was conducted in a in a chamber branched from a survey tunnel for an underground powerhouse constructed in Yamanashi prefecture, central Japan. The rock mass of the site consists of mudstone and sandstone of Shimanto supergroup sedimentating in late Cretaceous of Mesozoic era and Paleogene of Cenozoic era. The test block was mudstone measuring 50 cm long, 50 cm wide and 20 cm high, as shown in Figure 9. The test block was made as a specimen for the direct shear test by using a mechanical breaker and a small rotational boring machine without blasting so as to avoid disturbing or loosening the specimen. The test block was encapsulated with 10 cm thick reinforced concrete.

A series of direct shear tests was conducted on the four specimens in order to obtain cohesion and internal friction angle for planning the underground powerhouse. Different magnitudes of vertical load, V=125, 250, 500 and 750 kN, were applied to the four specimens via a hydraulic ram connected to a hydraulic pump, and they were kept constant during the test. The magnitudes of the vertical load correspond to 0.5, 1, 2, and 3 MPa as an averaged normal stress on the expected shear plane, which is the plane at the base of the specimen extended from the ground surface around the specimen. In addition, a shear load, S, is applied in the direction parallel to the strike of the bedding plane. Since the direction of the shear load has an angle 17 degrees from the horizontal, this load induces a normal stress component $S \bullet \sin 17^{\circ}/A$ on the expected shear plane as well as the shear stress component $S \bullet \cos 17^{\circ}/A$ along the plane, where A is the area of the expected shear plane. Thus, the normal stress on the expected shear plane is $(V+S \bullet \sin 17^{\circ})/A$, and increases with the increase of S in spite of keeping V constant.

S was increased by 80 kN for 5 minutes and then was kept constant for the following 5 minutes. By repeating this 10-minute cycle, S increases until the specimen experiences a shear failure and starts to slide along the expected shear plane. The testing method follows the guidelines for an in-situ direct shear test [28] published by JSCE (Japanese Society for Civil Engineers) and is almost the same as the suggested methods [29] of the ISRM (International Society for Rock Mechanics) with slight differences in block size, rate of shear displacement, etc.

Assuming Coulomb's failure criterion, a regression line is obtained for the maximum shear stresses, $S_o \bullet \cos 17^{\circ}/A$, and the maximum normal stresses, $(V+S_o \bullet \sin 17^{\circ})/A$, for the four tests, where S_o is the maximum shear load. From the obtained regression line, a cohesion of 3.16 MPa and an internal friction angle of 56.4° are obtained.

3.1 AE and Displacement Monitoring

The test block for which we monitored AE events is the block which was subjected to V = 500 kN. Setting positions of the AE sensors and displacement gauges are shown in Figure 9. Displacements are measured at ten points in total: four points (m, n, o and p) are for the shear displacement; another four points (i, j, k and l) are for the vertical displacement; and the remaining two points (q and r) are for the lateral displacement. Vertical and shear loads were measured by load cells set between the rams and the test block.

As a sensor for the AE monitoring, a piezoelectric transducer made of PZT (Pb(lead) zirconium titanate) having a resonant frequency of 67 kHz was used as the sensor for AE monitoring. The PZT element was set in the bottom of a cylindrical brass case having 40-mm diameter and 34-mm height. The cylinder was filled with silicon rubber for waterproofing [11]. Since the dominant frequency of the waveform actually recorded in the test is in the range 15 to 40 kHz, the resonant frequency of the sensor including the brass case should be within this frequency band.

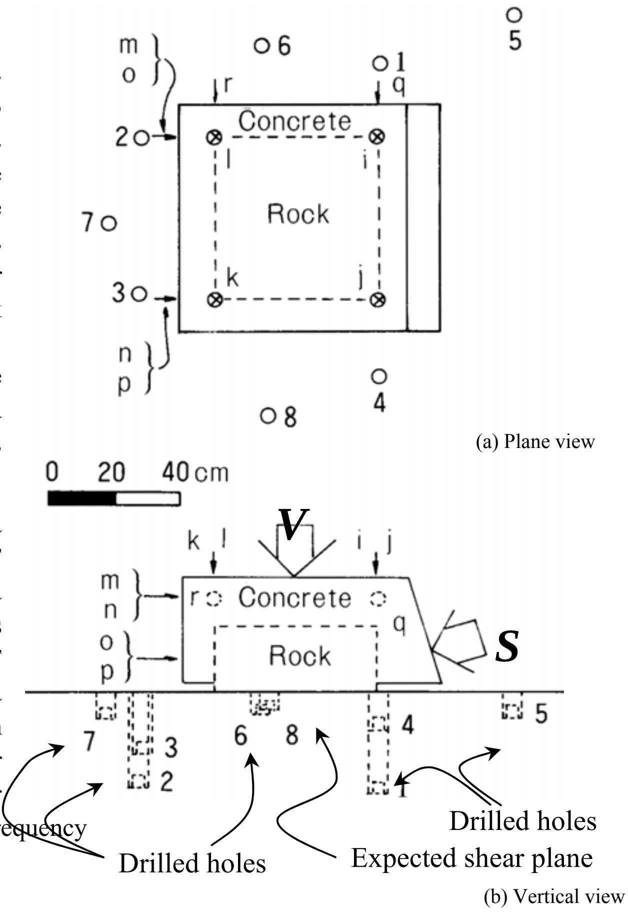

Figure 9 (a) Plane view and (b) vertical view of the test block for the in-situ direct shear test. Setting positions of AE sensors (numbers 1 to 8) and displacement gauges (letters i to r) are also shown. Two large open arrows show the directions of the vertical load, V, and the shear load, S, which are applied to the test block.

As shown in Figure 9, eight AE sensors are fixed with cement paste in the bottom of drilled holes having 66-mm diameter and depths up to 30 cm s around the test block.

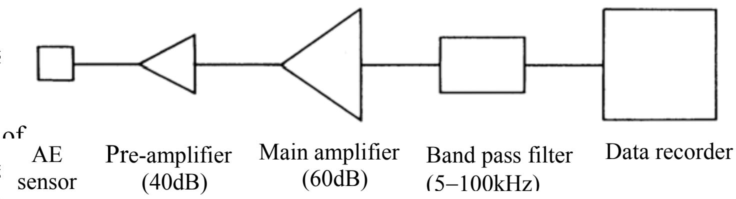

Figure 10 Schematic diagram of the AE measuring system.

Figure 10 shows the block diagram of the AE monitoring system. Since the test was conducted in 1984, the instruments are out of date. An AE signal received at each AE sensor was amplified 100 dB in total (40 dB in a pre-amplifier and 60 dB in a main amplifier) and recorded in a high speed tape recorder through a band pass filter of the frequency range from 5 to 100 kHz to eliminate noises. The tape recorder was used in a direct recording mode with a tape speed of 76.2 cm/s, covering the frequency range set by the filter.

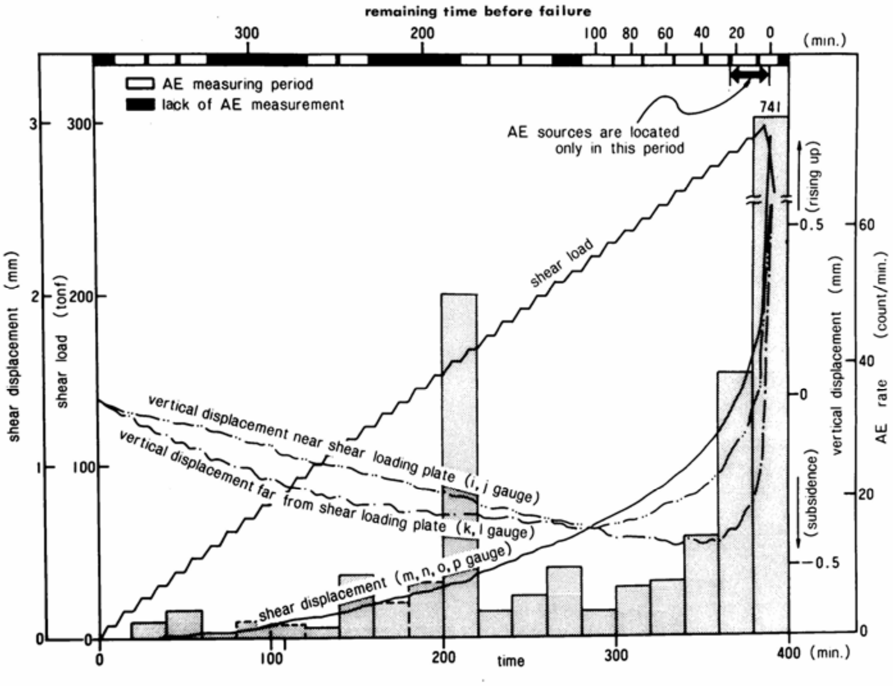

Figure 11 AE event rates, shear load, shear displacement and vertical displacements during the test.

3.2 Results

(1) AE Event Rates, Load and Displacements

The test took 6 hours and 40 minutes. Figure 11 shows the shear load, the shear and vertical displacements and AE event rates for every 20 minutes, with the lateral axis of the elapsed time. The AE event rates were counted for wave signals reproduced from the recorded tapes, by setting a constant discriminate level of 0.6 volt. The AE event rates shown in Figure 11 are average of those counted at Nos. 2 and 4 sensors. AE events were not recorded for some periods due to replacing the tape and other reasons, as shown by the black bars in the upper part of Figure 11. The AE event rates in such the periods were estimated from those just before and just after the periods, and were shown by the bar diagram of broken lines.

From 200 to 220 min, the AE event rate became large, and after that, it became small again. However, it increased again step by step around from 280 minutes, and showed large increase after 380 minutes, bringing the final failure of the test block with the burst of AE occurrence.

Hirama et al. [30] pointed out from their experience in many in-situ direct shear tests that the turn of the vertical displacement from downward to upward indicates to the start of final failure of the test block. From the view point, examining the records of the vertical displacements in Figure 11, the elapsed time of 280 minutes when the AE events rates started to increase almost corresponds to the time when the vertical average displacements measured at the points "i" and "j" close to the shear loading plate turned from downward to upward. Moreover, the elapsed time of 380 minutes when it started to show large increase almost corresponds to the time when the vertical average displacements measured at the points "k" and "l" close to the opposite side to the shear loading plate showed the turn.

(2) Two-Dimensional Source Location of AE Events

Since, in this test, the fracture accompanying AE events should be induced on the expected shear plane

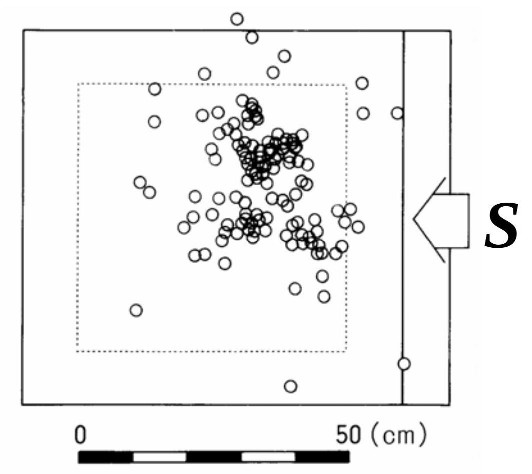

Figure 12. Distribution of all located AE epicentres.

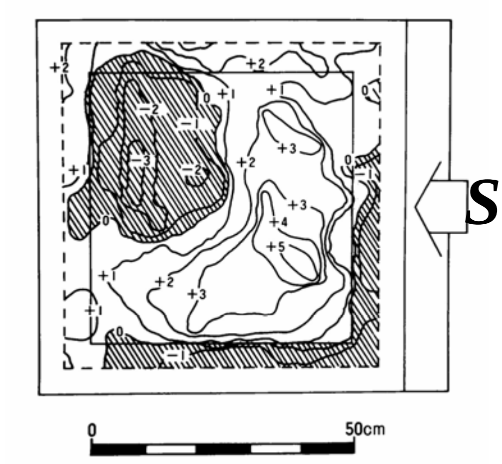

Figure 13. Contour of the fractured plane by the shear test. Numerals indicate the height in "cm". Hatched parts show concavities lower than the expected shear plane.

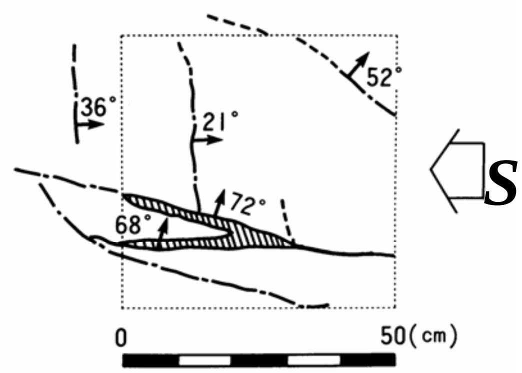

Figure 14. Sketch of the fractured plane. Solid, chain and broken lines show strikes of joints and arrows with numerals show their dip angles. A hatched part shows a loosening seam.

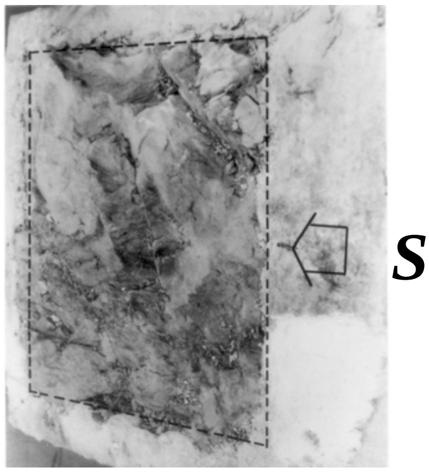

Photo 1 Fractured plane of the test block turned over. This photo was printed through the negative film in order to make the left and right hand sides (with respect to the direction of the shear load S) the same as those of Figures 12, 13 and 14. Note that "concave" and "convex" are still reversed between this photo and Figure 13.

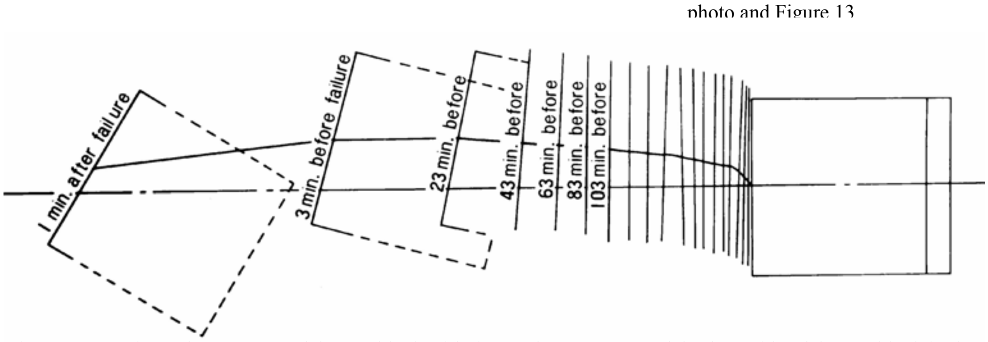

Figure 15. Horizontal movement of the test block with time. The movement of the front side of the test block is shown by drawn solid lines. (Displacement and rotational angle are exaggerated.)

corresponding to the ground surface line shown in Figure 9, AE sources were located two dimensionally under an assumption that they distributed on the plane. In this case, since P-wave velocity, 5.0 km/s, were measured in the test site, unknowns for the source location are three; two dimensional source coordinates, *x* and *y*, and occurrence time of the AE event, *t*. Thus, by the non-liner least square method, if P-wave initial motions could be read out along waveforms at more than four sensors, these three unknowns could be determined. Since the most of the AE events satisfying the condition were recorded only for the term closed to the final failure, the AE sources, that are the AE epicentres in this case, were located only for 22 minutes just before the shear load suddenly decreased as shown in Figure 11.

The recorded AE signals were reproduced on the tape speed of 1.19 cm/s, which is a speed of 1/64 to the recording tape speed, 76.2 cm/s. The reproduced AE signals were converted to digital data with a sampling time of 50μs that is 0.78μs in the real time, and an amplitude resolution of 10 bit. The 403 AE events were converted to digital data through this procedure, and the epicentres of 154 AE events out of them were located as shown in Figure 12. The arrow in the figure indicates the direction of the applied shear load *S*.

3.3 Discussion on the Located AE Epicentres in Comparison with Other Observations

Distribution of heights of the fractured plane, locations of joints and a loosening seam and horizontal movements of the test block with time could be compared with a distribution of the located AE epicentres.

Figure 13 shows distribution of heights of the fracture plane with contour lines, when the height of the expected shear plane corresponding to the ground surface was put to be zero. After the test, the fracture plane was covered with a wooden square frame having wires set in the same intervals in the two orthogonal directions along the frame so as to make grids, and the heights of the fracture plane were measured with a ruler at points of the grids using the frame plane as a reference of the height. In addition to this, to check the measured heights, the upper part of the test block separated along the fracture plane was turned over as shown in Photo 1, and the heights of the opposite side fracture plane were measured. While the hatched parts in Figure 13 show concavities lower than the ground surface, the open parts show convexities higher than it. This figure indicates that the centre of the AE clustering region shown in the right-upper part in Figure 12 corresponds to the convexities of +3 cm height.

Figure 14 shows the sketch of joints and a loosing seam observed on the fracture plane. This figure indicates that the AE clustering region in Figure 12 corresponds to the region of the intact rock surrounded with the joints and the loosening seam.

Photo 1 shows the fractured plane appearing on the upper part of the test block taken off and turned over. This photo was printed by turning over the negative in order to make the left and right hand sides (with respect to the direction of the shear load) the same as those of Figures 12, 13 and 14. Note that "concave" and "convex" are reversed between this photo and Figure 13. Considering these differences, we can see that the features of the upper fracture plane shown in Photo 1 correspond to the height distribution shown in Figure 13 and to the joints and the loosening seam observed on the lower fracture plane shown in Figure 14.

Figure 15 shows horizontal movement of the test block with time. This figure indicates that the test block turned clockwise for the 22 minutes while the AE events having the epicentres shown in Figure 12 were recorded.

From these measurements and observations, it could be concluded that the part of intact rock surrounded by the joints and the seam shown in Figure 14 was fractured with accompanying AE, and the specimen reached final fracture with turning around the convex part of +3 cm height shown in Figure 13. On the other hand, in the parts having the joints and the seam, AE events having large magnitude able to detect in the sensors did not occur. The above discussion elucidated that the distribution of AE sources corresponds to the observation of the fractured surface and the movement of the specimen. This also suggested that AE events detected in inhomogeneous rock masses usually encountered in field measurements occur in relatively hard and intact parts of rock masses. This suggestion should be considered when we monitor AE events prior to a rock burst to predict it and when we discuss stability of rock masses in underground chambers and rock slopes.

4 Conclusions

In this paper, at the first, we have introduced the results of DEM simulation for the uniaxial compression test of a rock specimen and discussed on the rock fracturing. The result indicates that the rock fracturing process is characterized by three typical phases as follows.

(1) During the first phase, tensile cracks were dominant. The microcracking in this phase is governed by inhomogeneous microstructures of rock such as pores, microcracks and grain boundaries.

(2) In the second phase, the number of cracks increases and the interaction between the cracks becomes stronger gradually. This induces coalescence of neighbouring cracks and results in clustering of microcracks.

(3) In the third phase, once a catastrophic fracture initiated at one key location, it grows again and again within a very short time. The catastrophic fracturing is guided by development of a process zone encompassing tensile cracks.

The results of our simulation could explain time-space distribution of microcracking activity in the course of a uniaxial compression test, and were well in agreement with the fracturing process deduced from AE measurements in the laboratory experiments conducted by previous researchers. In addition to this, the results provide the new findings to solve the conflict; the conventional theories and microscopic observations suggest that tensile cracks cause AE events, whereas an abundance of shear type AE events are observed in the experiments. Our simulation results indicate that the energy released from a tensile crack is very small comparing with that from a shear crack, due to the tensile strength much smaller than compressive strength. It is thought that such a small AE is easily buried in a noise and hard to be measured in an experiment. This is probably a reason why shear AE would be observed dominantly in an actual AE monitoring experiment. These results, including the new finding to solve the conflict, indicate that DEM is an effective numerical analysis technique for studying the fracturing process of inhomogeneous materials like rock.

In this paper, at the second, we have introduced the AE monitoring results of an in-situ direct shear test and discussed the relation between located AE events and geological inhomogeneity by comparing the joints, the loosening seam, height distribution of the fracture plane and displacement of the test block. As the results, the followings were found.

(1) The AE clustering region corresponds to the part of intact rock surrounded with the joints and the loosening seam.

(2) The AE clustering region also corresponds to the convex part higher than the expected shear plane that is the ground surface.

(3) The measurement of the horizontal displacement elucidated that the test block turned around the convex part at the final fracturing stage.

From these findings, it could be concluded that the part of intact rock surrounded by the joints and the seam was fractured with accompanying AE, and the specimen reached final fracture with turning around the convex part higher than the expected shear plane. This suggests that AE events detected in inhomogeneous rock masses usually encountered in field measurements occur in relatively hard and intact parts of rock masses. This suggestion should be considered when we monitor AE events prior to a rock burst to predict it.

References

1. Tang, C.A., Numerical simulation of progressive rock failure and associated seismicity, Int. J. Rock Mech. Min. Sci., 1997, 34(2). 249-261.
2. Chen, Z.H., Tang, C.A. and Huang, R.Q., A double rock sample model for rockbursts, Int. J. Rock Mech. Min. Sci., 1997, 34(6). 991-1000.
3. Mogi, K. Study of elastic shocks caused by the fracture of heterogeneous materials and its relations to earthquake phenomena, Bulletin of the Earthquake Research Institute, 1962, 40. 126-173.
4. Sellers, S. and Napier, J. A comparative investigation of micro-flaw models for the simulation of brittle fracture in rock, Computational Mechanics, 1997, 20. 164-169.
5. Rinne, M., Shen, B., Stephansson, O. and Röshoff. K. BEMF modelling of fracture propagation around a canister hole for spent nuclear fuel. Proc. of EUROCK, 2000. 369-374.
6. Cundall, P.A. and Strack, O.D.L. A discrete numerical model for granular assemblies，Geotechnique, 1979, 29(1). 47-65.
7. Potyondy, D.O. and Cundall, P.A. A bonded- particle model for rock, Int. J. Rock Mech. Min. Sci., 2004, 41. 1329-1364.
8. Shimizu, H.， Murata, S. and Ishida, T. Distinct element analysis for rock fracturing under uniaxial compression, Proc. of EIT-JSCE Joint Seminar on Rock Engineering, Bangkok, Thailand, 2007. 267-273.
9. Milev A.M. and Spottiswoode S.M. Effect of the rock properties on mining-induced seismicity around the Ventersdorp Contact Reef, Witwatersrand basin, South Africa, Pure and Applied Geophysics, 2002, 159, 165-177.
10. Ishida, T., Kanagawa, T., Uchita, Y. and Urayama, M. Fault-plane solutions of microseismicity induced by progressive excavations of a large underground chamber, Proc. of 3rd Int. Symp. on Rockburst and Seismicity in Mines, Kingston, 1993. 195-198.
11. Ishida, T., Kanagawa, T., Tsuchiyama, S and Momose, Y. High frequency AE monitoring with excavation of a large chamber, Proc. of 5th Conference on Acoustic Emission/Microseismic Activity in Geologic Structures and Materials, The Pennsylvania State University at June 1991), 1995. 479-490.
12. Ishida, T., Kanagawa, T., Uchita, Y. and Urayama, M. Acoustic emission mechanism and rock mass behavior as deduced from in situ measurements during progressive excavation of an underground powerhouse, Proc. of 8th International Congress on Rock Mechanics, Tokyo, 1995. 593-596.
13. Ishida, T., Nishikawa, T., Tanaka, M. and Shiotani, T. Acoustic emission monitoring for an unstable rock mass left after slope failure, Proc. of 5th Int. Symp. on Rockburst and Seismicity in Mines, Magaliesberg, South Africa, 2001. 29-33.
14. Ishida, T., Nishikawa, T. and Kitamura, H. Laser displacement monitoring for an unstable rock mass left on a failed slope, Proc. of EUROCK 2002, Madera Island, Portugal, 2002. 121-128
15. Tanaka, M., Kuwabara,K., Honma,M., Ishida,T., Kanagawa, T. and Mizuta,Y. Determination of crack direction in hydraulic fracturing by borehole acoustic emission sonde, Proc. of 4th Int. Symp. on Rockburst and Seismicity in Mines, Krakow, 1997. 409-413.
16. Nakayama, Y., Tanaka, M., Nishimura, H., Ueda, M. Ishida, T. and Mizuta T. Borehole AE monitoring during in-situ hydraulic fracturing stress measurements, Proc. of 4th North American Rock Mechanics Symp., Seattle, 2000. 1113-1119.
17. Ishida, T. Acoustic emission monitoring of hydraulic fracturing in laboratory and field, Construction and Building Materials, 2001, 15. 283-295.
18. Ishida, T., Chen, Q., Mizuta, Y. and Roegiers, J-C. Influence of fluid viscosity on the hydraulic fracturing mechanism, Transactions of the ASME, Journal of Energy Resource Technology, 2004, 126. 190-200.
19. Ishida, T., Kitano, K., Kinoshita, N. and Wakabayashi, N. Acoustic emission monitoring during in-situ heater test of granite, Journal of Acoustic Emission, 1991/92, 10(1-2). 42-48.
20. Lay, T. and Kanamori, H. An asperity model of large earthquake sequences, In Earthquake Prediction and International Review, ed. by Simpson D. and Richard P., Maurice Ewing Series, 4, AGU, Washington, D. C., 1981. 579-592.
21. Lay T., Kanamori, H. and Ruff L. The asperity model and the nature of large subduction zone earthquakes, Earthquake Pred. Res.; 1982, 1. 3-71.

22. Young, R.P. and Thompson B.D. Imaging dynamic fracture with acoustic emission and x-ray tomography, Proc. of 11th Cong. for ISRM, Specialized Session 04--Application of Geophysics to Rock Engineering (CD Rom), Lisbon, Portugal, 2007.
23. Ishida, T. and Kanagawa, T. Acoustic emission monitoring during in-situ direct shear test of rock, Proc. of 19th Int. Acoustic Emission Symp., Kyoto, Japan, 2008. 399-406.
24. Ishida, T., Kanagawa, T. and Kanaori, Y. Source distribution of acoustic emission during an *in-situ* direct shear test: Implication for an analog model of inhomogeneous rock-mass fracturing, Engineering Geology (will be submitted)
25. Ashby, M.F. and Sammis, C.G. The damage mechanics of brittle solids in compression, Pure and Applied Geophysics, 1990, 133(3). 489–521.
26. Krantz, R.L. Crack growth and development during creep of Barre granite, Int. J. Rock Mech. Min. Sci., 1979, 16. 23-35.
27. Lei, X.L., Nishizawa, O., Kusunose, K. and Satoh, T. Fractal structure of the hypocenter distributions and focal mechanism solutions of acoustic emission in two granites of different grain sizes, J. Phys, Earth, 1992, 40. 617-634.
28. Third Subcommittee in Committee on Rock Mechanics, Japan Society of Civil Engineers: Proc. of the Japan Society of Civil Engineers, 1978, 11. 37-46. (in Japanese)
29. International Society for Rock Mechanics Commission on Standardization of Laboratory and Field Tests: Suggested methods for determining shear strength in Rock Characterization Testing & Monitoring (ISRM Suggested Methods), edited by E. T. Brown, Pergamon Press, Oxford, England, 1981. 129-140.
30. Hirama, K., Maruyama, M. and Kuwabara, T.: Report of the Technical Research Institute Ohbayashi Corporation, 1983, 27. 102-106. (in Japanese).

RaSiM 7(2009): Controlling Seismic Hazard and
Sustainable Development of Deep Mines,
C.A. Tang(ed), Rinton Press, 17-32

MULTIPHYSICS OF COAL-GAS INTERACTIONS

JI-SHAN LIU, ZHONG-WEI CHEN, YU WU

School of Mechanical Engineering, The University of Western Australia, WA, 6009, Australia
Jishan@cyllene.uwa.edu.au

DEREK ELSWORTH

Department of Energy and Mineral Engineering, The Pennsylvania State University, 110 Hosler Building,
University Park, PA 16802-5000, USA

The advance of our understanding on coal-gas interactions has changed the way how we treat coalbed methane: from a mining hazard to an unconventional gas resource to a concurrent by-product of CO2 sequestration. When solid coal is removed from or a liquid (supercritical carbon dioxide) is injected into a coal seam, a chain of reactions is induced: gas sorption and flow, coal deformation, porosity change, permeability modification, and so on. In this lecture, we define this chain of reactions as coupled multiphysics. The term “coupled multiphysics” implies that one physical process affects the initiation and progress of another. The individual processes, in the absence of full consideration of cross couplings, form the basis of very well-known disciplines such as elasticity, hydrology and heat transfer. Therefore, the inclusion of cross couplings is the key to mathematically formulate the coupled multiphysics of coal-gas interactions. Although coal-gas interactions have been comprehensively investigated, all of these prior studies focus on one or more individual processes. They usually assume that these interactions are under conditions of invariant total stress where effective stresses scale inversely with applied pore pressures. Here we started with a new cross coupling relation between coal porosity and four (mechanical, hydrological, chemical and thermal) volumetric strains under variable stress conditions. A cubic relation between porosity and permeability is then introduced to relate coal storage capability (changing porosity) to coal transport property (changing permeability) also under variable stress conditions. These two relations (porosity model and permeability model) have been the key cross couplings that couple the multiphysics of coal-gas interactions. We implemented these two relations into a series of finite element models for the coupled multiphysics of coal-gas interactions from single poroelastic model to dual poroelastic model. These models couple the transport and sorption of a compressible fluid within a deformable medium where the effects of deformation are rigorously accommodated. This relaxes the prior assumption that total stresses remain constant and allows exploration of the full range of mechanical boundary conditions from invariant stress to restrained displacement. We applied these models to investigate the injectivity of CO2 under different in situ conditions, and reported the results in this lecture.

1 Introduction

From the 1970s onwards there has been a growing interest to produce coalbed methane as a fuel and now it grew from a little-known, high-cost operation to a competitive main-stream natural gas resource [3]. At the end of the 1980’s, this industry searched for methods to enhance production. The successes of Enhanced Oil Recovery (EOR) gave the coalbed methane industry the idea that gas injection could also be successfully applied in the unmineable coalbeds to enhance coalbed methane (ECBM) recovery [17]. Two main benefits can be obtained from ECBM with gas injection. One is to increase production rates of methane and to short return on investment; the other is to mitigate increasing concentrations of CO_2 in the atmosphere to release the global warming [20, 26, 47].

Carbon dioxide is known to have a greater affinity to coal than methane. Early laboratory isotherm measurements for pure gases have demonstrated that coal can absorb approximately twice as much CO_2 by volume as methane [59]. Other laboratory experiments showed that the ratio could be even larger at depths greater than about 800 meters, where the gaseous CO_2 changes to supercritical CO_2 [24,34]. Recent research on CO_2 sorption capacity of different ranks of United States coal has shown that this ratio may be as high as 10:1 in some low rank coals [54], which demonstrates that quite large amount of CO_2 can be storage in the unmineable coal seams. Stevens et al. recently estimated the worldwide coalbed CO_2 sequestration capacity to be 225 Gt [57], Kuuskraa et al. estimated the total global capacity could range from 300 to 964 Gt [21,35], which is significant to be compared to current anthropogenic CO_2 emissions of almost 30 Gt per year [26]. The amount of CBM resources can be withdrawn by using this technology is about 2980 to 9260 Tcf (84.38-262.21 Tm^3) [48].

The sorption process couples both physical and chemical processes [17]. Once coal and gaseous phase are brought together, it is in most instances likely that there will be some interactions between the coal and gas, which accompanies the physisorption and chemisorption activities. All gases below their critical temperature tend to adsorb as a result of general van der Waals interactions with the solid surface [1]; if the adsorption energy is large enough to be comparable to chemical bond energies, the chemisorption will happen which may be accompanied by chemical changes and likely to result in physical changes of the coal, e.g. Yong's modulus and Poisson's ratio [1,17]. It is well known that gases absorption/desorption will induce coal matrix swelling/shrinking. However, one of the technical obstacles faced in this technology is that CO_2 can cause a greater degree of coal matrix swelling or shrinkage compared to methane, which can cause profound changes in porosity and permeability of coalbed methane reservoirs during depletion or when under injection processes [9, 39,45], so differential swelling is caused by an excess strain produced by CO_2 over CH_4, which will partially block the cleat system of coal medium and have consequences in terms of permeability loss, with severe impact on CO_2 injection rate and CH_4 production rate [28,43] which has been proven from the Allison Unit pilot, finding that injection rate reduced from initial of 141×10^3 m^3/day to 85×10^3 m^3/day (by up to 40%) at the early stage of CO_2 injection, and the dramatic reduction in CO_2 injection rate also has been observed in other field trials [36] and confirmed in laboratory experiments [34,42]. This differential swelling/shrinkage also would affect coal matrix deformation, which in turn impacts the replacement of methane and CO_2 sequestration.

Additionally, the temperature is also a key factor controlling gases absorption/desorption and coal seam deformation. High temperature favors gas in the free state rather that the sorbed state. At higher temperatures the Langmuir constant decreases resulting in a lower initial slope of the isotherm [8]. Levy et al. have found for Australian coals a linear decrease in methane adsorption capacity of 0.12 m^3/tonne per 1°-increase in temperature over the temperature range of 20-65°C at 5 the gas pressure of 5 MPa [40]; meanwhile, higher gas injection temperature will swell the coal matrix more, which will negatively deteriorate gas transport and coal matrix deformation, and therefore the implementation of this technology.

The above analysis shows that CO_2-ECBM technology accompanies with multiphysics of coal-gas interactions, involving in the phenomena of geomechanics, fluid flow, geochemistry and thermodynamics. So far, many studies in the experiments, fields, and numerical analysis have been carried out to assess CO_2 storage capacity, understand adsorption/desorption dynamics during injection, characterize coal swelling and permeability, and develop predictive tools for ECBM operations. Andreas Busch [2] conducted an experiment to study the effects of grain sizes on the adsorption and desorption kinetics of CO_2 and CH_4 on a high volatile bituminous Pennsylvanian coal, and found that adsorption rates decreased with increasing grain size for all experimental conditions. Similarly, Basanta Kumar Prusty [6] carried out an experimental study using coal samples from different coal seams to investigate the ability of CO_2-ECBM and the effects of coal types on preferential sorption behaviour. In 2006, a field experiment of CO_2 storage with ECBM recovery was set up and performed in the upper Silesian coal basin in Poland to investigate the technical and economic feasibility of CO_2 storage under European conditions [17]. More recently, another experimental effort has been made to measure the differential swelling effect of CO_2/CH_4 on the macromolecular structure and to theoretically translate that effect in terms of porosity and permeability, where the real time permeability measurements were done to see the true effect of differential strain from CH_4 saturated coal core flooding experiments [49]. The image analysis technology was also used to measure the coal-gas interactions. For example, J. Denis *et al.* [27] contributed three-dimensional strain distribution in confined coal at microstructural level using high resolution X-ray computerized tomography data and image analysis to quantify the interactions of carbon dioxide with unconfined coal induced swelling; one different experiment was carried out to measure the CO_2 sorption-associated swelling and volumetric strains in consolidated coal under constant effective stress based on the dual-porosity theory [10]. The changes internal to the sample were evaluated by maps of density and atomic number determined by dual-energy X-ray computed tomography (X-ray CT) to calculate the macroporosity in the coal sample; scanning electron microscopy (SEM) and photographic images were used to identify the microlithotypes and microstructures.

Based on the experimental data and theoretical analysis, the permeability model, one of the most important transport properties of coal, has been widely developed as well. In 1995, the Seidle-Huitt Model was developed to describe the permeability change, assuming that all permeability changes are caused by the sorption-induced strain only, while elastic strain of coal is not included [52]. Another three of the most widely used permeability models are Palmer and Mansoori model (PM Model), the Shi and Durucan (SD) model, and the Advanced Resources International (ARI) model [44,45,55]. The PM model is a strain-based model, and considers the elastic deformation of coal under constant stress conditions. The SD model uses a stress-based formulation to correlate changes in the effective horizontal stress caused by the volumetric deformation and the cleat or pore compressibility. The ARI model describes the coal permeability using a semi-empirical correlation to account for the changes of coal porosity due to pore compressibility and matrix swelling/shrinkage [23]. However, although the influence of gas sorption-induced coal deformation on porosity and permeability has been widely studied in the above publications, these studies are all under the assumptions of the invariant total stress and homogenous system. In 2007, this assumption was relaxed and a new porosity and permeability model was derived by Zhang et al., which can be used at in-situ stress conditions [25].

Another totally different approach was carried out to investigate the permeability change characteristics related with CO_2 injection by using dual-porosity model. In this model, it is assumed that coal seam is a natural fractured reservoir for gas storage. The micro-pores and pores in coal matrix are the main storage space for gas, while the micro-fractures, fissures, fractures and faults build up the main passages for gas seepage and migration. Barenblatt et al. conducted the first theoretical study of the dual-porosity system in 1960 [5]. Jim Douglas et al. developed a dual-porosity model for saturated, two-phase, incompressible, immiscible flow in a naturally fractured petroleum reservoir and then approximated by a finite difference procedure [30]. Bai et al. extended the traditional dual-porosity concept to the behaviour of generalized multiporous media with emphasis on reservoir characteristics [41]. In 2007, the match-stick model, which describes the macroporous fracture network, was chosen to determine the fracture permeability and porosity by the average fracture spacing and the fracture aperture width [50]. Recently, G.X. Wang et al. [23] used an alternative approach to integrate the textural and mechanical properties to describe the anisotropy of gas permeability for CO_2- ECBM recovery and CO_2 geological sequestration in coal. This model accounts for the stress dependent deformation using a stress–strain correlation, which was developed by combining mechanical strain with sorption-induced strain for any given direction.

The numerical work regarding to coal-gas interactions of CO_2-ECBM has been significantly improved with the development of permeability models. Pan et al. [62] presented a simulation work using three different sorption models, named Extended Langmuir model (ELM), the Ideal Adsorbed Solution (IAS) model and the Two-Dimensional Equation of State (2D EOS) model to investigate the accuracy of the gas adsorption model comparing with the experimental adsorption data; John W. Larsen and F. Y. Wang [18,32] investigated the weakening and plasticization phenomena of coal mechanical properties, e.g. its softening temperature and its

Young's elastic modulus, possibly over the long time horizon of CO_2 storage due to coal uptake. The influence of gravity on CO_2 sequestration was investigated by Josh-Qiang Xu [31]. With a focus on the influence of the injection gas components was specifically studied by Durucan and Shi [53], concluding that the presence of the nitrogen component is capable of improving the efficiency of enhanced methane recovery significantly over pure CO_2 injection. Fokker [43] carried out a parametric study on the sensitivity of parameters on injectivity, and concluded that the permeability, the fracture conductivity and the cleat system porosity are the most sensitive parameters influencing the CO_2 injectivity.

Meanwhile, lots of studies based on dual-porosity models were conducted as well. Takeshi developed a numerical model to model ECBM recovery process by flue gas injection with assumption of a dual porosity system [58]; In 2005, a dual-porosity coalbed-methane simulator was used to model primary and secondary production of methane from coal for a variety of coal properties and operational parameters. The effects of the anisotropy of the permeability, the spacing between cleats, and the sorption isotherms for methane and CO_2 were investigated to optimize project design and operation [12]; meanwhile Grant S. Bromhal et al. carried out a simulation model to predict the maximum amount of carbon dioxide that could be sequestered in a coal seam and show how coal seam characteristics and injection practices will reduce the actual amount sequestered and conclude that as the Langmuir volume increases and the Langmuir pressure decreases, the amount of carbon dioxide sequestered (and methane produced) goes up [19]. Recently, a fully coupled dual-porosity model for anisotropic rock formations was developed to extend Biot's isothermal, linear poroelastic, isotropic dual-porosity model to an anisotropic dual-porosity system describing naturally fractured reservoirs [61]. In 2007, X.R. Wei [60] presented an alternative model of multicomponent gas diffusion and flow in bulk coals, focusing on CH_4-CO_2 counter-diffusion associated with CO_2-ECBM recovery, which was developed based on the bidisperse diffusion mechanism and the Maxwell–Stefan (MS) diffusion theory. More recently, Ebrahim Fathi [13] further investigated the effects of counter-diffusion and competitive adsorption on CO_2 injection and coalbed methane production, and one-dimensional theoretical framework suitable for a fundamental level investigation of binary gas storage and transport in coal seams considering a serial multi-continuum porous medium with triple porosity and dual permeability, focusing on the mass exchange and the interaction of micropores, marcopores and fractures. However, the geomechanical deformation was not taken into consideration in the above models.

Based on the assumption of homogeneous system, Zhang et al. [25] address a fully coupled gas deformation, gas transport and gas absorption/desorption FE model, but it's only suitable to single gas system. Connell et al. [37] has considered the role of coupled flow and geomechanical processes in the simulation of CO_2 enhanced coalbed methane recovery because of the sensitivity of coal permeability to the effective stress and the strain associated with gas sorption strain, but the influence of CH_4-CO_2 counter-diffusion phenomena was not taken into consideration in this study, which could play an important role for CO_2 replaces CH_4. Another several researches on dual-porosity coupled gas flow and coal deformation were discussed [11,41], but all the stress condition they used in their model is invariable.

Based on the literature review as presented above, it is concluded that although the influence of gas sorption-induced coal deformation on porosity and permeability has been widely studied, these studies are all under the conditions of invariant total stress. According to the principle of effective stress, the induced coal deformation is determined by the change in effective stress, which can be replaced by the change in pore pressure, under the assumption of null change in total stress. This is why terms representing effective stress or total stress are absent in all of these existing permeability models. This study seeks to incorporate the coal geomechanical deformation, gas transport, gas absorption/desorption and temperature in describing the multiphysics of coal-gas interactions involved in CO_2-ECBM technology based on our general permeability model [25], and the following main tasks will be discussed in details.

(1) Based on single gas flow system, the coal-gas interactions will be defined as a function of gas pressure,

mechanical deformation, temperature and chemical concentration, and the fully coupled multiphysical processes will be presented to quantify the net change in permeability, the gas flow, and the resultant deformation in a coal seam.

(2) A general porosity and permeability model will be modified to represent the interactions between binary gas transport and coal deformation, and implemented into a fully coupled coal deformation, CO_2 and CH_4 transport, and gas absorption/desorption under variable stress conditions. This model will be applied to quantify the mechanical responses of coal seam to the CO_2 injection under in situ stress conditions.

(3) In this work, a single porosity and permeability model was modified to represent both the primary medium and the secondary medium, and implemented into a fully coupled model incorporating coal deformation, CO_2 transport and gas sorption in the matrix system, and CO_2 flow in the fracture system. The novel dual-poroelastic model was applied to quantify the mechanical responses of coal seams to CO_2 injection under in situ stress conditions.

2 Multiphysics of Coal-Gas Interactions

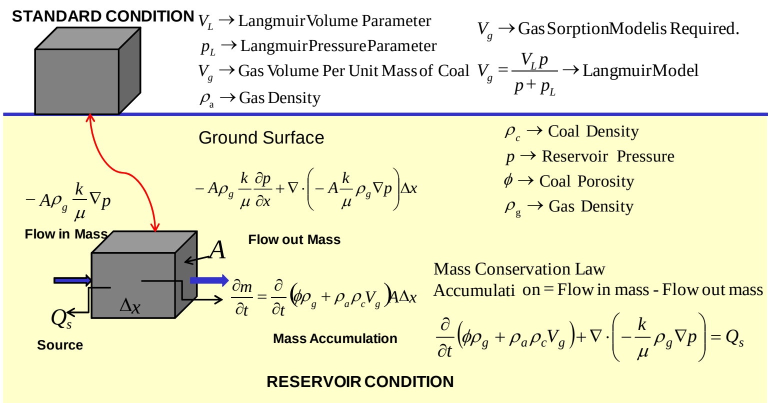

Figure 1. Application of mass conservation law to the derivation of gas flow in coal.

As illustrated in Figure 1, the gas flow equation is defined as

$$\frac{\partial}{\partial t}\left(\phi\rho_g + \rho_a\rho_c V_g\right) + \nabla \cdot \left(-\frac{k}{\mu}\rho_g \nabla p\right) = Q_s \tag{1}$$

In order to solve Eq. (1), most previous studies simplified the Eq. (1) into the following form:

$$S_g(p)\frac{\partial p}{\partial t} + \nabla \cdot \left(-\frac{k(p)}{\mu}\nabla p\right) = Q_s \tag{2}$$

Where $S_g(p)$ and $k(p)$ are defined as a function of gas pressure only. The gas flow was defined as a single-physics system by this approach. In our study, we define both S_g and k terms as a function of gas pressure, temperature, mechanical deformation and chemical concentration

$$S_g = S_g\left(p, T, \varepsilon_v, \varepsilon_s\right),\ k = k\left(p, T, \varepsilon_v, \varepsilon_s\right) \tag{3}$$

Substituting Eq. (3) into (2) yields

$$S_g\left(p,T,\varepsilon_v,\varepsilon_s\right)\frac{\partial p}{\partial t}+\nabla\cdot\left(-\frac{k\left(p,T,\varepsilon_v,\varepsilon_s\right)}{\mu}\nabla p\right)=Q_s \tag{4}$$

Eq. (4) must be solved simultaneously with other field equations such as mechanical deformation equation, energy conservation equation, and chemical transport equation. The multiphysics of coal-gas interactions were specifically illustrated in Fig. 2.

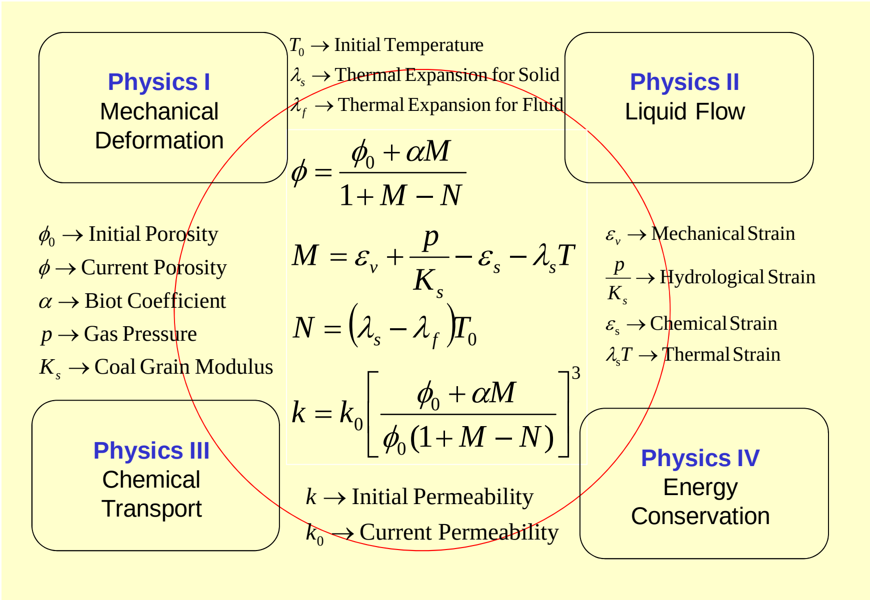

Figure 2. Multiphysics of Coal-Gas Interactions. Four physics are linked through a porosity and permeability model defined as a function of mechanical, chemical, thermal and hydrological volumetric strains.

As defined by Zhang et al., the general porosity model is as follows:

$$\phi=\frac{1}{1+M-N}\left[\left(1+M_0-N_0\right)\phi_0+\alpha\left(M-M_0\right)\right] \tag{5}$$

where $S_0=\varepsilon_{v0}+\left(p_0/K_s\right)-\varepsilon_L p_0/\left(p_0+P_L\right)-\lambda_s T$, $S_0=\varepsilon_{v0}+\left(p_0/K_s\right)-\varepsilon_L p_0/\left(p_0+P_L\right)-\lambda_s T_0$,

$N=\left(\lambda_s-\lambda_f\right)T$, $N_0=\left(\lambda_s-\lambda_f\right)T_0$.

Considering the cubic law relation between permeability and porosity of the porous media, we obtain

$$\frac{k}{k_0}=\left(\frac{\phi}{\phi_0}\right)^3=\left(\frac{1}{1+S}[(1+S_0)+\frac{\alpha}{\phi_0}(S-S_0)]\right)^3 \tag{6}$$

where k_0 is the initial permeability at the initial pressure p_0, porosity ϕ_0 and temperature T_0.

Equations (5) and (6) present a new porosity model and a new permeability model, respectively. Both models can be applied to variable stress conditions. If we consider $S<<1$, $S_0<<1$ and ignore the temperature influence on porosity change. The simplified expression for porosity is derived as

$$\phi=\phi_0\left\{1+\frac{\alpha}{\phi_0}\left[\varepsilon_v+\frac{p-p_0}{K_s}+\frac{\varepsilon_L P_L(p_0-p)}{(p_0+P_L)(p+P_L)}\right]\right\} \tag{7}$$

Eq. (7) clearly shows that the porosity of the coal is controlled by the matrix volumetric strain associated with effective stress, the grain volumetric strain and the gas desorption induced volumetric strain.

If $S << 1$, $S_0 << 1$, $K_s >> K$ and ignore the temperature influence on porosity change, the coal seam is under conditions of uniaxial strain, and the overburden load is unchanged, a simplified expression of porosity can be derived from Equation (5) as

$$\phi = \phi_0 + \frac{(1+\nu)(1-2\nu)}{E(1-\nu)}(p - p_0) - \frac{2(1-2\nu)}{3(1-\nu)}\left(\frac{\varepsilon_L p}{p+P_L} - \frac{\varepsilon_L p_0}{p_0+P_L}\right) \tag{8}$$

Which is the same as the model presented by Palmer and Mansoori (Palmer and Mansoori, 1998). Using the stress-strain relation and assuming ε_{33} is the direction of uniaxial strain and overburden load, the Palmer-Mansoori model can also be expressed as

$$\phi = \phi_0\left\{1 + \frac{1}{\phi_0}\left[\varepsilon_{33} + \frac{\varepsilon_L P_L (p_0 - p)}{(p_0+P_L)(p+P_L)}\right]\right\} \tag{9}$$

Comparing Equation (9) with Equation (7), the Palmer-Mansoori model is only applicable to conditions of uniaxial strain, constant overburden load, and infinite bulk modulus of the grains.

In the following section, one simulation example was presented to compare our model with PM one to verify the better suitability of our model. In this example, the methane desorption from a coal sample under the uniaxial strain state was simulated. The model geometry is shown in Figure 3(a). The right side is free while other three sides are constrained; the pressure on the right side is specified as 1 atmospheric pressure; zero fluxes on the other three sides are specified; the initial gas pore pressure in the coal is 6.2 MPa. The modelling results were presented in terms of the effect of coal bulk modulus ratios on the permeability and the comparison with the PM model, as shown in Fig. 3(b).

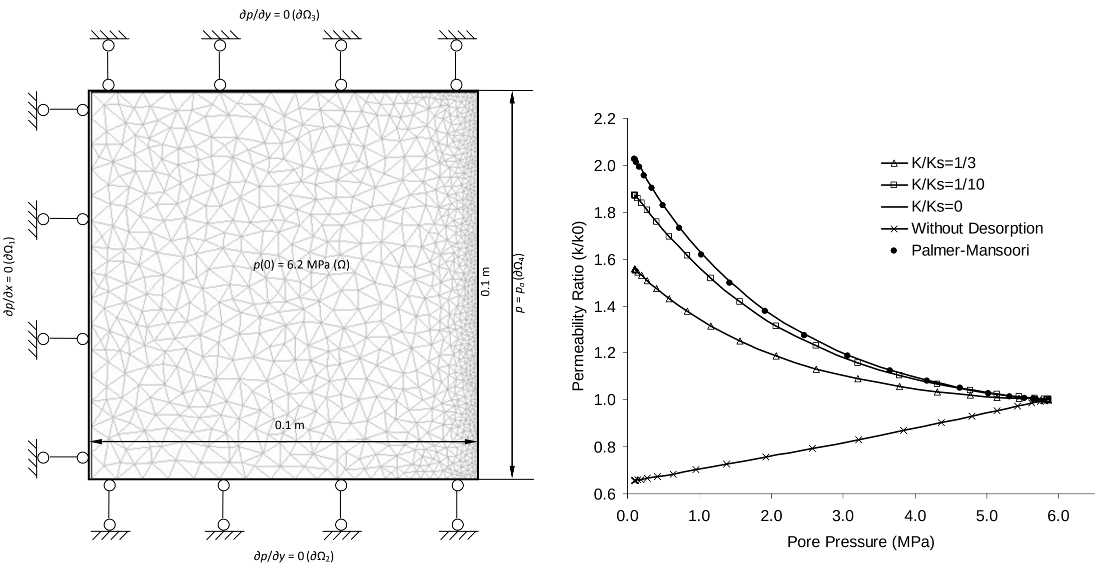

(a) (b)

Figure 3. (a) Simulation model of the gas desorption from a coal sample under the uniaxial plane strain state; (b) impacts of different bulk modulus ratio (K/Ks) and gas desorption on permeability ratio (k/k0).

Fig. 3(b) shows that the permeability ratio (k/k_0) increases due to gas desorption when pore pressure decreases. When the ratio of bulk modulus (K/Ks) changes from 1/3 to 0, the highest permeability ratio varies from 1.58 to 2.05. When the bulk modulus of coal grains (Ks) is assumed to be infinite, the simulation result is identical with the data calculated by the Palmer-Mansoori model.

3 Binary Gas Flow

In the following sections, we present the results of mechanical responses of coal to CO_2 injection to enhance coalbed methane recovery. Two simulations were presented to illustrate the resultant effects of the coupled gas transport, gas sorption and coal deformation. The first simulation was built to verify the coupled binary gas flow and coal deformation model through comparing the simulation results with the experimental data [56]. The second simulation was built to predict the mechanical response of coal seam to the CO_2 injection-induced binary gas transport.

3.1 Comparison with Experimental Data

The experimental sample is 334mm long and 69.50mm in diameter. The mean pore pressure was 4.3MPa. CO_2 was injected from the left side and flowed out from the right side. The injection rate is 6.0ml/h. Because the experimental model is axial symmetry, it can be simplified into a 2D plane strain model along the axial direction, as shown in Figure 4. Appropriate boundary conditions were applied to coupled coal deformation and gas transport problem. For the coal deformation model, the left side and bottom boundaries are constrained in horizontal direction and vertical direction, respectively; the overburden stress at the upper side is 7.91MPa, the right side was unconstrained. The coal property parameters were chosen from the experimental results, as listed in Table 1 [28,29,46,56]. For the binary gas transport models, the coal is initially saturated with CH_4 and the initial pressure is 4.3MPa and the injection rate is kept constant. The comparison between modelling results and experimental data is shown in Figure 5.

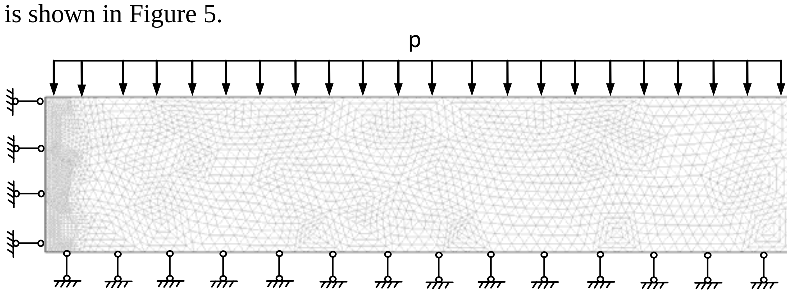

Figure 4 Schematic of the simulation model built based on the experiment conditions [56].

Table 1. Modeling Parameters for the Numerical Simulation

Parameters	Values	Parameters	Values
Young's modulus of coal (E , MPa)	2713	CO_2 Langmuir volumetric strain constant ($\varepsilon_{\infty 2}$)	0.0237
Young's modulus of coal grains (E_S , MPa)	8139	CH_4 Langmuir pressure constant (MPa)	2.07
Possion's ratio of coal (ν)	0.339	CO_2 Langmuir pressure constant (MPa)	1.38
Gas dynamic viscosity (μ , Pa·s)	1.84×10^{-5}	Initial porosity of coal (ϕ_0)	0.0423
CH_4 Langmuir volume constant ($V_{\infty 1}$, m^3/kg)	0.0256	Initial permeability of coal (k_0 , m^2)	3.0×10^{-17}
CO_2 Langmuir volume constant ($V_{\infty 2}$, m^3/kg)	0.0477	CH_4 Diffusion Coefficient (m^2/s)	3.6×10^{-12}
CH_4 Langmuir volumetric strain constant ($\varepsilon_{\infty 1}$)	0.0128	CO_2 Diffusion Coefficient (m^2/s)	5.8×10^{-12}

Fig. 5(a) shows that the simulation results match the experimental curve reasonably well, and the strain change characteristics is very close to the trendline of experimental data if we use polynomial to fit it. The largest error happens at the initial stage, but after two days the trend is very matchable with a mean error of 3.21%.

Sweep efficiency and displaced volume used in this paper are defined as follows:

$$\text{Sweep efficiency} = \frac{\text{moles of } CH_4 \text{ produced} \times 100\%}{\text{moles of } CH_4 \text{ initially in place}}, \quad \text{Displaced volume} = \frac{\text{moles of } CO_2 \text{ injected}}{\text{moles of } CH_4 \text{ initially in place}}$$

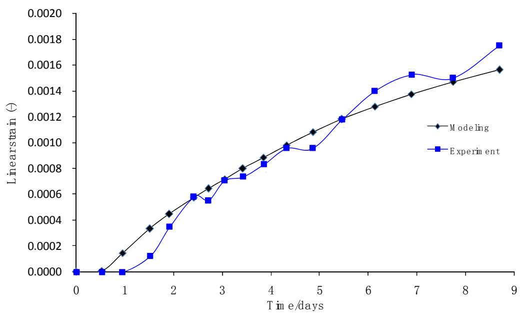

(a)

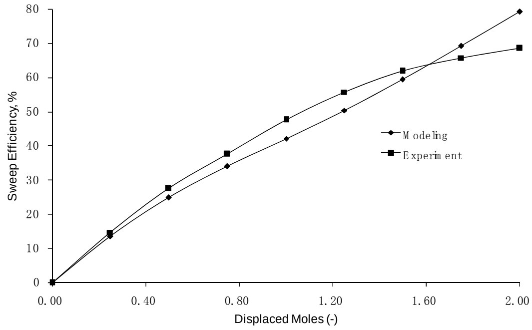

(b)

Figure 5 Comparison between modeling results and experimental data. (a) Differential swelling and coal deformation induced linear strain vs. time; (b) Sweep efficiency against displaced moles

Fig. 5(b) illustrates that the simulation results match experimental data reasonably well, even though the change trend for the modelling curve is more linear than the testing result. The largest error happens when the displaced volume is equal to two, with the error of 15.57%; the mean error value for the whole curve is 3.97%.

The successful match between modelled results and experimental data has demonstrated the validity of the FE model. In the following section, the model was used to predict the performance of CO_2-ECBM technology implementation in field scale.

3.2 Field Scale Response

In this simulation, a field scale model of one central injection well with four surrounding production wells was built to simulation the performance of CO_2-ECBM under in-situ conditions. Input parameters for this simulation are identical with the parameters used in section 3.1. The model geometry is 100m by 100m, as shown in Figure 6. For the coal deformation model, all four sides are confined in the normal direction the production and injection wells are unconfined. For the binary gas transport models, the coal is initially saturated with CH_4 and the initial pressure is 4.3MPa. The Neumann boundary conditions are specified at the four production wells, while the boundary condition of injection well is specified according to the simulation strategies (see Table 2). The following model results are presented under each condition in terms of the evolution of the permeability ratio and CO_2 injection rate, as shown in Figures (7) and (8).

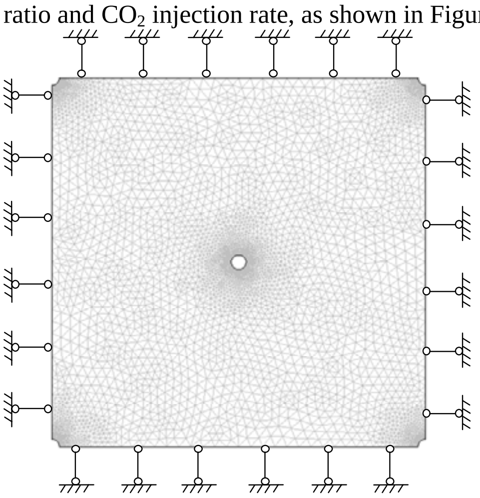

Table 2 Simulation strategies

Case 1	Investigation the impact of coal rank on the resulting response
	$E = 2.71MPa; 4.07MPa; 5.42MPa$
Case 2	Investigation the impact of initial permeability on the resulting response
	$k_0 = 3\times10^{-16}m^2; 3\times10^{-17}m^2; 3\times10^{-18}m^2$
Case 3	Investigation the impact of gas Langmuir strain constants on the resulting response
	$\varepsilon_{\infty 2} = 0.0119; 0.0237; 0.0474$

Fig. 6– The field scale model of one central CO_2 injection well with four surrounding production wells.

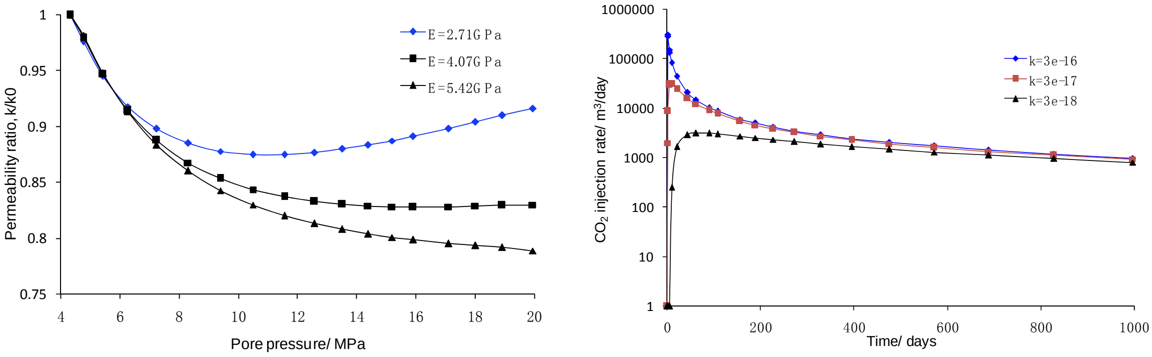

(a) (b)

Fig.7 – Simulation results (a) Sensitivity of permeability ratio to changes in coal Young's modulus vs. pore pressure; (b) Sensitivity of CO2 injection rate to changes in coal initial permeability vs. time.

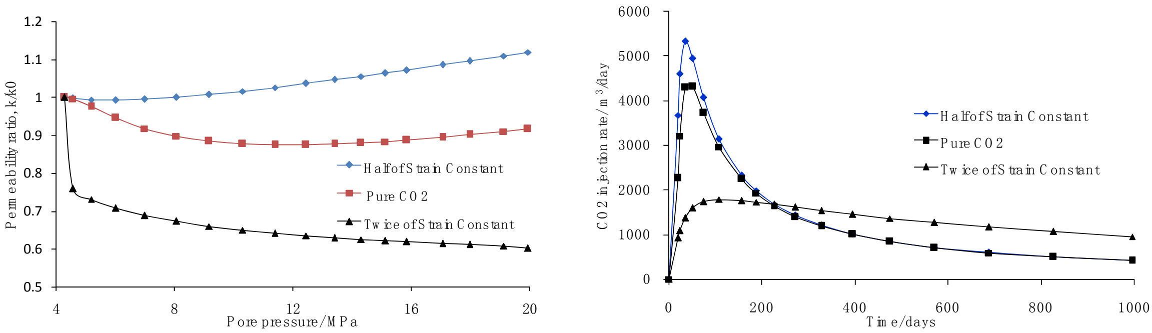

(a) (b)

Fig.8 – Sensitivity of the model to injection gas Langmuir strain constants.
(a) Sensitivity of permeability ratio to changes in injection gas Langmuir strain constants vs. pore pressure;
(b) Sensitivity of CO2 injection rate to changes in injection gas Langmuir strain constants vs. time

Figure 7(a) shows that increase to coal Young's modulus results in lower permeabilities as pore pressure increases. When E=2.71GPa, initially, the permeability decrease with gas injection until permeability ratio reducing to 0.87 (pore pressure is about 11MPa), followed by the permeability rebound with CO_2 injection. The simulation result demonstrates that the gas sorption-induced permeability change is dominant over the effective stress change induced in the initial stages; as injection proceeds, gas pressure increases progressively further into the medium, effective stresses concomitantly reduce and mechanical influences on the matrix dilation dominate. However, the permeability change trends for E=4.07GPa and 5.42GPa cases are different from the first one. The permeability decreases with the CO_2 injection for the whole injection process, which illustrates that the sorption-induced permeability change plays more significant role than mechanical influences. The reason is the higher coal Young's modulus is harder to deform, causing less porosity change. According to the cubic relation between porosity and permeability, it easily can be seen that less porosity change accompanies with smaller permeability change, which demonstrates that CO_2-ECBM technology can be carried out more easily in lower rank coal reservoir.

Figure 7(b) shows initial permeability has dramatic effects on CO_2 injection performance. The peak value of CO2 injection rate for $k=3\times10^{-16}m^2$ case is as high as 2×10^6 m^3/d, while the peak values for another two cases are only 3.1×10^4 and 3000 m^3/d respectively. Because when the initial permeability is larger, the convective velocity is higher, causing faster replacement. This finding still has an important indication for the implementation of this technology in shale and other low permeability mediums.

In case 3, half Strain Constant model is to imitate the binary gases injection of N_2 and CO_2, which has been tested that it could increase CO_2 injectivity dramatically [13]; twice Strain Constant model is to imitate the CO_2 affinity to other coals where have much larger Langmuir strain constants. Robertson and Christiansen [15] have shown that there is a large difference of sorption-induced strains of different coals ranks, which has also been proved by many experiments [29,56].

Simulation results show that the numerical model is very sensitive to changes in the injection gas Langmuir strain constants as shown in Fig. 8. In the first model, it demonstrates that the influence of effective stress change on permeability is dominant, while the impact of the sorption-induced permeability change is subordinative; the second model shows that gas sorption-induced permeability change is dominant over the effective stress change induced in the initial stages; as injection proceeds, mechanical influences take over the dominative role. However, the third model shows that the gas sorption-induced permeability change is always playing a major role during CO_2 injection process, all of which can be seen from Fig. 8 (a). Figure 8(b) shows that CO_2 injection rates are significantly affected by the Langmuir gas strain constants. The peak CO_2 injection rate is about 5500m^3/d for the first model, while the value decreased to 4300m^3/d with the constant increases, and the value even dramatically dropped to less than 2000m^3/d for the third model. From the above analysis we can seen that there is a strong dependence of permeability change on the changes of sorption-induced strain, strong gas sorption-induced strain capacity will negatively influence CO_2 injection rate and the replacement of CH_4, so reducing the strain capacity could be a useful way to improve CO_2 injection.

4 Dual Poroelasticity

In order to investigate the dual poroelastic response of coal seam to CO_2 injection, a simulation model was constructed. According to the geometry symmetry of the simulation model, a quarter of model was chosen to be analysed with 50m in length and 50m in width. The injection well with a diameter of 1m is located at the left-bottom corner of the model, as shown in Fig.9. Appropriate boundary conditions must be applied to coupled coal deformation and gas transport problems. For the coal deformation model, the left side and base are both rolled. In situ stresses are applied to the top and the right sides. The ratio of the horizontal in situ stresses (along page to across page) is kept as 1.5. For gas flow, a constant pressure of 8MPa is applied to the injection well. No flow conditions are applied to all the other boundaries. An initial pressure of 0.5MPa is applied in the model. A series of injection conditions as listed in Table 3 was simulated to investigate the mechanical responses of coal. Simulation results are presented in terms of (1) the impacts of modulus ratio, (2) the impacts of fracture frequency.

Impacts of Ratios of the Coal Bulk Modulus to the Coal Grain Modulus: Simulation results are shown in Figures (10). According to the analysis upon this issue, there are five contributing mechanisms to the storativity: free gas compression, gas absorption, coal grain deformation, coal shrinking or swelling, and coal bulk (skeletal) deformation. The contribution of each mechanism to the complete gas storativity is shown in Fig.10. As the matrix pore pressure increases, the volume of gas released (or sequestered) from the adsorbed-phase gas contributes about 87.6-93.9% to the total gas storativity. The volume of gas released from the free-phase gas contributes 6.1-12.2% to the total gas storativity, and that from bulk deformation contributes 0.38-3.44% to the total gas storativity. The contributions from the other mechanisms are less than 3.5% in total. These results indicate that gas sorption is the primary mechanism for gas production or sequestration.

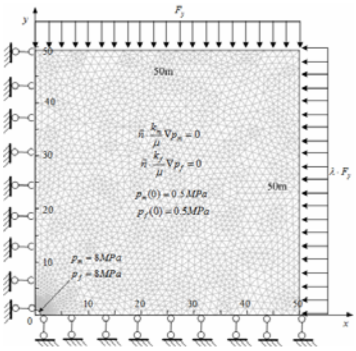

Fig.9. Quarter simulation model of CO_2 injection to a coal seam.

Table 3 Investigation of matrix pressure responses to CO_2 injection under different conditions

Case 1	Impacts of the ratio of coal bulk modulus to gain modulus on pressure responses to CO_2 injection
	$K/K_S = 1/2, \varepsilon_S \neq 0$; $K/K_S = 1/3, \varepsilon_S \neq 0$ $K/K_S = 1/10, \varepsilon_S \neq 0$; $K/K_S = 1/3, \varepsilon_S = 0$
Case 2	Impacts of fracture spacing on pressure responses to CO_2 injection
	$a = 0.25, \varepsilon_S \neq 0$; $a = 0.25, \varepsilon_S = 0$ $a = 0.5, \varepsilon_S \neq 0$; $a = 0.5, \varepsilon_S = 0$

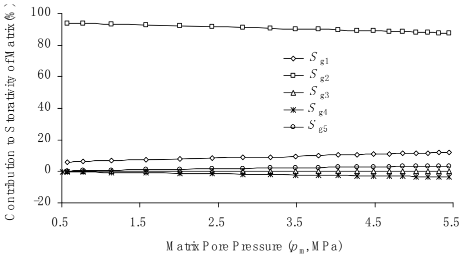

(a) (b)

Fig.10. Investigation the impact of skeletal and grain modulii on the resulting response. (a) contributions of each mechanism to gas storativity in the matrix: S_{g1} is the volume of gas released (or sequestered) from the free-phase gas; S_{g2} is the volume of gas released from the adsorped-phase gas; S_{g3} is the volume of gas released due to the coal gain deformation; S_{g4} is the volume of gas released due to coal grain swelling; S_{g5} is the volume of gas released (or sequestered) due to coal bulk (skeleton) deformation; (b) the relation between matrix permeability ratio and matrix pore pressure at a specific point of $x = 2$ and $y = 2$, adjacent to the wellbore.

Fig. 10(b) shows that for the simulation of $K/K_s = 1/3$ and $\varepsilon_v = 0$ (without sorption), the permeability ratio increases with an increase in the matrix pore pressure as expected with effective stress dependency. Conversely, for all other simulations, the permeability ratio decreases with an increase in the matrix pore pressure. These results show that the greater the modulus ratio, the faster the CO_2 diffuses into the matrix block, indicating that the Biot coefficient has a significant effect on CO_2 transport.

Impacts of Fracture Spacing: Four similar simulations were conducted and the simulation results are shown in Figures (11).

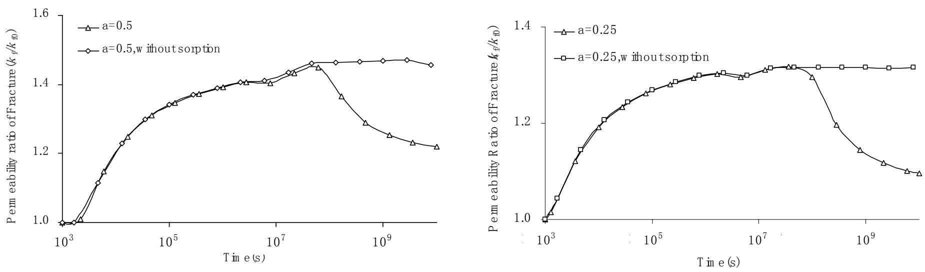

(a) (b)

Fig.11. The evolution of fracture permeability ratio with time at a specific location close to the wellbore ($x = 2$ and $y = 2$) for the cases of $a = 0.5m$ and $a = 0.25m$.

These analyses demonstrate the competitive changes in permeability in the fractures and matrix as the coal matrix swells. As fracture pressures are initially increased, effective stresses are reduced and fracture permeabilities concomitantly increased (Figure 11). Although gas pressures remain elevated, the evolution of sorption in the matrix results in swelling, which ultimately reduces fracture permeability as total stresses in the near wellbore ultimately build, even as fluid pressures remain constant (Figure 11). This process begins around 10^8 s. The key influence of sorption-induced swelling in augmenting total stresses is inferred from Figure 11 where absent swelling, fracture permeabilities are always increased with an increase in pore pressure. This influence of swelling-induced changes in total stresses is a key component of this analysis that cannot be accommodated where mechanical effects are only incorporated approximately for assumed constant total stresses.

5 Conclusions

In our study, we started with a new cross coupling relation between coal porosity and four (mechanical, hydrological, chemical and thermal) volumetric strains under variable stress conditions. A cubic relation between porosity and permeability is then introduced to relate coal storage capability (changing porosity) to coal transport property (changing permeability) also under variable stress conditions. These two relations (porosity model and permeability model) have been the key cross couplings that couple the multiphysics of coal-gas interactions. We implemented these two relations into a series of finite element models for the coupled multiphysics of coal-gas interactions from single poroelastic model to dual poroelastic model. These models couple the transport and sorption of a compressible fluid within a deformable medium where the effects of deformation are rigorously accommodated. This relaxes the prior assumption that total stresses remain constant and allows exploration of the full range of mechanical boundary conditions from invariant stress to restrained displacement. We applied these models to investigate the injectivity of CO_2 under different in situ conditions. Our major findings include:

(1) Our model fully reflects the influences of coal-gas interactions involved in permeability change and can be used in the variable stress conditions; the Palmer-Mansoori model may produce significant errors if loading conditions deviate from the assumptions of the uniaxial strain condition and the infinite coal grain bulk modulus.

(2) Coal rank has an adverse effect on the CO_2 injection performance. Increase of coal rank will exacerbate the dominant role of gas sorption on permeability reduction; the decrease of coal rank will enhance the role playing by the effective stress, so decreasing coal rank could be a useful way to improve CO_2 injection rate and enhance coalbed methane recovery;

(3) Initial permeability has significant impact on the performance of CO_2 replacing methane in unminable coalbed. The increase of coal permeability will accelerate the CH_4 replacement, which still has an important indication for the implementation of this technology in shale and other low permeability medium;

(4) Transport parameters, such as permeability and CO_2 injection rate, are very sensitive to changes in the injection gas Langmuir strain constants. Larger Langmuir strain constant will increase the impact of sorption on parameters changes and have a negative influence on implementation of CO_2 injection and CH_4 replacement, so trying to reduce the strain constant, such as using mixed gases like N_2 and CO_2, is an efficient solution to improve the gas recovery efficiency.

(5) Unlike the flow of slightly compressible fluids where no sorption is included, the gas sorption for this study is the primary mechanism for either gas production or sequestration. In this dual poroelastic model, there are five contributing mechanisms to the storativity, namely: free gas compression, gas absorption, coal grain deformation, coal shrinkage/swelling, and bulk skeletal deformation of the coal. Our simulation results indicate that the volume of gas released (or sequestered) from the adsorbed-phase contributes about 90% to the total gas content.

(6) Unlike dual poroelastic models for the flow of slightly compressible fluids where the coal grain modulus can be assumed large in comparison to the skeletal modulus, the coal grain modulus for this study may have significant impacts on response. Model results indicated that the permeability of the matrix is mainly affected by sorption-induced coal deformation. The grain modulus is an important parameter that affects the evolution of permeability when adsorption is taken into consideration. The greater the ratio of coal bulk modulus to coal grain modulus, the more rapid the reduction in matrix permeability ratio.

Acknowledgements

This work was supported by WA:ERA and by NIOSH under contract 200-2008-25702. This support is gratefully acknowledged.

References

1. Adamson, A.W., Gast, A. P.. Physical Chemistry of Surfaces, 6th edition. Wiley-Interscience Publications, ISBN 0-471-14873-3, 784, 1997.
2. Andreas Busch, Yves Gensterblum, Bernhard M. Krooss, et al.. Methane and carbon dioxide adsorption–diffusion experiments on coal: upscaling and modelling. International Journal of Coal Geology, 60 (2004), 151-168.
3. Ayers WB. Coalbed Methane Systems, Resources, and Production. AAPG Bulletin, 86(11) 1853-1890.
4. Bai M., Elsworth D., Roegiers J.-C.. Multi-porosity/multi-permeability approach to the simulation of naturally fractured reservoirs. Water Resource, Res., 29 (1993), 1621-1633.
5. Barenblatt, G.I, I.P. Zheltov, N.Kochina. Basic concepts in the theory of seepage of homogeneous liquids in fissured rocks. Prikl. Mat. Mekh, 24 (5), 852-864.
6. Basanta Kumar Prusty. Sorption of methane and CO_2 for enhanced coalbed methane recovery and carbon dioxide sequestration. Journal of Natural Gas Chemistry, 17 (2007), 29-38.
7. Brunauer, S.. Sorption of gases and vapors. Princeton University Press, Princeton, NJ, 1943.
8. Bustin, R. M., Clarkson, C. R.. Geological controls on coalbed methane reservoir capacity and gas content. International Journal of Coal Geology, 38(1998), 3–26.
9. Chikatamarla, L., Xiaojun, C.U.I., Bustin, R.M.. Implications of volumetric swelling/shrinkage of coal in sequestration of acid gases. Int. Coalbed Methane Symposium, 2004.
10. C. Özgen Karacan. Swelling-induced volumetric strains internal to a stressed coal associated with CO_2 sorption. International Journal of Coal Geology, 72 (2007) 209–220.
11. D. Elsworth and M. Bai. Flow-deformation response of dual-porosity media, J. Geotech. Engng. ASCE, 118(1992), 107-124.
12. Duane H. Smith, Grant Bromhal, W. Neal Sams, et al. Simulating Carbon Dioxide Sequestration/ECBM Production in Coal Seams: Effects of Permeability Anisotropies and the Diffusion-Time Constant. SPE-84423-PA, 2005.
13. Ebrahim Fathi, I. Yucel Akkutlu. 2008. Counter-Diffusion and Competitive Adsorption Effects during CO_2 Injection and Coalbed Methane Production. Society of Petroleum Engineers, SPE 115482.
14. Ekrem Ozdemir. Modeling of coal bed methane (CBM) production and CO_2 sequestration in coal seams. Coal Geology, 77 (2008) 145-152.
15. E.P. Robertson, R.L. Christiansen. Measurement of sorption-induced strain. Presented at the 2005 International Coalbed Methane Symposium, Tuscaloosa, Alabama. Paper No. 0532.
16. Frank van Bergen, Chris Spiers, Colin Peach. Investigation of CO_2 Interaction with Coal Under High Pressure. 6th European Coal Conference, 2006.
17. Frank van Bergen, Henk Pagnier, Pawel Krzystolik. Field experiment of enhanced coalbed methane-CO_2 in the upper Silesian basin of Poland. Environmental Geosciences, 13 (2006) 201–224.
18. F. Y. Wang, Z. H. Zhu, P. Massarotto, V. Rudolph. Mass Transfer in Coal Seams for CO_2 Sequestration. American Institute of Chemical Engineers, 53 (2007) 1028-1049.
19. Grant S. Bromhal,T, W. Neal Samsb, Sinisha Jikichc, et al. Simulation of CO_2 sequestration in coal beds: The effects of sorption isotherms. Chemical Geology, 217 (2005) 201– 211.

20. Gunter WD, Gentzis T, Rottenfuser BA, Richardson RJH. Deep coalbed methane in Alberta, Canada: a fossil resource with the potential of zero greenhouse gas emissions. Energy Conversion Management. 38(Suppl) (1997) 217-22.
21. Gunter, W. D., S. Wong, D. B. Cheel, G. Sjostrom. Large CO_2 sinks: Their role in the mitigation of greenhouse gases from an international, national (Canadian) and provincial (Alberta) perspective: Applied Energy, 61(1998) 209-227.
22. Guoxiang Liu, Andrei V. Smirnov. Modeling of carbon sequestration in coal-beds: A variable saturated simulation. Energy Conversion and Management, 49 (2007) 2849-2858.
23. G. X. Wang, P. Massarottoa, V. Rudolpha. An improved permeability model of coal for coalbed methane recovery and CO_2 geosequestration. International Journal of Coal Geology, 77 (2009), 127-136.
24. Hall, F.E., Chunhe Zou, Gasem, K.A.M., Robinson, R.L., Yee, D. Adsorption of pure methane, nitrogen, and carbon dioxide and their binary mixtures on wet Fruitland coal. SPE 29194, Eastern Regional Conference and Exhibition, Charleston, WV, 329-344.
25. Hongbin Zhang, Jishan Liu, D. Elsworth. How sorption-induced matrix deformation affects gas flow in coal seams: A new FE model. International Journal of Rock Mechanics and Mining Sciences, 45 (2007), 1226-1236.
26. IPCC. IPCC Special Report on Carbon Dioxide Capture and Storage. Cambridge University Press, Cambridge, New York, NY, USA, 2005.
27. J. Denis N. Pone, Michael Hile, Phillip M. Halleck, Jonathan P. Mathews. Three-dimensional carbon dioxide-induced strain distribution within a confined bituminous coal. International Journal of Coal Geology, 77 (2008), 103-108.
28. Ji-Quan Shi, Sevket Durucan. A numerical simulation study of the Allison unit CO_2-ECBM pilot: the impact of matrix shrinkage and swelling on ECBM production and CO_2 injectivity. Proceedings of 7th International Conference on Greenhouse Gas Control Technologies, 2004.
29. Ji-Quan Shi, Saikat Mazumder, Karl-Heinz Wolf, Sevket Durucan. Competitive Methane Desorption by Supercritical CO_2 Injection in Coal. Trans. Porous Med., 75 (2008) 35-54.
30. Jim Douglas, Jr., Jeffrey L. Hensley, Todd Arbogast. A Dual-porosity model for water flooding in naturally fractured reservoirs. Computer Methods in Applied Mechanics and Engineering, 87 (1991)157-174.
31. Josh-Qiang Xu. Modelling unsteady-state gravity-driven flow in porous media. Journal of Petroleum Science and Engineering, 62 (2008) 80-86.
32. John W. Larsen. The effects of dissolved CO_2 on coal structure and properties. International Journal of Coal Geology, 57 (2003) 63-70.
33. Jun Yi, I. Yücel Akkutlu, C.Özgen Karacan. Gas sorption and transport in coals: A poroelastic medium approach. International Journal of Coal Geology, 77 (2009) 137–144.
34. Krooss BM, Van Bergen F, Gensterblum Y, et al. High-pressure methane and carbon dioxide adsorption on dry and moisture-equilibrated Pennsylvanian coals. International Journal of Coal Geology, 51(2002) 69-92.
35. Kuuskraa, V. A., Boyer, J. N. Coalbed Gas 1—hunt for quality basins goes abroad. Oil and Gas Journal, OGJ Special—Unconventional Gas Development, 5(1992), 49–54
36. Law, D.H.-S. Enhanced Coalbed Methane Recovery & CO_2 Sequestration Projects in Canada and China: Single Well Micro-Pilot Tests, presented at the SPE ATW Enhanced CBM Recovery and CO_2 Sequestration, Denver, 2004, 28-29.
37. L.D. Connell, C. Detournay. Coupled flow and geomechanical processes during enhanced coal seam methane recovery through CO_2 sequestration. International Journal of Coal Geology, 77 (2008) 222-233.
38. L. J. Pekot, S. R. Reeves. Modeling Coal Matrix Shrinkage and Differential Swelling with CO_2 injection for Enhanced Coalbed Methane Recovery and Carbon sequestration Applications. Topical Report, U.S. Department of Energy DE-FC26-00NT40924, 2002.
39. Levine, J. R.. Model study of the influence of matrix shrinkage on absolute permeability of coal bed reservoirs. Coalbed Methane and Coal Geology, Geologic Society Special Publication, 109(1996), 197–212.
40. Levy, J., Day, S.J., Killingley, J.S.. Methane capacity of Bowen Basin coals related to coal properties. Fuel, 74 (1997) 1-7.
41. M. Bai, F. Meng, D. Elsworth, Y. Abousleiman et al. Numerical Modeling of Coupled Flow and Deformation in Fractured Rock Specimens. Int. J. Numer. Anal. Meth. Geomech., 23(1999), 141-160.
42. Mazumder, S. , Wolf, K-H.A.A , Bruining, H.. The Relationship between Coal Macromolecular structure and its Swelling. In: Proceedings International RECOPOL workshop Szcyrk (Poland), March 10-11, 2005.

43. P. A. Fokker, L.G.H van der Meer. The injectivity of coalbed CO_2 injection wells. Energy, 29 (2004.) 1423-1429.
44. Palmer, I., Mansoori, J.. How permeability depends on stress and pore pressure in coalbeds: a new model. SPE-52607.
45. Pekot, L.J., Reeves, S.R.. Modeling the Effects of Matrix Shrinkage and Differential Swelling on Coalbed Methane Recovery and Carbon Sequestration. U.S. Department of Energy. DE-FC26-00NT40924, 2000.
46. Raharjo Roy D., Freeman Benny D., Paul Donald R., Sanders Edgar S. Pure and mixed gas CH_4 and n-C4H10 permeability and diffusivity in poly. Polymer, 48 (2007) 7329-7344.
47. Reichle, D., Houghton, J. Kane, B. et al. Carbon Sequestration: Research and Development. U.S. DOE report, 1999.
48. Rice, D. Coalbed MethanesAn Untapped Energy Resource and an Environmental Concern. U. S. Geological Survey, Energy Resources Surveys Program, January 17, 1997.
49. Saikat Mazumder, Karl Heinz Wolf. Differential swelling and permeability change of coal in response to CO_2 injection for ECBM. International Journal of Coal Geology, 74 (2007), 123-138.
50. Satya Harpalani, Guoliang Chen. Influence of gas production induced volumetric strain on permeability of coal Geotechnical and Geological Engineering, 15 (1997) 303-325.
51. Sawyer, W.K., Paul, G.W., Schraufnagel, R. A.. Development and application of a 3D coalbed simulator. SPE Paper 90-119, 1990.
52. Seidle, J. P., Huitt, L. G.. Experimental measurement of coal matrix shrinkage due to gas desorption and implications for cleat permeability increases, Society of Petroleum Engineers, (1995) 575-582.
53. Sevket Durucan, Ji-Quan Shi. Imporving the CO_2 well injectivity and enhanced coalbed methane production performance in coal seams. Coal Geology, 77 (2008) 214-221.
54. Shi, J.Q. and Durucan S. Modeling of Mixed-Gas Adsorption and Diffusion in Coalbed Reservoirs. Soc. of Pet. Eng. SPE 114197, 2008.
55. Shi, J.Q., Durucan, S.. A model for changes in coalbed permeability during primary and enhanced methane recovery. SPE Reservoir Evaluation & Engineering, 8 (2005) 291–299.
56. S. Mazumder, K. H. A. A. Wolf, P. Van Hemert, Busch. Laboratory Experiments on Environmental Friendly Means to Improve Coalbed Methane Production by Carbon Dioxide/Flue Gas Injection. Transport in porous media, 75 (2007) 63-92.
57. Stevens S.H., Kuuskraa V.A., Spector D., Riemer P. CO_2 Sequestration in Deep Coal Seams: Pilot Results and Worldwide Potential. In Proceedings of the 4th International Conference on Greenhouse Gas Control Technologies, Interlake, Switzerland, August 30-September 2 (1998) 175-180.
58. Takeshi Sekiguchi , Sohei Shimada. Study on Enhanced Coalbed Methane Recovery by Flue Gas Injection. http://prelude.geosys.t.u-tokyo.ac.jp/index-j.html.
59. Wolf, K-H. A. A., Hijman, R., Barzandji, O. H., et al. Laboratory experiments on the environmentally friendly improvement of coalbed methane production by carbon dioxide injection: Tuscaloosa, Alabama, University of Alabama, 1999 International Coalbed Methane Symposium Proceedings, 279-290.
60. X.R. Wei, G.X. Wang, P. Massarotto, S.D. Golding, V. Rudolph. Numerical simulation of multicomponent gas diffusion and flow in coals for CO_2 enhanced coalbed methane recovery. Chemical Engineering Science, 62 (2007), 4193-4203.
61. Ying Zhaoa, Mian Chen. Fully coupled dual-porosity model for anisotropic formations. International Journal of Rock Mechanics & Mining Sciences, 43 (2006) 1128–1133.
62. Zhejun Pan, Luke D. Connell. Comparison of adsorption models in reservoir simulation of enhanced coalbed methane recovery and CO_2 sequestration in coal. International Journal of Greenhouse Gas Control, 3 (2008) 77-89.

RaSiM 7(2009): Controlling Seismic Hazard and
Sustainable Development of Deep Mines,
C.A. Tang(ed), Rinton Press, 33-46

THE ART OF ROCK SUPPORT IN BURST-PRONE GROUND

MING CAI and DENIS CHAMPAIGNE

Mansour Mining Inc.

Sudbury, Ontario, Canada

Rock support in burst-prone ground requires a good understanding of the rock mass behavior under high stress condition and the behavior and functionality of each rock support element. Seven principles, which can lead to making the right judgment and decision with regards to ground support in burst-prone ground, are presented. The success of using MCB conebolt based rockburst support in a few Canadian mines is illustrated along with our recent development to further improve the dynamic performance of MCB conebolt.

1 Introduction

A rockburst is a violent failure of hard brittle rock under high stress. Rockbursts can cause fatalities to workers in a split of a second. For example, on January 7, 1982, a rockburst (M_L = 3.2, Richter or local magnitude) struck the Taozhuang coalmine in Shandong Province in China, resulting in five deaths, six injuries, and permanent loss of mine stopes (500,000 tons of high grade coal). Rockbursts can also cause damage far beyond the source locations and it is one of the major causes of production disruptions in many deep mines around the world.

Mine wide seismic monitoring systems have been widely used in deep mines. A seismic monitoring system constantly monitors for rock noise in the mine. It can locate a seismic event and provide additional information about the event such as magnitude, moment, energy ratio, etc. Monitoring of seismic events in mines is a very useful tool in outlining potentially hazardous ground conditions and assisting mine management in effective re-entry decision. However, a seismic monitoring system cannot predict when and where a rockburst will happen and mine safety can only be guaranteed by proper engineering and effective rock support.

Due to large uncertainties in rock mass properties and boundary conditions (e.g., in-situ stress), all engineering design, calculations, and seismicity monitoring will have to rely on effective rock support as the final line of defense to safe guard workers, equipments, and mine operation. This is not to say that proper mine planning and rock engineering combined with seismic monitoring is not important, but emphasizes that rock support is an important consideration in order to overcome the rock mass property and behavior uncertainties so as to ensure a safe working environment in burst-prone ground. In addition to maintaining a safe working environment, proper rockburst support also ensures profitability for the mine by protecting the investment underground.

Rock support in burst-prone grounds differs from conventional rock support where controlling gravity induced rock falls is the main concern. Rock support in burst-prone grounds needs to address a few things such as dynamic loading and large rock dilation due to rock failure. Over the years, various lessons have been learned and experience gained, often in the bitterest ways. This paper intends to summarize some of those experiences in such a way that the art of rock support in burst-prone ground can be practiced by any engineers by following a few simple principles.

2 Rockburst Damage Mechanism

2.1 Rockburst Research

Extensive rockburst researches have been conducted in South Africa, Canada, Australia, and many other countries. One of the most comprehensive rockburst research studies in Canada from 1990 to 1995 eventually led to the publication of the Canadian Rockburst Support Handbook [6]. Multi-year mine seismicity research has been carried out in Australia and the Mine Seismicity Risk Analysis Program (MS-RAP) has been developed and used by the mining industry. The International Symposium on Rockburst and Seismicity in Mines (RaSim) has been the place for the exchange of ideas and discussion for engineering solutions since 1982. Those collective efforts have greatly improved our understanding of rockburst.

2.2 Rockburst Damage Mechanism

A rockburst is defined as damage to an excavation that occurs in a sudden or violent manner and is associated with a seismic event [5]. Rockbursts can be classified into three types [2]: (a) fault slip burst, (b) pillar burst, and (c) strain burst. When the event induced stresses exceed the capacity of the unsupported or supported rock, even temporarily, failure is initiated or triggered.

Typical rockburst damage to underground excavations include stress induced rock fracturing, bulking of roof and sidewalls, floor heave, shearing of rock, rock falls and ejections, etc. A rockburst can be self-initiated or trigged by a remote seismic event. Violent rock failure can be in any of the three forms – block ejection, seismically induced fall of ground, and rock fracture with dilation (strain burst). Quite often, all three forms of damage can be observed in a large rockburst event.

Severity of rockburst damage can be classified as minor, moderate, and severe [6]. For a typical opening of 5 by 5 m, the minor, moderate and severe damages can be characterized by fractured or loosened rocks of less than 0.25 m, 0.25 to 0.75 m, and more than 0.75 m, respectively. The degree of expected damage will determine the dynamic rock support demand. Under severe damage conditions, the rapid tunnel closure up to 300 mm or more is possible due to rock bulking. When a seismic wave reaches an opening, it can accelerate the blocks of rock and potentially eject the blocks out. The ejected blocks of rock possess kinetic energy; therefore, the applied rock support must be able to absorb or dissipate this kinetic energy. If the damage mechanism is associated with seismically induced rockfalls, it will be necessary to strengthen the support systems such that the factor of safety against failure under static conditions is significantly increased [6].

As stated before, violent rock failure cannot be avoided when mining at depth, hence, dynamic rock support is required to perform underground construction in seismically active mines. The demand on the support includes three aspects – dynamic energy absorption capacity, large displacement accommodation capacity, and load carrying capacity. All three of these are needed in order to ensure safety.

The role of rock support in underground construction can be classified into three major functions – reinforce, retain, and hold [6]. Under dynamic loading condition, the rock support system must be able to absorb energy and survive the rockburst event. There have been many publications on rockburst support (e.g., Hedley [2], Kaiser et al. [6], Ortlepp [8], and many others), but it is often hard for practicing engineers to master the essence of rock support in burst-prone ground. Hence, it is our intention to present the gained knowledge and experience in the form of a few easy-to-grasp guiding principles. These principles were gained through practical experience by many throughout the world and interaction with ground control engineers. We believe that a better understanding of the following seven principles is important to have a better rock support in burst-prone ground.

3 The Art of Rock Support in Burst-prone Ground

3.1 Avoid Rockburst Principle

The supreme excellence in rock support in burst-prone ground is to avoid rockburst conditions and the best rock support in burst-prone ground is no support at all. This may sound paradoxical but is completely true. Why fight if you can avoid it? The best strategy is to stabilize the rock without fighting against the loads and stresses in the rocks using heavy rock support. Ržiha, a famous nineteenth century German tunneling engineer, once commented on tunneling that – "*The true art in tunneling lies in the anticipation of the development of large rock pressure, which is far more effective than to find the means of resisting rock pressures which have already developed*." Strategies to mitigate and control rockburst risk and hazard are shown in Figure 1 and it is important to consider the order of priority when executing those strategies. The first thing to consider, of course, is to avoid rockburst risk and the last thing to do is to accept rockburst risk, which often means we need rockburst resistant rock support under this circumstance.

Methods to avoid rockburst risks include changing of drift location, use of different excavation shapes, changing the stope size and/or shape, altering mining sequencing and potentially switching mining methods. For example, a proper pillar design can eliminate the soft loading condition in a mine, thus prevent pillar bursts from happening. Re-entry management should be considered to avoid personal risk due to rockburst. No personnel should be permitted to work in areas where seismic activity is still high after a major event. Methods to transfer rockburst risk include destress blasting and altering timing of blasts. To minimize rockburst risk, backfill of mined stopes should be considered. When all these and other methods are exhausted and the rockburst problem is still present, we will have to accept the reality and institute effective rockburst support.

Avoiding difficulty and confrontation is one of the fundamentals of Tao in Chinese culture. If we can achieve this, we are following Tao in our professional work.

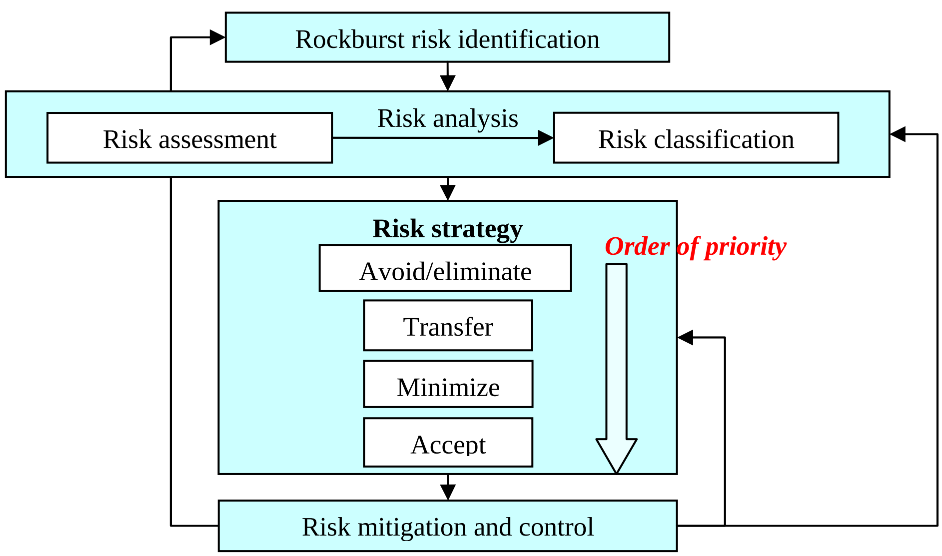

Figure 1 Rockburst risk mitigation and control.

3.2 Flexibility/Yielding Support Principle

When a seismic event occurs, rocks can be subjected to large impact loads. When brittle rock fails, it is always associated with large rock dilation. Therefore, the installed rock support system must be able to absorb dynamic energy while at the same time accommodate large rock deformation due to rock failure. Practical rock support has its limit in terms of capacity. Hence, the installed rock support system should focus on controlling the rock behavior after failure, not on preventing the rock failure from occurring.

In addition, when mining at depth, the excavation-induced stresses around underground openings are so high that rock fracturing is inevitable. The stresses are further elevated when the rock is loaded dynamically. In many situations, it is no longer possible to increase the load carrying capacity of the reinforced rock system economically, and the support behavior must be fundamentally changed to allow for yielding. Jager et al. [3] showed the dilation pressure resulting from brittle failure in a deep tunnel sidewall exceeded 0.4 MPa. When the rock fracturing process is dynamic, it is likely that the pressure will be considerably higher, exceeding the capacity of most practical rock support systems. For reference, the support pressure that can be achieved by a moderately dense pattern of rockbolts is about 0.1 MPa. To provide a support pressure of 0.4 MPa, very thick cast-in concrete would be required which is clearly not economically practical for most mining applications.

In general, rock pressure decreases with increasing rock deformation. If the rock support system is able to yield in a controlled fashion, we can reach a dynamic equilibrium in the whole deformation process and the system will eventually reach a new static equilibrium. Things in nature always try to reach an equilibrium – a cup of hot coffee sitting on the table will eventually reach room temperature, water tends to run down hill to a lower, more stable place, and a rock mass will deform to find its most natural bearing state itself.

Hence, the key point is that the rock support system must allow the rock mass to deform, which means that the rock support system must be yieldable. Yielding support system can tolerate large tunnel convergence without "self-destruction" of the system while providing necessary support to ensure safety and maintain serviceability of the tunnel. A yielding rock support system is a system in harmony with its surrounding rocks.

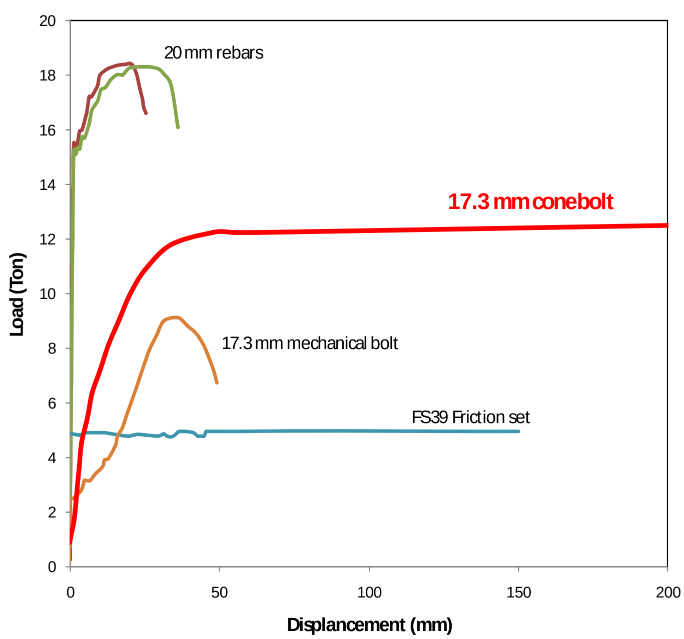

Figure 2 Load-displacement curves of various rock bolts (data except conebolt are from Stillborg [14]).

Cook and Ortlepp [1] first suggested the use of yielding support in the deep gold mines in South Africa. Not surprisingly, conebolts were first developed in South Africa. The conebolts were groutable yielding tendons developed by the Chamber of Mines Research Organization (COMRO) in 1987 [4] for use in cement grouted holes. Noranda Inc. added a mixing blade for use with polyester resin cartridges and the resulting conebolt was called the MCB (Modified Cone Bolt). When subjected to static loading, the cone functions as a wedge-style mechanical anchor similar to standard mechanical rockbolts. However, when subjected to dynamic loading, the MCB conebolt can yield or plow through the resin, thus absorbing the dynamic energy through controlled deformation. As can be seen from Figure 2, conebolts and friction sets can maintain their load carrying capacity while experiencing large deformation, and they are amongst the most widely used yielding support elements in deep underground mines. MCB conebolts have been successfully applied in some Canadian mines with severe rockburst problems and friction sets have been used for support in moderate bursting grounds. More discussions on the application of conebolt are presented in Section 4.

If we compare a rockburst to a storm, we often see large strong trees broken or rooted up due to high winds. However, when a bamboo is subjected to a similar storm, it bends and sways but is seldom broken. Let your rockburst support system emulate bamboo’s strength and flexibility.

3.3 Address the Weakest Link Principle

Standard support using rockbolts or rebars (or both) with wiremesh is widely used for ground support in Canadian mines. This type of rock support system is not effective when a rockburst strikes, not because the rockbolts do not have sufficient holding capacity, but because the link between the mesh and the bolts is weak. This linkage is the weakest link in the system. In fact, the surface retaining element is often the weakest link in most rock support systems. The connection between bolt and screen fails in 75-80% of large rockburst events. One example is given in Figure 3. The drift was supported by rockbolts and wiremesh. The ejected blocks from the rockburst stripped the mesh from the bolts yet most rockbolts were left in the wall with little damage to themselves and the plates were not even deformed. This picture clearly shows that the linkage between the bolts and the mesh was weak. Had the linkage been stronger, the damage might not have been as severe or could have been completely avoided.

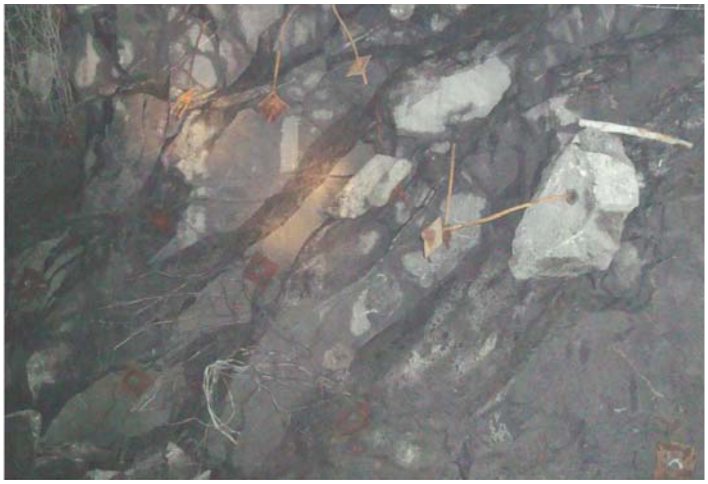

Figure 3 Rockburst damage to a drift at a mine in Canada. If the bolt mesh weakest link had been properly addressed, we might have seen a completely different picture.

A chain is only as strong as its weakest link. Most people seem to have no problem understanding this, however not everyone realizes that there is a weak link in rock support systems in use today in mines. In this case, the effectiveness of a rock support system comprised of rockbolts and mesh to resist the dynamic loading, does not depend on the strength and capacity of the bolts and mesh, but rather on the connection between the bolts and the mesh. Therefore, when designing rock support for burst-prone ground, we must address the problem of the weakest link. This problem has been recognized by a few researchers and a comprehensive investigation is provided by Simser [10].

The surface retention component failure is often caused by use of mesh with too low a strength, sharp-edged steel plates cutting the mesh, ejection at the mesh overlap, failure of the bolt threaded section, plate failure, failure of nut, etc. Hence, there are many ways to improve the capacities of the system's "weakest link." One example is the use of relatively large plates to connect the rockbolts to the wiremesh. At Otter-Juan Mine in Australia, they adopted 350×300 mm, 3 mm thick plates with 4 mm diameter wire mesh, and the end anchored thread bars proved effective in slight to moderate rockburst conditions [15]. In some Canadian mines, 300×300 mm #0 gauge (7.7 mm in diameter) mesh plates are used in combination with standard steel plates to provide a wider coverage area to prevent the plate from punching through wire mesh. In this case, the mesh thickness will also determine the degree of dynamic protection that the system can sustain. For years, the South Africans have successfully used a surface retention system called cable lacing for rockburst support. Rockbolts are installed with mesh and cables are woven through the yielding tendons in a diamond shape. The lacing increases surface retention and in the event of a rockburst, the mesh and cables work in tandem to capture the ejected rock and transfer the load to the surrounding tendons. A similar system is used in Canada. It comprises 30 cm wide 3 m long #0 gauge mesh straps. The above examples address the weakest link problem and the design strength can be increased or decreased based on each mine's individual needs following a thorough risk assessment.

Based on our experience, we recommend installing conebolts using relatively large plates (minimum 150×150 mm) and #0 gauge mesh straps. The reason is simple – we want to eliminate the weakest link in the rock support system. Addressing the weakest link in a rock support system often can result in greater system performance for a relatively smaller effort. We do not need a completely new chain; all we have to do is to replace the weakest link by a stronger one. Always remember that a rock support system is only as strong as its weakest link.

3.4 Integrated System Support Principle

The authors are often asked by miners and ground control engineers whether one "super" bolt can be developed to replace all other bolts to combat rockburst problems in deep mines. Our answer is always a big "No!" For example, extensive effort was put into the development of a "super" spray-on liner that was intended for use in highly stress ground. Spray-on liners have some sought after properties, however, it is doubtful if they can replace other surface support elements such as shotcrete, straps, lacing or mesh. Very often, we need a rock support system that is comprised of different rock support components. The clever ground control engineer looks to the combined effect of an integrated support system, and does not rely only on any individual element. He or she then has the ability to pick out the right combination of support elements and utilize the combined synergies.

In some people's mind, when you mention the term rockburst support, all they can think of is the application of conebolt or friction set. For example, they would think that rebars are too stiff and therefore conclude that rebars should not be used for rockburst support at all. The fact is that stiff rebars, in combination with mesh or shotcrete, can control the rock fracturing and hence rock dilation in hard rocks very well (when the stress is relatively low to moderate). When a rockburst strikes or when the rock stress is high, rebars can break (usually at the threaded section near the plate) and lose their holding or surface retention function. However, if we add conebolts with straps to the rock support system, we then form a two-tiered defense system. Rebars will reinforce the rock mass to ensure that it is not fracturing pre-maturely (static support). When the rock masses do fail, the yielding support will ensure that they are properly retained.

Similarly, some engineers do not like shotcrete in burst-prone grounds because they have seen that shotcrete became part of the "fly rock" when a rockburst occurred. The fact is shotcrete can be very useful to enhance the installed rockbolt and mesh rock support system. They will enhance the weak link between the bolt and mesh, and they can prevent key blocks from moving and therefore enhance the overall integrity of the rock mass. From our integrated system support approach, we understand that shotcrete is a very useful component in the team and we need to use it at the right place and at the right time when it is needed (this is like using defenders wisely in a sport game). To prevent shotcrete from flying off with rocks, a second layer of mesh can be used. Quite often, if conebolts and straps are installed over top of any applied shotcrete, the problem of "fly rock" can be resolved.

For this reason, we need to understand the function (reinforcement, hold, and retain) of each support component – rebar, rockbolts, friction sets, conebolts, cablebolts, wire mesh, shotcrete, lacing, straps, etc. Some support components have multiple roles in terms of the three support functions (reinforce, retain, and hold) but may be strong in one aspect and weak in the others. It is essential that the various support elements be combined to maximize their capabilities for support in burst-prone grounds. An effective rockburst support system is not the application of a single "super" bolt or liner, but rather the optimal use of various support components.

3.5 Simplicity Principle

Rockburst support does not necessarily have to be complicated. That means that the rock support elements should be relatively easy to be manufactured, installed, and maintained. Regardless how effective it is, if a rock support element is complicated to manufacture and the cost too high, operators will be reluctant to use it. If it is difficult to install and production is adversely affected, its acceptance by the mine operators and workers will suffer.

The new MCB33 conebolt is a good example of simplicity. The bolt is comprised of a smooth bar with a threaded end on one side to accommodate a nut and washer plate and a cone shape at the other end. It is relatively easy to manufacture and simple to install. The bolt is installed in a 33 mm drill hole using 30 mm resin cartridges. The 33 mm diameter is the standard drill bit size used in most Canadian mines for virtually all short bolt installations, i.e., 0.5 to 3 m bolt lengths. The use of resin instead of cement grout ensures quick installations and acceptance by both the mine management and the mine work force. One bit size means that a one pass bolting system can be implemented, greatly improving the bolting efficiency. In addition, the yielding mechanism of the MCB33 – cone plow through resin – can be easily understood by both engineers and miners alike. Ultimately all mine personnel need to understand the support elements and buy into the system to ensure their safety.

When it comes to rock support in burst-prone ground, it is always beneficial to follow Albert Einstein's advice – "*Make everything as simple as possible, but not simpler.*"

3.6 Cost-effectiveness Principle

By cost-effective, we mean two things – the rockburst support system should not cost a lot of money, and even though using rockburst support may cost extra money but it is money well spent. This first point needs no explanation at all and the second point seems to be difficult to be understood by many mine operators.

We know that making underground construction safe and reliable costs money. However, we must be very clear that spending money to ensure safety and spending it well are two different things. When a rockburst occurs, it usually comes as a BIG "surprise." In Canadian mines, if a worker is killed by a rockburst event, the mine could be shut down for an extended period of time during a lengthy investigation. When a critical access such as ramp is severely damaged by a rockburst event, it often means of loss production for months and the revenue loss is compounded by costly rehabilitation. It is estimated that the rehabilitation cost is 10 to 20 times higher than the initial development cost. The cost of a yielding support system (e.g., conebolt or other bolt system) may be slightly higher when compared to a standard rock support, however, if costly rehabilitation and lost production (and possibly litigation) can be avoided by using rockburst support systems, this is the most economical option. The key point is that if the price tag for a rockburst event is high, the cost of preventing it in the first place, using rockburst resistant rock support system, can be remarkably low (Figure 4). Many accidents have told us that prevention in burst-prone ground yields more benefits than cost.

However, it is not necessary to install rockburst support everywhere in a mine because this is excessively expensive. Therefore, we need to know or anticipate where rockburst damage could potentially occur. A few tools are available to assess the seismic hazard in a mine, such as analysis of microseismic monitoring data, integration of geology, and adaptive use of numerical modeling results. Unfortunately, rockburst risk assessment is still at its early development stage and coupled with the complex nature of rock mass property and excavation behavior, we will have to rely heavily on rock support to cushion the uncertainty with regard to location and severity of the rock mass damage due to a rockburst event.

For rock support in potentially high-risk rockburst grounds, a penny saved could be a dollar lost.

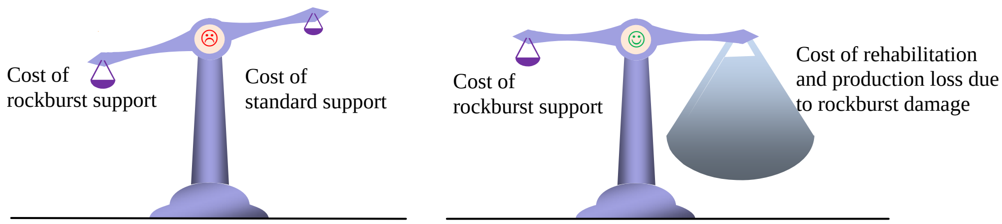

Figure 4 Illustration of cost-benefit for rockburst support.

3.7 Observational Construction (Anticipate and be Adaptable) Principle

Burst-prone ground conditions and rockburst damage severity potential change constantly. Where will the seismic event occur? How large of an event might it be? What mode of damage might it produce? We all understand that it is not possible to answer all of these questions. Therefore, it is unrealistic to have a fixed design that cannot be changed. In general, the choice of a particular rock support system depends on the ground conditions encountered, the mining sequence, available material, and the experience of the engineers and miners at the mine site.

In actual application, we have a good knowledge of the capacity of the rock support but a poor knowledge of the anticipated dynamic loads (demands). One may follow the guideline in the books (e.g. Canadian Rockburst Support Handbook [6]) to start his/her design of rock support, but the design needs to be verified and altered using field observation and monitoring. A few trial-and-errors are needed to assess the expected demand and then match it with appropriate rock support under given boundary conditions.

A good rockburst support system is the one that will stabilize the excavation for the conditions to be expected not only at the time of excavation, but also during the life of the operation. It should be capable of adapting to changes from these conditions as they are put into services. Adaptability is the ability of a system to adapt itself efficiently and quickly to changing circumstances. Adaptability means “survival of the fittest.” If a rock support system design cannot adapt to the changing ground condition, it is not going to be a good design.

When unexpected ground behavior is encountered, it is unwise to stick to old principles or old tricks. Let your underground excavation and rock support methods be regulated by the infinite variety of ground conditions. The art of rock support in burst-prone ground is not to rely not on the likelihood of the unexpected ground behaviors are not coming, but on our own readiness to receive them, not on the chance of the ground deformation forces are not attacking, but rather on the fact that we have made our rock support system unbeatable.

Wayne Gretzky, one of the most famous hockey players in NHL history, once said, "*Skate to where the puck is going, not where it is*." If you cannot anticipate, you will never become a good hockey player. Similarly, if you cannot anticipate, you will never become a good ground control engineer to combat rockburst. Your ability to anticipate and adapt can be greatly enhanced if you gain more underground experience (that is right, you have to go underground to see rockburst damage!). You ability to safe guard your fellow workers and company property can be significantly increased if you understand the seven principles (Figure 5) we outlined in this paper. As Ralph Waldo Emerson, an American essayist, philosopher and poet (1803 – 1882), said, "*As to methods there may be a million and then some, but principles are few. The man who grasps principles can successfully select his own methods. The man, who tries methods, ignoring principles, is sure to have trouble*."

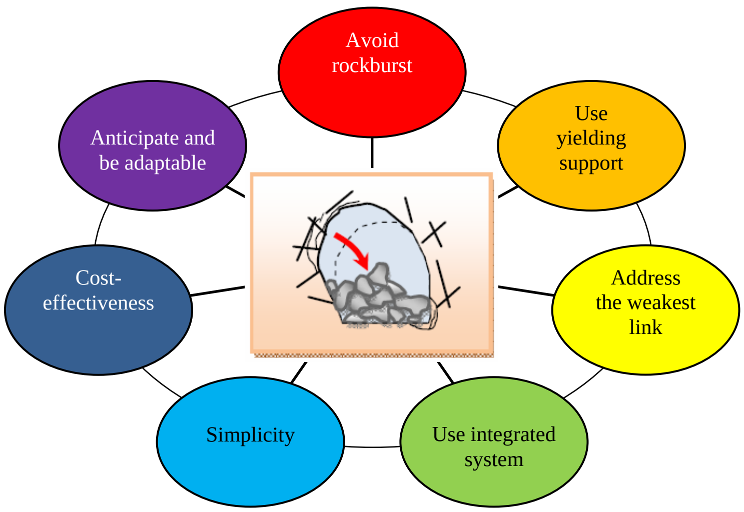

Figure 5 Summary of seven rockburst support principles (Rainbow Principles, as indicated by the color in the figure).

4 Case Histories and Recent Research and Development

4.1 Rockburst Support in Canadian Mines

Numerous methods exist to test a rock support system's dynamic energy absorption and effectiveness such as using a controlled blasting. For example, a test tunnel was reinforced with tensioned conventional end-anchored bolts on one side and yielding end-anchored bolts on the other and blasted with the same pattern and charge on both sides [8]. The test result convincingly demonstrated that yielding rockbolts could withstand the dynamic loading, whereas the other sidewall of a tunnel supported with conventional end-anchored rockbolts was destroyed.

As time passes, the effectiveness of the yielding support system has been proven by many practical applications in burst-prone mines around the world. In Australia, the use of conebolt for rockburst support had been proven effective at Big Bell Mine [16] and Beaconsfield Mine. Conebolt + strap yielding support system has been used in a number of mines in Canada and the results consistently show that the system works. At the Brunswick mine in Canada, several rockbursts severely damaged sections supported by conventional rock support system while the conebolt supported area was virtually undamaged [12]. On Oct. 13, 2000, a Mn=2.5

(Nuttli magnitude) rockburst event caused the collapse of an intersection involving approximately 1860 tons of material. A small portion of the crosscut immediately east of the intersection had MCB conebolts installed. The right-hand side of the tunnel was supported by 2.3 m conebolts in 1×1 m pattern with #0 gauge mesh straps and chainlink mesh. The left-hand side of the tunnel was supported only by rockbolts with chainlink mesh. The foreground of the area was supported by rebar and steel fiber reinforced shotcrete. After the rockburst event, it was revealed that the right-hand side of the tunnel suffered no visible damage at all while the rest of the area suffered severe damage. The intersection also collapsed despite the fact that it was supported by standard rebars, cablebolts, screen, and shotcrete. The good performance of the conebolt supported tunnel section held the ground so well that many people speculated that the rock might not be hit hard as the rest of the area. However, close onsite examination revealed that the conebolts had fulfilled their role to dissipate energy as some conebolts displaced as much as 180 mm [11]. Subsequence use of conebolt based rock support system at the mine site proved to be exceptionally well.

On September 11, 2008, a major rockburst (Mn=3.8, Nuttli) occurred following a series of seismic events immediately after a crown blast in the middle 100 orebody between 3050 and 3200 L, at Vale Inco Copper Cliff North Mine in Sudbury, Ontario, Canada. This large rockburst event, in association with other significant seismic events (Mn > 1.2), caused an enormous amount of damage. The damage was so widespread that it was extended from 2700 to 3710 L around the 100/900 orebody region. In total, more than 2500 tons of material was displaced at different locations on different levels, and most of the damage was observed to be associated mainly with major geological structures [17]. One of the reasons for the extensive damage was that the level of installed ground support was relatively light (a mix of resin rebars and mechanical bolts with wiremesh), and the support system has limited energy absorption and holding capacity. After the occurrence of the major event, mitigation plans were put in place to ensure that the remaining ore bodies can be mined safely and efficiently. The mine management swiftly adopted the conebolt based dynamic rock support system. On top of the primary support (#4 gauge welded wiremesh, 1.98 m FS46 (46 mm) friction bolts on a 1.22×0.76 m pattern for wall and 2.44 m resin rebars on a 1.22×0.76 m pattern for back), 2.34 m long MCB conebolts on 1.22×1.83 m pattern with #0 gauge mesh straps were implemented as the secondary (rockburst) support. On Feb. 2009, a Mn=2.9 (Nuttli) seismic event occurred in this same area causing further damage to the drifts; however all conebolt supported were undamaged [17]. Based on rockburst risk assessment, areas of high rockburst risks will be systematically supported by enhanced rock support using conebolts and straps.

Conebolt based rockburst support system has been successfully used at Vale Inco’s Creighton Mine and Garson Mine in Sudbury, Ontario, Canada. Over the last decade, the ground support system for Creighton Deep has been continuously improved based on trials and analyses of the ground response and stress levels. Primary support systems have been improved with the development and implementation of the FS46 friction sets for wall bolting and Swellex bolts when mining under or beside sand fill. In areas where secondary support (cablebolts) or rockburst support (conebolts with #0 gauge mesh straps) is required, the support is installed when driving the development, prior to driving any secondary crosscuts or approximately every four rounds. Delayed installation of conebolts and straps can cause various challenges over time, and the main challenge experienced is the difficulty to install conebolts due to ground deterioration from high in-situ stresses. Combined with other initiatives, the numbers of rockbursts have been reduced and the down times in the mine after major seismic events have been minimized. Today, damage after large seismic events (due to fault slip) is often minor or insignificant [7]. At Garson Mine, whenever the drifts passed the sub-vertical dyke of olivine diabase, strain burst resulted and damage occurred even when the standard rock support system (rockbolts with shotcrete or mesh) was used. After the introduction of conebolt based rockburst support at the mine site, no severe rockburst damages have been reported in the dyke areas.

Another convincing successful application of MCB conebolt based rockburst support system is at Xstrata’s Kidd Creek Mine in Timmins, Ontario, Canada. A magnitude Mn=3.8 seismic event, happened in January 6, 2009, causing extensive damage to four levels (6800, 6900, 7000 and 7100 L) at the mine. One drift supported by standard rock support with mesh and rebar totally collapse. A few pieces of mining equipments were buried and likely destroyed. Fortunately, the event occurred at about 4:40 a.m., as the nightshift at the mine was going off duty and heading to surface. No injuries were reported. Careful underground inspection by mine site ground control engineers (and the authors) confirmed that in areas where conebolt based rockburst support were installed, they were remarkably in good shape and that damage was extensive in adjacent areas where only standard rock support (rebars and meshes) was used. Currently, rehabilitation of the damaged areas is ongoing and it is expected that the whole rehabilitation will take at least six months (D. Counter (2009), personal communication).

4.2 The Next Generation Conebolt

Mansour Mining Inc. is the exclusive manufacturer of MCB conebolts (patented). Continuous research and development is being carried out to improve the performance of the product.

The South Africa conebolt is coated with wax and the MCB conebolt is greased to diminish the bonding between the grout and the bolt. However, spinning of the bolt to mix the resin can strip off almost all the coating, leading to unwanted bond between the bar and the resin. This has been demonstrated by static and dynamic tests in laboratory. The authors conducted a series pull tests using steel pipes. 1.2 m long conebolts (17.3 mm diameter) were installed in the pipes with fully encapsulated resin. After the resin is set, the cone section (about 0.1 m) was cut off and the remaining bolt was pulled until the bolt started to slide in the resin. It was found that for an embedment length of 0.94 m, the maximum load recorded was 127 kN, which is very close to the yielding load of the steel. St-Pierre et al. [13] conducted dynamic drop tests at CANMET and found that the influence of grease on the bolt behavior was not obvious. In two of their tests, the cones were cut off and a drop weight of 1016 kg from 0.5 m (5 kJ input energy) was used to test the dynamic capability of the smooth bars without cones. The resin embedment length was estimated at 1.2 m. The bar which was greased sustained six drops with a total input energy of 35 kJ and the non-greased bolt accepted five drops with a total input energy of 30 kJ. Note that 5 kJ impact energy is large enough to break a fully bonded rebar at the threads.

It is obvious from both the static and dynamic testing that grease is not doing a good job to debond the bolt from the resin. The fact that a smooth bar whether greased or not, can sustain reasonably high pull out loads or absorb certain amount of impact energy indicates that there is a reasonably large friction force existing between the bolt and the resin. A fully encapsulated smooth bar is, fundamentally, a friction bolt. The frictional force is distributed along the grouted section of the bolt and it becomes obvious that it will limit the cone's ability to plow through the resin when subjected to dynamic loading. Mansour Mining conducted dynamic drop tests in 2008 with an impact energy of 16 kJ (drop weight 1115 kg, drop height 1.5 m). Test results showed that greased bolts perform only slightly better on average than non-greased bolts (62.5% total displacement due to cone movement versus 50%). In addition, the test results showed that the bolt could withstand 16 kJ of impact energy 3 to 4 times before the bolt breaks. The maximum accumulated steel strain recorded was 10.4% before the bars broke. Again, this indicated that large friction component existed between the bolt and resin interface that prevented the cone to efficiently plow through resin under repeated loading.

In order to improve the static and dynamic performance of MCB conebolts, it has been realized for a long time that an effective debonding agent was required. We know that wax can be a good debonding agent; however, the manufacturing process is both complicated and costly.

Recently, the authors developed a new patented debonding agent in the form of a heat shrink plastic sleeve installed over the shaft of the bolt. Laboratory testing combined with in-situ pull tests confirmed the new system's functionality. Dynamic drop test at CANMET's Bell Corners testing laboratory confirmed that this new debonding agent is much more effective as a debonding agent over grease used in the original design.

There are currently two different cone sizes in use – MCB38 for 38 mm boreholes and MCB33 for 33 mm boreholes. Because rebars and rockbolts all use 33 mm boreholes, it makes much more economical sense to use the MCB33 conebolts, i.e., one bit and one resin. This eliminates one bit and one resin size from inventory. In addition, it is possible to install all standard and rockburst support systems in one pass. Hence, our recent research and development was focused on MCB33 conebolts. Our new design of MCB33 is presented in Figure 6.

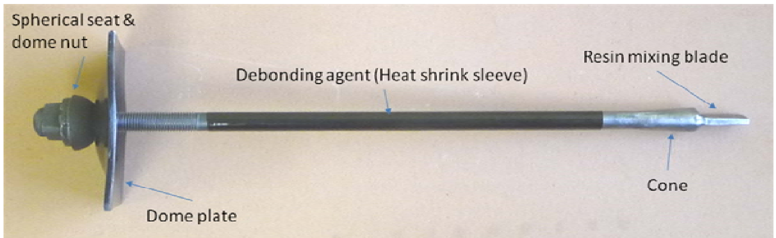

Figure 6 New design of MCB33 conebolt.

To prove our new design, 46 in-situ pull tests were performed at five mines, and eight dynamic drop tests were conducted at CANMET in April, 2009. Four plastic sleeve debonded conebolts (17.2 mm diameter) were tested at 16 kJ and the results are comparable to the results of previous tests using grease as the debonding agent. Dynamic drop test results showed that on average 99.6% of plate displacement was from cone plow on the first drop as compared to 82.9% in the old design. In the second drop, the cone plow percentages for the new and old designs are 75% and 29.2%, respectively. One new bolt showed an abnormal behavior in the second drop without cone plow. If this data were excluded, the cone plow would be 100% in the second drop for the new bolts. In the third drop, the cone plow percentages for the new and old designs are 99.6% and 4.7%, respectively. It is seen that the new design allows the cones to plow through the resin very effectively while the old design relied more on steel stretch to absorb the impact energy of repeated dynamic loading.

Three MCB33 with plastic sleeves were tested at 26 kJ impact energy (1784 kg weight, 1.5 m drop height). It resulted in 100% and 99.9% cone plows in the first and second drops, respectively. This means that all the impact energy was absorbed by cone plow in the test. In our previous drop tests on MCB conebolts, the highest impact energy tested was 22 kJ with significant steel stretch. Close to perfect cone plow at 26 kJ was very encouraging and we decided to use the last available bolt to test at a higher energy level. The bolt was subjected to a 33 kJ impact from a single drop (2229 kg weight, 1.5 m drop height) and survived. Cone plow constituted 76.3% of the total displacement and the steel stretch was 23.7% which represents of steel strain of only 5.6%. Figure 7 presents the relationship between bolt displacement and absorbed impact energy. Data other than MCB are obtained from Player et al. [9]. It is seen that when threadbars fail at the thread, the absorbed energy is very low (< 2 kJ). The fully bonded threadbars are tested using load transfer by separating the bolt in the middle of the installed pipe. The debonded threadbars have about 1.6 m debonded section which can allow the steel to stretch. All data points are from the first drop loading. Four threadbars failed but there were no conebolts failures on the first drop. A very good linear correlation between steel strain and energy absorption can be seen from the threadbar data. It is observed that the cement grouted South Africa conebolts and at least two of our old MCB conebolts follow the trend line, indicating that the dominant energy absorption mechanism of those conebolts had been steel stretch with very little cone plow. On the other hand, the new MCB design allows the cone to plow much more efficiently, and their capacities to absorb dynamic energy are thus substantially increased.

Theoretical consideration based on extrapolations of dynamic test data suggests that the 17.2 mm diameter conebolt may be able to absorb in excess of 40 kJ of impact energy in a single event. Previously tested largest single impact energy was only 22 kJ and our recent test has increased the energy to 33 kJ. With the success of our test, we anticipate that the new design of the conebolt may allow the bolt to absorb energy higher than 40 kJ in a single event. Future tests will be conducted to confirm this.

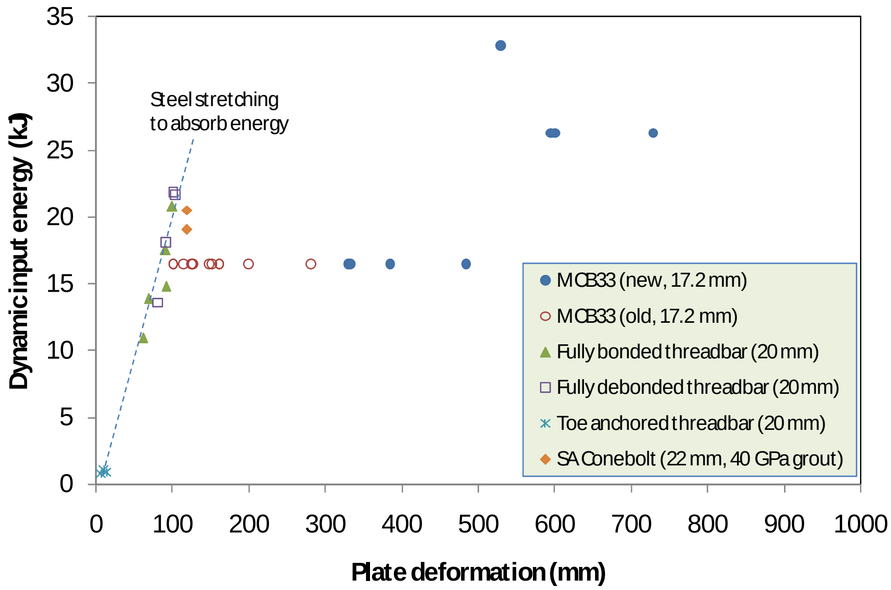

Figure 7 Energy dissipation of MCB33 and other bolts versus plate deformation. "New" and "Old" stand for plastic sleeve and grease debonded conebolts, respectively.

5 Conclusions

Rockbursts are a complex natural phenomenon occurring in deep underground construction. Much effort has been put into research to understand why it happens and to anticipate where it will happen. Unfortunately, due to the complexity of rock mass and the boundary conditions, we still do not have great confidence in our analysis and "prediction," at least the reality tells us so. As mining progresses to deeper grounds, violent rock failure cannot be avoided and it will have to be dealt with on a routine basis by implementing a rockburst resistant support strategy.

Rockburst support is not a mystery, not a skill that only a few can master. We present the art of rock support in burst-prone ground in seven principles. Once you understand them, you can make your right judgment and decision according to the ground condition. Because we have had the general principles previously determined, there will be no perplexity to know what to do when we are dealing with rockburst damage.

The use of yielding support is a key component when designing a rockburst support system. Although we place the principle of avoiding rockburst in the first place, however, when every effort has been taken to reduce the rockburst risk at a mine using sound mining methods etc, the risk will unfortunately not go away. Our final line of defense is not our ability to "predict" when and where a rockburst will occur, but rather on the fact that we have made our rockburst support system unbeatable. We present the observational construction principle (anticipate and be adaptive) as the last principle simply because this is the skill that we all need to have in order to win the battle against rockburst damage, and it is an effective skill to deal with uncertainty.

MCB conebolt based rockburst support systems have been proven to be very effective to mitigate/limit rockburst damage. Recent development at Mansour Mining Inc. has greatly improved the dynamic capability of the conebolt and it is expected that it will perform even better in severe rockburst situations. The new MCB33 conebolts can be used in a one-pass rock support system to facilitate rapid drift development in underground mines.

Acknowledgements

The authors wish to acknowledge Xstrata Nickel, Xstrata Copper, Kirkland Lake Gold, Vale INCO, and Goldcorp for their support during the field test of the development of the new MCB33 conebolt. The authors also wish to thank Mike Hill of Mansour Mining for assisting in-situ testing and CANMET for executing the dynamic drop test. Permission to publish the dynamic test results from Mansour Mining Inc. is gratefully acknowledged.

References

1. Cook, N.G.W. and Ortlepp, W.D. A yielding rockbolt. Chamber of Mines of South Africa Research Organization Bulletin, 1968, 14.
2. Hedley, D.G.F. Rockburst Handbook for Ontario Hardrock Mines. CANMET Special Report SP92-1E, 1992.
3. Jager, A., Wojno, L.N. and Henderson, N.B. New developments in the design and support of tunnels under high stress. In: Technical Challenges in Deep-level Mining, SAIMM Congress. 1990, 1155-1171.
4. Jager, A.J. Two new support units for the control of rockburst damage. In: Kaiser, P. K. and McCreath, D. R., editors. Rock Support in Mining and Underground Construction. 1992, 621-631.
5. Kaiser, P.K., Tannant, D.D. and McCreath, D.R. Drift support in burst-prone ground. In: Proc. 97th CIM Annual General Meeting. 1995, 277-288.
6. Kaiser, P.K., Tannant, D.D. and McCreath, D.R. Canadian Rockburst Support Handbook. Geomechanics Research Centre, Laurentian University, Sudbury, Ontario, 1996.
7. Malek, F., Suorineni, F. and Vasak P. Geomechanics strategies for rockburst management at Vale Inco Creighton Mine. In: Diederichs, M. and Grasselli, G. editors. ROCKENG09: Proceedings of the 3rd CANADA-US Rock Mechanics Symposium. 2009, 4234.
8. Ortlepp, W.D. The design of support for the containment of rockburst damage in tunnels an engineering approach. In: Kaiser, P.K. and McCreath, D.R. editors. Rock Support in Mining and Underground Construction. Balkema, 1992, 593-609.
9. Player, J.R., Thompson, A.G. and Villasescusa, E. Dynamic testing of threadbar used for rock reinforcement. In: Diederichs, M. and Grasselli, G., editors. ROCKENG09: Proceedings of the 3rd CANADA-US Rock Mechanics Symposium. 2009, 4030.
10. Simser, B. The weakest link: Ground support observations at some Canadian Shield hard rock mines. In: 4th International Seminar on Deep and High Stress Mining, Perth, Nov. 7-9, 2007.
11. Simser, B, Andrieus P, Gaudreau D. Rockburst support at Noranda's Brunswick Mine, Bathurst, New Brunswick. In: Hammah, R., Bawden, W., Curran, J. and Telesnicki, M. editors. NARMS 2002. University of Toronto Press, 2002, 1. 805-813.
12. Simser, B. Joughin, W.C. and Ortlepp, W.D. The performance of Brunswick Mine's rockburst support system during a severe seismic episode. J. South Afr. Inst. Min. Metall. 2002, 217-223.
13. St-Pierre, L. Hassani, F.P., Radziszewski, P.H. and Ouellet, J. Testing and analyzing the dynamic response of rock support elements. In: Proc. 4th Int. Symp. on High-performance mine production. 2007, 353-368.
14. Stillborg, B. Clausthal-Zellerfeld: Trans Tech Publications, 1994.
15. Turner, M.H. and Green, T. Threadbar bolts in a seismically active, high-stress, high-yield environment-Otter Juan Mine, Kambalda. In: Sixth International Symposium on Rockburst and Seismicity in Mines. 2005.
16. Turner MH, Player JR. Seismicity at Big Bell Mine. In: Proceedings Massmin 2000. The Australasian Institute of Mining and Metallurgy, 2000, 791-797.
17. Yao, M. Chinnasane, D.R. and Harding, D. Mitigation plans for mining in highly burst-prone ground conditions at Vale Inco Copper Cliff North Mine. In: Diederichs, M. and Grasselli, G. editors. ROCKENG09: Proceedings of the 3rd CANADA-US Rock Mechanics Symposium. 2009, 4045.

RaSiM 7(2009): Controlling Seismic Hazard and
Sustainable Development of Deep Mines,
C.A. Tang(ed), Rinton Press, 47-54

ROCK STRESSES, ROCK STRENGTHS AND SPALLING PREDICTION

JOHN A. HUDSON and JOHN P. HARRISON
Earth Sciences and Engineering
Imperial College, South Kensington, London SW7 2AZ, UK

To predict rock spalling around an underground excavation, a knowledge of the rock strength and the *in situ* rock stress state is required. Both these parameters usually show considerable variation at any given site, and therefore a methodology is required that captures this variation. In this paper, we combine recent research into the ratios between the magnitudes of the principal stresses and a fuzzy mathematics approach to rock parameter uncertainty to provide a methodology for approaching rock spalling/bursting estimation for rock engineering design. We present the effect of uncertainties in rock strength and *in situ* stress on the susceptibility to spalling in such a way that site investigation resources may be more effectively utilised,

1 Introduction

One of the difficulties encountered when designing underground excavations in regions of a high induced stress/rock strength ratio is the prediction of the extent to which either rock spalling or rockbursts will occur. This prediction is especially intractable because there is uncertainty regarding both the distribution of rock strength and the stress components (their magnitudes and directions).

Accordingly, it is useful to integrate recent findings concerning the distribution of different rock strength descriptors, research into the ratios between the magnitudes of the principal stresses and a fuzzy mathematics approach to rock parameter uncertainty, thus providing a realistic methodology for approaching rock spalling/bursting estimation. Additionally, in some rock masses, there can be significant inhomogeneity and anisotropy that needs to be taken into account. Thus, we also discuss how these may be considered as particular forms of variability, and show how they can be considered using the procedure presented.

The method for estimating the rock spalling potential is to compare the local rock strength adjacent to an underground opening with the stress concentration induced at that location. Therefore, in this paper we firstly discuss variability in rock strength, then variability in rock stress, and finally present a method using fuzzy arithmetic that allows these to be combined in order to establish the equivalent of a safety factor.

2 Variability of rock strength

Commonly, engineers characterise the rock strength through a single value, e.g. “the uniaxial compressive strength of the rock is 100 MPa”. Whilst in some cases this may be adequate, generally the inherent variability in rock strength should be taken into account. Figure 1 illustrates the variation in compressive strength of the crystalline rock types encountered at the Olkiluoto site in Finland (Hakala et al., 2009). Note that not only is there a wide spectrum of strengths (from less than 50 MPa to greater than 180 MPa), but the five rock types illustrated show different distributions of compressive strength (e.g. almost Gaussian for the veined gneiss, but more uniform for the mica gneiss). Clearly, the use of a single strength value may not be appropriate in these circumstances.

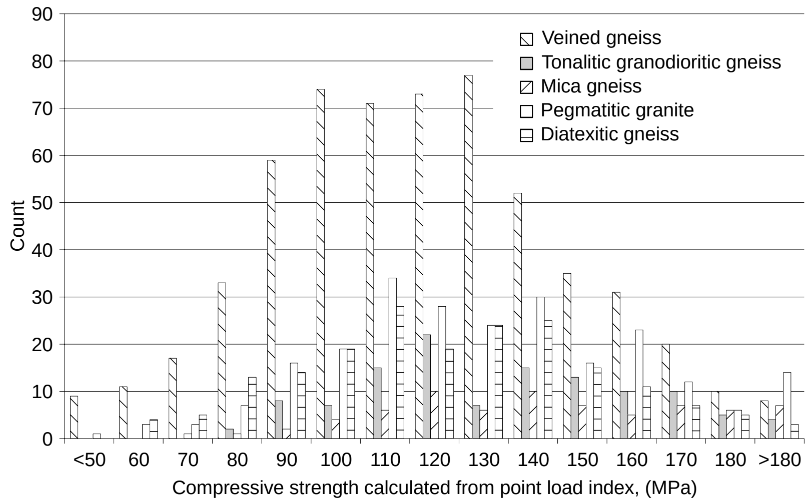

Figure 1 Variation of compressive strength for five rock crystalline rock types at the Olkiluoto site in Finland (after Hakala *et al.*, 2009).

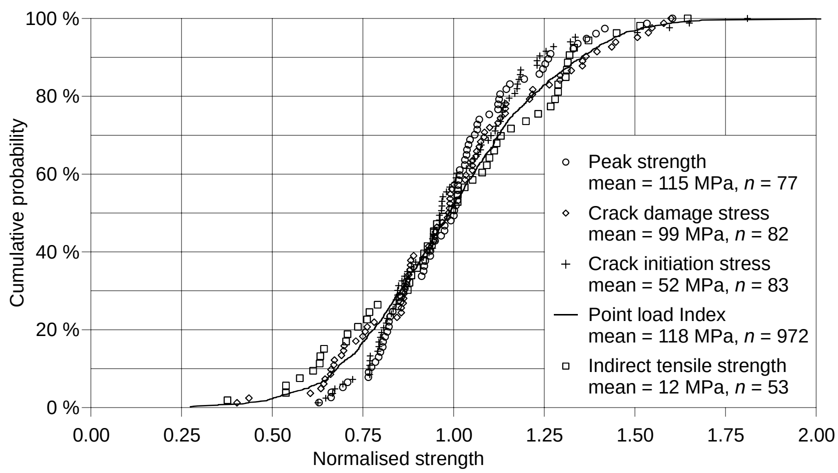

Figure 2 Cumulative distributions of different strength indices for the Olkiluoto rocks in Finland (after Hakala *et al.*, 2009).

However, in analyses of rock spalling, it is the in situ spalling strength that is used, rather than the uniaxial compressive strength directly. This spalling strength is related to the crack initiation strength, and is generally taken as a proportion of the uniaxial compressive strength, of the order of 60% for crystalline rocks (see, for example, Martin and Christiansson, 2009). Thus, it is important to establish whether the variation in this spalling strength is similar to that of the compressive strength. Analysis of the rock testing data from the Olkiluoto site supporting the data shown in Figure 1 allowed the construction of the normalised cumulative distribution curves in Figure 2, for the compressive strength, the crack initiation stress, and the crack damage stress. The point load strength and the indirect tensile strength (Brazilian test) have also been added. These results show that the distributions for the crack initiation stress and the peak strength are almost coincident — which indicates that the crack initiation stress can be accurately estimated from the compressive strength, assuming that the ratio between the two is known. In passing, we note that the point load strength and the crack damage stress are essentially coincident, but the distribution of these differs from that of the peak strength and crack initiation stress. In the analysis following later in this paper, we will therefore incorporate this variability of rock strength directly into the analysis.

3 Variability of in situ stress

It has long been known that the three principal components of the in situ stress state are not only variable, but also difficult to measure accurately. Moreover the stress state at any given depth in a rock mass can be perturbed by local changes in rock and geological structure. Together, these lead to marked variability in the stress state, as exemplified by the early data shown in Figure 3. These variations could arise from natural variability, or from incorrect values obtained due to the difficulties of measuring stress (Amadei and Stephansson, 1996).

To some extent this interpretation dilemma can be resolved through plotting the principal stress values in a different form. In Figure 4 we show more recent data from Australia (Lee et al., 2006), which show similar extreme variability to that in Figure 3. However, the authors suggested a different method of plotting these data: namely, instead of plotting the values against depth, to plot them against the first stress invariant (i.e. the sum of the three principal stresses). The result of this is shown in Figure 5 — where the data are visually much more coherent. Furthermore, the best straight lines through the data suggest the existence of distinct ratios between each principal stress and the first invariant.

In a previous paper (Harrison et al., 2007), we have noted that these ratios do seem to be similar in different locations (both geographical and geological). This paper also suggests the explanation for the phenomenon: that the Earth's crust is in a state of limiting equilibrium, and the stress ratios that can be sustained are constrained by the friction angle of the rock masses themselves. Indeed the paper goes on to suggest that the particular magnitudes of principal stress measured at a given location can vary, subject to the constraint offered by the frictional strength of the rock. This then leads on to a further analysis — using synthetic data — that shows how the ratios of the principal stress components are related to frictional strength (Figure 6). A comparison of Figures 5 and 6 immediately suggests that the Australian stress data are constrained by a rock mass friction angle of about 45°.

So, following the discussion on variability of rock strength in Section 2, and rock stress in this Section, we are now in a position to capture the variability of both parameters in an analysis of spalling potential. This is the subject of the material in Section 4.

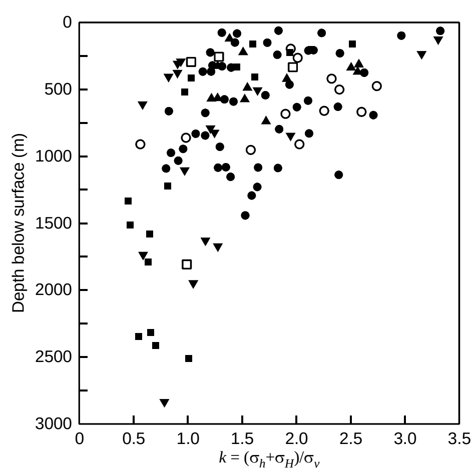

Figure 3 Variation of *in situ* stress principal values with depth below ground surface (after Hoek and Brown, 1980).

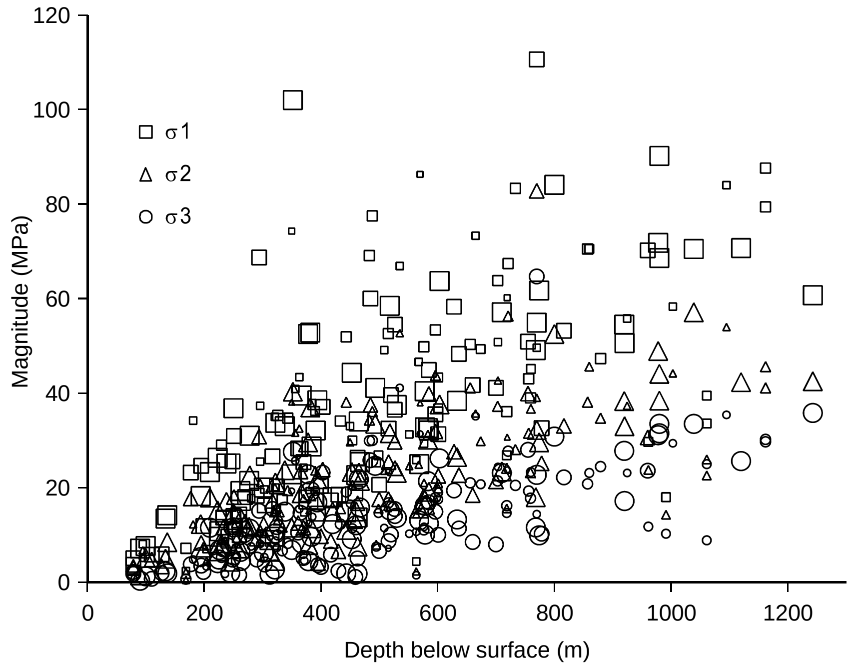

Figure 4 Australian measurements of principal stress magnitudes (after Lee *et al.*, 2006).

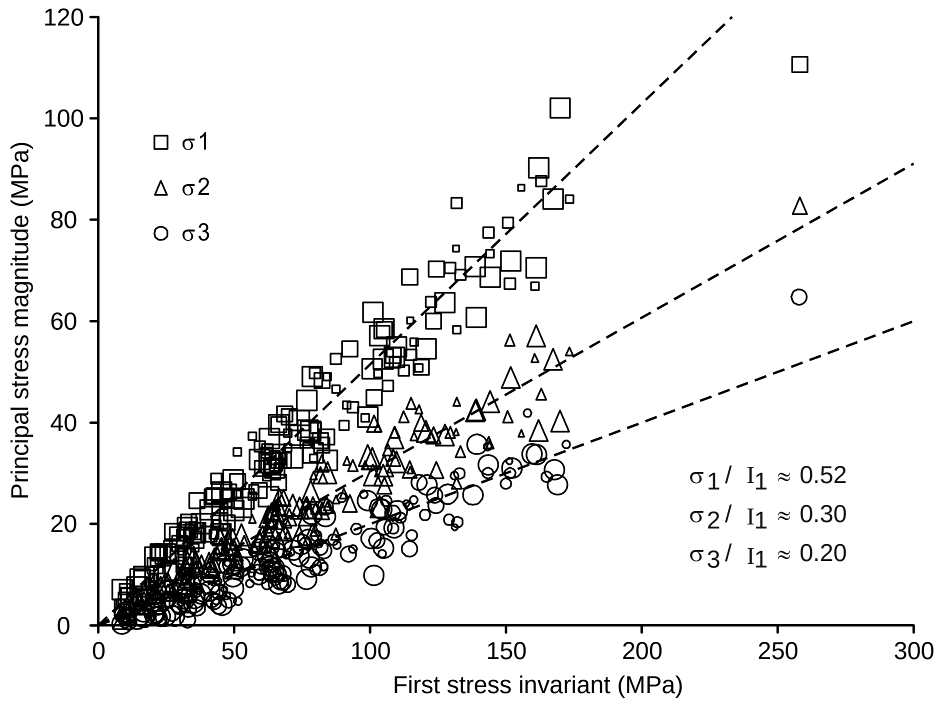

Figure 5 *In situ* stress data in terms of principal stress component and first invariant ($I_1 = \sigma_1+\sigma_2+\sigma_3$) as the independent variable (after Lee *et al.*, 2006).

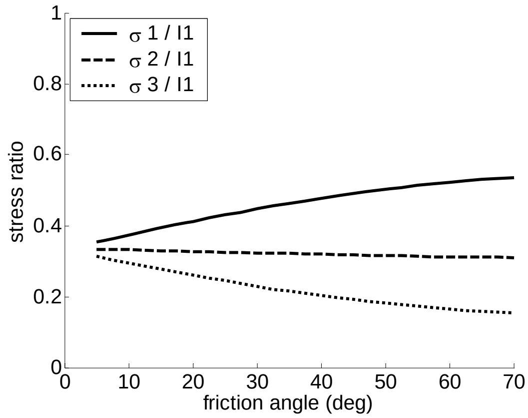

Figure 6 Ratios between principal stress components as a function of limiting rock mass friction angle (from Harrison *et al.*, 2007).

4 Effect of uncertainty in rock strength and in situ stress on susceptibility to spalling

At its simplest, the spalling potential of the rock at the boundary of a circular opening can be considered as the ratio of the induced circumferential stress and the rock spalling strength. Using the Kirsch solution, the factor of safety against spalling can be defined (Harrison and Hudson, 2009) as

$$F = \frac{\sigma_{spall}/\sigma_v}{3k-1} = \frac{\sigma_s}{3k-1} \text{ or } F = \frac{\sigma_{spall}/\sigma_v}{3-k} = \frac{\sigma_s}{3-k}\,. \tag{1}$$

Using the principles of fuzzy arithmetic (Kaufmann and Gupta, 1991) these relations can be extended to incorporate uncertainty which, in the context of this paper, can be considered to be variability in rock strength and in situ stress. This leads to

$$\hat{F} = \frac{\hat{\sigma}_s}{3\hat{k}-1} \text{ and } \hat{F} = \frac{\hat{\sigma}_s}{3-\hat{k}}\,, \tag{2}$$

where the hatted symbols, i.e. $\hat{\bullet}$, represent fuzzy extensions of the crisp values in equations 1. The two fuzzy numbers $\hat{\sigma}_s$ and $\hat{k}$ have been selected as being useful engineering variables.

For simplicity, and in the absence of any information to suggest greater sophistication, we assume that the fuzzy variables in equations 2 can be described by fuzzy triangular numbers as shown in Figure 7. A fuzzy number is an extension of the customary concept of number to encapsulate uncertainty. Thus, for the number shown in Figure 7, we are certain that the variable cannot take values less than 0.75 and more than 2.25. Furthermore, our certainty regarding the specific value of the variable is a maximum at 1.5; on either side of this value our certainty diminishes. The mode of a fuzzy number is defined as that value at which our certainty maximises (e.g. 1.5 in this example), and by definition this has associated with it a fuzzy membership value of unity. Here, as a convenient and concise means of introducing the concept of degree of uncertainty, we have chosen to define the range of variable values associated with the mode using the expression shown in Figure 7. Currently, there is no guidance for assessing the degree of uncertainty, and so for the purposes of illustration we have selected to take uncertainty values of 10%, 20% and 50% of the mode value. It should be noted that, although the definitions of mode and uncertainty are in some way analogous with those of mean and standard deviation, fuzzy numbers are not probability distributions, and they follow their own rules of arithmetic (Kaufmann and Gupta, 1991).

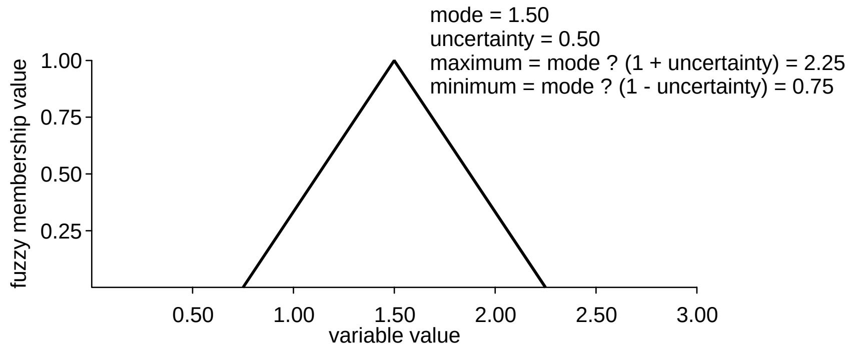

Figure 7 A triangular fuzzy number defined in terms of its mode and degree of uncertainty.

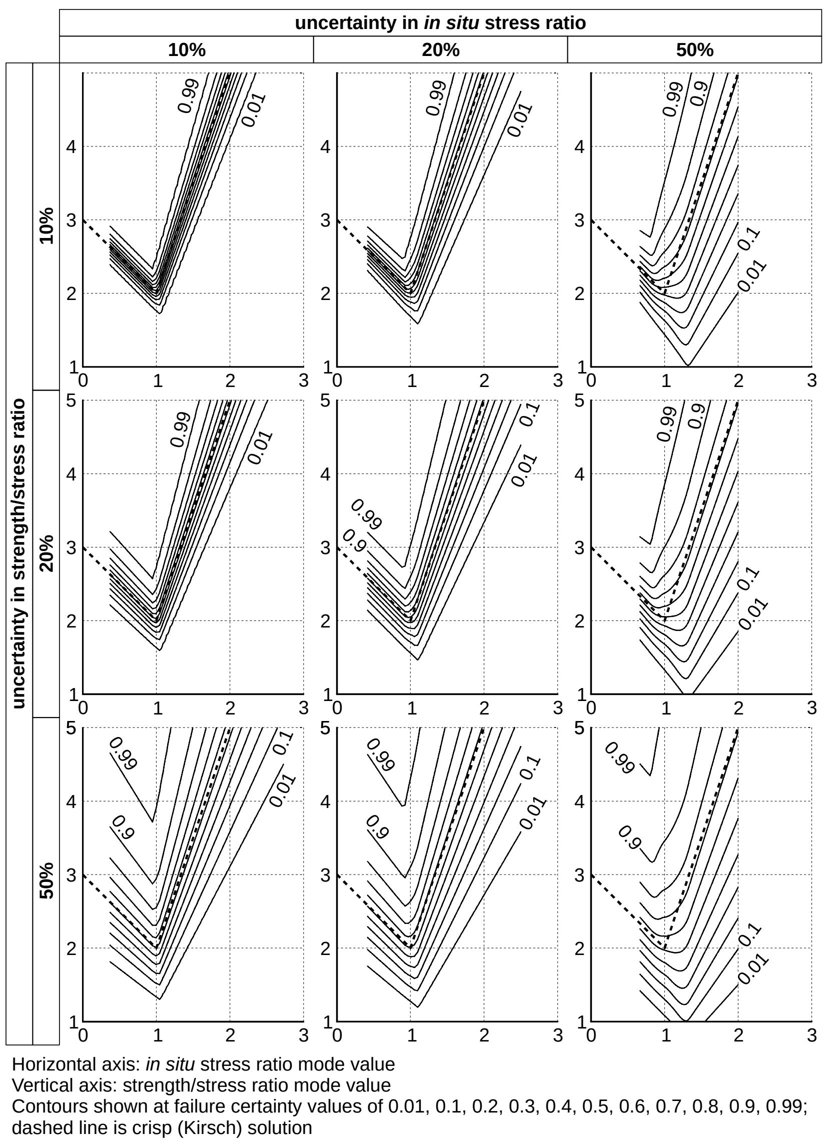

Figure 8 Effect of uncertainties in rock strength and in situ stress on susceptibility to spalling (from Harrison and Hudson, 2009).

Using these concepts, we can examine the spalling potential for various degrees of uncertainty in both the rock strength and the in situ stress, as shown in Figure 8. The contours in the Figure are of Failure Certainty Value, the degree of certainty that the rock mass will spall. The plots on the leading diagonal of this Figure clearly show how the contours of FCV close towards the crisp solution as uncertainty decreases (from 50% to 10%), and also indicate the relative effect of decreasing the uncertainty in the input parameters. Thus, if we consider the lower right hand plot, we can see that a reduction in the in situ stress ratio uncertainty (i.e. moving to the left, across the columns) closes the contours of FCV more rapidly than does the same reduction in the stress/strength ratio uncertainty (i.e. moving up, across the rows). A comparison of the plots at the top right and bottom left of the Figure shows this distinctly.

This analysis shows that spalling potential can only be accurately determined if variability, or uncertainty, in the governing variables is introduced explicitly in either the way we have demonstrated, or by analogous means e.g. Monte Carlo simulation. In the discussion presented above, we have implicitly assumed that the spalling strength of rock is a unique and crisply defined value. In fact, the failure of rock in general, and the spalling process in particular, is a progressive phenomenon involving a continuous breakdown process of the rock microstructure: at the free surface, fractures occur and the frequency of these attenuates away from the free face.

5 Discussion and conclusions

In this paper we have concentrated on the variability of rock strength and rock stress, and their influence in the prediction of rock spalling. It is evident that the analysis of rock spalling should include this variability, rather than using single values for strength and stress. We have shown how the parameters of strength and stress can be characterised in terms of their variability, and how these can be succinctly accommodated in a fuzzy, or equivalent, analysis.

It is critically important to remember that rock is a natural material, with its characteristics of discontinuousness, inhomogeneity and anisotropy — and hence the existence of the variability we have discussed. The corollary is that upon encountering regimes of different rock properties (e.g. varying strength due to different mineralogy, cementation, weathering or facies) or different stress states (e.g. different magnitudes of major principal stress, or maximum shear stress, due to the presence of major structural geological features such as faults), we should expect different values for the spalling potential. Although we have shown how to incorporate uncertainty due to variability, this only applies for a particular geomechanical regime. If there is overall change in the regime, then the spalling potential has to be re-evaluated using the new parameter values. It is emphasised that the variability illustrated in Figure 8 only applies for a specific set of circumstances; if these circumstances change, so may the variability.

The analyses described here are straightforward, do not require any specialised computer software, and are well within the capabilities of professional engineers. Guidance in their application is available from the second author at j.harrison@imperial.ac.uk.

References

1. Amadei, B. and Stephansson, S. Rock stress and its measurement. Chapman & Hall, 1996.
2. Hakala, M., Hudson, J.A., Harrison, J.P. and Johansson, E. Assessment of the potential for rock spalling at the Olkiluoto site. Posiva Working Report 2008-83. Available from www.posiva.fi, 2009.
3. Harrison, J.P., Hudson, J.A. and Carter, J.N.C. Is there a relation between the in situ principal stress magnitudes in rock masses? Proc. 1st Canadian-US Rock Mechanics Symposium, Vancouver, Canada. 2007.
4. Harrison, J.P. and Hudson, J.A. Incorporating parameter variability in rock mechanics analyses: fuzzy mathematics applied to underground rock spalling. Rock Mechanics and Rock Engineering, 2009. (in

press).
5. Hoek, E. and Brown, E.T. Underground Excavations in Rock. Institution of Mining and Metallurgy. 1980.
6. Lee, M.F., Mollison, L.J., Mikula, P. and Pascoe, M. In situ rock stress measurements in Western Australia's Yilgarn Craton. Proc. Int. Conf. In situ Rock Stress, Trondheim, Norway, 2006. 35-38.
7. Kaufmann A. and M.M. Gupta, 1991. Introduction to fuzzy arithmetic: theory and applications. New York, Van Nostrand Reinhold.
8. Martin, C.D. and Christiansson, R. Estimating the potential for spalling around a deep nuclear waste repository in crystalline rock. Int. J. Rock Mech. Min. Sci., 2009. 46. 219-228.

RaSiM 7(2009): Controlling Seismic Hazard and Sustainable Development of Deep Mines, C.A. Tang(ed), Rinton Press, 55-58

SEISMIC HAZARD EVALUATION IN UNDERGROUND CONSTRUCTION: THEORY AND PRACTICE

PETER KAISER

Centre for Excellence in Mining Innovation, Sudbury, Ontario, Canada

The nature of Web systems is substantially different from more conventional software systems. They are developed in shorter timeframes, often act as the direct interface between multiple stakeholders, meet a more generic set of requirements, and generally serve a less specific user group. They are often developed very quickly from templated solutions, using coarse-grained authoring tools, and by the efforts of a multi-disciplinary team. There is often considerable uncertainty on the part of the client as to their own requirements. The importance of defining the objectives of the system during the early stages of a project are generally acknowledged to be important, but access to the tools and templates can encourage developers to build too early. Often requirements are inadequately documented, or only emerge during development, or change as development proceeds.

1 Introduction

This keynote highlights recent developments in mining-induced seismicity research and development of procedures and tools for mine operators based on experience in the Sudbury Basin, Ontario, Canada. The basin hosts major copper-nickel sulphide deposits that have been minded since the early 1900's. With over a century of mining, most operations are producing at greater depth where seismicity is a concern and seismic monitoring is now standard practice.

Many mines and deep tunnels are plagued with strainbursts that are either triggered by seismic events or self-initiated due to stress concentrations near excavations. This topic will be covered in Part I for civil and mining applications. The rest of the paper is divided into three parts dealing with structurally-induced seismicity and the procedures and tools developed to aid mine operators in dealing with seismic hazard through the use of Seismic Excavation Hazard Maps, and finally with integrated modeling approaches for mine-wide seismicity assessment.

2 Stress Induced Seismicity –Strainbursts

Self-initiated rockbursts occur when the stresses near the boundary of an excavation exceed the rockmass strength and failure proceeds in an unstable or violent manner. The stress deviator near an excavation increases as an excavation is advanced and eventually, particularly in brittle rock, fails with various degrees of energy release. During mining, the stress state is further disturbed and may lead to a further stress increase and thus an increased strainburst potential. Finally, remote seismic events (e.g., fault slip events) may add a dynamic stress component and thus trigger strainbursts. In addition, the rockmass strength may degrade with time or with loss of confinement, leading to sudden failure. In either case the rockmass strength-to-stress ratio reaches unity and the rock fails. The failure process is sudden and violent if the stored strain energy in the rockmass is not dissipated by the supported rock near the excavation boundary. The strainburst potential is particularly high when the stiffness of the loading system, i.e., the mine stiffness, is lower (soft) than the unstable failure unloading stiffness of the volume of failing rock. The various causes of strainburst will be explained and guidelines for anticipated rock mass behavior prediction will be provided.

3 Mine Wide Seismic Migration - Channel Element Model

Mining-induced stress changes during excavation are generally associated with rockmass displacements, which are enhanced by chains of rotations of discontinuous rock mass blocks. These may lead to rockmass slip along pre-existing discontinuities or fracturing of massive or moderately jointed rock. As a result, seismic events not only occur in the rockmass near the boundaries of mine excavations or on excessively stressed geological structures; in deep mines, they can migrate far, at the mine-wide scale, from a triggering event. This type is more problematic and may be destructive to mining production due to their apparently unpredictable characteristics. The concept of gravity-driven and thus displacement dependent mine-wide seismicity migration will be explored. A novel approach, the Channel Element Model (CEM), based on rockmass displacement and chain-like rotational movement, will be introduced (Figure 1) and explored. CEM is a mathematical model that describes the time dependent migration and remote interactions from source disturbances. In contrast to mechanical contact interactions by the Discrete Element Method (DEM), or constitutive relations by the Finite Element Method (FEM) to model near source disturbance responses, the CEM describes the phenomenon of gravity-driven displacement and thus stress and rockburst migration.

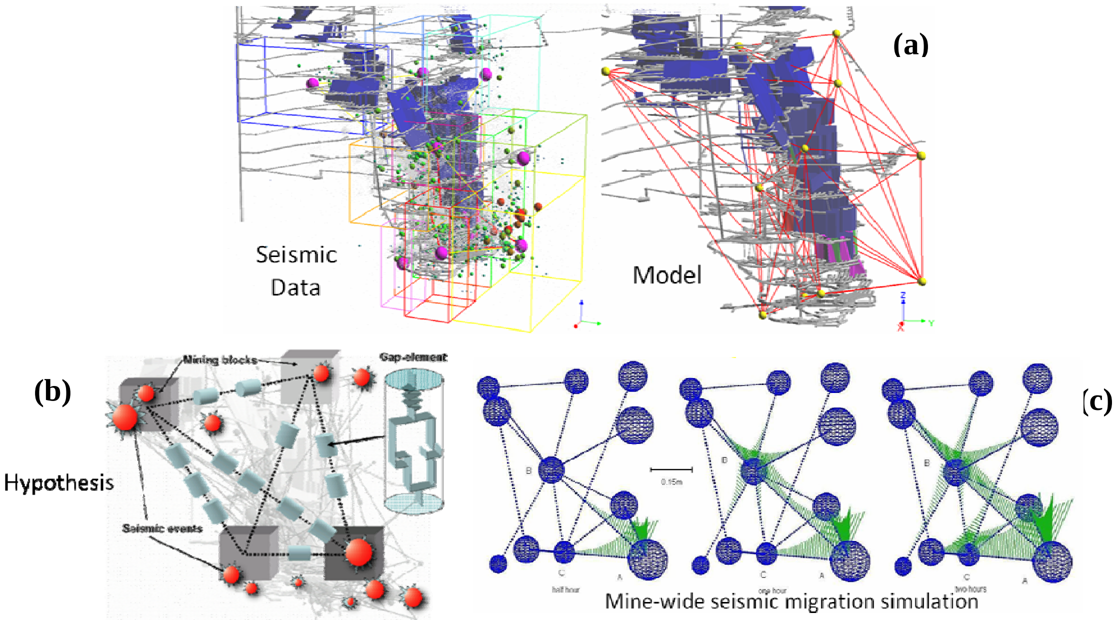

Figure 1: Mine-wide seismic migration model (Channel Element Model). (a) seismic data and (b) time linkages between events in mining blocks; (c) hypothetical model illustrating possible linkage characteristics consisting of time-dependent and deformation-dependent elements; (d) modeled migration patterns as a function of time (green showing influence function)

4 Scientific Visualization using Virtual Reality - Seismic Excavation Hazard Maps

MIRARCO has pioneered the use of virtual reality (VR) technology for solving complex problems in the underground mining. The technology, first introduced for earth modelling in the oil and gas sector, is well suited for multidisciplinary evaluation of information at all stages of the mining cycle. VR has proven to be beneficial in developing 3D geology models, planning exploration drilling and developing resource models. Furthermore, MIRARCO's developments has demonstrated that it can also be extended to handle spatiotemporal data used for planning mine infrastructure, optimizing stope sequences and using mine monitoring data to understand how production practices impact the safety of the operation. The latter is particularly relevant to deep mining where rockbursts can have an adverse effect on both safety and the economic viability of an operation. VR and visual interpretation is quickly shifting the data analysis paradigm for highly complex engineering problems. While we have been applying the technology to other fields such as stope stability assessments, in this section, we focus on the development and application of the Seismic Excavation Hazard Maps for deep mines (Figure 2). The technology has matured to the point where it now can be used on real-time data and it is thus fitting to integrate virtual reality and scientific visualizations methods, with large screen, immersive, stereoscopic visualization capability at mine sites. MIRARCO had established such facilities at Mines of Goldcorp, Vale Inco, and Kennecott (Rio Tinto). Related case examples will be used during the lecture.

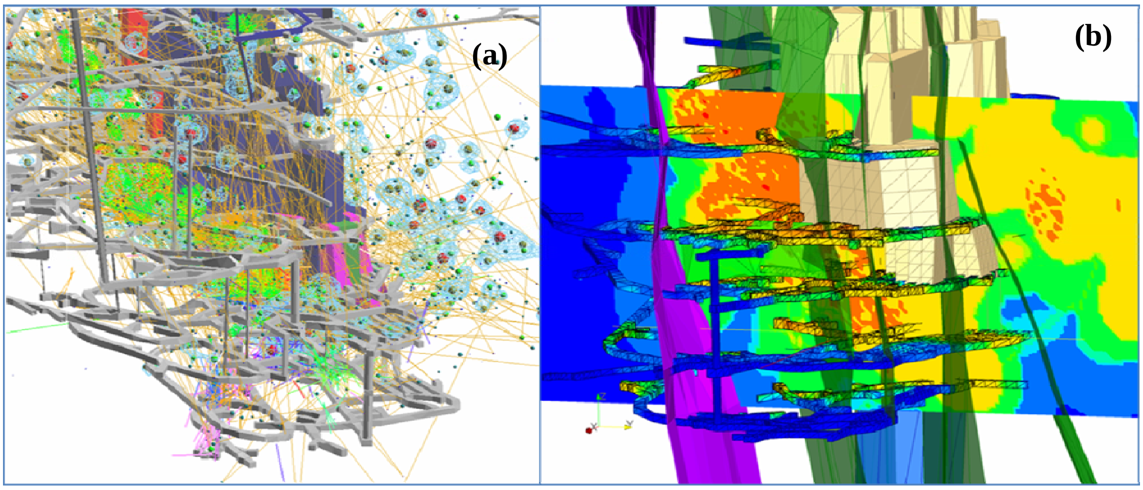

Figure 2: Seismic data processed to create the Seismic Excavation Hazard Map: (a) Seismic and micro-seismic data with colored density contours and time links (in yellow); (b) Seismic hazard map with drifts colored by hazard level (also shown is vertical plane of enquiry)

5 Integrated Modeling Approach - Garson Mine Case Study

Recent experience in structurally complex mining environments, such as the Sudbury Basin, a meteorite impact crater having undergone deformation from ancient tectonic collisions, shows that sudden shear deformation along large scale structural features (fault zones) can occur in unexpected areas and at distances (>200 m away from active mining areas). As mines move deeper the risk for unexpected major seismic events (>2.0 Mn; Nuttli magnitude) to occur increases. The mechanics of sudden seismic energy release in structurally complex environments requires the implementation of a global or holistic understanding of the structures, their characteristics, and interactions. Only then can the complex dynamic behavior of a mine involving geological structures, mining induced perturbation and occurrence of seismic events be captured. Based on such holistic models it is then possible to mitigate risks by implementing strategic geomechanical management practices in order to minimize hazardous ground exposure to mine personnel and ensure stakeholder value is maintained. This section discusses the use of an integrated approach using engineering geology models based on complex geologic, seismic data and numerical modeling data for one case study in the Sudbury Basin.

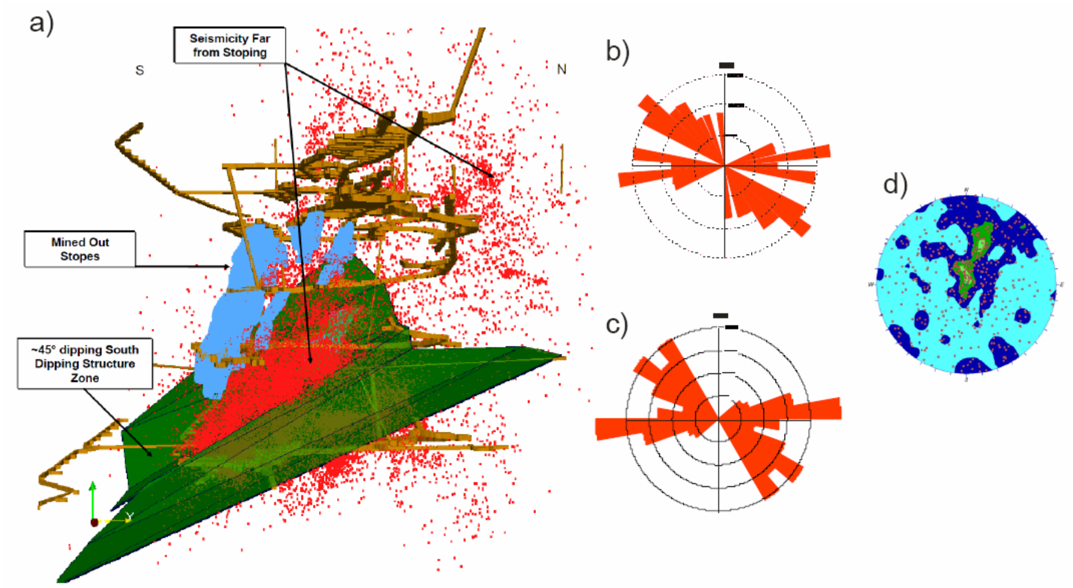

Figure 3: Seismic data related to geological structures: (a) Location of microseismic-events relative to mine infrastructure; (b) Rosette diagram of high density seismic trends; (c) Rosette diagram of the strike of the main structures; and (d) Stereographic projection of the orientation of seismically active planes determined from event processing (lower hemisphere equal angle)

Acknowledgments

The author is deeply appreciated to S. Maloney, P. Vasak, G. Wang and R.P. Bewick for their contributions of this paper.

RaSiM 7(2009): Controlling Seismic Hazard and
Sustainable Development of Deep Mines,
C.A. Tang(ed), Rinton Press, 59-72

PROBABILISTIC SEISMIC HAZARD ANALYSIS FOR MINING-INDUCED SEISMICITY

STANISŁAW LASOCKI

Faculty of Geology, Geophysics and Environmental Protection, AGH University of Science and Technology,
al. Mickiewicza 30, 30–059 Kraków, Poland

Many examples have shown that the seismic activity accompanying underground mining works can be hazardous both to underground staff and mining installations, as well as to ground structures. Due to their shallow focal depth, smaller as compared to natural earthquakes mining seismic events can give rise to damaging ground motion.

The probabilistic seismic hazard analysis (PSHA) is a standard tool to estimate expected seismic impacts of earthquakes. Mining-induced seismicity, however, significantly differs from the earthquake process. First, the seismic activity in mines is predominantly controlled by time-varying mining works, therefore the active zones are, by their nature, transient. Moreover, even during their lifetime, the activity of these zones is not stationary but changes considerable. Second, due to the heterogeneity of the rockmass fracturing process in mines, the magnitude distribution of seismic events induced by exploitation is complex and its modeling based on the Gutenberg-Richter's relation usually leads to large systematic errors of hazard parameters. Third, the ground motion resulting from weak mining seismic sources is strongly influenced by local path and site conditions and the attenuation relations from one region are poorly applicable to the other region. All these differences cause that the standard PSHA methods cannot be readily applied to mining seismic problems. A probabilistic approach to the seismic hazard assessment, radically adjusted to mining seismicity, is presented in this paper. In these modified procedures, locations and times of activity of the seismic zones that will be active in the future are deduced from programs of mining operations. From all mine areas of past seismicity experts select those whose mining and geologic conditions are expected to be similar to the conditions of the zones of future activity. Probabilistic characteristics of the seismic activity of these areas and their changes in time give rise to the alternative time dependent models of the future zone seismic activity. The model-free approach with the non-parametric kernel estimator of magnitude density is applied to represent the source size distribution. This approach ensures cumulative distribution function and related parameters estimate which are free from epistemic uncertainty and have of tolerable aleatory variability regardless the actual complexity of the underlying magnitude distribution. The attenuation relations, used to convert the probabilistic characteristics of the future seismic source into the probabilistic characteristics of the future ground motion, are identified from multiple acceleration signals recorded in the region under study and therefore are linked to local conditions. Estimation of the relative local amplification factors and the use of spectral ordinates in addition to the peak motion amplitudes reduces uncertainty of this step of the hazard analysis. The alternative possibilities of the seismic process development in the future zones and the variants of ground motion generation and propagation are combined with the logic tree approach. The presented mining-induced seismic hazard assessment method is illustrated be a practical example from Legnica-Głogow copper mining area in Poland.

1 Introduction

Many examples have shown that the seismic activity accompanying underground mining works can be hazardous both to underground staff and mining installations, as well as to ground structures. Due to their shallow focal depth, smaller, as compared to natural earthquakes, mining seismic events can give rise to damaging ground motion. Figure 1 presents ground motion generated by an induced seismic event from the underground copper mine Rudna in Legnica-Glogow Copper District (LGCD) in Poland. The event occurred on May 21, 2006 during mining works at the border of town Polkowice. The event magnitude was 4.2. The ground motion was recorded at the epicentral distance of about 1 km. The peak horizontal component of ground acceleration in the frequency band limited to 10 Hz was at that point PHA = 1.67 m/s^2, the peak horizontal velocity was PHV = 11.9 cm/s and the peak horizontal displacement was PHD = 1.6 cm. The elastic response spectrum of the *x*-component of ground motion (Figure 1d) has two distinct peaks, the one at about 6.5 Hz and the second one at about 3 Hz. The latter coincides with the first mode natural frequency of smaller private houses. Due to its epicenter location close to the inhabited area the event resulted in a considerable damage, and in a few cases parts of walls of older buildings were destroyed. Fortunately, the damage area was limited because the ground motion amplitude was fast decreasing with the increasing distance from the epicenter. The peak values of horizontal acceleration and velocity of the ground motion recorded at various epicentral distances from the source are shown in Figure 2. The area of significant seismic impact was apparently no farer than about 1.5 km from the source. At similar and short epicentral distances from the source, ground motion peak amplitudes were, however, much different.

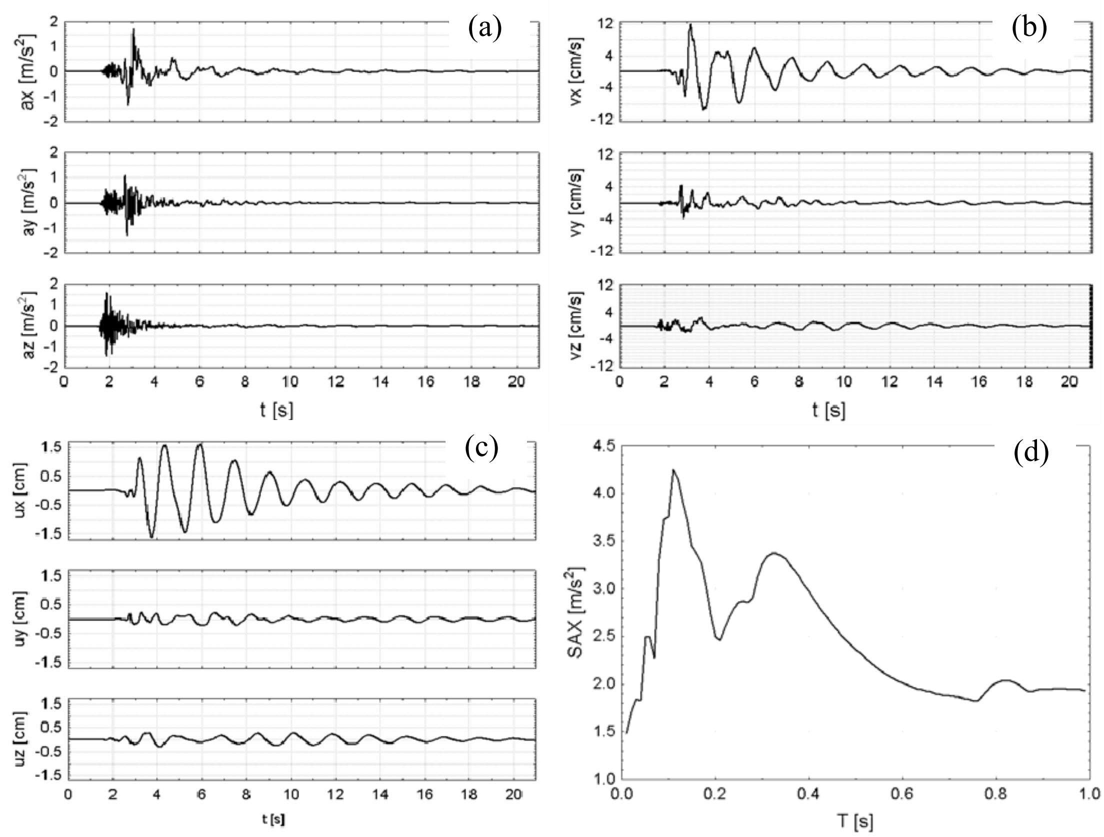

Figure 1 Ground motion recorded at the epicentral distance of 1 km from a mining seismic event of magnitude 4.2 that occurred in Rudna copper mine on May 21, 2006. (a) acceleration, (b) velocity, (c) displacement time history, (d) absolute acceleration response spectrum of *x*-component, damping 5%

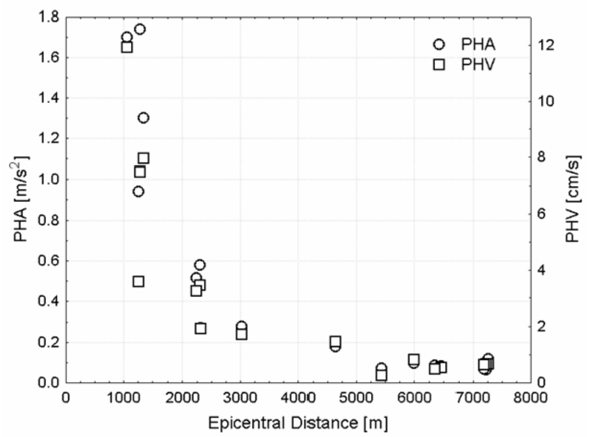

Figure 2 Recorded peak ground acceleration and peak ground velocity at various epicentral distances from the M4.2 mining seismic event from May 21, 2006.

The following conclusions can be drawn from the presented and similar examples:

- Mining seismic events occur at shallow depths and therefore, when the epicentral distance is short, these relatively weak events can generate strong ground motion which can result in considerable damage to ground objects;
- Ground motion due to stronger mining events can comprise significant low frequency components that can impact on structural elements of ground structures;
- Ground motion resulting from weak mining seismic sources is fast attenuated with the increasing distance from the source and is strongly influenced by local path and site conditions.

The probabilistic seismic hazard analysis (PSHA) is a standard tool to estimate expected seismic impacts of earthquakes. After the pioneer Cornell's work [2] the PSHA problem is usually formulated as estimating at the point on the surface (x_0,y_0) the limiting value, a_{max} of the ground motion amplitude parameter, $a(x,y;D)$ whose exceedance probability in D time units takes the assigned, usually small value, p:

$$p = \Pr\left(a\left(x_0, y_0; D\right) \geq a_{\max}\right). \tag{1}$$

For weak seismic sources, like those induced by mining operations, source dimensions are small compared to the distances to receiving points and under the assumptions on magnitude stability [13], the dependence of ground motion attenuation only on epicentral distance and many other the exceedance probability can be determined as:

$$\Pr\left(a\left(x_0, y_0; D\right) \geq a_{\max}\right) = \int_0^{\infty} \int_{m_{\min}}^{m_{\max}} f_r\left(r\left(x_o, y_o\right)\right) f\left(m \mid n \neq 0, D\right) \Pr\left(a \geq a_{\max} \mid m, r\right) drdm \tag{2}$$

where $f_r(r(x_0,y_0))$ is the probability density of epicentral distance to a receiving point, $r(x_0,y_0)$, implied by a source epicenter probability distribution and the receiving point location, $f(m|n\neq0,D)$ is the probability density of event size, m, conditional upon event occurrence in D time units, $[m_{min},m_{max}]$ is the event size range, and $\Pr(a\geq a_{max}|m,r)$ is the probability that the ground motion amplitude parameter, a, will be greater than a_{max} at the receiver point horizontally distanced of r from the seismic source of size m.

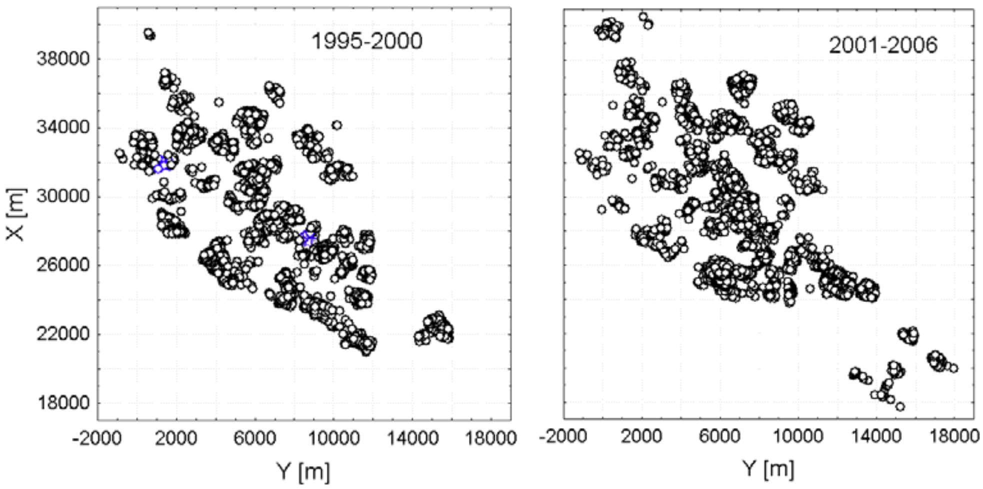

Figure 3 Distribution of seismic event epicenters over the LGCD area in two consecutive six year periods.

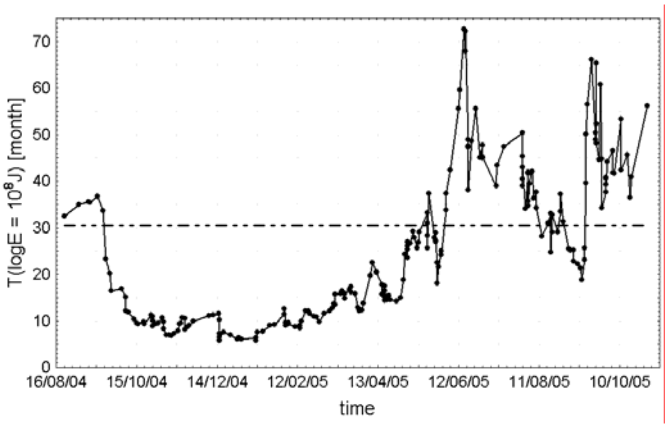

Figure 4 Variation in time of the return period of a 10^8 J and more energy mining event in an individual mining panel region. The mean return period, estimated from all events recorded in the considered 15 months is shown by a horizontal dashed line.

The seismic process in mines differs, however, from the earthquake process in such an extent that the PSHA must be radically adjusted before it can be used in mining-induced seismicity problems. The most important difference results from the fact that the seismic activity in mines is predominantly controlled by time-varying mining works, therefore the active zones are, by their nature, transient. This temporary nature of the mining-induced seismic zones is exemplified in Figure 3. The presented distributions of seismic event epicenters over the area of LGCD from two consecutive six year periods are distinctly different.

Moreover, even during their lifetime, activity of these zones is not stationary but changes considerable. Figure 4 shows estimates of the return period of seismic energy 10^8 J or greater events in a mining panel region. All the estimates have been evaluated in a moving time-window comprising a constant number of events and are attributed to the window middle dates. In the presented 15 months time the return period was systematically changing, being in some periods significantly greater than and in some other smaller than the mean return period estimated from all recorded events and shown by a horizontal dashed line.

The time-dependence of seismic process in mines means that both, the epicentral distance distribution, $f_r(r(x_0,y_0))$ and the conditional event size distribution, $f(m|n\neq0)$ depend on time. Although in our approach to the PSHA for mining-induced seismicity we assume that both these distributions are segmental stationary, however, the dependence of the exceedance probability (eq. 2) only on the duration of study period, D and not on the location of this period on time axis is no longer valid. PSHA results for mining induced seismicity are predictions linked to a prescribed time interval, $[D_1,D_2]$ say.

The second crucial from the point of view of PSHA, unique property of the seismic process in mines, is caused by the heterogeneity of mining rockmass fracturing. Magnitude distribution of seismic events induced by exploitation is complex and its modeling based on the Gutenberg-Richter's relation usually leads to large systematic errors of hazard parameters. The problem has been evidenced and thoroughly discussed in [8] and [11], whereas the unique properties of mining induced seismicity are summarized in [10] and [18] and the reference therein.

The third important characteristic of mining seismicity that must be taken into account in the PSHA results from the above mentioned strong influence of path and site conditions on ground motion. Due to that attenuation relations are very local and those from one region are poorly applicable to the other region.

Depending on the objective of a study we distinguish a regional and a local PSHA for mining induced seismicity. In both approaches locations and life-times of future activity zones are determined based on plans of mining works. Within the regional approach the cumulative impact of many future seismic zones is studied. To reduce the problem complexity it is assumed that probabilistic characteristics of the future zones seismicity will not change in time. These characteristics are deduced from the characteristics of zones active in the past that are the closest in space and time to the future zones.

Within the more detailed local approach an impact of one or maximum a few future seismic zones is predicted. In this approach, however, time changes of the probabilistic characteristics of the future zones seismicity are also taken into consideration. Seismic histories of selected past zones serve as alternative models of seismic activity in the future zones. Selection of the models is done by experts on geology and mining of the studied region. The alternatives are integrated with the use of logic tree approach.

The regional PSHA for mining seismicity was presented during the previous Rockburst and Seismicity in Mines Symposium in Perth in 2005 [9]. Here we discuss the local PSHA on an actual example of the analysis of seismic hazard caused by mining of one mine panel in the underground copper mine in LGCD.

2 Local PSHA for mining-induced seismicity

2.1 Seismic hazard problem of mine panel G-4/8

The Legnica-Glogow Copper District is located in south-west Poland. Copper-ore exploitation is carried on in three underground mines. In a flotation process some 6 per-cent of excavated rock is converted into an ore concentrate and directed to further processing. The rest, some 26 million tons per annum wastes [4], is dumped into the Żelazny Most repository. The repository covers an area of about 12.4 km^2 and is enclosed with 14 km long earth dams. The dams are systematically raised in order to increase the repository's capacity up to the planned final one billion meter cube [12].

The repository is located in an impact region of seismic activity connected with mining operation in the copper mines. Ground motion due to stronger seismic events could threaten the dams stability.

The presented here local PSHA was performed in 2005 in connection with planned exploitation in the mine panel G-4/8. The panel was designed to be located at about 500 m of the minimum horizontal distance to the repository dam. (Fig. 6). An earlier, regional PSHA had indicated that the seismic activity linked to this mining panel could have been hazardous to the dam.

The PSHA problem was formulated as predicting limiting values of ground motion posed on Żelazny Most repository structures by the seismicity induced by exploitation of the mine panel G-4/8. The ground motion parameters were the horizontal, *PHA*, and vertical, *PVA*, peak ground acceleration in the frequency band up to 10Hz. The limiting values were those whose exceedance probability was 0.1 (10 per-cent) in a prediction horizon, and the prediction horizon covered six year (2006-2011) planned period of mining works in the panel G-4/8.

2.2 Expected activity time and epicentre distribution in the zone of future seismic activity

It is assumed that the seismic activity that is expected to appear in the future is closely linked in time-space to mining works. Based on observational experience (e.g. [1], [3]) the future zone of seismic activity is supposed to extend over the area of planned mining works plus a 200-meter margin around the area and to last for the period of these works plus six month. Unlike in the regional PSHA, where seismic source epicenters are assumed to be uniformly distributed in such an area, within the local PSHA approach possible time changes of the epicenter distribution are also taken into considerations. We have, however, no reliable functional model of these time changes, neither of any other probabilistic characteristics of the future seismic activity. In this connection a compromising approach is accepted consisting in splitting the expected activity period into segments in which particular characteristics, e.g. the epicenter distribution, can be regarded as stationary. In the case of the epicenter distribution such segmentation of the activity period is based on detailed mining plans. Figure 5 shows a plan of exploitation of the panel G-4/8. Mining works are divided into four parts, presented by different shading, related to four consecutive time periods. Accordingly, four different epicenter distributions, associated with the respective time periods, were assumed. Each one was the uniform distribution in the respective part of the panel.

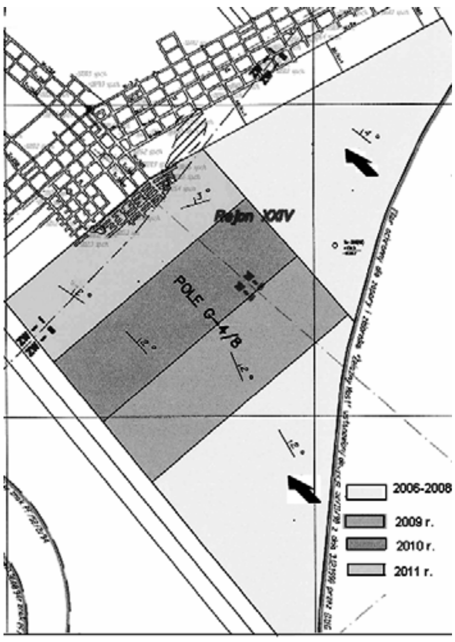

Figure 5 Exploitation plan of the panel G-4/8.

2.3 Models of future seismic activity

Characteristics of seismic activity of a future zone are obviously unknown and can be only deduced from the characteristics of the zones that were active in the past. Needless to say, accuracy of the PSHA results strongly depend on the degree of similarity between the activity of the past zones modelling the future zone activity and the actual activity of the future zone. In the case of local PSHA a selection of the past zones to model the future zone activity is based on the similarity of mining and local geological conditions of the past and future zones and is done by experts in the field. Figure 6 present a fragment of mining map showing schematically location of the planned panel G-4/8 and locations of other, already mined panels. The expert selected the panels G-22/4, XVIII/1 and G-23/4 to be used alternatively for modelling of the panel G-4/8 seismic activity. To overcome estimation problems resulting from small sample size and to enhance accuracy of estimates we added a fourth model consisting of combined activity connected with the panel G-22/4 and the panel XVIII/1. Moreover, due to the geographical proximity we included into the analysis also the activity of panels G-24/4 and G-6/7. This activity built two other models for the panel G-4/8 activity, but, as is shown below, weights of these two models were smaller than the weights of the first four expert-determined models. Hence, altogether six models of the panel G-4/8 seismic activity were distinguished: S1 related to the seismicity of the mine panel G-22/4, S2 related to G-23/4, S3 to XVIII/1, S4 to G-22/4+XVIII/1, S5 to G-6/7 and S6 to G-24/4. The models were grouped in two alternative groups. The first one, A1, consisted only of the expert selected models S1-S4 and the second one, A2 comprised the expert selected models, S1-S4 and the models resulted from the geographical proximity criterion, S5 and S6.

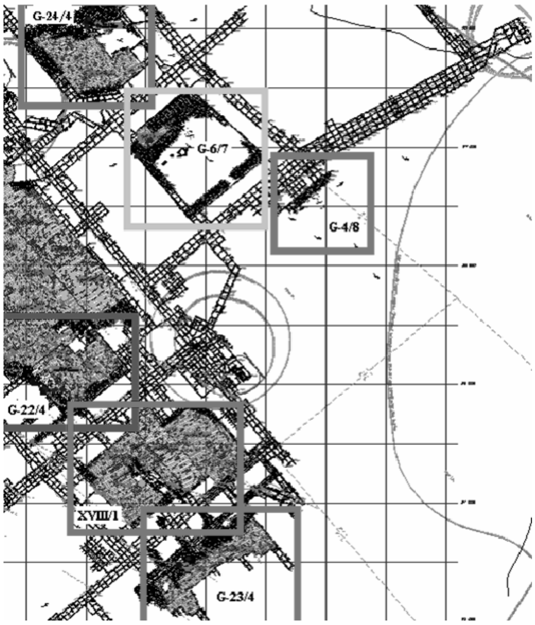

Figure 6 Location of the panel G-4/8 and the panels, which seismic activity modelled alternatively the activity of G-4/8.

In the next step, time variability of the seismic activity of each of the selected model-panels was analyzed in details with the aim to distinguish the periods for which this activity could be regarded as stationary. The activity was parameterized by the exceedance probability of E_p=10^8 J event occurrence in 6 months. The exceedance probability

$$R(\log E_p, D) = 1 - \exp\{-\lambda D[1 - F_{\log E}(\log E_p)]\}, \tag{3}$$

where λ is the mean event rate and $F_{\log E}(\bullet)$ is the cumulative distribution function of logarithm of seismic energy, combines the activity rate and the event size distribution and therefore is particularly suitable as a one-parameter representation of the seismic activity. It was used only to trace the time-variability of activity, thus the particular choice of its internal parameters: the event energy equal to 10^8 J and the waiting period equal to 6 months was not important. Every other combination of these two parameters would result in the same picture of the activity time-variation. The exceedance probability was calculated in a moving window comprising constant number of events. To enable estimation of R from a small number of events in the window, the unlimited Gutenberg-Richter relation based model for the logarithm of seismic energy distribution was applied in this part of the analysis. An example of variations in time of the exceedance probability, R is shown in Figure 7. In this case the whole period of activity, presented in the figure, was divided into 5 'stationary' segments. The division of all the G-4/8 activity models was the following: S1 – into 5 stationary segments, S2 – 2 segments, S3 – 1 segment, S4 – 5 segments, S5 – 4 segments, S6 – 2 segments.

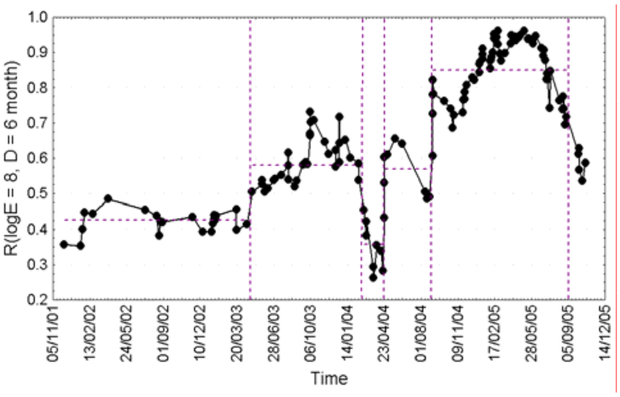

Figure 7 Time-changes of the seismic activity that was used as one of the alternative models of the panel G-4/8 activity. The vertical lines divide the whole time period into segments where the activity is regarded as stationary.

When active periods of past zones modeling the future zone activity are divided into stationary segments, the seismic data linked to these segments are used to estimate the respective mean activity rate and the event size distribution. Due to the mentioned in Introduction complexity of event size distribution of the seismic events in mines, the estimation of this distribution is done by means of a model-free method, namely the non-parametric, kernel density estimator [17]. We apply an adaptive version of this estimator, [16], [11] and the smoothing factor is selected based on a least-square validation criterion, [6]. The generic formula after Kijko [5] is used for the estimation of an upper limit of the event size distribution. Details of the approach are presented in the cited publications and the references therein. After this part of the analysis every stationary segment of every model of the future seismicity has its own activity rate, λ and event size distribution, $f_m(m)$ estimates.

The division into the stationary segments of every individual activity model is next mapped onto the planned period of mining works in the analyzed future activity zone and combined with the planned division of mining works in this zone. Such a combination leads to splitting of the period of expected seismic activity of the future zone into a number of consecutive segments. Each segment has its own probability density of event size, conditional upon event occurrence $f(m|n\neq 0,[D_b,D_e])$ (eq. 2), where $[D_b,D_e]$ time-interval defines this segment. This conditional probability density results from the activity rate, λ and event size distribution, $f_m(m)$ of the respective stationary segment of the activity model and takes the form of:

$$f\left(m \mid n \neq 0,\left[D_b, D_e\right]\right)=\frac{\lambda D f_m(m) \exp\left[-\lambda D\left(1-F_m(m)\right)\right]}{1-\exp(-\lambda D)} \tag{4}$$

where D=D_e-D_b, and $F_m(m)$ is the cumulative distribution of the event size. Furthermore, each segment has its own probability density of the epicentral distance to the receiving point, $f_r(r(x_0,y_0))$ (eq. 2), resulting from the epicenter distribution assumed for the respective part of the planned mining works. For instance, the combination of the division of activity model S1 into 5 segments having specific activity rates and the division of mining works of G-4/8 into four parts resulted in splitting the expected period of activity of G-4/8 into 7 consecutive segments. Each of these segments had a unique combination of the conditional distribution of event size, inferred from the model S1 and the epicentral distance distribution, implied by planned location of mining works within the panel G-4/8 (see: Section 2.2). Such a segmentation procedure applied to other activity models distinguished 5 segments for the model S2, 4 segments for the model S3, 7 segments for the model S4, 7 segments for the model S5 and 4 segments for the model S6.

2.4 Conditional probability of ground motion amplitude

The conditional probability of ground motion amplitude, $\Pr(a \geq a_{max}|m,r)$, given the event size m and the epicentral distance from the source, r, (eq. 1) results from a relationship linking the amplitude parameter to m and r. Such relationships are called in the engineering seismology the attenuation relations and usually take a form of the linear regression for the logarithm of amplitude parameter. In the mining-induced seismicity hazard problems, where sources are generally weak, the area of significant ground motion is limited to an epicentral region and its direct surrounding. Due to that an anelastic attenuation is less important than a geometrical spreading and site effects and the attenuation relation which we usually adopt reads, [9]

$$\log a(x,y) = \alpha + \beta \log E + \gamma \log \sqrt{r^2 + h^2} \tag{5}$$

where the logarithm of seismic energy, E stands for the events size, m, and α, β, γ, h are the coefficients specific for local conditions of ground motion propagation. The h is a common depth factor and ensures nonlinearity of the relationship (5) in the epicentral region. Occasionally, we enrich the attenuation relation (5) with relative local amplification factors, [15]. The coefficients of attenuation relations for ground motion generated by mining seismic events are very local and change strongly from one region to another, therefore their identification should be based on ground motion measurements from the region under study. In the case of the panel G-4/8 problem two these kind of relationships were available, referred to as R1 and R2, respectively. The one was identified from 165 ground motion signals recorded solely on the Zelazny Most repository dams, whereas the second one was constructed with the use of 961 signals recorded on the dams and in the western foreland of the repository. From the overall statistical quality standpoint the second model was much better than the first one.

The conditional probability of ground motion amplitude, $\Pr(a \geq a_{max}|m,r)$ is obtained from the upper limit of confidence interval of an attenuation relation. When a large number of observation is used to estimate coefficients of the relationship (5), the (1-2p)-probable approximate limits of the confidence interval for prediction for this relation read, [9]:

$$\log a(x,y) = \alpha + \beta \log E + \gamma \log \sqrt{r^2 + h^2} \pm z_p \sqrt{\mathbf{X}^{\mathbf{T}} \mathbf{C_b} \mathbf{X} + SEE^2} \tag{6}$$

where z_p is the critical value of standard normal distribution, $\mathbf{X} = \begin{bmatrix} 1 \\ \log E \\ \log \sqrt{r^2 + h^2} \end{bmatrix}$ and $\mathbf{X^T}$ is its transposition, $\mathbf{C_b}$ is the covariance matrix of regression (5) coefficient estimators, and SEE is the standard error of estimate. From (6) the conditional probability of ground motion amplitude reads

$$\Pr\left(a \geq a_{\max} \mid \log E, r\right) = 1 - \Phi\left(\frac{\log a_{\max} - \alpha - \beta \log E - \gamma \log\sqrt{r^2 + h^2}}{\sqrt{\mathbf{X}^{\mathrm{T}}\mathbf{C}_{\mathrm{b}}\mathbf{X} + SEE}}\right) \tag{7}$$

where Φ(•) is the standard normal cumulative distribution function.

2.5 Logic tree integration of alternative possibilities of source and propagation characteristics

The analysis steps described in 2.2 – 2.4 provide a number of alternative probabilistic characteristics of seismic source and a number of alternative attenuation relation. For the case of panel G-4/8 we had two groups of the source characteristics alternatives, A1 and A2. The groups comprise four: S1-S4 and six: S1-S6 alternatives. Each of the alternatives S1-S6 consisted of a certain number of unequal duration consecutive time segments, that in total covered the planned period of the seismic activity expected to appear during G-4/8 exploitation. For every segment, in turn, we had a unique combination of the two: the probability density of event size, conditional upon event occurrence in this segment and the probability density of epicentral distance to a receiving point. We had also two alternative attenuation relations, R1 and R2, hence two conditional probabilities of ground motion. All such alternative possibilities are integrated by means of the logic tree scheme (eg. [14], [7]).

The logic tree is a scheme of process development possibilities, consisting of branches and nodes. Each node is a point where the process branches into further possibilities whereas each branch represents one of these possible ways, which the process can take continuing from the node. One chain of branches starting from the beginning of process and ending at its end constructs a path. The logic tree scheme for the considered case of hazard associated with the panel G-4/8 seismicity, shown in Figure 8, consists of 20 paths.

Every logic tree branch has its own probability to be chosen, and the sum of these probabilities for all branches starting from a node equals one. The probability that the process follows a particular path equals to the product of probabilities of the branches comprising the path.

The branch probabilities for the scheme presented in Figure 8 were chosen somewhat arbitrarily in the following way:

(1) We had more confidence in the expert selected models of G-4/8 seismicity than in the models selected based on the geographical proximity criterion. Therefore the group A1 that comprised only the expert selected models received the branch probability Pr(A1)=0.6, whereas the probability of the group A2 including all the expert and the 'geographic' models was Pr(A2)=0.6.

(2) The expert did not discriminate the selected panels of past mining (G-22/4, G-23/4, XVIII/1) from the point of view of their usefulness to model the future seismicity of G-4/8. It was, therefore reasonable to attribute to these three possibilities equal probability. However, due to the practical reasons mentioned in Section 2.3, we constructed four alternative seismic activity models (S1-S4) from the seismic data linked to these three panels. To maintain the probabilities associated with these three panels equal, the branch probabilities of the alternative seismic activity models S1-S4 within the group A1 had to be: Pr(S1|A1)=2/9, Pr(S2|A1)=1/3, Pr(S3|A1)=2/9, Pr(S4|A1)=2/9.

(3) There was no reason to discriminate the panels of past mining that built the models of G-4/8 future activity within the group A2. Our belief that the expert selected models were more trustworthy than the 'geographic' models was expressed by the difference between the branch probabilities of A1 and A2 groups and by the fact that the expert selected models were included to both groups, whereas the geographic models only to A2. Taking into account also the above presented consequences of having four activity models from three mine panels indicated by the expert, the branch probabilities of the

seismic activity models S1-S6 within the group A2 were: Pr(S1|A2)=2/15, Pr(S2|A2)=1/5, Pr(S3|A2)=2/15, Pr(S4|A2)=2/15, Pr(S5|A2)=1/5, Pr(S6|A2)=1/5.

(4) As mentioned in 2.4 the attenuation relation R2 was much more reliable than the attenuation relation R1. Therefore we assumed that ground reaction to seismic excitation according to R2 had probability Pr(R2)=0.8, whereas that according to R1 – Pr(R1)=0.2.

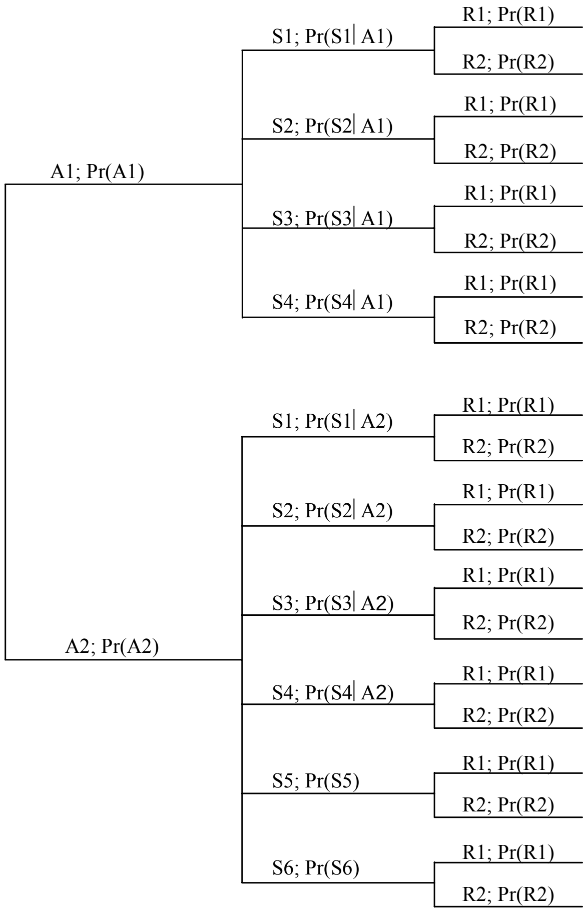

Figure 8 Logic tree used to integrate all possibilities of the seismic hazard linked to mining works in the mine panel G-4/8. See: text for further explanations.

One of the last things that should be addressed are consequences of the fact that in our approach a seismic activity model is split into a number of consecutive time segments, each having its own characteristics of the seismic activity. For instance let us consider the logic tree path #1: A1→S1→R1. The model S1 is divided into 5 segments. Let these segments be defined by $[D_1, D_2]$, $[D_2, D_3]$, $[D_3, D_4]$, $[D_4, D_5]$, $[D_5, D_6]$ time intervals of the expected total period of seismic activity linked to mining of G-4/8, $[D_1, D_6]$. Let the unique combination of the conditional probability density of event size and the probability density of epicentral distance be $\{f^{(1)}(m|n\neq0,[D_1,D_2]),\ .f_r^{(1)}(r)\},\ldots,\ \{f^{(6)}(m|n\neq0,[D_1,D_2]),\ .f_r^{(6)}(r)\}$, respectively. The total probability that in the time interval $[D_1, D_6]$ the ground motion amplitude exceeds at point (x_0,y_0) the value of a_{max} is

$$\Pr\left(a\left(x_0, y_0\right) \geq a_{\max}\right) = 1 - \prod_{k=1}^{5}\left[1 - \Pr_k\left(a\left(x_0, y_0\right) \geq a_{\max}\right)\right] \quad (8)$$

where $\Pr_k(a(x_0,y_0)\geq a_{max})$ is evaluated according to (1) using appropriate probability densities $f^{(k)}(m|n\neq 0,[D_k,D_{k+1}])$, $.f_r^{(k)}(r(x_0,y_0))$ and the conditional probability of ground motion resulting from the attenuation relation R1. The probability (8) determines chances to exceed a_{max} if the seismic hazard is controlled by factors constructing the path A1→S1→R1. Therefore the exceedance probability attributed to this path is

$$\Pr\left(a\left(x_0, y_0\right) \geq a_{\max} \mid Path\,1\right) = \Pr\left(A1\right)\Pr\left(S1 \mid A1\right)\Pr\left(R1\right)\left\{1 - \prod_{k=1}^{5}\left[1 - \Pr_k\left(a\left(x_0, y_0\right) \geq a_{\max}\right)\right]\right\}. \tag{9}$$

The total probability that $a(x_0,y_0)\geq a_{max}$ due to the seismic activity connected with mining of G-4/8 is:

$$\Pr\left(a\left(x_0, y_0\right) \geq a_{\max}\right) = \sum_{i=1}^{20}\Pr\left(a\left(x_0, y_0\right) \geq a_{\max} \mid Path\, i\right). \tag{10}$$

We have to invert eq. 10 because we are interested in the ground motion limiting value a_{max}, given the exceedance probability $\Pr(a(x_0,y_0)\geq a_{max})=p$. The inversion is done in an iterative way where a_{max} is being corrected unless its value fulfills the condition $\Pr(a(x_0,y_0)\geq a_{max})=p$. In the case of panel G-4/8 problem p was set to 0.1.

2.6 Results

In the PSHA for the Zelazny Most repository we calculated the limiting values of the horizontal and vertical peak ground acceleration along the repository dams. Figure 9a presents results of the analysis for the horizontal motion, whereas locations of the points for which the limiting values were evaluated is shown in Figure 9b. An area of the greatest expected impact is on the western dam in the region of points VIIIW and XIIW. The maximum peak horizontal acceleration value of the exceedance probability 0.1 in the future activity period of the region of panel G-4/8 was estimated to be 0.92 m/s^2.

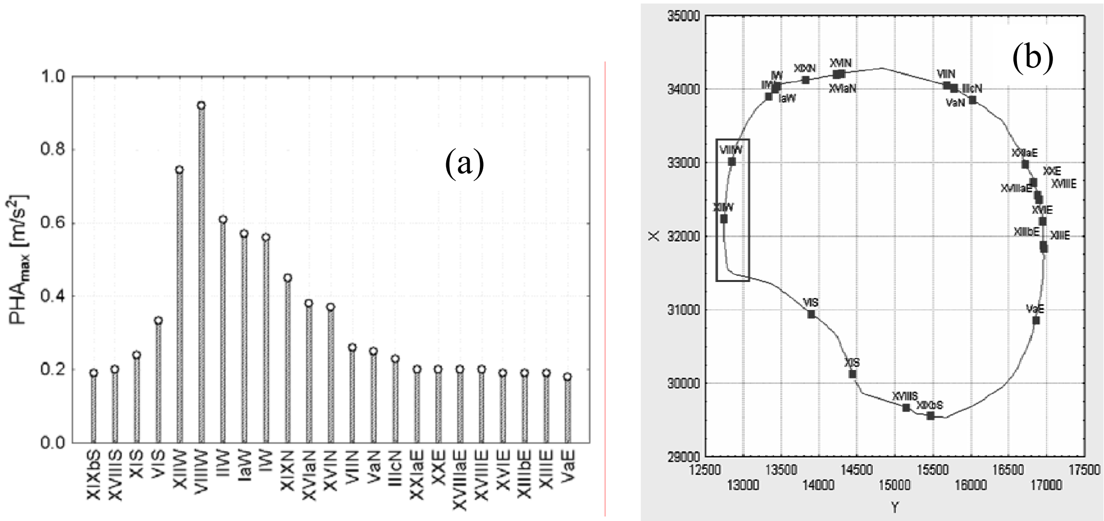

Figure 9 Results of PSHA for the region of Zelazny Most repository. (a) Predicted limiting PHA values at points along the repository dams for the years 2006-2011, linked to mining works in the mine panel G-4/8. (b) Location of the points from (a).

Another feature of the logic tree approach makes it particularly convenient in the PSHA in mining areas. In this scheme it is easy to conclude on possible results of various impact scenarios. We can analyse what could happen if exactly one of the path alternatives were selected as well as we can infer, modifying probability functions associated with particular branches, how mining plans changes (e.g. direction of front advance, work sequences, area mined etc.) can change the seismic hazard. Such an analysis led in the case of G-4/8 problem to turning opposite the front advance direction.

Acknowledgements

This work was prepared within the framework of the research project No. PBS-Grecja/10/2007, financed by the Ministry of Science and Higher Education of Poland during the period 2007 to 2009.

References

1. Cichy, A. and Lasocki, S. Some possibilities of statistical interpreting mining microseismological data from the point of view of estimating rockburst danger. Publs. Inst. Geophys. Pol. Acad. Sci. M-5 (155). 85-100, 1982. (in Polish with English abstract and figure captions).
2. Cornell, C.A. Engineering seismic risk analysis. Bull Seismol. Soc. Am. 58. 1583-1606, 1968.
3. Drzęźla, B., Białek, J., Jaworski, A., Bańka, P. and Słapa W. Distributions of the number and energy of mining shocks nearby active longwall excavations. Publs. Inst. Geophys. Pol. Acad. Sci. M-15 (235). 197-202, 1991 (in Polish with English abstract and figure captions).
4. Jasiński, A. and Janicki, K. Geological Conditions of Influence of Żelazny Most Tailings Dump on Subsurface Water. Proc. Symp. Warsztaty Górnicze, Szklarska Poręba 26-28 May 2003, (ed. E. Pilecka), Wyd. IGSMiE PAN, Kraków, 89-104, 2003. (in Polish).
5. Kijko, A. Estimation of the maximum earthquake magnitude, m(max), Pure Appl Geophys 161. 1655-1681, 2004.
6. Kijko, A, Lasocki, S, and Graham, G. Non-parametric seismic hazard in mines, Pure Appl Geophys 158, 1655-1675, 2001.
7. Kulkarni, R.B., Youngs, R.R., and Coppersmith, K.J. Assessment of confidence intervals for results of seismic hazard analysis. Proc. Eighth World Conf. on Earthquake Engineering, San Francisco, CA, July 21-28, 1984, 1, 263-270, 1984.
8. Lasocki, S. Quantitative Evidences of Complexity of Magnitude Distribution in Mining induced Seismicity: Implications for Hazard Evaluation. Proc. 5th Int. Symp. Rockbursts and Seismicity in Mines "Dynamic rock mass response to mining", Magalisberg, 17-20 September 2001 (eds. G. van Aswegen, R.J. Durrheim, and W.D. Ortlepp) SAIMM S27, Johannesburg, South Africa. 543-550, 2001.
9. Lasocki, S. Probabilistic analysis of seismic hazard posed by mining induced events, Controlling Seismic Risk, Proc Sixth Int. Symp. on Rockburst and Seismicity in Mines 9–11 March, Australia, (eds. Y. Potvin and M. Hudyma), Australian Centre for Geomechanics, Perth, Australia. 151–156, 2005.
10. Lasocki, S. Some unique statistical properties of the seismic process in mines, Proc. 1st Southern Hemisphere International Rock Mechanics Symposium SHIRMS 2008, Perth, 16-19 September 2008, (Potvin, Y., Carter, J., Dyskin, and A., Jeffrey, R., eds.), Australian Centre for Geomechanics, Australia. 667-678, 2008.
11. Lasocki, S. and Orlecka-Sikora, B. Seismic hazard assessment under complex source size distribution of mining induced seismicity. Tectonophysics 456, 28-37 doi:10.1016/j.tecto.2006.08.013, 2008.
12. Lewiński, J. and Wolski, W., eds. Part V – Waste Repositories. In Monograph of KGHM Polska Miedź S.A. (ed. A. Piestrzyński.), CBPM „Cuprum" Sp. z o.o., Wrocław. 787-912, 1996. (in Polish).
13. Lomnitz, C. Global Tectonics and Earthquake Risk, Elsevier Scientific Publishing Company, New York, 1974.
14. McGuire, R.K., and Shedlock, K.M. Statistical uncertainties in seismic hazard evaluations in the United States. Bull. Seismol. Soc. Am. 71. 1287-1308, 1981.
15. Olszewska, D., and Lasocki, S. Attenuation relation for the peak ground acceleration with local amplification for selected regions of Legnica-Głogów Copper District. WUG : Bezpieczeństwo Pracy i Ochrona Środowiska w Górnictwie 6. 19–20, 2006. (in Polish)
16. Orlecka-Sikora, B., and Lasocki, S., Nonparametric characterization of mining induced seismic sources. In: Potvin, Y., Hudyma, M. (Eds.), Controlling Seismic Risk, Proc Sixth Int. Symp. on Rockburst and

Seismicity in Mines 9–11 March, Australia, (eds. Y. Potvin and M. Hudyma), Australian Centre for Geomechanics, Perth, Australia. 555–560, 2005.
17. Silverman, B.W., Density Estimation For Statistics And Data Analysis. Monographs on Statistics and Applied Probability. Chapman and Hall, London, 1986.
18. Węglarczyk, S., and Lasocki, S. Studies of Short and Long Memory in Mining-Induced Seismic Processes, Acta Geophys. 2009. (in print)

RaSiM 7(2009): Controlling Seismic Hazard and Sustainable Development of Deep Mines, C.A. Tang(ed), Rinton Press, 73-74

PART I

UNDERSTANDING SEISMIC HAZARD

RaSiM 7(2009): Controlling Seismic Hazard and Sustainable Development of Deep Mines, C.A. Tang(ed), Rinton Press, 75-80

ANALYSIS OF SMOOTH BLASTING PARAMETERS ON TUNNELS IN SOFT-FRACTURED ROCK MASS

YU-HUA FU, XI-BING LI, LEI ZHANG, LONG-JUN DONG and JUN-JUN WU

School of Resources and Safety Engineering, Central South University

Changsha , 410083, P.R. China

YU-HUA FU

School of Application and Science, Jiangxi University of Science and Technology

Ganzhou, 341000, P.R. China

Smooth blasting may bring good blast effects in the case of high-intensity and integrity rock mass. However, it is difficult for smooth blasting to get a good blasting effect in soft-fractured rock mass if conventional methods are used to design parameters, due to a variety of existing weak surfaces. In this paper, for the soft and fractured rock mass, theoretical formula is put forward for designing parameters of smooth blasting based on coupled interaction theory of explosion shock wave and explosive gas-pressure. The proposed formula are validated by comparing with common parameters and local explosion examination. It is concluded that the formula can be applied to smooth blasting in the soft-fractared rock mass achieving good blasting effects.

1 Introduction

Smooth blasting effect depends on the rock conditions, detonator properties and blasting parameters [1]. Conventional methods of design parameters of smooth blasting are difficult to use to obtain the ideal blasting effect. This is because for soft broken rock mass their exists adverse guidance from forming blasting fracture surfaces during various structural weakness and weak interlayers [2], enormous energy consumption in the rock fracture zone, and rock mass damage in burden of the perimeter.

Smooth blasting parameters are used in accordance with the parameters at home and abroad currently. u the analogy works to be determined. It is impossible to conduct a comprehensive and reasonable inspection for the weak and broken rock in particular during making determination process of parameter, thus affecting the blasting effect; therefore, smooth blasting parameters should be determined by the rocks’ condition and explosives blasting mechanism. In the domestic smooth blasting parameters of theoretical calculation and blasting mechanism on many research [2-10], formed explosion stress waves and detonation gas comprehensive effect of smooth blasting to sew mechanism, obtained some useful conclusions and the theoretical calculation formula. This paper analyzes rock damage on the impact of the smooth blasting based on the stress waves and the blasting gas theory, and puts forward the theoretical calculation. Ways to create parameters of smooth blasting to soft-broken rock mass under the conditions of not considering damage and considering the injury.

2 General theoretical calculation of smooth blasting parameters

Smooth blasting parameters including charging structure and charge, hole spacing and the minimum resistance line. Smooth blasting parameters can be ascertained according to explosive gas and stress wave of explosion.

2.1 Charging structure and charge

Theoretical research and production practice has proved that the reasonable charging structure of smooth blasting in hole are decoupled charge, including the radial clearance and axial cushion decoupling charging structure , more the air as a coupling medium.

2.1.1 Charging structure parameters

Mainly is the coefficient of decoupling of radial Kd and coefficient of decoupling of axial Kl, the two are not mutually independent, but constrained to each other. Determine the parameters of explosive charging structure should be a comprehensive analysis of the following two aspects: it is necessary to make eye-wall initial shock pressure of radial not more than the dynamic compressive strength of rock; and it must make the initial tangential tensile force not less than the dynamic tensile strength of rock. Both established under the style:

$$p_r \le K_D S_c \tag{1}$$

$$K_a p_\theta = \lambda K_a p_r \ge S^D{}_t \tag{2}$$

In type, p_r for the initial eye-wall radial pressure , p_θ for the initial tangential tensile force; K_D for dynamic loads of rock strength increase coefficient, it is desirable K_D = 10, $K_D S_c$ for the dynamic compressive strength of rock; K_a for concentration coefficient of tensile stress, and its value can be obtained Figure 1 [4]; $S^D{}_t$ for the dynamic tensile strength of rock, which was less affected by the loading speed may consider it equal to anti-static tensile strength, that is $S^D{}_t = S_t$.

When both axial and radial-decoupling charge and ignore plug length, the eye wall of the initial pressure can be determined using the following equation

$$p_r = \frac{1}{8}\rho_0 D^2 K_d{}^{-6} K_l{}^{-1} n \tag{3}$$

Type ρ_0 for explosives density, D is detonation velocity, n for the gas pressure of burst collided with eye wall increasing in multiples, it is desirable n = 10.

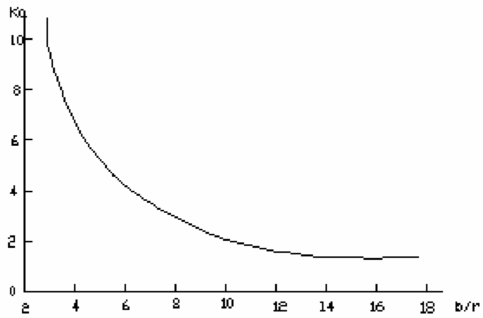

Figure 1 Curve for Stress concentration factor.

When using special small-volume explosives, the coefficient of decoupling of radial is identified, then the axial-decoupling coefficient:

$$\left(\frac{n\rho_0 D^2}{8K_D S_c K_d{}^6}\right) \le K_l \le \left(\frac{n\lambda K_a \rho_0 D^2}{8S_t K_d{}^6}\right) \tag{4}$$

2.1.2 Charge Calculation

When the radial and axial decoupling coefficient is determined, the charge concentration degree is defined

$$q_l = \frac{\pi d_c{}^2 \rho_0}{4K_l} = \frac{\pi d_b{}^2 \rho_0}{4K_l K_d{}^2} \tag{5}$$

q_l for the charge degree of concentration, d_c ,, d_b for charge diameter and hole diameter.

2.2 embrasure spacing E

Determine the borehole spacing has a variety of methods [6], currently being recognized is based on the conbine effect theory of stress wave and blasting gas. The propellant of stress wave produced in their respective borehole wall first, then the initial cracks in the explosion was born under the action of gas pressure, thus creating conditions for cross-cutting cracks can be approximated by the following balance to express [10]:

$$d_b p_b = (E - 2r_k) S_t \tag{6}$$

$$r_k = \left(\frac{\lambda p_r}{S_t}\right)^{\frac{1}{\alpha}} \frac{d_b}{2} \tag{7}$$

α is attenuation index for the stress wave , $\alpha = 2 - \lambda$;; r_k for the initial crack length; p_b for the strees when the gas filled embrasure, can be calculated by isentropic expansion process.

$$p_b = p_k \left(\frac{p_0}{p_k}\right)^{\frac{r}{k}} \left(\frac{v_c}{v_b}\right)^{r} = p_k \left(\frac{p_0}{p_k}\right)^{\frac{r}{k}} K_d{}^{-2r} K_l{}^{-r} \tag{8}$$

k for the entropy index(k =3);; r for the adiabatic index(r =1.2～1.3);; p_k for the critical pressure, calculated desirable 200MPa;; p_0 for initial average gas pressure can be determined using the following equation.

$$p_0 = \frac{1}{8} \rho_0 D^2 \tag{9}$$

According to the formula of 6 - 9 can get calculation formula of hole spacing E:

$$E = d_b \left[\left(\frac{\lambda p_r}{S_t}\right)^{\frac{1}{\alpha}} + \frac{p_k (p_0 / p_k)^{\frac{r}{k}} K_d{}^{-2r} K_l{}^{-r}}{S_t} \right] \tag{10}$$

2.3 Minimum resistance line W

$$m = \frac{E}{W} \tag{11}$$

m hole Concentration coefficient ,usually m =0.6～1.2, taking large values of hard rock, soft rock from a small value.

Blast injury on parameters of smooth blasting

Rock damage to smooth blasting process is complex and has a dual effect, on the one hand, rock damaged, reducing its strength and is conducive to the formation of long radial cracks, increasing the distance and the minimum resistance line; On the other hand, injury also increased the stress wave attenuation coefficient, the lateral stress coefficient reduced, making the explosion in the smooth layer generated by reducing the effective stress is not conducive to the achievement of the larger blast-hole spacing and minimum resistance.

Zhang Chengliang [11], such as the application of dynamic finite element program, set up two-dimensional elastic-plastic model of rock that do not consider the injury and consider the injury in the process of smooth blasting a numerical simulation, and compare the two kinds of model of the maximum effective stress change with distance relations. On this basis proposed: the resistance line and distance can be increased due to increase to hole spacing 1.1 - 1.2 times which do not considering the damaging effects of the blast.

Dai Jun ,Yang YongQi Analysis [12], if rock damage, the hole spacing should be reduce, and the greater degree of rock damage, the greater reduced value of spacing of smooth blasting.

4 Parameters of smooth blasting for damage of rock

After rock damage, its static uniaxial compressive strength, static uniaxial tensile strength and stress wave attenuation coefficient have the following relations:

$$S_{ce} = (1-\zeta)S_c \tag{12}$$

$$S_{te} = (1-\zeta)S_t \tag{13}$$

$$\alpha_e = \frac{\alpha}{1-\zeta} \tag{14}$$

ζ for rock damage factor, C_d for crack density caused by damage.

The decoupling coefficient can express by the following formula after rock damage:

$$\left(\frac{n\rho_0 D^2}{8K_D(1-\xi)S_c K_d{}^6}\right) \le K_l \le \left(\frac{n\lambda K_a \rho_0 D^2}{8(1-\xi)S_t K_d{}^6}\right) \tag{15}$$

Hole spacing:

$$E = d_b\left[\left(\frac{\lambda p_r}{[(1-\xi)S_t]}\right)^{\frac{1-\xi}{\alpha}} + \frac{p_k(p_0/p_k)^{\frac{r}{k}} K_d{}^{-2r} K_l{}^{-r}}{(1-\xi)S_t}\right] \tag{16}$$

Other formulas unchanged.

5 Engineering application

A mine in Henan province the main ore body is located in tectonic belt broken, the broken rock and ore body structure, low intensity, to be natural caving mining. Test mining block is located 505m - 540m level, and some electric rake tunnels are located in granite, mylonite migmatite of fragmentation, the electric rake design gross section 2.2m × 2.2m, length 40m - 48m. According to interior test, uniaxial compressive strength of rock check 30Mpa, uniaxial tensile strength 3Mpa, Poisson's ratio of 0.25.

hole diameter d_b = 40mm, the design hole length 1.5m. Selection 2 # Rock AN-TNT explosive, density ρ_0 = 1.0g/cm3, explosives detonation velocity D = 3200m / s, roll diameter drugs d_c = 25mm.

Based on the above theoretical analysis, we can see that the radial-decoupling coefficient K_d =1.6, uniaxial decoupling coefficient range from 2.54 $\leq K_l \leq$ 127, thus to know the degree of concentration of charge for 0.04kg/m$\leq q_l \leq$0.19kg/m , Combined engineering experience, check q_l =0.12kg/m ,,Calculated K_l =4.08

which can get hole spacing and the smallest resistance line , the results shown in Table 1.

Table 1 Electricity harrow roadway main parameters of smooth blasting

Ways to determine the parameters		K_d	K_l	q_l (kg/m)	E (mm)	W (mm)	m
Theory of Law	Excluding damage	1.6	4.08	0.12	527	759	0.69
	Included damage	1.6	4.08	0.12	474	683	0.69
Engineering analogy		1.6	4.08	0.12	500	600	0.83

6 Conclusion

The more broken the rock, the lower the strength, the quasi-static pressure, the more obvious, therefore, an explosive stress wave and quasi-static gas pressure should be included in weak and broken rock mass conditions when calculating smooth blasting parameters. Rock damage on the role of smooth blasting processes are complex, on the one hand, rock damaged, reducing its strength and is conducive to the formation of long radial cracks, increasing the distance the smallest surrounding hole resistance line. On the other hand, damage also increased the stress wave attenuation coefficient, the lateral stress coefficient reduced; making the explosion in the smooth layer generated by reducing the effective stress not conducive to the achievement of the larger blast-hole spacing and minimum resistance. Therefore, study of the impact of smooth blasting parameters excluding damage must also consider these two factors. The results of engineering examples show that the effect of smooth blasting is salient, which illustrates the theoretical parameters calculation formula having a certain reference value. Rock mass damaged, relevant hole distance and minimum resistance line should reduce.

References

1. Gao, A.X. and Yang, R.S. Blasting Engineering. Xuzhou: Chinese Mining Industry University Publishing House, 1999, 158-159.

2. Zong, Q. Study and Application of Soft Rock Tunnel Smooth Blasting Technology. Journal of China Coal Society, 2002, 27(1). 45-49.
3. Gao, J.S. and Zhang, J.C. Dynamical Analysis of Break Mechanism on Rock Blasting Metal Mine, 1989, 9. 7-13.
4. Gao, J.S., Yang, J. and Zhang J.C. Studies on The Direction and Mechanism of Rock Blasting Cracking Under The Action of Quasistatic Pressure. Explosion and Shock Waves, 1990, 10(1). 76-84.
5. Zong, Q. and Ma, Q.Y. Theoretical Analysis of Parameters of Smooth Blasting. Journal of Fuxin Mining Institute(Natural Science), 1994, 13(4). 21-25.
6. Ma, Q.Y. Definition of Hole-space and Burden in Smooth Blasting. Chinese Journal of Rock Mechanics and Engineering, 1997, 15(6). 590-594.
7. Zong, Q., Lu, P.J. and Luo, Q. Theoretical Study on Axial Decoupling Coefficients of Smooth Blasting With Air Cushion Charging Construction. Chinese Journal of Rock Mechanics and Engineering, 2005, 24(6). 1047-1051.
8. Dai, J. and Yang, Y.Q. Calculation of The Distance Between The Adjacent Delay-explosion Shotholes in Smooth Blasting. Explosion and Shock Waves, 2003, 23(3). 253-258.
9. Dai, J. The Controlled Contour Blasting Technique and Its Parameter Determination for Tunnel at Depth. Explosion and Shock Waves, 2004, 24(6). 493-498.
10. Wang, W.L. .Hole Blasting. Beijing, China.Coal Industry Publishing House, 1989, 193-244.
11. Zhang, C.L. and Li, X.P. Numerical Analysis and Parameters Option Based on Damage in Smooth Blasting.Journal of Wuhan University of Technology, 2006, 28(7). 86-89.
12. Dai, J. and Yang, Y.Q. Analyses of Controlled Perimeter Blasting in Damaged Rock. Journal of China University of Mining & Technology, 2000, 29(5). 496-499.

RaSiM 7(2009): Controlling Seismic Hazard and
Sustainable Development of Deep Mines,
C.A. Tang(ed), Rinton Press, 81-88

ANALYSIS OF ROCKBURST GENERATION MECHANISM INTRODUCED BY EXPLOSIVE STRESS WAVE PROPAGATION

HAO QIN and SHU-CAI LI

Research Center of Geotechnical and Structural Engineering, Shandong University,

Jinan, Shandong 250061, P.R.China

MING-BIN WANG

School of Science, Shandong Jianzhu University

Jinan, 250101, P.R. China

The rockburst records of many underground projects indicate that the static load theory has apparent limitation in the analysis of rockburst mechanism, as rockburst is closely related to explosion, when the elastic wave especially Rayleigh wave generated by explosion has remarkable disturbance effects on the surrounding rocks. Based on the elastic wave theory and fracture mechanics, the FEM simulations are carred out to study the propagation of the micro-cracks within the rock mass surrounding the tunnel under the conditions of Rayleigh wave effect.. The stress intensity factor of the micro-crack tip is acquired via the numerical extrapolation method at the displacement of nodes. The calculation results indicate that elastic wave is able to lead to the instantaneous augment of the winged crack tip stress intensity factor as well as the deflection of the crack propagation direction.

1 Introduction

Rockburst is a disastrous phenomenon which occurs in underground construction activities due to the internal strain energy suddenly released from surrounding rocks and transformed into kinetic energy. Rockburst has been studied intensely by many researchers because of the severe damage brought to personnel and equipment in construction activity process [1-10]. Researches on rock burst have great significance on both theory and engineering practice.

To explain the rockburst mechanism and predict its occurrence, scholars put forward many theories and methods, including strength theories such as the Griffith Theory, the Shear Theory, empirical formula [15], rigidity theory which is put forward by A.M.Linkov [16], energy theory [17] and the instability theory.

In the last 20 years, thesis [7-10] reported that the 1st and 2nd lines of Chinling Extro-long Tunnel were excavated employing TBM and drilling and blasting method respectively. During the process, rockburst records agree with the above conclusions. Text [8,11,14] reported that a rock burst of a diversion tunnel generally occurs from the working face in the 2-50 m range in Tianshengqiao and Er-tan and other large grade hydropower stations. Rockburst blasting generally occurs after a certain period of time, and is weakened with time elapsing. Text [11-13] came out with the core control measures in order to reduce the blasting of rock disturbances named “step-by-step excavation, light burst, reducing the volume of Charge” and “short-footage, weak blasting” and so on according to engineering practice.

2 Explosion Stress Wave along Tunnel Axial Direction

In tunnel blasting process, the same paragraph as a result of the use of detonators, the time lag difference of a same layer hole can be ignored, once of explosion can be generalized into a number of homologous cylindrical wave launching process. The propagation of cylindrical wave along radial directions is explicit not only in theory but also in test of construction activity process. However, that will be discussed here is not the explosion stress wave radial transmission but the axial spread. It is studied here that propagation of stress wave generated by present explosion in excavated tunnel and the stability of surrounding rock impacted by stress wave.

In tunnel blasting, the blast hole length is generally 3-5 m, sometimes even shorter. Clearly, this length is minimal in comparison with the length of the tunnel. If the tunnel side-wall of the vault ripped, at the same time also assisted blasting hole contours projected onto the surface of the excavation, then the disturbance of a shot of blasting can be translated into three separate surface vertical line source the Lamb issue, which is shown in Figure1.

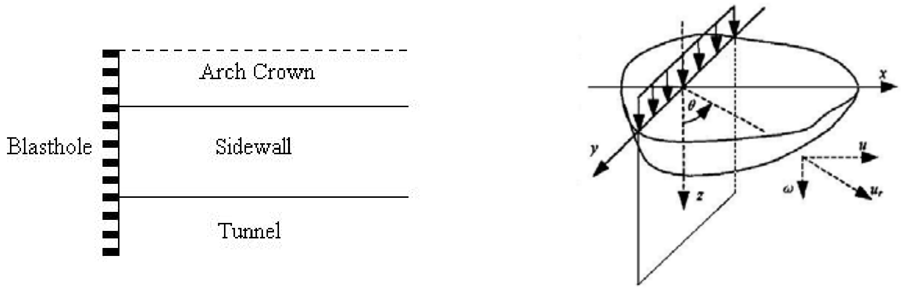

Figure 1. Model of tunnel blasting disturbing surrounding rock masses

Normal load $-P_0F(t)$ uniformly distributed along the y direction, at t = 0 moment applied to the surface of semi-infinite elastic medium at z =0. Uniform distribution along the y direction makes this issue into a plane problem. The mechanical model is based on the following equations:

$$\left.\begin{aligned} \nabla^2\phi(x,z,t) &= \frac{\ddot{\phi}}{V_P^2} \\ \nabla^2\psi(x,z,t) &= \frac{\ddot{\psi}}{V_S^2} \end{aligned}\right\}(-\infty < x < \infty, z > 0, t > 0) \tag{1}$$

$$\left.\begin{aligned} \phi(x,z,0) &= \dot{\phi}(x,z,0) \\ \psi(x,z,0) &= \dot{\psi}(x,z,0) \end{aligned}\right\}(-\infty < x < \infty, z \geq 0, t > 0) \tag{2}$$

$$\left.\begin{aligned} \sigma_z(x,0,t) &= -P_0\delta(x)F(t) \\ \sigma_{zy}(x,0,t) &= 0 \end{aligned}\right\}(-\infty < x < \infty, t > 0) \tag{3}$$

$$\lim_{r \to \infty} [\phi, \psi] = 0; r = \sqrt{x^2 + z^2} \tag{4}$$

Where: ϕ,ψ is scalar and vector potential function of the displacement vector field respectively. $\delta(x)$ is the Dirac generalized function.

Applied by the general explosion loads $P(t)=P_0\, e^{-kt}$, the displacement $[u_r(r,\theta,t),u_\theta(r,\theta,t)]$ of contour of surrounding rock of excavated tunnel can be solved from the above four formulas from(1) to (4). The solution is:

$$u_r\left(r,\frac{\lambda}{2},t\right)=\frac{P_0}{\lambda G}\left\{R_e\frac{V_Pt}{r}\left[\frac{\left(D^2+2\omega_P^2\right)}{R(\omega_P)}\frac{d\omega_P}{dt}\right]\cdot H\left(t-\frac{r}{V_P}\right)+D\sqrt{\left[\left(\frac{V_St}{r}\right)^2-1\right]}R_eH\left(t-\frac{r}{V_S}\right)\cdot\left[\frac{-2\omega_S\eta_P'(\omega_S)}{R(\omega_S)}\frac{d\omega_S}{dt}\right]\right.$$

$$\left.-\frac{D^2\left(D^2-2\xi_R^2\right)P_0}{2G\xi_R\left[R'(-i\xi_R)/i\right]}\delta\left(t-\frac{r}{V_R}\right)\right\} \tag{5}$$

$$u_\theta\left(r,\frac{\lambda}{2},t\right)=\frac{P_0}{\lambda G}\left\{R_eH\left(t-\frac{r}{V_P}\right)\sqrt{\left[\left(\frac{V_Pt}{r}\right)^2-1\right]}\left[\frac{i\left(D^2+2\omega_P^2\right)}{R(\omega_P)}\frac{d\omega_P}{dt}\right]+R_e\frac{V_St}{r}H\left(t-\frac{r}{V_S}\right)\cdot\left[\frac{-2i\omega_S\eta_P'(\omega_S)}{R(\omega_S)}\frac{d\omega_S}{dt}\right]\right. \tag{6}$$

Rayleigh wave present only when $\theta=\pi/2$, that is intersection line when tunnel vertical profile across with excavation contour cylinder surface.

3 Calculation of Dynamic Stress Intensity Factor

3.1 Calculation Model

In linear elastic problems, the displacement, stress and strain near the crack top changes in corresponding with the r -1/2 (r for the distance between crack tip and the calculation point) ,so crack tip is the singularity point of stress and strain. Using FE Method for solving fracture mechanics singular element is employed which move mid-point of the edge to the 1/4 edge-length position. Element type is determined as a two-dimensional 8-node high order element with quadratic displacement approximation function. Elements of the first row around the crack tip must be the singular elements (Barsoum [18], Ingraffa and Manu [19] and others researchers come out with a degenerated singular isoparametric elements and approach to obtain stress intensity factor based on the elements, the ordinary isoparametric element(node8,20)has simple formation, high precision and been widely used). Crack surface sliding is simulated using contact element which meet the Mohr-Coulomb criterion. Analysis shows that changes in μ values slightly impact the stress intensity factor, so set it to zero. In reality, there are quantity of micro-cracks which distribute in surrounding rock randomly, Beta is supposed as included angle between cracks and tunnel excavation contour.

This article was programmed computational procedures using APDL language, FEM model is shown in Figure 2. The tunnel surface boundary is applied displacement load. Displacement load function is determined by formula (5)& (6).

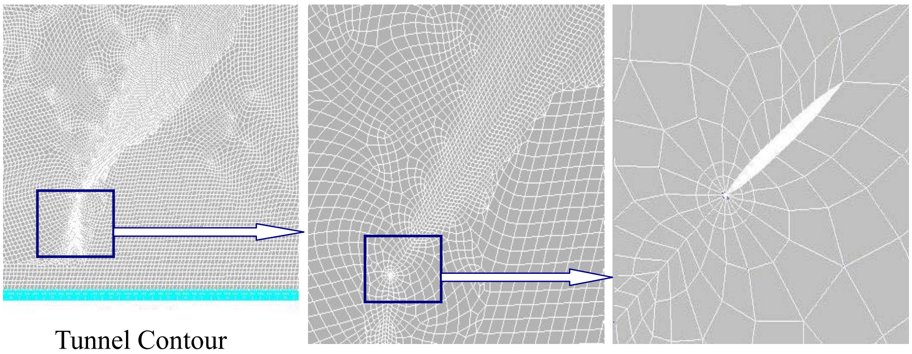

Figure.2 Crack opening due to dynamic stress wave

3.2 Numerical Extrapolation Method

In this paper, K factor is calculated employing a numerical extrapolation method proposed in literature [20] which inherited advantages of singular isoparametric element and effectively solve the problem that calculation of the K factor was influenced by the materials' size, shape and poisson ratio [19]. The precision and stability are improved.

Process of numerical extrapolation method is that identify the displacement of nodes belong to degenerated singular isoparametric elements and other elements around the crack tip which is on the crack surface. Apparent K factor is computed using following formula with displacement of these nodes [21].

$$K_i^* = \frac{E'}{2}\sqrt{\frac{\pi}{2r_i}}u_i(r_i,\pi) \tag{7}$$

According to the apparent K^* factor, K factor is obtained with minimal squares linear regression method.

$$K = \frac{1}{n}\left(\sum K_i^* - c\sum r_i\right) \tag{8}$$

Where

$$c = \frac{n\sum K_i^* r_i - \sum K_i^* \sum r_i}{n\sum r_i^2 - \sum r_i \sum r_i} \tag{9}$$

n is the amount of interpolation nodes, 4-5 nodes

r_i is distance between interpolation nodes and crack tip

Through the test of linear correlation coefficient fitting precision and interpolation interval were decided, the more linear correlation coefficient close to ±1, the higher interpolation precision. r_K is described as:

$$r_K = \frac{\sum\left(r_i - \bar{r}\right)\left(K_i^* - \overline{K^*}\right)}{\sqrt{\sum\left(r_i - \bar{r}\right)^2 \sum\left(K_i^* - \overline{K^*}\right)^2}}$$

4 Crack propagation direction

Once a crack has been initiated, the direction of propagation needs to be calculated using various criteria. Many comparative studies have been made for these different criteria [22], and the results are similar in terms of direction of propagation. For our developments, we chose the maximal normal stress criterion. The computation of the maximal stress is performed as follows (1)the integration points nearest to the crack tip are identified;(2)for each of them, eigenvalues and eigenvectors of the stress tensor are computed;(3)these eigenvalues provide the principal stresses and enable us to find the direction of propagation for each integration point;

The final direction of the crack propagation is obtained by a weighted average of each direction with respect to the distance between the integration point and the crack tip (Fig. 3). This technique enables to determine the direction of propagation without computing the stress intensity factors. Beta is assumed as included angle between crack propagation direction and tunnel excavation outline.

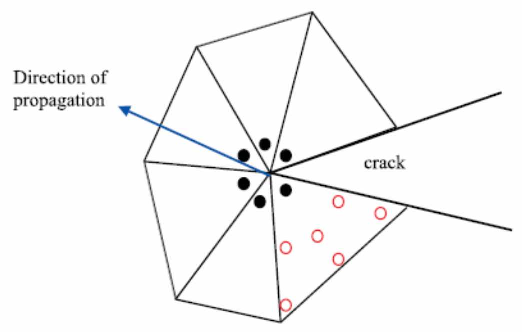

Figure 3. Zoom on the crack tip and computation of the crack propagation direction.

5 Results Discussion and Conclusion

Rayleigh wave is generated by superposed uneven P wave and uneven SV wave; when m=0.25, the ratio of major axis and minor axis, that is max=1.47. The particle movement track caused by Rayleigh wave which is generated along excavation contour surface by blasting pulse is irregular ellipse shaped and the surface disturbance is dominated by vertical displacement. From The results figure 4, Rayleigh stress wave especially its relatively steep fore-part lead to a large stress intensity factor values. For these micro-cracks which are already exist in the surrounding rock, the closer to horizontal the greater stress intensity factor. No matter what the angle of crack is, the majority of the crack propagation directions concentrate in the range form 70 to 110 degree to tunnel contour surface that present a trend that crack grow toward tunnel contour surface under the explosive stress wave. Since pressure resistance capacity of the rock is much larger than tensile capacity, the Rayleigh wave causes the formation of a series of tensional rapture surfaces which are vertical to the contour surface. The preliminary scale of the disturbance damage is probably very low; however, multiple Rayleigh wave disturbances may possibly cause macro-cracks.

Many blasting records of tunnel construction and controlling measures indicate that there is close relationship between rock burst and blasting. In present tunnel blasting, in order to speed up the construction progress or restricted by construction field, heavy loaded parallel cut smooth blasting is widely adopted, constituting the main factor which influences the stability of excavated surrounding rock during the latest blasting. The propagation of stress waves (formed in the latest blasting) in the excavated surrounding rock can be generalized as Lamb line source problem. After blasting, looking at a certain point in the contour surface of the excavated surrounding rock, *P* waves, *S* waves, and Rayleigh waves arrive sequentially, and,the Rayleigh wave with the largest amplitude dominates. Rayleigh waves will respectively generate tensional fracture surfaces which are vertical or parallel to the excavated contour surfaces in the surrounding rocks. The preliminary scale of the structural surfaces may be relatively small because the surrounding rock is disturbed by the stress wave for a plurality of times and macro fractures can form. In the stress environment of $\sigma_1>\sigma_2$, $\sigma_3=0$, the formation of rapture surfaces of different directions (or potentiality) may possibly prompt the surrounding rock to be damaged in the form of rock burst or peeling. The attenuation of P waves and the vertical distribution of Rayleigh waves can be used to explain the positional relation between the rock burst prevalence region and rock face as well as a plurality of rock burst phenomenon, such as the shape features of rock burst fragments.

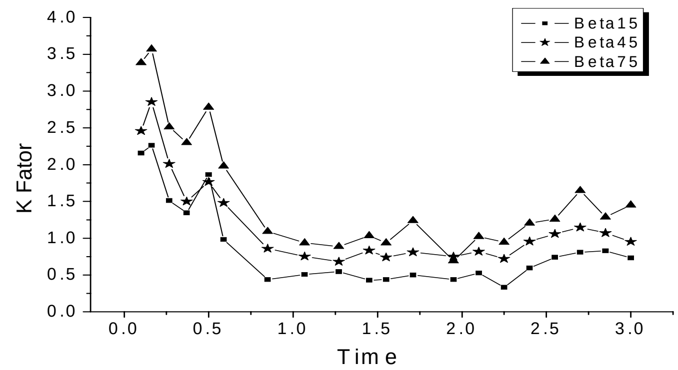

Figure 4 K factor of micro-crack in surrounding rocks under explosive pulse

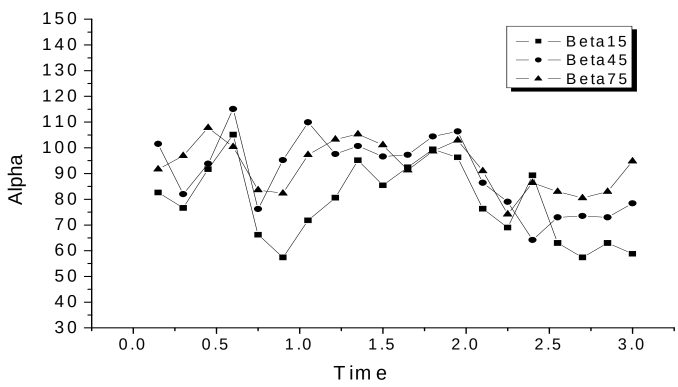

Figure 5 Crack propagation direction of micro-crack in surrounding rocks under explosive pulse

Acknowledgements

The authors wish to acknowledge the funding support from National Science Fund for Distinguished Young Scholars (A class): Rock and Fractured Rock Mass Constitutive Relations and Computing Technology (fund No. 50625927).

References

1. Morrison, R. G. K. Theory and the practical problem of rock bursts. Engineering and Mining Journal, 1948, 149(3). 6 6-72.
2. Brady, B. T. Anomalous seismicity prior to rock bursts implications for-earthquake prediction. Pure and Applied Geophysics, 1977, 115(1-2). 357-374
3. Guha, S. K. Seismological study of the rock bursts at the Kolar goldfield India. In:Proc. of Fourth International Congress. International Association of Engineering Geology, 1982.
4. Mueller, W. Numerical simulation of rock bursts. Mining Science &Technology, 1991, 12(1). 27-42.
5. Casten, U. and Fajklewicz, Z. Induced gravity anomalies and rock-burst risk in coal mines: a case history. Geophysical Prospecting, 1993, 41(1). 1-13.
6. Zhang, Z.Q. and Guan, B.S. Basic Analysis of Rock Bursting Occurrence Condition. Journel of the China Railway Society. 1998.
7. Liu, C. Some Aspects of TBM Construction at Early Stage of Qinling Tunnel 11. Modern Tunnelling Technology, 1998.
8. Li, C.J. Rock Burst Characteristics and Treatment Methods in Qinling tunnel.Modern Tunnelling Technology, 1999.
9. Liu, Y.Q. Experimental study on mechanical characteristics of twin tunnels with small spacing.Chinses Jouenal of Rock Mechanics and Engineering, 2000.
10. Zhang, K.C. and Zeng, J.F. Countermeasures for IBM Passing through Rock-Blasting Sectionin Qinling Tunnel. Modern Tunnelling Technology, 2000.
11. Zhou, D.P. and Hong, K.R. The Rockburst features of taipingyi tunnel and the prevention methods. Chinses Journal of Rock Mechanics and Engineering, 1995.
12. Gou, B. and Liu, Z.X. Discussion on Reasonable Round and Ratio during Construction of A Parallel Pilot in No. 2 Qinling Tunnel.Modern Tunnelling Technology, 1999.
13. Sun, J.P. Review on the Construction of Long Single Track Tunnel with Tyre Transportation. Modern Tunnelling Technology, 1998.
14. Zo. Study on the law of occurring rockburst hazard in underground engineering and its forcasting. The Chinese Journal of Geological Hazard and Control, 1992.
15. Peng, Z., Wang, Y.H. and Li,T.J. Griffith Theory and the Criteria of Rockburst. Chinese Journal of Rock Mechanics and Engineering, 1996, 15(Supp.). 491-495.
16. LIinkov, A.M. Rockburst and the Instability of the Rock Masses. International Journal of Rock Mechanics and Mining Sciences&Geotechnical Abstracts, 1996, 33(7). 727-732.
17. Pan, Y. and Wang, Z.Q. Research approach on increment of work and energy-catastrophe theory of rock dynamic destabilization. Chiese Journal of Rock Mechanics and engineering, 2004, 23(9). 1433-1438.
18. Barsoum, R S. On the use of isoparametric finite elements in linear fracture mechanics. Int J Num Meth Engng, 1976, 10. 25-37.
19. Ingraffea, A R and Manu, C. Stress2 intensity factor computation in three dimensions with quarter 2 point element. Int J Num Meth Engng, 1980. 15. 1427-1447.

20. Li, H.P.and Wu, X.T. Numerical extrapolated method for calculating sif accurately. Journal of Mechanical Strength. 2001, 23(2). 209-212.
21. Shen, C.K. Fracture Mechanics. Shanghai: Tongji University Press, 1996. 8-15.
22. Maiti, S.K. and Smith, R.A. Comparison of the criteria for mixed mode brittle fracture based on the preinstability stress-strain field. Part II: pure shear and uniaxial compressive loading, Int. J. Fract. 1984, 24. 5-22.

RaSiM 7(2009): Controlling Seismic Hazard and
Sustainable Development of Deep Mines,
C.A. Tang(ed), Rinton Press, 89-94

EXPERIMENTAL AND NUMERICAL STUDY ON ZONAL DISINTEGRATION OF DEEP TUNNEL

XU-GUANG CHEN, QIANG-YONG ZHANG, BO LIN, NING ZHANG, DE-JUN LIU and MING-BIN WANG

Research Center of Geotechnical and Structural Engineering, Shandong University

Jinan, 250061, P.R. China

With the increase of embedded depth of tunnel, the phenomenon of zonal disintegration that the fracture zone and the entire zone formed alternately in deep tunnel has been discovered in many tunnel projects. In order to investigate the failure mechanism of zonal disintegration, a series of similar materials laboratory tests have been carried out. The experimental results reproduced this phenomenon of zonal disintegration. In addition, numerical simulations using RFPA-Parallel system are conducted to compare with the experimental results. Based on the experimental and numerical results, it is concluded that the phenomenon of zonal disintegration is the result of circular tensile cracks developing spirally within surrounding rock mass, which is under the effect of principal stress in the tunnel direction.

1 Introduction

Zonal disintegration is the phenomenon where the fracture zone and entire zone appears alternately in the side walls of the tunnel when it is excavated in deep rock mass [1]. Zonal disintegration is confirmed with physical detection methods in many deep cave excavations home and abroad.

During the late 20th century, E.I.Shemyakin discovered the zonal disintegration in Taimyrskii Mine by electrical resisitivity well logging [2]. (Fig.1)

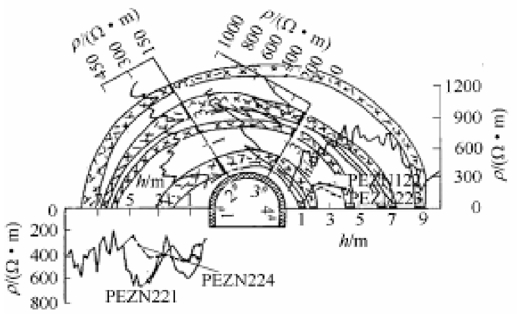

Figure 1 Zonal disintegration of Taimyrskii mine

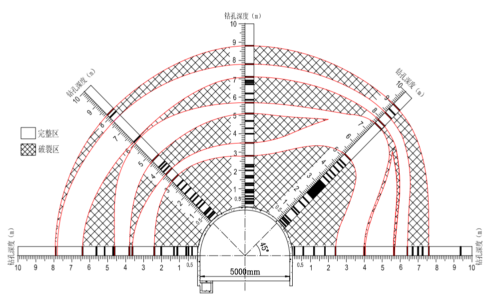

Figure 2 Zonal disintegration of Dingji coal mine of Huainan mine area

G.D.Adams and A.J.Jager discovered the fracture spacing phenomenon in Witwatersrand Gold Mine 2000～3000m deep using a periscope[3].

LI Shucai [4] observed and recorded the zonal disintegration phenomena using the television borehole camera. This confirmed the existence of zonal disintegration (Fig 2).

However, restricted by the conditions, monitoring and recording in the tunnel one can observe the phenomena merely in surrounding rock mass and can't record the formative processes of zonal disintegration. The price to carry out experiments in tunnels costs too much after it has been excavated. So, the most effective method to reveal the produce mechanism is to simulate the excavation process of the tunnel in the laboratory by reproducing the zonal disintegration phenomena.

2 Entity model experiment and computer simulation

Model includes the entity model and the computer simulation model. This two are complementary to each other and each has its merits.

Computer simulation is the methods which establish virtual model in computer to research the actual project by using the high speed calculate capacity in computer. It can simulate the anisotropism, anisotropic and discontinuity characters of the medium. It also can simulate the complex boundary condition and time-variation characters in projects. Compared to computer simulation, model experiment is weak in some aspect such as cost and time-consuming too much. However, unlike the virtual model, the physical model is the entity, when it fills the similarity principle, it can visually and truly reflect failure deformation in surrounding rocks and especially, can simulate some specific phenomena and ruin laws. One hand, this can verifies with mathematic models each other, the other, it can lay the foundation to discover some new mechanics phenomena and laws.

Take these two method – geomechanics model test and computer simulate together to research and analyze projects at the different angle, will use the different advantage and can be complementary to each other. Only by this, the characters of the projects will display, and the form process and mechanics mechanism of the zonal disintegration phenomena could be revealed.

In the computer simulation, Tang Chun'an[5]carried out the numerical tests on three-dimensional failure process of rock samples containing hole with RFPA-Parallel system running on Lenovo 1800 Cluster, reproducing fracture spacing (zonal disintegration) observed from rock mass around deep tunnels.

While in the geomechanics model experiment, the following two are the most typical models.

PanYishan made the model by using plaster with its dimensions 30cm×30cm×10cm. In the center of the model he preset a hole which its diameter is 6cm. This model is loaded by plane stress. This experiment only discovered cracks in the direction of the loading. Zonal disintegration phenomena are not discovered [6].

GuJincai manufactured the model using the cement mortar. He also reset the hole to simulate the cave after excavation. He discovered that in the high axial stress in the direction of the axes of the cave, many cracks appear in the surrounding rocks. And between cracks the entire zone existence. Zonal disintegration phenomena are confirmed by geomechanics model experiment [7].

According to the characters of the model experiment, we choose the rock blocks from the HUAINAN Coal Mine area DINGJI Coal Mine in which zonal disintegration phenomena is discovered to manufacture it to the test blocks and test its physical mechanical parameters. After this, we use the similar materials to simulate the rock mass from the coal mine to carry out the geomechanics model experiment. This experiment results good.

3 Introduction to the experiment

1) Physical and mechanics parameters test on test blocks from DINGJI cola mine rock mass

We choose the medium-sandstone in which bed stratum the zonal disintegration is discovered to carry out the test of physical and mechanics parameters (Fig.3).

Figure 3 mechanic parameters test on rocks from HUAINAN mine area

Results by the test, the mechanics parameters of the medium sandstone are shown as below:

Compression strength is 88.55Mpa, Tensile strength is 5.1Mpa, Modulus of deformation is 12.97GPA.

2) Introduction to the experiment

The steel drum is 380mm high and it’s inside diameter is 450mm. The wall thickness is 10mm. Take the similar material to manufacture the model and set it inside the steel drum. Inside the model reset the hole to simulate the deep tunnel. We made the model by this material called iron barites sand cementation material (IBSCM) [8], the diameter of the model is 160mm. The ax of the circular cave is in the direction of the central axes of the steel drum. In order to compress the model more evenly, we put a circular steel plate which is 50mm thick on the model.

The barites sand cementation material is mixed with iron ore powder, barites powder, sand, rosin, alcohol and gypsum powder. Iron ore powder, barites powder and sand are main materials: the solution of rosin and alcohol is glue; Gypsum powder is regulator.

This material has got a national patent in 2007. (Patent number: 200510104581.4). Proportion of similar material in this experiment is shown as below. (Table 1)

Table1 Proportion of similar material

I：B：S	Portion of the Gypsum	Concentration Of the solution of rosin and alcohol	Portion of the solution of rosin and alcohol
1：1.2：0.38	2.5%	7.5%	5.0%

Note：I means iron(in weight), B means barites powder (in weight),S means sand (in weight).

The parameters of the similar material are shown as below:

Compression strength is 3.2Mpa, tensile strength is 0.21Mpa.

Modulus of deformation is 520MPA. The similarity ratio is about 25.

The model is made placement in layers and tamped. After that it’s made a hole inside the models to simulate the cave. Then the model is maintained to 7 days to make the alcohol evaporated in order to strengthen the model. The model is compressed evenly on the 800T compression machine (Fig5).

Load values depend on the multiples of the compression strength of the material. The compression strength of this material is 3.2Mpa, so according to the surface area of the upper surface of the model, we can calculate the load values in 7 steps.(Table 2)

While in the actual load process, when the pressure reaches 180t which is about 4.5 multiples of the compression strength, the load values can’t raise more. This means that can’t compress the model more. Meanwhile the axial displacement of the model increases all of a sudden. This indicates that the model has been arisen significant deformation and the cave of the model maybe has already collapsed. So we stop the compression process and take down the steel drum.

Table 2 Values in loading procedure

Load steps	1	2	3	4	5	6	7
Multiples of the compression strength	1	2	3	4	5	6	7
Load values(T)	40	80	119	159	199	238	278

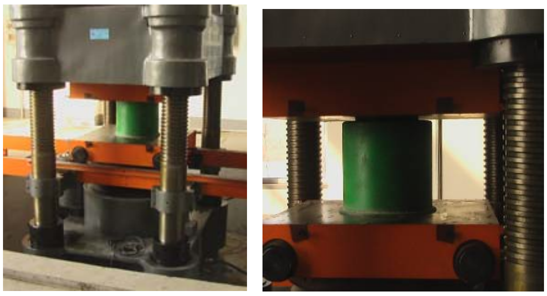

Figure 5 loading procedure on model test

4 Results comparison between the geomechanics model experiment and the computer simulate

Split the model at the different depth in the direction of the axes of the model, we can get the finally cracks distribution inside the model (Fig.6).

a) cracks distribution at the depth of 4–6cm b) cracks distribution at the depth of 8–10cm

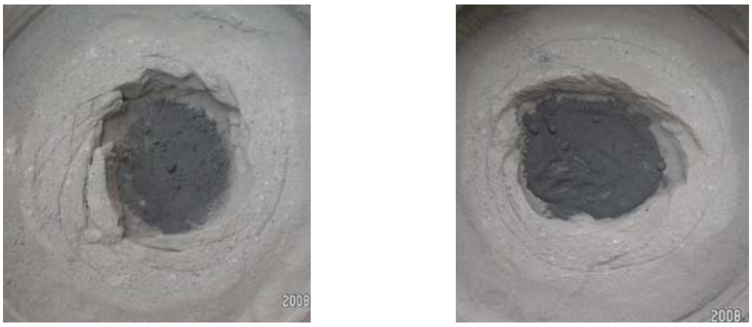

c) cracks distribution at the depth of 15–18cm d) Cracks distribution at the depth of 25cm

Figure 6 photos of model after destroy at the different depth in the direction of the axes of the cave.

The circular crack forms the entire circle. The cracks form 4 fracture zones and there is entire zones existence between the two adjacent fracture zones. So we confirmed the existence of the zonal disintegration phenomena in the model.

As shown in the photos of the fracture shapes of the model at the different depth, we can conclude rules as bellows:

1. Most circular cracks cut at some point. They don't form the entire circles.

Prof. Tang Chun'an [5] points: the phenomena which called zonal disintegration is the artificial scheme that connect the data (stress or displacements) got from the limited boreholes in surrounding rocks. He thinks, these schemes can't reflect the true situation of the cracks disputation and the fracture spacing factually. In fact, analyzing the scheme of zonal disintegration phenomena found in the tunnel mentioned in the references above, we can find that the circular cracks are not the continuous circles. There is fracture zone existed in isolation. And there is the situation of one fracture zone expanded to two fracture zones. This indicates that the expanding of the cracks is too complex and is influenced by sorts of factors. It's not the simple circular cracks.

2. Compared to the circular fracture zones, the fracture shapes look more like spirals. The fracture zones are not the concentric circles of the cave, they are spirals expanding outside endlessly which their center is the cave. This coincides with the fact result mentioned in the reference [5].

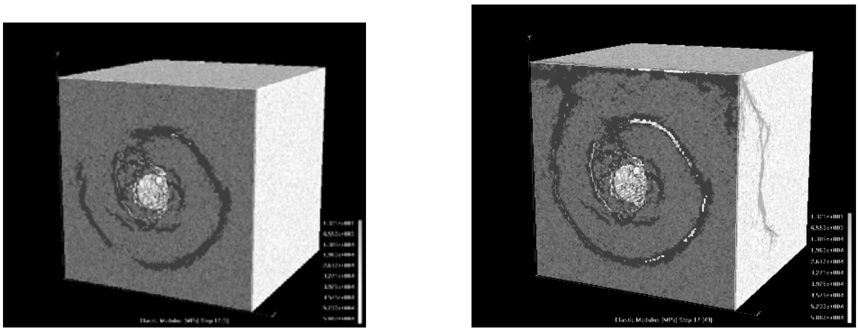

Figure 8.Fracture Spacing formation process obtained with RFPA

3. Along with the increasing of the depth of the models, the fracture zones expand gradually. At the depth of 4-6cm the fracture zones are concentrated in the range of 4-5cm away from the cave. While the outmost fracture zone is about 5cm away from the cave. When at the depth of 20cm, it expands to about 10cm away from the cave. It indicates that at the shallow area it's influenced by the end restrict effect. While the depth of the model approaches the middle of the model, the zonal disintegration phenomena becomes more significant.

5 Conclusions

1). Under greater axial compression, the zonal disintegration phenomenon may appear. The axial load is the important factor which causes the phenomenon.

2). The results between the similar material geomechanics model experiment and the computer simulation experiment are consistent. They all reproduce the zonal disintegration and prove its existence.

3).As seen from the cutaway view of the models, the fracture line is not the concentric circle of the cave; it is a discontinuous line which looks like a spiral generally. While seen from the form process of the zonal disintegration simulated by RFPA, the fracture line around the cave is also a spiral. The simulated material model and the computer simulation model reach the same result.

4). Similar to the experiment carried out by GU Jincai, when the ratio between the axial compression on the model and the compression strength of the material reached some relationships, the zonal disintegration phenomena appears. While the ratio is not constant, it changes along with the changing of the material. For example, in the experiment of GU Jincai, the ratio is 7.47, while in this paper it is 4.5. It indicates that the compression is not the single factor which results in the zonal disintegration. The phenomena are related to the mechanics parameters of the surrounding rocks.

This indicates when the axial compression on the model and the mechanics parameters of the rock, especially, the uniaxial compression strength of the rock mass reach some function relations, the generating condition of the zonal disintegration may be reached. The depth of the tunnel is not always the key factor which causes the phenomena. This paper speculates that zonal disintegration may also appear in some shallow tunnels when it reaches some function relationship between the stress surrounding rocks and the mechanics parameter. The stress in surrounding rocks where zonal disintegration happens is not always the high stress. It has not been discovered most likely because people haven't observed or monitored it yet.

Acknowledgments

This work was supported by a grant from the National Basic Research Program of China (973 Program) (No. 2009CB724607), National Natural Science Foundations of China (No. 40772173); Natural Science Foundations of Shandong Province (No.Y2007F52); New Century Excellent Talents in University(NCET-08-0336).The author is deeply appreciated to these supports.

References

1 Qian, Q.H. The characteristic scientific phenomena of engineering response to deep rock mass and the implication of deepness. Journal of East China Institute of Technology. 2004.27(1). 1-5.

2 Shemyakin, E. I., Fisenko, G. L., Kurlenya, M. V. Zonal disintegration of rocks around underground workings, part I:data of in-situ observations. Journal of Mining Science, 1986, 22(3). 157-168.

3 Adams, G. D., Jager, A. J. Etroscopic observations of rock fracturing ahead of the stope faces in deep-level gold mines. Journal of the South Africa Institute of Mining and Metallurgy,1980, (2). 115-127.

4 LI, S.C. Wang, H.P and Qian, Q.H. In-situ monitoring research on zonal disintegration of surrounding rock mass in deep mine roadways. Chinese Journal of Rock Mechanics and Engineering, 2008, 27(8). 1545-1553.

5 Tang, C.A. and Zhang, Y.B. Discussion 0n mechanism and evolution laws of fracture spacing in rock mass. Chinese Journal of Rock Mechanics and Engineering. 2008, 27(7). 1362-1369.

6 Pan, Y.S., Li, Y.J. and Tang, X. Study on zonal disintegration of rock. Chinese Journal of Rock Mechanics and Engineering. 2007, 26(Supp.1). 3335-3341.

7 Gu, J.C., Gu, L.Y. and Chen, A.M. Model test study on mechanism of layered fracture within surrounding rock of tunnels in deep stratum. Chinese Journal of Rock Mechanics and Engineering. 2008, 27(3). 433-438.

8 Zhang, Q.Y., Li, S.C. and Guo, X.H. Research and development of new typed cementitious geomechanics similar material for iron crystal sand and its application. Rock and Soil Mechanics, 2008, 29(8). 2126-2130.

RaSiM 7(2009): Controlling Seismic Hazard and Sustainable Development of Deep Mines, C.A. Tang(ed), Rinton Press, 95-100

EXPERIMENTAL STUDY ON THE ESTIMATION OF SEISMIC GROUND CHARACTERISTIC BY MICRO-TREMORS

BO-MING ZHAO

School of Civil Engineering, Beijing Jiaotong University

Beijing 100044, China

JING CHEN

Institute of Computing Technologies, China Academy of Railway Science

Beijing 100081, China

The seismic ground characteristics estimated by micro-tremors measurements and weak earthquake observation at the arrays set up in Kushiro district in Japan have been examined. It is suggested from these examinations that the micro-tremors measurements are usable as an effective tool to estimate the seismic site-specific characteristics. In this paper, the reliability of the micro-tremors measurements as a tool of estimating site-specific characteristics by comparing the estimation results at the arrays in the Kushiro and at another arrays in Kansai district are examined. These arrays are located in different conditions with respect to geological structure and micro-tremors source effect.

1 Introduction

Recent research into the methodology of reducing various damages caused by past weak earthquakes has presented problems urgent problems in seismic engineering concerning the qualitative and quantitative evaluations on the effects of surface geology on the characteristics of seismic ground motion. From the engineering aspects of these problems, the evaluation of the effects on surface geology is very substantial in the prevention of earthquake disasters with regard to destructive damages of the ground for various structures and urban facilities. The investigations of the damages caused by the Mexico Earthquake in 1985 to Mexico City and the Lome-Prieta Earthquake in 1989 to San Francisco showed that the surface geology had considerable effects on the characteristics of seismic ground motion, resulting in the concentration of the damages in a certain local district. The aim of this study is to qualitatively evaluate, from an interdisciplinary point of view, the effects of surface geology on the characteristics of seismic ground motion through the use of micro-tremor measurements [1, 5, 6, 8].

Micro-tremors have been proposed as a simple and effective tool to estimate the ground response characteristics on site [1, 2, 4, 5]. However, these proposals have not been summarized in their theoretical background and applicable conditions yet. In order to solve these problems, estimation results of micro-tremors and seismic motions from an array of observations [3, 7, 8] have been compared. In this paper, we discuss the reliability of seismic site-specific characteristics estimated from micro-tremors measurements by comparing the results from the Kushiro and Kansai district in Japan, located under different conditions with respect to geological structure and the micro-tremors source effect.

In this study, three site-specific characteristics are used to discuss the above-mentioned purposes. Specifically the characteristics consist of the predominant frequency, the spectral ratios of horizontal components between different sites (hereafter HH spectral ratio), and the spectral ratio of horizontal to vertical components ratio (hereafter HV spectral ratio).

2 Array Observation Procedures

Two different observation networks located in Kushiro and Kansai district are chosen as the observation areas in this spatial variation study. Fig.1 shows the location of all arrays in the two areas. Kansai district was an area hit by the Great-Hansin Earthquake (M_J=7.3) and Kushiro district is chosen partly because the area showed remarkable spatial variation of quake damages in 1993's Oki-Kushiro Earthquake (M_J=7.1).

The Kushiro observation networks were composed by two arrays (JSKA and CIKA). The JSKA-array locates in the Kushiro plateau. The diameter of the array is about 500m round Kushiro JMA, and 8 sites are installed on the plateau.

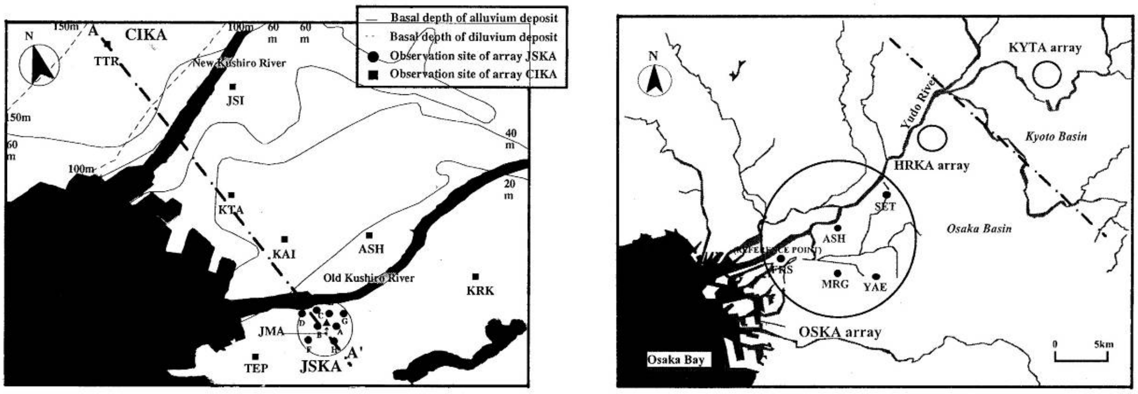

Figure 1. Location of observation points of JSKA-, CIKA-array in Kushiro district (left diagram), OSKA-, HRKA-, KYTA-array in Kansai district (right diagram).

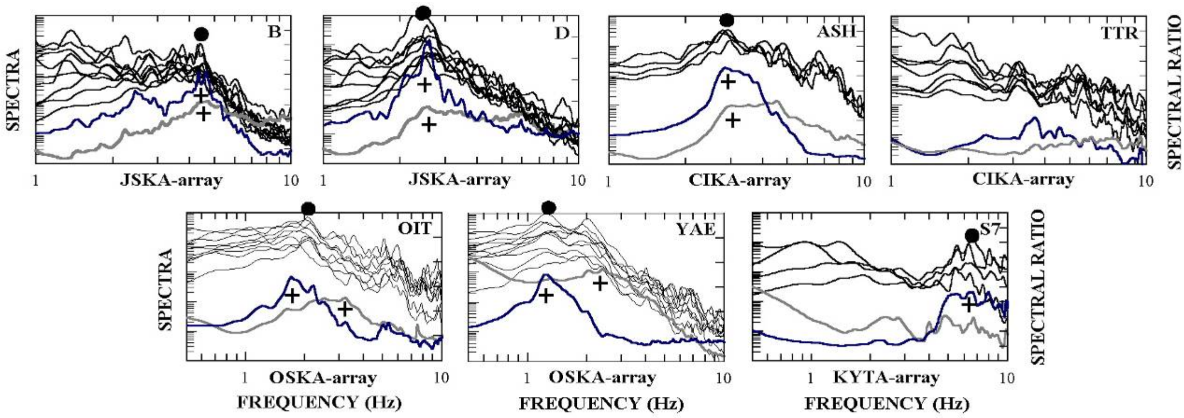

Figure 2. Amplification characteristics among micro-tremors spectra, micro-tremor HV spectral ratios and seismic motion spectra at JSKA-, CIKA- (Kushiro), OSKA- and KYTA-array (Kansai).

The shallow portions of the plateau are composed of soft volcanic ashes, and a hard Tertiary formation lies beneath it. The CIKA-array size approximately 6km×4km. Five sites are in the Kushiro alluvium plains west of

Kushiro River, and 2 sites are in the Kushiro plateau east of the river. The reason for that two different-size arrays were deployed is to examine to what spatial extent site responses from micro-tremors are in agreement with those of seismic motions. Three arrays in Kansai observation network that are OSKA-array, KYTA-array and HRKA-array are shown by circle of solid line in Figure 1 (right diagram) The large OSKA-array, the small KYTA- and HRKA-array are formed by five observation sites located on the alluvium layer of Osaka basin, seven observation sites located on the reclaimed land of the south of Kyoto basin, and four observation sites located respectively. The OSKA- and KYTA-array are used to estimate reliability of using micro-tremors measurements in different areas by comparing the results with Kushiro arrays. The HRKA-array is used to discuss what change are occurred for three characteristics whit other arrays deployed on soft surface ground (e.g., alluvium deposits).

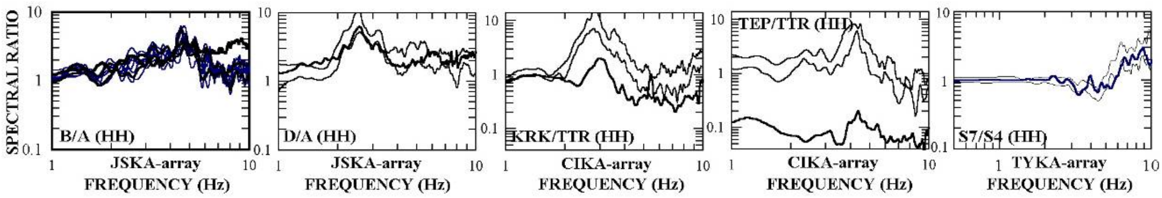

Figure 3. HH spectral ratios among micro-tremors and seismic motion for JSKA-, CIKA- and KYTA-array.

3 Predominant Frequencies of Power Spectra and HV Spectral Ratios

The predominant frequency of sediments has been estimated from micro-tremors for the simplicity of observation and analysis(10). However, it was often reported that the predominant frequency does not always reflects that of sediments. Therefore we compare predominant frequency estimated from seismic motions with one from the power spectra and from the HV spectral ratios of micro-tremors. Figure 2 show the typical analysis results as to JSKA-, CIKA-, OSKA- and KYTA-array in which micro-tremors power spectra (thick line), micro-tremors HV spectral ratio (bold line) and seismic motion spectra (dotted line). In this Figure, we find that the peak frequencies of seismic motions are observed at almost sites, where those of micro-tremors are observed either. We define the predominant frequency as the peak frequency, which appears in the power spectra of all seismic events, as shown by solid circles, the peak frequencies of micro-tremors, as shown by crosses.

As these sites, we found that the peak of micro-tremor HV spectral ratios are very conspicuous than the power spectra, and the frequency coincide with those of seismic motions. However, we also found that at some site (e.g., ASH, SET and YAE) micro-tremors power spectra show peak but their frequencies do not coincide with those of seismic motions exactly. On the other hand, in KAI site the micro-tremors and seismic motions don’t have clear peak in the whole frequency range.

As a result, it follows that observation of micro-tremors HV spectral ratios are more reliable and more effective than that of micro-tremors power spectra in estimating predominant frequencies of seismic motions.

4 HH Spectral Ratios between Different Observation Sites

In this section, it is examined whether spatial variation of seismic motions can be estimated by utilizing micro-tremors power spectral ratios with reference to a standard observation site. The examples of observation results of JSKA-, CIKA- and KYTA-array are indicated from Figure 3. The micro-tremors measurements obtained form that OSKA-array have not simultaneity. In this Figure, two thin lines denote the mean plus the standard deviation of seismic motions HH ratios and the mean minus the standard deviation of them; thick lines denote the micro-tremors HH spectral ratios. An example of the relation of a standard deviation and a scattering of HH spectral ratios is shown as to the B/A (HH) result. In small array JSKA and KYTA, space between two thin lines is narrow and show similar characteristics as to each weak earthquake event. As for the comparison between the seismic HH ratios and those of micro-tremors, values of the latter ratios are within limits of standard deviations of the former in the low frequency range concerning all the observation sites whether the spatial variation are shown or not. In large array CIKA, the spectral sharp is similar to each other, but the values are quite different in almost sites.

As mentioned above, micro-tremor HH ratios almost coincide with those of seismic motions concerning the small arrays, but they differ greatly concerning the large array CIKA. One of the reasons of this great difference might be that spatial distribution of micro-tremor sources (spatial density of sources and location of them at observation sites) is not uniform within the area of large array, because the spatial distribution of micro-tremor sources depends on the level of human activities and underground structures on site. These results suggest reliability of estimating the seismic spatial variation by utilizing the micro-tremor HH ratios, if the frequency range is restricted in small area.

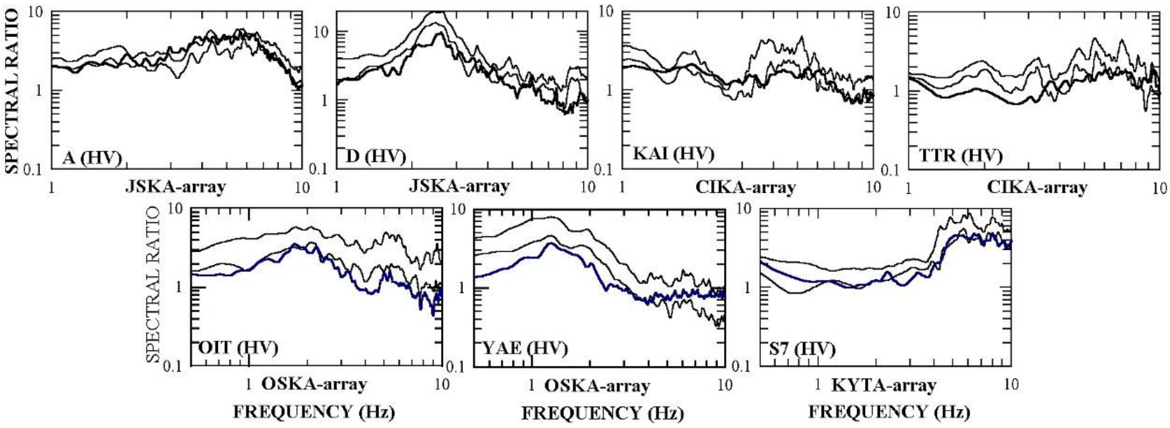

Figure 4. HV spectral ratios among micro-tremor s and seismic motion for JSKA-, CIKA-array (in Kushiro) and OSKA-,KYTA-array (in Kansai).

5 HV Spectral Ratio

HV spectral ratio can be utilized as a transfer function of estimating vertical components from horizontal one of seismic motions, if HV spectral ratios are supposed to be specific on each observation site. From this viewpoint, HV spectral ratios of micro-tremors are compared with these of seismic motions. Figure 4 show HV spectral ratios of JSKA-, CIKA-, OSKA- and KYTA-array. Two thin lines denote the mean plus and minus the standard deviation of seismic HV ratios, and thick lines denote micro-tremor HV ratios. In these arrays, it is found that micro-tremor HV spectral ratios indicate to be the same to seismic motions ones or the values are some smaller than that of seismic motions.

These results suggest reliability of estimating the vertical component from the horizontal one of seismic motions by using micro-tremor HV spectral ratios, if appropriate corrections are established with respect to the values of micro-tremor HV spectral ratios.

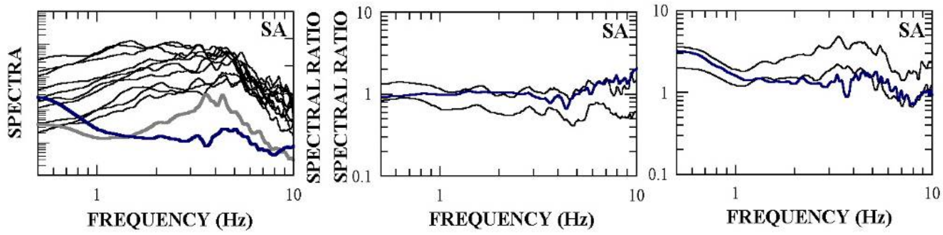

Figure 5. Compare micro-tremor s and seismic motions on power spectra, HV and HH spectral ratios for HRKA-array.

6 Results of the Hard Surface Ground

Figure 5 shows comparison results recorded at HRKA-array that has a diluvial surface layer (Vs=450m/s). In this case, power spectra of micro-tremors and seismic motions are clear in almost the same frequency range and show correlation, but the HV spectral ratios of micro-tremors do not show peak more clearly than power spectra. These results are contrary to those from soft surface ground. On the other hand, the HH, HV spectral ratios of micro-tremors and seismic motions are comparably flat in the all frequency range. As for the comparison between the seismic spectral ratios and those of micro-tremors, the both spectral ratios are agreement, and result is similar to those from soft surface ground.

7 Conclusions

In this study, the reliability of seismic site-specific characteristics is estimated from micro-tremor measurements by the experimental studies. The following conclusions are obtained from them:

(1) The high-frequency peak of HV ratios is identified with the predominant frequency of seismic motion with high accuracy, while a sharp-peak frequency of the power spectra is not always identified with it. This result indicates that the use of HV ratios is superior to estimate the predominant frequency on soft surface ground. However, the spectral peaks of horizontal components do not always coincide with those of weak earthquake ground motions.

(2) The HH ratios inferred from micro-tremors show better agreement with those from seismic motion, except high frequency range with respect to the smaller arrays. This result indicates that the spatial variation of seismic motion can be estimated from micro-tremor measurements to the area where the micro-tremor source characteristics are in spatial uniform.

(3) The HV ratios of micro-tremors closely coincide with those of the arrays of seismic motions. This result suggests the HV ratios can be utilized as transfer characteristics to predict vertical seismic motion from horizontal ones.

Acknowledgements

The author is grateful for support of Natural Science Foundation of China (No. 40674016), National Key Technology R&D Program (2008BAC38B04-03), and the Seismic Industry Foundation of Ministry of Science and Technology ([2007]203/8-53).

References

1. Horike, M. Inversion of Phase Velocity of Long-period Micro-tremors to the S-wave-velocity Structure Down to the Basement in Urbanized Areas, J. Phys Earth, 1985, 33. 59-96.
2. Irikura, K. and Kawanaka, T. Characteristics of Micro-tremors on Ground with Discontinuous Underground Structure, Bull. Disast. Prev. Res. Inst., Kyoto Univ, 1980, 30(3). 81-96.
3. Lachet, C., Hatzfeld, D., Bard, P.Y., Theodulidis, N., Papaioannou, C. and Savvaidis, A. Site Effects and Microzonation in the City of Thessaloniki (Greece) Comparison of Different Approaches, Bull. Seism. Soc. Am., 1996, 86, 1692-1703.
4. Kanai, K., Osada, T. and Tanaka T. Measurement of the Micro-tremors, Bull. Earthq. Res. Inst. Tokyo Univ., 1954, 32, 199-209.
5. Kanai, K., The Requisite Condition for the Predominant Vibration of Ground. Bull. Earthq. Res. Inst. Kyoto Univ, 1961, 35. 457-471.
6. Nakamura, Y. Inference of Seismic Responses of Surficial Layer Based on Micro-tremors Measurement, Report on Railroad Research, Railway Technical Research Institute, 1988, 4. 18-27.
7. Zhao, B. M., Horike, M., Takeuchi, Y. and Kawase, H. Comparison of Site-specific Response Characteristics Inferred from Seismic Motions and Micto-tremors, Journal of Seism. Soc. Japan (ZISIN), 1997, 2, 50, 67-87 。
8. Zhao, B. M., Horike, M. and Takeuchi, Y., Which Site-specific Characteristics Estimated from Micro-tremors Are Useful?, Journal of Struct. Constr. Eng. Architectural Inst. Japan (AIJ), 1998, 509. 69-75.

RaSiM 7(2009): Controlling Seismic Hazard and
Sustainable Development of Deep Mines,
C.A. Tang(ed), Rinton Press, 101-106

OBSERVATION AND ANALYSIS OF SPLITTING FAILURE ZONES IN BRITTLE SURROUNDING ROCK UNDER HIGH GEOSTRESS

QIAN-BING ZHANG and WEI-SHEN ZHU

Geotechnical & Structural Engineering Research Center, Shandong University

Jinan, 250061, P. R. China

LIN-FENG SUN

Fuzhou Investigation and Surveying Institute

Fuzhou, 350000, P.R. China

The Pubugou underground powerhouse is approximately 400 m below the ground surface. During excavation, a number of vertical splitting cracks appeared in the high wall of the busbar chamber. There are similar phenomena in Longtan, Er'tan, Laxiwa as well as other underground powerhouses. In order to investigate the numbers and distributions of these cracks, Borehole Television (BTV) observations, C-1 electrical resistivity tester and the developed self-made borehole probe were carried out in the four boreholes at regular intervals throughout testing, the distribution rules of the vertical splitting cracks and the disintegrated zones of surrounding rock masses can be obtained. The results indicate that the special geometrical position of the busbar chamber in the underground cavern group, the complicated geological conditions and the excavation method result in this phenomenon. Meanwhile, it can be observed that the deformation of the high wall consists of opening displacement and continuous displacement.

1 Introduction

Many large-scale underground hydropower stations have been built recently or are under construction in China. However, these underground caverns are mostly located in the high initial geostress fields which are strongly influenced by high mountains, steep slopes, and tectonic history. In some instances, the high horizontal principal stress will influence the stability of the caverns. Meanwhile, the surrounding rock masses are commonly hard and brittle rocks. Therefore, brittle failure will easily appear. The splitting of hard rocks in the neighbourhood of underground openings at distinct depths may be a common phenomenon [1]. A number of vertical splitting cracks have appeared in the high wall of the busbar chamber, such as in Longtan, Er'tan, Shisanling, Laxiwa, Pubugou as well as other underground powerhouses in China. The investigations of these phenomena are of great interest concerning the stability of the underground cavern group.

The similar phenomenon that is the parallel equidistant vertical splitting cracks exists in brittle rock pillars in several mines. However, only an analytical approximate model was presented based on the principles of the theory of elasticity and of linear elastic fracture mechanics [2]. Numerical simulation method for this phenomenon has been studied [3], but it was limited to the continuum method which is not able to simulate the generation of cracks. Elucidating this question by means of another method, Borehole Television (BTV) system was successfully applied at different sites of underground caverns for hydropower stations in Japan [4, 5]; however it could not investigate the mechanism of this phenomenon.

In the Pubugou underground powerhouse, a number of vertical splitting cracks appeared in the surrounding rock masses of the arch crown and sidewall of the busbar chambers during excavation, as shown in figure 1.

BTV observations and electrical resistivity measurement methods were carried out to investigate these phenomena at regular intervals and at different stages of the excavation.

Figure 1 Photos of circumferential splitting cracks in Pubugou hydropower station

2 Outline of the Site

The Pubugou hydropower station with a maximum output of 3300 MW is located on the Dadu River in Sichuan Province, which is the largest under construct hydropower stations in the Dadu River basin. The slope inclinations are 35°- 50° at the left bank and 45°- 60° at the right bank. Due to the river valley is very narrow, an underground powerhouse is the best choice for the project design. The underground cavern group mainly consists of the main power house, the transformer house, the surge chamber and the busbar chamber. The main power house has a width of 26.8 m, height of 70.1 m and length of 208.6 m. The underground cavern group is approximately 400 m below the ground surface. Although the axis of the underground caverns intersects the maximum principle *in-situ* stress at a small angle, the underground group is located at an area with high *in-situ* stress (up to 27MPa) and high seismic intensity (nearly 8 degree). They will influence the stability of the underground cavern group. The underlying geology surrounding the underground cavern group mainly consists of medium or fine-grained granites. The uniaxial strength of the rock is about 100 MPa.

BTV observation and electrical resistivity measurement method were carried out in the same 4 boreholes located in the sidewall of the main power house. The boreholes dip 5° from the horizontal having a length of 42 m and a diameter of 110 mm, as shown in figure 2.

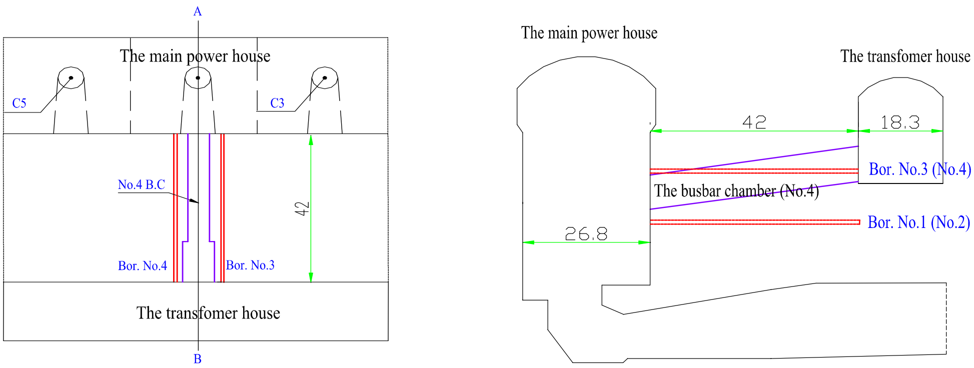

(a) Horizontal section at an elevation of 667.7 m (b) Cross section of A-B

Figure 2 Layout of the boreholes (unit: m)

3 Testing Methods

3.1. Borehole Television Observation

BTV system basically consists of a probe with a diameter of 75 mm housing the TV camera and a control unit. These two parts are connected by a 100 m long cable allowing observations to be carried out in the boreholes up to the depth of these boreholes. The orientation and the focus of the camera are adjusted by a remote control. Corresponding videos are displayed on the control unit screen. The pictures can be recorded by means of a video recorder and the TV screen shows the image at the actual size. They clearly revealed the cracks had been progressively generated in the wall area, as shown in figure 3.

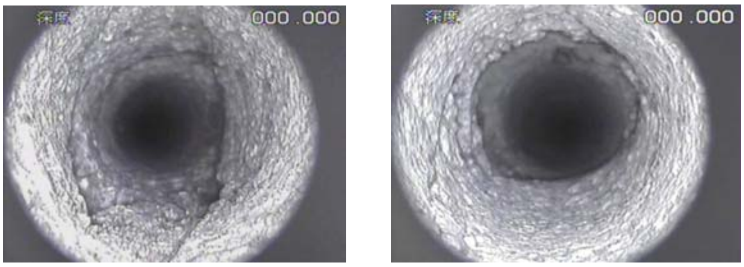

Figure 3 Pictures from the video recorder

Recently, the distributions and numbers of cracks under construction have been observed through BTV. In several underground cavern groups, BTV observations were carried out at regular intervals and at different stages during excavation, such as the opening and generation of cracks. In the Pubugou underground powerhouse, BTV observations were carried out six times at regular intervals in the following stages:

Table 1 Excavation stages and the frequency of testing

Observation	Stage of excavation
1	bench excavation completed down to 620 m elevation
2	excavation of the bottom of the main power house
3	excavation of the bottom of the surge chamber
4	excavation of the whole tail-water pipe
5	excavation of the whole caverns completed
6	one month after the completion of excavation

3.2. Electrical Resistivity Measurement Method

Electrical resistivity is one of the most important physical parameters on rocks. The degree of rock mass fracturing has great influence on electric resistivity, and generally electrical resistivity changes suddenly in the fractural location [6]. The variation of electrical resistivity of surrounding rock with the borehole depth can be measured. C-1 electrical resistivity tester and developed self-made borehole probe were carried out twice at regular intervals in the above four boreholes.

Electrical resistivity measurements are made with a four probes square device that has been specifically developed to perform field measurements. The device usually requires four electrodes: two electrodes called A and B that are used to inject the current (“current electrodes”) and two other electrodes called M and N that are used to record the resulting potential difference (“potential electrodes”), as shown in figure 4. The current electrodes A, B and the potential electrodes M and N can be placed in the boreholes. The self-made borehole probe basically consists of the PVC pipe equipping with stainless steel electrodes and connectors. The electrodes are made of stainless-steel cylinders to ensure a good contact between the electrodes and rock in the boreholes, as shown in figure 5. This measurement system is quite similar to permanent electrodes used, for example, by Daily et al. [7]. The array of the four-electrode is adopted the type of Schlumberger device. The geometrical distance between the electrodes A and B, and M and N are 90 cm and 40 cm respectively. During testing process, the water pipe was connected to the tail of the self-made probe and the self-made probe was put in the boreholes, and then water was injected into the borehole. Measurements were conducted at 25 cm intervals along the length of the borehole.

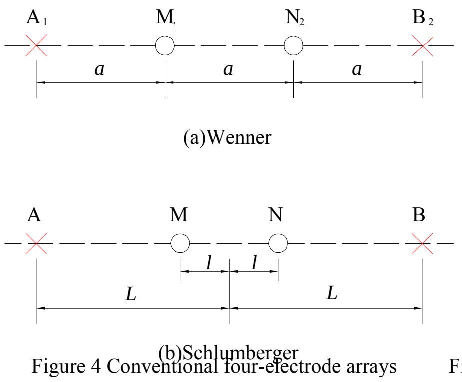

Figure 4 Conventional four-electrode arrays


Figure 5 PVC pipe equipped with stainless steel electrodes and connector

The electrical resistivity is calculated by the equation:

$$\rho = [\frac{2\pi}{(1/AM - (1/BM) - (1/AN) + (1/BN))}]\frac{\Delta V}{I} = K\frac{\Delta V}{I} \tag{1}$$

Where AM, BM, AN, and BN represent the geometrical distance between the electrodes A and M, B and M, A and N, and B and N, respectively. K is a geometrical coefficient that depends on the arrangement of the four electrodes A, B, M and N, the potential difference ΔV and the current intensity I can be measured by the C-1 electrical resistivity tester.

4 Results and Discussion

4.1. Observation Results by Borehole Television Observation

Figure 6 shows the frequency distribution and numbers of vertical splitting cracks observed during excavation in the boreholes No.1 and No.2.

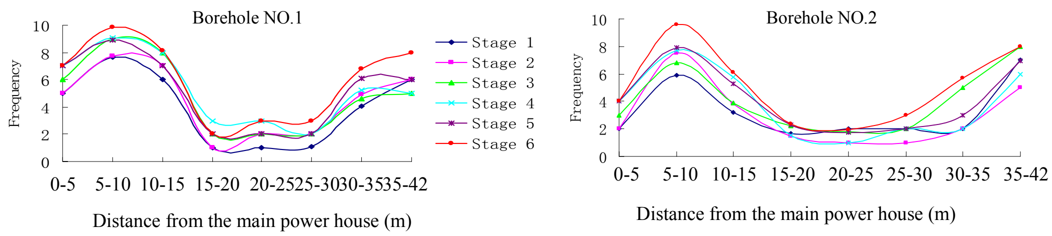

Figure 6 Relation between the number of cracks and the borehole depth in different stages

The observations clearly revealed that cracks had been progressively generated in the sidewall of the busbar chamber. One region where cracks generated largely during excavation was in the vicinity of the main power house with the depth of approximate 0-15 m in the busbar chamber. The other region was in the vicinity of the transformer house with the depth of approximate 0-7 m. Boreholes NO.3 and NO.4 had the similar results.

4.2. Measurement Results by Electrical Resistivity Measurement Methods

The electrical resistivity of rock mass would be decreased when the water was injected into the cracks of rock mass in the boreholes. A reference value of electrical resistivity on disintegrated zones of rock mass can be determined according to average electrical resistivity in every borehole, and the ones that greater than the reference value are intact rock. The average electrical resistivity is calculated by the equation [8]:

$$\rho_0^{(k)} = \frac{1}{N_k}\sum_{i=1}^{N_k}\rho_k(x_i)\ \ (0 < x_i \le L,\ k = 1,2,\cdots,5) \tag{2}$$

where k is the number of the borehole; i is the measuring point; $\rho_0^{(k)}$ is the reference value of electrical resistivity in the number k borehole; N_k is the total of the number k borehole; $\rho_k(x)$ is the resistivity distribution function of the number k borehole; x_i is the distance between the measuring point i and the orifice; L is the borehole depth.

The logarithms of testing results and reference values of the electrical resistivity could be calculated, and then the diagrams of rock mass fracturing distribution in the boreholes were drawn in figure 7. The regions that below the reference line represent the disintegrated zones of rock mass. However, the slash-filled regions located above the reference line indicate the intact rocks.

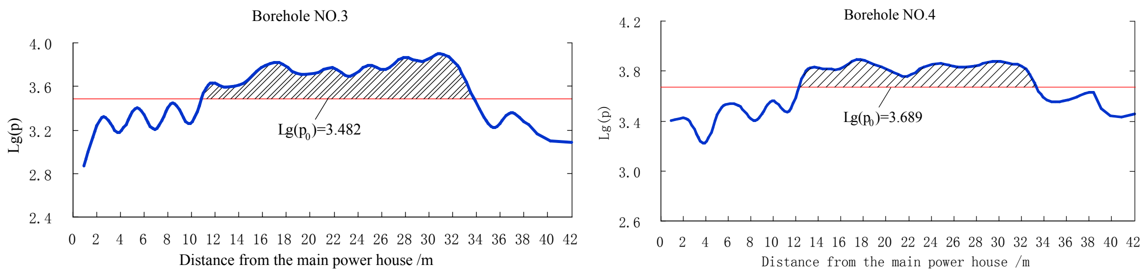

Figure 7 Logarithm of the electrical resistivity with borehole depth in the 5th stage.

From the above two diagrams, one region where the disintegrated zones of rock mass after excavation was in the vicinity of the main power house and with the depth of approximate 0-12 m in the busbar chamber. The other region was in the vicinity of the transformer house with the depth of approximate 0-8 m.

4.3. Discussion

The distribution rules of the vertical splitting cracks and the disintegrated zones of rock mass during excavation obtained by BTV observations and electrical resistivity measurements were similar. Due to the distance measurement errors in the boreholes existed in the two methods, only a slight difference in some place occurs, but the overall trend was consistent.

The distributions and numbers of cracks were directly observed through BTV. However, due to the mist and dust existed in the boreholes; it is difficult to completely rely on the video information and to determine accurately the degree of rock mass fracturing. Therefore, electrical resistivity measurement method was carried out to measure the variation of electrical resistivity of surrounding rock and to determine the disintegrated zones of rock mass. It is a new attempt that has been provided to more accurately determine the fracturing degree of rock mass in the boreholes.

5 Conclusions

In order to investigate the mechanism of the circumferential splitting cracks inside the high wall of surrounding rock of the busbar chamber during/after excavation, BTV observations and electrical resistivity measurement methods were carried out at regular intervals in the Pubugou underground powerhouse. Based on results from these two methods, the following conclusions are obtained:

The busbar chamber is located in the special geometrical position of the underground cavern group. Consequently, stress redistribution in this position was induced by a combination of the excavation effects of the main power house, the transformer house and the busbar chamber. Stress redistribution around the busbar chamber causes zones of tensile stress, which may locally exceed the rock strength.

This phenomenon is related to the orientation, magnitude and ratio of the initial geostress. In the Pubugou underground powerhouse, the orientation of the maximum principal stress intersects the axis of underground caverns at a small angle; meanwhile, it lies parallel to the extended direction of the splitting cracks. The maximum stress ratio is about 3:1. These factors can easily lead to vertical splitting cracks.

Excavation of underground caverns in highly stressed brittle crystalline rock at great depths may cause instability in form of axial splitting. In addition, drilling, blasting and the possible primary cracks will accelerate these cracks generation.

These two methods clearly reveal that the distribution rules of splitting cracks and disintegrated zones has been progressively generated in the wall area during monitoring process.

Acknowledgements

This work was financially supported by Natural Science Foundation of China (No. 90510019, 50874068, 59939190, and 50579033), National Basic Research Program of China (973 Program, No. 2002CB412705, 2007CB209407), and Natural Science Foundation of Shandong Province (NO.Y2008F22).

References

1. Fairhurst, C. and Cook, N.G.W. The Phenomenon of Rock Splitting Parallels to a Free Surface under Compressive Stress. In: Proceedings of 1st International Congress on Rock Mechanics. ISRM, 1966, 687-692.
2. Exadaktylos, G.E. and Tsouterlis, C.E. Pillar Failure by Axial Splitting in Brittle. International Journal of Rock Mechanics and Mining Sciences & Geomechanics Abstracts, 1995, 32(6). 551-562.
3. Li, N., Sun, H. and Yao, X.C., et al. Cause Analysis of Circumferential Splits in Surrounding Rock of Busbar Tunnels in Underground Powerhouse and Reinforced Measures. Chinese Journal of Rock Mechanics and Engineering, 2008, 27(3). 439-446. (in Chinese)
4. Hibino, S. and Motojima, M. Characteristic behavior of Rock Mass during Excavation of Large Scale Cavers. In: Proceedings of 8th International Congress on Rock Mechanics. ISRM, 1995, 583-586.
5. Uno, H. Evaluation of Loosened Zone around Underground Cavern Based on in-situ Measurement Results during Excavation Process. In: Proceedings of the 10th Japan Symposium on Rock Mechanics. 1998, 605-610.
6. Tomecka-suchon, S. and Rummel, F. Fracture-induced Resistivity Changes in Granite. International Journal of Rock Mechanics and Mining Sciences & Geomechanics Abstracts, 1992, 29(6). 583-588.
7. Daily, W. and Ramirez, A.L. Electrical imaging of engineered hydraulic barriers. Geophysics, 2000, 65. 83-94.
8. Shemyakin, E.I., Fisenko, G.L. and Kurlenya, M.V., et al. Zonal Disintegration of Rocks around Underground Workings, Part I: Data of in-situ Observations. Journal of Mining Science, 1986, 22(3). 157-168.

RaSiM 7(2009): Controlling Seismic Hazard and Sustainable Development of Deep Mines, C.A. Tang(ed), Rinton Press, 107-112

STUDY ON ACOUSTIC EMISSION CHARACTERISTICS OF REINFORCED EFFECT OF BOLT TO FRACTURE UNDER UNIAXIAL TENSILE CONDITIONS

NING ZHANG, SHU-CAI LI, MING-TIAN LI, LEI YANG, HUAI-FENG SUN

Geotechnical and Structural Engineering Research Center, Shandong University

Jinan, 250061, P.R. China

MINGTIAN LI

Department of Civil Engineering，Shandong Jiaotong University

Jinan, 250023, P.R. China

FENG SHEN

Nanjing Feng Hui Composites Co., Ltd

Nanjing, 211124, P.R. China

Laboratory tests on acoustic emission (AE) characteristics of modified cement mortar with three-dimensional through crack and anchorage are carried out under the conditions of uniaxial tensile loading. Stress-time curve and the relations of time with AE characteristics are obtained. In an effort to analyze the complete failure process of the specimen, the experimental results show that the effect of strengthening and crack arrest of bolt to fracture is obvious. In addition, AE parameters, e.g., energy and hit number, can reflect exactly the trend of stress. Furthermore, "Jumping phenomenon" occurs corresponding to the change law of stress-time. Besides,very little energy is released in linear elastic stage. AE energy is released continuously in the process of the bolt being pulled out from specimen. AE activity also occurs mainly in the process of the bolt being pulled out from specimen. From the location point of view, AE activity mainly concentrates in the end of the bolt slipping.

1 Introduction

Acoustic Emissions (AE) are commonly defined as transient elastic waves within a material caused by the release of localized stress energy. The released elastic wave is transferred to the electrical signal through the acoustic emission sensors, and then characteristic parameters are obtained from amplification and processing [1, 2]. This method can monitor the emergence of internal micro-cracks and the extension of macro-cracks continuously and timely. The other methods do not have these advantages [3]. AE technology is developing to be an indispensable method in rock mechanics tests.

Since AE technology has been applied in rock mechanics tests, large qualities of research results about the failure mechanism of brittle material have been obtained by many researchers. Zhao Xingdong [4] did experimental studies on AE activity characteristics of different rock samples. It was concluded that, AE location functioning relates directly to the attributes of rock samples. Wu Gang [5] did studies on the acoustic emission characteristics of rock material's failure during various stress states. Li Shulin etc [6] concluded that the Kaiser effect does not occur for rock samples subjected to simple loading. Xu Zhaoyong [7] studied the preliminary location of micro-cracks under true triaxial compression. Zhang Ru and Xie Heping [8] did an experimental study on acoustic emission characteristics of rock failure under uniaxial multilevel loadings, and they concluded that a relatively quiet period of AE appears before rock failure.

2 Acoustic Emission Location Algorithm

AE location algorithms are built on the basis of arrival time residual model. All the location method is in accordance with the P-wave arrival time except Scholz using the S-wave arrival time. Arrival time residual model is:

$$(X_i - X_0)^2 + (Y_i - Y_0)^2 + (Z_i - Z_0)^2 = V_i^2 \times (T_i - T_0)^2 \qquad (i = 1,2,\cdots,N) \tag{1}$$

Where (X_i , Y_i , Z_i) represents the coordinate position of the i-th AE sensor; V_i is the wave velocity; T_i is the arrival time of P-wave spreading to the i-th sensor.

The idea of least square method can be summarized as

(1) Subtracting the first row from the other terms of the formula (1), overdetermined Linear Equations can be obtained:

$$a_j X_0 + b_j Y_0 + c_j Z_0 + d_j T_0 = e_j \qquad (j = 1,2,\cdots,N-1) \tag{2}$$

where a_j , b_j , c_j , d_j , e_j are the coefficients after subtracting;

(2) Do the operation of least square to formula (2), receive the optimization solution vectors $[X_0, Y_0, Z_0, T_0]$;

(3) According to the preliminary locating results, speculate the rationality of each tunnel, remove the unreasonable tunnel, obtain the accurate locating result;

(4) Make the judgment of the solution and solve the error range.

3 Experiment

3.1 Samples Making

Use modified rubber powder-cement mortar as rock similar material. Choose Glass Fiber Reinforced Plastics (GFP), produced by Nanjing Feng Hui Composites Co., Ltd. to simulate the real bolts according to similarity principle. Mechanical properties of the similar materials and the GFP materials are listed in Table1. Geometry size of the specimen is $L_1 \times L_2 \times H$=70mm×70mm×140mm Hard resin sheet is choosen to make the preset crack. The dimension of preset crack is L_3=35mm and thickness 0.2mm The fracture is throughout.. Positions of preset crack and bolt in specimen are shown in Figure1.

Table 1 Mechanical properties of the similar materials and bolt materials

	Compressive Strength $\sigma_c/(MPa)$	Tensile Strength $\sigma_t/(MPa)$	Elastic Modulus $E/(GPa)$	Poisson Ratio ν	Bulk Density $\gamma/(g/cm^3)$
Similar materials	16.1	1.89	2.3	0.191	1.88
Bolt materials(GFP)	——	50	21	——	——

3.2 Test Loading Device

The test loading device is a 3000KN digital electro-hydraulic servo-rigid tri-axial rock testing machine. The stress, strain, displacement vs time curves can be drawled automatically by the collected data. Displacement control is used in this paper with a speed of 0.002mm/s.

3.3 Analysis System of AE and Parameter Setting

AE analysis system is produced by Physical Acoustic Corporation. PCI-8 card is used to reduce noise. The system can collect and store the waveform signals. 8 channels are used. Sampling frequency is 2MHZ and the threshold is 100mv. The sensor model is MICRO-30. The frequency domain is 100MHz~600KHz. Type 1220A-AST preamplifier with a gain of 40db is available. Positions of the sensors are shown in Figure 2.

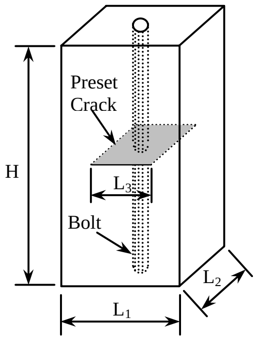

Figure 1 Arrangement of preset crack and bolt

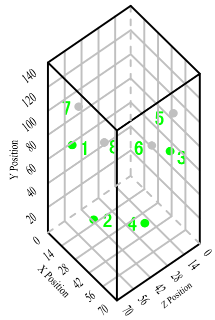

Figure 2 Location of sensors on the surface of specimen

3.4 Test Device

High strength binder is used to connect specimen and the rigid indenter. To decrease eccentric tension, steering knuckles are set on both ends of specimen. Due to the existing of high strength binder, the influence of noise signals to acoustic emission signals is eliminated. Receiving surfaces of sensors should be contacted completely with specimen, otherwise, AE signals is effected. Vaseline is used by some researchers to fix AE sensors. The author use the same method too and find that the method is inconvenient if the dimension of specimen is too small. The author consulted correlation papers [9], using silica instead of Vaseline as the coupling medium between sensor and specimen, and a better performance is achieved. Sketch of testing is shown in Figure 3.

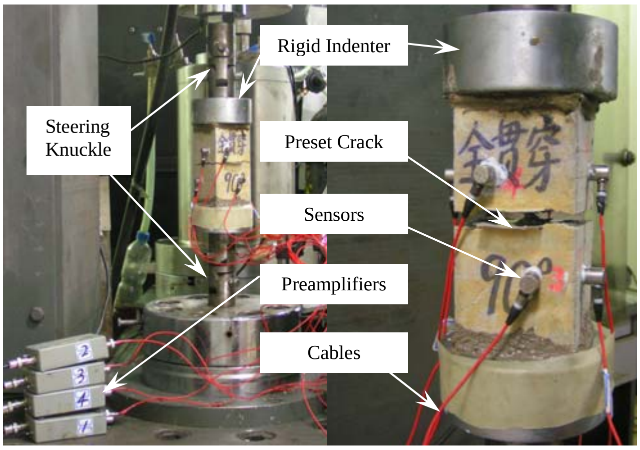

Figure 3 Sketch of testing

4 Experimental Results Analysis

4.1 Analysis of Whole Stress-time Curve of Specimen under Axial Tension

Displacement control is used in test and the loading rate is a fixed value. So the trend of stress-time curve and stress-strain curve is completed consistent. For the convenient of comparison with the following AE parameters-time curves, stress-time curve (Figure 4) is adopted here to analyze the whole failure process of specimen. It is found that the strengthening and crack arresting role is obvious. The bolt plays its role continuously even after the crack extends completely. Mechanical behavior of specimen on different stages of failure process can be reflected clearly according to the several feature points in Figure 4.

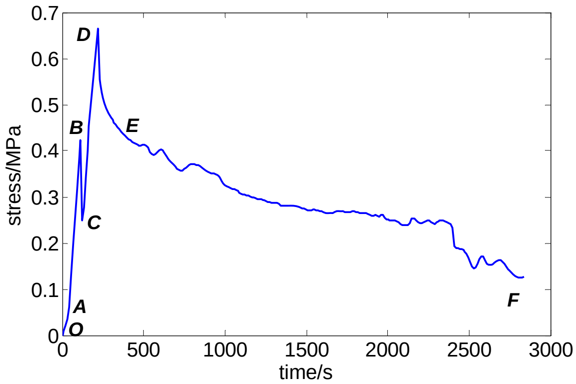

Figure 4 Measured whole stress-time curve of specimen under axial tension

Stage OA: In this stage, because of the influence of the fitting clearance of steering knuckles and the testing machine, the curve is up concave. Stage AB: It is linear elastic stage. In this stage, it is mainly linear elastic deformation. Micro-cracks in materials hardly extend. Monitored data, containing load, stress, strain and so on, increases in equal ratio. Stage BC: Crack initiation takes place in one side of the crack with smaller initial fracture toughness. The fracture develops rapidly to the specimen surface. Stage CD: With the increasing of axial load, crack develops to the other side crossing the bolt. Stage DE: Dislocation slip takes place between bolt and specimen, developing rapidly to the end of specimen. Anchorage length deceases with the process of dislocation slip. Finally, bolt slips along the full length. Stage EF: In this stage, bolt is pulled out gradually form one end of specimen. Stress decreases with the increasing of displacement.

By observation of the stress-time curve, “jumping phenomenon” can be found. The author holds that the “jumping phenomenon” is induced by transient slip between bolt and specimen.

4.2 Analysis of AE Parameters

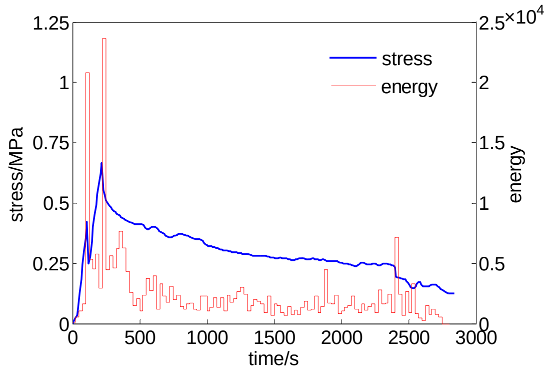

Figure 5 Relationship curves of time with stress and energy

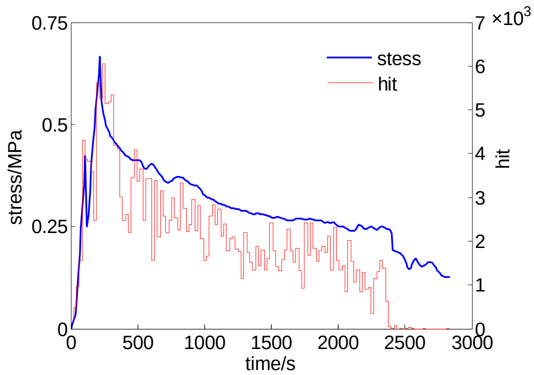

Figure 6 Relationship curves of time with stress and hit number

Observing Figure 5, it can be obtained that: in initial stage (OA) and linear elastic stage (AB), only very little energy is released from specimen. In the stable crack propagation stage (BC), the first “jumping phenomenon” takes place. In this stage, AE activity is mainly caused by micro-crack forming nucleation and preset crack rapidly extending. AE activity increases sharply near the crack, energy accumulates rapidly. One of the two boundaries with smaller initial fracture toughness extends firstly. The crack develops rapidly to the specimen surface. At the same time, accumulated energy is released transiently. The second “jumping phenomenon”, corresponding to stage CD & DE, is mainly caused by two aspects. On the one hand, the other boundary of the preset crack extends, on another other hand, the dislocation movement between the bolt and the specimen takes place with the increasing of axial load. In this time, more energy is released than the first jumping. The last stage (EF) is the stable release stage of AE energy. The characteristic of this stage is that the AE energy is released continuously. In this stage, small “jumping phenomenon” happens, which is caused by the same reason with the “jumping phenomenon” of stress-time curve.

Observing Figure 6, it can be found that hit number has the same change law with that of the energy. The hit-time curve accords better with the stress-time curve. As same as the energy, there is twice big “jumping phenomenon” takes place. From the time point of view, the twice jumping phenomenon of the hit number and that of the energy is simultaneous. Looking from the duration, the second jumping (bolt slipping, corresponding to stage BC) has a longer duration than the first one (preset crack extending, corresponding to stage DE), which according well with the testing phenomenon.

Because the three-dimension diagrammatic sketch generated by the AE software cannot clearly display the location of AE activity in specimen. Plane diagrammatic sketches are shown here. AE activity in different stages locating result of Y-X plane and Y-Z plane is shown in Figure 7.

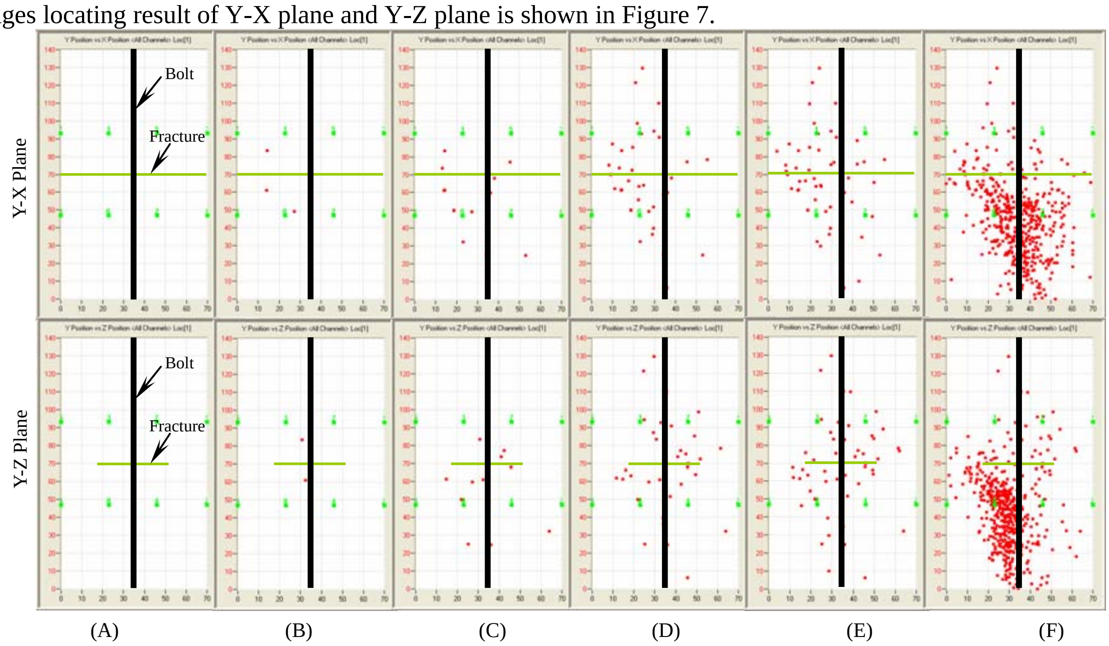

Figure 7 AE locating results

The figure numbering (A~F) of Figure 7 is respectively corresponding to the numbering of Figure4 in time. The following results can be obtained by studying the AE locating results. Before the preset crack extending, there is hardly AE activity and AE activity occurs mainly in the process of the bolt being pulled out from specimen, corresponding to stage EF. From the location point of view, AE activity mainly concentrates in one end of the bolt. This shows that the bolt has obvious crack reinforcement effect. Comparing the figures before and after preset crack extension, AE activity mainly concentrates near the fracture surface. While in quantitative terms, there is no big difference between them. This shows that AE activity caused by crack extension is very little. The author holds that the phenomenon is caused mainly for two reasons. On the one hand, the crack extension is a transient process; there is no enough time for sensors to monitor the signals. On the other hand, the preset crack is large in size compared with the dimension of specimen and it is also a throughout crack. So the author considers that extension of larger-size crack release less energy, in other words, less energy is needed for extension of a larger-size crack.

It should be indicated that, in the test, the gain value of the preamplifier is 40dB. In addition, the strength of the material is low. So, very few AE events are monitored in the whole failure process of the specimen. The monitored AE events mainly occur in the process of crack extension and the bolt slipping. However, the number of monitored AE events may increase under the premise of improving the gain value.

5 Conclusion

Acoustic emission studies on modified cement mortar with three-dimensional through crack and anchorage have been carried out. Reinforcement effects of bolt to crack are studied. The following conclusions have been drawn experimentally:

(1) Mechanical behaviors of specimen on different stages are obtained by analysing the complete failure process of the specimen. The bolt has obvious reinforcement effects to the preset crack, and the bolt plays its role continuously, even after the specimen completely faults.

(2) AE parameters, energy and hit number, can clearly reflect the change law of stress.

(3) Very little energy is released in linear elastic stage. AE energy is released continuously in the process of the bolt being pulled out from specimen.

(4) AE activity occurs mainly in the process of the bolt being pulled out from specimen. From the location point of view, AE activity mainly concentrates in one end of the bolt, around the bolt.

Acknowledgements

This work was financially supported by National Science Fund for Distinguished Young Scholars (No. 50625927), National Research Item of 973 (2007CB209407), and Natural Science Foundation of P. R. China (No. 40872203) .

References

1. Qin, S.Q. Li, Z.D. and Lin, Y.M. Micoprocess of Rock Fracture and Acoustic Emission. Journal of Northwest University of Technology, 1991, 12(3). 247-253.
2. Ba, J., Liu, L.Q. and Ma, S.L. A Summary on Acoustic Emission Source Location Methods in Rock Mechanics Experiment. NDT, 2004, 26(7). 342-348.
3. Zhao, X.D., Liu, J.P. and Li Y.H., et al. Experimental verification of rock locating technique with acoustic emission. Chinese Journal of Geotechnical Engineering, 2008, 30(10). 1472-1476.
4. Zhao, X.D., Chen, C.H. and Liu, J.P., et al. Experimental Study on AE Activity Characteristics of Different Rock Samples. Journal of Northeastern University (Natural Science), 2008, 29(11). 1633-1636.
5. Wu, G. and Zhao Z.Y. Acoustic emission character of rock materials failure during various stress states. Chinese Journal of Geotechnical Engineering, 1998, 20(2). 82-85.
6. Li, S.L., Yin X.G. and Wang, Y.J., et al. Studies on acoustic emission characteristics of uniaxial compressive rock failure. Chinese Journal of Rock Mechanics and Engineering, 2004, 23(15). 2499-2503.
7. Xu, Z.Y., Mei, S.R. and Zhuang, C.T., et al. Preliminary location of microcracks in several rock specimens under true triaxial compression. Acta Seismologica Sinica, 1994, 7(S). 51-59.
8. Zhang, R., Xie, H.P. and Liu, J.F., et al. Experimental study on acoustic emission characteristics of rock failure under uniaxial multilevel loadings. Chinese Journal of Rock Mechanics and Engineering, 2006, 25(12). 2584-2588.
9. Zhao, K., Deng, F. and Jin, J.F., et al. Wavelet analysis of Kaiser signal of rock acoustic emission and its application. Chinese Journal of Rock Mechanics and Engineering, 2006, 25(2). 3854-3858.

RaSiM 7(2009): Controlling Seismic Hazard and
Sustainable Development of Deep Mines,
C.A. Tang(ed), Rinton Press, 113-118

EXPERIMENTAL STUDY ON ROCKBURST PROCESSES OF LIMESTONE UNDER UNLOADING CONDITION IN DEEP ROADWAYS

LI-MING ZHANG and ZAI-QUAN WANG

College of science, Qingdao Technological University

Qingdao, 266033, P.R. China

The characteristics of rock failure under unloading condition are different from those under loading condition. Unloading confining pressure experiments are conducted to simulate the failure process of stress released during underground excavation. The deformation features, mechanical parameters and failure characteristics were obtained based on the results of triaxial unloading tests of limestone. Results show that strain energy stored in rock is large enough to cause rock failure when it is released. Rock will outburst when the maximum in situ stress is excessively greater than the uniaxial compressive strength of rock. In order to prevent the occurrence of rockburst, one of the basic methods is to release the strain energy in rock before excavation. Accordingly, the rock will not have a large amount of energy released to cause failure. In addition, rockburst can also be controlled or released by lowering the excavation speed or applying precautionary measures to control the displacement of surrounding rocks.

1 Introduction

In civil engineering fields such as hydroelectricity, communications projects, etc., there exist plenty of unloading circumstances due to excavation. Unloading due to underground excavating often necessitates stress adjustment in the rock mass near the free face and causes stresses to concentrate in certain areas. The behaviour of rock deformation and its failure characteristics under loading and unloading conditions are substantially different [1, 2]. Rockburst during excavation of underground engineering in areas of high geo-stress is a typical failure phenomenon due to unloading [3, 4]. However, most rock mechanical experiments are designed for loading condition, which is not relevant to the study of the stress states of rock masses during excavation. In recent years, studies on the unloading failure of rock masses have been developed with the demands of rock mechanics and engineering practices. Some researchers studied unloading characteristics of rock triaxial tests and gained some good results [1-7]. For making unloading failure mechanism clear and establishing effective rock unloading failure theory, more efforts must be expended. This study attempts to reveal the deformation and failure mechanism during confining pressure release through laboratory controlled experiments, and the application of experimental results to underground rockburst control are discussed.

2 Test condition and plans

Unloading mechanical conditions are simulated by the triaxial test and two typical test plans are applied. The experiments are carried out on an MTS815 servo-controlled testing machine. The testing procedure is described as follows:

(1) Plan 1: unloading test

Stage 1: Applying and increasing σ_1 and σ_3 to the destined value of σ_3 according to hydrostatic pressure.

Stage 2: Steadying σ_3 and steadily increasing σ_1 to a certain stress condition before the specimen is failure and the tress level is approximately around the proportion limit.

Stage 3: Pressure is decreased while axial deformation is maintained at a constant level. Slowly increasing σ_1 and gradually reducing σ_3 at the same time.

Stage 4: Once the specimen is broken, σ_3 shall stop unloading the confining pressure and keep constant, and continue applying axial strain until the stress differences of σ_1 - σ_3 doesn't decrease with axial strain.

(2) Plan 2: loading test

Loading test with constant confining pressure is carried out for the purpose of comparison.

3 Analysis of experimental results

3.1 Stress-strain relations

The results show that intense brittle failure happened in the process of unloading confining pressure. The experiment data are shown in Table 1.

Table 1 Experimental data of unloading rock specimens

Rock specimens	Confining pressure	Velocity of unloading confining pressure (MPa/S)	Failure confining pressure (MPa)	Failure stress difference	Velocity of loading axial stress (KN/S)
3#	40	0.2	25.8	180.2	1.5
4#	40	0.4	12.2	178.8	1.5
6#	40	0.6	14.6	155.4	1.5
5#	40	0.8	7.7	158.3	1.5
2#	30	0.2	17.5	159.5	1.5
7#	30	0.4	14.9	137.1	1.5
8#	30	0.6	10.2	126.8	1.5
9#	30	0.8	0.3	137.7	1.5
20#	30	0.2	19.9	158.9	1.5
21#	30	0.4	18.1	186.3	1.5
22#	30	0.6	14.8	149.6	1.5
12#	20	0.2	7.1	108.9	1.5
11#	20	0.4	4.5	104.5	1.5
10#	20	0.6	3.6	109.4	1.5
14#	10	0.2	0.7	127.3	1.5
13#	10	0.4	0.3	68.7	1.5
15#	10	0.6	0	79	1.5

Figure1 shows the relationship between axial stress and axial strain under unloading condition. Unloading condition has less effect on the forepeak stage of axial strain curve, σ_1 but much more on the post-peak stage, which is mainly manifested by curve shape differences between specimens. Contemporaneous unloading has greater effects on the curves of transverse strain σ_3 and volumetric strain σ_v , and after entering the unloading stage; variant gradient of σ_1 obviously increases. σ_v changes from compression to dilation deformation, which shows that during destruction due to unloading, the tension character is apparent and fracture surfaces are different.

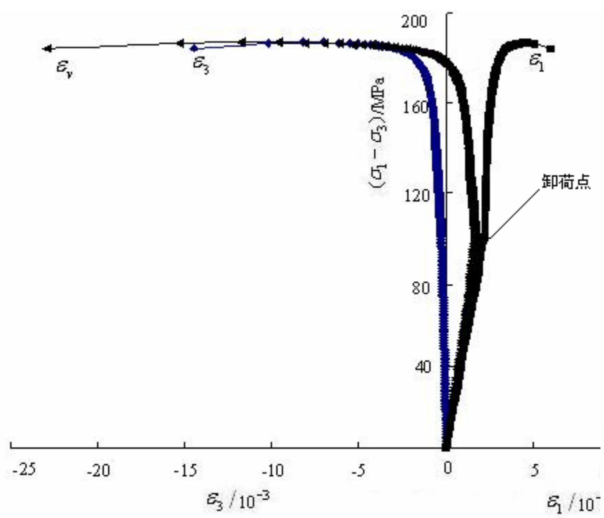

Figure 1 Complete stress-strain curve of 4＃under unloading test

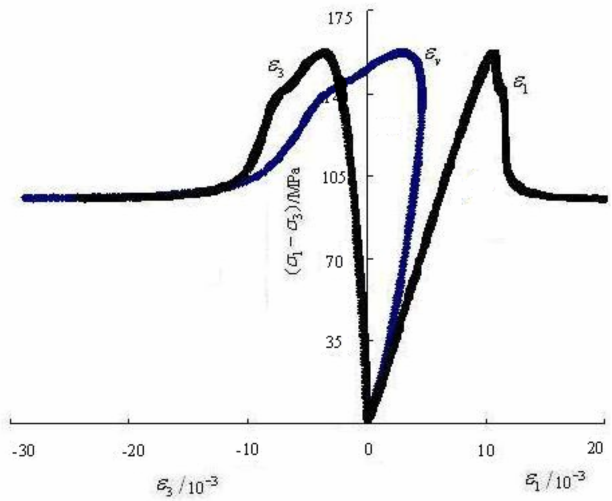

Figure 2 Complete stress-strain curve under loading test

Figure2 shows that the stress difference (σ_1-σ_3) and axial strain ε_1 have good linear relation prior to peak value under unloading condition and the strain rate nearly keeps constant with a certain slope, which shows that strain remains rising when the stress difference reduces. At the same time, the axial strain occurs rebounding, which is mainly due to applying the different axial loading modes in the test.

3.2 Variation characteristics of deformation modulus and Poisson ratio

Figure3 shows the relationship between confining pressure and deformation modulus under unloading condition. Figure4 shows the relationship between confining pressure and Poisson ratio under unloading condition. Results show deformation modulus decreased and Poisson ratio increased during the unloading stage, compared with Plan 2. Those variables decreased with increase in unloading velocity under the same initial confining pressure. However, they increased with increase in the initial confining pressure at the same unloading velocity.

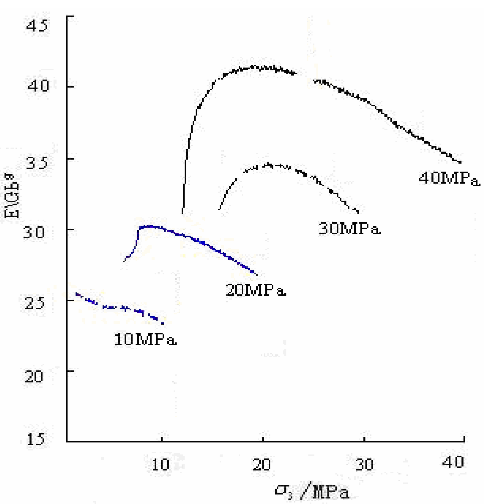

Figure 3 Relationship between confining pressure and deformation modulus

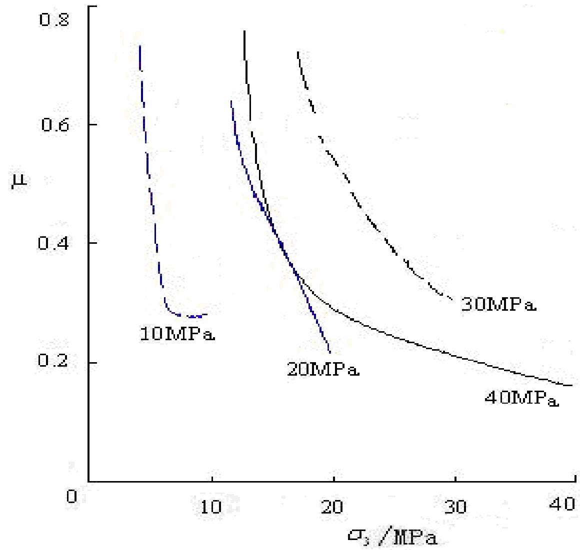

Figure 4 Relationship between confining pressure and Poisson

3.3 Failure modes

The results show failure modes of rock specimens can be classified into two types: tensile-shear and splitting-shear failure under unloading condition. Failure modes are related with confining pressure and unloading velocity. The failure angle increased with unloading velocity increasing under the same initial confining pressure. However, it decreased with the initial confining pressure increasing under the same unloading velocity. Failure patterns of the specimens under unloading condition are shear failure.

3.4 Strength analysis

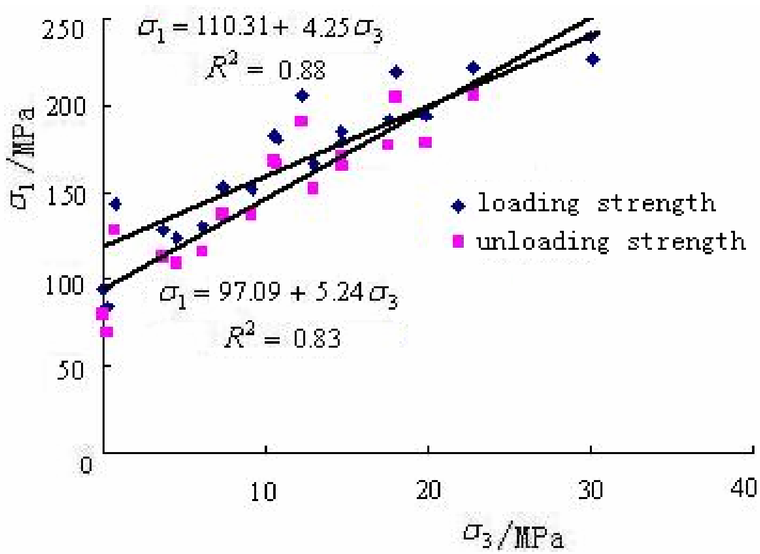

Figure 5 Strength values of specimens

Figure5 shows the relationship between axial stress and confining pressure. A linear relation between axial load bearing capacity and confining pressure means confining pressure has a large effect on axial load bearing capacity. Comprised with loading condition, the cohesion (c) of rock decreased but the internal friction angle (φ) increased in the process of unloading.

3.5 Effect of unloading velocity

Results indicate that the higher the unloading ratio, the lower the strength and the smaller the dilatational strain of the specimens are found. This means the more slowly the unloading ratio, the more time for fractures spreading and stress transferring in the specimens. So there are more fracture planes during the specimens breaking and the greater breakage.

4 Application experimental results to underground Rockburst control

In the unloading process during a tunnel excavation, the lateral pressure in the surrounding rock is released. The inherent stresses readjust, and failure of rock may occur if the adjusted stress state becomes overly critical. In areas where the in situ rocks are highly stressed, quick unloading due to tunnel excavation would result in a series of discontinuous tensile cracks parallel to the tunnel walls and the development of a “slaty” structure in the surrounding rock. Researchers used the scanning electron microscope to analyze some rupture planes of rockburst, which occurred in the Tianshengqiao hydropower station [8, 9]. They found the rupture planes were of the tensile-shear or tensile type, which supports the results of the experiments under unloading conditions. When this kind of “slaty rupture” develops further and propagates toward the interior, rockburst will occur [10].

Based on the experimental results, rock will outburst when the maximum in situ stress is excessively greater than the uniaxial compression strength. It is often difficult to measure the maximum in situ stress. But the core drilling can often show the stress state of the rock. For example, schistose and disc effects indicate that stress in the rock body is very high and outburst may happen. To prevent rockburst, one of the basic methods is to release the strain energy in the rock mass before excavation. After that, the rock will not have enough energy stored to cause failure. The authors have used the pre-boring method to release the strain energy and to prevent the outburst in coal mines. Rockburst could also be controlled or released by adjusting the speed of excavation, which is lowering the excavation speed in highly stressed areas, or taking some measures, such as NATM excavation techniques, to control the release of the displacement of surrounding rock.

5 Conclusions

Experimental results showed that: Deformation modulus decreased and Poisson ratio increased under unloading conditions. Those variables decreased with an increase in unloading velocity under the same initial confining pressure. Failure modes of rock can be classified into two types: tensile-shear and splitting-shear failure. The cohesion of rock decreased, but the internal friction angle increased under this unloading condition

Rockburst occur in the unloading process of tunnel excavation, and their characteristics are closely related to the deformation and failure characteristics of the rock. Rocks fail during the process of confining stress reduction, and the failure is associated with strain energy release. To prevent rockburst, one of the basic methods is to release the strain energy in the rock before excavation so the rock will not have a large amount of stored energy which releases to cause failure. Rockburst could be controlled or released by adjusting the speed of excavation.

Acknowledgements

The authors wish to acknowledge the financial support from the National Natural Science Foundation of China (no. 50674059) and Shandong Provincial Education Foundation (no. J07YB01 and no.J08LD54).

References

1. Ortlepp, W.D. The behavior of tunnels at great depth under large static and dynamic pressures. Tunnelling Underground space technology, 2001, 16(1). 41-48.
2. Wu, G. Comparison of failure effects of rock mass under loading conditions. Chin. J. Rock Mechanics and Engineering, 1997, 18(2). 13-16.
3. Wang, X. and Huang, R. Analysis of Deformation and Failure Features Characteristics of Rock under Unloading Conditions and Their Effects on Rock Burst. Chin. J. Mountain Research, 1998, 16(4). 281-285.
4. Xu, L. Research on the Experimental Rock Mechanics of Rockburst under Unloading Condition. Chin. J. Geotechnical Engineering, 2003, 22(1). 1-4.
5. You, M. and Hua, A. Triaxial confining pressure test of rock sample. Chin. J. Rock Mechanics and Engineering, 1998, 17(1). 24-29.
6. Wu, Y. And Li, J.D. Unloading properties of marble. Chin. J. Rock and Soil Mechanics, 1984, 5(1). 29-36.
7. Ren, J.X., Ge X.R., Pu Y.H. and et a1.Primary study of real-time CT testing of unloading damage evolution law of rock.Chin. J. Rock Mechanics and Engineering, 2000, l9(6).697-701.
8. Tan, Y. Analysis on the mechanism of rock burst. Chin. J. Hydrol Engineering Geology,1989, 16(1). 34-38.
9. Pan Yue,Liu Ying, Gu Shanfa. Fold Catastrophe Model of Mining Fault Rockburst. Chin.J. Rock Mechanics and Rock Engineering, 2001, 20(1). 43-48.
10. Gu, M.C., He, F.L. and Chen, C.Z. Rock Mechanics and Rock Engineering, 2002, 21(9). 1324-1329.

RaSiM 7(2009): Controlling Seismic Hazard and
Sustainable Development of Deep Mines,
C.A. Tang(ed), Rinton Press, 119-124

EXPERIMENT STUDY OF ROCK STRENGTH DEGRADATION

HOU-QUAN ZHANG, YONG-NIAN HE, LI-JUN HAN, BING-SONG JIANG

State Key Laboratory for Geomechanics and Deep Underground Engineering, School of Architecture and Civil Engineering, China University of Mining and Technology

Xuzhou, 221008 P.R. China

Rock material strength will degrade with the damage in the rock failure process. This paper reports one self-designed method to test rock strength degradation and introduce the technical routine, sample preparation (including its key technique) and experiment procedure in details. Through self-designed direct shear tests by XJ-1 portable type of shear apparatus, the relationships between shear stress and compressive stress of irregular rock samples which are produced in normal uniaxial and triaxial compressive experiments were obtained. Comparing the Coulomb strength curve gained by the direct shear tests with the ultimate Mohr circle envelope obtained from previous uniaxial and triaxial compressive experiments, it can be seen that the cohesion result measured by uniaxial and triaxial experiments before failure is obviously greater than that obtained by direct shear tests of irregular rock blocks. This difference mainly results from the damage in the rock failure processes of uniaxial and triaxial compressive experiments, not the deviation by the different testing methods.

1 Introduction

Under the long-term geological effect, mechanical properties of geological materials such as rock mass will degrade at a certain extent. For example, under the tectonic stress, micro cracks in rock mass will initiate, propagate and nucleate. Fracture happens ultimately. The material of rock blocks will be damaged at certain content, and its material strength will decrease. The degradation process of rock material strength accompanies with the damage in rock failure process [1].

However, many present analytical methods used to discuss high stress problems such as the slop stability and tunnel support are mostly based on the peak material strength. It is obvious that the calculated results are undoubtedly at risk. In contrast, the results calculated by residual strength are very cautious [2]. Therefore, a comprehensive understanding on real laws of strength degradation in rock failure has a much greater theoretical and practical significance, which will impel the deep investigation on the mechanical behaviour of rock after peak strength, promote the understanding of mechanical behaviour of other materials after failure, describe the characteristics of cracked rock mass in high stressed rock engineering properly and lay more reasonable scientific foundation for the selection of support design.

Although modern advanced techniques such as scanning electron microscopy, acoustic emission detecting, computed tomography, non-destructive testing and digital image [3-5] expedite the study on mechanical behaviour of rock before and after failure, the degradation investigation of rock strength after peak-load can’t attract much attention from rock scientists, and the related research report is very rare. Therefore, a kind of self-designed testing method for rock strength degradation is presented and discussed in this paper.

2 Experiment Description

2.1 Experiment Aim and Technical Routine

The purpose of this experiment is aimed to test the strength degradation of rock material after failure. At first, normal uniaxial and triaxial compressive experiments were carried out on the TATW-2000 rock triaxial testing machine developed by China University of Mining and Technology and Changchun Chaoyang Instrument and Experiment Limited Company to obtain original rock material strength. Then, the material strength of irregular damaged rock blocks which produced in previous normal compression tests was planed to test. But the material strength for damaged rock blocks can't be simply measured by normal compression or tension tests since they were irregular. The following testing method was adopted in this paper. Initially, the irregular rock blocks obtained from compression tests were moulded and embedded in a concrete 'shear box'. Secondly, the samples made from irregular rock blocks were performed self-designed direct shear tests by XJ-1 portable type of shear apparatus (see figure 1) developed by the engineering geological research laboratory in Chengdu Geological Institute [6] to obtain the relationship between shear stress and compressive stress in shear failure process. Thirdly, the degradation of material strength between rock samples before failure and rock blocks after failure was studied by the comparison with the ultimate Mohr circle envelope obtained in the uniaxial and triaxial compression experiments.

2.2 Sample Preparation

Some damaged rock blocks in (uniaxial and triaxial) compression tests with a certain section area were selected out and numbered. Then, rock blocks are moulded and embedded in a concrete 'shear box' (see Figure 2) in order that the load applied on the surface of shear box can be evenly transferred to rock blocks and formed uniform compressive and shear stresses. For more effectiveness in experiments, it is necessary that two ends of rock blocks should be reliably embedded in concrete box for a certain length. A clearance of 5mm between the upper and lower boxes was designedly left as a potential failure surface, which was parallel to the surface of moulding box in shear apparatus.

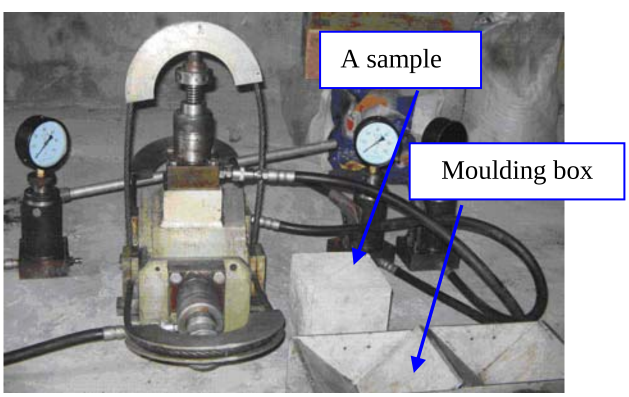

Figure 1. XJ-1 shear portable apparatus.

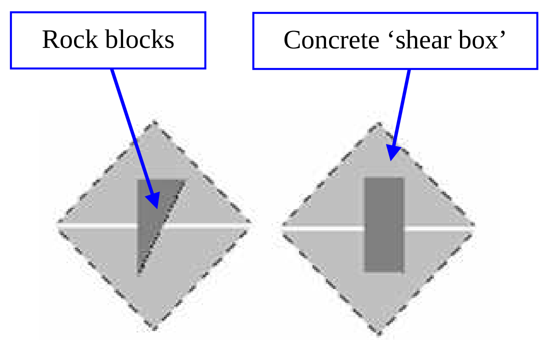

Figure 2. Scheme of sample preparation.

2.3 Experiment Procedure

(1) For more effectiveness in experiments, several groups of trial compression-shear tests should be performed to make sure that normal compressive stress on the 'shear box' is so appropriate that concrete 'shear box' can't produce a run-through fracture before shear failure of rock blocks. According the former groups of experiment results, an appropriate compressive stress was selected and used in the later testing.

(2) One shear sample was put in the lower shear box to make sure that the potential failure surface was parallel to the surface of lower shear box. Then, the upper shear box was put down to cover the sample.

(3) Adjust the extendible loading arm of jack to make sure that it didn’t elongate so long. Then, join the transmission setting with jack and made sure that pressure instrument worked well.

(4) Compressive stress was increased to a pre-designed value, recording it and maintaining this pressure.

(5) Then, increase the horizontal load until the shear sample produced an evident crack, recording the maximum shear stress and stop testing at this time.

(6) Put a soft paper on shear failure surface and draw an outline for the shear failure section using a pencil. Subsequently, count the area of shear failure surface using millimeter paper.

2.4 Key Technique for Key Step

The most important step in the whole experiment is preparing shear samples. Elaborate Preparation can make the experiment results represent the mechanical behaviour of rock blocks more properly. In preparing shear samples, the key technique is the reasonable mix proportion of concrete and curing condition. A reasonable proportion can produce a high strength of concrete ‘shear box’ so that it don’t produce macroscopic run-through cracks before shear failure of rock blocks and a good workability to make sure that a tight bonding between rock blocks and concrete ‘shear box’.

Concrete mix proportion. The design of concrete proportion should take into account three ratios between four kinds of materials: the ratio of water to cement, the ratio of sand to aggregate (stone and sand), and the ratio of aggregate to cement. The two important influential factors on concrete strength are the strength of cement and the ratio of water to cement. The ratio of sand to aggregate was determined by the voidage of stone and the ratio of water to cement. The quantity of water was selected based on the category of coarse aggregate, grain size and the requirement of concrete collapsing degree. According to the literature [7] and considering the requirement of sufficient workability and high strength for concrete ‘shear box’, the referenced concrete mix proportion in practice is listed in Table 1, Table 2 and Table 3.

Table 1. Concrete mix proportion.

Concrete type	Cement type	Stone type	Maximum grain size of crushed stone	Sand percentage	cement/sand/stone/water (weight, kN)
C40	42.5	Crushed stone	20	31	1:1.34:2.6:0.4
C50	52.5	Crushed stone	20	31	1:1.34:1.6:0.4

Table 2. Grading of crushed stone.

Grading size	25 mm	20 mm	10 mm	5 mm	2.5 mm
Referenced grading	0%~5%	15%~45%	70%~90%	90%~100%	95%~100%
Reality grading	0	45%	45%	10%	0

Table 3. Grading of sand.

Grading size	5mm	2.5mm	1.25mm	0.63mm	0.315mm	0.16mm
Referenced grading	10~0%	35~0%	65~35%	70~41%	92~70%	100~90%
Reality grading	0	20%	40%	20%	20%	0

Sample moulding. Before the moulding of samples, a thin layer of oil was smeared on the inside surface of moulding box for the convenience of sample’s separation from it in the future. Firstly, according to Table 1, Table 2 and Table 3, sand, stone and cement were mixed and blended up fully. It is noted that the ratio of water to cement must be strictly controlled in this process. Then, put the concrete mixture into the moulding box and agitate it for air bubbles come out from the concrete mixture. After smoothing the surface of concrete mixture, rock blocks were put into the center of concrete ‘shear box’. When the concrete mixture became solid, the upper half part of sample was knocked down from the moulding box. It almost spent ten hours preparing the upper part of shear sample from moulding to knocking off. In the same way, the lower half part of sample was moulded and embedded into the center of moulding box full of concrete mixture. A clearance of 5 mm was left between the upper and lower concrete ‘shear box’ as a pre-designed potential shear failure surface. After fourteen hours, the whole sample can be knocked out from the moulding box and the whole preparation of a shear sample was completed. It is noted that the upper part of shear sample should be preserved with water-covering curing when the lower part was moulded.

Concrete curing. Concrete curing has an important influence on its strength, especially for the earlier curing. When the sample was moulded, if concrete surface was dry, the inner water would transfer to the outer surface and made it difficulty for inner cement to hydrate. Even though the concrete surface was wet, owing to the water movement of cement’s hydration, the inner part would come into a dry state. Therefore, it was very necessary to supply water from outside to maintain the hydration of inner cement. Moreover, the upper part of sample should be maintained in time when it was knocked out from moulding box. According to the temperature and humidity conditions, natural curing using wet cloth to cover the sample was adopted in this testing. It was very necessary for the curing of concrete moulding in summer. Additionally, the curing should last for at least 15 days.

3 Experiment Results

The prepared samples had been performed direct shear tests by XJ-1 shear portable apparatus. The experiment results of different irregular rock blocks obtained are listed in table 4. Two representative shear failure patterns are shown in figure 3. The ultimate Mohr circle envelope obtained by uniaxial and triaxial compression experiments is shown in figure 4. The comparison of two strength curves obtained by compression experiments and compression-shear experiments is represented in figure 5.

It can be seen from Figure 5 that cohesion in Mohr strength curve obtained by compression experiments is obviously greater than that obtained by compression-shear tests. Maybe there arises one question that the difference is induced by two different testing methods, but the reference [8] reported that there were no much difference (almost 10% deviation) on cohesion in two strength curves obtained by direct shear tests using intact samples (different from damaged rock blocks in this paper) of saturated argillaceous siltsand, natural silty mudstone, saturated silty mudstone and compression (unaxial and triaxial) experiments using intact rock samples in the same way. So the main reason for this great difference (approximately 64% deviation) on cohesion is the material strength degradation of rock samples in failure process, not the deviation resulted by different testing methods in this investigation.

Table 4. Compression-shear experiment results of irregular rock blocks

Sample No.	Compressive stress	Shear stress	Sample No.	Compressive stress	Shear stress
1	4.25 MPa	11 MPa	7	3.72 MPa	12.38 MPa
2	6.21 MPa	11.5 MPa	8	7.42 MPa	14.54 MPa
3	7.38 MPa	13.77 MPa	9	7.92 MPa	15.61 MPa
4	12.19 MPa	16.25 MPa	10	8.53 MPa	15.54 MPa
5	5.89 MPa	12.14 MPa	11	10.75 MPa	16.41 MPa
6	8.6 MPa	14.04 MPa	12	12.04 MPa	17.68 MPa

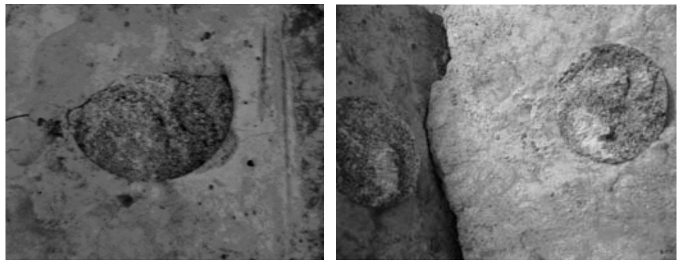

Figure 3. Two representative shear failure patterns of rock blocks

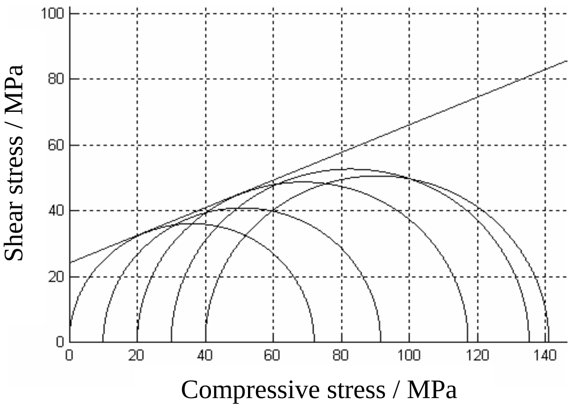

Figure 4. Ultimate Mohr circle envelop obtained by compression experiments

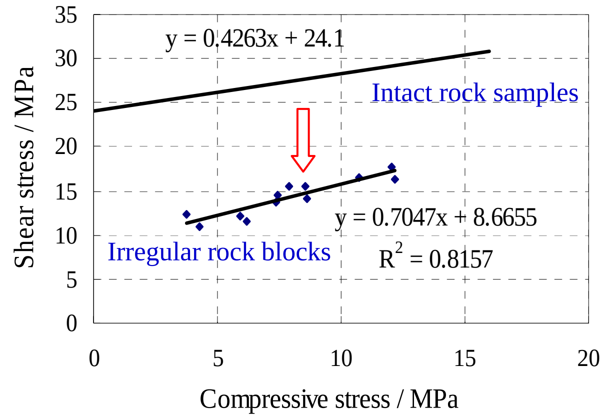

Figure 5. Comparison of strength

4 Summery

Through self-designed direct shear tests, the relationships between shear stress and compressive stress of irregular rock samples produced in normal compressive experiments were obtained. Comparing the Coulomb strength curve gained by the compression-shear tests with the ultimate Mohr circle envelope obtained from previous uniaxial and triaxial compressive experiments, it can be seen that the cohesion result measured by uniaxial and triaxial experiments before failure is obviously greater than that obtained by compressive-shear tests of irregular rock blocks. Moreover, it can be seen that this great difference mainly resulted from the damage in the rock failure process in uniaxial and triaxial compressive experiments, not the deviation by the different testing methods. So it can be concluded that rock material strength degrades with the damage development in the rock failure process.

Acknowledgements

This study was supported by NSFC (Nos: 50804046, 50774082 and 50490273) and Scientific Research Fund for youths of CUMT (No: 0B080240).

References

1. Chen, H.F. Constitutive Relations of Concrete and Soil. Translated by Yu, T.Q. China Architecture and Building Press, 2004.
2. Shen, Z.J. The Geomaterials Mechanics from Childhood to Adults. Geotechnical Engineering World, 2003, 6(12). 15-17.
3. Nie, B.S., He, X.Q. and Wang, E.Y. et al. Study on Electromagnetic Radiation and Acoustic Emission in Shearing Process of Coal. Journal of China University of Mining & Technology, 2002, 31(6). 609-611.

4. Chen, Y.L., Ge, S. and Wu, M. Study of Metal Magnetic Memory Induced by Stress Concentration. Journal of China University of Mining & Technology, 2004, 33(5). 592-595.
5. Chen, S., Yue, Z.Q. and Tham, L.G. Digital Image-base Numerical Modeling Method for Prediction of Inhomogeneous Rock Failure. International Journal of Rock Mechanics and Mining Science, 2004, 41. 939-957.
6. Zhou, J.J. Evolutionary Process and Strength Degradation of Rock Failure. China University of Mining and Technology Press, 2006.
7. Feng, N.Q. New Applicable Concrete Manual. Science Press, 2005.
8. Zhou, Y.H., Zhou, D.P. and Yang, T. et al. Experimental Investigation on Shear Strength Parameters of Jointed Rock Mass. Journal of Southwest Jiaotong University, 2005, 40(1). 73-76.

RaSiM 7(2009): Controlling Seismic Hazard and
Sustainable Development of Deep Mines,
C.A. Tang(ed), Rinton Press, 125-130

APPLICATION OF PLOW MINING IN THIN-SOFT SEAM WITH HARD ROOF

XIN-XIAN ZHAI, DONG-HAI CHEN, YONG-KANG REN

School of Energy Science and Engineering, Henan Polytechnic University

Jaozuo, 454000, P.R. China

Plow is one kind of coal winning machinery that has been widely used in mining thin seams in many countries. Based on the application of plow mining in China, the calculating method on aggregative indicator of seam plowability is probided. Herein, plowability of thin seams is divided into five categories, i.e., most easy to plow, easy to plow, normal to plow, difficult to plow and extremely difficult to plow. Using this method, the plowability for thin seams in Caoyao Coal Mine of Yima Coal Group, China is calculated. The calculated result indicates that the plowability of thin seam belongs to the category of normal to plow. This method provides the theoretical basis for the optimization of the schemes of coordination equipments of plow mining for thin seam

1 Status of Mining Technology with Plow

Plow is one kind of coal winning machinery which can automatically break up and load coal into thin seam coal faces with high gas content. Compared with the shearer, the plow has many advantages, such as its simple structure, its ability to be carried forward while shaving coal, and its continual mining with comprehensive mechanization. Plow mining is applicable to thin and medium thickness seams, on the geological conditions of whose hardness is less than 2.5 and dip angle is less than 25º. DBT Company of Germany of plows is the largest one, and its level of production technology is the highest in the world. The company has manufactured many types of plows, for instance towing hook, sliding-towing hook, and sliding plows. Presently, technical level of plow mining has developed into the following states: mining height 0.6-3.0m, maximum web 300mm, hardness of shaved seam 4, maximum speed of plowing 3m/min, diameter of plough chain Φ42mm, maximum power of plow 2×800kW, coal face length 300m. In Germany, almost all thin seams whose thickness are less than 1.6m, and the majority of medium-thickness seams whose thickness is 1.6-2.2m, have been excavated with plows. According to the statistics, Germany has more than 30 high-yield coal faces in thin seams whose thicknesses are less than 1.8m. Shearers were used for only one of the 30 coal faces, and the rest were all plow coal faces. Daily output of plows reached 5000t, annual output at plow coal face was more than 2 million tons[1, 2]. In Poland, the average number of plow coal faces was 65 every year. While the number was 150 per annum in Russia. In main coal-production countries e.g., Australia, South Africa, USA, etc., full automation plows have been widely used in thin seams. In USA, being maximum efficiency of productivity with plow, annual output at thin seam coal face has been more than 3 million tons.

Since the 1960s, China has successively imported foreign plow equipment. As geological conditions of seams were unsuitable, application of foreign plows in one mine was different from another. Output in some mines was much higher, but productive efficiency of plows in most mines was much lower. China has manufactured four kinds of plows. However, the output per coal face with a Chinese plow was similar to that of blasting coal face. The main reason for this is that plows made in China have some disadvantages, such as lower power and plowing speed, less adaptability to geological condition, and poorer reliability of components. Above reasons have resulted in more accidents and lower efficiency of production at coal faces [3,4,5]. Therefore, only several plows have been made in China in recent years, the state made plows are in a dead lock.

China has imported several sets of plows from DBT Company of Germany since 2002. The plows are used with Chinese equipment and have been widely applied in Xiaoqing Coal Mine of Tiefa Coal Group and other mines. Better benefits were acquired in these coal mines. There are reserves of 0.62 billion tons in thin seams whose thickness is less than 1.5m in Tiefa mining area. Proportion of the reserves in thin seams in Xiaoqing Coal Mine accounts for 73.75% of whole reserves. The first set of automation plow was tested in Xiaoqing Coal Mine in China. The length of test coal face was 150-200m. The average thickness of seam was 1.3m, its dip angle was 5-8º. The associated equipments at coal face were sliding plow of Gleithobel 9-34ve/4.7, PF 2.30/732 conveyer, SZZ764/160 transfer conveyor and hydraulic supports of ZY6400/09/20D type made in Beijing Coal Mine Machinery Factory. With this set of plow equipment, average daily production of 3911t, maximum daily production of 6480t and 1.5 million tons per year in 2002 were obtained, which created the best level of mining in thin seams in China, and realized safely mining with high-efficiency [6, 7].

With the successful application of full automation plow in Xiaoqing Coal Mine, enthusiasm on using plows significantly increased in coal mines in China. And most coal mines had a regard for mining thin seams. One after another, eight sets of automation plows were imported from 2001 to 2005. Compared with technology of the first set of imported plow, the later imported plows was improved in technical performance. The plow was type GH9-38Ve/5.7, its power 2×400kW, its productive capacity 900t/h, and the diameter of plough chain Φ38mm. The type of associated conveyer was PF3/822, its head engine with intersect and side unload was adopted.

In August, 2003，Malan Coal Mine of Shanxi Coking Coal Group imported plow from DBT Company of Germany, the maximum daily output in test coal face was 8600t, and annual output could reache one million tons[8]. Then, the fourth set of plow equipments was installed successfullyin Xiaoqing Coal Mine in March, 2008. The associated equipments of plow were jointly manufactured by Beijing Coal Mine Machinery Factory. At present, supports of ZY4800/06/16.5D are advanced in thin seam in the world, which can meet the requirement in thin seams with 0.6-1.65m thickness.

2 Studies on Plowability in Thin Seam

2.1 Analysis on influencing factors about seam plowability

Following way is mining with plow: plough cutter installed on the plow is guided by conveyer at coal face; plough head towed by plough chain is drawn along the entire coal face. Then coal is shaved from rib by plough cutter with a certain ploughing depth, the coal planed off is loaded into conveyer through the incline of plough head. Finally, the broken coal is conveyed out of coal face by conveyer. So plow mining is a perfect winning technology in thin seam. Due to variance in buried conditions of seam, such as thickness of seam, its dig angle, texture, harness, joint and cranny, as well as its roof and floor strata, above factors influence on seam plowability. The plowability affects on type of associated equipments at coal face, even influences on the feasibility about mining technology with plow.

There are four major factors influencing the thin seam plowability as following: (1) dig angle and thickness of seam; (2) its hardness, structure, and developing degree of joint and cranny of seam; (3) surrounding rock conditions of roof and floor strata; (4) geological structure and other factor.

2.2 Classification on thin seam plowability

According to plow mining practices in thin seams, seams plowabilities are divided into five categories, i.e., most easy to plow, easy, normal, difficult, and extremely difficult.

Main factors influencing plow mining are seam hardness, dig angle, thickness, texture, joint and cranny, geological structure, floor, immediate roof, main roof, and other factors. but the importances of above factors are different from each other. So during the process of comprehensive judgment on influence degree, the weight coefficient is cited to determine the significance of single factor. After dimensionless treatment for every single factor, the method of weight summation is used to obtain comprehensive quantization value, which can determine the feasibility of plow in thin seam. The value of weight coefficient for single factor is evaluated by experts, and final value is obtained with mathematics statistics. Statistical result is shown as table 1.

Table 1 Weight coefficient K_n about seam plowability by single influencing factor

Influencing factors	Hardness of seam	Thickness of seam	Joint and cranny	Texture of seam	Dig angle	Floor	Immediate roof	Main roof	Geological structure	Other factor
Weight coefficient k_n	0.1835	0.0685	0.0842	0.1494	0.0973	0.1024	0.0953	0.0448	0.1221	0.0525

In order to better quantitative analysis, the parameter of every single influencing factor is treated in quantization. Based on the result of plowability classification, the plowabilities are divided into five categories. Plowability indicator I is expressed with decimal grade. While zero denotes extremely difficult to plow, ten shows extremely easy to plow. According to the value of plowability indicator from zero to ten[9], seams plowabilities can be divided into five categories as shown as table 2.

Table 2 Classification on the seam plowability

Type	Extremely difficult	Difficult	Normal	Easy	Extremely easy
Classification Indicator I	$0 \le I \le 2$	$2 < I \le 4$	$4 < I \le 6$	$6 < I \le 8$	$8 < I \le 10$

In fact, all above ten single influencing factors influence on the seam plowability. But influencing degree of single factor is different from each other. Thus aggregative indicator ΣI about seam plowability is equal to a summation of plowability indicator of every single influencing factor multiplied by its weight coefficient.

$$\Sigma I = \sum_{10}^{n=1} k_n \cdot I_n \tag{1}$$

Before thin seam is excavated with plow, the influence of every single factor on plow mining should be considerate comprehensively. Firstly, based on geological conditions of thin seam, the influence of plowability indicator affected by single factor was calculated, and the indicator of single factor was obtained. After that, considering weight coefficient of every single factor, comprehensive indicator ΣI of seam plowability can be calculated. Finally, plow utilized result can be predicted directly in line with the value of plowability. Since this method is simple, easy and better maneuverability, it could be more widely used

Since the structure of plow is simple, it's easy operation and convenient maintenance. Electromotors are laid out on the two terminal of coal face. So, the cable need not be drawn, miners need not go after plow for working and labor intensity is much lower. At plow coal face, there are many advantages, the ratio of lump coal is higher; dust concentration is lower and so on. So long as the condition of thin seam is favorable for mining, the plow mining should be preferential chosen. During the study processing of plowability classification for seams, if the type of thin seam belongs to extremely difficult to plow, other coal wining technology should be considered. Otherwise, particular measure has been adopted, winning technology with plow can be employed.

3 Studies on the Plowability in Thin-soft Seam with Hard Roof

Whereas Caoyao Coal Mine has already come into anaphase, and its residual reserves are limited. In order to enhance mechanization level of coal mine, reduce working intensity and enhance productive capacity with safety and economic benefit, study of comprehensive mechanization mining in thin seam must be carried out.

3.1 Geological conditions of thin seam in Caoyao Coal Mine

Caoyao Coal Mine has excavates seam B_1 in Shannian coalfield. Its designed mine capacity was 0.3 million tons per year. The minefield is located in the east of coalfield, its checked productive capacity was 0.42 million tons per year in 2006, and annual output was 0.2316 million tons in 2007, residual service is 13.1 years. Presently, the mine has already come into anaphase in deep mining.

Seam B_1 is a minable one, its dip angle is 13-18º, average dip angle 15º. Average thickness of seam is 0.8-2.0m. The seam belongs to gentle inclined seam with unstable, soft and thin-medium thickness. Protodyakonov coefficient of the seam is 0.16. Thickness of roof with coarse-grained sandstone is 5.34-28.38m, average thickness is 17.00m. Roof lithology is off-white medium bedded felspar and quartz sandstone with coarse-medium grains. The stratum of roof has cross-bedding and wavy bedding. Its uniaxial compressive strength and tensile strength are 46.6-212.4MPa and 5.97MPa, respectively. Seam floor is black mudstone, charcoal mudstone and sand mudstone. In the floor, there are 62.5% of mudstone, 30% of charcoal mudstone and 7.1% of sand mudstone. And floor has rich concretion with pyrite, little fossil fragments of plant. Its lithology is soft, its uniaxial compression strength of rock is 18.43MPa.

3.2 Plowability in thin seam in Caoyao Coal Mine and associated equipments of plow

According to buried condition of seam and strata behaviors at coal face 2503 in Caoyao Coal Mine, geological structure and influence degree of other factors are general. Its dig angle is 8-18º; Hypothesis, included angle between main divisional planes in seam and running direction for plough cutter is 90°. Protodyakonov coefficient for seam partings is 4. Protodyakonov coefficient in floor stratum is 1.843. Interval of periodic weighting of main roof is 11m. Therefore, intensity index for immediate roof *D* is:

$$D = 10R_C \cdot C_1 \cdot C_2 = 10 \times 115.19 \times 0.34 \times 0.27 = 105.74(\text{MPa}) \tag{2}$$

Where, R_C——Uniaxial compressive strength of rock in immediate roof, 115.19MPa;

C_1——Influencing coefficient of joints and crannies, 0.34;

C_2——Influence coefficient of stratification thickness, 0.27.

According to above geological conditions, comprehensive indicator of seam plowability can be figured out:

$$\begin{aligned}
I &= \sum_{10}^{n=1} k_n \cdot I_n \\
&= k_1 I_1 + k_2 I_2 + k_3 I_3 + k_4 I_4 + k_5 I_5 + k_6 I_6 + k_7 I_7 + k_8 I_8 + k_9 I_9 + k_{10} I_{10} \\
&= k_1(10 - 2.4f) + k_2(-13.33h + 28.69) + k_3(-\frac{\phi}{15} + 10) + k_4(-2.25 f_g + 10) + \\
&+ k_5(90.51e^{-0.208\alpha}) + k_6(32 f_d^2 / 45 - 44 f_d / 45) + k_7(3.797 \times e^{0.0092D}) + k_8 5 + k_9 5 + k_{10}(10 - Q) \\
&= 0.1835(10 - 2.4 \times 0.16) + 0.0685(-13.33 \times 1.4 + 28.69) + 0.0842(-\frac{90}{15} + 10) \\
&+ 0.1494(-2.25 \times 4 + 10) + 0.0973(90.51e^{-0.208\times18}) + 0.1024(32 \times 1.843^2 / 45 - 44 \times 1.843 / 45) \\
&+ 0.0953(3.797 \times e^{0.0092\times105.74}) + 0.0448 \times 5 + 0.1221 \times 5 + 0.0525(10 - 5) \\
&= 5.2569
\end{aligned} \tag{3}$$

The thin seam is a gentle inclined and soft one with loose floor. The seam with complex structure contains partings. Immediate roof with higher strength is more stable. Above conditions that are beneficial for supporting coal face, are helpful to seam plowability. But its unstable buried conditions, large diversification thickness, and easy rib spalling, that have affected seam plowability. Based on comprehensive indicator of seam plowability, the thin seam in Caoyao Coal Mine belongs to normal type in line with plowability classification. Whereas, industrial test of plow mining in thin-soft seam can be carried out in Caoyao Coal Mine.

Table 3 Scheme of coordination equipments with Germanic plow at thin seam coal face in Caoyao Coal Mine

Serial number	Name of equipment	Type of equipment	Technical parameters	Manufacturer
1	Plow	Gleithobel 9-34ve/4.7	Diameter 34 mm of plough chain, Power 2×315kW, Productive capacity 900t/h,	DBT Company of Germany
2	Scraper conveyer	PF 2.30/732	Power 2×315kW, Rated capacity 900t/h	DBT Company of Germany
3	Transfer conveyer	SZZ764/160	Power 724kW, Transportability 1000t/h	Zhangjiakou Coal Mine Machinery Co. Ltd.
4	Crusher	PCM110	Power 110kN, Crushing capacity 1000t/h	Zhangjiakou Coal Mine Machinery Co. Ltd.
5	Hydraulic support	ZY4400/09/21D	Effective resistance 4400kN, Supporting height 0.9- 2.1m	Zhengzhou Coal Mine Machinery Co. Ltd.
6	Emulsion power pack	BRW315/31.5	Power 200kW, Rating pressure 31.5MPa, Rating flow 315L/min	Pingdingshan Coal Mine Machinery Co. Ltd.

Table 4 Scheme of coordination equipment withChinese plow at thin seam coal face in Caoyao Coal Mine

Serial number	Name of equipment	Type of equipment	Technical parameters	Manufacture
1	Plow	BH34/2×200	Power 2×200 kW, productive capacity 264-990t/h;	Zhangjiakou Coal Mine Machinery Co. Ltd.
2	Scraper conveyer	PF3/822	Power 2×400 kW	DBT Company of Germany
3	Transfer conveyer	SZZ764/160	Power 724kW, Conveying capacity 1000t/h	Zhangjiakou Coal Mine Machinery Co. Ltd.
4	Crusher	PCM110	Power 110kN, Crushing capacity 1000t/h	Zhangjiakou Coal Mine Machinery Co. Ltd.
5	Hydraulic support	ZY4400/09/21D	Effective resistance 4400kN, Supporting height 0.9- 2.1m	Zhengzhou Coal Mine Machinery Co. Ltd.
6	Emulsion pump	BRW315/31.5	Power 200kW, Rating pressure 31.5MPa, Rating flow 31.5L/min	Pingdingshan Coal Mine Machinery Co. Ltd.

Based on successful experiences of plow mining, the schemes of two sets of coordination equipments with plow were designed in line with geological conditions of thin seam in Caoyao Coal Mine, The main distinguish is different plow shown as table 3 and table 4: Germanic plow is used in one set; Chinese plow is employ in other set.

4 Conclusions

Plow is a coal winning machinery that can automatically break out, fall out, and load coal. It has been widely used in mining thin or less medium thickness seams. Currently, DBT Company of Germany has the highest technical level of plow manufacturing in the world. Automatic plows have been used at thin seam coal faces in most countries. Since 2002, several sets of plows imported from DBT Company and associated Chinese made equipments have been applied in Xiaoqing Coal Mine of Tiefa Coal Group and other coal mines. These mines have obtained better benefits, which promote associated equipments of plow and its mining technology to be quickly developed in China.

Based on the practices of plow mining in the world, the authors have put forward a calculating method using the aggregative indicator ΣI of seam plowability, in line with main influencing factors on swam plowability and importance degree of every factor. Plowability of thin seams is divided into five categories, i.e., most easy to plow, easy to plow, normal to plow, difficult to plow and extremely difficult to plow. According to geological conditions of thin seams B_1 in Caoyao Coal Mine and law of strata behaviors, comprehensive indicator of thin seam plowability can be worked out. This type of seam plowability is normal. Lastly, the scheme of two sets of associated equipment about plow mining in Caoyao Coal Mine was optimized, which have provided theoretical basics for the industrial test of mechanization mining with the plow. Research findings have operational significance on stability, high yield and sustainable development for senescent mines in thin seams in the west mining area of Yima Coal Group.

Acknowledgment

This project was financially supported by the National Basic Research Program of China (No. 2007CB209404) and the National Natural Science Foundation of China (No. 40638040/D0214). The authors acknowledges financial supports of the items.

References

1. Liu, Z.S. and Ma, Y. Development Status and Prospect of Plough in Domestic and Aboard. Coal Mine Machinery, 2006, 27(10). 1-3.
2. Yang, L.C. DBT Full Automatic Coal Plough Technology and Thin Seam Mining in China. Coal Science Technology, 2003, 31(8). 51-54.
3. Hua, Y.Q. Plough: An Effect Way to Solve Thin Seam Mining in China. Coal Mine Electromechanical, 2004, 8. 25-29.
4. Ma, F.B. and Chen, S.F. Development and Status of Plows in China. Coal Engineering, 2007, 1. 74-75.
5. Shi, Y.G. and Cui, S.Z. Application and Suggestion about plow. Coal Engineering, 2007, 8. 55-56..
6. Li, J.P., Du, C.L. and Zhang, Y.Z. Status and Development Trend of Mining Equipment in thin and extremely thin seams. Coal Science Technology, 2005, Vol.33, 6: 65-67.
7. Zhou, M.H., Huang, C.L. and Liu Y., et al. The Successful Application of Entire Autocontrol Plow System at Xiaonan Coal Mine. China Mining, 2004, 13(3). 51-53.
8. Yang, M.L. Application of roboticized Mining Technology Using Coal Plow in Malan Coal Mine. Coal Mining, 2004, 9(2). 30-31.
9. Liu, G.B. and Cheng, S.L. Optimization on Comprehensive Parameters of Plow Mining. Ground Stress and Strata Control, 2003, 20(3). 61-64.

RaSiM 7(2009): Controlling Seismic Hazard and Sustainable Development of Deep Mines, C.A. Tang(ed), Rinton Press, 131-136

NEW TECHNOLOGIES OF ROCK-LIKE MATERIAL DIRECT TENSILEEXPERIMENT AND ITS APPLICATION

LEI YANG, SHU-CAI LI, MING-TIAN LI, NING ZHANG

Geotechnical and Structural Engineering Research Center, Shandong University

Jinan, 250061, P.R. China

Due to the limitations of experimental equipments and technologies, direct tensile experiment of rock-like material has been deemed as one of the difficult laboratory tests to implement. After analyzing the advantages and disadvantages of several main methods for direct tensile experiment, some improvements are given for the conventional bonding method and fixture method. A location device for rock-like material bonding tensile experiment and a sample mold and its matching clamp for fixture tensile experiment are designed firstly. By using the improved equipments and technologies, accurate results can be obtained easily. Afterwards, uniaxial direct tensile experiments are carried out with rock-like mortar material, and tensile stress-strain curves are obtained. The results indicate that the force and deformation process in tensile condition of rock-like material is quite different from that of compressive condition. Tensile force and deformation process can be divided into four stages: flaws opening stage, elastic deformation stage, elastic and plastic deformation stage, and failure stage. The elastic deformation stage takes up the most proportion, wherein elastic strain proportion occupies about 2/3 of the total strain. After very little plastic deformation, the stress reaches the peak strength, when burst-like fracture forms in the sample and residual stress drops to zero suddenly.

1 Introduction

Generally speaking, all of the destruction behaviors of rock mass relate to the internal tensile stress. Therefore, study of rock mass mechanical characteristics under tensile load is important for engineering[1]. Uniaxial direct tensile experiment of rock and rock-like material is the most fundamental and effective method to study the tensile force and deformation characteristics of rock mass. Through direct tensile experimentation, the stress-strain curve can be obtained in addition to the tensile strength. The stress-strain curve is the foundation to conclude the constitutive relationship of rock mechanics [2]. Direct tensile experimentation of rock-like materials is difficult to implement because of the constraints of experimental equipments and technologies [3]. At present, the testing of tensile strength of rock-like material mostly resorts to indirect methods, such as the Brazilian test. Ssample stress status of the Brazilian test is much more complicated than that of uniaxial direct tensile experiment which causes errors affecting the precision of experimental results [4].

There are currently several traditional kinds of rock-like material direct tensile experiment methods and technologies. However, all of those methods have some disadvantages which affect the accuracy of results and the success rate of experiment. The key factor of brittle material direct tensile experiment is to ensure that tensile stress transfers through the sample axis, and the successful mark of these experiments is that fracture happens in the uniform section of samples [5]. By improving conventional methods, finding rock-like material direct tensile experiment methods with high accuracy and easy operation has important theoretical significance and application value for both the improvement of rock tensile experiments and constitutive relation conclusion of rock tensile force and deformation.

2 Conventional Rock-like Material Direct Tensile Experiment Methods

Nowadays, there are four main methods for direct test of tensile strength: pre-existing pull-piece method, tension-compression conversion method, bonding method, and fixture method. All these methods have advantages and disadvantages, as follows:

2.1 Pre-existing Pull-piece Method

Sample is usually with the shape of prism with variable cross section. Pull-pieces made of steel with high stiffness are pre-placed in the enlarged end parts of sample, showed in Fig 1. Testing machine clamps the pull-pieces to apply tensile loads[5]. This method has high success rate, but the process of sample preparation is complicated. Precise location of pre-placed pull-pieces is difficult, so the axial eccentricity may be caused.

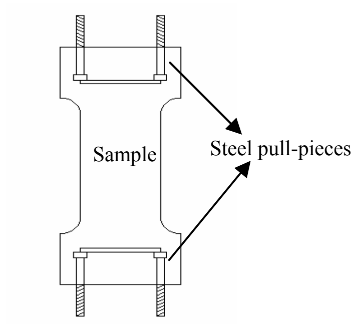

Figure 1 Pre-existing pull-piece method

(LU Peiyin, SONG Yupu. 2003)

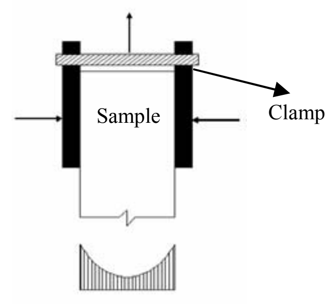

Figure 2 Conventional fixture method and stress

distribution on sample section

2.2 Tension-compression Conversion Method

The tension-compression conversion equipment must be designed and processed firstly. Sample is bonded to the internal ends of the conversion equipment. The equipment can convert the compressive load applied by testing machine to tensile load which is applied on the sample end parts[6]. This method has high success rate, but the deformation of conversion equipment would disturb experiment results. Furthermore, it is difficult to observe the failure process of samples in the conversion equipment.

2.3 Fixture Method

Reasonable clamps should be designed firstly according to experiment requirements. Sample is fixed in clamps through which the tensile load is applied by testing machine. Different clamping mode and sample shape effect experiment results greatly. One of the fixture method adopted commonly is to clamp the end of samples through friction, as showed in Fig 2. Stress concentration which effects test results usually exists in the clamping position.

2.4 Bonding Method

Sample is bonded to the pulling end parts of test machine through adhesive with high strength, as showed in Fig 3. The end planes of samples must be smooth and parallel to avoid eccentricity. Stress distributes uniformly across sample section, so fracture usually happen in uniform segment. The success of experiment depends on the selection of adhesive. This method usually takes a long experimental period and occupies much experimental resources. For some kinds of samples which need reprocessing after being bonded (for example, the resin material always needs freezing after being bonded), this method may have constraint.

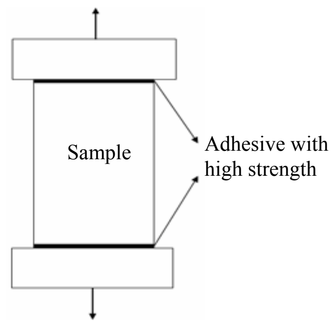

Figure 3 Conventional bonding method

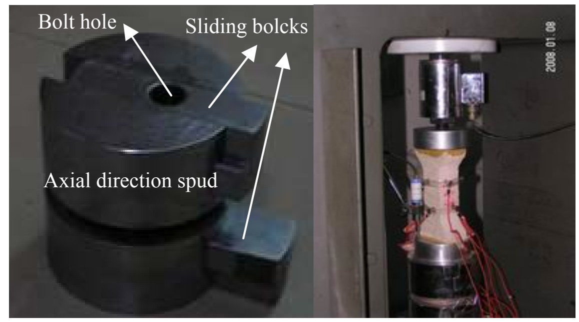

Figure 4 Bonding location device and its application

3 Improved Bonding Method and Fixture Method

In the above four methods, the bonding method and fixture method are adopted widely, which have advantage of uniform stress distribution and convenient operation respectively. To overcome disadvantages of these two methods, some improvements are employed for conventional equipments, and a location device for bonding tensile experiment and a sample shape and its matching clamp for fixture tensile experiment are designed.

3.1 Improved Bonding Method

To overcome disadvantages of conventional method, the location device for rock-like material bonding tensile experiment is designed, as showed in Fig 4. The device consists of two parts, and they are axial direction spud and two sliding blocks with "T" shape respectively. All parts of the device are made of steel with high stiffness so that the deformation of device can be neglected. The lower sliding block is fixed in test machine through bolt, and the upper sliding block is fixed in backing plate which is bonded with sample. After the bonded sample and backing plates are connected to the stress sensor, the axial direction spud can not only slide along the lower and upper siding blocks but also rotate freely along axis. Free slide and rotation is great helpful for axial location and guarantee of axial tension.

3.2 Improved Fixture Method

In order to avoid disadvantages and to increase success rate, some improvements are employed to the conventional fixture technology. First of all, the steering devices are designed and connected to the fixtures, which can shift direction freely and ensure that stress transfers through sample axis. Secondly, the shape of samples is designed as end region enlargement, and the enlarging region of samples is effective to decrease stress concentration of the clamping position. Then a piece of ebonite which is also helpful to decrease stress concentration should be put between sample and clamps. The improved fixture is showed in Fig 5. Verified by experiments, the shape of sample and its matching clamps can increase the experimental success rate greatly.

4 Mortar Material Uniaxial Tensile Experiment with Improved Methods

Both the improved bonding method and fixture method are adopted to conduct uniaxial tensile experiments of mortar material. Uniaxial tensile stress-strain curves are obtained, and sample failure process is observed during experiments. The mechanical and fracture features of rock-like material can be analysed with those results.

4.1 Experimental Material and Sample Shape

In order to simulate the physical and mechanical properties of rock material, such as heterogeneity, brittleness, non-linearity, finally the special mortar material is adopted as rock-like material. After testing, the maxing ratio by weight of raw material is determined as white portland 325R cement: riversand: water= 1: 2.34: 0.35. The main physical and mechanical parameters of special mortar material were tested and compared with sandstone, as showed in Table 1. The results indicate that all these parameters of mortar are in the range of those of sandstone. The tension-compression strength ratio of special mortar is 1/12.6, and the mortar material has good brittleness. At the same time, mortar material is heterogeneous material because of the mixing of cement and riversand. Therefore, all the physical and mechanical properties satisfy the experimental requirement. Special mortar material is a good substitution of sandstone.

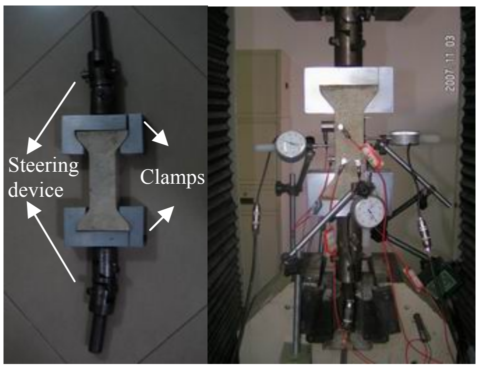

Figure 5 Tension clamps and its application

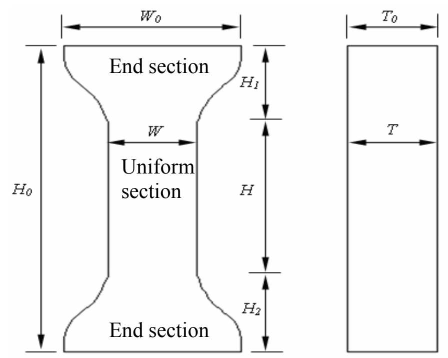

(a) Front view (b) Side view

Figure 6. Sample shape and size

Table 1. Physical and mechanical parameters of mortar material and sandstone

Parameter	σ_c /MPa	σ_t /MPa	E_C /Gpa	v	K_{IC} /MPa·m$^{0.5}$	ρ /g·cm^{-3}
Mortar	35.54	2.82	17.92	0.192	0.512	2.3
Sandstone	20~170	4~25	4.9~78.5	0.02~0.2	0.22~2.26	1.2~3.0

In order to decrease the stress concentration in bonding or clamping section of sample, sample shape is designed as end region enlargement, as showed in Fig 6. The size is: $W_0 \times H_0 \times T_0$=100mm×200mm×50mm, H_1= H_2=50mm, $W \times H \times T$=50mm×100mm×50mm. The end section and uniform section are connected by arc surface in order to decrease stress concentration degree.

4.2 Experimental Results and Analysis

4.2.1 Uniaxial Tensile Stress-strain Curve Analysis of Mortar Material

Uniaxial tensile stress-strain curve of mortar material sample is showed in Fig 7. The curve analysis indicates that uniaxial tensile force and deformation process can be divided into four stages. The first stage is microporosities and microcracks opening stage, corresponding to the OA part of curve (σ_A=13.8%σ_P, ε_A= 21.6% ε_T. σ_P is peak strength, and ε_T represents total strength). In this stage, curve is concave and nonlinear. The second stage is elastic deformation stage, corresponding to the AB part (σ_B=83.5%σ_P, ε_B=80.3%ε_T). The deformation of this stage is elastic, and curve is linear. Elastic deformation stage takes up the maximum proportion of the total curve. A great amount of elastic strain energy is accumulated in the sample. The third stage is elastic and plastic deformation stage, corresponding to the BC part (σ_C=σ_P, ε_C=93.4%ε_T). In this stage, non-recoverable plastic deformation occurs. The growth and interaction of flaws results in nonlinearity of curve. The elastic and plastic stage is short, and a little plastic deformation will lead to the stress reaching σ_P. The fourth stage is the failure stage, corresponding to the CD part. Sample fracture suddenly after σ_P with the bearing capability loss and elastic strain energy release.

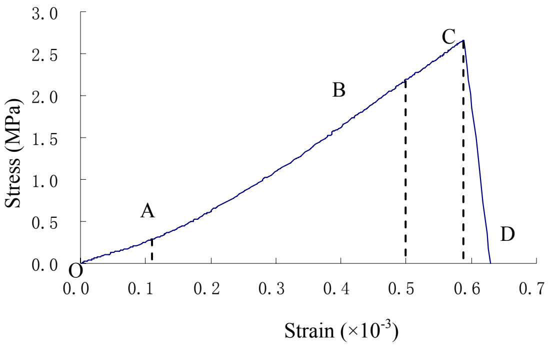

Figure 7. Uniaxial tensile stress-strain curve of mortar sample

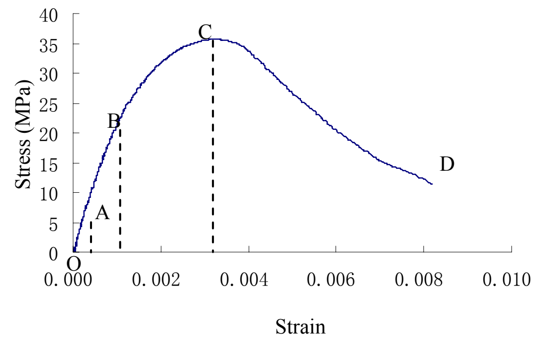

Figure 8. Uniaxial compressive stress-strain curve of mortar sample

Comparing with compressive stress-strain curve of mortar material(showed in Fig 8.), uniaxial tensile curve is quite different. The proportion elastic deformation stage takes up of tensile curve is much larger than that of compressive curve(Tensile elastic strain occupies about 2/3 of the total). Tensile failure stage is sudden without obvious softening period. During compressive failure process, significant softening stage and residual strength is observed. Therefore, the failure stage is the most obvious difference between tensile and compressive force and deformation process of mortar material.

Furthermore, tensile elastic modulus of mortar material is only 28.2% of compressive elastic modulus (E_t = 5.17Gpa, E_C=17.92GPa). In previous researches, many scholars also found the fact with rock material[7-9]. The fact has important significance on the engineering calculation and analysis.

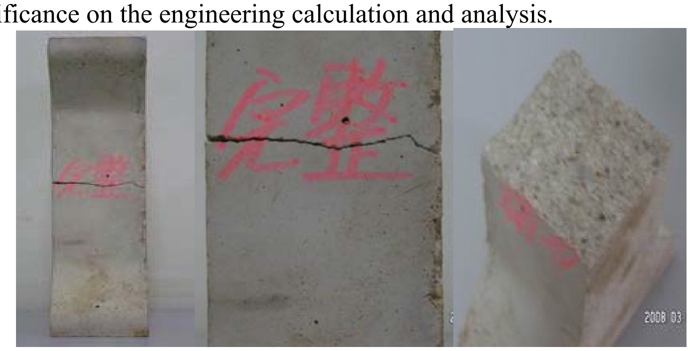

(a) Fractured sample (b) Fracture trace (c) Failure plane

Figure 7 Fracture trace and failure plane of fractured sample

4.2.2 Unianxial Tensile Failure Process of Mortar Material

The failure process of sample is analyzed through the observation of fracture trace and failure plane, showed in Fig. 7. In the flaw opening stage, the closed flaws gradually open under tensile stress, and a spot of new flaws initiate. In the elastic deformation stage, crack initiation rate increases, crack size grows bigger, and flaw amount increases, but the flaw influence is still little. In the elastic-plastic deformation stage, micro-cracks grow and form macro-cracks, and interaction between cracks becomes obvious. After the peak strength, the propagation rate of macro-cracks grows up, and failure plane is formed which leads to abrupt breaking.

Tensile fracture position is located in middle of sample. Fracture trace is horizontal line perpendicular to the direction of axial tensile stress only with little deviation near the sample corner. The shape of destroyed section is approximate plane perpendicular to axial direction with some asperities. The fracture trace direction deviation and destroyed section asperities are caused by the heterogeneity of mortar material. The flaws in material would attribute to stress concentration, which guides the fracture direction. Tensile fracture of mortar material is abrupt which is difficult to control and is dangerous to engineering.

5 Conclusion

Resulting from the constraints of experimental equipments and technologies, the direct tensile experiment of rock-like material is difficult to implement. All conventional methods for direct tensile experimentation have disadvantages. Some improvements are performed to the conventional methods, and a location device for bonding tensile experiment and a sample shape, and its matching clamp for tensile experiment are designed.

Both the improved bonding method and fixture method are adopted to conduct the mortar material uniaxial tensile experiment. The main physical and mechanical parameters of specially made mortar material are in the range of sandstone. Uniaxial tensile experimental results indicate that the rock-like material uniaxial tensile force and deformation process can be divided into four stages: pore opening stage, elastic deformation stage, elastic and plastic deformation stage, and failure stage. The elastic deformation stage takes up the most proportion which is about 2/3 of the total. After producing very little plastic distortion, the stress reaches the peak, and a burst-like sample destruction is caused. Tensile fracture happens in the middle of the sample. Fracture trace is approximately perpendicular to the direction of axial tensile stress. Comparative analysis shows that the failure process is the most obvious difference between tensile and compressive failure.

Acknowledgements

This work was financially supported by National Science Fund for Distinguished Young Scholars (No. 50625927), National Research Item of 973 (2007CB209407), and Natural Science Foundation of P. R. China (No. 40872203) .

References

1. Zhou, X.P., Zhang, Y.X. and Zhu, K.S. A study of complete stress-strain relation for mesoscopic heterogenous rocks under uniaxial tensile loading. Rock and Soil Mechanics, 2003, 24(S). 143-147.
2. Tao, L.B., Xia, C.C. and He, Z.M. Experimental studies on the total course stress-strain curves of granit specimens under tensile condition. Journal of Tongji University, 1997, 25(1). 34-38.
3. Jin, F.N.and Qian, Q.H. Uniaxial tension and mechanical model of rock.Chinese Journal of Geotechnical Engineering, 1998, 20(6). 5-8.
4. Dou, Q.F., Yue, S. and Dai G.F. Comparative study of rock dircect tensile experiment and splitting experiment. Underground Space, 2004, 24(2). 178-181.
5. Lu, P.Y. and Song, Y.P. Experimental investigation of fatigue behavior of concrect under cyclic tension loading at different temperatures. Engineering Mechanics, 2003, 20(2). 80-86.
6. Dai, G.F., Xia, C.C. and Yan, C. Testing study on deformation behavior of rock in Longtan hydropower project under tensile condition. Chinese Journal of Rock Mechanics and Engineering, 2005, 24(3). 384-388.
7. Perkins, T.K. and Krech, W.W. The energy balance concept of hydraulic fracturing. Society of Petroleum Engineers Journal, 1968, 8(1). 1-12 .
8. Hawkes, I. Mellor, M. and Gariepy, S. Deformation of rocks under uniaxial tension. Int J Rock Mech Min Sci & Geomech Abstr, 1973, 10. 493-507.
9. Stimpson, B. and Rui, C. Measurement of rock elastic moduli in tension and in compression and its practical significance. Canadian Geotechnical Journal, 1993, 30. 338-347.

RaSiM 7(2009): Controlling Seismic Hazard and Sustainable Development of Deep Mines,
C.A. Tang(ed), Rinton Press, 137-142

NUMERICAL SIMULATION OF THE SIZE EFFECT IN CIRCULAR TUNNEL ROCKBURST

XUE-BIN WANG
College of Mechanics and Engineering, Liaoning Technical University
Fuxin, 123000, P.R. China

YI-SHAN PAN
Rockburst Research College, Liaoning Technical University
Fuxin, 123000, P.R. China

XIAO-LIN WU
Institute of Computational Mechanics, Liaoning Technical University
Fuxin, 123000, P.R. China

Rockburst processes of two circular tunnels with different diameters are modelled by use of FLAC. Rock exhibits linear strain-softening behavior beyond the occurrence of failure, which is followed by ideal plastic behavior. A composite Mohr-Coulomb criterion with tension cut-off is used. Rectangular elements with the same size are adopted. The model is firstly loaded until a static equilibrium state is reached. Then, the excavation is modelling by using a written FISH function. Results show that, when the tunnel with small diameter is excavated, the surrounding rock with four V-shaped notches is still stable after rockbursts. However, when a large-diameter tunnel is excavated, the entire section of the tunnel will collapse and the surrounding rock will lose its stability since many shear bands occur and the maximum unbalanced force is always larger than a limit value.

1 Introduction

The size effect and stability problems have been extensively studied with conclusive results for the rock and concrete specimens [1-10]. Rockburst is a type of dynamic rock failure and can be regarded as a type of instability problem in the rock structure or system composed of strain that is localized in bands and the surrounding rock. The occurrence of rockbursts corresponds to the instability of the system with size-dependent rockbursts receiving less attention [6-7,9-13]. Wang and his co-workers presented the unstable criteria of rock or concrete specimens in uniaxial compression and direct shear tests [5-10]. In these studies, the specimen was treated as two parts after the peak strength was reached: the localized zone or band exhibiting strain-softening behavior and the elastic body outside the zone. The size of the zone and the distribution of the plastic strain in the zone were determined by the gradient-dependent plasticity. It was found that the stability of the specimen was closely related to the height of the specimen, or the size of the elastic part. These studies suggest that the unstable criteria are size-dependent.

Many studies regarding the size effect and stability problems have focused on the use of rectangular specimens. The size effects of tunnel rockbursts are not very well understood at the present. Shear bands or V-shaped rockburst notches can be usually observed in the tunnel wall after rockbursts [14-18]. Obtaining an analytical solution regarding the size effects of tunnel rockbursts is extremely difficult if the localized failure mode is taken into account. Numerical simulations can overcome the deficiencies of theoretical analyses.

In this paper, rockburst processes of two circular tunnels with different diameters are modelled by the use of FLAC. A FISH function is written to automatically delete the elements in tunnels. In the numerical simulation, a composite Mohr-Coulomb criterion with tension cut-off and a post-peak strain-softening relation was adopted. The present results reveal that the stability of the surrounding excavated rock after rockbursts is dependent on the diameter of the tunnel.

2 Model, Constitutive Relation and FISH Functions

2.1. Model and constitutive relation

Both the length and height of the model in plane strain are 1m. The unexcavated model is divided into 40000 rectangular elements with the same size. The model is subjected to a hydrostatic stress of 7.5MPa. The present calculation is in a small strain mode.

Here, two schemes are adopted. Scheme 1 is for the small tunnel with a diameter of 0.36m, while scheme 2 is for the large tunnel with a diameter of 0.41m.

In the elastic stage, the linearly elastic rock only has two constitutive parameters. Elastic modulus and Poisson's ratio are 26.6GPa and 0.21, respectively. The adopted failure criterion is a composite Mohr-Coulomb criterion with tension cut-off and the tension strength is 2MPa. Beyond the yield strength, the cohesion and internal friction angle linearly decrease with the plastic shear strain before the residual cohesion and internal friction angle are reached [19-20]. The initial cohesion and internal friction angle are 3MPa and 44˚, respectively, while the residual cohesion and internal friction angle are 0.1MPa and 38˚, respectively.

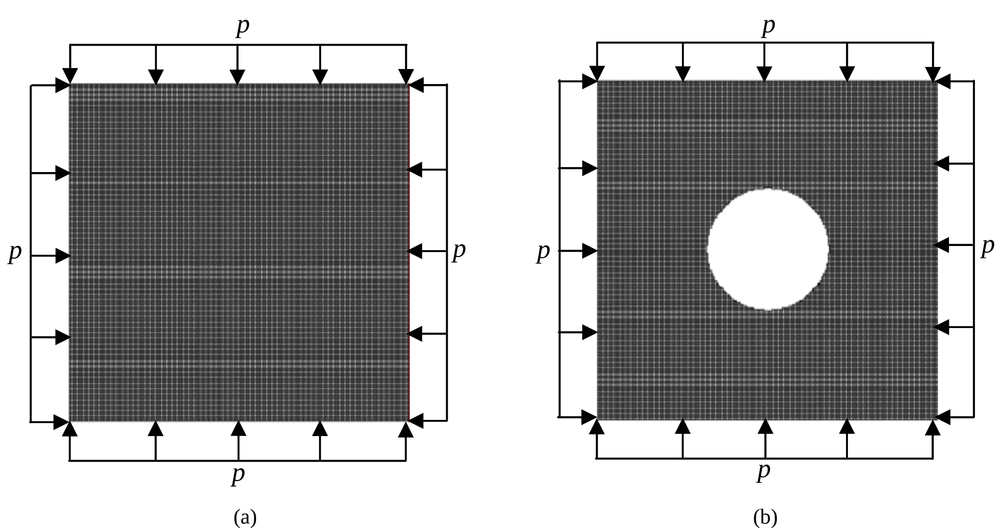

Figure 1 Model geometry and boundary conditions: (a) the model before excavation; (b) the model after excavation.

2.2. Calculation process and FISH function

The present numerical calculation includes the following three steps:

Firstly, the unexcavated model is established (figure 1(a)) and the calculation is conducted to reach a static equilibrium state. If the maximum unbalanced force is found to be smaller than a limit value (1.5×10^{-3}N), then the stresses model is believed to have reached a static equilibrium state.

Secondly, the tunnel is excavated. Figure 1(b) shows the excavated model in scheme 1 (small tunnel). After the tunnel is excavated, the static equilibrium state is violated due to the excavation disturbance.

Finally, the calculation newly begins for the excavated model. For scheme 1, it is found that a new equilibrium state can reach since the maximum unbalanced force can be smaller than the given limit value, i.e., 1.5×10^{-3}N. However, for scheme 2, the maximum unbalanced force is always larger than the limit value. Therefore, eventually, a plastic flow state occurs.

A FISH function is written to automatically delete the elements in the tunnel:

Firstly, the centroid of the model and the centroid of any element are obtained using the height and width of the model and the coordinates of nodes.

Secondly, the distance between them is determined.

Finally, if the distance is found to be smaller than the radius of the tunnel, then the element is set to be a null model to model the tunnel excavation.

3 Results and Discussions

Figure 2(a-j) and figure 3(a-e) show the failure processes of excavated models in schemes 1 and 2, respectively. Darker zones in figure 2(a-j) and figure 3(a-e) are called shear localized zones. Longer and narrower shear localized zones are usually called shear bands. Timesteps are also given in figure 2(a-j) and figure 3(a-e). It is noted that these timesteps are counted from the tunnel excavation (not counted from the application of the hydrostatic stress). Figure 2(k) and figure 3(f) show the monitored maximum unbalanced force-timestep curves in schemes 1 and 2, respectively.

3.1. Results for scheme 1 (small diameter)

It is found that the present model undergoes three deformational stages (figure 2(k)). In stage 1, the tunnel is not excavated and the model is subjected to the hydrostatic stress. With an increase of timesteps, the model tends to reach a static equilibrium state. In stage 2, after the tunnel is excavated the maximum unbalanced force increases and decreases continuously until a very small value is reached. In stage 3, the maximum unbalanced force is small enough so that it is invisible in figure 2(k), meaning that the excavated model has reached a new static equilibrium state.

Stage 2 can be roughly divided into three smaller stages, i.e., stages 2.1, 2.2 and 2.3 (figure 2(k)).

The stage 2.1 is from the tunnel excavation to 5000 timesteps after the tunnel excavation. In figure 2(a), no longer shear bands are found. The intensive shear strains are localized at twelve points. Outside these points, the shear strain concentrated zone is like a cirque. In figure 2(b), only eight points with intensive shear strain concentrations are observed. In figure 2(c), eight shear bands are originated from the surface of the tunnel, i.e., the eight strain localization points. After any shear band is initiated, it develops outwards. Eventually, it combines with its nearest neighbour to form a V-shaped rockburst notch (or called a “dog-ear”). Eight shear bands form four rockburst notches. In figure 2(d), the rockburst notches become deeper.

Rockbursts occurred in stage 2.1 correspond to the violent rockbursts in situ due to the very high maximum unbalanced force (about 70N) immediately after the tunnel excavation.

Stage 2.2 is between 5000 timesteps and 15000 timesteps after the tunnel excavation. In figure 2(e), a new shear band (marked by a character A in figure 2(e)) is initiated at the lower left corner of the tunnel. The shear band A and the adjacent horizontal shear band (marked by a character B in figure 2(e)) meet so that a larger V-shaped notch is formed. Afterwards, the other two larger V-shaped notches are formed one after another at the upper left corner (figure 2(f-g)) and lower right corner (figure 2(h)) of the tunnel. In stage 2.2, the peak of the maximum unbalanced force is lower than 30N, while it is about 70N in stage 2.1. Obviously, the magnitude of rockbursts occurred in stage 2.2 will be lower than that in stage 2.1 according to the peak of the maximum unbalanced force.

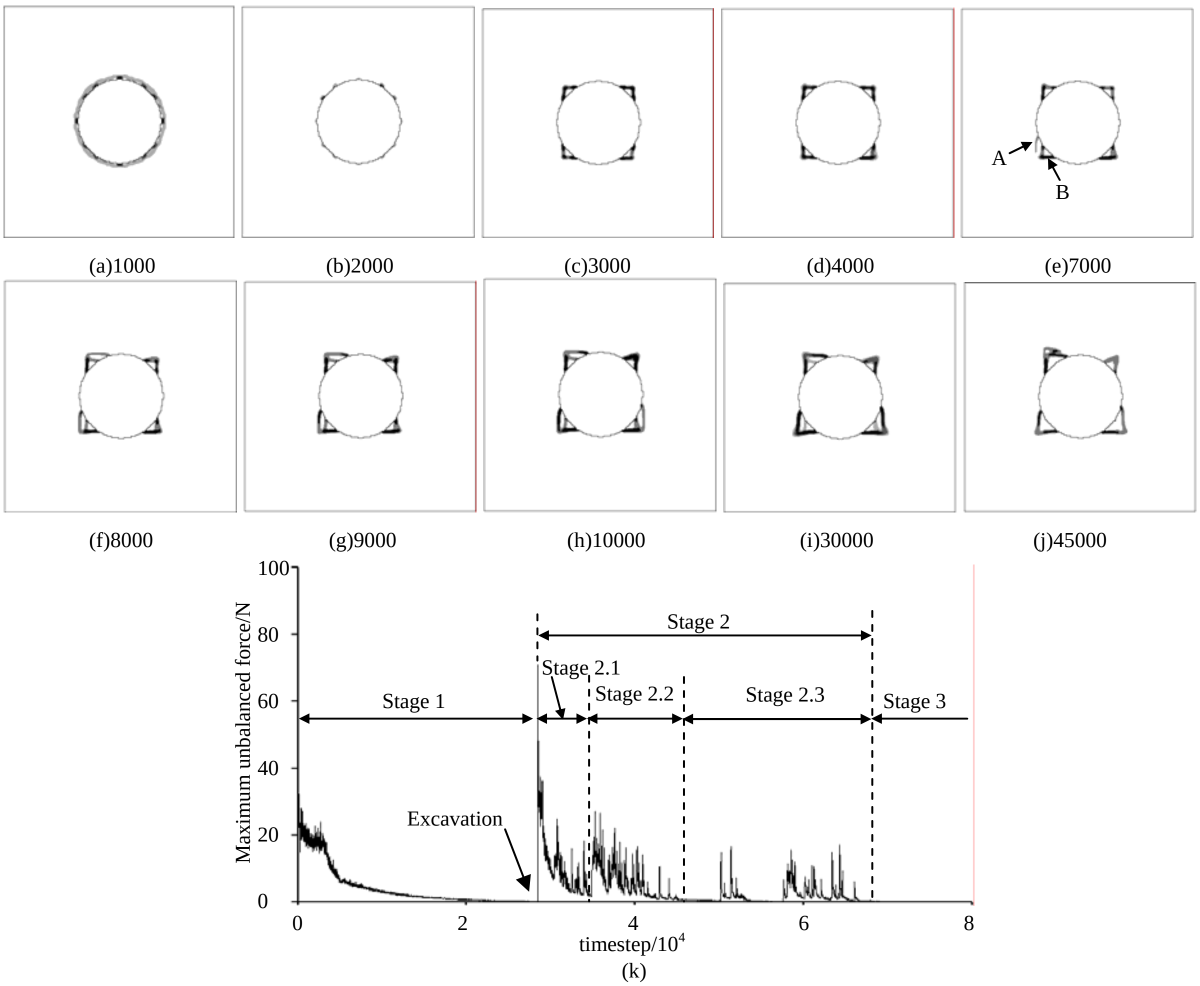

Figure 2 Failure process (a-j) of scheme 1 (small hole) at different timesteps and the maximum unbalanced force-timestep curve (k).

In stage 2.3 (timesteps are from 15000 to 35000 beyond the tunnel excavation), no new rockburst notches are found and only the depth of notches becomes larger. Though the maximum unbalanced force rapidly rises and then drops many times, rockbursts occurred at this stage correspond to minor rockbursts in situ since the maximum unbalanced force (lower than 20N) is relatively lower.

In stage 3 (beyond 45000 timesteps after the tunnel excavation), the maximum unbalanced force has dropped to an extremely small value, meaning that the excavated model has reached a new static equilibrium state after the minor rockbursts in stage 2.3. That is to say, the new tunnel geometry with four V-shaped notches is still stable.

Strictly speaking, after 7000 timesteps beyond the tunnel excavation, the deformational mode of the surrounding rock is not completely symmetric because there is a relatively small rockburst notch at the upper right corner of the tunnel. However, the asymmetric phenomenon is less apparent.

3.2. Results for scheme 2 (large diameter)

At 1000 timesteps beyond the tunnel excavation, the shear strain distribution in the surrounding rock is uniform in the circumferential direction (figure 3(a)). The highest shear strain is located at the position that is closest to the surface of the tunnel. At 3000 timesteps (figure 3(b)), four rockburst notches have been formed. Figure 3(b) is similar to figure 2(c-d). After that, the four notches become larger and larger with an increase of timesteps (figure 3(c-d)). Next, many longer shear bands initiate and propagate outwards (figure 3(e)). In this process, the symmetric deformational mode disappears. Moreover, the maximum unbalanced force is never lower than the limit value (figure 3(f)), which means that the entire tunnel section will collapse.

Obviously, the peak of the maximum unbalanced force after the tunnel excavation in figure 3(f) is higher than that in figure 2(k). Therefore, the magnitude of rockbursts occurred in scheme 2 will be higher than that in scheme 1.

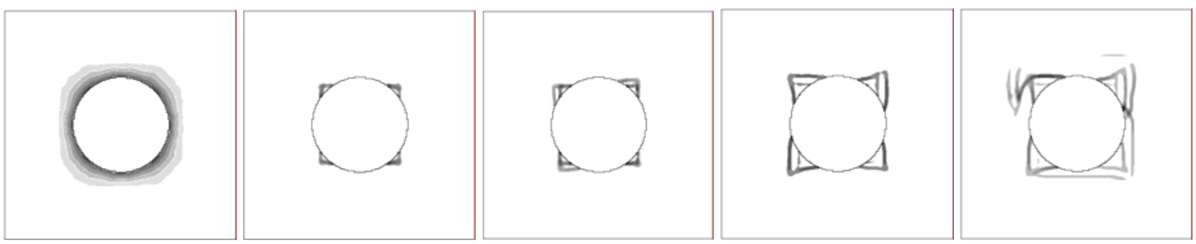

(a)1000 (b)3000 (c)5000 (d) 20000 (e)60000

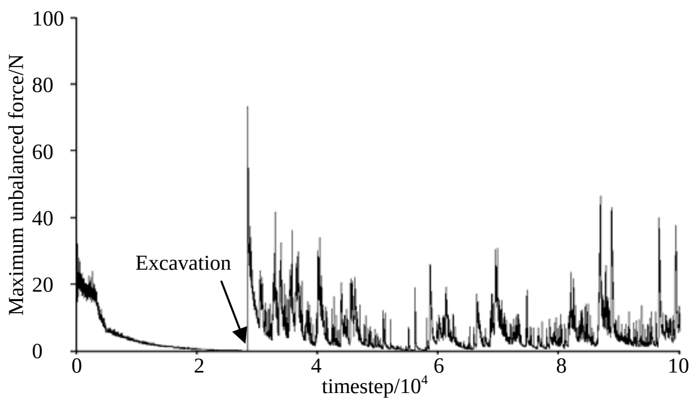

(f)

Figure 3 Failure process (a-e) of scheme 2 (big hole) at different timesteps and the maximum unbalanced force-timestep curve (f).

3.3. Experimental results and observations in situ

The experimental result by Lu and Wang [12] shows that the circular tunnel wall is destroyed in the form of four V-shaped rockburst notches. Their model is in a hydrostatic stress state, as is identical to the present calculation condition. Four symmetric V-shaped rockburst notches have been also observed in situ [12]. These results agree well with the present numerical results.

In fact, the observed number of rockburst notches by many researchers is 1 or 2 [14-18]. On one hand, possibly, the hydrostatic stress state cannot be always satisfied in situ. On the other hand, the heterogeneity of rock materials leads to the asymmetric deformational mode in situ.

Meng et al. [13] found that the magnitude of rockbursts increases with the tunnel size, which is in a good agreement with the present numerical results.

4 Conclusions

The stability of the excavated model is found to be dependent on the diameter of the tunnel. For the small tunnel, eight shorter shear bands form four small V-shaped rockburst notches and the surrounding rock remains stable after rockbursts. For the large tunnel, after larger rockburst notches appear, many longer shear bands are formed and propagate outwards. Moreover, the maximum unbalanced force never tends to be smaller than a very small value. Therefore, after the large tunnel is excavated, the surrounding rock easily loses its stability.

References

1. Jansen, D.C. and Shah, S.P. Effect of length on compressive strain softening of concrete. J. Eng. Mech., ASCE, 1997, 123(1). 25-35.
2. Van Mier, J.G.M., Shah, S.P. and Arnaud, M., et al. Strain-softening of concrete in uniaxial compression-report of the round robin test carried out by RILEM TC 148-SSC. Mater. Struct., 1997, 30(198). 195-209.
3. Tang, C.A., Tham, L.G. and Lee, P.K.K., et al. Numerical studies of the influence of microstructure on rock failure in uniaxial compression-Part II: Constraint, slenderness and size effect. Int. J Rock Mech. Min. Sci., 2000, 37(4). 571-583.
4. Pan, Y.S., Wang, X.B. and Li, Z.V. Analysis of the strain softening size effect for rock specimens based on shear strain gradient plasticity theory. Int J Rock Mech Min Sci, 2002, 39(6). 801-805.
5. Wang, X.B. Prediction of height effect, plastic deformation and fracture energy for high-strength concrete by linear shear softening constitutive relation based on energy conservation method. Magazine of Concrete Research, 2007, 59(5). 341-350.
6. Wang, X.B., Pan, Y.S. and Hai, L. Instability criterion of fault rock burst based on gradient-dependent plasticity. Chinese Journal of Rock Mechanics and Engineering, 2004, 23(4). 588-591. (in Chinese)
7. Wang, X.B. Unstable criterion of rock specimen subjected to shear failure in uniaxial compression based on energy principle. Engineering Mechanics, 2007, 24(1). 153-156,161. (in Chinese)
8. Wang, X.B., Size effect of shear fracture energy of concrete in uniaxial compression based on gradient-dependent plasticity. Key Engineering Materials, 2006, 312. 299-304.
9. Wang, X.B., Pan, Y.S. and Ma, J., Theoretical analysis of stability and unstable sliding of the system composed of shear band and elastic rock. Chin J Geotech Eng, 2002, 24(3). 360-363. (in Chinese)
10. Wang, X.B., Zhao, Y.F. and Zhang, Z.H., et al. Analysis on fault rockburst considering strain rate and strain gradient. Chinese Journal of Rock Mechanics and Engineering, 2003, 22(11). 1859-1862. (in Chinese)
11. Bazant, Z.P., Lin, F.B. and Lippmann, H. Fracture energy release and size effect in borehole breakout. Int J Num Anal Methods Geomech, 1993, 17. 1-14.
12. Lu, J.Y. and Wang, C.M., Study on back analysis for stress of rock mass from information of rockbursts. Journal of Yangtze River Scientific Research Institute, 1994, 11(3). 27-30. (in Chinese)
13. Meng, L.B., Li, T.B. and Zhou, H.C. Rock burst’s dimensional effect on the tunnels of a hydropower station. Water Power, 2008, 34(1). 29-31. (in Chinese)
14. Papanastasiou, P.C. and Vardoulakis, I.G., Numerical treatment of progressive localization in relation to borehole stability. Int J Num Anal Methods Geomech, 1992, 16. 389-424.
15. Gu, C. and Anand, L. Granular materials: constitutive equations and strain localization. J Mech Phys Solids, 2000, 48. 1701-1733.
16. Vardoulakis, I.G., Sulem, J. and Guenot, A., Borehole instabilities as bifurcation phenomena. Int J Rock Mech Min Sci, 1988, 25. 159-170.
17. Guenot, A., Borehole breakout and stress fields. Int J Rock Mech Min Sci, 1989, 26. 185-195.
18. Martin, C.D. The effect of cohesion loss and stress path on brittle rock strength. Can Geotech, 1997, 34. 698-725.
19. Wang, X.B., Effects of dilation angle on failure process and mechanical behavior for rock specimen with random material imperfections. The Chinese Journal of Nonferrous Metals, 2007, 17(7). 1063-1071. (in Chinese)
20. Wang, X.B., Failure process and stress-strain curve of plane strain rock specimen with initially random material imperfections. Key Engineering Materials, 2007, 353-358. 1133-1136.

RaSiM 7(2009): Controlling Seismic Hazard and
Sustainable Development of Deep Mines,
C.A. Tang(ed), Rinton Press, 143-148

GOB-SIDE ENTRY WITH LIMESTONE ROOF RETAINED BY ANCHORAGE CABLE AND INDIVIDUAL PROP SUPPORT

YUN-LIANG TAN

Education Ministry Key Lab of Mine Disaster Prevention and Control, Shandong University of Science and Technology, Qingdao 266510, P.R. China

LI-JUN ZHANG

Binhu Mine, Zaozhuang Mine Ltd, Zaozhuang, Shandong 277000, P.R. China

Theoretical analysis and in-situ tests are adopted to study the support method for gob-side entry with a limestone roof. A combinational method of the anchor cable and individual prop are put up, and it is shown that this combinational method is valid for cutting the roof with a certain hanging distance. It is also found that, because of the roof hanging effect, there exists an 8-metre-wide high stress concentrated zone in front of work face, and a concentrated load zone with 8 metres width lag behind work face. When main roof fractures, a rebound ahead of work face may occur, this can be used for forecasting both the time and the place of main roof fracturing.

1 Introduction

Gob-side entry retained for the next sublevel can cancel a coal pillar, reduce a new entry, and bring out prominent economic and social efficiency. However, gob-side entry retaining supports will undergo the two-time intensive mining affection and is difficult generally to maintain, which makes it a hot topic in coal mining engineering for some scholars in recent years. For example, through statistical and theoretical analysis are studied through the roof-cut load and the deformation of its pack-filling induced by the main roof breakage [1]. By analyzing the shearing stress distribution in bolts with the help of numerical simulation, it is found that the shearing effect of the bolt is not to be neglected in the gob-side entry of the fully-mechanized caving face [2]. With the help of UDEC software, the influences of the location of the main roof rupture, length of un-caved top-coal at the end of the working face, original road support, width of filling belt, filling way and strength of the filling belt on the stability of surrounding rocks of gob-side entry retaining in fully-mechanized top-coal caving mining face are analyzed [3]. A test of gob-side entry retaining technique has been done in the Daihe Coal Mine, by using bolt-mesh-cable supports in the roadway, dense I-steel pillar, and broken coal wall roadside supports [4]. In order to keep the gob-side entry retaining in fully-mechanized coalface with top-coal caving well, a three-step support process due is put forth: firstly, the original entry is reinforced with bolts, wire mesh, and cable (BBWC); secondly, the coal wall of the next coalface is enlarged and supported by BBWC; finally, the road packing is carried out [5]. By the equivalent material simulation test, the broken situation, shape of the main roof, and the influence of different supports on roof activity are analyzed [6]. Because both the roadside coal bearing capacity and the reinforcing effects of the roadside cable-support are two important factors for the gob-side roadway, they must be taken into account to analyze the support mechanism [7]. In order to estimate the gob-side roadway safety, a method for calculating the critical value of roof bedding separation is set up [8]. How to maintain the gob-side entry or roadway well by effective support is a key technique of the research. This article introduces a case study of the gob-side entry maintained technique under special geological conditions of a hard limestone roof and soft shale floor.

2 Gob-side Entry Support Design

2.1 Geologic Conditions

The trial entry is the haulage roadway of work face No. 16101 in Binhu Mine, its buried depth is 548 m. The work face incline length is 181 m and strike length is 651 m, its dip angle is 4° . The seam is stable in occurrence and 1.33 m in height, its hardness f=2.05. The roof strata above the seam are limestone with 4.9 m in thickness and with hardness f=2.3, and mudstone with 8.5 m in thickness orderly. The floor is mudstone with 4.5m, which is soft and fragile, argillaceous cement, hardness f=1.74.

2.2 Overburden Strata Components

Because the gob-side roadway is influenced by overburden strata movement, the first thing should be to make clear the basic law of overburden strata movement during the working face advances. Based on the strata movement theory put up by Song [9], the overburden layers affecting the work face and entry prominently can be named two parts of immediate roof and main roof (figure 1).

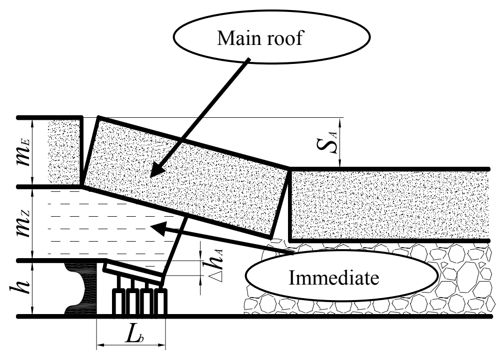

Figure 1 Structure of overburden strata

Immediate roof can collapse completely in goaf, so its thickness can be estimated by

$$m_z = \frac{h - S_A}{K_A - 1} \tag{1}$$

where m_z is the thickness of immediate roof, h is the extraction height; K_A is the expansion coefficient at the location of main roof contacting collapsed rock, S_A is the actual subsidence of main roof, if S_0 is the limit subsidence value keeping main roof un-break away, then $S_A \le S_0$.

In practice, S_A can be obtained from reference [10] as

$$S_A = K_S \cdot h \tag{2}$$

where Ks is the actual ration of subsidence of un-caved strata to extraction height h, it can be obtained by in-situ test.

For the work face No.16101 in Binhu Mine, Ks≈0.1. By taking K_A=1.25 and h=1.33 m into formulas (1), the immediate roof thickness is obtained as: m_z=4.788 m, it is just the thickness of limestone. Also, the main roof can be ensured as the mudstone with 8.5 m in thickness.

2.3 Fracturing Span of Roof

Incline length of work face is represented by *b*, the roof fractured span L_0 can be estimated by ref. [10]

$$\begin{cases} \beta = \sqrt{\dfrac{4[\sigma_t]m_i}{1.3\gamma}} \\ L_0 = \dfrac{\beta}{\sqrt{3-2\beta\dfrac{1}{b}}} \end{cases} \tag{3}$$

where $[\sigma_t]$ is the equivalent tensile strength of roof; m_i is the thickness of roof ; β is a transition parameter (m) ; *r* is the density of roof.

(a) Immediate roof. By laboratory test, it is shown the tensile strength of immediate roof is $\sigma_t = 6.5$ Mpa. By multiplying fissure factor, the rock body strength of immediate roof is obtained by $[\sigma_t]_z = \xi\sigma_t = 0.3\times 6.5 = 2.0$ Mpa**.** Substituting b=161 m, m_z=4.9 m into formulas (3), the initial fracture span of immediate roof is L_{z0}=21.6 m. According to the minimum of plastic power consumption in the roof fracture process, the lateral fracture span L_z is deduced as 1/3 of initial fracture span L_{z0}, i.e., $L_z \approx L_{zc} = L_{z0}/3 = 7.2$ m.

(b) Main roof. By a similar way of laboratory test, it is shown the tensile strength of main roof is $\sigma_t' = 2.26MPa$. By multiplying crocodile factor ξ=0.875, the rock body tensile strength of main roof is obtained by $[\sigma_t']_E = \xi'\sigma_t' = 1.98$ Mpa**.** So the initial fracturing span of main roof L_{E0}=33.5 Mpa, and lateral fracture span L_{ec}=16.8 m.

2.4 Support Design

Suppose the roof of gob-side roadway can be simplified as a cantilever beam acted a uniform load q_E form main roof, as shown in figure 2.

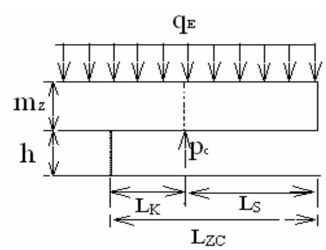

Figure 2 Cutting roof model of gob-side roadway

In order to cut roof effectively, the cutting force P_C supplied by support should satisfy the condition

$$P_C = \max\{P_1, P_2\} \tag{4}$$

where $P_1 = \gamma_z m_z L_s$ which is support force for the case of only immediate roof i.e. q_E=0, P_2 is the force needed for cutting the roof along the wall of god-side.

The limit tensile strength of immediate roof can be represented by

$$[\sigma_t]_z' = \frac{M}{W} = \frac{\frac{1}{2}(r_z m_z + q_E)L_s^2}{\frac{1}{6}m_z'^2} = \frac{3q' L_s^2}{m_z'^2} \tag{5}$$

where $q^{'}$ is the load density when roof begin to fracture in tensile form; $[\sigma_t]_z^{'}$ is the actual tensile strength after affected by roof movement, in-situ test shows $[\sigma_t]_z^{'} = 0.7[\sigma_t]_z$; $m_z^{'}$ is actual bending thickness after affected by roof movement; q_E is load density from main roof.

If let the gob-side entry bear sufficient subsidence but not bear the load from main roof, i.e. q_E =0, then

$$p_2 = q^{'} L_s = \frac{[\sigma_t]_z^{'} m_z^{'2}}{3L_s} \tag{6}$$

Consider the existed fissure, let $m_z^{'} = 0.5m_z$, $m_z = 4.9$ m, $[\sigma_t]_z^{'} = 1.4$ Mpa, $L_s = (L_{zc} - L_k) = 3.8$ m, P_2 is obtained as P_2=737.2 KN. Thus $P_c = \max\{P_1, P_2\} = 737.2$ KN/m.

2.4 Support Layout

In the case of anchor cable 15.2 mm in diameter is adopted for cutting roof along the gob-side line, the limit pull out force is P_a=220KN for each anchor cable, the bolts density along cutting line is 3.03 count.m^{-1}. In the case of individual prop with 2.8 m in height, the actual working force of each prop is 225 KN; the prop density along cutting line is 2.96 number.m$^{-1.}$ A combinatorial support disposal with two parts is as following:

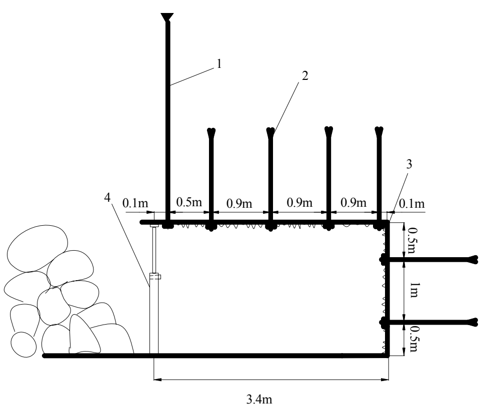

(a) Section map

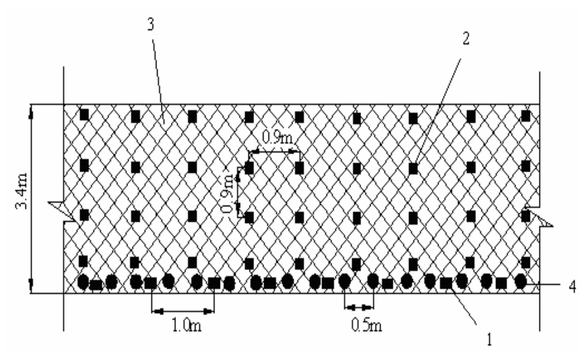

(b) Planar graph

Figure 3 Support disposal

(1-anchor cable, 2-anchor, 3-steel mesh, 4-individual prop.)

(a) For basic support, whorl steel bar with 18 mm in diameter 2000 mm in length, metal mesh with 300 mm in length and 1000 mm in width and resin with 18mm in diameter and 350 mm in length are adopted. The space between anchors is 900 mm

(b) For strengthening the cut support, along cutting line, an anchor cable with 5.5 m long was bonded by two rolls of resin with 18 mm in diameter and 350 mm in length, every other metre. At the same time, along cutting line, an individual prop is supported every other half metre, as shown in figure 3.

3 In-situ Test

The trial work is done in the haulage roadway of work face No. 16101 in Binhu Mine. In-situ observations show that the gob-side entry is maintained very well after roof movement. Much more, some interesting results are obtained.

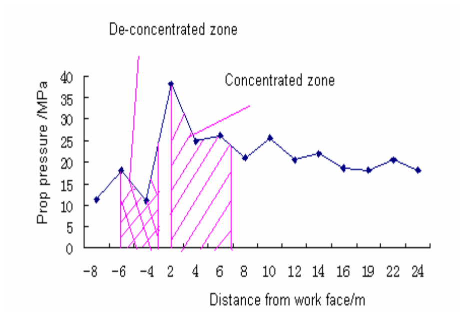

(a) No roof hanging case without main roof weighting

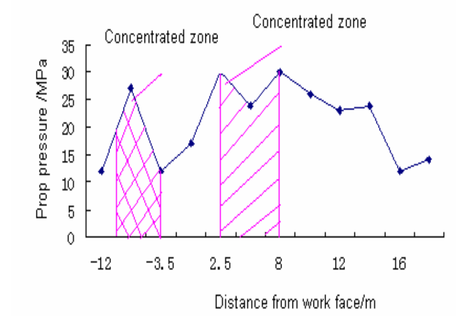

(b) Concentrated zone due to main roof weighting of no roof hanging

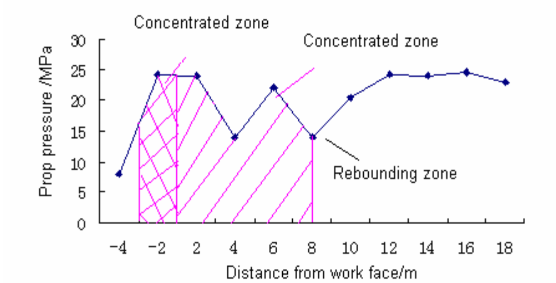

(c) Concentrated zone due to main roof weighting with roof hanging

Figure 4 Prop support pressure monitoring results

(a) Support load. As shown in figure 4, the obvious region affected by abutment pressure ahead of work face is 8m, and the obvious region affected by roof movement lag behind work face is 10 m. The main roof fracturing position is about ahead of work face 3 m. During the fracturing process, advance support load appears fluctuation and rebound. When roof is weighting, the individual prop load lag behind work face 10 m increases greatly if roof hanging distance exists largely, but the individual prop load lag behind work face only about from 3 m to 5 m increases if there is roof hanging.

(b) Convergence. Through convergence measurement, it is shown that the obvious deformation zone is about 10 m ahead of work face, which is about consistent to the load measurement results, as shown in figure 5.

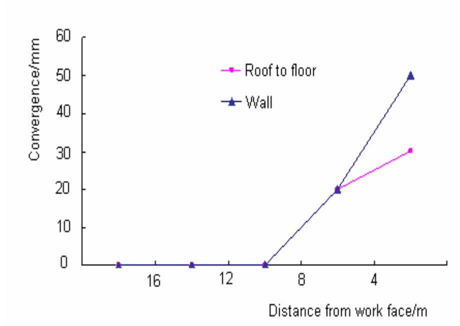

(a) Measuring base 4

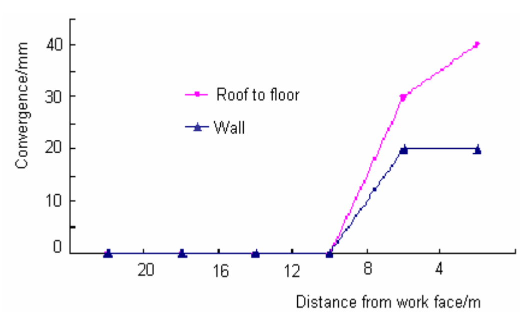

(b) Measuring base 5

Figure 5 Convergence curve

4 Conclusions

For Gob-side entry with a limestone roof, the combinational method of anchor cable and individual prop are successful for cutting the roof with a certain hanging distance, based on the strata movement analysis. Because of the hanging effect of the roof, there exists a high stress concentrated zone ahead of the work face by 8 m, and a concentrated load zone lag behind the work face by 8 m. When the main roof fractures, a rebound ahead of the work face can occur, this can be used to forecast when and where the main roof will fracture. During the main roof weighting, strengthening support measures must be adopted in the range of about 8 m wide in front of the work face and 8 m wide lag behind the workface, in order to correctly maintain the gob-side entry.

Acknowledgements

The study is supported by China Natural Science Fund (No. 50534080, No. 50674063), Shandong Province Natural Science Fund (Z2008F01), Project No. J06N04 of Educational Department of Shandong Province, Key Laboratory of Mine Disaster Prevention and Control of Education Ministry, Tai'shan Scholar Engineering Construction Fund of Shandong Province of China.

References

1. Qi, T.Y. Main Parameters of Pack-filling for Retained Gob-side Entry and Its Adaptability. Journal of China University of Mining & Technology, 28(2). 122-125.
2. Miao, X.X., Mao, X.B., Zhu, C.Q. and Liu, W.Q. Analysis on Shearing Deformation of Roof Support Bolt in Gob-side Entry of Fully-mechanized Caving Face. Journal of the China Coal Society, 30(6). 681-684.
3. Xie, W.B. Influence Factors on Stability of Surrounding Rocks of Gob-side Entry Retaining in Top-coal Caving Mining face. Chinese Journal of Rock Mechanics and Engineering, 23(18). 3059-3065.
4. Hua, X.Z., Zhao, S.H., Zhu, H. and Hu H.J. Research on Combined Support Technique of Gob-side Entry Retaining. Rock and Soil Mechanics, 27(12). 2225-2228.
5. Zhang, D.S., Ma, L.Q., Feng, G.M. and Miao, X.X. Technique of Gob-side Entry Retaining with Entry in Packing on Its Original Position in Fully-mechanized Coalface with Top-coal Caving. Chinese Journal of Rock Mechanics and Engineering, 24(7). 1164-1168.
6. Zhang D.S., Mao, X.B. and Ma, W.D. Testing Study on Deformation Features of Surrounding Rocks of Gob-side Entry Retaining in Fully-mechanized Coal Face with Top-coal Caving. Chinese Journal of Rock Mechanics and Engineering, 21(3). 331-334.
7. Hua, X.Z., Ma, J.F. and Xu, T.J. Study on Controlling Mechanism of Surrounding Rock of Gob-side Entry with Combination of Roadside Reinforced Cable Supporting and Roadway Bolt Supporting, and Its Application. Chinese Journal of Rock Mechanics and Engineering, 24(12). 2107-2112.
8. Shen, R.X., Liu, C.W. and Wu X.Y. Analysis and Calculation on Roof Separation Critical Values of Solid-Coal Roadway and Gob-side Roadway Supported with Bolts. Journal of Sichuan University (Engineering Science Edition), 39(3). 19-23.
9. Song, Z.Q. Applied Strata Mechanics. Publishing House of China University of Mining and Technology, 1988.
10. Tan, Y.L. The Plate Limit Analysis of the Fracture Length of Hard Roof Back of the Coalface. J. of Shandong Inst. of Min. and Tech., 8(3). 21-26.

RaSiM 7(2009): Controlling Seismic Hazard and Sustainable Development of Deep Mines, C.A. Tang(ed), Rinton Press, 149-156

MLE NEPHOGRAMS FOR STABILITY ANALYSIS OF STEEP SLOPES BASED ON MULTIVARIATE PHASE SPACE RECONSTRUCTION

ZHI-PING LIU, XIU-FENG HE and MIN HE

Institute of Satellite Navigation & Spatial Information System, Hohai University

Nanjing 210098, P.R. China

Deformation monitoring provides an important basis for identifying slope instability, and the maximal Lyapunov exponent (MLE) extracted from slope deformations indicates the dynamic features of nonlinear evolution. This paper investigates the phase space reconstruction of multivariate time series. Based on both phase space reconstruction of multivariable time series and the reversible and irreversible properties of time trajectories, the generalized estimation of MLE method is proposed to detect dynamic features buried in slope deformations using bi-directional search phase point. The developed method is characterized by its robustness, high accuracy and dimension flexibility. In the end, a case is studied for the Number Two steep slope at Xiaowan hydropower station according to the proposed method, and the results show that the MLE nephograms and stability zoning maps, derived from the developed method with the help of Ordinary Kriging tool, can effectively reveal the traction deformation mechanism of this slope from bottom to top and the result is in good agreement with actual deformation in the field. The validity of proposed method is proven and can be reliably used for stability analysis of slopes.

1 Introduction

Steep slopes are characteristic geological bodies in the environment or bearing layers of engineering structures in southwestern region of China [1]. They are predominately the first major geotechnical engineering and engineering geological problems that has to be considered in important construction projects. Both the nonlinear factors of internal mechanisms and the random factors of the external environment have influenced the deformation of slope projects [2], which are very complex evolution processes of a dynamic system. Theoretically, the complex dynamics system can be characterized by multivariable dynamic evolution, hierarchical structure, and information randomicity. However, it is almost impossible to model with the analytical method. Practice and research have verified the maximal Lyapunov exponent (MLE), the long-term average index rate for detecting convergence, and the divergence between adjacent tracks in the phase space reconstruction [3] as important indicators for quantitatively describing the dynamics features of system. Moreover, compared with the Kolmogorov entropy, Hausdorff dimension, information dimension, and correlation dimensions; MLE can provide more useful dynamics diagnosing for the chaotic system. Thus, MLE has been widely adopted for judging criteria of slope stability, and related work can be found in many technical papers [4-7].

The above mentioned achievements were useful for phase space reconstruction of the univariate time series. However, modern monitoring techniques (such as by GPS [8]) can efficiently obtain 3D deformation of geotechnical slopes. Theoretically, the multivariate time series contains more dynamics information of slopes than the univariate time series; therefore the MLE calculated from the multivariate time series is expected to be more accurate [9]. In addition, the prevention and control of large-scale spatial-temporal slopes deformation by hazards zoning are urgently important and are the purpose of this paper [10]. Section 2 will briefly discuss the phase space reconstruction of the 3D deformation series. On the basis of the irreversible and reversible properties of time trajectories in the phase space reconstruction, the generalized method for estimating MLE from multivariate time series is proposed using the bi-directional search phase point in section 3. To verify the rationality and viability of the developed method, section 4 will study deformation stability of the Number Two steep slope at the Xiao Wan hydropower station based on the novel method and Ordinary Kriging. Finally, in section 5 we present some useful conclusions and recommendations for ongoing work.

2 Phase Space Reconstruction of Multivariate Time Series

Supposing that n periods 3D deformation series have been obtained from monitoring points of a slope, the corresponding multivariate time series are $\left\{\left(x_i, y_i, z_i\right)\right\}_{i=1}^{n}$, where x_i, y_i, z_i are respectively the horizontal and the vertical deformations. Before reconstructing phase space, the raw 3D deformation series should be initialized as follow:

$$\tilde{s}_i = \frac{s_i - s_1}{\max\left(s_i\right) - \min\left(s_i\right)} \tag{1}$$

Where, $s \in \left\{x, y, z\right\}$.

The 3D deformation series normalized by equation (1) eliminating the influence of dimensional difference. In other words, $\left\{\tilde{x}_i\right\}_{i=1}^{n}$, $\left\{\tilde{y}_i\right\}_{i=1}^{n}$, and $\left\{\tilde{z}_i\right\}_{i=1}^{n}$ have the same initial value and value range. Then, the 3D deformation series transformed can be extended to the following phase space:

$$\begin{aligned}
\boldsymbol{V}_i\left(m_1, \tau_1; m_2, \tau_2; m_3, \tau_3\right) &= \left(\tilde{\boldsymbol{X}}_i^T;\ \tilde{\boldsymbol{Y}}_i^T;\ \tilde{\boldsymbol{Z}}_i^T\right) \\
&= \{\tilde{x}(t_i),\quad \tilde{x}(t_i+\tau_1),\quad \tilde{x}(t_i+2\tau_1),\quad \cdots,\quad \tilde{x}\left[t_i+(m_1-1)\tau_1\right]; \\
&\quad\ \tilde{y}(t_i),\quad \tilde{y}(t_i+\tau_2),\quad \tilde{y}(t_i+2\tau_2),\quad \cdots,\quad \tilde{y}\left[t_i+(m_2-1)\tau_2\right]; \\
&\quad\ \tilde{z}(t_i),\quad \tilde{z}(t_i+\tau_3),\quad \tilde{z}(t_i+2\tau_3),\quad \cdots,\quad \tilde{z}\left[t_i+(m_3-1)\tau_3\right]\}^T
\end{aligned} \tag{2}$$

Where, $\boldsymbol{V}_i$ is the phase point, $\tau_k = \omega_k \Delta t (k = 1, 2, 3)$ stands for the time-lag item, ω_k is the time-lag epochs, Δt is the sampling interval, and m_k is the embedding dimension of the phase space reconstruction.

It must be noted that, the different selecting method of reconstruction parameters has different effect on phase space reconstruction related to the accuracy of MLE. Currently, there are mainly two kinds of selection methods. under the assumption that time series are infinite length and have no observation error, the first viewpoint think that time-lag item and embedding dimension are unrelated, thus time-lag item and embedding dimension can be determined independently. The second one is just the opposite. They think both finite length and observation error are inevitably taken into account in actual application, that is to say, time-lag item and embedding dimension should be determined dependently. Most researchers agree the second viewpoint is more practical and reasonable in engineering practice [12]. Therefore, reconstruction parameters are determined using the prediction error minimization method [13] in this paper.

3 The Generalized Estimation of MLE Method for 3D Slope Deformation Using Bi-directional Search Phase Points

In the phase space reconstruction of multivariate time series, $\boldsymbol{V}_{\eta(i)}$ and $\boldsymbol{V}_i$ are the pair of the nearest neighbor phase points. Then, the distance between the nearest neighbor phase points can be defined as

$$\begin{aligned} D_i^0 &= \left\| \boldsymbol{V}_i - \boldsymbol{V}_{\eta(i)} \right\| \\ &= \frac{m_1}{M}\left\|\tilde{\boldsymbol{X}}_i - \tilde{\boldsymbol{X}}_{\eta(i)}\right\| + \frac{m_2}{M}\left\|\tilde{\boldsymbol{Y}}_i - \tilde{\boldsymbol{Y}}_{\eta(i)}\right\| + \frac{m_3}{M}\left\|\tilde{\boldsymbol{Z}}_i - \tilde{\boldsymbol{Z}}_{\eta(i)}\right\| \end{aligned} \tag{3}$$

Where, $M = \sum_{k=1}^{3} m_k$.

For every phase point V_i , after it and its nearest neighbor phase point evolve forward h_i^f steps along time trajectories, the distance evolving forward between the phase points can be written as

$$\begin{aligned} D_i^{h_i^f} &= \left\| \boldsymbol{V}_{i+h_i^f} - \boldsymbol{V}_{\eta(i)+h_i^f} \right\| \\ &= \frac{m_1}{M}\left\|\tilde{\boldsymbol{X}}_{i+h_i^f} - \tilde{\boldsymbol{X}}_{\eta(i)+h_i^f}\right\| + \frac{m_2}{M}\left\|\tilde{\boldsymbol{Y}}_{i+h_i^f} - \tilde{\boldsymbol{Y}}_{\eta(i)+h_i^f}\right\| + \frac{m_3}{M}\left\|\tilde{\boldsymbol{Z}}_{i+h_i^f} - \tilde{\boldsymbol{Z}}_{\eta(i)+h_i^f}\right\| \end{aligned} \tag{4}$$

Where, $1 \le h_i^f \le N_i^{fore}$, $N_i^{fore} = \min\left\{N-i, N-\eta\left(i\right)\right\}$. In the same way, the distance evolving backward h_i^b steps between the phase points can be written as $D_i^{-h_i^b}$.

Generally, the approximate relation of the distance evolving forward and the Maximal Lyapunov Exponent can be given by the following formula

$$\left\langle \ln D_i^{h^f} \right\rangle \cong \left\langle \ln D_i^0 \right\rangle + \mathrm{MLE}^f \cdot h^f \Delta t \tag{5}$$

where, MLE^f is the maximal Lyapunov exponent using forward search phase points, h^f are forward search steps whose range is from 1 to $\max\left(N_i^{fore}\right)$, and $\langle\cdot\rangle$ is average operator of all phase points.

According to the Lyapunov stability criterion [4], when $\mathrm{MLE}^f \le 0$, it signified that slopes deformation has no chaotic features and slope system is stable, and the larger its absolute value is, the higher stability is. When $0 < \mathrm{MLE}^f < \infty$, it signified that slopes deformation has chaotic features and slope system is unstable, and the larger its value is, the higher instability is.

Equation (5) can be obtained using small data sets method calculating MLE from univariate time series [3], however it would be more accurate and reliable by extending to multivariate time series. To improve further the accuracy and reliability of MLE, on the basis of the irreversible property of chaotic attractor [11], the irreversible and reversible properties of time trajectories is studied in the phase space reconstruction and the generalized estimation of MLE method is proposed for 3D deformation series using bi-directional search phase points.

Similar to forward search phase points, the distance evolving backward can also be devoted to calculating the maximal Lyapunov exponent:

$$\left\langle \ln D_i^{-h^b} \right\rangle \cong \left\langle \ln D_i^0 \right\rangle + \mathrm{MLE}^b \cdot h^b \Delta t \tag{6}$$

Where, MLE^b is the maximal Lyapunov exponent using backward search phase points, and h^b are backward search steps whose range is from 1 to $\max\left(N_i^{back}\right)$.

When $\mathrm{MLE}^f \times \mathrm{MLE}^b > 0$, it signified time trajectories is irreversible in the phase space reconstruction. Thus, according to equation (5) and (6), the generalized estimation of MLE method is proposed for 3D deformation series using bi-directional search phase points:

$$\left\{\left\langle \ln D_i^h \right\rangle + \left\langle \ln D_i^{-h} \right\rangle\right\} \cong 2\left\langle \ln D_i^0 \right\rangle + 2\mathrm{MLE} \cdot h\Delta t \tag{7-a}$$

Where, h are bi-directional search steps whose range is from 1 to $\min\left\{\max N_i^{fore}, \max N_i^{back}\right\}$.

When $\mathrm{MLE}^f \times \mathrm{MLE}^b \le 0$, it signified time trajectories is reversible in the phase space reconstruction. Thus, according to equation (5) and (6), the generalized estimation of MLE method is developed for 3D deformation series using bi-directional search phase points:

$$\left\{\left\langle \ln D_i^h \right\rangle - \left\langle \ln D_i^{-h} \right\rangle\right\} \cong 2\mathrm{MLE} \cdot h\Delta t \tag{7-b}$$

According to the above formulae and analyses, we would like to explore that the generalized estimation of MLE method is characterized by as follow:

- Since embedding dimension m_k reflects the complexity of time series, the distance weighted by m_k/M between the phase points in the multivariate phase space reconstruction is more robust than that in the univariate phase space reconstruction.
- If equation (5) is used to calculate MLE, the phase points in the back of V_i can not used as reference phase points. But if equations (6) - (7) are used to calculate MLE, all phase points can serve as reference phase points. Thus, the utilization ratio of the time series data is doubled, which is helpful for greatly improving accuracy and reliability furthermore.
- The generalized method has dimension flexibility, so it can not only be extended to higher dimensional multivariate time series, but also be reduced to the univariate time series.

The 3D deformation series is more complete and true in describing the changes of slopes monitoring points, and theoretically multivariable time series contains more dynamics information than univariate time series. Therefore, the MLE results obtained by the generalized method reflect more truly the deformation features of the slope system, and the slope stability can be measured more accurately.

4 Stability Analysis for the Number Two Steep Slope at Xiaowan Hydropower Station Using the MLE Results

The Xiaowan hydropower station, started in January 2002 and to be completed by the end of 2012, dam height 292 m, with an installed capacity of 4200 MW, is located on the middle reaches of the Lancang River in Yunan Province of China. Steep slopes in the river valley, with a "V" shape, result in critical problems for construction engineers. Thus, control of slope deformation and its stability has become important engineering problems in the Xiaowan project construction, and the Number Two steep slope, with the height of 700m, the average width of 190 m, the front edge elevation of 1130 m, the back edge elevation of 1590 m, and the average slope angle from 30 to 35 degrees, is the key of slopes monitoring. To verify the effectiveness of the generalized estimation of MLE method, a case study is implemented to probe into 3D deformation series of the 44 monitoring points situated at the Number Two steep slope from February to September 2004. With the aid of Ordinary Kriging approach, the MLE nephograms determined from the proposed method are shown in figure 1. The horizontal axis is the East coordinate with the origin of 13750 m, the vertical axis presents the North coordinate with the origin of 36700 m, and the bar stands for deformation velocity of seasons with the unit of mm/d.

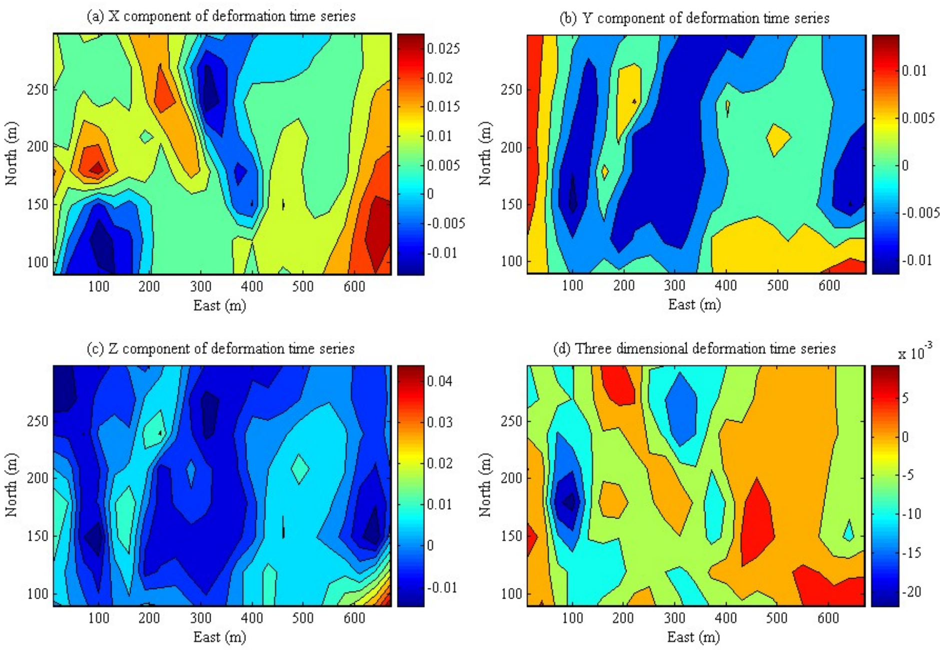

Figure 1 The MLE nephograms of the Number Two steep slope at Xiaowan hydropower station using different time series

From figure 1 it can be seen that there is great difference among MLE nephograms derived from different univariable deformation series. Then, if the Lyapunov stability theory is used to stability analysis, it is bound to lead to conflicting conclusions. Thus, the MLE nephograms calculating from the univariable deformation series nearly obtained reliable dynamics features of slope system. However, according to the MLE nephogram calculating from 3D multivariable time series, the Number Two steep slope is demonstrated with chaotic features in whole, which validates instability signs founded at the overall vertical elevation of this slope from 1245 m to 1600 m in January 2004. In addition, the continuous plane zone from 14050m to 14350m in east direction and from 36820m to 36980m in north direction is unstable based on MLE results from figure 1 (d), which almost agrees with the location of the large-scale toppling deformation at Yinshui Gully slope [14]. These indicate that MLE results from 3D multivariable time series can integrate completely 3D deformation features of monitoring points, so they can more realistically present dynamics features of slope system. To further verify the accuracy of the MLE results from 3D multivariable time series, stability zoning map of the Number Two steep slope, including the unstable zone and the basic stable zone, is shown in figure 2.

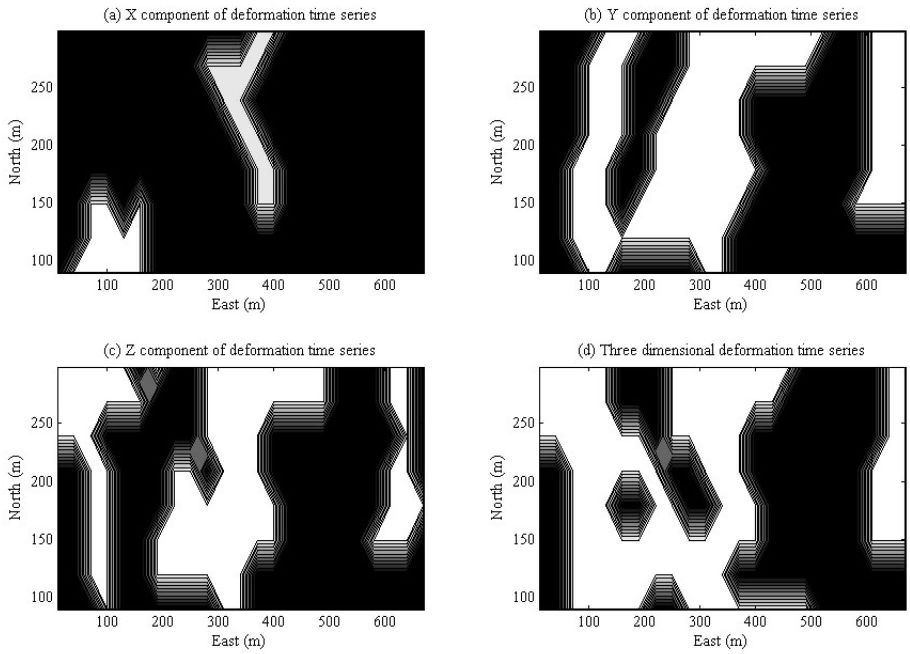

Figure 2 The stability zoning maps of the Number Two steep slope at Xiaowan hydropower station using different time series

In figure 2, black stands for unstable zone whose MLE is positive, while white stands for stable zone whose MLE is negative in figure 1. From figure 2 it is not difficult to find the stability zoning map from 3D deformation series is more accurate than that from other univariable deformation series. As shown in figure 2 (d), the unstable zone is located at the upper part of Yinshui Gully accumulation, which is adjacent to the gentle slope platform of Longtai Road in the north, to the ridge top of the Number Two steep slope in the south, and to Junmalutang Gully in the north-east. With the vertical deformation development depth of about 160 m, the large-scale toppling deformation zone can be detected from this unstable zone, while its surrounding zone is regarded as basically stable. The traction deformation mechanism of this slope from bottom to top also can be obtained by slope deformations and MLE results in figure 2.

From the view of slopes deformation reflecting internal mechanical behaviours, deformation stability of the Number Two steep slope, which are basically consistent with the conclusions derived from creep analysis of underground terranes and the actual deformation features, can be effectively disclosed using the MLE results from 3D deformation series. In fact, the above results are also agreement with the published achievement [14]. So, further control measures should be employed to prevent partly destabilization of the stable zone by improving the stability of unstable zone, because this slope stability has something to do with the drag sliding down caused by the bedrock failure of Yinshui Gully accumulation.

5 Conclusions

In this research, phase space reconstruction of 3D multivariate time series is investigated in detail. Through the use of bi-directional search phase points based on both irreversible and reversible properties of time trajectories, the generalized estimation of MLE method, characterized by robustness, accuracy and dimension flexibility, is developed for the 3D deformation series. In the end, the stability analysis for the Number Two steep slope at the Xiaowan hydropower station is carried through measurement of the accuracy and effectiveness of the novel method. Using the Lyapunov stability theory and the interpolation approach of Ordinary Kriging, both the MLE nephogram and the stability zoning map were derived from 3D deformation series. These demonstrated that the slope can be approximately classified by unstable zone and stable zones. The analyzed results are in agreement with the observed deformation features of the slope, and especially accurate for the traction deformation zones from 14050m to 14350m along the east direction and from 36820m to 36980m along the north direction. This presented research will present some references for the stability analysis of other slopes.

Acknowledgements

The work is supported by Nature Science Foundation of China (No. 50579013 and 50539110) and the S&T innovation foundation for graduates of Jiangsu Province in China (No. CX07B_137z).

References

1. Huang, R.Q. Main Characteristics of High Rock Slopes in Southwestern China and Their Dynamic Evolution. Advance in Earth Sciences, 2005, 20(3). 292-297. (in Chinese).
2. Fu, Y.X. and Liu Z.Q. Analytic Method and Application about Chaotic Slope Deformation Destruction Time-series. Journal of Wuhan University of Technology, 2003, 27(4). 473-476. (in Chinese).
3. Rosenstein, M.T. and Collins J. J. De Luca C. J. A practical method for calculating largest Lyapunov exponents from small data sets. Physica D, 1993, 65. 117-134.
4. Wu, Z.R. and Pan W.P. Research on Stability Criterion of Rock and Soil Slopes with Lyapunov Exponent. Chinese Journal of Rock Mechanics and Engineering. 1997, 16(3). 217-223. (in Chinese).
5. Huang, R.Q. and Xu, Q. Quantitative Analysis about Evolutive Characteristics of Geological Hazard Systems. Bulletin of National Science Foundation of China, 2000, 14(5). 265-269. (in Chinese).
6. Wang, L.G., Song, Y. and Miao, X.X. Lyapunov exponent of chaos feature in the processing of deformation failure for coal floor. Chinese Journal of Geotechnical Engineering, 2000, 24(3). 356-359.
7. Jiang, B.S., Han, L.J. and He, Y.N. Chaotic Prediction Method of Rock Mass Deformation in Depth. Chinese Journal of Rock Mechanics and Engineering, 24(16). 2934-2940. (in Chinese).
8. He, X.F., Sang, W.G. and Jia, D.Z. Deformation monitoring of steep rock slopes by means of GPS. Journal of Hydraulic Engineering, 2006, 37(5). 114-119. (in Chinese).

9. Lu, S. and Wang, H.Y. Calculation of the maximal Lyapunov exponent from multivariate data. Acta Physica Sinica, 2006, 50(2). 572-576. (in Chinese).
10. Tang, H.M., Lin, X.S. and Chen, H.K., et al. Risk zoning assessment of geological disaster in Wanzhou area, Chongqing City. The Chinese Journal of Geological Hazard and Control, 2004, 15(3). 1-5.
11. Zhang, Y., Chen, T.Q. and Chen, B. Extended Methods for Calculating Largest Lyapunov Exponent from Small Data Sets. Journal of University of Electronic Science and Technology of China, 2004, 33(3). 254-257. (in Chinese).
12. Ma, H.G., Li, X.H. and Wang, G.H., et al. Selection of Embedding Dimension and Delay Time in Phase Space Reconstruction. Journal of Xi'an Jiaotong University, 2004, 38(4). 335-338. (in Chinese).
13. Cao, L.Y., Mees, A. and Judd, K. Dynamics from multivariate time series. Physica D, 1998, 121. 75-88.
14. Yang, G.L., Huang, R.Q. and Yan, M., et al. Engineering Geological Study on a Large-Scale Topping Deformation at Xiaowan Hydropower Station. Journal of Engineering Geology, 2004, 14(2). 165-171.

RaSiM 7(2009): Controlling Seismic Hazard and Sustainable Development of Deep Mines, C.A. Tang(ed), Rinton Press, 157-164

RESEARCH ON DEVELOPING EXTENSION THEORY TO EVALUATEROCK STABILITY IN DEEP-UNDERGROUND ROCK ENGINEERING

JUN-ZHONG LIU, JIN-YU XU, XIAO-CONG LV and HAO-YANG SU

Engineering College, Air Force Engineering University

Xi'an, 710038, P.R China

In this paper, extension theory, which is developed on the basis of matter-element theory and conjunction function, is introduced to evaluate the stability of rock in deep depth. The extension theory takes into account the influences of high in-situ stress, high ground temperature and high hydraulic pressure on the mechanical characteristics of rock in deep depth. The traditional evaluation indices are modified to reflect the facts met in the deep-underground rock engineering and an extensional model is established to evaluate the stability of rock in deep-underground rock engineering. It reduces the error caused by subjective judgment and makes the results more objective by applying simple conjunction function to calculate the weight coefficient of evaluation indexes. Moreover, the extension theory is used to evaluate the rock quality in certain deep mines, which testifies that it is reasonable and feasible to introduce extension theory into rock stability evaluation in deep-underground rock engineering.

1 Introduction

With the development of economic construction and science & technology, the scale of underground engineering is expanding and the engineering is developing into deep underground gradually. Generally, the engineering with depth over 500 meters is defined as relatively deep underground rock mass engineering, with depth over 1000 meters is defined as super-deep underground rock mass engineering and that with depth over 2000 meters is defined as extremely-deep underground engineering [1]. Deep-underground rock mass engineering is in the environment of representative high geostress, high ground temperature and high hydraulic pressure. With the depth increasing, some geological disasters will happen, such as the enhancement of mine stress, the extension of surrounding rock's distortion, the rising of ground temperature, gas explosion, water bursting, and the frequency increase of impulsive ground press, etc [2]. In order to excavate the deep underground engineering rationally and scientifically, and to make the operation of deep underground engineering safely, it is necessary to evaluate the stability of surrounding rock in deep underground engineering correctly.

Extenics began with research of transformation rule and solution of non-compatible problems, which studies on the regular patterns and methods to resolve contradictory problems from qualitative and qualitative angles with formalized tools, by introducing matter element R=(N,C,V)=(matter, characteristic, value)and carry though transformation and operation [3]. The application of extension method on evaluation mainly lies in evaluation on product quality as well as rock mass classifying in engineering. Related researches can be got across a variety of newspaper. However, considering the characteristics of deep underground rock mass, there are still some shortages in aspects of high geostress, high ground temperature and high hydraulic pressure. Therefore, based on the research achievement made by predecessors, the reasonable modification to traditional extension evaluation method makes it in accord with the deep underground engineering, and serves stability evaluation of surrounding rock in deep underground rock mass engineering more availably.

2 Extension Evaluation Model

2.1 Ascertain Classical Matter-element

Classical matter-element can be expressed as follows:

$$R_{0i}=(N_i,C_i,V_i)=\begin{bmatrix} N_i & C_1 & V_{i1} \\ & C_2 & V_{i2} \\ & \vdots & \vdots \\ & C_n & V_{in} \end{bmatrix}=\begin{bmatrix} N_i & C_1 & \langle a_{i1},b_{i1}\rangle \\ & C_2 & \langle a_{i2},b_{i2}\rangle \\ & \vdots & \vdots \\ & C_n & \langle a_{in},b_{in}\rangle \end{bmatrix} \tag{1}$$

In the equation: R_{0i} means matter element, N_i means the evaluation sort, C_i means the evaluation index; V_i means the value range determined by C_i.

2.2 Ascertain Limited Matter-element

Limited matter-element can be expressed as follows:

$$R_P=(P,C_i,V_p)=\begin{bmatrix} P & C_1 & V_{p1} \\ & C_2 & V_{p2} \\ & \vdots & \vdots \\ & C_n & V_{pn} \end{bmatrix}=\begin{bmatrix} P & C_1 & \langle a_{p1},b_{p1}\rangle \\ & C_2 & \langle a_{p2},b_{p2}\rangle \\ & \vdots & \vdots \\ & C_n & \langle a_{pn},b_{pn}\rangle \end{bmatrix} \tag{2}$$

In the equation: P means the collectivity of evaluation sort, V_{pi} means the range of P.

2.3 Ascertain Matter Element

The matter element R which to be evaluated can be expressed as follows:

$$R=(p,C_i,v_i)=\begin{bmatrix} p & C_1 & v_1 \\ & C_2 & v_2 \\ & \vdots & \vdots \\ & C_n & v_n \end{bmatrix} \tag{3}$$

In the equation: v_i means the value of p, i.e., all the statistics of things to be evaluated.

2.4 Ascertain Dependence Degree of Each Evaluation Index on Each Grade

The dependence degree of each single evaluation index:

$$K_j(v_i)=\begin{cases}\dfrac{-\rho(v_i,V_{ij})}{\left|V_{ij}\right|},(v_i\in V_{ij})\\ 0.5,(v_i=a_{ij}\text{或}b_{ij})\\ \dfrac{\rho(v_i,V_{ij})}{\rho(v_i,V_{pi})-\rho(v_i,V_{ij})},(v_i\notin V_{ij})\end{cases} \tag{4}$$

In the equation: $\rho(v_i,V_{ij})=\left|v_i-\frac{a_{ij}+b_{ij}}{2}\right|-\frac{b_{ij}-a_{ij}}{2}$, $\left|V_{ij}\right|=\left|b_{ij}-a_{ij}\right|$, $\rho(v_i,V_{pi})=\left|v_i-\frac{a_{pi}+b_{pi}}{2}\right|-\frac{b_{pi}-a_{pi}}{2}$, i means parameter, and j means grade. (i=1, 2…n; j=1, 2…m)

2.5 Ascertain Dependence Degree on Grade j

The dependence degree of the matter element on grade j:

$$K_j(p)=\sum_{i=1}^{n}\omega_i K_j(v_i) \tag{5}$$

In the equation: ω_i means the weight coefficient of each evaluation index. $\sum_{i=1}^{n}\omega_i=1$.

2.6 Ascertain Evaluation Grade

If $K_{j^0}(p)=\max K_j(p)>0$, then p belongs to grade j^0 ,

If $K_{j^0}(p)=\max K_j(p)\le 0$, then p is not in the compartmentalized grade range and new swatch turns up,

Command:
$$\bar{K}_j(p)=\frac{K_j(p)-\min K_j(p)}{\max K_j(p)-\min K_j(p)} \tag{6}$$

$$j^*=\frac{\sum_{j=1}^{m}j\bar{K}_j(p)}{\sum_{j=1}^{m}\bar{K}_j(p)} \tag{7}$$

Then j^* is the grade variable eigenvalue of p.

3 Ascertain Weight Coefficient

In order to reduce the influence caused by subjective factors on evaluation result, the weight coefficient is ascertained through the simple conjunction function. The simple conjunction function is as follows [4]:

$$r_{ij}(v_i,V_{ij})=\begin{cases}\dfrac{2(v_i-a_{ij})}{b_{ij}-a_{ij}},v_i\le\dfrac{a_{ij}+b_{ij}}{2};\\ \dfrac{2(b_{ij}-v_i)}{b_{ij}-a_{ij}},v_i\ge\dfrac{a_{ij}+b_{ij}}{2};\end{cases}\qquad (i=1,2,\cdots,n;j=1,2,\cdots,m) \tag{8}$$

And $v_i\in V_{pi}$ $(i=1,2,\cdots,n)$, then:

$$r_{it^*}(v_i, V_{ij}) = \max_j \{r_{ij}(v_i, V_{ij})\} \tag{9}$$

If the larger sorts that the index C_i falls into, the larger weight coefficient is endowed, then:

$$r_i = \begin{cases} t^* \times (1 + r_{it^*}(v_i, V_{ij})), & r_{it^*}(v_i, V_{ij}) \geq -0.5 \\ 0.5t^*, & r_{it^*}(v_i, V_{ij}) < -0.5 \end{cases} \tag{10}$$

If the larger sorts that the index C_i falls into, the smaller weight coefficient is endowed, then:

$$r_i = \begin{cases} (m - t^* + 1) \times (1 + r_{it^*}(v_i, V_{ij})), & r_{it^*}(v_i, V_{ij}) \geq -0.5 \\ 0.5(m - t^* + 1), & r_{it^*}(v_i, V_{ij}) < -0.5 \end{cases} \tag{11}$$

The weight coefficient of C_i is:

$$\omega_i = r_i \Big/ \sum_{i=1}^{n} r_i \tag{12}$$

4 Modify Extension Evaluation Method

4.1 Geostress Modification of Evaluation Method

One of the most remarkable characteristic of deep rock mass is high geostress, which is the most primary reason for damage and instability of the wall rock in deep rock mass engineering. High geostress brings significant changes to the mechanical character of deep rock mass. Therefore, geostress must be taken into consideration when evaluating the stability of surrounding rock in deep rock mass engineering, and it is essential to be modified. Rock mass damnification criticality parameter Q is defined according to geostress and petrous strength character [5]. Line AB in Figure1 is Mohr-Coulomb Strength Criterion Line. When the rock mass to be evaluated is ascertained, its mechanical character is determinated, so the position of line AB is fixed and stress state of rock mass is also fixed as circular O_1 shows. The closer the circular O_1 is to line AB, the shorter d is, the more possible the rock mass is to damage. Define $Q = R / \overline{O_1 B}$ to make the approach degree quantitative It is obvious that $Q \in (0, 1)$. The closer the value of Q is to 1, the more serious the rock mass is damnified and the more possible damage is to emerge.

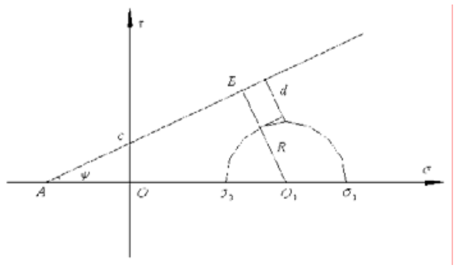

Figure 1 Mohr circular for the definition of rock mass damage risk degree factor Q

From the geometry of figure 1, we can get:

$$\left.\begin{aligned}&R=(\sigma_1-\sigma_2)/2\\&\overline{O_1B}=\overline{AO_1}\sin\varphi\\&\overline{AO_1}=\overline{AO}+\overline{OO_1}=c/\tan\varphi+(\sigma_1+\sigma_2)/2\end{aligned}\right\}\Rightarrow Q=\frac{R}{\overline{O_1B}}=\frac{\sigma_1-\sigma_3}{(\sigma_1+\sigma_3)\sin\varphi+2c\cos\varphi} \tag{13}$$

In the formula: R is radius of Mohr circular, σ_1 and σ_3 are the largest main stress and smallest main stress in rock mass geostress field respectively, c is cohesion and φ is angle of internal friction.

From the analysis above and considering the damnification and danger that geostress causes to rock mass, geostress modification coefficient is introduced to reflect the influence on wall rock sort caused by geostress. The modificatory method is as follows:

$$j^{*\prime}=j^{*}+6k \tag{14}$$

In the formula: $j^{*\prime}$ is grade variable eigenvalue after modifying; j^{*} is grade variable eigenvalue; k is geostress modification coefficient. The relationship between Q and k is as Table 1 shows.

Table 1 Stress reduction factor k

Q	0~0.2	0.2~0.4	0.4~0.6	0.6~0.8	0.8~1
k	0	0.05	0.1	0.15	0.30

4.2 Groundwater and Terrestrial Heat Deterioration Modification of Rock Block [5]

Deep rock mass engineering usually is located in the deep place under original groundwater water table. For the influence of high geostress, the groundwater pressure is often at a high level. Dissoluble rock water pressure is as high as 7*MPa* or even higher in the place with its depth more than 1000*m* [1]. In this situation the effect on rock mass caused by groundwater obviously strengthens, the main embodiment is the deterioration effect on rock mass structure surface and mechanical character of structure. As a result, the rock block strength in actual engineering is usually lower than that ascertained in conventional indoor experiment, and the integral rock strength index must be modified through groundwater deterioration. Rock strength water deterioration coefficient K_W is defined as follows:

$$K_W=\sigma_{UCS_W}/\sigma_{UCS} \tag{15}$$

In the formula: σ_{UCS} is single axis compression strength of rock; σ_{UCS_W} is single axis compression strength of rock deteriorated by water.

The experiment indicates that K_W is the function of rock hydrous quotiety because with rock hydrous quotiety changing the rock strength continuously changes [6]. The rock strength water deterioration coefficient must be ascertained according to actual engineering.

Another remarkable characteristic of deep rock engineering is high ground temperature. According to measuring, the deeper the rock is, the higher the ground temperature is [7]. The ground temperature grad varies from 30℃/*km* to 50℃/*km*. In some singular area the temperature can reach as high as 200℃/*km*. As a result, the temperature of deep rock is usually above 40~50℃. Generally, the change of one centigrade degree could bring stress change of 0.4~0.5*MPa*. In this situation, the rock mass is liable to damage because of heat expanding and cold shrinking, which deteriorates the quality of wall rock in engineering. Therefore, the rock block strength must be modified through heat deterioration. Rock heat deterioration coefficient K_T is defined as follows:

$$K_T = \sigma_{UCS_T} / \sigma_{UCS} \tag{16}$$

In the formula: σ_{UCS} is single axis compression strength of rock, σ_{UCS_T} is single axis compression strength of rock deteriorated by heat and K_T is the function of rock temperature.

K_W, K_T could be ascertained through indoor experiment or analogical coefficient method.

5 Application Examples

5.1 Ascertain Evaluation Index

In rock quality evaluation, different classifying methods choose different evaluation indexes. RMR Method (*Rock Mass Rating*) is a rapidly developing, widely used and relatively integrated classifying method in rock mass engineering. Therefore evaluation index is ascertained on the basis of RMR method, single axis compression strength of rock (σ_{UCS}), rock quality designation index (I_{RQD}), the joint spacing, filtering groundwater (W) and joint status are chose as indexes to be evaluated and all the indexes are classified into 5 grades. The classifying standard of each index lies in Table 2.

Table 2 Standard for index classification of surrounding rock stability

Grades	σ_{UCS} /*MPa*	I_{RQD} /%	Joint Spacing /*m*	W / ($L\cdot min^{-1}/10m$)	Joint Status
Ⅰ	250~300	90~100	2~3	0~5	9~10
Ⅱ	100~250	75~90	0.6~2	5~10	7~9
Ⅲ	50~100	50~75	0.2~0.6	10~25	4~7
Ⅳ	25~50	25~50	0.06~0.2	25~125	2~4
Ⅴ	0~25	0~25	0~0.06	125~250	0~2

5.2 Construct Matter Element

Classical matter-element and limited matter-element of rock mass stability evaluation are formed as follows:

$$R=(N,C,V)=\begin{bmatrix} N/C & N_1 & N_2 & N_3 & N_4 & N_5 \\ C_1 & \langle 250,300\rangle & \langle 100,250\rangle & \langle 50,100\rangle & \langle 25,50\rangle & \langle 0,25\rangle \\ C_2 & \langle 90,100\rangle & \langle 75,90\rangle & \langle 50,75\rangle & \langle 25,50\rangle & \langle 0,25\rangle \\ C_3 & \langle 2,3\rangle & \langle 0.6,2\rangle & \langle 0.2,0.6\rangle & \langle 0.06,0.2\rangle & \langle 0,0.06\rangle \\ C_4 & \langle 0,5\rangle & \langle 5,10\rangle & \langle 10,25\rangle & \langle 25,125\rangle & \langle 125,250\rangle \\ C_5 & \langle 9,10\rangle & \langle 7,9\rangle & \langle 4,7\rangle & \langle 2,4\rangle & \langle 0,2\rangle \end{bmatrix} \qquad R_P=(P,C,V_P)=\begin{bmatrix} P & C_1 & <0,300> \\ & C_2 & <0,100> \\ & C_3 & <0,3> \\ & C_4 & <0,250> \\ & C_5 & <0,10> \end{bmatrix}$$

In the formula: P is the collectivity of surrounding rock stability evaluation grades; C_1 is the single axis compressive strength of rock, C_2 is rock quality designation index, C_3 is the joint spacing, C_4 is filtering groundwater, C_5 is joint status and V_{pi} is the value bound of C_i.

5.3 Extensional Evaluation of Rock Stability

A gold mine engineering that was mentioned in reference is located in -330m ~ -380m [8]. Ground stress field is deadweight stress field, the unit weight on average is 26.5kN/m^3, Poisson Ratio is 0.28, groundwater and ground heat deterioration coefficient of rock based on indoor experiment are 0.76 and 0.97. Measurement results of evaluation index of three groups of rock mass lie in Table 4:

Table 3 Measurement results of indexes

SN	Rock Groups	σ_{UCS} /MPa	DM σ_{UCS}/MPa	I_{RQD} /%	Joint Spacing	W /($L\cdot min^{-1}$/10m)	Vein Status
1	Biotite Granites	65.10	47.99	78	0.4	20	5
2	Sericitolite Deposit Granites	54.62	40.27	40	0.77	11	4
3	Sericitolite Deposit Granite Cataclastic Rock	46.59	34.35	34	0.55	112.5	2

According to Table 3, the matrix of matter element on surrounding rock stability classifying is as follows:

$$R = \begin{bmatrix} P & C_1 & C_2 & C_3 & C_4 & C_5 \\ P_1 & 47.99 & 78 & 0.4 & 20 & 5 \\ P_2 & 40.27 & 40 & 0.77 & 11 & 4 \\ P_3 & 34.35 & 34 & 0.55 & 112.5 & 2 \end{bmatrix}$$

In the formula: P_i represents stability evaluation index of each rock group.

From conservative angle of view, in case that the larger sorts that the index i fall into, the more disadvantageous that the influence on the surrounding rock stability evaluation is, endow i with larger weight coefficient. The weight coefficient matrix of indexes is ascertained through equations (8-12).

$$W = \begin{bmatrix} 0.198 & 0.119 & 0.256 & 0.213 & 0.214 \\ 0.307 & 0.310 & 0.107 & 0.147 & 0.129 \\ 0.263 & 0.258 & 0.141 & 0.188 & 0.150 \end{bmatrix}$$

The evaluation results of surrounding rock stability could be ascertained with calculating formulas of relevant degree and assessing grade. The damnification and damage criticality index values of three rock masses are 0.439, 0.439 and 0.57, which are obtained through equation (13) and calculating rock mass stress field according to deadweight field calculating method. The evaluation results of three rock masses lie in Table 4.

Table 4 Evaluation results of surrounding rock stability

SN	$K_1(p)$	$K_2(p)$	$K_3(p)$	$K_4(p)$	$K_5(p)$	max	j^0	j^*	$j^{*\prime}$	Reference[4]
1	-0.5932	-0.2967	0.2481	-0.2143	-0.5250	0.2481	3	3.14	3.74	4
2	-0.6191	-0.3826	-0.1313	0.1156	-0.3973	0.1156	4	3.56	4.16	4
3	-0.6982	-0.5222	-0.3045	0.1599	-0.1955	0.1599	4	3.87	4.47	4

Evaluation results show that the result obtained through extension evaluation method coincides with the result of reference [5], which is obtained through wall rock quality evaluation method in deep rock mass engineering based on modified RMR method and the actual instance after the present rock mass being was dug. The method in this paper works out the grade variable eigenvalue of each rock mass and reflects the degree by which the eigenvalue leans to near the sort. For example, the stability grade of rock mass 2 is 4 and its variable eigenvalue is 4.16, that is to say, the actual stability grade is 4.16. The result conforms to actual instance better.

6 Conclusions

Extension evaluation method inextenso reflects the synthesized quality level of pattern through establishing multi-index assessing model and expresses the result with quantitative numerical value. It can be indicated from the evaluation results of the instance that it is feasible to evaluate surrounding rock stability in deep underground rock mass engineering which is a multi-index system. It is just an attempt to introduce extension evaluation method into evaluating surrounding rock stability in deep underground rock mass engineering. There are still some problems to be explored in both theory field and application field, such as the distributing of weight coefficient, the problem of ascertaining ground stress reduction factor and groundwater and ground heat deterioration coefficient, choosing of assessing index and classifying standard of grades, to make the result more consistent with the actual instance.

References

1. He M C, Lu X J, Jing H H. Characters of Surrounding Rock Mass in Deep Engineering and Its Non-linear Dynamic-Mechanical Design Concept [J].Chinese Journal of Rock Mechanics and Engineering, 2002, 21(8): 1215-1224.
2. Cai M F. Rock Mechanics and Engineering [M].Beijing: Press of Science, 2002.
3. Cai, W., Yang, C. Y. and Lin, W. C. Extension Engineering Method. Beijing: Press of Science, 2000.
4. Hu, B. Q. Application of extension assessment method to stability classification of surrounding rocks. Journal of Hydraulic Engineering, 2000 (2). 66-70.
5. Chen, Y. J., Wu, C. and Fu, Y. M. Study on Evaluation of the Surrounding Rock Quality in Deep Rock mass Engineering Based on the Revised RMR Method. Journal of Disaster Prevention and Mitigation Engineering, 2007, 27(2). 141-146.
6. Kang, H. P. Rock damage from water Effect. Hydrogeology Engineering, 1994 (3). 39-41.
7. Lin, M. C. Rock Thermal Physics and Its Application in Engineering. Chongqing: Chongqing University Press, 1991.
8. Chen, Y. J., Pan, C. L. and HU, M. B. Research on the problem of controlling the main roof of the underground mine workplace without the ore pillar in Xiangxi Gold Mine. West-China Exploration Engineering, 2001, (5). 1-3.

RaSiM 7(2009): Controlling Seismic Hazard and Sustainable Development of Deep Mines, C.A. Tang(ed), Rinton Press, 165-170

STUDY OF SPATIAL DISTRIBUTION AND FRACTAL DIMENSION OF AE EVENTS DURING ROCK FRACTURE

JIAN-PO LIU, YUAN-HUI LI and YU-JIANG YANG

School of Resources & Civil Engineering, Northeastern University

Shenyang, 110004, P.R. China

Rock is one kind of typical inhomogeneous brittle material with various deficiencies such as micro-cracks and voids. It will generate a large number of acoustic emission (AE) signals during damage process, when the rock is subjected to external loading. In this investigation,AE location technique is applied to study the three dimensional (3D) evolutionary process of micro-cracks initiation, propagation and coalescence during rock failure process. Meanwhile, the fractal characteristic of AE events is provided. The experimental results show that spatial distribution of AE located events enable to directly reflect the micro-crack initiation, propagation direction and spatial evolutionary. It is consistent between AE locate result and rock damage result eventually. In addition, although the fractal dimensions for different rock samples are not kept the same during rock fracture, they all drop to the minimum value before rock failure. This pnenomenon is an important referred indicator for the tremendous rock failure, which is helpful to the study of rock failure mechanism and in-situ rock mass monitoring.

1 Introduction

Acoustic emissions (AE) are transient elastic waves generated by the rapid release of energy from localized sources within materials such as metal, rock and concrete, when they undergo changes in the mechanical, thermal and hydraulic environment [1]. AE technique is a helpful tool to study the unstable failure process because it can monitor micro-crack initiation and propagation in brittle material continuously and in real-time. It is much better than the other methods, and it can be applied to study failure mechanics of brittle material. Rock failure is correlated with interior construction and previous micro-cracks, so the study of rock failure mechanics in microscopic view of micro-crack initiation, propagation, and coalescence processes are important. The spatial distribution of AE events form a point set, and every point is corresponding with a micro-crack face or micro-crack volume in rock. The spatial evolutional process of this point set has fractal characteristics. Through the calculation on fractal dimension, the fractal characteristics of micro-cracks spatial distribution can be obtained, and it is meaningful to study rock failure mechanism.

Many researchers have applied the AE technique to study the rock unstable fracture process, and they have obtained many valuable results. Through the AE location studies, Mogi pointed out that the pre-main rupturing micro-cracks tended to cluster along the main fracture plane [2]. Despite the comparatively poor locating accuracy of their experiments, the guideline used in their study attracted tremendous attention in the seismological circles. Byerlee and Lockner introduced the multi-channel tape recorder and computer into their locating studies, and they identified that the clustering of AE events coincided with the onset of creep [3]. With the view to keep away from the noise in seismic phase recognition controlled by the threshold value, Sondergeld adopted the operator-computer dialogue technique in his seismic phase recognition. He greatly enhanced the locating accuracy, and he displayed his data in a series of stereographic projections [4, 5]. Subsequently, Japanese seismologists undertook a number of studies in the same field and yielded results dealing with the formation of micro-crack gaps and the migration and concentration of microrupturings, etc [6].

However, few studies could depict the behaviour of spatial distribution of AE events in detail because of locating accuracy of their equipments, and none of them pointed out the critical value of AE distribution of rock failure which is very significant to the application of AE technique in mining and other geoengineerings.

The purpose of this paper is to study on the three-dimensional evolutionary process of micro-crack initiation, propagation and coalescence during rock failure process under uniaxial loading based on AE locating technique. Analysis on fractal characteristics has been carried out aiming at finding the critical value of rock unstable failure and providing foundation for rock mass monitoring in-situ.

2 Sample Material and Experimental Technique

2.1 Test specimens

Rock samples (70mm×70mm×150mm) for experiment were common brittle rock of granite, marble and gneiss and were prepared according to the international rock mechanics test criteria. The depth of parallelism, smoothness and verticality were agreed with the test standard.

2.2 Test equipment

The servo-controlled hydraulic testing machine with a maximum capacity of 3000KN was used in the experiment. It can record the value of load, stress, displacement and strain, and draw the curve of load-displacement and stress-strain instantaneously. A multi-channel, high-speed AE signal acquiring and analyzing system called HUS (Hyperion Ultrasonic System) was employed to acquire the AE signal. It can record the AE signals and waves in real-time. It also can record the temporal and spatial distribution of AE event in the specimen during loading and visually display them by the post processor in 3-D model. The threshed was set at 100dB to gain a high signal/noise ratio. The sampling frequency was set at 100mv. Figure 1 shows the system of the experimental instruments.

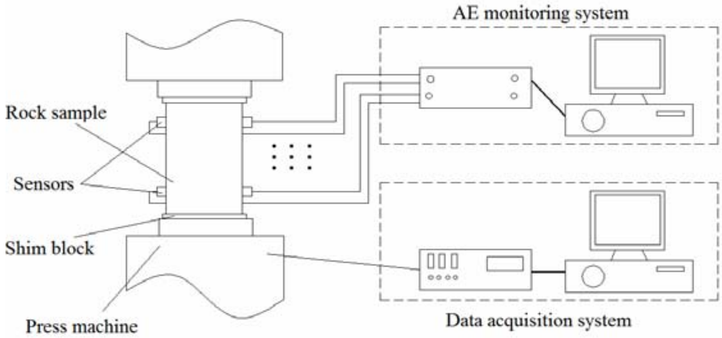

Figure 1 Arrangement of experimental instruments

2.3 Sensors arrangement

Eight Nano30 sensors with frequency sensitivities between 125Hz to 750 KHz and a 40 dB pre-amplification (1220A－AST) were used in the experiment. The sensors were fixed on rock face by gum band and was used vaseline for coupling. Plastic cushions were matted between pressing machine and specimen to eliminate noise generated by friction. Figure 2 shows the arrangement of AE sensors

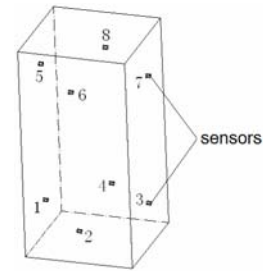

Figure 2 Arrangement of AE sensors

3 Experimental results and analysis

3.1 AE location results

There are two location algorithms of Simplex algorithm and Geiger algorithm in Hyperion Ultrasonic System. AE events location of the two algorithms is based on time difference of first arrival times of p-wave detected by the AE sensors. In this paper, Geiger algorithm [7] was used for AE events location. AE events position and occurred time will be calculated through Geiger algorithm according to the difference of sensors' coordinates and p-wave arrival times. The location error is also reflected by the color scale of AE events (Figure.3)

Figure 3 Error sketch of AE event

Figure 4(A) is the locate results of granite-1. During early load phase (0-42% of peak strength), micro-cracks in rock swarmed gradually and the AE events occurred much less. With the load increasing (42%-50.3% of peak strength), AE events began to cluster from the upper side to the middle of the rock specimen. When the load exceeded 50.3% of peak strength, AE events began to extend and formed a cluster band in vertical direction until rock unstable failure occurred finally. The AE locate result and rock damage (splitting damage) were consistent finally which suggested that spatial distribution of AE locate events can reflect micro-crack initiation, propagation direction and spatial evolutionary process directly. Figure 4(B) is the locate results of marbel-1. The homogeneous of marble is better than granite, so the AE events distribution is much scatter and without cluster phenomenon. The marble sample was broke completely at last which is in coincidence with the AE events location. Figure 4(C) is the locate results of gneiss-1. The AE location result of gneiss is similar with granite but the extend direction is from the lower side to the upper side. It is also consistent between AE locate result and gneiss damage result(splitting damage).

The experimental results show that spatial distribution of AE located events can directly reflect micro-cracks initiation, propagation direction and spatial evolutionary process. It is meaningful to the study on micro-cracks propagation and spatial state thoroughly and provides potential a method for forecasting rock unstable failure.

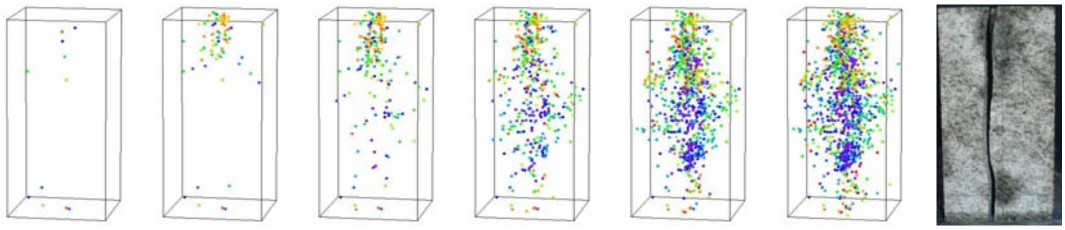

(a)0-42% (b)42%-50.3% (c)50.3%-53.7% (d)53.7%-59% (e)59%-72.9% (f)72.9%-100% (h)failure

(A) granite-1

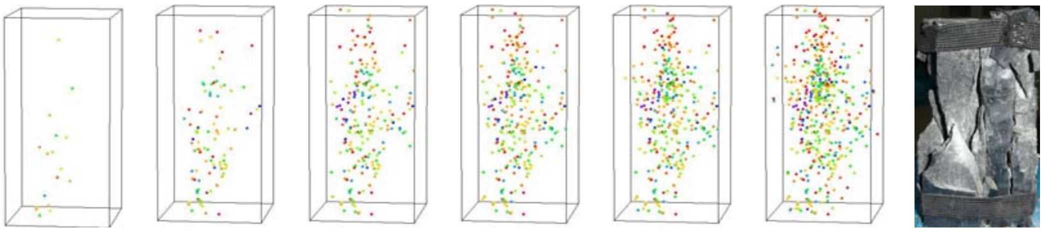

(a)0-25% (b)25%-35% (c)35%-38.8% (d)38.8%-42% (e)42%-48.6% (f)48.6%-100% (h)failure

(B) marble-1

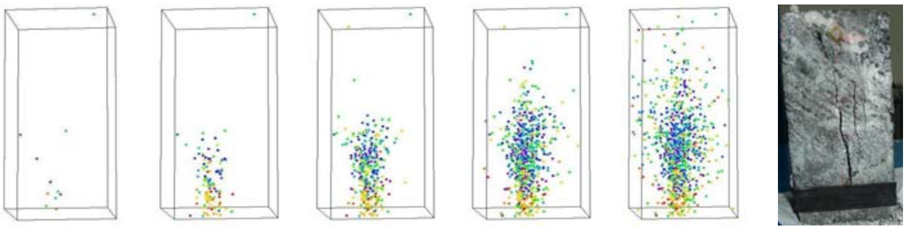

(a)0-44% (b)44%-58% (c)58%-68.3% (d)68.3%-77.4% (e)77.4-100% (h)failure

(C) gneiss-1

Figure 4 AE location results and crack propagation process for different rock samples

3.2 Fractal characteristic

In this paper, box dimension was applied to calculate the fractal characteristic of the spatial distribution of AE events. Box dimension is the most used dimension due to its convenience of mathematical computation and empirical estimation [8].

AE events fractal dimension is the measurement of micro-crack randomness reflecting the statistical regularity of micro-cracks in rock. Fractal dimension *D* of granite samples (Fig.5a, b) fluctuates in higher level during initial loading phase meaning that the micro-crack distribution is scatter. When the load reached 80% of peak strength the fractal dimension *D* fell down quickly. It indicated that the proportion of bigger AE events increased and the micro-cracks spatial distribution turned random to order. When the load reached peak strength, macroscopic cracks are formed, order degree of cracks reached the biggest and the fractal dimension *D* fell down to minimum value. The fluctuating time of fractal dimension *D* of marble (Fig.5c, d) is shorter than granite samples. It is mainly because the marble with high brittleness and will generate macroscopic cracks when under lower stress level and cause the fractal dimension D to fall down. The regularity of fractal dimension D of marble (Fig.5e, f) was different with granite and marble. Fractal dimension *D* rose before falling down which indicated that the proportion of micro-cracks was increasing. Before rock unstable failure, the generated macroscopic crack caused the fractal dimension *D* to fall down.

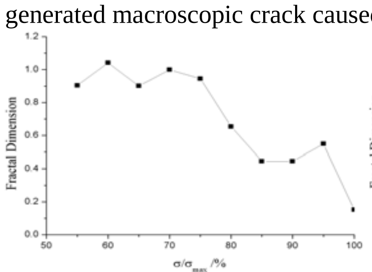

(a) granite-1

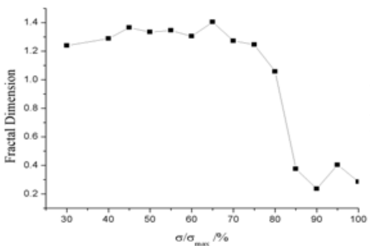

(b) granite-2

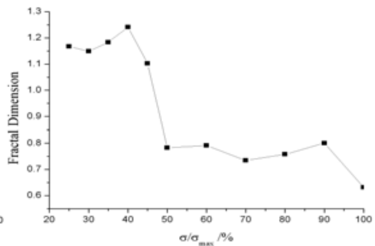

(c) marble-1

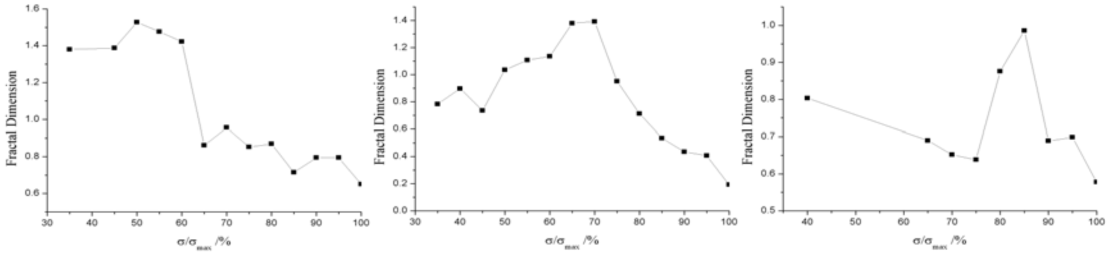

(d) marble-2 (e) marble-1 (f) marble-2

Figure 5 Relation curves of fractal dimension with stress levels for different rock samples

Fractal dimension *D* falls down when the stress reaches a special level during rock fracturing and arrive at the minimum value before rock unstable failure which reflects the fractal regularity of rock fracture. It illuminates that the rock failure process is a dimensionality reduction process. So, the fractal dimension D can be seen as a precursor of rock failure to monitor the rock mass stability.

4 Conclusion and Discussion

Rock failure comes from the processes of micro-cracks initiation, propagation and coalescence. The experimental results show that the spatial distributions of AE locate events can reflect micro-cracks initiation, propagation direction and spatial evolutionary process. The AE locating results and rock damage results are consistent with one another. This is significant for further study of micro-crack evolutionary process and spatial characteristics. Due to the difference of construction and material characteristics of different rocks, AE events can only reflect micro-crack stable propagation, but they can not reflect unstable propagation process. This still requires more research.

AE event fractal dimension is the measurement of micro-crack randomness which shows the statistical regularity of micro-cracks in rock. Although the fractal dimension *D* regularity is different with different rocks, but before rock failure the fractal dimension *D* will all fall down quickly. When there are rock failures, the fractal dimension *D* reaches the minimum value. This phenomenon can be seen as a precursor of rock failure and can be applied to forecast rock mass stability. During rock mass monitoring the critical value of fractal dimension *D* will not be stabled and will influence the monitoring precision accordingly. Combined analysis of Fractal dimension *D* and other parameters (such as *b* value) can be applied in-situ application to improve monitoring precision.

Acknowledgements

This work was financially supported by the State 863 projects of China (*NO.Z110607*) and the Program for New Century Excellent Talents of China (*NO. NCET-07-0163*). The authors also would like to thank Mr. X.D. Zhao, J. Tian and for their help in the tests, and Prof. Y. J. Wang for correcting the language.

References

1. Katsuyama, T. Application of Acoustic Emission Technique. Translated by Feng Xiating. Beijing: China Metallurgical Industry Press, 1996. (in Chinese)
2. Blanpied, M.L., Lockner, D.A. and Byerlee, J.D. Fault stability inferred from granite gliding experiments at hydrothermal comdition. Geophys. Res. Lett., 1991, 18. 609-612.
3. Byerlee, J.D. Acoustic emission in rock during fluid injection. Proceeding of the Third Congress of the international Society for Rock Mechanics, 1974, 633-637.

4. Sondergeld, C.H. and Estey, L.H. Acoustic emission study of microfracturing duing the cyclic loading of westerly granite. J. Geophys. Res, 1981, 1915-1924.
5. Sondergeld, C.H. and Estey, L.H. Source mechanisms and microfracturing during axial cycling of rock. Pure Appl. Geohyys, 1982, 151-166.
6. Kinichiro, K., Osamu, N., et al. Seismic gaps observed in uniaxial rock experiments. Earthquake, 1982, 91-102.
7. Geiger, L. Probability method for the determination of earthquake epicentres from the arrival time only. Bull. St. Louis Unic., 1912, 60-71.
8. Xie, H.P. Introduction to Fractal Rock Mechanics. Beijing: Science Press, 1996. (in Chinese)

RaSiM 7(2009): Controlling Seismic Hazard and Sustainable Development of Deep Mines, C.A. Tang(ed), Rinton Press, 171-176

EXPERIMENTAL STUDY ON SURFACE CRACK GROWTH IN ROCK –LIKE MATERIALS IN UNIAXIAL TENSION

MING-TIAN LI[1,2], SHUCAI LI[2], LEI YANG[2] and NING ZHANG[2]

1. Civil Engineering Department Shandong Jiaotong University

250023, Jinan China

2. Geo-technical and Structural Engineering Research Center, Shandong University

250061, Jinan China

Direct tension experiments with adhesive have been carried out for rock-like materials. Surface crack is pre-fabricated by placing polyester thin plate in the specimen. The specimen is then subjected to direct tension experiment to study the surface crack growth. Throughout this study, it is found that direct tension experiment with adhesive can be adapted to most rock-like materials and the pre-fabricated surface crack influences significantly the fracture mode of the rock-like materials. The pre-fabricated surface crack growth initiates from the front face, where the surface crack is located. In the front face, the surface crack exhibits obviously the propagation mode of two-dimension through crack. However, owing to the influence of the pre-existing surface crack, the crack propagation then deflects through the specimen and finally the fracture on the back face is not perpendicular to the loading direction but at acute angle with the loading direction. It is concluded that the acute angle is related to the dip angle and the depth of the pre-existing surface crack.

1 Introduction

In recent years, with the fast development of mining engineering and underground structural engineering crack propagation mechanisms and the techniques to halt crack growth have been paid much more attention by academic researchers and technicians than before. Owing to the natural or artificial reasons, in rock mass there always exist many flaws with various depth and dip angles that can be simplified as three dimensional surface cracks or internal cracks in fracture mechanics. A great number of engineering activities and experiments have proved that these cracks heavily influence the mechanical behaviour of rock mass, and unstable propagation of the cracks usually causes engineering disasters such as collapse of underground caverns, rock-burst in mining engineering and so on. Many researchers have carried out the study on three-dimensional crack growth. For instance Dyskin and co-authors [1-3] studied the propagation of three-dimensional internal cracks with rock-like materials such as transparent casting resin, cement, mortar and PMMA in uniaxial and biaxial compression, and demonstrated that three-dimensional crack growth in compression was qualitatively different from the two-dimensional case. Unlike two-dimensional cracking there are intrinsic limits on three-dimensional growth of wing cracks produced by a single pre-existing internal crack. In reality pre-existing cracks are three dimensional, so it will result in errors to apply the experiment results on two-dimensional crack growth to the engineering activities. Literatures [4, 5] investigated three-dimensional surface flaw growth for plate specimens of several kinds of materials including glass, plexiglass and marble in uniaxial compression and studied the influences of interaction of two crack surface of the closed crack on crack growth. They found that cracks may initiate from several points around the flaw tip. Literatures [6-8] investigated the three-dimensional crack propagation modes in transparent PMMA, marble and Gabbro specimens. In the experiments they observed a new propagation mode where an anti-wing crack was induced at a distance away from the flaw tip in the region of compression stress zone. Literature [9] conducted a series of uniaxial compression tests on frozen PMMA with several pre-existing three-dimensional cracks to investigate the mechanisms of crack propagation and coalescence. They found the propagation and coalescence of three-dimensional surface cracks are dependent on the crack depth and the crack configuration. Literature [10] carried out CT real-time scanning tests on rock-like materials-special ceramics specimens to investigate the three-dimensional internal crack growth. From CT image analysis, the damage evolution of the crack was attained. Although rock mass is always in multi-axial compression, local tension conditions may be caused because of excavation and so on. For instance during the excavation of large underground caverns their side walls, which are the most dangerous and worth to support, are always in tensile stress state. And enormous practices and experimental results have demonstrated that crack growth in tension is more unstable and dangerous than that in compression. Therefore the crack growth in tension heavily influences the stability of rock engineering. But little study on surface crack growth in rock-like materials in direct tension is carried out. So in this paper the surface crack growth in cement mortar in direct tension is studied.

2 Experimental Setup and Reparation

This experiment is conducted on the full-digital servo-controlled rock stiff tri-axial testing machine developed by Geo-technical and Structural Engineering Research Center of Shandong University by itself. This machine can adopt two controlling modes such as load and displacement, collect instrumental data automatically and meanwhile stress-strain relationships can be observed. So deformability properties and strength of the specimens can be calculated from the collected instrumental data.

Cement mortar is selected as specimen materials for this experiment because of its convenience, brittleness and easiness to form surface crack or internal crack in specimens. This special cement mortar is a mixture of cement, fine aggregate, special additives and water. In order to make sure the similarity between special cement mortar and sandstone a great number of mixing ratio tests are required to determine the best mixing ratio. The mechanical properties of the special cement mortar specimens with the best mixing ratio are in good agreement with those of the real sandstone as shown in table 1. From table 1 the special cement mortar can meet the requirements of this experiment.

Table 1 Physical and mechanical parameters of special cement mortar materials and sandstone

parameters	Compressive strength σ_c/MPa	Tensile strengh σ_t/MPa	Elastic modulus E/Gpa	Poission ratio ν	Toughness K_{IC}/MPa·m$^{0.5}$	Unit weight ρ /g·cm^{-3}
Special cement mortar	35.54	2.82	17.92	0.192	0.512	2.3
Sandstone	20～170	4～25	4.9～78.5	0.02～0.2	0.22～2.26	2.1

The test specimens are cuboids with even middle section and two widened ends and 100mm long (W_0), 200mm high (H_0) and 50mm wide (T_0) as shown in figure 1. The widened end is 50mm high (H_1=H_2) as shown in figure 1. And the even middle side is 50mm long (W), 100mm high (H) and 50mm wide (T) as shown in figure 1. In order to reduce stress concentration the even middle side is connected with two widened sides by smooth arc. Special mould is developed to make the test specimens during the experiments.

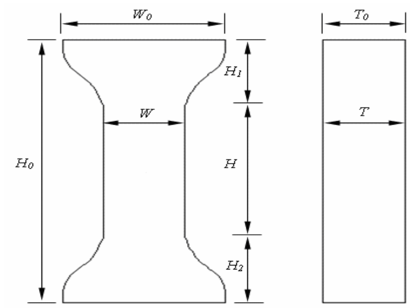

Figure 1 Schematic diagram of specimen shape and size

Initial pre-existing surface crack can be formed by placing polyester thin plate in the specimens while making them and its shape, size and dip angle can be set up according to the requirements. The selected polyester thin plate is 0.25mm thick with smooth surface. During the direct tension tests the crack remains always open, so interaction between surfaces of the crack may not be considered. The specimen shape and the size and position of pre-existing surface crack are shown in figure 2.

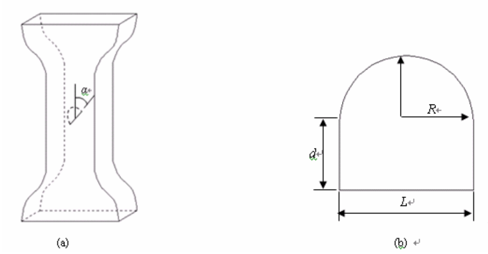

Figure 2 Specimen shape and the size and position of pre-existing crack (a) Specimen shape and crack position (b) the shape and size of pre-existing crack

Because the direct tension test is conducted with adhesive, specimen should be bound with the platens of the testing machine by adhesive with high strength as shown in figure 3. From the tests of tens of adhesives the architectural structure adhesive with tensile strength 19.9MPa and shearing strength more than 33MPa is selected finally. In order to make sure being stretched in the axial direction of the specimen the ends of the specimens should be ground finely. During binding specimens and platens a special axial orientation setup, which may realize the proper orientation and is patented, is developed.

Figure 3 Schematic diagram of experimental setup

3 Experimental Results and Discussion

In order to study surface crack growth and the influence of dip angle and the depth of the pre-existing surface crack on crack growth in rock-like materials a series of direct tension tests are conducted on the cement mortar specimens with various dip angle and depth of pre-existing surface crack. The typical crack growth modes are shown in figure 4-7. In order to compare the crack growth of the surface crack with that of the through crack, direct tension test of the specimen with through crack is performed and its crack growth is shown in figure 8.

Figure 4 Crack growth of the surface crack with the depth and dip angle of 1/4T and 30 degree respectively

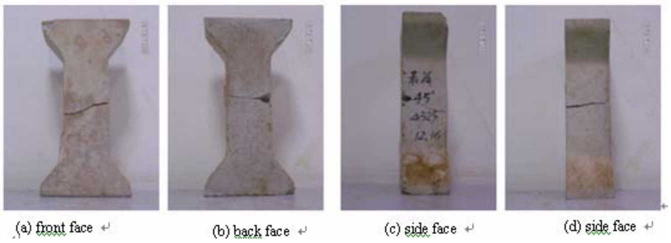

Figure 5 Crack growth of the surface crack with the depth and dip angle of 1/4T and 45 degree respectively

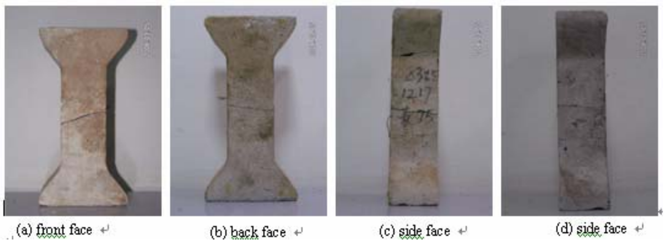

Figure 6 Crack growth of the surface crack with the depth and dip angle of 1/4T and 75 degree respectively

Figure 7 Crack growth of the surface crack with the depth and dip angle of 1/2T and 45 degree respectively

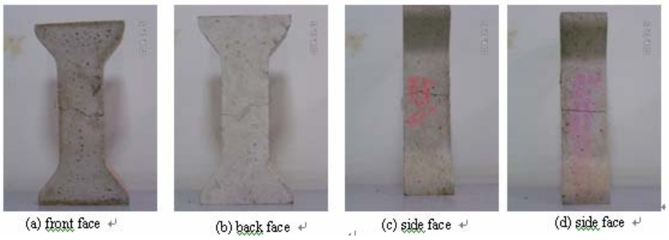

Figure 8 Crack growth of the through crack with the dip angle of 45 degree

From figure 8 the crack growth on the front face of the through crack is similar with that on the back face. Its growth direction as shown in figure 8 (a), (b) is about perpendicular with the loading direction and it is a typical tensile fracture. From figure 5(a) and figure 7(a), crack growth on the front face of the non-through surface crack is similar with that of the through crack, which exhibits obviously the growth mode of two-dimensional through crack, but the crack growth on the back face of the non-through surface crack as shown in figure 5(b) and figure 7(b), which is not perpendicular with the loading direction, is not similar with that of the through crack. And further experimental results of the crack growth of the specimens as shown in figure 4 and figure 6 also support this conclusion. And this penetrating acute angle between the growth direction on the back face of specimen and the loading direction is found to be related with the dip angle and the depth of the pre-existing surface crack as shown in table 2. From table 2 the penetrating angle on the back face increases with the increase of the dip angle of the pre-existing crack, but reduces with the increase of the depth of the pre-existing crack, which demonstrates that crack deflects through the specimen.

Table 2 Relation between penetrating angles and the dip angle and depth of surface crack

Depth of surface crack	Dip angle (degree)	Crack growth angle on the back face (degree)
1/4T	30	76
1/4T	45	80
1/4T	60	83
1/4T	75	85
1/2T	30	69
1/2T	45	76
1/2T	60	80
1/2T	75	81

According to elastic mechanics in the case of a specimen with through crack both the front and back faces are usually in plane stress state. Therefore crack growth on the front and back faces of the specimen with through crack shows the two-dimensional crack growth mode. However in the case of the specimen with non-through surface crack the front face is in plane stress state so crack growth on the front face is similar to the case of plane stress. But the other crack fronts of the non-through crack are embedded in the specimens, which is similar to the embedded internal crack. According to fracture mechanics in the case of through crack with length 2R the mode I stress intensity factor is shown as

$$K_{\mathrm{I}} = \sigma\sqrt{\pi R} \tag{1}$$

But in the case of embedded semi-circle crack with radius R the mode I stress intensity factor is shown as

$$K_{\mathrm{Iembedded}} = \frac{2\sigma\sqrt{R}}{\sqrt{\pi}} = \frac{2}{\pi}K_{\mathrm{I}} < K_{\mathrm{I}} \tag{2}$$

where σ is remote tensile loading, $R = L/2$ as shown in figure 2. So during the test surface crack growth will initiates from the front face of the specimens, and then influences the growth of the other crack fronts and finally causes the penetrating direction on the back face is not perpendicular with the loading direction.

4 Conclusion and Future Work

Owing to excavation and so on local rock mass in large underground caverns is usually in tension. And the rock mass is a typical quasi-brittle material whose tensile strength is much less than the compressive strength. So it is significant to perform crack growth in tension. Three-dimensional surface crack growth in direct tension is studied preliminarily and conclusions are drawn as below,

(1) Surface crack in rock-like materials initiates from the front face of the specimens and its growth exhibits the growth mode of two dimensional through crack, which is similar with plane stress case. However owing to the influence of the pre-existing crack surface crack deflects during its growth. And finally the fracture on the back face is not perpendicular with the loading direction but at acute angle with the loading direction.

(2) Surface crack growth in rock-like materials is very complex, and further study on growth path and growth criterion and so on should be carried out.

Acknowledgements

This paper is supported by the National Natural Science Foundation of China under Grand no.40872203, National Natural Science Funds for Distinguished Young Scholar under Grand no. 50625927, Natural Science Foundation of Shandong Province under Grand no.Q2008F03.

References

1. Dyskin, A.V. Germanovich, L.N. & Ustinov K B. A 3-D Model of wing crack growth and interaction. Engineering Fracture Mechanics, 1999, 63. 61-110.
2. Germanovich, A.V., Salganik, R.L., Dyskin, A.V., et al. Mechanisms of brittle fracture of rock with multiple pre-existing cracks in compression. Pure and Applied Geophysics, 1994, 143. 117-149.
3. Dyskin, A.V., Sahouryeh, E., Jewell, R.J., et al. Influence of shape and locations of initial 3-D cracks on their growth in uniaxial compression. Engineering Fracture Mechanics, 2003, 70. 2115-2136.
4. Teng, C.K., Yin, X.C., Li, S.Y., et al. Experimental Study of 3D Fracture in Plate Specimens with Non-penetrating Crack. Chinese Journal of Geophysics, 1987, 30(4). 371-378.
5. Yin, X.C., Li, S.Y., Li, H., et al. Experimental Study of interactions between Two Flanks of a Closed Crack. Chinese Journal of Geophysics, 1988, 31(3). 307-314 .
6. Wong, R.H.C., Huang, M.L., Jiao, M.R., Tang, C.A. Crack Propagation in Brittle solid Containing 3D Surface Fracture Under Uniaxial Compression. Chinese Journal of Rock Mechanics and Engineering, 2004, 22(Supp.1). 2145-2148.
7. Wong, R.H.C., Law, C.M., Chau, K.T., Zhu, W.S. Crack propagation from 3-D surface fractures in PMMA and marble specimens under uniaxial compression. Int. J. Rock Mech. Min. Sci., 2004, 41(3). 111-114.
8. Guo, Y.S., Wong, R.H.C., Zhu W.S., et al. Study on Fracture pattern of Open Surface Flaw in Gabbro. Chinese Journal of Rock Mechanics and Engineering, 2007, 26(3). 525-531.
9. Huang, M.L., Wong, R.H.C. Experimental Study on propagation and Coalescence Mechanisms of 3D Surface Crack. Chinese Journal of Rock Mechanics and Engineering, 2007, 26(9). 1794-1799.
10. Li, S.C., Li, T.C., Wang, G., Bai and S.W. CT Real-time Scanning Tests on Rock Specimens with Artificial Initial Crack Under Uniaxial Conditions. Chinese Journal of Rock Mechanics and Engineering, 2007, 26(3). 484-492

RaSiM 7(2009): Controlling Seismic Hazard and Sustainable Development of Deep Mines, C.A. Tang(ed), Rinton Press, 177-180

ANALYSIS OF INFRARED RADIATION DURING DEFORMATION OF BOLT AND ROCK

YUAN-MING JI

School of Mathematics and Physics, Qingdao University of Science & Technology

Qingdao, 266042, P.R. China

The infrared radiation experimental tests on bolt and rock in the process of loading were carried out. The results show that the infrared radiation temperatures rise wholly and uniformly before peak stress with increase of loading. The bolted rock presents local dissimilation in the thermal image after peak stress. The multi-layer round infrared radiation isothermal lines is formed around bolt. The temperature gradually reduces from inside to outside. There are two kinds of infrared omens for bolted rock fracturing, i.e., the infrared thermal image anomaly and curve of infrared radiation temperature and time anomaly, which reflect the spatial and temporal features of infrared omens respectively.

1 Introduction

Infrared technology has been widely applied to the fields of the mechanics characteristics and catastrophe of coal, rock, concrete, etc in the last two decades [1-5]. Infrared thermal imaging technique makes it possible to detect the infrared radiation (IR) temperature and the infrared radiant flux in non-contact and real-time modes. It can convert the surface temperature of the object into visual images. We can gain the stress fields by comparing the relationship between temperature and stress.

One kind of effectual and economy supporting technology is bolt support which has been applied in many engineering fields such as mining engineering, metallurgy engineering, hydroelectricity, and tunnel [6-10]. However, there are not effective techniques and devices to directly monitor the construction quality and work condition of the bolts. Accidents such as roof caving and breakage occurred frequently. The existing support theory cannot totally reveal the bolt support mechanism. It is necessary to study a new method in order to monitor the stability of tunnel rocks, the bolt support mechanism and disaster forecast. This paper studies the infrared radiation law of interaction between bolts and surrounding rock by the use of infrared detecting technology and simulation tests.

2 Experimental Devices and Method

2.1 Experimental Devices

A fully digital hydraulic server, EHG-UG500 with load precision 0.5%, was used for the uniaxial loading. A modern infrared thermal imaging system, TVS-8100MKⅡ, was applied for the infrared radiation detection and image recording. Its technical indices are detection spectrum 3.6~4.6μm, temperature sensibility 0.025℃, spatial resolution 320×240 pixels, temperature range –40~300℃. The imaging and recording speed are 60 frames/sec.

2.2 Similar Material

The similar material of rock was made up of sand, cement and gypsum in the test. Its matching is showed in table 1.The bolt material was new-type fiberglass bolt produced by China University of Mining and Technology. Its mechanics parameters are showed in table 2.Cement was 914 glue produced in Tianjin.

Table 1. Similar material matching and mechanics parameters

Material	Match	*E(Mpa)*	μ
Rock	Sand:cement:gypsum:water 13 : 8 : 1 : 1	301.7	0.2

Table 2. Similar material matching and mechanics parameters

Material	Length(mm)	*E(Mpa)*	Failing Load*(KN)*
Bolt	30	40000	153

2.3 Model Making

The similar material was mixed up according to proportion exactly, put into mould and tamped. The size of blocks was 70mm× 70mm× 70mm.The blocks were punched 30 days later, irritated into 914 glue at the same time and inserted bolt.

2.4 Experimental Method

The TVS system was aligned in level with the block and approximately 1m away from it. Loading was at the uniform velocity controlled at 0.01mm/s. In order to minimize environmental effects on the detection of IR radiation from the block surface, a paper box with a square hole, was used for enclosing both the block sample and the load platform.

3 Results and Discussion

Figure1 shows the infrared radiation isothermal lines of sample a2 at different loading stages. There is a bolt in the

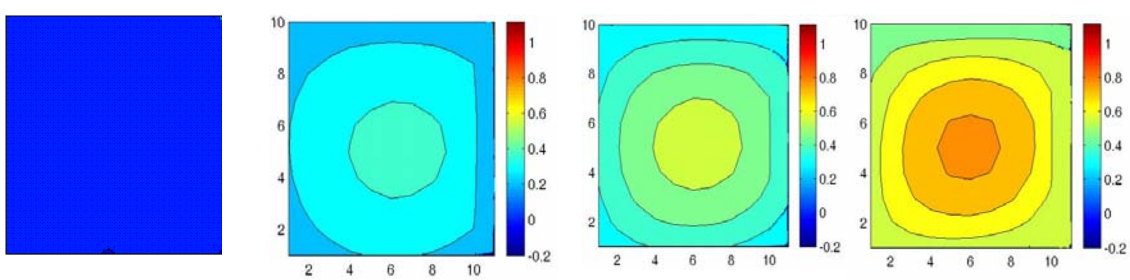

(a) 124s (b) 424s (c) 724s (d) 1004s

Figure1 IR image isothermal lines of sample a2 centre of sample a2. It can be seen that the surface IR temperature increases gradually and uniformly with loading from beginning to stress peak. The infrared images present local dissimilation after stress peak. The multi-layer round infrared radiation isothermal lines are formed around bolt. More close to the bolt centre, the temperature is higher. Farther from the bolt centre, the temperature is lower. The infrared temperature is gradually reduced from inside to outside. The original circular isotherm radius increase with the increase of rock deformation.

There are two kinds of infrared omens for bolted rock fracturing, i.e., the infrared thermal image anomaly and curve of infrared radiation temperature(IRT) and time anomaly, which reflect the spatial and temporal features of infrared omens respectively. The curve of infrared radiation temperature and time anomaly was temperature drop (Figure2).

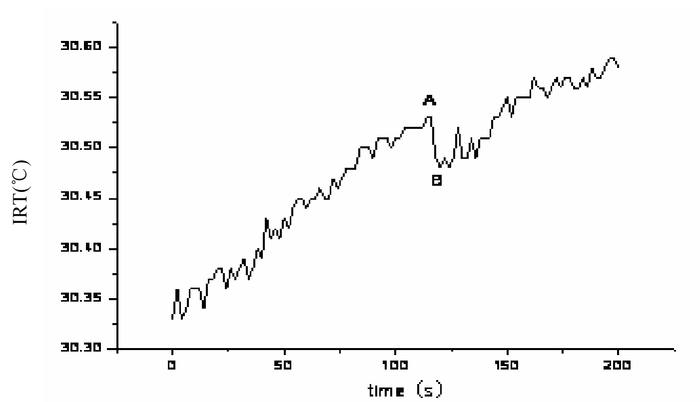

Fig.2 IRT-time curve of bolted rock fracture omens

Figure3 shows that infrared thermal image omen can be classified as high-temperature strip(section a) and low-temperature strip(section b). The infrared thermal images omens of bolted rock breakage are anomaly of temperature fields of infrared thermal image in the late stages of loading. The radiating the temperature anomaly of strip appeared. These strips responded to the bolted rocks breakage in the position and shape. The strip of different temperature fields respond to fracture of different nature. The high-temperature strip represents the shear fracture and low-temperature strip represents the extension fracture.

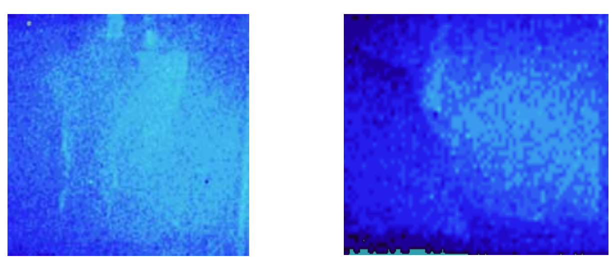

（a）　　　　　　　　（b）

Fig.3 IR image of bolted rock fracture

4 Conclusions

The infrared radiation experiments on bolt and rock in the process of loading were carried out, and the results are obtained. The infrared radiation temperatures rise wholly and uniformly before the stress peak with the increase of loading. The bolted rock presents the local dissimilation in the thermal image after the stress peak. The multi-layer round infrared radiation isothermal lines are formed around the bolt. The temperature gradually reduces from inside to outside. There are two kinds of infrared omens for bolted rock fracturing, i.e., the infrared thermal image anomaly and curve of infrared radiation temperature and time anomaly, which reflect the spatial and temporal features of infrared omens respectively. The curve of infrared radiation temperature and time anomaly is temperature drop. The infrared thermal image omen can be classified as a high-temperature strip and a low-temperature strip.

Acknowledgements

This research was supported by the National Natural Science Funds of China(Ratified No.50374069).

References

1. Luong, M.P. Infrared Thermography of Fracture of Concrete and Rock. Fracture of Concrete and Rock: SEM-RILEM International Conference, 1987.
2. Brady, B.T. and Rowell, G.A. Laboratory Investigation of the Electrodynamics of Rock Fracture, Nature, 1986, 321(29). 488-492.
3. Geng, N.G., Cui, C.Y. and Deng, M.D. Remote Sensing Detection on Rock Fracturing Experiment and the Beginning of Remote Sensing Rock Mechanics. Acta Seismologic Sinica, 1992,14(supp). 645-652.
4. Wu, L.X., Cui, C.Y. and Geng, N.G. Remote Sensing Rock Mechanics(RSRM) and Associated Experimental Studies. Int J Rock Mech Min Sci, 2000, 37(6). 879-882.
5. Terumi Inagaki, Yoshizo Okamoto. Surface Temperature Measurement near Ambient Condition Using Infrared Radiometer with Different Detection Wavelength Bands by Applying a Gray Body Approximation: Estimation of Radiative Properties for Non-metal Surface. Journal of NDT E International, 1996, 29(6). 363-369.
6. Chen, Y.G. and Lu, S.L. Strata Control around Coal Mine Roadways in China. Publishing house of China University of Mining and Technology, 1994.
7. Hart. New Development in Rock Bolting. Colliery Guardian, 1994, 7. 133-143.
8. Ji, Y.M.and An, L.Q. The Experimental Study with Infrared Radiation on the Interaction between Bolt and Surrounding Rock. Mining and Metallurgical Engineering, 2005, 25(3). 14-17.
9. Ji, Y.M.and An, L.Q. Simulated Experimental Study on Infrared Thermal Image of Bolt and Rock under Loading. Mechanics in Engineering, 2007. 29(4). 40-43.
10. Tan, Z.H., Tang, C.A., and Zhu, W.C. Experimental Study on Infrared Thermal Image for Failure Process of Granite with Fracture. Chinese Journal of Rock Mechanics and Engineering, 2005, 24(16). 2977-2981.

*RaSiM 7(2009): Controlling Seismic Hazard and
Sustainable Development of Deep Mines,
C.A. Tang(ed), Rinton Press, 181-188*

CHARACTERISTICS OF ACOUSTIC EMISSION ON THE EXPERIMENTAL PROCESS OF STRAIN BURST AT DEPTH

MAN-CHAO HE [1, 2], JIN-LI MIAO [1, 2], DE-JIAN LI [1, 2], FAN-JIANG ZENG [1, 2] and RUN-JIE MA [1, 2]

1 School of Mechanics and Civil Engineering, China University of Mining and Technology

Beijing, 100083, P.R. China

2 State Key Laboratory for GeoMechanics and Deep Underground Engineering

Beijing, 100083, P.R. China

Recently, a great development for strain rockburst tests has been made at China University of Mining and Technology in Beijing, which is represented by the design of a true triaxial rockburst test system to simulate the occurrence condition of in-situ rockburst. A series of rockburst tests by the system have been conducted, including the tests of Laizhou granite, Yaoqiao sandstone, Jiahe limestone, Jinping marble, and Nanshan coal. The information of force was collected and acoustic emission (AE) signals were also monitored by auxiliary equipment during all tests. Correlation dimension was studied for the AE amplitude, energy ratio, and ring-down count,. It is shown that the correlation dimensions change with different rocks and rockburst stages. In fact, the activity of AE for the marble sample was relatively weak and the granite was relatively strong. In addition, the signals of AE for the sandstone, limestone and the coal were strong due to the development of cracking and micro-pore within them.

1 Introduction

Rockbursts often occur in underground engineering, especially in hard rock mass at depth under high stress conditions. In order to simulate strain rockburst, some samples such as granite, limestone, sandstone, marble and coal have been conducted on true triaxial rockburst system at China University of Mining & Technology, Beijing, since 2006. The experimental system and methods were preliminarily introduced [1] with corresponding experimental results, including strain rockburst classification, process stages. The acoustic emission (AE) characteristics were reported by He [2] in details.

In this paper, we described a complementary study of the strain rockburst of five rocks on the AE fractal parameters of amplitude, energy ratio, ring-down counts, and the characteristics of AE cumulative energy during the rockburst process. The methodology makes use of a fracture model of AE in space with the amplitude of AE signals in order to measure the fracture of micro cracks [3]; which is a new to research strain rockburst experimental results.

There has been many well documented studies which have recorded the rate of occurrence of AE during true triaxial unloading; one specific study conducted analyses of the predominate cracks corresponding to AE events [4,5]. Further analysis focuses on fractal of AE parameters such as the amplitude and the energy release corresponding to micro-cracks of rock-like brittle materials under triaxial compression [6,7] and the theory models of AE [8,9]. A series of studies were conducted for fracture-evaluation of AE signals by Shiotani [10]. He also summarized the behavior of the AE parameters of ring-down count, energy count and improved *b*-value during the fracture tests of bending and shear. The rock failure due to pure macro-compressive and macro-tensile stresses (in one direction) was described by the laboratory recorded cumulative AE energy [11]. The tensile fracture propagation in sandstone under chevron-bend testing was studied with acoustic emission events [12] and the quantity fracture types at the peak load during fracture propagation were summarized.

Although the fractal methods are widely used to analyze the rock fracture characteristics with AE in uniaxial compressive, splitting, bending beam test and in situ rock blasting, etc. [13-15]; few reports [16] mentioned the rockburst fractal and mechanism with in situ micro-seismic data. Whereas, there are no reports on the analysis of AE characteristics for rockburst, under true triaxial unloading, that occur suddenly on one surface of the sample. Thus we focus on the behaviors and fractal dimensions of AE parameters to analyze the rockburst process characteristics.

2 Experiments and data analysis

The experimental system of rockburst is well described in the literature [1,2], and will not be described in detail here. It consists of true triaxial machine, data dynamic acquisition equipment and AE monitoring system.

2.1 Samples and experiments

Five different rock samples were prepared to simulate strain rockburst in laboratory by true triaxial test system via dynamic unloading one side of the sample at three directions stresses state. All the samples were rectangular-cube with approximately size of 150×60×30 mm produced by rock block of Laizhou granite, Yaoqiao sandstone, Jiahe limestone, Jinping marble and Nanshan coal in China. The mechanics and physics property of rocks are shown in Table 1 .

Table 1 Mechanics and physics of rocks

Rock type	Uniaxial compression strength (MPa)	Elastic modulus (GPa)	Possion ratio	Density (gcm^{-3})
Granite	131	21.1	0.23	2.58
Sandstone	104-113	14.6-25.0	0.23	2.41
Limestone	78	36.7	0.20	2.66
Marble	80-120	30.0-40.0	0.20-0.25	2.80
Coal	15-17	1.21-1.65	0.19-0.38	1.25

All samples were conducted at room conditions by an approximately loading stress-rate of 0.1-0.5MPa/s and unloading of 5-30MPa/s. The initial loading deviation stress is 2 MPa for coal and 10MPa for others. Every stage stress holds 5 min including the loading time of 0.3-1.0min. Normally, one stress state is kept about 30min, then one horizontal stress is unloaded suddenly, and one side of the sample is exposed. To observe whether rockburst occurs within 30mins after unloading, if not, reloading the force and increasing one or three directions stress, then unloading again after 30mins, rockburst test will end till the sample fails after one time unloading. The stress control process is shown in Figure 1.

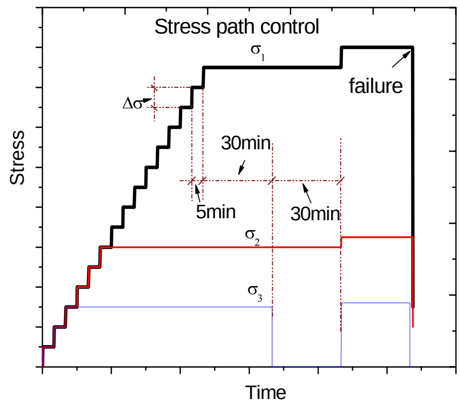

Figure 1 The stress path control process

Two piezoelectric transducers (18mm in diameter, resonant frequency of 150kHz) were mounted on the surfaces of outer steel plate contiguous to the sample. Grease of lubrication was used at the interface of sample and steel plate. The acoustic emission sampling was

1Mps and the stress sampling was 10kps. The force acquisition system includes 8 channels (sampling rate of 100 kHz, 16-bit resolution).

2.2 Rockburst experiments process

Herein we focus on the rockburst process from the final unloading to rockburst. Figure 2 (a), (b), (c), (d) and (e) show the stress paths of #19 granite, #6 sandstone, #3 limestone, #1 marble and #2-3 coal samples. The stresses states before unloading, just before rockburst, as well as the failure patterns and the lasting time from the final unloading to rockburst end for five samples were shown in Table 2.

Table 2 The testing results for all tests

Rock type	Stress before unloading (MPa)	Failure stress (MPa)	Failure pattern	Duration time
Granite #19	151.1/61.3/31.2	130.1/60.8/0	bucking-shear	28s
Sandstone #6	118.2/76.3/35.8	109.4/73.2/0	Ejection-spalling	4min10s
Limestone #3	123.1/63.6/30.9	110.9/61.9/0	Ejection-spalling	3min8s
Marble #1	106.6/39.4/22.1	104.1/39.4/0	Ejection-shear	24s
Coal #2-3	16.3/8.0/3.2	17.6/8.1/0	Ejection -splite	2min50s

Notes: The maximum principal failure stress was lower than that of prior to unloading except #2-3 coal sample

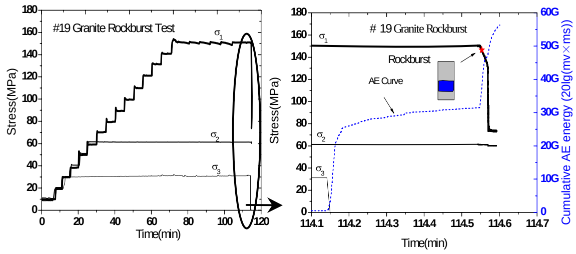

(a) #19 Rockburst stress path

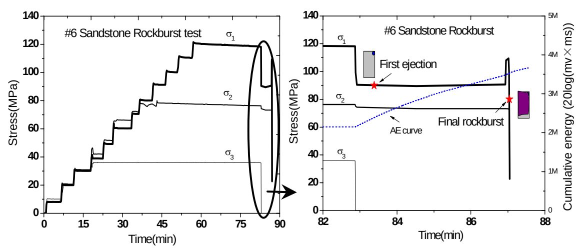

(b) #6 Rockburst stress path

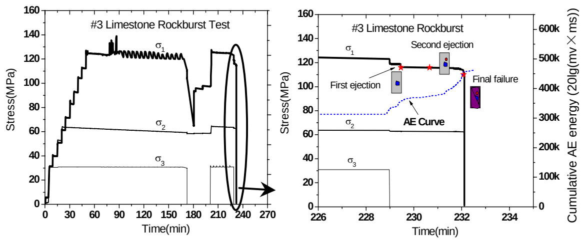

(c) #3 Rockburst stress path

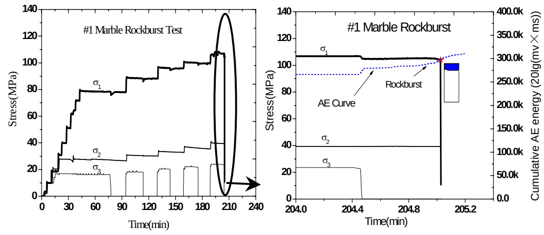

(d) #1 Rockburst stress path

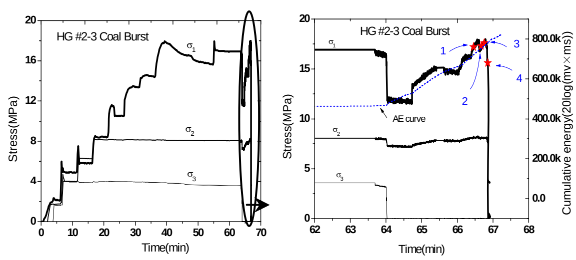

(e) #2-3 Coal burst stress path

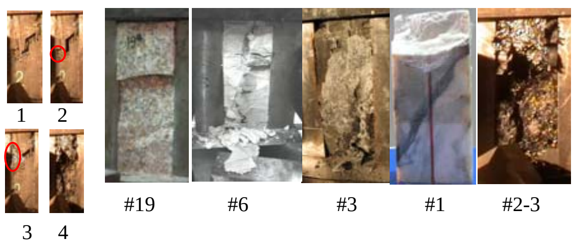

(f) Samples after failure

Figure 2 Stress paths and failure patterns of rockburst samples

For the #19 sample, rockburst occurred suddenly with the maximum principal stress dropping quickly at the moment of 28s after unloading. Buckling failure occurred in the lower-middle of the sample due to tensile-shear stress accompanied with clear sound. The total time from unloading to failure is 4min10s for #6, the first small grains ejection occurred in the right-upper of the sample at 24s after unloading and the final rockburst was caused by the maximum principal stress small increase. Platy rock fragments ejected from the sample surface and the failure sound could be heard clearly. The first thin fragment ejected in the middle of the #3sample at 28s after unloading, and the final failure occurred with an amount of fragments ejection accompanied with the sample collapsed entirely at 3min6s. #1 marble sample burst in the upper zone at 24s after unloading the minimum stress, and induced the maximum principal stress dropped quickly. Both the maximum and medium principal stresses of #2-3 dropped down when unloading the minimum principal stress. Coal burst occurred with the stress increasing slowly accompanying with twice ejections of thin fragments at the time of 2min 26s and 2min 39s and the final entire coal burst occurred at the moment of 2min50s after unloading. We may observe the samples failure patterns in Figure 2 (f).

2.3 Preliminary data analysis

The method to calculate correlation dimension (CD) of AE parameters such as energy ratio, ring-down count and amplitude is based on the intercalation theory and phase space reconstruction [17]. We define a sequence set with number *n* representing AE parameter time serials as follows.

$$X = \{x_1, x_2, \ldots x_n\} \tag{1}$$

One phase space of *m* dimensions can be generated. Firstly, a vector of *m* dimensions phase space is produced with *m* numbers from the beginning of AE sequence set. Secondly, the next vector is constructed with the same numbers from the second number of the set, and so on, we can obtain $N = n\text{-}m\text{+}1$ vectors. The corresponding correlation function is written as formula 3,

$$X_1 = \{x_1, x_2, \ldots x_m\} \tag{2}$$

$$W(r) = \frac{1}{N^2}\sum_{i=1}^{N}\sum_{j=1}^{N} H\left[r - \left|X_i - X_j\right|\right] \tag{3}$$

where *H* is Heaviside function and *r* is measure size. The slope of lg(*r*)-lg(*W*(*r*)) curve is the CD of AE parameter time series, the measure size *r* is determined as follows

$$r = k\frac{1}{N^2}\sum_{i=1}^{N}\sum_{j=1}^{N}\left|X_i - X_j\right| \tag{4}$$

where *k* is proportionality factor, and others have the same meaning as mentioned above.

According to relative research [14], the following results were calculated with $m = 4$ which has little effect to the correlative dimension.

3 Results

3.1 Curve of cumulative AE energy

Figure 2 (a) shows cumulative energy of AE during final unloading to rockburst of #19 granite sample, amounts of energy release suddenly at the moment of unloading and rockburst. See also in Figure 2 from (b) to (e), for the sandstone and coal, the cumulative energy release curves were approximately linear increasing after dynamic unloading. In another situation, like limestone and marble, it has the behaviour of rapid energy release during unloading, keeps calm relatively and increases quickly just before rockburst failure. In general, the cumulative AE energy release curve during unloading to rockburst can be grouped into three stages including dynamic unloading, stress redistribution and rockburst which are not completely corresponding with the four stages of rockburst process (i.e., calm, grains ejection, compound ejection and collapse).

It can be divided into three types for the cumulative energy curves. i) *high increase*, *keep calm*, *rapid increase again*, just as #19 granite sample; ii) *linear increase*, #6 sandstone and #2-3 coal belong to this type; iii) *small increase*, *keep constant*, *slow increase* which corresponds with #3 limestone and #1 marble sample.

3.2 Correlation dimension of AE amplitude, energy ratio and ring-down

Figure 3 (a) shows the CDs of AE amplitude, energy ratio and ring-down counts of #19 granite. CD value increases obviously after unloading and decreases prior to the final failure. The value seems varying with the damage intensity whether the stresses keep constant or decrease slightly which is very different from the sample loading test (such as uniaxial compressive test). The CD is from 0.0470 to 0.9652 of amplitude, from 1.1477 to 1.8845 of energy ratio, and from 1.4825 to 2.1759 of ring-down counts parameter, respectively.

The CD of amplitude of #6 sandstone increases gradually and reaches the peak value before final rockburst.

However, the CD peak value of energy ratio and ring-down counts appear more ahead compared with that of amplitude, see Figure 3 (b). Figure 3 (c) shows the CD of AE parameters of #3 sample. Lower value appeared before final rockburst. The value increases after post-failure except that of energy ratio. Figure 3 (d) is the CD variations of #1 marble. The CD peak value of amplitude occurred at post-failure, of energy ratio at the moment of rockburst and of ring-down counts at prior to rockburst. Figure 3(e) shows the varietal characteristics of #2-3 coal of CD. The CD increase slowly (for energy ratio and ring-down) or decreases (for amplitude) prior to coal bursting, the CD peak value of the three parameters is 2.3353, 1.9235 and 1.5788, respectively.

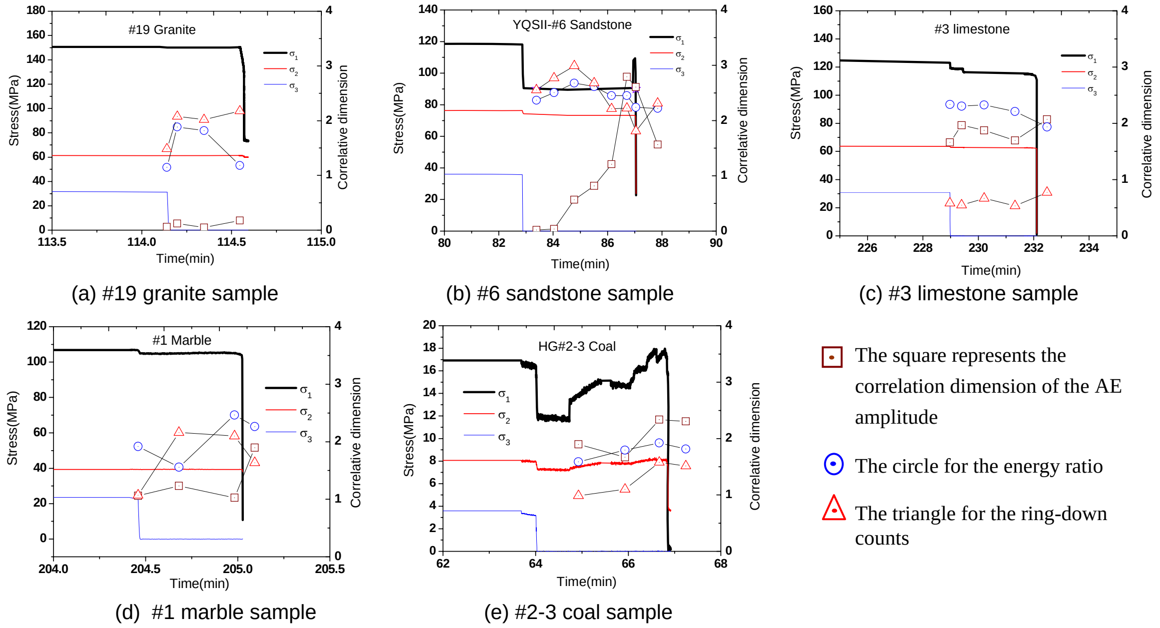

(a) #19 granite sample (b) #6 sandstone sample (c) #3 limestone sample

(d) #1 marble sample (e) #2-3 coal sample

Figure 3 Correlation dimension of AE

4 Discussions

4.1 Rockburst process and its physics behaviour

AE activities in stressed rock can be researched by the theory of damage dynamic crack for sub-critical crack growth of macroscopic cracks and population of micro-cracks [6]. The CD of AE parameters, such as energy ratio, amplitude and ring-down, exhibit a slight relationship with rockburst process.

In fact, in the stable stage of rockburst, the stress holds approximate constant, the micro-cracks may govern. Whether the AE rate increases slowly or fast is due to random local damage in the micro size such as dislocation or micro cracking. The differences for five rocks are more due to the texture and mineral components which reflects the mechanics property under external force.

AE energy release increase quickly just before rockburst. No obvious regularity has been found based on the CD when rockburst occurred in very small scale. The reason may be that boundary varies for rockburst test which is different from uniaxial or triaxial compression test. The AE behaviour has verified the damage evolvement due to inner stress redistribution in the sample though the apparent stress is constant.

The final rockburst stage is the most interesting and important phase in the catastrophic fracture of rock samples. In this stage, micro-cracking increases rapidly prior to dynamic rupture corresponding to the final unstable fracture, namely rockburst. In brittle rocks, such as granite, marble and limestone, the growth of initial cracks is in random and many of them are tensile micro-cracks (Shiotani[10] and Miao[18]). Shear cracks govern in the final rockburst collapse, AE rate increases rapidly most, but CD varying is not similar.

Figure 4 shows the CD of amplitude, energy ratio and ring-down counts of AE parameters. It appears that the varietal tendency of CD of amplitude for #1 marble, #3 limestone and #19 granite is similar during rockburst, part of reason is the similar rockburst stress paths and their homogeneous materials. In contrast, that of #6 sandstone and #2-3 coal samples vary opposite, which can be explained by the different rockburst stress paths and their porous materials property. For #1 marble, #2-3 coal and #3 limestone, the CD values of energy ratio increase just prior to rockburst, and reach the peak value at the moment of rockburst. But for #6 sandstone and #19 granite samples, the peak value occurs prior to rockburst, which may be due to stress again and the failure intensity such as local rockburst, entire rockburst or gradual rockburst. The more intensity and suddenly the rockburst occurred, or the stress increasing, the larger CD of energy ratio may be according to the rockburst failure phenomenon. Except that of #2-3 coal, others' CD calculated by AE ring-down counts decrease at the moment of rockburst.

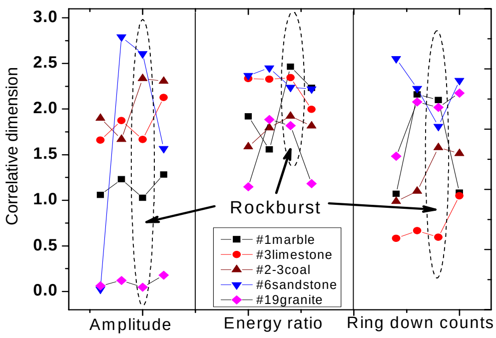

Figure 4 The correlative dimension of AE parameters (including amplitude, energy ratio and ring down counts. Four correlative dimension values, which were calculated at the stages of unloading, prior to rockburst, rockburst and post rockburst, respectively, are plotted for every AE parameter of five rocks).

The test results show that the CD of AE parameters during rockburst process, such as amplitude, energy ratio and ring-down counts, is not similar to the previous research results obtained under conventional test method controlled by force or deformation ([6], [3], [14]). The CDs change closely to the stress redistribution and the failure characteristics for rockburst test.

4.2 Implication of experimental results

The present experimental results of rockburst process for five rock samples show that rockburst is governed by stress and affected by rock's minerals components and texture. The AE energy increasing with varietal feature demonstrates the entire damage process though the macro- failure phenomenon is not obvious. We discovered that the cracking types (tensile or shear) are primarily affected by outer conditions, including the boundary condition, not only the applied force to the sample. AE energy release increase rapidly is almost related to rock failure in different sizes.

Another research is the result of correlative dimension of AE parameters, such as amplitude, energy ratio and ring-down counts. No obvious evidence illustrates the normal rule for rockburst process for different lithology test on the surface. The results of amplitude may be investigated in further with the suitable explanation for five rock samples.

5 Conclusions

The rockburst stress paths imply the rockburst's occurrence condition and intensity. For high strength rock, such as granite and marble, rockburst occurs suddenly after dynamic unloading accompanying with the rapid lowering of stress and a loud sound with failure. Otherwise, with regards to sandstone and limestone, the maximum principal stress dropped significantly when unloading the minimum principal stress suddenly causing rockburst with staggered small grains or thin fragments ejecting from the sample. Rockburst will occur intensely with stress increase to simulate in situ stress concentration. Damage generated in coal samples, caused by dynamic unloading and coal burst, occurs due to stress concentrates in mining.

The cumulative energy release parameter illustrates rapid AE increase with dynamic unloading prior to rockburst for granite and marble, linear increases for sandstone and coal, and terrace increases for limestone.

There is no normal rule for the correlation dimension varying tendency of the AE amplitude, energy ratio, and ring-down during the time from dynamic unloading to rockburst's end. We should pay attention to the dimension results calculated with the amplitude which may correlate to the stress path and lithology. It seems impossible to predict rockburst only based on AE parameters, which may explain the low accuracy of predicting rockburst according to the in situ micro-seismic data.

Acknowledgements

This work was supported by the National Basic Research Program of China (2006CB202200), the Major Program of National Natural Science Foundation of China (50490270), and Innovative Team Development Project of the Ministry of Education of China (IRT0656).

References

1. He, M.C., Miao, J.L., Li D.J. and Wang, C.G. Experimental study on the rockburst process of granite specimen at great depth. Chinese J. Rock Mech. Eng., 2007, 26(5). 865-876.
2. He, M.C., Miao, J.L., Feng, J.L. and Li, D.J. Development of strain rockburst test in China. 5th ARMS, November 24-26, (Iran, 2008)
3. Qin, S.Q. and Li, Z.D. Analysis on fractal distribution in space of acoustic emission event of rock. Applied Acoustics. 1992, 11(4). 19-21.
4. Chen, J.T. and Feng X.T. True triaxial experimental study on rock with high geostress. Chinese J Rock Mech. Eng., 2006, 25 (8). 1537-1543.
5. Hou, F. L. Experimential research on rockburst under true triaxial stress conditions. The fourth national rock dynamic acadamic conference proceedings, Chengdu, China, 1994, 201-207.
6. Lei, X.L., Koji Masuda, Osamu Nishizawa, et al. Detailed analysis of acoustic emission acivity during catastrophic fracture of faults in rock. Journal of Structural Geology, 2004, 26. 247-258.
7. Baud, P. and Meredith P.G. Damage accumulation during triaxial creep of Darley Dale sandstone from pore volumetery and acoustic emission. International Jornal of Rock Mechnics and Mining Science. 1997, 34. 3-4, paper No.024.
8. André Moura, Lei, X.L. and Osamu Nishisawa. Prediction scheme for the catastrophic failure of highly loaded brittle materials or rocks. Journal of the Mechanics and Physics of Solids, 2005, 53. 2435-2455.
9. Carpinteri, A., Chiaia, B. and Cornetti, P. On the mechanics of quasi-brittle materials with a fractal microstructure. Engineering Fracture Mechanics, 2003, 70. 2321-2349.
10. Shiotani, T., Ohtsu, M. and Ikeda, K. Detection and evaluation of AE waves due to rock. Construction and Building Materials, 2001,15. 235-246.

11. Ganne, P., Vervoort, A. and Wevers, M. Quantification of pre-peak brittle damage:Correlation between acoustic emission and observed micro-fracturing. International Journal of Rock Mechanics and Mining Sciences. 2007, (44). 720-729.
12. Backers, T., Stanchits, S. and Dresen, G. Tensile fracture propagation and acoustic emission activity in sandstone: The effect of loading rate. International Journal of Rock Mechanics and Mining Sciences. 2005, (42). 1094-1101.
13. Carpinteri, A., Lacidogna, G. and Pugno, N. Structural damage diagnosis and life-time assessment by acoustic emission monitoring. Engineering Fracture Mechanics, 2007,(74). 273-289.
14. Gao, F., Li, J.J., Li, X. Y. and Chen, J. Fractal analysis of the characteristics of acoustic emission of rock. Journal of Wuhan University of technology, 2005, 27(7). 67-69.
15. Yin, X.G., Li, S.L. and Tang, H.Y. Study on strength fractal features of acoustic emission in process of rock failure. Chinese Journal of Rock Mechanincs and Engineering, 2005, 24(19). 3512-3516.
16. Xie, H.P. Fractal character and Mechanism of rock bursts. Chinese Journal of Rock Mechanics and Engineering, 1993, 12(1). 28-37.
17. Grassberger. P. and Procaccia. J. Characterization of strange attractors. Phys. Rev. Lett. 1983, 50. 346-349.
18. Miao, J.L., He, M.C. and Li, D.J. Acoustic emission characteristics of granite under strain rockburst test and its micro-fracture mechanism. Chinese Journal of Rock Mechanics and Engineering, 2009. (Accepted)

RaSiM 7(2009): Controlling Seismic Hazard and
Sustainable Development of Deep Mines,
C.A. Tang(ed), Rinton Press, 189-194

ENVIRONMENTAL GEOLOGY DISASTERS PREVENTION OF KARST TUNNEL

YAN-HUI GE [1, 2], SHU-CAI LI [1], QING-SONG ZHANG [1], GUO-FU SUN [3] and MING-BIN WANG[4]

1 Department of Civil Engineering, Shandong Jiaotong University
Jinan, P.R. China

2 The Research Center of Geotechnical Engineering, Shandong University
Jinan, P.R. China

3 Department of Business Administration,Shandong University of Finance
Jinan, P.R. China

4 School of Science, Shandong Jianzhu University
Jinan, P.R. China

At present, environmental geology disasters are some critical problems which urgently need to be solved in tunnel construction in karst zones. In this paper, the environmental geology disasters caused by karst, collapse and water in the process of tunnel construction are described. The measures to prevent and control the disasters are summarized and the sustainable developmental concepts of tunnel design and construction are proposed for the tunnels which are under construction. The ecological environment can be protected by the measures which are proposed above.

1 Introduction

Western highway construction in China consists mainly of bridges and tunnels with tunnels becoming more and more prominent. Western China is mainly a karst zone, and the disasters of rock burst, water inrush, and collapse happen frequently during tunnel construction [1, 2]. If not handled properly, the soil erosion and collapse will cause problems of water resources shortage and ecological environment deterioration. Most karst tunnels have brought serious changes to people’s living environment which acts to counter the thought of sustainable development.

The karst tunnel is distributed widely in China. The Zhongliangshan tunnel of Xiangyu Railway built in the 1970s caused 37% of 48 spring exhaustion [3]. In the late 1980s, the disaster of water and mud inrush of the Nanling tunnel of Hengyang-Guangzhou Railway caused the land collapse, and the ecological environment was also influenced [4]. As water and mud inrush, the surface water in the area of the Dayaoshan tunnel of Beijing-Guangzhou railway was drained out, which caused 200 land collapses in the karst area and irreversible environment disease [5-7]. The environment and geology problems also occurred in a different degree in the Wulong and Yuanliangshan tunnels during construction and operation of Chongqing-Huaihua Railway [8~12]. The karst geology disasters are universal in the Yichang-Wanzhou Railway during construction. The special large water inrush disasters have occurred in the Maluqing and Yesanguan tunnel, which caused serious losses [13, 14]. If dealt with indirectly, more seriously environment geology disasters would occur in operation. There are more tunnels to be constructed in karst areas of western China and environmental disasters would be more. So the environment geology disasters are the problems to be dealt with urgently.

2 Tunnel geology disasters in Hurongxi highway

Tunnel geology disasters of Hurongxi highway are mainly caused by karst water, collapse and etc. There are some disasters have caused environment problems.

2.1 Water inrush

1) Water inrush in Tanjiaba tunnel

The buried depth is only 20m at the first pass area of Tanjiaba tunnel (K224+410～K224＋430), where karst extremely developed. There is a pool at the pass and the water of it is recharged by a karst spring. When the excavation came here, water inrush occurred and the spring stopped flow (Figure 1) and began to flow into the tunnel, which caused 5 land collapses occurred (Figure 2).

2) Water inrush in Qiyueshan tunnel

The K329＋615～K329＋525 section have a few outflows in the left and right of the exit of Qiyueshan tunnel, the inflow of water is about 500m3/h and controlled by the atmospheric rainfall directly. This area is located at the season changing belt and has well hydraulic connection with the karst depression at surface (Q17). There are many karst conduits and fractures in this section. When raining heavily, the inflow of water increases and the hydrops is about 400m (Figure 3). The construction is seriously influenced.

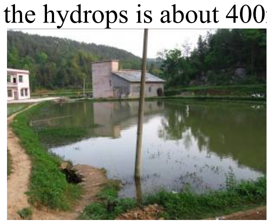

Figure 1 The spring stop flow

Figigure 2 Surface subsidence zones

Figure 3 The inflow picture of Qiyueshan tunnel

3) Water and mud inrush in Longtan tunnel

The ZK72+175.5～ZK72+176 section of Longtan tunnel occurred water and mud inrush, and the mud amount arrived about 1800m^3 in 13 minutes. After 3 times of gushing, the mud blocked the lower bench (Figure 4). If dealt with indirectly, the underground water would flow into tunnel and the balance of the original water field would be broken, which would cause the ecological environment broken.

4) Water inrush in Yesanguan tunnel

There were 9 times water and mud inrush into Yesanguan tunnel during excavation. The maximum hydrops was about 700m. The construction was influenced and ecological environment would be broken.

2.2 Collapse

1) Collapse in Qiyueshan tunnel

There are 3 collapses in the shallow buried section at Kangjia groove of Qiyueshan tunnel (Figure 5), where the overlaying surrounding rock is so broken, the collapses were caused by rain and incorrect construction method.

Figure 4 The water inflow and mud gushing of Longtan tunnel

Figure 5 The collapse and roof cave-in of Qiyueshan tunnel

2) Collapse in Zhucaowan tunnel
There is a slip block at the shallow buried section of the tunnel entrance and there is a cave at this area. Due to one month's raining caused the soil shear strength decreasing significantly, the collapse occurred.

3 Environmental disasters prevention

Sustainable development design and construction is necessary to prevent environment disasters. It means implementing dynamic design and information construction, applying comprehensive advance geology prediction, controlling auxiliary construction approaches strictly and using reasonable karst water treatment method on the basis of doing preliminary design well.

3.1 Design

1) Location design
High attention must be paid on the location design for most disasters caused by improper location design. Highway line must avoid or pass through the strong developed karst area, land collapse, area of soil or karst cave distributed densely, the contact zone of soluble and unsoluble rock, the enrichment area and discharge zone of karst water with large obliquity. The tunnel goes through the karst safety zone and underground watershed zone as much as possible to avoid disasters caused by karst and water. If can't avoid, apply dynamic design and information construction to prevent the disasters.
2) Construction drawing design
At the stage of construction drawing design, karst problems, which have been known or exist in possible, must be fully considered to avoid he disasters during construction or operation.

3.2 Dynamic design and information construction

The geological condition of karst tunnel is complex and so much uncertainty factors. Apply dynamic design and information construction, the disasters like collapse, water inrush and etc. can be avoided effectively.
1) Comprehensive advance geology prediction
The site occurred disasters like water inrush, collapse and roof fall is most at the section of karst developed or fault, like Maluqing and Yesanguan tunnel. The reason of water inrush are not finding out the unfavourable geological body forward or finding out but not making clear the dangerous. To avoid geological disaster, comprehensive advance geology prediction must be applied. Comprehensive advance geology prediction can help ascertain the characteristics of geological structure and hydrogeology features, the variety of surrounding rock, the characteristic and position of the unfavourable geological body and the dangerous degree of the unfavourable geological body and providing basis date for dynamic design and information construction.
2) Strengthen montoring
Monitoring in site is important link of the new Austrian tunnelling method and means of dynamic design and information construction. Through monitoring, the stability of surrounding rock, internal force of support system and deformation can be known, and disasters can be reflected by the data.
3) Choosing reasonable excavation method
The reasonable exaction method can be chosen on the basis of dynamic design and information construction. Exaction method is an important factor which influences the stability of the surrounding rock. According to the variety of the surrounding rock, choose reasonable excavation, adjust the form of primary support, control the excavation steps especially the leading length, and prohibit the violation construction.
4) Control auxiliary construction approaches strictly
At some section of tunnel, such as shallow buried, surrounding rock broken, karst developed the auxiliary construction approaches must be applying strictly. It main conclude advance long pipe-shed, leading conduit, forepoling bolt, curtain grouting and etc. Controlling auxiliary construction approaches strictly can strengthen

surrounding rock, improve the self bearing ability and the elastic resistance of surrounding rock and the stress conditions of the structure.

4 Environment disaster controlling

The principle of controlling environment disasters is mainly sticking to putting prevention first, but reasonable treatment measures should be taken to deal with the existing disasters.

4.1 Waterproof Design

1) The underground karst water design princple

Before 1980s, the principle of karst water controlling is giving priority to drainage of groundwater, which caused the groundwater lowering, surface water and spring drying up, ground kast collapses and ecological environment deterioration. At early 1980s, the principle changes to combining with resistant and drainage, depending on drainage. But the ecological environment deterioration problem did not change obviously. Until 1990s, the principle develops to combining with resistant and drainage, depending on resistant.

The principle of waterproof design depending on resistant is the main direction of karst water controlling for meeting the ecological environment protection. If closed grouting to make the structure into a closed waterproof layer, the water is excluded out of the tunnel and the original flow field of underground water will not change. The engineering cost and construction difficulty increase. The principle of combining with resistant and drainage, depending on resistant is appropriate.

2) Sustainable karst waterproof design

Sustainable karst waterproof design is choosing appropriate karst water controlling method, concluding closed resistant and combining with resistant and drainage, depending on resistant is appropriate. The emission is the maximum allowable amount to protect the ecological environment, which is the total water subtract the ecology balance using water.

At the low water pressure section, apply closed resistance. At the deep embedded and high water pressure section, apply combining with resistant and drainage, depending on resistant.

4.2 Treatment

1) Treatment principle

The treatment principle of tunnel existing collapse and karst water disasters should insist dealing with combining surface and inner of tunnel, depending on closed plugging but drainage limitation.

2) Treatment measures

Surface treatment method combines with block, cutting and exhaust. The measures include backfilling pitfall, isolating water with grouting in shallow layer of the surface, forming wall barrier with deep grouting and etc.

Treatment method inside tunnel is closed resistance or depending on closed plugging but drainage limitation. In addition, improving the waterproof ability of lining structure, strengthening the waterproof measures of construction joint, expansion joint and settlement joint can help avoiding the karst water disaster.

5 Grouting in Qiyueshan tunnel

5.1 Development of karst

1) Treatment principle

As mentioned above, water gushing at K329＋615～K329＋525 seriously influenced construction and would bring environmental disasters and hidden trouble to operation stage. The water pressure is about 65m at the section. To protect environment, karst water should be fully blocked by grouting.

2) Exploration by comprehensive geophysical prospecting

To applying grouting, the development of karst must be ascertained. Through GPR detecting, karst pipe and fractures distribution are clear (Figure 6). 10 drillings are implemented at the key point based on the GPR result. The drilling result shows that the GPR result is correct. It also shows the spatial distribution of the karst pipe and fractures (Figure 7).

5.2 Grouting scheme

According to the characteristic of karst water, technique and economic analysis of grouting, the composite grouting with Malisan and cement is the suitable.

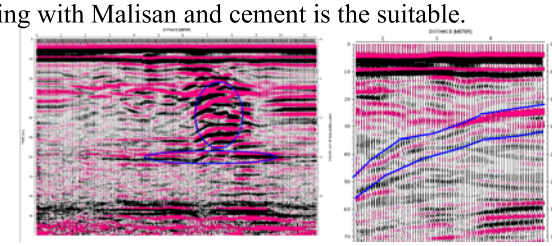

Figure 6 The result of GPR

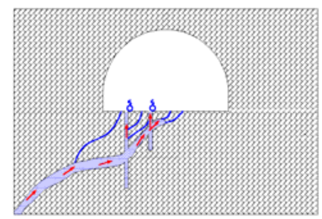

Figure 7 Vertical section of karst distribution

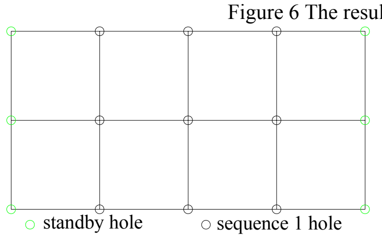

Figure 8 Hole arrangement of side wall

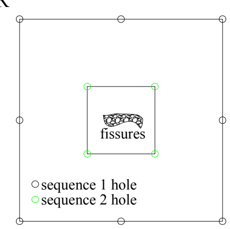

Figure 9 Grouting hole arrangement of floor

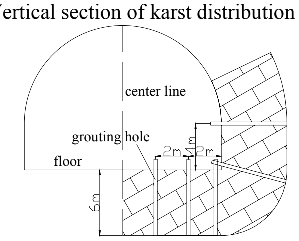

Figure 10 Vertical section of grouting hole

1) Grouting drillings arrangement

At the strengthen area arrange grouting hole (Figure 8, Figure 9) with Φ50mm and 6m (Figure 10) in depth. In the side wall grouting process, implement sequence 1 hole first, if not working, then standby hole. In the floor grouting process, implement sequence 1 hole, if not working, then sequence 2 hole. In the grouting process, the sequence should be adjusted according to practice. 6m thick reinforced region is formed by grouting.

2) Construction procedure

As the water gushing has the characteristic of large flow and fast flow rate. To avoiding cement grouting slurry, grouting to downstream of the karst pipe and fractures. Implement grouting to the fractures at the right of central axis first with Malisan. Then implement deep cement grouting at the left of central axis and use Malisan grouting to small fractures.

5.3 Detection of grouting effect

Inspecting with drilling and geophysical, the effect is well. After a rainfall season, there is non-leakage. The grouting in Qiyueshan tunnel solves the construction problem and prevents the environment geology disasters.

6 Conclusion

With the rapid development of highway and railway construction in western China, tunnel construction is happening more often. If little attention is paid to water inrush and collapse in construction, geology disasters will happen in the near future. Therefore, countermeasures must be studied to prevent the disasters.

1) Proposed the sustainable design and construction method by analyzing the existing and appearing problems in the construction of the Hurongxi highway. Especially, the sustainable karst waterproof design can protect the ecological environment in tunnel construction and operation.

2) Proposed the prevention principle and method of environmental geology disasters which are pre-grouting, strengthening surrounding rock and grouting to stop up water.
3) The treatment principle of tunnel existing collapse and karst water disasters should insist on dealing with surface and inner tunnels, depending on closed plugging but drainage limitation, protecting the water resources field and original land resources.
4) Grouting in the Qiyueshan tunnel disaster is dealt with water inrush by the principle mentioned above. The practice shows that grouting is successful in solving the problem and preventing environment geology disasters.

Acknowledgements

The authors gratefully acknowledge the supports of National Basic Research Program of China (973 Program,No.2007CB209407), national natural science foundation of China under the project No. 50539080, No.50874068 and natural science foundation of Shandong Province of China under the project No. Y2008F22.

References

1. Yu, N., Zhu, H.H. and Su, S.R. Analysis of Geological Hazards During Road Tunnel Construction and Corresponding Countermeasures. Underground Space, 2003, 23(2). 119-123.
2. Jiang, Y. and Wang, L.S. Problems of High Stress Rock Burst and Water Outburst and Countermeasures in Deep and Long Tunnels. Chinese Journal of Rock Mechanics and Engineering, 2002, 21(9). 1319-1323.
3. Bai, M.Z., Xu, Z.Y. and Wang, L.J. et al. Study on Water Outburst Geological Disaster of Tunnel Construction at Complicated Karst Zone. China Saftey Since Journal, 2006, 16(1). 114-118.
4. Wu, Z.S. Environmrntal Geolygy Problem of Tunnel in Karst Zone. Journal of Railway Engineering Society, 2006, (1). 70-73.
5. Xiong, X.J. Study and Controlling on Dayaoshan Tunnel Chinese Railways, 1997, (10). 39-42.
6. Chen C.Z. and Mou, R.F. Analysis of Karst Water Inflow System in Dayaoshan Tunnel. Journal of Engineering Geology, 1993, (9). 36-46.
7. Wang, M.S., Wang, F.Z. and Xu, J.C. et al. Scientific Research on and Construction of Dayaoshan Tunnel. China Institute of Rock Mechanics and Engineering Conference of the Seventh Academic Collection. Beijing: China Science and Technology Publishing House, 2002.
8. Su, H.F., Xi, J. and Chen, S.J. The Treatment of Water Flowing And Stability Analysis of Tunnel Support Structure on WuLong Tunnel. Railway Engineering, 2006, (6). 27-29.
9. Li, Z. and Du, M.H. The Analysis on Mud-piping and Study on Controlling Measures of YuanLiangShan Tunnel. West-China Exploration Engineering, 2005, (9). 208-209.
10. Zhang, M.Q. and Liu, Z.W. The Analysis on the Features of Karst Water Burst in the Yuanliangshan Tunnel. Chinese Journal of Geotechnical Engineering, 2005, 27(4). 422-426.
11. Gou, D.C., Wang, K. and Huang R.Q. et al. Distributing Character and Disposing Principal of Geologic Hazards Along Chongqing-Huaihua Railroad. Journal of Chengdu University of Technology, 2001, 28(2), 116-119.
12. Jin, X.F., Xia, R.Y. and Liang, B. Analysis of Bursting Water Source of Maluqing Tunnnnel, Yichang-Wanzhou Railway. Hydrogeology & Engineering Geology, 2007, 2. 71-74.
13. Wu, Y.X. The Transient-Electromagnetic Method Investigate Application in Yichang-Wanxian Railway Maluqing Tunnel. Chinese Journal of Engineering Geophysics, 2007, (2). 21-26.
14. Li, B., Bai, M.Z. and Xu, Z.Y. Risk Analysis of Karst Disasts during Constructing Yesanguan Tunnel of Yiwan Railway and Study on Its Countermeasures. China Saftey Since Journal, 2006, 16(9). 4-9.

RaSiM 7(2009): Controlling Seismic Hazard and
Sustainable Development of Deep Mines,
C.A. Tang(ed), Rinton Press, 195-202

CLASSIFICATION OF STOPE ROOF SAFETY BASED ON CATASTROPHE PROGRESSION METHOD AND ITS APPLICATION

HONG-JIANG CHEN, XI-BING LI, AI-HUA LIU and SHU-QUAN PENG,
School of Resources and Safety Engineering, Central South University
Changsha 410083, China

(This abstract is totally the same with the other paper "**SET PAIR ANALYSIS-VARIABLE FUZZY SET MODEL FOR UNDERGROUND GOAF RISK EVALUATION"**

KE-WEI LIU, XI-BING LI and HONG-JIANG CHEN
School of Resources and Safety Engineering, Central South University
Changsha 410083, China) Please check it and decide if accept it)

Collapse of mining stope roof is one of the common disasters in underground mines. In fact, the stability of the mining stope affects not only on the efficiency of resources exploitation, but also the safety of personal and their equipment. Therefore, how to evaluate and classify the safety grade of mining stope roof is very important to the choice of mining method, the determination of mining parameters, and the design of supporting system. It is a good idea to use catastrophe progression theory in safety classification of mining stope roof. First, the main principles and steps of catastrophe progression theory are introduced. Second, the main factors which will impact the safety grade of mining stope roof are identified and ordered, the index system of factors is determined as well. Finally, the catastrophic affiliated functional values of the samples are obtained to predict the safety grade of the mining stope roof. Some important results are concluded: (1) the inherent logic relation among indexes is used in catastrophe progression theory instead of the weight factor, so that the personal subjectivity can be reduced greatly and the results of the evaluation will be more objective; (2) the feasibility and effectiveness of catastrophe progression theory have been approved in real engineering cases. The results obtained are more objective and more quantitative; (3) there is no complicated calculations for the method of safety classification for mining stope roof based on catastrophe progression theory, it can be easily understood and accepted and it has a potential value in practice.

1 Introduction

Collapse of mining stope roof is one of the disasters occurring in underground mines. Classification standards and safety methods of mining stoop roofs have not been established because of different forms of geological conditions of mineral deposit, stope structures and roof falls. Based on rock mechanical tests, geological survey and rock mass failure monitoring, the classification method for stope surrounding rock stability was proposed according to the rock mass quality classification principle [1]. There are many natural and uncertain man-made factors effecting the stability analysis of the stope roof, so it is a very complex system, and the reliable results can't be obtained by only using single factor index or excessive subjective sensation. Recently, the fuzzy mathematics method [2], grey theory method [3] and artificial neural network method (ANN) [1, 4] are used to predict the stope roof safety and better results are obtained in practical application.

A new calculation model of catastrophe progression method is put forward in this paper to predict the safety classification of stope roof in underground mines. The new approach's feasibility and effectiveness based on catastrophe progression method are approved by several practical examples.

2 Basic concepts and evaluation process of catastrophe progression method

2.1 Basic concepts of catastrophe progression method

Catastrophe progression method is a comprehensive evaluation method based on catastrophe theory. Its characteristics of catastrophe progression method are mainly displayed: the weight is not adopted but the relative importance of all indexes is considered. The total evaluation index is established at first, and then it is divided by multi-hierarchical contradictory groups according to the evaluation purpose [5]. Different catastrophe systems are constructed by every layer indexes, and there are several commonly used catastrophe systems: cusp catastrophe system, swallowtail catastrophe system and butterfly catastrophe system. Optimization functions of several basic catastrophe models are showed in table 1, and the more about catastrophe progression method can be known from table.1

Table 1 Optimization functions of the four basic catastrophe models [6]

Catastrophe model	Control variables	State variable	potential function
Fold	*a*	*x*	$V(x) = x^3 + ax$
Cusp	*a,b*	*x*	$V(x) = x^4 + ax^2 + bx$
Swallowtail	*a,b,c*	*x*	$V(x) = x^5 + ax^3 + bx^2 + cx$
Butterfly	*a,b,c,d*	*x*	$V(x) = x^6 + dx^4 + ax^3 + bx^2 + cx$

Note： $V(x)$ is the potential function of the state variable x. The coefficient a, b, c, d indicated the control variable of system.

State variable and control variables of system potential function are two contradictory aspects, and their relations are showed in Figure.1. As shown in the Figure.1 *b*, the primary control variable *a* is in the left hand and the secondary control variable *b* is in the right hand. The total evaluation index in this system is divided into two sub-indexes, and it is called cusp catastrophe system. If the total evaluation index is divided into three sub-indexes or four sub-indexes, the system is called as swallowtail catastrophe system (Figure.1 *c*) or butterfly catastrophe system (Figure.1 *d*).

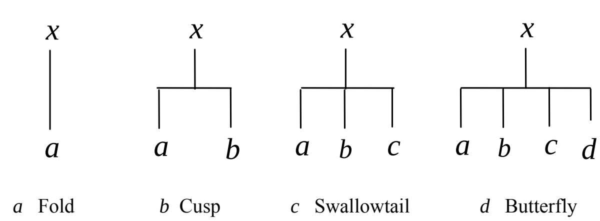

Figure1. Several catastrophe model systems

2.2 Evaluation process of catastrophe progression method

2.2.1 Establishing the catastrophe assessment indexes system

According to the internal effect mechanism of the system, it is decomposed into a new multilayer system which is built with several evaluation indexes. To obtain the more concrete quantifying indexes, some indexes may have to be decomposed further. The decomposition will be stopped until the metered indexes are obtained .Usually, the number of control variables should not be more than 4, so the sub-indexes of a single index should be less than 4 accordingly.[7]

2.2.2 Normalization for the control variables of catastrophe model.

(1) Non-dimensional quantities of original data

The indexes of system usually have different dimension and unit. To eliminate the non-commensurability of indexes, the range transform method is utilized for making indexes be-dimensionless. The dimensionless indexes will be obtained by the transforming steps as follows:

Index type A: the index is better while it is bigger:

$$y_{ij} = \frac{x_{ij} - x_{\min(j)}}{x_{\max(j)} - x_{\min(j)}} \tag{1}$$

Index type B: the index is better while it is smaller:

$$y_{ij} = \frac{x_{\max(j)} - x_{ij}}{x_{\max(j)} - x_{\min(j)}} \tag{2}$$

Where y_{ij} - dimensionless data; x_{ij} - original data; $x_{\max(j)}$-the maximum value in line j; $x_{\min(j)}$ - the minimum value in line j. If the value of the control variable is between 0 and 1, data processing is not needed. They can be used directly to catastrophe progression calculation.

(2) The normalization of control variables [8]

According to catastrophe theory, the normalization formulas of control variables are as follows:

A) For the cusp catastrophe system: $x_a = \sqrt{|a|}$, $x_b = \sqrt[3]{|b|}$ (3)

B) For the swallow tail catastrophe system: $x_a = \sqrt{|a|}$, $x_b = \sqrt[3]{|b|}$, $x_c = \sqrt[4]{|c|}$ (4)

C) For the butterfly catastrophe system: $x_a = \sqrt{|a|}$, $x_b = \sqrt[3]{|b|}$, $x_c = \sqrt[4]{|c|}$, $x_d = \sqrt[5]{|d|}$ (5)

2.2.3 Obtaining the catastrophic affiliated functional values

According to the normalization formula, the catastrophe progression values can be deduced from initial fuzzy affiliated functional values. Two principles must be considered in the calculation [9]: complementary and noncomplementary principle.

A) In the case of complementary principle, the control variables (a, b, c, d) in the system can make up each other's shortage, so the average value of x_a, x_b, x_c and x_d can be used as x value in the system, which is calculated by $x = (x_a + x_b + x_c + x_d)/4$.

B) In the case of noncomplementary principle, the control variables in the system can't make up each other's shortage, so the smallest value among x_a, x_b, x_c and x_d can be used as x value in the system, which is calculated by $x = \min(x_a, x_b, x_c, x_d)$.

In the same manner, the total catastrophic affiliated functional values can be obtained through the recursive calculation layer by layer.

3 Classification of stope roof safety based on catastrophe progression method

3.1 Establishing indexes system of stope roof safety

Although a number of factors may influence the stability of stope roof, but as considering the basic characteristics of stope roof safety, ten representative indexes have been chosen in classification of stope safety based on catastrophe progression method, these indexes are the rock quality designation $RQD(f_1)$, the uniaxial compressive strength $R_c\,(f_2)$, the internal friction angle of the structural plane $\varphi_r\,(f_3)$, the unit absorption of rock mass $\omega\,(f_4)$, the rate of AE event $C(f_5)$, the AE energy $E(f_6)$, the coefficient $m(f_7)$between AE events number and amplitude distribution, the exposure degree of soft interbedded layer (f_8), the crevasse coefficient $J_v\,(f_9)$and the exposed area of stope $S(f_{10})$.

According to the analysis of stope roof-fall in the reference 1, it's apparent that the influences of different factors on the effects of stope roof-fall are different. The importance of the factors affecting on the stability of stope roof is in the order of :$RQD(f_1) > R_c\,(f_2) > \varphi_r\,(f_3) > \omega\,(f_4) > C(f_5) > E(f_6) > m(f_7) > (f_8) > J_v\,(f_9) > S(f_{10})$.

The multi-level target structure of integrated evaluation was built up with these factors above and the sequence must be in response to the factors' significance as shown in Figure.2, the primary indexes were listed prior to the secondary ones.

3.2 Classification of stope roof Safety

According to the rock classification system and the concrete practical experiences, the criterion of stope roof safety classification is built. The classification of stope roof safety related to threshold value of every factor is listed in table 2.

Since the samples must be uniform and representative, interpolation method was adopted to construct the training sample sets.Because indexes $RQD(f_1)$, $R_c(f_2)$, φ_r (f_3) , $m(f_7)$ belong to the index type A, the formula (1) is used. On the other hand, indexes $\omega(f_4)$, $C(f_5)$, (f_8), $J_v(f_9)$, $S(f_{10})$) and $E(f_6)$ belong to the index type B, the formula (2) is used. Table 3 shows the catastrophe progression values of training samples based on the catastrophe progression principle.

According to the training sample classification and the catastrophe progression result, a system with five ranks from Ⅰ (better) to V (worse) for evaluating stope roof safety is put forward as shown in table 6. (where *a* indicates catastrophe progression value)

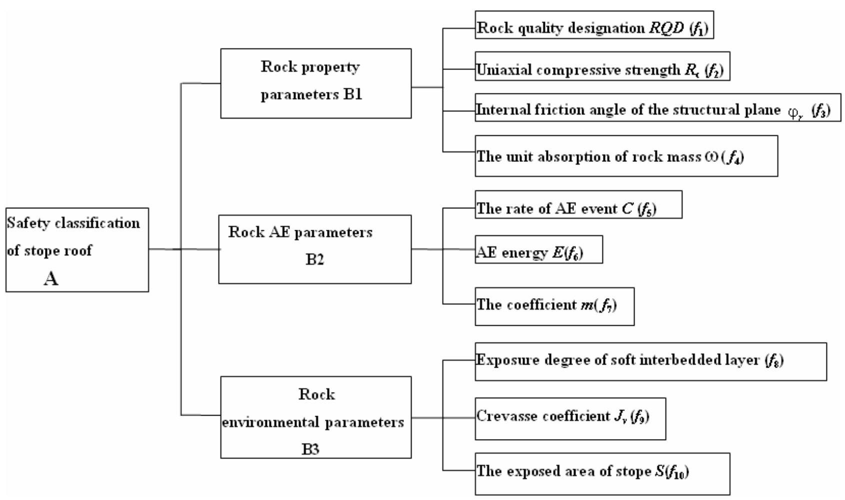

Figure2 The assessment indexes system for classification of stope roof safety

Table 2 Classification Standard of stope roof safety

Classification indexes	f_1	f_2	f_3	f_4	f_5	f_6	f_7	f_8	f_9	f_{10}
I(better)	90～100	＞200	＞45	＜10	＜5	＜300	＞3.0	＜1	＜4	＜50
II(good)	75～90	100～200	40～45	10～30	5～10	300～350	2.5～3.0	1～2	4～8	50～100
III(normal)	50～75	50～100	35～40	30～50	10～15	350～400	2.0～2.5	3～4	8～16	100～150
IV(bad)	25～50	25～50	30～35	50～70	15～20	400～450	1.5～2.0	5～7	16～30	150～200
V(worse)	＜25	＜25	＜30	＞70	＞20	＞450	＜1.5	＞8	＞30	＞200

Table3 Training sample of stope roof safety classification based on catastrophe progression

No.	f_1	f_2	f_3	f_4	f_5	f_6	f_7	f_8	f_9	f_{10}
1	90	200	45	10	5	300	3	1	4	50
2	87	180	44	14	6	310	2.9	1.2	4	60

3	85	160	43	18	7	320	2.8	1.4	5	70
4	80	140	42	22	8	330	2.7	1.6	6	80
5	78	120	41	18	9	340	2.6	1.8	7	90
6	75	100	40	30	10	350	2.5	2	8	100
7	70	90	39	34	11	360	2.4	3	10	110
8	65	80	38	36	12	370	2.3	3.4	12	120
9	60	70	37	40	13	380	2.2	3.5	14	130
10	55	60	36	45	14	390	2.1	4.8	15	140
11	50	50	35	50	15	400	2	4	16	150
12	45	45	34	55	16	410	1.9	5	18	160
13	40	40	33	60	17	420	1.8	6	20	170
14	35	35	32	62	18	430	1.7	6.5	24	180
15	30	30	31	67	19	440	1.6	7	26	190
16	25	25	30	70	20	450	1.5	8	28	200
type	A	A	A	B	B	B	A	B	B	B

Note: A indicates the index type A; B indicates the index type B.

Table4 Normalization of the control variables

No.	f_1	f_2	f_3	f_4	f_5	f_6	f_7	f_8	f_9	f_{10}
1	0.866667	1	1	1	1	1	1	1	1	1
2	0.826667	0.885714	0.933333	0.933333	0.933333	0.933333	0.933333	0.971429	1	0.933333
3	0.8	0.771429	0.866667	0.866667	0.866667	0.866667	0.866667	0.942857	0.961538	0.866667
4	0.733333	0.657143	0.8	0.8	0.8	0.8	0.8	0.914286	0.923077	0.8
5	0.706667	0.542857	0.733333	0.866667	0.733333	0.733333	0.733333	0.885714	0.884615	0.733333
6	0.666667	0.428571	0.666667	0.666667	0.666667	0.666667	0.666667	0.857143	0.846154	0.666667
7	0.6	0.371429	0.6	0.6	0.6	0.6	0.6	0.714286	0.769231	0.6
8	0.533333	0.314286	0.533333	0.566667	0.533333	0.533333	0.533333	0.657143	0.692308	0.533333
9	0.466667	0.257143	0.466667	0.5	0.466667	0.466667	0.466667	0.642857	0.615385	0.466667
10	0.4	0.2	0.4	0.416667	0.4	0.4	0.4	0.457143	0.576923	0.4
11	0.333333	0.142857	0.333333	0.333333	0.333333	0.333333	0.333333	0.571429	0.538462	0.333333
12	0.266667	0.114286	0.266667	0.25	0.266667	0.266667	0.266667	0.428571	0.461538	0.266667
13	0.2	0.085714	0.2	0.166667	0.2	0.2	0.2	0.285714	0.384615	0.2
14	0.133333	0.057143	0.133333	0.133333	0.133333	0.133333	0.133333	0.214286	0.230769	0.133333
15	0.066667	0.028571	0.066667	0.05	0.066667	0.066667	0.066667	0.142857	0.153846	0.066667
16	0	0	0	0	0	0	0	0	0.076923	0

Table5 The result based on catastrophe progression method of training samples

No.	Catastrophe progression value	Safety classifications	No.	Catastrophe progression value	Safety classifications
1	0.99711	I	9	0.908605	III
2	0.98618	II	10	0.893515	III
3	0.97848	II	11	0.875878	III
4	0.969183	II	12	0.848428	IV
5	0.961557	II	13	0.823401	IV
6	0.949825	II	14	0.790408	IV
7	0.933874	III	15	0.738213	IV
8	0.922168	III	16	0.248409	V

Table6 The catastrophe progression value and safety grades

catastrophe progression value	$1.000 \geq a \geq 0.99711$	$0.99711 > a \geq 0.94185$	$0.94185 > a \geq 0.84843$	$0.84843 > a \geq 0.24841$	$0.24841 > a \geq 0.000$
Safety classifications	I	II	III	IV	V

4 Applications

Nine samples from reference 1 and 4 were chosen for testing (see table 7), the corresponding catastrophe progression value was obtained as shown in table 8. The forecasting result indicated that the accuracy rate is 100%.

It is clearly demonstrated that the catastrophe progression method used for predicting the classification of stope roof safety is much more convenient and highly efficient.

For the third test sample, the catastrophe progression value of the classification of stope roof safety is calculated as follows.

(1) For the second level of the multi-level target structure of integrated evaluation:

Step 1:

Because $RQD(f_1)$, $R_c(f_2)$, φ_r (f_3) and $\omega(f_4)$ accord with the butterfly catastrophe system, then

$x_a = a^{\frac{1}{2}} = \sqrt{0.5} = 0.707107$, $x_b = b^{\frac{1}{3}} = \sqrt[3]{0.285714} = 0.65863$, $x_c = c^{\frac{1}{4}} = \sqrt[4]{0.5} = 0.840896$, $x_d = d^{\frac{1}{5}} = \sqrt[5]{0.5} = 0.870551$.

According to the complementary principle, the index "B_1: Rock property parameters" is

$x_{B_1} = (x_a + x_b + x_c + x_d)/4 = 0.769297$;

Step 2:

Because the rate of AE event $C(f_5)$, AE energy $E(f_6)$, the coefficient $m(f_7)$ between AE events number and amplitude distribution accord with the swallowtail catastrophe system, then

$x_a = a^{\frac{1}{2}} = \sqrt{0.5} = 0.707107$, $x_b = b^{\frac{1}{3}} = \sqrt[3]{0.5} = 0.793701$, $x_c = c^{\frac{1}{4}} = \sqrt[4]{0.5} = 0.840896$.

According to the complementary principle, the index "B_2: Rock AE parameters" is

$x_{B_2} = (x_a + x_b + x_c)/3 = 0.780568$;

Step 3:

Because exposure degree of soft interbedded layer (f_8), crevasse coefficient $J_v(f_9)$ and the exposed area of stope $S(f_{10})$ accord with the swallowtail catastrophe system, then

$x_a = a^{\frac{1}{2}} = \sqrt{0.6428571} = 0.801784$, $x_b = b^{\frac{1}{3}} = \sqrt[3]{0.692308} = 0.88464$, $x_c = c^{\frac{1}{4}} = \sqrt[4]{0.5} = 0.840896$.

According to the complementary principle, the index "B_3: Rock environmental parameters" is

$x_{B_3} = (x_a + x_b + x_c)/3 = 0.84244$;

Table7 Data material of test sample

No.	f_1	f_2	f_3	f_4	f_5	f_6	f_7	f_8	f_9	f_{10}
1	95	200	45	10	5.0	300	3.0	1.0	4	50
2	82.5	150	42.5	15	7.5	325	2.75	1.5	6	75
3	62.5	75	37.5	40	12.5	375	2.25	3.5	12	125
4	37.5	32.5	32.5	60	17.5	425	1.75	6.0	23	175
5	25	25	30	70	20.5	450	1.5	8.0	30	200
6*	55	109	45	52	11.6	496	2.45	5	10	135
7*	61	109	20	58	9.6	359	2.04	7	17	167
8@	58	105	40	55	11.2	481	2.53	5	11	128
9@	60	105	25	56	9.5	365	2.12	7	16	166

Note: *indicates that the data are from reference 1 and @ indicates that the data are from reference 4.

Table8 The classification result of catastrophe progression

No.	Catastrophe progression value	Practical results	ANN method	Catastrophe progression method
1	0.998584	I	I	I
2	0.977353	II	II	II
3	0.918626	III	III	III
4	0.80562	IV	IV	IV
5	0.092151	V	V	V
6*	0.88545	III	III	III
7*	0.854621	III	III	III
8@	0.882608	III	III	III
9@	0.856146	III	III	III

Note: * indicates that the data are from reference 1 and @ indicates that the data are from reference 4.

(2) For the first level of the multi-level target structure of integrated evaluation

Because rock property parameters(B_1),rock AE parameters(B_2) and rock environmental(B_3) accord with the swallowtail catastrophe system, then

$x_a = a^{\frac{1}{2}} = \sqrt{0.769297} = 0.877096$, $x_b = b^{\frac{1}{3}} = \sqrt[3]{0.780568} = 0.92074$, $x_c = c^{\frac{1}{4}} = \sqrt[4]{0.84244} = 0.958042$,

According to the complementary principle, $x = (x_a + x_b + x_c)/3 = 0.918626$.

Because the catastrophe progression value is between 0.94185 and 0.84843, the safety grade of the third test sample was III.

In the same manner, the catastrophe progression values of other test samples can be calculated by computer and then the safety grades can be found out easily according to the safety classification standards (table 6).

5 Conclusions

（1）The weight factor is not used in catastrophe progression theory, the inherent logic relation between indexes are analyzed so as to reduce significantly the subjectivity of people. The model based on the catastrophe progression theory can make the evaluation results more objective.

（2）The model deduced in this paper for predicting the safety grade of stope roof is influenced by the representation and veracity of the original engineering materials. In practice, the model is built from the more comprehensive sample database and will be more consistent and accurate through collecting more engineering example materials.

（3）The case studies show that the feasibility and effectiveness of catastrophe progression method are valid. The results obtained can provide a good and viable reference for decision makers in the disposal of stope roof.

（4）It is clearly demonstrated that the method used in the present research is much more convenient and highly efficient in predicting the safety grade of a stope roof. However, several problems still exist in the method, such as the assignment of some factors which are controlled artificially, and further studies are certainly needed.

Acknowledgements

The authors wish to acknowledge the collaborative funding support from the 973 Project of China (2007CB209402) and academic degree innovation project of Hunan (1343-74236000013). In particular we wish to thank Ke Gao, and Yi-fang Deng for their contributions to this research project.

References

1. Cao, Q.L. and S, Y.F. Classification of stope roof safety with artificial neural networks.Mining and Metallurgical Engineering, 1995, 15(3). 8-11.
2. Zhou, K.P. Fuzzy Comprehensive Evaluation on stability of stope roof. Hunan Nonferrous Metals, 1994, 10(1). 1-4.
3. Zhou K.P. An analysis of stability and ambiguity prediction of settlement regularity for stop roof. Mining Research & Development, 1994, 14(4).44-49.
4. Liu, H.X., Wu, X.Z. and Hu, W. Study on Different Adjusting Amplitudes for the Velocity and Temperature Distribution at the Exit of Tip Cavity. Journal of Southern Institute of Metallurgy, 2004, 25(1). 20-24.
5. Huang, Y.L. Application of catastrophe Progression Method to Evaluation of Sustainable Usage of Water Resource.Arid Eaviroamcatal Monitoring, 2001, 15(3). 167-170.
6. Chen Y.F., Sun, D.Y. and Lu G.F.Application of catastrophe progression method in ecological suitability assessment: A case study on Zhenjiang new area. Acta Ecologica Sinica, 2006, 26(8). 2587-2593.
7. Chen, H.J., Li, X.B. and Gao, K. On the application of catastrophe progression method to predicting the likely mining collapse accidents. Journal of Safety and Environment, 2008, 8(6). 108-111.

8. Wan, W.L, Yang, C.F.and Wang, D.J. Application of catastrophe theory evaluation method in assessment of economic profit & productivity of mine. Mining Engineering, 2006, 4(2). 5-7.
9. Jiang J.C. Catastrophe theory and its application in the safety engineering. Journal of Nanjiing University of Chemical Technology, 1999, 21(1). 24-28.

RaSiM 7(2009): Controlling Seismic Hazard and Sustainable Development of Deep Mines, C.A. Tang(ed), Rinton Press, 203-208

SET PAIR ANALYSIS-VARIABLE FUZZY SET MODEL FOR UNDERGROUND GOAF RISK EVALUATION

KE-WEI LIU, XI-BING LI and HONG-JIANG CHEN
School of Resources and Safety Engineering, Central South University
Changsha 410083, China

Underground goaf risk evaluation is a complicated uncertainty system issue. Based on the set pair analysis (SPA) and the variable fuzzy sets theory, a new fuzzy comprehensive classification model was established for underground goaf risk evaluation. Considering the geologic condition and engineering status of underground goaf, five factors such as the span, area, height and depth of underground goaf were taken into account. In order to test this new model, ten risk underground goafs in Dabaoshan mine were evaluated through it. Compared with the results of fuzzy synthetic evaluation method and uncertainty measurement method, the results show that the proposed method used to evaluate the risk of underground goaf is feasible and effective, and more objective.

1 Introduction

In recent years, the continuous socio-economic development has created a great demand for mineral resources. In China, underground exploiting is a main form of mine exploiting, and the subsidence in the goaf district leads to the destroying of land resource due to underground exploiting. Recently, underground goaf is one of the major dangers in mining [1, 2], therefore, the treatment of underground goaf is of great importance.

Set pair analysis is a new system analysis method that was advanced by Chinese scholar ZHAO Keqin in 1980s [3]. Since its development, set pair analysis has been applied to many areas. Reference [4] uses set pair analysis in an oil depot management system; Reference [5] and reference [6] are both demonstrate its application in water assessment; Reference [7] uses the method to evaluate the stability of a stope roof. These applications all indicate that set pair analysis is a better tool and method to identify and deal with certainties and uncertainties.

2 Set pair analysis-variable fuzzy set model

2.1 Basic Ideas of Set Pair Analysis

Set pair is a pair which is composed of two sets that have certain connection. Basic ideas of set pair analysis are: It analyzes characteristics of a set pairs in a certain context. Then find the shared characteristics, the opposite characteristics of the two pairs. And find differences of neither shared nor opposite characteristics of the two sets. This establishes the same-indefinite-contrary degree of connection expression of the two sets in a certain context: $\mu = a + bi + cj$. Then it can expend to more than two sets' condition. In the end, we can further study the relevant issues on basis of this system [3].

2.2 Degree of Connection μ

According to the internal effect mechanism of the system, it is decomposed into a new multilayer system which is built with several evaluation indexes. To obtain the more concrete indexes for quantization ,some indexes must be decomposed .The decomposition will be stopped until the metered indexes are obtained .Usually, the number of control variable should not excess 4,so the sub-indexes of a single index should be less than 4 accordingly.[7]

Degree of connection is an important concept of set pair analysis [5]. It can be expressed as:

$$\mu = S/N + (F/N)i + (P/N)j \tag{1}$$

where N is the total number of the characteristics that the two sets have; S is the number of the shared characteristics of the two sets; P is the number of the opposite characteristics of the two sets; F=N-S-P is the number of neither shared nor opposite characteristics of the two sets; S/N is the same degree of the two sets in a certain context; F/N the different degree of the two sets in a certain context; P/N is the opposite degree of the two sets in a certain context; j is the coefficient of the opposite degree, provides value -1; i is the coefficient of the differences degree, $i \in [-1,1]$.

For convenience, we request $S/N=a$, $F/N=b$, $P/N=c$, then the expression (1) can be written as:

$$\mu = a + bi + cj \tag{2}$$

Because a and cj are certainties, bi is an uncertainty, the expression (2) includes both certainty and uncertainty.

2.3 Comprehensive Evaluation Model.

Underground goaf risk evaluation is a typical and complicated uncertainty system problem. In order to simplify the evaluation procedure and improve the accuracy and reliability of results, a new method to construct relative difference degree was proposed in this paper. According to the ideas of set pair analysis and nondeterminacy characteristics, the methods of fuzzy set pair analysis were advanced on the basis of the fuzzy degree of connexion.

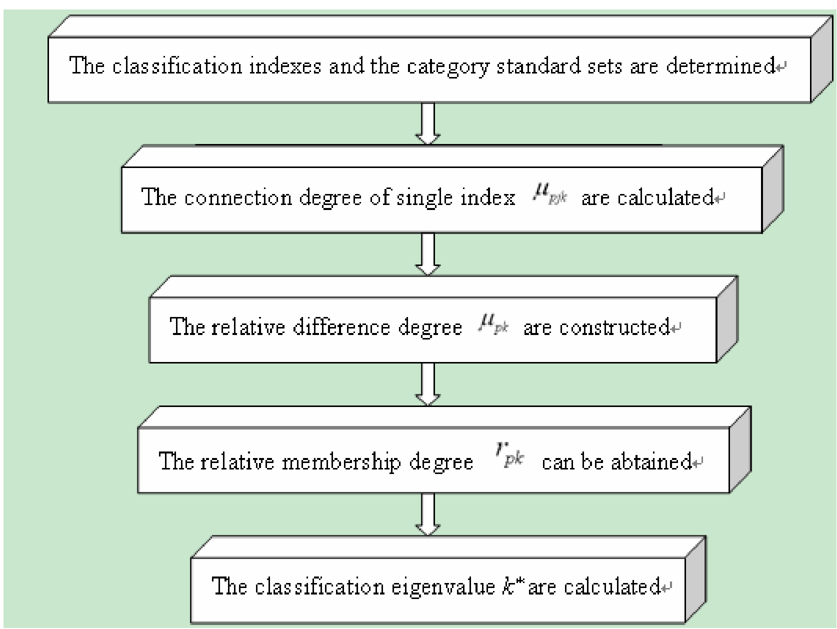

Figure 1 Flow chart of set pair analysis-variable fuzzy set model

The explicit evaluation process as follows [8]:

(1) The classification indexes and the category standard sets of underground goaf risk evaluation are determined;

(2)The connection degree of single index μ_{pjk} between sample index value $x_{pj}(p=1,2,\cdots,n \quad j=1,2,\cdots,m)$ and underground goaf risk degree $k(k=1,2,\cdots,K)$ are calculated;

(3)Combining with the weight ϖ_j of the classification indexes, the relative difference degree μ_{pk} between the samples and the standard grades *k* of underground goaf risk evaluation are constructed;

(4) Then the relative membership degree r_{pk} can be obtained based on the relative difference degree μ_{pk};

(5) According to the relative membership degree r_{pk}, the classification eigenvalue k^* is calculated in order to describe which risk degree the sample belong to. The concrete operating procedure is shown by Fig.1.

If x_{pj} was located in the range of class *k*, then $\mu_{pjk}=1$; and if x_{pj} was located in the range of adjacent class *k*+1 or *k*-1, then $\mu_{pjk}\in[-1,1]$; otherwise, $\mu_{pjk}=-1$. Finally, according to the same-indefinite-contrary assessment principle, the formula of approaching degree between sample index value x_{pj} and *k* are:

a) When the difference degree coefficient i in risk degree Ⅰ，

$$\mu_{pj1}=\begin{cases}1 & x\in\left[0,S_{i(1)}\right]\\ 1-\left|\dfrac{2(x-S_{i(1)})}{S_{i(2)}-S_{i(1)}}\right| & x\in\left[S_{i(1)},S_{i(2)}\right]\\ -1 & x\in\left[S_{i(2)},+\infty\right)\end{cases}\tag{3}$$

b) When the difference degree coefficient *i* in risk degree Ⅱ，

$$\mu_{pj2}=\begin{cases}1-\left|\dfrac{2(S_{i(1)}-x)}{S_{i(1)}-0}\right| & x\in\left[0,S_{i(1)}\right]\\ 1 & x\in\left[S_{i(1)},S_{i(2)}\right]\\ 1-\left|\dfrac{2(x-S_{i(2)})}{S_{i(3)}-S_{i(2)}}\right| & x\in\left[S_{i(2)},S_{i(3)}\right]\\ -1 & x\in\left[S_{i(3)},+\infty\right)\end{cases}\tag{4}$$

c) When the difference degree coefficient *i* in risk degree Ⅲ，

$$\mu_{pj3}=\begin{cases}1-\left|\dfrac{2(S_{i(2)}-x)}{S_{i(2)}-S_{i(1)}}\right| & x\in\left[S_{i(1)},S_{i(2)}\right]\\ 1 & x\in\left[S_{i(2)},S_{i(3)}\right]\\ 1-\left|\dfrac{2(x-S_{i(3)})}{S_{i(4)}-S_{i(3)}}\right| & x\in\left[S_{i(3)},S_{i(4)}\right]\\ -1 & x\in\left[0,S_{i(1)}\right] or [S_{i(4)},+\infty)\end{cases}\tag{5}$$

d) When the difference degree coefficient *i* in risk degree Ⅳ，

$$\mu_{pj4}=\begin{cases}1 & x\in\left[S_{i(3)},S_{i(4)}\right]\\ 1-\left|\dfrac{2(S_{i(3)}-x)}{S_{i(3)}-S_{i(2)}}\right| & x\in\left[S_{i(2)},S_{i(3)}\right]\\ -1 & x\in\left[0,S_{i(2)}\right] or [S_{i(4)},+\infty)\end{cases}\tag{6}$$

In the formula (3) ～ (6)， $S_{i(1)}$、 $S_{i(2)}$、 $S_{i(3)}$、 $S_{i(4)}$ denote respectively the threshold value of every risk degree j; x is the observed index of the underground goaf risk evaluation. Then combining with the weight ϖ_j of the classification indexes, the relative difference degree μ_{pk} between the samples and the standard grades k of underground goaf risk evaluation can be calculated by formula (7),

$$\mu_{pk}=\sum_{j=1}^{m}\varpi_j\mu_{pjk}\tag{7}$$

In the formula (7), ϖ_j is the weight of the classification indexes, we can get it. These results indicated that the closer between the value of μ_{pk} and -1, the more difference between the sample *p* and classification *k*, then the sample *p* tends to other classification and vice versa. Corresponding relative membership degree r_{pk} can be obtained based on the relative difference degree μ_{pk} as distortion caused by the maximum membership degree follows:

$$r_{pk} = \frac{1+\mu_{pk}}{2} \tag{8}$$

Usually, the maximum membership degree principle is used for underground goaf risk evaluation. To avoid the principle, the eigenvalue k^* is adopted to quantity assessment. The calculation formula is:

$$k^* = \sum_{k=1}^{K} k \cdot \left| \frac{r_{pk}}{\sum_{i=1}^{K} r_{pi}} \right| \tag{9}$$

3 Application of Set Pair Analysis-Variable Fuzzy Set Model for Underground Goaf Risk Evaluation

According to related studies[10,11], five factors that influence the stability of underground goaf were taken as the impact factors for evaluation, such as Quality indexes of rock , Span of goaf , Area of goaf ,Height of goaf and Depth of goaf (respectively using X_1 ,X_2 ,X_3 ,X_4 ,X_5 as indicators).The evaluation set is {C_1 ,C_2 ,C_3 ,C_4 },namely Ⅰ, Ⅱ,Ⅲ, Ⅳ, they denote very high risk, high risk , general risk and low risk respectively. The classification standard and the evaluation set are shown in Table 1.

Table 1 Classification criterion of quantitative indexes in underground goaf risk evaluation

Classification	Quality indexes of rock(X_1)/%	Span of goaf (X_2)/*m*	Area of goaf (X_3)/m^2	Height of goaf (X_4)/*m*	Depth of goaf (X_5)/*m*
Ⅰ (C_1)	＜40	＞120	＞2700	＞30	＞400
Ⅱ (C_2)	40～50	80～120	1200～2700	20～30	200～400
Ⅲ(C_3)	50～60	40～80	800～1200	8～20	100～200
Ⅳ(C_4)	＞60	＜40	＜800	＜8	＜100

Table 2 Estimation and measured data of risk evaluation indexes of underground goaf

Serial number of underground goaf	Quantitative indexes				
	Quality indexes of rock (X1)/%	Span of goaf (X2)/m	Area of goaf (X3)/m2	Height of goaf (X4)/m	Depth of goaf (X5)/m
1	38	85	5190	15.0	260
2	56	60	1230	8.0	260
3	35	62	2560	14.5	290
4	48	73	1740	22.0	280
5	43	60	1920	16.5	280
6	47	160	6890	26.3	305
7	55	26	2870	15.8	305
8	57	96	2260	21.0	335
9	67	60	1200	10.0	335
10	53	85	3970	60.0	240

Table 3 The evaluated results of underground goaf and comparison

Serial number	r_{p1}	r_{p2}	r_{p3}	r_{p4}	Set pair analysis-variable fuzzy set model		fuzzy synthetic evaluation method	uncertainty measurement method
					Classification	Eigenvalue k^*		
1	0.4850	0.7067	0.5150	0.0833	II	2.11	II	II
2	0.0640	0.5800	0.9360	0.4200	III	2.86	III	III
3	0.4713	0.7933	0.5287	0.1817	II	2.21	II	II
4	0.2320	0.9650	0.7680	0.0350	II	2.30	II	II
5	0.3160	0.8417	0.6840	0.1583	II	2.34	II	II
6	0.5860	0.4000	0.2210	0.2000	I	1.02	I	II
7	0.2000	0.2300	0.5370	0.5700	IV	3.96	IV	IV
8	0.3763	0.8600	0.6237	0.1400	II	2.26	II	II
9	0.1350	0.5333	0.7250	0.4667	III	2.82	III	III
10	0.4650	0.5400	0.5350	0.0600	II	2.12	II	II

The Dabaoshan polymetallic deposit is located Guangdong province. As a result of sublevel open stope mining and unlicensed mining by native, big and small stoped out areas were made under the well. It is urgent to exploit plentiful ore in the north of one of the largest stoped out areas called 576, which comes to millions of steres. According to the hydrogeology condition, environmental factors and structure parameters of underground goaf, 10 underground goafs have been chosen as evaluation objects. The basic situations of them are shown in Table 2.

To verify the correctness and effectiveness of the new model, the sample data from 17 refs are used to do some comparative analysis with other models such as fuzzy synthetic evaluation model and uncertainty measurement model. The results are shown in Table 3.

4 Conclusions

(1) A set pair analysis-variable fuzzy set model is established for underground goaf risk evaluation in this paper. In this model, the potential uncertainties are considered. A combination of qualitative and quantitative phase analysis is achieved. By comparing the results between a practical example and other methods, it was proven that the proposed model used to evaluate the underground goaf was feasible, effective, and more objective.

(2) The method can be used efficiently to evaluate underground goaf. This method is easy to understand and operate. Compared with other assessment methods, set pair analysis has comprehensively analyzed certainties and uncertainties, and its assessment result is more precise. Set pair analysis is suitable to be widely used in all areas.

(3) Except for the assessment of three-element connection number introduced in this paper (good, general, and poor), there are assessments of four-element connection number and five-element connection number, and even more elements [8]. Also, each has its own characteristics.

Acknowledgements

The authors wish to acknowledge the collaborative funding support from 11th Five Years Key Programs for Science and Technology Development of China (2007BAK24B01-4) and academic degree innovation project of Hunan (1343-74236000013). In particular we wish to thank Li xi-bing, Liu ai-hua, Peng shu-quan, Gao ke, and Deng yi-fang for their contributions to this research project.

References

1. Gu, D.S. and Li,X.B. Modern mining science and technology for metal mineral resources.Beijing: China Metallurgical Industry Press,2006.

2. State Administration of Work Safety. State technological development programming of work safety—non-coal mine domain research bulletin (2004-2010). Beijing: State Administration of Work Safety, State Administration of Coal Mine Safety, 2003.
3. Zhao, K.Q. Set Pair Analysis and its preliminary Application. Zhejiang: Zhejiang Science and Technology Press, 2000.
4. Zheng, X.B. and Chen, G.M. Safety comprehensive assessment method based on set pair analysis and its application. Journal of Harbin Institute of Technology, 2006,(2). 290-293.
5. Ren, Y.L.and Zhu, M.F. Comprehensive assessment method based on set pair analysis and its application. Microcomputer Information, 2007(36). 220-222.
6. Lu, M., Zhang, Z.Y.and Shi, Y.Z. Application of set pair analysis to evaluation of water safety. Journal of Hohai University: Natural Sciences), 2006(5). 505-508.
7. Wang, Q.S.and Li, X,B. Evaluation on surrounding rock quality of tunnel based on set pair analysis method. International Young Scholar Symposium on Rock Mechanics , 2008,8(6). 346-350.
8. Wang, M.W, Li, L, and Jin, J.L. Set pair analysis-variable fuzzy set model for evaluation of stability of surrounding rock. Chinese Journal of Geotechnical Engineering, 2008, 30(6). 941-944.
9. Science and Technology Developmental Limited Company of Changsha Tuojin. Study on current safety synthetic evaluation situation of underground in Dabaoshan mine.Changsha:School of Resources and Safety Engineering,Central South University,2005.
10. Iang W.D, Li, X.B.and Hu, L.Q. et al. Stability analysis of ground above excavated area based on grey fixed weight cluster.Mining and Metallurgical Engineering, 2002, 22(4).15-17.(in Chinese)
11. Gong, F.Q., Li, X.B., Dong, L.J. and Liu, X.L. Underground goaf risk evaluation based on uncertainty measurement theory. Chinese Journal of Rock Mechanics and Engineering, 2008, 27(2). 323-330.

RaSiM 7(2009): Controlling Seismic Hazard and
Sustainable Development of Deep Mines,
C.A. Tang(ed), Rinton Press, 209-214

STUDY ON TEST METHOD AND FORMATION MECHANISM OF CLASS Ⅱ ROCK BEHAVIOR

SHAO-JIE CHEN, FA-ZHU LI, WEI-JIA GUO and YONG-JIE YANG

Key Laboratory of Mine Disaster Prevention and Control，Shandong University of Science and Technology

Qingdao, 266510, P.R. China

FA-ZHU LI, ZHI-QIANG PU

Daizhuang Colliery, Zibo Mining Group Co., Ltd

Jining 272175 , P.R. China

Class Ⅱ curve is the manifestation of rock sample' unstable failure, which is important for the prediction of geotechnical engineering calamities such as rock burst etc.. In this paper, several typical sedimentary rocks' class Ⅱ curves are obtained by combined loading control mode of axial-displacement and circumferential-displacement on MTS test system. The formation mechanism of class Ⅱ curve is analyzed based on test results. The occurrence of class Ⅱ curve needs two conditions. The first one is appropriate loading mode. The circumferential displacement should be used as the loading control variable in sample failure process. The second condition is that the rock presents brittleness property and can amass some elastic energy. Only when the variable with maximum change rate is used as the loading control parameter in different stages of the whole stress-stain curve, the class Ⅱ curve may be obtained. For the post-peak phase of class Ⅱ curve, the elastic energy amassed in the rock can cause the sample collapse, when the circumferential displacement increases rapidly without loading. In the meantime, if the loading rate of circumferential displacement is less than the change rate caused by its broken down, the MTS will unload. At the same time, the sample failure caused by elastic energy released makes the circumferential strain increasing and the axial strain reducing. Rock samples with the same mechanical properties are characterized as Class I or Ⅱ， which are controlled by different loading control mode.

1 Introduction

The complete stress-strain curves under uniaxial compression can reveal the mechanical properties of rocks. This test is clearly formulated in "Proposed Methods for Rock Mechanics Testing" [1] of ISRM and in "Rules of Rock Mechanics Testing" [2,3]of Chinese Ministry of Coal, Ministry of Water Resources and other departments. Cube or cylinder samples are loaded with an axial compression force of a specific frequency until the force reaches a specific level or the sample fails, and then the force is recorded to monitor sample failures. The loading can be controlled with strain or stress. Axial displacement control is instead used to stop loading after the sample failure or test halt. Rock's axial compressive strength and deformation tests are defined definitely but no uniaxial post-failure or complete stress-strain tests in those proposed methods and rules. In general, the complete stress-strain curves can be divided into two types as class Ⅰ and classⅡ, as shown in Figure 1.

Class Ⅰ and classⅡcurves of rocks under uniaxial compression perform visually with a variety of different properties, formation of which depends on several factors such as rock's mechanical characteristic, tester's property and loading control mode, etc. In order to obtain a classⅡcurve, many researchers have used different methods to control loading. Some researchers studied on class Ⅰ especially classⅡcurves and obtained those through experimentation in foreign [4-7]. Domestic researchers made some researches on classⅡcurves with numerical simulation or response modes instead of experiments [8-12]. ClassⅡcurve is the performance form of rock unstable failure, and the studying about it is very important for the prediction of geotechnical engineering calamities such as rock burst etc.

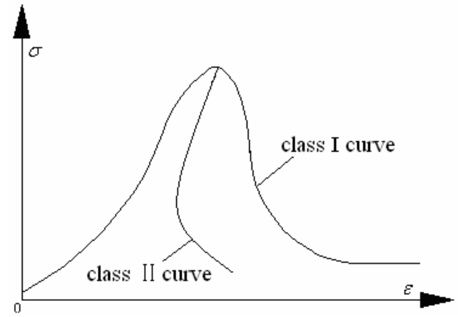

Figure l Complete stress-strain curves of rocks under uniaxial compression

2 Test conditions

Uniaxial compression tests controlled with stroke show that the process of rock destruction takes place in 1S [13,14]. It is not easy to properly control displacement to make the rock smooth failure, and it is very difficult to obtain classⅡcurves in experiment.

Table 1 Dimensions and mechanical parameter of samples

	Loading controlled with axial displacement; classⅡcurves prospected					Loading controlled with circumferential displacement; classⅡcurves prospected				
lithology	serial number	diameter (mm)	high (mm)	elastic modulus (MPa)	uniaxial compressive strength(MPa)	serial number	diameter (mm)	high (mm)	elastic modulus (MPa)	uniaxial compressive strength(MPa)
limestone	L11	49.5	98.96	18826.62	101.7944	L21	49.5	99.94	18927.88	93.2834
	L12	49.5	102.10	19709.77	102.4660	L22	49.5	100.13	16820.65	82.4385
	L13	49.5	99.90	18095.28	97.4575	L23	49.5	100.50	18404.01	92.1597
	L14	49.5	97.60	18474.01	82.1945	L24	49.5	97.82	17857.32	74.6132
	L15	49.5	98.72	18654.19	85.2297	L25	49.5	100.18	18509.86	82.5586
sandstone	S11	49.2	100.68	10501.62	68.6411	S21	49.2	100.23	11020.94	70. 9166
	S12	49.2	100.24	13445.74	75.5002	S22	49.2	100.34	10195. 38	60. 3022
	S13	49.2	100.00	10271.77	69.0075	S23	49.2	99.90	10746.89	63.5573
	S14	49.2	100.38	10136.76	67.4908	S24	49.2	100.25	9813.17	58. 2985
	S15	49.2	100.78	9977.12	63.8973	S25	49.2	98.89	10494.83	65. 1607
coal	C11	49.2	100.80	1641.02	10.5022	C21	49.2	100.19	2001.93	9.2899
	C12	49.2	100.70	1552.68	9.1901	C22	49.2	99.53	1828.31	8.3418
	C13	49.2	100.20	1532.66	8.1386	C23	49.2	97.83	1363.62	7.9956
	C14	49.2	100.72	2178.42	12.0677	C24	49.2	98.60	1257.14	6.5704
	C15	49.2	100.16	1743.43	11.4405	C25	49.2	99.20	1508.28	7.3145
red sandstone	RS11	48.6	100.40	1310.60	5.5502	RS21	48.6	100.32	1187.94	6.1433
	RS12	48.6	100.02	1289.58	5.4966	RS22	48.6	100.61	1306.61	6.2680
	RS13	48.6	100.43	1323.21	5.7814	RS23	48.6	100.37	1295.63	6.2248
						RS24	48.6	100.29	1274.98	6.1915

Remark: The red sandstone sample of RS21# puts up classⅡcurve loaded with circumferential displacement control.

These tests are carried on with servo-hydraulic test system of MTS815.03 which is produced in company MTS of USA. Its stiffness of load frame with 10.5×109N/m stores wee elastic energy then actualizes rigid compression tests. Data are collected automatically with full computer control and the minimal mum sampling time is 50 μs . Tests can be controlled by load or axial displacement or circumferential displacement.

In order to study classⅡcurve bitterly, four kinds of typical sedimentary rocks are tested in this paper. Those are collected in Jining mining area as limestone, sandstone, coal and red sandstone with favorable homogeneity。Rock samples are cylinder with diameter of 48.6 ~ 49.5mm and high 97.60 ~ 102.10mm, as shown in Table 1.

Under loading controlled with axial displacement, the axial strain is increasing, and the classⅡcurve can't be obtained during the whole test. In order to study rock's natural failure progress and gain classⅡcurve, the sample is loaded with the combined control mode axial displacement & circumferential displacement. Firstly, the sample is loaded slowly with axial displacement control until there is obvious circumferential displacement in it, then the load switch into circumferential displacement control. The circumferential strain increases more rapidly than that of axial strain and the loading with circumferential displacement control can make the sample destroy relative stability in sample's failure progress. Furthermore, the class I curve is obtained with axial displacement control mode completely in the tests. Test method and formation mechanism of lassⅡcurve can be analyzed combined with the two kinds of curves. In order to minimize the impact of discrete of sedimentary rock, the samples with same lithology are collected in the same region and same stratum.

3 Class Ⅱ curve compression test and results analysis

3.1 Uniaxial compression tests of typical sedimentary rock

J.A.Hudson[4] obtained rock's classⅡcurves of stress-strain on servo system controlled with the feedback signal of lateral displacement or displacement. M.Terada[5] obtained classⅡcurves with the control parameter of acoustic emission rate. S.Okubo[6] obtained classⅡcurves with the feedback signal of non-elastic volume strain rate also. S. Okubo and Y. Nishimatsu [7] obtained class I andⅡcurves with different parameters of linear combination feedback signal of stress – strain.

In this paper, class I curves of four kinds of typical sedimetary rocks are obtained under uniaxial compression controlled with axial displacement of 0.01mm/s, class Ⅱcurves of those rocks are obtained with combined control of axial-dis & circumferential-dis. During class Ⅱ curve test, loading is controlled with axial displacement firstly and switched with circumferential displacement while the change speed of circumferential displacement is closely to the predetermined value. The speeds of axial and circumferential displacement are both 0.005mm/s.

3.2 Test results

Elastic modulus and uniaxial compressive strength of each sample tested are listed in Table1.

Limestone and sandstone perform obvious elasticity and brittleness commonly. Those samples are tested straightway after processed, and class Ⅱ curves of five limestone specimens and five sandstone specimens are obtained with combined control of axial-dis & circumferential-dis. Typical class I andⅡcurves of limestone and sandstone are respectively shown in Figure2 and Figure3.

Coal and red sandstone have considerable plasticity themselves, and then it is difficult to obtain classⅡcurves of those rocks. In order to study the test method and formation mechanism of lassⅡcurve better, the coal samples soak in water for 18 hours and the red sandstone samples soak in water for 45 hours, which can reduce their strength and brittleness and increase plasticity. Under these conditions, class Ⅱ curves of five coal specimens and three red sandstone specimens are obtained but those characteristics of class Ⅱ are not obviously. Typical class I andⅡcurves of coal and red sandstone are respectively shown in Figure4 and Figure5 . The C22# coal curve characteristic of classⅡ is very inconspicuous, as shown in Figure 6. At the same time, the sample of RS21# red sandstone has class I curve, as shown in Figure7.

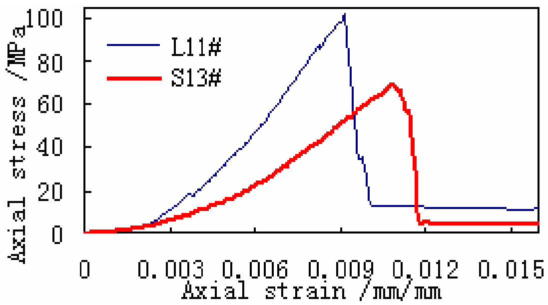

Figure 2 Typical class I curves of limestone and sandstone

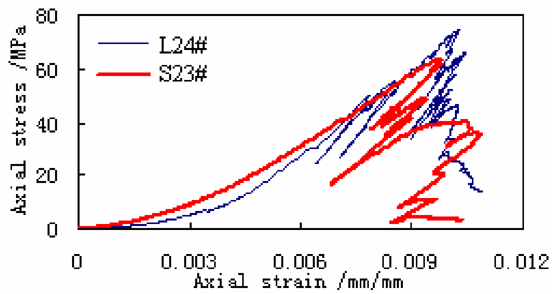

Figure 3 Typical class Ⅱ curves of limestone and sandstone

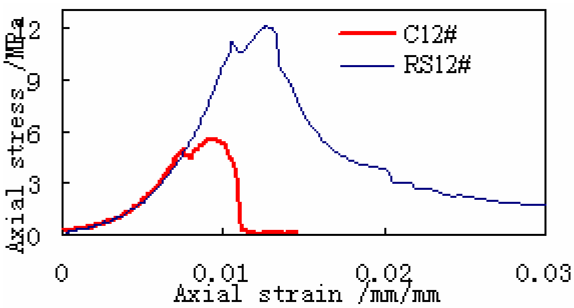

Figure 4 Typical class I curves of coal and red sandstone

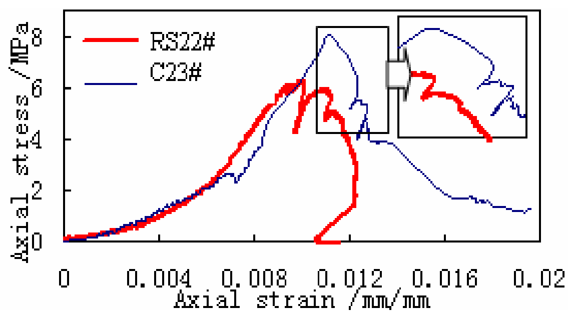

Figure 5 Typical class Ⅱ curves of coal and red sandstone

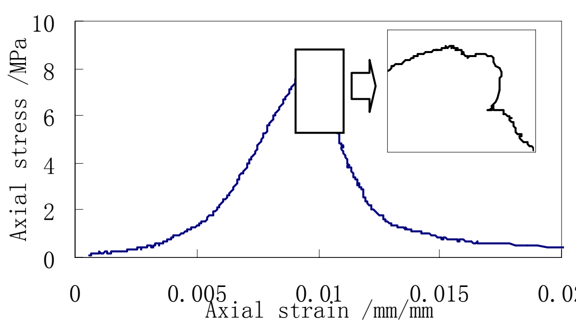

Figure 6 Class Ⅱ curves of C22# coal sample

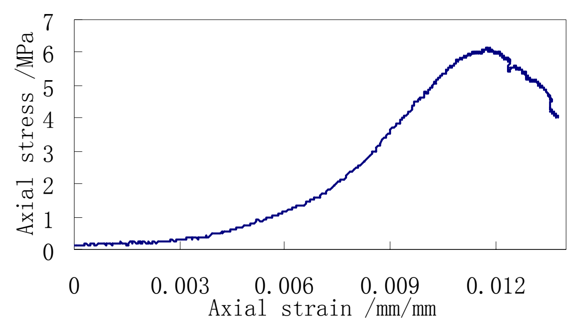

Figure 7 Class Ⅱ curves of RS21# red sandstone sample

3.3 Analysis of test results

In this paper, 19 samples of limestone, sandstone, coal and red sandstone are tested under uniaxial compression of class Ⅱ curve, and the results is comparatively perfect. Those soft rocks of coal and red sandstone have class Ⅱ curves after soak also. Only one sample of red sandstone with lower elastic modulus and strength after soak 45 hours has class I curve even loaded with combined control of axial-dis & circumferential-dis slowly. On the whole, the combined loading control mode of axial-dis & circumferential-dis is a simple and feasible method for class Ⅱ curve of rock.

We can discover that from class I and Ⅱ curves of same lithology rock samples as below. Rock samples with the same mechanical properties are characterized as Class I or Ⅱ, which are controlled by different loading control mode. Axial displacement control and circumferential displacement control are respectively used before and after sample entering in plastic phase to load on sample, then the class Ⅱ curve can be obtained. However, limestone, sandstone, and other significant brittle rocks break down frequently in split second. It is difficult to obtain smooth stress-strain curves of brittle rock.

We can discover that from class Ⅱcurves of different lithology rock samples as below. Brittle rock with high elastic modulus and strength is prone to be characterized as classⅡ. Along with elastic modulus and strength reducing, the classⅡcharacter weak rock become inconspicuously gradually. While both elastic modulus and strength are very low, the rock sample is almost characterized as no-brittle. It is difficult to obtain classⅡ curve of this kind rock regardless of which load control used.

The macro failure of rock is made from a large number of discrete micro- ruptures accumulating. Those micro- ruptures occur before and after the peak of the whole stress-strain curve. Each brittle micro- rupture may bring the shape of class Ⅱ,just as micro- rupture before the peak of L24 # limestone sample in Figure3 and after the peak of C22 # coal sample in Figure6.

4 Formation mechanism of class Ⅱ curve

There are two different views on class Ⅱ curve[14]. Some researchers consider that class Ⅱ curve is not real and it is the feint caused by improper load control method or lack of feedback sensitivity of tester. Others think that class Ⅱ curve does exist. It marks the instability spread of material destroy and break, and it is inherent mechanics property of some materials.

Elastic energy is accumulated in the progress of rock sample pressed. The test results show that class I and Ⅱcurves are stable or unstable failures of rock samples. The occurrence of class Ⅱ curve needs two conditions. The first is appropriate loading mode. The circumferential displacement should be used as the loading control variable slowly in sample failure process. Second, the rock possesses brittleness property and can amass some elastic energy. Only the variable with max change rate is used as the loading control parameter in different stages of the whole stress-stain curve, the class Ⅱ curve may be obtained.

While sample turn into post-peak phase of class Ⅱ curve, the elastic energy amassed in itself can lead it break down, and the circumferential strain increases rapidly without loading. Its rate is far greater than that of axial strain. When the loading rate of circumferential strain is less then the change rate of axial strain, it less then the change rate caused by destruction also, though the sample is loaded as the circumferential displacement increasing. This progress is not loading but unloading on sample. At that time, the tester indenter unloads on sample. At the same time, the sample failure caused by elastic energy releasing makes the circumferential displacement increase（circumferential strain increase）and the axial displacement increase (axial strain reduces). Since the failure progress is discontinuous, rock especially brittle rock samples have repeated loading and unloading courses. Class Ⅱ curve is essentially obtained in the unloading phase during brittle rock being pressed to destroy.

Class Ⅱ curve is the manifestation of rock sample unstable failure. The character degree of class Ⅱ indicates the feasibility of that rock burst occurs in the geotechnical engineering this lithology. The study about it is very important for the prediction of geotechnical engineering calamities such as rock burst etc. For example, the failure time of coal is regarded as an important judging standard of rock burst orientation at home and abroad.

5 Conclusions

(1) Class Ⅱ curve of rock can be obtained with the combined control load mode of axial-dis & circumferential-dis on MTS. Only the variable with max change rate is used as the loading control parameter in different stages of the whole stress-stain curve, the class Ⅱ curve may be obtained.

(2) Class I and Ⅱcurves are stable or unstable failures of rock samples. Rock samples with the same mechanical properties are characterized as Class I or Ⅱ， which are controlled by different loading control modes.

(3) Class Ⅱ curve is essentially obtained in the unloading phase during brittle rock being pressed to destroy. The occurrence of a class Ⅱ curve needs two conditions. The first is appropriate loading mode. The circumferential displacement should be used as the loading control variable slowly in sample failure process. Second, the rock possesses brittleness property and can amass some elastic energy.

(4) Along with elastic modulus and strength reducing, the classⅡ character weak rock became inconspicuous gradually. While both elastic modulus and strength are very low, it is difficult to obtain classⅡ curve of this kind rock regardless of which load control used.

Acknowledgements

Supported by NSFC(50874070) and Naturl Science Foundation of Shandong(Y2008F01) and Open Foundation Subject of State Key Laboratory For Geomechanics & Deep Underground Engineering(SKLGDUE08002X) and Research Project of "SUST Spring Bud" (06540040108).

References

1. Test Standardization Committee in Lab and Field of International Rock Mechanics Academy. Proposed Methods for Rock Mechanics Testing. Coal Industry Publishing House,1982.
2. Ministry of Geology and Mineral People's Republic of China. Geological Publishing House, 1988.
3. Ministry of Water of Resources People's Republic of China . Program Publishing House of China, 1999.
4. Hudson, J.A., Brown, E.T.and Fairhurst, C. Optimizing the control of rock failure in servo-controlled laboratory tests. Rock Mechanics, 1971,3. 217-224.
5. Terada M, Yanagitani T, Ehara S. AE rate controlled compression test of rocks . In:Proc. The 3rd Conf. on Acoustic Emission Micro seismic Activity in Geologic Structures and Materials.Clausthal: Trans. Tech., 1984. 159-171.
6. Okubo S, Terada M, Ehara, S. A study on the time dependent micro fracturing and strength of Oshima granite. Tectonophsics,1982, 84. 343-362.
7. Okubo S, Nishimatsu Y. Uniaxial compression testing using a linear combination of stress and strain as the control variable. International Journal of Rock Mechanics and Mining Sciences and Geomechanical Abstracts, 22(5): 323-330.
8. Pan, P.Z., Feng, X.T.and J.A. Hudson. Numerical simulations of Class I and Class II uniaxial compression curves using an elasto-plastic cellular automaton and a linear combination of stress and strain as the control method. International Journal of Rock Mechanics and Mining Sciences, 2006,(43). 1109-1117.
9. Wang, M.Y., Yan, D.J.and Zhou, Z.S. et al. Discussion on complete stress-strain curves of rocks under uniaxial compression.Chinese Journal of Rock Mechanics and Engineering, 17(1). 101–106.
10. Li, X.K.and CescottoS. Finiteelement analysis for gradient plasticity and modeing of strain localization. Acta Mechanica Sinica, 28(5). 575–584.
11. Pan, Y.S., Xu, B.Y.and Wang, M.Y. Study on plastic strain gradient and class II behavior of rock. Chinese Journal of Geotechnical Engineering, 21(4). 471–474.
12. Qian, J.S.and Wu, K.R. The experimental and numerical studies on Classes I,II fracture mode on concrete. Journal of Chongqing Institute of Architecture and Engineering, 15(4). 79–88.
13. Chen, S.J., Guo, W.J.and Yang, Y.J. et al. Experiment on rock burst orientation of coal seam. Mining Safety & Environmental Protection, 34(2). 10-14.
14. You, M.Q. Strength and Deformation Failure Progress of Rock Samples, Beijing: Geological Publishing House. 2000.

RaSiM 7(2009): Controlling Seismic Hazard and
Sustainable Development of Deep Mines,
C.A. Tang(ed), Rinton Press, 215-222

IMPLEMENTATION OF THE GARFORD DYNAMIC BOLT AT KANOWNA BELLE MINE

RICHARD P VARDEN
Senior Geotechnical Engineer
Kanowna Belle Mine
Barrick Gold Corporation
Kalgoorlie Western Australia 6430

Kanowna Belle is a high risk seismically active mine, the introduction of the Garford Dynamic bolt has given confidence to the design and control of this seismic risk through the specific engineered design of the bolt. Since the introduction of the bolt there has been a significant learning curve resulting in a well installed bolt in a high seismic risk environment. The paper starts with a summary of the bolt design processes, first reported in [5] then moves on to the implementation of the bolt and learning's over the past few years. The concept of placement of the bolt is to target high risk seismic areas, these being mainly when development intersects structures and in ore drive development ahead of a stoping front. The majority of bolts placed to date are in the lower part of the mine where stoping is not yet advanced and no significant events have occurred, only one significant event has occurred close to an area supported with Garford Dynamic bolts, but little damage occurred. From overcoring of the Garford Dynamic bolt it has been deduced that the dynamic mechanism does work, but is dependent on installation and resin mixing quality.

1 Introduction

1.1 Overview of Kanowna Belle Mine – Location, Geological Setting and Mining Method

The Kanowna Belle Gold Mine is located 18 km NE of Kalgoorlie and 2 km west of the historic gold mining centre of Kanowna, Western Australia.

The Kanowna Belle deposit is hosted by sedimentary volcaniclastic and conglomeratic rocks, which are separated into hangingwall and footwall sequences by a major, steeply SSE dipping zone of structural disruption. The orebody strikes East West, varies from 5 – 50 m in width with an average dip of 65°. The strike length is 500 m with a down- plunge extent greater than 1400 m.

The main structural feature of the deposit is the Fitzroy fault, varying width and dip – a undulating feature dipping on average 65° and is gouge filled in some areas, but mainly a zone of highly broken rock. The fault forms the footwall in A,B and C block and the hanging wall of the ore zone in D and E block and this is encompassed by a footwall and hanging wall shear zone, which can be up to 30 m wide. Three felsic units occur in the footwall, which terminate at the Fitzroy fault. A number of splay structures off the fault exists. These are sub-parallel to the fault and occur either side of the fault. They are substantial in length and down dip strike. Figure 1 shows a plan view of the generalised geology for Kanowna Belle. [1]

The mine has been split into five mining blocks, A block – mined out, B – partly mined, C – currently mining almost complete, D – currently mining, E – developing. The mining method is long-hole open stoping, with 30 m sublevels. Sequencing is centre out bottom up with paste fill.

The rockmass has an intact rock strength measured between 90 to 140 MPa. Up to 4 joint sets are present throughout the mine with local areas (stopes) having 2 to 3 joint sets. In general the rock mass can be described to be fair to very good, with the exception of the Fitzroy fault being very poor, [2].

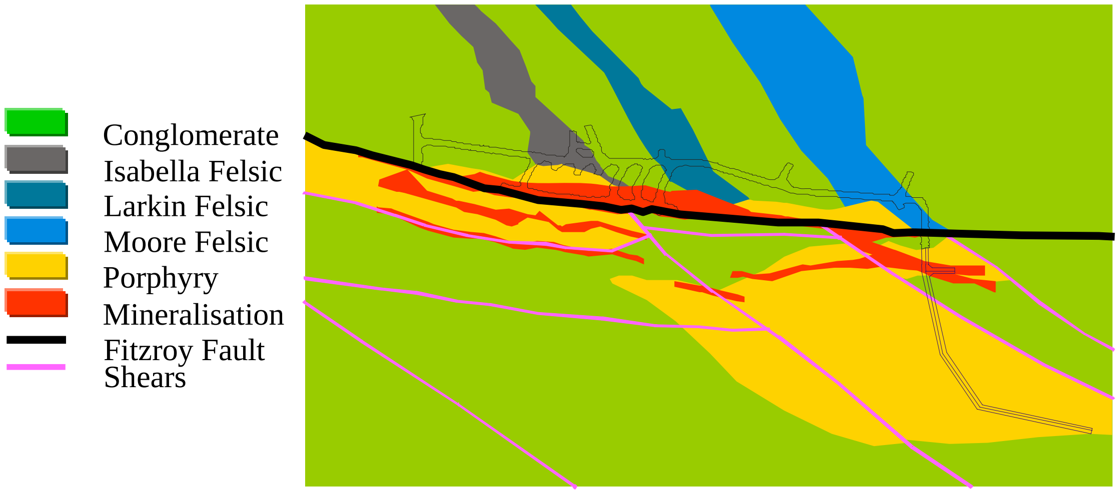

Figure 1 Generalised geology of Kanowna Belle.

The major principal stress at 1000 m is 75 MPa and is horizontal (124/06). In general walls are more affected by stress than the backs. This due to the high horizontal stress acting on the walls, whereas the backs, with an arched profile, are in compression and have been stable in observed seismic events.

2 Review of the Development and testing results of the Garford Dynamic Bolt

The development and test work carried out on Garford Dynamic bolt has been reported on in the paper Development and Implementation of the Garford Dynamic Bolt at the Kanowna Belle Mine presented at The Australian Institute of Mining and Metallurgy in April 2008 [3]. This section summarises this work so as to give an understanding to the reader of the implementation of the bolt.

2.1 Technical description of the Garford Dynamic bolt

Figure 2 shows the Garford Dynamic bolt now installed at Kanowna Belle. The bolt consists of a 24 mm mild steel solid bar with a M24 thread. The resin mixing devices is 350 mm long, 43 mm in diameter coarse threaded steel sleeve crimped on to the end of the bolt. The dynamic section is a Patented sliding anchor mechanism that is pressed on to the bolt below the mixing device.

The remainder of the bolt is covered in a polyethylene sleeve; this de-bonds the bolt behind the dynamic section. When the bolt is subjected to a ground movement the bolt is forced through the constriction and elongates.

2.2 Summary of WASM testing on the Garford Dynamic bolt

The Western Australian School of Mining (WASM) was commissioned by Kanowna Belle to test Garford Dynamic bolt in their dynamic test facility,[4][5] . The objectives was to test the static and dynamic abilities of the bolt, compare resin verses cement grout and to assess the bolt for weakness and consistency of performance.

Tests were carried out in simulated boreholes into which, bolts were installed with a jumbo [5]. Two configurations of the Garford Dynamic bolt were tested. The second configuration was based on recommendations by A. Thompson [6] made to the first bolt configuration. Two main technical issues were identified. The first related specifically to the pull of the bar through the anchor ferrule without achieving the tensile strength of the element. The second issue related to the generally poor implementation of resin bolts in the underground metalliferous mining industry. [7]

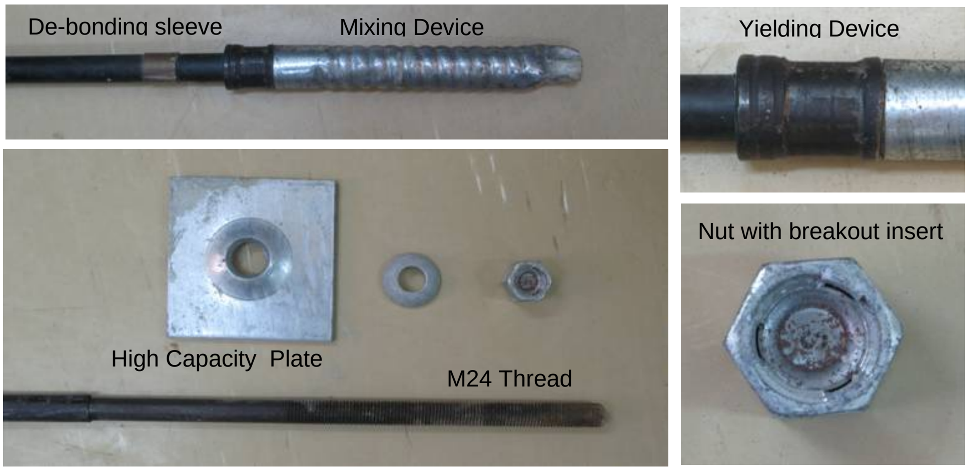

Figure 2. The Garford Dynamic bolt.

2.2.1 Dissection of simulated boreholes

The simulated boreholes with jumbo installed and resin encapsulation bolts were dissected after dynamic loading. This examination showed;

- the mixing device was very effective, however best performance was achieved by rotating the bolt and slowly pushing the bolt through the entire length of the resin,
- an over-drill allowance of 100mm to 150mm at the end of the hole allowed the resin bag to move to the end of the hole and not wrap around the mixing device,
- A resin length of 240mm below the yielding device on the bolt was sufficient to break the shaft of bolt once the end stop mechanism was reached.

It is highly recommended that readers read a copy of the paper [7] by the R. Varden et al, which describes the testing of the bolt in more detail.

3 Support System Design

3.1 Bolt pattern

Figure 3 Shows the support design issued. The standard pattern is 0.75 m staggered pattern for the side walls and 1.2 m x 1.5 m spacing in the backs.

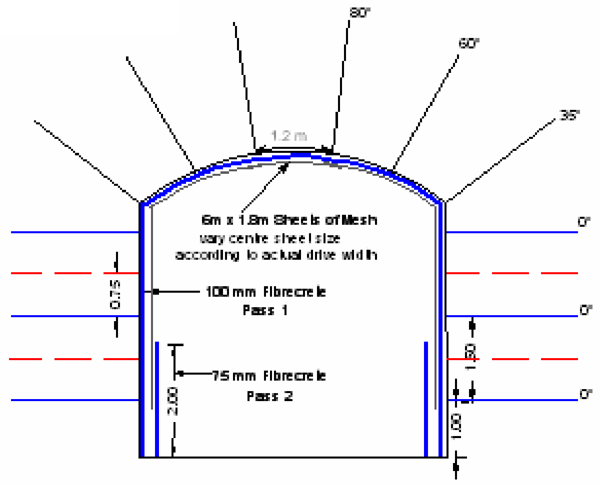

Figure 3. Support layout for Dynamic support

Bolting patterns were calculated from a range of ejection velocities resulting in residual energy demand for the bolt. This was then used to rate the bolt stability at probably damage/ground movement expected. These calculations were based on observed depth of damage ranging from 1 m to 1.5 m. [7]

3.2 Design criteria

Backs: Arched excavation shape and key blocks locked in by in-cycle fibrecrete, 100 mm thick. Empirical observations shows that historic dynamic failures mainly occurs along the walls. High horizontal clamping stress act to clamp backs together.

Walls: not locked in by an arched shape, but allowed to deform into opening, i.e. potential to 'flap' in a dynamic situation. Relaxation occurs along walls, allowing a seismic event to push blocks into the opening. If the wall integrity is maintained, the arched shape is maintained improving stability of the backs. Historically seismic damage has been mainly along development walls to a maximum observed depth of 1.5 m.

3.3 Surface support design

Fibrecrete has been designed to be sprayed to 100 mm on the first pass and the mix is a high strength 550 KJ and high fibre content 45 Kg of steel fibres. The justification behind this is to spray the best possible mix to suit short term and long term strength requirements. 28 day strength is 40 MPa, with 1 day strength typically reaching 18 MPa and greater. The second pass of fibrecrete to 2 m above the floor is for protection of the lower bolts and mesh from equipment damage.

The mesh used is a standard mesh size used in Australia, 5.6 mm wires with a 100 x 100 mm aperture. Mesh is from the lowest wall bolt, 1 m above the floor, to the lowest bolt on the other wall. The mesh is placed over the fibrecrete, this is, in an event that results in ejection, allows the broken fibrecrete to be retained.

3.4 Placement strategy

Kanowna Belle's strategy for placement of dynamic support is by analysis of seismic risk of specific area, this is covered in more detail in paper [7]. Essentially dynamic support is placed on and around structures that are seismically active. For example the felsic contacts are a known source of seismicity and these contacts are known and instructions for dynamic support are issued before these contacts are intersected. In areas where the structure is not known, but seismic monitoring indicates a structure support instruction can be changed to dynamic support. Dynamic support can be "turned on and turned off" as required.

4 Bolt Implementation at KB

The Garford dynamic bolt has been used at Kanowna Belle for last two and a half years. Since installation was first started there has been a large improvement in the quality and operator ability. The paper [5] outlined a number of installation issues, these are listed below with solutions and the current state of installation quality. Other implementation issues and design issues have been reported. The bolts are also being installed at the Raleigh mine and these problems have also been reported. The Raleigh operation uses similar equipment, but drive dimensions are different, however some of the problems are relevant to Kanowna belle and have been reported in this paper.

4.1 Installation issues reported in [7] and performance to-date:

- Operators unfamiliar with bolts, leading to poor installation: this has mainly been a matter of time to gain experience with the installation method. The main problems with operator installations are:
    - Bolt being bent before being fully installed due to miss alignment of the bolt and hole.
    - Resin setting before bolt fully installed due miss alignment, not enough feed rate.
    - Plastic sheath stripping off – miss alignment of bolt, catching on mesh and or on plate.
    - Resin not setting – either under spun or over spun, operator not spinning for specified time.
- Other problems not directly related to operator error:
    - The plate, 200 x 200 mm was found to damage the mesh, especially on irregular surfaces.
    - Medium set resin often resulted in operators trying to break out the nut before the resin had set. Mixing with medium set resin took at least 1 minute and 40 seconds, this is likely due to the large annulus of the hole to bolt diameter: 46 mm to 24 mm on the bar.
    - Operators unable to install bolts according to the required bolting design due to the machine installing the bolts being unable to install low bolts.
    - At the over lap between cuts an additional bolt is required for the new sheet of mesh. Initially an additional Garford yielding bolt was used, but after review it was considered that the first Garford bolt, i.e., the bolt installed at the face of the previous cut was sufficient in controlling ground movement. For the overlap a 3 m friction bolt is now used.
    - When installing 3 m bolts it was found that the mixing mechanism was not turning, but the bolt was tuning inside the mixing mechanism resulting in the resin not mixing.
    - In seismically damaged ground, (this refers to an area that was damaged during development before the implementation of the dynamic bolts), it was not possible to install the dynamic bolts due to collapsing of the holes.

4.2 Modifications and changes to the system

- The high- load plate was attached to a "butterfly" plate, 400 x 278 mm to increase the area in contact with the mesh.
- Fast set resin introduced. This has allowed operators to install more quickly and has improved their confidence and ability to install bolts to a higher standard.
- The use of an "augur" spiral drill steel has allowed drilling through and cleaning holes in poor ground to be improved allowing installation of resin and the bolt.
- In an area where rehabilitation was being carried out the operator would drill all the holes, install all the resin and then start installing the bolts. This resulted in many bolts not being installed properly due to collapsing holes and additional bolts had to be installed. When a bolt is installed it is important to drill, insert the resin and then install the bolt before moving on to the next hole.
- The low sidewall bolts were originally designed to be installed at 0.5 m above the floor. This was changed to 1 m due to the boom arrangement not allowing the bolt to be installed lower than this. When friction bolts are installed a bolt at 0.5 m is feasible due to the installation dolly arrangement.
- The mixing mechanism was spot welded onto the bar. Previously the mixing mechanism had only being crimped on to the bar. This spot welding is only sufficient to prevent the mixing device from rotating and does not interfere with the dynamic capabilities of the bolt.
- De-bonding sheath retaining device was modified to reduce the chance of the plate catching on it and ripping the plastic off during installation.

4.3 9560 OD94 installation failure and subsequent solutions

The 9560 ore drive was subjected to several large damaging seismic events during development. This occurred before the Garford dynamic bolts were brought to site. Before stoping was started in this area it was recognised that the seismic risk was high and that this would be an ideal area to start implementation of the dynamic bolt. Some success was achieved on the 9590 level, (level above 9560), but the attempts on the 9560 and 9530 levels failed. This was due to the ground being broken and the holes subsequently falling in when the drill rod was withdrawn and the inexperience of the jumbo operators. The solution resulted in doubling of surface support, i.e. 75 mm of fibrecrete with mesh and friction bolts to 1 m off the floor – original support design, followed by and additional layer of 100 mm of high fibre content (40 kg/m^3 steel fibres) fibrecrete and mesh and friction bolts, with the lower 2 m sprayed with 75 mm fibrecrete.

The result of this "double" surface support was successful. Subsequent large seismic events ranging between 1.6 to 2.7 local magnitude resulted in little damage. Most of the damage was cracking of the fibrecrete, bulging of the sidewalls and ejection of the friction bolt plates. Rehabilitation was required on some of the events and this has consisted of re-bolting of bolts that lost their plates and re-fibrecreting, meshing and bolting the worst areas.

5 Quality Assurance and Quality Control

5.1 Quality Assurance and Quality Control at Kanowna Belle

To determine that the Garford Dynamic bolt is functioning the supplier and the mine have developed a pull test that tests the dynamic, static and to an extent the installation quality. This test allows a small amount of movement to occur on the dynamic unit. This is kept to about 10 mm, which would not significantly change the performance of the bolt. In addition to onsite pull tests the manufacture is testing the dynamic unit at the factory at a rate of every 100 units.

Other QAQC systems used at the mine are regular inspections and auditing of the installation and installed product by on site geotechnical engineers. This includes the geotechnical engineer speaking to the operators to get feedback on the installation practices. This has resulted in several improvements to the system to be achieved and early detection of problems. Training has been provided by the supplier and by site geotechnical engineers.

5.2 Overcoring test work from Raleigh Mine

Raleigh, a joint venture operation owned by Barrick and Rand Tribune in Kalgoorlie, also uses the Garford Dynamic bolt. In a recent overcoring program of standard resin grouted bolts (Posimix Bolts), two Garford yield bolts were over-cored, in addition two additional tests were conducted at WASM. WASM undertook the overcoring and test work of all bolts. Below is the conclusion of the tests conducted on the Garford yielding bolts.

Results[8]:

- In general it can be concluded that the yielding mechanism is working, but integrity of the resin is critical to ensure a fixed point that allows the mechanism to be mobilised
    - Poor mixing can result in: dynamic unit not being encapsulated, not encapsulated behind unit, poor resin, layered resin – multiple layers – poor load transfer
    - De-bonding proportion works, less than 1 ton developed
    - For one bolt the yielding mechanism functioned properly for 25 mm yield, then started to stretching the bar instead of yielding.

Figure 4 shows the load-displacement of the yielding unit, the insert shows the yielding mechanism and yielded bar after testing

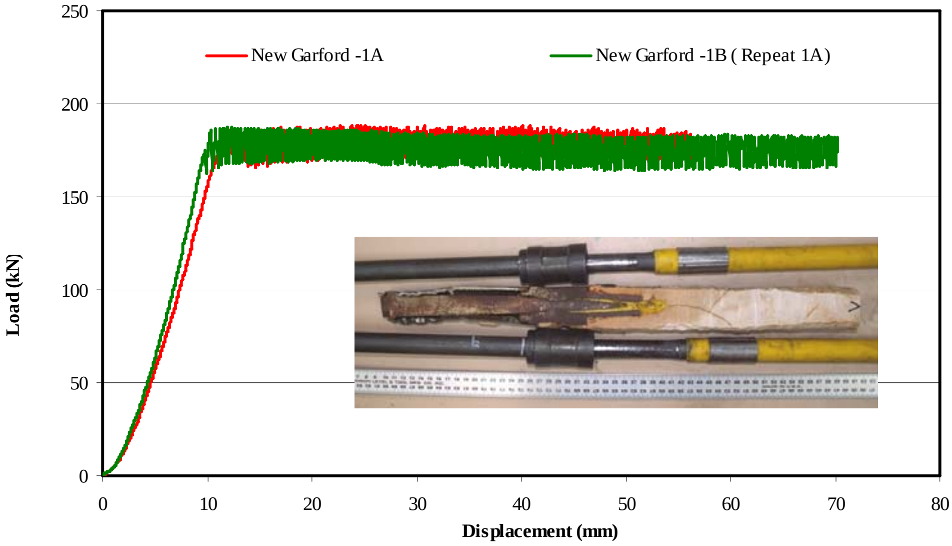

Figure 4. Load- displacement results for Garford bolt mechanism [2]

6 Even at the 9470 OD18

To date there has been no significant seismic event to conclusively test the Garford Dynamic bolt. The majority of installations has been in the lower section of the mine where future stoping is expected to result in seismicity. Additionally in combination with improved development layout design and sequencing the seismic risk has been reduced in many areas. There has been one large event resulting in some minor damage, which may well have been far more significant if dynamic bolts had not been installed. This occurred on the 9470 ore drive 18 immediately after the mass blast of the DA1644 stope. The result was up to 1.5 m of floor heave to 10 m behind the stope and cracking of the fibrecrete in the sidewalls. It is likely that the level of support did reduce damage, as friction bolts may well have had their plates ejected and the 75 mm shotcrete may have broken up more. Some minor rehabilitation would have been required, it so happened that no rehabilitation was required. This area is very active and the risk for the next stope is high.

7 Conclusions

The Garford dynamic bolt is an engineered bolt that has been extensively tested, but performance is dependent on installation quality. Since the initial implementation of the bolt to the mine, the installation ability and techniques have been significantly improved by personnel installing the bolts. Several modifications have been made to the bolt design allowing a more effective installation and improving the overall system. The bolt has only been subjected to one event where minor damage occurred and no other significant event has occurred in areas where the bolt is installed. This is mainly due to most bolts being installed in areas where no stoping is occurring and where layout designs has changed allowing reduced risk of damage.

Acknowledgements

The author wishes to acknowledge the work conducted by WASM, especially John Player who conducted the dynamic test work. DSI, the supplier of the Garford bolts, especially Gary Davy with whom I had a number of discussions with. Ronald Lachenicht, colleague and mentor and Barrick Kanowna for the opportunity to implement the Garford bolt and publish this paper.

References

1. Beckett, T.S., Fahey, G.J., Sage, P.W. and Wilson, G.M. Kanowna Belle gold deposits in Geology of Australian and Papua New Guinean Mineral Deposits. Eds: D.A.Berkman and D.H. Mackenzie, 1998, 201-206, The Australian Institute of Mining and Metallurgy: Melbourne.
2. Hoek, E., Kaiser, P.K.and Bawden, W.F. Support of Underground Excavations in Hard Rock. 1997 A.A. Balkema, Rotterdam.
3. MERIWA Project, M349a, 2005, Dynamic testing of support for underground mines-project sponsored by industry and MERIWA, conducted by Western Australian School of Mines.
4. Player, J. Dynamic Testing of Garford Yielding Solid Bolt for Barrick - Kanowna Belle Kalgoorlie, WASM-Curtin University, 2007.
5. Player, J. Dynamic testing of Jumbo installed Garford Yielding Solid Bolt into simulated boreholes for Barrick-Kanowna Belle, Research Report, July 2007.
6. Thompson, A. and Player, J., Implementation of dynamic load resistant rockbolts at Kanowna Belle Gold Mine WAS School of Mines, 2005, Draft report.
7. Varden, R., Lachenicht, R., Player, J., Thompson, A., Villaescusa, E., Development and Implementation of the Garford Dynamic Bolt at Kanowna Belle Mine. The AusIMM 10th Underground Operators Conference, April 2008, Launceston, Tasmania.
8. Villaescusa, E., and Hla, Saw. A. Evaluation of resin grouted and Garford bolt performance using bolt overcoring techniques. CRC Mining Western Australian School of Mines Curtain University of Technology, January 2009, report supplied to Raleigh Mine Barrick.

RaSiM 7(2009): Controlling Seismic Hazard and
Sustainable Development of Deep Mines,
C.A. Tang(ed), Rinton Press, 223-228

INVESTIGATION OF THE COAL BUMP LIABILITY THROUGH MICROSCOPIC EXPERIMENTS

YAO-DONG JIANG, YI-XIN ZHAO and JIE ZHU

State Key Lab of Coal Resources and Safe Mining，School of Mechanics, Architecture and Civil Engineering，
China University of Mining and Technology, Beijing, 100083, P.R. China

The investigation on the mechanism of coal bumps is always one of the hot topics in the field of mining and rock mechanics all over the world. Coal mine bumps are sudden failures near mine entries which may expel large amounts of coal and rock into the face area and cause damages to underground openings and to equipments. Persistent bump problems not only threaten the safety of mine workers, but also have caused the abandonment of large coal reserves. Researchers have made a large effort to understand, anticipate, and control this kind of hazard and achieved lots of helpful results. This paper describes a series of microscopic experiments finished to analyze the relationship between bump-prone property and microstructureal characteristics of coal. The micro-process of unstable cracking in coal and the development process of coal bumps induced by propagation of fractures were analyzed systematically. Moreover, a bump liability indices based on the microstructure parameters of coal was proposed to determine the bump potential of coal.

1 Introduction

Coal bump is defined as a sudden release of the geologic strain energy that can expel large amounts of coal and rock into the face area, which has been recognized as a sudden catastrophic failure of coal. It can result in fatalities and injuries to underground workers and has caused serious problems to underground coal mining worldwide in the past 100 years. In the past ten years, coal bumps have increased in occurance with rapid development of coal mining in China. Statistics show that several decades of bumps accidents occurred and caused hundreds of fatalities and injuries in the period from 1997 to 2008. Coal bumps are historically one of the most dangerous damaging disasters to underground mining safety in China. The other three destructive damages are rock fall, coal and gas outburst, and water inrush. So understanding the mechanism of coal bumps becomes more and more urgent.

In recent years, many attempts have been made to understand the mechanisms of coal bumps [1~5] and methodologies were developed and proposed to predict the hazard based on seismicacoustic or electromagnetic emissions [6~8]. However, the investigations on the mechanism of coal bumps can be classified into three categories: first is theory analysis, which is composed of (1) system modelling by elastic-plastic theory [9~11] and Chaos or fractal theory [12] to analyze the bump process; (2) the evaluation on the potential liability of coal bumps triggered by geological structures, progressive mining and blasting based on the theories of strain localization and coal petrology [13~15]; and (3) the research on the features of accumulation and dissipation of strain energy by various indices. Second is the experimental research works conducted in laboratories, which are primarily concerned with the macroscopic physic-mechanical properties (i.e. bursting liability indices of coal) and the structure features of 'coal-surrounding rock' system [16~18]. Little attention is paid to the microscopic features of bump-prone coal. The third part is numerical simulation. Various kinds of numerical modelling codes are developed or adopted to analyze the mechanisms of coal bumps according to data from the geophysical and geomechanical survey [19~24]. The results of earlier investigations provided further knowledge of the process that occur in a bump, and could help to improve our understanding of coal bumps mechanism.

The objective of this study is to investigate the microscopic properties of bump-prone coal and the micro-process of unstable cracking in coal. A bump liability based on the microstructure parameters of coal is proposed to determine the bump potential of coal.

2 Experiments on the microscopic properties of bump prone coal

Previous investigations indicate that the microscopic properties and the micro-cracking features of coal affect the bump prone conditions significantly [25, 26]. Two experiments were conducted to analyze the relationship between bump-prone property and micro-structural characteristics of coal. In addition, the development process of coal bumps induced by propagation of fractures was analyzed systematically.

2.1 Microcracking features in bump prone coal

The Three Points Loading Test with the Scanning Electron Microscopy (SEM) observation was conducted to three samples from No.12 coal seam in Zhaogezhuang mine (Samples Num: ZGZ-TPL1, ZGZ-TPL2 and ZGZ-TPL3) and three samples from 8727# working face, No.11 coal seam in Xinzhouyao mine (Samples Num: XZY-TPL1, XZY-TPL2, XZY-TPL3). And a bump occurred just at 8727# working face after sampling. Fortunately, there was nobody working there at that time and the samples influenced by a bump can be collected from the site (Samples Num:XZYCH-TPL4 and XZYCH-TPL5). Figure 1 presents the load-stoke curves of three samples. The test results show that the failure of samples without any damages caused by bumps is characterized by brittle and sudden failure features, but the samples influenced by a bump are characterized as the viscous ductile failure. Moreover, the strength of the coal samples influenced by the bump is obvious decreased compared to the samples without being influenced by the bump, see Figure 1(b) and Figure 1(c). So it is proved that the thermodynamic process of coal bump do influence the internal micro-structures of coal. And according to the information from bump sites studies and the theories of coal petrology, coal bumps are always accompanied by repaid increasing of temperature in surrounding coal. So the generated heat and rapid release of strain energy can exacerbate the damage in coal mass and affect the physic-chemical properties of coal.

The several significant decreasing stages of load are shown in the load-stoke curves. The results illustrate the sudden propagation of micro-cracks and unstable cracking features in the coal specimen. The following features best explain the thinning out, propagation, influx and coalescence of cracks in the specimen:

(1) Microcracking initiates as the load increasing to the 20%~30% of the peak load. The initiation of cracks is generally adjacent to the primary defects where the stress concentrated or the weak zone connected different macerals, see Figure 2(a).

(2) The initiation and thinning out of cracks depended mainly on the variation of stress gradients. And the direction of crack tip and the propagation speed are determined by the magnitude of stress and micro-structures distribution in the specimen, shown in Figure 2(b).

(3) The nonlinear features such as bifurcation and chaos are found in the process of influx and coalescence of crack sets in the bump prone coal. And Figure 2(c) and Figure 2(d) present the mutual inhibition and competition of different crack sets in the failure process. It is revealed that the coalescence and propagation of main crack can induce the closure of other secondary cracks. In addition, the path of micro-cracking is concentrated in the stratification planes of specimen or the macerals with relatively smaller micro-hardness. The fractal characteristics are revealed in the geometrical features of cracking path.

(4) Based on the analysis of micro-cracking features in the bump prone coal, the Least Energy Consumption Principle can be adopted to describe the micro-process in the development process of coal bumps.

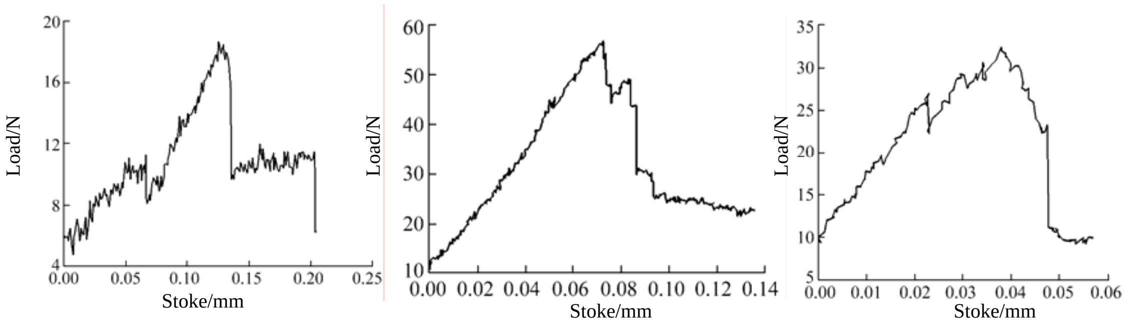

(a) (b) (c)

Figure 1 Relation curves between load and displacement in the three bending test for the specimens of (a) ZGZ-TPL2, from No.12 coal seam in Zhaogezhuang mine; (b) XZY-TPL1, from No.12 coal seam in Xinzhouyao mine; (c) XZYCH-TPL4, influenced by a bump, sampling from No.12 coal seam in Xinzhouyao mine.

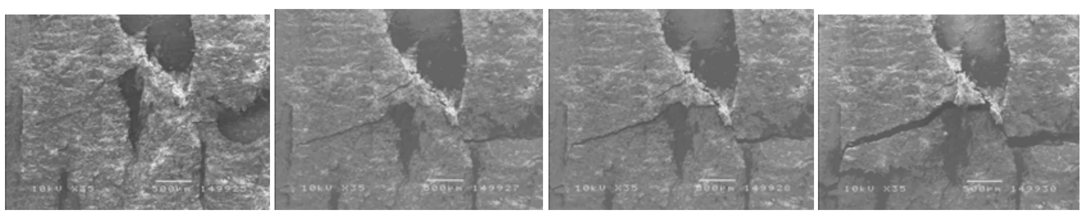

(a) P = 11. (b) P = 15.8 N (c) P = 18.7 N (d) P = 25.6 N

Figure 2 Crack propagation characteristics in the specimen of XZYCH-TPL4 with the loading increasing.

2.2 Maceral analysis on the bump prone coal

Thermodynamic process in the mining conditions is influenced by not only the unstable propagation of cracks, but also the macerals in the coal. So a bump liability indice ξ is proposed based on the analysis of the micromechanical properties of bump prone coal. The samples are from the No.7, No.9, No.12 coal seams in Zhaogezhuang mine and No.11 coal seam in Xinzhouyao mine. Table 1 illustrates the sampling features and positions. The X-Ray Diffraction (XRD) method was applied to achieve the diffraction pattern and XRD parameters of different coal samples. The comparison analysis was carried out to the bump-influenced coal and original coal. In addition, the macerals and the vitrinites reflectance in different samples were studied to analyze their influences to the properties of bump prone coal.

Table 1. Sampling positions and features description

Sample Num	Sampling place	Depth/m	Description*
ZGZ-M1	West 1# crosscut in 13 panel, No.9 coal seam, Zhaogezhuang	-1100	Coal and gas outburst prone seam
ZGZ-M2	West 1# crosscut in 13 panel, No7 coal seam, Zhaogezhuang	-1100	No outburst and bump liability seam
ZGZ-M3	East 4# crosscut in 12 panel, No12 coal seam, Zhaogezhuang	-1000	Extremely bump liability seam
XZYCQ1	8727# working face, No.11 coal seam,Xizhouyao (before a bump)	-300	Moderate bump liability seam
XZYCH1	8727# working face, No.11 coal seam, Xizhouyao (after a bump)	-300	Moderate bump liability seam

* The bursting liability of different coal seams were determined by failure duration index, energy index and bursting energy index [26].

Based on the theory of petrology, the microstructure features of coal are determined by the three parameters: the interlamellar spacing of aromatic layer (d_{002}), the average packing thickness of microcrystalline laminas (L_c), and the diameter of aromatic layer (L_a). These three parameters can be calculated by the following formula:

$$\left.\begin{aligned} d_{002} &= \frac{\lambda}{2\sin\theta_{002}} \\ L_c &= \frac{0.94\lambda}{\beta_{002}\cos\theta_{002}} \\ L_a &= \frac{1.84\lambda}{\beta_{100}\cos\theta_{100}} \end{aligned}\right\} \quad (1)$$

Where λ is the wave length of X ray, θ_{002} and θ_{100} are the peak positions of 002 and 100 peaks respectively (Unit is degree (°)), and β_{100}, β_{002} are the full width at half maximum of 002 and 100 peaks (Unit is radian).

Then the bump liability indices $\xi=(L_a-L_c)/L_c$ can be proposed to determine the bump potential of coal. And it is found that the bigger of ξ value, the more dangerous and liability to bump in the coal seam.

Test results show that the ξ values of ZGZ-M1, ZGZ-M2, ZGZ-M3, XZYCQ1 and XZYCH1 equal to 0.135, 0.154, 0.162,0.930, and 0.427 respectively, which indicate that coal bumps can be triggered more easily at No.11 coal seam in Xinzhouyao mine compared with other three coal seams in Zhaogezhuang mine even at the same geological and mining conditions. The results can also illustrate the reasons of the bumps occurrence critical depth in Xinzhouyao mine is just 300m, but ranges up to about 860m in Zhaogezhuang mine. It is also proved that energy dissipation in bump preparation process affect the mechanical properties of coal as the decreasing of ξ value in the bump influenced coal. Table 2 presents the macerals amounts in different samples. The results demonstrate that the samples composed of more vitrinites and inertinites have more potential to bump. Table 3 presents the vitrinites reflectance of different samples, which indicates that the maximum vitrinites reflectance (R_{max}) and the minimum vitrinites reflectance (R_{min}) are not sensitive to the bump prone indices separately. But the value of $|R_{max}-R_{min}|$ can be used to assess the bump liability: the smaller of the value of $|R_{max}-R_{min}|$, the less potential of coal bumps. Results also show that microstructure features can determine the bump liability and the historical stratigraphic evolution can be recorded by the microstructures in coal.

Table 2. The statistics table of macerals in different coal samples

	Sample Number	ZGZ-M1	ZGZ-M2	ZGZ-M3	XZYCQ1
Vitrinite	Desmocollinites	7.6	10.6	3.0	19.5
	Homocollinite	49.3	4.8	45.3	11.0
	Telinite	15.7	32.2	20.9	41.2
	Corpocollinite	4.7	7.4	2.6	3.7
	Vitrodetrinit	1.2	0.4		
Inertinite	Semifusinite	2.9	10.2	11.5	10.2
	Fusinite	4.9	9.2	9.3	5.3
	Detritus	2.5	16.6	4.8	4.3
	Macrinite		0.4		0.2
	Micrinite		0.6		
	Sclerotinite		0.6		
Exinite	Sporophyte		0.6		1.8
	Cutinite				
	Resinite				
Minerals	Clay mineral	2.4	5.8	0.2	2.2
	Pyrite			2.2	0.2
	Carbonatite	8.8	0.6	0.2	0.4
	Others				

Table 3. Reflectance ratio of vitrinites in different samples

Sample Number	R_{min}/%	R_{max}/%	$R_{o,max}$/%	$\|R_{max}-R_{min}\|$/%	Observation point num
ZGZ-M1	1.10	1.17	1.14	0.15	20
ZGZ-M1	1.11	1.21	1.16	0.08	20
ZGZ-M1	1.19	1.24	1.22	0.18	20
XZYCQ1	0.76	0.85	0.81	0.15	20

* R_{max} is the maximum vitrinites reflectance, R_{min} is the minimum vitrinites reflectance, and R_o,max is the average vitrinites reflectance.

3 Conclusions

Coal bumps can be characterized as the unstable release of energy that is non-uniform in space, and which is associated with yielding that occurs with progressive mining. Many variables can affect the bump- prone conditions. This paper aims to investigate the microstructures features of bump-prone coal and to evaluate the bump liability according to the microstructure parameters of coal. The following conclusions had been drawn regarding to the microstructures features of bump-prone coal and their potential applications in understanding coal bumps mechanisms:

(1) It was proved that energy dissipation in the bump preparation process affects the mechanical properties of coal significantly. The initiation of cracks is generally adjacent to the primary defects where the stress concentrated or the weak zone connected different macerals. The initiation and thinning out of cracks depended mainly on the variation of stress gradients. And the direction of crack tip and the propagation speed were determined by the magnitude of stress and micro-structures distribution in the specimen.

(2) The nonlinear features such as bifurcation and chaos were found in the process of influx and coalescence of crack sets in the bump prone coal. The path of micro-cracking was concentrated in the stratification planes of specimen or the macerals with relatively smaller micro-hardness. The fractal characteristics were revealed in the geometrical features of cracking path.

(3) A bump liability indices $\xi=(L_a-L_c)/L_c$ was proposed to determine the bump potential of coal. It was found that the bigger the ξ value, the more dangerous and liable to bump in the coal seam. The macerals analysis revealed that the coal, composed of more vitrinites and inertinites, had more potential to bump because the micro-hardness and the micro-brittleness were higher. The value of $|R_{max}-R_{min}|$ can be adopted to evaluate the liability of coal. The smaller of the value of $|R_{max}-R_{min}|$, the less potential of coal bumps. The results also indicated that the microstructure features can aid to determine the bump liability and the historical stratigraphic evolution can be recorded by the microstructures in coal.

Acknowledgements

The research is financially supported by the National Natural Science Foundation of China under grant No. 50704034, the Major State Basic Research Development Program Fund under grant No. 2006CB202203 and the State Scientific Support Fund under grant No. 2006BAK03B06. These supports are gratefully acknowledged.

References

1. Grouch, S.L.and Fairhurst, C. Mechanics of coal mine bumps. AIME Transactions, 1974, 256. 317–322.
2. Burgert, W.and Lippmann, H. Models of translatory rock bursting in coal. International Journal of Rock Mechanics Mining Science & Geomechanics Abstract, 1981, 18. 285-294.
3. Salamon, M.D.G. Energy considerations in rock mechanics fundamental results. Int J S Afr. Inst. Min. Metall, 1984, 84. 237-246.
4. Maleki, H., Wopat, P.F.and Repshe, R.C. et al. An analysis of violent failure in U.S. Coal mines: case

studies. In: Proceedings-Mechanics and Mitigation of Violent Failure in Coal and Hard-Rock Mines. Spokane, 1995, 95(1), 5-25.

5. Maleki, H., Zahl, E.G. and Dunford, J.P. A hybrid statistical-analytical method for assessing violent failure in U.S coal mines. DHHS(NIOSH) Publication, 1998, 99(114). 139-144.
6. Arabasz, W.J., Nava, S.J.and Phelps, W.T. Mining seismicity in the Wasatch Plateau and Book Cliffs coal mining districts, Utah, U.S.A. In S.J. Gibowicz & S. Lasocki (eds), Rockbursts and Seismicity in Mines-Proceedings of the 4th International Symposium on Rockbursts and Seismictiy in Mines. Krakow, 11-14 ,1997, Rotterdam: Balkema .
7. Fujii, Y., Ishijima, Y. and Deguchi, G. Prediction of coal face rockbursts and microseismicity in deep longwall coal mining. Int. J. Rock Mech. Min. Sci. & Geomech. Abstr.34(1). 85-96.
8. McGarr, A. Some applications of seismic source mechanism studies to assessing underground hazare. In N.C. Gay & E.H. Wainwright (eds), Rockbursts and seismicity in Mines-Proceedings of the Sympoium on Seismicity in Mines: SAIM Johannesburg, 1984, 199-208.
9. Lippmann, H. Meckanicks of “Bumps” in coal mines: a discussion of violent deformations in the sides of roadways in coal seams. Appl. Mech. Rew. 40(8). 1033-1043.
10. Lippmann, H. Mechanical considerations of bumps in coal mines. In C. Fairhurst (ed.), Rockbursts and Seismicity in Mines-Proceedings of the 2th International Symposium on Rockbursts and Seismictiy in Mines., Mineapolis, 1988,8(10). Rotterdam. Balkema. 279-284.
11. Jiang, Y.D., Zhao, Y.X., and Liu, W.G. et al. Investigation on three-dimensional model of translatory coal bumps in deep mining. Chinese Journal of Rock Mechanics and Engineering. 24(16). 2864-2869. (in Chinese)
12. Xie, H. and Pariseau, W.G. Fractal character and mechanism of rockburst. Int. J. Rock Mech. Min. Sci. 30(2). 343-350.
13. Shepherd, J., Rixon, L.K. and Griffiths, L. Outbursts and geological structures in coal mines: a review. Journal of Rock Mechanics Mining Science and Geomech Abstr. 18. 267-283.
14. Vardoulakis, I. Rock bursting as a surface instability phenomenon. Journal of Rock Mechanics Mining Science and Geomech Abstr. 21. 137-144.
15. Jiang, Y.D., Zhao, Y.X.and Song, Y.Q. et al. Analysis of blasting tremor impact on roadway stability in coal mining. Chinese Journal of Rock Mechanics and Engineering, 24(17). 3131-3136.
16. Kidybinski, A. Bursting liability indices of coal. Journal of Rock Mechanics Mining Science and Geomech Abstr, 1981, 18. 295-304.
17. Babcock, C.O. and Bickel, D.L. Constraint-the missing variable in the coal burst problem. In C.H. Dowding & M.M. Singh (eds), Rock Mechanics in Productivity and Protection-Proceedings of the 25th Symposium on Rock Mechanics. Littleton. 639-647.
18. Cao, Y.X., He, D. and David, G.C. Coal and gas outbursts in footwalls of reverse faults. International Journal of Coal Geology. 48. 47–63.
20. Zubelewicz, A. and Mroz, Z. Numerical Simulation of Rockburst Processes Treated as Problems of Dynamic lnstability. Rock Mechanics and Rock Engineering.16. 253-274.
21. Baradet, J.P. Numerical modeling of a rock burst as surface bucking. In C. Fairhurst (ed.), Rockbursts and Seismicity in Mines-Proceedings of the 2th International Symposium on Rockbursts and Seismictiy in Mines., Mineapolis, 8-10 June 1988, Rotterdam: Balkema. 81-85.
22. Cundall, P.A. and Lemos, J.V. Numerical simulation of fault instabilities with a continuously-yielding joint model. In C. Fairhurst (ed.), Rockbursts and Seismicity in Mines-Proceedings of the 2th International Symposium on Rockbursts and Seismictiy in Mines., Mineapolis, 8-10 June 1988. Rotterdam: Balkema. 147-152.
23. Muller, W. Numerical simulation of rock bursts. Mining Science and Technology. 12. 27-42.
24. Tang, C.A. Numerical simulation of rock failure and associated seismicity. Int. J. Rock Mech. Min.Sci. 34(20). 49-262.
25. Zhao, Y.X., Jiang, Y.D. and Zhang, Y. The relationship between bump-prone properity and microstructure characteristics of coal. Journal of China Coal Society, 2007, 32(1). 64-69.
26. Jiang, Y.D., Zhao, Y.X., Liu, W.G. et al. Investigation on the mechanism of coal bumps and relating experiments. Science Press, 2009.

RaSiM 7(2009): Controlling Seismic Hazard and Sustainable Development of Deep Mines, C.A. Tang(ed), Rinton Press, 229-234

ROCK MASS RELAXATION MECHANISM AND REINFORCEMENT METHOD OF FOUNDATION EXCAVATION OF SUPER HIGH ARCH DAM

PENG LIN, ZI-CANG LI, JIN-XIE JIN, QIANG YANG and WEI-YUAN ZHOU

State Key Laboratory of Hydroscience and Engineering, Tsinghua University

Beijing 100084, China

As for those arch dams constructed in high in situ stress valley, foundation excavation may lead to stress and strain energy release and rock mass relaxation, and then cause shallow stability problem, which has few successful examples for us to learn how to design and reinforce the foundation for super high arch dam with complicated geo-condition. In this paper, a detailed discussion was conducted focusing on the characters, types of rock mass relaxation and loose mechanisms of excavated foundation of super high arch dam. Based on the calculation of anti-shear and anti-sliding safety factor of dam interface, system treatment measures, such as grouting, drainage, backfill concrete and reinforced bolts, are proposed.

1 Introduction

Along with the vigorous development of hydropower resources, many super high arch dams are constructing in the southwest region of China. The stability of these arch dams is a key and important problem in the process of design and construction [1]. In general, these super high arch dams are constructed in high in situ stress valleys. Rock masses at both abutments are subjected to stresses resulting from the weight of the overlying strata and locked-in stresses of tectonic origins with stress concentration as an especially serious consideration in the bedrock of the valley. When dam grooves are excavated for the dam foundation, the stress field is locally disrupted and a new set of stresses are induced in the rock surrounding the foundation interface (dam-rock foundation contact surface). Excavation leads to stress release and relaxation of the rock mass causing shallow stability problems in the rock foundation. Knowledge of the magnitudes and directions of these in situ and induced stresses is an essential component of foundation interface excavation. In many cases, the strength of the rock is exceeded and the resulting instability can have serious consequence on the behaviour of an interface excavation.

According to current design specifications for concrete arch dams [2], the foundation excavation should reach intact or fresh rock mass for high arch dams with a height less than 200m, otherwise specific research should be carried out, taking into account the safety, current construction technology, and current expertise for high arch dams. The stability interface between the dam and foundation of high arch dams is illustrated through anti-slide stability of arch abutments, i.e. In addition, for the overall stability of the arch dam, the mechanical parameters of arch abutments should be the same with that of the foundation to calculate the anti-slide stability. However, it should allow for shallow sliding; such as unloading rock masses and weak structural planes, whether their anti-slide stabilities should be checked lacks specific regulation.

For example, the Xiaowan hydropower station [3, 4] under construction in China is situated on the Meigong River in the Yunnan province and is located on complex rock foundations with high wall that are steep and narrow. Besides the several large faults and geological altered rock zones, its most troublesome problems were found in the river bed with high geo-stresses with relaxed rocks. Large and deep relaxed zones in dam foundations are subjected to high geo-stresses with enginering excavation. Important precautions must be taken to prevent the dam foundation from sliding. Thus, proper treatments are necessary in foundation interface areas to ensure that three-dimensional compression states increase the anti-shear strength and carrying capacity of the rock mass.

In this paper, the main characteristics of the rock mass relaxation of the foundation interface are analyzed, and the rock mass of foundation interface relaxation mechanism of high arch dams is elaborated. On the basis of this analysis, a treatment system is proposed to keep the stability of interface of arch dam in the 300m height level.

2 Characters of rock mass relaxation

Based on the summary of characters of excavation rock mass of super high arch dam in China[5-7], The main patterns of rock mass relaxation including (a) Crack propagation along existing joints; (b) Onion skin phenomenon; (c) Unloading relaxation and return elasticity ;(d) Rockburst

Relaxation rock mass is those bare rock mass when excavation of foundation interface in highly geostress region, stress distribution will change and regulate, the elastic stain energy will release lead shallow rock mass loose along uncovered direction.

2.1 Crack propagation along existing joints

In areas with high arch dams, cracks and joints are close and invisible in intact rock mass without releasing stress before excavation. For example, horizontal joint in Xiaowan arch dam is in crack form, i.e, cracks and joints of rock mass near interface are close before excavation[3];There are invisible cracks in the rock mass of Xiluodu arch dam before excavation[1]. In the process of excavation, rock mass, the phenomenon that cracks propagate along existing joints is always noticeable, which includes two types(1) along joint with a single incline angle, see in Figure 1; (2) along rock blocks formed by combination joints, and occur creep deformation of rock blocks.

Figure 1 Cracks opening along existing single joint

Figure 2 “onion skin” phenomenon

2.2 “Onion skin” phenomenon

The rock mass relaxation is similar as “onion skin”, the thickness of layers of loose rock is about 0.5cm～5cm, see in Figure 2. These releasing rock mass is very disadvantageous for shallow stability of dam foundation.

2.3 Unloading relaxation and return elasticity

Unloading relaxation is very conspicuous in complicate excavation structural area, for example, rock mass close to outlet of grouting tunnel, concrete replace tunnel et al, and see in Figure 3.

Figure 3. Rock mass loose of opening

Figure 4. Image of rockbursting

2.4 Rockburst

When excavation of dam interface in hard brittle rock under high stress, rock will tend to fail in a violent manner; i.e, it will burst. A rockburst is defined as damage to an excavation that occurs in a sudden or violent manner and is associated with (not caused by) a seismic event. Figure 5 illustrates rockburst in the right bank of Xiaowan arch dam with elevation 962m[3], the areas is about $2m^2 \sim 3m^2$.

In conclusion, some characters of rock mass relaxation in process of excavation includes: (1) excavation unloading loose phenomenon of abutments and degree of unloading loose is related to distribution of geotechnical stress and rock mass structure. (2) Excavation unloading loose varies in different elevation in the same bank, and it is more noticeable in lower elevation, especially in the valley with high in situ stress. (3) Excavation unloading loose varies in different parts of the same elevation, it is more noticeable in the dam heal than that in the dam toe. (4) Excavation unloading loose is related to rock mass integrity, higher stress in integrate foundation rock mass leads to conspicuous relaxation, and it is not so conspicuous in rock mass with developed structural plane. (5) Excavation unloading loose is conspicuous in areas with complicated excavation, such as tunnels of grouting, drainage, concrete replacement.

3 Rock mass relaxation mechanisms

Based on foregoing characters of rock mass relaxation, the rock mass relaxation mechanisms are analyzed in following:

3.1Rock mass condition

As we all know, if strength of rock mass is low, rock mass have no high strain energy even if in site stress is high. However, if rock mass is hard rock with compresses around rock mass, and the large amounts of strain energy that can be stored in hard rock under high stress, and rock mass will be loose due to excavation-induced stresses. In general, the region stress is high, and site stress σ_1 is greater than 20 percent of compressed strength of rock mass.

3.2 Strainbursts

Strainbursts are defined as damage to an excavation resulting from a violent release of stored strain energy. The amount of damage is a function of the excavation size and stress magnitude of foundation interface. From an energy dissipation point of view, considering the maximum capacity of practically feasible reinforcement system, sever rockburst condition can be defined as condition when the failure depth exceeds 1.5m.

3.3 Self-initiated rock mass relaxation

These rock mass relaxation occur when the stresses near the boundary of an excavation exceed the rock mass strength, and failure rock mass is not dissipated during the fracturing process. It will occur when the stiffness of the loading system is softer than the post-peak stiffness of failing rock.

3.4 Fracturing with rock mass bulking

Fracturing with rock mass bulking- occurs when static and dynamic stresses exceed the rock mass strength. In brittle rock, fracturing of rock mass around an excavation is associated with a sudden volume increase or bulking of the failing rock. This bulking can be reduced by rock reinforcement measure as discussed in following context but the grouting also include deformable retaining and holding components to prevent unraveling of broken rock between bolts.

If there is horizontal crack in shallow rock mass of bedrock foundation after excavation, leakage occurs in opening of foundation rock mass under sonic test, and these cracks are close before excavation. According to digital imaging study of internal borehole, developed horizontal cracks of foundation rock mass consist of types as follows according to maturity and style of development: ①horizontal cracks propagate in concentration, showed as flake and lamellicorn, with width of 1cm～5cm, spalling appears in borehole locally and the development is within limited depth, as shown in Figure 5a ② horizontal cracks develop in strip, but rock mass are crushing by squeezing, spalling is conspicuous in borehole and it is within limited depth, as shown in Figure 5b ③Only one horizontal crack develop in shallow area of borehole, and the borehole is complete and cracks develop in deep area of borehole(mostly close),as shown in Figure 5c

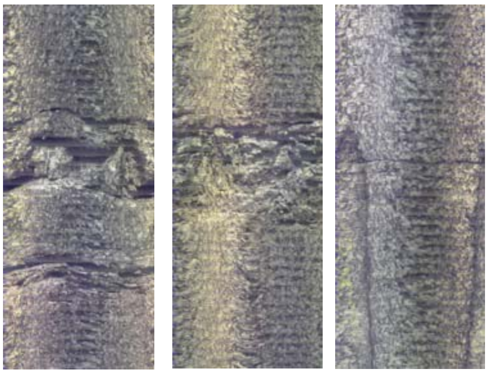

a b c

Figure 5 Full photos of internal borehole [3]

4 Reinforcement method

Relaxation mechanisms of rock mass has been discussed above in dam interface, and how about the stability analysis of dam interface? The stability analysis of super arch dam interface focuses on foundation (including abutments), and there are some existing methods [7-9].

According to investigation of some arch dams home and abroad, the instability and failure of dams always result from weak area in foundation and interface involving the rock mass properties or relaxation. Which cause tensile stress concentration in dam heel and weak area in foundation, and then lead to crack and failure of dam. The crack in interface are due to shear failure, crack appears and propagates in dam simultaneously. Thus, it is very important to adopt appropriate reinforcement method based on the results of integrity safety factor of dam and foundation by employing numerical simulation.

4.1 Surface safety factor of dam interface

Based on failure mechanism discussed above, the key to check stability of dam interface lies in investigation of 3D body surrounding the lower part of dam and interface, and surface sliding mechanism along dam interface is not accurate. In this situation, thrust of arch should be taken into account, stress in lower part of dam will transfer to two banks, thus dam will not slid along dam interface unless $L/H \geq 5$.Sliding along interface should be taken into account for gravity dam, however, tensile crack exists in interface and principles stress is in 3D spatial for arch dam. Thus, numerical simulation to check the stress condition of dam interface, tensile crack in the upstream surface, compression stress concentration in the downstream surface, and the stability safety factor in interface should be analyzed by 3D stress mode.

Surface safety factor is used to verify the M-C elastoplastic yielding criterion of river bed dam section along shallow loose surface, i.e. overall anti-sliding safety factor. The gravity is taken into account for concrete, and the downstream rock mass is regard to be resistance block, the gravity of concrete is distributed between dam body and resistance block, resistance force can be calculated according to limit equilibrium state of resistance block, and then anti-sliding safety factor in dam section can be calculated. Table 1 lists Surface safety factors of Xiaowan arch dam. The results also the safety factor of bottom interface (From both banks to elevation 975 m) is lower than that of both abutments. Thus, the low surface safety factor zone should be reinforced by various treatment measures. Detail calculating method about surface safety factor illustrated in reference [6].

Table 1 Surface safety factors of Xiaowan arch dam (consideration uplift pressure)

From both banks to river bed Depth under dam interface				From both banks to elevation 975 m Depth under dam interface				From both banks to elevation 1050m			
2m		4m		2m		4m		2m, 5m depth between river bed to elevation 975m and 975～1050m, respective		4m, 5m depth between river bed to elevation 975m and 975～1050m, respective	
K_{sh}	K_{sl}	K_{sh}	K_{sl}	K_{sh}	K_{sl}	K_{sh}	K_{sl}	K_{sh}	K_{sl}	K_{sh}	K_{sl}
0.91	1.28	1.14	1.88	1.05	1.48	1.32	2.16	1.49	2.22	1.64	2.58

K_{sh} denotes anti-shear safety factor ; K_{sl} denotes anti-sliding safety factor

4.2 Reinforcement method of engineering

Prior to application of shotcrete, all loose rock mass shall be removed and the surface thoroughly cleaned, Loose rock removal and cleaning of surfaces, to which attachment of shotcrete is questionable as determined by the Engineer, shall first be scoured with an air-water jet, Cleaned surface shall be kept damp.

Where a weathered zone in rock mass is encountered or exposed rock surfaces have been damaged from exposure to air, including drying, cracking, spalling, disintegrating, etc., all such damaged rock shall be removed, and additional rock bolts, drilling and grouting shall be installed in the damaged areas as directed by the engineer. After rock bolting has been installed and approved, the rock surface shall be scoured, cleaned, and kept damp as described above.

These defects in abutments and dam interface are designed to be strengthened by reinforced measures, such as replacement with concrete plugs, reinforced bolts or cement grouting. Especially, its most troublesome problems were found in river bed with high geo-stresses with relaxed rocks. Large and deep relaxed zones in dam foundations are to be emerged by high geo-stresses with enginering excavation. Important means are needed to prevent dam foundation sliding. Another important problem for cracking prevention is to construct virtual joint in upstream dam heel.

Since the permeability of the foundation including joints, shears, fault zones and solution cavities have dominate effect on stress of dam heel and stability, the treatment, drainage before upstream dam heel is used to beneficiate the stability foundation, and for sure protect the water enter into dam.

Another, the safety monitor for foundation deformation during construction and operation period is very important for saving reservoir operation safety.

5 Conclusion

It is very significant for the stability of the dam to study the rock mass relaxation mechanism and reinforcement measures of the foundation excavation of the super high arch dam.

The main patterns of rock mass relaxation including crack propagation along existing joints, the onion skin phenomenon, unloading relaxation, return elasticity, and rockburst.

The condition of rock mass relaxation exists in hard rock that can store large amounts of strain energy under high stress, and rock masses with looses due to excavation-induced stresses. The main relaxation mechanism includes strain bursts, self-initiated rock mass relaxation, and fracturing with rock mass bulking.

Based on the analysis of the surface safety factor of the dam interface of the super arch dam, a system treatment measure, such as grouting, drainage, backfill concrete and reinforced bolts is proposed.

Acknowledgments

This research work was supported by National Natural Science Foundation of China (No:10772095), National excellent State Key Laboratory Foundation of China（50823005）and Foundation of State Key Laboratory of Hydroscience and Engineering （2008-TC-2）. The authors wish to express sincerest gratitude to Kunming Hydroelectric Investigation & Design Institute of SPC, Kunming, China for providing field data.

References

1. Wang, R. K., Lin, P.and Zhou W.Y. Cracking and stability problems of high arch dams on complicated rock foundations. Chinese J. of Rock Mech. and Eng., 2007, 26(10). 951-958.(in Chinese)
2. Design criteria for concrete arch dam, DL/T5436-2006, National Development and Reform Commission of the People’s Republic of China,2007.(in Chinese)
3. Report on effect and reinforcement method for foundation excavation of Xiaowan arch dam, Kunming Hydroelectric Investigation and Design Institute, China Hydropower Engineering Consulting Group Co, 2006. (in Chinese))
4. Zhou, W.Y., Lin, P., Yang, Q.and Yang, R.Q.，The challenging problems with the super large Xiaowan arch dam under construction, 11th Congress of the International society for rock mechanics, Ribeiro e Sousa, Olalla & Grossman(eds), Taylor & Francis Group, London, 567-570,2007.
5. Li, Z., Chen, F.and Zheng, J. B. Key study on super high arch dam, CEPP, 2004.(in Chinese)
6. Lin, P., Wang, R. K., Zhou, Y. N.and Zhou, W.Y. Study on shallow unloading mechanism and stability of foundation interface of super high arch dam，soil mechanics, 2008, 29 (Supp). 8-14.(in Chinese)
7. Zhou, W.Y., Lin P., Yang, R.Q., Yang Q., Method and application of geomechanics model test on high arch dam. Beijing：China Water Power Press，2008.(in Chinese)
8. Foundations for dams, Asilomar conference grounds pacific grove, California, 1974, American Society of civil Engineers, New York.
9. Lin, P., Wang, R. K., Yang, Q., Zhou, Y. N.and Zhou, W.Y., Reinforcement force analysis and evaluation for downstream toe of high arch dam, 5th Asian Rock Mechanics Symposium (ARMS 2008), Tehran, Iran, 2008, 953-958.

RaSiM 7(2009): Controlling Seismic Hazard and
Sustainable Development of Deep Mines,
C.A. Tang(ed), Rinton Press, 235-238

STUDY ON PREVENTION AND CONTROL OF ROCK BURST IN DEEP-LYING DEPOSIT

SHAO-ZE YU

Civil＆Environment Engineering School, University of Science and Technology Beijing

Beijing, 100083, P.R. China

Rock burst is often found in deep mining engineering. The backfilling method in a deep mine is presented in this paper. The technology and process of the backfilling method are firstly introduced. The results and effects of backfilling method are then discussed taking rock burst problems into account. After that, in order to prevent the disaster of rock burst, many researches are undertaken to optimize the dimensions of mining method and make a suitable mining sequence. Finally, integrated means is proposed to develop road ways, where bolt and wire mesh are effective means to control the occurrence of rock burst. The results show that the backfilling method is a feasible and highly efficient mining method for deep-lying deposit.

1 Introduction

To avoid the occurrence of rock burst, we designed a copper mine in China with mitigating measures incorporated in the design. The depth of this copper deposit under study is between 700 m ~ 1150 m. The ore body is located in the axis of an anticline, with its attitude coinciding with the anticline axis. The strike length of the ore body is 1810 m and the width ranges between 300 m and 800 m, with the average thickness being about 40 m. The lithology of hanging wall rock is marble, whereas that of the footwall rock is sandstone or siltstone. The ore hosts some pyrite, hence the possibility of the occurrence of spontaneous combustion. The maximum principal stress has a magnitude of 30 ~ 38MPa of the original rock lies along the strike of the deposit. Rock burst phenomena was observed during mine development [1]. For example, there were some rock ejections leading to bolts and wire mesh being thrown out. The sound of rock burst lasted for 20 days [4]. The output level of this mine is 10,000 t/d with a stope producing roughly 2400 t/d. It is tagged as a highly efficient mine in China, with uninterrupted operation in recent years.

2 Characters of the mine rock burst

Rock burst is a phenomenon that causes the elastic strain energy of rock to be spontaneously released. It may be harmful to the safety of the personnel and equipments underground. There are two types of mine rock burst. One is caused by mining activity, which usually occurs at working faces of high stress concentration, the consequence thereof being the likelihood of catastrophic damage. The second is caused by the stress redistribution in a large region [2], with scale generally larger than the afore-mentioned, and the resultant damage being more serious in some cases.

The study of Spottiwoode and Prout showed that filling body/media can effectively control and reduce the movement of country rock. Salamon has an equation to his credit employed in calculating the quality of the filling material in backfilling. It is as follows:

$$M = \frac{1}{\sigma}\int_0^{\sigma} \varepsilon d\sigma \quad (1)$$

M − Backfilling quality parameter.

σ − Stress when the material is compressed.

ε − Strain when the material is compressed.

The backfilling body plays the following roles in ground support:

(a) Improvement of pillar strength

If the room is fully filled, the strength of the pillar can greatly be improved, because the filling body can provide surrounding pressure to the pillar and can greatly improve the residual strength too.

(b) Reduction of rock burst energy. Backfilling body can reduce the velocity and acceleration of the particle in the country rock [2].

The research findings of American Spokane proved the function of backfilling. Thus, backfilled mines are reported to have a reduction of 42 percent in energy releasing ratio, as compared to, mines which were not backfilled. Backfilling body plays a crucial role in the absorption of rock burst energy. The research of LAC company has also shown that the velocity was reduced by 30~50% in filling body. In a conclusion, filling up goafs as a measure to control rock burst is considered feasible.

3 The prevention and control of rock burst in this copper mine

The daily output of this mine is 10,000 t of raw ore, so a more efficient mining method must be selected in order not to hamper the designed output level. However, the occurrence of rock burst, high temperature and the possibility of spontaneous combustion in this mine, makes exploitation a daunting task or a challenge.

Through comprehensive technical and economic comparison in addition to engineering experience and the trend of modern mining technology, the decision to employ stage room mining method was made, which implied mined out stopes will be filled. It is a well known fact that backfilling body prevents ore from spontaneous combustion and simultaneously serves as a support for the country rock. This mining method has a better mining recovery and it is proven to be more efficient.

Prevention of rock burst and mine safety were ensured through the following measures:

(1) Optimized the parameters of stage room mining method

Three-dimension elastic and plastic finite element software was employed in the calculation of stope dimensions, orthogonal experiment principal was used in an experiment which used pillar widths of 10 m, 12m, 16m, 18m and 20m; Room widths of 50 m, 75 m and 90 m; The height being the thickness of the ore body. The result showed that the width of pillar is the most important in factor in stress distribution. The wider the pillar width, the lesser the stress near the perimeter of pillar, but the width and length of the room is on the contrary. Conclusion was therefore drawn based on the equipment size and practical experience [6], that the dimension 78 m x 18 m was optimum and safe, therefore should be used.

Though the country rock and ore body are stable, the room was considered a little bigger for a deep-lying deposit, so other alternatives were resorted to in order to reduce and control the occurrence of rock burst. The deposit was divided into several panels and temporary pillars for the panels were designed. Panel width of 100 m and temporary pillar of width 18 m were used. This led to separately mining each panel more efficient.

Generating a good mining sequence is another important factor in the prevention of rock burst. A mining sequence commencing from the center of a deposit and then extending to the extreme ends of the deposit (along strike) was used. One stope out of every four is selected for mining in the first step, which is equivalent to widening the width of the pillar. Mining is undertaken through drilling, blasting, mucking, hauling and dumping. Vertical array of fan-patterned holes are used with two or three arrays of blastholes initiated simultaneously during blasting. Mining progresses from the bottom to the top allowing gradual expansion of the goaf. The goaf is then filled with high concentration of all-tailings cement slurry after a stope is completely mined out.

(2) High concentration All-tailings used to fill goaf.

Used high concentration all-tailings slurry to fill the goaf. The constituent of the filling material is primarily tailings. The vertical sand depot concentrates the slurry directly from the concentrator. It can continuously receive the slurry from the top of depot and make the high concentration slurry from the bottom, the clean water flows out for reuse. The concentration of the slurry from the depot is about 70% but finally reaches 76%. The vertical sand depot produces slurry at a rate of $50m^3/h$. The slurry gravitates to the goaf and cures after several weeks. Almost no water seeps out of the slurry during this period, so no cement is lost and pollution is curtailed. The goaf is also filled with waste rock. Construction of tailing dam is therefore no longer required. This is a breakthrough, thus making it possible for all the tailings to be continuously sent underground for the purpose of backfilling. This is an advance technology in the world.

Both exploitation and face development are conducted expeditiously in order to pave the way for goafs to be fully filled. As a way of ensuring the smoothness of the perimeters of stopes, smooth blasting is used along the borders of stopes.

(3) Prohibited entry of equipments and personnel into the goaf

Ore loading is conducted in the roadways; the thickness of the blasted ore is 10~15 m (At least), thereby making the working faces safe. The remnant ore on the floor of the stope is loaded and transported by remote controlled scraper, so personnel or equipments are not exposed to the potential dangers in the goaf, except the remote scrapers.

(4)Used integrated means to excavate the road way

The existing rock burst in the mine is very different from most mines with rock burst problems, there exists significant amount of ground pressure as compared to other mines, and therefore, the supporting system must have strong resistance of static pressure and withstand sudden release of kinetic energy of rock, so the following measures to control the rock burst in the roadways [3] were taken.

(a) In accordance with the principles of rock mechanics, roadway must be parallel to the direction of maximum principal stress or could be slightly angled.

(b) Designed 4~5 cutting holes which are two times longer than the normal blastholes. These set of blastholes are firstly initiated to the release the stress pile up in advance. Rock burst usually happened within 2~4 hours after blasting. Strict plan/schedule was therefore adopted for tunnelling.

(c) Used smooth blasting method to minimize the disturbance of the country rock, hence contributing to the roadways retaining their designed shape and enabling the full use of the country rock's inherent ability to support the ground.

4 Conclusion

This mine has been in operation for more than two years and it has proven that backfilling is a good means to control rock burst. With rapid development in backfilling technology, the cost of backfilling is steadily declining. Currently, the trend is to use the backfill mining method for the exploitation of deep-lying deposit and the importance of optimizing mining method and sequencing parameters can not be over-emphasized. In roadway development, the use of appropriate construction methods is also helpful to control and reduce risk of rock burst. The bolt, wire mesh and shot-crete are effective ways to support roadways. The high efficient mining is feasible in the deep-lying deposit.

References

1. Peng, H.S., Gu, D.S.and Deng, J. Technical Evaluation of Backfill Mining Method and Tentative ideas for Backfill Stopping in Dongguashan Mine. Mining research and Development, 1997.
2. Guo, R., Pan, C.L. and Feng, T. Mechanism of Backfill on Rock burst Control and an initial Research of Exploitation of a Deposit. Nonferrous metals, 1999.
3. Guo, R. and Yu, R.C. Design of support work in Drift Having Rock burst Danger. China Mining Magazine, 2002.
4. Zhu, F.C., Pan, C.L., and Jia, M.T. Analysis of the Rock burst machenism of Dongguashan Deposit. Metal mine. 2002.
5. Yang, C.X., Luo, Z.Q. Analysis and Control of Unstable Mode of Laneway with Rock burst Possibility in deep Mine Mining and metallurgical Engineering, 2007.
6. Yang, C.X., Luo, Z.Q., Hu, G..B., Jia, L.Z. and Jia, M.Z. Research on the techonolgy of high efficient and safe mining of deep-lying deposit. Mining Technology, 2006.

RaSiM 7(2009): Controlling Seismic Hazard and
Sustainable Development of Deep Mines,
C.A. Tang(ed), Rinton Press, 239-244

ANALYSIS ON LIMIT TIME OF SUBCRITICAL CRACK GROWTH IN DIFFERENT ROCKS UNDER COMPRESSIVE-SHEAR STRESSES STATE

JIANG-TENG LI PING CAO DE-SHENG GU and CHAO WU

School of Resources and Safety Engineering, Central South University,

Changsha, 410083, P.R. China

Subcritical crack growth parameters of double torsion specimens made of ore, lherzolite, marble and granite were tested using Instron1342 type electro hydraulic servo test machine. The relations of the mode-I stress intensity factor K_I versus the subcritical crack growth velocity (V) were obtained by the double torsion constant displacement load relaxation method. The curves of crack relative length (l/b) and crack growth time (t) of four rocks under compressive stresses state were discussed according to subcritical crack growth parameters and subcritical crack growth equation, and the limit time was obtained respectively. The results show that there are turning points on curves of crack relative length (l/b) and crack growth time (t) of all four rocks. Cracks grow stably, i.e. subcritical crack growth, before the turning point. Cracks grow, encounter and integrate catastrophically after the turning point. There is not a gradual stage from crack stability growth to crack instability growth, i.e. rock mass instability is sudden. The curves of crack relative length l/b and crack growth time t move to right with increase of Young modulus, which implies that limit time increases consequently.

1 Introduction

Rock is usually under compressive-shear stresses. The geological hazards in rock engineering, such as land slide, rockburst and seism, are related to rupture under compressive-shear stresses state. A lot of engineering cases and experiment results show that rock rupture happens because of cracks propagation, growth and integration. Many researches show that cracks kink to the mode-I fracture under compressive-shear stresses [1-5].

In fracture mechanics, crack growth occurs when the stress intensity factor reaches the fracture toughness of the material. However, slow crack growth also occurs when the stress intensity factor is less than the fracture toughness. This phenomenon is called subcritical crack growth. The reasons may be listed as follows[6]: (1) The stresses at the crack tip increase in the process of forming micro-cracks and interspaces, (2)The chemical bond fracture stresses decrease by the effects of environmental medium. The crack grows catastrophically in rock mass and engineering instability happens after the subcritical cracks propagate to a certain extent usually, which results in rock engineering instability relating to subcritical crack growth limit time. So, studies of the subcritical crack growth laws, fracture properties and their testing data are important to rock engineering long-term stability.

In this paper, subcritical crack growth parameters of double torsion specimens made of ore, lherzolite, marble and granite and were tested using an Instron1342 type electro hydraulic servo test machine. The relationship of the mode-I stress intensity factor K_I versus the subcritical crack growth velocity V were obtained by the double torsion constant displacement load relaxation method. The curves of crack relative length l/b and crack growth time t of four rocks under compressive stresses state were discussed according to subcritical crack growth parameters and subcritical crack growth equation, and the limit time was obtained respectively.

2 crack growth model under compressive-shear stresses state

Suppose initial cracks, which length is $2a$, which inclination is β , is subjected to σ_1 and σ_2（$\sigma_1 \leqslant 0,\ \sigma_2 \leqslant 0$，$\sigma_1$ is maximal principal stress）(see Fig. 1(a)). When effective shear stress is up to critical value, initial cracks propagate along θ direction, which is angles between growth direction and initial crack, and wing crack was appear consequently. According to Refs. [7,8], the stress intensity factor of wing crack, K_I^{wing} , can be expressed as follows：

$$K_I^{wing} = K_I^{isol} + K_I^{\inf l} \tag{1}$$

Where K_I^{wing} is the stress intensity factor of wing crack, K_I^{isol} denotes the stress intensity factor of single wing crack, which length is equal to l , under compress load σ_1 and σ_2, $K_I^{\inf l}$ denotes the effect initial cracks which length is equal to $2a$ to the stress intensity factor of wing crack , under compress load σ_1 and σ_2. The relation was shown in Fig. 1.

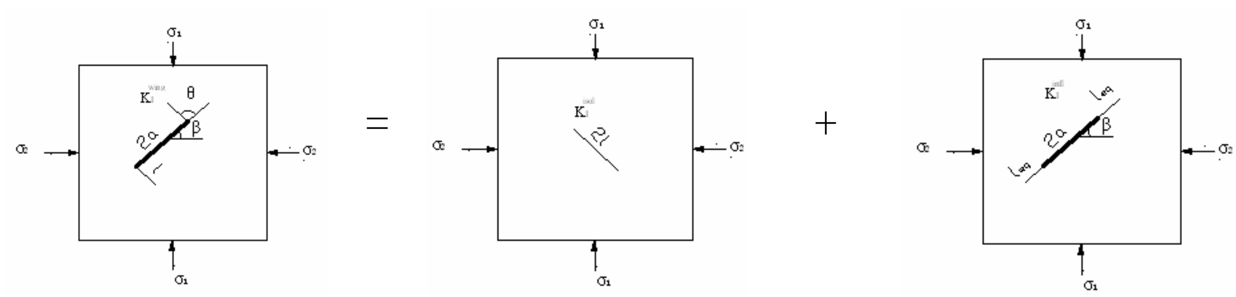

（a） （b） （c）

Figure 1 The stress intensity factor superposition of wing cracks

K_I^{isol} can be expressed by

$$K_I^{isol} = \frac{1}{2}[(\sigma_1 + \sigma_2) + (\sigma_1 - \sigma_2)\cos 2(\theta + \beta)]\sqrt{\pi l} \tag{2}$$

$$K_I^{\inf l} = -3\tau_{eff}\sqrt{\frac{a + l_{ea}}{\pi}}\sin^{-1}(\frac{a}{a + l_{eq}})\sin\theta\cos\frac{\theta}{2} \tag{3}$$

Where $l_{eq} = \frac{9}{4} l \cos^2\frac{\theta}{2}$

Eq.(3) shows the contributes of initial cracks to the stress intensity factor of wing cracks. Eq.(4) can be obtained by superposition Eq.(2) and Eq.(3)

$$\begin{aligned} K_I^{wing} &= -3\tau_{eff}\sin\theta\sqrt{\frac{a + l_{eq}}{\pi}}\sin^{-1}(\frac{a}{a + l_{eq}})\sin\theta\cos\frac{\theta}{2} \\ &+ \frac{1}{2}[(\sigma_1 + \sigma_2) + (\sigma_1 - \sigma_2)\cos 2(\beta + \theta)]\sqrt{\pi l} \end{aligned} \tag{4}$$

Eq.(4) indicates the relation of wing cracks stress intensity K_I^{wing} and wing crack length l and initial crack geometry parameters.

3 K_I-V relation

The relation between subcritical crack growth velocity and the stress intensity factor at the tips of crack is taken into account when subcritical crack growth velocity is studied usually. The most common empirical equation used to describe subcritical crack growth in rock is based on the power law formulation of Charles[9], and is given by:

$$V = v_0 \exp(-H/RT) K_I^{\ n} \tag{5}$$

Where: V is subcritical crack growth velocity, H the activation enthalpy, R the gas constant, K_I the stress intensity factor, T the absolute temperature. v_0 and n are constant. At a constant temperature, equation (5) can be rewritten as

$$V = AK_I^{\ n} \tag{6}$$

No dimension crack growth power equation can be expressed by[9,10]

$$\frac{\partial(l/b)}{\partial t} = \frac{A}{b} K_I^{\ n} \tag{7}$$

Where A, n are subcritical crack growth parameters, which are gained by experiment. b denotes space between crack (see in Fig. 2.) .

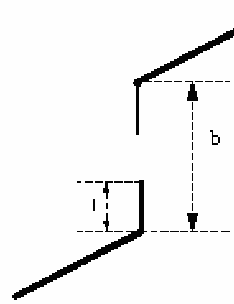

Figure 2 Wing crack interaction

Eq. (8) can be obtained by substituting Eq. (4) into Eq. (7)

$$\frac{\partial(l/b)}{\partial t} = \frac{A}{b}\{-3\tau_{eff}\sin\theta\sqrt{\frac{a+l_{eq}}{\pi}}\sin^{-1}(\frac{a}{a+l_{eq}})\sin\theta\cos\frac{\theta}{2} + \frac{1}{2}[(\sigma_1+\sigma_2)+(\sigma_1-\sigma_2)\cos 2(\beta+\theta)]\sqrt{\pi l}\}^n \tag{8}$$

It shows the relation between crack relative length l/b and time t. The curve of crack relative length l/b and time t can be obtained by numerical solution of Eq. (8). Subcritical crack growth limit time was obtained consequently.

4 Subcritical Crack Growth Parameters Testing

Subcritical crack growth parameters A and n were tested by the double torsion constant displacement load relaxation method. The specimen of double torsion is shown in Fig. 3, which is a rectangle plate. There is a longitudinal groove on the bottom surface, and the crack front proceeds along a straight line starting from a machined initial notch and guided by a side groove thus producing a relaxation of the load. The specimen is treated as two elastic torsion bars. According to references [11-15], the stress intensity factor K_I and the subcritical crack growth V can be obtained for small deformation when the width of torsion bar is much larger than its thickness (see Eq.(9) and Eq.(10)).

$$K_I = P w_m \left[\frac{3(1+\nu)}{w d^3 d_n}\right]^{\frac{1}{2}} \qquad (9)$$

$$V = \frac{da}{dt} = \frac{w d^3 E y}{6 w_m^2 P^2 (1+\nu)} \frac{dP}{dt} \qquad (10)$$

Where *P* is the applied load, w_m is the moment arm of the torsion, *v* is Poisson's ratio, *d* is the thickness of the specimen, d_n is the thickness of the specimen minus the groove depth, *W/2* is the width of torsion bar, *E* is Young modulus, *t* denotes time.

It can be seen that the stress intensity factor K_I and subcritical crack growth velocity are independent of the crack length, which is very useful in the subcritical crack growth research. The relation between the subcritical crack growth *V* and the stress intensity factor K_I can be established by Eq.(9) and Eq.(10).

Average logK_I-log*V* coordinate points in logarithm coordinates are shown in Fig. 4. Subcritical crack growth parameters were listed in tab. 1.

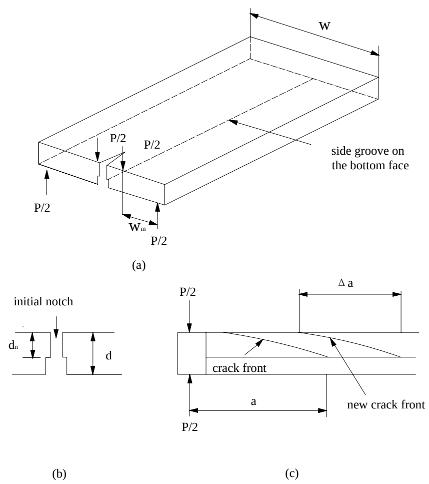

(a) specimen shape (b) cross-section in width (c) cross-section in length

Figure 3 The schematic diagram of double torsion specimen

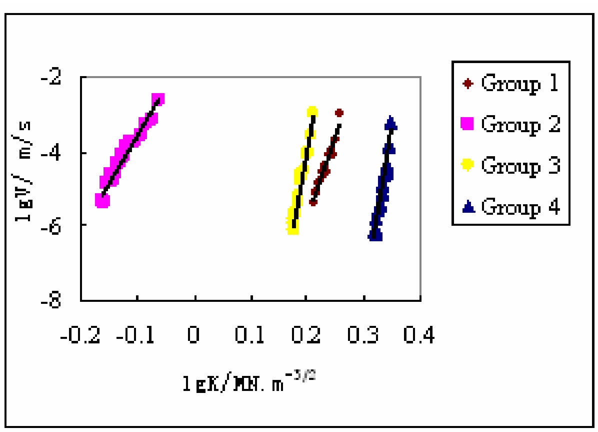

Fig.ure4 The average K_I-*V* curve of four kinds of rocks

Table 1 Subcritical crack growth parameters

Group	Material	*A*	*n*
1	Ore	4.39E-15	50.384
2	Lherzolite	0.210985	25.863
3	Marble	3.26E-16	75.228
4	Granite	5.67E-34	95.943

5 Analysis on limit time of subcritical crack growth

The curves of crack relative length l/b and time t of ore, lherzolite, marble and granite（$a=0.01m$，$b=0.1m$，$\beta=45°$，$\sigma_1=10$MPa）are respectively given in Fig. 5. It can be seen that crack relative length l/b - time t curves move to right with increase of Young modulus E, which implies that limit time increases consequently. The relation between the subcritical crack growth limit time t_s and Young modulus E is shown in Fig. 6. The limit time of subcritical crack growth of ore, lherzolite, marble and granite are given in Tab. 2

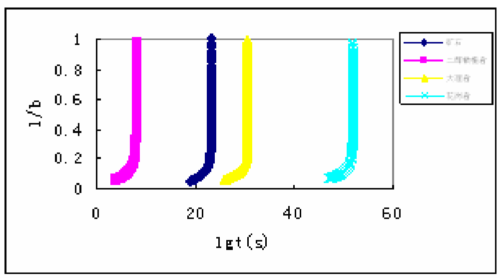

Figure 5 The curve of crack relative length l/b and time t of four kinds of rocks

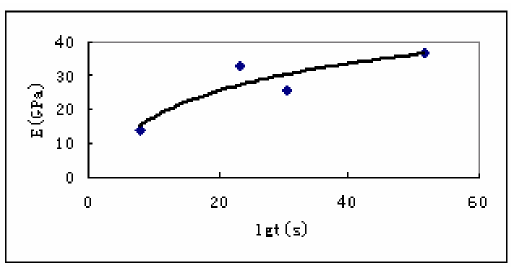

Figure 6 The subcritical crack growth limit time ts versus Young modulus *E*

Table 2 Subcritical crack growth limit time（s）

Material	Ore	Lherzolite	Marble	Granite
subcritical crack growth limit time	1.63E+23	1.1E+08	3.4E+30	4.38E+51

6 Conclusions

In this paper, subcritical crack growth parameters of double torsion specimens made. Ore, lherzolite, marble and granite were tested using an Instron1342 type electro hydraulic servo test machine. The relationship of the mode-I stress intensity factor K_I versus the subcritical crack growth velocity V were obtained by the double torsion constant displacement load relaxation method. The curves of crack relative length l/b and crack growth time t of four rocks under compressive stresses state were discussed according to subcritical crack growth parameters and the subcritical crack growth equation, and the limit time was obtained respectively. The main consequences can be summarized as follows:

（1）There are turning points on curves of crack relative length l/b and crack growth time t of all four rocks. Cracks grow stably, i.e. subcritical crack growth, before the turning point. Cracks grow, encounter and integrate catastrophically after the turning point, and there is not a gradual stage from crack stability growth to crack instability growth, i.e. rock mass instability is sudden. The curves of crack relative length l/b and crack growth time t move to right with increase of Young modulus E, which implies that limit time increases consequently. The results correspond to practicality.

（2）The curves of crack relative length l/b and crack growth time t of ore, lherzolite, marble and granite move to right with an increase of E, which implies that limit time increases consequently.

Acknowledgements

This research has been supported by China Postdoctoral Science Foundation(20060400264) and by the National Nature Science Foundation of China(50774093).

References

1. Nemat-Nasser S, Horii H. Compression-induced non-planar crack extension with application to splitting, exfoliation and rockbursts. J. Geophys. Res, 1982, B87. 6805-6821.
2. S.Melin, When does a crack grow under mode II conditions. Int. J. of Fract, 1986, 30. 103-104.
3. B.Cotterell and J. R. Rice. Slightly curved or kinked cracks. Int. J. of Fract, 1980, 16(2). 155-169.
4. H. Horii and S. Nemat-Nessar, Compression induced microcrack growth in brittle solids. Phil. Trans. R. Soc, 1986, 319. 337-374.
5. S. Nemat-Nessar. Non-coplanar crack growth. In Proceedings of the ICF International Symposium on Fracture Mechanics. Science Press,185-197, Beijing, People’s Republic of China, 1983.
6. Zhang, F.F., Wang, F.C., Lu,J. Fracture mechanics. Beijing. China Architecture & Building Press, 1981.(in Chinese)
7. Chen, F. Study on theory and experiment of compressive-shear fracture. ChangSha. Central South University, 2002.
8. P.Baud, T.Reuschle. and P.Charlze. An improved wing crack model for the deformation and failure of rock in compression. Int. J. Rock Mech. Min. Sci. & Geomech. Abstr., 1996, 33(5). 539-542.
9. J.M.Kemey. A Model for Non-linear Rock Deformation Under Compression Due to Sub-critical Crack Growth. Int. J. Rock Mech. Min. Sci. & Geomech. Abstr., 1991, 28(6). 459-467.
10. Miao, X.X., An, L.Q. and Zhai, M.H. Model of Rockburest for Extension of Slip Fracture in Palisades. Journal Of China University Of Mining & Technology, 1999, 28(2). 113-117.
11. Sun, S.F. material mechanics, Beijing: People Education Press, 1979.(in Chinese)
12. M. Ciccotti, G.Gonzato. and F. Mulargia. The double torsion loading configuration for fracture propagation: an improved methodology for the load-relaxation at constant displacement. International Journal of Rock Mechanics & Mining Sciences, 2000, 37 (7). 1103-1113.
13. M. Ciccotti, N. Negri. and G. Gonzato, et al. Practical application of an improved methodology for the double torsion load relaxation method. International Journal of Rock Mechanics & Mining Sciences, 2001, 38 (4) . 569-576.
14. Li, J.T. Study on instability and time dependence of pillar in hard rock mass. central south university, 2005.
15. Cao, P., Li, J.T. and Yuan, H.P. Testing study of subcritical crack growth and fracture toughness in different rocks.Transactions of Nonferrous Metals Society of China. 2006，16(3). 709-713.

RaSiM 7(2009): Controlling Seismic Hazard and
Sustainable Development of Deep Mines,
C.A. Tang(ed), Rinton Press, 245-250

MECHANISMS OF MICROSEISMIC EVENTS OCCURRED IN A DEEP HARD-ROCK MINE OF CHINA

CHUN-LAI WANG, AI-XIANG WU and XIAO-HUI LIU
School of Civil & Environment Engineering, University of Science & Technology Beijing,
Beijing, 100083, P.R. China

XUE-WEN JI, XIANG LI, QING-WEN YAN, XUE-GUI HUANG and XIAO-BING HOU
Yunnan chihong Zn & Ge Co. LTD
Qujing, 654212, P. R. China

The eighth orebody is being mined in the Huize Lead & Zinc mine, which is a deep mine in Yunnan chihong Zn & Ge Co. LTD. in China. In situ rock stresses were tested in different levels, the results indicated that the rock mass was in a state of high compressive stress. The basic problems such as high in-situ rock stress, fault structure, plentiful groundwater, etc. were concluded in the eight orebody. The microseismic events were generally induced because of the stress changes, excavation and geologic discontinuities in the deep hard-rock mine. By analyzing these reasons, the microseismic events occurred in brittle rock masses and geologic discontinuities, and the mechanisms of microseismic events occurrence were deduced. In the deep mine, the digital microseismic monitoring system was established in eighth orebody, the microseismic activity was recorded during the deep hard-rock mining, which made it possible to locate high stress concentration zones. Providing important implications for rockburst forecast based on the ongoing microseismic activity.

1 Introduction

The eighth orebody of the Huize Lead & Zinc mine is a rare large-sizes and rich multimetal orebody in Yunan chihong Zn & Ge Co., LTD. in China. The characteristics of the orebody are tremendous geology reserves, high ore grade, and rare multimetals such as: like germanium, silver, and cadmium. The complicated geological conditions of the orebody are unprecedented in China and include the water, deepness, fragmentary and their difficulty together. The distance between the eighth orebody and the Niulanjiang River is only 900 meters, which may cause accidental mine water invasion in the case that rock layer is broken by mine activity. The depth of the orebody is 1,280 meters from the ground in the mine, which is one of the deepest metal mines in China. It is located in the Yunnan-Kweichow Plateau and is high in-site stress because of the deepness of the mine. Under the high stress environment, as the rock mass yields and fails, the fracture of rock mass would be caused by the compressed stress and shear stress. Associated with this fracturing, microseismic events often occur in brittle rock masses and geologic discontinuities. Rockbursts have occurred locally in the mine, and the threats of rockbursts to mining safety and production is greatly increasingly. In order to improve rockburst forecasting based on the ongoing microseismic activity, the mechanisms of the microseismic events occurrence in a deep hard-rock mine needs to be discovered behind the violent failures.

Microseismicity is the response to deformation and failure of rock mass. A microseismic event is the sudden release of potential or stored energy in the rock. The released energy is then radiated as seismic waves. A rockburst is defined as a mining-induced microseismic event that causes damage to openings in the rock. The vagueness of the term rockburst is evident here, since this definition says nothing of how large the damage should be. These definitions have been used by for instance Cook [1], Salamon [2] and Ortlepp and Stacey [3].

2 Geology of the study area

The mining area is located at the southwestern edge of Yangtze metaplatform, and at the northeastern end of thrust structure zone of Kuangshanchang—Jinniuchang anticline on the eastern edge of the northeastern fold beam in Yunnan. The developing northeastern folds, faults, along-faults and near-faults in the mine area are favorable to the spacial distribution of mineral deposit. The structure of mine area was patterned toward the northeast-southwest direction, which was characterized firstly by schuppen structure, and secondly by the northwestern-southeastern structure [4].

Generally, the strata is divided from upper to lower, i.e.(1) Maping formation of upper Carboniferous(C3m):purple and grayish purple argillaceous striped breccia limestone with purple mud stone; (2) Weining formation of middle Carboniferous(C2w):grey middle-thick layer-like limestone with oolitic limestone; (3) Baizuo formation of lower Carboniferous(C1b):grayish white, ecru and pinkish red middle-coarse-grained dolomite with light grey limestone; (4) Datang formation of lower Carboniferous(C1d):grey crypto-crystal limestone, a layer of 0.3-3.5m brown black fine siltstone and purple mud stone on bottom; (5) Third member of Zaige formation of upper Devonian(D3zg3):grey crypto-crystal limestone and yellowish white, pinkish red middle-grained dolomite. Qilinchang orebody occurred in the middle-lower of Baizuo formation of lower Carboniferous, whose strike was N12°- 25°E, dip direction was SE and dip angle was 54°-65°.

3 Mechanisms of microseismic events occurrence

3.1 Stress induced microseismic events

3.1.1 Compress stress

It was speculated that stiff rock with high uniaxial compressive strength and high Young’s modulus could store more strain energy than softer and more deformable rock. But, brittle and the soft rocks consume almost the same amount of stored strain energy when brittle rock have a steeper unloading curve than soft rocks. Figure 1 shows that the failure process in excavating is violent in an intact and brittle part of the rock mass because the stiffness of surrounding rock is lower than the unloading stiffness of brittle rock. Conversely, the failure process is non-violent [5-6].

Microseismic events are either compressive failures of the rock mass or slip on a discontinuity. The state of stress satisfying a yield criterion is an essential theoretical question for microseismicity. Yield (failure) can be aseismic or seismic depending on local strain energy density and the energy required to induce yield under the state of rock mass confinement at the locus of rock failure [7-8].With the generation of stopes in the mine, microseismic events occurred when the pillars were fractured. Table 1 is the in-site stress state in the mine.

Table 1 In situ rock stress distribution in different levels

Postion /level	1391m			1261m		
Direction	S70°E	vertical compressive stress	N20°E	S70°E	vertical compressive stress	N20°E
Compress stress/MPa	22.1	21.5	18	26.4	25	22.3

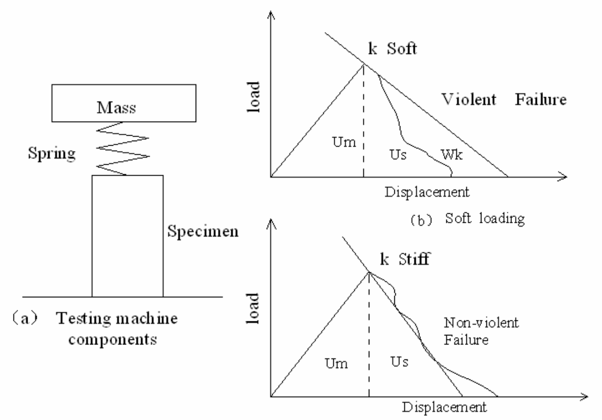

Figure 1 Model of the interaction between e.g., surrounding rock and ore (from Hedley 1992)

3.1.2 Shear stress

The recurrence time of microseismic events can be modelled reasonably well as a Poisson process. In the eighth orebody of the mine, the failure of most tunnels 'shoulder' was induced by the shear stress. Figure 2 shows the failure of shotcrete layer induced by shear stress in-site. The microseismic events occurred during the failure process of tunnel 'shoulder'. At the same time, S waves are easy to be monitored by the established monitoring system. It is possible to predict microseismic events given sufficient knowledge of shear stresses. But the most important work for predicting the occurrence of microseismic events is to accurately analyze where and when the shear stress concentrated on.

Figure 2 The failure of shotcrete layer induced by shear stress

3.2 Mine induced microseismic events

The different mining models induced microseismicity have the same basic mechanisms but occur on different scales. A large amount of work has been spent on solving the problem of predicting microseismicity. One problem is the difficulty of understanding exactly why they occur. The theory involves gradual stress and strain accumulation, which is suddenly released by movement along the mining surrounding rockmass.

A mining-induced seismic event cause's damage to openings in the rock, the released energy is then radiated as microseismic waves [9]. The type of microseismic events occurs in close proximity to excavations, and is a direct result of the stress redistribution around the excavations. It is most likely to occur where the stress is highest. The characteristic of this type of microseismic events is the coincidence of damage and failures. That is, the location of the damage and the location of the energy release are one or the same. Several types of failures belong to this type, the three most common fracturing are strain burst, pillar burst and face burst [10].

3.3 Geologic discontinuities

The geologic discontinuities conditions include geological structures (joints, faults, folds etc.) of rock mass and its characteristics are the strength and stiffness of the intact rock and the joints, water pressure etc. High stress levels may lead to massive failures in the rock mass and large plastic deformations. If the rock mass is of high quality and consists of brittle high strength rock types, the risk for violent failures increases. The failures can, in such cases, be relatively restricted to the area closest to the opening or result in rapid movements along geological structures leading to microseismicity phenomena.

Fault structures exit in eighth orebody in the mine, the local rock mass is at high in-site stress concentration, the moving of fault structures cause the maldistribution of stress state, which is disturbed by the fault structures activity leading to locally increased or decreased stresses. Microseism is the rock mass response to deformation and failure. The released energy is then radiated as seismic waves. A rockburst is defined as a mining-induced seismic event that causes damage to openings in the rock. These definitions have been used by for instance Cook (1976) [1], Salamon (1983) [2] and Ortlepp and Stacey (1994) [3].

The theory involves gradual stress and strain accumulation, which is suddenly released by movement along the geologic discontinuities. A simple model demonstrating the mechanism of slip on a fault is shown in Fig. 3.

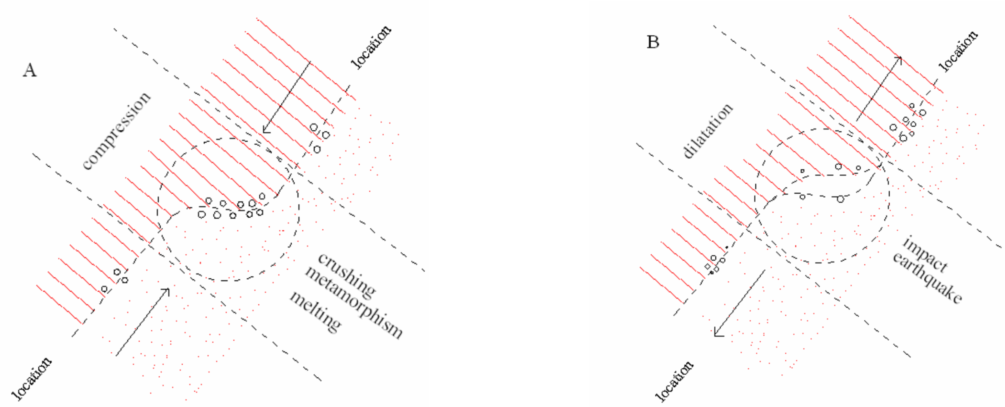

Figure 3 Microseismic events in the geologic discontinuities

4 Preventing method

Some different methods are used to predict and explain dynamic disasters. One of methods is preventing seismicity and microseismic monitoring which is an important tool for many mines today. The 24 channels full-digital microseismic monitoring system (ISS International, South Africa) was established in this mine in Aug. 2007 to monitor microseismic events in deep mining under the condition of complex development water. This monitoring system consists of a data acquisition unit and a three-dimensional array of uniaxial and triaxial accelerometers, and a total of 12 uniaxial and triaxial sensors. The sensors were distributed evenly within the area of interest and located at various elevations covering the full height of the caverns. The system automatically processes source parameters of the microseismic events and continuously displays three-dimensional source locations. It can predict the occurrence and magnitude of any seismic event, periodical interpretation of the processed data enables assessment of the stability and integrity of the caverns. The microseismic monitoring system could achieve the basic condition of monitoring dynamic disasters, like rockburst, mine earthquake, water bursting.

5 Conclusions

The geological conditions of the eight orebodies in the Huize mine are described. By analyzing the influencing factors of microseismic events occurrence, the compressive stress, shear stress, mining and geologic discontinuities were thought of as the main factors. The in-site stresses were tested at 1391m level and 1261m level in eighth orebody of this mine, which showed that the area belongs to high in-site stress, so that, it easily leads to the occurrence of microseismic events. Therefore, the microseismic monitoring system was established in the eighth orebody of this mine, which was for real-time monitoring of the microsismic events activity during the deep hard-rock mining, providing important methods for rockburst forecast based on the microseismic events activity.

Acknowledgments

We thank the financial support from the Key Technology P&D Program supporting project of the National ‘Eleventh Five-Year-Plan’ of China (No.2006BAB02A01).

References

1. Cook, N.G.W. Seismicity Induced by Mining. Engineering Geology, 1976, (10), 99-122.
2. Salamon, M.D.G. Rockburst Hazard and the Fight for Its Alleviation in South African Gold Mines. Proc. Symp. Rockbursts: prediction and control (London). London: Institution of Mining and Metallurgy, 1983, October. 20. 11-36.
3. Ortlepp, W.D. and Stacey, T.R. Rockburst Mechanisms in Tunnels and Shafts. Tunnelling and Underground Space Technology, 9(l). 59-65.
4. Tang, S.H. and Chen, J. The Law and Mechanism of Rockburst Occurring in Huize Lead-Zinc Mine. In: Fifth International Conference on Case Histories in Geotechnical Engineering, (New York, 2004).
5. Kristina, L. Seismicity in Mines, (Sweden, 2004).

6. Zhu, J.R., Pan, Y. and Wang, C.L. et al. Kaiser Used to Estimate In-site Stress in Huize Lead-Zine Mine. Mining Technology, 2008, 8(2), 26-55(in Chinese).
7. Hedley, D.G.F. Rockburst Handbook for Ontario Hardrock Mines. Ottawa: Canada Communication Group, 1992.
8. Wawersik, W.R. and Fairhurst, C. A Study of Brittle Rock Fracture in Laboratory Compression Experiments. Int. J. Rock Mech. Min. Sci. & Geomech. Abstr., 1970, (7), 561-575.
9. Gibowicz, S.J. and Kijko, A. An Introduction to Mining Seismology. San Diego: Academic Press, 1994.
10. Ortlepp, W.D. Rock Fracture and Rockbursts, An Illustrative Study. Johannesburg: The South African Institute of Mining and Metallurgy, 1997.

RaSiM 7(2009): Controlling Seismic Hazard and Sustainable Development of Deep Mines, C.A. Tang(ed), Rinton Press, 251-254

REVIEW ON ROCKBURST PREDICTION UNDER HIGH STRESS CONDITIONS

YAN-FEI XIONG, ZHENG-CAI DONG, YAN-LI MA and CONG-YIN WANG

Command Institute of Engineering Corps of PLA,

Xuzhou,221004, P.R. China

Rockburst is one type of dynamic stability geo-hazard under high stress conditions in underground rock engineering. Due to the serious damage to workers and facilities caused by rockburst, much research has been conducted. Some recent research work on rockburst prediction is discussed in this paper, such as RBF (Radial Basis Function) Neural Network, AdaBoost combination learning method, case reasoning, grey relational analysis theory, and the grey whitenization weight function cluster theory.

1 Introduction

Rockburst is a familiar type of geo-hazard with dynamic stability in the underground engineering of rocks under the high stress conditions of mining. It threatens the safety of builders, equipment and influences the process of engineering directly. Thus, it has become one of the most puzzling problems of underground engineering. The prediction of rockburst`s orientation is the basis for rockburst prevention.

In section 2 we introduce rockburst`s characteristics and classification and introduce the main effective cause of rockburst in section 3. In section 4, we state the research method of rockburst prediction, such as RBF (Radial Basis Function) Neural Network, AdaBoost combination learning method, case reasoning, grey relational analysis theory, and the grey whitenization weight function cluster theory. Finally, we conclude with some general observations and recommendations for ongoing work.

2 Characteristics and classification of rockburst

The rockburst usually shows signs of exfoliation, serious side and roof falling, and is sometimes accompanied with noise, rock ejecting, fierce energy release and underground works abruptly wrecking. The characteristics of rockburst can be summed up with the following facets[1]:

(1) The wall rock is hard and brittle. The uniaxial compressive strength of the rockburst's rock is larger than 50Mpa.

(2) The surrounding rock surface of the rockburst hole is generally dry.

(3) In the tunnel process, rockburst occurs more frequently within 3 times the diameter range of the working face, often occurring in the parts where the surrounding wall surfaces and cross-section are non-circular, and cavity walls are easily focused on parts of the stress.

(4) The depth for rockburst can be large or small; therefore, the depth is unimportant for the occurrence of rockburst.

(5) Rockburst occurs at different times, immediately after excavation, or some hours or days later.

According to the location and energy released, rockburst can be divided into the following three types[2]:

(1) Rockburst happens when the surrounding table rocks burst suddenly with PIPIPAPA noise, just like machine-gun firing, which is called rock shooting.

(2) Sudden rockburst caused by pillar or large-scale destruction of wall rock.

(3）Rockburst caused by changed move of fault.

3 Main effective cause of rockburst

Rockburst is a dynamic failure phenomenon which the surrounding rock occur brittle fracture and release elasticity potential energy under high stress and many other factors. From stress, lithology and energy, Ref [3,4] has put forward three different criterion for judging whether occurring rockburst:

(1)stress coefficient (P): it is the ratio of the largest chamber tangential stress σ_θ and the uniaxial compressive strength of rock σ_c. Rockburst is related to stress, which shows that the bigger stress coefficient is, the greater possibility of rockburst occurrence is.

(2)Rock brittleness coefficient (R): Rock brittleness coefficient refers to the ratio of rock uniaxial compressive strength σ_c and tensile strength σ_t. Rockburst is related to lithology, which shows that the bigger rock brittleness coefficient is, the greater possibility of rockburst occurrence is.

(3) Elastic energy index (W_{et}): When the rock sample is loaded to(0.8～0.9) σ_c, energy must be consume. And then the rock sample is unloaded to 0.05 σ_c, elastic energy must be released. Elastic energy index is ratio of consuming energy to load and elastic energy from unloading. The rockburst occurrence is related to energy. That is to say, the bigger W_{et} is, the greater the possibility and intensity of rockburst is.

4 The advanced process forecast of rockburst

4.1 RBF(Radical Basis Function) Neural Network in rockburst forecast utilization

The RBF neural network is one kind of forward feed type neural network, as shown in Figure1. The input level constitutes by the signal source node. The second level is hide level, and number nodes of it regards needs to decide. The third level is the output level, to response to the input pattern. Space's transformation is nonlinear from the input space to the hideaway, and the activation function of hidden node is RBF. The function is nonlinear, locally and centrosymmetric. The mapping of the function is shown as following[7]:

$$y_i = f_n(x) = w_0 + \sum_{i=1}^{n} \omega_i \Phi(\|X - c_i\|) \tag{1}$$

Where: ω_i is weight, X is input vector, Φ is RBF, $\Phi(\|X-c_i\|) = \exp\left(-\frac{\|X-c_i\|^2}{\sigma_i^2}\right)$. c_i and σ_i is data central and width of basis function, n is the number of centre.

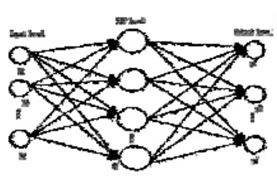

Figure1. The structural graph of RBF

In the rockburst simulation, we can quote the MATLAB software package's RBF Networks toolbox directly to simple program.

4.2 Classification and prediction of rockburst using Adaboost combination learning method

Boosting is the newest data getting method of forecast learning system, and the AdaBoost(auto-adapted Boost)is representative. This algorithm has obtained application successfully in many machine learning question, especially applies in the decision tree. Combination learning method which combine AdaBoost and ANN(Artificial Neural Network) classify and predict rockburst with rockburst sample[8].

4.3 Artificial neural networks for prediction rockburst in deep mining

The artificial neural networks have the strong misalignment dynamic handling ability, in does not need to know the data asked when distributed form and variable relations, it can, from the organization basis massive actual material establish each kind of factor and the output result misalignment mapping through the training study knowledge relate it are carry on the revision through the network outlet error's feedback to the network parameter, the automatic control each influencing factor asked weight, thus realizes the network mapping ability[10].

Based on the above Artificial Neural Networks Theory, 4 steps should be necessary, which is applied to forecast to solve the deep mining rockburst as following: to establish appropriate network architecture, that is to determine the number of input and output for the level neuron, of the implicit strata and of every implicit strata neuron, to establish collection of study sample and expectation output, to train network till its restraining, and to forecast using restraining network.

4.4Rockburst prediction method based on Grey Whitenization Weight Function

The rocks in every underground work will be selected as cluster objects to forecast rockburst disaster and intensity, with $i(i=1,2,\cdots)$ .That is to say:

$$i=\{rock\,under-excavation_1, rock\,under-excavation_2,\cdots\} \tag{2}$$

The rockburst disaster's major effect factor is to take as the cluster target, with j(j=1,2,3). Then[11]:

$$j=\left\{\sigma_\theta/\sigma_c, \sigma_c/\sigma_t, W_{et}\right\} \tag{3}$$

where: σ_θ is the maximum tangent stress of rock, σ_c is uniaxial compressive strength of rock, σ_t is uniaxial tension strength of rock , $f(\varepsilon)$ is loading curve, $f_1(\varepsilon)$ is unloading curve, $\varepsilon_r, \varepsilon_e, \varepsilon_p$ is total strain, elastic strain and model strain , W_{et} is rockburst forecast target, $W_{et}=\dfrac{\int_{\varepsilon_p}^{\varepsilon_\tau} f_1(\varepsilon)d\varepsilon}{\int_0^{\varepsilon_\tau} f(\varepsilon)d\varepsilon-\int_{\varepsilon_p}^{\varepsilon_\tau} f_1(\varepsilon)d\varepsilon}$.

The cluster ash classification will be divided into 4 kinds based on rock destruction form, the rockburst disaster destructiveness, and use k(k=1,2,3,4) to represent.

Then: $k=\{\text{no rockburst(RB}-1),\ \text{low rockburst(RB}-2),\ \text{medium rockburst(RB}-3),\ \text{violent rockburst(RB}-4)\}$

For convenient to express, we use i refer to the its cluster object the albinism number which has regarding the jth cluster target. The rock underground structure work that need to forecast will be taken as a cluster object, then the cluster coefficient of the works is :

$$\sigma_i^k = \sum_{j=1}^{3} f_j^k(x_{ij})\eta_j^k, \quad k = 1,2,3,4 \tag{4}$$

where: η_j^k is the j target about the k subclass power. According to the experts' experience and analysis to the rockburst material, the weight of various clusters target would be determined respectively that:

$$\eta_1 = 0.4,\ \eta_2 = \eta_3 = 0.3 \tag{5}$$

The cluster vector which constructs by the above cluster coefficient σ_i is:

$$\sigma_i = \left(\sigma_i^1, \sigma_i^2, \sigma_i^3, \sigma_i^4\right) \tag{6}$$

If $\sigma_i^{k^*} = \max_{1\le k\le 4}\left\{\sigma_i^k\right\}$, then the rank of rockburst disaster in the rock of underground structure work that's forecasted belongs to ash class k^*.

5 Conclusions

Rockburst occurrence is one kind of special power geology process, which is restricted based on various condition factors; such as the rock mass structure and performance, the geologic structural condition, hydro geological conditions, and the stress field after excavation adjustment. Breeding, evolution, suggestion of rockburst is a misalignment process, the rockburst occurrence mechanism all can not be clarified completely and, consequently, the existing rockburst prediction theory is not mature. In some rockburst forecast methods introduced above, the accuracy of Grey Relational Analysis, Fuzzy AHP, Case Reasoning Pattern Recognition, and rockburst based on Maxwell equation's forecast are high. If study is continued, perhaps an even better precision may be reached.

Reference:

1. Xu, L.S. Current Research Situation of Problems Related to High Ground Stress and Rock Blasting. Technology of Highway and Transport, 2002, 12(4). 48-51(in Chinese).
2. Yang, J. and Wu, X. Comprehensive Forecasting Method of Estimating Rockburst. Chinese Journal of Rock Mechanics and Engineering, 2005, 24(3). 411-416(in Chinese).
3. Wang, Y.H., Li, W.D. and Li, Q.G. et al. Comprehensive Method for Estimating Rockburst FUZZY. Chinese Journal of Rock Mechanics and Engineering, 1998, 17(5), 493-501(in Chinese).
4. Hoek, E. and Brown, E.T. Underground Evaluation in Rock. London: Institute of Mining and Metallurgy, 1980.
5. Liu, J.H., Feng, T. and Yuan, J. Rockburst Prediction Method Based on the Nonlinear Grey Model of Classification. Chinese Journal of Underground Space and Engneering, 2005, 12(1). 821-824(in Chinese).
6. He, X.F. and Xiao, H.F. Study on the Mine Rockburst Based on Maxwell Equations. Physic and Engineering, 2007, 17(3). 47-50. (in Chinese)
7. Pei, L. and Yang, Z.R. Prediction Forecast of Rockburst Based on RBF Neural Network. Coal Technology, 2008, 27(3). 137-139.(in Chinese)
8. Ge, Q.F. and Feng, X.T. Classification and Prediction of Rockburst Using Adaboost Combination Learning Method. Rock and Mechanics, 2008, 29(4). 943-948.(in Chinese)
9. Su, G.S., Zhang, X.F. and Yan, L.B. Rockburst Prediction Method Based on Case Reasoning Pattern Recognition. Journal of Mining & Safety Engineering, 2005, 25(1). 63-67.(in Chinese)
10. Song, C.S. and Li, D.H. Artificial Neural Networks for Prediction Rockburst in Deep Mining. Journal of Henan Polytechnic University (Natural Science), 2007, 26(4). 365-369.(in Chinese)
11. Xie X.B. and Pan, C.L. Rockburst Prediction Method Based on Grey Whitenization Weight Function Cluster Theory. Journal of Henan University (Natural Sciences), 2007, 34(8). 17-21.(in Chinese)

RaSiM 7(2009): Controlling Seismic Hazard and
Sustainable Development of Deep Mines,
C.A. Tang(ed), Rinton Press, 255-260

A PRELIMINARY STUDY OF SIZE EFFECT BEHAVIOUR OF ROCK SPECIMENS

XIAO-RUI ZHOU, WEI GUO and JUN-JIE LIU

Institute of Civil Engineering and Architecture, Dalian University

Dalian 116622, China

To completely recognize size effect, this paper discusses a relative compressive strength experiment which adopts different size specimens using granite porphyry (100×100×20mm) and Diorite (130×100×80mm). Results show that the size effect has obvious differences on the strength of the specimens, the characteristics of the rupture state of specimens, stress-temperature coupling, acoustic emissions, etc. The essence is that the specimens store different elastic strain energies with a difference of magnitude. The elastic strain energy is mainly used in the rupture of specimens; large size specimens and isometric granular texture specimens appear cutting ejection, also called rock burst, before rupture. On the contrary, small size specimens and porphyritic texture specimens do not appear cutting ejection before rupture, and the elastic strain energy is converted into acoustic energy which is used for increasing heat of specimens. The above performance of size effect under the stress plays an important role for research, the mechanism of rock burst, which is happened in deep underground surrounding rock, design and construction, the security maintenance, and the monitoring and prediction of earthquake.

1 Introduction

The change of ground stress is related to some phenomenon which are as follows: the phenomenon of dynamic disaster such as rock burst [1, 2, 3] which happens in the process of underground engineering excavation, the phenomenon of temperature increment of coal mass [4, 5] which turns up in the process of roadway head of coal mine, the phenomenon of geothermal anomaly which happens before major earthquake, and the physical phenomenon of infrared radiation energy and microwave radiation energy of rock following the rock stress changing which is found in the research of remote sensing on earthquake prediction [6].

The size effect appearing in specimens under sustained stress has a long research history and has been recognised clearly [7, 8, 9]. The size effect based on specimens which have same material but different sizes shows the different strength, and it is hypothesized that this is the cause of size effect due to the defects and heterogeneity in the internal structure. Through the preliminary experiment of rock specimens in this paper, the author also found that the size effect has significant performance in the rupture-form, temperature increment and the characteristics of acoustic emission strength. These three performances of size effect of rock specimens have an important application meaning in engineering.

2 Overview of experiment

2.1 Specimens of experiment.

The granite porphyry and the diorite are used in experiment. Granite porphyry belongs to hypabyssal rock, its petrological characteristics are flesh-colored, holocrystalline porphyritic texture, blocky structural, density and have the biggest orthoclase phenocryst which are 5-8mm. Granite porphyry have a mineral association of orthoclase, quartz, and biotite etc, the uniaxial compressive strength is 100-180MPa [10] (coarse-grained granite is 120-140MPa, medium-grained granite is 160-180MPa), and the size is 100×100×20mm. Diorite belongs to abyssal rock, its petrological characteristics are gray, holocrystalline isometric granular texture, blocky structure, compact. Diorite have a mineral association of hornblende, plagioclase, and biotite etc, the uniaxial compressive strength is 130-300MPa [10], and the size is 130×100×80mm.

2.2 Experiment equipment and performance of technical parameters.

Compression test machine is YEW3300 computer screen display press machine which is produced in Changchun New Test Instruments Ltd, the maximum load is 3000KN, and accuracy is 1%. Thermodetector is Optris non-contact infrared thermometer which is produced in Germany, whose measuring range is -32~530℃, precision is ±1%, temperature resolution is 0.1℃, response time is 300ms.

2.3 Dealing with the experiment data by real time recording

The press machine and the infrared thermometer are connected with a computer through the USB interface. The experiment data of load (KN), temperature (℃), time (s) are recorded by real time in the experiment process, the records of load-time data are storied in the form of Excel and the temperature-time data are storied in the form of dat. Meanwhile real time load-time and temperature-time change curve are drawn automatically, and the digital and graphical form can show the changing on computer screen.

3 Experiment results analysis

3.1. Characteristics of stress-change experiment curve

With the increasing of stress, the process of deformation and fracture of rock specimens is roughly shown by three stages. (Figure 1, Figure 2)

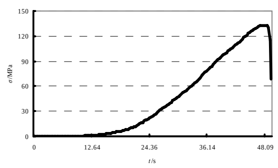

Figure 1 The experiment curve which is stress with time-varying load of diorite specimens

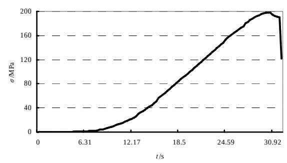

Figure 2 The experiment curve which is stress with time-varying load of granite porphyry specimens

3.1.1 Approximately straight line elastic deformation stage.

The stress-time experiment curve shows the change is just like a straight line on the condition when the stress is under 15MPa, which can be regarded as elastic deformation stage.

3.1.2 Oblique linear elastic-plastic-cracking and deformation stage.

With the stress on Diorite being 15 ~125MPa, and Granite porphyry 25~180MPa, the stress-time experiment curve shows that oblique line change observably, which can be regarded as elastic-plastic-cracking and deformation stage, and on the condition when the stress is ±100MPa, it reached plastic deformation stage.

3.1.3 Parabola type ruptures stage.

Stress-time experiment curve shows parabolic change on the condition that the stress reaches maximum stress (rupture stress) 132MPa (Diorite) and 195MPa (Granite porphyry), and it is also called the specimens rupture and deformation stage.

3.2. Characteristics of temperature-change experiment curve

Stress-temperature experiment curve is shown in Figure 3 and Figure 4. The characteristics of diorite temperature-time experiment curve (Figure 3), roughly correspond to the three deformation stages which mentioned above, but the change rate of the second stage and its pre-stage manifests less significant than the stress-time experiment curve. On the condition that the stress reaches 100MPa and the temperature is from 17.4℃ rising to 18.3℃ (the temperature of diorite), and the temperature increment is $\triangle T_{<100MPa}$=0.9℃. At the times of specimens rupture, the temperature rapidly rising from 18.3℃ to 20.25℃ in less than 1 second. The temperature increment is $\triangle T_{>100MPa}$=2.2℃, and the whole temperature increment $\triangle T$=2.85℃.

The characteristics of granite porphyry temperature-time experiment curve (Figure 4) do not show the characteristic which correspond to the above-mentioned three stages, but shows several rectangular jump morphologies. At first, it fluctuates between 23.6℃ and 23.8℃ (roughly corresponds to stress <15MPa stage). Then fluctuates between 23.8℃ and 23.9℃ (roughly corresponds to stress±100MPa stage), and it appears 23.7℃ once. The whole temperature increment is little $\triangle T$=0.3℃.

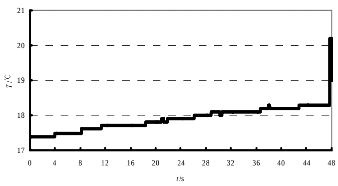

Figure 3 The experiment curve which is temperature with time-varying load of diorite specimens

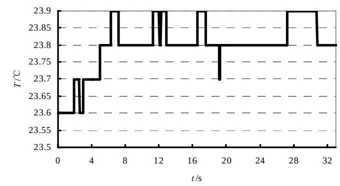

Figure 4 The experiment curve which is temperature with time-varying load of granite porphyry specimens

3.3 Analysis for the specimens by comparing between stress-temperature experiment curves

Through comparing and analyzing the characteristics of tress-temperature-time experiment curve of rock specimens from Figure 3 and Figure 4 that can obtain some cognition as follows.

3.3.1 Experiment results compared with predecessors.

The former [6] experiments with rock specimens proved that existence stress-temperature coupling effect. With the sustainable increase of stress, the temperature becomes higher and higher, and the process of specimens temperature increment is close to its deformation stage, which performances have three stages: 1) At elastic deformation stage, the temperature increasing amplitude is low, and the temperature increment is $\triangle T$=0.3~0.8℃. 2) When stress reaches 100MPa that equivalent to 81% of rupture stress, and the temperature rising suddenly at the transition from elastic deformation stage to plastic deformation stage. The temperature increment is $\triangle T$=1.4~3.6℃. 3) The temperature rising suddenly once more before specimens rupture. The temperature increment is $\triangle T$=1.6~5.5℃ and its average is 3.2℃.

3.3.2 Size effect.

This experiment with the same experiment materials as in literature [6], but different corresponding stress proves the size effect really existence. The height of relatively smaller specimens need much more stress than the bigger one when it failure (the height of specimens are 18cm in literature [6]), and the rupture stress for the former is up to 180MPa, and the latter 123MPa.

The major way of specimens rupture is tensional rupture, but state of ruptures between different size specimens exist differences. The deformation fracture of small size specimens performs the whole axial rupture, but the big one performs conical rupture accompanied by ejection.

3.3.3 Rock structure (Grain size).

It is not only related to size effect, but also to the structure of material, in another word, we can say it is related to particle size and uniformity of rock crystallization phase. The change of temperature of coarse grained texture rock following by stress is less than fine grained one [6]. Granite porphyry is porphyritic structure with larger feldspar phenocryst, but diorite is isometric granular texture.

3.4 Characteristics and analysis of the acoustic emission of specimens

3.4.1 Sound description.

Without detecting the acoustic emission with specialized equipment, this paper only offers the qualitative analysis for the sound when specimens rupture. It is observed that the rock of two different types and different sizes produce totally different characteristics of acoustic emission in the process of specimens compression test until the beginning of the rupture. Acoustic emission of small size specimens has low-frequency sound, and no cutting ejection phenomena, from deformation to rupture. Acoustic emission of large size specimens has high-frequency sound at the beginning, and finally, with it ruptured, there is crisp sound, at the same time the cutting ejection phenomena happened. This phenomenon is called rock burst.

3.4.2 Relationship between the stress field, acoustic emission and temperature field.

According to the experiment results of literature [6], the relationship between temperature-change of specimens followed by stress-change and specimens deformation stage is closed. Acoustic emission protrudes three stages, corresponding to the initial elastic deformation, initial plastic deformation and the stage before the rupture. Furthermore, it becomes stronger one stage by another. With the acoustic emission, the temperature rising suddenly once more before rupture, and then specimens ruptures. In addition, the relationship between acoustic emission and temperature shows cross-change. In another word, the temperature keeps invariant when acoustic emission happens and acoustic emission quiet when temperature rising suddenly.

3.5 Energy explanation of size effect

It is analyzed that the size effect has three forms of performance, which is the form of specimens rupture, the amplitudes of the temperature increment and the strength of acoustic emission. On the one hand the three performances are related to the accumulation of elastic strain energy, specimens with different size in the compression process, the accumulation of energy is different which small size specimens have low accumulation of energy for its stress acting on small volume, on the contrary, large size specimens have high accumulation of energy for its stress acting on large volume. When rock (assumed to be rectangular columnar) force at elastic strain state, the accumulation of strain energy E_ε as follows,

$$E_\varepsilon = \frac{\sigma^2 \cdot V}{2E}^{[1]} \tag{1}$$

In the formula, σ is the stress that acting on square rock body, kg/cm^2, E_ε is the elastic modulus of rock, kg/cm^2, V is the volume of square body, cm^3.

On the other hand, these three performance are related to work and energy conversion for different size of specimens in the stress process. From (1) can know that the greater stress loaded on the specimens and the volume of specimens, the greater strain energy E_ε accumulated. The phenomenon of large-size specimens rupture with cutting ejection (rock burst) is response to the release of more energy. The variable quantity of temperature measuring point in deep is greater than the surface [6], that is, the warming amplitudes in the internal of specimens are greater, which reflecting the more strain energy storage in the internal of rock or specimens. The acoustic emission characteristic of large-size specimens has a performance of high-frequency, as well as high-energy release.

The problem of energy of size effect can through many groups corresponding experiment, general consideration work of loading process, strain energy, thermal energy (reflected by temperature), sound energy (reflected by acoustic emission) and the work of specimens rupture etc to explore the quantitative relation of conversion and balance between work and energy except (1).

4 Conclusions

It can be confirmed in the experiment that the size effect can be demonstrated three ways: 1) the rupture form of specimens; 2) specimen's temperature increment under the stress; 3) and the acoustic emission characteristics of specimens rupture. These three phenomenon mentioned above in essence is a process of elastic strain energy storage and release.

The stress-temperature coupling effect of rock specimens is obviously related to size effect. Specimens' temperature increases with stress until the specimen failure, which is when the temperature rises to the highest value, then the temperature drops, and the critical state appears before the specimens rupture, which shown a greater increment in stress and the temperature rapidly rise. In this experiment, the height of specimens are 8 cm and 2cm, the temperature increment of former (large size) is 9.5 times of the latter's.

There are some obvious differences in acoustic emission characteristics with different sizes. The acoustic emission of large-size specimen is high-frequency short waves, and is accompanied by the phenomenon of cuttings ejection (rock burst). Oppositely, the acoustic emission of small-size specimens are low-frequency long waves without cuttings spatter phenomenon.

Further experimental testifying and theoretical analysis is needed to find the differences of experiment results between this experiment and the predecessors. The present recognition is that it may be related to the loading rate of the press machine during the process of experiment. Previous experiments did not mention the factors of the loading rate and there may have been no consideration of loading rate on stress-temperature coupling effect.

Acknowledgements

The author would like to thank the financial support by the National Natural Science Foundation of Liaoning (Grant No. 2050772).

References

1. Zhang, Z.Y., Wang, S.T. and Wang, L.S. Engineering geological analysis axiom. Beijing: Geological Poblishing House, 1990, 283-357. (In Chinese)
2. Zhang, X.G., Li, Z.Y. and Zheng, D.H. etc. Special Engineering Geology. Beijing: Geological Poblishing House, 1994, 148-173. (In Chinese)
3. Yan, X.Z. Coal Mine Geology. Xuzhou: China University of Mining &Technology Press, 1993, 255-350. (In Chinese)
4. Guo, L.W., Yu, Q.X. Jiang, C.L. and Wang, K. Testing Study on the Variation of Coal Temperature During the Process of Coal and Gas Outburst. Chinese Journal of Rock Mechanics and Engineering, 2000, 19(3). 366-368. (In Chinese)
5. Jiang, C.L. and Yu, Q.X. The Mechanism of Coal and Gas Outburst Spherical Shell Instability Hypothesis. Safety in Coal Mines, 1995(2). 17-25. (In Chinese)
6. Deng, M.D., Geng, N.G. and Cui, C.Y. etc. The Study on the Variation of thermal State of Rocks Caused by the Variation of Stress State of Rocks. Earthquake Research in China, 1997, 13(2). 179-185. (In Chinese)
7. Xu, D.H. and Feng, W.Y. Concrete Material Practical Guide. Beijing: China Building Material Industry Press, 2005, 102-111. (In Chinese)
8. Yang, M.Q. and Chi, Y. Mechanism of Size Effect of Concrete Sample. Journal of Fuzhou University (Natural Science), 1992(1): 87-94. (In Chinese)
9. Huang, H.Y., Yang, G.Y. Shen, C.M. Wang, S.R. and Zhang Y.D. Numerical Analysis of Concrete Strength Size Effect on Meso-level. Concrete, 2007(4). 11-16. (In Chinese)
10. Liu, B.C. The General for Mine Rock Mechanics. 1982, 30-104. (In Chinese)

RaSiM 7(2009): Controlling Seismic Hazard and
Sustainable Development of Deep Mines,
C.A. Tang(ed), Rinton Press, 261-268

STUDY ON LOCALIZATION AND BIFURCATION OF GEOMATERIALS WITH DAMAGE EFFECT

DAN ZHENG

College of Safety Science and Engineering, Liaoning Technical University, Fuxin, 123000, China;

ZHONG-CHANG WANG

College of Civil and Architectural Engineering , Dalian University, Dalian 116622, China

LIAN-SHAN SHEN and HAI-JIAO WANG

College of Information Engineering, Dalian University, Dalian 116622, China

To obtain the damage effect in the process of elasto-plasticity deformation of geomaterials, the isotropic damage loading-unloading equation and damage variable are introduced to the non-continuous bifurcation. The critical hardening modulus, localized orientation angle with consideration of stiffness degradation, and dilatancy are set up. The relationship of the localized orientation angle and the maximal hardening modulus depends on the degree of damage, and the initial Poisson's ratio of rock is explored. Comparative analyses are conducted to study the bifurcation of uniaxial tension-compression samples under the conditions of plane stress and plane strain. The variation of the orientation angle of localization and the maximum hardening modulus depends on the initial Poisson's ratio and the degree of damage, and the sum of the orientation angle under tension and compression conditions is 90°. Also, there are plane stress and plane strain cases of the maximum hardening modulus which is independent of the uniaxial compression and tension.

1 Introduction

Bifurcation is an abrupt change of a system parameter's qualitative behaviour when it fluctuates and reaches a certain critical value [1]. Continuity mechanics method is applied to catch the moment and location of bifurcation for localization analysis when bifurcation happens. So many scholars [1-3] just discussed bifurcation instability relating to elasto-plasticity deformation, and they neglected the damage effect. A large number of defects appear with dilatancy and stiffness degradation. Elasto-plasticity deformation and damage effect are two kinds of nonlinear characteristics that must be considered when material bifurcation instability is analyzed. Assuming isotropic damage, damage variable and the loading-unloading equations are introduced to non-continuous bifurcation. With consideration of stiffness degradation and dilatancy causing Poisson's ratio to increase, the maximal hardening modulus and localized orientation angle are theoretically derived. The relationship of the localized orientation angle and the maximal hardening modulus depends on the degree of damage, and the initial Poisson's ratio is explored. Comparative analyzes are conducted to study the bifurcation of uniaxial tension-compression samples under the conditions of plane stress and plane strain.

2 Derivation of Constitutive Equation for Damage Increment

Constitutive relation of traditional isotropic damage can be expressed as:

$$\boldsymbol{\sigma}_{ij} = \mathbf{D}_{ijkl}\boldsymbol{\varepsilon}_{kl}\,,\quad \mathbf{C}:\mathbf{D} = \mathbf{I}_4 \tag{1}$$

where $\mathbf{C}$ is flexibility tensor, $\mathbf{I}_4$ is fourth order identity tensor and $\mathbf{D}_{ijkl}$ is modulus tensor of elastic damage. It can be expressed as follows [4]:

$$\mathbf{D}_{ijkl} = (1-d)\mathbf{D}^0_{ijkl}\,,\quad \dot{\mathbf{D}}_{ijkl} = -\dot{d}\mathbf{D}^0_{ijkl}\,,\quad \mathbf{C}_{ijkl} = \hat{d}\mathbf{C}^0_{ijkl} \tag{2}$$

where $\mathbf{D}^0_{ijkl}$ is initial elastic modulus tensor and d is damage variable. Depending on the former plastic strain, loading-unloading equation is introduced:

$$F(\boldsymbol{\sigma}_{ij}, \lambda) = 0 \tag{3}$$

where λ is an internal variable in flex field. G is damage potential equation and $\dot{\varepsilon}^{\mathrm{d}}_{ij}$ is damage strain, then constitutive relation of increment is as follows:

$$\dot{\boldsymbol{\sigma}}_{ij} = \mathbf{D}_{ijkl}\left(\dot{\boldsymbol{\varepsilon}}_{kl} - \dot{\boldsymbol{\varepsilon}}^{\mathrm{d}}_{kl}\right) \tag{4}$$

Applying non-associated flow rule, the following can be found:

$$\dot{\boldsymbol{\varepsilon}}^{\mathrm{d}}_{kl} = \dot{\lambda}\mathbf{g}_{kl} \tag{5}$$

where $\mathbf{g}_{kl} = \partial G \big/ \partial \boldsymbol{\sigma}_{kl}$ is gradient equation. According to consistency condition, there is equation as follows:

$$\dot{F} = \frac{\partial F}{\partial \boldsymbol{\sigma}_{ij}}\dot{\boldsymbol{\sigma}}_{ij} + \frac{\partial F}{\partial \lambda}\dot{\lambda} = \mathbf{f}_{ij}\dot{\boldsymbol{\sigma}}_{ij} - H\dot{\lambda} = 0 \tag{6}$$

where $\mathbf{f}_{ij} = \partial F \big/ \partial \boldsymbol{\sigma}_{ij}$ is gradient equation of loading equation, $H = -\partial F \big/ \partial \lambda$ is hardening or softening modulus and $\dot{\lambda}$ is non-negative damage multiplicator.

Using flexibility tensor, flow rule can be expressed as:

$$\dot{\boldsymbol{\varepsilon}}^{\mathrm{d}}_{pq} = \dot{\lambda}\mathbf{M}_{ijkl}\boldsymbol{\sigma}_{rs} \tag{7}$$

where $\mathbf{M}_{ijkl}$ is initial flexibility tensor.

From equations (5) and (7), we can get:

$$\mathbf{g}_{ij} = \mathbf{M}_{ijkl}\boldsymbol{\sigma}_{kl} \tag{8}$$

And from equation (4)-(6), the following can be obtained:

$$\dot{\lambda} = \frac{1}{A}\mathbf{f}_{ij}\mathbf{D}_{ijkl}\dot{\varepsilon}_{kl}\,,\quad A = H + \phi_{pq}\mathbf{D}_{pqrs}\mathbf{M}_{rsuv}\boldsymbol{\sigma}_{uv} > 0 \tag{9}$$

Taking equation (9) into equations (4) and (5), the constitutive relation of increment can be found:

$$\dot{\boldsymbol{\sigma}}_{ij} = \mathbf{D}^{\mathrm{ed}}_{ijkl}\dot{\varepsilon}_{ij} \tag{10}$$

where $\mathbf{D}^{\mathrm{ed}}_{ijkl}$ is tangent modulus tensor of elastic damage.

$$\mathbf{D}_{ijkl}^{\mathrm{ed}} = \begin{cases} \mathbf{D}_{ijkl}, & \text{elastic loading} \\ \mathbf{D}_{ijkl} - \dfrac{1}{A}\mathbf{D}_{ijkl}\mathbf{M}_{abcd}\boldsymbol{\sigma}_{cd}\mathbf{f}_{xy}\mathbf{D}_{xykl}, & \text{damage loading} \end{cases} \tag{11}$$

Damage loading or unloading criterion obeys complementary condition:

$$\dot{F} \le 0, \dot{\lambda} \ge 0, \dot{F}\dot{\lambda} = 0 \tag{12}$$

According to the proposal [5] of Carol, damage factor and initial flexibility tensor can be expressed as follows:

$$\dot{\lambda} = \dot{\hat{d}} = \frac{\dot{d}}{(1-d)^2}, \quad \mathbf{M}_{ijkl} = \mathbf{C}_{ijkl}^0, \quad \mathbf{g}_{ij} = \mathbf{C}_{ijkl}^0\boldsymbol{\sigma}_{kl} = \boldsymbol{\varepsilon}_{ij}^0 \tag{13}$$

The following damage loading equation [6] is selected:

$$F = f\left(w^0, \hat{d}\right) - r\left(\hat{d}\right), \quad w^0 = \frac{1}{2}\boldsymbol{\sigma}_{ij}\mathbf{C}_{ijkl}^0\boldsymbol{\sigma}_{kl} \tag{14}$$

where f is crack driving force and r is radius of yield surface.

Damage hardening modulus H is:

$$H = -\frac{\partial F}{\partial \lambda} = -\frac{\partial f\left(w^0, \hat{d}\right)}{\partial \hat{d}} + \frac{\partial r\left(\hat{d}\right)}{\partial \hat{d}} \tag{15}$$

Gradient equation of loading equation can be expressed as:

$$f_{ij} = \frac{\partial F}{\partial \boldsymbol{\sigma}_{ij}} = \frac{\partial f\left(w^0, \hat{d}\right)}{\partial w^0}\mathbf{C}_{ijkl}^0\boldsymbol{\sigma}_{kl} = \frac{\partial f\left(w^0, \hat{d}\right)}{\partial w^0}\varepsilon_{ij}^0 \tag{16}$$

Taking equations (14)-(18) into equation (9) and according to (2), the following can be found:

$$A = -\frac{\partial f\left(w^0, \hat{d}\right)}{\partial \hat{d}} + \frac{\partial r\left(\hat{d}\right)}{\partial \hat{d}} + 2(1-d)w^0\frac{\partial f\left(w^0, \hat{d}\right)}{\partial w^0} \tag{17}$$

Then damage tangent modulus is:

$$\mathbf{D}_{ijkl}^{\mathrm{ed}} = (1-d)\mathbf{D}_{ijkl}^0 - \frac{(1-d)^2\left(\partial f / \partial w^0\right)}{\partial r/\partial \hat{d} - \partial f/\partial \hat{d} + 2(1-d)w^0\,\partial f/\partial w^0}\boldsymbol{\sigma}_{ij}\boldsymbol{\sigma}_{kl} \tag{18}$$

3 Damage Effect in Analysis of Bifurcation

Non-continuous bifurcation is decided by singularity of damage tensor $\mathbf{Q}_{il}^{\mathrm{d}}$.

$$\mathbf{Q}_{il}^{\mathrm{d}} = \mathbf{n}_j\mathbf{D}_{ijkl}^{\mathrm{ed}}\mathbf{n}_k \tag{19}$$

where n_j ($j = 1, 2, 3$) is unit normal vector of localized feature face. Prerequisite of non-continuous bifurcation is:

$$\det[\mathbf{Q}_{il}^{\mathrm{d}}] = 0 \tag{20}$$

According to the following eigenvalue:

$$\mathbf{Q}_{il}^{\mathrm{d}}y_l^{(i)} = \lambda^{(i)}\mathbf{Q}_{il}^{\mathrm{d}}y_l^{(i)} \quad \text{(i=1, 2, 3)} \tag{21}$$

And according to symmetric positive definiteness of $\mathbf{D}_{ijkl}^{\mathrm{ed}}$ and Q_{il}^{d}, $\left(\mathbf{Q}_{il}^{\mathrm{d}}\right)^{-1} = \mathbf{P}_{il}^{\mathrm{d}}$, equation (21) can be expressed as follows:

$$B_{jl}y_l^{(i)} = \lambda^{(i)}y_j^{(i)} \qquad \text{(i=1, 2, 3)} \tag{22}$$

where $\mathbf{B}_{jl} = \boldsymbol{\delta}_{jl} - \dfrac{1}{A}\mathbf{P}^{\mathrm{d}}_{ji} b_i a_l$, $a_l = \mathbf{f}_{mn}\mathbf{D}^{0}_{mnkl}\mathbf{n}_k$, $b_i = \mathbf{n}_j\mathbf{D}^{0}_{ijst}\mathbf{g}_{st}$

If $\mathbf{P}^{\mathrm{d}}_{il}$ and $\mathbf{Q}^{\mathrm{d}}_{il}$ are nonsingular, $\mathbf{B}_{jl}$ must be nonsingular. The equation $\lambda = 1$ has double eigenvalue of equation (22), and the third eigenvalue is obtained.

$$\lambda^{(3)} = 1 - \frac{1}{A} a_i \mathbf{P}^{\mathrm{d}}_{ij} b_j \tag{23}$$

If B_{ji} is singular, $\lambda^{(3)} = 0$ and according to equation (10), the hardening modulus is found when localization happens.

$$H = -\mathbf{f}_{ij}\mathbf{D}_{ijkl}\mathbf{g}_{kl} + \mathbf{n}_j\mathbf{D}_{ijst}\mathbf{g}_{st}\mathbf{P}^{\mathrm{d}}_{il}\mathbf{f}_{mn}\mathbf{D}_{mnkl}\mathbf{n}_k \tag{24}$$

$\mathbf{D}^{0}_{ijkl} = \mathbf{D}^{\mathrm{e}}_{ijkl}$, where $\mathbf{D}^{\mathrm{e}}_{ijkl}$ is isotropic elastic tensor, then follow is found from equation (2)

$$\mathbf{D}_{ijkl} = 2G^{\mathrm{d}}\left[\frac{v^{\mathrm{d}}}{1-2v^{\mathrm{d}}}\delta_{ij}\delta_{kl} + \frac{1}{2}\left(\delta_{ik}\delta_{jl} + \delta_{il}\delta_{jk}\right)\right] \tag{25}$$

where G^{d} and v^{d} are damage shear modulus and Poisson’s ratio, and they can be expressed as:

$$G^{\mathrm{d}} = (1-d)G\,,\quad v^{\mathrm{d}} = \frac{3\nu_0 + (1-2\nu_0)d}{3-(1-2\nu_0)d} \tag{26}$$

where G and ν_0 are shear modulus before damage and initial Poisson’s ratio.

Direction of $H^{\mathrm{d}} = \max H(\mathbf{n}_i)$ is the same as the critical localization’s, and the following can be obtained:

$$\frac{H}{2G^{\mathrm{d}}} = 2n_k\mathbf{f}_{kl}\mathbf{g}_{ij}\mathbf{n}_j + \frac{v^{\mathrm{d}}\left[\mathbf{n}_i\left(\mathbf{g}_{ss}\mathbf{f}_{ij} + \mathbf{f}_{ss}\mathbf{g}_{ij}\right)\mathbf{n}_j - \mathbf{f}_{ii}\mathbf{g}_{ss}\right]}{1-v^{\mathrm{d}}} - \mathbf{f}_{ij}\mathbf{g}_{ij} - \frac{\mathbf{n}_i\mathbf{f}_{ij}\mathbf{n}_j\mathbf{n}_k\mathbf{g}_{kl}\mathbf{n}_l}{1-v^{\mathrm{d}}} \tag{27}$$

where $f_{\mathrm{v}} = \mathbf{f}_{ii}$, $\bar{\mathbf{f}}_{ij} = \mathbf{f}_{ij} - \dfrac{1}{3}\delta_{ij} f_{\mathrm{v}}$, $g_{\mathrm{v}} = \xi f_{\mathrm{v}}$, $\bar{\mathbf{g}}_{ij} = \xi\bar{\mathbf{f}}_{\mathbf{ij}}$ and $\xi = \left(\partial f\left(w^0, \hat{d}\right)\big/\partial w^0\right)^{-1}$

where f_{v} , $\bar{\mathbf{f}}_{ij}$, g_{v} and $\bar{\mathbf{g}}_{ij}$ are the first invariant and deviator of yield equation $\mathbf{f}_{ij}$ and gradient equation of damage potential equation $\mathbf{g}_{ij}$.

It is supposed that $\bar{f}_i\,(i = 1, 2, 3)$ is principal value of $\bar{\mathbf{f}}_{ij}$, and the following can be defined:

$$r = \varphi\left(f_{\mathrm{v}} + g_{\mathrm{v}}\right),\quad k = \frac{1}{2}\sum_{i=1}^{3}\bar{f}_i\bar{g}_i + \frac{2}{3}\varphi f_{\mathrm{v}} g_{\mathrm{v}} \tag{28}$$

Taking equation (28) into equation (27), normalized hardening modulus can be obtained.

$$\frac{H}{4\xi G^{\mathrm{d}}} = \sum_{m=1}^{3}\left(\bar{f}_m^{\,2} + r\bar{f}_m\right)n_m^2 - \psi\left(\sum_{l=1}^{3}\bar{f}_l n_l^2\right)^2 - k \tag{29}$$

where $\varphi = \dfrac{1+v^{\mathrm{d}}}{6\left(1-v^{\mathrm{d}}\right)}$ and $\psi = \dfrac{1}{2\left(1-v^{\mathrm{d}}\right)}$.

Considering geometry constraint conditions $\sum_{j=1}^{3} n_j^2 = 1$, Lagrange's method of undetermined multipliers is used to structure extreme value in unrestrained conditions, in order to obtain maximum.

$$L = \frac{H}{4\xi G^{\mathrm{d}}} - \beta\left(\sum_{j=1}^{3} n_j^2 - 1\right) \tag{30}$$

where β is Lagrange multiplier. Extremum condition of hardening modulus H is:

$$\frac{\partial L}{\partial n_i} = 2A_i \mathbf{n}_i = 0, \quad \frac{\partial L}{\partial \beta} = -\left(\sum_{j=1}^{3} n_j^2 - 1\right) = 0 \tag{31}$$

For $A_i = \bar{f}_i^2 + r\bar{f}_i - 2\psi m\bar{f}_i - \beta$ and $m = \sum_{i=1}^{3} \bar{f}_i n_i^2$, H_{ij} is defined as:

$$H_{ij} = \frac{\partial^2 L}{\partial \mathbf{n}_i \partial \mathbf{n}_j} = \begin{bmatrix} H_{11} & H_{12} & H_{13} \\ H_{21} & H_{22} & H_{23} \\ H_{31} & H_{32} & H_{33} \end{bmatrix} \tag{32}$$

where $H_{ij} = 2A_i\delta_{ij} - 8\psi\bar{f}_i\bar{f}_j \mathbf{n}_i \mathbf{n}_j$.

Because n_i does not identically equals to 0, $A_i \equiv 0$ according to equation (31).

$$\begin{bmatrix} \bar{f}_1^2 & \bar{f}_1\bar{f}_2 & \bar{f}_1\bar{f}_3 \\ \bar{f}_1\bar{f}_2 & \bar{f}_2^2 & \bar{f}_2\bar{f}_3 \\ \bar{f}_1\bar{f}_3 & \bar{f}_2\bar{f}_3 & \bar{f}_3^2 \end{bmatrix} \begin{bmatrix} n_1^2 \\ n_2^2 \\ n_3^2 \end{bmatrix} = \frac{1}{2\psi} \begin{bmatrix} \bar{f}_1^2 + r\bar{f}_1 - \beta \\ \bar{f}_2^2 + r\bar{f}_2 - \beta \\ \bar{f}_3^2 + r\bar{f}_3 - \beta \end{bmatrix} \tag{33}$$

If $h_i = \begin{bmatrix} \bar{f}_1 n_1 & \bar{f}_2 n_2 & \bar{f}_3 n_3 \end{bmatrix}$, $\mathbf{H}_{ij} = -8\psi h_i^{\mathrm{T}} h_j$.

If $\bar{f}_1 \geq \bar{f}_2 \geq \bar{f}_3$ and $\bar{f}_1 \neq 0$, the following can be found according to (32):

$$\beta\left(\bar{f}_1 - \bar{f}_2\right) = -\bar{f}_1\bar{f}_2\left(\bar{f}_1 - \bar{f}_2\right), \quad \beta\left(\bar{f}_1 - \bar{f}_3\right) = -\bar{f}_1\bar{f}_3\left(\bar{f}_1 - \bar{f}_3\right) \tag{34}$$

(1) When $\bar{f}_1 > \bar{f}_2 > \bar{f}_3$, equation (34) can not be satisfied simultaneously. There is no maximum value in hardening modulus in equation (31).

(2) When $\bar{f}_1 = \bar{f}_2 > \bar{f}_3, \beta = -\bar{f}_1\bar{f}_3$.

When $\bar{f}_1 \neq 0$ and $\bar{f}_3 \neq 0$, it is obtained according to assumption and equation (32):

$$\bar{f}_1\left(n_1^2 + n_2^2\right) + \bar{f}_3 n_3^2 = \frac{1}{2\psi}\left(\bar{f}_1 + \bar{f}_3 + r\right) \tag{35}$$

And according to equations (31) and (35), the following can be obtained:

$$n_3^2 = -\frac{\bar{f}_3 + (1-2\psi)\bar{f}_1 + r}{2\psi\left(\bar{f}_1 - \bar{f}_3\right)}, \; n_1^2 + n_2^2 = 1 - n_3^2 \tag{36}$$

For $0 \leq n_3^2 \leq 1$:

$$\bar{f}_3 + (1-2\psi)\bar{f}_1 + r \leq 0, \quad \bar{f}_1 + (1-2\psi)\bar{f}_3 + r \geq 0 \tag{37}$$

(3) When $\bar{f}_1 > \bar{f}_2 = \bar{f}_3$, $\beta = -\bar{f}_1\bar{f}_3$ and:

$$n_1^2 = -\frac{\bar{f}_1 + (1-2\psi)\bar{f}_3 + r}{2\psi\left(\bar{f}_1 - \bar{f}_3\right)}, \; n_2^2 + n_3^2 = 1 - n_1^2 \tag{38}$$

$$\bar{f}_3 + (1-2\psi)\bar{f}_1 + r \leq 0, \quad \bar{f}_1 + (1-2\psi)\bar{f}_3 + r \geq 0 \tag{39}$$

When non-continuous bifurcation happens, the maximal hardening modulus is:

$$H^{\mathrm{db}} = G^{\mathrm{d}}\xi\left[\psi\left(\bar{f}_1 + \bar{f}_3 + r\right)^2 - \bar{f}_1\bar{f}_3 - k\right] \tag{40}$$

In figure 1, if $r \geq 0$, $\bar{f}_1 > \bar{f}_2 > \bar{f}_3$ and $n_2 = 0$, localized orientation angle θ_{cr} is:

$$\tan^2\theta_{\mathrm{cr}} = \frac{n_3^2}{n_1^2} = -\frac{\bar{f}_3 + (1-2\psi)\bar{f}_1 + \varphi\left(f_{\mathrm{v}} + g_{\mathrm{v}}\right)}{\bar{f}_1 + (1-2\psi)\bar{f}_3 + \varphi\left(f_{\mathrm{v}} + g_{\mathrm{v}}\right)} \tag{41}$$

4 Analysis of Localized Uniaxial Sample under Plane Condition

Bifurcation theory of localized isotropic damage is used to calculate and analyze the localization of uniaxial tension-compression samples under the conditions of plane stress and plane strain. In order to compare the bifurcation characteristic of uniaxial tension-compression samples under the conditions of plane stress and plane strain, figure 2 to figure 5 show dependency of localized orientation angle or maximal hardening modulus on degree of damage d and initial Poisson's ratio ν_0 under different conditions where Poisson's ration $\nu_0 = 0.3$ and damage variable $d = 0.5$.

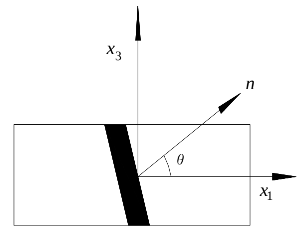

Figure 1 Orientation angle of localization for plane problems

In table 1 and figure 2 to figure 5, it is shown that localized orientation angle and maximal hardening modulus depend on initial Poisson's ratio and degree of damage under the conditions of plane stress and plane strain. Under condition of plane stress, localized orientation angle will be decrease, if initial Poisson's ratio or the degree of damage increases. In the compression condition declining rate of localized orientation angle is lower than that in tension condition. With the same degree of damage or initial Poisson's ratio, localized orientation angle will be bigger than that of compression to tension. Under condition of plane strain, localized orientation angle will increase, if initial Poisson's ratio or the degree of damage increases. In the tension condition increasing rate of localized orientation angle is higher than that in compression condition. With the same degree of damage or initial Poisson's ratio, localized orientation angle will increase from tension to compression. The sum of localized orientation angle under tension and compression conditions is 90°. Furthermore, there are plane stress and plane strain cases of the maximum hardening modulus that is independent of compression and tension. Maximum hardening modulus will increase while the degree of damage or initial Poisson's ratio increases. In the plane stain case, increasing rate of maximum hardening modulus is higher than that in plane stress case. With the same degree of damage or initial Poisson's ratio, maximum hardening modulus will increase from plane strain to plane stress, so does the effective range of Poisson's ration.

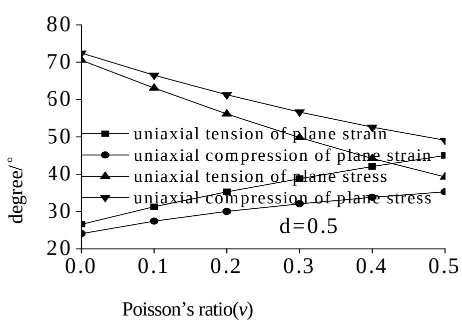

Figure 2 Comparison of dependency of localization orientation on Poisson's ration under different conditions

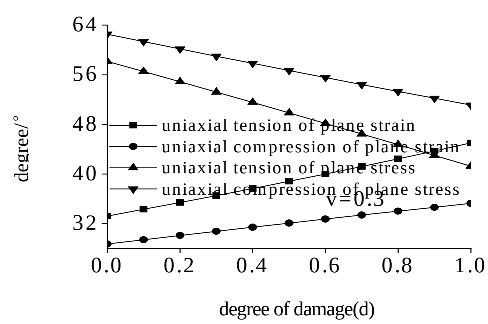

Figure 3 Comparison of dependency of localization orientation on degree of damage under different conditions

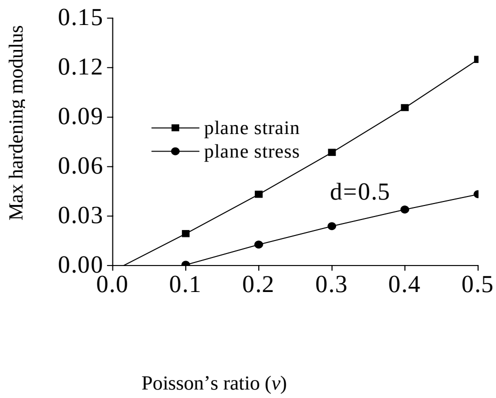

Figure 4 Comparison of dependency of maximal hardening modulus on Poisson's ratio under different conditions

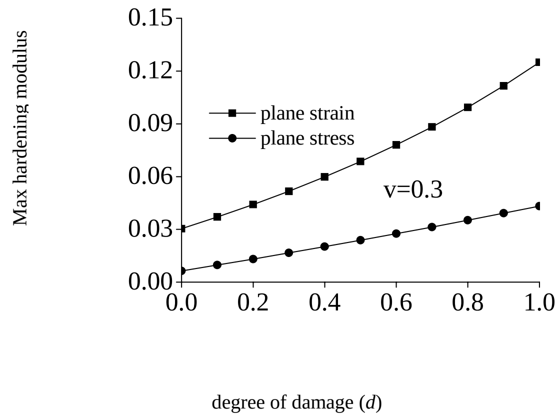

Figure 5 Comparison of dependency of maximal hardening modulus ratio on degree of damage under different conditions

5 Conclusions

The localized orientation angle and maximal hardening modulus depends on the initial Poisson's ratio and degree of damage. The sum of the localized orientation angle under tension and compression is 90°.

There are plane stress and plane strain cases of the maximum hardening modulus which is independent of the uniaxial compression and tension.

Acknowledgements

The author would like to thank the financial support by the National Natural Science Foundation of P. R. China (Grant No. 50809008).

References

1. Lu, Q.S. Bifurcation and Singularity. Shanghai: Publication of Education of Science and Technology of Shanghai, Nonlinear Science Series, Second Edition, 1997.
2. Ottosen, N.S. and Runesson, K. Properties of Discontinuous Bifurcation Solutions in Elasto- plasticity. International Journal Solids and Structure. 1991, 27(4). 401-421.
3. Yin, G.Z. and Xian, X.F. The bifurcation analysis of shear band of rock under the plane strain condition. Journal of China Coal Society, 1999, 24(4). 364-367.
4. Carol, I., Rizzi, E. and Willam, K. A unified theory of elastic degradation and damage based on a loading surface. International Journal of Solids and Structures, 1994, 31(20). 2835-2865.
5. Carol, I., Rizzi, E. and Willam, K. An 'extended' volumetric /deviatoric formulation of anisotropic damage based on a pseudo-log rate. European Journal of Mechanics-A/ Solids, 2002, 21(5). 747-772.

6. Ju, J.W. Isotropic and anisotropic damage variables in continuum damage mechanics. Journal of Engineering Mechanics, ASCE, 1990, 116(2). 2764-2770.

RaSiM 7(2009): Controlling Seismic Hazard and
Sustainable Development of Deep Mines,
C.A. Tang(ed), Rinton Press, 269-274

TIME-SPACE CALCULATION MODEL OF LAND DEFORMATIONS DUE TO PUMPING

CHUN-HUI ZHANG HONG-LIANG YUE and LI HUANG

School of Civil Engineering, Hebei University of Science and Technology

Shijiazhuang, 050018, P.R. China

YONG-JIANG YU

College of mechanics and Engineering, Liaoning Technical University
Fuxin, 123000, P.R. China

YANG YANG

Center for Material Failure Modeling Research, Dalian University

Dalian 116622, China

It is extremely important to study the calculation method of land deformations because of how dramatically they threaten the safety of peoples' lives and estates. Because of the difficulties of choosing the soil constitutive model and measuring the parameters, the calculation method based on Biot's consolidation theory is not presently perfect. In this paper, adopting the combination of one dimension consolidation differential equation and the stochastic medium theory, a new space-time calculation model of land deformation due to pumping is created. First, based on one dimension consolidation differential equations, the semi-experience model for land subsidence's time effect is presented. Second, based on analyzing the space distribution laws of land subsidence, by the stochastic medium theory the space distribution calculation model of land subsidence is set up. Third, synthetically analyzing the time effect and the space distribution characteristics, a new time-space calculation model of land subsidence due to pumping is presented, and the time-space calculation model of the surface tilting, the surface level movement, the surface level deformation and the surface curvature is set up as well. Five parameters are needed when the model performs. Those parameters could be determined by experience formula or displacement back analysis. Lastly, a case of single pumping well is introduced, and the time-space laws of land deformations are calculated through the new calculation model. The calculating results show that the calculation model could nicely reflect the time and space characteristics of land deformations due to pumping, and could expediently, accurately and rapidly calculate land deformations.

1 Introduction

With the development of the society and the economy, the demand for water resource rapidly increases. In many cities groundwater is pumped. With the pore water pressure declining for pumping and the effective stress on soil increasing, the soil is compressed and land deformations appear. Land deformations seriously threaten the safety of people's lives and estates. For example, (1) because of the differential settlement, the building's tilt, deform, and even are destroyed; (2) the safe factor of dykes loses; (3) the pipes such as drained pipes, water pipes, and communication pipes are twisted off. [1]. ¥ 290 billion has been lost in the last forty years in Shanghai, China. With the further development of China, the damage of the land deformation due to pumping will be much more serious. Therefore it is very important and significant to study the calculation method of land deformations for the prevention and control of the damage.

Biot's three-dimension consolidation theory is the main calculation method of land deformations due to pumping at present [2, 3]. However there are still some difficulties in calculating the land deformations through the theory. On one hand, it is too complicated to obtain the analytical solution. On the other hand, there are some difficulties in obtaining the numerical solutions, too. First, it is difficult to set up or select the constitutive model of the soil which could accurately reflect the elasticity, plasticity and viscidity of the soil. Second, accurately measuring the parameters of the soil is difficult. Lastly, the calculation field of the land deformation due to pumping is too big and complicated to grid finite elements. In this paper, a new space-time calculation model of land deformations due to pumping is set up adopting the method of mechanics reasoning combined with statistic mathematics. The results of case study show that the new model could nicely reflect the time-space effects of land deformations.

2 Calculation Model

Saturated soil consists of soil grain and water. When groundwater is pumped out of the aquifer, pore water pressure (PWP) will be lower and effective stress on the soil will increase, as a result the soil is compressed and land subsidence and land deformations appear. The voids for clay are so thin that it takes long time for water to flow out, so the soil compression and land subsidence takes markedly on time effect. The time effect of land subsidence due to pumping could be considered with Terzaghi's one dimension consolidation.

2.1 Time Effect of Land Subsidence

For clay supposes (1) the soil compression and the seepage are one-dimensional(Vertical) and the coefficient of permeability is constant ; (2) The soil is homogeneous and fully saturated; (3) The soil particles and water are incompressible, (4) Strains are small and Darcy's law is valid, (5) additional stress is applied one time. One dimension consolidation equation is [4]:

$$\frac{\partial u}{\partial t} = C_V \frac{\partial^2 u}{\partial z^2} \tag{1}$$

Where $C_V=10k(1+e)/\gamma_w a$ is the consolidation coefficient, k is the permeability coefficient, e is the average void ratio during consolidation of soil, γ_w is the unit weight of water, a is the compression coefficient.

Considering the initial and boundary conditions, the solution for the excess pore water pressure u at the depth z and time t is [4]:

$$u = \frac{4\sigma}{\pi}\sum_{m=1}^{\infty}\frac{1}{m}\sin\frac{m\pi z}{2d}\exp(-m^2\frac{\pi^2}{4}\frac{C_V}{d^2}t) \tag{2}$$

Where m is the odd positive integer, σ is the additional stress, d is the maximum drainage distance.

According to Hooker's law and (2), the average degree of consolidation at time t is written as follows:

$$U = \frac{WT_i}{WT_E} = 1 - \frac{8}{\pi^2}\sum_{n=0}^{\infty}\exp(-[\frac{(2n+1)\pi}{2}]^2\frac{C_V}{d^2}t) \tag{3}$$

Where WT_i is the land subsidence at time t_i , WT_E is the maximum land subsidence.

For equation (3) has a quick convergence, it could be written as follows:

$$U = \frac{WT_i}{WT_E} = 1 - \frac{8}{\pi^2}\exp(-\frac{\pi^2}{4}\frac{C_V}{d^2}t) \tag{4}$$

Specifying $\alpha=8/\pi^2$, $\beta=\pi^2 C_V/4d^2$, Substituting α and β into (4), alternatively (4) is written as follows [5]:

$$U = \frac{WT_i}{WT_E} = 1 - \alpha\exp(-\beta t) \tag{5}$$

Alternatively, the equation could be written [5], too:

$$WT_i = WT_E[1-\alpha\exp(-\beta t)] \tag{6}$$

Through equation (6), the time effect is depicted during the consolidation.

2.2 Space Distribution of Land Subsidence

The soil deformation mainly depends on the effective stress change of the soil. Many studies and statistical analysis for land subsidence observational data show [6-7] that the space distribution of land subsidence caused by groundwater exploitation takes on the characteristics shown in figure 1. Compared to land subsidence caused by mine exploitation, there is the similar law. Since land subsidence caused by mine exploitation could be perfectly calculated by the stochastic medium theory, it is feasible that the space distribution of land subsidence caused by groundwater exploitation is calculated by the theory. If a pumping well of (x, y) leads to total pressure head loss of Δp at (X, Y) in the earth surface, the land subsidence of (X, Y) could be calculated with the stochastic medium theory [6]:

$$w(X,Y) = w\iiint_V \frac{1}{R}\exp((-\frac{\pi(X-x)^2}{R^2})+(-\frac{\pi(Y-y)^2}{R^2}))\frac{a\Delta p\gamma_w}{1+e_0}\mathrm{d}x\mathrm{d}y\mathrm{d}z \tag{7}$$

where R is the influence radius.

If the land subsidence at the well is known at time t, for the axisymmetric coordinate system (Fig.1 and Fig.2) the subsidence of the point X from the well at the time is:

$$w(X) = w\int_{-\infty}^{X}\frac{2}{R}\exp(-\frac{\pi X^2}{R^2})\mathrm{d}x \tag{8}$$

Equation (8) is the integral function for normal probability density. The relationship of the density function *f(x)*, the influence radius *R* and the subsidence *w(X)* could be seen in figure 2.

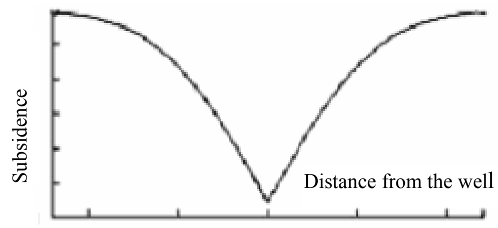

Figure.1 Character curve of surface subsidence caused by groundwater exploitation

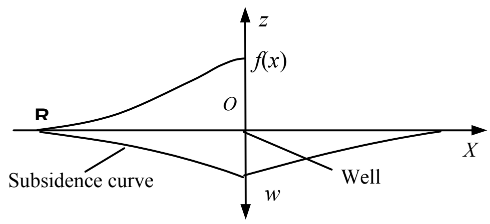

Figure.2 Subsidence curve and probability density

In equation (8), the space distribution characteristics of the land subsidence is reflected.

2.3 Land deformation calculating models taking the time and space into Account

The effects of the time and the space of land subsidence are coupled during groundwater exploitation. In equation (6), the time effect is described. In equation (8), the space effect of land subsidence is reflected. So the coupled calculating model taking the time and the space into account could be given:

$$w(X) = WT_E\{1-\alpha\exp(-\beta t_i)\}\int_{-\infty}^{X}\frac{2}{R}\exp(-\frac{\pi(X-x)^2}{R^2})dx \tag{9}$$

When equation (9) is performed, WT_E, α, β, and R should be fixed firstly, then the land subsidence could be calculated at any point at any time. Let $A\left(\frac{X}{R}\right)=\int_{-\infty}^{x}\frac{2}{R}\exp\left(-\frac{\pi X^2}{R^2}\right)dx$, and (9) could be written [8]:

$$w(X)=WT_E\left[1-\alpha\exp(-\beta t_i)\right]A\left(\frac{X}{R}\right) \tag{10}$$

The land tilt, level movement, level deformation and curve calculating equation at any point at the time of t_i are written as follows [8]:

The land tilt is:

$$I(X)=I_{\max}A'\left(\frac{X}{R}\right)=\frac{WT_E\left[1-\alpha\exp(-\beta t_i)\right]}{R}A'\left(\frac{X}{R}\right) \tag{11}$$

The level movement is:

$$D(X)=D_{\max}A'\left(\frac{X}{R}\right)=bWT_E\left[1-\alpha\exp(-\beta t_i)\right]A'\left(\frac{X}{R}\right) \tag{12}$$

The level deformation is:

$$\varepsilon(X)=\varepsilon_{\max}A''\left(\frac{X}{R}\right)=1.52b\frac{WT_E\left[1-\alpha\exp(-\beta t_i)\right]}{R}A''\left(\frac{X}{R}\right) \tag{13}$$

The curve is:

$$K(X)=K_{\max}A''\left(\frac{X}{R}\right)=1.52b\frac{WT_E\left[1-\alpha\exp(-\beta t_i)\right]}{R^2}A''\left(\frac{X}{R}\right) \tag{14}$$

(10)-(14) is the time-space calculating model of land deformation due to pumping. Where $A\left(\frac{X}{R}\right)$, $A'\left(\frac{X}{R}\right)$ and $A''\left(\frac{X}{R}\right)$ could be calculated by reference[8]. X is the distance from the well to the calculation point, b is the level movement coefficient between 0.3-0.5.

2.4 Calculating parameters

Five calculating parameters are needed when the model performs: WT_E, α, β, R and b. Here two methods, namely experiential method and back analysis of displacement are introduced.

1) Experiential method

α and β of theory values could be written as follows:

$$\alpha=\frac{8}{\pi^2},\ \beta=\frac{\pi^2}{4}\frac{C_V}{d^2} \tag{15}$$

For multi-layer soil, β could be calculated as follows:

$$\beta=\frac{\sum\beta_i H_i}{\sum H_i} \tag{16}$$

Where β_i and H_i are the coefficient and thickness of No i soil lay, respectively.

WT_E could be calculated by the summation of the soil compression of all sublayers [9]:

$$WT_E=\sum_{i=1}^{n}\frac{a_{i(1-2)}}{1+e_{0i}}\Delta p_i\Delta h_i \tag{17}$$

Where $a_{i(1-2)}$ is the compression coefficient of No i sublayer soil, e_{0i} is the initial void ratio of No i sublayer soil, Δp_i is the additional stress caused by groundwater exploitation, Δh_i is the thickness of No i sublayer soil. Make $\alpha=8/\pi^2$, $\beta=\pi^2C_V/4d^2$, and the time effect of land subsidence could be calculated.

The influence radius could be calculated as follows [9]:

For unconfined flow:

$$R=2S\sqrt{HK_d} \tag{18}$$

For confined flow:

$$R = 10S\sqrt{K_d} \tag{19}$$

Where S is the total head pressure loss, H is the thickness of the aquifer，K_d is the average permeability coefficient (m/d). b is a experimental coefficient between 0.3-0.5.

2) Displacement back analysis method

If there are available observation data of land subsidence, the calculating parameters could be calculated as follows:

$$f(WT_E,\alpha,\beta,R)=\min\left\{\sum_{j=1}^{n}\left[w_j(WT_E,\alpha,\beta,R)-\overline{w_j}\right]^2\right\}^{0.5} \tag{20}$$

Where n is number of data, w_j is the calculating data of land subsidence by formulas (10), $\overline{w_j}$ is the observational data of the land subsidence.

Simplex method is used to solve (20), and the back analysis program S-DCX is developed in Matlab.

4 Case Study

There is a pumping well from No.2 confined aquifer in Shenyang city, Liaoning province. Now it is the third year to dewater, and it is steady confined flow. There have been observation data for two years. Those observation data could be seen in Table 1 and Table 2.

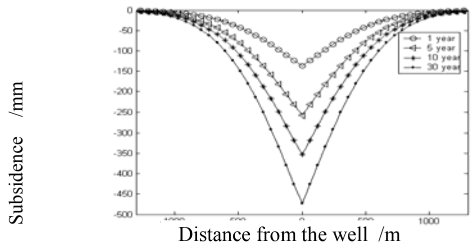

Figure 3 Land subsidence

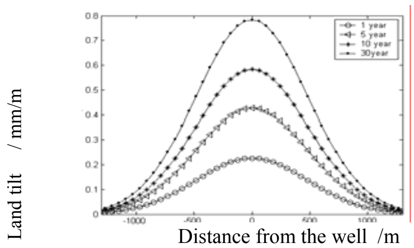

Figure 4 Land tilt

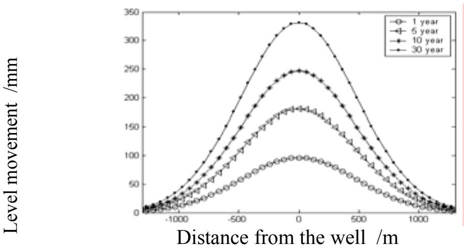

Figure 5 Land level movement

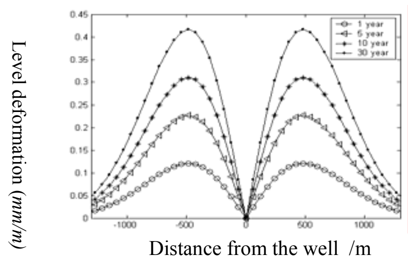

Figure 6 Land level deformation

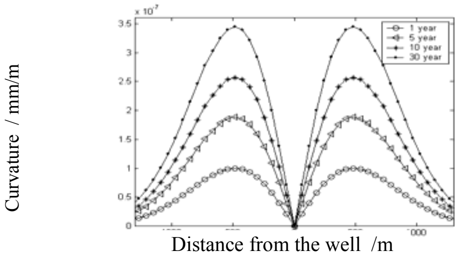

Figure 7 Land curvature

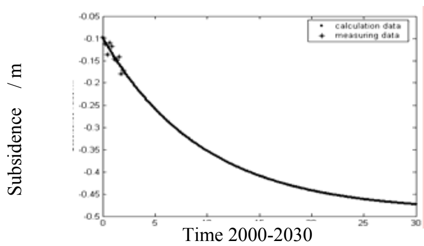

Figure 8 Maximum land subsidence

Firstly, with the observation data in Table1 and 2, α, β, WT_E and R are solved through equation (20) and S-DCX. They are: α=0.8, β=0.105, WT_E= 0.49, R=1209. Then b is 0.3 according to experience. The time and space distribution laws of land deformation are calculated with the calculating model in this paper, and results could be seen between Fig.3 and Fig.7. The evolvement of the maximum land subsidence VS time could be seen in Fig.3. From Fig.4, it could be found that land subsidence increases with the increasing time, however its increasing rate decreases. In space, the nearer to the well the calculation point is, the subsidence is bigger. Land tilt(fig.4) and land level movement(fig.5) is similar as well. From fig.6 and fig.7, land level deformation and culture is maximum at the 0.42R, which shows the land deformations are more harmful to the buildings at the 0.42R. In fig.8, the calculating data by the model in the paper is closed to observation data, which shows the model is reliable.

Table 1 Subsidence observation data at the edge of dewatering well

Time /d	36	72	180	255	365	545	720
Land subsidence of the well /mm	5.1	11	23	41	45	75	93

Table 2 Surface subsidence from the well

Distance from the well /m	0	120	240	360	480	600	720	840	960	1080	1200	1320
Land subsidence /mm	93	76	57	39	31	19	14	8	4	2	1	0.5

Note: It is the 720th day.

4 Conclusions

Analyzing the time and space distribution characteristics and laws of land subsidence due to pumping, a new calculation model of land deformations is presented. The model could not only expediently and rapidly calculate land deformations, but also avoid the constitutive model of soil. For these reasons, it is superior to numerical methods based on Biot's theory.

References

1. Yu, G., Zhang, C., Pan, Y.and Liu, F. Research progress and prospect of strata subsidence calamity prediction. In: Land Subsidence Proceedings of the Seventh International Symposium on Land Subsidence, Shanghai, China, 2005, 825-836.
2. Biot, M. A. Theory of elasticity and consolidation for a porous anisotropic solid. Journal of Applied Physics, 1955, 26. 182-185.
3. Zhang, Y.and Xue, Y. Present situation and prospect on the mathematical model of land subsidence due to pumping, Chinese Journal of Geological Hazard and Control, 2002, 13(2). 1-6. (In Chinese)
4. Chen, X. Soil mechanics and foundation. Beijing: Tsinghua University Press, 1998. 106-112.(In Chinese)
5. Pan, L. and Xie, X. Observational settlement prediction by curve fitting methods. Rock and Soil Mechanics, 2004, 25(7). 1 053-1 058. (In Chinese)
6. Zhang, C., Yu, G. and Yang, L. Computerization research and predicting model of surface subsidence caused by pulling out underwater. Journal of Liaoning Technical University, 2004, 23(4):463-465. (In Chinese)
7. Yang, J., Liu, B. Stochastic medium predicting model of surface subsidence caused by pulling out water. Hydrogeology and Engineering Geology, 1999, (5),11-13. (In Chinese)
8. He, G., Yang, L. Mine subsidence theory. Beijing: Coal Industry press, 1995, 15-60. (In Chinese)
9. Li, B. Manual for chinese civil engineers. Shanghai: Shanghai technological press,1985, 321-352.(In Chinese)

RaSiM 7(2009): Controlling Seismic Hazard and
Sustainable Development of Deep Mines,
C.A. Tang(ed), Rinton Press, 275-278

STUDY OF DYNAMIC COMPRESSIVE PROPERTIES OF CONCRETE

PING GUAN and PENG LIU

Key Laboratory for Prediction & Control on Complicated Structure System of the Education Department of Liaoning Province, Dalian University, Dalian 116622, China

Dynamic loading to the rock structure and concrete structure is inevitable during use; such as wind load, seismic load and explosion impact load for underground rock structure. Dynamic load is an important factor for structure design. In this paper, the uniaxial dynamic compressive test was carried out on concrete specimens under different stain rates using a large static and dynamic electro-hydraulic servo testing system. The effect of stain rate on concrete failure modes, compressive strength, elastic modulus, peak strain and Stress-Strain curve are studied. The experiential formula for dynamic strength of concrete which changes with strain rate is given. The test indicates that the concrete compressive strength increases with the elastic modulus and peak strain also increases as the strain rate goes up.

1 Guidelines

Concrete is a material which is sensitive to the strain rate. The load experienced on concrete structure changes significantly in strain rate. For example, creep strain rate is less than 10-6/s, the strain rate under seismic loading is between 10-3/s and 10-2/s, the strain rate of impact loads is about 100/s-101/s, the strain rate of explosion loading reaches 102/s over. The strength, stiffness and ductility (or brittleness) of concrete structure are subject to the effects of loading rate [1,2]. Obviously, it will have a lot of errors if concrete structural calculation with the static mechanical parameters. This article focuses on the dynamic strength characteristics and failure characteristics of concrete material under seismic loading (the strain rate were 10-5/s, 10-4/s, 10-3/s and 10-2/s respectively), it is to provide the necessary test basis for a comprehensive understanding of the dynamic constitutive relation of concrete and its engineering application.

2 Experiment Process

2.1 Experimental Equipment

The experiment had been done in the Structures Laboratory of the State Key Laboratory of Coastal and Offshore Engineering at Dalian University of Technology, using a large static and dynamic electro-hydraulic servo testing system. Visual C++ programming software system was employed in the tests to control and collect data, with the minimum acquisition cycle being up to 2μs. In addition, a pair of displacement transducers (LVDT) were fixed to measure the displacement, and load sensor was used on the force direction The measurement system used, with a response frequency of actuators being up to 10.0Hz, applies a loading at maximum rate of 5×103KN/s, with a control precision of precision loading of 1.5%.

2.2 Designing and Making of Specimens

The concrete specimens used in the experimental study were cubic, 100mm×100mm×100mm, with design strength of 20 MPa. The materials used were type 32.5R Portland cement produced by Seagull in Dalian, general river sand, of which fineness modulus is 2.68, crushed gravel (the maximum grain size is 15mm), and tap water.

The cubic specimens were cast in steel moulds, and compacted by vibration. Having been demoulded in the next day, they put in a water tank for 3days, after cured in a fog room for 28 days, and then naturally cured in the laboratory.

3 Experimental Results and Discussion

3.1 Failure Modes of the Specimens

It is column-type failure for concrete specimens under uniaxial compression, because of the adoption of antifriction measures. Concrete produced compression distortion in the loading direction, tensile distortion in other two directions. With the increase of principal stress, the two lateral strain exceed the concrete ultimate tensile strain, they formed two groups of crack faces that parallel with side surface of specimen. Finally crack surface runs through the concrete specimen, then column-type failure is observed, which is shown in Figure 1.

3.2 Compressive Strength of Concrete

Data of the ultimate compressive strength of concrete in different loading rate are listed in Table 1. As can be seen from Table 1, ultimate compressive strength of concrete increased with the increase of strain rate. By taking the strength at strain rate of 10-5/s as the quasi-static compressive strength of concrete, the compressive strength of concrete increase by 12.6%, 21.2% and 35.6% respectively while the strain rate was 10-4/s, 10-3/s and 10-2/s.

Table 1 Compressive ultimate strength of concrete under various strain rates

No.	Loading rate (s^{-1})			
	10^{-5}	10^{-4}	10^{-3}	10^{-2}
1	20.43	23.23	22.42	26.43
2	19.94	22.49	26.14	26.20
3	19.93	22.21	24.56	29.12
average	20.10	22.64	24.37	27.25

The failure process of concrete materials under dynamic loading is different from that under static loading. Especially in high strain rate, the failure surfaces of concrete specimens were more smoothing and kilter, with more destructiveness of crude aggregates. It is because that after increase of loading rate, the ability of through a higher strength region enhanced, with less energy consumption, and it finally cause more destructiveness of crude aggregates and increase of strength. Through the crack shapes, the damage crack shapes of concrete were got closer to linear as the strain rate increases.

The relationship between dynamic compressive strength of concrete and strain rate is expressed with the following empirical formula.

$$f_d / f_s = a + b \lg(\dot{\varepsilon}_d / \dot{\varepsilon}_s) \tag{1}$$

Fitting by least square method, formula (1) can be changed to

$$f_d / f_s = 1.0 + 0.1155 \lg(\dot{\varepsilon}_d / \dot{\varepsilon}_s) \qquad (2)$$

where $\dot{\varepsilon}_d$ denotes the dynamic strain rate, the unit of which is s^{-1}; $\dot{\varepsilon}_s$ denotes the quasi-static strain rate, the value of which is 10^{-5}/s; f_d denotes the concrete compressive strength under dynamic strain rate and f_s denotes the compressive strength under quasi-static strain rate.

3.3 Peak Strain of Concrete

The values of peak strain are listed in Table 2. Table 2 shows that, the values of peak strain of concrete under uniaxial compression are increasing slightly with the increasing of strain rate. The increasing range is very small, so it can be thought no change approximately.

Table 2 Peak strain of concrete ($\mu\varepsilon$)

Test	Strain rates (s^{-1})			
	10^{-5}	10^{-4}	10^{-3}	10^{-2}
1	983	1168	1185	1168
2	903	1000	1048	1100
3	989	973	1000	1123
Average	958	1047	1078	1130

3.4 Elastic Modulus of Concrete

The slope of concrete compressive stress-strain curve (σ-ε) is elastic modulus, or deformation modulus. In this paper, the elastic modulus value is a secant elastic modulus which is calculated from the strain corresponding to 30% of peak stress. Table 3 lists different rates of the elastic modulus of concrete.

Table 3 Elastic Modulus of concrete under various strain rates

No.	Loading rates (s^{-1})			
	10^{-5}	10^{-4}	10^{-3}	10^{-2}
1	1.74	2.08	2.60	3.06
2	1.45	2.03	2.62	3.03
3	1.78	2.14	2.54	2.99
Average	1.66	2.08	2.59	3.03

The relationship between dynamic elastic modulus of concrete and strain rate is expressed with the following empirical formula.

$$E_d / E_s = c + d \lg(\dot{\varepsilon}_d / \dot{\varepsilon}_s) \qquad (3)$$

where $\dot{\varepsilon}_d$ denotes the dynamic strain rate, the unit of which is s^{-1}; $\dot{\varepsilon}_s$ denotes the quasi-static strain rate, the value of which is 10^{-5}/s; E_d denotes the elastic modulus under dynamic strain rate; E_s denotes the elastic modulus under quasi-static strain rate and c, d denote regression coefficient.

By fitting, formula (3) can be changed to

$$E_d / E_s = 0.9946 + 0.2824 \lg(\dot{\varepsilon}_d / \dot{\varepsilon}_s) \qquad (4)$$

3.5 Stress-strain Curve of Concrete

Four stress-strain curves of concrete under different strain-rate are given in Figure 2. These curves can reflect the concrete compressive characteristics. It can be seen in Figure 2, in spite of the strain rate, the shapes of the stress-strain curves of concrete and the complete curve of concrete under static load are basically similar. The only differences between them are the changes of peak stresses, peak strains, and initial elastic modulus.

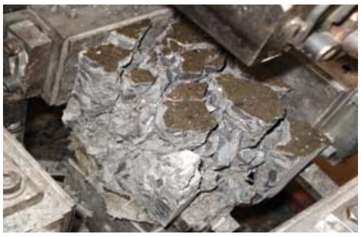

Figure 1 Typical failure modes of concrete under uniaxial compressive

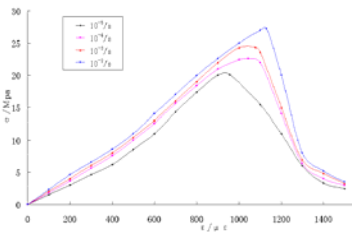

Figure 2 Stress-strain curve of concrete under various strain rates

4 Conclusions

(1) With antifriction measures being taken, the failure mode of the concrete specimens under uniaxial compression is discovered to be column-type failure.

(2) With the increase in strain rate, the compressive strength of concrete increases significantly, and the elastic modulus and peak strain of concrete increase also.

(3) The relationship formulas of dynamic compressive strength and strain rate, dynamic elastic modulus and strain rate are given in this paper.

(4) Stress-strain curves of the concrete under different strain rates are given in this paper.

Acknowledgements

The author would like to thank the financial support by the National Natural Science Foundation of P. R. China (Grant No.90410012)

References

1. Yan, D.M. and Lin, G. Actuality and prospects of experimental studies on the dynamic properties of concrete. Water Sciences and Engineering Technology, 2006, 4. 1-6.
2. Wang, Z., Lin, G. and Lu J.Z. A uniaxial rate dependent constitutive model for concrete materials. Journal of Dalian University of Technology, 2000, 9(5). 597-601.
3. Yan, D.M. and Lin, G. Experimental Study on the Uniaxial Dynamic Compression Properties of Concrete. Water Sciences and Engineering Technology, 2005, 6. 8-10.
4. Xiao, S.Y.,Lin,G.and Lu, J.Z. Effect of strain rate on dynamic behavior of concrete in compression. Journal of Harbin University of Civil Engineering and Architecture, 2002, 5. 35-39.
5. Ahmad, S.H. and Shah, S.P. Behavior of hoop confined concrete under high strain rates. ACI J, 1985, 82(5). 634-647.

RaSiM 7(2009): Controlling Seismic Hazard and
Sustainable Development of Deep Mines,
C.A. Tang(ed), Rinton Press, 279-282

STUDY OF THE FRACTURE OF ROCKBURST NOTCHES OF CIRCULAR CAVERNS

YI-MIN SONG and HUI-JI SHI

Department of Engineering Mechanics, Tsinghua University, Beijing 100084;

YI-SHAN PAN

Institute of Mechanics and Engineering, Liaoning Technology University,

Liaoning Fuxin 123000

The study of the fracture of rockburst notches of circular caverns is presented. A numerical solution of the full-field stress distribution of rockburst notches was obtained by Kolosov-Muskhelishvili's complex variable function method. A method to determine the fracture of rockburst notches is proposed using the Mohr-Coulomb criteria as the fracture criterion. Considering the effect of high stress concentration, a characteristic length is introduced in the tip of rockburst notches. The rockburst notches will fracture when the stress state of a point on the circle, where the characteristic length is the radius, meets the fracture criteria. The characteristic length is then obtained through experimentation. The purpose of this paper is to provide a reference for engineering applications through a quick-solver method for the fracture of rockburst notches of underground openings.

1 Introduction

In rock engineering, a rockburst is one of the major geological disasters. Field observations showed that the size and the frequency of rockbursts would increase with increasing excavation depth [1]. The v-shaped (triangular) or dog-eared notches will be generated on the surrounding rock after rockburst. Rockburst notches change the structure of the original chamber and cause the stress redistribution. The tip of rockburst notches has a high stress concentration. In high stress conditions, the geometry of rockburst notches configurations can greatly influence the load bearing capacity of the rock structure and consequently its stability. A second or even more rockbursts may occur when the external stress, such as excavation, is introduced [2]. At the same time, the experiment found that the fracture extended of rockburst notches is the basis of zonal disintegration formation. The study on the fracture of rockburst notches has important implications.

The geometry of rockburst notches is irregularly, Kolosov –Muskhelishvili's complex variable function method is used to analyze the stress distribution. As it is noted by Cheatham, an exact elasticity solution for a breakout configuration is quite similar to the initial circular cavity breakout shape which was published by Mitchell. By using the method of complex potential functions of Muskhelishvili, Mitchell has solved the stress concentration problem for a symmetrical hole whose boundary consists of three intersecting circles.

However, it would appear that the evaluation of the full-field stress distribution around the hole, and consequently the stress-gradient effect, has not been pursued by the author. G.E.Exadaktylos presented a semi-analytical plane elasticity solution of the circular hole with diametrically opposite notches in a homogeneous and isotropic geomaterial [3]. Due to the limitations of semi-analytical method to solve the complex configuration, in this paper, the numerical simulation is used to study the stress distribution of rockburst notches. On the base of the aforementioned study, we proposed a method to determine the fracture of rockburst notches. The Mohr-Coulomb criteria are used as the fracture criterion. Considering the effect of high stress concentration, a characteristic length is introduced in the tip of rockburst notches, and the rockburst notches will fracture when the stress state of a point on the circle, where the characteristic length is the radius, meet the fracture criteria. The characteristic length is obtained by experimentation. The purpose of this paper is to provide a reference for engineering applications.

2 The stress analysis of rockburst notches of circular cavern

2.1 Mechanical model

Through the results of in-situ observation [4] and the theoretical and experimental study [5], the shape of rockburst notches is a sharp triangular or v-shaped configuration under high stress. Therefore, the circular hole with diametrically opposite V-shape notches in a homogeneous and isotropic geomaterial is used as the calculation model of this article. As shown in Fig.1, this model is in a state of plane strain, far-field load is N_1, N_2, h_0 is the depth of the rockburst notches, r_0 is the radius of cavity, and ϑ_0 is the angle of rockburst notches. σ_r is the radial stress, σ_θ is the circumferential stress , $\tau_{r\theta}$ is the shear stress.

2.2 The stress analysis of rockburst notches of circular cavern

Kolosov -Muskhelishvili complex variable function method is applied to analyze the stress distribution. First, the position of every point in the physical z-plane with $z = x + iy = \omega(\xi)$ is mapped into the unit circle in the ξ -plane by complex function. Then, the stress distribution of z-plane is solved by the potential functions $\phi(\xi)$ and $\varphi(\xi)$.

2.2.1 the conformal mapping and coefficients

The conformal mapping formula is:

$$z = \frac{a_0}{\xi} + \sum_{k=1}^{n} a_{2k-1}\xi^{2k-1} \qquad |\xi| \le 1 \tag{1}$$

The transform coefficients calculated by the method of literature [3]. Coefficient matrix can be expressed as:

$$AX = B \Leftrightarrow (A^T A)^{-1} A^T B \tag{2}$$

T represents the transpose matrix;-1 stands for the inverse matrix; A is coordinate matrix of the point on unit circle of mapping; B is coordinate matrix of the point of the border in z-plane; X is variables column vector.

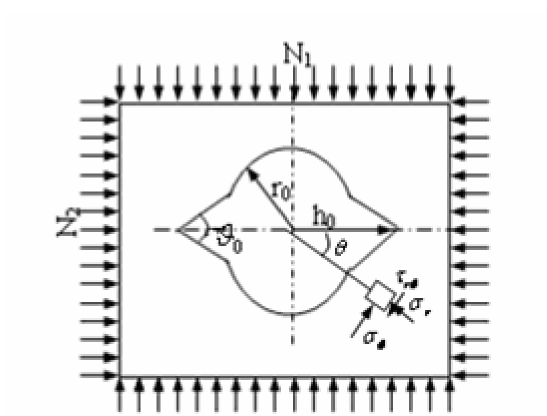

Figure 1 the mechanical model of rockburst notchesse

After the first estimation of the constant coefficients a_0, a_{2k-1} $(k = 1,2,\cdots,n)$, the new points on the border of the opening at the z-plane are calculated by the mapping function, subsequently, for each point predicted by the mapping function, the intersection of the line that connects this point and the centre of coordinates with the prescribed physical boundary is used as the new z-value, these new z-values are next substituted into the system ,which is solved for the estimation of the new improved values of a_0, a_{2k-1} $(k = 1,2,\cdots,n)$. This iterative procedure is continued until a prescribed small error is achieved.

2.2.2 The calculation of the potential function $\phi(\xi)$, $\varphi(\xi)$

Z-plane stress distribution being expressed by the potential function $\phi(\xi)$ and $\varphi(\xi)$ as follows:

$$\sigma_\theta + \sigma_r = 4\,\mathrm{Re}[\frac{\phi'(\xi)}{\omega'(\xi)}] \quad , \sigma_\theta - \sigma_r + 2i\tau_{r\theta} = \frac{2\xi^2}{\rho^2\overline{\omega'(\xi)}}\{\overline{\omega(\xi)}[\frac{\phi'(\xi)}{\omega'(\xi)}]' + \varphi'(\xi)\} \tag{3}$$

The potential function $\phi(\xi)$ and $\varphi(\xi)$ can be expressed as:

$$\phi(\xi) = A_0\omega(\xi) + \phi_0(\xi), \qquad \varphi(\xi) = B_0\omega(\xi) + \varphi_0(\xi) \tag{4}$$

where A_0 and B_0, which are the far-field stress conditions, can be expressed as:

$$A_0 = \frac{1}{4}(N_1 + N_2) \quad , \quad B0 = -\frac{1}{2}(N_1 - N_2) \tag{5}$$

And $\phi_0(\xi), \varphi_0(\xi)$ can be expressed respectively as:

$$\phi_0 = \sum_{n=1}^{\infty}\alpha_n\xi^n \qquad \varphi_0 = \sum_{n=0}^{\infty}\beta_n\xi^n \tag{6}$$

The calculation formula of $\phi_0(\xi)$, $\varphi_0(\xi)$ is:

$$\phi_0(\xi) + \frac{\omega(\xi)}{\overline{\omega'(\xi)}}\overline{\phi_0'(\xi)} + \overline{\varphi_0(\xi)} = f_0 \tag{7}$$

Equation (7) is fitted by a certain number of discrete points which are selected at the border of ξ-plane, $i = 1,2,\cdots,2n$ represent the number of discrete points. ξ_i, $(f_0)_i$ is the corresponding value of the discrete points respectively.

$$\begin{aligned}&(\xi_i + \frac{\omega(\xi_i)}{\overline{\omega'(\xi_i)}})\alpha_1 + (\xi_i^2 + 2\frac{\omega(\xi_i)}{\overline{\omega'(\xi_i)}}\xi_i^{-1})\alpha_2 + \cdots + (\xi_i^n + n\frac{\omega(\xi_i)}{\overline{\omega'(\xi_i)}}\xi_i^{-(n-1)})\alpha_n \\ &+ \beta_0 + \beta_1\xi_i^{-1} + \cdots + \beta_n\xi_i^{-(n-1)} = (f_0)_i\end{aligned} \tag{8}$$

According to Equation (8), $2n$ equations can be derived, the coefficient matrix α_n, β_n which are obtained by solving these linear equations, and substituted into the formula (4) and (6), then $\phi(\xi)$, $\varphi(\xi)$ can be solved.

3 The study on the fracture of rockburst notches of circular cavern

The Mohr-Coulomb criteria are used as fracture criterion, which is:

$$\sigma_\theta = q\sigma_r + \sigma_c \tag{9}$$

here

$$q = \frac{1+\sin\phi}{1-\sin\phi} \quad , \quad \sigma_c = \frac{2c\cos\phi}{1-\sin\phi} \tag{10}$$

where ϕ the friction angle, and c is the cohesion.

Considering the effect of high stress concentration, a characteristic length R_0 is introduced in the tip of rockburst notches, and the rockburst notches would fracture when the stress state of a point of the circle, where the characteristic length is the radius, meets the fracture criteria. The characteristic length is obtained by the experiment ion.

4 Conclusions

Through the numerical analysis, some conclusions can be drawn:

1) The numerical analysis is used to study the full-field stress distribution of rockburst notches. A method is proposed to determine the fracture of rockburst notches of circular caverns, and is also applicable to the arbitrary shape rockburst of caverns.

2) The biaxial compression test of the chamber model has been completed, and the characteristic length of the siltstone specimen has been obtained through experimentation.

3) This numerical analysis method can be used as a quick-solver for the fracture of rockburst notches of underground openings.

References

1. Qian, Q.H. and Li, S.C. A Review of Research on Zonal Disintegration Phenomenon in Deep Rock Mass Engineering. Chinese Journal of Rock Mechanics and Engineering, 2008, 27(6).1278-1284. (in Chinese)
2. Wang, J.L. and Hong, K.R. Rock Bust of Division Channel of Taipinyi Hydrorlectrical Station and its Control. West-China Exploration Engineering, 1995, 7(1). 87-89. (in Chinese)
3. Exadaktylos, G.E., Liolios, P.A.and Stavropoulou, M.C. A semi-analytical elastic stress-displacement solution for notched circular openings in rocks. International .Journal of solids and structures, 2003, 40. 1165-1187.
4. Ewy, R.T. and Cook, N.G.W. Deformation and fracture around cylindrical openings in rock-I, II. Int .J. Rock Mech. Min. Sci.&Geomech.Abstr, 1990, 27(5). 387-427
5. Martin, C.D., Kaiser, P.K., mccreath, D.R. and Hoek, B. Parameters for predicting the depth of brittle failure around tunnels. Can. geotech. J. 1999, 36. 136-151

*RaSiM 7(2009): Controlling Seismic Hazard and
Sustainable Development of Deep Mines,
C.A. Tang(ed), Rinton Press, 283-290*

QUANTITATIVE ANALYSIS OF RELIABILITY ASSESSMENT INDEXES OF MINE VENTILATION NETWORK SYSTEM

HONG-DE WANG and YUN-DONG MA

School of Civil and Safety Engineering, Dalian Jiaotong University

Dalian 116028, China

In order to prevent the hazards of rock burst, spontaneous fire in deep-level mines, and to ensure that ventilation runs safely and reliably; the variation trends and the distribution rules of the air flow in deep-level mine are analyzed. Based on the network flow theory and statistics principle, the density functions of the air quantities in the airways are established. With the maximum likelihood estimation (MLE), the rationality of the parameters in the air quantities distribution functions are verified. By the mean of the disjoint minimal path set algorithm, the reliability assessment models of the mine ventilation network are found. All of the calculation processes are processed in the environment of MATLAB and VC++. The results indicate that the indexes of the quantitative analysis confirm the practical situation of the ventilation network system in Daliuta Coal Mine.

1 Introduction

Research on the reliability of mine ventilation network system began in the 1980s. Some domestic and international scholars have probed into this question and obtained some results such as: the determination of reliability indexes of the ventilation network system [1, 2], the investigation of airflow distribution theory of the ventilation network [3] and the establishment of the reliability model [4]. The mine ventilation network system, however, is a complex system which consists of multi-links, is time-dependent, and also non-linear. So the reliability indexes, which can only be determined by expert's experience, lack a scientific foundation.

Based on fluid network theories and statistics methods, and according to the analysis to the trend of variations of airflow in mine ventilation network system; the distribution rule of the reliability assessment indexes is founded, and the quantitative assessment model is set up. The references will be offered for the reconstruction, the daily maintenance and the management of the ventilation network system.

2 Reliability assessment task frame of mine ventilation network system

Mine ventilation system is an organism with strong coupling characters, and it is crossed connected with air paths and ventilated constructions. According to the characteristics of ventilation network, consulting the research practices to ventilation technology and management in domestic and abroad, together with the reality of Daliuta Coal Mine, the reliability assessment task frame of the ventilation network is constructed. It is a model with series-wound, shunt-wound and bypass. The aim is to realize to assess the reliability of ventilation network system by mean of the analysis and forecast to the reliability indexes of its subsystems.

3 Estimation of the density functions of air-quantity distribution in airway

3.1. Forecast of the Air-quantity distribution and the air-quantity rate in airway

Based on the statistics analysis principle, the air-quantity distribution of airway i is respected that there are how many percent of the testing samples $(q_i + \Delta q)$ of q_i keeping into the observation section at different moments during a certain periods of time.

According to the observation to the sample $(q_i + \Delta q)$ at different periods of time, the relations of the air-quantity observation section with the sample records in this airway can be founded, so the estimation value of the air-quantity distribution can be calculated. Form the relations between the sample values of this observation section and the total air-quantity (q_i), the records of air-quantity which fall into this section can be found out, and the mean air-quantity rate can be calculated.

If N_0 is taken as the gross sample of air-quantity in airway i during a certain periods of time, and $n(q_i)$ as the records of the samples which don't fall into the observational sections, $N_f(q_i)$ as the records of the samples which fall into the observational sections. So the estimate value $\widehat{D}(q_i)$ (q_i don't fall into the observational section) and $\widehat{U}(q_i)$ (q_i fall into the observational section) can be shown as:

$$\widehat{D}(q_i) = \frac{n(q_i)}{N_0}, \qquad \widehat{U}(q_i) = 1 - \widehat{D}(q_i) = 1 - \frac{n(q_i)}{N_0} = \frac{N_f(q_i)}{N_0} \tag{1}$$

So the mean air-quantity distribution density ($\overline{f}(q_i, \Delta q)$) and the mean air-quantity rate ($\overline{\lambda}(q_i, \Delta q)$) during $[q_i, q_i + \Delta q]$ in airway i can be shown as:

$$\overline{f}(q_i, \Delta q) = \frac{1}{\Delta q}\left[\widehat{U}(q_i + \Delta q) - \widehat{U}(q_i)\right] = \frac{\Delta N_f(q_i)}{N_0 \Delta q},$$

$$\overline{\lambda}(q_i, \Delta q) = \frac{\overline{f}(q_i)}{\widehat{D}(q_i)} = \frac{\Delta N_f(q_i)}{n(q_i)\Delta q} = \frac{\Delta N_f(q_i)}{\Delta q\left[N_0 - N_f(q_i)\right]} \tag{2}$$

where, $\Delta N_f(q_i)$ is records of air-quantity keeping into observational section, $\Delta N_f(q_i) = N_f(q_i + \Delta q) - N_f(q_i)$.

3.2 Density Function of airway reliability distribution

Considered $q_{i1}, q_{i2}, \cdots, q_{in}$ as the sample sets of q_i, if the records of the samples are enough, the air-quantity distribution density in airway i can be estimated approximately. The process is as follows:

Firstly, takes 20401 transportation laneway of Daliuta Mine as an example, the experiment data of the air-quantity distribution in the airways is acquired and analyzed. The detailed process is shown in table 1.

Secondly, $f(q_i)$ is calculated. The steps are as bellow:

Step 1: Calculate the extreme deviation R_i . $R_i = \max\{q_i\} - \min\{q_i\}$ = 60.73–41.24=19.49.

Step 2: Calculate the group distance *C*: *C*=*R*/*K*=19.49/20=0.9745 ≈ 1(m^3/s). *K* is the number of groups.

Step 3: Confirm the frequency w_i : $w_i = M_i / M$, M_i is the frequency, M is the total frequency.

Step 4: Draw the histogram of w_i , just as in figure 2. It is in normal distribution approximately.

In order to verify the correctness of the distribution curve in Figure 2, the mean air-quantity rate of each observational section is calculated with formula 2 based on M_i and w_i in table 1. The results are shown in table 2.

From table 2, the mean air-quantity rate is increased, namely the air-quantity fault rate is increased in this transportation laneway. So the density function of this laneway can be described:

$$f\left(\mu_i, \sigma_i^2\right) = \frac{1}{\sigma_i \sqrt{2\pi}} \mathrm{e}^{-\frac{(q_i - \mu_i)^2}{2\sigma_i^2}} \tag{3}$$

where, q_i is as random sample, and μ_i as mean value, σ_i^2 as variance, σ_i as standard deviation.

$$\mu_i = \sum_{k=1}^{20} \overline{q}_{ik} \cdot \omega_k \ , \quad \sigma_i^2 = \sum_{k=1}^{20} \left(\overline{q}_{ik} - \mu_i\right)^2 \cdot \omega_k \tag{4}$$

Table 1 List of the air-quantity data processing

Group mark	Group distance lower bound ($m^3 \cdot s^{-1}$)	Group distance upper bound ($m^3 \cdot s^{-1}$)	Group distance median $\overline{q}_i$ ($m^3 \cdot s^{-1}$)	Frequency(M_i) (records)	Frequency(ω_i) (records^{-1})
1	41	42	41.5	1	3.472×10^{-3}
2	42	43	42.5	2	6.944×10^{-3}
3	43	44	43.5	4	1.389×10^{-2}
4	44	45	44.5	9	3.125×10^{-2}
5	45	46	45.5	11	3.819×10^{-2}
6	46	47	46.5	13	4.514×10^{-2}
7	47	48	47.5	20	6.944×10^{-2}
8	48	49	48.5	28	9.722×10^{-2}
9	49	50	49.5	35	0.1215278
10	50	51	50.5	52	0.1805556
11	51	52	51.5	39	0.1354167
12	52	53	52.5	20	6.944×10^{-2}
13	53	54	53.5	15	5.208×10^{-2}
14	54	55	54.5	11	3.819×10^{-2}
15	55	56	55.5	9	3.125×10^{-2}
16	56	57	56.5	7	2.431×10^{-2}
17	57	58	57.5	6	2.083×10^{-2}
18	58	59	58.5	4	1.389×10^{-3}
19	59	60	59.5	1	3.472×10^{-3}
20	60	61	60.5	1	3.472×10^{-3}

Table 2 Mean air-quantity rates

Group mark	$\bar{q}_i$ (m^3·s^{-1})	$\bar{\lambda}_i$ (s^{-1})	Group mark	$\bar{q}_i$ (m^3·s^{-1})	$\bar{\lambda}_i$ (s^{-1})
1	41–42	0.003 472	11	51–52	0.345 133
2	42–-43	0.006 969	12	52–53	0.270 270
3	43–44	0.014 035	13	53–54	0.277 778
4	44–45	0.032 029	14	54–55	0.282 051
5	45–46	0.040 441	15	55–56	0.321 429
6	46–47	0.049 808	16	56–57	0.368 421
7	47–48	0.080 645	17	57–58	0.500 000
8	48–49	0.122 807	18	58–59	0.666 667
9	49–50	0.175 000	19	59–60	0.500 000
10	50–51	0.315 152	20	60–61	1.000 000

According to the formulas above, the mean value, the variance and the standard deviation of 20401 transportation laneway in this mine are μ_i =49.75, σ_i^2 =11.3866, σ_i =3.3744. The distribution density curve of the laneway is shown in Figure 3, and the distribution density function is as bellow:

$$f\left(\mu_i,\sigma_i^2\right)=\frac{1}{\sqrt{2\pi}\sigma_i}\mathrm{e}^{-\frac{(q_i-\mu_i)^2}{2\sigma_i^2}}=\frac{1}{\sqrt{2\pi}}\cdot\frac{1}{3.3744}\cdot\mathrm{e}^{-\frac{(q_i-49.75)^2}{2\times 11.3866}}$$

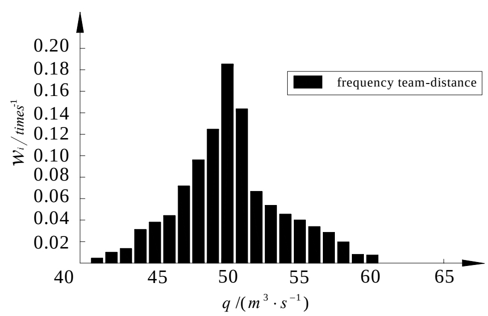

Figure 2 Draft of frequency group-distance distribution

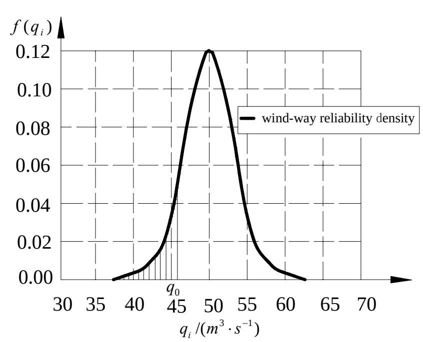

Figure 3 Density function curves of airways reliability

3.3 parameters assessment in the similar airway

Based on the data acquired, analyze the internal relation between the samples and the gross. Known the failure probability density function of airways [5]:

$$f(\mu,\sigma^2)=\frac{1}{\sqrt{2\pi}\sigma}\exp^{-\frac{1}{2}\left(\frac{q-\mu}{\sigma}\right)^2}$$

where, the μ and the σ^2 need to be estimated. The likelihood function is shown as below:

$$L(\mu,\sigma^2)=\prod_{j=1}^{n}\frac{1}{\sqrt{2\pi}\sigma}\exp\left[-\frac{1}{2}\left(\frac{q_j-\mu}{\sigma}\right)^2\right]$$

So we can know the estimate values of μ and σ^2:

$$\hat{\mu}=\frac{\sum_{j=1}^{n}q_j}{n}\quad,\quad \hat{\sigma}^2=\frac{\sum_{j=1}^{n}(q_j-\hat{\mu})^2}{n} \tag{5}$$

Based on μ_i =49.75 and σ_i =3.3744 of 20401 transports laneway, μ = [49.5669, 50.0808], and σ = [3.1089, 3.3948] on 95% confidence level, and the true value falls into the confidence interval.

4 Reliability Index's Substantiation and Computation to Wind Network

4.1 Reliability measurement indexes of airways [6]

1) *Airway reliability*. Takes into account of the stochastic disturb of wind-resistance and wind-pressure, as well as other factors in ventilation network, the reliability of the airway i is shown as:

$$R_i(q_i)=\int_{q_{i1}}^{q_{i2}}\frac{1}{\sqrt{2\pi}\sigma_i}\mathrm{e}^{-\frac{(q_i-\mu_i)^2}{2(\sigma_i)^2}}dq_i \tag{6}$$

The boundary condition about air-quantity of the airway i is as bellow:

$$q_{i1}=v_{i1}\cdot S_i\,,\,q_{i2}=v_{i2}\cdot S_i \tag{7}$$

2) *Cumulative failure rate of an airway*. Takes into account of the stochastic disturb of wind-resistance and wind-pressure, as well as other factors, the probability of air-quantity, of which the air quantity don't keep into $[q_{i1},q_{i2}]$ at airway i, is shown as below:

$$F_i(q_i)=1-R_i(q_i) \tag{8}$$

3) *Failure probability density of an airway*. The probability of q_i cannot keep into its reasonable interval $[q_{i1},q_{i2}]$ per unit time, shown as $f_i(q_i)$:

$$f_i(q_i) = \frac{\mathrm{d}F_i(q_i)}{\mathrm{d}q_i} = \frac{1}{\sigma_i\sqrt{2\pi}}\exp\left[-\frac{(q_i-\mu_i)^2}{2\sigma_i^2}\right] \quad , \quad q_{i1} \le q_i \le q_{i2} \tag{9}$$

4.2 Computations of the airway reliability

1) *Analytic method*. The shaded area $\Phi(q_0)$ in figure 4 is the probability of air-quantity less than q_0 in the airway, so the probability which the air-quantity more than q_0 is $R_i(q_0) = 1 - \Phi(q_0)$. The reliability of this airway by IRC:

$$R_i = P\{q_{i1} < q_i < q_{i2}\} = \Phi(q_{i2}) - \Phi(q_{i1}) \tag{10}$$

Takes 20401 laneway of Daliuta Coal Mine as an example, q_{i1} =40m^3/s, q_{i2} =55m^3/s. The reliability in this airway:

$R_i = \Phi(q_{i2}) - \Phi(q_{i1}) = \Phi(55) - \Phi(40) \approx 0.939430 - 0.001926 = 0.937504$

2) *Maximum likelihood estimation*. The formula estimated is described as the following:

$$R_{\mathrm{i}}(q_i) = \int_{q_{i1}}^{q_{i2}} f(q_i)\mathrm{d}q_i \tag{11}$$

The estimated value of reliability at 95% confidence interval of 20401 transportation lane:

$$R_i(q_i) = \int_{40}^{55} f(q_i)\mathrm{d}q_i = \int_{40}^{55}\frac{1}{\sqrt{2\pi}}\cdot\frac{1}{3.3744}\cdot \mathrm{e}^{-\frac{(q_i-49.75)^2}{2\times 11.3866}}\mathrm{d}q_i \approx 0.936642$$

The difference between the estimated value (0.936642) and the true value of analytic result (0.937504) of this airway is 0.000862. It is obvious that the estimated value is reasonable.

Likewise, the reliability index value of all kinds of Intake or Return in mine can be figured out.

4.3 Disjoint minimal path set algorithm of the ventilation network reliability [5]

In ventilation network, takes L_i as the compatibility minimal path, and L_{kdis} as the incompatibility minimal path, the relationship of them:

$$L_{idis} \cap L_{kdis} = \varnothing (i \ne k) \tag{12}$$

$$\bigcup_{i=1}^{n} L_i = \bigcup_{k=1}^{m} L_{kids} \tag{13}$$

With “Delete-Keep” algorithm to estimate the reliability of a wind network system is as follows:

Define a vector $E_i(i = 1,2,\cdots,n)$ of n dimension for each minimal path set of the ventilation network. Each component of vector E_i is a binary digit.

Calculate T_k:

$$T_k = \sum_{k=1}^{n} E_k (k = 1,2,\cdots,n) \tag{14}$$

Calculate the i incompatibility minimal path L_{kdis}. Suppose $k = 1$, $L_{idis} = L_1$, and then $k = k + 1$, to compare T_k with E_k. There are some E_k of zero at the non-zero position in T_k. Write down their positions in T_k from large to small (or from small to large) and set them as $k_1, k_2, \cdots, k_r$.

In L_{kdis}, the intact airway corresponds to 1, the failure airway to –1, and 0 to that not included in the network. The disjoint minimal path matrix S of the ventilation network is shown as bellow:

$$S = \prod_{i=1}^{n} L_{kdis} \tag{15}$$

Reliability R_w of the ventilation network system is calculated as bellow:

$$R_w = \sum_{i=1}^{n} P\{L_{kdis}\} \tag{16}$$

5 Conclusions

Based on the fluid network theory, the definition of the reliability index in the mine ventilation network is given. The forecast formula about mean air-quantity distributing density and mean air-quantity rate of airways are deduced. The fit-check assessment method about the air-quantity distribute density is brought forward as well. It is confirmed that fluid distribution rule of airflow in the laneway approximately obeys normal distribution.

The method of maximum likelihood estimation is applied to deduce the formula about the dots estimation and interval estimation of air-quantity distribution parameters. Matlab statistical toolbox is employed to solve this problem.

$\Phi(q_{i1})$ is reflects the probability of air quantity insufficient at airways, and $\Phi(q_{i2})$ is reflects the probability of air-quantity ultra limits. The smaller the $\Phi(q_{i1})$, the smaller the probability the air-quantity is insufficient; contrarily, the larger the probability. The smaller the $\Phi(q_{i2})$, the larger the probability the air-quantity is at ultra limits; contrarily, the smaller the probability .

The disjoint minimal path set algorithm is suitable to complex systemic reliability solution processes like ventilation networks. The method is validated by the case of the ventilation network of Daliuta Coal Mine.

Acknowledgements

The author would like to thank the financial support by the National Natural Science Foundation of P. R. China (Grant No. 50809008).

References

1. Zhou, X.Q., Wu, B. and Du, H.B. Theoretical study on fundamental conceptions in mine ventilation theory. Journal of China University of Mining & Technology, 2003, 32(2). 133–137. (In Chinese)
2. Cheng, Y.G. and Wang, D.M. The reliability analysis of a mine ventilation system. Journal of Taiyuan University of Technology, 1998, 29(7). 432–436. (In Chinese)
3. Lowndes, I.S. Review of mine ventilation system optimization. Transactions of institution of mining and metallurgy. Mine Industry, 1996,105. 114–126.
4. Xu, R.L. Theory of Ventilation Network. Beijing: Coal Industry Press, 1993, 2: 103–108. (In Chinese)
5. Xiao, D.H. Reliability Engineering. Beijing: Aviation Press, 1985, 11. 16–20. (In Chinese)

6. Wang, H.D. and Ma, Y.D. Study on reliability theory for mine ventilation system and its application. Beijing: Coal Industry Press, 2004,7. 48–53. (In Chinese)

RaSiM 7(2009): Controlling Seismic Hazard and
Sustainable Development of Deep Mines,
C.A. Tang(ed), Rinton Press,291-296

SIGNIFICANCE ANALYSIS OF THE SLAG AND FLY ASH INFLUENCE ON THE STRENGTH OF HIGH-STRENGTH CONCRETE

YIN WU, DA-GUO WANG and FENG CHEN

Geotechnical & Structural Engineering Institute, Dalian University

Dalian 116622, China

Through an analysis of the results of the test, this paper discusses the impact of slag and fly ash on the strength of high performance concrete under the conventional material and common technological method. It explains how to make the most appropriate mixture of slag composite admixture, fly ash, water reducing agent, and different water cement ratios. This is turn regulates the relationship of the early strength and the later strength on the premise of satisfying the concrete performance requirement. The best combination in which the function of each component has been put into full use is also found in this paper.

1 Introduction

A lot of studies and project instances show that the use of the high efficient water reducing agent and the high active mineral admixture, such as silica fume and mineral slag, will make the concrete strength improves greatly. Silica fume has very high activation, so it is widely used in the high strength concrete in a lot of countries, but because of the low output and the high price in China, it is only considered when the concrete strength is higher than 80Mpa. On the contrary, with the abundant source and the low price, fly ash is a good application prospect, however, it reacts slowly in the early hydrating period, its activation is relatively bad, and the early strength is weak. For those reasons, the application of fly ash is limited in the high strength concrete [1, 2]. So, in order to find out the best combination in which the function of each component has been put into full use, it is necessary to analysis and study the combined effect of slag, fly ash and water reducing agent.

2 The chosen raw materials

2.1. High efficient water reducing agent

Through comparative tests on β naphthyl sulfonate formaldehyde condensate and many kinds of complex surface activation material: HIP-A, HIP-AA, HIP-HF100, HIP-A100, and comparing with the test [3], it is found that the effects of several kinds of high efficient water reducing agent are not obvious. But the viscidity of mixture, the early strength and the increment of strength of model in later stage are greatly different. So the high efficient water reducing agent HIP-A100 which can give a better comprehensive result is adopted Quality index of HIP-A100 type high efficient water reducing agent [4].

2.2. Cement

The cement of 525# of “Starfish” is adopted [4], whose redundant coefficient is relatively higher and admixture adaptability is better.

2.3. Slag and fly ash

The I grade slag and fly ash (0.045mm tail over 7.5%) is adopted .See technical specification in [4].

2.4. Aggregate.

The adopted coarse aggregate is broken stones of 5~25mm (continuous grading). The fine aggregate is the sand of fineness modulus 2.7~3.00.

3 Analysis of the test result

3.1. Strength influence of water cement ratio

In this test water cement ratio is between 0.25~0.31, the percentage of HIP-A100 is 1.2% and that of slag is 40%,finally the compressive strength of 3 days, 7 days and 28 days are all measured (Fig. 1) [3, 4]. Test shows that when the water cement ratio changes between 0.25~0.31, slump flow and slump loss do not change greatly, but the viscosity drops to a great extent [5], all of the above have an actual significance to improve concrete performance. So, on condition of satisfying the strength, it is necessary to employ the water cement ratio as big as possible.

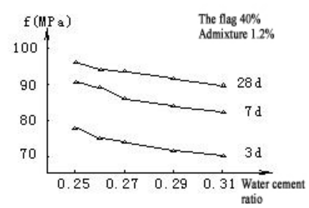

Figure 1 Relative water cement ratio and the concrete compressive strength

3.2. Strength influence of slag, fly ash

Slag and fly ash admixture are adopted in this text to go on single-admixture and double-admixture comparative tests. Concrete viscidity is minimum when the slag is mixed only, concrete viscidity is maximum when the fly ash is mixed only, the viscidity of double mixed with slag and fly ash is close to that of single mixed with the fly ash only [4]. we can find out from the relational curve of single mixed with the slag only and the relational curve of compressive strength of concrete (Fig.2) that the concrete strength increases to some extent when the percentage of slag mixture is between 10%~30%, the strength reduces with mixture amount increasing when the percentage of the slag mixture is between 30%~50%.The concrete strength when the percentage of slag mixture is 40% is basically the same with strength of concrete without slag admixture, for that when the slag is rubbed into ultra fine power, the gelation capacity which must depends on the effect of activator is still very weak. The amount of cement reduces, so the amount of $Ca(OH)_2$ produced in hydration course reduces, the activation can't be totally excited, which leads to the fact that the strength and the cohesion decrease.

We can find out from the relational curve of single mixed with the slag only and compressive concrete strength, the concrete strength especially the early strength decrease obviously with the increment of fly ash. But the strength increases sharp on the later stage, In order to guarantee the early strength the amount of fly ash should be limited within a certain range.

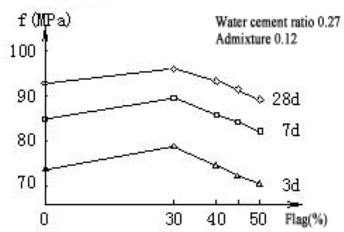

Figure 2 Compressive concrete strength of single mixed with slag only

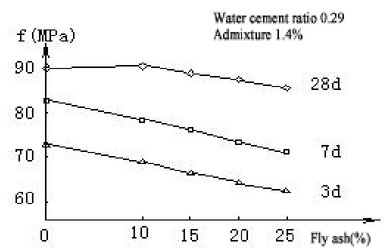

Figure 3 Compressive concrete strength of single mixed with fly ash only

We can find out from the relational curve of double missed with slag and fly ash together and the concrete strength, the amount of slag mixture and fly ash mixture influences the compressive strength comparatively, the strengths of 3days and 7days decreases obviously ,especially when the amount of fly ash is large, the strength of 28d increases obviously. When the mixture topographic effect, micro-aggregate effect and volcanic ash effect, also known as the effects of lubrication, thinning pore and gelatinization, act at the same time, it not only increase the later strength but also decreases the hydration heat, the slump loss and the alkalinity, which does the favour of the modification effect. So, by adjusting the amount of mixture, we can guarantee the early strength and accelerate the later strength t by a relatively large range.

As Fig 5 shows, the compressive strength of high performance concrete mixed slag and fly ash is up with the change of the age. It is shown that the concrete strength increases constantly with the growth of the age under the condition of the active slag 25%, the fly ash 10%, the relative water cement ratio percentage 0.26, HIP-A100 admixture 1.2% and sand cement percentage 35%.

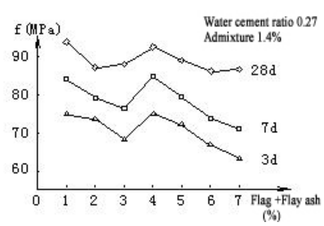

Figure 4 Amount of slag, fly ash (double-admixture) and the concrete strength

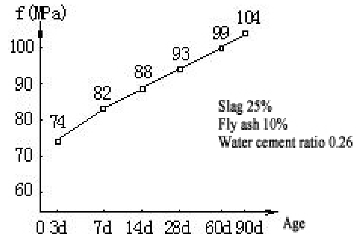

Figure 5 The compressive concrete strength is up with the age

3.3. Significance analysis of the influencing factors

As the mentioned results of the test show, the remarkable influencing factors of concrete strength are water cement ratio, the percentage of slag and fly ash, the percentage of admixtures. On the condition of the sand cement percentage 37%, through orthogonal test it can find out the influencing factors. The method of inverted slump tube is adopted to survey the time how much the all of mixtures spend to flow out, the time are considered as the evaluation index of viscidity. The concrete fluidity is evaluated synthetically by outflow time, slump flow and slump loss.

What the orthogonal test in which the slag mixture is mixed singly shows (Tab. 1-1 and Tab. 1-2), the viscidity and slump flow change greatly, when the relative water cement ratio varies form 0.24 to 0.28, the outflow time decreases rapidly; slump flow increases obviously too, the slump loss does not change significantly. The changes of the amount of slag and admixture influences greatly to slump flow, weakly to other factors. The most important factor that influence greatly to compressive strength is water cement ratio; the second most important factor is the amount of slag mixture. When relative water cement ratio is between 0.24~0.26, it almost has no influence to compressive strength. The amount of slag mixture has great influence to the compressive strength of 3 days and 7 days, however, after 7 days, the influence becomes weaker and weaker with the time. The appropriate amount of admixtures has little influence to strength.

The double-admixture orthogonal test, in which the fly ash replaces part flag, shows that (Tab. 2-1 and Tab. 2-2) water cement ratio is still the main influence of concrete fluidity. Besides we can find out that the amounts of slag and fly ash influence the short time compressive strength greatly, especially when the amount of fly ash is larger, the strengths of 3 days and 7days increase obviously; the strength of 28 days has no difference with the single-admixture strength. So, in order to guarantee the early strength the percentage of fly ash admixture should not be higher than 20%. Within the specific limit the difference of the amounts of slag and fly ash is utilized to regulate the relation of the early strength and the later strength.

Table 1-1. The orthogonal test single mixed with slag

Number	Water cement ratio	Cement+Slag (%)	Admixture (%)	Outflow time (sec)	Slump flow (mm)	Slump loss (mm)	Compressive strength (Mpa)		
							3days	7days	28days
1	1(0.24)	1(75+25)	1(1.0)	100	200	450	77.3	85.2	90.8
2	1	2(65+35)	2(1.2)	60	210	485	78.7	80.1	92.7
3	1	3(55+45)	3(1.4)	73	230	540	71.9	85.2	85.5
4	2(0.26)	1	2	29	195	485	80.6	81.4	89.9

5	2	2	3	12	210	550	75.1	83.2	89.6
6	2	3	1	21	235	565	76.8	79.7	88.2
7	3(0.28)	1	3	13	205	560	76.1	77.5	87.2
8	3	2	1	18	210	575	77.1	75.0	82.5
9	3	3	2	10	215	545	65.2	77.3	83.9

Table 1-2. The statistics to the orthogonal test single mixed with slag

Index factor	Outflow time			Slump flow time			Slump loss time			Strength of 3days			Strength of 7days			Strength of 28days		
	1	2	3	1	2	3	1	2	3	1	2	3	1	2	3	1	2	3
K1	78	47	46	213	200	215	492	498	530	76.0	78.0	77.1	83.5	81.4	80.0	89.7	89.3	87.2
K2	21	30	33	213	210	207	533	537	505	77.5	77.0	74.8	81.4	79.4	79.6	89.2	88.3	88.8
K3	14	35	33	210	227	215	560	550	550	72.8	71.3	74.4	76.6	80.7	82.0	84.5	85.9	87.4
Leave	64	17	13	3	27	8	68	52	45	4.7	6.7	2.7	6.9	12.0	2.4	5.2	3.4	1.6

Table 2-1. The orthogonal test double mixed with slag and fly ash

Number	Water cement ratio	Slag + Fly ash （%）	Admixture （%）	Outflow time （sec）	Slump flow （mm）	Slump loss （mm）	Compressive strength（Mpa）		
							3days	7days	28days
1	1(0.24)	1(30+10)	1(1.0)	36	240	583	74.4	80.4	89.4
2	1	2(20+20)	2(1.2)	40	235	543	67.4	80.6	89.6
3	1	3(10+30)	3(1.4)	31	230	560	58.7	73.0	88.1
4	2(0.26)	1	2	15	235	578	74.4	78.6	89.1
5	2	2	3	20	225	570	65.2	73.5	84.5
6	2	3	1	23	230	570	56.6	63.9	88.3
7	3(0.28)	1	3	12	230	610	63.4	72.0	84.3
8	3	2	1	14	210	580	59.1	67.5	81.0
9	3	3	2	14	220	560	53.0	64.9	84.0

Table 2-2. The statistics of the orthogonal test double mixed with slag and fly ash

Index factor	Flowing out time			Slump time			expand time			Strength of 3days			Strength of 7days			Strength of 28days		
	1	2	3	1	2	3	1	2	3	1	2	3	1	2	3	1	2	3
K1	36	21	24	235	235	227	562	590	578	66.8	70.7	63.4	78.0	77.0	70.6	89.0	87.6	86.2
K2	19	25	23	230	223	230	573	564	560	65.4	63.9	64.9	72.0	73.9	74.7	87.3	85.0	87.6
K3	13	23	21	220	227	228	583	563	580	58.5	56.1	62.4	68.1	67.3	72.8	83.1	86.8	85.6
Leave	23	4	3	15	12	3	21	27	20	8.3	14.6	2.5	9.9	9.7	4.1	5.9	2.6	2.0

3.4. Survey of other mechanics performance

On condition of water cement ratio 0.26、slag cement ratio 25%、fly ash cement ratio 10%、HIP-A100 admixture 1.2%、sand cement percentage 35%, the model tested about various mechanical indexes in the Tab.3, has the higher early strength, the compressive strength of 28 days is more than 90Mpa. We can see from the Tab.3, the size effect of the model is obvious, bending strength and split-tensile strength have no obvious increase, the splitting tensile strength is low and the tensile strength does not increase with the compressive strength, the elastic modulus is twice as many as that of common concrete.

Table.3. Test result of other mechanical performance

Age	Cubic compressive strength(Mpa)		Axial compressive strength(Mpa)	Bending strength(Mpa)	Split-tensile strength(Mpa)	Elastic modulus (Mpa)
	$150\times150\times150mm^3$	$100\times100\times100mm^3$				
28d	87.7	93.1	88.4	11.3	5.75	4.62×104

4 Conclusions

It can be concluded from the test:

1) The most important factor of compressive strength is water cement ratio when the water cement ratio varies within the range of 0.24-0.28. The second most important factor is the amount of slag mixture. The concrete strength of 28 days is near 90Mpa when the water cement ratio is between 0.26-0.28.

2) When the water cement ratio is between 0.25-0.31, the concrete strength increases to some extent on condition that the percentage of slag mixture is 10%-30%. However, the concrete strength decreases with the increase of the percentage of slag mixture when that in the concrete is between 30%-50%.The strength of the plain concrete is the basically same as that of concrete in which the percentage of slag mixture is near 40%.The amount of admixture influences greatly to the strength of 3 days and 7 days, while the effect of the admixture becomes weaker and weaker after 7 days.

3) When slag is single mixed in the concrete, the fly ash of the different kinds and grades has different influences to the strength, but the effect of the high quality fly ash is the same as that of first grad fly ash. With the growth of amount of fly ash, the concrete strength, especially the early concrete strength, decreases obviously, on the contrary, the later strength increase greatly. To guarantee the strength of the first stage, the percentage of fly ash should not be more than 20%.

4) When the slag and the fly ash are mixed together in the concrete, they influence the compressive strength obviously in the short period, especially when the mount of fly ash mixture is higher; the strength of 3days and 7days decreases obviously and the strength of 28days does not vary greatly. Therefore, it can be concluded that the different amount of slag and fly ash can be used to adjust the relation of the early strength and the later strength.

Acknowledgements

The author would like to thank the financial support by the National Natural Science Foundation of P. R. China (Grant No. 50809008).

Reference

1. Feng, N.Q. High performance concrete construction. Beijing: China Mechanical Industry Press, 2004. (In Chinese)
2. Chen, Z.Y., Zhu, J.Q. and Wu, P.G. High strength concrete & application. Beijing: Tsinghua University Press, 1992. (In Chinese)
3. Wu, Y. and Guan, P. Study on factors of influence on strength of high performance concrete. New Building Materials, 2005, (7). 1-5. (In Chinese)
4. Wu, Y. and Guan, P. Study on the strength and pumping performance of high strength concrete with slag and fly-ash. Journal of Dalian University, 2003, 24(6). 36-40. (In Chinese)
5. Wu, Y. Shang, X.L. and Zhao, D. S. Compound technology of C80 high performance pumping concrete. Journal of Liaoning Technical University, 2004, 23(5). 627-629. (In Chinese)

RaSiM 7(2009): Controlling Seismic Hazard and Sustainable Development of Deep Mines, C.A. Tang(ed), Rinton Press, 297-300

STUDY OF THE RELATIONSHIP BETWEEN DAMAGE AND AE ENERGY ACUMULATION OF COAL SAMPLES BASED ON THE UNIAXIAL COMPRESSION TEST

XIAO-BIN YANG and YUE-PING QIN

State Key Laboratory of Coal Resources and Safe Mining, China University of Mining and Technology

Beijing, 100083, China

DA-GUO WANG

Center for Material Failure Modeling Research, Dalian University

Dalian 116622, China

Rockburst is the result of a dynamic instability phenomenon of surrounding rock in underground projects in deep high-geostress zones. The prediction and mechanism of rockburst are important issues in many underground projects. The study of the mechanical and physical properties of rock under different loads and physical chemistry conditions is the primary consideration for rockbursts. The relationship between the damage and the AE energy accumulation has been studied by the uniaxial compression test in this paper. First, several coal samples are tested under the uniaxial compression test to obtain the curves of the stress-strain and the AE energy accumulation and strain, which are then fitted by a logarithmic function. Second, based on the Damage Rock Mechanics Theory and the energy conservation equation, the damage evolution model of coal is constructed through analysis of the experimental data. The damage factor varies with the strain and is given by analyzing the experimental data which yields the values of the material constant in the theoretical model. Third, through the relationship between the AE energy accumulation strain and the damage factor strain, the relationship between the AE energy accumulation and the damage factor can be obtained. Based on the damage evolution model and the AE detection method, the results of this paper will provide a theoretical reference for rockburst prediction in coal mines.

1 Introduction

A rockburst [1] or gas outburst in a coal mine is a sudden and violent expulsion of coal or coal and gas from the surrounding coal mass. Possible effects of rockbursts or gas outbursts include： injuries, fatal accidents, damage to equipment, construction and production delays, and higher costs of construction and operation. There is a need for the development of suitable methods for the prediction and control of rockbursts or gas outbursts, particularly for safe and economical underground excavation for construction or mining in burst-prone ground. As to the mechanism of the rockburst, the theoretical assumptions have been formed by scientists at home and abroad. But the theoretical framework is still based on the continuum of elastic-plastic mechanics, so the theoretical results of this research have considerable differences with engineering practice.

The damage theory has been applied to study the stress evolution under the coal mine and understands the mechanism of rockbursts. Although the damage theory has been developed for fifty years now [2], there has not been a generally accepted theory. Dougil, Dragon etc. were the first scholars to introduce the damage concept to study mechanical response in the rock material, put forward an elastic-plasticity constitutive relation to reflect strain-softening phenomena of rock materials, and set up a model of continuum damage mechanics. As the continuous development and improvement of rock damage research, a lot of research results have been obtained in the experimental observations of rock meso-damage, the rock damage constitutive model, numerical simulation and engineering applications [3-10].

In the present paper, three coal samples under uniaxial compression and acoustic emission test are conducted to experiment; through the measured experimental data analysis, and taking the non-linear property of rock, the damage evolution equation of coal is found; then deduce the relation between damage and acoustic emission (AE) energy accumulation. The results of this paper will provide theoretical guidance for the safe and efficient produce for the engineering to avoid rockburst.

2 Uniaxial Compression Test of Coal samples

The MTS815.02S type of electro-hydraulic servo rock mechanics test system is applied, and the main technical parameters of this test system as: axial compressive pressure is 1700kN, confining pressure is 45MPa, stiffness of the frame is 10.5×10^9N / m, the sensitivity of servo valve is 290Hz, the minimum sampling time is 50 μs, number of channel sampling is 10, the maximum diameter of the sample is 100mm and the maximum height is 200mm.

Using the same loading rate and the data sampling time, three coal samples has been prepared to experiment, and the experimental condition is shown in table 1. During the loading process, with the evolution of damage, not only the stress-strain relationship would change, but also the volume expansion, acoustic emission, electro-magnetic radiation would change, too. In order to study the relation between these physical parameters and damage, set up a quantitative relationship between acoustic emission and damage, the stress and AE energy accumulation varied with the strain are obtained, shown in Figure 1 and Figure 2. In figure 2, the "da31e" presents the experimental data, and the "da31f" presents the fitting results.

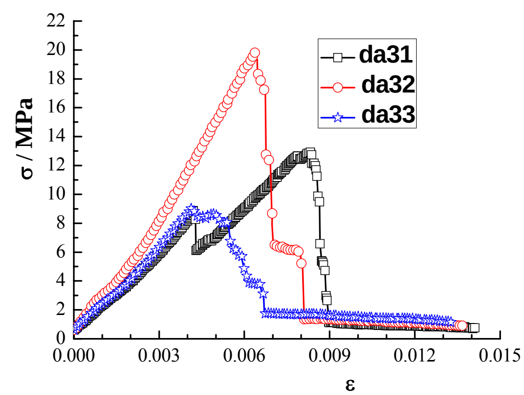

Figure 1 under the uniaxial compression, the stress-train curve of the three coal samples

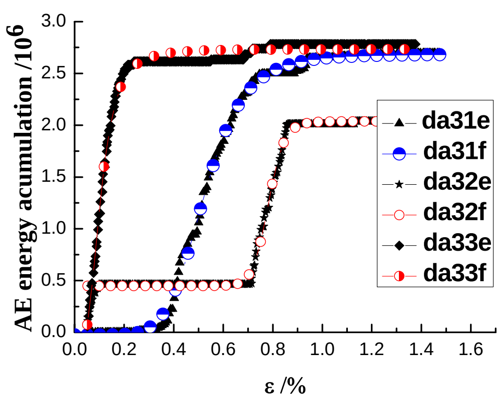

Figure 2 under the uniaxial compression test, the AE accumulated energy varied with the strain for the three coal samples.

Table.1 the table of the uniaxial compression experiment under controlling the axial strain rate

Samples	D /mm	H /mm	Strain rate /mm·s^{-1}	Sampling time /s	Maximum load /kN
da31	49.0	94.1	3/960	1.0	24.0
da32	49.5	99.4	3/960	1.0	39.0
da33	49.2	97.7	3/960	1.0	17.4

Through analyzing experimental results of the strain and AE energy accumulation, the relation of which can be obtained by fitting the data, the relation shown as following:

$$AE = \frac{A_1 - A_2}{1 + (\varepsilon - \varepsilon_0)^p} + A_2 \tag{1}$$

Where $A_1, A_2, \varepsilon_0, p$ are material constants, which can be obtained by fitting the experimental data, as to the three coal samples, the values of them shown in table 2.

Table.2 the table of material constants of the three coal samples for the AE and strain relation

samples	A_1	A_2	ε_0	p
da31	-0.025	2.684	0.525	6.524
da32	0.448	2.037	0.782	24.81
da33	-0.183	2.733	0.104	3.333

3 Damage model and the relation between damage and AE energy accumulation

From the figure 1, the curves of the stress- strain shows that the tress does not vary with strain linearly before the peak value, that is to say the stress has a nonlinear relation with the strain. So considering the nonlinear property of rock material, applying the damage theory, the damage and damage evolution function can be deduced by the energy conservation equation, just as the follow:

$$D = 1 - \left(\frac{n}{(j+1)} \frac{E_0^l}{\gamma} \varepsilon^{j+1} + 1 \right)^{\frac{1}{1-n}} \tag{2}$$

$$dD = \frac{j+1}{n-1} \left(\frac{n}{(j+1)} \frac{E_0^l}{\gamma} \right)^{\frac{1}{1-n}} \varepsilon^j d\varepsilon \tag{3}$$

where j, l, n are material constants, γ is the Energy consumption rate of damage, E_0 is the initial elastic modulus, D is damage factor. j, l, n, γ and E_0 can be obtained by analyzingthe experimental data, which shown in table 3.

Table.2 the value of the parameters in the damage evolution equation of the coal samples

samples	j	n	γ	l	E_0(MPa)
da31	1.36	2.5	0.87	0.8	2.7
da32	1.4	1.25	0.08	0.88	2.5
da33	1.32	1.28	0.035	1.1	2.6

Substituting equation (2) into equation (1), the relation between the AE energy accumulation and damage can be obtained:

$$D = 1 - \left(\frac{n}{(j+1)} \frac{AE(\varepsilon) \cdot E_0^l}{\gamma} + 1 \right)^{\frac{1}{1-n}} \tag{4}$$

where

$$AE(\varepsilon) = \left(\frac{A_1 - AE}{AE - A_2} \right)^{\frac{j+1}{p}} \tag{5}$$

Through the equation (4) and the AE energy accumulation data obtained from the AE experiment, the curves of the AE energy accumulation and damage is shown in Fig. 3 for the three coal samples.

4 Conclusions

Through experimental testing and theoretical analysis, several conclusions can be drawn:

(1) Under the uniaxial compression and acoustic emission experiment, the curves of stress and AE energy accumulation with strain have been obtained; shown in Fig.1 and Fig.2.

(2) From Fig.1 and Fig.2, there is an indirect relation between the AE energy accumulation and the sample strength: the higher the strength, the lower the AE energy accumulation

(3) A formula of the AE energy accumulation and strain has been obtained by fitting the experimental data.

(4) Based on the damage theory and energy conservation equation, and also considering the nonlinear property of coal, the damage function and damage evolution function can be found.

(5) A formula of the relationship between the AE energy accumulation and damage has been found.

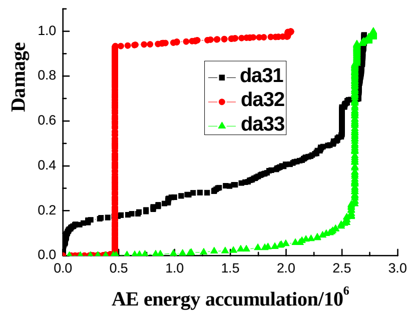

Fig.3 damage varied with the AE accumulated energy for the three coal samples

Acknowledgements

The author would like to thank the financial support by the China Postdoctoral Science Foundation (Grant No. 2008440445) and the National Natural Science Foundation of P. R. China (Grant No. 50809008).

References

1. Jaeger, J.C. and Cook, N.G.W. Fundamentals of rock mechanics. London: Chapman & Hall, 1979.
2. Yu, S.W. and Feng, X. Q. Damage mechanics. Beijing: Tsinghua university press, 1997. (in Chinese)
3. Qin, Y.P. Discussion on damage mechanics model and constitutive equation of rock. Chinese Journal of Rock Mechanics and Engineering, 2001, 20(4). 560-562. (in Chinese)
4. Li, S.M., Qi, W. and Liu, H.S. Development of the rock's damage theory**.** World Geology, 2001, 20(1). 72-78. (in Chinese)
5. Zhou, T.Q., Li, Z.X. and Jia, J.B. Parametric Variational Principle for Coupled Elasto-Plasticity Damage Problem Analysis. Journal of Southeast Univwrsity, 2001, 20 (3). 391-393. (in Chinese)
6. Zhang, Q.Y. and Xiang, W. Constitutive model for energy damage of jointed rockmass and its engineering application. Journal of engineering geology, 1999, 7(4). 311-314. (in Chinese)
7. Li, G.P. The mechanism of compression-shear damage for rock mass with its application to rockburst. Chinese jounal of geotechnical engineering, 1997, 19(6).50-55. (in Chinese)
8. Zofia, M., Grażyna, C.S., Stanisław M. and Jerzy Z. Binary gas sorption/desorption experiments on a bituminous coal: Simultaneous measurements on sorption kinetics, volumetric strain and acoustic emission. International Journal of Coal Geology , 2009, (77). 90–102
9. Manoj, N.B. and Vladimir P. Fatigue and dynamic energy behavior of rock subjected to cyclical loading. International Journal of Rock Mechanics & Mining Sciences, 2009, 46. 200– 209
10. Jan, V., Vladimír, R., Tomáš, L. and Roman, Ž. Application of autocorrelation analysis for interpreting acoustic emission in rock. International Journal of Rock Mechanics & Mining Sciences, 2008, 45. 1068-1081.

RaSiM 7(2009): Controlling Seismic Hazard and Sustainable Development of Deep Mines, C.A. Tang(ed), Rinton Press, 301-306

NUMERICAL FORWARD MODELLING AND INVERSION OF ELECTRICAL RESISTIVITY TOMOGRAPHY FOR MONITORING CRACK GROWTH IN ROCK

BIN LIU, SHU-CAI LI amd SHU-CHEN LI

Geotechnical & Structural Engineering Research Center of Shandong University

Jinan, 250061, China

The initiation and growth of crack are important features of rock fracturing and burst. Microseismic monitoring and sound reflection technique are main methods to monitor the initiation and growth of crack. However, it is difficult to apply tomography to study crack initiation and growth using conventional methods. Electrical Resistivity Tomography (ERT) is usually used to image geological body and metal mine, and has been proved to be useful. The resistivity of crack is higher than surrounding rock, which is the essential condition to use ERT technique to monitor the crack. In this paper, Finite Element Method (FEM) based on Preconditioning Conjugal Gradient (PCG) algorithm is used for the first time to model the ERT for crack growth. Jacobian preconditioning matrix is the key technique to solve the large linear system in FEM, by which the calculation speed is greatly improved. In order to precisely locate the crack, geophysical inversion technique (smooth least-squares method) is used to calculate the distribution shape of crack. The result of 2D inversion is consistent with the process of crack growth. Throughout this study, it is concluded that it is feasible to monitor crack growth with ERT technique.

1 Introduction

As a dynamic failure process, rock burst results from the creation and growth of cracks. Therefore, rock burst can be predicted by monitoring crack growth. Microseismic monitoring technique are one of the important methods to predict rock fracturing, crack creation and growth, which has been widely applied in deep mines in South Africa, Canada and Australia. In addition, other physical quantities or parameters are sensitive to rock fracturing are also necessary information for rock burst prediction [1, 2, 3]. For instance, in former Soviet, Poland and Germany, the resistivity method was used to monitor rock displacement and fracturing. Brace W F [4] first conducted experiment about resistivity variation associated with rock fracturing, and proposed some failure mode and mechanism. Thereafter, this method is mainly applied in seismic prediction, and massive tests are conducted. With increasing mining depths and dynamic disasters, the resistivity method is introduced into mine project to monitor rock fracturing. Stopinskl W in Poland [5] used this method to predict rock burst and roof fall and got the initial achievement. In China, Jin-qi Zhou and Rui Feng studied the mechanism of resistivity variation in the rock fracturing process, and used ERT technique to monitor crack growth [6].

In this paper, FEM based on PCG algorithm is used to model the ERT for crack growth, by which the calculation speed is greatly improved. In order to locate the crack precisely, geophysical inversion technique is used to calculate the position and distribution shape of the crack. The result shows that it is feasible to predict crack growth and rock burst with the ERT technique.

2 FEM modelling of ERT

2.1 FEM for solving point source electrical field problem [7,8,9]

In 3D geoelectric section, variational problem of point source field is expressed as follows:

$$\begin{cases} F(u)=\int_{\Omega}\left[\frac{1}{2}\sigma(\nabla u)^{2}+\sigma'\nabla u_{0}\bullet\nabla u\right]d\Omega+\int_{\Gamma_{\infty}}\left[\frac{1}{2}\frac{\sigma\cos(r,n)}{r}u^{2}+\frac{\sigma'\cos(r,n)}{r}u_{0}u\right]d\Gamma \\ \delta F(u)=0 \end{cases} \quad (1)$$

Where u_0 is normal potential, u is abnormal potential, σ_0 is conductivity of surrounding rock, σ is conductivity of anomalous body, and $\sigma'=\sigma-\sigma_0$.

The solved region Ω is subdivided with eight-node hexahedron. The abnormal potential u in the cell is calculated through tri-linear interpolation. And the elemental coefficient matrix is obtained by calculating integration in element. And the global stiffness matrix is composed with elemental coefficient matrix, which is expressed as Eq. (2). And the normal potential $\boldsymbol{u}_0$ has analytical solution.

$$F(u)=\sum F_e(u)=-\frac{1}{2}\mathbf{u}^T\sum\overline{\mathbf{K}}_e\mathbf{u}+\mathbf{u}^T\sum\overline{\mathbf{K}}'_e\mathbf{u}_0=\frac{1}{2}\mathbf{u}^T\mathbf{K}\mathbf{u}+\mathbf{u}^T\mathbf{K}'\mathbf{u}_0 \quad (2)$$

Here, $\overline{\mathbf{K}}_e=\sigma(\overline{\mathbf{K}}_{1e}+\overline{\mathbf{K}}_{2e})$, $\overline{\mathbf{K}}'_{\mathrm{e}}=\sigma'(\overline{\mathbf{K}}_{1e}+\overline{\mathbf{K}}_{2e})$. $\overline{\mathbf{K}}_{1e}$ is expansive matrix of the elemental coefficient matrix by calculating volume integration of the first part in Eq.(1).And $\overline{\mathbf{K}}_{2e}$ is expansive matrix of the elemental coefficient matrix by calculating boundary integration of the second part in Eq.(1).

Linear equations are obtained by calculating the variation of Eq. (2), as follows:

$$\mathbf{Ku}=-\mathbf{K'u}_0 \quad (3)$$

Abnormal potential of each node is calculated with Eq. (3). And total potential v is obtained by Eq. (4).

$$v=u+u_0 \quad (4)$$

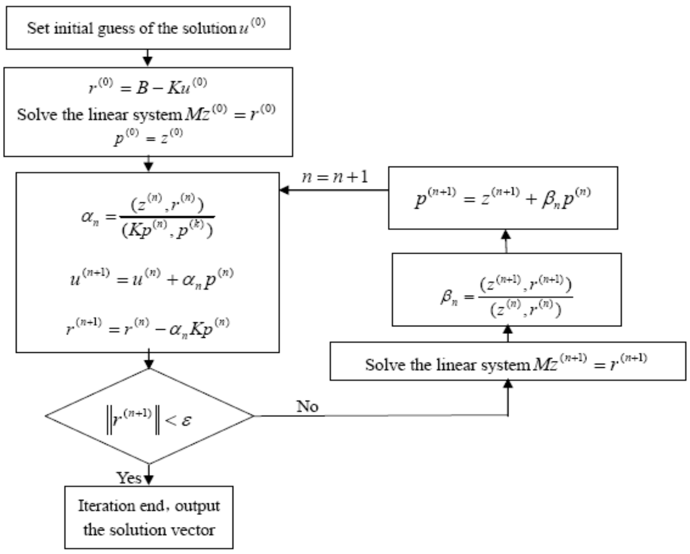

Figure 1 The process of PCG algorithm

2.2 Solving large linear systems with PCG

In this paper, PCG algorithm is used to solve large linear system. And PCG algorithm is introduced in Figure 1. Eq. (3) can be transformed into Eq.(5),as follows:

$$\mathbf{Ku} = \mathbf{B} \quad (5)$$

Where, $\mathbf{B} = \mathbf{K'u_0}$.

For PCG algorithm, the preconditioning matrix $\mathbf{M}$ must meet condition that is easy to solve its inverse matrix. In this paper, the diagonal block matrix in Jacobian Iteration is used as preconditioning matrix, the inverse matrix of which is easy to be solved.

2.3 Numerical modelling of ERT for crack growth

Fractures or cracks in rocks are thin planar features of high resistivity, embedded in a more conductive bulk volume. Cracks have a major influence on the electrical resistivity of bulk material, which is the essential condition to use ERT to monitor crack growth. Two numerical experiments with 3D FEM are carried out to evaluate the effect of the ERT [10, 11, 12]. Figure 2 is schematic diagram of the rock sample with crack. The side length of the rock in x, y and z direction is 1.3m, 0.4m and 0.8m respectively. And a crack is designed with an electrical resistivity of $1\times10^5\,\Omega m$ and a width of $2\,mm$, and the red line is survey line. In the first model, a vertical crack is designed, and elevation of the growth process of crack is described in Figure 3, and the mark L represents the length of crack. ERT is carried out with a Wenner array of 59 electrodes separated by 0.04 m spacing. The forward modelling results are in Figure.4, and its longitudinal axis represents polar distance and its vertical axis represents the layer number in data structure of ERT. In the second one, an inclined crack is designed with an angle of 30° with Y direction (Figure.5), and the modelling result is in Figure.6.

The result of both of the numerical experiments shows that the ERT method is very sensitive to the crack growth. The red colour zone with higher resistivity is the reflection of crack .However, the distribute shape of red zone is greatly different from the shape of crack. For the second model, the red zone does not reflect inclined angle of crack, the shape of which is almost the same as the first. So inversion must be carried out to obtain the feature of crack.

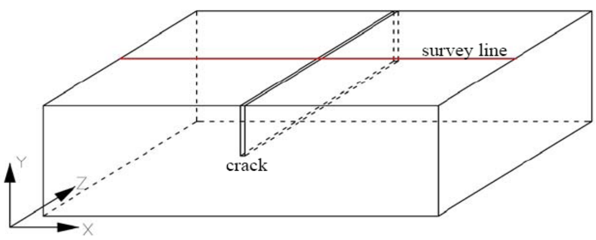

Figure 2 Schematic diagram of crack in the rock sample

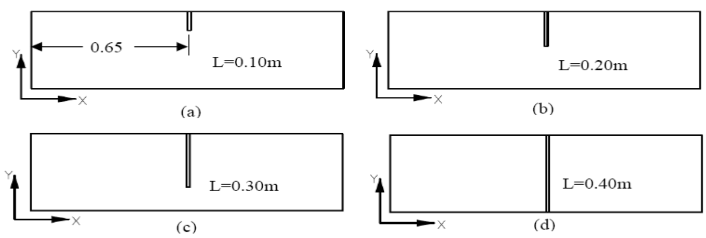

Figure 3 Elevation of growth process of crack in the first model

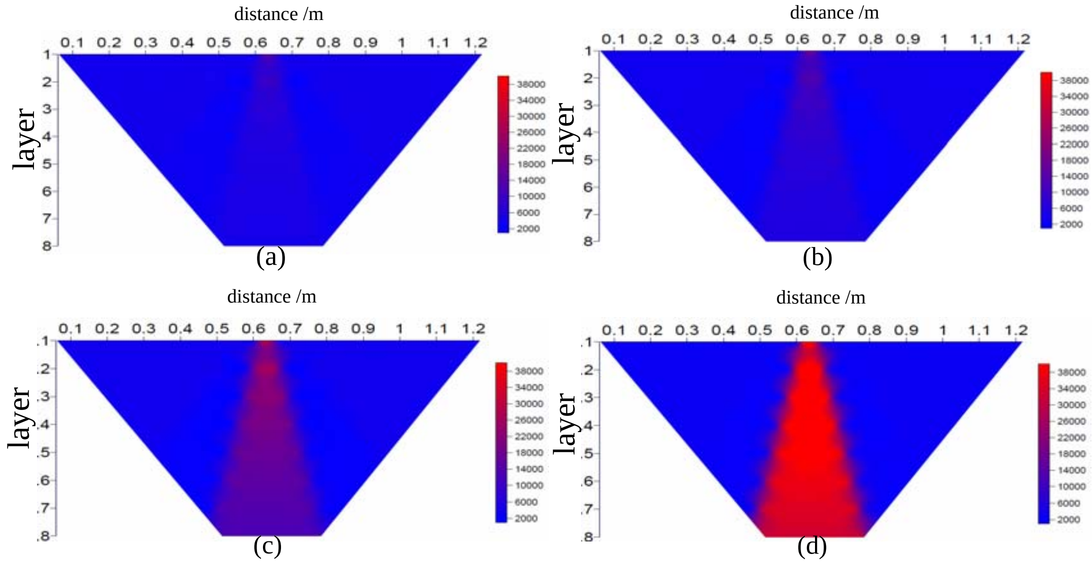

Figure 4 Forward modelling results of ERT for the first model

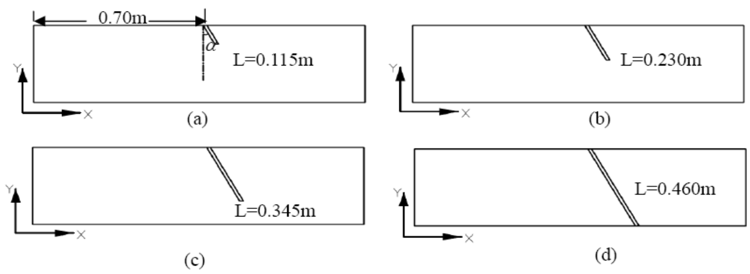

Figure 5 Elevation of growth process of crack in the second model

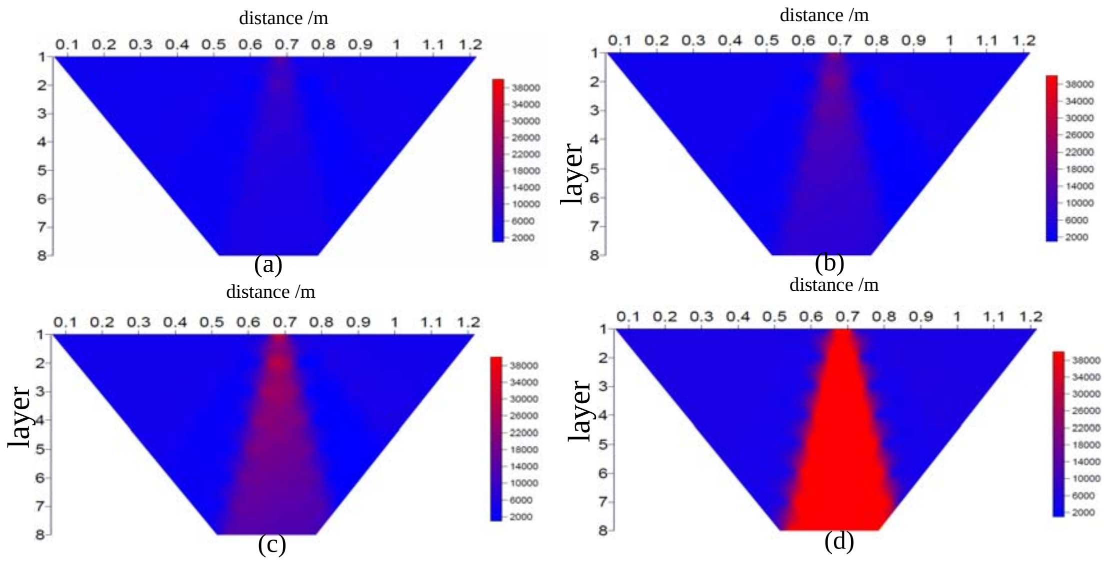

Figure 6 Forward modelling results of ERT for the second model

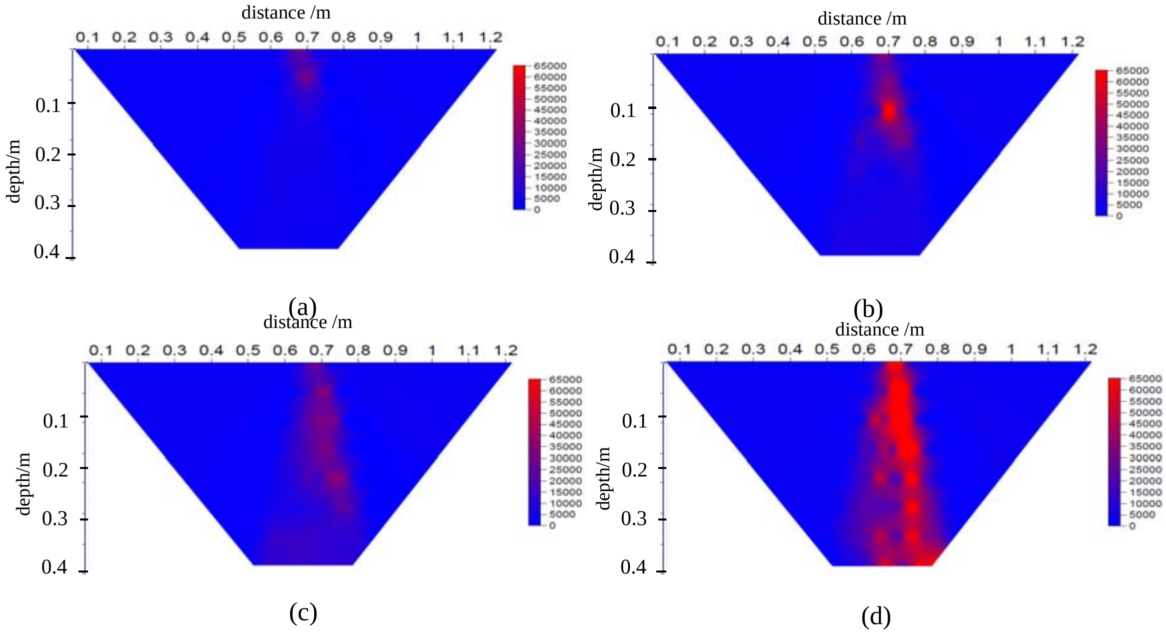

Figure 7 Inversion result of ERT for the second model

3 Inversion for ERT

3.1 Algorithm of smooth least-squares inversion

If we desire to obtain the resistivity structure and crack feature from our measure data, we must solve a nonlinear optimization problem. In this paper, inversion problem is linearilized, and smoothness operator matrix is introduced into the inversion equation. The inversion equation with smooth least-squares method is expressed in Eq. (6).

$$(\mathbf{A}^T\mathbf{A}+\lambda\mathbf{C}^T\mathbf{C})\Delta m=\mathbf{A}^T\Delta d \quad (6)$$

Where λ is Lagrange constant, $\mathbf{A}$ is sensitivity matrix and $\mathbf{C}$ is smoothness matrix [13].

3.2 Inversion example

For saving calculation time, 2D inversion is carried out. Take the second model for example, smooth least-squares inversion is performed. The inversion converges after 17 iterations. The results are shown in Figure.7. There are several conclusions from the results as follows:

(1)The red zone in inversion result is much closer to the distribute shape of crack than that in modelling result. In general, the change of red zone in four photos is consistent with the growth of crack.

(2)The resistivity of red zone is lower than the crack, which results that the width of red zone is slightly greater than that in model.

(3)The angle of red zone with Y direction is about 15° while the angle of crack is 30°, and the tolerance error of which is large consequently.

4 Discussion

In this paper, there is only one crack in rock, and multi-crack rock is not considered. For single crack, satisfied tomography consistent with the rock sample can be obtained with 2D inversion method. However, for multi-crack rock sample, it is difficult to obtain satisfied result by 2D inversion method. So it is necessary to study 3D inversion method for ERT.

5 Conclusions and Future Work

In this paper, numerical modelling and inversion is carried out to study the ERT for crack growth. The result of 2D inversion is basically consistent with the process of crack growth. The result shows that measure date is sensitive to the crack growth and good effect is got to monitor the crack growth by this method.

The work in this paper demonstrates the feasibility of this method to monitor crack growth in theory. Experiments need to be carried out to checkout the practicality of this method and provide the means to make the method better.

Acknowledgements

The authors would like to deeply appreciate the project supported by the State Program of National Natural Science of China (Grant No. 2007AA11Z131; 50727904; 50874068) and National Basic Research Program of China (973 Program, No.2007CB209407).

References

1. Li., T.J.Wang., Y.H. etal..Fractal properties of crack in rock and mechanism of rock-burst. Chinese Journal of Rock Mechanics and Engineering, 2000, 19(1). 6-10.
2. Li., D.C.Ge., B.C. etal..Mechanism and tests of mine disaster prediction by resistivity method.Coal geology & exploration, 1999, 27(6). 62-65.
3. Yang.,Z.G.Yu., R.C. etal. Application of microseismic monitoring to deep mines. Chinese Journal of Rock Mechanics and Engineering, 2008, 27(5). 1066-1073.
4. BraceW,F., et al. Electrical resistivity changes in saturated rocks during fracture and frictional stiding. J. G. R, 1968; 73 (4) . 130-131.
5. Stop insk l W. P recursory rock resistivity variations related to mining tremors. A cta Geophys. Po l. , 1982; 30 (4) . 367-379.
6. Hao, J.Q.Feng,.J R.Zhou, I.G. etal. Study on the mechanism of resistivity changes during rock cracking. CHINESE JOURNAL OF GEOPHYSICS, 2002,45(3). 426-435.
7. Xu., S.Z. The Finite Element Method in Geophysics. Beijing: Science Press, 1994.
8. Wu., X.P.Xu.,g.m.Li.,S.C.T he calculation of three-dimensional geoelectric field of point source[J]. CHINESE JOURNAL OF GEOPHYSICS, 1998,41(6). 848-855.
9. Lei., G.Y. Preconditioned technique and PCG algorithm. Advances in Mathematics,1992,21(2). 129-139.
10. Jeanne, T.Anatja,S.,etal. Numerical modelling of direct current electrical resistivity for the characterisation of cracks in soils. Journal of Applied Geophysics 62 (2007) . 313–323.
11. Samouëlian, A., Richard, G., Cousin, I., Guérin, R., Bruand, A., Tabbagh, A. Three-dimensional crack monitoring by electrical resistivity measurement. European Journal of Soil Science, 2004, 55. 751–762.
12. Samouëlian, A..Cousin, I..Richard, G. Tabbagh, A., Bruand, A., Electrical resistivity imaging for detecting soil cracking at the centimetric scale. Soil Science Society of America Journal, 2003,67(5).1319–1326.
13. Ruan, B.Y., Yutanka,M. urakami. Xu, S.Z. 2-Dinversion programs of induced polarization data.Computing technique for geophysical and geochemical exploration,1999,21(2). 116-125.

RaSiM 7(2009): Controlling Seismic Hazard and Sustainable Development of Deep Mines, C.A. Tang(ed), Rinton Press, 307-312

RESEARCH ON THE EVALUATION OF RELIEVE-SHOT EFFECT BY MICROSEISM

CAI-PING LU and LIN-MING DOU

State Key Laboratory of Coal Resources and Mine Safety, China University of Mining and Technology

Xuzhou Jiangsu, China

HUI-MIN LI

Chongqing Vocational Institute of Engineering

Chongqing, China

By weakening the strength of coal and rock materials, relieve-shot can reduce the rockburst proneness. The accurate assessment of the effect has an important significance for guiding rockburst prevention. Using the TDS-6 microseismic (MS) collection system, MS activities during the process of deformation, fracture and failure of the compound coal-rock samples retrieved from Sanhejian Coal Mine are measured. The results show the negative correlation between the intensity of the specimen deformation and failure, as well as micro-cracks scale and main frequency of MS signals. With the increase in load, micro-fissures continue to expand, grow and converge accompanied with energy release, low-frequency signals gradually increase along with high-frequency components. By field MS monitoring, relieve-shot signals show the wider frequency band, the main frequency distribution in 0-300Hz, and a multi-peak feature. The low-frequency signals reveal the failure scale of macro-crack in coal and rock materials. The lower the main frequency is, the better the effect of relieve-shot is. When roof fracture is induced by relieve-shot, the main frequency distribution is 0-100Hz, showing that the macro-fissures and main fractures are formed in coal and rock materials, the accumulated elastic energy is released, and the extent of stress concentration is reduced greatly. Therefore, by analyzing the frequency spectrum characteristic parameters of MS signals around the relieve-shot and damaged roof, the relieve-shot effect can be evaluated accurately.

1 Introduction

Deep-hole control relieve-shot of coal and rock materials is one of the most direct and effective means to prevent rockburst. Effective tests of relieve-shot have an important significance for guiding dynamic rockburst prevention. However, the implementation of relieve-shot on site lacks the guidance of theoretical laws and the key parameters are determined on the basis of experience. Unreasonable blasting parameters may lead to an unsatisfactory result causing a resonance effect of explosion waves throughout the coal and rock materials inducing rockburst. An example of such an instance occurred at 23:22 on November 3, 2001 when a relieve-shot caused a serious rockburst on the downward bottom of a 3407 (1) working face in Huafeng Coal Mine. The rockburst invoked the roadway section to shrink up to 50%-90%, a 20m section of roadway was completely destroyed, there was severe deformation, transportation equipment in the headentry was displaced, a worker was killed, and many were injured in the tragedy [1].

At the present, some domestic scholars have conducted research on the evaluation of the relieve-shot effect. For example, DOU Linming et al. [2,3] proposed a test of the relieve-shot effect using the characteristic parameters change law of electromagnetic emission (EME), before and after blasting. QI Qingxin et al. [4] tested the relief effect of deep-hole blasting for rockburst prevention by monitoring stress change. From related-literature retrieval, researchers focus mainly on the blast-induced vibration wave propagation and attenuation laws in different medium; as well as the evaluation of the safety of surface structures. For example, Ak. Hakan

[5] discovered that 98% of the frequency values of blasting signals were between 4-40 Hz, and established the relation curve between the peak particle velocity (PPV) and frequency spectrum. Mostafa [6] proposed an artificial neural network for the prediction and control of blasting vibrations in thr Assiut (Egypt) limestone quarry. Karel. Holub [7] discovered that nearby PPV stations and main frequency can reveal the mechanic parameters of coal and rock materials, and are the best criterion to assess vibration damage to surface structures. Y.K. Wu [8] realized that main frequency of blast-induced vibration wave can be used to assess the stability and safety of structures. Cengiz Kuzu [9] studied the blast-induced vibration wave attenuation law in relation to the charge and the propagation distance. Manoj. Khandelwal [10] proposed a new neural network for the prediction of ground vibration and frequency through consideration of all possible influencing parameters of rock mass, explosive characteristics and blast design. TIAN Yunsheng [11] discussed the frequency spectrum characteristics of blast-induced vibration wave from foundation pit excavation, and revealed that the frequency change rule in relation to blasting distance, charge volume, blasting method and elevation. ZHANG Qingsong [12] discovered that blast-induced micro-fissure can restrain high frequency vibration wave, frequencies distributed mainly in the low frequency band (20-95Hz).

As a consequence of the above, the propagation and attenuation laws of blast-induced vibration waves in different mechanical properties medium have been studied in greater detail. Especially, in respect to the correlation between PPV and main frequency spectrum of MS signals has been discussed extensively, which establishes the foundation on evaluation of the stability and safety of surface buildings induced by blasting. However, the studies on the evaluation of the relieve-shot effect with MS characteristic parameters evolution law are rarely reported, yet there need for further study in depth.

2 Mechanism of deep-hole control blasting

According to the explosion dynamics and elastic kinetic theory, the shock wave disseminated from blasting hole acts on the hole wall, under impulsive dynamic load, the hole wall and the surrounding coal and rock medium are caused excessive grinding, and form crush compression ring. On the border of the crush ring, the shock wave attenuates to become stress wave, and propagates to the surrounding medium in the form of elastic wave. Although its intensity is below the limit of medium compressive strength, but tangential tensile stress generated by the stress wave may still be higher than the tensile strength of medium, and break medium to form the radial fissures linked with crush area. With continuous propagation of stress wave, its intensity gradually attenuates. Blast-induced gas generates quasi-static stress field after stress wave completely attenuates, wedges the open fissures on the blasting hole wall, generates stress concentration on crack tip, with further expansion of cracks, then forms intersectional fissures net around blasting holes.

Because propagation velocity of the stress wave is much larger than expansion velocity of the cracks, when the peak intensity of the stress wave attenuates to be below the medium intensity, cracks formed will continue to expand. When stress wave propagates to the control hole wall, immediately generates stress wave reflection. The superposition of reflection tensile wave and stress field of the radial fissures tip prompt the radial and circumferential fissures to further expand and greatly increase fracture area.

As coal and rock medium inhomogeneity, cracks cannot expand along the direction of the initial force and derive *S* wave, that is, the blast-induced *S* wave is secondary wave. Because blasting directly generates *P* wave, the four quadrants of *P*-wave first motion distribution are positive direction. Another the direct action of blast-induced gas causes strong vibration of coal and rock materials, the waveform and amplitude as well as the attenuation rate depend primarily on the volume charge, the general attenuation time is longer. Therefore, the MS waveform of relieve-shot is divided into two parts, respectively vibration wave generated by blast-induced gas and vibration wave evoked of coal-rock medium.

As a consequence of the above, the deep-hole control blasting can generate a columnar crush compression ring and impenetrate crack surface along the line of centres direction of the blasting and control holes in the medium. The impenetrate crack surface is the key point to weaken the coal and rock materials strength by deep-hole control blasting.

3 Correlation between coal-rock crack scale and MS frequency spectrum

Studies [13] show the correlation between MS main frequency and crack intensity of coal and rock materials as well as the scale effect. So, the research on MS signal spectrum evolution rules in the process of coal and rock deformation and fracture can reveal blast-induced fissures generation, expansion intensity and scale, in order to evaluate relieve-shot effect.

3.1 Samples process

Coal and rock samples are collected from 9202 working face in Sanhejian Coal Mine. In accordance with coal industry standards, coal and rock samples are processed into the specimen 50mm in diameter, and sawn into cylinder about 20, 30, 35, 70mm in height, at last, both ends are grinded smoothly. According to different height ratio and combining type, the compound specimens are glued into standard samples (Φ50mm×100mm).

3.2 Test system

Load device is *SANS* material testing machine which can control the loading speed precisely, used to measure the stress-strain complete curve in the process of coal and rock samples loading (as in figure 1). Experiments are conducted by cyclic loading type, the first loading speed is 0.5kN/s until load reaches 70% of sample compressive strength value, and then starts to unload until the ultimate load is about 0.5kN, finally begins to load again until impact failure.

MS signals are collected with TDS-6 system developed by China University of Mining and Technology and State Seismological Bureau, the system is composed by six sub-stations and a central station.

3.3 System parameters

MS system chooses all band (1-100Hz), respectively set STA/LTA=1.2, scan time is 1s. The maximum voltage value is 5000mV. Record way uses trigger, when substation collection data is bigger than the trigger threshold value set, MS event will be recorded from 10s before the event beginning until 30s after the event end.

Figure 1 Real photo of press machine and MS collection station

3.4 Test results and analysis

Figure 2 is amplitude-time curves of MS signals recorded in the process of deformation, fracture and impact failure of compound coal-rock samples. Space lacks for a detailed description of all samples. So a substation collection result of part samples is given in this paper.

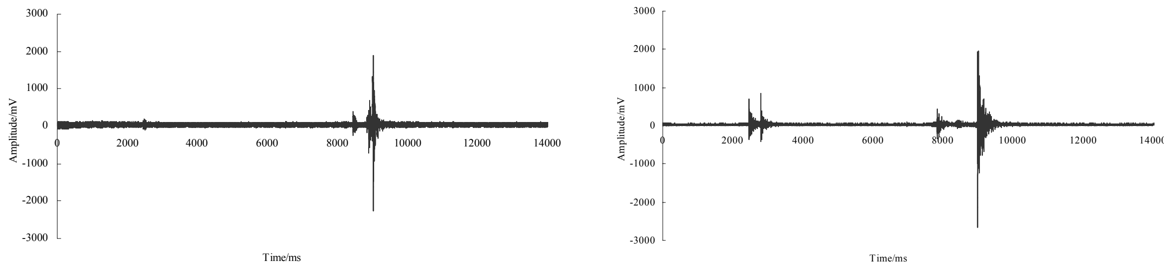

(a) Amplitude-time curve of No.1 substation (RC4 sample)   (b) Amplitude-time curve of No.1 substation (RC5 sample)

Figure 2 Amplitude-time curves of MS signals

The original signals are denoised with band elimination filter, by time-frequency analysis, the frequency spectrum distribution of MS precursory and main shock signals are obtained. Figure 3, 4 are respectively the frequency spectrum distribution curves of RC4 and RC5 samples.

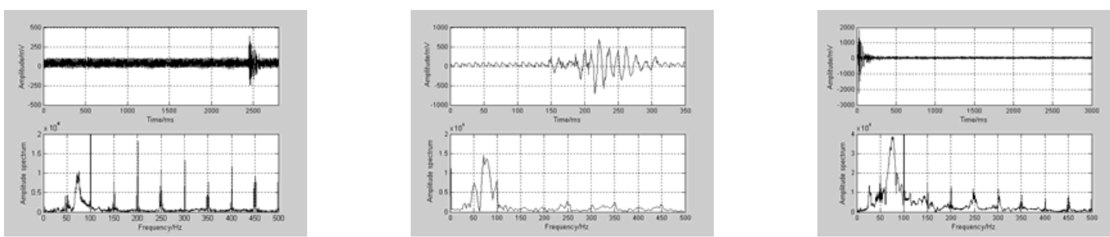

(a) Spectrum of No.1 precursory signal   (b) Spectrum of No.2 precursory signal   (c) Spectrum of main shock signal

Figure 3 Frequency spectrum distribution of RC4 sample

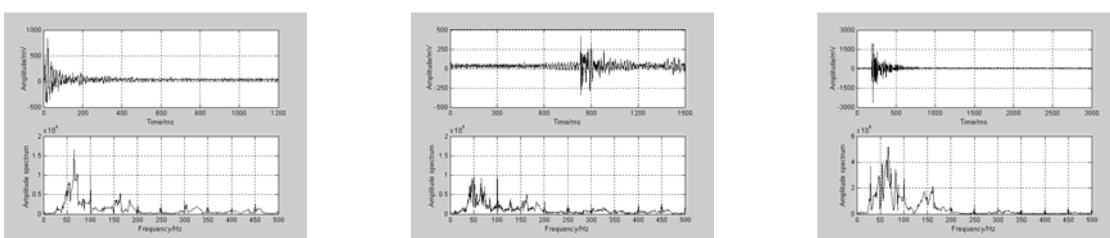

(a) Spectrum of No.1 precursory signal   (b) Spectrum of No.2 precursory signal   (c) Spectrum of main shock signal

Figure 4 Frequency spectrum distribution of RC5 sample

From above figures, there are the obvious precursory signal series before compound samples impact failure. According to frequency spectrum distribution, the main frequency of precursory signals begins to move to low frequency band with rise in intensity of deformation and fracture. Obviously the low frequency signals (<50Hz) gradually increase. When impact failure, the signals show the broadband character, main frequency distributes in 0-250Hz, but the low frequency signals (<50Hz) components increase, the center frequency moves to the low frequency band. Among the high frequency signals are mainly generated by microcracks expansion. According to the interval time of precursory and main shock signals, as load increase, the main frequency gradually moves to the low frequency band in the process of microcracks growth, expansion and convergence. For relieve-shot, when MS signals main frequency gradually reduces and the low frequency components increase, which show that lots of macrofissures have been internally generated, relieve-shots obtain remarkable results.

4 Field monitoring and evaluation of relieve-shot effect

7206 working face locates Sanhejian Coal Mine west wing belonged to typical deep high-stress concentration region. Coal seam No.7 identified is strong rockburst tendency. Rockbursts had happened in 7206 working face when drilling headentry. For example, on October 16, 2008, six blasting holes were prepared in headentry face, the explosive charge was 15Kg, detonation occurred on 10:54, roof fracture was induced respectively at 17 and 30 minutes after relieve-shot, which caused about 4-5t coal to eject at both sides about 1.0m deep, the farthest ejection distance was about 10m. In order to evaluate the relieve-shot effect effectively, and provide reasonable key parameters, MS monitoring system was used for evaluation.

4.1 Introduction of MS monitoring system

The present MS monitoring system of Sanhejian Coal Mine is renovated and expanded based on the original 4 single-component substations. Existing system has 12 three-component substations, of which 10 substations arrange at -500m,-700m,-800m,-900m main levels underground. Other 2 substations are located respectively in two surface boreholes to avoid the mining influence and reduce data error. The horizontal spacing of substations is about 3km. Recording way uses event-triggered. Absolute time error of GPS clock is less than 1ms. The system begins to operate in August 2008, the initial operation shows that the three-dimensional positioning error is less than 50m.

4.2 MS monitoring results and analysis of relieve-shot

Table 1 is the relieve-shots and roof actions induced statistical result in 7206 working face headentry during the time of November 11, 2008 to November 13, 2008.

Table 1 Statistical result of relieve-shots and roof actions induced

Blasting time	Number of blasting hole	Explosive charge	Number of roof action	Destructive condition
10: 50(11)	6	12Kg	1	Nude roof 1-1.2m on face
10: 45(12)	6	12Kg	1	Nude roof 0.8-1m on face
10: 22(13)	5	12Kg	1	Nude roof 0.8-1m on face

Figure 5 is MS waveform and frequency spectrum distribution of roof action induced by relieve-shot.

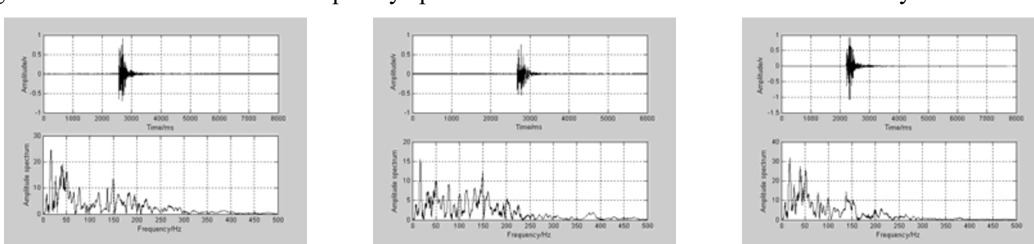

(a) Nov 11, 2008 (b) Nov 12, 2008 (c) Nov 13, 2008

Figure 5 MS waveform and frequency spectrum distribution of roof action

According to MS frequency spectrum distribution of roof action, the wider frequency band, the frequency spectrum distribution in 0-300Hz and a multi-peak feature are known. 0-100Hz low frequency signals are the predominant components, which reveal the failure scale of macrocracks induced in coal and rock materials. The lower the main frequency is, the better the relieve-shot effect is.

5 Conclusions and Future Work

In this paper we have analyzed the negative correlation between the main frequency of MS signals and crack intensity of coal and rock materials, as well as the scale effect through experimentation. Specifically, field MS monitoring results show that the lower the main frequency is, the better the effect of relieve-shot is. The main focus is the monitoring and evaluation of the relieve-shot effect.

Indeed, the insights into this work can potentially promote a greater precision of the relieve-shot effect. We believe that it is important to control dynamically rockburst intensity on the basis of reasonable blasting parameters. Rather, we need to be able to reveal the relation between the MS main frequency distribution and key blasting parameters.

Considerable work still remains in this area, both in terms of diagnosing and analyzing the blast-induced MS signals and in the more detailed exploration of the relationship between main frequency distribution and key blasting parameters based on laboratory experiments and field tests.

Acknowledgements

The authors wish to acknowledge the collaborative funding support from the National Key Project of Scientific and Technical Supporting Programs (2006BAK04B02, 2006BAK03B06). In particular we wish to thank WU Xingrong, GONG Siyuan, CAO Anye, HE Hu, CHEN Ligao, and HE Gang for their contributions to this research project.

References

1. Li, X.Y. Zhang, X.F. Accident cause analysis and prevention measures of typical deep mine heavy pressure bump. Coal Science and Technology , 2003, 31(2). 15-17.
2. Dou, L.M. He, Y. Zhang, W.D. Hazards of rock burst in coal face and its control. Chinese Journal of Rock Mechanics and Engineering, 2003, 22(11). 1866-1869.
3. Lu, C.P. Dou, L.M., Wu, C.G. et al. Electromagnetic emission testing method for the effect of relieve-shot based on energy mechanism. Chinese Journal of Rock Mechanics and Engineering, 2005, 24(6). 1014-1017.
4. Qi., Q.G. Lei, Y. Li, H.Y et al. Theory and application of prevention of rock burst by break-tip blast in deep hole. Chinese Journal of Rock Mechanics and Engineering, 2007, 26(Supp.1). 3522-3527.
5. Hakan, A.Melih Iphar, Mahmut Y., et al. Evaluation of ground vibration effect of blasting operations in a magnesite mine. Soil Dynamics and Earthquake Engineering, 2009, 29. 669-676.
6. Mostafa, Tantawy, Mohamed. Artificial neural network for prediction and control of blasting vibrations in Assiut (Egypt) limestone quarry. International Journal of Rock Mechanics & Mining Sciences, 2009, 46. 426-431.
7. Karel Holub, Vladimír Petroš. Some parameters of rockbursts derived from underground seismological measurements. Tectonophysics, 2008, 456. 67-73.
8. Wu, Y.K. Hao, H. Zhou, Y.X. Propagation characteristics of blast-induced shock waves in a jointed rock mass. Soil Dynamics and Earthquake Engineering, 1998, 17. 407-412.
9. Cengiz Kuzu. The importance of site-specific characters in prediction models for blast-induced ground vibrations. Soil Dynamics and Earthquake Engineering, 2008, 28. 405-414.
10. Manoj Khandelwal, T.N. Singh. Prediction of blast induced ground vibrations and frequency in opencast mine: A neural network approach. Journal of Sound and Vibration, 2006, 289.711-725.
11. Tian, Y.S. Li, Z.J. Wang, X.G. et al. Spectra characteristics of blasting vibration wave from foundation pit excavation. Blasting, 2005, 22(4). 29-31, 50.
12. ZHANG Qingsong, LI Liping, LI Shucai, et al. Experimental study of blasting dynamic vibration of closely adjacent tunnels. Rock and Soil Mechanics, 2008, 29(10). 2655-2660.
13. LU Caiping, DOU Linming, WU Xingrong, et al. Experimental and empirical research on frequency-spectrum evolvement rule of rockburst omen microseismic signals of coal-rock. Chinese Journal of Rock Mechanics and Engineering, 2008, 27(3).519-525.

RaSiM 7(2009): Controlling Seismic Hazard and
Sustainable Development of Deep Mines,
C.A. Tang(ed), Rinton Press, 313-318

THE MECHANISM OF ROCKBURST AND THE CONTROL COUNTERMEASURE IN DEEP-WELL TOUGH ROCK

YAO CHENG, YONG-LI ZHANG and YU-LIN MA

College of Mechanics and Engineering, Liaoning Technical University

Fuxin, 123000, P.R.. China

Rockburst is a kind of dynamic buckling geologic disaster. The elastic strain energy, which is stored in the rock, is released suddenly while mining hard brittle rock under high stress. Rockburst results in relaxation, exfoliation, and ejection. It threatens the safety of the crew and equipment and often occurs in metal mines, but also arises in coal mining. Presently, domestic and foreign experts are researching technology for the forecasting and control of rockburst. Though mechanisms of rockburst have been understood to a certain extent and preventive measures are adopted in practice, the problems of rockburst are not solved radically. Based on the geological conditions of the Dataijing coal pit in the Muchengjian coal mine of Beijing, calculations of stress distribution on the wall rock by the cusp model of catastrophe theory have been performed with research on the mechanism of rockburst in the Dataijing coal pit. Several countermeasures have been put forth to prevent rockburst: reasonable set up out of the tunnel, change of physical and mechanical properties, and stress conditions of wall rock, and improvement of explosion and supporting characteristics. It is a simple and effective measure that advance boreholes can release parts of the stress to prevent the rockburst.

1 Introduction

Rockburst is a type of dynamic buckling geologic disaster. It threatens the safety of the crew and equipment impacting the progress of work. It is one of the most difficult engineering problems often occuring in metal mines. It also arises in colliery drivage. Presently, domestic and foreign experts are researching the technology of forecasting and control on rockburst. Though mechanisms of rockburst have been known to a certain extent and preventive measures have been adopted in practice, the problems of rockburst are not solved radically. It is imperative to solve them in the worldwide mining community.

Mainly research of the Dataijing coal pit which is in Muchengjian coal mine of Beijing Haohua energy resource Co, LTD. pertained to its biggest roadway which was used for centralized transportation and was composed of hard rock. Rockburst occurred when coal was mined in -210m, -310m and -410m levels of the roadway and was increasing drastic with the increase in depth. Several casualty accidents occurred and it impacted drivage and seriously imperilled lives. Based on the classification of rockburst designed by Guo Zhi[1], Tan Yi'an[2], et al, the rockburst which happened above -210m is weak (Class Ⅰ); it is occurred moderately between -210m and -410m (Class Ⅱ); and occurred intensely below -410m (ClassⅢ).

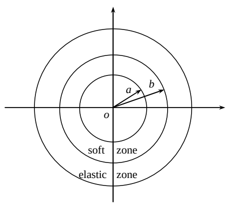

Figure 1 A analytical model of circular tunnel

2 The calculation of stress multi-layered distribution on wall rock

Dig up a circular tunnel with a radius of a when ground stress is p. As the ground stress is small, the whole wall rock is in the elastic state. In the incompressibility condition, radial displacement is u, strain components are ε_r and ε_θ, stress components are σ_r, σ_θ and σ_z, equivalent strain is $\bar{\varepsilon}$, equivalent stress is $\bar{\sigma}$ and ultimate load is p_e in elastic range by elastic theory.

When $p > p_e$, the radius of soft zone is b. The stress-strain curves are two parts that are soft zone and elastic zone. The relation between stress and strain is

$$\sigma = \begin{cases} E\varepsilon & (\varepsilon \le \varepsilon_c) \\ E\varepsilon \exp\left(1 - \dfrac{\varepsilon}{\varepsilon_c}\right) & (\varepsilon > \varepsilon_c) \end{cases}, \tag{2.1}$$

where ε_c is strain respond to peak strength σ_c.

In 3-D, substitution of $\bar{\sigma}$ and $\bar{\varepsilon}$ in the stress and strain of above formula respectively give new formula.

In the soft zone, by the incompressibility condition and geometric equation, we find dislocation $u = \dfrac{u_0 a}{r}$, strain components $\varepsilon_r = -\dfrac{u_0 a}{r^2}$ and $\varepsilon_\theta = \dfrac{u_0 a}{r^2}$, equivalent strain $\bar{\varepsilon} = \dfrac{2u_0 a}{\sqrt{3} r^2}$ and equivalent stress

$$\bar{\sigma} = \frac{\sqrt{3}}{2}(\sigma_\theta - \sigma_r) = E\frac{2u_0 a}{\sqrt{3} r^2}\exp\left(1 - \frac{2u_0 a}{\sqrt{3}\varepsilon_c r^2}\right), \tag{2.2}$$

where u_0 is dislocation in the rim of cave, $\bar{\varepsilon}(b) = \dfrac{2u_0 a}{\sqrt{3} b^2} = \varepsilon_c$ and $\bar{\sigma}(b) = E\varepsilon_c = \sigma_c$.

By taking $\bar{\sigma}$ in the balanced equation and boundary condition $\sigma_r(a) = 0$, yield σ_r and σ_θ.

$r = b$ is the common boundary between soft zone and elastic zone. The radial stress is

$$q = \sigma_r(b) = \frac{\sigma_c}{\sqrt{3}}\left[1 - \exp\left(1 - \frac{2u_0}{\sqrt{3}\varepsilon_c a}\right)\right]. \tag{2.3}$$

The circumference stress is

$$\sigma_\theta(b) = \frac{\sigma_c}{\sqrt{3}}\left[3 - \exp\left(1 - \frac{2u_0}{\sqrt{3}\varepsilon_c a}\right)\right]. \tag{2.4}$$

In the soft zone, $r \ge b$. Elastic theory yields other components.

In the common boundary between soft zone and elastic zone, $\bar{\sigma}(b)=\sigma_c$, so $q=p-\frac{\sigma_c}{\sqrt{3}}$. By dislocation continuity condition, $b^2=\frac{2Eu_0a}{3(p-q)}=\frac{2Eu_0a}{\sqrt{3}\sigma_c}$. Let $\zeta=\frac{b^2}{a^2}$. By $\bar{\varepsilon}(b)=\varepsilon_c$ and radial stress continuity condition, $\zeta=1-\ln\left(2-\frac{\sqrt{3}p}{\sigma_c}\right)$.

3 cusp catastrophe theory of rockburst

In the elastic zone, Deformation energy Π^e is

$$\Pi^e=2\pi\int_b^R\frac{1}{2}(\sigma_r\varepsilon_r+\sigma_\theta\varepsilon_\theta)r\mathrm{d}r=\frac{2\pi E}{3\zeta}u_0^2 \qquad (3.1)$$

In the soft, zone deformation energy Π^s is

$$\Pi^s=2\pi\int_a^b\left(\int_{\varepsilon_c}^{\varepsilon_i}\bar{\sigma}\mathrm{d}\bar{\varepsilon}\right)rdr=\pi\sigma_c\varepsilon_ca^2\left[2\zeta-2-\zeta\exp\left(1-\frac{2u_0}{\sqrt{3}\varepsilon_ca\zeta}\right)+\exp\left(1-\frac{2u_0}{\sqrt{3}\varepsilon_ca}\right)\right] \qquad (3.2).$$

Then total energy of position in the wall-rock deformation system is

$$\begin{aligned}\Pi&=\Pi^e+\Pi^s\\&=\pi e\sigma_c\varepsilon_ca^2\left[\frac{2u_0^2}{3\varepsilon_c^2a^2e\zeta}+\frac{2\zeta-2}{e}-\zeta\exp\left(-\frac{2u_0}{\sqrt{3}\varepsilon_ca\zeta}\right)+\exp\left(-\frac{2u_0}{\sqrt{3}\varepsilon_ca}\right)\right]\end{aligned} \qquad (3.3)$$

Based on cusp catastrophe theory[3，4，5], equation of equilibrium state is $\frac{\mathrm{d}\Pi}{\mathrm{d}u_0}=0$,

Thus, cusp $u_g=\sqrt{3}\varepsilon_ca\frac{\zeta\ln\zeta}{\zeta-1}$ by $\frac{\mathrm{d}^3\Pi}{\mathrm{d}u_0^3}=0$. Stiffness is $K^e=\frac{\mathrm{d}^2\Pi^e}{\mathrm{d}u_0^2}=\frac{4\pi E}{3\zeta}$ in the elastic zone.

It is $K_g^s=\frac{\mathrm{d}^2\Pi^s}{\mathrm{d}u_0^2}=-\frac{4\pi eE(\zeta-1)}{3\zeta}\zeta^{-\frac{\zeta+1}{\zeta-1}}<0$ in the soft zone. So stiffness ratio is defined by

$$K=\frac{K^e}{\left|K_g^s\right|}=\frac{\zeta^{\frac{\zeta+1}{\zeta-1}}}{e(\zeta-1)}. \qquad (3.4)$$

The equation of equilibrium state is expressed at the cusp and neglect higher order term, then equilibrium hood face M is $4x^3+2ux+v=0$, where $x=\frac{u_0-u_g}{u_g}$, $u=\frac{3(\zeta-1)^2(K-1)}{\zeta\ln^2\zeta}$ and $v=\frac{3(\zeta-1)^2(2K\ln\zeta+\zeta^2-1)}{\zeta^2\ln^3\zeta}$.

Singularity set S is $\begin{cases} 4x^3 + 2ux + v = 0 \\ 6x^2 + u = 0 \end{cases}$. When only $u \le 0$, the equation of equilibrium state is so unsteady that rockburst happens. $u \le 0$, then $K \le 1$ which is the necessary condition of rockburst. When $\zeta > 5.2$, $K < 1$ and $\frac{b}{a} > 2.28$.

Branching point set B is $8u^3 + 27v^2 = 0$,

i.e.

$$8\zeta(\zeta - 1)^2 (K - 1)^3 + 9(2K \ln\zeta + \zeta^2 - 1)^2 = 0. \qquad (3.5)$$

We have $\zeta = 5.5$, and hence depth of critical soft zone is $b^* = 2.35a$.

When ground stress is smaller, surrounding radial dispersion u_0 is smaller in the tunnel and $u_0 < u_g$. The wall-rock equilibrium state is below equilibrium hood face. x moves upward along equilibrium hood face with the ground stress increasing. u_0 increases with the ground stress. When x is at the crease of hood face, wall rock is critical equilibrium state. If it is disturbed, u_0 increases more. When x is at the middle of equilibrium hood face, wall rock is unsteady equilibrium state. Because this state is not exist, x jumps at the equilibrium point of top of corresponding hood face. Now wall rock is equilibrium state again.

The smooth crease equation is $6x^2 + u = 0$, then $x = \pm\sqrt{-\frac{u}{6}}$

i.e. displacement of convergence is

$$u_F = u_g\left[1 - \sqrt{-\frac{u}{6}}\right] = \sqrt{3}\varepsilon_c a\left[\frac{\zeta \ln\zeta}{\zeta - 1} - \sqrt{\frac{\zeta(1-K)}{2}}\right] \qquad (3.6)$$

in corresponding surrounding tunnel of critical equilibrium point F.

The displacement of convergence is

$$u_H = u_g\left[1 + \sqrt{-\frac{u}{6}}\right] = \sqrt{3}\varepsilon_c a\left[\frac{\zeta \ln\zeta}{\zeta - 1} + \sqrt{\frac{\zeta(1-K)}{2}}\right] \qquad (3.7)$$

in corresponding surrounding tunnel of new equilibrium point F after kick.

After rockburst, the value of kick is

$$\Delta u = 2u_g\sqrt{-\frac{u}{6}} = \varepsilon_c a\sqrt{6\zeta(1-K)} \qquad (3.8)$$

The potential energy is $\Pi(u_F)$ at F. It is $\Pi(u_H)$ at H.

The energy which is released in per unit length after rockburst is

$\Delta\Pi = \Pi(u_H) - \Pi(u_F)$

$$= 2\pi\sigma_c\varepsilon_c a^2\left[\frac{4\ln\zeta}{\zeta-1}\sqrt{\frac{\zeta(1-K)}{2}} + e\zeta^{\frac{\zeta-3}{\zeta-1}}\sinh\sqrt{\frac{2(1-K)}{\zeta}} + e\zeta^{-\frac{2\zeta}{\zeta-1}}\sinh\sqrt{2\zeta(1-K)}\right]. \quad (3.9)$$

Basal area of rock gangway is $S = 12.6m^2$ in Dataijing. Hence the radius of circular tunnel is $a = 2m$. Mechanical parameters of rock are compression strength $\sigma_c = 128.7MPa$ and Young's modulus $E = 22.5GPa$. Then $\zeta = 5.5$, ratio of rigidity is $K = 0.96$, depth of critical soft zone is $b^* = 4.7m$, displacement of convergence is $u_F = 0.035m$ before rockburst, displacement of convergence is $u_H = 0.048m$ after rockburst, value of kick of displacement of convergence is $\Delta u = 0.013m$ and energy which is released in per unit length when rockburst is $\Pi = 2.58\times10^7 J$. Because they are influenced by many factors, they are more than computational values.

The type calculates is $\zeta = 5.5$, The ratio of rigidity is $K = 0.96$, The Critical softened zone depth is $b^* = 4.7m$. Before the rock outburst has, the tunnel restraining displacement is $u_F = 0.035m$,After the rockburst occurs, the tunnel restraining displacement is $u_H = 0.048m$, The restraining displacement kicking value is $\Delta u = 0.013m$, Each meter long tunnel rockburst emit energy is $\Pi = 2.58\times10^7 J$. Because actual situation many kinds of factor influences, possibly compared to predicted value big somewhat.

4 The prevention countermeasures of rockburst

The rocks of rockburst are hard, high intensity and big elastic modulus which are the common characters. The increase of deep underground pressure is the internal factor by which the rockburst can occur. The secondary factors are deep inclined coal seam, special geological structure, high level of stress and tectonic stress involved in. In view of the actual conditions, choose the proper prevention countermeasures. According to the conditions of Dataijing coal pit, the prevention countermeasures are following.

4.1. Tunnel's reasonable arrangement

To security angle's advantage, tunnel's direction should be the same as the direction of maximum principal stress of ground stresses to avoid the effect of supporting pressure. Arrangement should be in the fine rock layer. Because the roadway of Dataijing coal pit has been formed, the directions of transport tunnels are not changed. For minimizing rock-door project and avoiding harmful effects of the pressure of fixed supporting, it avails to the maintenance of transport roadway and reduce the impact of rockburst on the transport tunnels.

According to theoretical analysis, the shape of cross-section of roadway effects on the stress redistribution of wall rock. Choose the appropriate shape of cross section. A circular cross-section is better. However, combined with Dataijing coal pit, vault connects with wall as far as possible smoothly for the multicenter arch. It can reduce the degree of stress concentration. Determine specifications and quality standards of roadway. According to the requirements of light burst, additional digging is not more than 150mm, allowable deviation of clear width is -50 ~ 200m, clear height is -30 ~ 300mm, the rate of eye marks is not less than 60% and there are no obvious cracks.

4.2. Improving the process of blasting

Blasting may impact on rockburst. Adopt rilling and blasting method on the rockbust area. And take the short driving footage. Reduce the amount of drugs to control the effect of light burst. Thereby reduce the phenomenon of stress concentration. Class Ⅰ and Ⅱ rockburst areas use a full-face excavation method in order to reduce disturbance of the surrounding rock as far as possible. Intense rockburst zones have recourse to the method of excavation division in order to reduce the extent of the damage. In the course of construction, it should minimize the possibility of rockburst by the blasting vibration. Ahead of drilling, release stress, loosen blasting or shock blasting to reduce the stress of rock mass. Energy is released before excavating.

4.3. The support technology

It should spurt cold water with pressure on the possible locations. The method may reduce the intensity of the surface layer of wall rock and soften it. It's able to release the elastic energy in the stress concentration area. Water permeates the internal of rock. It reduces the strength and elastic modulus of rock and improves the capacity of plastic deformation of rock. It slows down rockburst. Spurting water should be between blasting and removed. It should advance with uniform speed and there is no blind spot.

In addition, temporary protection facilities should be used. It should hang wire netting on the wall near rockburst site to prevent ejection from wounding and equipment. Grid should be dense enough to prevent ejection.

5 Conclusions

1. By means of the CUSP model of catastrophe theory, the physical process of rockburst occurring on a circular chamber has been studied. It not only describes the instability process of rockburst more deeply, but also obtained the critical depth of the plastic softening area of the chamber that is valuable in the control engineering of rockburst. The chamber displacement jump and energy liberation have been derived. The influence of rock parameters on rockburst has also been discussed.

2. The intrinsic relationship between energy dissipation, energy release and the failure of rock are discussed. Based on energy principles, the mechanism and characteristic of rockburst are pointed out prove that rockburst is a geological disaster which happens in hard brittle rock masses which accumulated lots of energy. The stress state and failure location of rockburst in the surrounding rock of underground excavation are analyzed by integrating the surrounding rock stress distribution of a circular shaped tunnel.

3. Sections of a stress-strain curve of the complete rock failure process are regarded as constitutive relationship, based on which, the state of a circular chamber under hydrostatic pressure is analyzed. The stress zone is divided into the softened area and elastic area. A model established on the basis of theory of catastrophe is discussed by potential function. A criterion for occurrence of rockburst is given and compared with measured data. It has been proven that this theory is effective. Several countermeasures of preventing rockburst are put forth: reasonable lay out of the tunnel, release of the stress of advance on the borehole, changing physical-mechanical properties and stress conditions of the wall rock, reinforcement of the wall rock, changing the deep-hole blasting to shallow blasting, spraying water on the gunite supports and advancing boreholes. These are all simple and effective measures to prevent rockburst.

References

1. Guo, Z. Applied Mechanics of Rock Masses. Beijing Earthquake Publishing House, 1996, 190-200.
2. Tan, Y.A. Types and Treatments of Rockbust. Geoscience, 1991, 5(4). 450-456.
3. Fei, H.L., Xu, X.H. and Tang, C.A. Research on Theory of Catastrophe of Rockburst in Underground Chamber. Journal of China Coal Society, 1995, 20(1). 29-33.
4. Shan, X.Y. et al. The Possibility of Forecasting the Rockburst by Catastrophe Theory. Mine Surveying, 2000, (4). 36-37.
5. Pan, Y.S., Zhang M.T. and Li, G.Z. The Study of Chamber Rockburst by the CUSP Model of Catastrophe Theory. Applied Mathematics and Mechanics, 1994, 15(10). 893-900.

RaSiM 7(2009): Controlling Seismic Hazard and Sustainable Development of Deep Mines, C.A. Tang(ed), Rinton Press, 319-326

SEISMIC MAGNITUDE-FREQUENCY RELATION: A MAXIMUM ENTROPY APPROACH

JIAN DENG, HUAI-SHENG PENG and DE-SHENG GU

School of Resources and Safety Engineering, Central South University, Changsha 410083,China

Statistical approach provides a reasonable basis for seismic hazard assessment in specific tectonic regions (e.g. metal mines) as well as for the earth as a whole. The Gutenberg-Richter (G-R) law has been widely used to describe the seismic magnitude-frequency relationship. However, a number of studies show that the G-R relationship does not satisfactorily hold for seismicity in the high-magnitude range. Furthermore, the nonlinearity of the magnitude-frequency relationship can appear for very small events. In this paper, a new seismic magnitude-frequency relation is derived from the concept of entropy and the principle of maximum entropy, by considering the first and second order moment of magnitude.The proposed framework covers the well known G-R formula as a special case, and provides a reasonable theoretical explanation of it. Furthermore, given the mean and variance of earthquake occurrence, the maximum entropy principle generates a new seismic magnitude-frequency relation, which agrees with observed data remarkably well.

1 Introduction

Statistical approach to the analysis of seismic events on earth or in metal mines provides a reasonable basis for seismic hazard assessment. The problem of developing stochastic models for earthquake occurrence has been raising strong interest among seismologists and mining engineers [1]. The Gutenberg–Richter (G-R) law expresses the relationship between the magnitude and total number of earthquakes in any given region and time period [2].

$$\log N = a - bM \tag{1}$$

Where N denotes the number of the earthquakes with magnitudes greater than or equal to M, and *a* and *b* are parameters describing regional seismicity. However, a number of studies report that the G-R relationship does not satisfactorily hold for seismicity in some magnitude ranges, and the nonlinear magnitude frequency equation was proposed [3]. If the magnitudes of seismic events are assumed to be independent, identically distributed random variables, the probability density function is subjected to exponential distributions [1], as can be seen by reformulation of Eq.(1). The frequency of extreme earthquake events can be characterized by the Generalized Pareto Distribution [4]. However, in certain cases, deviations from the Pareto at the very end of the tail may occur, in particular for large samples signalling a novel regime.

An alternative approach to the distribution fitting comes from the modern information theory in which a robust measure of probabilistic information, namely the entropy, has been developed. The principle of maximum entropy has been used with varying degrees of success, in fields such as structure safety [5,6], hydrology[7], seismicity [8,9], probabilistic engineering mechanics [10], etc. However, only the first moment (i.e. the mean value) was considered in the analysis of seismic magnitude frequency relation using the maximum entropy principle. In this paper, the maximum entropy principle was introduced and the maximum entropy distribution was derived on the constraints of moments. A new seismic magnitude-frequency relation is proposed by using the concept of entropy and the principle of maximum entropy. The proposed approach covers the well known G-R formula as a special case, and provides a reasonable theoretical explanation of it.

2 Maximum entropy principle

The modern information theory is a quantitative approach to the notion of information largely based on probability theory and statistics. The maximum entropy (MaxEnt) principle was proposed as a rational approach for choosing a consistent probability distribution, amongst all possible distributions, that contains minimum spurious information. The principle states that the most unbiased estimate of a probability distribution is that which maximizes the entropy subject to constraints supplied by the available information, e.g., moments of a random variable. The distribution so obtained is referred to as the *most unbiased*, because its derivation involves a systematic maximization of uncertainty about the unknown information. Given the moment constraints only, the entropy maximization was proved to be a uniquely correct method of probabilistic inference that satisfies all the consistency axioms. If the random variable is a continuous variable with density function $f(x)$ over the interval [*a*,*b*], Shannon's measure of entropy (uncertainty) of the random variable is given by

$$H[f(x)] = -\int_a^b f(x)\ln f(x)dx \tag{2}$$

The available constraints are presented as

$$\int_a^b f(x)dx = 1 \tag{3}$$

and

$$\int_a^b f(x)g_r(x)dx = a_r\,, \quad (r = 0,1,...,M) \tag{4}$$

where a_r is a sample realization of moments of the function $g_r(x)$, and M is the highest order of moments considered in the analysis. Use of the Euler-Lagrange equation of the calculus of variations gives the maximum entropy distributions as follows

$$f(x) = \exp[-\lambda_0 - \sum_{r=1}^{M}\lambda_r g_r(x)] \tag{5}$$

where $\{\lambda_i\}_{i=0}^{M}$ is the Lagrangian parameters. Eq.(5) is the derived maximum entropy density function. The (*M*+1) Lagrangian parameters $\{\lambda_i\}_{i=0}^{M}$ can be obtained by solving the following set of (*M*+1) nonlinear integral equations

$$\int_a^b g_r(x)\exp[-\lambda_0 - \sum_{i=1}^{M}\lambda_i g_i(x)]dx = a_r \tag{6}$$

And

$$\int_a^b \exp[-\lambda_0 - \sum_{i=1}^{M}\lambda_i g_i(x)]dx = 1 \tag{7}$$

Specifically, provided that moment constraints are given, i.e. $g_r(x) = x^r$, maximum entropy distributions are

$$f(x) = \exp[-\sum_{r=0}^{M}\lambda_r x^r] \tag{8}$$

3 Seismic magnitude-frequency relation

One of the remarkable characteristics from the derived maximum entropy density function in Eq.(5) is that most of the classical theoretical probability distributions can be derived from the maximum entropy principle provided that appropriate moments are specified. Three very well known Entropy distributions are the Uniform, Exponential and Normal Distributions, which correspond, respectively, to special cases of M=0, M=1 and M=2. Seismic magnitude-frequency relation are derived as follows.

3.1 Mean value of magnitude is provided

If the arithmetic mean μ is prescribed, then the maximum entropy problem is to maximize the entropy

$$H[f(x)] = -\int_a^b f(x)\ln f(x)dx \tag{9}$$

Subjected to

$$\int_a^b f(x)dx = 1, \int_a^b xf(x)dx = \mu \tag{10}$$

Solution of Eqs.(9) and (10), the maximum entropy density function is obtained as

$$f(x) = \exp(-\lambda_0 - \lambda_1 x) \tag{11}$$

Where the Lagrangian parameters λ_0 and λ_1 can be expressed as functions of μ, a and b.

Different seismic magnitude ranges considered will lead to the following three cases:

(1)Case 1 for $a = 0, b = m_1$: The seismic magnitude range of x is $[0, m_1]$, the maximum entropy magnitude distribution in Eq.(11) can be described as a truncated exponential distribution

$$f(M) = \frac{\beta e^{-\beta M}}{1 - e^{-\beta m_1}} \tag{12}$$

where β is a parameter, which can be expressed as a function of the magnitude mean value μ, but β is a more useful parameter. Meanwhile, the probability of the magnitude can be estimated by

$$F(M) = \frac{N}{T} \tag{13}$$

where N is the number of the earthquakes with magnitudes greater than or equal to the seismic magnitude M, T is the number of the earthquakes with $M \geq 0$. We obtain

$$\frac{N}{T} = \int_M^{m_1} f(M)dM = \frac{e^{-\beta M} - e^{-\beta m_1}}{1 - e^{-\beta m_1}} \tag{14}$$

Or

$$\log N = \log T + \log(\frac{e^{-\beta M} - e^{-\beta m_1}}{1 - e^{-\beta m_1}}) \tag{15}$$

This is the seismic magnitude frequency relation based on truncated exponential distribution derived from maximum entropy principle. This relation was demonstrated to agree with observed data both at small and large magnitudes. The parameters β and T can be obtained from the parameters a and b in Eq.(1) [8].

$$\beta = 2.3b(1 - e^{-\beta m_1}) \approx 2.3b \quad (16)$$

And

$$T = 10^a \quad (17)$$

(2) Case 2 for $a = 0, b = +\infty$: The seismic magnitude range of x is $[0, +\infty]$, the maximum entropy magnitude distribution is a simple exponential distribution

$$f(M) = \beta e^{-\beta M} \quad (18)$$

Similar to Eq.(14), we obtain

$$\frac{N}{T} = \int_M^{+\infty} f(M)dM = e^{-\beta M} \quad (19)$$

Rewrite Eq.(19),

$$\log N = \log T - 0.434\beta M = a - bM \quad (20)$$

This is the seismic magnitude frequency relation based on exponential distribution. This relation exactly coincides with G-R relation shown in Eq.(1), which considers only the arithmetic mean magnitude (μ) in maximum entropy principle.

(3)Case 3 for $a = m_0, b = +\infty$: The seismic magnitude range of x is $[m_0, +\infty]$, the Lagrangian parameters in Eq. (11) are

$$\lambda_0 = -\lambda_1 m_0 - \ln(\lambda_1) \quad (21)$$

And

$$\lambda_1 = \frac{1}{\mu - m_0} \quad (22)$$

The maximum entropy magnitude distribution is

$$f(M) = \lambda_1 \exp[-\lambda_1(M - m_0)] \quad (23)$$

Similar to Eq.(14), we obtain

$$\frac{N}{T} = \int_M^{+\infty} f(M)dM = e^{\lambda_1 m_0 - \lambda_1 M} \quad (24)$$

Rewrite and log the equation

$$\log N = \log(T) + 0.434\lambda_1 m_0 - 0.434\lambda_1 M \quad (25)$$

This is also a linear seismic magnitude frequency relation which coincides with Eq.(1).

3.1 First-order and second-order moment of magnitude are provided

If the first order moment (or mean) μ and second order moment (or variance) α^2 are prescribed, then the maximum entropy problem is to maximize the entropy

$$H[f(x)] = -\int_0^{+\infty} f(x) \ln f(x) dx \quad (26)$$

Subject to

$$\int_0^{+\infty} f(x)dx = 1, \int_0^{+\infty} xf(x)dx = \mu, \int_0^{+\infty} x^2 f(x)dx = \sigma^2 \tag{27}$$

The maximum entropy density function is

$$f(x) = \exp(-\lambda_0 - \lambda_1 x - \lambda_2 x^2) \tag{28}$$

This is a truncated normal distribution. The λ_0 is the normalizing parameter, which is a function of λ_1 and λ_2. The maximum entropy density function can also be written as the form standard normal distribution

$$f(x) = \frac{1}{a\sigma\sqrt{2\pi}} \exp[-\frac{(x-\eta)^2}{2\alpha^2}] \tag{29}$$

where parameters η and α can be expressed as functions of μ and σ^2, $a > 0$ is a normalization constant, which can be calculated from the normalization condition and equals to

$$a = \Phi(\frac{\eta}{\alpha}) \tag{30}$$

Meanwhile, the probability of the magnitude can be estimated by

$$F(M) = \frac{N}{T} \tag{31}$$

Then

$$\frac{N}{T} = \int_M^{+\infty} \exp(-\lambda_0 - \lambda_1 x - \lambda_2 x^2)dx = \int_M^{+\infty} \frac{1}{a\alpha\sqrt{2\pi}} \exp[-\frac{(x-\eta)^2}{2\alpha^2}]dx \tag{32}$$

The right part of Eq.(32) can be viewed as the normal cumulative distribution function Φ, then

$$\frac{N}{T} = \frac{1}{\Phi(\frac{\eta}{\alpha})}[1 - \Phi(\frac{M-\eta}{\alpha})] \tag{33}$$

Rewrite and log the equation

$$\log N = \log T - \log[\Phi(\frac{\eta}{\alpha})] + \log[1 - \Phi(\frac{M-\eta}{\alpha})] \tag{34}$$

This is a new nonlinear seismic magnitude frequency relation based on truncated normal distribution derived from maximum entropy principle. The parameters T, η and α can be obtained from observed data. This is a nonlinear curve-fitting (data-fitting) problems, which can be solved by Gauss-Newton method.

4 Examples

Consider a set of r magnitude frequency data points, $(N_1, M_1), (N_2, M_2), \cdots, (N_r, M_r)$ and a curve (relation) $N = f(M, \beta)$ that in addition to the variable N also depends on t parameters, $\beta = (\beta_1, \beta_2, \cdots, \beta_t)$ with $r \geq t$. It is desired to find the vector of parameters such that the curve fits best the given data in the least squares sense, that is, the sum of squares of residuals (SSR)

$$R = \sum_{i=1}^{r} R_i^2 \; , R_i = N_i - f(M_i, \beta) \tag{35}$$

is minimized, where R_i is the individual residuals (errors) for $i = 1,2,\cdots,r$. The smaller the SSR, the better the established seismic magnitude frequency relation. The other two criteria being used in comparison are the maximum individual residuals and average residuals. Comparison was made among three maximum entropy based relations: G-R linear relation in Eq.(20); nonlinear relation based on truncated exponential distribution in Eq.(15); and nonlinear relation based on truncated normal distribution in Eq.(34) proposed in this paper.

Table 1 In-situ data on Seismic magnitude-frequency relation for example 1

M	5.9	5.8	5.7	5.6	5.5	5.4	5.3	5.2	5.1	5.0
N(*M*+*dM*)	1	1	0	0	6	1	3	5	3	3
N(*M*)	1	2	2	2	8	9	12	17	20	23
M	4.9	4.8	4.7	4.6	4.5	4.4	4.3	4.2	4.1	4.0
N(*M*+*dM*)	5	11	13	8	14	11	22	17	22	15
N(*M*)	28	39	52	60	74	85	107	124	146	161

Notes: *M* is the seismic magnitude; *N*(*M*+*dM*) is number of the earthquakes between magnitude *M* and *M*+d*M*; *N*(*M*) is number of the earthquakes with magnitudes greater than or equal to *M*.

Table 2 Parameter comparison among three relations for example 1

	G-R relation	Exponential based relation	Normal based relation
Model parameters	*a*= 6.9389	β =2.6071	η =4.2445
	b= 1.1335	m_1 =5.9	α =0.6343
		T = 8688230.39	T = 222.0679
SSR	0.4172	0.6794	0.1445
Maximum residuals	0.2901	0.3806	0.2578
Average residual	0.1248	0.1535	0.05925

Table 1 lists the in-situ Japanese seismic magnitude-frequency data[11], from which an analytical relation needed to be established. The three model relations are fitted to the data and the model parameter are illustrated in Table 2. For the three comparison criteria values in Table 2 (SSR, maximum residual, and average residual), the proposed relation based on truncated normal distribution are the smallest, which shows that the proposed model is best-fitted to the data and better than G–R linear relation and nonlinear relation based on truncated exponential distribution. This result is illustrated in Figure 1(a).

In the second example, in-situ seismic magnitude-frequency data in Table 3 comes from Taiwan, China. Only shallow earthquakes were considered from the year of 1958 to 1986 [11]. From Table 4 and Figure 1(b), same results can be obtained as Example 1, as expected.

Table 3 In-situ data on Seismic magnitude-frequency relation for example 2

M	4.7	5.0	5.3	5.6	5.9	6.2	6.5	6.8	7.1	7.4	7.7	8.0
N(*M*+*dM*)	210	150	76	62	36	25	12	9	3	1	1	1
N(*M*)	594	384	234	150	88	52	27	15	6	3	2	1

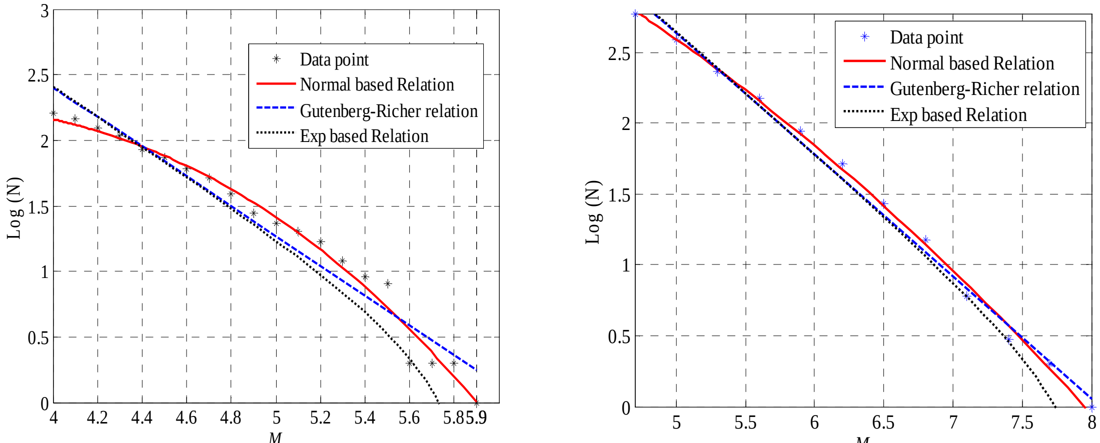

(a)For example 1 (b) For example 2

Figure 1 comparison among three relations

Table 4 Parameter comparison among three relations for example 2

	G-R relation	Exponential based relation	Normal based relation
Model parameters	a= 6.9455	β =1.9806	η =0.5208
	b= 0.8611	m_1 =8.0	α =0.1783
		T =8821135.26	T =39992.99
SSR	0.06965	0.5868	0.02449
Maximum residuals	0.1243	0.6813	0.09426
Average residual	0.06861	0.1337	0.03630

5 Conclusion

This paper explained a new seismic magnitude-frequency relationship from the concept of entropy and the principle of maximum entropy, by considering the first and second order moment of magnitude.

The maximum entropy principle is utilized to determine the distribution of earthquake magnitude. If the maximum entropy principle was constrained by the mean value of seismic magnitude and no upper magnitude bound is given, exponential distribution can be readily generated, which in turn the well known G-R relation can be explained. When an upper bound is assumed, the truncated exponential distribution can be produced and Berrill and Davis's relation is then confirmed. More interestingly, if the maximum entropy principle was constrained by the first and second moment (i.e. mean and variance) of seismic magnitude and no upper magnitude bound is given, truncated normal distribution can be generated, on which the new seismic magnitude-frequency relation is based.

$$\frac{N}{T}=\frac{1}{\Phi(\frac{\mu}{\sigma})}[1-\Phi(\frac{M-\mu}{\sigma})] \tag{36}$$

Comparison studies in two examples showed that the proposed model is best-fitted to the data and better than G-R linear relation and nonlinear relation based on truncated exponential distribution. However, what the parameters in our new relation represent in seismology need to be further investigated.

Acknowledgements

Supports from NSFC (Nos 50574098 and 50404010), Hunan NSF (05jj10010), program for NCET-07-0860 in universities, SRFDP-200805330029 and SRF for ROCS, SEM were acknowledged by the authors.

References

1. Gibowicz SJ, Kijko, A. An introduction to mining seismology. New York: Academic press, 1993
2. Gutenberg,B, Richter,CF. Seismicity of the Earth and Associated Phenomena(2nd ed.). Princeton: Princeton University Press, 1954
3. Chen, S.J.Tao.,J.Q.Wang.,Z.C., et al. Nonlinear characteristics of magnitude frequency relationship. Journal of seismological research, 1997, 20(3). 303-310 (in Chinese)
4. Pisarenko, V.F. Sornette, D. Characterization of the frequency of extreme earthquake events by the Generalized Pareto Distribution. Pure and applied geophysics, 2003, 160(12). 2343-2364
5. Pandey, MD. Direct estimation of quantile functions using the maximum entropy principle. *Structural Safety*, 2000;22(1). 61-79
6. Deng.,J. Pandey, MD. Estimation of the maximum entropy quantile function using fractional probability weighted moments. Structural Safety, 2008,30(4). 307-319
7. Deng, J, Pandey MD. Estimation of quantile function from censored samples using partial minimum cross entropy and partial probability weighted moments. Journal of Hydrology, 2008, 363(1-4). 18-31
8. Berrill, JB, Davis, RO. Maximum entropy and the magnitude distribution. Bulletin of the Seismological Society of America, 1980, 70(5). 1823-1831
9. Feng, LH. Maximum entropy principle and seismic magnitude frequency relation. Seismology and geology, 2003, 25(2). 260-264 (in Chinese)
10. Deng, J. Pandey MD. Estimation of minimum cross-entropy quantile function using fractional probability weighted moments. *Probabilistic Engineering Mechanics*, 2009,24(1). 43-50
11. Chen, E.L. Reform of magnitude frequency relationship and its application to some seismic zones. Northwestern Seismological Journal, 1993, 15(3). 33-36 (in Chinese)

RaSiM 7(2009): Controlling Seismic Hazard and
Sustainable Development of Deep Mines,
C.A. Tang(ed), Rinton Press, 327-332

PROBE INTO THE RELATIONSHIP BETWEEN CRACK EXPANSION AND ROCK BURST

LI- CHUN RUI, PENG-YONG WEI and PAN-JUN FENG

Coal Mining & Designing Branch, Coal Research Institute

China Coal Society of Rock Mechanics and Support Professional Committee,

Beijing 100013, P.R. China

QI -QING XIN, KANG -LI JUN

China Coal Research Institute,

Beijing, 100013, P.R. China

The physical processes of rock burst are described from the viewpoint of crack propagation. The crack propagation is explained as the "intrinsic factor" of rockburst, the energy release during rockburst is considered as the "energy factor", and the fracture zone is considered as the "structural factors" for rockburst. The relationship between crack-related "three factors" and rock burst is established, in order to provide a theoretical basis to microseism and earth sound technology for predict rock burst.

1 Introduction

“Pressure bump” or “Pressure burst” is damaged rock that behaves dynamically. It is one of major possibilities for disasters in process of mining. Rocks flexibility can cause a sudden, fierce, and quick release which is a danger in the course of coal production. It can lead to slope instability causing instantaneous destruction and accompanied by impact dust, with the possibility of personal injury. This phenomenon is called “rock burst” [1] and is present in metal mines, tunnels and other areas where excavation takes place [2].

2 Mechanism of rock burst related to cracks

Rock burst mechanism is the physical processes and principles for which coal (rock) body deforms and destruction mechanics processes take place; both are linked with rock burst with separate conditions and reasons that are independent of each other. With the basic mechanism, it is possible to correctly understand the causes of rock burst, set up the criteria for discriminate, understand the control theory and establish effective prevention and control measures.

About the occurrence of rock burst mechanism have been much discussed, Zhang-Mengtao, PAN-Yishan, etc. think rock burst happen relevant with the coal (rock) expansion of cracks, the violent rupture, and according to solid dielectric rupture theory, discussed rock burst occurrence mechanism [3]. Miao-Xiexing Zhang-Xiaochun, think rock burst relate to coal parietal and spall plate structure, and analysis of coal wall cracked plate structure formation and destruction law, give the stress criterion of crack growth, run-through and subsequent formation of spall plate structure unstable pressure conditions [4]. Tang Chun-an, Qiao-He think that rock burst caused by elastic-brittle characteristics micro shell element without intermission rupture [5]. Tan-Yian according as the rock broken state when rock burst occur, proposed the rock burst formation of three stages, namely "splitting into plate - shear into pieces - pieces chip ejection"[6]. From the results of scholars before, rock burst and cracks expand have some association.

Recent years, technical means of rock burst mechanism constantly improve. In lab experiments, along with scanning electron microscopy, CT, magnetic resonance imaging technologies etc. development, to coal (rock) cracks leading to final breakdown process has been more clearly. In scene monitoring, use microseismicity, earth sound monitoring equipment, on coal (rock) break down, crack extension monitoring, accumulated valuable data. This give the relationship between rock burst and coal (rock) cracks expand, expatiate rock burst mechanism provides a sufficient basis.

3 Relationship between cracks expand and rock burst

After analysis the results of previous scholars, we can see that the occurrence of rock burst and rock rupture have some relate. The occurrence of rock burst process is rock crack initiation, extended to disrupt and rupture eject process.

3.1 rock burst gestation

According to rock mechanics treatise [7], rock rupture refers to the cracks expand, cohesion disappears suddenly, joints and fissures instantly separate, and release elastic energy.

According to micro observation during rock load [8], at nearly peak stress, micro-cracks near the shear surface more congestion, become a plume array (see Fig 2). Dyskin and Germanovich approve the direction of its initial fracture roughly parallel to the maximum pressure axis [9]. Near the rock broken, Rock interior exist obvious micro-cracks localized region, until develop to a non-elastic band. Micro-cracks and deformation is concentrated in this region, and merge into macro-cracks, the formation of macro-cracks merge have unexpected forms and progressive forms[10], which relate to the rock strength, stiffness and other property-related, that is, relate to the internal factors .

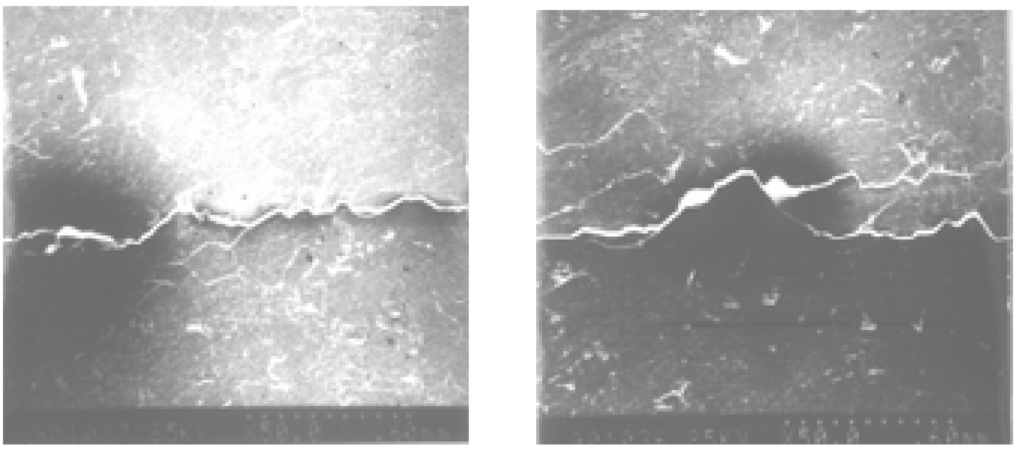

Figure2 SEM photos of Crack Growth

After stress get to peak, the load-bearing capacity of rock reduce accompanied by deformation increasing. If in common experimental machine, because of lack of rigidity, at the beginning of peak intensity or a little pass, rock breaking destruction will happen suddenly, which similar to rock burst happen. So the stress at near peak, when the micro-cracks localized and merge into macro-cracks unexpected, this provide rock burst for breeding conditions. Through drill cuttings method to predict rock burst is essential to determine whether the stress close to ultimate strength, to observe whether there have localize changes, localize destruction.

3.2 rock burst occurrence

Rock burst occurrence accompanied by the enormous energy release. In general believed that rock burst energy from the broken rock and surrounding rock elastic energy stored [11]. Assume the broken rock elastic energy fully release when rock burst happened, according to the formula $\Theta = \sigma_p^2 V / 2E$ to estimate broken rock released elastic energy. V for the volume of broken rock, σ_p for the average stress in rock before broken, E is modulus of elasticity.

Table 1 rock burst magnitude and energy

	Zaozhuang Mine	Laohutai Mine	Xinzhouyao Mine	Mentougou Mine	Beipiao Mine
Quake Magnitude M	M0.7	M1.2	M2.1	M3.0	M3.8
Quake energy E	1.52e13	2.97e13	7.44e13	1.68e15	4.11e16
Broken rock's Energy Θ	1.77e13	1.68e13	1.87e13	1.25e14	2.13e14
$\Theta / E\%$	116%	56.5%	25.13%	7.4%	5.18%

Table 1 shows the seismic network monitored several rock burst energy level. From the table, we can see that the greater the magnitude of rock burst, the smaller the broken body energy released per cent of total energy, or even worse by two orders of magnitude. This indicate the larger magnitude rock burst energy released mainly from the surrounding rock be stored as elastic. At smaller magnitude rock burst, the broken body of the energy released by a higher proportion. Means at this time the energy mainly by rock rupture released. Rock compression test in lab often see specimen partial rupture and produce spalling fly off, and the testing machine load does not decline, as is the case of the simulation.

Rupture zone instability and eject is rock burst external performance, and in order to study when the energy release, need to find the rupture zone instability criterion, for this we have bring the theory of unlimited domain contains body in elasticity [12]. The theory suggests that when the local deformation happened in rock mass, the elastic modulus in strain concentration area significantly decreased because of intensive fractured, as if in a uniform medium contains a low elastic modulus inclusion, and its mechanical state changed, become into a surround rock and inclusion composed balance system (Fig 3-a), when the rupture zone is very narrow, they can be degraded as the fault plane or fracture surface (Fig 3-b).

In order to obtain above structure inclusion-rupture zone unstable condition, we carried out an analytic calculation. In this system, fracture medium accord to rupture constitutive equations described [13], elastic surround rock tally with Hooke's law incremental forms $d\sigma = Dd\varepsilon$ .The equilibrium conditions can be used variation form give as

$$\delta\prod = \int_{V_S} \delta(d\varepsilon)^t D d\varepsilon dV + \int_{V_i} \delta(d\varepsilon)^t D_{cp} d\varepsilon dV - \int_V \delta(du)^t dp dV - \int_F \delta(du)^t dq dF = 0$$

There

$$D = \begin{bmatrix} \lambda+2G & \lambda & 0 & 0 & 0 & 0 \\ & \lambda+2G & \lambda & 0 & 0 & 0 \\ & & \lambda+2G & \lambda & 0 & 0 \\ & & & G & 0 & 0 \\ & & & & G & 0 \\ & & & & & G \end{bmatrix}$$

λ and G are Lame elastic coefficient, D_{cp} is a variable relate to yield function, V_s denote elastic surround rock, V_i indicated fractured zone (inclusion), $V = V_s + V_i$, F is force regional borders, dp is incremental of physical load (gravity , stress, etc.).

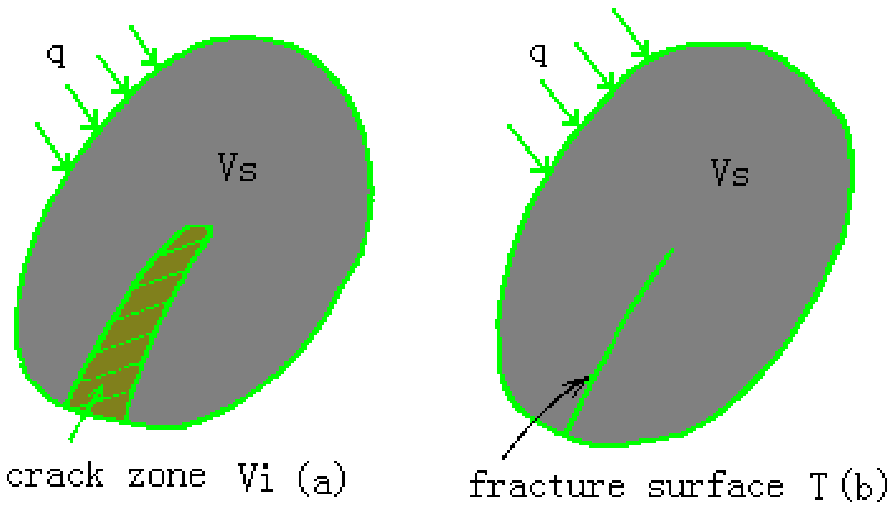

Figure 3 Rock-inclusion zone diagram

To any strain variety field $\delta\varepsilon$. If quadric variation $\delta^2\prod$>0, the system is balance stabilize; When $\delta^2\prod$= 0, it's in state of indifferent equilibrium. That is, the stability of peristalsis; If at least have one strain field cause $\delta^2\prod$<0, the system is in a non-steady state, that is critical state.

From instability criterion can be seen, inclusion's soften nature is a necessary condition for system instability. Because if the inclusion is not a softening medium, as D is positive definite matrix and D_{cp} is half positive definite, constantly have $\delta^2\prod$>0, state is stable. In addition, to soften fissures, faults and other media, only in the plastic loading criterion function l>0, could D_{cp} be negative (if l≤0, when $D_{cp} = D$). If take physical force dq as advance abutment pressure changes, which will calculate the deformation field, only when l>0 could possible being rock burst, if l≤0 will not trigger.

3.3 rock burst termination

About crack arrest theory there have strength bulwark, fissure disjunction, sudden unloading etc... However, most scholars believe that the expand fissures often stopped at old macro-cracks, at discontinuity surface. Thus, although the expand process have crack initiation and accelerate process, but to the plastic medium containing cracks, the cracks expand just started may be terminated at "old" cracks surface, so this relax the intensity energy, not easy to trigger rock burst.

We use the stress relief blasting, coal seam cutting, hydraulic pressure to crack and other means, that is, through artificial increase fracture region, so that depress concentration, thereby reducing the extent of localized deformation, reduce inclusion and surround elastic rock. So that terminate expand of fissures in the plastic region at interface of cracks. Make it does not have the conditions for energy storage or energy could be released.

4 Conclusion

1) Through analysis, it was discovered that rock burst occurs in rock mass close to the ultimate strength and that deformation is localized and produces strain at the localization zone. Micro-fissures in the region merge together to form macro-cracks; which expand and become unstable. This causes instability in rock-inclusion system, leading to suddenly release of elastic energy. When the rock-inclusion restores to stable conditions, the cracks are stabilized and slows down causing the rock burst to terminate.
2) From fracture mechanics theory, rock burst occurs at strain concentration zone after macro-cracks expand. We can use the strain concentration zone, rupture intensive region or vibration and sound caused by micro-cracks expand, as the precursor to forecast the rock burst.

Acknowledgements

The present work is funded “973” project entitled "Coal (Rock) and gas force disasters behave and mechanical conditions research." (2005CB221504-04).

References:

1. Qi, Q.X., Dou, L.M. Rockburst Theory and Technology. Xuzhou: China University of Mining and Technology Press, 2008.3
2. Qi, Q.X. Mao, D.B. between rock burst rock burst, mine quake relationship and numerical simulation study, Journal of Rock Mechanics and Engineering, 2003.11.52-57
3. Zhang, M.T. Pan.,Y.S, etc. Rock burst Mechanism, Journal of Fuxin Mining Institute, 1985.3. 27-33
4. Zhang, X.C. Miao, X.X. Rock burst spall plate model and experimental study, Journal of Rock Mechanics and Engineering, 1999.10. 5-10
5. Qiao, H. Tang, C.A. rock burst and mining-induced rock failure process of numerical simulation new method, Journal of Geomechanics ,1999.3.5-10
6. Tan, Y.A. the formation mechanism of rock burst, Hydrogeology and Engineering Geology, 1989.1. 30-34
7. Xie, H.P. Chen., Z.H. Rock Mechanics, Science Press, 2004.5
8. Lai, Y. Zhang, Y.X. rock macro meso-damage composite model and crack propagation law, Rock Mechanics and Engineering 2008,27 (03). 40-44
9. Dyskin., A.V and Germanovich L.N. Model of rock burst caused by cracks growing near free surface. Rock bursts and Seismicity in Mines. Rotterdam: Balkema, 1993. 169-174
10. Zhang., H.Y.Li.,T.J.the mesomechanics experimental analysis to formation mechanism of rock burst,

Journal of Inner Mongolia Polytechnic University, 1997.3. 44-47
11. Dou., L.M. Zhao., C.G. Rock burst coalmining disaster prevention. Xuzhou: China University of Mining and Technology Press, 2006.
12. Xu, Z.L. Elasticity Concise Guide, Higher Education Press, 1996
13. Yin,Y.Q. Zhang., H.simulated earthquake strain softening mathematical model, Journal of Geophysical, 1982, 25.5. 26-31

RaSiM 7(2009): Controlling Seismic Hazard and
Sustainable Development of Deep Mines,
C.A. Tang(ed), Rinton Press, 333-338

A NEW METHOD TO PREDICT THE SPLITTING CRACKS OF THE SURROUNDING ROCK MASSES IN UNDERGROUND OPENINGS BASED ON ENERGY DISSIPATION PRINCIPLE

XIAO-JING LI，WEI-SHEN ZHU, WEI-MIN YANG and YONG LI

Geotechnical & Structural Engineering Research Center, Shandong University

Jinan, 250061, P.R. China

During the excavation of the underground openings of Ertan Hydraulic Project in P. R. China, a large range of longitudinal splitting cracks zone appeared in the rock pillars between the main house and transformer house that were within the deep embedded and high-pressured surrounding rock masses. In order to study and predict the failure zone and the quantities of cracks, plate theory and energy dissipation principle are used together, which have been verified by numerical analyses. The prediction formula is set up. It can estimate the crack numbers of the failure zone. In addition, using the finite differential software Flac3D, the strain-softening model is adopted, as it is appropriate for brittle rock masses, by tracing the whole process of elastic energy variation of each element and memorizing the energy difference of before and after failure. Accordingly, the splitting cracks are predicted. The numerical analysis results are almost agreed with the results by prediction formula.

1 Introduction

The failure modes of the surrounding rock masses of the underground caverns in the Ertan Hydraulic Project are complicated because of the rock mass structures and in-situ stresses. For the large scale underground caverns (the excavation width is up to 20m and excavation height is up to 60m), the primary potential failure mode of the surrounding rock mass is mainly block failure [1].

When doing the excavations in underground caverns under the condition of high in-situ stresses, some failure zones appear almost inevitable. As to the intact brittle rock masses, the formation and developing procedure of the plastic zones are usually also accompanied by the phenomena just like splitting cracks, alling ribs and rockburst, and even more serious disaster like earthquake, which can greatly endanger construction safety. Therefore, it is very important to study the energy variations of the failure zones in the process of excavations and ultimately make a judgment on the stability of the surrounding rock masses [2, 3, 4, 5, and 6].

The splitting failure of the surrounding rock masses in the underground caverns of Ertan Hydraulic Projects has been further studied based on the fundamental principals of the energy dissipation, combined with plate buckling theories and numerical simulation analyses. A generalized prediction model for splitting cracks has been proposed and utilized by Ertan Project for validation.

2 The fundamental principle for analyzing splitting failure based on energy method

As we know, the surrounding rock mass in the underground caverns before excavations maintains a balanced three-dimensional stress state. After excavations, there are loading and unloading zones in the rock mass, which keeps an elastic state. In the meantime, there is no macroscopical irreversible process in the rock media, but a uniform deformation state.

3 Study on the destabilization of rock pillars based on plate buckling theory

3.2 The critical load of the buckling plate

As the rock mass among the splitting cracks is simplified to be a buckling plate, so two supporting boundaries can be simplified to be a simply supporting restrict and free restrict for the other two boundaries. Then $N_x = -N$, $N_y = 0$, $N_{xy} = 0$, and replace the loads with the known values in equation 3.1-1. The following equation 3.2-1 can be gained:

$$D\nabla^4 \mathrm{w} + \mathrm{N_x}\frac{\partial^2 w}{\partial x^2} = 0 \tag{3.2-1}$$

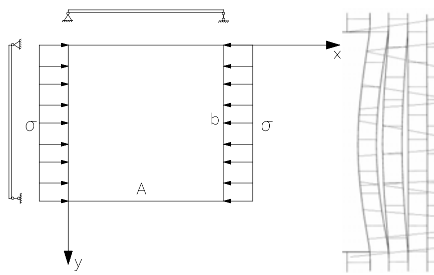

Figure 1 The sketch of thin plate buckling mode

The critical stress value of the buckling plate can be determined through calculations:

$$\sigma_{cr} = \frac{\pi^2 E t^2}{3L^2} \tag{3.2-3}$$

After determining the critical stress value, the relieving energy value can also be determined:

$$W_s = \frac{1}{2}\int_{-0.5b}^{0.5b}\int_{-0.5L}^{0.5L} \sigma_{cr}\left(\frac{\partial u}{\partial x}\right)^2 dxdy = \frac{\pi E b t^4 \sigma_t}{36L^2 \sigma_{cr}} \tag{3.2-4}$$

The energy expression is closely related to the tensile strength of the rock mass and the compressive strength of the slim plate, which can pretty reflect the energy change in the process of forming the splitting cracks in the surrounding rock mass.

3.3 The energy dissipation analysis of the buckling plate

In order to qualitatively describe the splitting failure in vicinity of the underground caverns, the uneven distribution of the stress induced by excavations can be neglected. Assuming that N splitting cracks whose length is all L form in an area of $A \times L \times b$, and the interval of the cracks is t .

According to the energy equation [8], $WD = SE + nW_s$ (3.3-1), the following can be got:

$$\left(\frac{\sigma_1 - \sigma_3}{2}\right)\varepsilon ALb = \left(\sigma_1^2 + 2\sigma_3^2 - 4v\sigma_1\sigma_3 - 2v\sigma_3^2\right)\frac{ALb}{2E} + \frac{\pi E b^2 t^4 \sigma_t}{36L^3\sigma_{cr}} n \tag{3.3-2}$$

From the above equation 3.3-2, the number of the splitting cracks can be determined. The relationship between the number n and the splitting failure depth A is $n = \frac{A}{t} - 1$ or $n = \frac{A}{t}$.

With the purpose of verifying the correctness of this formula, the related parameters of Ertan Project has been adopted to make a validation for this formula. So the energy equation can be simplified as below:

$$\frac{\sigma'_{cr}}{2}\varepsilon AL = \sigma'^2_{cr}\frac{AL}{2E} + \frac{b\sigma_t}{12\pi L}t^2 n \tag{3.3-3}$$

Let $\eta_1 = \frac{\sigma'_{cr}}{2}\varepsilon L$, $\eta_2 = \sigma'^2_{cr}\frac{L}{2E}$ and $\eta_3 = \frac{b\sigma_t}{12\pi L}$ be constants, and the following expression can be related with A , n and t :

$$\left(\eta_1 - \eta_2\right) A = \eta_3 t^2 n \tag{3.3-4}$$

If the splitting failure depth and the average width of the cracks interval can be observed in situ, the number of the cracks can be estimated. If the number of the cracks can be calculated through $n = A/t$, the width of the cracks is $t = (\eta_1 - \eta_2)/\eta_3$, and then t =0.72m can be achieved. This value may be the minimum of the width, and the corresponding number of cracks is approximately 28.

4 Numerical analysis on splitting failure based on energy method

According to the above analysis, the total energy in rock mass SD includes: (1) the elastic strain energy (SE); (2) the dissipated energy induced by cracks extending (W_s), that is $SD = SE + nW_s$.

This energy assumption would be totally utilized to the energy dissipation. The following method will be accepted to check the energy variations: in the numerical simulations, the strain softening model which is appropriate for brittle rock mass has been adopted, tracing the whole process of elastic energy variation of each element, memorizing the energy difference of before and after failure, that is $U_i = SD_i - SE_i$, then the whole accumulated energy of the elements in plastic zones is equal to the energy relief induced by excavations, that is nW_s .

For making good use of the numerical results, the energy expression for each element can be defined below:

(1) The elastic strain energy of the ith element before failure:

$$SE_i = V_i\left[\left(\sigma_1^2 + \sigma_2^2 + \sigma_3^2\right) - 2\nu\left(\sigma_1\sigma_2 + \sigma_1\sigma_3 + \sigma_3\sigma_2\right)\right]/\left(2E\right) \tag{4-1}$$

(2) The elastic strain energy of the ith element while failing:

$$SD_i = V_i\left[\left(\sigma^{*2}_1 + \sigma^{*2}_2 + \sigma^{*2}_3\right) - 2\bar{\nu}\left(\sigma_1^*\sigma_2^* + \sigma_1^*\sigma_3^* + \sigma_3^*\sigma_2^*\right)\right]/\left(2\bar{E}\right) \tag{4-2}$$

Where $\sigma_1, \sigma_2, \sigma_3$ are the principal stresses of each element before failure, and $\sigma_1^*, \sigma_2^*, \sigma_3^*$ are the principal stresses of each element while failing. ν and E are the Poisson's ratio and elastic modulus before failure, and $\bar{\nu}$, $\bar{E}$ are the Poisson's ratio and elastic modulus after failure. For the sake of simplicity, the Poisson's ratio and elastic modulus would never change before and after failure, the energy change in the failure zones can be expressed as below:

$$U = \sum_{i=1}^{n} SD_i - \sum_{i=1}^{n} SE_i \tag{4-3}$$

The details introduced above reflect the energy change in the whole surrounding rock mass which splitting failure occurs by means of tracing the energy change of each element before and after failures, which can be convenient to check the applicability whether the energy method can be used in studying the splitting failure.5 The case study of Ertan project

4.1 Geology descriptions

The surrounding rock mass of Ertan project belongs to the fresh and rigid simaite in Indo-Chinese epoch. The rock mass is hard and intact. The structural planes have few failures. In a word, the rock mass is the brittle rock media under high in-situ stress. There is no perforative softening structural plane in this project.

Table 1 shows the physico-mechanical parameters of the rock mass.

Table 1 The physico- mechanical parameters of the rock mass

Rock mass	γ (KN/m^3)	E (GPa)	c (MPa)	σ_c (MPa)	σ_t (MPa)	μ	φ (°)
Simaite	27.8	35	30	140	6.24	0.22	45

4.2 The main hydraulic buildings

In the underground caverns group, the three parallel caverns are the main powerhouse, the transformer house and the surge chamber. The direction of the axis is N6E. The dimensions of the three caverns are as following: the main powerhouse 280.3m×25.5m×60.5m (length×width×height), the transformer house 199.0m×17.4m×25.0m (length×width×height), the surge chamber 203m×19.5m×58.1m (length×width×height) and the other tailrace tunnel 888.1m×16m×16m (length×width×height).

The horizontal intervals of the three caverns are 35m and 30m respectively. The three underground caverns are approximately 80m away from the left shoulder of the arch dam. The average buried depths are between 250m and 450m. The lateral thickness of the rock mass is about 300m.

4.3 The numerical results analyses

The energy variations have been qualitatively analyzed in the procedure of excavations. Therefore, for the sake of simplicity, the main caverns are only taken into account, the structural planes like joints and faults aren't considered and only one type of rock mass is thought over.

In the numerical model, the horizontal direction of the transverse section is defined as X-direction; the vertical direction is defined as Y-direction, and the longitudinal axis direction is Z-direction. The numerical model is a quasi three dimensional model, as only thickness of 10m along the longitudinal axis is considered. The strain softening model in Flac3D is adopted in analyzing the brittle failures of the hard rock mass.

Six typical parts were selected to analyzing the influences of the energy variations on the rock mass shown in Fig. 3.

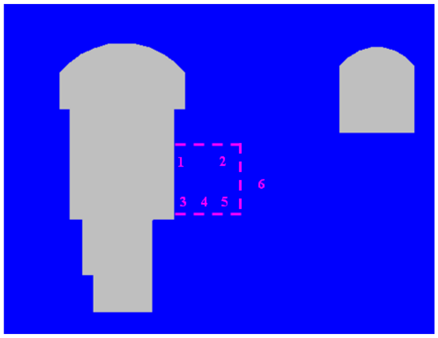

Fig.3 The key zone layout sketch

The following figures show the energy dissipations of the elements from No.1 to No.6.

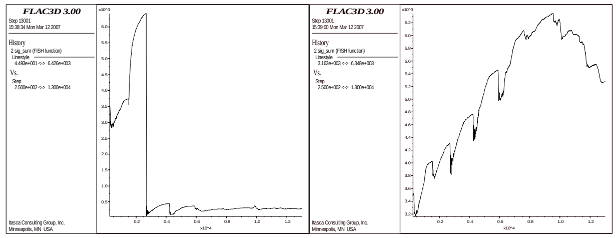

Fig.4 The energy dissipation of No.1 & No.2 zone with the time-step

The elements of No.1 and No.3 are in vicinity of the side walls. The two elements appear obvious mutation in energy dissipation. The reason is that the radial stresses of the surrounding rock mass release duo to the excavations. Although the tangential stresses increase, the total elastic energy would diminish in total. The decrements of the two elements are 6280J and 5349J respectively. It's also concluded that the energy of the elements tends to be steady owing to the less influences of the subsequent excavations.

The element No.4 is a little farther away from the side walls. Some great energy changes also occurred because of the excavations, and the changed energy value is 3106J that is relatively smaller compared with the elements of No. 1 and No. 3. The disturbance of the surrounding rock mass induced by excavations gradually decrease as the depths increase.

The element No.2 is much farther away from the side walls than element No.4. The changed energy value is only 600J.

Compared elements No.1, No.3 and No.4 with elements No.2 and No.5 in the energy change curves, it is concluded that the energy of elements No.1, No.3 and No.4 increases in the initial period of time since the stress variations result in the increment of the elastic energy and dissipated energy is used to perform the cracks extending. The energy variation curves of elements No.2 and No.5 firstly increase and have a sudden drop, but the final energy is still larger than the initial that can demonstrate the energy of this part increases after excavations.

The element No.6 is outside of the selected splitting area. This element is in an elastic state in the whole process of numerical simulations. The energy variations maintain a rising tendency. The each excavation step has little impact on this element, and the maximum energy variation is only 100J.

Fig.7 shows the total energy dissipation change of main house surrounding rock with the excavations.

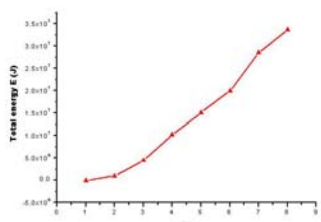

Fig.7 The total energy dissipation change of main house surrounding rock with the excavations

Seen from Fig.7, the energy dissipation change maintains a rising tendency with the excavations, almost as an elastic rising. When the eighth excavation step is completed, the dissipated energy is up to be $\Delta U = 3.36e7J$. Combined with the proposed cracks number predicting formula on basis of the energy method, the number of cracks in this selected area can be estimated, $n = \Delta U / W_s$, where $W_s = \dfrac{\pi E b t^4 \sigma_t}{36 L^2 \sigma_{cr}}$. Finally, n=21 can be worked out, which is similar to the number worked out by Equation 3.3-4. Therefore, it's feasible to predict the cracks numbers in the splitting failure areas based on the energy method.

5 Conclusions

(1) Assuming the total energy in rock mass SD includes: (1) the elastic strain energy (SE); (2) the dissipated energy induced by cracks extending (W_s), that is $SD = SE + nW_s$ according to the energy dissipation principles.

(2) By means of the plate buckling theory in elasticity theories, the failure of the rock pillars in the surrounding rock mass has been studied. The critical load and the dissipated energy have also been achieved.

(3) Combined with the above two conclusions, a generalized prediction model for the number of splitting cracks has been proposed and utilized to Ertan Project for validation. Some consistent results have been accomplished.

(4) The fact that the lengths of cracks change with in-situ stresses has not been considered. The energy of the plates among cracks is regarded to be the same. Therefore, it is necessary to modify the predicting formula by considering more impact factors.

Acknowledgements

This work was financially supported by Natural Science Foundation of P. R. China (No. 90510019, 59939190, and 50579033) and National Research Item of 973 (2002CB412705).

References

1. Zhu, W.S. Sun, A.H. Sui, B. Systematic Analysis of Underground Cavern Groups in Background for Ertan Project. Underground Space, 2005, 1,1-5
2. Xie, H.P., Ju, Y.L. Li.,Y. Criteria for strength and structural failure of rocks based on energy dissipation and energy release principles. Chinese Journal of Rock Mechanics and Engineering, 2005, (17). 3003-3010.
3. Bieniawski, Z. T. Mechansim of brittle fracture of rock, Parts I, II and III. Int. J. Rock Mech. Min. Sci. Geomech. Abstr., 1967, 4(4). 395-430.
4. Vardoulakis I. Rockbursting as a surface instability phenomena. Int J Rock Mech Min Sci & Geomech Abstr,1984, 21(3).137-144.
5. Chinnasane, Damodara Reddy. Brittle rock rating for stability assessment of underground excavations.. Ph. D. Thesis, Laurentian University of Sudbury, Canada, 2004.
6. Tang.,C.A. Lin., P. Wong., R,H,C.Chau.,K.T. Analysis of crack coalescence in rock-like materials containing three flaws-Part Ⅱ:numerical approach. International Journal of Rock Mechanics and Mining Sciences, 2004, 38(7). 925-939.
7. Xu.,Z.L.. Mechanics of Elasticity. Higher Education Press, 1990, 132-134.
8. LI., X.J.The study on experiment and theory of splitting failure in great depth openings[Ph. D. Thesis]. Jinan:Shandong University, 2007
9. Salamon,M.D.G. Energy Considerations in Rock Mechanics: Fundamental Results. J. South Afr. Inst. Min. Metall., 1984, 84.233-246.
10. Su., G.S.Feng., X.T.Jiang.,Q.Chen.,G.Q.. Study on new index of local energy release rate for stability analysis and optimal design of underground rockmass engineering with high geostress. Chinese Journal of Rock Mechanics and Engineering, 2006, 25 (12). 2453-2460.
11. Itasca Consulting Group Inc.. FLAC3D manual. USA:ItascaConsulting Group Inc.,1997.

RaSiM 7(2009): Controlling Seismic Hazard and
Sustainable Development of Deep Mines,
C.A. Tang(ed), Rinton Press, 339-342

EXPERIMENTAL STUDY OF THE INFLUENCE OF WATER ON MARBLE ROCK BURST TENDENTIOUSNESS

ZHI-QIANG KANG, YAN-BO ZHANG and FU-PING LI

College of Resources and Environment, Hebei Polytechnic University, Tangshan 063009, P.R. China

HeBei Province Key Laboratory of Mining Development and Safety Technique, Tangshan 063009, P.R. China

Rock burst phenomenon is simulated by using marble samples in laboratory tests. Moreover, the mechanism of rock burst of hydrous marble and drying marble is also investigated, respectively. Rock acoustic emission characteristics of round-hole sample under bilateral compression are recorded. The relationship of rock burst, acoustic emission characteristics in hydrous marble and drying marble samples are analyzed. The results show that water plays an important role in preventing and curing rock burst. In addition, it is feasible for acoustic emission to forecast rock burst.

1 Introduction

There is an extremely complicated natural stress field in the magma of the Earth's crust. Mining work can cause variations of natural stress field, redistributing the stress in rock and creating stress concentration. In certain conditions, elastic strain energy, gathering in the rock, can bring nonlinear distortion of the rock when it overruns the elastic critical state. Rock outburst takes place when nonlinear distortion is strenuous [1,2,3]. The rock outburst has become one of the international problems which threatens the builders and security of equipment directly, and it is influencing the rate of progress.

The inner energy is released when a rock changes its form. The released energy spreads through sound waves, and we named this phenomenon rock sound emission [4,5]. Rock sound emission is caused by cracks from the accumulating of misplacement, disturbing of crystal lattice or extends and spreads outwards from the original disadvantage of non-plastic fracture, as well as the energy released by the changes of inner structure which is caused by the above reasons. The investigating of characteristics of sound emission in the process of rock distortion has great significance to probe into the mechanism of magmatic body outburst destabilization and to prevent, cure, and forecast rock outburst [6,7,8].

2 Experiment method

The samples of rock outburst simulation experiment is from a certain mine in Hebei province , with a bit of cranny, size 150×150×50mm^3 and along with a round hole, diameter 20mm , in the center. Misalignment of each end and surface of the samples is no greater than 0.05mm. Surfaces are smooth. Place the dry samples under room temperature more than 2 months to dry it naturally, and place the hydrous samples in water for 48 hours before using.

The bilateral compression mode to simulate the happening of rock output under the two-dimensional stress condition, which the experiment adopted, is similar to real conditions. Experiment equipment: press machine (500t), hydraulic jack, YD-28 style dynamic strain indicator. AE-04 sound emission and check system. Record the stress, strain and character of sound emission during experiment.

Experiment load approach: load side pressure σ_2 to 50MPa at certain speed then keep it steady, load axle pressure σ_1 until the sample rock is destroy.

3 Rock outburst happening phenomena and analysis

Experiment shows that rock outburst happen obviously both dry and hydrous conditions. When the axle stress arrives to some degree the pieces separates from side-wall of the hole with bathtub shape. The peeling of layer becomes more obviously and the pieces of hole's side-wall springs out while loading pressure, and new peeled layer comes forth in deep of the inner hole wall. The whole hole cracks suddenly because of standing under load when loaded to limit stress.

Table 1 Dry and hydrous marble rock outburst happening state

Hydrous level of the sample	Name of the sample	Sound of the inside hole σ/σ1%	Pieces ejection σ/σ1%	The hole broken entirely σ/σ1%
Water contain	Awh01	79.5	85.4	100
	Awh02	78.4	85.1	100
	Awh03	79.1	83.9	100
	Awh04	80.3	85.2	100
Range		78－81	83－86	100
Dryness	Aym01	71.0	75.3	100
	Aym02	68.0	74.9	100
	Aym03	69.4	76.1	100
	Aym04	73.6	77.6	100
Range		68－74	75－78	100

Note: σ/σ1% is main stress taken the percentage of limit stress during the progress of standing stress.

Experiment shows rock outburst of the hydrous marble is obviously delayed. From the data of table 1 we can see as follows: In the dry sample experiment hole walls of the rock sample makes a sound when experimental main stress takes around 70 percent of limit stress while in the hydrous experiment it is around 80 percent, and the pieces separated from hole side-wall help rock outburst when the main stress added to about 75 percent of the limit stress while in the hydrous sample experiment it is about 85 percent. Another result is the huge differences in the time of obvious rock outburst phenomenon. The obvious rock outburst phenomenon of the dry samples came into being at about 170 seconds while hydrous ones at about 360 seconds, the two time has a discrepancy more than one time.

In the simulation experiment, the strength of white marble decreased by 15% to 25% after containing water. Analysis indicates that the decreasing of rock strength may be influenced by the following two hydrous qualities of rock: Firstly, under the effect of erosion the rock density decreases and the porosity increases which result the decreasing of rock strength. Secondly, under the effect of softening and water soak, rock's physical condition changes and the surface energy between inner rock granules reduces because of the joining of water molecular. At the same time hydrating changes radii of the mineral ion and influences the rock mechanics property resulting in the decreasing of rock strength and the increasing of plastic yield shares. White marble is mainly formed of calcite. Its rigidity is 3, relatively low. Calcite has a relatively strong property of erosion and softening which lead to an obviously decreasing of the strength after containing water.

Table 2　Young’s modulus of dry and hydrous marbles

Rock style	Young’s modulus E(×104Mpa) (dry)	Young’s modulus E(×104Mpa) (hydrous)
Marble	3.45~4.0	2.67~3.2

Experiment also shows there is some reduction on the rock outburst acuteness degree. As a result of the water influence rock strength decreases, plastic yield shares increases and elasticity shares decreases (see to table 2). All those lead to the reduction of gathered elastic energy and rock outburst acuteness degree as well as lagging the happening time of rock outburst.

4　Character of sound emission in the rock outburst simulation experiment

The sound emission is somewhat different between hydrous samples and dry samples. In dry conditions sound emission incident rate has no predictive peak value but energy rate has. In hydrous conditions both sound emission incident rate and energy rate have a predictive peak value.

At the very beginning of loading, sound emission rate increases constantly and rises to the peak value rapidly and then it keeps the peak value until the limit stress reaches to around 95%. Sound emission rate falls to low level rapidly when the limit stress is beyond 98%. Before the main destroy sound emission keeps relatively peace, and the time is 5-30 seconds (see to Figure 1).

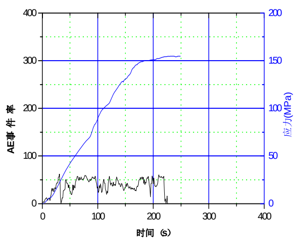

Figure 1　dry sample stress and incident rate—time curve

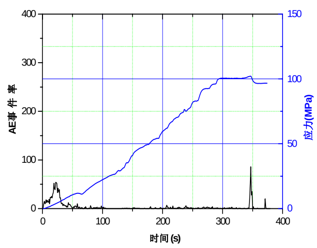

Figure 2　hydrous sample stress and incident rate—time curve

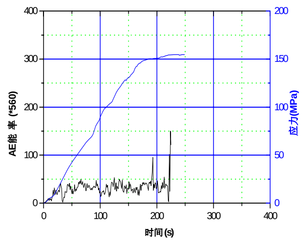

Figure 3　dry sample stress and energy rate—time curve

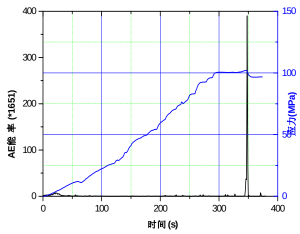

Figure 4　hydrous sample stress and energy rate—time curve

Energy rate varies markedly in the whole loading progress and has two peak values. It appears predict peak value before the main broken. The sound emission also a relatively peace time from the appearance of predict peak value to the happening of main broken. Generally the time is 5-20 seconds. (see to Figure 3)

Regular of the sound emission energy rate has no obviously change after the samples contain water (see to Figure 4) while the incident rate, appearing predict peak value, has an evident change (see to Figure 2). White marble mainly formation is calcite. It has relatively big crystal grain and low strength besides calcite is easily softened by water, therefore at the start of loading, the micro-crack junk period, micro-cracks inner the rock and micro-spaces between crystal granules close soon under the pressure, giving a sign of sound emission with greater energy.

With the increasing of main stress, the rock steps into elastic distortion period and the spaces between crystal granules become extremely tiny. At this time the stress which samples stand is not great enough to form new cracks, but the distortion leads slippage between some closed crack's surfaces. It gives a few sound emission signs and a little energy, so that in this period the sound emission rate can keep in a low level.

At about 80% of limit stress, the combining force between crystal granules can't resist the strength of external applied load so crystal granules begin to separate and sound emission incident rate begin to add. With the increasing of strain, the forming of micro-cracks in the weak surface extends gradually at the direction of parallel to the main stress, and speeding. At about 98% of the limit stress, the extending speed reaches to max and the sound emission appears peak value, after that the extending speed gradually decreases and the sound emission signs become weaker until the rock outburst main broken has done.

The relatively peace time of energy rate before main broken is longer than that of sound emission incident rate. Generally it is 10-35 seconds.

5 Conclusion

There are many factors that affect the occurrence of cavern rock outbursts, such as the conditions of lithology and crustal stress, the structure of magmatic body, the method of construct, etc. Mining depth and geologic structure can also affect rock outburst. The inside curve of the tunnel turning and the corner of fracture surfaces are generally the sensitive areas to rock outburst. In practice, excluding the method of keeping away from strong crustal stress area and considering rock property to reduce rock outburst and to decrease the acuteness degree of rock outburst, injecting water to substructure can also reach the goal.

Sound emission incident rates and energy rates appear at double their peak values when the white marbles are hydrous. Both sound emission incident rates and energy rates have a period of relatively peaceful times before the main is destroyed, and the time is about 5-30 seconds. It is feasible to forecast rock outburst by taking advantage of the double peak value property and the relatively peaceful period of sound emission.

Acknowledgements

The authors wish to acknowledge the funding support from HeBei Province Natural Foundation (No E2008000410) and HeBei Province Education Office of China (No 2007454). At the same time, acknowledge the laboratory support from The HeBei Province Key Laboratory of Mining Development and Safety Technique

References

1. Corner,B. Seismic research associated with deep level mining rock burst prediction and vibration damage to buildings in South Africa. Geophysics, 1985, 50(12). 2914-2915
2. Rudajev,V.Sileny J. Seismic events with non-shear component II. rock bursts with implosive source component . Pure and Applied Geophysics, 1985, 123(1). 17-25.
3. Senfaute,G.Chambon ,C. Bigarre,P, etal. Spatial distribution of mining tremors and the relationship to rockburst hazard. Pure and Applied Geophysics, 1997, 150(4). 451-459.
4. Tang., C.A. Numerical Simulation on Progressive Failure Leading to Collapse and Associated Seismicity Int.J,Rock Mech1&Min.Sci, 1997 (2): 249-261.
5. Xue.,TH. Xiang., Y.Q. Guo., F.Z.. Numerical method to determine mechanical parametersof engineering design in rock masses . Journal of Zhejiang University Science, 2004, (7). 884-889.
6. Tarantola A, and Valette B. Inverse problem quest for information . Geophysics. 1982, (50). 159-170.
7. Fedorvo, V. V. Regrression problems with controllable variables subject to error . Biometrika , 1974 (61). 49-55.
8. Spence W. Relative epicenter determination using P-wave arrival time differences . Bull. Seism. Soc. Am. 1980 (70). 171-183.

RaSiM 7(2009): Controlling Seismic Hazard and
Sustainable Development of Deep Mines,
C.A. Tang(ed), Rinton Press, 343-346

ANALYSIS OF THE CAUSES OF MICROSEISM INDUCED BY UNDERGROUND MINING--TAKING A MINE IN BEIPIAO MINING AREA AS AN EXAMPLE

XIAO-GUANG ZANG, GUO-YAN WANG, GUANG-MING YU and YONG-ZHAN PAN

Qingdao Technological University

Qingdao, 266033, P.R. China

GUO-YAN WANG

Liaoning Technical University

Fuxin, 123000, P.R. China

YONG-ZHAN PAN

Henan University of Science and Technology

Luoyang, 471003, P.R. China

A mine in Beipiao mining area is one of collieries which are exploited deeper than others in our country. As a result, mining induced microseismicity has happened 1550 times since 1971. The microseismicity is called mine seismicity because most of them take place in the mining area. Mine seismic events happen mostly in geological structure zone and mining area, and are characterised by shallow focus, strong intensity, comparatively concentrated focus and so on, and their occurrence is periodicity. There is a close relationship between mine seismicity and many factors such as regional earthquake activities and mining activities. In this paper, based on the research of mutual relationship of geological structure, ground stress, mining conditions and characteristics of mine seismicity, it is concluded that Taiji mine seismicity is induced by mining activities under the regional stress field. The characteristics and laws of the mine seismicity are analyzed.

1 Introduction

Earthquakes take place frequently in the Taiji coal mine in the Beipiao mining area since it was established in 1971. Earthquakes have occurred l550 times from when it was constructed to June 1986 with a maximum magnitude of 3.8. The earthquakes can be felt an area of 1200 km^2, and the intensity can reach up to seven degrees. Many underground buildings around the shaft and the laneway are damaged after many earthquakes. This causes great threat to mine production and personnel safety, becoming another natural disaster in the deeper mining area [1-2]. There is a certain connection between mining activities and earthquakes. The microseism is called mine seismicity because most of it occurs in the mining area. Based on the characteristics of mine seismicity, geological structure conditions, tectonic stress field state, and mining conditions in the Taiji coal mine; it was concluded that mine seismicity is induced by mining under the regional tectonic stress field. Mechanisms and causes of mine seismicity are preliminary studied in this paper.

2 The characteristics of mine seismicity

Beipiao mining area is located in western Liaoning in China, where there is no strong earthquakes in history. Weak earthquakes with Ms≥2.0 happened in many areas such as Yixian, Chaoyang, Beipiao and so on after Ms 4.5 Tangshan earthquake occurred in Heibei province in 1976. All the results show that tectonic stress is gathered and released under the influence of strong earthquake activities in adjacent area. It has happened 1550 times for mine seismicity in Taiji coal mine till 1986, among them Ms≥1.0 mine seismicity for 4 times and Ms≥2.0 mine seismicity for 18 times. Based on microseismic monitoring, deformation observation and underground rock stress analysis for a few years, the characteristics of mine seismicity are shown as followed.

⑴The characteristics of mine seismicity are shallow focus and strong intensity. When Ms≥1.0, it can he felt in Taiji area. When 1.5<Ms<2.0, the buildings are damaged slightly. When Ms≥2.0, the buildings are damaged obviously both underground and ground.

⑵Compared with common earthquakes, there are many characteristics such as long period for seismic phase, surface wave development of short period and fast decay rate and so on.

⑶There is a close relation between mine seismicity and mining area. The investigation results show that about 70% mine seismicity with Ms ≥ 2.0 take place around the fault No.8-13. There is relative movement of both sides for fault and the direction of movement is towards gaft.

⑷There is a good relationship between mine seismicity and seismicity of outer area. When the frequency of regional seismic is increased, strain energy release of mine seismicity in the mining area is strengthened at the same time.

⑸Mine seismicity is constrained by regional seismic and its occurrence is periodicity. The probability of mine seismicity occurrence is high in March, April and August.

3 Geological and stress situation of mine seismicity occurrence

3.1 Geological situation

Beipiao coalfield is located in western Liaoning mountain area, where is located in the compound position of Tianshan-Yinshan structural belt and the second settlement belt of new cathaysian system. The subordinate tectonic is located in southeast of Heicheng-Kazuo depression area. Taiji mine is located in western coalfield. Faults from north to south such as Longtan fracture, Tayingzi fracture, Jinshanzi fracture, NanTianmen fracture and so on are showed as Figure 1. There are many characteristics for the faults such as similar trend, parallel arrangement, equidistant distribution, regional shear fracture and so on. Geological structure is relatively simple in Taiji area. Strike of coal measures are near EW, dip 50° -60° . There are many high angle faults, strike in the direction of NNE and NW, which divided the coal seam into many blocks with different length.

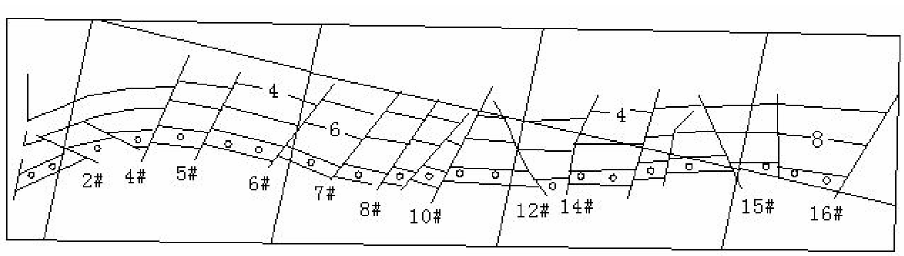

Figure 1 Geological structure in mining area

3.2 Actualities of the regional stress field

There were many changes in the process of geological history in Beipiao mining area according to the analysis of geological structure. At the beginning of the Jurassic Yanshan movement a series of coal basins were produced, strike in the direction of EW because of the strong pressure role in the direction of SN. During the middle Jurassic period, stress field is strengthened further. Until the late Jurassic, torsion in the direction of NS is appeared in addition the continuing stress in the direction of SN. Then, the direction of regional principal stress is changed gradually to NE.

In the level of -700m of Taiji mine rock stress is measured. The maximum principal stress is 53.5MPa in the direction of EW and nearly horizontal. The azimuth of the main axis is 84°, the dip 15°. In the level of -550m the observation results of deformation are showed in table 1. The distance between traverse points is compressed, which are cross the faults. The direction of traverse is almost EW in parallel to coal measures.

Table1. Compress quantity of distance

Number of traverse points	E3-E4	E2-E3	W8-W9	W10-W11	W13-W14
Number of fault	F13-1	F12	F8	F7	F6
compress quantity（mm）	-125	-81	-113	-52	-26

In short, it is stress in the direction from NE to NEE and nearly horizontal in the regional stress field.

3.3 Mining conditions and characteristics of rock

Compressive strength of coal seam in Taiji mine is 8.2-12.2MPa, shear strength 4.38-9.915Mpa. The roof and floor of coal seam are composed of coarse-grained sand or sandstone, compressive strength 49.9-105.2Mpa, and shear strength 37.9-80.4Mpa. The basement of coal measures is conglomerate layer with thick about 30-60m, compressive strength 36.9-83.3Mpa and shear strength 35.3-93.5MPa. Hydrogeological conditions are relatively simple. Both coal seam and strata of the roof and floor belong to poor water bearing layer. Current production level is -550m that is the vertical depth of 722m. Usually long wall and short wall hydraulic mining are adopted by mining methods. Roof management adopts natural subsidence method. The length of strike is from 200m to 400m with faults as the boundary of mining area.

4 Causes of mine seismicity

Many geologists and physicists believe earthquakes are induced by the release of stress energy suddenly which is accumulated in certain parts of the geological structure [3-4]. Mine seismicity activities in the Taiji area are frequent in a certain period and its occurrence echoes with seismicity in outer areas. Based on analysis of mechanism, mining conditions and other factors, the causes of mine seismicity in the Taiji area is shown as follows:

4.1 The main factor of mine seismicity----regional stress

Seismic geological data shows that pressure stress field is in the direction of NE in Northern China, with the axis of the principal compressive stress in the direction of NEE and the principal tensile stress in the direction of NNW is near horizon. The Taiji area is located in the north-east of Northern China. According to the measurement of rock stress and analysis of focal mechanism, the principal stress in the Taiji area is compressive stress in the direction of EW and near horizontal. This is opposite of the stress field in North China. It is the main factor of mine seismicity occurrence in mining area.

4.2 The factors of inducing mine seismicity-- mining and rock mechanical properties

The roof becomes gradually more coarse and thick from the east to west in the entirety of the mining area, which is almost composed of coarse-grained sandstone and conglomerate. Before mining, underground rock stress is in a balance. This stress balance is destroyed and the principal stress increases after mining. The minimum principal stress perpendicular to the strike of the coal seam is reduced. When the mining area is large enough and the minimum principal stress decreases to an certain extent, the rock is destroyed.

4.3 The condition of mine seismicity occurrence-- boundary of mining area ie faults

Damage occurs in the weak part of the rock, as does mine seismicity. Fault is the weak part of the rockmass. The floor of the coal seam moves to the goaf under the influence of exploitation. It affects the rockmass instability when exploitation of both sides is out of balance. The results show that mining activities are corresponding to mine seismicity in the Taiji coal mine.

Conclusions can be obtained as followed based on the analysis. Large stress is accumulated in the Taiji mining area under the role of the principal compressive stress field in the direction of NE and near horizonal. The original stress balance is destroyed and stress is redistributed under the influence of mining activities. Mine seismicity takes place when the stress redistribution reaches at ultimate strength of coal or rock which leads to the activation of faults and the release of accumulated energy in the form of seismic waves.

Acknowledgements:

The authors thanks for sustain from key Natural Science Fund of China (No:50434020); the National Natural Science Fund of China (No: 50874064；50804026) and Natural Science Fund of Shandong Province.

References

1. Mining bureau of Beipiao. Integrative Report of Characteristics and Laws of Mine Seismicity in Taiji. 1986.10.
2. Dong, R.S. Xu, Shijie. About Mine Seismicity-Take Taiji Coal Mine as an Example. Journal of Catastrophology. 1990(1). 65-66.
3. Song, J.S. Liu, D.Y. Wang.,E etc. Cause and mechanism of mine’s fault-type earthquake and its forecast. Mining Engineering. 2007, 5(3). 16-18.
4. Li, T. Cai., M.F. Cai., M. A Discussion on Classification of Mining-induced Seismicity. Chinese Journal of Rock Mechanics and Engineering. 2006.sup.2. 3679-3686.

RaSiM 7(2009): Controlling Seismic Hazard and
Sustainable Development of Deep Mines,
C.A. Tang(ed), Rinton Press, 347-352

SWALLOWTAIL CATASTROPHE MODELING OF THE INSTABILITY OF LAYERED ROCKS

TIAN-JUN ZHANG
College of Sciences, Xi'an University of Science and Technology
Xi'an, 710054, P.R. China

SHU-GANG LI
School of Energy, Xi'an University of Science and Technology
Xi'an, 710054, P.R. China

XING-HU ZHU
Dalian Mechsoft Co., Ltd
Dalian 116600, P.R. China

TIAN-CAI ZHANG
Xinjiang Oil Field Survey and Design Institute
Karamay 834000, P.R. China

A layered rock in underground works is simplified as a rectangular plate and the mechanical model of a rock plate simply supported on four sides is established based on the deformation and force features of the rock under practical engineering conditions. The mechanical mechanism of collapse of the rock plate under the combined action of in-plane stress, vertical stress and dynamic loads during production disturbance is studied using the catastrophe theory. The total potential function and the bifurcation-set equation are derived for the rock system when it undergoes swallowtail catastrophe. The study shows that the instability collapse of layered rocks in underground works under the combined action of in-plane stress, vertical stress and dynamic loads during production disturbance accords with the swallowtail catastrophe model. Ultimate frequency of catastrophe instability of rock plates is given in the paper, which has certain guiding significance in controlling rock collapse instability.

1 Introduction

Many rock structures in underground works, such as the ceiling, floor, and side plates of the mining tunnel, are sometimes more like plate structures. During mining production, dynamic loads can easily cause dynamic instability phenomena such as rock outburst, coal outburst, and coal and gas outburst in these structures. The changes in these dynamic instability phenomena are discontinuous. It is uniquely advantageous to study these phenomena by using catastrophe theory. For the past few years, Chinese scholars, Pan [1], Qin [2], Li [3] and Yin [4] have used catastrophe theory to study problems of rock mechanics, including rock outburst in underground tunnel, slope instability and rock failure process. In this paper, the dynamic loading action during mining production is taken into consideration and the swallowtail catastrophe model is used to regard the layered rock as rock plate. The instability characteristics of the layered rock which is under combined action of in-plane stress, vertical stress and dynamic loads during production disturbance are analyzed.

2 Geomechnical Model of Rock Plate

Based on the data observed on site, the layered rock is simplified as a plate model as shown in Figure 1. The coordinate system is indicated in the figure. For the sake of computing simplification, it is assumed that the rock plate has equal thickness. Let the thickness of the plate be *h*, the length along *x* axis be *a*, the width along *y* axis be *b*, the longitudinal load be *Px* and *Py* (horizontal geostress caused by rock deadweight and rock formation), the distribution intensity of the transverse load be *q*, and the modulus of elasticity of the plate be *E*. The upper and lower constraints of the bearing sides are regarded as simply supported constraints. Generally, the constraints of the bearing sides of rock are regarded as simply or fixedly supported constraints. When the bearing side is well bound with the surrounding rock, the constraint is considered fixedly supported; when the binding force is not strong, the constraint is considered simply supported. In this paper, the constraints of the bearing sides are regarded as simply supported constraints.

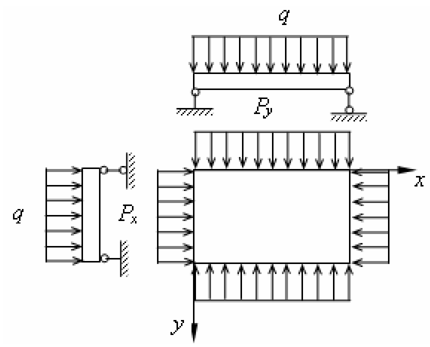

Figure 1 Rock plate mechanics model.

When the dynamic load during production disturbance is considered, the deflection equation of the rock plate can be expressed with the following trigonometric series [5]:

$$w = A\sin(\omega t + \varphi)\sin\left(\frac{\pi x}{a}\right)\sin\left(\frac{\pi y}{b}\right) \tag{1}$$

in which w is the deflection, A is the amplitude, ω is the frequency, and φ is the phase angle.

3 Potential Function of the System

The total potential V can be expressed as the combination of strain energy U and load potential of the structure:

$$V = U + \sum_{i=1}^{n} P_i \delta_i$$

in which P_i is the load acting on the structure, δ_i is the corresponding displacement, n is the number of loads. For the rock plate model in this study, the total potential of the system can be expressed as:

$$V = U - P\delta - \iint qw dx dy - E_k \tag{2}$$

in which P is the static load acting in the rock plate plane, q is the uniformly distributed load vertical to the rock plane, and E_k is the work done by the dynamic load.

When the thickness of the rock plate is between 1/5 and 1/8 of its width, it is regarded as thin plate. According to the bending theory of thin rock plate with small deflection, the deformation components $\varepsilon_z, \gamma_{yz}, \gamma_{zx}$ can be omitted, thus the deforming potential of the rock plate can be expressed as:

$$U = \frac{1}{2}\iiint\left(\sigma_x\varepsilon_x + \sigma_y\varepsilon_y + \tau_{xy}\gamma_{xy}\right)ds_x ds_y dz \tag{3}$$

in which ds_x, ds_y and dz are infinitesimal elements taken form the deformed rock plate. And among them, ds_x and ds_y are the infinitesimal arc length along the curvature lines on the equilibrium surface.

The strain components of the thin plate can be expressed with the deflection equation as

$$\varepsilon_x = \frac{\partial u}{\partial x} = -\frac{\partial^2 w}{\partial x^2}z, \varepsilon_y = \frac{\partial v}{\partial y} = -\frac{\partial^2 w}{\partial y^2}z, \gamma_{xy} = \frac{\partial v}{\partial x} + \frac{\partial u}{\partial y} = -2\frac{\partial^2 w}{\partial x \partial y}z \tag{4}$$

And the stress components of the rock plate can be expressed with the deflection equation as

$$\sigma_x = -\frac{Ez}{1-\mu^2}\left(\frac{\partial^2 w}{\partial x^2} + \mu\frac{\partial^2 w}{\partial y^2}\right), \sigma_y = -\frac{Ez}{1-\mu^2}\left(\frac{\partial^2 w}{\partial y^2} + \mu\frac{\partial^2 w}{\partial x^2}\right), \tau_{xy} = \tau_{yx} = -\frac{Ez}{1+\mu}\frac{\partial^2 w}{\partial x \partial y} \tag{5}$$

Substitute Equations (4) and (5) into Equation (3) and integrate z from $-t/2$ to $t/2$, the deforming potential can be expressed as

$$U = \frac{D}{2}\iint\left(\nabla^2 w\right)^2 ds_x ds_y - (1-\mu)D\iint\left[\frac{\partial^2 w}{\partial x^2}\frac{\partial^2 w}{\partial y^2} - \left(\frac{\partial^2 w}{\partial x \partial y}\right)^2\right]ds_x ds_y \tag{6}$$

in which $\nabla^2 = \frac{\partial^2}{\partial x^2} + \frac{\partial^2}{\partial y^2}$ and the bending stiffness of the thin plate $D = \frac{Et^3}{12\left(1-\mu^2\right)}$.

When the deflection of the rock plate is very small, the infinitesimal arc length along the axial directions can be approximately expressed with the deflection equation as

$$ds_x = \left[1 + \left(\frac{\partial w}{\partial x}\right)^2\right]^{\frac{1}{2}} dx, ds_y = \left[1 + \left(\frac{\partial w}{\partial y}\right)^2\right]^{\frac{1}{2}} dy \tag{7}$$

By Green formula and substituting Equation (7) into Equation (6), the following equation is obtained:

$$U = \frac{D}{2}\iint\left(\frac{\partial^2 w}{\partial x^2} + \frac{\partial^2 w}{\partial y^2}\right)^2\left[1 + \left(\frac{\partial w}{\partial x}\right)^2\right]^{\frac{1}{2}}\left[1 + \left(\frac{\partial w}{\partial y}\right)^2\right]^{\frac{1}{2}} dxdy \tag{8}$$

Taking the Taylor expansion of the integral function of Equation (8) and integrating it gives

$$U = \frac{D\pi^8 ab}{18}\left(\frac{1}{a^2} + \frac{1}{b^2}\right)^2 A^2 \sin^2\left(\omega t + \varphi\right) \tag{9}$$

The work done by the loads parallel with the plate plane during buckling process is

$$W_1 = \frac{1}{2}\iint\left[N_x\left\{\left[1 + \left(\frac{\partial w}{\partial x}\right)^2\right]^{\frac{1}{2}} - 1\right\} + N_y\left\{\left[1 + \left(\frac{\partial w}{\partial y}\right)^2\right]^{\frac{1}{2}} - 1\right\} - 2N_{xy}\frac{\partial w}{\partial x}\frac{\partial w}{\partial y}\right]dxdy \tag{10}$$

In Equation (10), replacing N_x with p_x , N_y with p_y , and N_{xy} with 0 results in

$$W_1 = P_x \int_0^a \int_0^b \left\{ \left[1 + \left(\frac{\partial w}{\partial x} \right)^2 \right]^{1/2} - 1 \right\} dxdy + P_y \int_0^a \int_0^b \left\{ \left[1 + \left(\frac{\partial w}{\partial y} \right)^2 \right]^{1/2} - 1 \right\} dxdy \tag{11}$$

The work done by the loads vertical to the plate plane is

$$W_2 = \iint qwds_x ds_y = \iint qA \sin(\omega t + \varphi) \sin\left(\frac{\pi x}{a} \right) \sin\left(\frac{\pi y}{b} \right) \left[1 + \left(\frac{\partial w}{\partial x} \right)^2 \right]^{\frac{1}{2}} \left[1 + \left(\frac{\partial w}{\partial y} \right)^2 \right]^{\frac{1}{2}} dxdy \tag{12}$$

Let the unit-area mass of rock plate be $\overline{m}$ (including the rock plate's own mass and the mass vibrating with the rock plate). The kinetic energy can be expressed as

$$E_k = \frac{1}{2} \iint \overline{m} \left(\frac{\partial w}{\partial t} \right)^2 dxdy \tag{13}$$

Integrating Equation (13) gives

$$E_k = \frac{\overline{m} ab\omega^2 \cos^2(\omega t + \varphi)}{8} A^2 \tag{14}$$

The total energy of the system is

$$V = U - W_1 - W_2 - E_k \tag{15}$$

After expanding Equations (11) and (12) with Taylor formula and truncating the fifth term, substitute Equations (9) and (14) into Equation (15). Let

$$m = \left(\frac{qa\pi^6}{4b^3} + \frac{12qa\pi^2}{b^3} + \frac{qb\pi^6}{4a^3} + \frac{12qb\pi^2}{a^3} - \frac{q\pi^6}{4ab} - \frac{2q\pi^2}{ab} - \frac{3qa\pi^4}{b^3} + \frac{3qb\pi^4}{a^3} \right) \sin^5(\omega t + \varphi)$$

$$p = \left(\frac{5qb\pi^4}{6a} - \frac{9qb\pi^2}{a} + \frac{5qa\pi^4}{6b} + \frac{28qa}{b} - \frac{9qa\pi^2}{b} \right) \sin^3(\omega t + \varphi)$$

$$r = \left[\frac{Dab\pi^8}{18} \left(\frac{1}{a^2} + \frac{1}{b^2} \right) - \left(\frac{P_x b\pi^2}{8a} + \frac{P_y a\pi^2}{8b} \right) \right] \sin^2(\omega t + \varphi) - \frac{\overline{m} ab\omega^2 \cos^2(\omega t + \varphi)}{8}$$

$$Z = -\frac{4qab}{\pi^2} \sin(\omega t + \varphi)$$

Then Equation (15) is reduced to

$$V = mA^5 + pA^3 + rA^2 + zA \tag{16}$$

Let

$$A = \sqrt[5]{\frac{1}{m}} x - k, u = p\left(\sqrt[5]{\frac{1}{m}} \right)^3, v = r\left(\sqrt[5]{\frac{1}{m}} \right)^2, o = z\sqrt[5]{\frac{1}{m}} \tag{17}$$

Then the expression of the system's total potential is reduced to a swallowtail catastrophe model, with u, v, and o as the control variables, with x as the state variable.

$$V(x) = x^5 + ux^3 + vx^2 + ox \tag{18}$$

Its phase space is composed of the state variable and the three control variables.
By $V'(x) = 0$, the equation of the equilibrium curve M is obtained:

$$V' = 5x^4 + 3ux^2 + 2vx + o = 0 \tag{19}$$

By $V''(x) = 0$, the cusp-set equation of the equilibrium curve M is obtained:

$$V'' = 20x^3 + 6ux + 2v = 0 \tag{20}$$

By eliminating x from Equations (19) and (20), the bifurcation-set equation is obtained. Under the combined action of in-plane stress, vertical stress and dynamic loads, points that meet Equation (20) form the swallowtail curve on the control surface, as shown in Figure 2. Therefore, for the established mechanics model of rock plate, the structure is unstable and can change suddenly from one state to another only when the in-plane stress, vertical stress and dynamic loads meet Equations (19) and (20). The bifurcation set of the rock plate system is shown in Figure 3. Where, (a) is the bifurcation-set section diagram when u is greater than 0; while (b) is the bifurcation-set section diagram when u is less than or equal to 0.

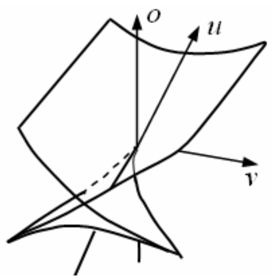

Figure 2 Bifurcation-set Diagram of swallowtail catastrophe model

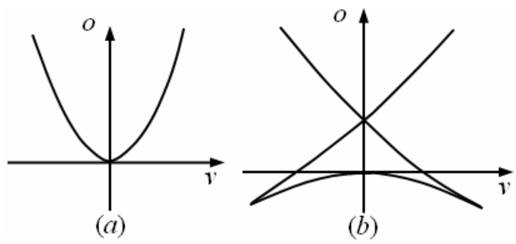

Figure 3 The section diagrams of bifurcation set

When the rock plate is in the state of plane equilibrium under the action of longitudinal loads in certain distribution manner, to determine whether the state is stable or not, it is only necessary to determine whether the equilibrium state resumes after the disturbance force is removed. Therefore, when the rock plate enters the bending state from the plane state, the work done by the longitudinal force is equal to the added deformation potential energy. So the limit load is

$$\frac{4D\pi^6}{9}\left(\frac{b}{a}+\frac{a}{b}\right)^2 = p_x b^2 + p_y a^2 \tag{21}$$

When the actual loads on the rock plate approach the limit load, the rock plate instability collapse is closely related with the frequency of the loads vertical to the plane.

By $\frac{\partial}{\partial A}(U - E_k) = 0$, the frequency when rock plate instability collapse occurs shall meet the following condition:

$$\frac{4D\pi^8}{9\overline{m}}\left(\frac{1}{a^2}+\frac{1}{b^2}\right)^2 = \omega^2 \cot^2(\omega t + \varphi) \tag{22}$$

From Reference [6], it is known that the intrinsic frequency is

$$\omega_0 = \frac{k}{a^2}\sqrt{\frac{gD}{q_i}} \tag{23}$$

in which, k is an dimensionless factor dependent on the rock side ratio a/b, g is the acceleration of gravity, and D is the bending stiffness of the rock plate.

By computing verification, it is found that the frequencies obtained from Equations (22) and (23) are basically the same, with a difference of 1%.

4 Conclusion

Layered rocks in underground works can be simplified as a rock plate model. The instability collapse of rocks under the action of in-plane stress, vertical stress and the dynamic loads during production disturbance can be explained with the swallowtail catastrophe model. The ultimate frequency of the rock plate instability given in the paper is very close to the intrinsic frequency of the rock plate. The result is instructive to efficient control of layered rock instability collapse.

Acknowledgements

The authors wish to acknowledge the funding support from the National Natural Science Foundation of China (50874089) and from the Special Scientific Research Foundation of Shanxi Education Department (08JK366).

References

1. Pan., Y. and Wang.,Z. Fold Catastrophe Model of Rock Outburst in Narrow Coal Pillar. Rock and Soil Mechanics, 2004, 25(1). 23-30.
2. Qin.,S. Jiao J. J. and Wang S. A Cusp Catastrophe Model of Instability of Slip-buckling Slope. International Rock Mechanics and Rock Engineering, 2001, 34(2). 119-134.
3. Li ., J.and Cao., P. Analysis of Pillar Stability in Hard Rock Mass by Longitudinal Splitting Based on Catastrophe Theory . Journal of Central South University of Science and Technology, 2006, 37(2). 371-375.
4. Yin., Y.and Du., Y. Swallowtail Catastrophe of Earthquake Process. Acta Seismologica Sinica, 1994, 16 (4). 416-422.
5. Xu., Z. Mechanics of Elasticity. Higher Education Publishing House. 2006.
6. Cao., G. Vibration of Elastic Rectangular Rock Plate. China Construction Publishing House. 1983

RaSiM 7(2009): Controlling Seismic Hazard and
Sustainable Development of Deep Mines,
C.A. Tang(ed), Rinton Press, 353-358

THE INFLUENCE OF ABNORMAL STRESS DISTRIBUTION ADJACENT TO ALTERATION ZONE ON ROCK BURST

LE-WEN ZHANG, DAO-HONG QIU, SHU-CAI LI and HUAI-FENG SUN

Geotechnical and Structural Engineering Research Center,

Shandong University, Jinan 250061, P.R.China

Normally, there is an abnormal stress distribution adjacent to alteration zone, and the abnormal stress distribution directly affects the stability of tunnel and the accident of rock burst when deep-buried tunnels cross the alteration zone. This paper studies the influence of alteration zone thickness and lateral pressure coefficient to abnormal stress distribution by systematic numerical simulation. Both test design method of orthogonal and uniform and finite difference method are applied to get regular results. Besides, take the actual tunnel engineering of Riverside Hydropower Station as an example to analyze the principal stress distribution near alteration zone and predict grading of the rock burst.

1 Introduction

After spending a long time in “three high stress and one disturbance” of complicated geomechanical environments, organization structure、basic behaviour characteristics and engineering responses of deep rock masses begin to take basic changes. This is also the fundamental reason leading to catastrophes that have occurred suddenly and on multiple occasions. Deep-buried long tunnels have the characteristics of long extension 、deep burial 、long construction period, and multiple engineering geology problems. These characteristics become the controlling works in numerous multi-linear constructions. As one of the major geological disasters of deep-buried long tunnels, rock bursts are caused mainly because excavation unloading leads to surrounding rock happening brittle failure and elastic strain energy stored in the rock mass is released suddenly, which eventually leads to phenomenon of burst, spilling, and ejection [1,2,3].

The recent study showed that there is usually abnormal ground stress in the vicinity of the alteration zone, and from the alteration zone a certain distance there is a zone which has an obvious increase in stress. The tunnel more than 700 meters depth has its ground stress near the high stress areas of alteration zone which usually forms a rock burst in this intensely increased area. Considering of a number of factors, a systematic study of deep tunnel and the abnormal stress areas distribution near alteration zone, it has enormous practical significance and value of engineering applications to determine the magnitude of stress increase, and analyze its effect on rock burst influences, thus ensuring tunnel excavation and security [4].

In this paper, we take the abnormal stress near alteration zone as well as tunnel stress fields influenced by alteration zone as the main simulation objects, through the numerical simulation test systems to study the influences of alteration zone thickness and side pressure coefficient to the abnormal distribution of power and its rockburst degrees. On the basis of the riverside hydropower station tunnel, this paper studies the influences of alteration zone to the distribution of ground stress and rockburst degrees, and draws some useful conclusions. They have played a guiding role to actual construction projects.

2 Quasi-three-dimensional numerical analysis of results

2.1 Numerical simulation program

In this paper, drawing up to calculate the regional rock check for 90m×60m; selecting 400m as rock depth. By using linear elastic rock model in numerical experiment to study effects of different side pressure coefficient of ground stress and different alteration zone thickness on initial rock stress field.

Table 1. 4 factors and 4 levels of numerical test

factors levels	angles of alteration zone S1	side pressure coefficient of ground stress S2	alteration zone thickness S3	Alteration zone length in the y-axis projection S4（m）
1	30°	0.5	1	30
2	45°	1.0	3	40
3	60°	1.5	6	45
4	75°	2.5	10	48

Based on the table 1 in different conditions, the 16 kinds of numerical experiments program in table 2 are obtained by the orthogonal experiments, applied software FLAC-3D to numerical simulation.

Table 2. Numerical test schemes

contions	1	2	3	4	5	6	7	8	9	10	11	12	13	14	15	16
S1	30°	30°	30°	30°	45°	45°	45°	45°	60°	60°	60°	60°	75°	75°	75°	75°
S2	0.5	1	1.5	2.5	0.5	1	1.5	2.5	0.5	1	1.5	2.5	0.5	1	1.5	2.5
S3	1	3	6	10	3	1	10	6	6	10	1	2	10	6	3	1
S4	30	40	45	48	48	45	40	30	40	30	48	45	45	48	30	40

2.2 typical working condition results

Figure 1 is the quasi-three-dimensional displacement diagram of working conditions S1 = 45, S2 = 0.5, S3 = 3, S4 = 45m, and the calculation results under other working conditions are basically the same as Figure 1, only values are different. From the figure we can see that the displacement of significant change in the region link up to form a quadrilateral of the diamond-shaped pattern.

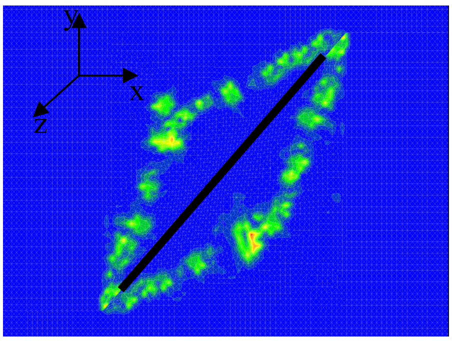

Figure 1 Displacement cloud picture

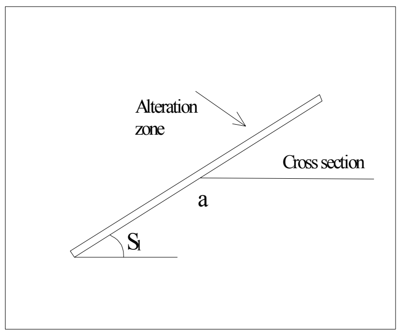

Figure 2 Research area diagram adjacent to alteration zone

At both ends of the alteration zone, the more near the alteration zone, the change is greater in its displacement. But the displacement near the central alteration zone does not change significantly. By comparison, a mutation occurred in a certain distance away from the alteration zone (diamond-shaped border). This is similar to the flow of fluid mechanics phenomenon, namely: in a given initial stress field the alteration zone has played a role in shielding discontinuity. The original uniform stress flow vector will deviate from the original straight-line path. However, bypassing the alteration zone, the disturbance became smaller. In the distant enough, the stress flow vector will then revert to the original uniform flow field [5].

2.3 The alteration zone thickness on the stress field change impact studies

Thickness are one of the major characteristics of alteration zone.The existing literature shows that in the different geological conditions , the thickness of alteration zone will be very different, maybe from a few meters to tens of meters. In this paper, we use less mechanical modules as its alteration zone or its filler when finite element mesh are subdivided to simulate and to study the influence of alteration zone thickness on the original rock stress field changes.

Representation working conditions S1 = 45, S2 = 2.5, S4 = 45m, under the condition of four different alteration zone thickness, the maximum principal stress value on profiles "a" of Figure 2 are shown in Figure 3.

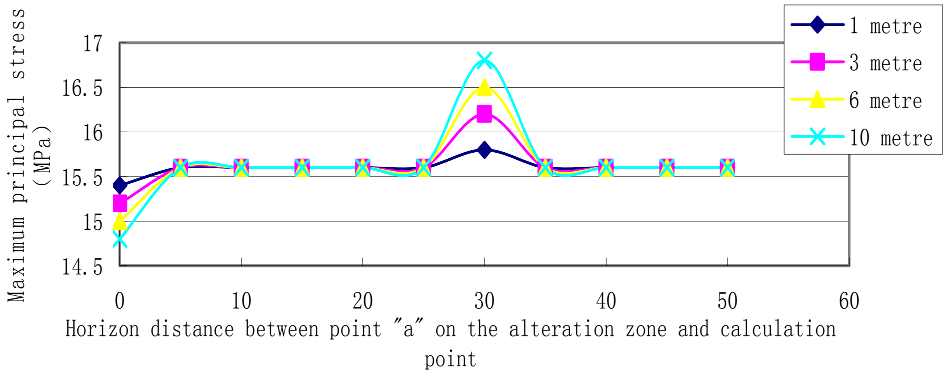

Figure 3 Variation of the maximum principal stress vs alteration zone thicknesses changes

As similar flow problem described in the previous section, in the alteration zone at 30m horizontal distance from point a, the stress difference has a larger mutation. Less than 5m, the stress difference that is close to the alteration zone is large as well. In a point (X =30): alteration zone compare with non-alteration zone of the largest 7.7% change. Because of the role of alteration zone, where X = 30 may form a distinct stress concentration zone, namely where X = 30 is that of a rock burst intensity enhanced area. And the thickness of alteration zone greater, the intensity of rockburst increase greater in amplitude.

2.4 Geostress lateral pressure coefficient λ of the stress field change impact studies

In the only self-weight stress field, on the basis of depth of underground caverns we can estimate initial stress field. However, according to the measured data at home and abroad, the majority of strata in the region there are horizontal structural(tectonic) stress, so that the level of stress σh is greater than the vertical stress σr. And maximum horizontal stress and vertical stress ratio, namely, lateral pressure coefficient λ, is generally 0.5-5.5. This section to develop lateral pressure coefficient λ 0.5,1.0,1.5,2.5 respectively for four. Studying four stress field in the vicinity of the alteration zone of the stress anomaly. Representation of condition S1 = 45 , S3=1m、S4 = 45m, under the condition of four different geostress lateral pressure coefficient, the maximum principal stress value on profiles "a" of Figure 2 are shown in Figure 4.

The line in this chart is stress difference on profiles "a" of Figure 2 when lateral pressure coefficient λ = 2.5. In a point (X =30): alteration zone compare with non-alteration zone of the largest 7.7% change. It can be seen that where the X = 30 also can form an obvious zone of stress concentration area under the above condition. Here is a rock burst intensity areas for rockburst region. The general law is that, when λ> 1.0, the greater of the lateral pressure coefficient, the intensity rockburst increase greater in amplitude.

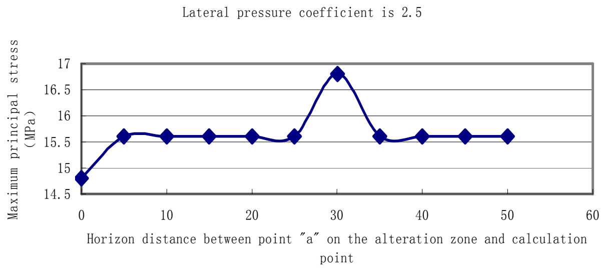

Figure 4 Variation of the maximum principal stress vs distance to alteration zone when λ= 2.5

3 Engineering application

3.1 Engineering situation

Riverside hydrodypower Station is located in the south-eastern part of Sichuan Province Ganzi Tibetan Autonomous Prefecture, located in Jiulong county level on the left bank of the Yalong River tributary river on the Jiulong River ,who is "one reservoir five stage" a finally stage to develop power plants. Hydrodypower Station use dam intake, mainly led by the Department of Buildings hub, water system and underground power house, etc. Total capacity of the hydrohydropower Station is 1,330,000 m^3, and the station installed capacity of 330MW is the second large-scale hydropower projects.

Water diversion system is mainly composed of water diversion tunnel, surge shaft at room, high-pressure pipelines, etc. Diversion tunnel is located on the left bank of Jiulong River. Diversion tunnel is from the intake to the surge shaft, hole-line length of about 8.5km, excavation diameter 8.4m, depth of tunnel 100 ~ 1694m. Diversion tunnel in upstream of Bailong Temple landslide has a buried depth of about 100 ~ 200m, while in downstream of Bailong Temple landslide has a larger buried depth of about 300~1694m. The entire depth of > 300m long hole above 4824m, the total length of 53%, which is deeply buried tunnel.

3.2 Finite element model

The impacts of alteration zone to the secondary stress field distribution under Riverside hydropower station tunnel excavation mainly achieve two categories. Firstly，analyzing the initial three-dimensional stress field around tunnel area, then based on the analysis of the initial stress field in three-dimensional calculation, further evaluating the secondary stress field of the environment under the conditions of the tunnel excavation, as part of the tunnel excavation rockburst forecast to meet the engineering requirements of the stress field of environmental information .

The three-dimensional analysis of the initial stress field of the tunnel area is mainly through the establishing the tunnel project area geomechanical model and the finite element numerical simulation to implement ,which based on studies of the tunnel project of regional geological conditions and the regional stress field investigations .

In the establishment of three-dimensional finite element model, in accordance with the right hand rule, YZ plane takes the plane that nearly perpendicular to the direction of the tunnel extension, and XY plane take the plane that parallel to the tunnel extends from the planar direction, Y direction is positive upward. The above selection of border computing model, both to enable the principal mechanical characteristics of the geological and topographical features are reflected in the calculation of results, and be able to ensure that sufficient calculation accuracy. In order to ensure accuracy and at the same time facilitate the division of units, the discretization of three-dimensional model used 10-node isoparametric tetrahedral units. In delineating the finite element mesh, using different accuracy of mesh: using a higher mesh density on the most affected region in the alteration zone ,while in the auxiliary calculation region using relatively lower mesh density [6,7,8].

3.3 The results of finite element analysis

From the calculation results we can see: the re-distribution of secondary stress field in surrounding rock is caused by the tunnel's excavation, cross-section of tunnel excavation in rock is all at state of compressive stress.

The results at home and abroad show that, there are many reasons to result in rockburst. The influencing factors include lithology, the initial stress state of the tunnel, depth, surface topography, excavation cross-section form and excavation methods, but among these factors, the formation lithologic conditions and the size of stress are two decisive factors generating rockburst. At the present stage rockburst stress criteria commonly used include Rb/σ1 criterion, Zhenyu Tao criterion and Luessen criterion, the criteria in Table 3.

Table 3. Stress criterion of rock burst

Criterion Type	Rb/σ1 criterion	Zhenyu Tao criterion Rc/σ1	Luessen criterionσθ/Rc
None rockburst	>6	>14.5	<0.2
Weak rockburst	3~6	14.5~5.5	0.2~03
Medium rockburst		5.5~2.5	0.3~0.55
Strong rockburst	<3	<2.5	>0.55

Note: σ1 for the maximum principal stress of rock; σθ for the tangential stress of rock; Rc for the uniaxial compressive strength of surrounding rock; Rb for saturated uniaxial compressive strength

It can be drawn from the above three stress criteria: there is closely relation between rockburst intensity and the size of surrounding rock stress after cavern excavation. For diversion tunnel of the Riverside hydropower Station, because lithology consistent and rock mechanics parameters on both sides of the alteration zone are basically the same, the surrounding rock stress situation in the tunnel are key factors that impact rockburst intensity after excavation. Therefore the degree of stress concentration plays a vital role on the occurrence of rock burst intensity.

Figure 5 is the maximum principal stress value of the arch crown.

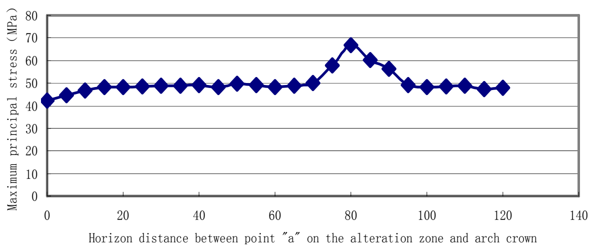

Figure 5 Variation of the maximum principal stress along the tunnel top arch

It can be drawn from Figure 5: the distribution of maximum principal stress in vault is similar to the stress distribution of quasi-three-dimensional "a" profile in above section. In area whose horizontal distance from the alteration zone around the 79m (ie, Figure 1 in the diamond-shaped border), the maximum principal stress shows greater mutation, which is in line with "flow around phenomenon" described in the previous section.

By the stress increasing to reach 36 percent, the maximum principal stress value reaches 68Mpa. From the judgement of the rock burst prediction given in front, we can conclude that the zone of high stress rock burst near the alteration zone has reached a strong rockburst degree.

Now current excavation has crossed the alteration zone. The actual situation of tunnel excavation shows that: strong rockburst happened in area which distances the alteration zone 80m away, rockburst duration of more than 12 hours. And it resulted in a 5×7×4.5m (L×W×H) explosion pit in the vault and spandrel department. It can be seen that the calculation results and the actual situation reach the basic agreement.

4 Conclusion

This paper uses the systematic analysis method by considering the key elements such as the alteration zone thickness and lateral pressure coefficient of ground stress to study the stress distribution anomaly near the alteration zone. Also, the paper analyzes rockburst in surrounding rock under an influence of the alteration zone. The following conclusions are found:

(1) In the quasi-three-dimensional calculations we only consider the influence of a single alteration zone structure. The maximum principal stress distribution near the middle of the alteration zone takes on a certain degree of volatility, and the stress mutation phenomenon happens in the area from alteration zone a certain amount of distance. Eventually stress shows the "flow around" phenomenon near the entire alteration zone, forming a particular form, which is a diamond-shaped area of stress concentration distribution.

(2)When other conditions are in the same circumstances, the greater the alteration zone thickness and the lateral stress coefficient, the sudden increase of amplitude in principal stress difference of specific parts is larger due to the impact of diamond stress concentration area.

(3)In three-dimensional finite element analysis of the Riverside hydropower station tunnel, the vault and spandrel of the tunnel under the influence of the alteration zone, the distribution of principal stress difference in a particular location happened the phenomenon of sudden increase, because of the impact of the diamond with stress concentration, thus increasing the intensity of rockburst.

Acknowledgements

The authors wish to acknowledge the collaborative funding support from the National Basic Research Program of China (NO: 2009CB724607) and Natural Science Foundation of Shandong Province (Y2007F53).

References

1. Jiang., F.Z. Xing.,X.D.. Zhu.,D.S.. The current status and developing tendency of rock blasting forecast at home and abroad[J]. Industrial Safety and Dust Control, 2003, 29(8). 19-22.
2. Xu.,S.D. Summary of Rock Explosion Prediction and Counter Measure, Northwest Water Power, 2005, 2(2). 14-17.
3. Xu., L.S. Wang., L.S.Li.., Y.L.. Study on mechanism and judgement of rockbursts, Rock and Soil Mechanics, 2002, 23(3), 300-303.
4. Zhou., P.Wu., J.M.Sun.,Y.H. etc. Forecast of Rockburst and Analysis of the Influence Factors, hongshuiriver[J], 2004, (1).71-74.
5. Zhu.,W.S..Ruan.,Y.S. Li.,X.J. etc. Abnorma Stress Distribution Adjacent to a Fault and it's Influence on Stability of Tunnel[J], Chinese Journal of Underground Space and Engineering, 2008, 4(4). 685-689.
6. Deng.,J. Zhu.,H.H. Ding.,W.Q. Finite element simulation of whole excavation operation of a unequal-span double-arch tunnel[J]. Rock and Soil Mechanics, 2004, 25(3). 476-480.
7. Wang., X.Q. Yang.,L.D. Gao.W.H. Dynamic monitoring and FEM simulation analysis of an expressway tunnel with unsymmetrical loadings[J]. Chinese Journal of Rock Mechanics and Engineering, 2005, 24(2). 284-289.
8. Tang., J.P. Pan.,Y.S. Li.,Y.J. Numerical simulation of deep-level rokcburst in Fuxin coalfield[J]. Journal of Coal Science & Engineering (China), 2005, 11(1). 13-16.

RaSiM 7(2009): Controlling Seismic Hazard and
Sustainable Development of Deep Mines,
C.A. Tang(ed), Rinton Press, 359-364

SYNERGETIC EFFECT AND VISIBLE SIMULATION ON AE IN ROCK MASS FAILURE PROCESS

GUANG-MING YU

Qingdao Technological University

Qingdao, 266033, P.R. China

CHUN-AN TANG

Center for Rock Instability and Seismicity Research, Dalian University of Technology

Dalian, 116024, P.R. China

YONG-ZHAN PAN

Qingdao Technological University, Qingdao, 266033, P.R. China

Henan University of Science and Technology, Luoyang, 471003, P.R. China

GUO-YAN WANG

Qingdao Technological University, Qingdao, 266033, P.R. China

Liaoning Technical University, Fuxin, 123000, P.R. China

CHANG-FENG YUAN

Qingdao Technological University, Qingdao, 266033, P.R. China

AE is an indicator of rock mass fracturing. Synergetics is used to study the AE characteristics in the rock mass fracturing process. The laws of rock mass fracture are further studied through the relationship between AE and damage evolution. AE count rate is taken as the order parameter to study the rock mass failure process. Firstly, the evolutionequation of the AE order parameter is established according to the relationship of AE and damage. Secondly, solutions of stationary state and nonstationary state are obtained and analyzed. The synergetic characteristics of AE are described in generalities. At last, the AE phenomena of rock mass break is simulated with the RFPA software. The synergetic effects of rock mass AE are verified through numerical simulation. The suitability of the AE technique for rock damage process analysis was further demonstrated.

1 Introduction

Acoustic Emission, shortened to AE， is a natural phenomenon describing the partial release of strain energy with elastic waves when deformation or damage occurs in materials or structure (Ji, 2004). AE technology is successfully applied in many fields such as: material engineering, pressure container evaluation, and structural integrity evaluation.

Since 1959, AE technique is used as a nondestructive, non-contact, and real-time technique to study the progressive damage processes and failure mechanisms of rock mass subjected to given load. Experimental studies showed that the AE phenomena might be generated from crystal dislocation, crystal slipping, generation and expansion of cracks. AE signals are affected by many dynamic and static factors; such as material feature, deformation characteristic, and damage propagation, etc. Therefore, AE signals are very complicated and difficult to recognize and quantify. Now applications of AE technique in rock mass failure progress are restricted and limited. New theories and methods are necessary to introduce and study AE laws of rock mass.

Modern nonlinear science offers new points of view to the study of rock mass AE. Hirata (1987) pointed out the fractal characteristics and dimensions of AE changed with stress and deformation during the rock failure progress, Xie (1997) analyzed the mutation phenomenon during rock mass damage, and Yu (2004) studied the chaos effect of cracks evolution in rock mass, etc.

In this paper, synergetics is used to explore the study of rock mass AE laws while AE laws of rock mass are simulated visibly with RFPA to verify the theoretical results.

2 Synergetics description of rock mass AE

2.1 Relationship between AE parameter and damage evolvement of rock mass

Qin (1992) pointed out that sum of AE counts in the plastic deformation is

$$N = A'\left[\left(\frac{K}{K_c}\right)^{4m} \bullet \left(\frac{\ln K - \ln K_c}{4m} - \frac{1}{16m^2}\right) + \frac{1}{16m^2}\right] \tag{1}$$

Where $A^{/}$ is a constant; m is a parameter about material characteristic and experiment condition; K is stress intensity factor; and Kc is the critical stress intensity factor.

From equation (1), when material characteristic and experiment condition are fixed, more cracks means more AE counts, and most AE counts occur during the cracks expansion.

Qin (1993) pointed out that in the course of microcracks generation and propagation, the relationship between AE counts and the expansion of crack is as follows:

$$\frac{d\varphi}{dt} = \xi \frac{dl}{dt} \tag{2}$$

Where $d\phi / dt$ is AE rate, ξ is a parameter decided by material characteristic and experiment condition. dl/dt is crack expansion speed.

As above-mentioned, most AE signals generate from the dehiscence and expansion of microcracks. AE parameters change with the evolution of damage in the rock mass.

2.2 Evolvement equation of AE order parameter of rock mass

2.2.1 Selection of order parameters

There are many parameters describing rock mass AE. Two main kinds of change rates are used to study AE signals changes in the rock mass failure process. One is AE count rate N_0, which means the sum of AE signals in a stated time. The other is AE count rate of large-scale N_b, which means the sum of AE signals of large-scale in a stated time. N_0 is corresponding with crack enlarging and N_b is corresponding with large-scale cracks enlarging. It is obvious that AE signals changes with the expansion of cracks. So N_0 and N_b can be as order parameters describing the damage process of rock mass.

2.2.2 Deduction of main equation of order parameters evolution

Harkris (1963) pointed out that the increment rate of bifurcation counts of crack expansion is proportional to the square of original large-scale counts. So the equation of large-scale counts can be showed as follows:

$$\frac{dN_0}{dt} = (-r_0 + i_0)N_0 + \alpha_0 N_b^2 \tag{3}$$

Where r0 is attenuation coefficient of N0, i0 is increment coefficient of N0. Both of them are positive numbers. And a0 is relevant coefficient associated with the influence of large-scale AE signals.

Evolvement equation of Nb in view of the influence of N0 can be shown as follows:

$$\frac{dN_b}{dt} = \left(-r_b + i_b\right)N_b + \alpha_b N_o \tag{4}$$

The meaning of every coefficient is just as above. Supposing that large-scale AE signals increment rate is proportional to the AE counts.

Based on the two equations and using method of thermal insulation elimination, the main equation of order parameter N0 can be obtained.

Supposing

$$\frac{dN_b}{dt} = 0 \tag{5}$$

Substituting it into Eq. (4), we can get

$$N_b = \frac{\alpha_b}{i_b - r_b} N_o \tag{6}$$

Substituting Eq. (6) into Eq. (3), we can get main equation of the order parameter as follows:

$$\frac{dN_o}{dt} = mN_o + nN_o{}^2 \tag{7}$$

Where m=i0-r0 and $n = \frac{\alpha_0 \alpha_b^2}{(i_b - r_b)^2}$

2.2.3 Analysis of main equation of order parameters evolution

2.2.3.1 Steady-state solutions and stability analysis

In Eq. (7), supposing

$$\frac{dN_0}{dt} = 0 \tag{8}$$

Two steady-state solutions can be obtained as follows:

$$N_{01} = 0 \tag{9}$$

$$N_{02} = -\frac{m}{n} \tag{10}$$

N_{01} is the AE counts of rock mass without loads, so it is a steady-state solution about the equilibrium condition obviously.

The linear stability of N_{02} can be analyzed with perturation method, supposing δ is the infinitesimal disturbance, namely

$$N = N_{02} + \delta \tag{11}$$

and

$$\left|\frac{\delta}{N_0}\right| << 1 \tag{12}$$

Substitute Eq. (11) into Eq. (7) and omit the differential quadratic term of δ ,

$$\frac{d\delta}{dt} = -m\delta \tag{13}$$

Then we get

$$\delta(t) = \delta(0)e^{-mt} \tag{14}$$

Where $\delta(0)$ is initial disturbance.

It is known from Eq. (7) that stability of N_{02} depends on notation of m. If *m* is positive number, steady state solutions of equation (14) are stable. Namely, when rate of increase of AE event is over its decrement, the order of AE signals is stable. As the same way, if m is negative number, the steady state solutions are unstable, and the order of AE signals is stable.

2.2.3.2 Nonstationary state solutions and stability analysis

Nonstationary-state solution of Eq. (7) is

$$N_o(t) = \frac{1}{k_1 + k_2 e^{-mt}} \tag{15}$$

Where, $k_1 = -\frac{m}{n}$, $k_2 = \frac{1}{N_o(0)} + \frac{n}{m}$, $N_o(0)$ N0(0) is the initial value of order parameter under certain condition.

When m is positive number, namely i_0 is over r_0, increment coefficient of AE event is over its decrement coefficient. It happens during the cracks progressive expansion in the early stage of load. In this course, AE counts rate increases gradually with the load growth.

When m is equal to zero, the AE counts rate keeps relative stable and the AE change rate is at the critical condition. And main equation of order parameters is

$$\frac{dN_o}{dt} = nN_o{}^2 \tag{16}$$

Then we get

$$N_o(t) = \frac{N_o(0)}{1 - N_o(0)nt} \tag{17}$$

Where $N_0(t)$ is the initial value of the AE counts rate corresponding to the critical condition. During this stage, if *n* is less than zero, namely α_o is less than zero, the order parameter of $N_0(t)$ will decrease as time increase. For the system of rock mass, the inner stresses redistribute with the frequent big break events, and AE counts in the unit time decrease. If n is over zero, the order parameter of $N_0(t)$ will increase gradually with time increment. Once the value of $N_0(0)nt$ decreased to 1, AE counts in the unit time will approach to infinite, and the system catastrophe will happen. When m is less than zero, namely i_0 is less than r_0, increment coefficient of AE event is less than its decrement coefficient. From Eq. (16) we see that AE counts rate decreases gradually with the load growth.

3 Synergetics description to AE of rock mass fracture process

AE phenomena of rock mass can be described as follows: in the early stage of loading, original and new cracks extend gradually, and AE counts increase steadily with time increasing. When load increased to certain value, all kinds of cracks extend rapidly and AE counts increase fast. During the stage, rock mass catastrophe will happen with the discontinuous damage. After this failure process, stresses in rock mass redistribute and the speed of cracks expansion decrease to another stable value. The AE counts decrease correspondingly. Then with load increasing, a new cycle begins as above. So, the AE counts change laws can be generalized to the cycle of relatively steady increasing, catastrophe, attenuation, relatively steady increasing and catastrophe. It is found that AE counts are mainly increasing before the yield strength of rock mass and AE counts are mainly decreasing after the yield strength of rock mass.

4 Numerical simulation of rock mass AE

Damage processes of rock mass are simulated with the software of RFPA. The loading is controlled by displacement. The size of sample is 150 mm×150 mm. Poisson's ratio is 0.2. The compression strength is 30 Mpa and Young's modulus is 30000Mpa, every step of loading is 0.001 mm. The results of simulation are shown as Fig.1 to Fig.6.

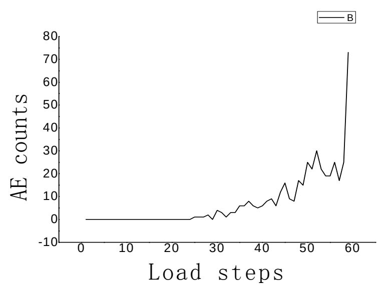

Fig.1 AE counts of step 1-59

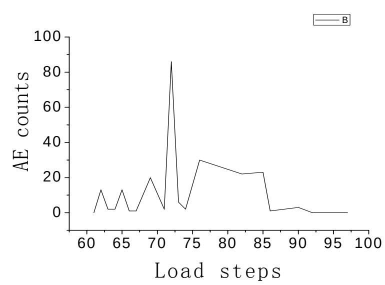

Fig.2 AE counts of step 61-97

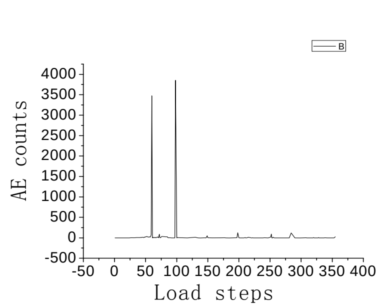

Fig.3 AE counts of the entire course

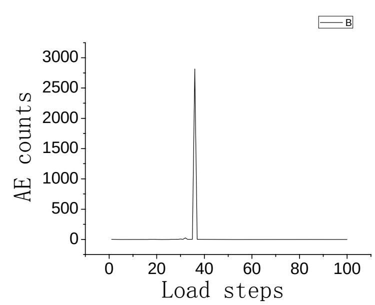

Fig.4 AE counts of step 60 (magnified 100 times)

Fig.1 shows the AE counts change trend of step 1-59. AE counts are zero at the beginning of loading. Before the critical value, the fracture intensity factors of original cracks increase progressively along with load increasing. Then with the load increasing, existing cracks extended rapidly and the AE counts are mainly increasing. Along with every big fracture, the stresses redistributed and the AE counts decreased in the following short stage. Fig.2 shows the AE counts change trend of step 61-97. The sample fractured at step 60. From step 61 to step 65, the cracks extended rapidly and AE counts fluctuated in wide range. With the load increasing, the sample fractured again at step 73. AE counts decreased fast in large range. Then AE counts are mainly decreasing till the load end. Fig.3 show the changing AE counts of the entire course. The catastrophe characteristic in the damage process is that the AE rate maximum at the failure is bigger than other's in large scale. When the load approached to maximum, AE counts increase rapidly and reached the maximum in very short time. AE counts decreased fast along with the sample catastrophe. Then the AE rate began to increase progressively till next catastrophe. Fig.4 is AE counts of step 60 magnified by 100 times. It has the same characteristic with Fig.3 obviously. Fig.5 and Fig.6 are stress maps of steps before and after the sample catastrophe respectively. Although the strain difference of both steps is less than 7×10^{-6}, the catastrophe took place. The simulated results are accordant with the theoretical solutions with synergetics. From Fig.4 and Fig.5, we can see that AE rate change law of every little fracture is similar to the one of catastrophe. Also, the AE rate scale is invariant at the critical point of catastrophe.

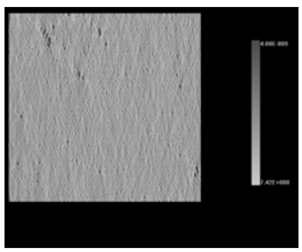

Fig.5 Stress map of step 59

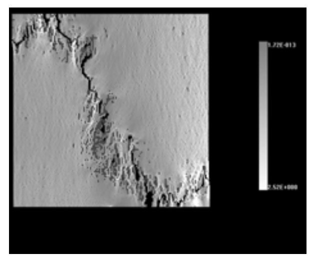

Fig.6 Stress map of step 60

5 Conclusions

AE technique is a nondestructive, non-contact and real-time technique used broadly in rock and soil engineering. For the first time, synergetics is used for exploratory study of rock mass AE laws. AE laws of rock mass are simulated with RFPA to verify the theoretical results. The research results do not only have theoretical value for understanding the AE laws of the rock mass damage process, but also practical meanings for application of AE technique in rock and soil engineering.

Acknowledgement

The authors are very thankful for support from the Natural Science Key Fund of China (No.50434020), Natural Science Fund of China (No. 50874064, 50804026) and Natural Science Key Fund of Shandong Province.

References

1. Ji, H.G. Study and application of AE of rock mass material. Beijing: Coal Industry Press, 2004.
2. Takayuki H. Fractal Structure and Spatial Distribution of Micro-fracturing in Rock. Geophysics J.R. 1987, 90: 23-29.
3. Xie, H.P. Fractal rock mechanics. Beijing: Science Press, 1997.
4. Yu, G.M., Dong, C.S. and Pan, Y.Z. Fractal characteristic and chaos effect of rock mass cracks. Transaction of Qingdao Institite of Architecture and Engineering, 2004, 1: 1-6.
5. Qin, S.Q. Study and application of AE of rock. Shenyang: Northeast University, 1992.
6. Qin, S.Q. Basis of rock AE. Chengdu: Press of Southwest Traffic University, 1993.
7. Harkris, T.E. The theory of branching process. New York, Springer, 1963.
8. Tan, Y.L., Wang, Y.J. and Zhu, F.S. Study of self-organization of overburden activity. Transaction of rock mechanics and engineering, 1997, 16(3): 258-265.

RaSiM 7(2009): Controlling Seismic Hazard and
Sustainable Development of Deep Mines,
C.A. Tang(ed), Rinton Press, 365-370

MODEL FOR ROCK-CONCRETE-LIKE MATERIAL CRACKING DUE TO CORROSION EXPANSION OF REBAR AND UNIFORM SHEAR AT INFINITY

MING-BIN WANG[a,b]

[a]*School of Science, Shandong Jianzhu University*
Jinan, 250101, P.R. China
[b]*Research Center of Geotechnical and Structural Engineering , Shandong University*
Jinan, 250061 , P.R. China
morganwmb@sdjzu.edu.cn

SHU-CAI LI

Research Center of Geotechnical and Structural Engineering ,Shandong University
Jinan, 250061 , P.R. China

XU YANG

School of Science, Shandong Jianzhu University
Jinan, 250101, P.R. China
yangxu@sdjzu.edu.cn

The failure mechanism of rock-concrete-like material due to rebar corrosion and uniform shear at infinity is investigated. Based on the series expansion technology in the complex potential theory established by Muskhelishvili, the complex stress functions can be established. Then, in conjunction with the principle of superposition, the expression of tangential stress in rock-concrete-like material may be analytically deduced. Furthermore, by considering Faraday's equation, the equation of the time of rock-concrete-like material cracking due to rebar corrosion under transverse seismic response is obtained. It is found that the applied shear at infinity may accelerate the initiation of cracks. The existence of corrosion product can change the location of cracking. The ratio of the shear modulus between the reinforced bar and the rock-concrete-like material has little effect on the initiation of cracking. The possibility of rock-concrete-like material cracking increases with the increase of the relative corrosion depth.

1 Introduction

Corrosion of reinforced bar in rock-concrete-like material has been identified as being one of the most predominant factors responsible for the deterioration of the engineering structures. The serviceability and the durability of the engineering structures can be seriously affected by the rebar corrosion. It is found that the damage to the rock-concrete-like material due to rebar corrosion is in the form of expansion, cracking and eventually the spalling of the concrete cover [1]. Ohtsu and Yosimura [2] analyzed the crack propagation and crack initiation due to the rebar corrosion based on the concept of the linear elastic fracture mechanics and the boundary element method (BEM); Du [3] showed a finite element model to analyze the effect of corroding rebar on the surrounding concrete, then the model was applied to explore the effect of rebar radial expansion, due to the formation of corrosion product, on the cracking of concrete cover. The non-linear analysis of concrete cover requirement for FRP (fiber reinforced polymer) reinforced members subjected to high temperatures ranging from 20°C to 100°C was discussed[4]. At the same time, some useful analytical models have also been introduced to predict the time of cover cracking. Bhargavaa et al. [5-6] presented a mathematical model to predict the time required for cover cracking and the loss weight of corrosion of reinforced bars in corrosion affected reinforced concrete structures; Wang and Liu [7-8] proposed a simple analytical model to demonstrate the effect of the rebar corrosion on reduction of the bond strength. Piltner and Monteiro [9] presented a 2-D model to analyze the expansive reaction in concrete by using the theory of complex potentials established by Muskhelishvili[10]. A mathematical model that predicts the time from corrosion initiation to corrosion cracking was presented [11]. However, the applied stresses at infinity in the aforementioned literatures weren't almost considered. A number of experimental studies have been extensively done to investigate the radial expansion of corroded reinforcement and its effects on engineering structures [12-17].

In view of the aforementioned discussion it becomes necessary to determine the effect of rebar corrosion on structural stability. However, the foretime references modeled the effect of the corrosion expansion by prescribing a uniform radial displacement and assumed the stresses at infinity were zero, i.e., there was no influence from boundaries at a finite distance, apparently, the assumption may not be realistic for some problems. In order to examine the influence of uniform stresses at infinity on the crack initiation, the action of corrosion expansion and loading at infinity on the rock-concrete-like material cracking are both considered in the paper. By using Muskhelishvili's method and in conjunction with the Faraday's equation to predict when cracking will occur as a result of corrosion expansion and uniform shear at infinity in rock-concrtet-like material structures. The effects of the loading at infinity, the ratio between rebar and surrounding rock-concrete-like material and the corrosion penetration on the initiation of crack are discussed.

2 Method of solution

Assuming uniform corrosion on the surface of rebar and uniform shear at infinity, the current problem is modeled with reference to figure 1 and a rebar of radius r_1 is surrounded by reaction product. The boundary between reaction product and rock-concrete-like material lies on $r=r_2$. The x- and y-axes are taken with their origin at the center of the rebar, and the structure is subjected to uniform shear τ_0 at infinity. The domains of the rebar, corrosion product and rock-concrete-like material are denoted by index 1, 2 and 3, respectively.

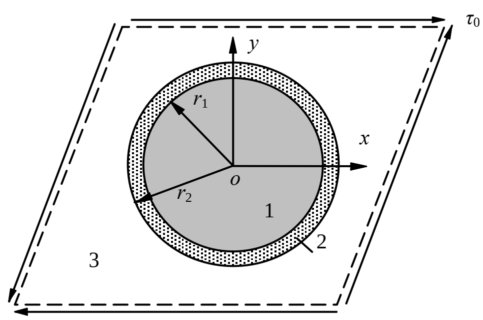

Figure1 Model used to estimate the stresses under the action of corrosion expansion and uniform shear at infinity.

For the plane problem shown in Figure1, all the physical quantities are expressed in terms of two complex potentials $\varphi(z)$, $\psi(z)$ and their derivatives, where $z=x+\mathrm{i}y$.

$$\sigma_\theta + \sigma_r = 2[\varphi'(z) + \overline{\varphi'(z)}] \tag{1}$$

$$\sigma_\theta - \sigma_r + 2\mathrm{i}\,\tau_{r\theta} = 2\,\mathrm{e}^{2\mathrm{i}\theta}[\bar{z}\varphi''(z) + \psi'(z)] \tag{2}$$

$$F_x + \mathrm{i}\,F_y = -\mathrm{i}[\varphi(z) + z\overline{\varphi'(z)} + \overline{\psi(z)}] + (\text{an arbitrary constant}) \tag{3}$$

$$2G(u_r + \mathrm{i}\,u_\theta) = \mathrm{e}^{-\mathrm{i}\theta}[\kappa\varphi(z) - z\overline{\varphi'(z)} - \overline{\psi(z)}] + (\text{an arbitrary constant}) \tag{4}$$

$$\kappa = (3-\gamma)/(1+\gamma)\ (\text{plane stress}),\quad \kappa = (3-4\gamma)\ (\text{plane strain}) \tag{5}$$

Firstly, only the expansive reactions are considered [9]. It is assumed that as a result of the expansive reactions, radius r_2 expands uniformly with $u_r(r=r_2)=\bar{u}_{r2,3}$. The two complex functions in domain 3 yield

$$\varphi_3^1(z) = 0\,,\quad \psi_3^1(z) = bz^{-1} \tag{6}$$

where b is real. From the boundary condition, the expression of b results in, $b=-2G_3r_2\bar{u}_{r2,3}$. Moreover, the hoop stress in domain 3 due to the boundary at $r=r_2$ yields

$$\sigma_{3\theta}^1 = -b\big/r^2 = 2G_3\bar{u}_{r2,3}\big/r^2 \tag{7}$$

Next, let's only consider the action of uniform shear at infinity, and then the stress potentials φ_1^2(z), ψ_1^2(z), φ_2^2(z), ψ_2^2(z), and φ_3^2(z), ψ_3^2(z) for domains 1, 2 and 3 in proper forms are written as:

$$\varphi_1^2(z) = \sum_{n=0}^{\infty} k_{2n} z^{2n+1}\,,\quad \psi_1^2(z) = \sum_{n=0}^{\infty} l_{2n} z^{2n+1} \tag{8}$$

$$\varphi_2^2(z) = \sum_{n=0}^{\infty} (W_{2n} z^{2n+1} + V_{2n} z^{-(2n+1)})\,,\quad \psi_2^2(z) = \sum_{n=0}^{\infty} (Q_{2n} z^{2n+1} + R_{2n} z^{-(2n+1)}) \tag{9}$$

$$\varphi_3^2(z) = \sum_{n=0}^{\infty} (K_{2n} z^{2n+1} + F_{2n} z^{-(2n+1)})\,,\quad \psi_3^2(z) = \sum_{n=0}^{\infty} (L_{2n} z^{2n+1} + H_{2n} z^{-(2n+1)}) \tag{10}$$

The above expressions must satisfy the continuity conditions, that is

$$\left.\begin{aligned} F_{1y} + \mathrm{i}\,F_{1x} &= F_{2y} + \mathrm{i}\,F_{2x} \\ u_{1x} + \mathrm{i}\,u_{1y} &= u_{2x} + \mathrm{i}\,u_{2y} \end{aligned}\right\} \text{when } |z| = r_1\,,\quad \left.\begin{aligned} F_{2y} + \mathrm{i}\,F_{2x} &= F_{3y} + \mathrm{i}\,F_{3x} \\ u_{2x} + \mathrm{i}\,u_{2y} &= u_{3x} + \mathrm{i}\,u_{3y} \end{aligned}\right\} \text{when } |z| = r_2 \tag{11}$$

Substituting Eqs.(8)-(10) into Eq.(11), and noting the stress state at infinity, the following equations are derived:

$$K_{2(n-1)} = L_{2n} = l_{2n} = V_{2n} = F_{2n} = Q_{2n} = H_{2(n+1)} = W_{2(n+1)} = R_{2(n+1)} = k_{2(n+1)} = 0 \ (n \ge 1) \tag{12}$$

$$L_0 = \mathrm{i}\,\tau_0\,,\ \mathrm{Im}W_2 = -\frac{a_2a_5\,\mathrm{Im}L_0}{a_1a_4 - a_2a_3}\,,\ \mathrm{Im}V_0 = -\frac{a_1a_5\,\mathrm{Im}L_0}{a_1a_4 - a_2a_3}\,,\ \mathrm{Im}Q_0 = [\frac{(\kappa_2\,G_1/G_2+1)r_1^{-2}a_1a_5}{(G_1/G_2-1)(a_1a_4-a_2a_3)} + \frac{3a_2a_5r_1^2}{a_1a_4-a_2a_3}]\mathrm{Im}L_0 \tag{13}$$

$$\mathrm{Im}\,R_2 = [\frac{(\kappa_2\,G_1/G_2 - \kappa_1)r_1^{-2}a_3a_7}{(G_1/G_2+\kappa_1)(a_3a_6 - a_4a_5)} - \frac{a_1a_5r_1^2}{a_1a_4 - a_2a_3}]\,\mathrm{Im}\,L_0\,,\ \mathrm{Im}k_2 = -\frac{G_1/G_2\,(1+\kappa_2)a_2a_5}{(G_1/G_2+\kappa_1)(a_1a_4 - a_2a_3)}\,\mathrm{Im}L_0 \tag{14}$$

$$\mathrm{Im}\,l_0 = [\frac{a_1a_5r_1^{-2}}{G_1/G_2 - 1} + \frac{3a_2a_5r_1^2}{G_1/G_2 + \kappa_1}]\frac{(1+\kappa_2)\,G_1/G_2}{a_1a_4 - a_2a_3}\,\mathrm{Im}\,L_0 \tag{15}$$

$$\mathrm{Im}\ F_0 = -[1 + \frac{(\kappa_2G_1/G_2+1)r_1^{-2}r_2^2}{G_1/G_2 - 1}]\frac{a_1a_5\ \mathrm{Im}\ L_0}{a_1a_4 + a_2a_3} + 3(r_2^4 - r_1^2r_2^2)\frac{a_2a_5\ \mathrm{Im}\ L_0}{a_1a_4 - a_2a_3} + r_2^2\ \mathrm{Im}\ L_0 \tag{16}$$

$$\mathrm{Im}H_2 = -[r_2^4(3r_1^2 - 4r_2^2) - \frac{(\kappa_2G_1/G_2-\kappa_1)r_1^6}{G_1/G_2+\kappa_1}]\frac{a_2a_5\,\mathrm{Im}L_0}{a_1a_4-a_2a_3} - [r_1^2 + \frac{(\kappa_2G_1/G_2+1)r_1^{-2}r_2^4}{G_1/G_2-1}]\frac{a_1a_5\,\mathrm{Im}L_0}{a_1a_4-a_2a_3} + r_2^4\,\mathrm{Im}L_0 \tag{17}$$

$$W_0 = R_0 = k_0 = H_0 = 0\,,\ \mathrm{Re}W_2 = \mathrm{Re}V_0 = \mathrm{Re}Q_0 = \mathrm{Re}R_2 = \mathrm{Re}k_2 = \mathrm{Re}l_0 = \mathrm{Re}F_0 = \mathrm{Re}H_2 = 0 \tag{18}$$

where, $a_1 = (\kappa_2\ G_1/G_2 - \kappa_1)(G_3/G_2 - 1)r_1^3r_2^{-3} - (G_3/G_2\ \kappa_2 + 1)(G_1/G_2 + \kappa_1)r_2^3r_1^{-3}$,

$a_2 = (G_1/G_2 + \kappa_1)(G_3/G_2 - 1)r_1^{-1}r_2^{-3} - (G_3/G_2 + 1)(G_1/G_2 + \kappa_1)r_2^{-1}r_1^{-3}$,

$a_3 = -3(G_1/G_2 - 1)(G_3/G_2 + \kappa_3)r_1^3r_2 - (G_3/G_2 + \kappa_3)(G_1/G_2 - 1)r_2^3r_1$

$a_4 = (G_1/G_2\ \kappa_2 + 1)(G_3/G_2 + \kappa_3)r_1^{-1}r_2 - (\kappa_2\ G_3/G_2 - \kappa_3)(G_1/G_2 - 1)r_2^{-1}r_1$, $a_5 = (G_1/G_2 - 1)(\kappa_3 + 1)r_1r_2$

The hoop stresses in the surrounding rock-concrete-like material may be written as follows

$$\sigma_{\theta 3}^2 = -(\mathrm{Im}\,L_0 + 3r^{-4}\,\mathrm{Im}\,H_2)\sin 2\theta \tag{19}$$

From figure 2, it can be found that the hazardous positions will happen at θ=135° and θ=-45°.By applying the principle of superposition, the tangential stress in rock-concrete-like material is expressed as

$$\sigma_{3\theta} = \sigma_{3\theta}^1 + \sigma_{3\theta}^2 \tag{20}$$

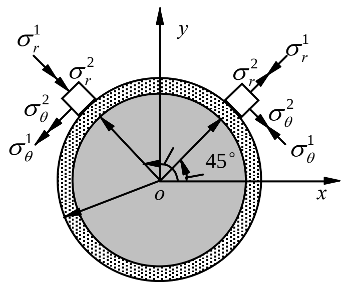

Figure 2 Determination for hazardous location.

3 Time determination for the first crack initiation

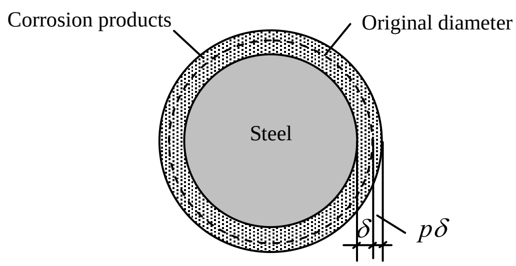

Figure 3 Model used to estimate the stresses developed during the corrosion of reinforced rock-concrete-like material.

The corrosion mechanism of rebar decreases the original cross-section of the bar, but generates corrosion products that occupy greater volume than the rebar did initially. Therefore, it is useful to define a "coefficient of expansion" p, which relates the penetration of corrosion, δ, to the expansion of the corrosion product (Figure.3).

The tensile hoop stress at the interface, i.e., r=r_2, is expressed as

$$\sigma_{3\theta}^1 = 2G_3\, \bar{u}_{2,3} / r_2 \tag{21}$$

The displacement at the interface is, $\bar{u}_{2,3}$=$p\delta$, therefore, Eq.(21) becomes $\sigma_{3\theta}^1 = 2G_3\ p\delta / r_2$. The reacted mass of steel, m, during the corrosion process may be determined by Faraday's equation as

$$m = Ita/(nF) \tag{22}$$

where I is the current, t is the time, a is the atomic mass, n is the equivalents exchanged, and F is the Faraday's constant. The corrosion rate ζ can be obtained by dividing Eq.(22) by t and by the surface area A :

$$\zeta = ia/(nF) \tag{23}$$

where i, the current density, is given by I/A, The rate of penetration, dδ/dt, during the corrosion process can be determined from dividing Eq.(23) by the density of the metal. For steel (n=2), the equation becomes:

$$\mathrm{d}\,\delta/\mathrm{d}\,t = 0.0116i \quad \text{(mm/year)} \tag{24}$$

with i in μA/cm^2. Integrating Eq.(24), it becomes, δ=0.0116it,with time, t, in years. Eq.(21) becomes:

$$\sigma_{3\theta}^1 = 0.0232\, G_3 itp / r_2 \tag{25}$$

Assuming the first crack develops at time t_c when the hoop stress reaches the tensile strength of the rock-concrete-like material f_t, i.e., t_c=$f_t r_2$/(0.0232$G_3 ip$). It is found that t_c is proportional to the rebar radius and inversely proportional to the current density. When the uniform stress at infinity are considered, we obtain

$$t_c = (f_t - \sigma_{3\theta\max}^2) r_2 / (0.0232 G_3 ip) \tag{26}$$

4 Factor analysis for the crack initiation

4.1. The effect of uniform shear at infinity on the crack initiation

When the magnitude of uniform shear at infinity τ_0 is low, the damage of the rock-concrete-like material may not occur. From Eqs.(19) and (26) , It may be found that the maximal tensile hoop stress $\sigma_{3\theta\max}^2$ caused by τ_0 may happen at the interface, i.e., $r=r_2$, for θ=135° and θ=-45°, which can accelerate the crack initiation.

When τ_0 is enough big so that, only due to the action of τ_0, the crack initiation can be caused, i.e., the tensile hoop stress due to τ_0 can exceed to the surrounding rock-concrete-like material tensile strength without considering the existence of corrosion expansion. For such case, Eq.(26) becomes negative value and insignificant. For this case we can take $G_2=G_3$ in Eq.(19), the first crack will appear at the interface, i.e., $r=r_2$, for θ=45° and θ=-135°. However, the first crack will appear at θ=135°and θ=-45° when the corrosion products exist, in other words, the existence of corrosion product changes the location of crack initiation.

4.2. The effect of shear modulus ratio between rebar and surrounding rock-concrete-like material (Γ) on the crack initiation

Here, we take G_2/G_3=0.01, δ/r_2=0.1 and $\gamma_1=\gamma_2=\gamma_3$=0.3. The variations of $\sigma_{3\theta\max}^2/\sigma_1$ with Γ ($\Gamma=G_1/G_3$) are shown in figure 4, it may be observed that $\sigma_{3\theta\max}^2/\sigma_1$ monotonically decreases with increasing Γ. But the influence of Γ on $\sigma_{3\theta\max}^2/\sigma_1$ is not significant.

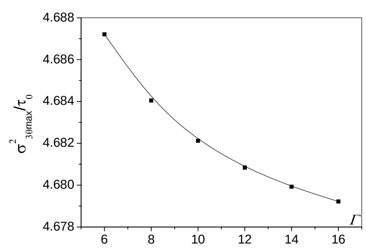

Figure 4 Variations of maximal interface hoop stresses with the ratios of shear modulus.

4.3. The effect of corrosion penetration on the crack initiation

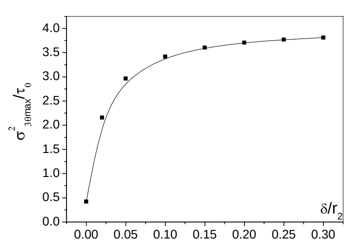

Figure 5 Variations of maximal interface hoop stresses with the penetration of corrosion.

Here, we take $\gamma_1=\gamma_2=\gamma_3$=0.3， $\Gamma=G_1/G_3$=10 and G_2/G_3=0.01. The variations of $\sigma_{3\theta\max}^2/\sigma_1$ with corrosion penetration are plotted in figure 5, it may be found that $\sigma_{3\theta\max}^2/\sigma_1$ increases with increasing the value of δ/r_2. Recalling Eq.(21), $\sigma_{3\theta\max}^1$ also increases with increasing the value of δ. Thus, the crack initiation becomes greatly easy with increasing the corrosion penetration. But when no corrosion products exists (δ/r_2=0), $\sigma_{3\theta\max}^2/\sigma_1$will change the location, for example, $\sigma_{3\theta\max}^2/\sigma_1$ will appear at θ=135° and θ=-45° when the corrosion products exist, However, $\sigma_{3\theta\max}^2/\sigma_1$ will appear at θ=45° and θ=-135° when no corrosion products exist.

5 Conclusion

Muskhelishvili's method was used to determine the stress fields caused by the corrosion expansion and uniform stresses at infinity. The equation of cracking time of the surrounding rock-concrete-like material is established in conjunction with the foretime literature. The influences of uniform shear at infinity, the shear modulus ratio between the rebar and the surrounding rock-concrete-like material and the corrosion penetration on the crack initiation are numerically demonstrated in the paper.

Acknowledgments

The authors would like to deeply appreciate the national project support of China (Grant No. 50625927; 060422002, 50539080; 2007AA11Z131; 2007CB209407).

References

1. Mehta, P.K. and Monterio, P.J.M. Concrete Microstructure, Properties and Materials. 1st ed. Chennai (India), Indian Concrete Institute, 1997.
2. Ohtsuand, M. and Yosimura, Y. Analysis of Crack Propagation and Crack Initiation Due to Corrosion of Reinforcement. Construction and Building Materials, 1997, 7-8. 437-442.
3. Du, Y.G., Chan, A.H.C. and Clark, L.A. Finite Element Analysis of the Effects of Radial Expansion of Corroded Reinforcement. Computers and Structures, 2006, 84. 917-929.
4. Abdalla, H. Concrete Cover Requirements for FRP Reinforced Members in Hot Climates. Composite Structures, 2006, 73. 61-69.
5. Bhargava, K., Ghosh, A.K. and Mori, Y. et al. Modeling of Time to Corrosion-induced Cover Cracking in Reinforced Concrete Structures. Cement and Concrete Research, 2005, 35. 2203-2218.
6. Bhargava, K., Ghosh, A.K. and Mori, Y. et al. Model for Cover Cracking Due to Rebar Corrosion in RC Structures. Engineering Structures, 2006, 28. 1093-1109.
7. Wang, X.H. and Liu, X.L. Modeling Bond Strength of Corroded Reinforcement without Stirrups. Cement and Concrete Research, 2004, 34. 1331-1339.
8. Wang, X.H. and Liu, X.L. Bond Strength Modeling for Corroded Reinforcements. Construction and Building Materials, 2006, 20. 177-186.
9. Piltnera, R. and Monteirob, P.J.M. Stress Analysis of Expansive Reactions in Concrete. Cement and Concrete Research, 2000, 30. 843-848.
10. Muskhelishvili, N.I. Some Basic Problems of the Mathematical Theory of Elasticity. Noordhoff. Groningen, 1953.
11. Maaddawy, T.E. and Soudki, K. A Model for Prediction of Time From Corrosion Initiation to Corrosion Cracking. Construction and Building Materials, 2007, 21. 190-197.
12. Andrade, C., Alonso, C. and Rodriguez, J. et al. Cover Cracking and Amount of Rebar Corrosion: Importance of the Current Applied Accelerated Tests. In: Sjostrom C, Editor. Durability of Building Materials and Components, London: E&FN Spon, 1996, 7. 263-273.
13. Liu, Y. and Weyers, R.E. Modelling the Time-to-corrosion Cracking in Chloride Contaminated Reinforced Concrete Structures. ACI Materials Journal, 1998, 95(6). 675-681.
14. Clark, L.A. and Saifullah, M. Effect of Corrosion on Reinforcement Bond Strength. In: Forde M, Editor. Proceedings of 5th International Conference on Structural Faults and Repairs. Edinburgh: Engineering Technical Press, 1993, 3. 113-119.
15. Al-Sulaimani, G.J., Kaleemullah, M. and Basunbul, L.A. et al., Influence of Corrosion and Cracking on Bond Behavior and Strength of Reinforced Concrete Members. ACI Structures Journal, 1990. 87(2), 220-231.
16. Rasheeduzzafar, S., Al-Saadoun, S.S. and Al-Gahtani, A.S. Corrosion Cracking in Relation to Bar Diameter and Concrete Quality. Journal of Materials in Civil Engineering, 1992, 4(4). 327-342.
17. Williamson, J.S. and Clark, L.A. Pressure Required to Cause Cover Cracking of Concrete Due to Reinforcement Corrosion. Magazine of Concrete Research, 2000, 52(6). 455-467.

RaSiM 7(2009): Controlling Seismic Hazard and
Sustainable Development of Deep Mines,
C.A. Tang(ed), Rinton Press, 371-376

DYNAMIC DESCRIPTION OF STRATA MOVEMENT BASED ON MICROSEISMIC MONITORING

HONG SHI
Department of Civil Engineering, Shandong Jiaotong College
Jinan, 250023, P.R. China

FU-XING JIANG
School of Civil and Environmental Engineering, Beijing University of Science & technology
Beijing, 100083, P.R. China
Jiangfuxing1@163.com

Generally, the precision of microseismic locating monitoring determines the application of monitoring result in mining engineering. To improve the location precision and location speed, this paper presents the improved microseismic location method for the reading and processing of the data on the arrival time of strata movement, solving methods of the equations, and the dynamic illustration of the location result. In addition, this paper also reports how to predict the occurring time, location, scale and developing direction of strata rupture, how to describe the strata movement course, and how to show the mechanism of strata movement.

1 Introduction

The rupture of the strata structure is always accompanied by sound waves, so the microseismic signals contain lots of useful information on the strata destruction and the geological defect activation process This can be used to predict the mechanics of the strata movement and decide if the strata structure is destroyed. It is a noticeable research trend to fully understand the strata movement hazard [1-8]. The precision of microseismic location monitoring determines the application of monitoring results to mining. This paper combines the microseismic signals according to their arriving time being close to each other in order to reduce the error of regarding strata as uniformity speed field and solves locating equations based on the Gauss-Newton method in order to advance the precision and stability of the answers. This paper analyzes how to predict the occurring time, location, scale and developing direction of strata rupture during a period of time, how to describe the strata movement course, and how to show the mechanism of strata movement. Its written for the purpose of providing the methods and means for study of the rule between the rupture field and the stress field of strata.

2 Microseismic locating method

According to the microseismic monitoring principles, the coordinate of each sensor and the time of the signal received is known, what is unknown is the place and occurring time of microseism. Suppose the space coordinate of the microseism focus is (x_1, x_2, x_3), the occurring time is x_4, (a_i, b_i, c_i)is the space coordinate of each monitoring station or detector, and t_i is the time for arrival of wave P of the microseism signal. Because wave P travels fast, and the longwall face of a mine is of a strike of 1000~2000m, of a tendency of 150~250m and of a cave height of 2~8m, the distribution area of the stress caused by mining is located at a distance of 50~150m near the mining area, the area which can be monitored in mining has a small circumference of several hundreds of meters. The author thinks that the elastic wave is hardly influenced by the stratum surface and density when it travels after the strata rupture, so, suppose wave P travels at a normal speed of V, the relationship of MS focus and the sensors will satisfy the locating equation.

3 Improved Microseismic locating method for strata movement on a small scale

3.1. Improved method of the location data processing

The data on the arrival of the microseismic wave will be read by the microseismic instrument automatically. The space coordinate of each sensor and effective data on the arrival of the microseismic wave will form the corresponding location data matrix.

In the reference[8], the location software on strata movement on a small scale is mentioned which processing the location data by 4-4 random combination and subarea location according to the arrival time. There is a problem on this method: The combination fomed by the random combination is arbitrary among all the possible ones and the number of the location results is not the number of all the combinations, so the strata rupture position shown by the microseismic location result is arbitrary among all the possible combinations and sometimes the location result is highly discrete and fails to fully show the strata rupture due to the loss of certain comparatively ideal location results. The subarea location according to the arrival time can reduce the arbitrariness and discreteness of the location result, but, the location result which is reasonable when the effective data are of a small amount. There will show that there is a large difference beween the results of the same rupture according to the subarea location when the effective data are of a large amount. Take the A16 event for example, which happened in Huafeng Mine at the time of 19: 26: 04, January 24, 2005, nine groups of effective data are received, and the location results are (3135,5102,-796,0.033)and(3184,5192,-809,0.051)(the first three numbers stand for the space coordinate of the microseism focus and the last one for the rupture time) respectively after averaging by random combination and subarea location. The mining plan and profile chart show that the rupture point (3135,5102,-796,0.033)is in the aleutite of 8.2 m above six layers of coal and the rupture point (3184,5192,-809,0.051)is in the sandstone at the bottom of four layers of coal, so the two location results show a difference of about 100m. Though the near-point priority locating method is used, the influence of the location result is not certain when the large data on the arrival time are ignored.

According to the improved locating method, the principle of the 4-4 combination location is combining according to the arriving time of signals being close to each other, that is, put the microseismic location matrix in order the arriving time of signals from big to small, then use 4-4 combination according the order, so, each event has n-3 location results (n stands for the number of the effective data read by the detector). A sensor is generally put in the same hard stratum. If the arrival time of the signals is similar, that shows the microseismic wave travels through the similar strata with the similar distance. The location precision can be improved by reducing the error due to regarding stratum as uniformity speed field. At the same time, when the effective data are combined according to certain rule, the point combination of the same plane can be largely reduced which can result in the reducing of the location error of the rupture height and the possibility of having an ill-conditioned equation. Take the above mentioned A16 event for example, the six location results combined according to the arriving time of signals being close to each other will be (2913.4,4932.6,-679.42,-1.8032), (3278.5,5073.4,-827.42,25.871),(3136.5,5117.1,-769.24,33.195),(3235.6,4940.9,786.57,34.57),(3233.5,5123.7,-772.18,72.657),(3201.4,5092.4,-782.46,78.799). The wave shape of this event is like a hill and the time duration is short. It means the rupture occurs in the hard rock. The mining plan and profile chart show the six location results are all in the sandrock above four layers of coal.

3.2. Improved calculating method

The locating equation is generally as follows:

$$\begin{cases} f_1(x)=(a_1-x_1)^2+(b_1-x_2)^2+(c_1-x_3)^2-v^2(t_1-x_4)^2=0, \\ f_2(x)=(a_2-x_1)^2+(b_2-x_2)^2+(c_2-x_3)^2-v^2(t_2-x_4)^2=0, \\ f_3(x)=(a_3-x_1)^2+(b_3-x_2)^2+(c_3-x_3)^2-v^2(t_3-x_4)^2=0, \\ f_4(x)=(a_4-x_1)^2+(b_4-x_2)^2+(c_4-x_3)^2-v^2(t_4-x_4)^2=0 \end{cases} \quad (1)$$

The locating equation (1) is a nonlinear equation set, different scholars and experts proposed different ways of solving it , most of them use a linear system[7-9]. In reference[8], Newton method is used . But, this method needs the calculating of $\partial^2 f$ which is complicated and has the local convergence which may cause instability of the location result. In the optimization toolbox of Matlab, Gauss-Newton method is use in solving the nonlinear equation set. The Gauss-Newton method changes the solving of the nonlinear equation set (1) into solving the optimization of the target function. Its iterative formula is:

$$\begin{cases} x^{k+1}=x^k+\Delta x_k \\ [F^{'}(x^k)^T F^{'}(x^k)]\Delta x_k=-F^{'}(x^k)^T F(x^k) \end{cases} \quad (k=0,1,\cdots) \ (2)$$

This method is different from the direct use of Newton method in solving the equation (1). Formula (2) only needs the calculating of ∂f , which is comparatively easy. Also, in formula (2), Δx_k is descending direction and it can be used for one-dimensional search. *fsolve* in the optimization toolbox of Matlab can be used to solve the locating equation (1).

3.3. Dynamic illustration of the strata rupture locating

The microseismic location result of the strata rupture can be obtained by using the file M in the Matlab. In the reference[8], the processing of the location results is averaging the space coordinate of all the location points, viewing the average value as the rupture point. But the strata rupture is a gradual process, so the microseismic location result should show the rupture area.

(1) the rupture sequence of a microseismic event

The signals received by detectors of different places are from their nearby ruptures, so, if an event has more than four effective signals, there will be more than one location results each showing the rupture of different places with the arriving time as the occurring time. Each microseismic event contains information on the position, nature, and movement of the rupture, so the several location results of the same event can show the strata rupture sequence, namely, several location results of the same event may contain different information on the movement of the strata in terms of strata rupture, fault activation, strata sliding, etc. If several location results of the same event is put in the order according to the rupture time from small to big, the location point sequence can be used to show the rupture point sequence. Take the A21 event for example, which happened in Huafeng Mine at the time of 12:39:49, January 20, 2005, the location results are: ①(3220.5,4980.9,-786.0,64.4); ②(3223.4,4989.9,-788.8,64.4); ③(3217.8,5027.7,-778.6,66.3); ④(3222.7,5052.9,-776.1,67.6); ⑤(3227.5,5038.6,-775.7,67.9); ⑥ (3221.7,5070.4,-845.8,98.2); ⑦ (3211.0,5067.0,-773.5,102.5); ⑧(3396.1,5019.9,-963.9,143.6). The mining plan and profile chart show that rupture ①,②,④and⑤ are in the aleutite of 9.5m above the working surface of four layers of coal; rupture ③ is in the sandstone of 6.3 m above the aleuvite of 9.5m; rupture ⑦ is in the sandstone of 9.7m under the aleutite of 9.5m; rupture ⑥ is in the sandstone of 9.0m under four layers of coal; rupture ⑧ is in the entity coal area. The location result shows that the rupture occurs in the aleuvite of 9.5m first and then causes the rupture of the hard stratum above it which, while sinking, causes the further rupture of the aleutite of 9.5m, and later all the above strata movement cause the rupture of the sandstone of 9.7m, thus the movement of the strata of nearly 45m above the working surface cause the rupture of the hard stratum under the four layers of coal. The above analysis shows that the strata movement of this event is from the top to the bottom. The location results ①~⑦are between x=3200~3230 and y=4970~5100, the position of the work surface of the four layers of coal is near y=4845, the rupture area is far from the work surface, and there are in the rupture area several fault of various direction, so it can be concluded that the cause of the rupture is the activation of fault.

(2)Dynamic illustration of the strata rupture location

The location of a microseismic event may show the strata rupture sequence which includes information on the rupture of the strata of different position and nature, but the information on one event is not enough to determine the strata rupture course. After a period of microseismic monitoring, the information on a certain stratum movement is known from many microseismic events of different time, so from many microseismic events the complete information on certain stratum movement can be obtained; by using many location results of certain stratum movement, and putting different events and the different location results of the same event in order according to the occurring time respectively, we can analyze the position, time, scale, and direction of such strata movement as strata rupture and fault activation as the mining progresses, thus understanding the strata rupture sequence of a period.

1)Dynamic movement course of the strata rupture

The rupture sequence of a period can help predict the time, position, scale, and direction of the strata rupture and show the movement course. Fig.1 is the microseismic plan of Huafeng Mine, Shandong Province from January 20~23, 2005, the dotted line refers to the lane of the four layers of coal, and the position of the working surface is near y=4850~4860. The relevant researches already show that the rupture point near the working surface is mainly caused by the strata breaking while the rupture far from the working surface by the fault activation, so the rupture about 80~100m ahead of the working surface in Fig.1 (the rectangle shadow region) should be caused by the strata breaking. Fig.1 shows that on January 20, 2005, there are many rupture points in the area 80~100m ahead of the working surface, rupture ① and ② is (3235.3,4947,-785.4,55.7) and (3187.9,4942.6,792.1,42.3)of02_44_35;rupture③and④is(3230.3,4931.8,780.5,47.5)and(3192.4,4953.8,793.5,43.8) of 10_13_49; rupture ⑤ and ⑥ is (3239.5,4965.6-788.6,107.7) and (3225.8,4937.9,-773.5,108.1) of 12_13_38; and rupture ⑦ is (3223.6,4953.4,-783,57.9) of 21_08_07, which tells that the strata move comparatively violently at this time. But during January 21~22, 2005, as the working surface progresses, the rupture points of this area sharply reduces, rupture ⑧and ⑨ are (3171,4958,-758,62.1) of 05_13_37 on January 21 and (3226,4954,-772,96) on January 22, which tells that the strata begin to move less violently and in the following days there are almost no rupture points in this area which shows that from January 22, the strata almost stops moving. The profile chart of the strata rupture of each day shows that putting the rupture points in order according to occurring time can help predict the strata movement course. The profile chart of the strata in Fig.2 shows that rupture ① is in the sandstone of 9.7m above the working surface of four layers of coal; rupture ② is in the sandstone of 4.2m near the bottom of four layers of coal; rupture ③ is in the sandstone of 9.7m above the working surface of four layers of coal; rupture ④ is in the sandstone of 4.2m near the bottom of four layers of coal; rupture ⑤ is in the sandstone of 9.7m above the working surface of four layers of coal; rupture ⑥ is in the aleutite of 9.5m above the working surface of four layers of coal; rupture ⑦ is in the sandstone of 9.7m above the working surface of four layers of coal. So, the strata ruptures are mainly in the hard strata of the floor and the roof of the coal. The four layers of coal are mined by fully-mechanized sublevel caving technology and the mining thickness is 6.3m and the sandstone of 9.7m above is in the coal roof. The strata movement should be like this: the mining of coal layers causes the movement of the hard strata in the roof and the floor and the movement of the roof causes the movement of the aleutite of 9.5m above it. The rupture ⑧ of 05_13_37 on January 21 is in the sandstone of 9.2m under the sandstone of 9.7m above the working surface; the breaking of the sandstone of 9.7m in the roof causes the its sinking which mainly causes the breaking of the hard thick stratum under it. The rupture ⑨ is in the aleutite of 9.5m and its movement is caused by the breaking and sinking of the sandstone of 9.2m under it. To sum up, the strata movement range above the working surface is 35m and the strata movement range under the working surface is 8m, and the cause of the strata movement is the breaking of the hard strata in the roof and floor after mining.

2)Dynamic illustration of the fault activation

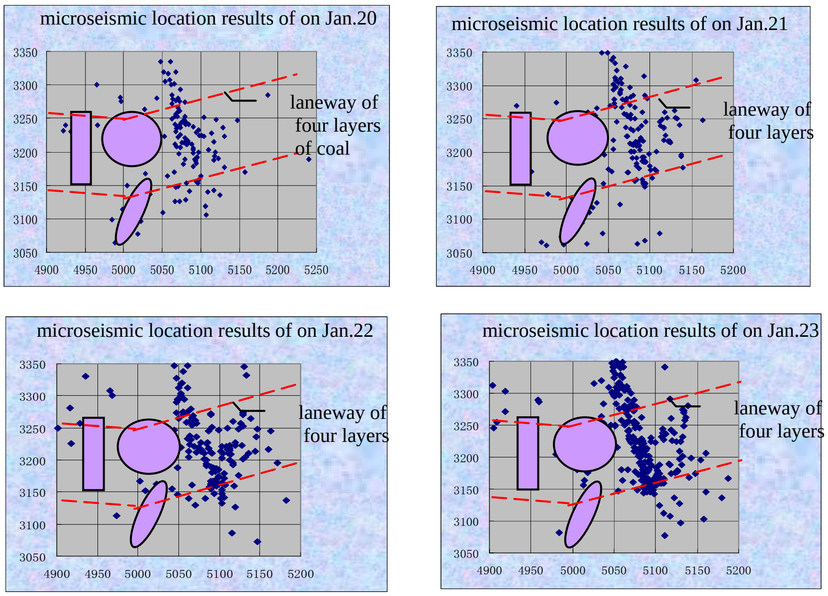

Fig.1 Microseismic monitoring results

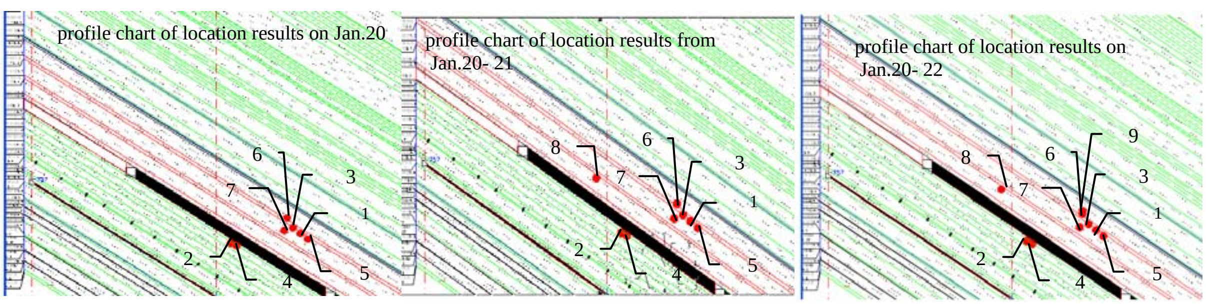

Fig.2 The profile chart of location results

The strata rupture sequence of a period can also help predict the movement course of the fault activation. Because the distance of the influence of the four-layer coal mining on the fracture is up to 350m[6], the strata rupture far from the working surface is mainly caused by the fault activation as is illustrated in Fig.1(the rupture points in and in front of the circular and oval area).Take the fault in the oval area for example, on January 20, the distribution of the rupture points in the oval area is even;on January 21, there are more rupture points than the previous day, which shows that the fault activation moves more actively; from January 22~23, there is a gradual decrease of the rupture points, which shows that the fault moves slowly in this area. By using the same method, one can see from the location result plan from January 20~23 that there is a gradual increase of the rupture points in the circular area as the working surface progresses, which shows that the fault activation movement becomes more violent. The same location results also show that with the progressing of the working surface, the mining of four layers of coal influence the faults ahead at a distance of 350m, and as the working surface further progresses, the fault activation movement in front of the working surface gradually begins, as is illustrated in Fig.1. On January 20, the rupture points of the faraway fault activation movement is near y=5125m; on January 23, the rupture point moves to y=5150m. This example is based on the monitoring of a short period, and the monitoring of long time can be used for the dynamic monitoring of the fault movement for the purpose of predicting the time, position, direction and scale of the fault activation.

4 Conclusions

This paper makes a contrastive analysis of the microseismic monitoring results by combining the location data according to the 4-4 random combination and combination of the microseismic signals according to their arriving times being close to each other. The combination of the microseismic signals according to their arriving times being close to each other can be helpful in the full use of all the effective data, improvement of location precision, and reducing the random of location results and the error due to regarding stratum as uniformity speed field.

By analyzing the location results of Huafeng Mine, the author holds that the Gauss-Newton iterative method based on nonlinear optimization can be used to solve the locating equation to advance the precision and stability of an answer and to reduce the probability part convergence of the solution of equation. The optimization toolbox of Matlab method can also be used to simplify the editing of the program codes.

The strata rupture is a gradual process, so, the time, position, scale and direction of the strata rupture can be known by putting in order the rupture sequence of a microseismic event and the strata rupture sequence of a certain period according to the occurring time and drawing the plan and profile chart of the rupture points. The rupture movement course can also help make a dynamic description of the course of strata movement and reflect the strata movement mechanism. This trial method still welcomes further research.

Acknowledgements

The authors wish to acknowledge funding support from the National Natural Science Foundation of China(40674017）and the Docter Foundation of Shandong Province(2008BS08003).

References

1. Jiang, F.X. and Luo, X. Application of Microseismic Monitoring Technology of Strata Fracturing in Underground Coal Mine. Chinese Journal of Geotechnical Engineering, 2002, 24(2): 147-149.
2. Jiang, F.X., Yang, S.H. and Luo, X. Spatial fracturing progresses of surrounding rock masses in longwall face monitored by microseismic monitoring techniques. Journal of China Coal Society, 2003, 28(4): 357-360.
3. Mendecki, A.J. Seismic monitoring in Mines. London: Chapman and Hall, 1997.
4. Luo, X. and Hatherly, P. Application of microseismic monitoring to characterise geomechnic conditions in longwall mining. Exploration Geophysics, 1998, 29:489-493.
5. Luo, X., Hatherly, P. and Gladwin M. Application of microseismic monitoring to longwall geomechanics and safety. Proc. 17th Conf. Ground Control in Mining, (Morgantown, USA, 1998).
6. Jiang, F.X.,Yang, S.H. and Cheng, Y.H. A Study on Microseismic Monitoring of Rock Burst in Coal Mine. Chinese Journal of Geophysics, 2006, 49(5): 1511-1516
7. Li, H.Y., Jiang, F.X., Yang, S.H. Research and Application of Microseismic Monitoring Location of Strata Fracturing Based on Matlab. Journal of China Coal Society, 2006, 3: 7-11.
8. Luo, X. and Hatherly, P. Understanding of high gas emissions at Appin Colliery through microseismic monitoring. Proc. Int. Mining Tech.' 98 Symp, (Chingqing, China, 1998).

*RaSiM 7(2009): Controlling Seismic Hazard and
Sustainable Development of Deep Mines,
C.A. Tang(ed), Rinton Press, 377-380*

ANALYTIC SOLUTION OF VERTICAL INCIDENT P WAVE AMPLITUE REFLECTED AT THE FREE SURFACE IN A VISCOELASTIC MEDIUM

BO ZHANG, SHU-CAI LI and QING-SONG ZHANG

Geotechnical and Structural Engineering Research Center, Shandong University

Jinan 250061,China

The analytic solution of vertical incident *P* wave reflected at free surface in viscoelastic medium was presented in this paper. The analytic solution of vertical incident *P* wave reflected at free surface in elastic medium was firstly obtained through elastic wave theory. Combining the analytic solution with elastic wave theory with that of the viscoelastic theory, the analytic solution of vertical incident *P* wave amplitude reflected at free surface in viscoelastic medium was obtained.

1 Introduction

The viscoelastic material and viscoelastic theory have been used in many fields, such as rock rheology [1, 2, 3] and so on. The wave propagation problem in viscoelastic medium is often solved using the correspondence principle of viscoelastic theory, which solves the problem in elastic medium and can be used to solve the problem in a viscoelastic medium [4, 5, 6].The analytic solution of the vertical incident *P* wave amplitude reflected at free surface in elastic medium has been presented in numerous documents[7,8]. However, the analytic solution of vertical incident *P* wave amplitude reflected at free surface in viscoelastic medium has not been presented so far. In this paper the analytic solution of the vertical incident *P* wave amplitude reflected at free surface in elastic medium was obtained primarily through the elastic wave theory. Combining the analytic solution of the reflected amplitude in elastic wave theory with the viscoelactic theory, the analytic solution of the vertical incident *P* wave amplitude reflected at the free surface in viscoelastic medium was obtained.

2 The analytic solution of vertical incident *P* wave amplitude reflected at free surface in elastic medium

The incident *P* wave with random angle r1 to the free surface is shown in Figure1.

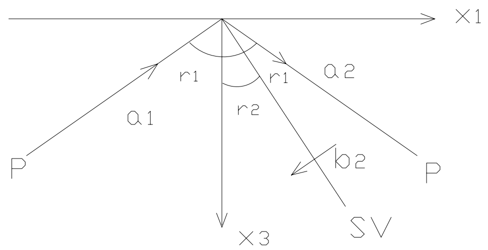

Figure 1 The incident P wave with random angle to free surface

In the fig.1, the x_1x_2 plane is the free surface of medium, the x_1x_3 plane is the incident plane. The area of $x_3<0$ is empty space, the area of $x_3 \geq 0$ is the medium of wave propagation. *a*1 is the incident *P* wave with incident angle r1, *a*2 is the reflected *P* wave with reflection angle r1 , *b*2 is the reflected *SV* wave with the angle r2 of reflection. The density of medium is ρ .

The potential functions of incident wave *a*1and reflected wave *a*2, *b*2 [7]are as follows

$$\phi_1 = A_1 e^{i(k_{p1}x_1 - k_{p3}x_3 - \omega \cdot t)} \tag{1}$$

$$\phi_2 = A_2 e^{i(k_{p1}x_1 + k_{p3}x_3 - \omega \cdot t)} \tag{2}$$

$$\varphi_2 = A_2 e^{i(k_{s1}x_1 + k_{s3}x_3 - \omega \cdot t)} \tag{3}$$

where

$$k_{p1} = (\omega / v_p)\sin r_1 \qquad k_{p3} = (\omega / v_p)\cos r_1$$

$$k_{s1} = (\omega / v_s)\sin r_2 \qquad k_{s3} = (\omega / v_s)\cos r_2$$

Where ω is the angular velocity of wave, v_p is the velocity of *P* wave, v_s is the velocity of *S* wave.

And the displacements of *P* wave and *S* wave can be written as

$$u_p = \nabla\phi\,, \quad u_s = \nabla \times \varphi \tag{4}$$

By substituting (1),(2)and(3)into (4)

$$u_{p1} = iA_1(k_{p1}i_1 - k_{p3}i_3)e^{i(k_{p1}x_1 - k_{p3}x_3 - \omega \cdot t)} = a_1 e^{i(k_{p1}x_1 - k_{p3}x_3 - \omega \cdot t)} \tag{5}$$

$$u_{p2} = iA_2(k_{p1}i_1 + k_{p3}i_3)e^{i(k_{p1}x_1 + k_{p3}x_3 - \omega \cdot t)} = a_2 e^{i(k_{p1}x_1 + k_{p3}x_3 - \omega \cdot t)} \tag{6}$$

$$u_{s2} = iB_2(-k_{s3}i_1 + k_{s1}i_3)e^{i(k_{s1}x_1 + k_{s3}x_3 - \omega \cdot t)} = b_2 e^{i(k_{s1}x_1 + k_{s3}x_3 - \omega \cdot t)} \tag{7}$$

Where u_{p1} is the displacement of incident *P* wave, u_{p2} is the displacement of reflected *P* wave, u_{s2} is the displacement of reflected *S* wave, $a_1 = iA_1(k_{p1}i_1 - k_{p3}i_3)$, $a_2 = iA_2(k_{p1}i_1 + k_{p3}i_3)$ and $b_2 = iB_2(-k_{s3}i_1 + k_{s1}i_3)$ are the amplitudes of incident and reflected waves.

Using eqs. (5),(6)and(7) the amplitudes in horizontal and vertical directions at free surface can be solved

$$U_1 = 2\cos r_1 \sin 2r_2 \cdot a_1 / \Delta \tag{8}$$

$$U_3 = -2\cos r_1 \cos 2r_2 \cdot a_1 / \Delta \tag{9}$$

where

$$\Delta = \cos^2 2r_2 + (v_s / v_p)^2 \sin 2r_1 \cos 2r_2 \tag{10}$$

where U_1 is the amplitude in horizontal direction and U_3 is the amplitude in vertical direction.

When the incident *P* wave is in vertical direction, then r1=0，r2=0，and using eqs.(8),(9)and (10) the amplitudes can be written as

$$U_1 = 0 \tag{11}$$

$$U_3 = -2a_1 \tag{12}$$

It can be seen that the amplitude at free surface in vertical direction is two times as high as that of incident P wave from eq. 12.

3 The analytic solution of vertical incident *P* wave amplitude reflected at free surface in viscoelastic medium

The boundary conditions of semi-infinite viscoelastic bar are

$$u(0,t) = U\cos(-\omega \cdot t) \tag{13}$$

$$u(\infty,t) = 0 \tag{14}$$

The motion differential equation of semi-infinite viscoelastic bar is [4]

$$\rho\sum_{k=0}^{m} p_k \frac{\partial^{k+2}u}{\partial t^{k+2}} - \sum_{k=0}^{n} q_k \frac{\partial^{k+2}u}{\partial x^2 \partial t^k} = 0 \tag{15}$$

By eqs.(13),(14)and (15),the displacement of wave propagated in semi-infinite viscoelastic bar is written as

$$u(x,t) = Ue^{-ax}e^{i(-kx-\omega t)} \tag{16}$$

where, when the viscoelastic medium is Kelvin material the k and a are written as[4]

$$k^2 = \frac{\rho E_k \omega^2}{2\left(E_k^2 + \eta_k^2\omega^2\right)}\left[\sqrt{1+\frac{\eta_k^2\omega^2}{E_k^2}}+1\right] \tag{17.a}$$

$$a^2 = \frac{\rho E_k \omega^2}{2\left(E_k^2 + \eta_k^2\omega^2\right)}\left[\sqrt{1+\frac{\eta_k^2\omega^2}{E_k^2}}-1\right] \tag{17.b}$$

when the viscoelastic medium is Maxwell material the k and a are written as

$$k^2 = \frac{\rho\omega^2}{2E_m}\left[\sqrt{1+\frac{E_m}{\omega^2\eta_m}}+1\right] \tag{18.a}$$

$$a^2 = \frac{\rho\omega^2}{2E_m}\left[\sqrt{1+\frac{E_m}{\omega^2\eta_m}}-1\right] \tag{18.b}$$

where the E_k is the elastics modulus of spring and the η_k is the viscosity coefficient of damper in Kelvin model, the E_m is the elastics modulus of spring and the η_m is the viscosity coefficient of damper in Maxwell model. The meaning of k is wave number and the meaning of a is attenuation factor of wave propagated in viscoelastic medium.

When the incident *P* wave is at vertical direction in viscoelatic medium, by substituting eq.(16) into eq.(5) the eq.(5) can be written as

$$u(x_3,t) = a_1 e^{-ax}e^{i(-kx_3-\omega t)} \tag{19}$$

where the a_1 is shown in eq.(5) and a,k are shown in eqs. (17)and(18).

By using eqs.(12)and(19) the analytic solution of vertical incident *P* wave amplitude reflected at free surface in viscoelastic medium can be written as

$$U_1 = 0 \tag{20}$$

$$U_3 = -2a_1 e^{-ax_3} \tag{21}$$

where U_1 is the amplitude in horizontal direction and U_3 is the amplitude in vertical direction.

It can be seen that the amplitude at free surface in vertical direction is $2e^{-ax_3}$ times as high as that of incident P wave from eq. 18.The amplitudes of wave decay at exponential form with the increase of propagation distance and the decay coefficient is e^{-ax}.

4 Conclusions

The analytic solution of the vertical incident P wave amplitude reflected at free surface in the elastic medium was primarily obtained through the elastic wave theory. The amplitude at free surface in the vertical direction is two times as high as that of incident P wave. Combining the analytic solution of the reflected amplitude in the elastic wave theory with that of the viscoelactic theory, the analytic solution of vertical incident P wave amplitude reflected at free surface in viscoelastic medium was obtained. The amplitude at free surface in vertical direction is $2e^{-ax_3}$ times as high as that of incident P wave, in the viscoelastic medium the amplitudes of wave decay at exponential form with the increase of propagation distance and the decay coefficient is e^{-ax}.

Acknowledgments

This research was supported by Chinese National Natural Science Funds for Distinguished Young Scholar (50625927)， National Natural Science Foundation of China (40872203) and National Basic Research Program of China (973 Program,No.2007CB209407).

References

1. Schmid, D.W., Dabrowski, M. and Krotkiewski, M. Evolution of large amplitude 3D fold patterns: A FEM study. Physics of the Earth and Planetary Interiors, 2008, 171: 400-408.
2. Maurizio, B. and Claudio, F. Analytical models of deformation and residual gravity changes due to a Mogi source in a viscoelastic medium. Tectonophysics, 2008, 163: 375-384.
3. Moresi, L., Quenette, S. and Lemiale, V., et al. Computational approaches to studying non-linear dynamics of the crust and mantle. Physics of the Earth and Planetary Interiors, 2007, 163: 69-82.
4. Zhou, G.Q. Viscoelastic Theory. University of Science and Technology of China Press, 1996.
5. HyukIm, S. and Huang, R. Wrinkle patterns of anisotropic crystal films on viscoelastic substrates. Journal of the Mechanics and Physics of Solids, 2008, 56: 3315-3330.
6. Chaillat, S. and Bui, H.D. Resolution of linear viscoelastic equations in the frequency domain using real Helmholtz boundary integral equations. Comptes Rendus Mécanique, 2007, 335: 746-750.
7. Yang, B.J. Elastic wave theory. Northeast Normal University Press, 1990.
8. Degrande, G. and Geraedts, K. An electronic learning environment for the study of seismic wave propagation. Computers & Geosciences, 2008, 34: 569-591.

RaSiM 7(2009): Controlling Seismic Hazard and
Sustainable Development of Deep Mines,
C.A. Tang(ed), Rinton Press, 381-386

THE DYNAMIC DISTURBANCE AS A MECHANISM TO TRIGGER THE ROCKBURST AROUND THE UNDERGROUND OPENING

WAN-CHENG ZHU

Center for Rock Instability and Seismicity Research, Box 138, Northeastern University
Shenyang, 110004, P.R. China

CHUN-AN TANG

Center for Rock Instability and Seismicity Research, Dalian University of Technology
Dalian, 116024, P.R. China

YU-JUN ZUO

Research Center for Numerical Tests on Material Failure, Dalian University
Dalian, 116622, P.R. China

SHAN-YONG WANG

Centre for Geotechnical and Materials Modelling, Civil, Surveying and Environmental Engineering
The University of Newcastle, Callaghan, NSW 2308, Australia

Rock bursts occur when a highly stressed rock mass at depth is triggered by a dynamic disturbance. The Realistic Failure Process Analysis (RFPA) numerically simulates the occurrence of rock bursts around the deep rock tunnel, which are triggered by a dynamic disturbance. The effects of waveforms from dynamic disturbances and tunnel depth on the occurrence of rock bursts are studied. The numerical results indicate that dynamic disturbances are one of the most important mechanisms that govern the stability of underground openings. When tensile stress induced by static in-situ stress caused by dynamic disturbance are superposed at a location to enhance the total tensile stress, the contribution of dynamic disturbance to trigger rock bursts becomes greater with the increase of tunnel depth.

1 Introduction

In the past several decades, a vast majority of works related to the mechanism of rock busts have been undertaken. It is believed that that a detailed understanding of the damage mechanisms and the proper application of this knowledge to mining and support of excavations will lead to a reduction in the hazard posed by rockbursts [1]. It is well accepted that the occurrence of rockbursts is dependent on many factors such as in-situ stress conditions, geological structures, rockmass strength, excavation methods and excavation size, rock blasting and earthquakes [2-4]. However, the possession of the large accumulated elastic energy in the rockmass is only a prerequisite for rockburst occurrence, the external disturbances, such as the unloading due to excavation and the dynamic disturbance excited by blasting or earthquakes, may be the one of the necessary key factors to trigger the rockburst. For instance, the control of rockburst hazards with blasting practices is started with the recognition that roughly 75% of rockbursts occur with, or in the hour following, a blast [5]. With the underground mining goes deeper, the more elastic strain energy accumulated in the rock mass, the rock bursts become even more severe as one of the mining catastrophes. Therefore, it is of great significance to consider the dynamic disturbance as a key factor to trigger the rock bursts in deep underground mining.

The effective rock burst model should be capable of describing the complete stress-strain behaviour of rock both in the elastic as well as in the pre- and post-failure phases in order to describe the beginning and development of dynamic fracture processes of rockmass. This kind of model to describe the failure process of rock subjected to dynamic loading has been proposed in some work of authors based on RFPA Code [6-7]. In this work, the RFPA-Dynamics is extended to simulate the dynamic failure of statically pre-stressed rock triggered by dynamic disturbance, which provides a method to clarify this kind of rockburst mechanism.

2 Numerical model of tunnel

In the following simulations, the tunnels with horseshoe-shaped cross sections are considered. The specific geometries and loading conditions for this model are shown in Fig.1. The failure process of this tunnel under combined static and dynamic loading is simulated with RFPA-Dynamics.

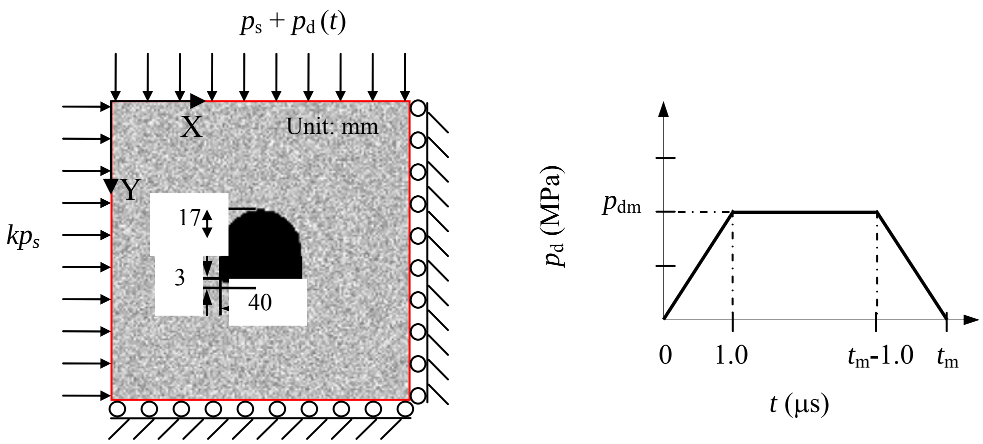

(a) Model setup (b) Dynamic disturbance $p_d(t)$

Fig.1 Model configuration of underground tunnel (here k is lateral pressure coefficient for static in-situ stress, while p_{dm} and t_m are amplitude and duration of dynamic disturbance, respectively.)

The numerical specimen of tunnel has a common dimension of 150mm×150mm, and is composed of 150×150 quadrilateral iso-parametric finite elements. The Young's modulus and unconfined compressive strength of this rock is 58 GPa and 150 MPa, respectively. To enable recognition of the mechanisms leading to the collapse of the tunnel under different lateral pressure coefficients, the excavation process, rock support and reinforcement are not considered in the numerical simulations. The rock is assumed heterogeneous with its mechanical properties defined by a Weibull distribution with the parameters listed in Table 1. In previous studies [6-7], the parameters used in the constitutive model were calibrated in detail.

Table 1 Weibull distribution parameters of rock material

Rock Parameter	Value
Homogeneity index	3.0
Mean elastic modulus	70 (GPa)
Mean compressive strength	510 (MPa)

The static in-situ stress condition is a very important factor to govern the stress distribution and damage zone around the tunnel [7]. Therefore, the effect of lateral pressure coefficient k is firstly considered in the simulations. For the static analysis, in order to calculate the stress redistribution induced by excavation, the applied boundary stresses in the vertical and horizontal directions that are denoted as p_s and kp_s, respectively, where k is usually called lateral pressure coefficient, is applied incrementally until the pre-specified in-situ stresses are attained. The bottom and right sides of the model domain is prevented from displacement in vertical and horizontal directions, respectively.

As regards the dynamic loading conditions, the dynamic stress, which is simplified as a trapeziform stress pulse p_d(t), as defined in Fig.1b, is applied at the top surface of model domain. For the dynamic stress (or dynamic disturbance), two parameters including amplitude (p_{dm}) and duration (t_m) of dynamic stress are involved in the numerical simulations in order to analyze the effect of the dynamic stress waveform on the failure of this tunnel.

3 Numerical results

The different in-situ stresses under a fixed lateral pressure coefficient are applied before the application of dynamic disturbance. The failure pattern at t = 30 μs under lateral pressure coefficient of 0.1 is shown in Fig.2, in which the depth of the tunnel, as well as the amplitude of dynamic disturbance, is varied to show its effect on occurrence of rockburst. In general, solely under the dynamic disturbance, the spalling occurs at the roof of the tunnel when p_{dm}=25 MPa, and the spalling crack becomes longer with the increasing amplitude. When the effect of in-situ stress is considered, for instance, at the depth of 700 m (p_s = 17.5 MPa), the damage zone around the opening is reduced even though the amplitude of dynamic disturbance is increased to 50 MPa. If the contribution of coupled static and dynamic loading is considered, as the tunnel goes deeper, the higher in-situ stress is induced, and the damage around the opening, especially at the roof, become widely distributed.

At a specified depth of the opening, the increase of the amplitude of the dynamic disturbance triggers the more evident spalling at the roof. When the amplitude of dynamic disturbance is 12.5 MPa, the extent of the damage zone becomes wider with the increase of depth of tunnel, however the dynamic spalling at the roof is not obviously found even though the depth is increased to 2400 m. Under this lateral pressure coefficient (k = 0.1), the static tensile stress caused by static in-situ stress and dynamic tensile stress caused by reflection of compressive stress wave at the perimeter of opening are superposed to contribute to the tensile damage at the roof. The consideration of static in-situ stress may facilitate the formation of damage zone at the roof; however, the damage at the roof may prevent the transmission of stress wave, and therefore, the static in-situ stress does not contribute too much to initiation of the spalling crack there. When the combined contribution of static in-situ stress and dynamic disturbance is considered, for the tunnel at the depth (for example, depth is 1600 m or 2400 m), the dynamic disturbance with lower amplitude (p_{dm}=12.5 MPa) is sufficient to trigger the dynamic spalling at the roof.

(a) p_s = 0 MPa (no static stress)

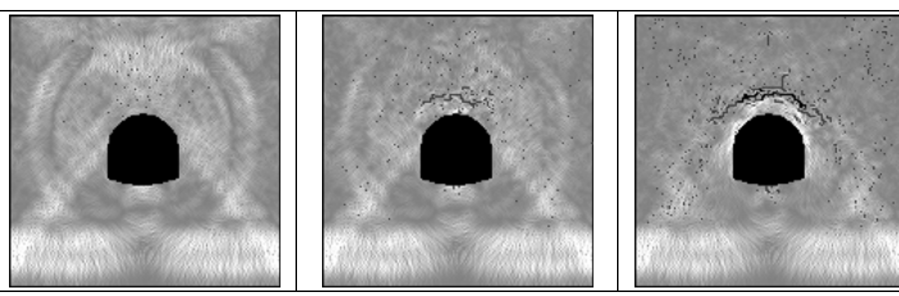

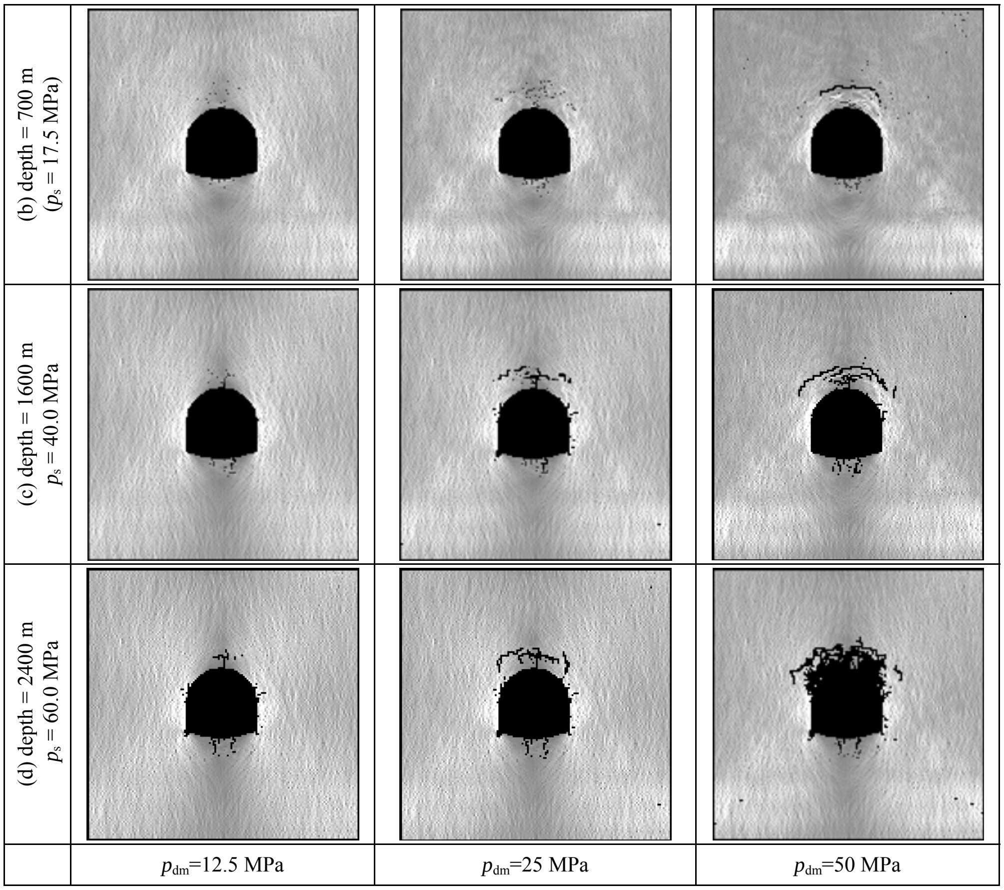

Fig.2 The maximum shear stress at t = 30μs of the tunnel at different depth and under dynamic disturbances with varied amplitude (k = 0.1, t_m = 6μs)

When the lateral pressure coefficient k = 2.0, as shown in Fig.3a, if no in-situ stress is considered in the simulations, a marked deterioration of ground condition around opening is found. However, the damage zone around the opening is greatly reduced when the effect of static in-situ stress is considered. Then, as the tunnel goes deeper, higher compressive stress at the roof is induced, the dynamic spalling never occurs at the roof at depth of 2400 m. Thereafter, under this in-situ stress condition (k = 2.0), the dynamic spalling at the roof is not rather prone to occur with the depth.

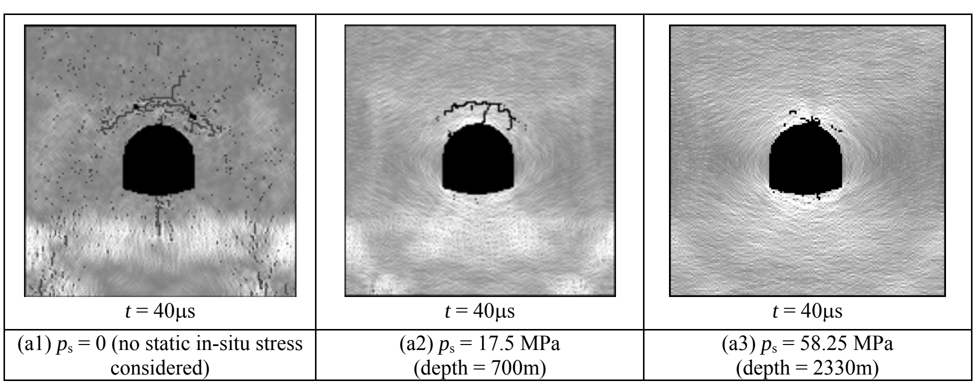

(a) The dynamic disturbance is applied in Y direction

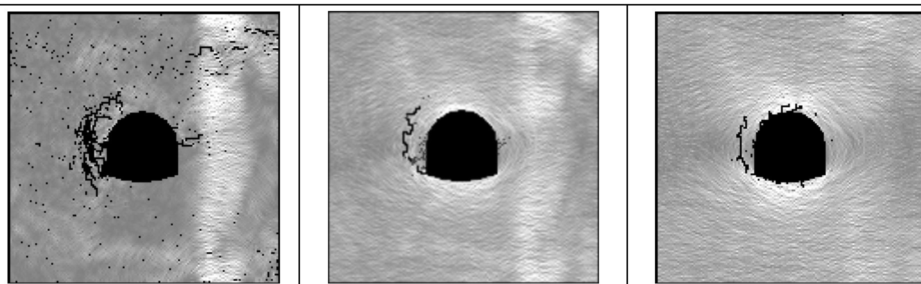

$t = 40\mu s$	$t = 40\mu s$	$t = 40\mu s$
(b1) $p_s = 0$ (no static in-situ stress considered)	(b2) $p_s = 17.5$ MPa (depth = 700m)	(b3) $p_s = 58.25$ MPa (depth = 2330m)

(b) The dynamic disturbance is applied in X direction

Fig.3 The maximum shear stress of the tunnel at different depth and under dynamic disturbances in different directions ($k = 2.0$, $t_m = 6\mu s$, p_{dm}=50 MPa)

However, if the dynamic disturbance is applied at the left boundary of the model domain in X direction, as shown in Fig.3b, the increase of depth of the opening tends to induce more widely distributed damage around the tunnel. The spalling at the left sidewall does not extend with the depth, but the damage at the roof also occurs at the depth of 2330 m. In this regard, the contribution of the dynamic disturbance to trigger the failure (or rockburst) around the tunnel is also affected by which direction it is applied.

4 Conclusions

The dynamic disturbance can be a factor to trigger the instable failure of rock and to induce rockburst around the tunnel at depth. In the paper, the numerical code RFPA-Dynamics is used to simulate the rockburst triggered by a dynamic disturbance. This simulation suggests that the consideration of the static in-situ stress does not always induce more severe damage around the tunnel. Depending on the static stress induced around the tunnel, the existence of the static in-situ stress sometimes may restrain the occurrence of dynamic spalling. In general, when the tensile stress induced by static in-situ stress and that is caused by dynamic disturbance are superposed at a location to enhance the tensile failure, the contribution of dynamic disturbance to triggering rockburst tends to be severe and with increasing tunnel depth. Otherwise, the contribution of the dynamic disturbance to facilitate the occurrence of rockburst can only be concluded based on the numerical simulation according to the specific in-situ stress conditions and characteristics of the dynamic disturbance.

Acknowledgements

The present work is funded by National Science Foundation of China (Grant Nos. 50504005, 50874024 and 50874020), the National Basic Research Program (“973 program”) of China (Grant No. 2007CB209405), the Key Project of Chinese Ministry of Education (No. 108038), the Program for New Century Excellent Talents in University of China (Grant No. NCET-06-0291), Liaoning Provincial Natural Science Foundation of China (Grant No. 20082027) and the Scientific Research Foundation for the Returned Overseas Chinese Scholars of State Education Ministry. This support is gratefully acknowledged.

References

1. Durrheim, R.J., Haile, A. and Roberts, M.K.C., et al. Violent failure of a remnant in a deep South African gold mine. Tectonophysics, 1998, 289: 105-116.
2. Linkov, A.M. Rockbursts and the instability of rock mass. International Journal of Rock Mechanics and Mining Sciences and Geomechanical Abstracts, 1996, 33(7): 727-732.

3. Mansurov, V.A. Prediction of rockbursts by analysis of induced seismicity data. International Journal of Rock Mechanics and Mining Sciences, 2001, 38 (6): 893-901.
4. Wang, J.A. and Park H.D. Comprehensive prediction of rockburst based on analysis of strain energy in rocks. Tunnelling and Underground Space Technology, 2001, 16: 49-57.
5. Whyatt, J.K., Blake, W., Williams, T.J. and White, B.G. 60 years of rockbursting in the Coeur D' Alene District of northeastern Idaho, USA: lessons learned and remaining issues. In Proceedings of the 109th Annual Exhibit and Meeting, Society for Mining, Metallurgy, and Exploration (Phoenix, AZ, 2002).
6. Zhụ, W.C. and Tang, C.A. Numerical simulation of Brazilian disk rock failure under static and dynamic loading. International Journal of Rock Mechanics and Mining Sciences 2006, 43(2): 236-252.
7. Zhu, W.C. Liu, J. and Tang, C.A., et al, B.H. Simulation of progressive fracturing processes around underground excavations under biaxial compression. Tunnelling and Underground Space Technology, 2005, 20 (3): 231-247.

RaSiM 7(2009): Controlling Seismic Hazard and
Sustainable Development of Deep Mines,
C.A. Tang(ed), Rinton Press, 387-398

STUDY OF SEISMIC SOURCE MECHANISMS IN MINES OF THE VERKHNEKAMSKOYE POTASH DEPOSIT

DMITRIY A. MALOVICHKO

Mining Institute, Ural branch of the Russian academy of sciences

Perm 614007, Russia

For over 13 years a routine seismic monitoring has been carried out at six of the mines in the world's second largest potash deposit, the Verkhekamskoye, Perm region, Russia. The observed level of seismicity is rather low in the mines. On average about 1-2 events with seismic energies from 100 J up to 50 kJ are recorded daily. The seismicity doesn't show any direct temporal and spatial correlation with mining operations. The sources are located within the areas which were mined in the past several years or up to several decades ago. We believe that the observed seismicity can be regarded as a source of information about the fracture processes in the mined out areas. This interpretation is important for safe mining, as the integrity of horizons above the excavations needs to be controlled to exclude possibility of flooding of the mine.

An investigation of source mechanisms of seismic events was undertaken. The waveforms of the majority of events are rich in low frequency surface waves (0.5 – 2 Hz) which is explained by the proximity of both the sensors and the sources to the earth's surface and consistent layered geology of the deposit. The standard inversion technique for surface waves was applied to the seismic monitoring data (64 largest events occurred in the mines Solikamsk-1, -2 and -3 in 2004). The analysis of both amplitude and phase properties of the obtained point sources (single forces and moment tensors) was done in terms of mechanisms which are possible in these mining conditions viz. shear and tensile failures in host rocks, rock falls in the excavations and pillar bursts. The application of the above technique points to rock falls and horizontal tensile failures as the most likely mechanisms for the majority of the events. These mechanisms produce synthetic surface waves which fit the observed ones quite well.

The acquired experience of previously done and current studies of seismic sources in the mines of the Verkhnekamskoye potash deposit makes it possible to conclude that it is a rock fall that is the most probable mechanism of the local seismic events.

1 Introduction

1.1 Seismic Monitoring at the Verkhnekamskoye Potash Deposit

The Verkhnekamskoye potash deposit is situated in the Western Urals in the Perm region (Russia). Currently five mines operate there from one to three productive horizons (in sylvinite and carnallite zones) laying at the depth of 140 to 420 m (figure 1). The room-and-pillar method is used in the mines [11]. The geometrical parameters of the rooms are: length 150-190 m, width 3 – 15 m, height up to 10 m. Width of the pillars is 3 – 18 m.

The seismological observations in the deposit started in 1995. The observations are carried out using arrays of short period vertical geophones SM3-KV (having flat frequency response from 0.5 to 70 Hz) installed underground. The spatial configuration of the arrays is close to planar because of small variation of depth of the productive horizons and the excavations layouts. The average distance between the seismic sites is 2 km.

Seismic events associated with mining are routinely registered by the seismic systems. Waveforms of the events are represented by the wavelets of compressional (P) and much more intensive shear (S) waves. The frequency range of these waves is 8-20 Hz.

Because of the planar near-horizontal configuration of the seismic systems the vertical position of seismic events sources is poorly determined. Some features of the observed waveforms (small amplitudes of P waves in comparison to S waves for the vertical components, absence of high apparent velocities of propagation of seismic waves through the arrays) make it possible to suggest that seismic sources are in the vicinity of the mining level. This conclusion is similar to the one obtained for micro-seismic events in the potash mines of Saskatchewan deposit [6].

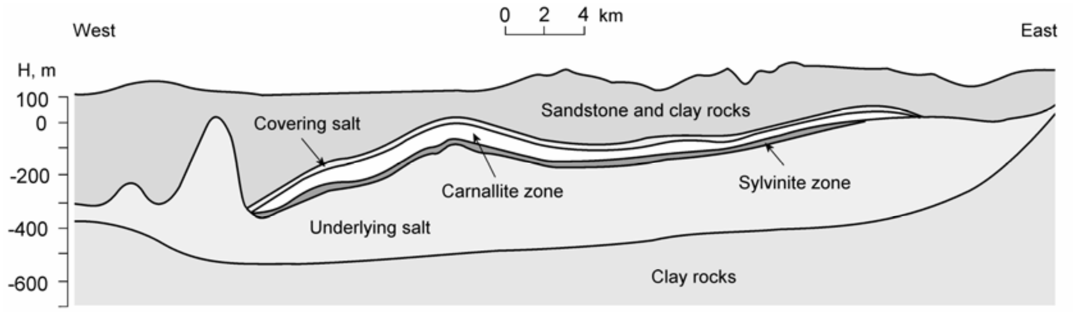

Figure 1 Geological section of the Verkhnekamskoye potash deposit

The sources of seismic events are usually located within the areas which were mined long time ago: from several years to decades. The observed seismicity can be regarded as a source of information about the fracture processes in the mined out areas. This interpretation is important for safe mining, as the integrity of horizons above the excavations needs to be controlled to exclude possibility of flooding of the mine. Thus the catalogues of mine-induced events are used for examination of the seismic regime of the mines. Seismically active zones are identified and their time history is analyzed. This assists in guiding active mining measures such as backfill [8].

1.2 The 'Low Frequency' Seismic Events

The waveforms of some mine-induced events are complicated by intensive low frequency (0.5 – 2 Hz) waves (figure 2). The numerical modelling of seismic wavefield for the Verkhnekamskoye deposit [9] makes it possible to interpret these low frequency waves as Rayleigh ones. The presence of Rayleigh surface waves in seismic monitoring data (which is quite rare in mining seismology) could be explained by a consistent layered structure of the deposit and the proximity of the earth's surface to the level of seismic sources and sensors.

Events with intensive Rayleigh waves have been named 'low frequency'. An analysis of the possible source mechanisms of the 'low frequency' events was done in [10]. As it was shown there, a classical seismic source model in the form of expanding shear crack does not reproduce the waveforms of the 'low frequency' events. Double couple point sources with reasonable parameters would generate predominantly high frequency body waves. Dynamical processes such as pillar bursts, rock falls, dynamical floor failures, which are observed in potash mines have been tried as possible sources of the 'low frequency' seismic events. The equivalent point sources have been determined for these processes. Synthetic waveforms for the constructed point sources have been calculated and compared with the seismograms of the 'low frequency' events. It has been found that only rock falls could generate Rayleigh waves of the observed intensity.

An interesting feature in the waveforms of some large 'low frequency' events is observed. It is a splitting of the shear waves. An additional phase S1 appears approximately 1 second before the arrival of the more intensive phase S2. This splitting could be interpreted as a result of a rock fall. If this is a case, then the week phase S1 would be associated with a detachment of the collapsed mass, while the much more intensive phase S2 would correspond to the impact of the collapsed block to a floor of the excavation. The time difference t_0 between the arrivals of S1 and S2 is equal to the free fall time of the collapsed mass. For $t_0 \approx 1$ s we have free fall distance (or height of the excavation) $H = gt_0^2/2 \approx 4.9$ m which seems plausible for the mining environments of the Verkhnekamskoye potash deposit.

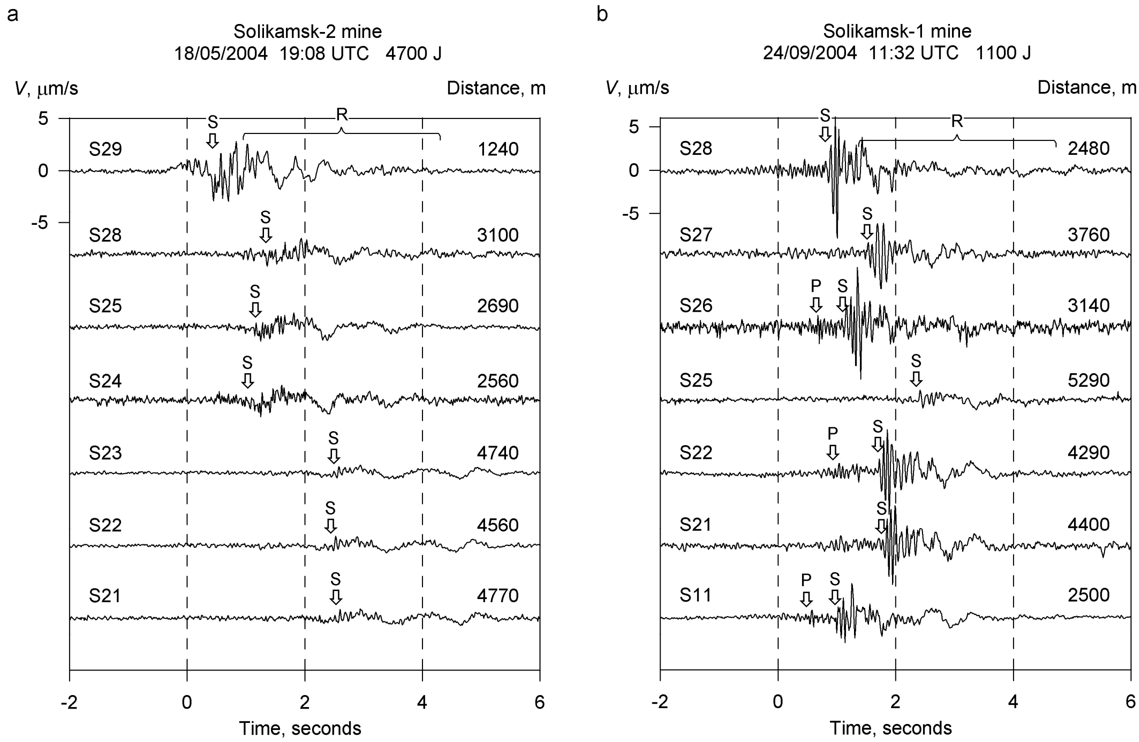

Figure 2 Examples of the 'low frequency' seismic events

To summarize, the previous investigations point to the importance of rock falls as seismic source mechanisms in the mines of Verkhnekamskoye deposit. In the present paper we undertake additional study of the source mechanism independent from those discussed above. The traditional seismological tool of equivalent seismic point source inversion was applied both to 'low frequency' events and events with less pronounced surface waves. The results of the inversion will be interpreted in terms of source processes which are most probable for the Verkhnekamskoye deposit.

2 Method

2.1 Seismic Point Source Inversion using Surface Waves

A study of source mechanisms based on surface (Rayleigh and Love) seismic waves is essentially developed and widely used in crustal and global seismology. It occurs that similar approaches are efficient at much smaller scale, in particular for the monitoring conditions in the Verkhnekamskoye potash deposit. Surprisingly, in spite of the lateral heterogeneities in the rock mass of the deposit (see figure 1), the low frequency part of the observed seismic signals (in the range 0.6-0.95 Hz) could be successfully modelled using fundamental mode of Rayleigh wave for the 1D layered half-space medium model. The quality of modelling of surface waves in the higher frequency range (0.95-2 Hz) becomes worse, probably due to the inadequacy of the 1D medium model. Therefore, given the geological conditions of the Verkhnekamskoye deposit and the configuration of the monitoring system it turns out that it is possible to investigate the mechanisms of seismic sources through a 'keyhole', i.e. as they radiate surface waves in 0.6-0.95 Hz frequency band.

A simple technique of surface-waves-based point source inversion was implemented. Theoretical waveforms of Rayleigh waves are calculated using method of Reflection and Transmission Matrices described in [7]. The source position and origin time used in the Rayleigh waves modelling are known according to the location based on P and S wave arrivals. The observed and theoretical waveforms of Rayleigh waves were band-pass filtered in the range 0.6-0.95 Hz. Then they were used to construct a linear system of equations for the source time functions (STF). This was done independently for the case of single force $F_i(t)$ and for the case of dipoles $M_{ij}(t)$. The systems are solved through SVD decomposition.

2.2 Analysis of the Inversion Results

The near-horizontal layout of the seismic sites in the mines of the Verkhnekamskoye deposit leads to some ambiguity in the surface-waves-based inversion results for equivalent point sources which are symmetric with respect to a vertical axis. This implies that the surface waves which are modelled by vertical force could be equally well modelled using either vertical dipole or two equal orthogonal horizontal dipoles.

In the case of the mines of the Verkhnekamskoye deposit different in nature source processes have axisymmetric point source equivalents. In particular a rock fall would correspond to a vertical force, pillar burst would correspond to a set of orthogonal dipoles with equal horizontal ones (see Appendix 1). Thus an additional analysis of the point source inversion results is desirable. The phases of the inverted source time functions are found to be useful for distinguishing among axisymmetric sources. For instance, in the case of a rock fall the average phase φ_F of the STF of the equivalent vertical force must be roughly equal to $-\pi/2$, if the moment of impact of the collapsed block is chosen as the origin time. For the pillar burst the STF of equivalent point source should have step-wise pulse shape with a negative sign, therefore the average phase φ_M of the vertical dipole STF must be roughly equal to $-\pi/2$. For a horizontal tensile failure the sign of the STF is opposite which will result in $\varphi_M = \pi/2$.

Taking into account the above arguments, the following scheme of the point source inversion and analysis of its results was drown up (figure 3).

1) The waveforms in the 0.6-0.95 Hz band are inverted for two equivalent point sources, namely for single force or for force dipoles (seismic moment tensor). The correlation of observed and synthetic Rayleigh waves in the 0.6-0.95 Hz range is used as a measure of the inversion quality. The subsequent analysis is carried out in parallel for the two cases: (a) inverted single force $F_i(t)$ and (b) inverted moment tensor $M_{ij}(t)$.

2) The axial symmetry of the point source is investigated.

2a) In the case of the single force this was aimed to identify rock fall sources, for which points source equivalent has vertical component dominating over horizontal ones (see Appendix 1). The parameter $\theta_F = |F_z| / \sqrt{F_x^2 + F_y^2 + F_z^2}$ was chosen as a measure of symmetry with respect to vertical axis. It was assumed that $\theta_F > 0.8$ is acceptable for provisionally classifying the source as a rock fall.

2b) In the moment tensor case axial symmetry should be used to discriminate between symmetric sources, for instance pillar burst or horizontal tensile failure, and asymmetric ones, such as shear failure. The parameter $\theta_M = \sqrt{0.5(M_{xx} + M_{yy})^2 + M_{zz}^2} / \sqrt{M_{ij}^2}$ was selected as a measure of the symmetry with respect to a vertical axis. The fully axisymmetric point source corresponds to $\theta_M = 1.0$. For the most probable asymmetric source – shear failure with arbitrary strike, dip and rake - the parameter θ_M will be less than 0.7 with 90% probability. So the value $\theta_M = 0.7$ was chosen as a separator between asymmetric and axial symmetric source processes.

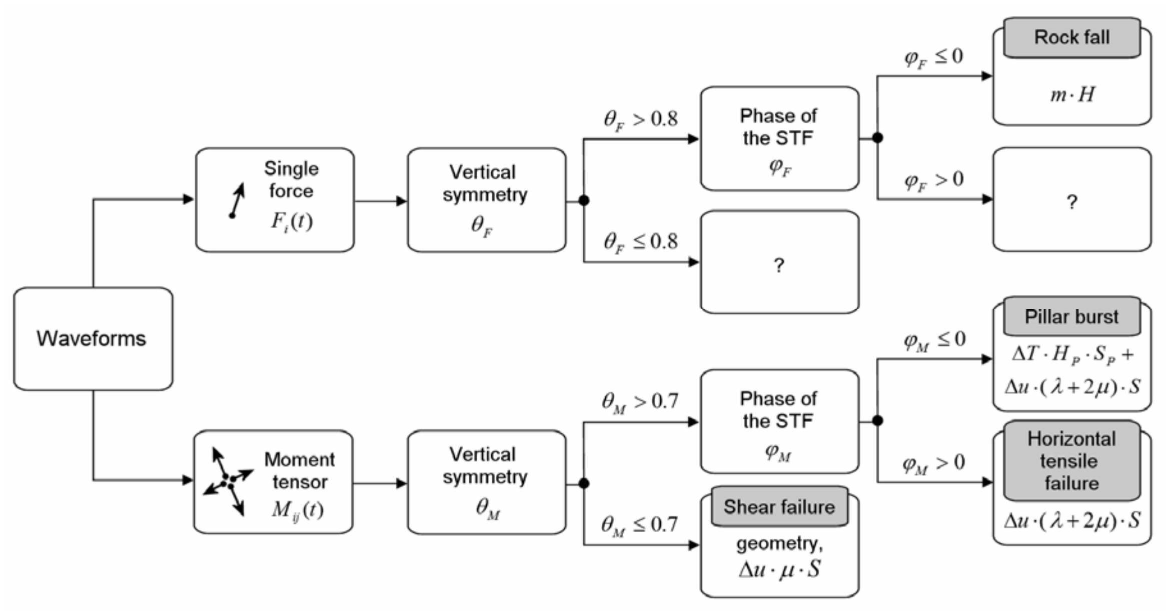

Figure 3 Flowchart for the inversion and analysis of seismic point sources

3) The average phase of the source time function is calculated.

3a) A rock fall is announced as probable source mechanism in the event that the phase of single force φ_F is within the interval $(-\pi..0]$.

3b) The phase of point source for the pillar burst φ_M will be in the interval $(-\pi .. 0]$ and the phase for the horizontal tensile failure φ_M will be in $(0 .. \pi]$.

4) The geometrical and mechanical parameters of the source processes are estimated from the amplitude spectrum of the inverted STF.

4a) The product mH is calculated from the low frequency plateau of the reduced amplitude spectrum $|F_z(f)/2\pi f|$ (figure A2).

4b) The generalized characteristics of pillar burst, horizontal tensile and shear failures ($\Delta T\, H_P\, S_P + \Delta u(\lambda + 2\mu) S$, $\Delta u(\lambda + 2\mu) S$ and $\Delta u\, \mu\, S$ - see Appendix 1) could be estimated from the amplitude spectra of the moment tensor components $|M_{ij}(f)|$.

3 Results

The above described inversion of surface waves and the analysis of the inverted sources were applied to seismic monitoring data of Solikamsk-1, -2 and -3 mines obtained in the period January-September of 2004. We selected 64 largest events recorded by at least 5 sites. The results of inversion and analysis of point sources for these events are summarized in figure 4.

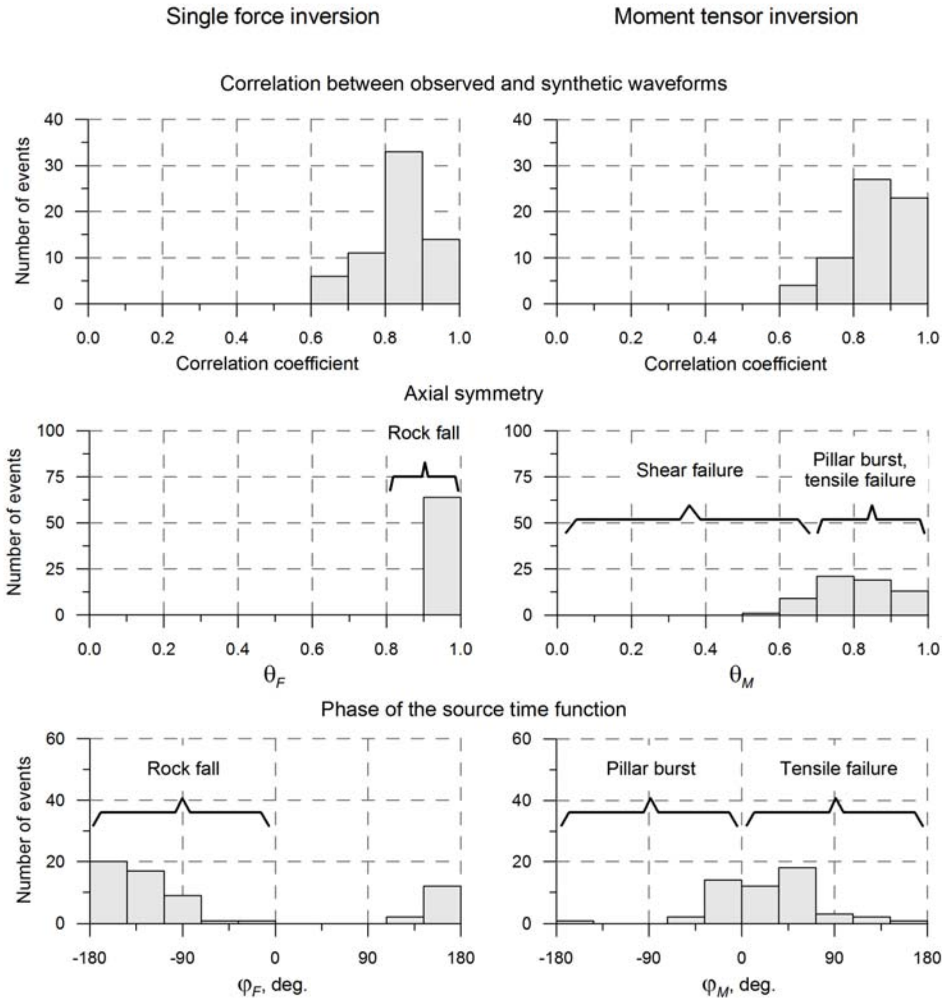

Figure 4 Results of the point source inversion for 65 seismic events occurred in 2004 in Solikamsk-1,-2 and -3 mines

A strikingly good agreement between synthetic and observed waveforms was observed for most of the selected events. This is illustrated in figure 5. The mean coefficient of correlation between the observed and synthetic waveforms was more than 0.8 for 75% of events (figure 4). A slightly worse match can be noted for the single force inversion due to the smaller number of degrees of freedom as compared to the moment tensor case.

We consider it of interest to note the strong symmetry of the inverted sources with respect to the vertical axis. For instance, all events have $\theta_F > 0.9$ (figure 4) which means that they could be modelled by a vertical force. Similarly, the inverted moment tensors demonstrate that the events could be associated with either pillar bursts or horizontal tensile failures. Only 10 events we found with $\theta_F \leq 0.7$ and this could be attributed to some shear failure admixture.

From the analysis of the phase φ_F of the single force STFs (figure 4) one can conclude that the majority of the events (48 from 64, i.e. 75%) could be interpreted as rock falls. A similar analysis of the phase φ_M of the vertical dipoles STFs shows that more then half of the events (36 from 64, i.e. 56%) could be associated with horizontal tensile failure. A pillar burst mechanism is possible in 27% cases (17 events from 64).

The intensity of the source processes was quantified in terms of generalized parameters. For instance, in the case of the rock falls this parameter is mH and it varies from $2 \cdot 10^5$ to 10^7 kg·m.

4 Conclusions

The main result of the implemented surface-waves-based point source inversion is that two alternative source mechanisms are possible for most of the large events observed in the Solikamsk-1, -2 and -3 mines during 2004. These events could be associated either with a rock fall or with a horizontal tensile failure.

The acquired experience of investigating seismic source in the mines of the Verkhnekamskoye potash deposit could be summarized in the following way:

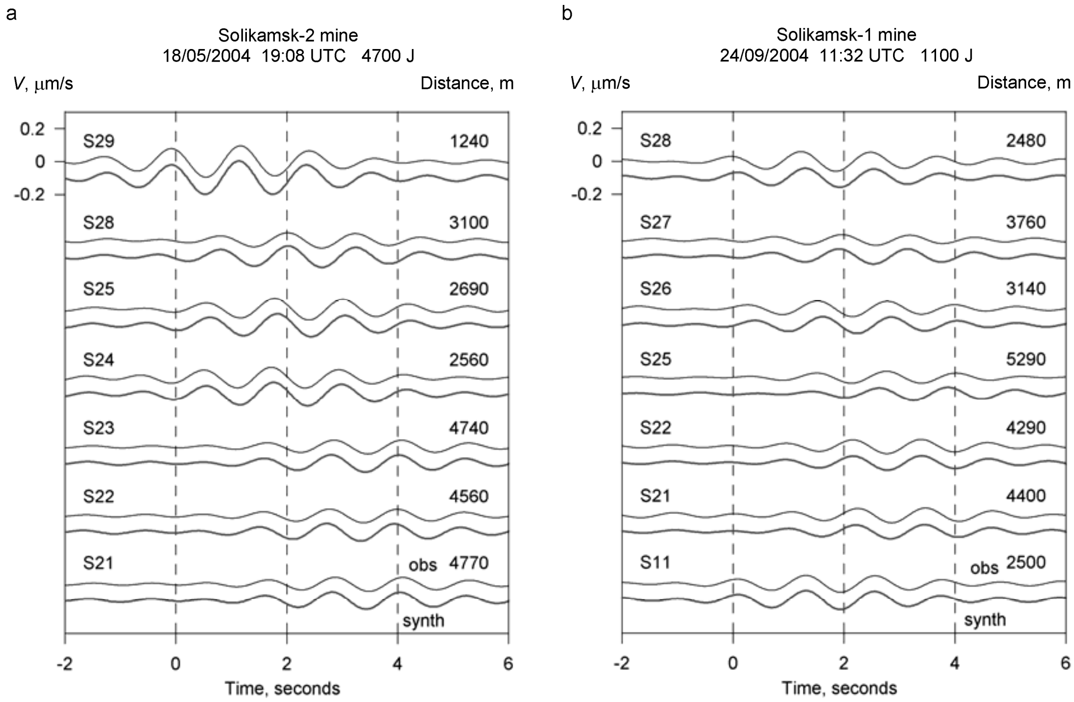

Figure 5 Comparison between observed (upper) and modelled (lower) seismograms of Rayleigh wave for events shown in the Figure 2

The modelling of seismic wavefields in the Verkhnekamskoye deposit mining and monitoring environments points to rockfalls as the sole most probable mechanism of radiating surface waves with frequency in the range 0.6-3 Hz and with amplitudes commeasurable with higher frequency body waves [10]. Other theoretically possible source processes would radiate predominantly body waves.

The presence of duplicating arrivals of shear waves in the waveforms of some large events could be explained by two phases of a rock fall, i.e. by the detachment and impact of the collapsed block.

The surface waves observed for most of the large events could be confidently modelled in two possible ways: either as a vertical force with source time function corresponding to a rock fall or as a vertical dipole with source time function of tensile failure.

On the basis of these facts we may conclude that rock falls are behind most of the seismic activity in the mines of the Verkhnekamskoye deposit.

The results described above demonstrate also that surface waves could be a useful provider of information about source processes in mining environments. In some cases layered structure of the rock mass within a mine make it possible to numerically simulate these waves using a simple 1D medium model. This opens the door to the use of numerous efficient techniques developed in crustal seismology.

Acknowledgements

The author would like to thank Dr. Sergey L. Younga from Institute of Physics of the Earth (Moscow) for the valuable ideas concerning appropriate measure of axial symmetry of the seismic moment tensor. In particular the author wishes to thank Dr. Assen Ilchev from ISS International Ltd. for interesting discussions and comprehensive help in improvement of the text of the paper.

References

1. Aki, K. and Richards, P.G. Quantitative seismology: theory and methods, University Science Books, 2002.
2. Anandakrishnan, S., Taylor, S.R., and Stump, B.W. Quantification and characterization of regional seismic signals from cast blasting in mines: a linear elastic model, Geophys. J. Int., 1997, 131. 45-60.
3. Backus, G. and Mulcahy, M. Moment tensors and other phenomenological description of seismic sources-I. Continuous displacements, Geophys. J. R. astr. Soc., 46, 1976, 341-361.
4. Dolgov, P.V., Polyanina, G.D. and Zemskov, A.N. Methods of prediction and prevention of gas-dynamic events in potash mines, Nauka, USSR, 1987. (in Russian)
5. Fukao, Y. Single force representation of earthquakes due to landslides or the collapse of caverns, Geophys. J. Int., 122, 1995, 243-248.
6. Prugger, A.F. and Gendzwill, D.J. Fracture mechanism of microseisms in Saskatchewan potash mines. Proc. of the 3rd International Symposium on Rockbursts and Seismicity in Mines, Kingston, 1993 (ed. P.Young), Balkema. 239-244.
7. Kennett, B.L.N. The seismic wavefield. Volume1: Introduction and theoretical development, Cambridge, 2001.
8. Malovichko, A.A., Sabirov, R.H. and Akhmetov, B.Sh. Ten years of seismic monitoring in mines of the Verkhnekamskoye potash deposit. Proc. of the 6th International Symposium on Rockburst and Seismicity in Mines, Perth, 2005 (eds. Y. Potvin & M. Hudyma), ACG, 367-372.
9. Malovichko, D.A. and Baranov, Yu.V. Application of numerical modelling for analysis of underground recordings of seismic events. Proc. of the 5th Symposium on Rockbursts and seismicity in mines, Megaliesberg, 2001 (eds. G. van Aswegen, R.J. Durrheim, W.D.Ortlepp) SAIMM, 479-482.
10. Malovichko, D.A. Study of "low-frequency" seismic events sources in the mines of the Verkhnekamskoye potash deposit. Proc. of the 6th International Symposium on Rockburst and Seismicity in Mines, Perth, 2005 (eds. Y. Potvin & M. Hudyma), ACG, 373-377.
11. Methodical manual of mining in the Verkhnekamskoye potash deposit. Ed. V.A. Soloviev, Nedra, 1992 (in Russian).
12. Takei, Y. and Kumazawa, M. Phenomenological representation and kinematics of general seismic sources including the seismic vector modes, Geophys. J. Int., 121, 1995, 641-662.
13. Taylor, S. R. False alarms and mine seismicity: An example from the Gentry mountain mining region, Utah, Bull. seism. Soc. Am., 84, 1994, 350-358.

Appendix 1: Equivalent Seismic Points Sources for Dynamic Processes in Mines of the Verkhnekamskoye Potash Deposit

Assume that we have Green's function $\mathbf{G}(\mathbf{x}, \xi, \omega)$ which is valid in a domain V of medium with an exception of a certain part of it V_0. Here $\mathbf{x}$ and ξ correspond to points in the medium, ω is the frequency[a]. The part V_0 in which the Green's function is not valid will be called the 'physical source region'. For instance, in theoretical seismology, the Green's function for elastic medium characterized by the stiffness tensor $c_{klij}(\mathbf{x})$ is used as a rule. The 'physical source region' in this case could be domain of a 'localized, temporary failure' [3], where the assumed elastic strain-stress relation does not hold. Besides that the 'physical source region' could contain strong heterogeneities not parameterized by $c_{klij}(\mathbf{x})$ [7].

Seismic radiation from the 'physical source region' V_0 could be described in terms of displacement $\mathbf{u}(\mathbf{x}, \omega)$ and traction $\mathbf{T}(\mathbf{u}(\mathbf{x}, \omega), \mathbf{n})$ on the boundary ∂V_0. Here $\mathbf{n}$ corresponds to the unit normal to ∂V_0.

The representation theorem and the Taylor's expansion of the Green's function relative to $\xi^{\mathbf{0}} \in V_0$ makes it possible to describe the low-frequency part of seismic wavefield at point $\mathbf{x}$ outside of the 'physical source region' in the following way:

$$u_s(\mathbf{x}, \omega) = F_i(\omega) G_{si}(\mathbf{x}, \xi^{\mathbf{0}}, \omega) + M_{ij}(\omega) \left. \frac{\partial G_{si}(\mathbf{x}, \xi, \omega)}{\partial \xi_j} \right|_{\xi=\xi^{\mathbf{0}}} + \dots .$$

That is the observed seismic wavefield is the result of action of the equivalent point source in the point $\xi^{\mathbf{0}} \in V_0$. This point source includes:

a) single force with components:

$$F_i(\omega) = \iint_{\partial V_0} T_i(\mathbf{u}(\xi, \omega), \mathbf{n}) \; dS(\xi),$$

b) force dipoles with components:

$$M_{ij}(\omega) = \iint_{\partial V_0} \left[T_i(\mathbf{u}(\xi, \omega), \mathbf{n}) (\xi_j - \xi_j^0) - c_{klij}(\xi) \, \mathrm{u}_k(\xi, \omega) \, n_l \right] dS(\xi),$$

and multipoles of higher orders.

Let us apply the above representation to the dynamic processes presumed and observed in potash mines of the Verkhnekamskoye deposit [4]. These processes are shear or tensile failures near the excavations, rock fall in excavations and dynamic pillar failure (pillar burst) (figure A1).

Shear and Tensile Failure

The surface of shear or tensile crack Σ_S could be chosen as surface of the 'physical source' ∂V_0 (figure A1a). Then the equivalent point source of the lowest order will be a set of force dipoles (figure A1b):

$$M_{ij}^S(\omega) = -\iint_{\Sigma_S} c_{klij}(\xi) \, \mathrm{u}_k(\xi, \omega) \, n_l \; dS(\xi) \; .$$

---

[a] The notations from Aki and Richards monograph [1] are used as far as possible. Subscripts indicate the Cartesian components of vectors and tensors, and repeated indices imply summation

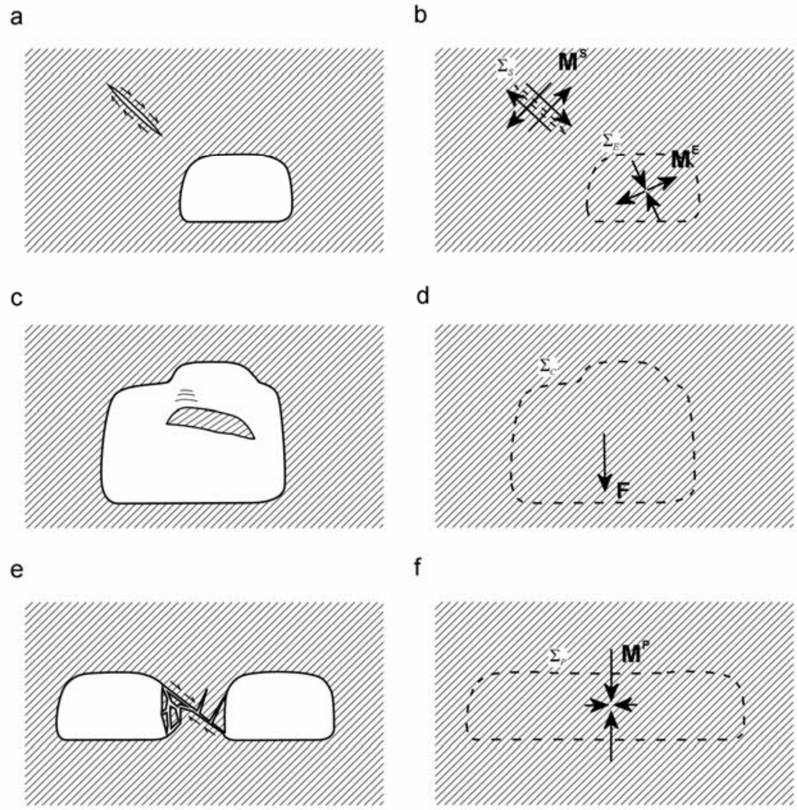

Figure A1. Dynamic processes in potash mines and their equivalent seismic point sources: shear failure in ambient rock mass (a, b); rock fall (c, d); pillar burst (e, f)

In the case of homogeneous isotropic medium around the crack ($c_{klij}(\xi) = \delta_{kl}\delta_{ij}\lambda + (\delta_{ki}\delta_{lj} + \delta_{kj}\delta_{li})\mu$) the equivalent for shear crack will be a pair of force couples (double couple) and equivalent for tensile crack will be a set of vector dipoles [1].

It's important to note that abovementioned source equivalents must be used with Green's function $\mathbf{G}(\mathbf{x}, \xi, \omega)$ that takes into account presence of heterogeneities not described by $c_{klij}(\mathbf{x})$ in the vicinity of the crack. For instance if the excavation Σ_E is near the shear or tensile crack (figure A1a) and nevertheless we want to use the Green's function for homogeneous space or layered half space, then it's necessary to add secondary source (figure A1b) with seismic moment:

$$M_{ij}^{E}(\omega) = -\iint\limits_{\Sigma_E} c_{klij}(\xi)\, \mathrm{u}_k(\xi, \omega)\, n_l \; dS(\xi) \;.$$

The secondary source reproduces the effects of distortion (or scattering) of waves radiated by the primary source (shear or tensile crack) on the surface of the excavation. If the length of seismic waves under study is larger than the distance between the crack and the heterogeneity (excavation), then the primary and the secondary sources could be combined, i.e. the low frequency seismic radiation will be described by a point source with seismic moment tensor $M_{ij}^{S}(\omega) + M_{ij}^{E}(\omega)$.

Thus for shear or tensile failure in mines we could expect equivalent seismic source in a form of a double couple or vector dipoles which are complicated by additional dipoles terms reflecting the deviation of the medium in the vicinity of the crack from homogeneous isotropic model.

Rock fall

It makes sense to choose the whole excavation with collapsing block of rocks as the 'physical source region' (figure A1c-d). Then the lowest order equivalent point source will be a single force:

$$F_i(\omega) = \iint_{\Sigma_C} T_i(\mathbf{u}(\xi, \omega), \mathbf{n})\ dS(\xi)\,, \tag{A1}$$

where Σ_C is the surface of the excavation.

The source time function of the equivalent single force could be written in the time domain from arguments about behavior of traction $\mathbf{T}(\mathbf{u}(\mathbf{x}, \omega), \mathbf{n})$ on the surface Σ_C during the process of rock fall. The vertical component of the traction will be essential in (A1) in the course of the process. In that case the vertical component F_Z of equivalent single force will dominate over the other components. The onset of the source time function of F_Z will have positive sign (in the coordinate system with upward vertical axis) and will correspond to a rebound of the ambient rock mass due to the detachment of the block (figure A2a). The amplitude of this positive pulse is constant during the free fall period $\sqrt{2H_1 / g}$ and equals mg, where m is the mass of the block, H_2 is the height of the free fall and g is the gravitational constant. The subsequent negative pulse corresponds to the impact of the block on the floor of the excavation. The shape of this pulse is determined by the nature of the impact. The more inelastic the interaction of the block with the floor, the lower will be the frequency content of the pulse. The time integral to infinity of the source time function must be zero due to the momentum conservation law. It is noteworthy that similar source time functions are used for the description of seismic radiation from:

- large scale collapses in mines [13];
- casting of rocks in the course of open pit blasts [2].

There are two interesting features of the source time function amplitude spectrum (figure A2b) which are independent from the details of the impact. If we assume that the velocity of the block doesn't change sign in the course of both free fall and impact to the floor then:

- the low frequency part of the spectrum has an asymptotic straight section. Its slope is equal to the product of mass of the block m and its total motion during free fall and the impact $H = H_1 + H_2$, i.e. $|F_z(\omega)| \to \omega m H$ as $\omega \to 0$;
- the slope has its maximum value for $\omega \to 0$.

So the universal characteristic of a rock fall mH could be estimated from the low frequency range of equivalent single force time function. The same result was obtained in a different way for various kinds of processes associated with mass advection (landslides, cavern collapses, etc.) in [12, 5].

Pillar Burst

When inelastic deformation occurs within the pillar then it is reasonable to choose as 'physical source region' the pillar itself and the neighbouring excavations (figure A1e-f). In this case the lowest order equivalent point source will be seismic moment:

$$M_{ij}^{P}(\omega) = \iint\limits_{\Sigma_P} \left[T_i(\mathbf{u}(\boldsymbol{\xi}, \omega), \mathbf{n})(\xi_j - \xi_j^0) - c_{klij}(\boldsymbol{\xi})\, \mathrm{u}_k(\boldsymbol{\xi}, \omega)\, n_l \right] dS(\boldsymbol{\xi}) \,,$$

where point $\boldsymbol{\xi}^{\mathbf{0}}$ is in the middle of the pillar, Σ_P is the boundary of the chosen 'physical source region'.

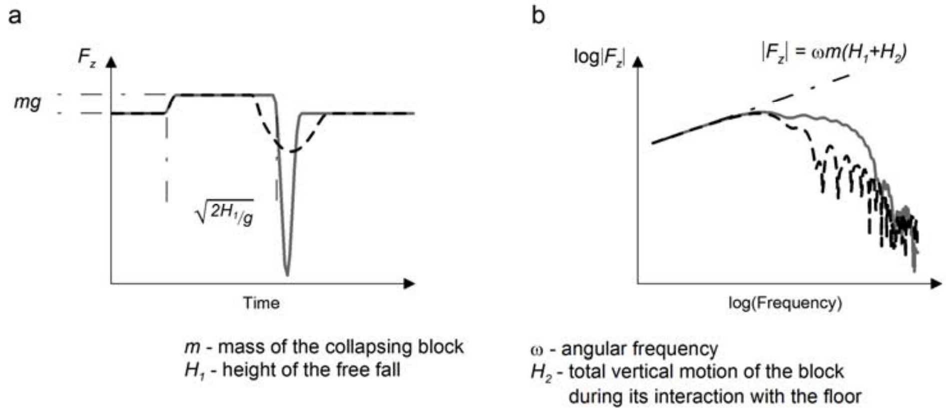

Figure A2. Source time function of the vertical force equivalent to a rock fall in time (a) and frequency (b) domains. Two cases of interaction of the falling block with excavation floor are presented, one of which (grey lines) is more 'elastic' (i.e. has smaller interaction time) than another (black dashed line). The total block motion $H_1 + H_2$ is the same in both cases

If we assume that:

- the material around the pillar and the neighbouring excavations is elastic, homogeneous and isotropic (i.e. $c_{klij}(\boldsymbol{\xi}) = \delta_{kl}\delta_{ij}\lambda + (\delta_{ki}\delta_{lj} + \delta_{kj}\delta_{li})\mu$);
- the vertical component of displacement $\mathbf{u}(\mathbf{x}, \omega)$ on the top and bottom of the surface Σ_P is larger than the horizontal components and also larger than the displacement in other parts of Σ_P during the pillar burst;

then the following expression for moment tensor could be obtained:

$$M_{ij}^{P}(\omega) \approx -\frac{1}{i\omega} \begin{pmatrix} \Delta u\, \lambda\, S & 0 & 0 \\ 0 & \Delta u\, \lambda\, S & 0 \\ 0 & 0 & \Delta T\, H_P\, S_P + \Delta u\,(\lambda + 2\mu)\, S \end{pmatrix},$$

where Δu is the average convergence of top and bottom parts of Σ_P, S is the horizontal area of top (or bottom) part of Σ_P, ΔT is the average drop of vertical traction below (or above) the pillar, H_P is the height of the pillar, S_P is the horizontal area of the pillar.

The expression above tends to the equivalent point source model of a closing crack [1] as the height of the pillar H_P goes to zero.

It's interesting to note that vertical component of the moment tensor M_{zz}^{P} prevails over horizontal ones and its magnitude depends both on the traction drop ΔT and the displacement drop Δu.

Thus, under the assumptions made, the equivalent seismic point source for the pillar burst is made of a set of vector linear dipoles of negative sign. The generalized characteristic of the pillar burst $\Delta T\, H_P\, S_P + \Delta u\,(\lambda + 2\mu)\, S$ could be estimated from the magnitude of the most intensive (vertical) dipole.

RaSiM 7(2009): Controlling Seismic Hazard and
Sustainable Development of Deep Mines,
C.A. Tang(ed), Rinton Press, 399-406

MOMENT TENSORS OF MINING TREMORS – DETECTION TOOL OF THE MODE OF ROCK-MASS FRACTURING: MECHANISM OF DEEP EVENTS ON OCTOBER 24 AND OCTOBER 12, 2005 IN MOAB KHOTSONG MINE, S.AFRICA

JAN SILENY

Institute of Geophysics, Academy of Sciences

Bocni II/1401, 14131 Praha 4, Czech Rep.

Contrary to natural earthquakes, where the features of the geological environ without void spaces and the character of loading naturally favor shear slip, in foci of seismic events induced by man-made activities there is a physically based reason for occurrence of non-shear processes. Especially in mines, the existence of mined-out cavities enables implosive events which are improbable among natural earthquakes. In particular, great depth of excavation typically occurring in gold ore mining results in extreme loading of mine structures underground. High stress concentrations cause collapsing of excavated cavities, which is reflected by specific non-double-couple (non-DC) mechanisms. Apart from mining tremors, natural earthquakes of a tectonic origin may occur in the area where mining activity takes place. The mechanism in the moment tensor (MT) representation, in particular the DC vs. non-DC issue, is an important discrimination instrument. To develop it into a reliable methodological tool it is however vital to assess properly errors in the MT retrieval and especially errors in the non-DC component determination, which is vulnerable to possible deterioration of the quality of records, station distribution, event location and velocity structure modelling. We demonstrate the approach on data from Moab Khotsong mine, S.Africa: we determine complete moment tensors of two tremors, discuss the reliability of the retrieval, interpret their decomposition into equivalent forces, check the significance of the dominance of the DC component by an F-test and hypothesize on this basis about their tectonic origin.

1 Introduction

The mechanism is one of the most important parameters of an earthquake focus and of foci of artificially induced events as well. Its determination from seismic data is usually not easy because its signature into the data is coupled with the effects of propagation from the focus to the point of observation. To decouple the latter, we need to know the response of the medium – the Green's function - in sufficient detail, which is rarely available. This hampers the resolution of the source parameters including the mechanism. They are biased the more the higher is the frequency of seismic records. Thus, whereas in the long periods (LP) available in teleseismic and regional distances the waveform inversion is straightforward and has became a routine task (e.g., [3] for teleseismic inversions, [2] for regional studies), short-period (SP) records from weak earthquakes are much more difficult to invert. Several case studies with SP data were performed (e.g., [4]), but the resultant mechanism seems to be rather dependent on the frequency band employed in the inversion. Performing the inversion in the spectral domain, the amplitude of the low-frequency plateau may be evaluated from integrals of displacement and velocity records [18]. Taking into account the frequent lack of knowledge about the true parameters of the medium resulting in our inability to simulate well local SP waveforms, it is more robust to parametrise the waveforms and invert these parameters which are, e.g., the amplitudes of first onsets of individual seismic phases or their polarities [15]. In this way, in fact, the ignorance about the medium hampering the synthesis of accurate Green's functions, is overcome by the skill of the interpreter in picking the amplitude of a seismic phase.

Most of the methods currently applied to determine the mechanism by inverting seismic data apply the concept of the moment tensor (MT). This formalism allows describe a general dipole source, i.e. all sources with zero net force. The double couple (DC) – a superposition of two single couples which balance their moments – is one of them. Being the body force equivalent of a shear slip along a planar fault (embedded in an isotropic medium), it is traditionally accepted in earthquake seismology as the mechanism of tectonic earthquakes. Violating some of the assumptions mentioned above results however in appearance of non-DC components even for a shear-slip: bending of the fault [5], and anisotropy in the focal zone [7]. In mining environment where there are void spaces and the stress field is more complex than the tectonic loading due to its concentration on the cavities and stress concentrators, more general processes in the foci of seismic events may be expected resulting in a more general system of forces than the balanced couple of dipoles, e.g., [9,10,14,17]. For their description just the unconstrained moment tensor can be advantageously applied. For a comprehensive overview of seismic events with a non-double-couple (non-DC) mechanism see [5,11]. It should be stressed that non-DC components of the mechanism retrieved from seismic data need not be necessarily real phenomena generated by the source, but due to the coupling of the source and propagation in seismic data they can be artifacts of a poor modeling of the medium and/or inexact hypocenter location [8]. For instance, spurious non-DC mechanisms can be due to oversimplifying the near-surface structure [1], or neglecting anisotropy [16].

The aim of the paper is to search for mechanisms of mining induced events by using the moment tensor (MT) source model. We will process seismograms recorded underground from a couple of events having occurred in the deep gold mine Moab Khotsong in South Africa. We invert 3-component amplitudes with signs of direct P and S waves, which provides a better control of the match of the synthetics to the data in comparison to inversion of complete waveforms, and allows to obtain an estimate of the confidence of the resolved mechanism taking into account inexact modeling of the medium [15]. In accordance with the most widely accepted MT decomposition into an isotropic part (ISO), DC and compensated linear vector dipole (CLVD), we will determine the percentage of these "elementary mechanisms" in the resolved MT and check how the mechanism departs from a pure DC, the body force attributed to tectonic earthquakes.

2 Data

The parameters of the two deep seismic events from the Moab Khotsong mine are listed in Tab. 1. The distribution of the stations across the focal sphere for each of the events is displayed in Fig. 1.

Table 1. Parameters of two deep seismic events from Moab Khotsong mine. From left to right the date, localization, number of stations having recorded the particular event.

date	location			obs
	NS	EW	Z	
Oct 24 2005 2:32:15.178	-26780.4453	4454.1421	4611.7358	22
Oct 12 2005 6:10:37.731	-26805.3477	3848.0876	3570.0176	28

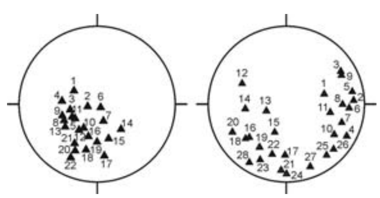

Figure 1 Focal sphere coverage for the events from Tab. 1. Left - event on Oct 24, 2005, right – Oct 12, 2005. Equal area projection of lower hemisphere

The rock mass is supposed to be isotropic and homogeneous, no data about its anisotropy or inhomogeneity are available. Therefore, only direct P and S phases propagating along straight-line rays connecting the hypocenter and a station are anticipated. The reality is obviously more complex and possible inhomogeneity causes the ray bending, but the deviation is supposed not to be large in the short hypocenter distances of the stations. Therefore, a large decline of the polarization of the 1st onset (supposed to be the direct P wave), which may occasionally occur in the data, should be interpreted either as the absence of P arrival (e.g., due to observation in a nodal plane of the source) or as a mis-arrangement of the channels for individual components or a polarity flip.

Large decline of the 1st onset polarization from the straight-line ray was indeed frequently observed during the initial inspection of the data, and a mis-arrangement of the component channels was detected at number of stations. However, even after correcting such gross errors in the data at some stations a large mismatch persists. In the following, several examples of the waveforms are shown which exhibit both consistency of the polarization with the ray or a pronounced deviation, on the other hand. Let us denote as the angle of inclination of P-polarization from the ray, and the angle of inclination of S-polarization from the plane perpendicular to the ray.

A perfect alignment of the polarizations of both P and S waves from event on Oct 24 can be observed at station #7 (hypocenter distance 2533 m), Fig. 2: =30, =10. The waveform is very simple here and there is no doubt about the points of picking the amplitude at the P and S wave.

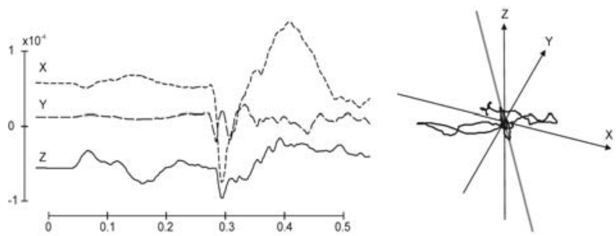

Figure 1 3-c ground displacement waveform (left) and corresponding particle motion diagram in a 3-D view (right) from event on Oct 24, 2005 at the station #7. x-component – fine dash, y-component – rough dash, z-component – solid line, straight-line ray connecting the source and the station in the particle motion diagram – grey line. Time on horizontal axis in seconds.

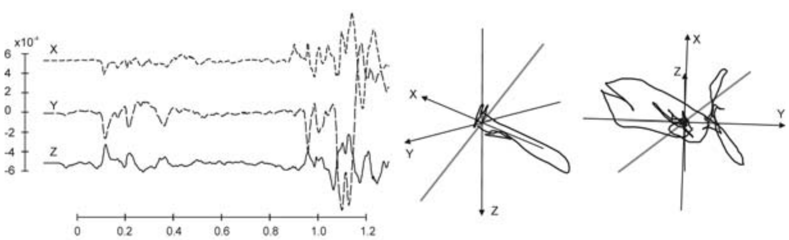

Figure 3 3-c ground displacement waveform (left) and corresponding particle motion diagrams in a 3-D view from event on Oct 12, 2005 at the station #1. Middle – particle motion diagram of the 1st sub-event, right – the 2nd sub-event. For details see the caption of Fig. 2.

Contrary to the event Oct 24, 2005, which was a simple single event, the event on Oct 12, 2005 is a double event. It is well seen on the waveform at the station #1 (at the distance 1727 m from the focus), Fig. 3. The 1st sub-event is well consistent with the ray in the polarizations of both P and S arrivals (=180 and =70), while in the following one the direction of P arrival surprisingly does not follow the ray at all (=820). Taking into account the fit of the 1st sub-event, the decline at the 2nd one cannot be caused by a mis-orientation of the sensor. The reason must be physical, e.g. a different ray path, reflection etc. of the signal traveling from the same source (however the large amplitudes at the 2nd sub-event weaken the hypothesis), or a completely different focus unrelated to the 1st sub-event. For a credible explanation, a re-localization should be done and a waveform modeling possibly by using empirical Green's function approach. This is, however, beyond the scope of this study. Due to the unresolved complexity of the generation of the 2nd sub-event, in the following we will be dealing with 1st sub-event only.

3 Selection of suitable P and S phases

In summary, in Tab. 2 and 3 the deviation angles and determined by the polarization analysis are presented for events Oct 24 and Oct 12, respectively.

Table 2 α,β - rectification angles (Fig. 4). (x,y,z) – x,y,z-component missing, (b) – bad signal.

No	1	2	3	4	5	6	7	8	9	10	11	12	13	14	15	16	17	18	19	20	21	22
α [^{0}]	9	8	50	(y)	31	18	3	12	(x)	(z)	54	16	(b)	10	5	3	17	12	23	(z)	19	26
β [^{0}]	24	6	61		10	8	1	3			39	15		12	11	4	23	6	0		2	1

Table 3 α,β - rectification angles (Fig. 4). For details see caption of Tab.2; in addition, (i) – integration failed.

No	1	2	3	4	5	6	7	8	9	10	11	12	13	14	15	16	17	18	19	20	21	22	23	24	25	26	27	28
α [^{0}]	18	35	9	(x) (z)	87	8	30	44	6	62	79	(b)	23	12	(i)	(z)	19	43	21	(x)	27	46	4	(y)	22	12	(x)	11
β [^{0}]	7	5	6		49	9	17	30	17	40	62		2	24			1	12	6		16	32	13		4	2		1

The most frequent loss of the data is the failure to record all three components at a station, while a corrupted signal appears only occasionally (station #13 for event Oct 24, #15 for Oct 12). For some of the stations, large deviations of the polarization from the ray remained even after the careful checking the sensor orientation and the polarities of individual component channels. They cannot be explained by a reasonable heterogeneity or anisotropy of the rock massif, and we are not able to apply a correction. Therefore, we have set an ad hoc threshold value of 500, and the data exhibiting larger deviations we exclude from the inversion. For the event Oct 24 this is just single station #3, for Oct 12 stations #5, 10 and 11. Thus, in summary, for the inversion we have got a data set containing P and S amplitudes at 16 stations (namely Nos. 1-3, 5-8, 12, 14-19, 21, 22) for the event Oct 24, and at 18 stations (Nos. 1-3, 6-9, 13, 14, 17-19, 21-23, 25, 26, 28) for event Oct 12.

4 Synthesis of Green's functions

Data available for description of the response of the rock massif were velocities of P and S wave only, assuming an isotropic and homogeneous medium. The values are vP=6200 m/s and vS=3650 m/s. It should be noted that a high accuracy of the value of seismic velocities is not critical in our approach, as small variation of the velocity introduces mainly changes in arrival times, which is not involved at all during the amplitude inversion.

5 Inversion of amplitudes of direct P and S phases

The homogeneity of the medium implies the propagation of the waves along straight-line rays connecting the hypocenter with the observational site. Therefore, the predicted polarization of the direct P and S wave in an isotropic homogeneous medium is along the ray and perpendicularly to it, respectively. However, we have detected some inclination of the polarizations from these predicted directions in the data. Therefore, before inverting the data, it is reasonable to reduce them for the observed inclinations. The procedure for the P and S polarization is displayed in Fig. 4.

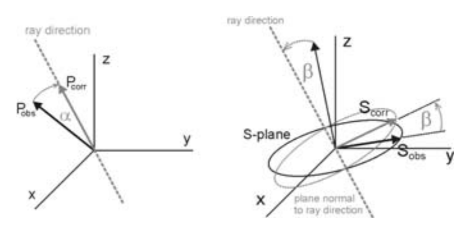

Figure 4 Scheme of reducing a P amplitude inclined from the ray direction (left), and reducing an S amplitude inclined from the plane perpendicular to the ray.

Thanks to description of the mechanism by means of the complete moment tensor (i.e. without the double-couple constraint, see the next section) the inversion task is linear, in particular, N linear equations for 6 unknowns are to be solved, in matrix form

$$G\ m = d \qquad (1)$$

where G is the (Nx6) matrix of Green's functions, m is 6-component column vector containing the moment tensor components, and d is N-component column vector with the data – P and S amplitudes. To solve it, we use the singular value decomposition (SVD), and take advantage of the library routine from Numeric Recipes [12]. The reliability of the solution is tested by evaluating the condition number – the ratio of the largest and smallest singular value, which should not exceed about tens.

The linear inverse theory provides an explicit formula for an estimate of the error of the solution of (1) provided that the data covariance matrix CD is available, which describes the uncertainty involved in the data d. It is the posterior covariance matrix of the model parameters Cm (i.e., the components of the moment tensor in our case)

$$Cm = (GTCD\text{-}1G)\text{-}1 \qquad (2)$$

A noise in the data is not the single cause of uncertainty of the solution of (1). The other one is the uncertainty in the estimate of the Green's function G, i.e. the inexact knowledge of the location of the event and/or the parameters of the rock massif. Then, if this error of the forward modeling is described by the covariance Ct and the distribution of errors of both the data and the forward modeling are Gaussian, the matrix CD in (2) can be understood as a generalized data covariance containing both the data and forward modeling uncertainties

$$CD = Cd + Ct \qquad (3)$$

We did not estimated Cd explicitly: in general, there is little noise on the records and, therefore, the error in P amplitudes is negligible. The error in S amplitudes is however not only the ambient noise but also the P coda which may persist behind the S arrival. In the current stage of the study, we neglect this error, and consider only the error due to inexact forward modeling. For this purpose we use the deviations of the P and S polarizations from the ray and the plane perpendicular to the ray, respectively, which we determined during the inspection of the seismograms. They, in fact, describe departures of the data reflecting the real properties of the rock massif from the synthetic polarizations predicted by the simplified model of the medium, thus reflecting the bias due to mismodeling of the rock massif. Of course, estimate of the error due to the neglect of inhomogeneity and anisotropy of the rock massif, which cause a bending of the ray and departures of the polarizations out of the ray coordinates is simplified only, because it considers only the geometry of the polarizations vs. ray direction but does not deal with the change of amplitude. Therefore, we should consider the errors of the mechanism obtained from these simplified assumptions as lower estimates.

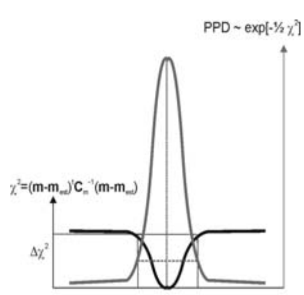

Figure 5 Sketch of constructing the confidence region of the model parameters m (horizontal axis), vertical axis: right – posterior probability density, left – least-squares sum

Once we obtain the posterior covariance matrix of the moment tensor Cm, it is useful to convert it into more illustrative quantities for understanding the uncertainty of the mechanism. For this purpose, confidence regions of the principal axes and that of the MT decomposition are advantageous. The former describe the uncertainty in the retrieved orientation of the source mechanism, the latter presents the uncertainty in determination of individual components of the moment tensor – isotropic part (ISO), double couple (DC) and compensated linear-vector dipole (CLVD). We define the confidence region in a standard way as the part of the model space around the estimated solution mest, which has a priori specified probability content, e.g., which contains 95% of all solutions of the inverse problem which can be obtained taking into account the variability of the data described by the data covariance CD. For its construction the exponential posterior probability density (PPD) corresponding to Gaussian distribution is applied, and we search for a region of the model space around mest which satisfies

$$(\mathbf{m}\text{-}\mathbf{m}_{est})^T \mathbf{C}_m^{-1} (\mathbf{m}\text{-}\mathbf{m}_{est}) \leq \Delta\chi^2 \qquad (4)$$

where $\Delta\chi^2$ is a quantity dependent on the number of degrees of freedom and the confidence level. Schematically the procedure is drawn in Fig. 5. For event Oct 24, 2005 the match of synthetics to the data is fairly good: the root mean square normalized by the norm of the data is low enough, NRMS = 0.12. The inversion can be considered as reliable because the condition number is small as well, CN = 6.6. For event Oct 12, 2005 it is even better than for event Oct 24, 2005: NRMS = 0.09, i.e. the variance reduction more than 90%. The reliability of the inversion expressed by the condition number of the data kernel is also better, CN = 3.4 only.

6 Decomposition of the complete moment tensor

Moment tensor is a phenomenological quantity which is comprehensive in describing the source but not illustrative enough by itself. Therefore, it is decomposed into components describing individual types of force systems, which reflect various modes of fracturing or slip. Splitting the moment tensor into isotropic (describing volume changes) and deviatoric part is unique, decomposition of the deviatoric part can be done in many ways (e.g., into two double couples etc.), but a most common way of the decomposition has been established by the seismological practice and accepted widely by the seismological community, namely the decomposition of the deviatoric part of the moment tensor into a double couple (DC) and a system of three couples called compensated linear-vector dipole: a dipole along the tensional or pressure principal axis of the moment tensor, complemented by two mutually perpendicular dipoles acting in the plane perpendicular to the principal dipole and of the opposite sign to it. The contents of the individual components in the complete moment tensor (MT), i.e. the isotropic component (ISO), the double-couple (DC) and the compensated linear-vector dipole (CLVD) is expressed by their percentages and visualized by two types of plot. It is (a) the traditional plot of zones of compression of the radiated P wave – for the DC sources exclusively investigated in seismology it is so called fault-plane solution or "beach ball", plot of two quadrants of compression bordered by the nodal lines. For more complex sources than the DC the zones of compression are no more the quadrants encircled by the DC nodal lines but may be larger or smaller and apart from the nodal lines, depending on the type and magnitude of the non-DC source components. The other type of plot is (b) Riedesel and Jordan display [13]. Descriptive vectors of the complete moment tensor, and the individual "elementary mechanisms" are defined on the basis of principal axes and principal values of the MT and projected onto the focal sphere. Then, the content of each of the elementary mechanisms in the retrieved MT is visualized by the distance of descriptive points for the MT and the ISO, DC and CLVD mechanisms on the projection of the focal sphere. Moreover, if we are able to assess the uncertainty of the moment tensor based on the estimate of error in the data and in the forward modeling by posterior covariance matrix of the moment tensor, we can transform it into confidence zones of the principal axes and the confidence zone of the MT decomposition. The latter one provides us with an insight if the MT retrieved can be interpreted as one of the elementary mechanisms into which we decompose the complete MT. For instance, if this confidence zone constructed for a priori specified probability level contains the DC elementary mechanism, we may conclude that the solution can be considered as a pure DC taking into account the errors in the input into the inversion. This is just the case of the events Oct 24 and Oct 12, 2005, see Figs. 6 and 7.

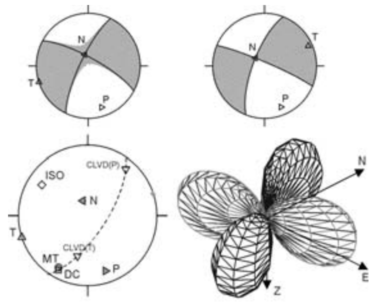

Figure 6 Mechanism of the event Oct 24, 2005. Top left – moment tensor (MT) solution: traditional plot of the fault-plane solution (nodal lines of the DC part), and the zone of compressions (grey) corresponding to the complete MT. Principal axes of the moment tensor: T – tensional axis, P – pressure axis, N – null axis. Top right – pure double-couple (DC) solution: plot of the fault-plane solution (compressions – grey), T – tensional axis, P – pressure axis, N – null axis. Bottom right - 3-D display of the P-radiation pattern of the complete MT: grey lobes – compression, black – dilatations. Bottom left – display of the decomposition of the moment tensor by Riedesel and Jordan [13] together with estimate of 95% confidence zones (grey zones) based on the inclination angles α, i.e. taking into account the mismodeling of the medium by considering straight-line rays. Complete moment tensor and the elementary mechanisms related to decomposition are marked by: MT - circle, ISO - diamond, DC - square and CLVD - triangle down. The proximity of the MT projection to ISO, DC and CLVD projections expresses the amount of the isotropic component, double couple and compensated linear vector dipole in the complete moment tensor. The dashed line displays the locus of deviatoric moment tensors. T,N and P: principal axes of the MT. MT decomposition: DC 87%, ISO(explosion) 3%, CLVD along P-axis 10%.

7 Discussion and conclusions

In the mechanisms of both events there is a large prevalence of the DC. The non DC components are consistently of the same type (isotropic explosion and a CLVD along the pressure axis) for both events, but they are not significant taking into account the error in the retrieved MT based on the estimate of the mismodeling: the confidence zone of the MT decomposition absorbs or touches the DC elementary mechanism. Therefore, despite the appearance of non-DC components in the retrieved MT, the events may be considered as pure shear events. It is confirmed also by the F-test comparing how the data are matched by the MT model (allowing non-DC components), and a pure DC model. In the F-test, the probability is quantified that the better match of the synthetics to the data for the MT model than for a DC model is not achieved by chance. For both events, the values of the F-probability are low (11% for the Oct 12 event, 22% for the Oct 24 event), indicating that the non-DC components retrieved in the MT solution are insignificant. The orientations of the principal axes are similar for the MT and DC model for both events: the cumulative deviation of T and P axes is 150 and 250 for the event Oct 24 and Oct 12, respectively. The shear-slip mechanism strongly supports the hypothesis arisen already on the basis of the great depth of both events situated far below the mining area, namely that they are of a tectonic origin, possibly not related to the mining activity at all. As concerns the orientation, they are close to a vertical strike-slip with a small dip-slip component only. A comparison with the tectonic setting at the site would be helpful for assigning them to the particular fault.

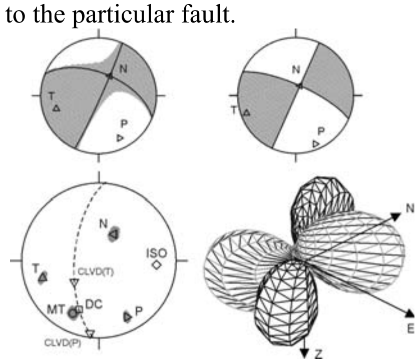

Figure 7 Mechanism of the event Oct 12, 2005. MT decomposition: DC 76%, ISO(explosion) 9%, CLVD along P-axis 15%. For the details see the caption of Fig. 6.

Acknowledgements

I thank the authorities of the Moab Khotsong Mine, AngloGold Ashanti Limited for providing the data. The study was partly performed during my stay at the ISS International, Stellenbosh, S. Africa in 2005. The Czech Rep. Grant Agency supported the study under Grant No. 205/09/0724.

References

1. Bean, Ch., Lokmer, I. and O'Brien G., 2008. Influence of near-surface volcanic structure on long-period seismic signals and on moment tensor inversions: Simulated examples from Mount Etna. *J. Geophys. Res.*, **113** (B08308), doi:10.1029/2007JB005468.
2. Braunmiller, J., Kradolfer, U., Baer, M. and Giardini, D., 2002. Regional moment tensor determination in the European–Mediterranean area-initial results. Tectonophysics, 356, 5-22.
3. Ekstrom, G., Dziewonski, A.M., Maternovskaya, N.N. and Nettles, M., 2005. Global seismicity of 2003: centroid-moment-tensor solutions for 1087 earthquakes, Phys. Earth Planet. Int., 148, 327-351.
4. Ferdinand, R.W. and Arvidsson, R. The determination of source mechanisms of small earthquakes and revised models of local crustal structure by moment tensor inversion, Geophys. J. Int., 2002, 151, 221-234.
5. Frohlich, C.. Earthquakes with non-double-couple mechanisms. Science, 1994, 264. 804-809.
6. Julian, B.R., Miller, A.D., and Foulger, G.R. Non-double-couple earthquakes. 1.Theory, Rev. Geoph, 1998,36. 525-549.
7. Kawasaki, I., and Tanimoto, T.. Radiation patterns of body waves due to the seismic dislocation occuring in the anisotropic source medium, Bull Seismol. Soc. Am, 1981, 71. 37-50.
8. Kuge, K. and Lay, T.. Data-dependent non-double-couple components of shallow earthquake source mechanisms: effects of waveform inversion instability, Geophys. Res. Lett, 1994, 21. 9-12.
9. McGarr., A. An implosive component in the seismic moment tensor of a mining induced tremor, Geophys. Res. Lett, 1992, 19. 1579-1582.
10. McGarr., A. Observations concerning diverse mechanisms for mining-induced earthquakes. In: Rockbursts and Seismicity in Mines, Potvin & Hudyma (eds.), ACG, Nedlands, W. Australia, 2005, 107-111.
11. Miller, A.D., Foulger, and Julian, B.R.. Non-double-couple earthquakes. 2. Observations, Rev. Geophys, 1998, 36. 551-568.
12. Press, W.H., Teukolsky, S.A., Vetterling, W.T. and Flannery B.P. Numerical Recipes. The art of Scientific Computing, 1992, Cambridge University Press, Cambridge.
13. Riedesel, M.A. and Jordan, T.H. Display and assessment of seismic moment tensors, Bull. Seism. Soc. Am, 1989, 79, 85-100.
14. Rudajev, V. and Sileny, J. Seismic events with non-shear component II. Rock bursts with implosive source component, Pure Appl. Geophys, 1985, 123, 17-25.
15. Sileny, J. and Milev, A. Seismic Source Mechanism - Source Mechanism of Mining Induced Seismic Events - Resolution of Double Couple and Non Double Couple Models, Tectonophysics, 2008, 456, 3-15, doi:10.1016/j.tecto.2006.09.021.
16. Sileny, J. and Vavryčuk, V. Approximate retrieval of the point source in anisotropic media: numerical modelling by indirect parameterization of the source. Geophys. J. Int., 2000, 143, 700-708.
17. Talebi, S. and Coté, M. Implosional focal mechanisms in a hard-rock mine. In: Rockbursts and Seismicity in Mines, Potvin and Hudyma (eds.), ACG, Nedlands, W. Australia, 2005, 113-121.
18. Trifu, C.I., Angus, D. and Shumila, V.. A fast evaluation of seismic moment tensor for induced seismicity, Bull. Seismol. Soc. Am, 2000, 90. 1521-1527.

RaSiM 7(2009): Controlling Seismic Hazard and
Sustainable Development of Deep Mines,
C.A. Tang(ed), Rinton Press, 407-414

WAVEFORM EFFECT ON PRE- AND POST-FAILURE FATIGUE PROPERTIES OF SANDSTONE

MANOJ NAMDEO BAGDE
Central Institute of Mining and Fuel Research, Regional Center, MECL, Nagpur 440 006, India

VLADIMIR PETROŠ
Faculty of Mining and Geology, VŠB-TU, Ostrava 70833, Czech Republic

The effect of loading waveform on the pre- and post- failure fatigue properties of sandstone subjected to uniaxial cyclic loading was investigated. The sinusoidal, ramp and square waveforms were used at cyclic loading frequency of 5Hz and peak amplitude of 0.05 mm. The loading waveform was found to be of the great significance and affected the fatigue behaviour. Fatigue behaviour was found to be a function of the dynamic energy of the load and the shape of the waveform. Damage accumulateed most rapidly under square waveforms with a high energy requirement. A ramp waveform was the least damaging of those considered. This study has practical significance in understanding the behaviour of rock and rock masses within the excavation systems subjected to dynamic cyclic loads.

1 Introduction

The understanding how dynamic loading influences fatigue in rock has a great significance in predicting cyclic fatigue in excavation systems prone to extreme rock-burst loading; however, there is almost rare literature on the topic. The work presented herein extends consideration to other waveforms than triangular and dynamic-cyclic-loading to improve the understanding of damage mechanisms of rock and rock masses subjected to severe cyclic fatigue and dynamic loads.

Among the first comprehensive studies on cyclic fatigue of rock was a Burdine´s [1] investigation of Berea sandstone strength under uniaxial and triaxial compresion. Hardy and Chugh [2] detected a cyclic fatigue effect in three hard rock types tested in uniaxial compression. They employed the traingular stress-time loading path were found to had advantage over the sinusoidal path. Attewell and Farmer [3] concentrated their efforts in understanding the deformational behaviour of rock under uniaxial cyclic compression. Haimson et al. [4, 5, 6] investigated the effect of repetitive stresses on strength, deformation and fabric in four rocks under four major loading configurations: cyclic stress-controlled, triangular in shape, and had a frequency of 1 cycle per second. Their results showed that hard rocks were significantly weakened by cyclic loading. Zhenyu and Haihong [7] studied the behaviour of rocks using two loading waveform: sinusoidal and triangle and reported that, the deformation caused by the sinusoidal waveform loading was larger than that by the triangle waveform loading. In their recent publications, Li et al. [8,9] studied the mechanical properties and presented a fatigue-damage model for jointed rock masses and dry, frozen and saturated sandstone samples with intermittent cracks subjected to dynamic cyclical loading in stress control mode using a ramp waveform. Bagde and Petros [10] studied the effect of loading frequency and amplitude using sinusoidal waveform on sandstone rocks and found that rock behaviour was greatly influenced. Apart from the studies on rock, Gong and Smith [11] investigated the effect of waveform and loading sequence on the low-cycle fatigue life of spruce wood.

2 Rock samples and test equipment

The rock samples were obtained from the rock-burst prone Darkov coal mine in the Ostarva-Karvina coal basin in the Czech Republic. Tests were conducted on sandstone rocks obtained from the borehole cores in the saddle layer sandstone, at the depth ranging from 588 to 607 m below MSL The sandstone were described macroscopically as: medium-grained, light grey sandstone with streaks (accumulated organic mass). The streaks were sporadically convergent, oriented diagonally (round 25^o) to the axis of the core. The samples were of 1:1 diameter to length ratio with average diameter of 47.5 mm and possible end, size and other testing effects were ignored. Samples were prepared and tested according to ISRM testing procedure and guidelines [12]. The average physical properties and sonic test results are provided in Table 1

Table 1. Physical properties and laboratory sonic test results for tested sandstone rock

Physical properties		Sonic -dry samples				Sonic-saturated samples			
γdry (kg/m3)	γsat (kg/m3)	Vp (m/s)	Vs (m/s)	νd	Ed (GPa)	Vp (m/s)	Vs (m/s)	νd	Ed (GPa)
2540	2578	3256	2268	0.02	27	3875	2222	0.17	33

The testing equipment was MTS-816 rock test system. The MTS controller consists of hardware components and software applications that provide closed-loop control of servo-hydraulic test equipment. For more details about the testing equipment kindly refer to author's paper [10].

The tests were conducted with axial displacement controlling loading system and the dynamic load was specified as a sine, ramp and square (Figure 1) cyclic compressive respectively for a given set of test conditions. In the begining of the test, the axial displacement target set point was set equal to an amplitude simulated. The axial displacement target set point was increased continuously till the failure of the sample and if possible till residual stress is reached to obtain complete pre- and post-failure curve. Amplitude refers to an absolute (± value), equal to one-half of the total range. For example, an amplitude entry of 0.1 mm means + 0.1 mm and – 0.1 mm, for a total travel of 0.2 mm.

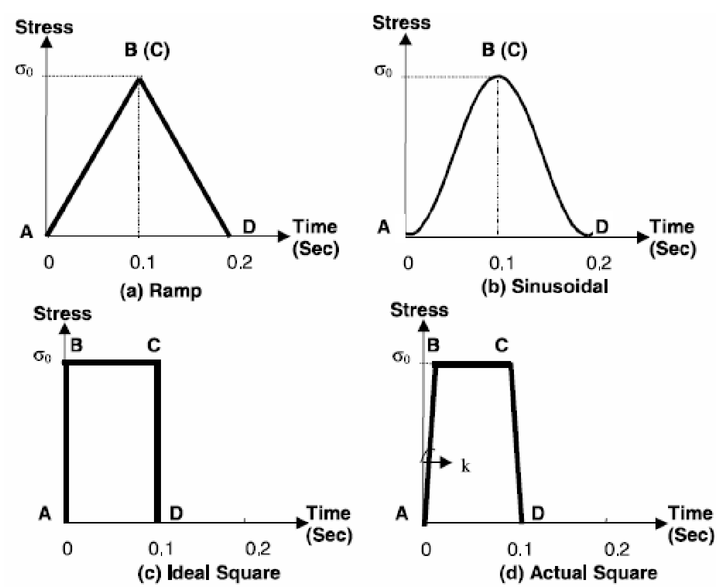

Figure1. Schematic waveforms

The shape of a waveform determines the loading/unloading rate, the rate of change in the loading/unloading rate, and the residence period at the peak stress. Figure 1 illustrates three waveforms with a load frequency of 5 Hz and a peak stress σ_0. Segment AB reflects the loading rate, BC reflects the residence period, and points B and C reflect the rate of change in the loading rate. It is clear that, in traingular and sinusoidal waveforms, point B and C overlap, indicating the residence period is zero. The ideal function for a square waveform is shown in Figure 1(c); however, the actual function used in the tests might be close to that shown in Figure 1(d). Detailed information on these waveforms is given in Table 2. Gong and Smith [11], reported that the actual square function used in the tests was close to that shown in Figure 1(d) and the value of k reported by them was 20 at a load frequency of 0.5 Hz.

Gong and Smith [11] of the opinioned that square waveforms were the most severe because they had a high loading rate and high change in loading rate, and a long residence period. According to them triangular waveforms had been found less damaging than sinusoidal waveform, even though they have a large peak change in loading rate (Table 2). According to them, the loading rate occupies a prime role, rather than the peak change in loading rate. The loading rate is not a constant for a sinusoidal waveform. The average loading rate $(d\sigma/dt)_{av}$ is $\pm 10\sigma_0$ for a sinusoidal waveform. This equals the loading rate for a traingular waveform with the same frequency. The maximum loading rate for a sinusoidal wavefrom is $\pm 5\pi\sigma_0$, i.e., $\pm 15.7\sigma_0$. This is thus 57% larger than the loading rate for a traingular waveform. It is well known that loading rate strongly influenced the rock behaviour. The detailed discussion about the maximum loading rate in a waveform and its influence on fatigue rock behaviour in uniaxial cyclic dynamic loading conditions follows.

Table 2. Characteristics of waeforms of Figure 1

Waveform	Loading function	Loading rate (MPa/s)	Change in loading rate at point B	Residence period (s)
Traingular/Ramp	Segment AB:$\sigma=10\sigma_0 t$ Segment BD: $\sigma=10\sigma_0(0.2\text{-}t)$	Segment AB:$10\sigma_0$ Segment BD: $-10\sigma_0$	$20\sigma_0$	0
Sinusoidal	$\sigma=(\sigma_0/2)[1\text{-}\sin(10\pi t+\pi/2)]$	$-5\pi\sigma_0.\cos(10\pi t+\pi/2)$	0	0
Square (ideal)	Segment AB:t=0 Segment BC:$\sigma=\sigma_0$	Segment AB:∞ Segment BC:0	∞	0.1
Square (actual)	Segment AB: :$\sigma=k\sigma_0 t$ Segment BC:$\sigma=\sigma_0$	Segment AB: :$\sigma=k\sigma_0$ Segment BC:0	$k\sigma_0$	≈0.1

3 Evaluation of rock properties

The data from the uniaxial cyclic loading tests were analysed to obtain peak fatigue strength (σ_{fp}), valley fatigue strength (σ_{fp}), average fatigue strength (σ_{fd}), fatigue life (T_{fl}), peak fatigue residual strength (σ_{fr}), post failure negative slope (S_{pf}), average Young's modulus (E_{avd}), secant Young's modulus (E_{sd}), axial stiffness (A_{sd}) at 50 % of the maximum stress, post failure modulus (E_{pf}) at 50% of maximum stress, dynamic energy (D_e) and stress energy (S_e) released by the rock.

The stress-strain curves were analysed for strength and defomation properties using a computer programme developed in MATLAB. An illustration of stress and modulus computation from peak-valley data using a computer programme is given in Figure 2. The peak fatigue strength (σ_{fp}) and valley fatigue strength (σ_{fv}) reported here is the maximum stress obtained from peak and valley curves. While, the fatigue strength (σ_{fd}) is the average of the above two. The fatigue life (T_{fl}) is the time corresponding to the peak fatigue strength (σ_{fp}). The peak fatigue residual strength (σ_{frp}) reported here is the residual strength corresponding to the peak curve. The post-failure negative slope (S_{pf}) is determined from the post-failure peak and valley curves and average value is reported here. The stress-strain curves were analysed for deformation properties like average Young's modulus (E_{avd}) and secant modulus (E_{sd}) according to the procedure outlined in ISRM suggested method [12]. Average Young's modulus (E_{avd}) was determined from the average slopes of the more-or-less straight line portion of the stress-strain curve. The secant modulus (E_{sd}) was calculated from zero force to 50% of the maximum load sustained by the rock. The post–failure modulus (E_{pf}) reported here is the average modulus determined from post-failure curve at 50% of the maximum stress. Since, the data were recorded in peak-valley mode in cyclic loading conditions, peak and valley curve were obtained separately and analyzed independently to calculate modulus values as shown in Figure 2 using a computer program developed in MATLAB. Then the modulus values obtained from the peak and valley curves were averaged and reported here.

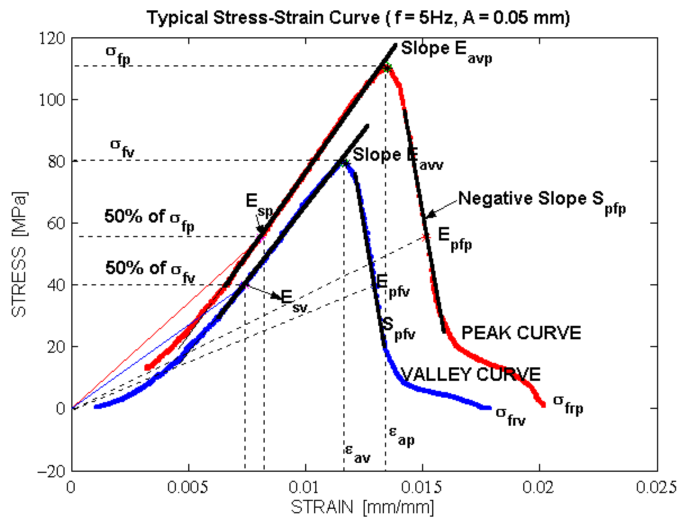

Figure 2. Typical stress-strain curve with illustrating evaluation of various parameters from peak-valley data in uni-axial cyclic loading

The average axial stiffness (A_{sd}) throughout loading of the rock is calculated using the formula:

$$A_{sd} = \Delta Stress/\Delta Strain, \quad (1)$$

where, A_{sd} is the average axial stiffness (i.e. modulus of deformation or Young's modulus over the elastic interval or reversible modulus) in GPa, ΔStress is the differential stress (or double stress amplitude) in GPa and ΔStrain is the differential strain (or double strain amplitude) obtained from the corresponding peak-valley data. The calculated axial stiffness using formula (1) was plotted against the axial peak stress as shown in Figure 3. The reported value of the axial stiffness was the average value estimated at 50 % of the peak axial stress sustained by the rock.

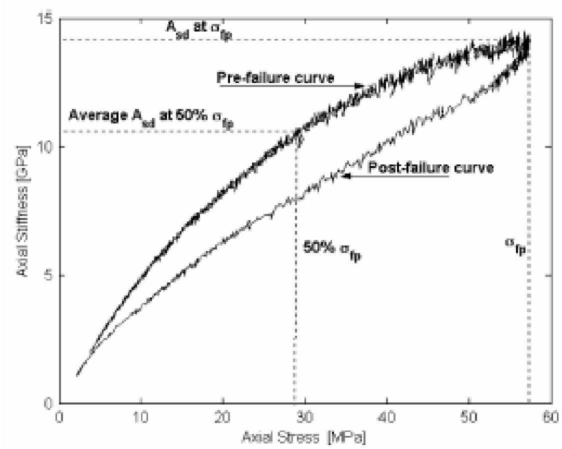

Figure 3. Axial stiffness *vs* peak axial stress plot illustrating calculation of average axial stiffness at 50% of the peak fatigue strength

The dynamic energy released by the rock is determined using the formula:

$D_e = (\Delta\text{Stress x }\Delta\text{Strain x f})/2,$ (2)

where, D_e is the dynamic energy sustained by the rock in MW/m^3, and f is the frequency in Hz. The dynamic energy determined using peak-valley data throughout the loading were plotted against time as shown in Figure 4. The reported value of the dynamic energy is the average determined from the asymptotic linear part of the curve at its peak.

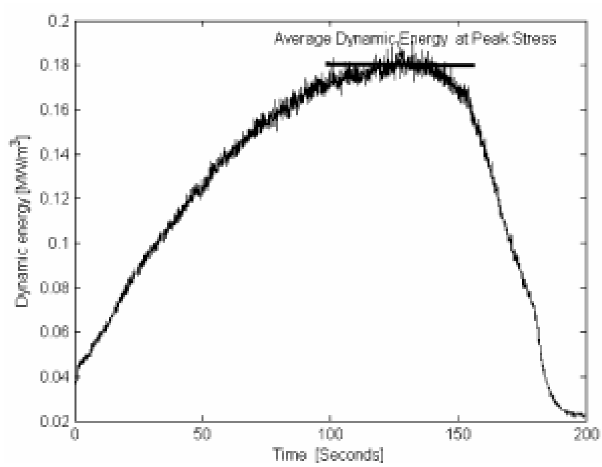

Figure 4. Time *vs* dynamic energy plot illustrating calculation of dynamic energy nearer to or at peak fatigue strength

According to the damage theory, the stress energy released by the rock can be described as:

$S_e = \sigma_{fp}^2 / 2E_{avd}$, (3)

where, S_e is the stress energy released in MJ/m^3, σ_{fp} is the peak fatigue strength sustained by the rock in MPa, and E_{avd} is the average Young's modulus in MPa. Using equation (3), stress energy released by the rock was determined.

4 Experimental results and discussion

Tests were conducted to study the effect of waveform on the fatigue behaviour of sandstone rock in uniaxial cyclic loading conditions. The sinusoidal, ramp and square waveforms were used with a load frequency of 5 Hz and amplitude of 0.05mm.

4.1 Fatigue strength of the rock

The fatigue strength obtained was higher in the case of ramp loading waveform compared to sinusoidal and square loading waveforms (Figure 5). Thus, it could be concluded that ramp loading waveform is more uniform in loading and unloading as compared to sinusiodal and square. Waveform is known to affect fatigue life and according to Gong and Smith [11], square waveforms are the most severe testing condition and result in the shortest fatigue life at a given loading frequency. However, it was found that fatigue life (Figure 6) is least in sinusoidal and residual strength (Figure 5) is higher in square waveform and thus exception. This could be due to the sample disturbance. The post-failure negative slope (Figure 7) found higher in ramp, followed by sinusiodal and least in sqaure waveform. The least post-failure negative slope in sqaure waveform suggests that under such condition rock would fail in more brittle manner due to residence period and high loading rate compared to others.

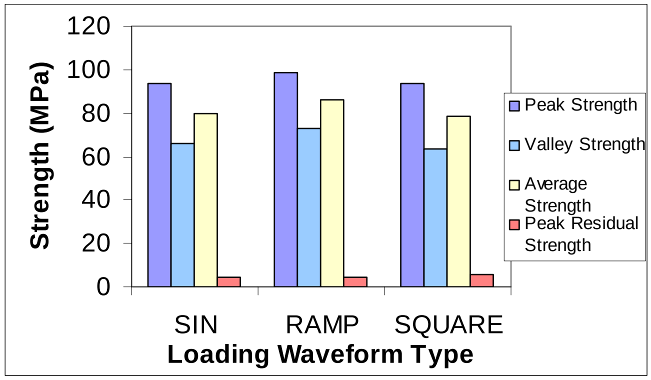

Figure 5. Strength with loading waveforms

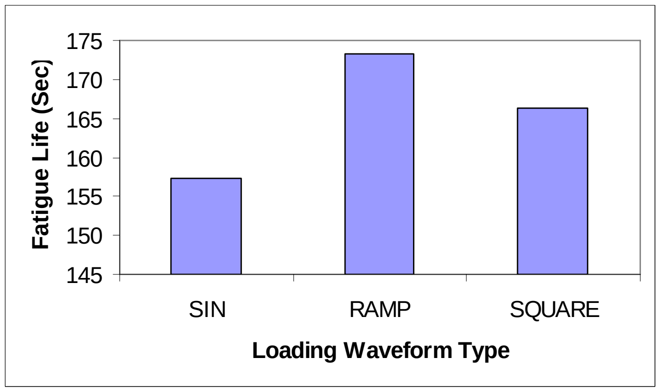

Figure 6. Fatigue life with loading waveforms

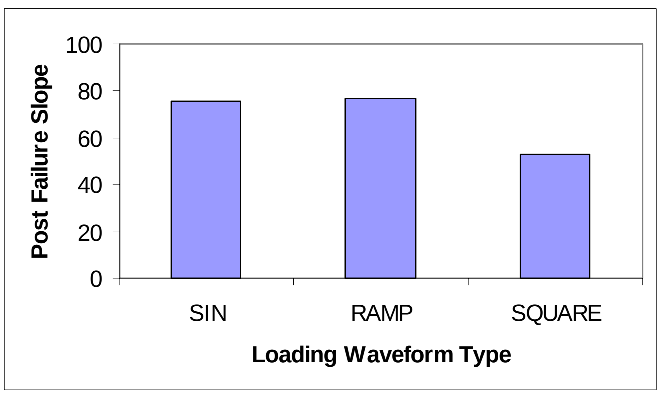

Figure 7. Post-failure slope with loading waveform

4.2 Deformation properties of the rock

The average Young´s modulus (E_{avd}) was higher in ramp waveform compared to other waveforms considered (Figure 8). In sinusoidal waveform, it was least. The secant modulus was least in square waveform and higher in sinusoidal waveform. The reversible modulus was higher in ramp, followed by sinusoidal and least in square waveforms. Post-failure modulus was least in square waveform. It seems that damage accumulated most rapidly under square waveforms compared to others. The maximum loading rate in a waveform strongly influences the damage accumulation in rock. According to Eberhardt [13], the larger the disparity between the secant and the Young's modulus values, the greater the initial crack density.

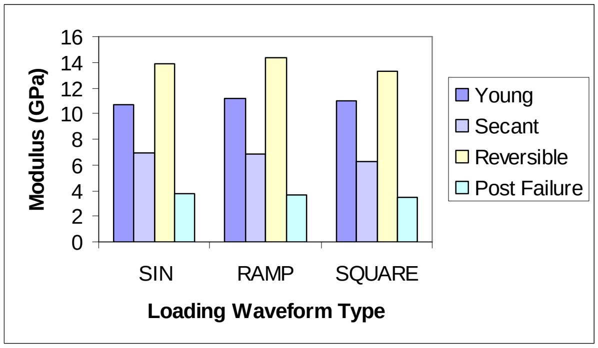

Figure 8. Modulus with loading waveforms

4.3 Eenergy response in the rock

Dynamic energy (D_e) utilized to cause rock failure was least in ramp waveform compared to sinusoidal and square (Figure 9). In the case of square waveform, it was found that the dynamic energy requirement was more to cause failure of the rock. Thus, it could be concluded that a ramp waveform is the least damaging of those considered. Damage accumulated most rapidly under sqaure waveforms with a high dynamic energy requirement and followed by sinusoidal and ramp waveforms. This findings demonstrated that it is the loading rate or loading waveform that mainly contributed to damage in rock, rather than the work done. This observation supported the proposition proposed by Gong and Smith [11] based on their findings on wood. They reported that the higher the workdone per cycle during low cycle fatigue tests, the shorter the time to failure will be. Though, dynamic energy was higher in square waveform, it had a shorter fatigue life and lower fatigue strength with exception of sinusoidal in the case of fatigue life. This could be due to nature of the material, the extent of anisotropy or heterogenity or sample disturbance and the mode of loading etc. Stress energy (S_e) released by the rock was highest in ramp, followed by sinusoidal and least in square waveform (Figure 10). As discussed earlier, sqaure waveform are the most severe testing condition and have the shortest fatigue life and a sinusiodal waveform is more severe than a traingular one. Henc, it could be hypothesised that stress energy released during compressive cyclic loading is a function of the workdone and the shape of the waveform.

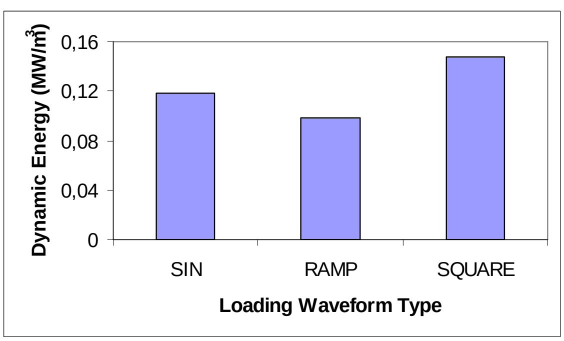

Figure 9. Dynamic energy with loading waveforms

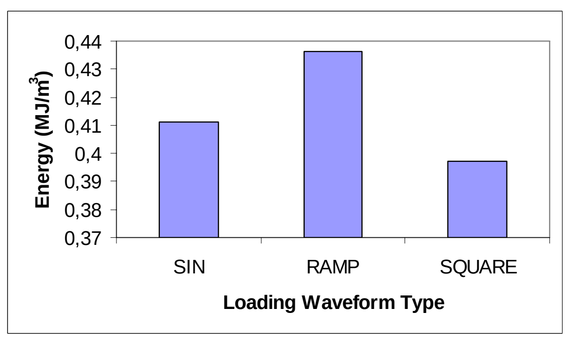

Figure 10. Stress energy with loading waveforms

5 Conclusions

This study focused on investigating the effects that waveform and amplitude have on the dynamic cyclic fatigue behaviour of intact sandstone rock. Based on work presented, the following conclusions are drawn:

Fatigue behaviour of rock subjected to uniaxial cyclic compression is a function of the shape *of* waveform and the workdone by the load. Damage accumulates most rapidly under sqaure waveforms with a high dynamic energy requirement. A ramp waveform is less damaging compared to square or sinusoidal waveforms. A ramp type waveform found to be uniform in loading and unloading with less dynamic energy requirement to cause failure in the rock samples for a given loading frequency and amplitude. The loading waveforms strongly influences the damage accumulation (accumulated deformation) under cyclic loading conditions. It is found that the maximum loading rate in a waveform strongly influences the damage acumulation in rock. The type of loading waveform affects the various pre- and post-failure rock properties in uniaxial cyclic loading conditions.

From the discussed results, the micro-fracturing process was found to be the main cause of rock failure. This finding suggests that strength degradation begins with the initiation of the micro-fracturing process, termed crack initiation, and can end in failure at stresses well below the uniaxial compressive strength of the material. Thus, the identification of these processes and their associated mechanisms are of key interest in predicting both the short and long term stability of an excavation. According to many researchers, the prediction of rock bursts and earthquakes is still a mystery, even after a long history of research. Therefore, concentrated efforts are made to improve rock burst control measures.

Acknowledgement

This piece of research on the “stress-deformation behaviour of rock at dynamic stress“ is supported by Grant Agency of Czech Republic under Grant No. 105/01/0042. The authors are thankful for this support.

References

1. Burdine, N. T. Rock failure under dynamic loading conditions. Soc. Petr. Eng. J. 1963, 3. 1-8.
2. Hardy, H. R. and Chugh, Y. P. Failure of geologic materials under low-cycle fatigue. In Proc. Sixth Canadian Symp. on Rock Mechanics, Montreal, 1970, 33-47.
3. Attewell, P. B. and Farmer, I. W. Fatigue behaviour of rock. Int. J. Rock Mech. Min. Sci. 1973, 10. 1-9.
4. Haimson, B. C. and Kim, C. M. Mechanical behaviour of rock under cyclic fatigue. In Stability of rock slopes, Proceedings of the 13th Symposium on Rock Mechanics, New York, ASCE, Cording E. J. (Editor), 1972, 845-863.
5. Haimson, B. C. Mechanical behaviour of rock under cyclic fatigue. In Advances in Rock mechanics, Proc. of the 3rd Congress of the Int. Soc. for Rock Mechanics, National Academy of Sciences, Washington, D. C., Vol. II, 1974, 373-378.
6. Haimson, B. C. Effect of cyclic loading on rock. In Dynamic Geo-technical Testing, ASTM STP 654, American Soc. for Testing and Materials, 1978, 228-245.
7. Zhenyu, T.and Haihong, M. An experimental study and analysis of the behaviour of rock under cyclic loading. Int. J. Rock Mech. Min. Sci. and Geomech. Abstr, 1990, 27(1). 51-56.
8. Li, N., Chen, W., Zhang, P., and Swoboda, G. The mechanical properties and a fatigue-damage model for jointed rock masses subjected to dynamic cyclical loading. Int. J. Rock Mech. Min. Sci. 2001, 38. 1071-1079.
9. Li, N., Zhang, P., Chen, Y., and Swoboda, G. Fatigue properties of a cracked, saturated and frozen sandstone samples under cyclic loading. Int. J. Rock Mech. Min. Sci. 2003, 40. 145-150.
10. Bagde, M. N. and Petros, V. Waveform effect on fatigue properties of intact sandstone in uniaxial cyclic loading. Rock Mech Rock Eng, 2005; 38(3). 169-196.
11. Gong, M., and Smith, I. Effect of waveform and loading sequence on low-cycle compressive fatigue life of spruce. J. of Materials in Civil Engineering, 2003, 15 (1). 93-99.
12. Fairhurst, C. E. and Hudson, J. A. Draft suggested method for the complete stress-strain curve for intact rock in uniaxial compression. In International Society for Rock Mechanics Commission on Testing Methods, Fairhurst, C. E. and Hudson, J. A. (Co-ordinators), Int. J. Rock Mech. Min. Sci. 1999, 36. 279-289.
13. Eberhardt, E. Brittle rock fracture and progressive damage in uniaxial compression. Ph. D. Thesis. College of Studies and Research, Department of Geological Sciences, University of Saskatchewan, Saskatoon, 1998, 334p.

RaSiM 7(2009): Controlling Seismic Hazard and
Sustainable Development of Deep Mines,
C.A. Tang(ed), Rinton Press, 415-426

CHARACTERISTICS OF THE PROCESSES TAKING PLACE AT THE SOURCES OF HIGH ENERGY TREMORS OCCURRING IN THE UPPER SILESIAN COAL BASIN IN POLAND – REGIONAL CHARACTER OF THE PHENOMENON

KYSTYNA STEC

Laboratory of Seismology and Seismic, Central Mining Institute

40 166 Katowic, pl. Gwarków 1

Seismic observations in the Upper Silesian Coal Basin carried out by the Upper Silesian Regional Seismic Network of Central Mining Institute date back to the 1950s. More than 61 000 mine tremors of energy $E \geq 10^5$ J (local magnitude $M_L \geq 1,6$) occurred over the period of 1974 to 2008. From the analysis of the seismic source location relative to mine faces and from the analysis of the tectonic structures location, two types of seismicity have been distinguished. These are called respectively mining and regional types of seismicity. The former one is strongly associated with the mining activity and seismic events that occur in the vicinity of active mining excavations. These events are, as a rule, energetically relatively weak. The latter one results from the interaction between mining and tectonic factors. These seismic events appear to be located in tectonically disturbed zones (faults) and the sources are visibly more energetic. They can also be intensely felt on the surface.

1 Introduction

Mining exploitation in the Upper Silesian Coal Basin conducted since more than 200 years causes equilibrium disturbance in the stress field distribution in the rock medium. The symptoms of this disturbance constitute dynamic phenomena in the form of rock mass tremors and rockbursts. The first documented mine tremor registrations originate from the beginnings of the 20st century [15]. In 1929 the first seismic station was established in Racibórz. Over the period 1929 – 1944 in the area of the Upper Silesian Coal Basin five seismic stations were active, with optical registration in the framework of the so-called regional system. In 1965 a seismological station at the first mine started and since this time systematic increase in the number of mine stations, up to 43 maximally in 1980s, was observed. Parallel with the development of mine networks the regional network was modernised. Seismic observations in the Upper Silesian Coal Basin carried out by the Upper Silesian Regional Seismic Network of the Central Mining Institute date back to the 1950s. More than 61000 mine tremors of energy $E \geq 10^5$ J (local magnitude $M_L \geq 1.6$) occurred over the period of 1974 to 2008. The intensity level of seismic phenomena is very differentiated, from non-perceptible to the people to strong ones having the character of weak earthquakes (seismic energy $E \geq 10^9$ J, $M_L \geq 4.0$).

The majority of tremors in the Upper Silesia constitute pure mining-related tremors connected with the change of the system of stresses and deformations caused by direct extraction. These are tremors of low or medium seismic energy value ($10^2 \div 10^7$ J, $M_L = 0.1 \div 2,7$). The focus of these phenomena occurs within the fronts of mined longwalls [7, 10, 11, 14].

Every few months, tremors of so-called regional character occur; their seismic energy is high, of the order of $10^8 – 10^9$ J, their focus are connected with geological-tectonic structures and accompanying them zones of natural stress concentrations and rock mass weakness in the form of different types of defects. This activity is caused by changes of the stress system resulting from summing up of residual and neotectonic stresses with stresses caused directly by underground mining [12, 16, 17].

Seismic tremors originate as a result of action of determined forces on the rock medium structure, what causes the characteristic development of dynamic processes and finds its reflection in the character of seismic radiation and indirectly in seismograms of registered tremors. The rock fracturing process can be determined on the basis of parameters describing the focal mechanism, calculated using the seismic moment tensor inversion method [1]. The results of hitherto realised investigations into the focal mechanism allowed to determine more precisely the variability of tremor focal mechanism according to the tectonic features of the region, position of tremor focus towards the longwall front and existing mining events [4, 6, 7, 9, 10, 11, 12, 14, 16, 17].

The parameters, which also describe broader the geomechanical processes occurring in the tremor focus, are source parameters calculated after the assumption of an appropriate model. One of the simplest and simultaneously most often used models is the Brune's model [2]. The simultaneous analysis of focal mechanism parameters and source parameters allows to indicate the characteristic features of tremor focus and thus to give the most probable hypothesis of their reasons.

2 Analysis of high-energy tremors of regional character from the "Bobrek" colliery

In 2007 and 2008 under the city of Bytom occurred two high-energy tremors: the first tremor of 9 February 2007, 2.45 p.m. of seismic energy E = 1.0E+09 J (M_L = 3.8) and second of 12 December 2008 with energy E = 7.0E+08 J (M_L = 3.7). These tremors have not caused effects in the workings of the mined longwall 1 in seam 503 in the "Bobrek" mine, but simultaneously have caused slight damages in several dozen of buildings in Bytom (falling of single roof tiles and damages of chimneys) and were strongly felt in a large area (within the radius up to 12 km).

In order to investigate the character and genesis of these tremors a number of geophysical analyses were carried out. For this purpose seismograms obtained on the basis of registrations of the mine seismological network of "Bobrek" mine and Upper Silesian Regional Seismological Network of Central Mining Institute as well as questionnaire of macroscopic feelings of tremors in the area of Upper Silesia were used.

2.1. Source mechanism

In using the method of mine tremor source mechanism determination we can establish the type of process responsible for the mine tremor source mechanism. As a result of calculations we determine three tremor focus models described by three types of seismic moment tensor [13]:

- the total tensor possesses the isotropic component I describing the source volume variations (explosion /+/ or implosion /-/, CLVD component corresponding with uniaxial compression /-/ or tension /+/ and DBCP shearing component described by a double pair of forces,
- the deviatoric tensor (change of form without volume change) has a CLVD component and DBCP shearing component,
- the pure shearing tensor possesses only the CBCP component – a shearing one.

The accuracy of source mechanism determination was controlled using the solution quality factor Q defined by Wiejacz [13], calculated for each mine tremor being studied. This index, Q, depends on: the source sphere coverage; a coefficient defining the shear solution approximation; and the error of the scalar seismic moment determination. The Q index ranges from 0 to 100%. The results for Q < 40% have been discarded. The source mechanism is presented as a lower-hemisphere projection with the shaded and white regions indicating compression and dilatation, respectively.

The seismic moment tensor inversion method has been applied to mine tremors from the "Borek" coal mine for two high-energy tremors. Calculations of the seismic tensor moment have pointed out that in the solution decidedly dominated the shearing component over explosion and uniaxial compression. The Tables 1, 2 present the calculation results.

Table 1. Parameters of source mechanism of the tremor of 9 February 2007 from "Bobrek"

<table>
<tr><td colspan="9">Date
2007-02-09</td><td colspan="9">Time
14:45</td><td colspan="9">Energy, J
1.0E+09</td><td colspan="9">Coordinates, m (SG system)
6420 | 50</td></tr>
<tr><td colspan="12">Full solution
Reverse fault
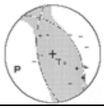</td><td colspan="12">Deviatoric solution
Reverse fault
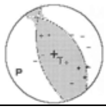</td><td colspan="12">Double couple solution
Reverse fault
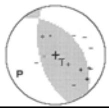</td></tr>
<tr><td colspan="12">M_{ij}, Nm
-0,295E+13 -0,892E+14 -0,192E+14
-0,892E+14 -0,165E+15 0,808E+14
-0192E+14 0,808E+14 0,191E+13</td><td colspan="12">M_{ij}, Nm
-0,333E+14 -0,941E+14 -0,128E+14
-0,941E+14 -0,162E+15 0,823E+14
-0,128E+14 0,823E+14 0,196E+15</td><td colspan="12">M_{ij}, Nm
-0,379E+14 -0,922E+14 -0,139E+14
-0,922E+14 -0,158E+15 0,815E+14
-0,139E+14 0,815E+14 0,196E+15</td></tr>
<tr><td colspan="6">M_o, Nm
0,193E+15</td><td colspan="6">M_T, Nm
0,216E+15</td><td colspan="6">M_o, Nm
0,218E+15</td><td colspan="6">M_T, Nm
0,221E+15</td><td colspan="6">M_o, Nm
0,218E+15</td><td colspan="6">M_T, Nm
0,218E+15</td></tr>
<tr><td colspan="4">I, %
-3</td><td colspan="4">CLVD, %
-6</td><td colspan="4">DBCP, %
91</td><td colspan="4">I, %
-</td><td colspan="4">CLVD, %
-2</td><td colspan="4">DBCP, %
98</td><td colspan="4">I, %
-</td><td colspan="4">CLVD, %
-</td><td colspan="4">DBCP, %
100</td></tr>
<tr><td colspan="3">ΦA, °
171</td><td colspan="3">δA, °
56</td><td colspan="3">ΦB, °
320</td><td colspan="3">δB, °
38</td><td colspan="3">ΦA, °
166</td><td colspan="3">δA, °
56</td><td colspan="3">ΦB, °
319</td><td colspan="3">δB, °
38</td><td colspan="3">ΦA, °
165</td><td colspan="3">δA, °
56</td><td colspan="3">ΦB, °
318</td><td colspan="3">δB, °
38</td></tr>
<tr><td colspan="3">ΦP, °
248</td><td colspan="3">δP, °
9</td><td colspan="3">ΦT, °
127</td><td colspan="3">δT, °
72</td><td colspan="3">ΦP, °
244</td><td colspan="3">δP, °
9</td><td colspan="3">ΦT, °
120</td><td colspan="3">δT, °
74</td><td colspan="3">ΦP, °
244</td><td colspan="3">δP, °
9</td><td colspan="3">ΦT, °
119</td><td colspan="3">δT, °
74</td></tr>
<tr><td colspan="6">Q, %
55</td><td colspan="6">ERR, Nm
0,185+14</td><td colspan="6">Q, %
62</td><td colspan="6">ERR, Nm
0,184+14</td><td colspan="6">Q, %
68</td><td colspan="6">ERR, Nm
0,185+14</td></tr>
</table>

M_{ij} – seismic moment components, M_o – scalar seismic moment, M_T – full seismic moment, I – percentage share of isotropic component, CLVD – percentage share of component corresponding with uniaxial compression /-/ or tension /+/, DBCP – percentage share of shearing component, ΦA,B – azimuth of plane A,B, δA,B – dip of plane A,B, ΦP,T – trend of axis P,T, δP,T – plunge of axis P,T, Q – coefficient of solution quality, ERR – tensor error

Table 2. Parameters of source mechanism of the tremor of 12 December 2008 from "Bobrek"

<table>
<tr><td colspan="9">Date
2008-12-19</td><td colspan="9">Time
23:45</td><td colspan="9">Energy, J
7.0E+08</td><td colspan="9">Coordinates, m (SG system)
6620 | -380</td></tr>
<tr><td colspan="12">Full solution
Reverse fault
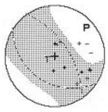</td><td colspan="12">Deviatoric solution
Reverse fault
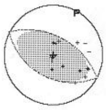</td><td colspan="12">Double couple solution
Reverse fault
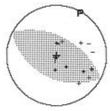</td></tr>
<tr><td colspan="12">M_{ij}, Nm
0,558E+14 -0,311E+15 -0,100E+15
-0,311E+15 -0,331E+14 -0,324E+15
-0,100E+15 -0,324E+15 -0,954E+14</td><td colspan="12">M_{ij}, Nm
-0,836E+15 -0,401E+15 -0,140E+15
-0,401E+15 -0,281E+15 -0,675E+14
-0,140E+13 -0,675E+14 0,112E+16</td><td colspan="12">M_{ij}, Nm
-,820E+15 -0,430E+15 -0,134E+15
-0,430E+15 -0,226E+15 -0,680E+14
-0,134E+15 -0,680E+14 0,105E+16</td></tr>
<tr><td colspan="6">M_o, Nm
0,814E+15</td><td colspan="6">M_T, Nm
0,818E+15</td><td colspan="6">M_o, Nm
0,106E+16</td><td colspan="6">M_T, Nm
0,109E+16</td><td colspan="6">M_o, Nm
0,317E+14</td><td colspan="6">M_T, Nm
0,317E+14</td></tr>
<tr><td colspan="4">I, %
10</td><td colspan="4">CLVD, %
3</td><td colspan="4">DBCP, %
87</td><td colspan="4">I, %
-</td><td colspan="4">CLVD, %
9</td><td colspan="4">DBCP, %
93</td><td colspan="4">I, %
-</td><td colspan="4">CLVD, %
-</td><td colspan="4">DBCP, %
100</td></tr>
<tr><td colspan="3">ΦA, °
326</td><td colspan="3">δA, °
58</td><td colspan="3">ΦB, °
123</td><td colspan="3">δB, °
34</td><td colspan="3">ΦA, °
297</td><td colspan="3">δA, °
50</td><td colspan="3">ΦB, °
118</td><td colspan="3">δB, °
41</td><td colspan="3">ΦA, °
298</td><td colspan="3">δA, °
50</td><td colspan="3">ΦB, °
118</td><td colspan="3">δB, °
40</td></tr>
<tr><td colspan="3">ΦP, °
47</td><td colspan="3">δP, °
12</td><td colspan="3">ΦT, °
270</td><td colspan="3">δT, °
73</td><td colspan="3">ΦP, °
28</td><td colspan="3">δP, °
4</td><td colspan="3">ΦT, °
204</td><td colspan="3">δT, °
86</td><td colspan="3">ΦP, °
28</td><td colspan="3">δP, °
4</td><td colspan="3">ΦT, °
206</td><td colspan="3">δT, °
86</td></tr>
<tr><td colspan="6">Q, %
62</td><td colspan="6">ERR, Nm
0,708+14</td><td colspan="6">Q, %
68</td><td colspan="6">ERR, Nm
0,717+14</td><td colspan="6">Q, %
69</td><td colspan="6">ERR, Nm
0,747+14</td></tr>
</table>

The focal mechanism of these tremors is reverse. The nodal planes have azimuth NW–SE. The main compressing stresses P are almost horizontal and have an azimuth close to the direction NE–NW, and the tension stresses T are close to the vertical and have an azimuth corresponding with the direction NW–SE. When analysing the focal mechanism of these tremors from the aspect of investigations conducted by Teper [12] concerning the seismotectonic model of the northern part of the Upper Silesian Coal Basin we can ascertain that the system of stresses acting in the tremor focus and stresses determining the state of rock mass deformations formed during the youngest orogenesis, resulting from the structural analysis, are characterised by natural similarity. Namely, as it is visible from Figure 1 presenting the stress model of UPCB, the direction for compression stresses P corresponds with the direction of compression C, and the direction of stresses T corresponds with the direction of tension T. Moreover, the direction of reverse faults is close to the azimuths of nodal planes determined in focus mechanism solution.

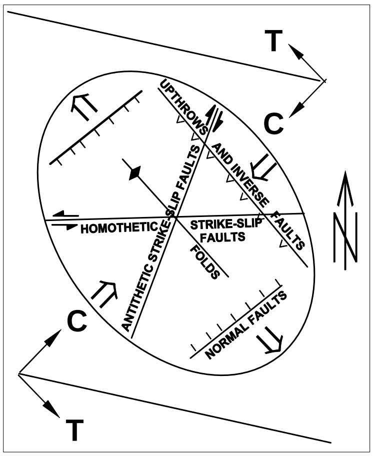

Figure 1. Schematic representation of spatial distribution of deformation complex characteristic for the regime remaining from the Upper Carboniferous through Alpine phases to contemporary movements in the Upper Silesian Coal Basin in the western part of the investigation area (block tectonics zone) and arising in the eastern part of investigations (fold-block tectonics zone) in the Alpine, neotectonic and contemporary stress field [12]

Taking into consideration the relationships presented above we can hypothetically conclude that the solution of the mechanism of focus reflects the system of residual or neotectonic stresses occurring in deep structures of the Upper Silesian Coal Basin. The confirmation of dependences of strong seismic phenomena occurrence on the tectonic factor presents the publication based on ten-years' investigations comprising seismic activity, tectonics and geodynamics of the Upper Silesian Coal Basin area and mining exploitation parameters [16, 17]. As the main contemporary seismogenic structure were acknowledged the discontinuities of the crystalline base running subparallel to boundary zones of the second order between segments of the Upper Silesian massif called blocks: Tarnowskie Góry, Bytom and central block. In the north this is the discontinuity under the Bytom syncline axis.

2.2. Source parameters

The seismic source parameters illustrate the characteristic features appearing in tremor focus. The calculations of parameters of the tremor source of 9 February 2007 and the tremor of 12 December 2008 were carried out using the MULTILOK programme developed in the Laboratory of Seismology and Seismic Prospecting of the Central Mining Institute. The source parameters on account of full not re-controlled record were determined from the seismogram of tremor registered by the Upper Silesian Regional Seismological Network. From the displacement courses the amplitude spectrum was calculated and on the flat part of the spectrum the spectral level Ω_0 and the point of crossing of the flat and inclined part determining the corner frequency f_0 (Fig. 2) were determined.

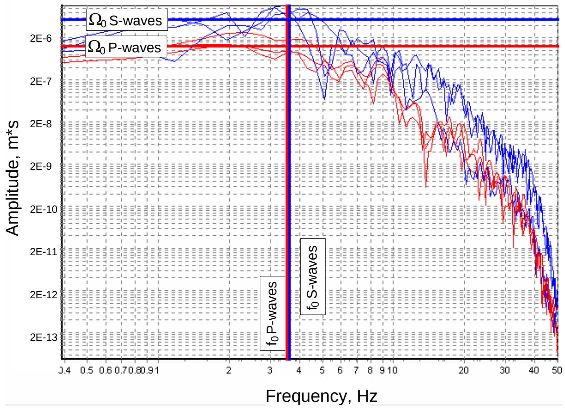

Figure 2. Ground displacement spectrum of the 9 February 2007, 2.45 p.m. of seismic energy E = 1.0E+09 J (M_L = 3.8) mine tremor with the low frequency level and corner frequency indicate (blue colour – S-waves, red colour – P-waves)

The results of source parameter calculations presents Table 3.

Table 3. Source parameters

Date	Time	Energy, J	Source parameters					
			M_0, Nm	R_0, m	f_o, Hz	$\overline{D}$, *m*	$\Delta\sigma$, Pa
2007-02-09	14:45	1.0E+09	4.7E+14	185	3.6	1.2E-02	2.4E+07
2008-12-12	23:45	7.0E+08	8.5E+14	228	4.5	9.9E-02	3.1E+07

M_0 – seismic moment, f_o – corner frequency, R_0 – focus radius, $\Delta\sigma$ – stress drop, $\overline{D}$ – average displacement in the focus

The obtained values of source parameters for the analysed tremors indicate the regional character of these phenomena. The corner frequency (frequency at which the maximum seismic energy is emitted) is low. As a rule for typically mining-related tremors the corner frequency is decidedly higher. The seismic moment is a very high moment as for tremors from the Upper Silesian Coal Basin area. The focus radius is a very high too. The displacement in the focus was exceptionally high. The high drop of stresses in the tremor focus, which manifests the high concentration of initial stresses in the focus area. High displacement in the focus and a high seismic moment are characteristic for tectonic tremors of regional character. Summing up, the large size of the tremor focus, considerable decrease of stresses in the focus and very high seismic energy in the focus indicate that these tremors could not occur at a distance lower than 500-1000 m from the underground workings of longwall 1 in the seam 503, because they would cause the destruction of these workings.

2.3 Spatial location of focus tremors

For the determination of the genesis of tremors very essential is to define the depth of their focus. Calculations of the focal mechanism were carried out for the depth interval from -200 to -1200 m above sea level (from -480 m to -1480 m counting from the terrain surface). The best solution determined on the basis of analysis of the Quality index Q of the solution and lowest error ERR were obtained for the depth 1280 m counting from the surface level, i.e. over 500 m under the occurrence level of seam 503 in the longwall 1 area.

The location in the spatial system has been carried out also by means of the MULTILOK programme. The option was used allowing to localise tremors in the 3D system, modified by the Powell's method. For location the seismogram of tremor registered by the mine seismological network of the "Bobrek" colliery was used. The depth of seismometric stations is differentiated from -300 to -900 m, counting from the terrain level, what allows to carry out calculations of the vertical component of tremor focus. The obtained result indicates that the focus depth amounts to about 1250 m (below terrain level), i.e. also about 500 m under the seam 503. To be sure, seismometric stations were not at disposal at this depth, thus the accuracy of location is limited, but at the spatial network to the level -900 m most certainly the tremor must have occurred decidedly below 1000 m.

Deep, strong tremors from the Bytom syncline area that took place in the 1950s of the previous century (deeper than the mining level) were the subject to a detailed analysis by [3]. It became evident that after the installation of instruments for tremor registration in Upper Silesia, numerous and weaker mining-related tremors could be separated from sporadic and strong regional – tectonic tremors.

The deep position of focus of analysed tremors explain also their strong feelings in a big area within the radius of 10-15 km from the epicentre and relatively low amplitudes of surface vibration acceleration in the tremor epicentre as for such a high seismic energy (about 600 mm/s^2). In the case of weaker and shallower mining-related tremors more than once in the epicentral area an acceleration impulse with higher amplitude (even up to 1000 mm/s^2) was registered. Such impulse is registered in the case of shallow tremors, in a small area around the epicentre, and then it is subject to strong suppression and at the distance of several km in general it is not felt.

It results from macroeconomic questionnaires carried out that the maximum tremor intensity from macroscopic observations according to the MSK scale amounted in the epicentre to $I_0 = 6$, and at the distance of 2.5 km from the epicentre the intensity $I_0 = 4$. Using the formula for vibration intensity with the distance and depth:

$$I_o\text{-}I=3\log\,[(r^2 + h^2) / h^2] \qquad (1.)$$

where: h – focus depth, r – distance from the epicentre

and after the acceptance of macroscopic data we obtain for the depth 1250 m from the earth surface $I_0 = 4^{th}$ degree (2.5 km from the epicentre) – result accordant with macroseismic observations.

However, in the case of acceptance of the hypothetical focus depth at the level of the mined seam 503 – (750 m from earth surface) the intensity at the distance of 2.5 km from the epicentre can be determined on the boundary of the second and third degree. This result absolutely does not coincide with macroseismic observations, what constitutes the subsequent proof confirming the tremor focus depth, considerably higher than the level of the mined seam 503, and at the same time its regional character.

3 Source mechanism of the mine tremors occurring in the vicinity of local tectonic structures from the „Knurów" colliery

3.1. Focal mechanism

The subsequent examples of tremors, which originated at overlapping of mining-related and tectonic stresses were the tremors that occurred at the "Knurów" colliery in the area of longwall 17 mined in the seam 361. The Tables 4 – 7 present specifications of seismological parameters of analysed tremors and calculation results of mechanism parameters. The three first tremors for full solution of the seismic moment tensor were characterised by reverse slide mechanism with very high share of the shearing component. The focus of tremor of 12 September 2007 for full solution contained 11% of explosive component, 17% of uniaxial tension component and 71% of shearing component (Table 4). The second tremor of 26 October 2007 for full solution was characterised below 1% of the explosive component, 11% of uniaxial tension component and 89% of shearing component (Table 5). The tremor of 7 November 2007 for full solution has pointed out also 86% of the shearing component. The remaining components amounted to: 7% explosive component and 7% uniaxial tension component, respectively (Table 6). The focus mechanism of tremor of 29 November 2007 was of normal slide type. The share of the shearing component was 80%, implosive component 8% and uniaxial compression component 12% (Table 7).

Table 4. Source mechanism parameters of the 12th September 2007

Date			Time			Energy, J			Coordinates, m (SG system)		
12.09.2007			5:53			$1\cdot10^7$			22521		10883
Full solution Reverse fault				Deviatoric solution Reverse fault				Double couple solution Reverse fault			
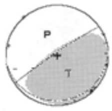				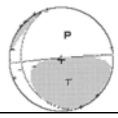				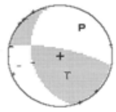			
$M_{ij,}$ Nm				$M_{ij,}$ Nm				$M_{ij,}$ Nm			
0,79E+09	0,79E+09	0,79E+09		-0,57E+14	-0,22E+15	-0,77E+15		-0,22E+15	-0,25E+15	-0,35E+15	
0,79E+09	0,79E+09	0,43E+15		-0,22E+15	-0,67E+14	0,12E+15		-0,25E+15	-0,94E+14	-0,28E+13	
0,79E+09	0,43E+15	0,13E+16		-0,77E+15	0,12E+15	0,12E+15		-0,35E+15	-0,28E+13	0,22E+15	
M_o, Nm		M_T, Nm		M_o, Nm		M_T, Nm		M_o, Nm		M_T, Nm	
0,10E+16		0,14E+16		0,75E+15		0,81E+15		0,56E+15		0,46E+15	
I, %	CLVD, %	DBCP, %		I, %	CLVD, %	DBCP, %		I, %	CLVD, %	DBCP, %	
11	18	71			15	85				100	
ΦA, °	δA, °	ΦB, °	δB, °	ΦA, °	δA, °	ΦB, °	δB, °	ΦA, °	δA, °	ΦB, °	δB, °
180	62	00	28	266	87	164	16	181	74	166	33
ΦP, °	δP, °	ΦT, °	δT, °	ΦP, °	δP, °	ΦT, °	δT, °	ΦP, °	δP, °	ΦT, °	δT, °
270	17	90	73	10	40	160	46	34	23	156	52
Q, %		ERR, Nm		Q, %		ERR, Nm		Q, %		ERR, Nm	
48		0,34E+14		55		0,29E+14		59		0,36E+14	

Table 5. Source mechanism parameters of the 26th October 2007

Date			Time			Energy, J			Coordinates, m (SG system)		
26.10.2007			3:01			$2\cdot10^7$			22498		11109
Full solution Reverse fault				Deviatoric solution Reverse fault				Double couple solution Reverse fault			
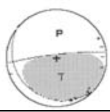				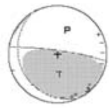				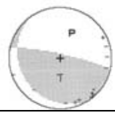			
$M_{ij,}$ Nm				$M_{ij,}$ Nm				$M_{ij,}$ Nm			
-0,34E+15	-0,19E+15	-0,13E+16		-0,79E+14	-0,99E+14	-0,44E+15		-0,16E+15	-0,15E+15	-0,64E+15	
-0,19E+15	-0,95E+14	0,21E+15		-0,99E+14	-0,59E+14	-0,38E+14		-0,15E+15	-0,59E+14	-0,12E+15	
-0,13E+16	0,21E+15	0,44E+15		-0,44E+15	-0,38E+14	0,24E+15		-0,64E+15	-0,12E+15	0,22E+15	
M_o, Nm		M_T, Nm		M_o, Nm		M_T, Nm		M_o, Nm		M_T, Nm	
0,14E+16		0,14E+16		0,45E+15		0,47E+15		0,69E+15		0,69E+15	
I, %	CLVD, %	DBCP, %		I, %	CLVD, %	DBCP, %		I, %	CLVD, %	DBCP, %	
0,2	10,8	89			8	92				100	
ΦA, °	δA, °	ΦB, °	δB, °	ΦA, °	δA, °	ΦB, °	δB, °	ΦA, °	δA, °	ΦB, °	δB, °
264	82	133	12	278	82	154	14	283	81	149	14
ΦP, °	δP, °	ΦT, °	δT, °	ΦP, °	δP, °	ΦT, °	δT, °	ΦP, °	δP, °	ΦT, °	δT, °
1	37	164	52	18	36	175	51	21	35	181	53
Q, %		ERR, Nm		Q, %		ERR, Nm		Q, %		ERR, Nm	
48		0,59E+14		53		0,35E+14		60		0,46E+14	

Table 6. Source mechanism parameters of the 7th November 2007

<table>
<tr><td colspan="3">Date
07.11.2007</td><td colspan="3">Time
10:07</td><td colspan="3">Energy, J
$5\cdot10^8$</td><td colspan="3">Coordinates, m (SG system)
22508 | 11070</td></tr>
<tr><td colspan="4">Full solution
Reverse fault
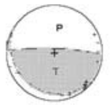</td><td colspan="4">Deviatoric solution
Reverse fault
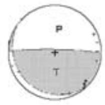</td><td colspan="4">Double couple solution
Reverse fault
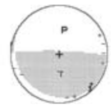</td></tr>
<tr><td colspan="4">$M_{ij,}$ Nm
-0,22E+16 -0,11E+16 -098E+16
-0,11E+16 -0,38E+14 0,57E+14
-0,98E+16 0,57E+14 0,45E+16</td><td colspan="4">$M_{ij,}$ Nm
-0,22E+16 -0,11E+16 -0,98E+16
-0,11E+16 -0,28E+14 -0,38E+14
-0,98E+16 -0,38E+14 0,22E+16</td><td colspan="4">$M_{ij,}$ Nm
-0,29E+16 -0,13E+16 -0,12E+17
-0,13E+16 -0,64E+14 -0,17E+15
-0,12E+17 -0,17E+15 0,30E+16</td></tr>
<tr><td colspan="2">M_o· Nm
0,11E+17</td><td colspan="2">M_T · Nm
0,12E+17</td><td colspan="2">M_o· Nm
0,11E+17</td><td colspan="2">M_T · Nm
011E+17</td><td colspan="2">M_o· Nm
0,13E+17</td><td colspan="2">M_T · Nm
0,13E+17</td></tr>
<tr><td>I, %
7</td><td colspan="2">CLVD, %
7</td><td>DBCP, %
86</td><td>I, %</td><td colspan="2">CLVD, %
0,1</td><td>DBCP, %
99,9</td><td>I, %</td><td colspan="2">CLVD, %</td><td>DBCP, %
100</td></tr>
<tr><td>ΦA, °
272</td><td>δA, °
80</td><td>ΦB, °
123</td><td>δB, °
11</td><td>ΦA, °
270</td><td>δA, °
84</td><td>ΦB, °
135</td><td>δB, °
9</td><td>ΦA, °
271</td><td>δA, °
83</td><td>ΦB, °
130</td><td>δB, °
9</td></tr>
<tr><td>ΦP, °
7</td><td>δP, °
35</td><td>ΦT, °
175</td><td>δT, °
54</td><td>ΦP, °
6</td><td>δP, °
38</td><td>ΦT, °
174</td><td>δT, °
51</td><td>ΦP, °
6</td><td>δP, °
39</td><td>ΦT, °
175</td><td>δT, °
52</td></tr>
<tr><td colspan="2">Q, %
45</td><td colspan="2">ERR, Nm
0,34E+15</td><td colspan="2">Q, %
52</td><td colspan="2">ERR, Nm
0,27E+15</td><td colspan="2">Q, %
60</td><td colspan="2">ERR, Nm
0,36E+15</td></tr>
</table>

Table 7. Source mechanism parameters of the 29th November 2007

<table>
<tr><td colspan="3">Date
29.11.2007</td><td colspan="3">Time
21:45</td><td colspan="3">Energy, J
$6\cdot10^6$</td><td colspan="3">Coordinates, m (SG system)
22462 | 11121</td></tr>
<tr><td colspan="4">Full solution
Normal fault
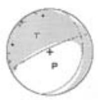</td><td colspan="4">Deviatoric solution
Normal fault
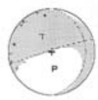</td><td colspan="4">Double couple solution
Normal fault
</td></tr>
<tr><td colspan="4">$M_{ij,}$ Nm
-0,13E+15 -0,31E+15 0,19E+16
-0,31E+15 0,47E+15 -0,63E+15
0,19E+16 -0,63E+15 -0,11E+16</td><td colspan="4">$M_{ij,}$ Nm
-0,14E+15 -0,32E+15 0,19E+16
-0,32E+15 0,52E+15 -0,41E+15
0,19E+16 -0,41E+15 -0,38E+15</td><td colspan="4">$M_{ij,}$ Nm
-0,98E+13 -0,40E+15 0,17E+16
-0,40E+15 0,24E+15 -0,48E+15
0,17E+16 -0,48E+15 -0,23E+15</td></tr>
<tr><td colspan="2">M_o· Nm
0,22E+16</td><td colspan="2">M_T · Nm
0,25E+16</td><td colspan="2">M_o· Nm
0,19E+16</td><td colspan="2">M_T · Nm
0,22E+16</td><td colspan="2">M_o· Nm
0,19E+16</td><td colspan="2">M_T · Nm
0,19E+16</td></tr>
<tr><td>I, %
-8</td><td colspan="2">CLVD, %
-12</td><td>DBCP, %
80</td><td>I, %</td><td colspan="2">CLVD, %
-11</td><td>DBCP, %
89</td><td>I, %</td><td colspan="2">CLVD, %</td><td>DBCP, %
100</td></tr>
<tr><td>ΦA, °
246</td><td>δA, °
80</td><td>ΦB, °
13</td><td>δB, °
16</td><td>ΦA, °
254</td><td>δA, °
86</td><td>ΦB, °
359</td><td>δB, °
13</td><td>ΦA, °
254</td><td>δA, °
86</td><td>ΦB, °
359</td><td>δB, °
13</td></tr>
<tr><td>ΦP, °
170</td><td>δP, °
52</td><td>ΦT, °
326</td><td>δT, °
34</td><td>ΦP, °
177</td><td>δP, °
45</td><td>ΦT, °
332</td><td>δT, °
40</td><td>ΦP, °
176</td><td>δP, °
48</td><td>ΦT, °
332</td><td>δT, °
40</td></tr>
<tr><td colspan="2">Q, %
40</td><td colspan="2">ERR, Nm
0,11E+15</td><td colspan="2">Q, %
47</td><td colspan="2">ERR, Nm
0,11E+15</td><td colspan="2">Q, %
55</td><td colspan="2">ERR, Nm
0,12E+15</td></tr>
</table>

The solution of the tremor mechanism for full tensor against the background of seam map sector presents the Figure 3. For the tremor of 12 September 2007 the direction of nodal plane azimuth can be correlated (within the limits of calculation error 20°) with the strike of the Knurów fault situated at the eastern side of the panel, and for the remaining tremors the direction of the modal plane azimuth is parallel to the strike of the fault zone which limits from the south the longwall 17 area. The exceptionally high share of the shearing component in the mechanism of focus testifies that in this area occur very high influence of stresses originating from tectonic structures. The type of reverse mechanism (displacement on the fracturing plane upwards) can indicate that in consequence of stress equalisation in the fault zone as a result of rock mass "relief" could arise fracturing of sandstone layers occurring at a high distance above the seam. On processes of this type can indicate the lack of equilibrium in the stress field distribution in a large area, because both in the north-western part of the "Knurów" colliery as well as on the eastern side at the "Budryk" colliery several seams were mined out. It should be also mentioned that the analysed tremors have not caused any effects and were not felt in underground workings. Thus the investigations carried out can indicate that the reason of occurred tremors was not only direct mining of the longwall 17, but there followed overlapping of mining-related stresses with residual stresses occurring in the fault zone.

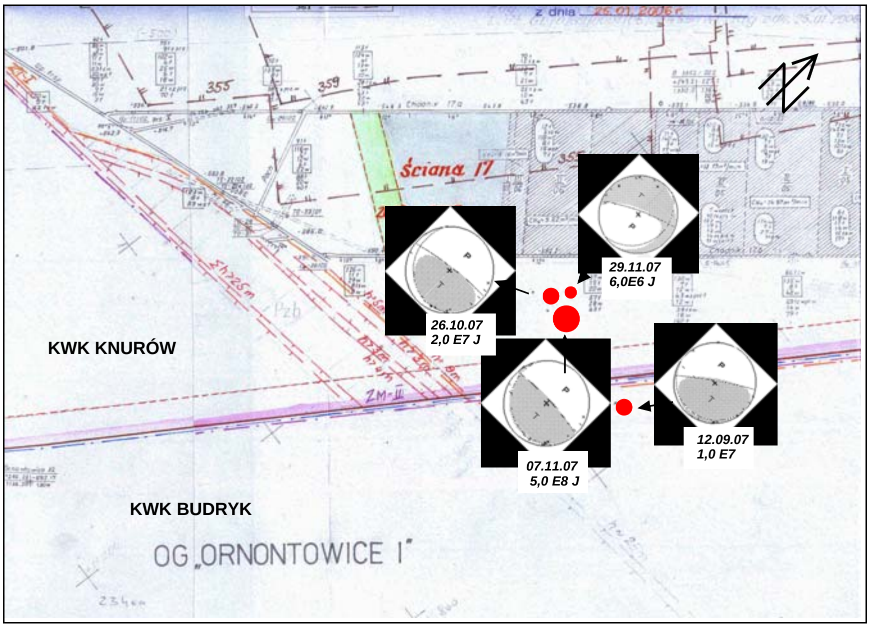

Figure 3. Position of tremor focus and their mechanism against the background of seam map sector

3.2. Spectral parameters

The spectral parameters of the source of analysed tremors were calculated from seismograms of the Seismological Network of the "Knurów" colliery. The results of source parameter calculations (averaged values from selected not re-controlled channels of the seismological network for the wave S presents Table 8.

Table 8. Source parameters

Date	Time	Energy, J	Source parameters				
			M_0, Nm	R_0, m	f_o, Hz	$\bar{D}$, m	$\Delta\sigma$, Pa
2007-09-12	14:45	1.0E+07	7.20E+11	73	6.8	1.38E-03	8.06E+05
2007-10-26.	23:45	2.0E+07	1.08E+12	72	7.5	2.16E-03	2.26E+06
2007-11- 07	10:07	5.0E+08	4.52E+13	104	5.8	4.24E-02	1.74E+07
2007-11- 29	21:45	6.0E+06	4.52E+11	82	4.2	2.35E-03	5.69E+06

The obtained values of source parameters for the analysed tremors indicate the regional character of these phenomena; their reason can be the trend to equalise tectonic residual stresses activated through conducted mining in the fault zone. The corner frequency is low and amounts on the average to 6 Hz. The seismic moment of analysed phenomena amounts from $4.52 \cdot 10^{11}$ Nm for the tremor of 29 November 2007 to $4.52 \cdot 10^{13}$ Nm for the tremor of 07 November 2007. By the largest focus radius equal to 102 m was characterised the tremor of 07 November 2007. The remaining tremors had radii equal to 73, 72 and 82 m. The displacement in the focus was from $1.38 \cdot 10^{-3}$ m for the tremor of 12 September 2007 to $4.24 \cdot 10^{-2}$ m for the tremor of 07 November 2007. The stress decrease, which means the difference between the stress in the focus before the tremor and stress after the tremor was very high and amounted maximally to $1.74 \cdot 10^{7}$ Pa for the tremor of 07 November 2007 and $2.26 \cdot 10^{6}$ Pa for the tremor of 26 October 2007, $8.05 \cdot 10^{5}$ Pa for the tremor of 12 September 2007 and $3.35 \cdot 10^{6}$ Pa for the tremor of 29 November 2007.

4 Mine tremor source mechanism induced by mining exploitation at the "Staszic" colliery

At the "Staszic" colliery on 23 February 2008 at 7.30 p.m. and 7.32 p.m. occurred two high-energy tremors, the first one with energy 8.0E+06 J ($M_L = 2.7$), and the second with energy 2.0E+07 J ($M_L = 2.9$), which led to the loss of functionality of workings in the area of longwall I (cross-cut Asea, transport incline). After tremor occurrence since 23 February 2008 extraction activities on longwall I was stopped on account of damages of workings. For these two tremors and remaining tremors with energy E ≥ 5.0E+03 J ($M_L \geq 1$) from the period 8 December 2007 – 29 March 2008 calculations of focal mechanism calculated using the seismic moment tensor inversion method. The specification of analysed tremors of shearing type of mechanism and explosive character presents Table 10.

From the analysed group of phenomena 23 tremors were characterised by the shearing type of focal mechanism. The fracturing process in the case of these tremors took place at the normal fault, and in their mechanism distinctly dominated the shearing component (from 60 to 75%). Figure 4 presents the position of analysed tremors and their focal mechanism for total solution of the seismic moment tensor of tremors with energy E ≥ 1.0E+05 J ($M_L = 2.7$) against the background of seam map sector. The direction of nodal planes and the corresponding with them fracture direction in the focus for high-energy tremors of 23 February 2008 with energy 8.0E+06 J ($M_L = 2.7$) and with energy 2.0E+07 J ($M_L = 2.9$), as well as of 25 February 2008 with energy 1.0E+05 J ($M_L = 1.7$) and of 29 March 2008 with energy 2.0E+05 J ($M_L = 1.8$) had the azimuth NE–SW or N–S. This direction, within the limits of the calculation error ± 20° was parallel to the course of the cross-cut Asea and transport incline and to the line of mined longwall front.

In the light of analysis carried out we can formulate the hypothesis that the reason of high-energy tremors causing the rockburst in the eastern panel could be exceeding of stresses in sandstone layers occurring above the seam 501, in the left zone of non-mined rock mass between the edges in seam 510, which are parallel to workings conducted in the seam 501. The direction of fracturing in focus of the remaining tremors with lower energies in the majority of cases had also the azimuth NE–SW as well as NW–SE and E–W.

For 12 phenomena one has obtained the type of focus of explosive character. The total tensor contained from 44 to 50% of explosive component, from 43 to 50% of the uniaxial tension component and from 0.5 to 17% of the shearing component. The high share of explosive and uniaxial tension components in the focal mechanism of this type indicates the domination of explosive processes in the seam as a result of overburden layer pressure.

Table 10. Specification of seismological parameters and parameters of focal mechanisms, which occurred during longwall I mining, in the seam 501/II over the period from 8 December 2007 to 29 March 2008 (NO- normal fault, RE – reverse fault)

Date	Time		Energy, J	Coordinates SG system, m		Tensor's components,%			Tape of focal mech.
	h	m		X	Y	I	CLVD	DBCP	
2007-12-10	4	52	1.0E+04	22522	-13776	-20	-20	60	NO
2007-12-12	23	25	2.0E+04	22528	-13777	-20	-20	60	NO
2007-12-17	12	20	6.0E+03	22428	-13717	-20	-20	60	NO
2007-12-23	8	36	8.0E+04	22421	-13822	-20	-20	60	NO
2007-12-29	22	17	7.0E+03	22432	-13767	-15	-15	70	NO
2008-01-24	9	29	4.0E+04	22379	-13719	-20	-20	60	NO
2008-02-13	11	49	3.0E+04	22485	-13790	-20	-20	60	NO
2008-02-16	15	13	6.0E+04	22407	-13661	-20	-20	60	NO
2008-02-19	9	59	2.0E+04	22428	-13569	-20	-20	60	NO
2008-02-21	10	39	2.0E+04	22424	-13658	-20	-20	60	NO
2008-02-22	7	8	8.0E+04	22383	-13679	-17	-20	63	NO
2008-02-22	16	36	2.0E+04	22414	-13717	-19	-20	61	NO
2008-02-23	16	21	2.0E+04	22433	-13702	-20	-20	60	NO
2008-02-23	19	30	8.0E+06	22457	-13631	-20	-19	61	NO
2008-02-23	19	32	2.0E+07	22322	-13622	-13	-17	70	NO
2008-02-23	19	42	2.0E+04	22474	-13668	-19	-20	61	NO
2008-02-23	20	15	1.0E+04	22430	-13614	-11	-14	75	NO
2008-02-23	21	0	2.0E+05	22358	-13858	-19	-19	62	NO
2008-02-24	14	44	2.0E+04	22465	-13621	-20	-20	60	NO
2008-02-25	1	37	2.0E+05	22306	-13638	-12	-18	70	NO
2008-02-25	10	10	1.0E+05	22389	-13692	-20	-20	60	NO
2008-03-25	14	6	3.0E+05	22286	-13640	-11	-14	75	NO
2008-03-29	5	18	3.0E+05	22295	-13643	-18	-20	62	NO
2007-12-08	2	5	7.0E+03	22599	-13833	46	47	7	RE
2007-12-19	23	24	5.0E+03	22458	-13776	50	49	1	RE
2007-12-22	17	7	8.0E+03	22547	-13822	49	48	3	RE
2008-01-06	6	40	6.0E+03	22503	-13748	49	49	2	RE
2008-01-12	23	1	6.0E+03	22394	-13708	50	49	1	RE
2008-02-13	6	5	5.0E+03	22324	-13589	44	43	13	RE
2008-02-13	6	7	5.0E+03	22334	-13591	49	49	2	RE
2008-02-13	22	8	9.0E+03	22460	-13821	43	40	17	RE
2008-02-20	21	12	5.0E+03	22454	-13638	49	49	2	RE
2008-02-22	14	31	5.0E+03	22410	-13670	50	49	1	RE
2008-02-23	6	58	8.0E+03	22417	-13659	49	49	2	RE

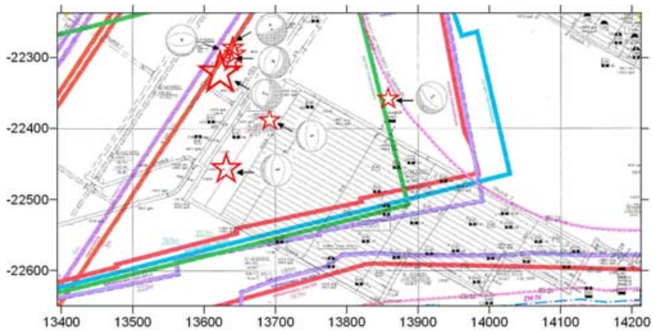

Figure 4. Focal mechanism of tremors with energy E ≥ 1.0E+05 J (M_L = 1.7) against the background of seam 501/II map sector

5 Summary

The results of investigations of tremor focus mechanism and source parameters carried out in different regions of the Upper Silesian Coal Basin allow to obtain information about destruction processes of rock mass disturbed by conducted mining exploitation. A distinct variability of mechanisms of focus of registered tremors according to the region's tectonic features, location of the tremor focus towards the longwall front and existing extraction events was stated.

Two types of seismicity were separated, the so-called mining and mining-tectonic seismicity. The first type of phenomena is directly connected with the conducted mining activity and occurs in the neighbourhood of active mine workings. There are phenomena weaker with respect to energy and are characterised in the majority by the explosive type of the of mechanism.

The second type of mining-tectonic seismicity originates as a result of connection of mining-related and residual stresses occurring in deep structures of the Upper Silesian Coal Basin.

These are high-energy tremors, occurring in regions of tectonic zones, frequently felt by the population on the surface. The most often type of mechanism of focus of these tremors is the normal slide mechanism with the appearing horizontal displacement in the tremor focus. The azimuth of disruption planes and their dips for these phenomena correlate with the strike and dip of faults, in the vicinity of which the focus of tremors are located.

References

1. Aki, K.and Richards, P.G. Quantitative Seismology. Theory and Methods, Freeman, San Francisco, 1980.
2. Brune, J.N. Tectonic stress and the sperctra of seismic shear waves from the earthquakes. J. Geophys. Res, 1970, 75. 4997-5009.
3. Budryk, W.: Skutki wstrząsów w kopalniach górnośląskich. Arch. Górn. i Hutn. 2, 1955s, 227-290.
4. Dubiński, J., Mutke, G.and Stec, K. 1999: Rozwiązania w sejsmologii górniczej poprawiające efektywność oceny stanu zagrożenia sejsmicznego. W: Geologia t.25, Akademia Górniczo-Hutnicza, Kraków, 45-58.
5. Dubiński, J.and Stec, K. Relationship between focal mechanism parameters of mine tremors and local strata tectonics. W: Dynamic rock mass response to mining. Red. G. Van Aswegen, R.J. Durrheim W.D. Ortlepp. The South African Institute of Mining and Metallurgy, 2001, Johannesburg, 113-118.
6. Gibowicz, S. J. Relations between source mechanism and the ratio of the S over P wave energy for seismic events induced by mining, Acta Montana, 1996, ser. A, No. 9 (100). 7-15.
7. Gibowicz, S. J., Domański, B.and Wiejacz, P. The focal mechanism and source parameters of seismic events induced by mining, Acta Montana, 1996, ser. A. No. 10 (102). 1-18.
8. Idziak, A.F., Teper, L. Zuberek, W.M., Sagan, G.and Dubiel, L.: Mine tremor mechanisms used to estimate the stress field near the deep rooted fault in the Upper Silesian Coal Basin. W: Rockbursts and Seismicity in the Mines, Red. S. J. Gibowicz, S. Lasocki. Balkema/Rotterdam/ Brookfield 1997, s. 31-37.
9. Stec, K. Analiza mechanizmów ognisk wstrząsów górniczych występujących w GZW. W: Geomechaniczne i sejsmologiczne modele ognisk wstrząsów górniczych, Akademia Górniczo-Hutnicza, Kraków, 1999, 53-73.
10. Stec K. Charakterystyka mechanizmu ognisk wstrząsów górniczych z Obszaru Górnośląskiego Zagłębia Węglowego", Wiadomości Górnicze 4/2005, 168-174.
11. Stec K. Characteristics of Seismic Activity of the Upper Silesian Coal Basin in Poland". Geophysical Journal International, Blackwell Publishing Ltd, 2007, V 168, 757-768.
12. Teper L. Wpływ nieciągłości podłoża karbonu na sesjmotektonikę północnej części Górnośląskiego Zagłębia Węglowego. Wyd. Uniw. Śląskiego, Katowice, 1998.
13. Wiejacz P. The SMT software, PAN, Warszawa, niepublikowane, 1994.
14. Wiejacz, P. Source mechanisms of seismic events inducend at Ziemowit coal mine: comparison with mining information. Publ. Inst. Geoph. Pol. Acad Sci. 1995, M-19, 15-32.
15. Wierzchowska, Z. Przyczyny wstrząsów na Górnym Śląsku, Główny Instytut Górnictwa, Katowice, 1961, Komunikat 268.
16. Zuberek, W.M., Teper, L., Idziak, A.F.and Sagan G. Tectonophysical approach to the description of mining induced seismicity in the Upper Silesia. W: Tectonophysics in Mining Areas. Red A. Idziak, Wyd. Uniw. Śl., Katowice, 1996, 79-98.
17. Zuberek, W.M., Teper, L., Idziak, A.F.and Sagan, G. Seismicity and tectonics in the Upper Silesian Coal Basin, Poland. W: proc. XIII Int. Cong. of Carboniferous-Permian. Prace Państw. Inst. Geol., Kraków 1997. nr 157, 199-207.

RaSiM 7(2009): Controlling Seismic Hazard and
Sustainable Development of Deep Mines,
C.A. Tang(ed), Rinton Press, 427-434

STUDY OF ROCKBURST BASED ON THE HIERARCHY OF ROCK MECHANICS SYSTEM

JUN HAN

College of Resource and Environment Engineering, Liaoning Technical University

No 47, zhonghua road, Fuxin city,Liaoning province, China

HONG-WEI ZHANG

College of Resource and Environment Engineering, Liaoning Technical University

No 47, zhonghua road, Fuxin city,liaoning province, China

SHENG LI

College of Resource and Environment Engineering, Liaoning Technical University

No 47, zhonghua road, Fuxin city,liaoning province, China

This research aims to the mechanism of rockburst in Haizhou coal mine. The numerical simulations were used to get the geological structure environment, mining induced stress and failure of roadway. The geological structure - sediment system, coal - rock system and floor strata system are divided and the hierarchy and nonlinear of them are discussed. The research shows that Gaode syncline is an inhomogeneous factor and the nearer the roadway is to Gaode syncline, the higher is the stress. This is the reason that rockburst closed to Gaode syncline. The interlayer in roadway make the stress of roadway to increase to 3～6 MPa than the case of no interlayer. So when rockburst occurs, the floor heave is main way of failure of sounding rock.

1 Introduction

Rockburst is a serious threat to the safety of mining because of its sudden and violent destruction. Many scholars and engineers have researched and put forth significant theories and viewpoints, such as Intension Theory (G.Brāener, 1965), Rigidity Theory (Cock et al, 1965; Blake, 1972), Energy Theory (Cock, 1965; Denkhaus, 1969; Salamon, 1970; Crouch, 1974; Petukhov, 1979), Bursting Liability Theory (Bieniawski, et al, 1969), Instability Theory(ZHANG M, 1987), Catastrophe Theory (PAN Y, 1992), Fractal Theory(XIE H, 1993) and Fracture Mechanics (Lippmann, 1987; Dyski et al, 1992). The consensus of opinion has not been built up to now. This conclusion can be found in literatures that discuss the mechanism and its influences, and that the energy of rockburst comes from two types of interactional stress fields, the in-situ stress field and mining induced stress. So, research needs to be done on the rockburst mechanism, prediction and prevention of rockburst, and the original mining induced stress field.

The rockburst phenomenon in Fuxin mining was severe. Rockburts occurred in six of the coal mines. Since 2002, 14 large rockbursts occurred in the Wulong coal mine. Thirty five rockbursts have occurred in the Haizhou coal mine since 2000. Gaode coal mine, Wangying coal mine and Dongliang coal mine are the other mines that have had rockburst disasters. From Sep, 1990 to Oct, 2004, more than 2,079 mining seisms ($M_L \geq 1.0$) occurred, and at least 66 of the mining seisms had $M_L \geq 3.0$. The strongest mining seism with M_L of 3.8 occurred in the Wulong coal mine on June 16th, 2002. The rockburst mechanism was an urgent and significant scientific problem, and much work has been done to curb the rockbursts in the Fuxin mining area. PAN Y summarized the reasons including the complex geological tectonic, deeply mining higher gas content and higher gas press [1]. TANG J considered that the rock burst type of Wulong coal mine was coal mass compressed [2]. In this paper the authors take rockburst as a stability problem of rock mechanics system. Based on the hierarchy of system, the mechanism of rockburst is studied. Finally, prediction and prevention of rockburst is discussed.

2 Rockburst and its characteristic of Haizhou coal mine

Haizhou coal mine lies in Fuxin basin, west of Liaoning province at longitude 121°41′ east and latitude 42°02′ north. The coal measure is Fuxin formation, Jurassic Period. The Gaode syncline and Gaode anticline were main structures in Haizhou coal mine. Its strike was NNE.

Since 2000, rockbursts were frequently occurred in Haizhou coal mine. According to conservative statistics, there were 35 rockbursts in Haizhou coal mine and the intensity and frequency were increased year-by-year. Such as 6 in 2005, 12 in 2006 and 12 in 2007. The ‘2.14’ gas explosion was caused by a rockburst which made 214 people death at 14 Feb, 2005 [3].

Some characteristics could be found according to these rockbursts in Haizhou coal mine. Firstly, most of rockbursts are located at Gaode syncline, the main structure of Haizhou coal mine (Figure 1). This is an obviously concentrative region. Secondly, the damage of roadway after rockburst has the same characteristic - floor heave. The magnitude of floor heave is usually 0.4-0.5 m and the maximum value is 1.3 m. Some roadway’s roof has a certain extent of subsidence.

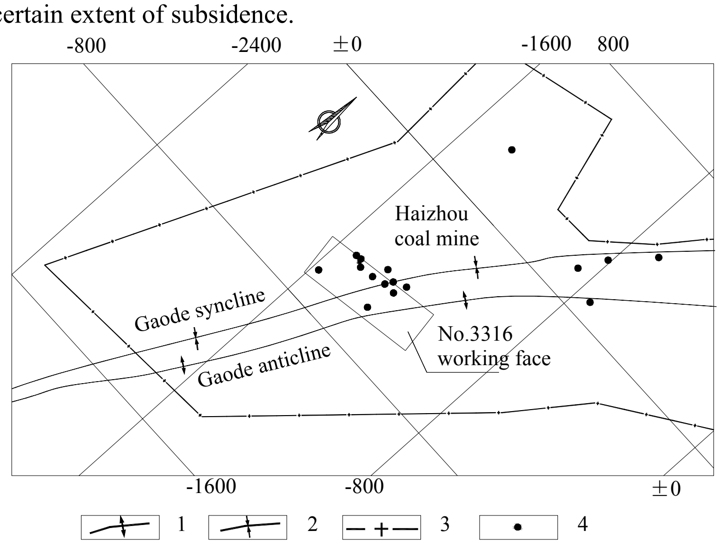

Figure 1 Relation between rockburst and syncline
1-anticline; 2-syncline; 3-boundary; 4-rockburst

3 Rockburst mechanism of Haizhou coal mine

3.1 The hierarchy of rock mechanics system

The coal seam and surrounding rock is considered as a rock mechanics analysis system at rock mechanism study [4] [5]. One system is always composed of some subsystems, at same time it could be looked upon as a subsystem to its parent system, namely hierarchy. The hierarchy is one of characteristic of system, rock mechanics system is no exception. Rock mechanics system is an open system, which exchange and transmit energy, matter and information with the inner and external environment (subsystem and parent system). At the disturbance of the outside world, the rock mechanics system would release energy through internal deformation and micro-fracture of subsystem to maintain itself stability and integrity.

In the rockburst mechanism study of Haizhou coal mine, the whole problem is divided into three levels of system. The coal - rock system is one of them, there is a higher level system – geological structure - sedimentary system, which is a composite of geological structure, coal measure etc. In the internal of coal - rock system, there is the floor strata system, a subsystem composed of various rock strata (Figure 2).

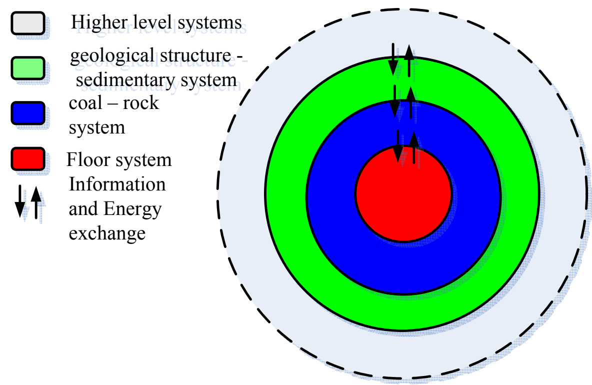

Figure 2 Hierarchy of rock mechanics system

3.2 The geological structure - sediment system

In this section, the reason that most of rockbursts located at Gaode syncline is analyzed. Syncline is one of structures because of rock's bend deformation under the force in crust. The mechanics system of syncline could be divided into three parts: upper layer, neutral layer and lower layer. The upper layer is compressive and the lower layer is tensile. The neutral layer is neither tensile nor compressive. Axis of syncline's stress (tensile or compressive) is greater than limb (Figure 3). Coal measure is composed of multilayer and the friction force of each layer is different, the stress state of syncline is complex much more [6].

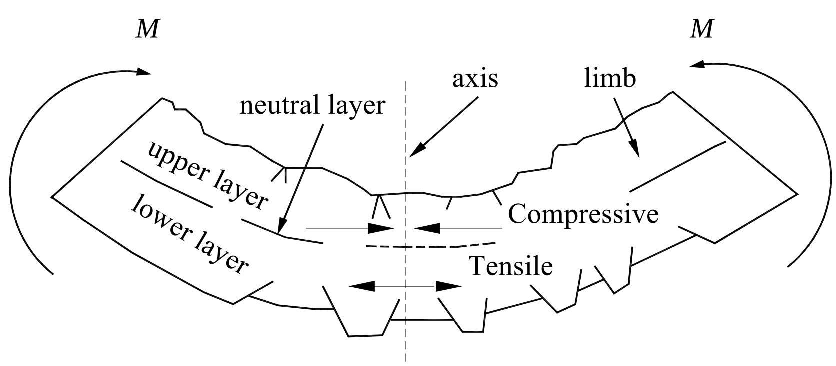

Figure 3 Mechanics sketch of the syncline

To know the stress state of Gaode syncline, in-situ stress was measured with hollow inclusion (HI) technique. The measurement result shows that: (1) the major and minor principle stress is horizontal and interim principal stress is vertical approximately, and (2) The orientation of major principal stress is 100.3°-102.3° and the magnitude of major principal stress is 29.45~31.89 MPa. The orientation of major principal stress is coincident to XIE F (2004) [7]. The inclination between axis of Gaode syncline and major principal stress is

55°-85°, so the stress state of Gaode syncline is similar to its forming state (Figure 3). Under this high stress, much strain energy is accumulated in the coal and rock mass. At this stress state, the coal – rock is prone to failure. Because No.3316 working face lies in the axis of Gaode syncline, coal – rock has accumulated much more strain energy. The Tectonic stress provides power for rockburst. The Gaode syncline is an inhomogeneous factor of the geological structure – sediment system. So the rockburst is prone to occurred close-by it.

3.3 The coal - rock system

The coal – rock system is a subsystem of geological structure - sediment system. It is the main space that the original and mining induced stress are contemporary and interactive. Whereas rockburst in No.3316 working face was most frequent and serious, in this paper take it as an example to analysis the relation between rockburst and mining induced stress. The No.3316 working face lies in the center of No.331 panel. The Gaode syncline crossed it (Figure 4). The coal seam of No.3316 longwall working face is complex with 0.2~0.3 m interlayer in it.

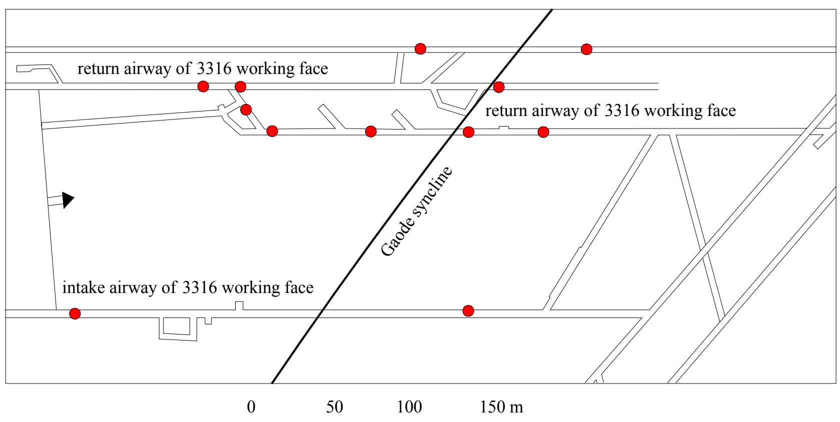

Figure 4 Layout of 3316 workface

According the geological condition and coal – rock configuration, establish the two-dimensional numerical calculation model for FLAC^{2D} software. The model considers a slice of the rock mass 360 m wide and up to 100 m high and contains 360 elements along the width and up to 100 elements along the height. The upper border of the model was applied a compressive stress which equiv to gravity of overlying strata. A linearly varying compressive stress was applied in horizontal. The physical and mechanical parameters of rock (coal) are shown in Table 2. The criterion of material failure in this calculation is Mohr-Coulomb relation, which is a linear failure surface corresponding to shear failure [8]:

$$f_{\tau} = \sigma_1 - \sigma_3 \frac{1+\sin\varphi}{1-\sin\varphi} - 2c\sqrt{\frac{1+\sin\varphi}{1-\sin\varphi}} \tag{1}$$

Where, σ_1 and σ_3 were the major principal stress and minor principal stress; C and φ were cohesion and friction angle. When f_s>0, the material would be shear failure. Generally speaking, the tensile strength of rock is very low, according to the tensile strength criteria ($\sigma_3 \geq \sigma_T$) to determine whether or not rock is failure.

Table 2 Physical and mechanical parameter of model

Type of rock	Density (kg/m^3)	bulk module /MPa	Shear module /MPa	Tensile strength /MPa	Cohesion /MPa	Friction angle /(°)
gritstone	2600	28395	18699	4.0	8.6	38
fine sandstone	2662	12103	10642	8.18	9.86	39
Coal	1366	1293	890	2.17	2.54	40
siltstone	2458	9609	6909	2.58	4.3	54
interlayer	2000	5000	3000	2.0	3.0	40

The calculation result of mining induced stress is shown in Figure 5. When the longwall face proceeds, abutment pressures will form around the edges of the gob and superimpose on those created during entry developments. The length of stress increased zone is 50 ~ 60 m in front of the working face. The stress value was 24 ~ 40 MPa and The peak stress located at 6 ~ 8 m ahead of working face and the stress concentration coefficient is 2.4. According to the results, mining induced stress in No.3316 working face is remarkable. The range of stress increased zone is forgoing and the magnitude of mining induced stress is large. So there will be much more elastic strain energy in the coal – rock system. When the speed of stress increase of coal – rock system is faster than the speed of stress relaxation, rockburst is likely to happen.

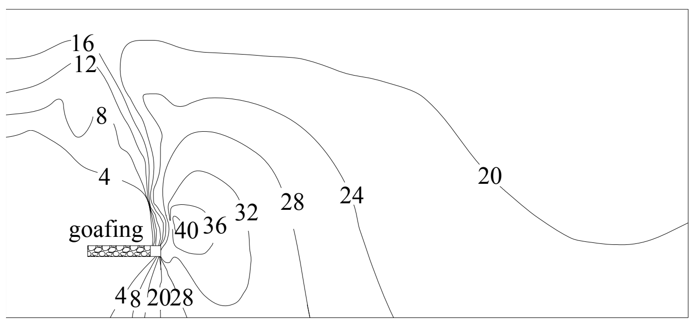

Figure 5 Distribution of mining induced stress

3.4 The floor strata system

In view of the roadway damage characteristic after rockburst, the RFPA^{2D} (Rock Failure Process Analysis System) is the appropriate tool to analyze rock's failure process of the No.3316 return airway. The RFPA^{2D} software is based on the principle of finite element method to analyze the failure process of rock - like material. Considering the non-homogeneous properties of rock materials, the statistical physics methods, namely, Weibull distribution is used to describe the disperse property of micro-mechanical body [9].

There is normally 0.5~2 m interlayer in the floor of No.3316 return airway. To know the relation between interlayer and floor heave, two type models were established, no interlayer in floor and an interlayer in floor. The calculation model is divided into 216 × 230 units and the cell dimension is 250 mm × 250 mm. The model's high and width are 54 m and 57.5 m (Figure 6).

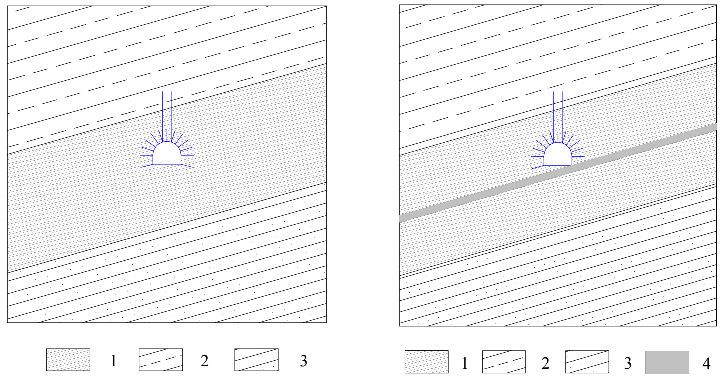

(a) (b)

Figure 6 Model of return airway of 3316 working face

1-coal; 2-siltstone; 3-fine sandstone; 4- interlayer

(a) no interlayer in floor; (b) an interlayer in floor

Regardless of whether the interlayer in floor, stress concentration appears in the top and bottom of roadway, and at top the stress values is 21 ~ 24 MPa. The difference is that where there has an interlayer, the bottom stress value is 24 ~ 30 MPa, mainly concentrated in interlayer and its bottom, affecting area of about 4 m. Without interlayer, the stress of roadway floor is about 21 ~ 24 MPa and the affecting area is 4 ~ 5 m. so the interlayer has a significant influence to the stress state of floor (Figure 7).

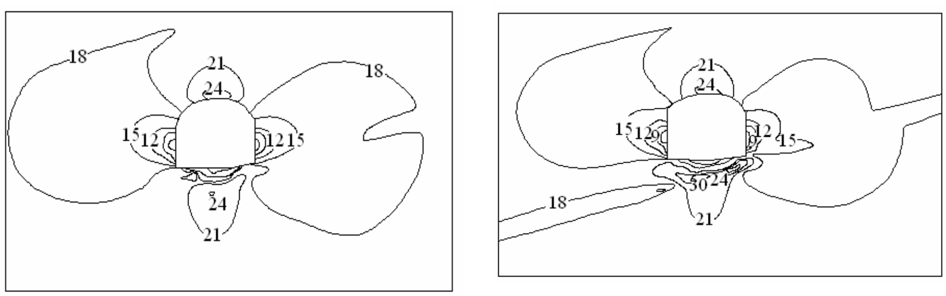

(a) (b)

Figure 7 Stress of roadway at different surrounding rock(coal)structure

(a) no interlayer in floor; (b) a interlayer in floor

Studies have shown that when the floor was stratified, the floor heave could occur at some stress condition. Set B as width of roadway, t as thickness of stratification, when the following conditions were met floor heave was likely to happen, that is, [10]

$$\begin{cases} t \le (1/8 \sim 1/15)B \\ p_{cr} \ge \beta(4\pi^2 EI / B^2) \end{cases} \tag{2}$$

Where, p_{cr} - extrusion force parallel to bedding direction, N; β - coefficient about joint development degree; EI - flexural stiffness of floor. According the formula, the rock strata thinner, the greater width of roadway, the critical buckling load p_{cr} required is smaller, the more prone to floor heave. Contrarily the width of roadway and thickness of interlayer is determinate; extrusion force parallel to bedding is greater the roadway also tend to floor heave.

RFPA^{2D} showed the Destroy evolvement of roadway (Figure 8). The floor is remarkable and the side is slight.

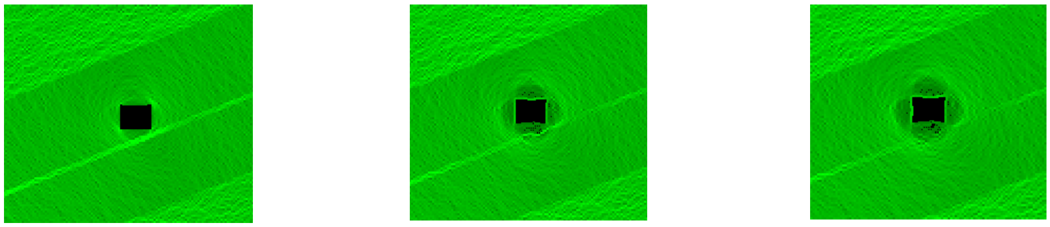

(a) step 1 (b) step 10 (c) step 16

Figure 8 Destroy evolvement of roadway

4 Conclusions

(1) Based on the hierarchy of the rock mechanism system, the three levels of system, geological structure – sediment system, coal – rock system, and floor strata system are divided. A feasible way to analyze the mechanism and appearance of rockburst is too study the inheterogeneity and nonlinear behaviors of the system.

(2) The Gaode syncline is an inhomogeneous factor of the geological structure – sediment system. The nearer the roadway is to the Gaode syncline, the higher the stress is. This is the reason that rockburst occurred in the Gaode syncline. Floor heave was the main reason the coal – rock failed.

Acknowledgments

The work presented in this paper was financially jointly supported from the National Natural Science Foundation of PR China (Grant No. 50874058) and the Research Fund of The State Key Laboratory of Coal Resources and Mine safety, CUMT (Grant No. 08KF01). Special thanks to Fuxin Mining Group and Haizhou coal mine.

References

1. Pan, Y.S., Li, Z.H. and Tang, X. Research on rockburst for highly gassy deep mine in Fuxin coal mining. Chinese Journal of Rock Mechanics and Engineering, 2005, 24:5202-5205. (in Chinese)
2. Tang, J.P., Li, Y.J. and Pan, Y.S. Numerical simulation of deep-level rockburst using ANSYS FEM software. Journal of Disaster Prevention and Mitigation Engineering, 2005, 25(3):271-274. (in Chinese)
3. Li, T., Cai, M.F. and Wang J.A. Mining–induced seismicity in China. Seismological Research of Northeast China, 2005, 21(3):1-26. (in Chinese)
4. Zhang, M.T., Xu, Z.H. and Pan, Y.H., et al. A united instability theory on coal burst and outburst. Journal of China Coal Society, 1991, 16(4): 48-53. (in Chinese)
5. Wang, L.G., Huang, R.Q. and Wang, Y.J., et al. Movement Stability Theory and Application of Rock Mechanics System. Beijing: Geological Publishing House, 1998. (in Chinese)
6. Han, J., Zhang, H.W. and Huo, B.J. Discussion of coal and gas outburst mechanism of syncline. Journal of the China Coal Society, 2008, 33(8): 908-913. (in Chinese)
7. Xie, F.R., Cui, X.F. and Zhao, J.T., et al. Regional division of the recent tectonic stress field in China and

adjacent areas. Chinese Journal Geophysics, 2004, 47(4): 654-662. (in Chinese)

8. Itasca Consulting Group Inc. FLAC (Version3.3) Users' Manul. 1996.
9. Tang, C.A. and Zhao, W. RFPA^{2D} system for rock failure process analysis. Chinese Journal of Rock Mechanics and Engineering, 1997, 16(5):507-508. (in Chinese)
10. Jiang, Y.D. and Lu, S.L. Investigation of mechanism of floor heave of roadway. Journal of China Coal Society, 1994, 19(4): 343-351. (in Chinese)

RaSiM 7(2009): Controlling Seismic Hazard and
Sustainable Development of Deep Mines,
C.A. Tang(ed), Rinton Press, 435-440

ACOUSTIC EMISSION CHARACTERISTICS AND MECHANICAL BEHAVIOR OF SKARN UNDER UNAXIAL CYCLIC LOADING AND UNLOADING

SU-CHAO XU
School of Resources and Civil Engineering，Northeastern University
Shenyang, 110004，P.R. China

XIA-TING FENG and BING-RUI CHEN
State Key Laboratory of Geomechanics and Geotechnical Engineering
Institute of Rock and Soil Mechanics，Chinese Academy of Sciences
Wuhan, 430071, P.R. China

Strength variation and acoustic emission characteristics of skarn under uniaxial cyclic loading and unloading tests are studied using MTS equipment and the PAC AE acquisition system. The results indicate that in the loading and unloading process, if there is no remarkably local failure occurring in the loading process, the unloading process might strengthen the rock sample with an increasing amplitude of 30%. If local failure occurs and non-renewable cracks appear in the loading process, the unloading process facilitates the slippage of planes of cracks and accelerates the breakdown rate. Meanwhile, the results also indicate that the uniaxial compression curve of skarn can be generally divided into four stages: pressure consolidation, elastic, plastic, and peak post which occurs with different acoustic emission conditions. There is an apparent relative quiet stage of acoustic emission signals before failure. In addition, skarn has the anti-Kaiser effect under cyclic loading and unloading with the felicity ratio decreasing and increasing in cycles Acoustic emission also exists in the unloading process with equal quantity and intensity to the loading process.

1 Introduction

In the field of Rock Engineering, the cyclic loading and unloading effect is very common. For example, in room and pillar mining methods, the stress concentration and redistribution occurs periodically with the different excavation sequences at different levels. Therefore, the pillars have to bear cyclic loading and unloading to some extent. Since the strength characteristics and deformation laws of rock under cyclic loading and unloading are significantly different from the statistic condition, it is necessary to make careful analysis and intensely research the strength characteristics and deformation laws of rock under cyclic loading and unloading to gain a better understanding. In this aspect, Ge Xiurun [3] has done research on the fatigue test of rock. With the development of monitoring methods, AE monitoring is becoming more and more important within the laboratory and practical engineering [1, 2]. Meanwhile, we can certainly understand the inner damage of the samples under loading. Li Shulin etc.[4,5,6] has performed a lot of work is this area.

We begin in Section 2 by introducing the test design and methods, including the testing rock produced area, grouping of this experiment, and the instruments used.

In section 3 we investigate the collected experimental data from the cyclic loading and unloading test, and justify our assertion that the strength of the rock will increase. By comprehensive analysis of the different results of the tests, we safely come the conclusion that if there is no remarkably local failure in the loading process, then the unloading process will strengthen the rock sample with the increasing amplitude of 30%; and if the local failure happens and the nonrenewable cracks appears in the loading process, then the unloading process will facilitate the slippage of planes of cracks and accelerate the breakdown rate.

In section 4 we then explore the acoustic emission data including hits, counts, energy etc. The results also indicate that: the uniaxial compression curve of skarn can be generally divided into four stages: pressure consolidation, elastic, plastic, peak post which with different acoustic emission characteristics. There is an obviously relative quiet stage of acoustic emission signals before failure. In addition, skarn has the anti-Kaiser effect under cyclic loading and unloading and the felicity ratio decrease with the increasing of cyclic times. Acoustic emission also exists in the unloading process with equal quantity and intensity to the loading process.

Finally, in section 5 we conclude with some beneficial conclusions.

2 Test design and methods

The rock of the test was mined from the multi-metal ore mine called Shi Zhuyuan in Chenzhou of Hunan province. The samples were made in ϕ 50×100mm and the accuracy satisfied the “rock experimental rules of hydroelectric project”.

This test is consisted of groups. The first group is uniaxial compression, which has 3 samples. The second is once cyclic loading and unloading test, which has 3 samples either and is unloading at the 80% of the predictive strength by the first group. The last group is cyclic loading and unloading, which has 9 samples and is unloading at the 50% of the predictive strength by the first group, and then cycles with the increment of 10Mpa each time until the wholly failure.

The test was conducted at Wuhan Rock and Soil Mechanics Institute of Chinese Academy of Sciences with the MTS equipment. The acquirement of AE was finished by the acoustic emission instrument with 16 channels imported from PAC company in America.

3 Strength Variation

3.1 uniaxial compression

For the purpose of predicting the unaxial strength of skarn, the uniaxial compression test was firstly conducted. The strength of the three samples is respectively: 12# 115.45Mpa, 6# 85.35Mpa, 21# 38.92Mpa. The 21# sample came into the yielding stage too early due to the natural structural defects, so the estimated strength of skarn of uniaxial loading is 100Mpa computed by the other samples.

3.1 .1 strength variation under once cyclic loading and unloading

Based on the estimated strength computed in the uniaxial compression test, the samples in this group were firstly loaded to 80Mpa, then unloaded to 5Mpa, and then loaded continuously till the failure. The strength of 13#, 20#, 1# samples are respectively 107.22Mpa, 124.79Mpa, 80.45Mpa. It is worth noting that 1# sample also came into the yielding stage too early due to the natural structural defects. So, the strength of 13# and 20# were higher than the estimated strength with the increment of 10% to 20%. Therefore, unloading happens before the peak strength, the linear characteristic of deformation can be enhanced in the next loading process with the a little bit enhancement of young’s modulus and yielding strength.

3.1 .2 strength variation under multi cyclic loading and unloading

The samples in this group were firstly loaded to 50Mpa based on the estimated strength computed in the uniaxial compression test either, then unloaded to 5Mpa, and then cycled the loading and unloading process with the strength increment of 10Mpa each time, finally loaded continuously till the failure. Table 1 is the detailed strength of samples in this group. Among them, the strength of 11#, 17#, 24# samples fell obviously in the early loading process, and it indicates that local distruction happens in the sample and leads the sample to failure quickly. The strength of the other 6 samples were higher than the estimated strength with the increment of 33%. Moreover, the effective average strength of the third group is also higher than the second group with the increment of 17Mpa and amplitude of 15%.

Table 1 strength of samples under cyclic loading and unloading

number	strength	number	strength	number	strength
10	127.29	27	111.78	19	105.96
4	119.06	22	171.18	11	82.35
2	164.61	17	57.07	24	76.45

Synthesize the results of strength of the three groups, we can inferred conservatively that the strength might increased with the increasing of cyclic times. This will naturally let us consider that it is the unloading process that raising the strength of specimens, however, the results of 11#, 17#, 24# also tell us the unloading process will facilitate the developing of the cracks instead of strengthening the samples if the local distruction happens in the loading process. Figure 1 is the stress- strain curve of 4# sample under cyclic loading and unloading. The young's modulus of the second loading process is a little bit higher than the first one, behind that, the young's modulus has almost no changes in the latter cyclic process. When the sample came into yielding process, the young's modulus began to diminish constantly till the wholly failure. Figure 2 is the stress-strain curve of 17# sample under cyclic loading and unloading. From Figure 2, we can distinctly see that the stress fell dramatically at the level of nearly 60Mpa, and it indicates that local distruction happens inside the sample, so the young's modulus afterwards diminished remarkably and macroscopic cracks occurs which leading the specimen collapse rapidly.

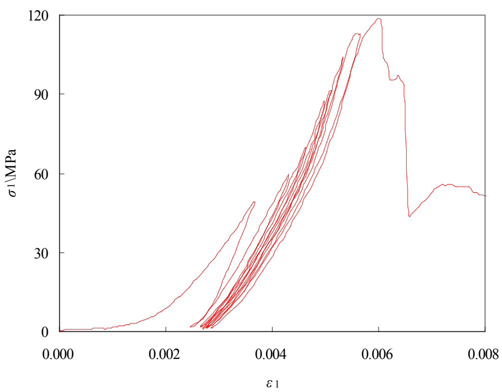

Figure 1 cyclic loading and unloading axial stress-strain curve of 4# sample

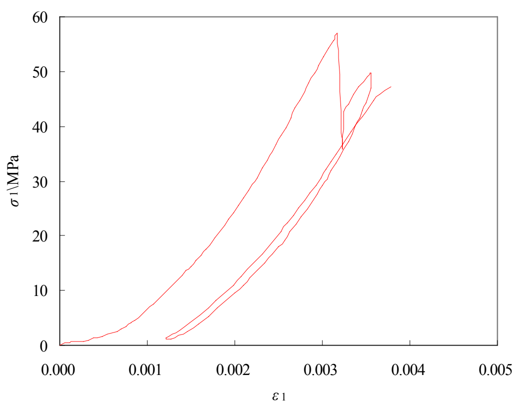

Figure 2 cyclic loading and unloading axial stress-strain curve of 17# sample

Comprehensive analysis of the two typical stress-strain curve was made, and with the purpose of finding the failure reason, the author holds that:

1. If there is no obvious local distruction in the loading process and only a few new born cracks occurs, the interbedded structure will be revitalized and adjusted in the unloading process, and so, the sample get strengthen due to the increasing of frictional strength. In summary, the unloading process is beneficial for the strengthening of the rock.

2. If local distruction happens and macroscopic cracks occur in the loading process, at this time, unloading will facilitate the slippage of the macroscopic cracks, so the specimen collapse rapidly in the next reloading stage.

4 Acoustic emission characteristics

Acoustic emission (AE) is a burst of high frequency elastic waves emitted by a local failure such as microcracking or pore collapsing in rock. It is observed in rocks that AE is detected only during the first loading to a given stress state under compression. If the previously applied stress state is exceeded, the AE events are again observed. This is the so-called Kaiser effect. It is formally described as the absence of detectable AE events until the load imposed on the material exceeds the previous applied level.

The Kaiser effect was first observed in metals by Kaiser. The investigations of the Kaiser effect in geomaterial started to be reported in the end of the 70's. The motivation for the study of the Kaiser effect in geomaterials at the beginning was to estimate geostresses. It seems, however, that no satisfactory results have been reported on this subject to date. The conclusions obtained are contradictory regarding what the stress estimated by means of the Kaiser effect represents. There are, at least, three different explanations: the historical maximum stress or the tectonic stress, the currently existing stress and the maximum differential stress. It has not been reported that the three dimensional in-situ stress state has been estimated by means of the Kaiser effect. It seems that the theoretical and technical problems of estimating geostresses by means of the Kaiser effect have not been successfully solved so far. The Kaiser effect is actually a measure of damage which has been developed in a material subjected to a load. In general, rocks do not exhibit a yield surface as metal materials. The formalism of plasticity is not appropriate to study the failure process in rocks. In describing brittle rocks where deformation and failure are due to the growth and coalescence of cracks, the concept of damage is useful. It is known that AE is associated with the development of damage in rocks (microcracking and pore collapsing). The Kaiser effect may be used to detect and assess the amount of damage that has been developed in rocks.

Figure 3 is the relation curve of time with stress and AE (accumulate counts), from this figure, we can know that the curve of AE process can be divided into 4 stages: AB is process of consolidation of natural cracks with little AE events, and the AE counts increased very slowly releasing little energy. BC is the linear deformation stage with nearly no increasing of AE counts and there is no high energy events happened. This indicates that it is mainly elastic deformation happens with no development of cracks. CD is the plastic stage with steadily increasing of AE counts acquiring a lot of high energy signals. This shows that the sample began to deteriorate and new born cracks occur with the increment of stress. Meanwhile, the cracks developed steadily. DE is post-peak stage with dramatically increasing of AE counts at the three obviously stress falling point, high energy signals occurs continuously. This result has some similar trends with Mogi's [7] research results.

By carefully examining Figure 3 and Figure 4, we can find that there is a relatively quiet period of AE before peak strength. In this period, AE hits, counts, energy are all at a relatively low level. This is very similar to the phenomenon that quiet period occurs before heavy earthquake, rock burst, other significant geo disasters etc. The similarity tells us comparability exists between results of monitoring and laboratory test. So, the laboratory results can provide some guidance for the prediction of geo disaster in practical engineering.

From Figure 5, we can know that the AE signals occur dramatically before the stress exceeding the previous maximum value. Lochner [8] noted that only a part of rocks have Kaiser effects. So, we can say that the specimen in this test has an anti- Kaiser effect, or in other words, it has Felicity effect. The felicity ratio is a measure of the quality of rocks, giving a quantitative measure of the extent to which the rock can be safely loaded.

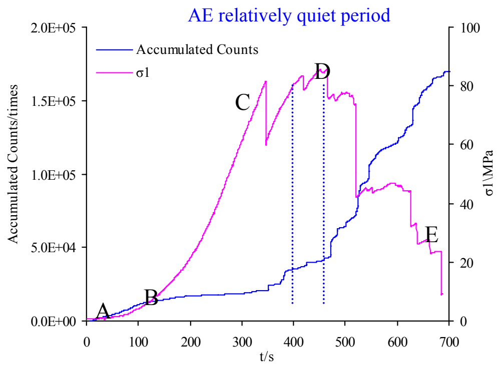

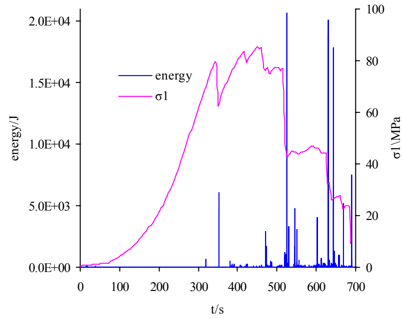

Figure 3 Relation of time with stress and AE (accumulate counts) for skarn under uniaxial loading

Figure 4 Relation of time with stress and AE (energy) for skarn under uniaxial loading

The definition of Felicity Ration:

$$FR_i = \frac{P_{i+1}}{P_{i\max}} \tag{1}$$

In which, FR_i is Felicity Ratio of the ith cycle; P_{i+1} is the stress level in the (i+1)th cycle when large amount of AE occurs; $P_{i\max}$ is the previous maximum stress level. The felicity ratio goes down as the cyclic times increasing. The felicity effect may be due to two mechanisms. One is the frictional sliding on pre-existing fractures. Another is the development of new fractures. The former usually generates sparse AE bursts due to the breakage of asperities on the surfaces of pre-existing fractures. The latter will generate continuous AE bursts. If the fracture is stable in the loading cycles, that is, the fracture does not develop unless load is increased, the Kaiser effect would show up during reloading. If the fracture becomes unstable at a certain load level, that is, the fracture continues even without further increase in load, AE resulting from the fracture of rock would recover at a level lower than the maximum load of the previous cycle when the specimen is reloaded.

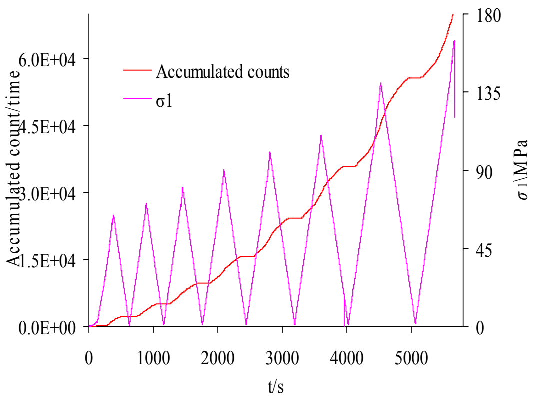

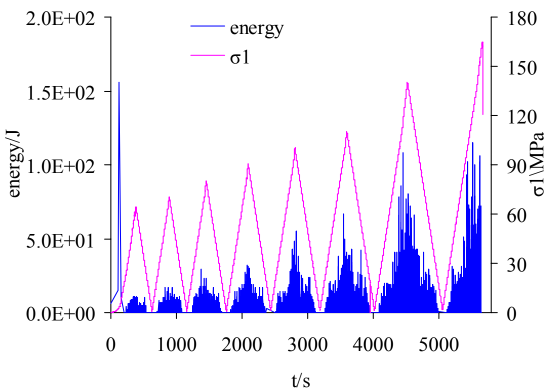

Figure 5 Relation of time with stress and AE (accumulate counts) for skarn under cyclic loading unloading

Figure 6 Relation of time with stress and AE (energy) for skarn under cyclic loading unloading

The relation of time with stress and AE energy is shown in Figure6. We can find that AE signal is still active in the unloading process which is equal to the loading in the quantity and intensity. This result is different from the reports of others, and the reason, in my opinion, is mainly the natural cracks and structure of the material in your test.

7 Conclusions and Future Work

In this paper we analyzed the results of the strength and AE characteristics of skarn under cyclic loading and unloading. Specifically, we have focused on the increase of strength and the anti-Kaiser effect. However, under the condition of this test, we can give the conclusions as follows:

(1) In the loading and unloading process, if there is no remarkably local failure in the loading process, then the unloading process might strengthen the rock sample with an increasing amplitude of 30%,

(2) If local failure occurs and nonrenewable cracks appear in the loading process, then the unloading process will facilitate the slippage of planes of cracks and accelerate the breakdown.

(3) The uniaxial compression curve of AE can generally be divided into four stages: pressure consolidation, elastic, plastic, and peak post which with different acoustic emission conditions.

(4) There is an relatively clear quiet stage of acoustic emission signals before failure.

(5) Skarn has the anti-Kaiser effect under cyclic loading and unloading, and the felicity ratio decreases with the increasing of the cycle time

(6) Acoustic emission also exists in the unloading process with equal quantity and intensity to the loading process.

Acknowledgements

Financial supports from the Hi-Tech Research and Development Program of China (863Program) under Grant No. 2006AA06Z117, National Natural Science Foundation of China under Grant No.50539090 and the Knowledge Innovation Program of the Chinese Academy of Sciences under Grant No. 0711031Q01 are gratefully acknowledged.

References

1. TengShanBangJiu. Application of AE techniques. Beijing Metallurgical Publishing House, 1996.
2. Qin, S.Q. Outline of Rock AE techniques. Chengdu: Southwestern Communications University publishing house, 1993.
3. Ge, X.R., Jiang Y. and Lu Y.D., et a1. Testing study on the fatigue deformation law of rock under cyclic loading. Chinese Journal of Rock Mechanics and Engineering, 2003, 22: 1581-1585 (in Chinese).
4. Li, S.L, Yin, X.G. and Wang, Y.J. Study on acoustic emission characters in whole process of rock damage under uniaxial compression. Chinese Journal of Rock Mechanics and Engineering, 2004, 21: 1203-1207 (in Chinese)
5. Mansurov, V.A. Acoustic emission from failing rock behaviour. Rock Engineering, 1994, 27 (3): 173-182.
6. Holcomb, D.J. and Costin, L.S. Detecting damage surfaces in brittle materials using acoustic emissions. Transactions of the ASME, 1986, 53: 536-544.
7. Mogi, K. Study of elastic cracks caused by the fracture of heterogeneous materials and its relations to earthquake phenomena. Bulletin of the Earthquake, Research institute, 1962, 40: 125-173.
8. Lochner, D.A. The role of acoustic Emission in the Study of Rock Fracture. Int. J. Rock. Mech. Min. Sci. & Geomech. Abstr. 1993, 30(7): 883-899.

RaSiM 7(2009): Controlling Seismic Hazard and
Sustainable Development of Deep Mines,
C.A. Tang(ed), Rinton Press, 441-448

STUDY ON THE METHODS OF PREDICTING BLASTING-INDUCED GROUND VIBRATION INTENSITY

ZHI-XIN YAN, PING JIANG and JIAN DUAN
School of Civil Engineering and Mechanics, Lanzhou University, Lanzhou，730000，P.R. China
LI YAN
School of Electronic and Information Engineering, Xi'an Jiaotong University, Xi'an, 710049, P.R. China

HOU-YU WANG
Air Force Engineering Design & Research Bureau, Beijing，100077，China

Blasting works with the use of explosive energy. It is an economical means for rock and soil excavation for both ground and underground engineering projects. Blast-induced ground vibration has negative consequences on nearby structures. The peak particle velocity produced by ground vibration is often used to evaluate the risk of blasting induced seismicity. There have been some empirical equations for predicting peak ground vibration velocity; however, these equations are invalid under the situation that specific conditions used for deduction can not be met. Ground vibration is complex and influenced by numerous parameters. In this paper, empirical equations and the Fourmap Method for calculating ground vibration intensity are investigated. In addition, a new method using an artificial neural network to predict the peak ground vibration velocity is proposed.

1 Introduction

Explosion is a fierce, quick power emission process. The method of using the power produced in explosions to achieve certain engineering purposes is called blasting. Powder was brought to world by the Chinese early in 600 A.D. In the 17th century, Marlin and Weigel from Germany made the first application of engineering blasting by blasting rock. In the 19th century, dynamite, which was invented by Alfred Nobel, increased the efficiency of road building, mining engineering and many other fields. It is widely accepted that applying explosive forces in road building and mining applications marks the real beginning of the Industrial Revolution.

Engineering blasting has significantly developed in many fields of national economic construction since the 20th century. Blast scale per project has reached the quantity of 120kg. It is widely accepted that engineering blasting, which is able to perform jobs that are unserviceable to humans and machines, is a specific way of construction. Shock waves, especially ground vibrations due to blast seism, are drawing increasing attention and are turning into the most common of social public pollution. In order to control the ground vibration due to blasts within the bearing limit of targets, the prediction of vibration on targets should be considered during design. Prediction results are most importantly used to target the security and blasting cost for the project. Therefore, the study methods for predicting blast seism intensity is urgent for the use of prediction, controlling and secure blast execution.

2 Empirical Formula Method

There are many factors which can affect the blast seismic intensity. Generally, these factors can be presented as function below:

$$A = f\,\text{(Explosive Source Variable, Transmission Medium Variable, Parameters of Apparatus)}$$

A is the maximum amplitude of ground vibration, f is non-specific function form.

Every item in f contains several variables which can be influenced by numerous, complicated factors. It is necessary to take the types and characteristics of explosive, explosive quantity, position and depth of embedment, aperture dimension and aperture network parameters of blast hole, method of explosion initiation, detonation interval and explosive scale in different phases of millisecond blasting, geophysical parameters of transmission medium, characteristics of explosive pores, the effects of transmission route, the capability parameters of apparatus such as testing reaction capability and sensitivity, etc into consideration. In a word, blast seism can be affected by factors including variation of distance between blast sources and measuring sites, the change of transmission route or wave mode, geological background of measuring site, partial geotechnical conditions around measuring site, the capabilities and embedding manner of vibration pick-up, etc. As influencing factors of blast seism are great in amount and have very complicated relations between each other, it is actually impossible to assert blast seismic intensity with comprehensive consideration of all the factors[1, 2, 3]. Therefore, Similarity Method, which studies the functional relation between dependent variables and residual few independent variables with all variables stored and viewing some independent variables as constants, is the general choice. The measuring data of ground vibration shows that the main factors which influence the ground vibration intensity are explosive quantity and distance to blast center. Therefore, if we approximately select explosive quantity and distance to blast center as primary variables, the amplitude of ground vibration intensity can be present as function below:

$$A = KQ^n R^{-m} \qquad (1)$$

A is maximum amplitude of ground vibration; Q is explosive quantity; R is distance to blast center; K、n、m are ground constants。

Concretely speaking, several primary forms are shown as below[1,3]:

The ground vibration peak velocity empirical formula used by Japanese:

$$V = K\frac{Q^{0.75}}{R^2} \qquad (2)$$

V is peak particle velocity produced by ground vibration (cm/s); Q is explosive quantity (kg); R is distance to explosive center (m); K is ground coefficient, K=100～900.

P. B. Attewell and his colleagues did some statistical analysis about the blast seism measuring data obtained in European Quarry and put forward a ground vibration peak velocity empirical formula in 1965:

$$V = K\left(\frac{Q}{R^2}\right)^{\alpha}$$

（3）

V is peak particle velocity produced by ground vibration (peak to peak) (cm/s); K and α are ground coefficients, K ranges from 0.013 to 0.148, with an average of 0.051； α ranges from 0.640 to 0.960, with an average of 0.840.

United States Bureau of Mines did some statistical analysis about the blast seism measuring data obtained in 20 quarries and building sites, these data are obtained with distance to explosive center ranging from 44.2 m to 966 m, explosive quantity ranging from 3.6 kg to 2095 kg. The measuring targets are limestone, diorite and dolomite. J. R. Devine put forward a ground vibration peak velocity empirical formula in 1966:

$$V = K\left[\frac{R}{Q^{1/2}}\right]^{-\alpha}$$

（4）

V is peak particle velocity produced by ground vibration (cm/s); R is distance to explosive center (ft); Q is explosive quantity (b); K and α are ground coefficients; $\frac{R}{Q^{1/2}}$ is converted distance (ft/lb$^{1/2}$); K ranges from 0.657 to 4.04, with an average of 1.85; α ranges from 1.083 to 2.346, with an average of 1.536.

Садовский, M. A. from Soviet Russia put forward a ground vibration peak velocity empirical formula which is shown as below:

$$V = K\left(\frac{Q^{\beta}}{R}\right)^{\alpha}$$

(5)

V is peak particle velocity produced by ground vibration (cm/s); Q is explosive quantity (b); R is distance to explosive center (m); K and α are ground coefficients, for rock: K ranges from 30 to 70, with an average of 50; for soil: K ranges from 150 to 250, with an average of 200; α ranges from 1 to 2.

With the analysis of blast seism test made in Zhengjiang, Chongqing, Anqing, Shaoguan, etc[4,5], the author finds that Садовский, M. A. Empirical Formula does well in presenting the relation between vibration velocity V, distance to explosive center R, explosive quantity Q under the situation different from urban blasting one, that is, a situation with relatively large explosive quantity and distant vibrated targets. After making variance analysis and regression analysis with $\beta = 1/3$ and $\beta = 1/3$, the researchers found that when $\beta = 1/3$, F is relatively large, surplus standard deviation is comparatively small. Therefore, setting $\beta = 1/3$ is appropriate in general situations, except for some specific situations which setting $\beta = 1/2$ is better. The ranges of K, α and f are:

K=90～160

α=1.45～1.8

f=15～100 Hz

Many velocity wave diagrams and frequency spectra of ground particle vibration show that, being different from the conclusions made in reference [6], there is no direct proportional relation between velocity and frequency.

When doing Throw Blasting

$$V = \frac{K}{\sqrt[3]{f(n)}}\left(\frac{Q^{1/3}}{R}\right)^{\alpha} \qquad (6)$$

$f(n)$ is blasting impact exponential function which can be got with considering the suggestions of Boleskov.

$$f(n) = 0.4 + 0.6n^3$$

The formulas upon are generally obtained on the basis of using ball charging blasting method.

On the basis of empirical formulas put forward by Садовский, M. A, combining the characteristics of seism, Feng Shuyu, Leiyi and other native scholars brought in correction coefficient K' ,which is adapted to demolition blasting, as amending coefficient to improve the application of empirical formulas put forward by Садовский, M. A. The amended formula for calculating ground vibration velocity in demolition blasting is shown as below[7]:

$$V = KK'\left(\frac{Q^{1/3}}{R}\right)^{\alpha} \tag{7}$$

K ranges from 0.25 to 1.0, if measuring site is close to blast source and spatial surface of blasted mass is lack, take the larger one; otherwise, take the minor one.

From the formulas introduced upon, we can see that although the primary variables selected are the same with each other, the measuring data are obtained under different ground conditions with different apparatus; the correlative regression coefficients calculated from these data are quite different from each other. As a result, it is rather difficult to apply these formulas in actual situations. In China, formula (5) and (6) are general choices for predicting peak velocity in blasting seism.

3 Fourmap Method

In 1983, D. A. Anderson put forward Fourmap Method[8]. which is based on measuring the vibration waveform of single explosive charge and using linear superposition model as simulation model. A figure with frequency as abscissa, delay time between pores or segments as ordinate can be drawn. On this figure, the amplitude of superposition corresponding to frequency is shown in depth of points; the appropriate delay time can be got by analyzing the depth of figure. The degree of depth is called the cancellation of wave or phase interference. Although the reliability of this method is greatly influenced by the accuracy of detonator delay time and the repeatability of single hole blasting waveform, it is still advantageous under certain constant geological conditions. To improve this method, it is necessary to bring in model analysis. The fact that transfer function remains constant when the geological structure of blast point and measuring point is constant makes it possible to predict the problem of superposition in blasting seism accurately, of course, the accuracy of detonator delay time can't be neglected.

4 Neural Network Predicting Method

Although much effort has been made on finding the way to explore the attenuation law of blast seism, nowadays widely used empirical formula methods (Садовский Empirical Formula Method, etc) are rather deficient, sometimes even completely invalid in predicting vibration velocity because of the complexity of blast mechanism and geological conditions of blast vibration transmission. Especially under the situation that blast center is very close to measuring point, for example, urban controlled blasting conditions, of which distance from protected targets to blast center is only 2-3m, traditional empirical formula methods are completely useless.

It is imperative to explore a brand new method of predicting peak value in blast seism.

Artificial Neural Network operates by simulating the structure and function of neural network in creatures. It has capabilities such as large-scale parallel calculation, distributed storage and processing, self-organization, self-adaption and self-study. It is suitable for analyzing problems which the consideration of numerous factors and conditions is needed; it is especially efficient in processing inaccurate or fuzzy information[9,10]. In recent years, Artificial Neural Network has been applied in many fields; it may be effective in associating the intricate relation between blasting effects and correlative variables.

To bring Artificial Neural Network BP Model into the prediction of peak velocity in blast seism, input parameters, which are primary factors that influence blast seism, of artificial neural network models should be determined at first. Blast seism is a rather complicated kinetic process which can be influenced by rock type, degree of weathering, types and characteristics of explosive, transmission route of blast vibration, aperture dimension and aperture network parameters of blast hole, etc. A specific blast project should be investigated from the point of blasting power emission. The artificial neural network with factors, such as distance between maximum explosive quantity point and measuring point, taken into consideration can be accurately achieved by applying a 3-layer artificial neural network model which has m nerve cells on 1st layer, 2m+1 nerve cells on hidden layer, n nerve cells on output layer[11].

The blast seism due to rapid development of urban communication and shallow underground excavation engineering projects has increasing harmful effects upon ground structure and environment, especially buildings. The minor ones make people uncomfortable and cause other physiological responses, the worse ones even make roads crack. Next the prediction and analysis of ground vibration in blast seism will be made by combining an city underground excavation engineering project.

This underground engineering is 1000 meters long, with a designed span of 12m. Surroundings rock is sandstone, its solidity coefficient ranges from 3 to 6. The joint and fracture of the surrounding rock in this underground engineering is scarcity and its integrity is good. The overburden layer on tunnel roof has a thickness ranges from 14 to 15m and a miscellaneous fill layer of which thickness ranges from 1 to 2m. The engineering is excavated on the basis of an original pilot tunnel, that is, pilot tunnel is existent at first, tunnel roof is excavated later, after that 2 ancipitous surroundings rock is extended. Lastly, the designed cross section is formed[12].

Since the blasting seismic wave transmission in rock is a rather complex kinetic process, correlative factors such as the features of explosives, explosive quantity, explosive charging structure, denotation mode, blocking condition, rock mass structure, geologic structure, rock mass structure, hydrogeology and geomorphologic shape, etc. can affect blasting earthquake. Moreover, it is hard to ascertain the kinetic characteristics of rock medium accurately, therefore, the transmission of blasting vibration is very complex. Blasting earthquake wave is random and transient. In this single tunnel excavation engineering, except for explosive quantity Q and distance between explosive center and measured point R, factors such as rock characteristics, rock mass structure, hydrogeology, geomorphologic shape, charging varieties, charging structure, denotation mode, blocking condition, etc. generally remain constant. As a result, an Artificial Neural Network Model with 2 input units is applied in research.

In this tunnel excavation engineering, except for explosive quantity and the distance to the explosive center, other factors such as rock characteristics, rock mass structure, hydrogeology, geomorphologic shape, charging varieties, charging structure, denotation mode, blocking condition, etc. generally remain constant. As a result, on the basis of blasting vibration measuring, according to Садовский, M. A Empirical Formula, the vertical velocity V_{em} and horizontal radial velocity V_{rm} and horizontal tangential velocity $V_{\tau m}$ can be get by the least squares the linear regression fitting. They are shown as below:

$$V_{em} = 105.6\left(\frac{\sqrt[3]{Q}}{R}\right)^{1.7} \tag{8}$$

$$V_{rm} = 83.8\left(\frac{\sqrt[3]{Q}}{R}\right)^{1.74} \tag{9}$$

$$V_{\tau p} = 30.74\left(\frac{\sqrt[3]{Q}}{R}\right)^{1.56} \tag{10}$$

You can know that the vertical velocity V_{em} is the most, then horizontal radial velocity V_{rm} is the second, and horizontal tangential velocity $V_{\tau m}$ is the smallest among them.

Take 30 samples of 40 existing data in the project as exercising samples. Explosive quantity, distance to explosive center and corresponding vertical velocity V_{em}, horizontal radial velocity V_{rm}, horizontal tangential velocity $V_{\tau m}$ have been gotten in measuring data. Therefore, a 3-layer artificial neural network model which, concretely speaking, consists of input layer which contains 2 input units and output layer which contains 3 output units is chosen for learning and prediction. After repeating debugging, the hidden layer which consists of 5 units is relatively more precise. As a result, 2-5-3 network structure is selected as the network structure. For making comparison to evaluate the accuracy of Artificial Neural Network, the blast conditions (explosive quantity Q, distance to explosive center R) of latter 20 samples are taken as inputs . By ranking the ratio of explosive quantity from larger ones to smaller ones, with the predicted results obtained, the curves of vertical peak vibration velocity V_{em}, radial peak velocity V_{rm}, tangential peak velocity $V_{\tau m}$ and corresponding predicted value V_{ep}、V_{rp} and $V_{\tau p}$ are calculated and shown in figure 2, figure 3 and figure 4.

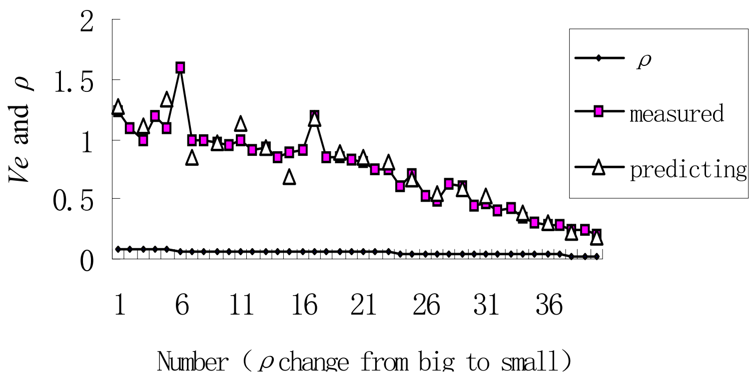

Figure.1. Measured vertical velocity V_{em} and predicting results V_{ep}

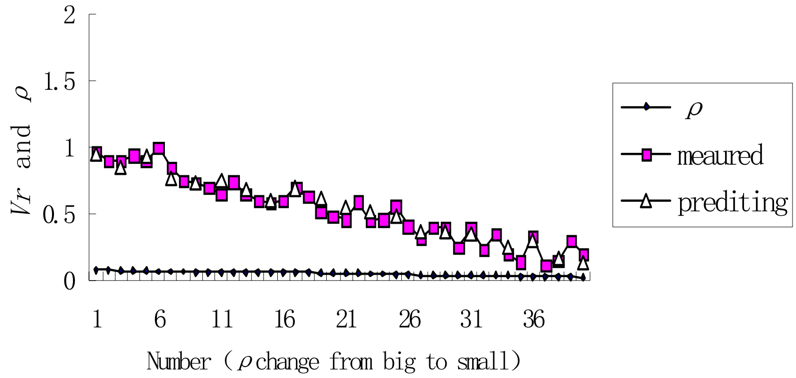

Figure. 2. Measured radial velocity V_{rm} and predicting results V_{rp}

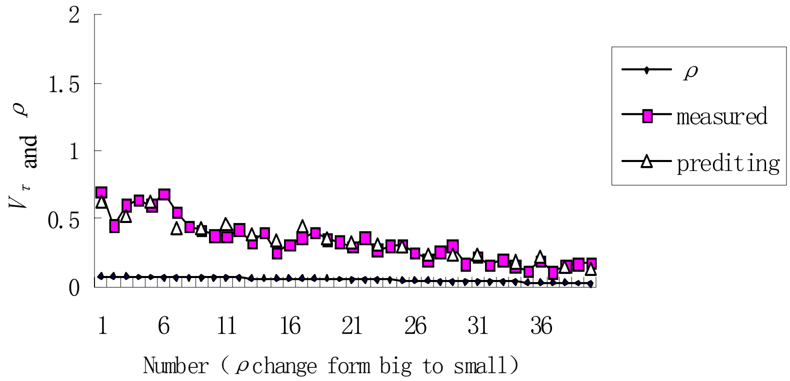

Figure. 3. Measured tangential velocity $V_{\tau m}$ and predicting results $V_{\tau p}$

5 Thinking and Conclusions

With the expansion of the economy, engineering blasting is becoming increasingly used in blasting projects; whereas, it used to be an unusual means of construction. The impact of related blast seism is becoming more and more conspicuous; reliable prediction of blast seism intensity is an impending need for decreasing blast seismic damage. However, traditional empirical formula methods are deficient forms of prediction, and are sometimes completely invalid. Therefore, the method of predicting peak values in blast seism must be improved. Latest accomplishments include the Empirical Formula Method, Fourmap Method, and especially the Artificial Neural Network.

On the basis of exploring the Empirical Formula Method and Fourmap method, with existing problems taken into consideration, the artificial neural network model was established. BP Artificial Neural Network is programmed in C programming language. The prediction of peak vibration velocity is achieved through study of the record of blast vertical velocity V_e, horizontal radial velocity V_r and horizontal tangential velocity V_τ in underground excavation engineering projects. The curve indicating a relationship between measured data, prediction data, and the explosive quantity ratio ρ is drawn. Conclusions are drawn as below:

（1） Measuring data, as the basis for the empirical formula, are obtained with different apparatuses. As regression results differs under different ground geological conditions in situations with relatively larger explosive quantity, the distance to blast center and low accuracy requirements, the geological conditions of blasting sites should be kept similar with each other. Obviously, the Empirical Formula Method is not able to satisfy the need of burgeoning engineering blasting today;

（2） Artificial Neural Network can be applied in the prediction of peak values in blast seism;

（3） Superior prediction of peak values in blast seism can be obtained by measuring data as exploratory samples;

（4） Predicted values of Artificial Neural Network and measured values present an exponential relationship along with the variation of explosive quantity ratio ρ;

（5） Linear Superposition Model of Fourmap Method has a certain value.

References

1. Zheng, F., Duan, W.D., Zhong, D.W. and Sun, B.Y. The Exploration about Present Situation of Blasting Seism Study and Problems. Blasting, 2006, 23(1): 23-26.
2. Singh, T.N. Artificial Neural Network Approach for Prediction and Control of Ground Vibration in Mines. Mining Technology, 2004, 113: 251-256.
3. Zhang, X.L. and Wang, S.H. Impact of Blasting Seism. Beijing: Earthquake Publishing House, 1981.
4. Yan, Z.X., Wu, D.L. and Xu, M. The Study of Blasting Seismic Effect and Security. Geomechanics, 2002, 23(2): 201-203.
5. Yan, Z.X., Jiang, P., Chen, G.Y. and Wang, H.Y. Study on Blasting Vibration Safety at Weigang Iron Mine. China: 2006ISSST, 2006, 10: 1188-1190.
6. Tang, C.H., Yu, Y.L. and Wang, J.H. Preliminary Exploration about Safety Criterion in Blasting Seism. Non-ferrous Metals, 2001, 53(1): 1-4.
7. Feng, S.Y., Lei, Y. and Gu, Y.C. Urban Controlled Blasting. Beijing: China Railway Publishing House, 1987.
8. Xu, Q.J., Mao, Z.Y. and Zhang, Q.M. Analysis of Prediction of Deep Hole Millisecond Blasting Seism. Explosion and Shock Waves 1998. 18(2). 182-186.
9. Zurada, J. M. Introduction to Artificial Neural System. West Publishing Company, 1992.
10. Smith, M. Neural Networks for Statistical Modeling. NY: Van Nostrand Reinhold, 1993.
11. Yan, Z.X. Study on Structure Demolition and Blasting Vibration Effect. Chongqing: Chongqing University Dissertation, 2002.
12. Li, Y.M. and Ni, Z.F. The Characteristics on Surface Vibration of Blasting in underground Engineering. Chinese Journal of Rock Mechanics and Engineering, 1997, 16(3): 274-278.

RaSiM 7(2009): Controlling Seismic Hazard and
Sustainable Development of Deep Mines,
C.A. Tang(ed), Rinton Press, 449-456

UNDERSTANDING OF THE OCCURRENCE OF ROCKBURSTS IN TUNNELS BASED ON 3D STRESS ANALYSIS

DI-YUAN LI, XI-BING LI and ZI-LONG ZHOU

School of Resources and Safety Engineering, Central South University, Changsha， 410083, P.R. China

Rockburst usually occurs in tunnels at depth. Some critical factors control the occurrence of rockburst, such as the in-situ stress, the strength of rock mass, the release rate of strain energy and the existing faults. So far, the analysis of rockburst occurrence has mainly concentrated on a two-dimensional stress state in tunnels. In reality, the rockburst frequency has been reported not only related to the distances to the tunnel face but also to the time interval of blasting rounds. In this paper, a 3D stress analysis has been carried out in a deeply located circular tunnel with both the Mohr-Coulomb criterion and the Hoek-Brown criterion. The variation of principal stress versus the advance direction of the tunnel has been obtained. The maximum principal stress concentration occurs at about 20 m away from the heading face. It is predicted that strong rockburst may take place in the tunnel by the criteria of maximum tangential stress. After that, a case study of 3D stress analysis at the Qinling road tunnel in China has been modelled by FLAC3D. The maximum frequency of rockburst occurs neither near the tunnel heading face nor just after excavation by blasting. The delaying effect of maximum principal stress in numerical modelling is similar to the delayed effect of rockburst occurrence in the tunnel. From the 3D numerical stress analysis, the occurrence of rockburst can be better understood.

1 Introduction

During several decades rockbursting has been a major concern in both deep mines [1-5] and highly in-situ stressed tunnels [6-9]. An extensive library of literature on the subject has accumulated and considerable research effort has been devoted to the understanding and explanation of the mechanism of the phenomenon. According to Ortlepp's definition[10], rockburst is a seismic event which causes violent and significant damage to the tunnel or the excavations of the mine. It involves rapid convergences and oscillation of the excavation walls, followed by slabbing and failure of the rock immediately adjacent to the excavation. This violent release of energy has been observed on a scale ranging from the explosion of small rock fragments to the collapse of the excavation.

Some critical factors control the occurrence of rockburst, such as the in-situ stress, the strength of rock mass, the release rate of strain energy and the existing shear faults. Durrheim[11] investigated 21 rockburst cases and pointed out that the source mechanism is often controlled by the mine layout, and regional geological structures such as faults and dykes. While local rock conditions and support systems strongly influence the location and severity of damage. Two kinds of rockburst, strain rockburst and fault-induced rockburst, are recognized now. So far, the numerical analysis of rockburst occurrence has been mainly in a two-dimensional stress state for tunnels or mines [12-14]. In reality, rockbursts may take place even in places far from the excavation face. The rockburst frequency has been reported not only related to the time interval of blasting, but also to the distances to the tunnel face[15].

In this paper, a 3D stress analysis was done in a deeply located circular tunnel with both the Mohr-Coulomb criterion and the Hoek-Brown criterion. The stress distribution and the failure zone of the tunnel, versus the advance direction, have been obtained. The results of the stresses surrounding a tunnel face are compared with the analytic solutions. After that, a case study of stress analysis at Zhongnanshan highway tunnel in China has been carried out. The failure zones and the stress difference have been calculated with FISH language in FLAC3D. The results of the numerical simulation have been compared with the site observation. From the 3D numerical stress analysis, the occurrence of rockburst can be better understood.

2. Material Model

2.1. Mohr-Coulomb model

The Mohr-Coulomb model is the conventional model used to describe shear failure in soils and rocks. The criterion is expressed by:

$$\tau' = c' + \sigma_n' \tan\phi' \tag{1}$$

where c' is the cohesive strength, and ϕ' is the friction angle. σ_n' and τ' are the normal stress and shear stress respectively. The Mohr-Coulomb criterion for triaxial data can also be given by:

$$\sigma_1' = \frac{2c'\cos\phi'}{1-\sin\phi'} + \frac{1+\sin\phi'}{1-\sin\phi'}\sigma_3' \tag{2}$$

where σ_1' and σ_3' are the major and minor effective principle stresses at failure, respectively.

2.2. Hoek-Brown model.

The Hoek-Brown failure criterion characterizes the stress conditions that lead to failure in intact rock and rock masses. The failure surface is nonlinear and is based on the relation between the major and minor principal stresses. The model incorporates a plasticity flow rule that varies as a function of the confining stress level. The "generalized" Hoek-Brown criterion is:

$$\sigma_1' = \sigma_3' + \sigma_{ci}\left\{m_b \frac{\sigma_3'}{\sigma_{ci}} + s\right\}^a \tag{3}$$

The parameters are calculated by the following formulas:

$s = \exp\left(\frac{GSI-100}{9-3D}\right)$, $m_b = m_i \exp\left(\frac{GSI-100}{28-14D}\right)$, $a = 0.5 + \frac{1}{6}\left(e^{-GSI/15} - e^{-20/3}\right)$, $\sigma_c = \sigma_{ci}s^a$ and $\sigma_t = -\frac{s\sigma_{ci}}{m_b}$

where:

- σ_c , σ_t are the compressive and tensile strength of the rock mass, respectively; σ_{ci} is the uniaxial compressive strength (UCS) of the intact rock material
- *GSI* is Geological Strength Index
- m_i is material constant
- *GSI,* m_i value can be obtained from the guideline published by Hoek.
- m_b is reduced value of material constant
- *D* is a factor depending on the degree of disturbance to which the rock mass has been subjected by blast damage and stress relaxation. D varies from 0 for undisturbed in situ rock mass (excavated by TBM) to 1 for disturbed rock mass.

3. 3D Numerical Stress Analysis

3.1. Calculation Model and Parameters

A deeply located circular tunnel with an opening diameter of 10 m is shown in Figure 1. The surrounding rock mass are supposed to be hard rock. After reviewing some literatures about hard rock study, the physical and mechanical parameters from the testing data on Lac du Bonnet grantie by Hajiabdolmajid [16] are adopted in this paper. The parameters both M-C material and H-B material are given in Table 1. The in-situ stress is supposed to be very high with a vertical compression stress *P* and two horizontal stress K*P* in both x-direction and y-direction. The original point of the coordinate system is located at the centre of the tunnel and the model size is 50m *50 m* 50m in x, y, z direction.

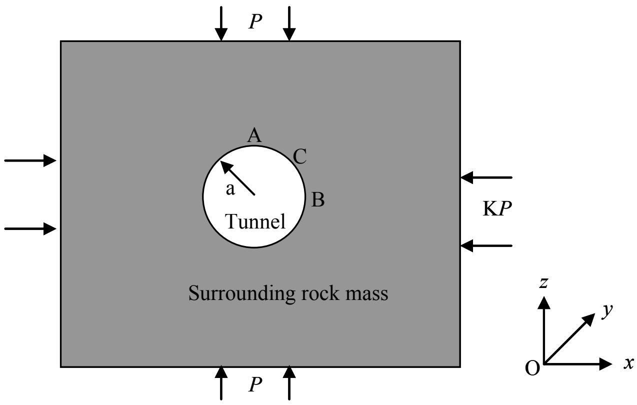

Figure 1. Problem geometry, coordinate system and the in-situ stress state around a deep circular tunnel.

Table 1. Mechanical parameters of Lac du Bonnet granite in the process of numerical modelling[16]

Mohr-Coulomb material				Hoek-Brown material							
E,GPa	ν	*c*,MPa	ϕ	*GSI*	σ_{ci} ,MPa	σ_{ti} ,MPa	m_i	m_b	*s*	σ_{cm} ,MPa	σ_{tm} ,MPa
60	0.2	25	48	90	224	10	28.11	19.67	0.329	128	-3.7

3.2. Stress Distribution around Tunnel

In the two dimension elastic stress analysis, the analytic solutions for the stress distribution around a circular opening are as follows:

$$\left.\begin{aligned}
\sigma_{rr} &= \frac{P}{2}[(1+K)(1-\frac{a^2}{r^2})-(1-K)(1-4\frac{a^2}{r^2}+3\frac{a^4}{r^4})\cos 2\theta] \\
\sigma_{\theta\theta} &= \frac{P}{2}[(1+K)(1-\frac{a^2}{r^2})+(1-K)(1+3\frac{a^4}{r^4})\cos 2\theta] \\
\sigma_{r\theta} &= \frac{P}{2}[(1-K)(1+2\frac{a^2}{r^2}-3\frac{a^4}{r^4})\sin 2\theta]
\end{aligned}\right\} \tag{4}$$

where, *a* is the radius of the circular opening; *P* is the vertical stress, *K* is the horizontal stress coefficient and *θ* is the angle in polar coordinate system.

As pointed out that there are two kinds of rockburst phenomena in tunneling engineering, strain burst and fault-slip burst. In this paper, we mainly discuss the strain burst problem. Therefore, faults and discontinuities were not considered in the numerical modelling. The in-situ stresses around the tunnel were supposed to be: *P*=30 MPa and K=2.

The tunnel was excavated 5m for every blasting round and 8 blasting rounds were modelled in the numerical simulation. Since the analysis was concentrated on the stress-induced rockburst, rock support was not involved. Zone stresses at three typical point around the tunnel, A (0, 2.5, 5.1), B (5.1, 2.5, 0) and C (3.6, 2.5, 3.6) were monitored (shown in Fig. 1).

The principal stresses at these points were monitored with the advancing direction of the tunnel face, see in Figure 2. In this figure, it is seen that the major principal stress of zone A reaches the maximum value when the distance to the tunnel heading face is about 20 m. A new stress balance is achieved after three or four excavation rounds in the surrounding rock masses.

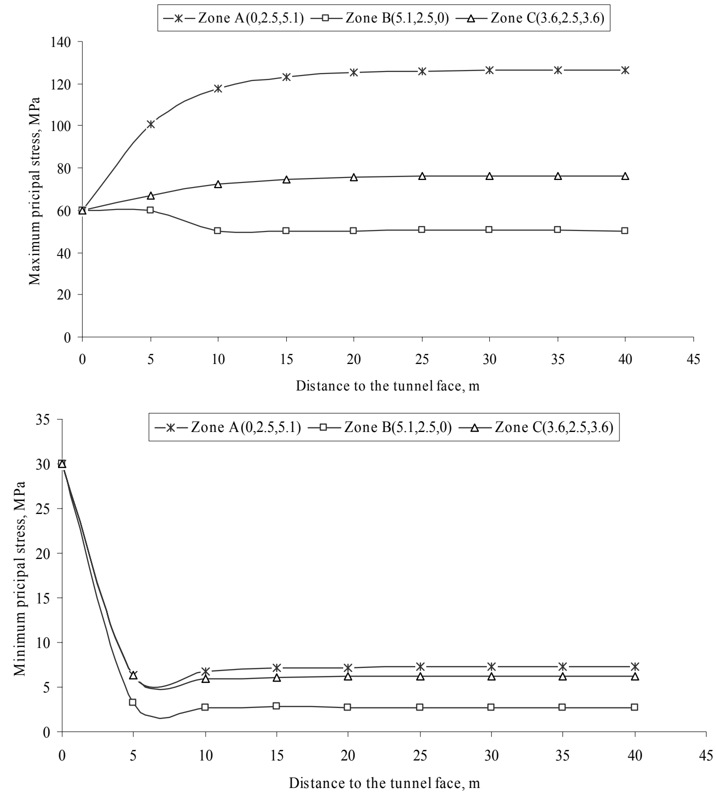

Figure 2. The variation of the principal stresses (σ_1 and σ_3) at zone A, B and C with the advancing of tunnel face (by M-C material).

The distribution of principal stresses in the x-z plane is shown in Figure 3. This plane is located at y=2m when the tunnel is advanced to the location of y=40m. It can be seen that the major principal stresses are concentrated at the tunnel vault and bottom. The stress distribution is almost the same either for the Mohr-Coulomb material or for the Hoek-Brown material.

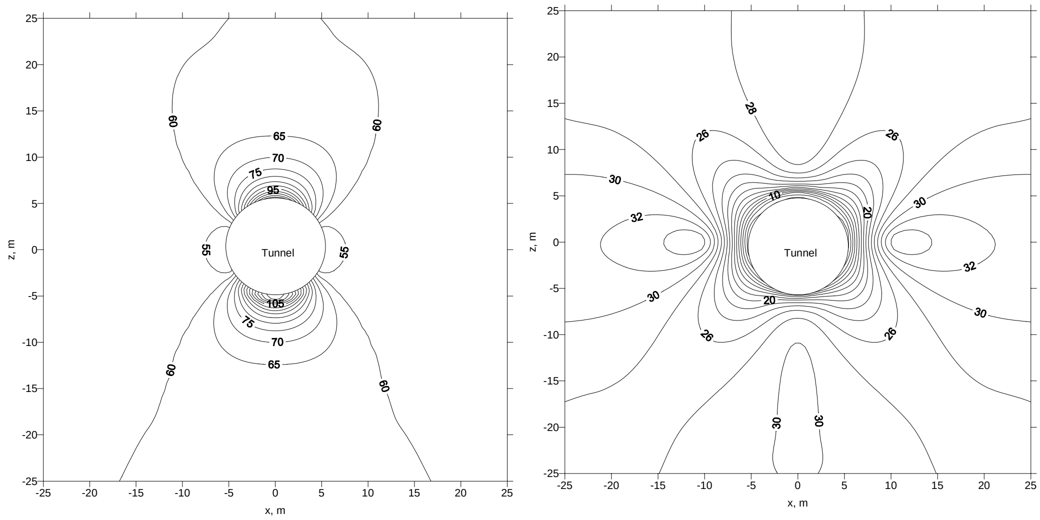

a. Major principal stress (σ_1, unit: MPa) b. Minor principal stress (σ_3, unit: MPa)

Figure 3. The distribution of the principal stresses around the tunnel after excavation in the X-Z plane at y =2 m location

The distribution of the major principal stress along the tunnel excavation direction is shown in Figure 4. This plane is located at x=0m when the tunnel was advanced to the location of y=40m. It can be seen that the major principal stress contours are curved near the tunnel face. It shows that the maximum stress concentration occur some distance away from the tunnel heading face, which is called delaying effect of maximum principal stress in this paper.

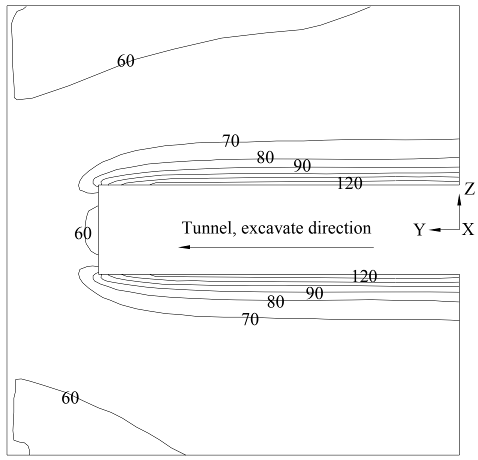

Figure 4. The distribution of major principal stress along the excavate direction around the tunnel (unit: MPa).

3.3. Criterion to Predict Rockburst

Some stress and strain criterions are used to predict the occurrence of rockburst, for example, the criterion of elastic strain energy, the criterion of rock brittleness and the criterion of tangential stress. The last one can be used here since 3D stress analysis was adopted in this paper. This criterion considers both the state of in-situ stress in the rock mass as well as the mechanical properties of rock. The criterion of tangential stress is expressed by:

$$T_s = \frac{\sigma_\theta}{\sigma_c} \tag{5}$$

where, σ_θ is the tangential stress in rock mass surrounding the opening and σ_c is the uniaxial compressive strength of rock. The preliminary study shows that[17]:

1. T_s<0.3, then no rockburst;
2. T_s=0.3-0.5, then weak rockburst;
3. T_s=0.5-0.7, then strong rockburst; and
4. T_s>0.7, then violent rockburst.

Throughout the 3D numerical analysis, the maximum tangential stress surrounding the tunnel has been obtained about 120 MPa and shown in Figure 3 and 4. Even though the uniaxial compressive strength of the Lac du Bonnet granite is as high as 224 MPa, the T_s value near the tunnel vault and the base is ranging from 0.5 to 0.6. So it indicates that strong rockburst may occur. The failure mode can perform as slabbing or spalling around the stress concentration place.

4. Case Study in Qinling tunnel

4.1. Reported Rockbursts in Qinling tunnel

Located in the Shaanxi province, China, the Qinling Zhongnanshan tunnel consists of four tunnels: two railway tunnels and two road tunnels. With a length of 18.02 km the road tunnel is currently the longest double tube road tunnel in the world. The gross cross section of the road tunnels is 12.8 × 10.5 m, accommodating three driving lanes. Excavation of the road tunnels was completed in 2004. High in-situ stresses led to the occurrence of rockburst when the tunnel was excavated at depth over 750m. According to the site investigation [15], the reported occurrence of rockburst had relationship not only to the distances to the tunnel face but also to the time interval of blasting round. The frequency of rockbursts and the exponential fitting curve are shown in figure 5.

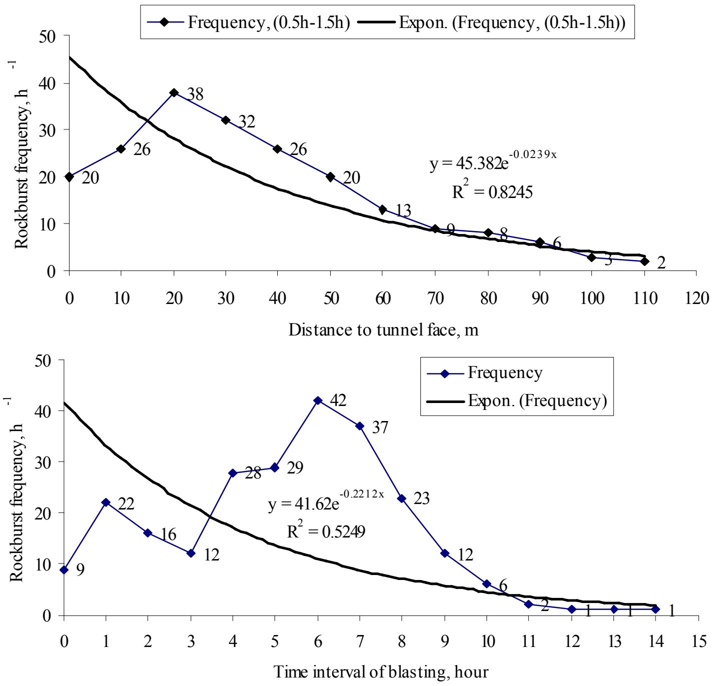

Figure 5. The reported occurrence of rockburst and the exponential fitting curve in Qinling tunnel [15].

From figure 5, it can be clearly seen that the maximum frequency of rockbursts did occur neither near the tunnel heading face nor just after excavation by blasting. The maximum number of rockbursts occurred at about 20m away from the tunnel face and it took place about 6 hours later after blasting. The delaying effect of rockbursts exited in tunnel excavation like the delaying effect of major principal stress in the numerical modelling.

4.2. 3D Stress Distribution and Potential Rockburst Area

The in-situ stress and the mechanical property of the surrounding rock mass in the numerical modelling are adopted from studies by others[15, 18], see details in table 2.

Table 2. In-situ stresses and mechanical properties of the rock mass in the 3D stress analysis of Qinling tunnel

In-situ stress, MPa			Mohr-Coulomb material					
σ_{xx}	σ_{yy}	σ_{zz}	E, GPa	ν	c, MPa	Φ, friction angle °	φ, dilation angle, °	σ_t ,MPa
35.0	15.0	28.0	29.0	0.215	1.90	57	10	1.13

The size of the model is 32m*50m*56.6m in x, y and z direction, respectively. There are 56000 zones and 62883 grid points in this model. Since it is a large 3D model, a half symmetric model is adopted in the numerical simulation. The excavation is divided by two stages, firstly the upper radial part (5m every round) and then the lower brick part (5m every round). In this calculation, 5 excavation rounds, which mean the total advancing distance of 25m, are taken into consideration.

Based on the Mohr-Coulomb theory, the high differential stress between the major and the minor principal stress can lead to shear failure of the rock mass. In this study, the differential stress is obtained by FISH language in FLAC3D and the contour diagram is shown in figure 6. The failure state of surrounding rock is also shown in figure 6. It can be seen that shear failure occurred at the place with high differential stress. The contour line of differential stress also becomes a little curved near the tunnel heading face along the advancing direction. This phenomenon indicates that the maximum frequency of rockburst may occur some distance away from the heading face. In this tunnel, rockburst may take place at the tunnel vault and also the bottom because of high differential stresses there.

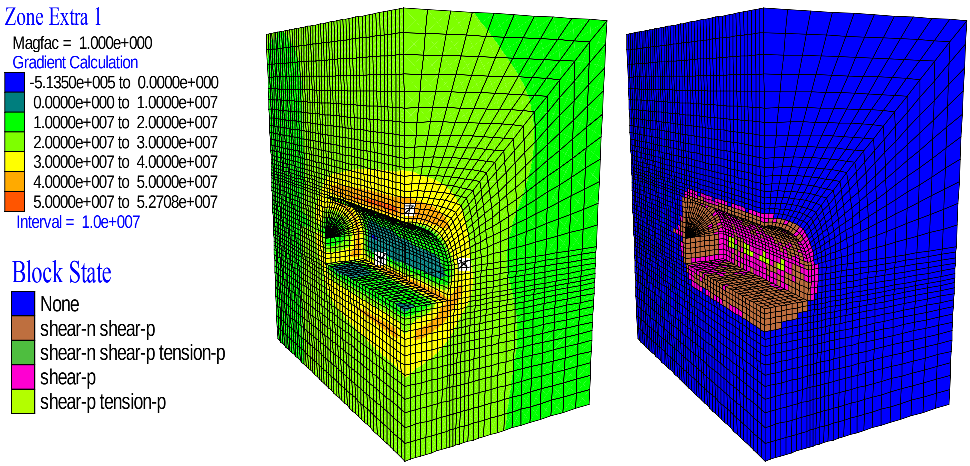

(a). Zone differential stress: σ_1- σ_3 (b). Zone block state: plastic area

Figure 6. Contour diagram of the differential stress and the failure state after 25 m tunnel excavation in the 3D numerical analysis.

According to the site description and statistics of rockbursts in reference[15], there were spalling rocks in the sideway of the tunnel and some rock falling down from the vault. Loud noise accompanied with the stress release after excavating. The depth of spalling or slabbing failure zone usually ranged from 0.6m to 2.1m. The phenomena can be observed by the plastic volume surrounding the tunnel after excavation.

5. Conclusions

(1) A deep circular tunnel was modelled with both the Mohr-Coulomb and Hoek-Brown criterion. The stress distribution was almost the same by these two criterions. The major principal stress contour lines are curved near the tunnel face. The maximum principal stress concentration occurred at about 20m away from the tunnel heading face. After 3D stress analysis, it is predicted that potential strong rockburst may take place surrounding the tunnel with the criterion of maximum tangential stress.

(2) Occurrence of rockburst has a relationship not only to the distances to the tunnel face, but also to the time interval of the blasting round. The maximum frequency of rockburst did not occur near the tunnel heading face nor just after excavation by blasting. The delaying effect of rockburst occurred in the tunnel is similar to the delaying effect of maximum principal stress in numerical modelling. The results of numerical analysis about rockbursting place and spalling volume in the Qinling tunnel were coincident with the site investigation.

Acknowledgements

The research was supported by the Natural Science Foundation of China under grants Nos. 10872218, 50674107. The first author wishes to acknowledge the China Scholarship Council to give the financial support to study in Norway as a jointed PhD student.

References

1. Dowding, C.H. and Andersson, C.A. Potential for rock bursting and slabbing in deep caverns. Engineering Geology, 1986, 22(3): 265-279.
2. Fujii, Y., Ishijima, Y. and Deguchi, G. Prediction of coal face rockbursts and microseismicity in deep longwall coal mining. International Journal of Rock Mechanics and Mining Sciences, 1997, 34(1): 85-96.
3. Cai, M., Wang, J. and Wang, S. Prediction of rock burst with deep mining excavation in linglong gold mine. Journal of University of Science and Technology Beijing: Mineral Metallurgy Materials (Eng Ed), 2001, 8(4): 241-243.
4. Tang, L., Pan, C. and Xie. X. Study on rockburst control in deep-seated hard ore deposit. Yanshilixue Yu Gongcheng Xuebao/Chinese Journal of Rock Mechanics and Engineering, 2003, 22(7): 1067-1071.
5. Li, T., Cai, M.F. and Cai, M. A review of mining-induced seismicity in China. International Journal of Rock Mechanics and Mining Sciences, 2007, 44(8): 1149-1171.
6. Broch, E. and Sørheim, S., Experiences from the Planning, Construction and Supporting of a Road Tunnel Subjected to Heavy Rockbursting. Rock Mech. Rock Engng., 1984, 17: 15-35.
7. Ortlepp, W.D. and Stacey T.R. Rockburst mechanisms in tunnels and shafts. Tunnelling & Underground Space Technology, 1994, 9(1): 59-65.
8. Lu, Q., et al. Comprehensive study on prediction of rockburst in deep and over-length highway tunnel. Yanshilixue Yu Gongcheng Xuebao/Chinese Journal of Rock Mechanics and Engineering, 2005, 24(16): 2982-2988.
9. Zuo, Y.J., Li, X.B. and Zhou, Z.L. Determination of ejection velocity of rock fragments during rock burst in consideration of damage. Journal of Central South University of Technology (English Edition), 2005, 12(5): 618-622.
10. Ortlepp, W.D. Rock fracture and rockbursts: an illustrative study, Johannesburg: South African Institute of Mining and Metallurgy, 1997.
11. Durrheim, R.J., et al. Factors influencing the severity of rockburst damage in South African gold mines. Journal of The South African Institute of Mining and Metallurgy, 1998, 98(2): 53-57.
12. Muller, W. Numerical simulation of rock bursts. Mining Science & Technology, 1991, 12(1): 27-42.
13. Tang, C.A., et al. A new approach to numerical method of modelling geological processes and rock engineering problems - continuum to discontinuum and linearity to nonlinearity. Engineering Geology, 1998, 49(3): 207-214.
14. Cai, M., Kaiser, P.K. and Morioka, H., et al. FLAC/PFC coupled numerical simulation of AE in large-scale underground excavations. International Journal of Rock Mechanics and Mining Sciences, 2007, 44(4): 550-564.
15. Guo, Z. Rock bursts and countermeasures in Zhongnanshan highway tunnel. Modern Tunnelling Technology, 2003, 40(6): 58-62.
16. Hajiabdolmajid, V., Kaiser, P.K. and Martin, C.D., Modelling brittle failure of rock. International Journal of Rock Mechanics and Mining Sciences, 2002, 39(6): 731-741.
17. Wang, J.A. and Park H.D. Comprehensive prediction of rockburst based on analysis of strain energy in rocks. Tunnelling and Underground Space Technology, 2001, 16(1): 49-57.
18. Lu, M. and Dahle, H. Design of rock caverns in high in-situ stress rock mass, in Rock Mechanics in Underground Construction: ISRM International Symposium 2006 : 4th Asian Rock Mechanics Symposium, Leung C. F. and Zhou Y.X., Editor, World Scientific: Singapore, 2006.

*RaSiM 7(2009): Controlling Seismic Hazard and
Sustainable Development of Deep Mines,
C.A. Tang(ed), Rinton Press, 457-462*

ROCKBURST PREDICTION IN PUBUGOU HYDROPOWER STATION

RU ZHANG, HE-PING XIE, JIAN-HUI DENG, WEN-PING FEI AND MING-ZHONG GAO

State Key Laboratory of Hydraulics and Mountain River Engineering,

College of Hydraulic and Hydroelectric Engineering, Sichuan University

In southwest China, many Hydropower Stations in construction are located in high geostress regions. Rockburst has taken place in the underground powerhouse of the Ertan, Pubugou, and Jinping Hydropower Stations. Research on rockburst prediction in the Pubugou Hydropower Station has been studied as the following procedure. Initially, according to the Barton Stress criterion and the initial stress, the rockburst possibility is assessed as the slight-moderate level. Next, granite rock samples are obtained from the underground powerhouse, and Elastic Deformation Energy Index *Wet* is tested. Herein, rockburst possibility is also evaluated as the slight-moderate level. Lastly, the disturbed stress distribution during excavation is calculated through 3D numerical simulations. The results show that the slight-moderate rockbursts tends to occur in some places of the main cavern, and intensive rockbursts trend to happen in few places. These research results are in accordance with the field observations.

1 Introduction

Rockburst is a geology hazard which is often encountered during excavation in high-stress underground works, caused by the violent release of stored strain energy. It is a type of dynamic phenomenon, not a static or quasistatic phenomenon. High geostress and excavation disturbance are the main external factors which are necessary conditions of rockburst; while hard, integrity and brittle rock mass are the main internal factors in which high elastic strain energy is liable to be stored[1, 7, 9,11,12].

Since it was brought forth in 1978, rockburst has been a concern of scholars all over the world. And many scholars suggested various theories and prediction methods. However, there isn't a common understanding about the definition of rockburst until today. Rockburst often occurs suddenly and intensely, which can cause injury to builders and damage to equipment make it an international engineering puzzle in underground works[2-6, 8, 10].

Due to the complexity of rock mass and the variety of influencing factors, it is very difficult to predict space-time distribution of rockburst exactly. The results of various prediction methods should be analyzed comprehensively. We think rockburst prediction may be described by the following three stages,

(a) Feasibility study and primary design period: in this stage there isn't a global stress adjustment for surrounding rockmass with lots of energy being accumulated. Rockburst possibility research should be done in this stage. The target is to understand rockburst possibility by means of field geostress and indoor rock characteristics.

(b) Primary design and earlier construction period: in this stage there is a stress adjustment for the surrounding rockmass, and energy is accumulated, dissipated and released. Rockburst trend prediction research should be done in this stage. The target is to determine the rockburst area approximately, providing the major area for field monitoring. This will be implemented mainly by means of 3D numerical simulation. The key problem is to select suitable rockburst criterion.

(c) Construction period: in this stage there is global stress adjustment for the surrounding rockmass, and energy is dissipated and released. Rockburst field prediction and forcasting should be done in this stage. The target is to predict rockburst near monitoring sections, and predict rockburst for the whole engineering area when conditionally necessarily.

In southwest China, there are many Hydropower Stations in construction. During the last several years, in these very high geostress regions, rockburst has taken place in underground power houses such as the Ertan, Pubugou, and Jinping Hydropower Station and so on. Detailed research on rockburst prediction has been done at the Pubugou Hydropower Station. The research was concentrated mainly on the former two stages, i.e. rockburst possibility and trend prediction.

2 General layout

Pubugou Hydropower Station is a huge project with comprehensive beneficence. Except for power generation, it also has functions as flood control, sediment retention etc. The project is composed of gravelly clay core rockfill dam, underground power house, open spillway and flood discharge tunnel on the left bank, and emptying tunnel and Niri River diversion works on the right bank(Figure 1).

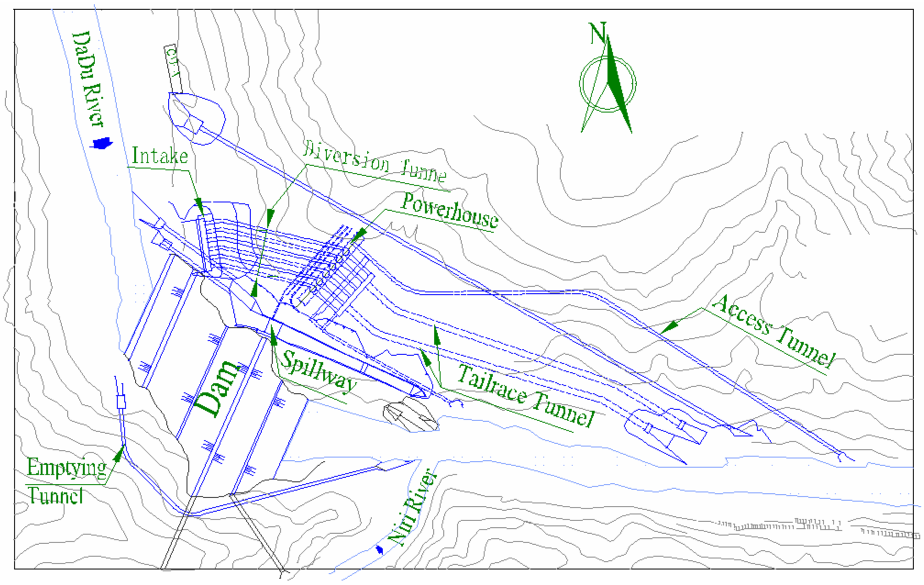

Figure 1 General layout of Pubugou Hydropower Station

Underground powerhouse of Pubugou Hydropower Station lies in granite rock mass on left bank. It is composed of six intake tunnels, main power house, power transformer chamber, tailwater gate chamber and two non-pressure tailwater tunnels. The power house is 294.10m×30.7m×70.175m. The length of main house is 208.6m, auxiliary powerhouse is 25.5m, and erection bay is 60m. The width of power house on the upper side of crane beam is 30.7m, and under crane beam is 26.8m. The power house is divided into nine stages when excavated and supported, power transformer chamber is divided into three stages, tailwater gate room is divided into six stages and tailwater tunnel is divided into three stages.

3 Rockburst possibility research

3.1. Pancake Cores Phenomenon

Except emptying tunnel on the right bank, main underground hydraulic structures of Pubugou Hydropower Station are in granite rockmass on the left bank. And rockmass quality is good. Poor assemblage of structural plane and rockburst hazard caused by high geostress are main geological factors which affect rockmass stability.

During excavation of 45# exploratory cavern, rockburst occured for more than 10 times. Most rockbursts occured at arch corner of upstream, spalling as shape of onion skin and platy. During geostress test drilling, there is the phenomenon of Pancake cores.

3.2. Geostress Measurement

The maximum principal stress at Pubugou Hydropower Station is σ_1=21.1~27.3MPa. The ratio between self-weight stress (σ_H) and vertical stress (σ_z) is less than 50%, indicating the tectonic stress is dominant. The average value of σ_1:σ_2:σ_3 equals to 1:0.65:0.27, showing deviatonic stress is larger.

The ratio between uniaxial compressive strength and maximum principal stress is σ_c:σ_1=3.9~7.6, and ratio between tensile strength and maximum principal stress is σ_t :σ_1=0.28~0.38. According to Barton Stress criterion, rockburst possibility was assessed as slight-moderate level.

3.3. Elastic Deformation Energy Index Wet

High geostress is main external factor which leads to rockburst but it is not sufficient factor. Under the same geostress condition, whether rockburst will happen or not depends on deformation characters of rock mass, and this could be illustrated by Elastic Deformation Energy Index *Wet*.

Elastic Deformation Energy Index *Wet* could be acquired by the following test: the rock sample is loaded to 80%~90% of the peak strength while doing uniaxial compression test, then it is unloaded to zero. Elastic Deformation Energy Index *Wet* is the ratio between unloading curve area and area of loading and unloading curve(Figure 2), i.e.

$$W_{ET} = \frac{\phi_{SP}}{\phi_{ST}}$$

ϕ_{SP} is elastic deformation energy, while ϕ_{ST} is plastic deformation energy.

Table 1 shows rockburst possibility criterion according to Elastic Deformation Energy Index *Wet*. Figure 3 and table 2 is experimental results of rock samples from underground powerhouse of Pubugou Hydropower Station.

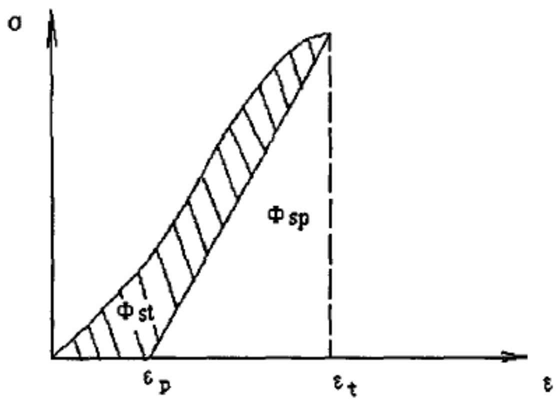

Figure 2 The schematic diagram of *Wet* measurement

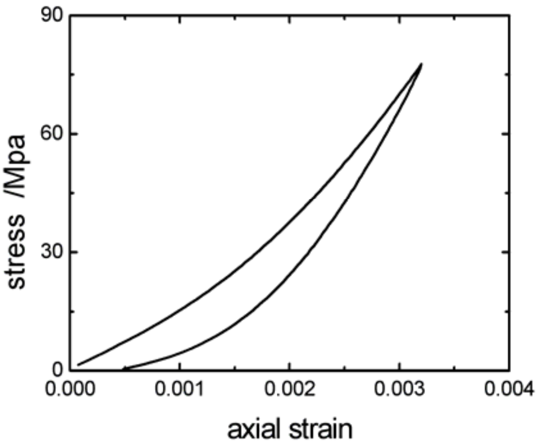

Figure 3 *Wet* measurement curve of wei1-7 rock sample

Table 1. Rockburst possibility criterion - Elastic Deformation Energy Index *Wet* (according to Kidybinski)

Wet	<2	No rockburst possibility
	2~4.9	Slight-moderate rockburst possibility
	≥5	Catastrophic rockburst possibility

Table 2. Experimental results of Elastic Deformation Energy Index *Wet*

Sample number	Diameter /mm	Height /mm	Elastic Deformation Energy Index *Wet*	Forecasting results
Wei1-6	49.5	105.3	4.75	Slight-moderate rockburst possibility
Wei1-7	49.3	105.7	2.42	Slight-moderate rockburst possibility
Chang2-1	49.5	103.9	1.91	No rockburst possibility

4 Rockburst trend prediction research

Using 3-D ANSYS FEM software, firstly geostress distribution in the rock mass of underground powerhouse in Pubugou Hydropower Station is fitted; Next, secondary stress distribution during excavation is simulated. According to Barton and Wanglansheng Stress Criterion, rockburst possibility during excavation is also predicted. The 3-D finite element model is shown in Figure 4 and Figure 5.

4.1.Geostress Fitting

Three methods is used while fitting geostress distribution: linear fitting of measuring points stress, optimization of initial displacement, optimization of initial loading. After comparison the third method is chosen.

4.2. Rockburst Trend Prediction

Secondary stress distribution during excavation in the rock mass of underground powerhouse in Pubugou Hydropower Station is simulated. According to Barton and Wanglansheng stress criterion, we got critical values of rockburst possibility(table 3). And rockburst trend prediction is analyzed after every excavation step(Figure 6, only the fourth and eighth step is chosen).

From comprehensive analysis of rockburst trend prediction, we could learn that,

(a) During excavation there is rockburst possibility of slight-moderate level, and there is little possibility of catastrophic level.

(b) Horizontal stress is much larger than vertical stress, rockburst possibility before the first three steps is lower than next six steps. From the fourth step, stress concentration in local area is more serious, and rockburst possibility is also larger.

(c) Single criterion is one-sided while analyzing rockburst trend prediction. Comprehensive analysis according to various criterion should be carried out. For Pubugou Hydropower Station, Barton criterion is conservative compared with Wanglan Sheng criterion.

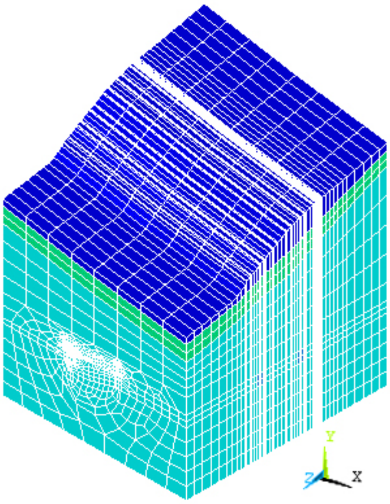

Figure 4 3D Finite Element Model

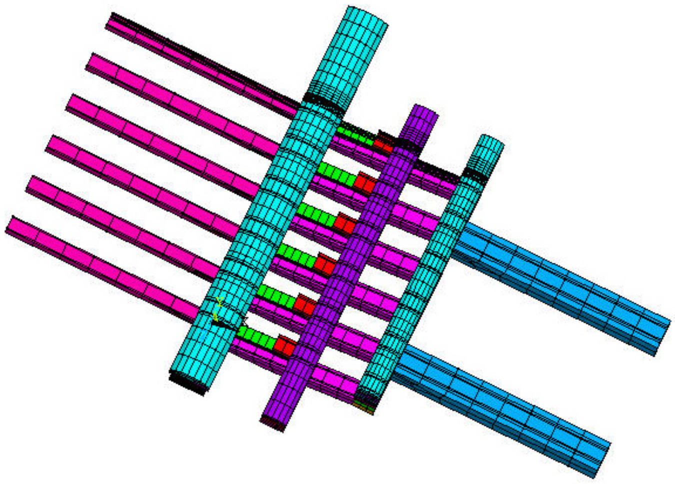

Figure 5 FEM model of underground powerhouse

Table 3. Critical values of rockburst stress criterion (unit: Mpa)

Criterion	No rockburst	Slight-moderate rockburst	Catastrophic rockburst
Barton stress criterion	<28	28~56	>56
Stress criterion of Wanglan Sheng Erlangshan tunnel	<42	42~98	>98

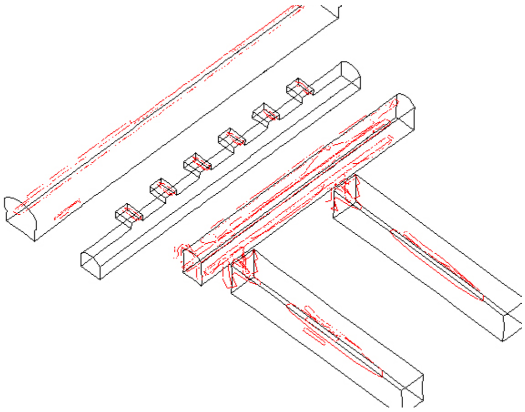

Figure 6 (a) Rockburst trend prediction of fourth excavation step

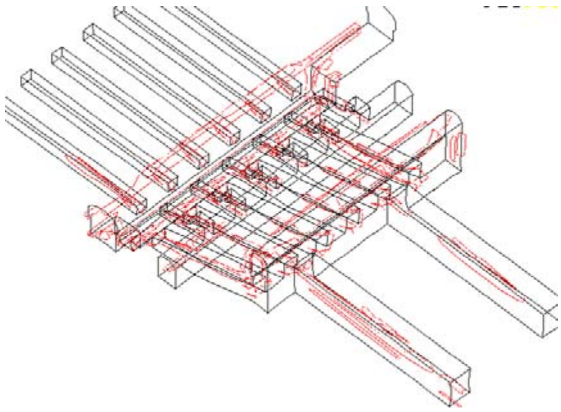

Figure 6 (b) Rockburst trend prediction of eighth excavation step

5 Conclusions

(a) Due to complexity of rock mass and variety of influencing factors, it is very difficult to predict space-time distribution of rockburst exactly. The results of various prediction methods should be analyzed comprehensively and may be described by the following three stages,

The purpose of rockburst possibility research during feasibility studies and the primary design period, is to target and understand rockburst possibility by means of geostress distribution and indoor rock tests. Rockburst trend prediction during primary design and the early construction period, targets the rockburst area approximately, providing the major area for field monitoring. The target of Rockburst field prediction and forecasting during the construction period is to predict rockburst near monitoring sections, and predict rockburst for the whole engineering area when conditionally necessarily.

(b) Detailed research on rockburst prediction in the underground powerhouse of the Pubugou Hydropower Station has been done. The research work was concentrated mainly on rockburst possibility and trend prediction.

Initially, according to Barton Stress criterion and initial stress value, rockburst possibility was assessed as a slight-moderate level. Next, the granite rock samples were obtained from the underground powerhouse and the rockburst possibility index *Wet* was tested and the rockburst possibility is also evaluated as the slight-moderate level. Lastly, the disturbed stress distribution during excavation was calculated through the 3D numerical simulation. According to the Wang Lansheng Stress Criterion, slight-moderate rockbursts tend to occur in some places of main cavern, and only in a very few places is intensive rockbursts likely. These research results were obtained in accordance with the facts in the field.

Acknowledgements

The authors wish to acknowledge the funding support from the National Natural Science Foundation of China (Grant no. 50639100, 50620130440, 50221402) and international collaborative project from Science and Technology Ministry of China (Grant no. 2007DFB60100).

References

1. Mansurov, V. A. Prediction of Rockbursts by Analysis of Induced Seismicity Data. International Journal of Rock Mechanics & Mining Sciences, 2001, 38: 893-901.
2. Lu, C., Mai,Y.W. and Xie, H. A Sudden Drop of Fractal Dimension: A Likely Precursor of Catastrophic Failure in Disordered Media. Philosophical Magazine Letters, 2005, 85(1): 33-40.
3. Poplawski, R.F. Seismic Parameters and Rockburst Hazard at Mt Charlotte Mine. Int. J. Rock Mech. &Min. Sci, 1997, 34(8): 1213-1228.
4. Frid, V. Electromagnetic Radiation Method Water-Infusion Control in Rockburst-Prone Strata. Journal of Applied Geophysics, 2000, 43: 5-13.
5. Fuji, Y., Ishiji, Y., Ma, E. and Deguchi, G. Prediction of Coal Face Rockbursts and Microseismicity in Deep Longwall Coal Mining. Int. J. Rock Mech. &Min. Sci, 1997, 34(1): 85-96.
6. Linkov, A. M. Rockbursts and the Instability of Rock Masses. Int. J. Rock Mech. &Min. Sci, 1996, 33(7): 727-732.
7. Srinivasan, C., Arora, S.K. and Benady, S. Precursory Monitoring of Impending Rockbursts in Kolar Gold Mines from Micoseismic Emissions at Deeper Levels. International Journal of Rock Mechanics & Mining Sciences, 1999, 36: 941-948.
8. Grodner, M. Delineation of Rockbursts Fractures with Ground Penetrating Radar in the Witwatersrand Basin, South Africa. International Journal of Rock Mechanics & Mining Sciences, 2001, 38: 885-891.
9. Arora, S.K., Willy, Y. and Srinivasan, A.C., et al. Local Seismicity Due to Rockbursts and Near-Field Attenuation of Ground Motion in the Kolar Gold Mining Region, India. International Journal of Rock Mechanics & Mining Sciences, 2001, 38: 711-719.
10. Moura, A., Lei, X.L. and Nishisawa, O. Self-Similarity in Rock Cracking and Related Complex Critical Exponents. Journal of the Mechanics and Physics of Solids, 2006, 54: 2544-2553.
11. Lei, X.L. and Satoh, T. Indications of Critical Point Behaviour Prior to Rock Failure Inferred from Pre-Failure Damage. Tectonophysics, 2007, 431: 97-111.
12. Moura, A. and Lei, X.L. Prediction Scheme for the Catastrophic Failure of Highly Loaded Brittle Materials or Rocks. Journal of the Mechanics and Physics of Solids, 2005, 53: 2435-2455.

RaSiM 7(2009): Controlling Seismic Hazard and Sustainable Development of Deep Mines, C.A. Tang(ed), Rinton Press, 463-466

FORMATION OF INELASTIC STRAIN ZONES NEARBY STOPES IN SLICE MINING OF STEEP ORE BODIES

VASILY BARYSHNIKOV and LIDIA GAKHOVA

Institute of Mining, Siberian Branch, Russian Academy of Sciences

54 Krasny Prospect, 630091 Novosibirsk, Russia

The authors analyze the cut and fill mining variants in steep ore bodies. An approach is offered to evaluate mining condition on junction of sublevels in the course of the ascending and descending cutting and to decide on the stope supporting by the numerical modelling of the stress-strain state with the known strengths of the ore and fill masses.

1 Introduction

Mining of steep ore bodies entails specific technological and geomechanical problems. Such is the horizon mining of subvertical kimberlite bodies at “Alrosa” Joint-Stock Company.

Slicing with consolidated backfill is employed in Internatsionalnaya underground kimberlite mine, the vertically occurring kimberlite body is elliptic in cross-section. There are several mining horizons, and a number of sublevels can concurrently be developed at each level. The cut-and-fill mining involves 5÷6 m wide and 3.5÷5.5 m high stopes. Depending on the stability of stopes, slicing may be either ascending or descending.

The efficient and safe slicing requires monitoring of variations in geomechanical conditions during sublevel mining and in the character of rock pressure manifestation depending on features of the stress-strain state formation in the vicinity of stope. It is possible to predict variations in geomechanical state in the course of mining by the numerical modelling of the mining stages. The numerical modelling with application of strength criteria allows identifying potential post-limit deformation zones in rocks. The use of a criterion is specified by analyzing the actual conditions, prevailing at a mining stage under consideration.

2 Geomechanical evaluation of horizon mining stages

The geomechanical conditions specify the main stages in the extraction of a level, differing essentially by rock pressure manifestations associated with the stress state formation nearby stopes; namely, formation of an undercutting layer in a virgin rock mass, raising or descending extraction of levels, access level extraction, ascending mining of parting levels.

To analyze the mining conditions at different production stages, numerical modelling of the rock mass stress-strain state was performed by the boundary integral equation method [1]. The experimental data on the natural stress field parameters were assumed according to [2, 3]: vertical stresses $\sigma_z = \gamma H$, horizontal stresses $\sigma_x = \sigma_y = \lambda\gamma H$, where H is mining depth, γ - weight of overlying rocks, λ is thrust coefficient (λ=0.7 for kimberlites, λ=1 for host rocks).

The laboratory test data indicate appreciable variability of physico-mechanical properties of kimberlites and host rocks by the types and occurrence depth. The ultimate compressive strength of the host rocks ranges from 31 MPa at depth of 600 ÷ 700 m to 54 MPa at depth of 1300 ÷1400 m.

The formation of an undercut level in a virgin rock mass requires maintaining stable temporary pillars subjected to vertical stresses induced by the weight of overlying rocks. Figure 1 shows the curves of the horizontal and vertical stress concentration coefficients in the roof and walls of stopes when the stopes are extracted next by one. The analysis data on the stress-strain state of the rock mass under slicing in two and three stages at depths of 600 m ÷ 960 m are generalized and used to evaluate the stability of stopes by the compressive strength criterion (σ_c) depending on mining depth and kimberlite strength (Fig. 2). For the indicated depths, the walls of all second-stage stopes 5 m x 3.5 m in size (Fig. 2*a*) and most of the second-stage stopes 5 m x 5 m (Fig. 2*b*) appear unstable and require supporting.

The upward mining results in unloading the roof and floor of the level parted by from the mined-out space by one level from the vertical and partially horizontal stresses, typical of virgin rock masses.

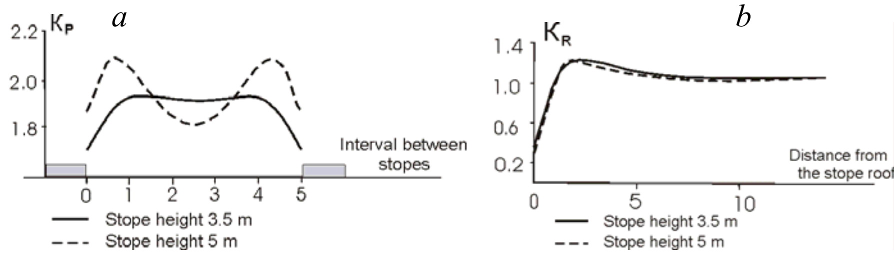

Figure 1. Stress concentration coefficients in cutting kimberlite body in virgin rock mass: *a* — σ_z in a pillar between stopes (K_p); *b* — σ_x the stope roof (K_R)

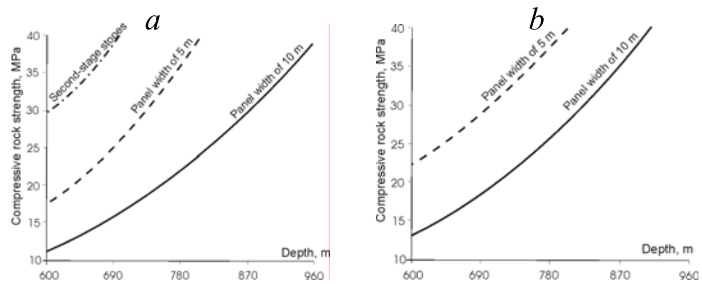

Figure 2. Evaluation of stability of stope walls in a cut: *a* – stopes 5 m ×3.5 m; *b* – stopes 5 m×5 m.
Note: area above a curve – the stope wall is stable; area under a curve – the stope wall is unstable

The concentration of horizontal stresses gradually grows as the height of mining in the ore roof increases. In these conditions the need for the support is evaluated relative to the minimum strength of kimberlite.

When forming a cut in the upward mining, the concentration of horizontal stresses in the roof of stopes in the central section of the ore body is especially hazardous and complicates their maintenance in the stable state. Peculiarities of the stress state formation in the roofs of the stopes are shown in Figure 3. Figure 4 presents the generalized data on the roof stability depending on mining depth and compressive strength of kimberlite, for stopes in the upward cut level.

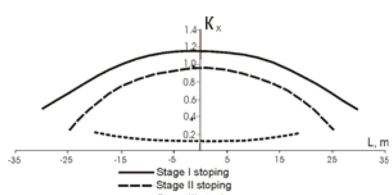

Figure 3. Variations in the horizontal stress concentration coefficients (K_x) in the roofs of entry ways, stopes of the second and third stages in upward mining versus distance (L) to the centre of the ore body

The upward mining of a ceiling between adjacent stoping fronts is characterized by the complete unloading of the ceiling from vertical stresses. Thereby the horizontal stresses grow substantially with the reduction in the ceiling thickness.

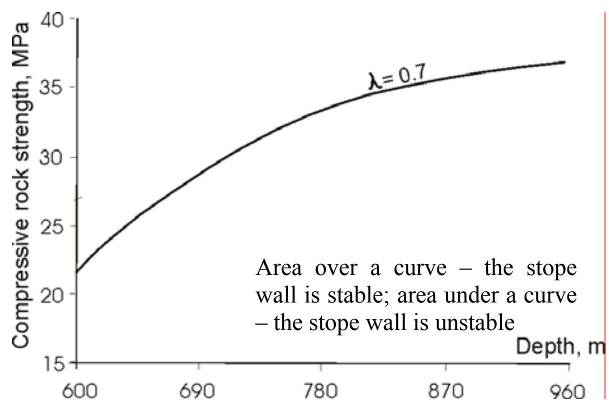

Figure 4. Roof stability in stopes in the centre of the ore body during the upward cutting

The generalized criterion for evaluation of rock outcrop stability was taken as the most suitable criterion to evaluate the rock mass stability at the stope contour [4]:

$$\frac{\lambda\gamma H}{\sigma_c} < \frac{1}{K_\sigma} \text{ or } K_\sigma < \frac{\sigma_c}{\lambda\gamma H}, \qquad (1)$$

where σ_c is uniaxial compressive strength limit for a rock mass (in the vicinity of rock outcrops), K_σ is coefficient of stress concentration in a rock mass, γ is specific weight of a rock mass, λ is lateral-thrust factor, H is mining depth, m.

We use the nomogram in Figure 5 to check the fulfillment of the stability criterion (1). With the known parameters of the rock mass strength and pillar-mining depth, the nomogram makes it possible to evaluate the ceiling thickness, at which the stope roof at overlying level reaches the critical state.

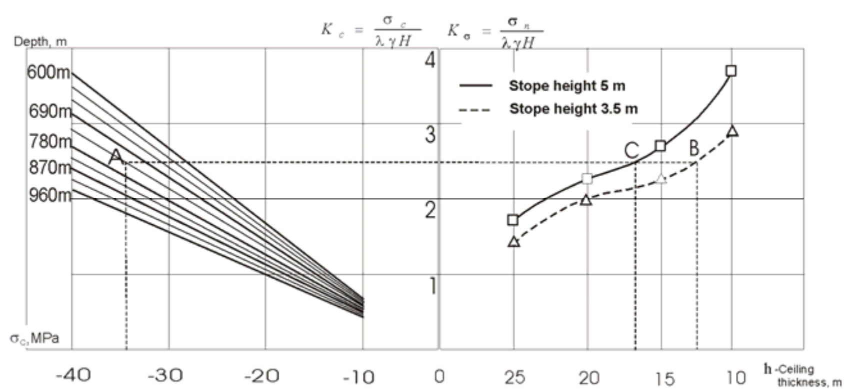

Figure 5. Nomogram to evaluate the stability of the central stope roof for level under mining

The size of the potential failure zones can be obtained by Mohr-Coulomb- criterion used to estimate the size of the non-elastic deformation areas by means of comparing the shearing stresses in a rock mass in the vicinity of an area under mining with the rock-mass cohesion (C):

$$\sigma_{c\partial} = \frac{\sigma_1 - \sigma_2}{2\cos\varphi} + \frac{\sigma_1 + \sigma_2}{2} tg\varphi, \qquad (2)$$

where $\sigma_1 > \sigma_2$ are principal stresses; φ is internal friction angle.

Classification of the rock stability in terms of size of the inelastic deformation zone proposed in [4] permits to relate the conventional rock stability categories with the dimensions and configuration of the potential failure zones, built in compliance with (2).

To work out the support measures for stopes or transition to downward mining, the category of the rock mass stability is determined from nomograms with account for the size of inelastic deformation zones at the known cohesion. The nomograms in Figure 6 are given as examples of evaluation of the inelastic deformation zone dimensions based on shearing stresses for the depth of 600 – 960 m when the crown pillar (ceiling) height is 15 m and the heights of stopes are 3.5 m and 5 m.

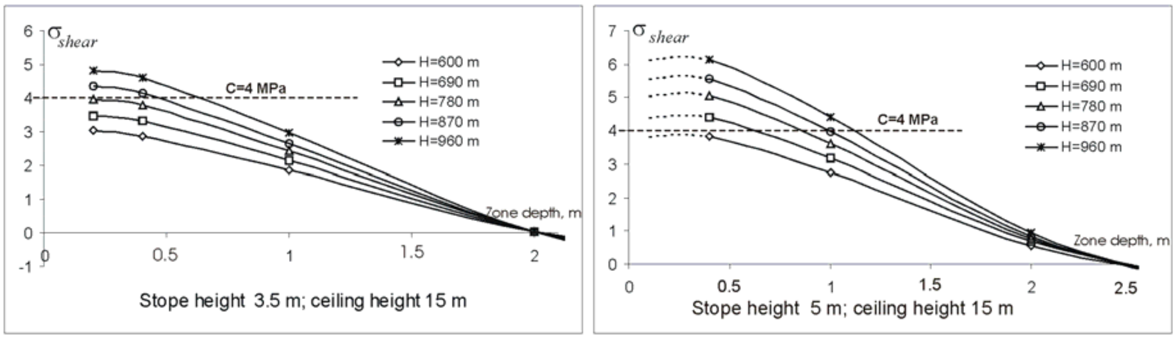

Figure 6. Shear stresses in the roof of stopes under development

3 Conclusions

The stability of the roof and walls of stopes in sublevel slicing in a virgin rock mass is evaluated for both upward and downward mining. The evaluation involves the use of numerical modelling data on the stress-strain state of the rock mass during the level mining and the known values of the rock mass strength and mining depth.

The upward mining conditions are considered. The transition to the downward mining of Internatsionalnaya kimberlite ore body at the sublevel contact zones and need in the roof support at stopes are substantiated. The forecast data on probable roof failure volumes in stopes in depth of the inelastic deformation zones allow establishing the optimal parameters of the stope support system.

4 References

1. Gakhova, L., Calculation Program for the Stress-Strain State of a Rock Mass of Block Structure by Boundary Integral Equation Process (ELB2D). RosAPO. Registration Certificate No. 960814.

2. Production Procedures (Interim Operating Procedure) for Stowing Operations at the Internatsionalny Mine in 2004 – 2006, Yakutniproalmaz (Mirny, 2004).

3. Baryshnikov, V., Gakhova, L. and Kramskov N., Stress State of Ore Mass in the Ascending Slice Mining System. Journal of Mining Science, 38 (6). pp. 608-611.

4. Bulychev, N., Mechanics of Underground Structures. Nedra (Moscow, 1989).

RaSiM 7(2009): Controlling Seismic Hazard and
Sustainable Development of Deep Mines,
C.A. Tang(ed), Rinton Press, 467-472

APPLICATIONS OF THE TRANSIENT ELECTROMAGNETIC METHOD IN UNFAVORABLE GEOLOGICAL BODIES WITH WATER OR MUD DETECTION

MAO-XIN SU, SHU-CAI LI, YI-GUO XUE and DAO-HONG QIU
Research Center of Geotechnical and Structural Engineering, Shandong University
Jinan,250061, P.R. China

Experience shows that unfavorable geological bodies containing water or mud in front of the tunnel working face play a great role in the tunnel construction. The transient electromagnetic method (TEM) is sensitive to the low resistive bodies. Usually, the unfavorable geological bodies can be considered as a low resistivity interbed as conducting the geological forecast. On the basis of the whole space theory, this paper intends to use the TEM equivalent conductance plane method on the detection of the low resistivity interbed in front of the tunnel working face. This will be done by combining the apparent longitudinal conductance and its differential imaging,. Some characteristics and laws of the detection are concluded through the computation and the analysis, which can be used to guide the actual TEM tunnel geological forecast and improve the precision and accuracy of TEM detection.

1 Introduction

China is a mountainous country with complicated underground hydrogeology in the construction of water conservancy and hydropower. With rail and road tunnels, some unfavorable geological bodies with water or mud are usually located, with implications such as water inrush, mud inrush and roof fall. These will seriously affect the construction progress, moreover; it will result in significant security incidents. Therefore, it is particularly important to detect these unfavorable geological bodies with water or mud.

There's several geological forecast methods to detect these bodies with water or mud [1-3], but the transient electromagnetic method (TEM) [4,5] is undoubtedly the best. In particular, TEM is sensitive to low resistivity, non-destructive nature, low cost and high efficiency; and it is widely used in the detection of the fracture zone and the fault with water and mud in front of the tunnel working face. Due to the unfavorable geological bodies in front of the tunnel working face that usually exist with a shape of interbed, these bodies' forecast can be studied as a low resistivity interbed detection. In domestic and foreign regions, there is little lecture material on the system study of the low resistivity detection in front of the tunnel working face. For example, some application research of certain geological bodies detection[6-8] and some thin-layer detection research in the condition of half-space[9-11]. For example, in the two 3D conductance thin layers, the author of Tang Xingong has research of computing the electromagnetic responses of different distance emit sources. In 2007, Xue Guoqiang studied the thin-layer detection ability of different geoelectric models with some meaningful conclusions. However, TEM detection in the tunnel is Whole-space problem and can not simply copy the detection method and some conclusions on the ground. Thus, the study of the detection of low resistivity layers in front of the tunnel working face using the whole-space TEM becomes very meaningful. The equivalent conductance plane method is a TEM interpretation method which is built on the whole space theory. In this article, we intend to use this method, import the genetic algorithm to numerical compute, and lastly, combine the apparent longitudinal conductance differential imaging[12]. With this combination, we can have a corresponding research to the detection of low resistivity interbed in front of the tunnel face.

2 TEM whole-space detection principle

The TEM detection of the tunnel working face is different form the detection on the ground, the ground's prospecting is a half-space problem, and the tunnel working face detection is a whole-space problem, so the detection method in tunnel can not copy the methods of the ground's. The theory and methods of Whole-space must be used in the tunnel. Now, in TEM, the equivalent conductance plane method [4] is based on the whole-space theory [13]. In addition, the apparent longitudinal conductance have a sensitive response to the low resistivity conductive thin-layer, which will help to detect low-resistivity geological body with mud and water. Therefore, this article will use the equivalent conductive plane method to have a study on the detection of low-resistivity interbed in front of the tunnel working face in front of the introduction of detection study.

2.1 Principle of the equivalent conductance plane method

As shown in Figure 1, there is a vertical circular loop close to the tunnel working face, which carry a step current, and the power supply disconnected at the moment t = 0:

$$I(t) = \begin{cases} I & t < 0 \\ 0 & t \geq 0 \end{cases}$$

Where, t is the survey time, and $I(t)$ is the current value in the vertical circular loop.

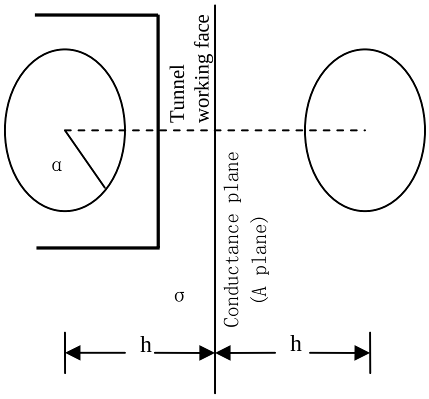

Figure 1 Schematic diagram of tunnel working face conductance plane

When the power supply disconnected, due to electromagnetic induction, electromagnetic response will be generated in 3D space in front of the tunnel working face. the electromagnetic response can be approximatively instead by the electromagnetic field which generated by the eddy current in the infinite large conductance plane A. in order to compute the electromagnetic by eddy current, put a falsehood source instead of the eddy current in the conductance plane, and the electromagnetic value of any point in the 3D space can be computed through the falsehood source.

2.2 Calculation of apparent longitudinal conductance and it's differential imaging

Because the article length problem, the calculation of apparent longitudinal conductance and its differential imaging will not be described in detail. the specific calculation methods and steps can be found in literature [4]. It is note that, as the calculation of the apparent longitudinal conductance need to import one assistant function $\varphi(\overline{m})$,when the function $\varphi(\overline{m})$ is used to establish objective function of the inversion problem, the value of apparent longitudinal conductance is not linear. Under the conditions, local search is easy to get into a best small value. For resolve this problem, the article import a global optimization algorithm - adaptive shrinkage genetic algorithm in the feasible region [13]. In the paper, the apparent longitudinal conductance and it's differential imaging calculations are based on this genetic algorithm.

3 Forward modelling of the low resistivity interbed

In order to make the forward modelling have more practical guide, the choice of simulation parameters as much as possible close to the practical conditions. Moreover, as the applied forward modelling and inversion of TEM still the 1D computation, all the numerical simulation in the article is the 1D geoelectric model calculations.

In general, the fault with water or mud, fissure and fracture zone is low resistivity. Therefore, the geoelectric model can be equal to low resistivity interbed. We mainly study the TEM characteristics and resolution of low resistivity interbed, two different thickness low resistivity interbed forward modelling will be discuss follow. Considering the geology and electromagnetic environment, the thin-layer geoelectric model parameters are: $\rho_1 = \rho_3 = 200\Omega.m$, $\rho_2 = 20\Omega.m$, $H_1 = 30m$, $H_2 = 1m$, and H_3 as be infinite, see model NO.1 in Figure 2; Thick layer geoelectric model parameters are: $\rho_1 = \rho_3 = 200\Omega.m$, $\rho_2 = 20\Omega.m$, $H_1 = 30m$, $H_2 = 20m$, and H_3 as be infinite , see model No.2 in Figure 3. Both central loop device launch side is 3 meters and 6 turns. Forward simulation results in Figure 4 and Figure 5 below.

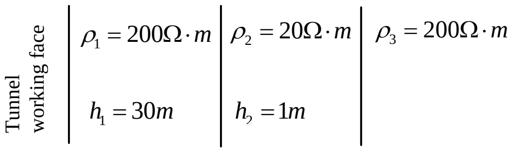

Figure 2 Geoelectric model No.1

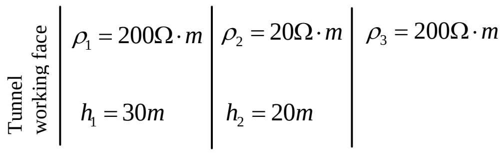

Figure 3 Geoelectric model No.2

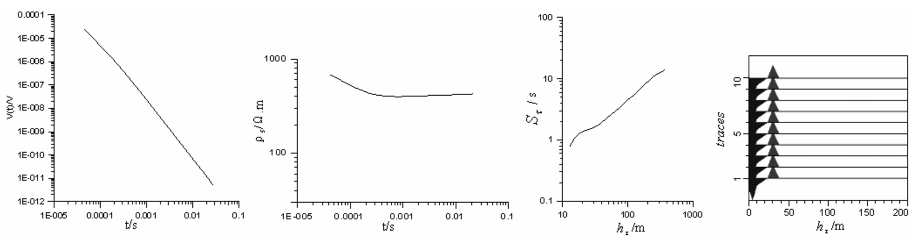

(a) (b) (c) (d)

Figure 4 Forward results of geoelectric model No.1 ((a) voltage decay curve (b) apparent resistivity curve (c) apparent longitudinal conductance curve (d) apparent longitudinal conductance differential imaging)

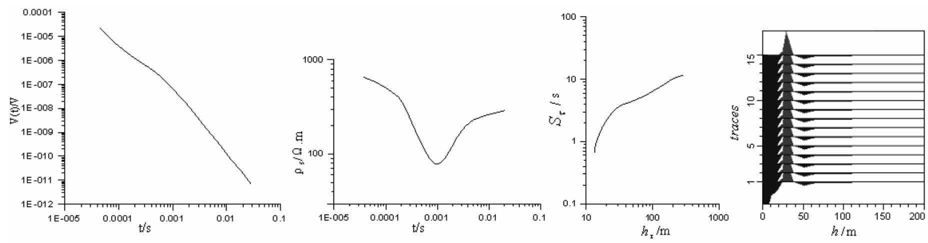

(a) (b) (c) (d)

Figure 5 Forward results of geoelectric model No.1 ((a) voltage decay curve (b) apparent resistivity curve (c) apparent longitudinal conductance curve (d) apparent longitudinal conductance differential imaging)

Figure 4a-d gives the numerical simulation of the low resistivity thin-layer geoelectric model. Thinner fault with water or mud in front of the tunnel working face can be equivalent to such a geoelectric model. In model 1, the middle layer is thinner, only 1m. From the result of the curve, we can see that attenuation of voltage (electromotive force sensor) basically do not see the response of thin layer; apparent resistivity curve is difficult to confirm the response of the middle interlay, too; However, from the apparent longitudinal conductance curve, the response turn point appear, and the electric interface of apparent longitudinal conductance differential imaging is so evidence. The interface location is about thirty meters distance from the tunnel working face, which accordant with the given model. Because the thinner interbed, although the top interface of the interbed can be clearly show, the bottom interface of the interbed is not show.

Figure 5a-d gives the numerical simulation of the low resistivity thick-layer geoelectric model. Thicker fault with water or mud in front of the tunnel working face can be equivalent to such a geoelectric model. In model 2, the middle layer is 20m. From the forward modelling result, although the interbed thickness increased, bun, in the decay voltage curve, the interbed response is not obvious; while the apparent resistivity anomalies are more evidence, which is the same as typical 'H' type [4] geoelectric model response curve. Of course, the location of the interbed response can be clearly identified. Besides, not only the first electric interface can be identified, but also the second, which is accordance with the model 2. However, to the apparent longitudinal conductance differential imaging, as the low resistivity interbed become thicker, the amplitude value become big and have a certain continue characters, which will disturb the interpretation of the interbed behind.

From the forward modelling result, when the low resistivity interbed top interface can not be show use the decay voltage curve and the apparent resistivity curve. however, by the means of apparent longitudinal conductance and the apparent longitudinal conductance differential imaging babes on the genetic algorithm, we can see the top interface of the low resistivity interbed response. In addition, from the forward modelling calculation of the geoelectric model above, the electric interface response effect of apparent longitudinal conductance differential imaging is the best, secondly is the apparent longitudinal conductance, third is apparent resistivity, the last is decay voltage. For the identify of the low resistivity interbed, usually, the more thicker of the layer, the response is more obvious, the electric interface is clearer. If the low resistivity interbed is relative thicker, the apparent longitudinal conductance differential imaging of the interface have a amplitude continuous character, which will disturb the interpretation of the interbed behind. Under the conditions, synthesis interpretation had better to be adopted, including apparent longitudinal conductance differential imaging, the apparent resistivity curve and the others geophysics exploration methods or the geology data.

4 Application example

In order to verify the application effect of the equivalent conductance plane based on the genetic algorithm which include the apparent resistivity and the longitudinal conductance and differential imaging, a certain tunnel TEM forecast application example in western China will be show as follow.

In the example, terrane in front of the tunnel working face is located in the limestone zone, where the fissures and joints are development, corrosion is serious. In order to effectively detect the unfavorable geology body with water or mud, the data collection parameters is: the central loop device, probe receive, loop side is 3 meters, loop is 6 turns and the point distance is 0.4 meters. The detection result as figure 6.

It is note that, In figure 6c, dashed line express as the conclude structure face, and thick solid line is the structure face after excavation.

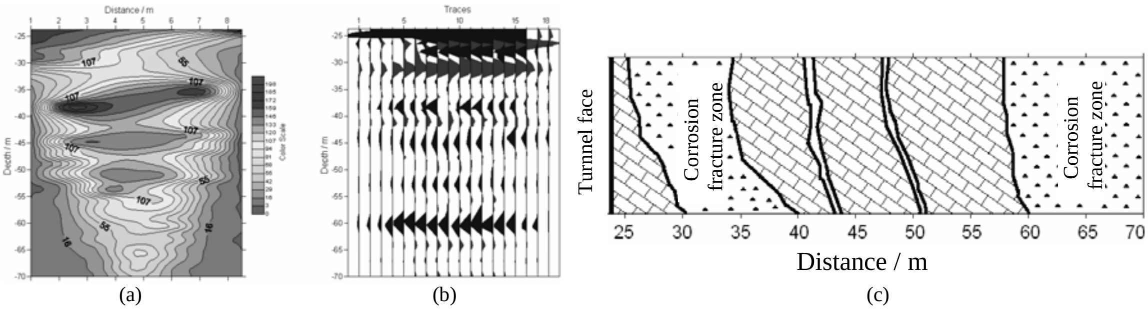

Figure 6 Results of tunnel detection ((a) section of apparent resistivity contour lines (b) apparent longitudinal conductance differential imaging (c) the results of excavation and interpretation)

According to the raw collect data, the interpretation depth is from 25m to 70m. from the apparent resistivity contour lines in figure 6c, there is an obvious low resistivity interbed. In the apparent longitudinal conductance differential imaging of figure 6b, there is a high amplitude interface about 30m distance in front of the tunnel working face. Both good corresponding to the excavation. Hower, the response interface information of apparent longitudinal conductance differential imaging is more rich and nicety. Especially, some thinner structure face or the lithology interface have a certain response, for example, there is a evidence interface response respectively in the location of 43m and 53m, the excavation results prove that two location develop fissures with water, which argue that the apparent longitudinal conductance differential imaging is a much well identify method to the low resistivity interbed judgement. Besides, the interface in 60m location is accord with the excavation result. However, apparent longitudinal conductance differential imaging can only show the variation of the longitudinal electrical nature and the depth information, can not see the apparent resistivity of different space location, also can not intuitively line out the abnormity. Therefore, when have a interpretation by the equivalent conductance plane method, both apparent resistivity and apparent longitudinal conductance differential imaging should be combined to process the interpretation and judgement.

5 Conclusions and future work

Detection of low resistivity interbeds in front of the tunnel working face is very important to the geological forecast In addition the low resistivity interbed often contains water and mud, and if it had not been forecasted, it can bring about evcavation dangers in the tunnel causing accidents or casualties. Therefore, it's important and significant to study of the detection of the low resistivity interbed in front of the tunnel working face. Combined with the analysis and research above, to the low resistivity interbed's detection, some conclusions and recommendations as follows:

(1) TEM conductance plane based on the equivalent genetic algorithm is effective to detect the low resistivity interbed in front of the tunnel face.

(2) The greater the thickness of the low resistivity in front of the tunnel working face, the more sensitive of the interface response; regardless of the voltage transient electromagnetic decay curve, the apparent resistivity curve, apparent longitudinal conductance curve, and the apparent longitudinal conductance differential imaging, on the contrary, it is not easy to distinguish. In the four methods, the apparent longitudinal conductance differential imaging is the most sensitive response of the interface which can show the thinner low-resistivity interbed interface, the next is respectively the longitudinal conductance, apparent resistivity and voltage decay curve.

(3) If the interbed is thicker, using the apparent longitudinal conductance differential imaging can not only see the top interbed interface, the bottom interface can be shown. However, because the top interface response

amplitude is stronger, and also with a certain continuity which will disturb the bottom interface of interbed, or deeper interface interpretation, thus the repression and identification should be processed in the TEM data.

(4) The apparent longitudinal conductance differential imaging can identify the electric property layer in a higher sensitivity and signal-to-noise ratio (SNR) in detail.

(5) When making the geological forecast by TEM, it is best to combine the apparent longitudinal conductance differential imaging and apparent resistivity contour lines. This can obtain a lot of geological information in front of the tunnel working face, and the interpretation results will become more complete and accurate.

In order to make TEM interpretation more accurate and reliable, apart from enhancing the SNR from signal acquisition, in the use of the equivalent conductance plane based on the genetic algorithm, the apparent resistivity section contour and the apparent longitudinal conductance differential imaging should be combined for interpretation. At the same time, the interpretation should closely combine with the geological and drilling data; as a result, the interpretation will become more accurate and effective.

Acknowledgements

The authors wish to acknowledge the funding support from 863 Research Development Plan Under grant no. 2007AA11Z131; National Natural Science Foundation of Special Funds for Equipment Under grant no. 50727904; Post-Doctoral Innovative Projects In Shandong Province Under grant no. 200703076.

References

1. Li, S.H., Li, S.C. and Zhang, Q.S., et al. Forecast of karst fractured groundwater and defective geological conditions. Chinese Journal of Rock Mechanics and Engineering, 2007, 26(2):217-225.
2. Li, S.S., Xue, Y.G. and Zhang, Q.S., et al. Key technology study on comprehensive prediction and early-warning of geological hazards during tunnel construction in high-risk karst areas. Chinese Journal of Rock Mechanics and Engineering, 2008, 27(7):1217-1307.
3. Wang, M.S. Hydrogeological and geological forecast of tunnel construction in the karst district. Railroad Survey, 2004, 1:7-10.
4. Li, X. Theory and application of transient electromagnetic sounding. Xi’an: Shanxi science & technology press, 2002.
5. Niu, Z.L. Theory of time domain electromagnetic. Chang sha: Zhongnan university press, 2007.
6. Li, X. and Guo, W.B. Application of TEM to exploration of water gushing channel way in coal field. Journal of Xi’an Engineering University, 2000, 22(3):35-38.
7. Wu, Y.X. The transient electromagnetic method investigate application in yichang wanxian railway maluqing tunnel. Chinese journal of engineering geophysics, 2007, 4 (1):21-26.
8. Duan, Z., Li, T.B. and Li, Y.S., et al. Application of transient electromagnetic methods geological forcast technology in Tong Luoshan. Modern tunnelling technology, 2008, 45(2):45-62.
9. Tang, X.G., Hu, W.B. and Yan, L.J., et al. Transient electromagnetic response to a 3-D thin plate in a layered earth. OGP, 2000, 5(5):628-633.
10. Xue, G.Q. and Deng, X. Capacity of Transient Electro-Magnetic (TEM) method for detecting thin layer. 2007, 42(6):709-713.
11. Xue, G.Q. and Li, X. The technology of TEM tunnel prediction imaging. Chinese J. Geophys, 2008, 51(3):894-900.
12. Guo, C., Liu, B.Z. and Bai, D.H. Prediction of water disasters ahead of tunneling in coal mine using continuous detection by UWTEM. Sysmology and Geology. 2006, 28(3):456-462.
13. Li. X. Application of the adaptive shrinkage genetic algorithm in the feasible region to TEM conductance thin layer inversion. Applied Geophysics, 2005, 2(4):204-211.

RaSiM 7(2009): Controlling Seismic Hazard and Sustainable Development of Deep Mines, C.A. Tang(ed), Rinton Press, 473-482

DISCUSSION ON DYNAMIC MECHANISM OF ROCKBURST AND ADVANCE STRESS RELEASE METHOD IN ROCKBURST PREVENTION

QI-HU ZHU

State Key Laboratory of Water Resources and Hydropower Engineering Science, Wuhan University

Wuhan, 430072, P.R. China

WEN-BO LU

State Key Laboratory of Water Resources and Hydropower Engineering Science, Wuhan University

Wuhan, 430072, P.R. China

YI LUO

State Key Laboratory of Water Resources and Hydropower Engineering Science, Wuhan University

Wuhan, 430072, P.R. China

MING CHEN

State Key Laboratory of Water Resources and Hydropower Engineering Science, Wuhan University

Wuhan, 430072, P.R. China

Through analyzing the stress state of surround rocks, the spatial distribution of rockbust, the stability of tunnel wall and the relationship between rockburst and section area, the static load theory is not appropriate for investigating rockbust. To the underground projects excavated with the drilling and blasting method, the vibration damage induced by blast loading and high in-situ stress transient unloading is the key factor in gestation stage of rockburst. In this paper, the vibration of surrounding rock under different dynamic loads is studied by finite element method. It is found that the prevention mechanism of rockburst by advance stress release can be considered as the result of releasing high in-situ stress in steps, which reducing the vibration damage of surrounding rocks and restraining the gestation of rockburst to the maximal degree.

1 Introduction

Rockburst is a complex phenomena of instability in surrounding rocks[1], of which the process can be divided into two basic stages, the process of gestation, i.e. the gradual damaging process, in which the crack is generating and expanding, and the process of eruption, i.e. the release of residual strain energy, in which the rock mass loses its stability[2].

Rockburst causes not only overexcavation, threat to the safety of constructors and equipments, but also, when it is severe, causes earthquake, thus is attracting people's attention. Over decades, numerous rockburst data were recorded by the scholars and engineering technicians over the world on the type of surrounding rock, the characteristic of in-situ stress, the spatial distribution of rockburst events, the feature of rockburst pit and fragmentation, the sound emission of rockburst process, electromagnetism radius and micro seismic vibration, etc[3~4]. But until now, there is no complete and reasonable explanation of this phenomena, which is to say that, no complete acknowledge is formed about the generating mechanism of rockburst. It is also because of the retardation of the study on the mechanism, that slows down the development of prevention technology over rockburst on the basis of it, causing severe rockburst accident in large-scale underground projects[5].

2 The static load theory and limitation in rockburst study

2.1 Strength theory of rockburst

It is believed by strength theory that, the rockburst is the damage occurring when the redistribution of stress reaches the strength of the rock mass. Its major idea is that the load is close to strength, and is generally judged by σ_θ / R_c, where σ_θ is the tangential stress of the surrounding rock and R_c is the uniaxial compressive strength of the rock mass. The stress state in rockburst of several actual engineering examples is given in Table 1, which shows that σ_θ is below or far below R_c when rockburst took place in most of the projects. After excavation of underground project, the stress on surrounding rock is redistributing, and σ_θ is increasing. However, according to the Mohr-Coulomb criteria, the increase is not enough to crush the surrounding rock. The explanation in paper [6] is that, because of the size effect, the strength determined indoor is much higher than it actually is. When rockburst takes place, it is believed that σ_θ is still close to the strength of rock mass. Indeed, the size effect in joint rock mass is obvious, but it is indicated by large amount of actual data[7] that, most rockburst, especially those severe, were generated in the surrounding rock of high density and no crack, sharing the patten of higher strength with higher severity. So, even the size effect exists, rockburst is not the damage in which stress is close to the strength. All the above shows that, as a type of surrounding rock instability, rockburst should have other forming mechanism besides static compression and shear damage.

Table 1 Examples of rockburst in engineering

Project name	σ_θ (MPa)	R_C (MPa)	σ_θ / R_c	Rockburst
Diversion tunnel of Tianshengqiao-Ⅱ hydropower station	30.0	88.7	0.34	moderate
Diversion tunnel of Jinping-Ⅱ hydropower station	98.6	115.0	0.82	moderate or weak
Diversion tunnel of Yuzhixi hydropower station	90.0	170.0	0.53	moderate or weak
Sewage tunnel, Norway	75.0	180.0	0.42	moderate
Kan-etsu tunnel, Japan	89.0	236.0	0.38	moderate or strong
Huggura road tunnel, Norway	62.5	175.0	0.36	moderate
Tunnel of forsmark nuclear power station, Sweden	50.0	130.0	0.38	moderate
Erlangshan road tunnel, K261+939	40.1	77.0	0.52	moderate

2.2 Spatial distribution of rockburst

The spatial distribution of rockburst is always attracting attention in projects, and lots of precious data is accumulated. Most of rockburst occurs within a certain distance to tunnel face, peak section is moving forward while the tunnel face is. The rockburst occurred in the diversion tunnel of Tianshengqiao hydropower station is mainly within the distance of 5~10m to the tunnel face[8], and is of 2~10m in the left bank diversion tunnel of Ertan hydropower station. The rockburst is the most strong after the excavation, and is weakened gradually[9].

Under current technical condition, the circular footage of drilling and blasting method is around 3~5m, for 6~7h in time. The larger is the section area, the longer is the circular time. That is to say, after the blasting, there is enough time for the stress adjustment in surrounding rock within the current blasting footage. So according to the static theory of rockburst, rockburst should happen mainly in the current blasting footage, instead those finished. The actual spatial distribution of rockburst illustrates that rockburst should have other mechanism besides static theory.

2.3 Stability of surrounding rock with TBM excavation and extra-deep borehole wall

After concluding the conditions of rockburst in various underground engineering home and abroad, it is pointed out by paper [7] that, under the same geological condition, it is possible for the tunnel with TBM excavation not to have rockburst, while to have for that with drilling and blasting method. The above theory is matched by relative rockburst data in the excavation with TBM and drilling and blasting method in Qinling extra-long tunnel Line Ⅰ and Ⅱ[10], which is hard to be explained by the static load theory of rockburst.

Required by the study and develop of technology, extra-deep borehole is used more and more popular. It is not rare to find a oil prospecting borehole deeper than 5000m, but their walls are rarely crushed by stress[11]. The extra-deep borehole, KTB, in Bavaria, Germany, was 9100m deep, and its complete hard rock was not crushed by high in-situ stress[12]. In the 1990s, there were over 1500 extra-deep boreholes over the world. The wall stability of extra-deep borehole shows that, for complete surrounding rock, as long as the disturbance to the surrounding rock in the excavation is small enough, even if the tangential stress is far over the compression stress of rock mass, it is not necessary to have brittle failure. The static load theory can't form a complete knowledge of the generation of rockburst yet.

2.4 Relationship between rockburst and section area

Large amount of rockburst data reveals that, tunnels with larger section area are more apt to have rockburst or greater rockburst in excavation. It is pointed out by paper [9] that, in excavating the diversion tunnels, the level of intensity and frequency of rockburst is obviously more than that in excavating pilot headings. According to elastic mechanics theory, after the excavation of underground projects with round section, tangential stress of surrounding rock on or around the contour is independent to the diameter of the section, which can't explain the rockburst phenomena above.

3 Dynamic mechanism of rockburst

Static load theory has important meaning in the study on rockburst, but it can't explain all the mechanism of rockburst. Lithology, in-situ stress and stress adjustment induced by excavation are the background and basis of rockburst generation. However, other factors should be there besides these.

In the drilling and blasting excavation, blast stress wave, which is produced by initiation of blasthole, will certainly damage the rock mass around the excavation face, such as extension and expansion of existing cracks, formation of new cracks, decrease of sonic wave speed of rock mass, increase of seepage coefficient and so on. The blasting excavation of rock mass, companied by rock fragmentation and piling, accomplished the transient unloading of in-situ stress on the contour. The study of Lu Wenbo, etc.[13~14], shows that under medium or high stress condition, the vibration induced by transient unloading of in-situ stress can not be ignored in the response of surrounding rock, and can even be the key factor in controlling the vibration on surrounding rock. So, the vibration induced by in-situ stress transient unloading will do further damage on the surrounding rock. In the mean time, the stress wave produced by the rockburst itself, the excavation disturbance and so on will also overlay on the surrounding rock, intensifying the damage. Macro damage might not be done by single act of the above dynamic load, but multiple disturbance of stress wave will induce accumulative damage and deterioration of local environment in micro, mesolevel dimension. These can be concluded as dynamic problems of rockburst gestation, damage of rock mass is the key factor of forming rockburst. With the ongoing increase of rock mass damage, finally, the large-scale dynamic expansion of cracks is caused, accompanied by strain energy transient release, the surrounding rock lose its stability in form of rockburst, it can be concluded as the dynamic problems in rockburst eruption. The peak vibration velocity is well related with the damage it dose on rock mass. In projects, the peak vibration velocity is taken as monitoring and controlling criteria to surrounding rock. With dynamic finite element method, the surrounding rock response under blast loading and transient unloading of in-situ stress is studied, the effect of the rock mass damage induced by dynamic load in the gestation stage is discussed.

3.1 Calculation model of surrounding rock vibration induced by dynamic load

Blast loading and in-situ stress transient unloading are both belonging to dynamic load when excavation under high in-situ stress[15]. Consider excavating a circular tunnel with small section area in infinite rock mass under static water pressure, and it is formed by full-face blasting, plane strain model is approximately taken. As shown in Figure 1, to simplify the process, the diameter of the tunnel is taken as 10m, surrounding rock is taken as granite with density of 2700kg/m^3, elastic modulus of 44.2GPa, Poission ratio of 0.23, longitudinal wave speed of 5250m/s. On the tunnel face, there arranged namely 2 rounds of cut holes, 3 rounds of breaking holes, 1 round of buffer holes and contour smooth blasting holes, short-delay blasting is designed with an interval of 25~50ms from center to edge.

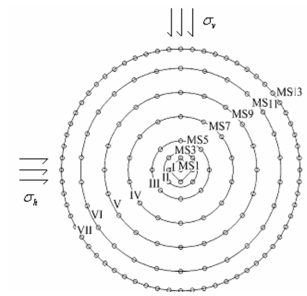

Figure1 Blasting design for tunnel excavation

3.2 Blast loading

Adopting sectional short-delay blasting in rock mass excavation, the energy of vibration induced by blasting can be distributed in time and space. Along with the development of blast material and accessary, parameter design and construction techniques, acceptable effect of controlled short-delay blasting can be achieved in engineering, so it can be confirmed that the initiation of blastholes are carried out in layers, and the blast loading produced is affecting the reserving rock mass alone. Triangle blast loading as in Figure 2 is adopted in analysis, t_r and t_d are relatively the rising time and positive pressure time. It is indicated that[16] the duration of pressure is about hundreds of milliseconds.

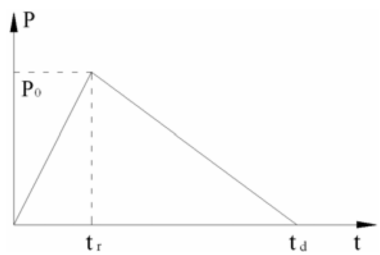

Figure 2 Blast loading assumed

Table 2 blasting parameters and calculated blast loading

Blasthole sequence	Blasthole type	Loading radius r_i (m)	Charge diameter (mm)	P_0 (MPa)	Equivalent blast loading *(MPa)
I	Cut holes	0.70	42.0	1445.0	50.00
II	Cut holes	0.80	42.0	1445.0	42.73
III	Breaking holes	1.20	32.0	282.7	12.60
IV	Breaking holes	2.20	32.0	282.7	12.02
V	Breaking holes	3.20	32.0	282.7	11.81
VI	Buffer holes	4.20	28.5	141.1	5.84
VII	Smooth blasting holes	5.00	20.0	43.6	3.73

In calculating the dynamic response of surrounding rock induced by blast loading, the blast loading of every delay of detonator is regarded as acting equally on the line of blastholes, to reduce calculation work. According to the blasting parameters and the formula mentioned in paper [6], the calculated result of the equivalent blast loading of each round of blastholes are shown in Table 2, while t_r and t_d are relatively taken as 0.10ms and 0.60ms.

3.3 Excavation Load

By analysing the mechanical process of rock mass in-situ stress unloading, Lu Wenbo[17] calculated the duration of excavation unloading of in-situ stress, that the unloading duration of open-pit bench blasting excavation is about 10~100ms, and that of full-face tunnel excavation is shorter than of deep hole bench blasting. It is obvious that the duration of excavation unloading is much longer than blast loading, while the purpose of millisecond delay time is to separate the dynamic effect of blast loading in each delay. So the additional effect of transient unloading of each layer can't be avoid, resulting the detonation of next round of blastholes before complete unloading of current layer. Therefore, after the detonation of contour blastholes, the in-situ stress unloading on the excavation contour can be regarded as a one-time unloading controlled by contour blastholes, as shown in Figure 3. In calculating the dynamic response of surrounding rock induced by transient unloading of excavation load, the stress curve on excavation contour is presented by Polygonal Line①, which is the composition of far field stress (Line②) and unloading curve③.

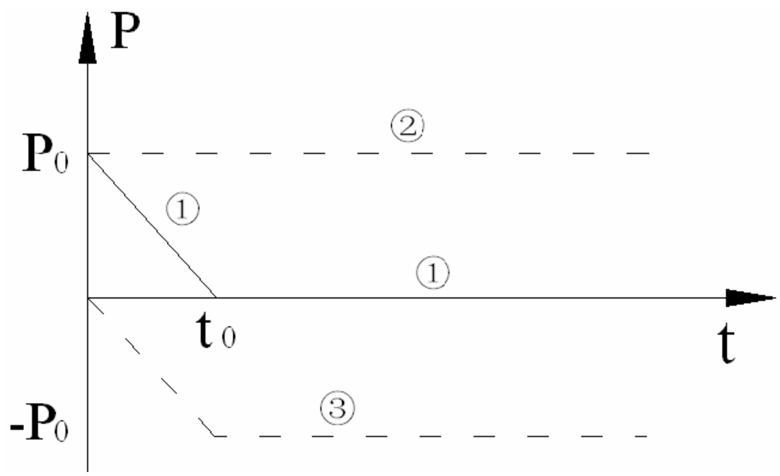

Figure3 The transient unloading of in-situ stress

The duration of in-situ stress unloading, t_0, can be calculated by crack extending velocity between blastholes after the detonation of contour holes, the transgression velocity of high temperature and high pressure gas, as well as the unloading wave transmission velocity in blasting gas[17]. With regard to the feature of the lay-out of the blastholes in the example of this paper, the unloading duration of the contour blasthole is 5ms.

3.4 Surrounding rock vibration induced by dynamic load

It is shown in Figure 4 and Figure 5 the surrounding rock peak particle velocity (PPV) induced by blast loading and transient unloading of excavation load under different in-situ stress condition.

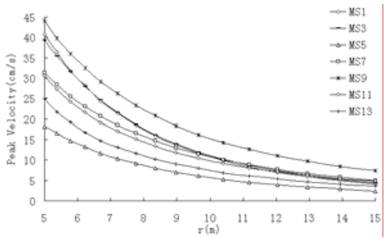

Figure4 Attenuations of radial PPV induced by blast loading

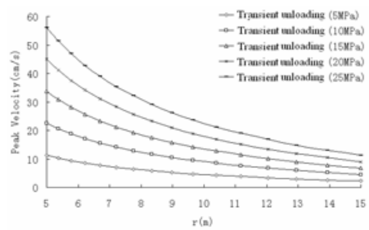

Figure5 Attenuations of radial PPV induced by transient unloading of in-situ stress

According to Figure 4 and 5, through comparing the PPV induced by blast loading and excavation load, the dynamic effect under different in-situ stress condition can be evaluated quantificationally.

The higher is the in-situ stress level, the greater is the PPV induced by transient unloading of excavation load. When the in-situ stress is 20MPa, the PPV induced by excavation load is more than that induced by blast loading.

In drilling and blasting excavation, blast loading will certainly cause the damage on surrounding rock. Under high in-situ stress condition, we can't ignore the vibration of surrounding rock induced by excavation load, which will necessarily aggravate the damage. The gestation process of rockburst is just the development of the damage on surrounding rock. In drilling and blasting excavation of underground projects, the dynamic effect of blast loading and excavation load together induced rockburst, and that is a good explanation to the question why there is much lower chance of rockburst in TBM excavation than in drilling and blasting excavation. It is also indicated by calculation that, the higher is the in-situ stress the higher the chance of rockburst is.

4 Application of advance stress release in rockburst prevention

While full-face drilling and blasting excavation would do more disturbance on surrounding rock and be more apt to induce rockburst, advance release of initial in-situ stress can be adopted in preventing rockburst. In Qinling Zhongnan mountain extra-long tunnel excavation, the full-face excavation is replaced by pilot heading excavation to release in-situ stress in steps, relieve the hazard of rockburst. There was a section of 510m, where pilot heading was adopted and great effect was achieved[18]. In excavating the diversion tunnel of Yongle hydropower station, severe rockburst occurred, pilot heading excavation was adopted in preventing rockburst[19].

Model is established as in Figure 6 to analyse the effect of advance stress release in preventing rockburst. The physical and mechanical parameters of rock mass and calculation condition are the same with the example in Section 3, while the radius of pilot heading is R. First excavating the pilot heading, then expanding the pilot heading to contour designed, so in-situ stress is released in two steps, and the vibration on surrounding rock is induced. Figure 7 shows the change of PPV induced by pilot heading excavation and tunnel expanding excavation with the variation of R.

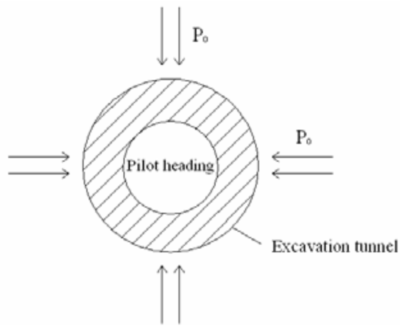

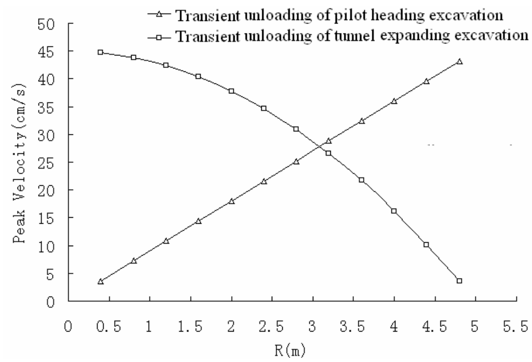

Figure6 The model of pilot heading

Figure7 Attenuations of radial PPV induced by transient unloading of in-situ stress

Known from Figure 7, release the in-situ stress in steps can reduce the vibration of surrounding rock greatly. With the radius of pilot heading increasing, vibration of the surrounding rock induced by pilot heading excavation is increased, while that induced by tunnel expanding excavation is reduced. Neither too small nor too large is the radius of pilot heading can't efficiently reduce the vibration. When the radius of pilot heading is 3.1m, the vibration on surrounding rock induced by excavation load is minimum, and the pilot heading has the best prevention effect.

The mechanism of advance stress release preventing rockburst is to release high in-situ stress in steps, reducing the vibration of surrounding rock induced by excavation load transient unloading and the damage on rock mass, and restraining the gestation of rockburst greatly, so as to prevent rockburst efficiently.

5 Conclusions

(1)A large amount of rockburst data is analysed, it is indicated that static load theory has significant meaning to rockburst research, while has obvious limits. Rockburst should be defined as a dynamic problem of damage accumulation and transient crack extension on large scale.

(2)The vibration of surrounding rock induced by dynamic load is studied by FEM, the results show that rockburst is result by a combined action of blast loading, excavation load and other dynamic load. The more is the surrounding rock disturbed by the excavation, the higher is the chance of rockburst.

(3)Advance stress release has obtained good effect in preventing rockburst. With the result of FEM calculation, the mechanism of preventing rockburst by advance stress release is well understood. Through the release of high in-situ stress in steps, the vibration on surrounding rock induced by transient unloading of excavation load is reduced, and so is the disturbance on rock mass.

This paper is only a initial discussion on the dynamic mechanism of rockburst. Further studies are needed on important problems such as the extent of damage on surrounding rock induced by dynamic effect, the dynamic criterion of rockburst, the optimized design of pilot heading and so on.

Acknowledgements

The work was subsidized by the National Science Fund for Distinguished Young Scholars(Project 50725931), the National Natural Science Foundation of China(Project 50779050) and the National Natural Science Foundation of China(Project 50639100).

References

1. Xu, L.S., Wang, L.S. and Li, Y.L.Study on Mechanism and Judgement of Rockburst. Rock and Soil Mechanics, 2002, 23(3). 300–303.
2. Sun J.S., Zhu Q.H. and Lu, W.B. Numerical Simulation of Rock Burst in Circular Tunnels under Unloading Conditions. Journal of China University of Mining & Technology, 2007, (4). 552-556.
3. Corner, B. Seismic Research Associated with Deep Level Mining: Rock Burst Prediction and Vibration Damage to Buildings in South Africa. Geophysics, 1985, 50(12). 2914-2915.
4. Rudajev, V. and Sileny, J. Seismic Events with Non-shear Component Ⅱ: Rock Bursts with Implosive Source Component. Pure and Applied Geophysics, 1985, 123(1). 17-25.
5. Baumgardt, D.R. and Leith, W. The Kirovskiy Explosion of September 29, 1996: Example of A CTB Event Notification for A Routine Mining Blast. Pure and Applied Geophysics, 2001, 158(11). 2041-2058.
6. Dowding, C.H. adn Andersson, C.A. Potential for Rock Bursting and Slabbing in Deep Caverns. Engineering Geology, 1986, 22. 265-279.
7. Guan, B.S. and Zhang, Z.Q. Study on Basic Conditions of Rockburst in Tunnel. Journal of Railway Engineering Society, 1998, (Supp). 326-330.
8. Zhang, J.S., Lu, J.Y. and Jia, Y.R. Study on Rockburst in Diversion Tunnel of Tianshengqiao-Ⅱ Hydropower Station. Water Power, 1992, (3). 34-37.
9. Shi, H.G. Analysis of Rockburst in Diversion Tunnel of Ertan Hydropower Station. Design of Hydroelectric Power Station, 1995, 11(3). 34-40.
10. Zhang, K.C., Zeng, J.F. and Zhang, J. et al. Countermeasures for TBM Passing Through Rock-blasting Section in Qinling Tunnel. Modern Tunnel Technology, 2000, 21(4). 34-38.
11. Li, J.Y., Guo, D.R. and Qiu, Z.S. et al. Research and Development Trend of Borehole Stability. Journal of China University of Petroleum(Edition of Natural Science), 1993, 17(Supp). 85-92.
12. Cai, X.L. The Progress of Contineental Deep Drilling Program of The Federal Republic Germany. Geology-geochemistry, 1992, (6). 30-33.
13. Lu, W.B., Jin, L. and Chen, M. et al. Study on the Mechanism of the Loosing of the Jointed Rock Mass Caused by the Dynamic Unloading of Innitial Stress During Rock Blasting. Chinese Journal of Rock Mechanics and Engineering, 2005, 24(Supp.1). 4653-4657.
14. Lu, W.B., Chen, M. and Yan, P. et al. Studr on Cibration Characteristics of Surrounding Rock Induced by Tunnel Excavation Under High In-situ Stress. Chinese Journal of Rock Mechanics and Engineering, 2007, 26(Supp.1). 3329-3334.
15. Yan, P. Study on Mechanism of the Vibration Induced by Dynamic Unloading During Rock Excavation. Wuhan: Doctoral Dissertation of Wuhan University, 2008.
16. Lu, W.B. and Tao, Z.Y. Theoritical Analysis of the Pressure-variation in Borehole for Pre-spliting Explosion.

Explosion and Shock Waves, 1994, 14(2). 140-147.

17. Lu, W.B., Zhou, C.B. and Chen, M. et al. Research on Transient Characteristics of Excavation Unloading. Chinese Journal of Rock Mechanics and Engineering, 2008, 27(11). 2184-2192.
18. Guo, Z.Q. Rockburst and Countermeasures in Zhongnanshan Highway Tunne. Modern Tunnelling Technology, 2003, 40(6). 58-62.
19. Yan, Z.H. Forecast and Treatment of Rock-burst in Tunnel Construction. Journal of Shijiazhuang Railway Institute, 2003, 7. 34-36.

RaSiM 7(2009): Controlling Seismic Hazard and
Sustainable Development of Deep Mines,
C.A. Tang(ed), Rinton Press, 483-490

APPLICATION OF MICROSEISMIC MONITORING TO CHARACTERIZE OVERBURDEN MOVEMENT IN ISOLATED LONGWALL MINING

AN-YE CAO

State Key Laboratory of Coal Resource and Mine Safety, China University of Mining & Technology

Xuzhou, 221008, P.R. China

LIN-MING DOU

State Key Laboratory of Coal Resource and Mine Safety, China University of Mining & Technology

Xuzhou, 221008, P.R. China

YUN QU

Baodian Coal Mine, Yanzhou Mining Group

Zhouchen, 273513, P.R. China

HENG JIANG

State Key Laboratory of Coal Resource and Mine Safety, China University of Mining & Technology

Xuzhou, 221008, P.R. China

Characterization of rock failure propagation is one of the most essential requirements in mine microseismic (MS) monitoring for dynamic hazard prevention. This paper illustrates the application for MS monitoring to characterize the fracture process associated with overburden movement in the mining progress of LW10302, an isolated working face in B.D. Coal Mine. The results show that the seismic signals correspond to the different failure mechanisms which show different characteristics in waveform features, and have demonstrated that fracture propagation monitored by MS monitoring fits well with the movement of the overburden structure. The study will greatly benefit the understanding of stress distribution around the longwall face and the control of rock burst hazards in mines.

1 Introduction

The safety and productivity of underground mining can be severely impacted by seismic activity. Mining-induced seismic events, which are induced by the sudden release of elastic strain energy in rock mass, are associated not only with superficial structure movement triggered by new stress concentration with mining operations, but also related to large geological discontinuities, affected by the extent and means of mining [1]. Rock bursts are particular cases of seismic events induced by mining activity that results in damage to underground workings and in some cases, injury and loss of life [2]. Since the first report of destructive seismicity (rock burst) in a South Stanford Coalmine in Britain in 1738, mining-induced tremors have been recorded and reported in many countries. The occurrence of rock bursts has become the most serious and least understood problem in deep mining operations throughout the world [3].

In China, the key problem of rock burst control is the lack of effective and reliable monitoring network in most mines. Many monitoring technologies, such as electromagnetic emission (EME), seism-acoustic emission (AE), drillings, et al, have been conducted in an effort to evaluate and forecast the dynamic hazard [4]. However, due to the limited monitoring range or no continuous data recording, the effective prediction and control of rock burst is still a challenge using the above methods.

Microseismic (MS) monitoring, which has retained the attention of much of the scientific and engineering communities this years, has been proven as a powerful tool to quantify mining-induced seismicities and can contribute valuable information to the studies on mining dynamic hazard prevention. The significant advantages of this technology are its remote, safe and real-time monitoring, accurate 3D location and multiple parameters determination.

In the last 10 years, rock bursts and strong tremors exist in several coal mines in Yanzhou Mining Group, and the problems become progressively more severe as the mining depth and the volume of extraction increase. This paper uses MS monitoring as the major investigation tool, and try to have a better understanding of the fracture propagation and overburden movement in the mining process of LW10302, an isolated working face in B.D. Coal Mine.

2 Description of the site

B.D. Mine has a coal production history for about 20 years and the production now has exceeded 6 Mt per year. As the mining depth and intension increase, strong mining-induced tremors have been a major dynamic hazard in recent years. The strongest tremor monitored by the local seismology network on Sep 6th, 2004 had the magnitude M_L=3.7, which shook the ground and made the abutment pressure underground increased largely.

The main working face now, LW10302, which mined the Upper No.3 coal seam, is an isolated working face surrounded by three sides mined areas in its early mining period. As shown in Figure 1, LW10301 on the north (the first face mined in No.10 Mining District) has mined both the Upper and Lower No.3 coal seams, while LW10303, 10304 and 10305 on the south side have just mined the Upper No.3 coal seam. After LW10302 was retreated about 570m (Since 1 Jan, 2009), both the Upper and Lower No.3 seams in LW10303 and other faces on the south side haven’t been mined.

The Upper No.3 coal seam of about 5.8m thickness is being mined some 460m below the ground surface. The immediate roof of about 3 m thickness is mainly composed of siltstone, while the main roof strata is composed of medium sandstone, with the thickness of 16m. Additionally, there is a key fine sandstone stratum of nearly 200m in thickness (which is called primary key strata), approximately 135m above the coal seam. The strength of the fine sandstone roof is high with UCS values over 80 MPa. In the mining process, the primary key strata overlying the isolated and surrounding faces moved together and ruptured drastically and frequently. A certain amount of strong tremors induced by the key strata fracturing were recorded.

3 Installation of the MS Monitoring System

A microseismic monitoring study was carried out in B.D. Mine since 1 Jul, 2008. The monitoring system "SOS" is produced by Central Mining Institute in Poland. It provides an efficient tool for transmission, recording and analysis of seismic events that occurred in mining process. It comprises 20 single component geophones (DLM 2001), DLM-SO Receiving Station and AS-1 Seismic Recording System. The geophone has a natural frequency of 4.5 Hz and velocity sensitivity of 32 V/m/s. Fifteen of the geophones were installed underground on the bolt inserted and glued into the floor to a depth of 1.5 m, while other five ones (N0 9, 10, 18, 19, 20) were installed on the ground surface. The microseismic data captured by the geophones was transmitted in the form of current signals via cables to the receiving station which is connected with the seismic recording system. The geophone configuration covers major mining areas and it was hence expected that the rock fracturing associated with mining progress can be detectable.

The following data acquisition parameters were set for the monitoring experiment: Gain=1, Sampling frequency=512Hz, recording length=12s, P-wave velocity =4100 m/s underground and =2450 m/s on the surface. The microseismic system was in good operational condition during the monitoring period. In the last 8 months, more than 7500 seismic events associated with roof and floor breakages were recorded and located, revealing detailed fracturing patterns around LW10302 and surrounding faces.

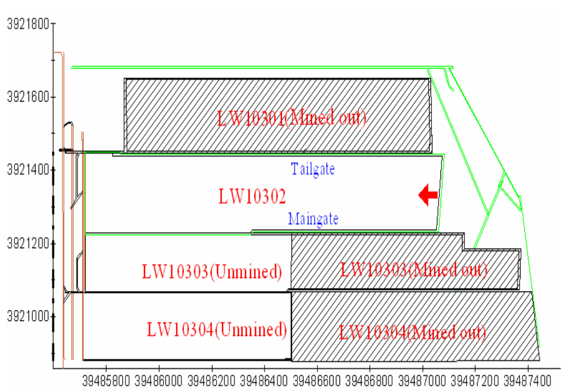

Figure 1 Layout of LW10302 and surrounding faces

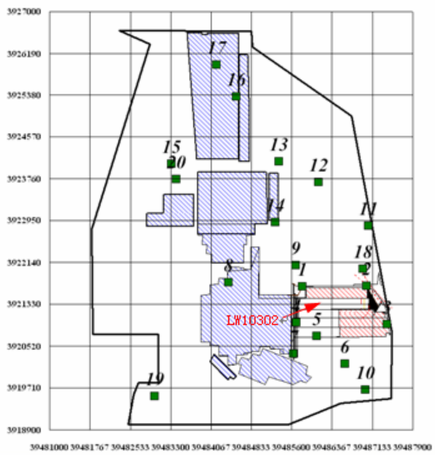

Figure 2 Configuration of the geophone stations in B.D. Mine

4 Characterization of seismic events

Seismic events recorded around LW10302 between 1 Jul, 2008 and 28 Feb, 2009 have been processed (LW10302 had been retreated about 860m). Most of the sources radiated energies ranging from 10^2 to 10^4J. 33 strong tremors with the energies released over 10^5J have been located, revealing the overburden movement of the overlying key strata.

The signals corresponding to different failure mechanisms show different characteristics in frequency, waveform duration, energy released, et al. Therefore, the events recorded around LW10302 can be classified into 3 groups in terms of energy radiated and waveform features.

(1) Low energy events (10^2~10^4J)

A considerable number of the low energy events were recorded throughout the mining process. Most of them were located behind the retreat line of working face and moved with the advance of the face. The low energy events are characterized by dominant frequency of 0-40Hz, short waveform duration of 500~2000ms and maximum amplitude order of 10^{-6}~10^{-5}m/s (Figure 3). In addition, these events always have clear P-wave arrivals and the ratio of S- to P-wave energy (E_S/E_P) ranges from 3 to 10. The occurrence of the low energy events have demonstrated duo to tensile fracturing of the surrounding rock, such as roof caving, horizontal tensile crack, delamination, et al.

(2) Shear fracturing events (10^4~10^5J)

Nearly 60 events released energies ranging from 10^4-10^5J, which showed different waveform features from the low energy events. This type of events is mainly characterized by low dominant frequency of 0-20Hz, long waveform duration of 1000~3000ms and maximum amplitude order of 10^{-6}~10^{-4}m/s (Figure 4). These events present strong S-wave signals and small P-wave arrivals. E_S/E_P always ranges from 20 to 1000. The occurrence of these events may be the result of shear rupture of the inferior key strata (main roof, et al) and partial fracture of the super-thick primary key strata.

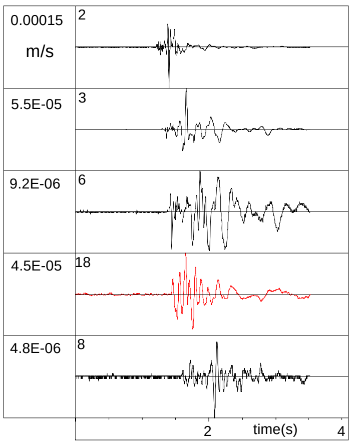

Figure 3 Typical low energy events recorded at 11:02:07 on 14 Nov, 2008 (E=7.20×10^3J, E_S/ E_P=3.6)

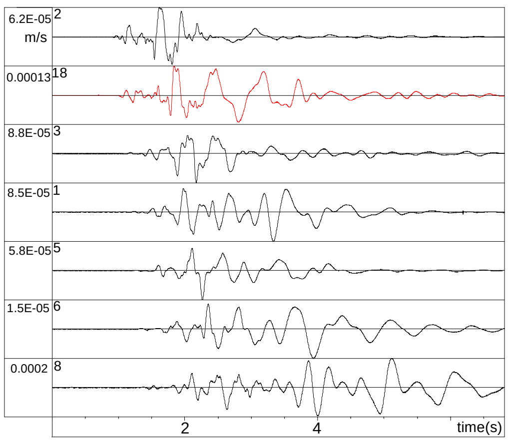

Figure 4 Typical shear fracturing event recorded at 01:37:45 on 15 Nov, 2008 (E=3.78×10^4J, E_S/ E_P=55.3)

(3) Strong tremors (>10^5J)

A certain number of strong tremors occurred during the mining process, which made the building on the ground shake slightly and the abutment pressure underground increase. Fortunately, these tremors didn't induce rock burst hazard and cause no injury underground. Most of the sources were located in the super-thick fine sandstone, which means the strong tremors are mainly the result of shear fracturing of the primary key strata. The tremors are characterized by lower dominant frequency of 0-5Hz, quite longer waveform duration, and much higher energy ranging from 10^5-10^7J (Figure 5).

5 Interpretation of microseismic activities

In general, the microseismicity observed was associated with longwall production (Figure 6). During the period when there was no production (18 Jul-19 Jul, 2008, 4 Jan-9 Jan, 2009, 26 Jan-29 Jan, 2009), the microseismic activity decreased significantly. There is evidence that fracturing detected around LW10302 through MS monitoring was induced by the mining activity.

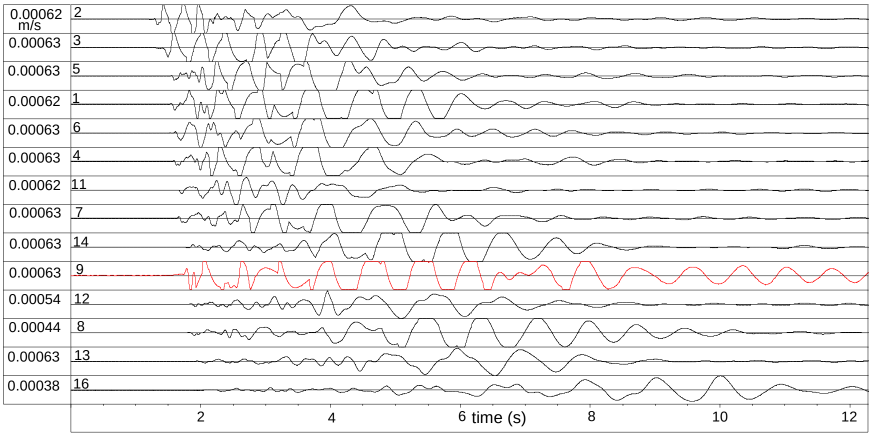

Figure 5 Typical strong tremor recorded at 01:37:45 on 15 Aug, 2008 (E=5.32×10^6J, E_S/ E_P=43.3)

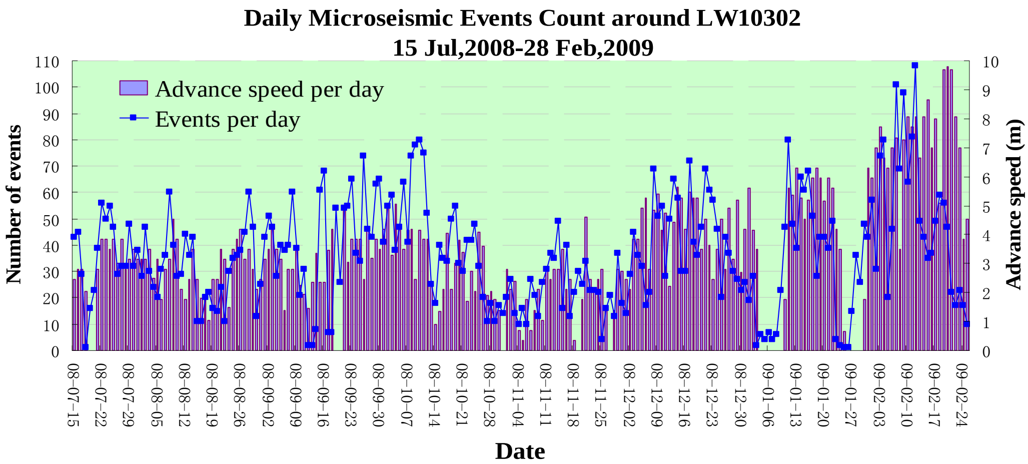

Figure 6 Daily numbers of events and longwall retreat speed for the monitoring period 15 Jul, 2008 to 28 Feb, 2009

Although both the Upper and Lower No.3 coal seam had been mined out in LW10301, the ratio of width to depth of the face is less than 0.5, which means the fracture height had just developed about 100-150 above the coal seam and there was almost no large fracturing in the super-thick primary key strata because of the limited mining area. Conversely, the total mining area of LW10303, 10304 and 10305 is so large that all the overlying strata had caved and ruptured fully, and the fracture height had developed to the ground surface [5,6]. Therefore, the overlying strata on the south side had no great impact on the mining of LW10302. After LW10302 was mined for a period, the overburden of LW10301 and 10302 would move together and make the risk of strong tremor, even rock burst be larger than the normal working face. Figure 7 shows the simple vertical cross-section view of the fracturing structure of the overlying strata before LW10302 was mined.

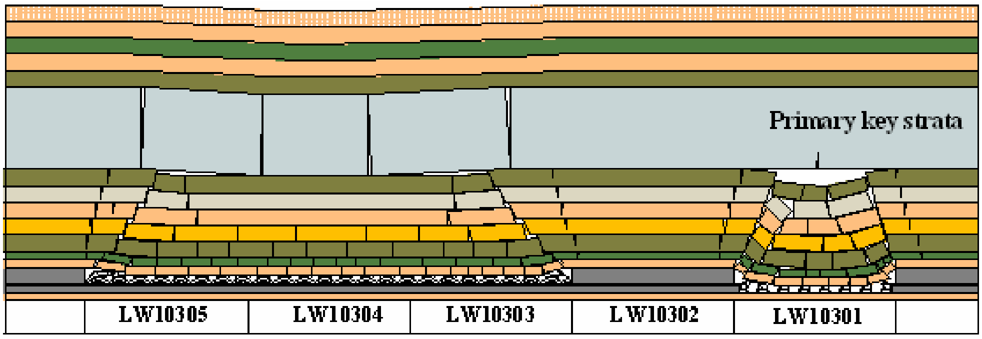

Figure 7 Vertical cross-section view of the strata structure, along vertical direction of the face, before LW10302 was mined

Shown in plan view of event (10^2~10^5J) locations relative to longwall process (Figure 8), from 15 Jul, 2008 to 28 Feb, 2009, most of the events occurred within the roof and floor of LW10301 and 10302. From 15 Jul to 31 Aug, 2008, an event trend can be viewed with an angle leaning backward about LW10302 and small amount of events started to occur within LW10301. Starting from 1 Sep, 2008, more events propagated within the surrounding strata of LW10301, and all the events moved forward with the advance of the face. Since 1 Dec, 2008, events occurred in a trend forward ahead of the faceline, which means the fractures extended gradually from caving zone to the abutment pressure zone. Since 1 Jan, 2009, LW10302 was retreated over the terminal mining line of LW10302, a small part of events occurred within the strata of LW10303, near the maingate side of LW10302. The changes of the event distribution revealed very detailed fracturing patterns within LW10302 and surrounding faces.

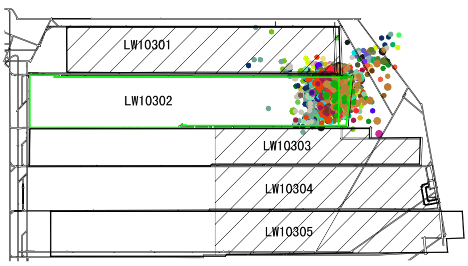

(a) 15 Jul- 31 Aug, 2008

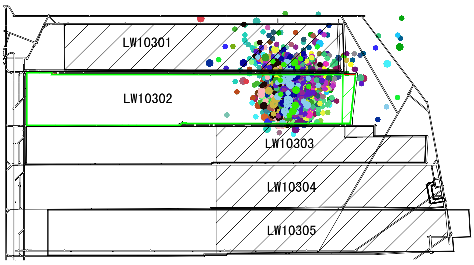

(b) 1 Sep- 31 Oct, 2008

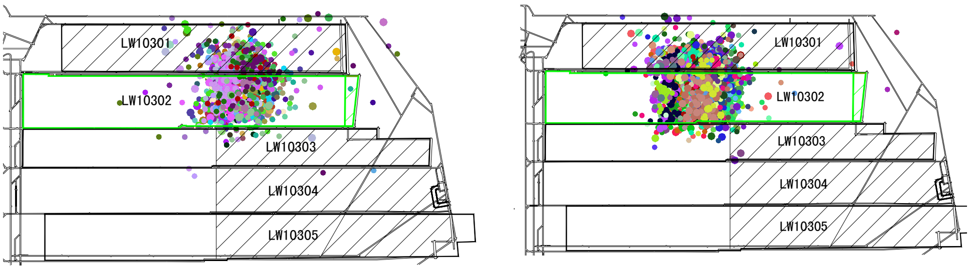

(c) 1 Nov- 31 Dec, 2008 (d) 1 Jan- 28 Feb, 2009

Figure 8 Plan view of event locations (10^2~10^5J), for the period 15 Jul, 2008- 28 Feb, 2009

Unlike the low energy events distributed within multiple roof and floor strata, the strong tremors were mainly associated with the large scale movements of the super-thick primary key strata. As shown in the plan view of the strong tremor locations (Figure 9), all of the tremors were located within LW10301 and 10302.Actually, strong tremors which relate to large fracture size can occur where the face interaction can allow failure zones to develop in the overburden as faces interacted. Obviously, the large overburden structure of LW10301 and 10302 can meet this condition. According to the source locations, the strong tremors occurred first above the caving zone of LW10301 and 10302. After the face was treated over 300m, some tremors started to occur ahead of LW10302. This means the key overburden started to rupture after it hanging over the caving zone for a certain length. The similar rupture process was repeated according to the strong tremors recorded.

On the vertical cross-section of event locations (Figure 10), looking along the face, all the strong tremors occurred within the primary key strata. This indicated that the strong tremors were mainly associated with shear fractures as a result of large scale key strata movements. In addition, the tremors gradually moved upward from the lower part of the key strata, and then downward again, which fits well with the changes of mining geometry of the interacted longwall faces.

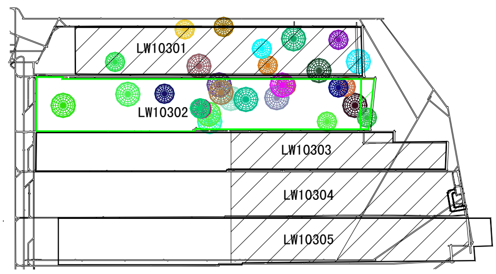

Figure 9 Plan view of the strong tremors, for the period 15 Jul, 2008- 28 Feb, 2009

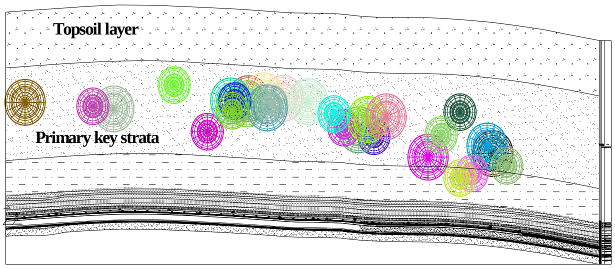

Figure 10 Vertical cross-section view of the strong tremor locations, along the face, for the period 15 Jul, 2008- 28 Feb, 2009

Nearly 200 large-diameter drilling holes (the diameter is 115mm, drilling depth is over 17m) were drilled into the coal wall of the roadways to relieve pressure in advance before LW10302 was mined. Additionally, most of the strong tremors occurred above the caving zone and were located far away from the working face, the energies radiated from the source attenuated largely before the seismic waves arrived at the coal seam. This may be the main factors why those strong tremors didn't induce rock burst and cause no injury underground.

6 Conclusions

In this paper, the analysis of microseismic events in the isolated working face, LW10302 in B.D. Coal Mine, indicates that MS monitoring can provide invaluable information to characterize the mining-induced seismicity and reveal the failure patterns in the roof and floor strata associated with longwall mining.

Different characteristics in waveform features and seismic energies were found between low energy events and strong tremors. Low energy events are mainly characterized by relatively high frequencies, short waveform duration, clear P-wave arrival, while strong tremors present much lower dominant frequencies, quite long waveform duration, developed code waves and strong S-wave components.

The study has demonstrated that fracture propagation fits very well with the movement of overburden structure and the stress regime around the face. In the mining process of LW10302, most of the events were located within the surrounding strata of LW10301 and 10302. In general, low energy events were distributed in multiple roof and floor strata, while the strong tremors occurred almost primarily within the super-thick key strata and appeared to relate to shear fracturing associated with large scale overburden movement.

The results indicate that source location is quite essential for the determination of failure patterns associated with mining, thus the improvement in source locating accuracy is still an important issue in MS monitoring. Further effort should be made to determine the failure mechanisms of the events and more information of the source needs to be obtained. Undoubtedly, more knowledge of the failure modes associated with mining will greatly benefit the alleviation and prevention of rock burst hazards in mines.

Acknowledgements

The authors wish to acknowledge the funding support from the National Basic Research Program of China (973) (2005CB221501), National Eleventh Five-year Key Science & Technology Project (2006BAK04B02, 2006BAK04B06) , National Natural Science Foundation of China (50474068) and State Scholarship Fund of China Scholarship Council ([2007]3020). In particular, we wish to thank Jiang He, Xue-feng Xu and Zheng-liang Zhang for their contributions to this research project.

References

1. He, X. S., Li, S.Y. and Pan, K. Mining seismicity, gas outburst and the significance of their relationship in the study of physics of earthquake source. ACTA SEISMOLOGICA SINICA, 2007, 20(3). 332-347.
2. Li, T., Cai, M.F. and Cai, M.A. review of mining-induced seismicity in China. International Journal of Rock Mechanics & Mining Sciences, 2007, (44). 1149-117.
3. Gibowicz, S.J. and Kijko, A. An introduction to mining seismology. San Diego: Academic Press, 1994.
4. Dou, L.M. and He, X.Q. Theory and Technology of Rock Burst Prevention. Xuzhou: China University of Mining and Technology Press, 200.
5. Xie, W.B., Chen, X.X. and Zhen, B.S. Study of the numerical simulation in engineering mining. Xuzhou: China University of Mining and Technology Press, 2005.
6. Zhou, Y.F., Hu, Y.F. and Guo, Z.Z. Mining-induced damage and its protection. Xuzhou: China University of Mining and Technology Press, 1996.

RaSiM 7(2009): Controlling Seismic Hazard and Sustainable Development of Deep Mines, C.A. Tang(ed), Rinton Press, 491-498

MECHANISMS OF HUMIDITY INDUCED DEFORMATION OF ROCK SALT

THOMAS SPIES & JÜRGEN HESSER

Federal Institute for Geosciences and Natural Resources (BGR), Hanover, Germany

In rock engineering, e.g. tunnelling, mining or underground disposal, deformation and stress have to be monitored to evaluate stability of cavities and hydraulic integrity of the rock mass. For the interpretation of such results and as a basis for the prognosis, laboratory investigations must be performed under defined loading by stress, temperature and humidity, to determine the material behaviour of the rock. Within this study a long-term laboratory test was performed to investigate the mechanisms of deformation of rock salt samples in connection with changes of humidity. In salt mines such humidity changes occur for instance as a result of ventilation or of backfilling of rooms using salt concrete. As known from former creep tests, the deformability of rock salt strongly increases at higher levels of humidity but it was not known by which mechanisms this is controlled. In the specially designed laboratory test acoustic emission and active ultrasonic measurements were used to characterize the damage evolution. The results document that increased humidity in the sample leads to an increase of ductility as well as to an increase of damage and cohesion loss.

1 Introduction

Underground cavities in rock salt are mined for mineral extraction, the storage of fluids and for the disposal of toxic or radioactive waste. The safe construction and operation of the cavities must be assured as well as the long-term safety after the closure of the workings. Therefore geomechanical investigations have to be performed with the aim to estimate and to predict the state of stresses and the deformations with regard to the mechanical stability and hydraulic integrity of the rock mass. Especially the detection and monitoring of zones with generation and development of microcracks or macrofractures are very important tasks in geomechanics which can be addressed by use of ultrasonic measurements very effectively [1].

Many investigations on the thermo-mechanical behaviour of rock salt were performed with the result that the physical mechanisms are well-known which control the distinct nonlinear behaviour of rock salt. They are described in different constitutive models with application in numerical codes [2], [3]. The influence of humidity on the creep deformation of rock salt was included in the constitutive model of [4]. On this basis reliable predictions of the deformation and stress behaviour in the long-term are possible.

But the question of understanding the influence of humidity on the ductility of salt and the evolution of the damage of the micro- and macrostructure still remains. This requires specific laboratory testing and field experiments. In this context acoustic emission measurements (AE) and active ultrasonic measurements are very useful methods as they provide results on damage of the rock with high sensitivity and resolution [1], [5].

2 Observation of Humidity effects on the deformation of rock Salt

The remarkable difference between rock salt and most other rocks is the fact that rock salt is capable of creep deformation under conditions of state existing in the depth of underground workings. In many investigations in the lab and in the field the non-linear creep behaviour has been observed and constitutive models were developed. The most important mechanism of creep in rock salt in the given range of conditions of state is the movement of dislocations in the crystals (dislocation glide). An often established relation for this creep mechanism is the combination of the Norton law for the stress dependence and the Arrhenius law for the dependence on temperature T. The following formulation was derived from uniaxial creep tests [4]:

$$\dot{\varepsilon}_{cr}(\sigma,T) = A \cdot exp[-\frac{Q}{R \cdot T}] \cdot [\frac{\sigma}{\sigma^*}]^n \qquad (1)$$

where έcr denotes the stationary creep (deformation) rate in 1/d, A is a factor considering the kind of rock salt under consideration (stratigraphy, distribution of grain size, amount of impurities, etc.) in 1/d, the activation energy Q has been determined to be 54 kJ/mol, R is the universal gas constant ($8.314 \cdot 10^{-3}$ kJ/(mol K), σ is the uniaxial load in MPa and σ* is the normalization stress of 1 MPa. The exponent n was determined to be 5. In tests investigating the influence of stress and temperature usually the humidity of the air in the test chamber is kept at a level of 45% relative humidity representing normal humidity conditions.

Variation of the humidity in the chamber leads to a large variation of the creep rates as a function of humidity [4]. Fig. 1 shows these results for a fixed mechanical load of 14 MPa at (fixed) room temperature in form of a factor which is the ratio of creep rates at a given humidity in relation to that in case of dry air (relative humidity r.h. = 0).

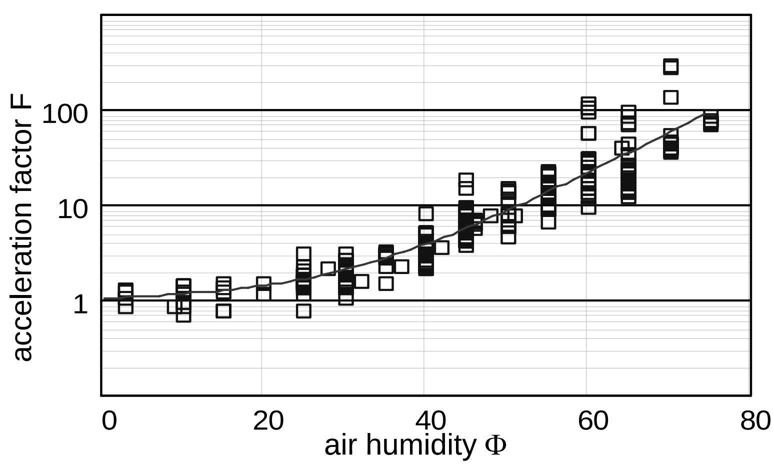

Figure 1 Results of uniaxial tests on rock salt samples with variation of relative humidity, load 14 MP: ratio of creep rates at a given humidity level to creep rate of dry air [4].

The line in the data scatter can be represented by the function $Fh(\Phi) = 1 + c_1 . \sinh(c_2 . \Phi)$, $c_1 = c_2 = 0.1$. Creep rate can then be written as:

$$\dot{\varepsilon}_{cr}(\sigma,T,\phi) = F_h(\phi) \cdot A \cdot exp[-\frac{Q}{R \cdot T}] \cdot [\frac{\sigma}{\sigma^*}]^n \qquad (2)$$

It can be stated that the influence of humidity on creep rates in the uniaxial tests is high as factors of increase amount up to more than 100.

Further evidence of humidity influence on the deformation of rock salt came from AE measurements in salt mines [6]. Fig. 2 shows an example of located events in a section of the Morsleben mine in Germany using

24 sensors. The measurements are performed in different mine sections and the results are used as a contribution for the evaluation of integrity and stability in the mine, for details see [7]. The rates of located AE events in Fig. 2 clearly show a seasonal variation in the time period from January 1998 to December 2002.

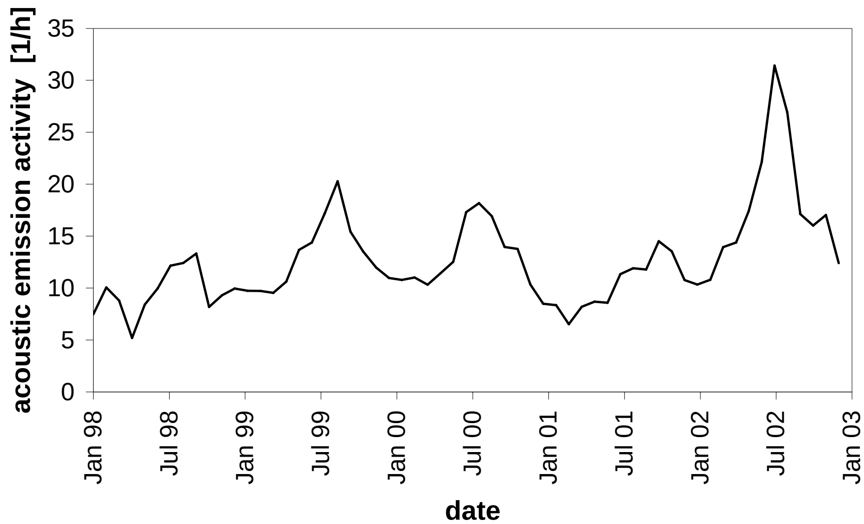

Figure 2 Seasonal variations of AE activity in a section of a salt mine (monthly average of AE rates).

In the months of summer the AE activity was high whereas in winter and spring it was low. A detailed evaluation of the AE locations showed that the additional events in summer are located in pillars and in the contour zones of the cavities. Because there was no mining activity in this mine section during the observation time, climatic conditions were assumed to influence the AE activity. Based on information from the staff of the repository, temperature changes could be estimated to by only about ±2 °C during the whole year in the mine section. But the relative humidity amounts to about 20 % r. h. in winter and increases up to 60 % r. h. in summer. This oscillation of the relative humidity correlates very well with the oscillation of the AE activity. Therefore significant influence of humidity due to seasonal variations on AE activity is concluded. Similar observations from long-term AE measurements in other salt mines were reported by [8] as well as from back filling of cavities in the Morsleben mine using salt concrete [7]. So it is expected that not only creep deformation rate is increasing as a result of higher humidity as shown by the creep tests in the laboratory but also the rate of microfracturing processes in the rock salt.

3 Aim and Layout of the laboratory investigation

In a specially designed laboratory test the question of the mechanisms leading to the observed effects was addressed. Can the observed increases of deformation rates and also microcrack activity be traced back to humidity induced processes in the structure of the rock salt accompanied by the increase of ductility as described by [9] or by a local reduction of the cohesion as described by [10]? The increase of ductility would be a consequence of several possible processes as humidity assisted recovery by the reduction of dislocation density and the removal of dislocation pile up or the process of pressure solution in the pore space (solution at stress concentrations and recrystallization in the pressure shadow). On the other hand local cohesion could be reduced by the weakening of ionic bonds of the rock salt lattice at the tips of microcracks where stress concentrations occur. At these locations of high surface energy films of adsorbed water may form and interact with the material. The increase of ductility acting alone would not imply irreversible increases of volume and damage in the rock in contrast to the loss of local cohesion. The aim of this study is the better understanding of the humidity induced processes in rock salt to be considered within the prediction of damage, integrity and stability in rock engineering projects.

The test should resemble conditions in the salt mine as close as possible. Because of the fundamental character of this investigation a sample of pure rock salt with a mid grain size was used to avoid effects due to complex mineralogical composition or complex distribution of grain sizes. With respect to former lab tests it was necessary to create stress states above the dilatancy boundary in stress space. Above this boundary microcacks form in the material resulting in an irreversible volume increase called dilatancy. Such stress conditions are met in the excavation damaged zone around and between cavities in the mine or at boundaries of materials with different mechanical behaviour. Thus humidity in from of vapour or brine films can penetrate into the structure of the rock salt sample especially into cracks or pores. Considering these items a deformation controlled uniaxial compression test was performed with a constant axial compression rate of $1{\cdot}10^{-8}$ s^{-1}. In contrast to creep tests at constant stress levels in this procedure the stress is increasing as a result of deformation such again resembling conditions in a salt mine where observed deformation rates due to the convergence of cavities are roughly constant after some month after construction. In the test radial deformation of the sample was measured as well to estimate volume change.

To qualify the humidity induced damage of the rock salt sample AE activity was monitored and ultrasonic travel times were measured. 12 small AE transducers of 8 mm diameter and 5 mm height were mounted at the surface of the cylindrical sample. The frequency range was between 100 kHz and 1GHz. The sample had a height of 25 cm and a diameter of 10 cm. The equipment was able to monitor AE rate in the sample and to conduct active ultrasonic measurements during mechanical loading between any combination of AE transducers, one acting as source and one acting as receiver. Active ultrasonic measurements were used to characterize damage in the sample by determination of the reduction of seismic velocities resulting from increasing damage caused by micro- and macrofracturing. Observing ray paths between all transducers offers the possibility to determine anisotropy effects caused by the damage. For each ray path between sources and receivers the seismic velocities v_P of P waves were determined once or twice a day using the determined travel times. In relation to the velocity at the beginning of the lab test, the velocity changes were determined as a function of time (or axial compression) to characterize the progress of the damage. This variation of the velocities was calculated using $\Delta v_{P,rel} = 100\ \% \cdot (v_P - v_{P0}) / v_{P0}$ where $\Delta v_{P,rel}$ the variation of seismic velocity in relation to velocity at the beginning of the lab test in %, v_P is the current seismic velocity in m/s, and v_{P0} is the seismic velocity at the beginning of the lab test in m/s. v_{P0} was in the range of 4500 m/s showing slight variations with ray paths.

The rock salt sample was situated in a climatic chamber with air conditioning to warranty defined test conditions of temperature and humidity. During the whole duration of the lab test constant temperature of 22 °C was maintained. In the first phase of the experiment relative humidity in the climatic chamber was kept constant at about 45 % r. h. until an axial compression of 1.8 % was reached. This was achieved after about 21 days under constant compression rate as mentioned above. From experience it could be expected that then cracks were generated in a sufficient amount and moisture could penetrate into the crack network of the rock salt sample. In the second phase of this experiment the relative humidity was raised to a value of 70 % relative humidity. This condition was held constant for about 4 weeks. At the end of this phase an axial sample compression of 4.1 % was obtained. After that humidity was reduced to a value of 45 % r. h. again in a time interval of about 3 days.

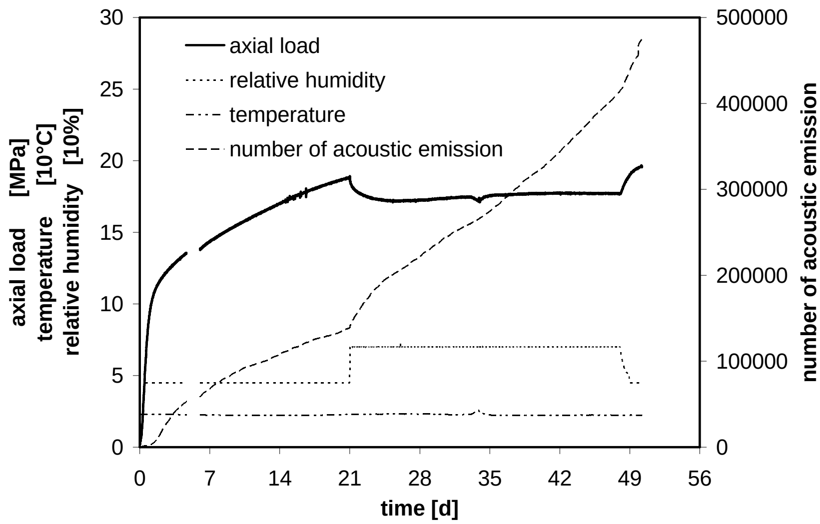

Figure 3 Axial load, temperature, relative humidity and number of AE.

4 Test results

Fig. 3 shows a compilation of data collected during the test as a function of time: axial load of the sample, temperature and relative humidity in the climatic chamber and the number of AE recorded during the lab test. The 6th day showed a data loss caused by a stop of the control unit. In this time interval the deformation was kept constant, so it was possible to restart the test at the same point without any difficulties. In the first 21 days at constant relative humidity of 45 % a hardening curve typical of rock salt was recorded with an increase of the axial stress or flow stress. The maximum possible load was not reached in this first test phase as short term uniaxial strength β^D amounts to about 25 MPa. As the axial compression was increasing at constant rate the development of the number of AE was increasing in this time interval as the flow stress did.

Humidity was changed from 45 % to 70 % at day 21. A significant reduction of the axial stress from 18.5 MPa to 17 MPa was determined although the axial compression rate was constant throughout the whole test. After the humidity induced stress relaxation took place the axial load was increasing again but very slightly in comparison to the first three weeks so that it actually stayed nearly constant. The maximum load in the second test phase of relative humidity 70 % amounted to 17.7 MPa for about 4 weeks. The number of AE was rising immediately after the relative humidity was increased. Except of the transient phase between the 21st and 25th day the number of AE was increasing nearly linearly until day 37 implying a constant AE rate which was at a higher level than in the first test interval before the humidity increase. From the 6th week of the lab test the AE curve was rising progressively.

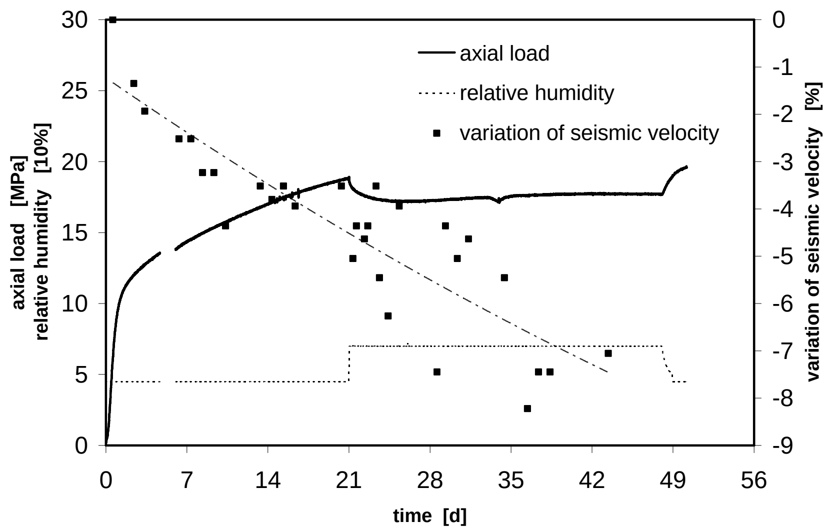

Figure 4 Axial load, relative humidity and variation of the seismic velocity in vertical direction.

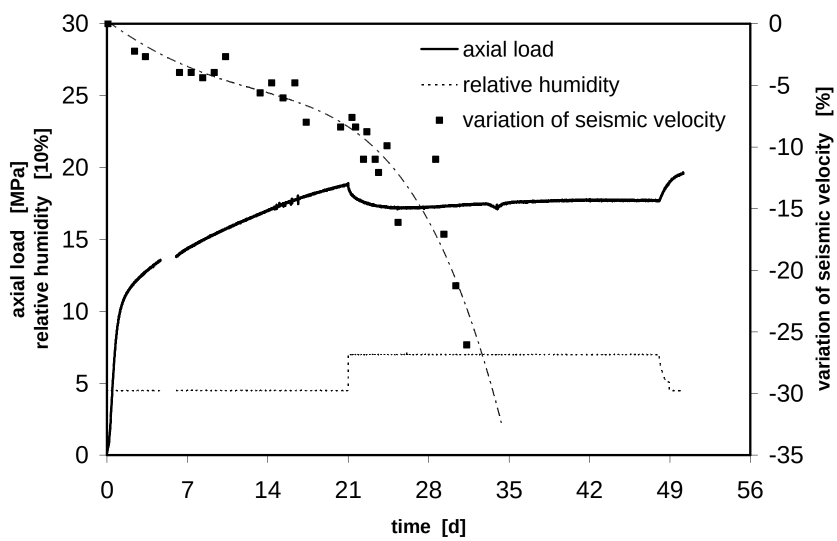

Figure 5 Axial load, relative humidity and variation of the seismic velocity in radial direction in the middle of the sample.

After the 48th day the relative humidity was reduced again to a value of 45 %. In Fig. 3 it can be seen that the axial stress was increasing immediately. Also the number of AE was rising significantly. At the end of the test shortly before failure the volume of the sample had increased by 3.8 %.

Fig. 4 displays the axial load of the sample, the relative humidity in the climatic chamber and the variation of the seismic velocity in the vertical direction which is the ray path parallel to the mechanical load and Fig. 5 displays the same quantities but for a selected ray path in radial direction perpendicular to the load. Seismic velocities were determined up to day 43 as later accumulated damage led to strong damping of the waves which did not admit determination of travel times any more. The seismic velocities in the radial direction show a stronger decrease than those in vertical direction. Additionally the influence of the variations of humidity can be observed in the case of waves in radial direction but not clearly for waves in perpendicular direction.

5 Interpretation

In the first test phase with a constant relative humidity of 45 % a typical hardening curve of the axial stress and an increase of the number of AE was observed. AE was caused by generation of intracrystalline microcracks in rock salt sample and by opening of grain boundaries. Both kinds of microfracturing are called 'microcracks' in this paper. The generation of microcracks led to an irreversible volume increase. At the same time the deformation produced strain hardening which causes stress concentrations especially at the tips of the microcracks.

The increase of the relative humidity to a level of 70 % resulted in a sudden reduction of the axial stress or flow stress. Afterwards the axial stress was increasing only very slightly and it remained on a comparative low level although deformation increased. Thus a strong change in the hardening behaviour was observed. With the change of the relative humidity the AE rate increased without delay. Both effects are caused by additional humidity penetrating into the microcracks and pores in the structure of the rock salt sample. The sudden drop of flow stress and the following very slow increase indicates a sudden increase of ductility. Additionally the increase of AE rate indicates an increase of the activity of microfracturing processes. It is concluded that water films at the tips of microcracks weakened ionic bonds at these locations. From the mechanical point of view this effect results in the reduction of cohesion.

The AE activity remained high in the test interval with 70 % relative humidity. Thus microcracks were growing and new ones were produced continuously by the reduction of cohesion at crack tips. They grew together leading to the formation of first macrofractures in the rock salt sample. This is concluded from the AE rate increasing after the 37th day of testing.

At the end of the lab test, the reduction of the relative humidity instantaneously led to a significant increase of the flow stress by re-establishment of the hardening behavior of the first test phase at the same level of humidity. This was caused by the pile up of dislocations, the increase of dislocation density as well as the reduction of pressure solution processes due to the less available humidity in the microcrack network. But in contrast to the beginning of the lab test, now, after axial compression of 4.1 % during 7 weeks, the rock salt sample was damaged in a way that the re-established hardening deformation and the larger flow stress caused progressive damage in the still existing solid material bridges in the rock salt sample. Coalescence of the micro- and macrofractures finally led to creep failure of the sample around 20 MPa axial stress well below the uniaxial short term strength in the range of 25 MPa as expected for ductile materials. This is supported by the strong increase in AE rate after the reduction of humidity.

The very sensitive reactions of the stress and the AE activity to the changes of relative humidity show that the influence of the humidity on the ductility and the fracturing behaviour in rock salt can be switched on and off without retardation. These instantaneous reactions depend on the availability of humidity at the tips of microcracks and pores and they indicate that the relevant processes mostly take place at the grain boundaries as inner surfaces of the material quickly reached by humidity changes outside the sample.

The development of seismic velocities is in full agreement with the above interpretation. The effects can be observed clearer in the velocities of radial ray paths than with vertical ray paths. This is explained be the load geometry in case of compression where the axial load is much higher than the radial load amounting to zero in case of uniaxial tests. This results in cracks oriented in vertical direction as cracks develop perpendicular to the smallest component of normal stress. P waves travelling in radial direction und thus polarized in this direction will interact with vertical cracks very strongly whereas in case of those travelling in vertical direction interaction will be much less. So these results illustrate the capability of active ultrasonic measurements to monitor accumulating damage during laboratory tests. It is also demonstrated that because of the preferred orientation of microcracks due to load geometry, ray path perpendicular to the smallest stress component have to be chosen in order to monitor damage adequately. In the present test the observed seismic velocities indicate the strong increase of damage after the increase of the relative humidity.

6 Summary and conclusions

In this study the mechanisms of humidity induced creep in rock salt were investigated by performing a specially designed long-term laboratory test. Creep deformation, flow stress and damage in form of micro- and macrofracturing were monitored by mechanical and ultrasonic measurements during uniaxial compression at constant rate. Relative humidity around the sample was controlled and varied. Humidity influenced the mechanical properties of rock salt strongly when a network of cracks was created in the sample by dilantancy due to high mechanical loading in shear. Then humidity entered the sample and the increase of relative humidity resulted both in higher ductility of the sample as well as in an increase of damage. The increase in ductility is observed by instantaneous changes of the hardening behaviour after humidity changes. Possible reasons for the ductility increase are humidity assisted recovery by the reduction of dislocation density and the removal of dislocation pile up as well as solution/recrystallization processes in the pore space [9]. In the case of humidity decrease these processes are reversed. Additionally an increase of microcrack activity and damage was observed when humidity was increased. This was documented by the results of AE and active ultrasonic measurements. The corresponding mechanism as described by [10] is the weakening of ionic bonds due to the formation of water films at the tips of microcracks where strong stress concentrations occur.

References

1. T. Spies, 2001: The South African Institute of Mining and Metallurgy, Symposium Series 27. 167 - 172; Johannesburg.
2. O. Schulze, U. Heemann, F. Zetsche, A. Hampel, A. Pudewills, R.-M. Günther, W. Minkley, K. Salzer, Z. Hou, R. Wolters, R. Rokahr and D. Zapf, 2007: Proceedings of SaltMech6, Taylor & Francis, London. 77 – 88.
3. A. Hampel and U. Hunsche, 1999: Engineering Geology 52 . 271 – 291.
4. U. Hunsche and O. Schulze, 2001: Proc. of the Fifth Conf. on the Mech. Behavior of Salt (MECASALT V), Bucharest 1999. 73 – 87, Lisse: Balkema.
5. D. Budzinski; Spies, T.; Alheid, H.-J.; Weber, J.R.; Eisenblätter, J. 2004. Rock Engineering – Theory and Practice; Proc. EUROCK 2004 & 53rd Geomechanics Colloquy, Salzburg: 421-424. Verlag Glückauf Essen, ISBN 3-7739-5995-8.
6. J. Hesser and T. Spies, 2007: Proceedings of SaltMech6, Taylor & Francis, London. 45 -52.
7. T. Spies, J. Hesser, J. Eisenblätter, 2004: Progress in Acoustic Emission XII, Tokyo, Metropolitan University, 361.
8. T. Spies, D. Meister and J. Eisenblätter, 1997. Proc. IV. Intern. Symp. on Rockbursts and Seismicity in Mines, Krakau: 135 - 139, Rotterdam : Balkema.
9. J.M Le Cleac'h,.and A. Ghazali, Deveughele, M. & Bruhlet, J., 1996. The Mechanical Behaviour of Salt, Proc. 3rd Conference, Palaiseau (France), 231 – 236, Trans Tech Publications, Clausthal.
10. Brodzky & Munson, 1991: Proc. 32nd US Symp. on Rock Mechanics, Univ. of Oklahoma, 703 – 712.

RaSiM 7(2009): Controlling Seismic Hazard and Sustainable Development of Deep Mines, C.A. Tang(ed), Rinton Press, 499-504

STUDY OF THE MECHANICAL PROPERTIES OF COAL FACE THICK –HARD TOP COVER ROCK UNDER THE PRESSURE OF OVERLYING ROCK

YU YANG & DONG-NING DU

The Research Center of Mining Damage and Control Engineering. Liaoning Technical University

Fuxin 123000, China

BING LIANG

Mechanics and Engineering College. Liaoning Technical University

Fuxin 123000, China

There are often two or more neighbouring thick and hard rock plates in the overlying rock layers during mining. In fact, more than one rock layer affects the characteristics of overlying rock layers when the compound effects in the second layer, or multi-hard layers, take place. Rock burst may occur in the case of larger mining depths. As a result, it is necessary to study the mechanical property of thick–hard rock layers under the press of overlying rock. Based on the plate theory, the mechanical property of thick-hard rock layers is studied and the mechanical model of the thick-hard layers are set up and analyzed. The formula of calculating the maximum deflection of the thick-hard layers and the formula of deformation of roof strata are also worked out. At the same time, the paper advanced the equation and method to calculate the vertical displacement of thick-hard roof pressed by overlying rock. This provides the theoretical basis for control of the strata and surface subsidence by injecting the caving zoon, which is conducive to the prevention and prediction of rock burst. At last, a computing example was given to compute the thick-hard roof subsidence.

1 Introduction

China's coal seam occurrence condition is complicated. Thick-hard top cover rocks are often encountered in coal mining with overlying rocks. About one third includes hard roof seams and distributed in more than half of the mining area. With the development of the comprehensive mechanization of coal mining technology, approximately 57% of the fully mechanized coal mining is faced with strong pressure to fall hard board. In particular, the thin layer (thickness <2m) directly on top of the hard roof face is widely distributed. For instance, rocks overlying thick hard board exist in many mines, such as China's Datong, Shanxi, Inner Mongolia, Beijing, etc. Thick hard board hangs open in a large scale during exploitation and the pressure is intense when mine caving occurs. If not handled properly in advance, it often leads to the serious consequences. Therefore, it is of significance to study the relevant theory and technology of controlling the thick hard board [1, 2].

2 Analysis of adaptive condition of thick hard top cover

It is reasonable to take the rock as a plate, either from the geometry or mechanical properties. When the overlying rock hard is more than half hard, and the ratio of the thickness of the roof rocks (or the thickness of laminate) and the shortest edge is larger than 1/5 -1/3, the thin plate theory is not applicable. In the study of Sr Seoul Jin, an academician of the former Soviet Union Academy of Sciences, when rock plate $t/b \le 1/5$ (t stands for rock plate thickness, and b is the length of shortest side of rock plate), the thin plate theory is allowed to use. While the study of A. A. Borisov, an academician of former Soviet Union, shows that, when $t/b \le 1/3$, thin plate theory can also be used in practice. But when rock plate $t/b>1/3$, it should be regarded as a thick plate. In the paper, it is agreed that, when $t/b \le 1/5$, the thin plate theory is can be used to analyze the mechanical properties of the roof rock. And when $t/b>1/5$, the thick plate theory is applicable. When the old roof panel is thick-hard rock, it can be analyzed as isotropic, and at that time the rock plate is under the clamped state [3-8]. The mechanical properties of clamped and laminated board are analyzed as follows.

3 The establishment of the state equation of clamped laminated plate

The clamped laminated plate is showed in figure 1 (a). The upper surface is evenly distributed pressure q. The whole laminated plate has p layer(s), with isotropic materials, and the axis direction is as shown in the figure. Arbitrary layer $j(j=1,2,\ldots,p)$ of enlarged figure is shown in figure 1 (b) below. Divide layer j into k_j thin layer and its thickness is $d_j=h_j/k_j$. The boundary reactions on the thin layer are $P(0)$,$P(a)$,$Q(0)$, and $Q(b)$. Establish the state equation of the first thin layer(j_1)in the local coordinate system [9]:

$$\begin{aligned}&\frac{d}{dz}\left[U_{mn}(z)\quad V_{mn}(z)\quad Z_{mn}(z)\quad X_{mn}(z)\quad Y_{mn}(z)\quad W_{mn}(z)\right]_{j1}^{T}=\\&D_j\left[U_{mn}(z)\quad V_{mn}(z)\quad Z_{mn}(z)\quad X_{mn}(z)\quad Y_{mn}(z)\quad W_{mn}(z)\right]_{j1}^{T}+\left\{B_{mn}(z)\right\}_{j1}\end{aligned} \tag{1}$$

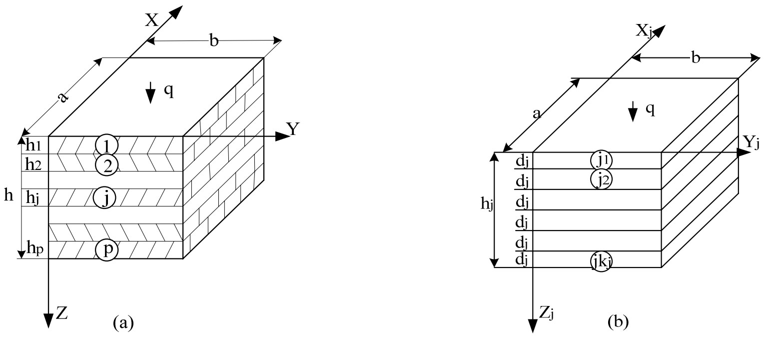

Figure 1. Thick laminated plate around with clamped sides

In the formula(1), D_j is determined by the single-layer clamped rock plate mechanical model, where the elastic constants should be calculated based on the material of layer j. Array $\left\{B_{mn}(z)\right\}_{j1}$ can be written as follow:

$$\left\{B_{mn}(z)\right\}_j=\left\{\begin{matrix}0\\0\\0\\\frac{2}{a}(P_n^{(0)}(z)-(-1)^m P_n^{(a)}(z))\\\frac{2}{b}(Q_m^{(0)}(z)-(-1)^n Q_m^{(b)}(z))\\0\end{matrix}\right\}\qquad (m\neq 0, n\neq 0) \tag{2}$$

4 Solution of clamped laminated plate mechanical quantity

As long as the thin-layer is thin enough, it is reasonable to believe that the reaction force on thin layer boundary along the *Z* direction is in the linear distribution. If each layer of the laminated plates is very thin, it is not necessary to separate layer of the laminated plates into thinner layers. If some layers are thick, the partition number of thin layer should be determined by the accuracy requirements. In the spreadsheet process, gradually increase the number of thin layer, if the significant figure required to reserve is almost unchanged when it is divided into K_j(j=1,2,…,p) thinner layers, the result can be taken as the accuracy value, which satisfy accuracy requirement [1,9-10].

The solution of equation (1) is as follow:

$$R_{j1}(z) = G_j(z)R_{j1}(0) + C_{j1}(z), z \in \left[0, d_j\right] \tag{3}$$

Where: $R_{j1}(z) = \left[U_{mn}(z) \quad V_{mn}(z) \quad Z_{mn}(z) \quad X_{mn}(z) \quad Y_{mn}(z) \quad W_{mn}(z)\right]_{j1}^{T}$;

$R_{j1}(0) = \left[U_{mn}(0) \quad V_{mn}(0) \quad Z_{mn}(0) \quad X_{mn}(0) \quad Y_{mn}(0) \quad W_{mn}(0)\right]_{j1}^{T}$;

$G_j(z) = e^{D_j \cdot z}$;

$C_{j1}(z) = \int_0^z e^{D_j \cdot (z-\tau)} \left\{B_{mn}(\tau)\right\}_{j1} d\tau$

It goes on the analogous derivation for the second thin layer as follow:

$$R_{j2}(d_j) = G_j(d_j)R_{j2}(0) + C_{j2}(d_j) \tag{4}$$

According to the displacement and stress continuity conditions between the two thin layers, it should be $R_{j1}(d_j)=R_{j2}(0)$. It can be derived that $R_{j2}(d_j) = \left[G_j(d_j)\right]^2 R_{j1}(0) + G_j(d_j)C_{j1}(d_j) + C_{j2}(d_j)$.

Followed by analogy, finally it can link the under surface mechanical quantity of k_j thin layer with the upper surface mechanical quantity of the first thin layer by the following formula:

$$R_{jk_j}(d_j) = E_{jk_j} R_{j1}(0) + \overline{E}_{jk_j} \tag{5}$$

In the formula: $E_{jk} = \left[G_j(d_j)\right]^k$,

$$\overline{E}_{jk_j} = \left[G_j(d_j)\right]^{k_j-1} C_{j1}(d_j) + \left[G_j(d_j)\right]^{k_j-2} C_{j2}(d_j) + \cdots + G_j(d_j)C_{j,k_j-1}(d_j) + C_{jk_j}(d_j)$$

Formula (5) is applicable for any layer in figure (1).

When j=1, 2, there is $R_{1k_1}(d_1) = E_{1k_1}R_{11}(0) + \overline{E}_{1k_1}, R_{2k_2}(d_2) = E_{2k_2}R_{21}(0) + \overline{E}_{2k_2}$

In the formula above, $R_1k_1(d_1)$ and $R_2k_2(d_2)$ are the undersurface mechanical quantity of the first layer and the upper surface mechanical quantity of the second layer. According to the displacement and stress continuity conditions between the two layers, $R_1k_1(d_1)$ and $R_2k_2(d_2)$ should be equal. Thus, take the second formula into the first formula, as the result $R_{2k_2}(d_2) = E_{2k_2}E_{1k_1}R_{11}(0) + E_{2k_2}\overline{E}_{1k_1} + \overline{E}_{2k_2}$.

Followed by analogy, finally it can link the undersurface mechanical quantity of the whole laminated plate with the upper surface mechanical quantity by the formula:

$$R_{pk_p}(d_p) = \prod R_{11}(0) + \overline{\Pi} \tag{6}$$

In the formula: $\Pi = \prod_{j=p}^{1} E_{jk}$;

$$\overline{\Pi} = E_{pk_p}(E_{p-1,k_{p-1}} \cdots E_{2k_2}\overline{E}_{1k_1} + E_{p-1,k_{p-1}} \cdots E_{3k_3}\overline{E}_{2k_2} + \cdots + \overline{E}_{p-1,k_{p-1}}) + \overline{E}_{pk_p}.$$

$R_{11}(0)$ in formula (6) is called as the initial value. The $\prod$ is a six order square matrix, and the $\overline{\Pi}$ is a six order array. Under normal circumstances, the external force on the upper and under surface of the laminated board is given in advance. Therefore, formula (6) is actually the matrix equation of six displacement components as well as the undetermined constant for the laminated board. Spread the formula and extract three lines 3, 4, 5 out of it.

$$\begin{Bmatrix} U_{mn}(0) \\ V_{mn}(0) \\ W_{mn}(0) \end{Bmatrix} = \begin{bmatrix} \Pi_{31} & \Pi_{32} & \Pi_{36} \\ \Pi_{41} & \Pi_{42} & \Pi_{46} \\ \Pi_{51} & \Pi_{52} & \Pi_{56} \end{bmatrix}^{-1} \left[\begin{Bmatrix} Z_{mn}(d_p) \\ X_{mn}(d_p) \\ Y_{mn}(d_p) \end{Bmatrix} - \begin{bmatrix} \Pi_{33} & \Pi_{34} & \Pi_{35} \\ \Pi_{43} & \Pi_{44} & \Pi_{45} \\ \Pi_{53} & \Pi_{54} & \Pi_{55} \end{bmatrix} \begin{Bmatrix} Z_{mn}(0) \\ X_{mn}(0) \\ Y_{mn}(0) \end{Bmatrix} - \begin{Bmatrix} \overline{\Pi}_3 \\ \overline{\Pi}_4 \\ \overline{\Pi}_5 \end{Bmatrix} \right] \tag{7}$$

When the upper surface of the board is only under the even pressure q, spread q by Z-progression form, $Z_{mn}(0) = -\dfrac{16q}{mn\pi^2}$ (m,n=1,3,5,….), And because $X_{mn}(0)=Y_{mn}(0)=X_{mn}(d_p)=Y_{mn}(d_p)=Z_{mn}(d_p)=0$, the following formula is obtained.

$$\begin{Bmatrix} U_{mn}(0) \\ V_{mn}(0) \\ W_{mn}(0) \end{Bmatrix} = \begin{bmatrix} \Pi_{31} & \Pi_{32} & \Pi_{36} \\ \Pi_{41} & \Pi_{42} & \Pi_{46} \\ \Pi_{51} & \Pi_{52} & \Pi_{56} \end{bmatrix}^{-1} \left[\frac{16q}{mn\pi^2} \begin{Bmatrix} \Pi_{33} \\ \Pi_{43} \\ \Pi_{53} \end{Bmatrix} - \begin{Bmatrix} \overline{\Pi}_3 \\ \overline{\Pi}_4 \\ \overline{\Pi}_5 \end{Bmatrix} \right] \tag{8}$$

Undetermined constant can be obtained by satisfying the bottom boundary conditions, and then $[\overline{\Pi}_3 \;\; \overline{\Pi}_4 \;\; \overline{\Pi}_5]^T$ and $[U_{mn}(0) \;\; V_{mn}(0) \;\; W_{mn}(0)]^T$ are calculated. So the initial value is known. Using formula (3) and making $j = 1$, the first thin layer mechanics quantity of the first layer can be obtained. The first thin layer under the surface of the mechanical quantity obtained can be considered as the initial value of the second thin layer. Take the analogy, the mechanical quantity of the first layer can be solved all. Similarly, the whole laminated can be solved.

Boundary conditions can be determined by the following formula.

The condition is satisfied, which is that for x=0, at point a, w=v=0; for y=0, at point b, w=u=0. But the following formula is remained to be satisfied.

$$x=0, \text{ at point } a,\ u=0; y=0, \text{ at point } b,\ v=0 \tag{9}$$

The condition (x=0, a, u=0;y=0, b, v=0) needs to satisfy. It can take the formula expressed by u, v into formula (9). Owing to the upper surface of the board is under uniform pressure, it is bound to the following formula.

$$\left.\begin{aligned} \sum_m [u_{mn}(z)]_j &= 0 \\ \sum_n [v_{mn}(z)]_j &= 0 \end{aligned}\right\} \tag{10}$$

5 Sinkage calculation example of thick hard top cover laminated plate model

Based on the above mechanical model and deformation analysis of thick hard board, the relevant mechanical quantity can be solved by the use of the procedures related to the preparation of laminated plate [10]. To meet the need, the plate as shown in figure 2 of the laminated plate examples is solved by using the following solution of the boundary clamped around the two layers together under the conditions of the solver. Due to the difference of the mechanical properties and the property of rock between up and down, so the coal layer can be considered the separate stratum between the overlying rock layer and the under thick bedding layers of rock when the model been established [11]. All mechanical parameters of each layer are shown in table 1.

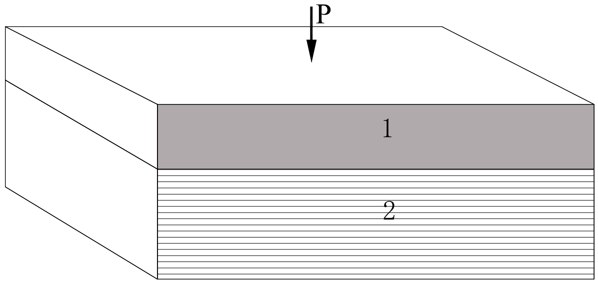

Figure 2. The model of calculating the deformation of two thick and hard rock plates

Tab1. Mechanical parameter of the thick laminated plate

Rock number	body force ($N \cdot m^{-3}$)	elastic modulus (GPa)	Poisson ratio	cohesion (MPa)	cohesion (°)	thickness (m)
1	24000	30	0.31	28	35	7.0
2	25000	40	0.24	30	40	14.6

According to practical coal mining, the face width is a = 80m, and the length changes with the advancing face ranging among 0-180m. The pressure on the laminated board rocks and soil changes into evenly distributed pressure P = 6.6MPa. The calculation result is shown in table 2.

6 Conclusion

Overlying strata in the mining area has an impact on the mining of overburden rock deformation, fracture, and the entire process of moving; usually more than one two-tiered roof is adjacent to the hard rock. The traditional theory of rock pressure only considers the impact of pressure behaviour of the first layer above the coal seam on mining hard rock. In fact, when there are compound effects in the second layer or multi-hard layers, more than one rock layer affects the characteristic of overlying rock layers. As a result, studying the mechanical properties of thick–hard rock layers under the pressure of overlying rock has important scientific and practical value. At the same time, a detailed study of different types of roof structures in the overburden rock deformation can lay a foundation for the implementation of technology of falling surface subsidence control.

Tab2. Stress and displacement of the central point on the underside of the plate

Plate length (m)	M,n	I_1,I_2	displacement (m)
40	m=1…79 n=1…19	5,6	0.085
80	m=1…99 n=1…19	5,6	0.197
100	m=1…99 n=1…39	5,6	0.254

120	m=1…199 n=1…29	5,10	0.303
140	m=1…179 n=1…19	10,10	0.518
160	m=1…79 n=1…79	5,6	0.703
180	m=1…219 n=1…399	5,10	0.914

Acknowledgements

The author would like to thank the financial support by the National Natural Science Foundation of P. R. China (50804020), the Liaoning Provincial Office of Education Science Foundation project (2008273), Liaoning Province Dr Start Fund Projects (20081103), and the Liaoning Provincial Key Laboratory of Education-funded Project (07194).

References

1. Jing, Z.M. and Xu, L.S. Coal mine hard roof Control. Beijing: Coal Industry Press, 1994.
2. Yang, Y. Research on the collapse rock pour fill overlying strata movement control mechanism. Liaoning Technical University Doctoral Dissertation, 2007 .(In Chinese)
3. Yang, Y.Q. Plate theory. Beijing: China Railway Press, 1980.(In Chinese)
4. S. Timoshenko. Shell theory. Beijing: Science Press, 1977.
5. Kang, J.R and Wang, J.ZH. Mining Overlying strata mechanics model and fracture failure conditions analysis. Journal of the coal, 2002, 27 (1): 16 -20.(In Chinese)
6. Gao, F., Qian, M.G. and Miu, X.X. Force deformation analysis of given deformation Old Roof. Journal of Rock Mechanics and Engineering, 2000, 19 (2): 145-148.
7. Tang, C.A. Disaster during the process of Rock failure. Beijing: Coal Industry Press, 1993.(In Chinese)
8. Salarnon, M.D.G. Elastic analysis of displacements and stresses induced by the mining of seam or roof deposis, J.S.Afr, Inst. Metall. 1963, 63.
9. Xu, Z.L. Elasticity. Beijing: Higher Education Press, 1979.(In Chinese)
10. Fan, J.R. Strong thickness laminated plate and shell precise theory. Beijing: Science Press, 1985.(In Chinese)
11. Li, H. Thick hard board mechanical analysis and application. China University of Mining master's degree thesis,2006.(In Chinese)

RaSiM 7(2009): Controlling Seismic Hazard and Sustainable Development of Deep Mines, C.A. Tang(ed), Rinton Press, 505-512

AN HARMONY MODEL OF ANISOTROPIC ELASTIC-PLASTIC DAMAGE FOR SATURATED ROCK

YING-FA LU[1,2], HUI SUN[1,2], TAO YAN[1] and XINXING WU[1]

1. Key Laboratory of Geological Hazards on Three gorges Reservoir Area (China Three Gorges University), Ministry of National Education, Yichang, Hubei 443002, China

2. School of Civil Engineering, Wuhan University, Wuhan, Hubei 430071, China

The research of anisotropic mechanical behaviors of rock is of importance; natural rock mass is anisotropic and its failing type is also non-isotropic. In this paper, an elastic-plastic damaged harmony model has been proposed; elastic deformation, damaged irreversible deformation and plastic deformation can be identified respectively. A second rank damage sensor is employed to characterize the induced damage; damage evolution is related to the propagation conditions of micro-cracks. A specific form of strain free energy is used to obtain effective elastic stiffness; the limited scopes of damage parameters are deduced. The determination of anisotropic parameters is proposed by virtue of a tri-axial laboratory test, and the mechanical behaviors of different loading paths are simulated. The comparison between testing data and numerical simulations yields similar results overall. The model is then used to simulate the coupled hydraulic mechanical responses in different loading paths. The numerical results also show the proposed model is suited to describe the main features of porous hydraulic mechanical behaviors of rock.

1 Introduction

Rock geo-materials exhibit a rich series of complex behaviors. Despite the study of numerous researchers [1, 2], the fundamental mechanical characteristics of rock still remain a challenge; particularly for anisotropic porous medium. The main consequences of saturated rock can be summarized: **a**. deterioration of elastic properties and non-linearity of stress-strain relation; **b**. induced material anisotropy and significant volume dilatation; **c**. irreversible deformation; etc. These fundamental features have to be considered in constitutive models of geo-material. Some researchers [3, 4] believe irreversible deformations come from damage of geo-materials, are assumed to develop under compressive stress, and are obtained as the method proposed by Yazdani [5]. In this paper, the irreversible deformations are thought to be natural characteristics of geo-materials, and are obtained by virtue of conventional plastic theories.

2 Continuous Damage Model

In order to develop a continuous damage model, an energy based approach is used to determine the effective elastic stiffness tensor. Some simplified assumptions are adopted: the initial damaged material has a linear isotropic elastic behavior, the influence of interaction between micro-cracks on the free energy function is so small that the latter can be expressed as a linear function of damage sensor, only short-term behavior will be discussed. The following free energy function is used:

$$G^b(\sigma,D)=\frac{1+\upsilon_0}{2E_0}tr(\sigma:\sigma)-\frac{\upsilon_0}{2E_0}(tr\sigma)^2+a_1tr(D)(tr\sigma)^2+ \\ a_2tr(\sigma:\sigma:D)+a_3tr(\sigma)tr(\sigma:D)+a_4tr(D)tr(\sigma:\sigma) \tag{1}$$

Where a_1, a_2, a_3, a_4 are introduced to characterize micro-crack contributions to the free energy; E_0 and υ_0 are initial elastic coefficients; D is damage variable; σ is stress tensor. Differentiation of free energy function leads to the effective strain-stress relations:

$$\in_{ij}-\in_{ij}^r=\frac{\partial G(\sigma,D)}{\partial\sigma}=S(D):\sigma_{kl} \tag{2}$$

Where $\in_{ij}^r$ is irreversible deformation, Considering the characteristic of free energy, the compliance matrix $S(D)$ can be composed into initial elastic compliance component S^0 and added damage compliance component S^d.

$$S=S^0+S^d \tag{3}$$

Where

$$S_{ijkl}^0(D)=\frac{1+\upsilon_0}{2E_0}(\delta_{ik}\delta_{jk}+\delta_{il}\delta_{jk})-\frac{\upsilon_0}{E_0}\delta_{ij}\delta_{kl} \\ S_{ijkl}^d(D)=\frac{1}{2}a_2(\delta_{ik}D_{jl}+\delta_{il}D_{jk}+D_{ik}\delta_{jl}+D_{il}\delta_{jk}) \\ +a_3(\delta_{ij}D_{kl}+D_{ij}\delta_{kl})+a_4tr(D)(\delta_{ik}\delta_{jl}+\delta_{il}\delta_{jk}) \tag{4}$$

The limited scope of four parameters a_1, a_2, a_3, a_4 in Eq.(4) will be presented. Thermodynamic considerations require that the deformation energy of an elastic material should always be positive. For isotropic material, the requirements are satisfied if $E_0>0$ and $-1<\upsilon_0<0.5$. For the anisotropic material, the deformation energy per unit volume is $\{\sigma\}^T[S]\{\sigma\}/2$. A more rigorous form of analysis, which considers all the elastic parameters, can be given for deformation free energy. Therefore, the criteria for positive strain energy can be read in the following form:

$$E_0>0;-1<\upsilon_0<0.5;\ a_1>0; \\ a_2>0;\ a_3<0;\ a_4>0;\ a_2+a_3>0; \\ 9a_1+a_2+3(a_3+a_4)+1/K_0>0 \tag{5}$$

Where $K_0=E_0/3(1-2\upsilon_0)$.

Based on plenty of test data, the mechanisms of different micro-crack growth have been studied; for most geo-materials, the most plausible mechanism is so-called sliding crack model [2, 6]; In this criterion, a mixed mode involving tensile mode Ⅰ and shear mode Ⅱ is considered, the mode Ⅱ becomes dominant as micro-crack grows, the principal stress determining growth conditions are normal and shear stresses applied to micro-crack. The crack propagation criterion is employed in the following form:

$$F(\sigma,r,\mathrm{n})=\sqrt{r}[f(r)\tau_n+\sigma_n]-C_t=0 \\ f(r)=t\left[1+C_1\frac{(1-r)^2}{(1-r_0)^2}\right] \tag{6}$$

Where $\sigma_n=\vec{n}\cdot\sigma\cdot\vec{n}$ and $\tau_n=\vec{n}\cdot\vec{\tau}\cdot\vec{n}$, $\vec{\tau}=\overrightarrow{n^l}-\sigma^m$; σ^m is mean stress on sliding plane; r_0 is initial damage effective variable; r is damage effective variable; C_t is equivalent material toughness; t and C_1 are model parameters; the scalar valued function $f(r)$ defines the proportion of applied stress field .

In Eq. (4), the damage internal variables should present the orientation, the distribution and the propagation of induced micro-cracks. The internal variable used widely is the second-order tensor $\overline{D}$. The second rank tensor can be expressed explicitly as follows [1]:

$$\overline{D} = \sum_k d^K(A)(\overline{n} \otimes \overline{n})_k \tag{7}$$

Where dk(A) denotes the crack density related to de-cohesion area A; $\overline{n}$ is the unit normal of crack. If the micro-cracks can be idealized as penny-shaped micro-defects, the second-order tensor $\overline{D}$ can be given by the eigenvalues:

$$D = \sum_{i=1}^{3} D_i V^i \otimes V^i \tag{8}$$

Where V^i is unit normal vector; D_i is area of micro-crack de-cohesion. However, most contain the initial damage, a randomly oriented set of initial micro-defects is assumed, considering initial state, the induced damage tensor $\overline{D}$ is characterized by relative variation of micro-crack density with respect to initial state:

$$\overline{D} = \sum_k \left(\frac{l^3 - l_0^3}{b^3}\overline{n} \otimes \overline{n}\right)_k = \sum_k ((r^3 - r_0^3)\overline{n} \otimes \overline{n})_k \tag{9}$$

Where l_0 is average radius of initial micro-cracks; b is a characteristic length at the onset of accelerated micro-crack interaction; $r = l^3/b^3$ is micro-crack-based internal damage variable.

The irreversible deformations corresponding to sliding of microstructure and misfit of crack surfaces exist, and they can be described by the conventional plastic theories; the yielding function can be proposed in the following form:

$$F^p(\sigma, \gamma^p, n) = \left[\sigma_n + f^d\left(\gamma^d\right)\tau_n\right] - C_t\left[1 + f^p\left(\gamma^d\right)\right] = 0 \tag{10}$$

Where $\gamma^d = \sqrt{2e_{ij}{}^p \cdot e_{ij}{}^p/3}$; $e_{ij}{}^p = \in_{ij}{}^p - \in_{ij}{}^p\ \delta_{ij}/3$; the function $f^d\left(\gamma^d\right)$ and $f^p\left(\gamma^d\right)$ are presented in the following forms:

$$\begin{aligned} f^d\left(\gamma^d\right) &= C_t\left(1 + \frac{C_1}{C_2\gamma^p + 1}\right) \\ f^p\left(\gamma^d\right) &= \left(\frac{1}{\sqrt{r_0}} - 1\right)\exp\left(-C_2\gamma^d\right) \end{aligned} \tag{11}$$

Where C_2 is constant coefficient. When $\gamma^d = 0$, the Eq. (11) corresponds the yielding stress plane, $f^d(0) = C_t(1 + C_1)$, $f^p(0) = 1/\sqrt{r_0} - 1$; when $C_2\gamma^d \to \infty$, the Eq. (11) corresponds the peak stress plane, $f^d(\infty) = C_t$, $f^p(\infty) \to 0$. The corresponding plastic potential is taken as follow:

$$G_d = h_d{}^2 q^2 + h_c{}^2 p^2 \tag{12}$$

Where h_d , h_c are constant coefficients; q, p are deviatoric stress and mean stress respectively

3 Calibration of Model Parameters

The relation ships of deviatoric stresses ($\sigma_1 - \sigma_2$) and strains ($\in_1, \in_2$) based on data of conventional tri-axial tests (Fig.1) can be plotted respectively. A process of unloading-reloading cycle at arbitrary point of damaged segment of stress-strain curves can be performed; the two linear equations (D_1E_1, D_2E_2) can be determined. By virtue of the slopes ($L_1, L_1/\upsilon_{21}$) and the intersections (b_i) at each points (E_1, E_2) with strain axes respectively for the linear equations, the three parameters, can be obtained; the fundamental equations are given as follows:

$$a_3 = \frac{S^d_{2211}}{D_{22}}; \quad a_4 = \frac{S^d_{1111}}{4D_{22}};$$

$$a_2 = \frac{1}{2D_{22}} \frac{\in^E_{22} - \in^r_{22}}{\sigma_{22}} - \frac{5}{2}a_3 - 2a_4 \tag{13}$$

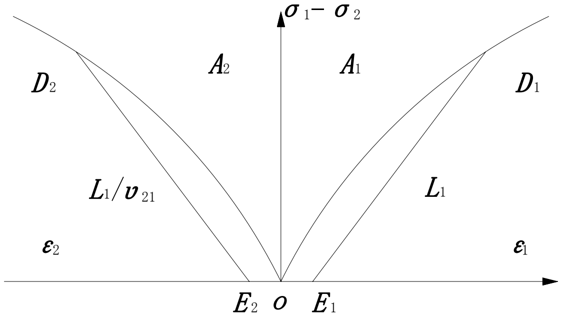

Figure 1 Diagram of parameter determination of proposed model

For the initial isotropic coefficients (λ_0, μ_0) ,they can be obtained by using of straight lines(OA_1, OA_2). The two parameters (h_c, h_d) present plastic deformations. The other 5 parameters involved in the damage criterion (C_t, r_0, t, C_1) and plastic yield function (C_2) can be determined by the macroscopic non-linear yield and failure condition of material with different confining pressures, and plastic strain characteristics.

4 Hydraulic Mechanical Coupled Damage

The preceding model is extended to the modeling with water pressure. The state variables are composed of strain tensor of bulk medium ($\bar{\in}$), damage tensor ($\bar{D}$), and change of fluid content per unit volume of bulk medium (ξ).It is assumed that the thermodynamic potential can be expressed as follows:

$$W = G\left(\bar{\in}, \bar{D}\right) - \xi M(\bar{D})\bar{\alpha}(\bar{D}) : \bar{\varepsilon} + \frac{1}{2}M(\bar{D})\xi^2 \tag{14}$$

The first function (G) represents the strain energy function of saturated porous elastic damages bulk medium; G is given for saturated porous medium without water pressure. The second part represents porous elastic coupling behaviors with water pressure, the scalar (M) depending on damaged tensor is Biot's modulus, the symmetric second rank tensor ($\alpha_{ij} = \alpha_{ji}$) defines the anisotropic. By assuming a linear state law for saturating fluid, the stress-strain relations can be inverted to obtain the following strain-stress equations:

$$\bar{\in} = \bar{S}(\bar{D}) : \bar{\sigma} + \bar{S}(\bar{D}) : \bar{\alpha}(\bar{D})P \tag{15a}$$

$$\xi = \left[\frac{1}{M(\bar{D})} + \bar{S}(\bar{D}) : \bar{\alpha}(\bar{D}) : \bar{\alpha}(\bar{D})\right]P + \bar{S}(\bar{D}) : \bar{\alpha}(\bar{D}) : \bar{\sigma}, \tag{15b}$$

where $\bar{S}$ is the fourth rank elastic compliance tensor of damaged bulk medium for drained conditions. By taking theoretical analyses for every stationary damage state, some relative formula can be obtained in forms:

The change of fluid content per unit volume of bulk medium

$$\frac{\xi}{\rho_0} = (S_{iiijj} - \frac{C_{iikk}S_{kkjj}}{3K^s})\sigma_{jj} + [S^*(\bar{D}) - \frac{1}{K^s} + \phi(S_f - \frac{1}{K^s})]P \tag{16}$$

Where $\eta(\bar{D}) = S^*(\bar{D}) - 1/K^s + \phi(S_f - 1/K^s)$; $S^* = S_{iiijj}$; S_f denotes the compressibility coefficient of fluid; ϕ is the porosity of geo-materials; ρ_0 is the density of fluid; $S_s = 1/K^s$ is the bulk compressibility of the so lid grains.

Biot's modulus:

$$M(\bar{D}) = \frac{K^s}{(1 - C_{iijj}/(9K^s)) + \phi(K^s/K^f - 1)} . \tag{17}$$

The generalized Skempton coefficients tensor ($\bar{B}(\bar{D})$)

$$P = -\frac{1}{3}\bar{B}(\bar{D}) : \sigma \ ; \ B_{ii}(\bar{D}) = \frac{[3S_{iijj}(\bar{D}) - 1/K^s]}{\eta(\bar{D})} . \tag{18}$$

5 Application

The proposed model is used to simulate conventional triaxial compression tests. The tests used were performed for sandstone; the average porosity is about 25%, hydrostatic compression tests have shown that the initial behavior of material is quasi-isotropic. The parameters proposed model are obtained as follows:

$$\begin{aligned} &E_0 = 20000MPa, \upsilon_0 = 0.2, a_2 = 24.82\times10^{-6}MPa^{-1}, \\ &a_3 = -14.99\times10^{-6}MPa^{-1}, \quad a_4 = 1.55\times10^{-6}MPa^{-1}, \\ &C_t = 37.5MPa, t = 1.50, r_0 = 0.25, C_1 = 4.17243, \\ &C_2 = 4700, h_c = 0.43, h_d = 0.67 \end{aligned} \tag{19}$$

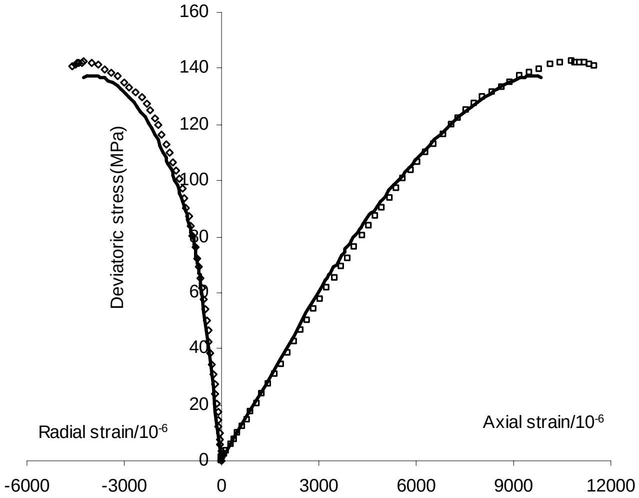

Figure 2 Simulation of saturated triaxial tests(continuous lines are numerical results) with confining pressures (40MPa)

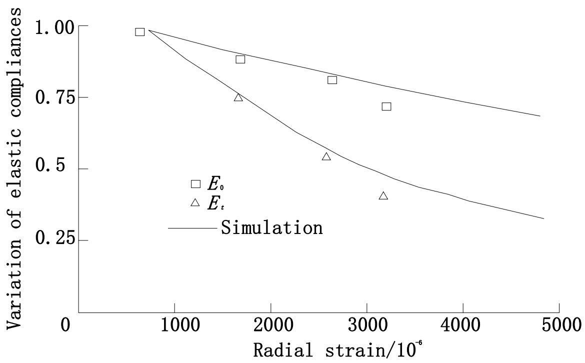

Figure 3 Variations of effective elastic modules as function of radial strain under confining pressure (40MPa)

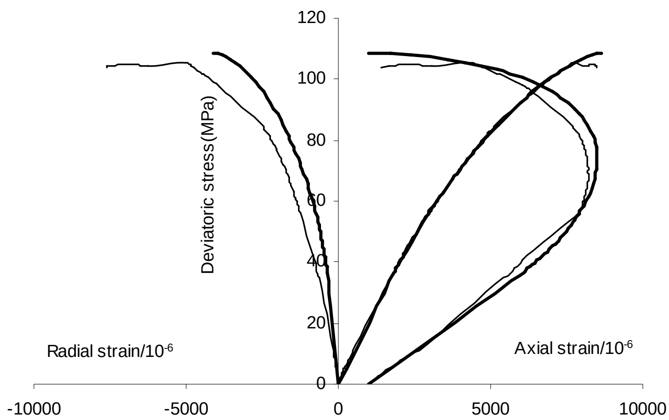

Figure 4 Simulation of non-drainage triaxial pressure tests (continuous lines are numerical results) with confining pressure (20MPa)

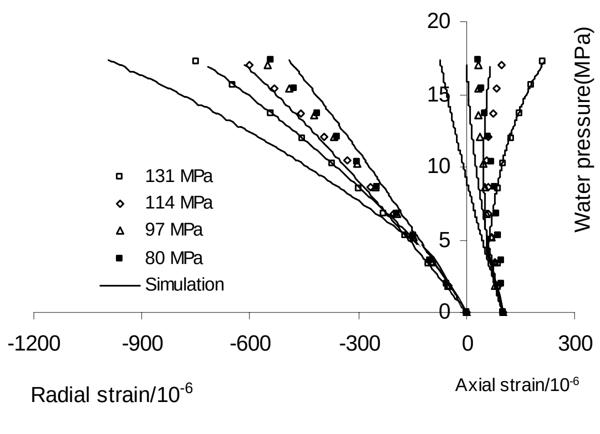

Figure 5 Simulation of injection triaxial test under different deviator (continuous lines are numerical result s) with confining pressures (50 MPa)

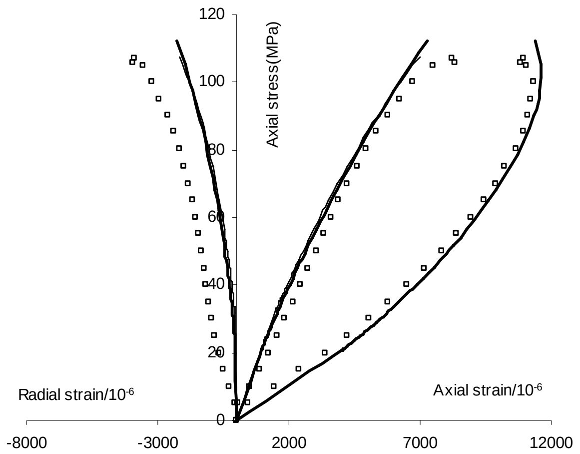

Figure 6 Simulation of proportional loading and non-drainage triaxial test(continuous lines are numericalresults) with proportional coefficient (50MPa).

In Fig.2, the comparisons between numerical simulation and testing data for conventional triaxial test are given under confining pressures ($P_c = 40MPa$); in Fig.3, the variation of effective axial modulus ($E_a = C_{1111}/C^0_{1111}$) and radial modulus ($E_r = C_{2211}/C^0_{2211}$) are compared with test data under confining pressure ($P_c = 40MPa$).The proposed model is available to describe the main features of induced damage on saturated material without water pressure. The theory is applied to simulate the coupled porous mechanical behaviors. For the non drainage condition, the unite volume fluid content is equal to zero ($\xi = 0$) and the modulus (K_f) of water compressibility can be obtained by making use of the testing Skempton coefficient ($B = 0.415$).The numerical simulating curve is presented in Fig.4 for confining pressure ($P_c = 20MPa$) under non-drainage. Mechanical tests under different deviator have been performed under confining pressure ($P_c = 50MPa$).The propagation of radial deformation is more radical than axial deformation (Fig.5). This test is conducted under a coefficient ($x = \sigma_{11} / \sigma_{22}$) between axial stress and confining pressure. The sample is loaded until a fully failure occurs, the testing result with $x = 5$ is show n in Fig.6. From the all-above results between testing data and numerical simulation, they are acceptable on the simulation of anisotropy, volumetric dilatation and failure stress under different loading paths for saturated rock without water pressure and with water pressure.

Acknowledgements

The author would like to thank the financial support by the National Natural Science Foundation (Grant No. 50779030), the National Natural Science Important Foundation (Grant No.50879044) and the National Natural Important Projection Foundation (2008BAB29B03)of P. R. China.

References

1. Kachanov, M. Effective elastic properties of cracked solid: critical review of some basic concepts. A SM E, App l. Mech. Rev, 1992, 45 (8): 304-335.
2. Kemeny, J.M. A model for nonlinear rock deformation under compression due to subcritical crack growth. Int. J. Rock Mech. Min. Sci, 1991, 28: 459-467.
3. Shao, J.F. and Rudnick, I.J.W. A microcrack-based continuous damage model for brittle geo-materials. Mechanics of Materials, 2000, 36: 52-63.

4. Lu, Y.F. and Shao, J.F. Modelling of anisotropic damage in brittle rocks under compression dominated stresses. Int. J. Numer. Anal. Meth.Geomech., 2002, 26: 230-247.
5. Yazdani, S.and Schreyer, H. L. An anisotropic damage model with dilatation for concrete. Mech. Mater, 1988, 7: 231-244.
6. Nemat-Nasser, S. and Horri, H. Micro-mechanics: overall properties of heterogeneous materials. North-Holland, Amsterdam, 1993.

RaSiM 7(2009): Controlling Seismic Hazard and
Sustainable Development of Deep Mines,
C.A. Tang(ed), Rinton Press, 513-518

NUMERICAL ANALYSIS OF PANIC MINE ROCK BURST MECHANISM

CHUN-RUI LI, JUN-FENG PAN and YONG-WEIR PENG
Coal Mining & Designing Branch, Coal Research Institute,
China Coal Society of Rock Mechanics and Support Professional Committee,
Beijing 100013, P.R.China

QING-XIN QI, LI-JUN KANG
China Coal Research Institute,
Beijing, 100013, P.R.China

Coal (rock) layer mechanical properties and in-situ stress are the main factors that influence rock burst occurrence. Bases on the practice of Panic mine production, it is found that the coal (rock) seam mechanics strength and stiffness parameters and the ratio between three principal stresses generated by tectonic stress and gravity are the key factors which influence rock burst in the coal mining process. This paper uses numerical analysis method to study the influence of the ratio of principal stress, pillar size, roof strength and stiffness on rock burst conditions.

1 Introduction

Pertaining to the research of rock burst mechanism, domestic and foreign scholars have put forth many theories. According to modern applied mechanics, the main theories are: strength theory, energy theory, stiffness theory, coal (rock) instability theory, burst trend theory, three criterion theory and holding theory [1]. Dr. Qi Qing-xin through lab and scene experiments analysis, found rock burst always exists in the areas of fault, fold, anticline, changing area of coal seam thickness, litho logy change area etc. Rock burst has a close relationship with the structure of coal and rock [2].For reasons given above, rock burst is affected by the intrinsic factor (burst trend), force source factor (stress concentration or high energy storage and dynamic perturbation), coal (rock) mass structure factors (with weak face and easily lead to mutations slip interface). That is the "three-factor theory" [3]. In fact, if the coal (rock) did not have a burst trend have high stress concentrations, enough proof resilience, weak face or soft sheaf, it would not generate local rupture, damage, instability and slip, and there would no rock burst. Thereby, intrinsic factors, force factors, and structure factors are three indispensable factors which result in rock burst.

2 Geological conditions and cases of rock burst in Panic mine

Most of the XinWen mining area is characteristic of deep mining. The coal mining geology of Panic mine is very complex with the coal seam obliquity at 35～40º and the mining depth reaching up to 800m. In recent years, rock burst is the main roof disasters. In order to control the rock burst efficiently, Coal Research Institute has tested the burst trend to the 19＃coal seam, roof and floor. According to "coal seam burst trend sort and index determination" and dynamic break time of the 19＃coal, impact energy index, elastic energy index educe the seam burst trend belongs to the Ⅱlevel, which is the weak burst trend. From the "coal seam burst trend sort and index determination " and the 19＃coal seam, the compound roof slate bend energy index is 127.92kJ. This is judged to be at the Ⅲ level, and has the highest burst trend roof [4]. We also tested the combined specimen and determined the compressive strength is higher than that of the pure coal specimen with the dynamic ruptured time becoming shorter. The phenomenon has shown 19# coal seam combine with hard floor, not only affect elastic energy accumulate, but also influence the speed of energy release. The combine seam enhances the burst trend. September 26, 2001, shock phenomenon happened under the lower triangular of 4194 western work place. Coal-winning machine and 180m glide machine moved out 0.8m,the influence of transport laneway is 12m, the top of lane whole offset 0.5m. The main reason is goaf hanging roof did not emit in time, and aside the depth of burial has been 780m, at its own gravity, resulting in rock burst. In June 10, 2004, rock burst happened during the tunneling. Bring out work head 10m scope spurts fall off partially. The main reason is that the laneway is near the F8-1 fault (faller 20m), located in footwall, because of the traction by the fault, the lower part of rock formed an anticline fold and accumulate a large amount of energy. April 27, 2005, Happened 2.5 level rock burst in 4196 work face lower laneway. The top of lane way from the coal face wall within 128m scope protrude1.5m, the below of the lane way from outlet within 22m protrude 0.4m. No obvious damage to roof and floor [5]. According to analysis of geological conditions and reasons of rock burst, the main factors to rock burst are: (1) coal(rock) mechanical properties, including the burst trend of 19# coal seam , stiffness and strength of roof and floor plate; (2) tectonic stress, the mine rock burst often happen nearby folds, faults and other tectonic. That is to say, the relationship is very close between the proportion of the three principal stress and rock burst; (3) roof structure, roof structure and the rock burst have very close relationship, roof strength and stiffness are an important factor to engender stress concentration of coal [6]. Combination above analysis, planed to use numerical simulation method find rock burst mechanism in Panic mine.

3 Numerical model establish

In order to go into study mechanism rock burst of Panic 19# coal, according to the phenomenon release in the mine, adopt FLAC3D software do research. FLAC3D software has the strong function in simulated three-dimension mechanical behavior of rock and yield damage. It also has powerful function for faults, bedding, joints and other weak faces and structure of friction contact surface [7]. 1) Geometric model: set up model seam dip angle by 26°, work face length set up by 80m, section of the coal pillar by 16m, taking the other 30m to eliminate the impact of boundary. Finally set up the model length by 180m; work face strike length by 60m, that is, to achieve face first weighting and two periodic weighting. Cutting lane width is 6m, both ends residual 30m as to eliminate boundary impact. Finally, length of model is 126m; model height accord with integrated histogram and face disclose state, taking into 50m top plate and 15m roof plate, total height of the model is 170m. 2) Constitutive model and boundary conditions: Parameters of the model refer to literature Panic coal rock burst research report [4], the constitutive model adopt Drucker-Prager equation. The four elevation borders are simply supported boundary, hemline border is fixed boundary, imposed uniform loading above the model and its value is the gravity by depth.

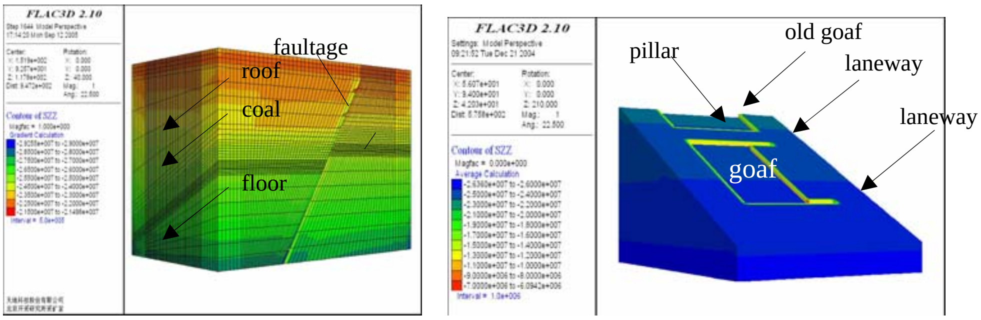

Figure 1 Numerical simulation model of Panic Mine

4 Panic Mine rock burst Mechanism Analysis

1）Geostress factor：

On the analysis of geostress effect, we must first understand the specific mine stress direction and the magnitude. Panic mine in 4193 east laneway using stress relief method to measure [8], the results of stress magnitude as shown in table 1.

Table 1 Measured stress data sheet (Map)

σ_x	σ_y	σ_z	τ_{xy}	τ_{yz}	τ_{zx}
17.27	8.11	14.35	-0.77	1.31	0.07

According to the stress components and stress state characteristic equation [9], calculated that, $\sigma_1 = 17.35$、$\sigma_2 = 14.61$、 $\sigma_3 = 7.79$. The test results show that, 4193 east transport lane roof stress distribute mainly is horizon stress component, principal stress distribution near horizontal ,stress σ_1 as main(σ_1 / σ_2 =1.19, σ_1 / σ_3 =2.23). Because of the direction of maximum horizontal principal stress is not parallel with the roadway axis（Angle approximate 20.5°）,and easily lead to odds stress, making underside of the roof and roadway impose force and get deformation [10]. In the numerical simulation analysis, σ_1 and σ_2 are two horizontal principal stress, σ_1 parallel with the lane axial, σ_2 vertical with the axial, σ_3 for the principal stress. In order to analyze the ratio of stress change effect on mine rock burst, and reference” Maximum principal stress map”and“Zone map of tectonic stress”[8],so the numerical simulation consider three kinds of programs, that is

$\sigma_1 : \sigma_2 : \sigma_3 = 1.0:1.0:1.0$, $\sigma_1 : \sigma_2 : \sigma_3 = 1.2:0.8:1.0$ and $\sigma_1 : \sigma_2 : \sigma_3 = 0.8:1.2:1.0$.

Part of stress concentration cloud figure about numerical simulation as shown in Figure 2. Part of stress changing law as shown in Figure 3.

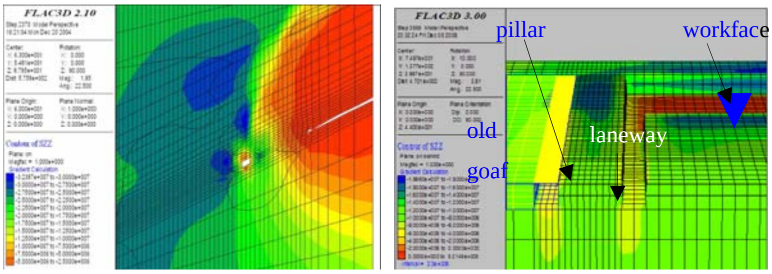

(a). Longitudinal profile (b). Cross section

Figure 2. Stress concentration cloud figure

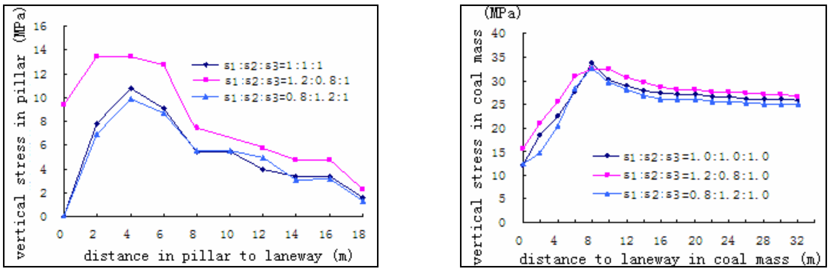

(a). Stress of pillar during tunneling (b). Stress of coal during work face advancing

Figure 3. Vertical stress changes

In stress factors analysis, according to principal stress different ratios analysis, we can receive that: (1) To tunnelling: The smaller of principal stress σ_2 ,the greater peak vertical stress in pillar, concentrations more stronger This deduce, the ratio of principal stress during tunneling to occur rock burst have an extremely important impact. (2) To work face advance: The greater of principal stress σ_2, the greater vertical stress peak in face, concentrations stronger. According to the simulation conclusions, in the face early extracting, the ratio of principal stress change affected section pillar stress significantly, while after the face advancing more than 48m that is, lie in nearly stability phase, the effect of ratio changes significantly decreased.

2）Coal pillar width factor:

In mining process, section coal pillars are the main areas of stress concentration, in its vicinity has become rock burst mainly zone [11]. So, in order to understand the mechanism of rock burst, we need to understand the coal pillar stress distribution law, and clear the relationship of coal pillar width to rock burst affection. In the numerical simulation analysis, we analyzed five kinds of coal pillar width, that is 8m、12m、16m、20m and 24m. Part of stress distribution law as shown in Figure 4.

From Figure 4 (a) we know that, since the width of the coal pillar different, the degrees of stress concentration in work face is different. To 8m, 12m and 16m small coal pillar, stress concentration factor is relatively small, the impact to lane way possibly very small. But to 20m and 24m coal pillar, because of they are wider, makes face stress peak position get close to lane way, stress peak is also more higher, stress concentration factor caused by is larger. Under this concentration, may have a more serious impact to lane way. As face forward, because of coal pillars destruction, lower side of up lane way concentrate relatively high vertical stress. When coal pillars width different, the degree of stress concentration is different, see Figure 4 (b). For 8m, 12m and 16m coal pillar, face stress peak away from the lane way, therefore the impact would small. As for 20m and 24m pillar, which makes stress peak position close to lane way. Thus, unreasonable width of coal pillar located may have a more serious impact.

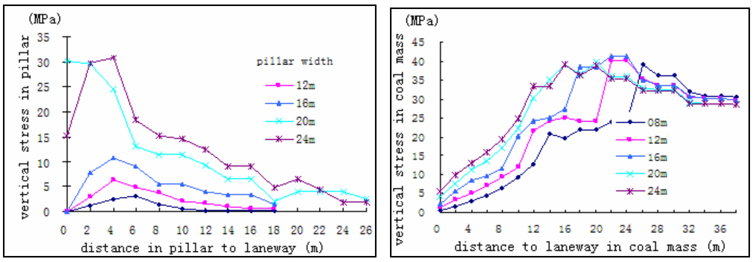

(a). Pillar stress during tunneling (b).Coal stress during face advancing

Figure 4 Vertical stress distribution when different width of coal pillar

3）Roof mechanics parameters factors:

The impact to rock burst as roof mechanics parameters factors change, in the application of numerical simulation analysis, we consider three kinds of roof conditions: (1) According to the lab measurement set the roof elastic modulus, tensile strength and cohesion; (2) The parameter value reduced to 50% to determine; (3) The first parameter value reduced to 20% to determine.

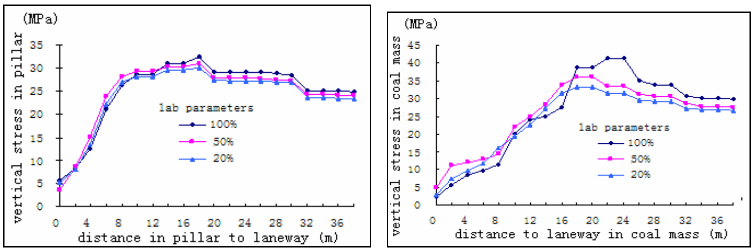

(a). Stress in pillar (b). Stress in coal mass

Figure 5 Stress distribution under different roof conditions

From Figure 5(a) we know that, the changing of roof conditions makes little effect to pillar stress distribution. However, the impact will greater when the roof weighting. If larger roof fall, it will induce impact to coal pillar, and make the stress in coal pillar with greater increase. The larger of roof strength and stiffness, the larger impact to coal pillar, the probability of burst trend is larger, too. From Figure 5(b) we know that, roof conditions changing to face vertical stress distribution have great affected. The greater strength and stiffness, the greater peak value of stress concentration, but the stress peak is further away from the lane way, the impact will be small. Changes in roof conditions also have great impact to face front abutment pressure distribution. When roof strength and stiffness reduce a certain extent, the front abutment pressure will be greatly reduced; the face roof will reduce burst risk.

5 The main conclusions

1) During laneway tunneling, the smaller the principal stresses σ_2; the greater the peak value of the vertical stress in the coal pillar while the concentration will be stronger. During the extraction of the work face, the

principal stress ratio change to the front abutment pressure impact is larger in initial stages; while in the normal recovery period, the impact is relatively smaller to front abutment pressure.

2) The width of the coal pillar has a greater impact to laneway with larger coal pillars having more of an effect compared to smaller ones. When the width of a coal pillar is bigger than 20m, the upper laneway burst risk is bigger.

3) Roof condition changes have big influences on rock burst. Especially during roof weighting, pillar stress distribution, and the work face front abutment pressure law.

4) Comprehensive analysis of the crystal stress factor, coal pillar factor, and roof condition factor impacts both sides of the laneway and the upper half of the workface. Among them, the strongest impact is coal pillars. Therefore reasonable stay for coal pillars is a key issue to solve Panic mine rock burst.

Acknowledgements

The present work is funded by the National Science and Technology support plan key project issues – “Deep mining coal (rock) dynamical disaster multi-parameter identification and solve risk key technology and equipment” (2006BAK03B06).

References:

1. Qi, Q.X. and Dou, L.M. Rockburst Theory and Technology. China University of Mining and Technology Press, 2008.
2. Qi, Q.X. Layered structure of coal (rock) mass destruction to rock burst theory and practice. Coal Mining & Designing Branch, Coal Research Institute, 1996.
3. Qi, Q.X., Liu, T.Q. and Shi, Y.W. Rockburst instability mechanism of sliding friction. Mine pressure and Roof Management, 1995(3, 4):174-176
4. Qi, Q.X. Panic coal mine rock burst research report. Coal Mining & Designing Branch. Coal Research Institute, 2007.
5. Zhu, J.W. and Liu, X.Z. Deep special rock burst reason and countermeasures. Shandong Coal Science and Technology, 2006.
6. Qi, Q.X., Ji, Z.E. and Pan, J.F. Xinwen coal mine deep mining rock burst reason and treatment technology. Beijing Coal Industry Press, 2007.
7. Theory and Background in FLAC3D. Itasca Consulting Group, Inc. 2004.
8. Wang, Z.H., Zhang, H.W. and Shi, Y.S. Geo-Dynamic division in the Xinwen Panic mine. Journal of Liaoning Technology University, 2005, (3):23-28.
9. Wu, J.L. Elastic mechanics. Higher Education Press, 2004.
10. Qi, Q.X. and Kang, L.J. Laneway Stress Numerical Study. Coal Science and Technology, 1994, 22:31-35.
11. Qi, Q.X. and Kang, L.J. Surround laneway conditions and stress state analysis. Mine pressure and Roof Management, 1994, 1:44-49.

RaSiM 7(2009): Controlling Seismic Hazard and
Sustainable Development of Deep Mines,
C.A. Tang(ed), Rinton Press, 519-524

SEISMIC WAVE INPUT STUDY ON NONLIEAR THREE-DIMENSIONAL VISCOELASTIC ARTIFICIAL BOUNDARIES

SHU-CAI LI

Geotechnical and Structural Engineering Research Center, Shandong University

Jinan 250061,China

BO ZHANG

Geotechnical and Structural Engineering Research Center, Shandong University

Jinan 250061,China

In this paper the seismic wave motion input method on three-dimensional nonlinear viscoelastic artificial boundary was presented. Taking the assumption that the far field medium out of the computing field is viscoelastic material and the medium in the computing field is elastic-plastic material, the radiation damping of far field medium was simulated with three-dimensional nonlinear artificial viscoelastic boundary. The force applied on the artificial boundary to implement the seismic wave input can be expressed with the displacement and velocity of the input seismic wave, which makes the seismic wave easy to input.

1 Introduction

The seismic wave propagates to the upper structure through the foundation, and the seismic response of the structure can be transmitted to the foundation conversely, which is called foundation-structure interaction. The exact seismic wave input is the precondition to solve the foundation-structure interaction problem. Many seismic input methods have been presented recently such as inputting displacement [1] or acceleration [2], large mass method [3] and so on. However, these methods are not suitable to solve foundation-structure interaction problem when the viscoelastic artificial boundary was used. A seismic wave input method for the viscoelastic boundary was presented in this paper [4] called the equivalent boundary force method [5]. In this method the force is applied on the viscoelastic boundary nodes to implement seismic wave input. The force applied on the three dimensional linear viscoelastic boundary is presented in this paper [6]. However, the force applied on the three dimensional nonlinear viscoelastic boundary has not been presented in any paper. In this paper taking the assumption that the far field medium out of the computing field is viscoelastic material and the medium in the computing field is an elastic-plastic material; the radiation damping of far field medium was simulated with the three-dimensional nonlinear viscoelastic artificial boundary. The force applied on the artificial boundary to implement the seismic wave input can be expressed with the displacement and velocity of the input seismic wave, which make the seismic wave simple to input.

2 Equivalent boundary force method

When the viscoelastic boundary is used to solve foundation-structure interaction problems, the standard of exact seismic wave input is that the displacements and stresses of the artificial boundary are the same with those of the original wave field [4].

$$u(x_B, y_B, z_B, t) = u_i(x_B, y_B, z_B, t) \tag{1}$$

$$\sigma(x_B, y_B, z_B, t) = \sigma_i(x_B, y_B, z_B, t) \tag{2}$$

where $u_i(x_B, y_B, z_B, t)$ and $\sigma_i(x_B, y_B, z_B, t)$ are the displacement and stress in original wave field, $u(x_B, y_B, z_B, t)$ and $\sigma(x_B, y_B, z_B, t)$ are the displacement and stress of nodes at viscoelastic boundary.

By applying a force $F_B(t)$ on the node at viscoelastic boundary to input seismic wave (Figure.1),the stress of node at viscoelastic boundary is

$$\sigma(x_B, y_B, z_B, t) \cdot A = F_B(t) - f_B(t) \tag{3}$$

where A is the area where the force $F_B(t)$ influence and

$$f_B(t) = C\dot{u}_i(x_B, y_B, z_B, t) + Ku_i(x_B, y_B, z_B, t) \tag{4}$$

where C and K are the parameters of viscoelastic boundary,

By substituting eqs.(2)and(4) into (3),the force $F_B(t)$ applied on the viscoelastic boundary nodes can be written as

$$F_B(t) = \sigma_i(x_B, y_B, z_B, t) \cdot A + C\dot{u}_i(x_B, y_B, z_B, t) + Ku_i(x_B, y_B, z_B, t) \tag{5}$$

The force applied on the viscoelastic boundary nodes to implement seismic wave input can be obtained from eq.5.

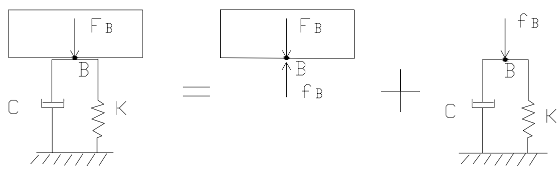

Figure 1. Schematic diagram of viscoelastic boundary and equivalent boundary force

3 Three dimensional nonlinear viscoelastic artificial boundary

The one and two dimensional nonlinear viscoelastic boundary have been presented in paper[7] and the three nonlinear viscoelastic boundary have been presented in paper [8] (Figure 2).

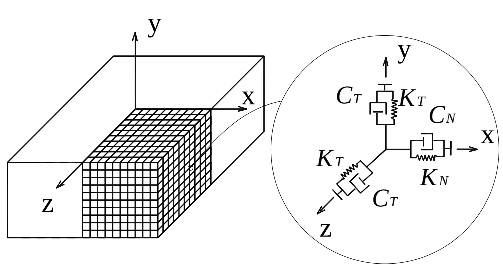

Figure.2 Three dimensional viscoelastic boundary

The three nonlinear viscoelastic boundary was deduced In paper [8] through the assumption that far field medium is Kelvin viscoelastic material. The parameters of three nonlinear viscoelastic boundary in normal direction[8] is written as

$$K_N = K\frac{k_1^2(a_1 - 1/R) + a_1^2(a_1 + 1/R)}{(a_1 + 1/R)^2 + k_1^2} + \frac{4}{3}G_k\left[\frac{3}{R} + \frac{k_1^2(a_1 - 1/R) + a_1^2(a_1 + 1/R)}{(a_1 + 1/R)^2 + k_1^2}\right]$$

$$+\frac{4}{3}\eta_k k_1\omega\left[-1+\frac{1}{R^2}\frac{1}{(a_1+1/R)^2+k_1^2}\right] \tag{6}$$

$$C_N = Kk_1\left[1-\frac{1}{R^2}\frac{1}{(a_1+1/R)^2+k_1^2}\right]+\frac{4}{3}G_k k_1\left[1-\frac{1}{R^2}\frac{1}{(a_1+1/R)^2+k_1^2}\right]$$
$$+\frac{4}{3}\eta_k\left[\frac{3}{R}+\frac{k_1^2(a_1-1/R)+a_1^2(a_1+1/R)}{(a_1+1/R)^2+k_1^2}\right] \tag{7}$$

The parameters of three nonlinear viscoelastic boundary in tangential direction[8] is written as

$$K_T = G_k(a_2+\frac{2}{R})-\eta_k\omega k_2 \tag{8}$$

$$\mathrm{C_T} = \eta_k(a_2+\frac{2}{R})+G_k k_2/\omega \tag{9}$$

where

$$k_1^2 = \frac{\rho\omega^2(K+\frac{4}{3}G_k)}{2\left[(K+\frac{4}{3}G_k)^2+(\frac{4}{3}\eta_k\omega)^2\right]}\left(\sqrt{1+\frac{(\frac{4}{3}\eta_k\omega)^2}{(K+\frac{4}{3}G_k)^2}}+1\right) \tag{10}$$

$$a_1^2 = \frac{\rho\omega^2(K+\frac{4}{3}G_k)}{2\left[(K+\frac{4}{3}G_k)^2+(\frac{4}{3}\eta_k\omega)^2\right]}\left(\sqrt{1+\frac{(\frac{4}{3}\eta_k\omega)^2}{(K+\frac{4}{3}G_k)^2}}-1\right) \tag{11}$$

$$k_2^2 = \frac{\rho\omega^2 G_k}{2[G_k{}^2+(\eta_k\omega)^2]}\left(\sqrt{1+\frac{(\eta_k\omega)^2}{G_k{}^2}}+1\right) \tag{12}$$

$$a_2^2 = \frac{\rho\omega^2 G_k}{2[G_k{}^2+(\eta_k\omega)^2]}\left(\sqrt{1+\frac{(\eta_k\omega)^2}{G_k{}^2}}-1\right) \tag{13}$$

where G_k , η_k and K are rigidity modulus, viscosity coefficient and bulk modulus of Kelvin viscoelastic material[9].

4 The boundary equivalent force of three dimensional nonlinear viscoelastic boundary

In this paper the assumption is taken that the far field medium out of the computing field is viscoelastic material, the medium in the computing field is elastic-plastic material and the input seismic wave is plane decaying wave in vertical direction.

The displacement expression of input seismic wave is

$$u_i(R,t) = f_j(R)\cdot g(R+ct) \tag{14}$$

The velocity of input seismic wave is

$$\dot{u}_i(R,t)=\frac{\partial u_i(R,t)}{\partial t}= f_j(R)\cdot c\cdot g'(R+ct) \tag{15}$$

where $f_j(R)$ is the decaying function of input seismic wave and $f_j(R)=1/R$,when the input seismic wave is P wave, $c=c_p=\sqrt{(\lambda+2G)/\rho}$,and when it is S wave, $c=c_s=\sqrt{G/\rho}$, ρ is the density and λ, G is the lame constants of material in computing field.

4.1 Input P wave in vertical direction

When the seismic wave is input in vertical direction, $u_x=u_z=0$, $u_y=u_i$,the stress of original wave field is

$$\sigma_i=\sigma_y=(\lambda+2G)\frac{\partial u_y}{\partial y}=(\lambda+2G)\frac{\partial u_i}{\partial R}=(\lambda+2G)[f_j'(R)g(R+c_pt)+f_j(R)g'(R+c_pt)] \tag{16}$$

By using eqs.(14),(15)and(16), the stress of original wave field is written as

$$\sigma_i=-\frac{\lambda+2G}{R}u_i+\rho c_p\dot{u}_i \tag{17}$$

By substituting eq.(17) into (5),the force applied on the viscoelastic boundary to implement *P* wave input in vertical direction is written as

$$\begin{aligned} F_{BN}(t)&=\sigma_i(x_B,y_B,z_B,t)\cdot A+C_N\dot{u}_i(x_B,y_B,z_B,t)+K_Nu_i(x_B,y_B,z_B,t)\\ &=\left(K_N-\frac{\lambda+2G}{R}\cdot A\right)u_i+\left(\rho c_p\cdot A+C_N\right)\dot{u}_i \end{aligned} \tag{18}$$

where K_N, C_N is shown in eqs.(6),(7) and A is shown in eq.(3)

4.2 Input S wave in vertical direction

When the seismic wave is input in vertical direction, $u_y=u_z=0$, $u_x=u_i$,the stress of original wave field is

$$\tau_i=G(\frac{\partial u_x}{\partial y}+\frac{\partial u_y}{\partial x})=G\frac{\partial u_i}{\partial R}=G[f_j{}'(R)\cdot g(R+c_pt)+f_j(R)g'(R+c_pt)] \tag{19}$$

By using eqs.(14),(15)and(19), the stress of original wave field is written as

$$\tau_i=-\frac{G}{R}u_i+\rho c_s\dot{u}_i \tag{20}$$

By substituting eq.(20) into (5),the force applied on the viscoelastic boundary to implement S wave input in vertical direction is written as

$$\begin{aligned} F_{BT}(t)&=\tau_i(x_B,y_B,z_B,t)\cdot A+C_T\dot{u}_i(x_B,y_B,z_B,t)+K_Tu_i(x_B,y_B,z_B,t)\\ &=\left(K_T-\frac{G}{R}\cdot A\right)u_i+\left(C_T+\rho c_s\cdot A\right)\dot{u}_i \end{aligned} \tag{21}$$

where K_N, C_N is shown in eqs.(8),(9) .

It can be seen from eqs.(18),(21) that the force $F_B(t)$ applied on the viscoelastic boundary to implement seismic wave input can be expressed with the displacement and velocity of input seismic wave, which makes the seismic wave input easy to implement.

5 Numerical verification

An example was done with ANSYS to verify the accuracy of seismic wave input method presented in this paper. The computing model is shown in Figure.3, the parameters of computing model are: shear modulus $G = 5292$ MPa, Poisson ratio $v = 0.25$, density $\rho = 2700$ kg/m^3, the material out of the computing field is Kelvin viscoelastic material, viscosity coefficient $\eta = 100000$ MPa·d. The domain of computing field is $|x| \le 381m$, $|z| \le 381m$, $y \le 381m$, the size of element is $\Delta x = \Delta y = \Delta z = 38.1m$, the observation point $A(0,0,0)$ is the center point at top surface. The input wave is shown in Figure.4. The displacement time history of observation point $A(0,0,0)$ is shown in Figure.5.

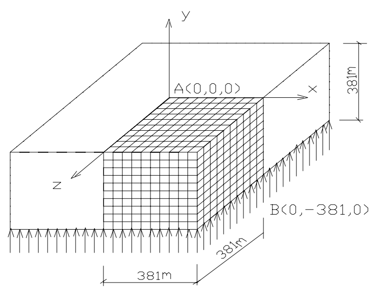

Figure.3 Computational model for input seismic wave

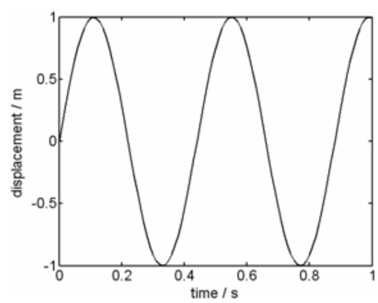

Figure.4 Displacement time-history of input wave

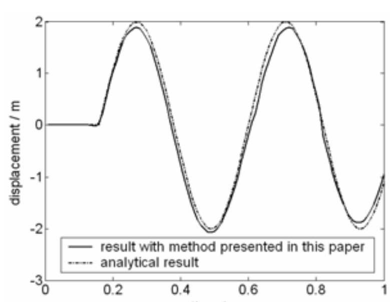

Figure.5 Displacement time-history of observation point

It can be seen that the result obtained in this paper is agreement with the analytic result [9].

6 Conclusions

The exact seismic wave input is a needed precondition to solve the foundation-structure interaction problem. Taking the assumption that the far field medium out of the computing field is a viscoelastic material and the medium in the computing field is elastic-plastic material, the radiation damping of far field medium was simulated with a three-dimensional nonlinear viscoelastic artificial boundary. The seismic wave input method used for nonlinear viscoelastic boundary was researched in this paper. The force $F_B(t)$ applied on the viscoelastic boundary to implement seismic wave input can be expressed with the displacement and velocity inputs of the seismic wave. This makes the seismic wave input easy to implement, and the accuracy of this method was verified through numerical examples.

Acknowledgments

This research was supported by Chinese National Natural Science Funds for Distinguished Young Scholar (50625927), National Natural Science Foundation of China (40872203) and National Basic Research Program of China (973 Program, No.2007CB209407).

References

1. Federica, D., Giuliano, B. and Laura, D.S., et al. Seismic facies and sedimentary processes on the continental rise off Wilkes Land (East Antarctica): evidence of bottom current activity. Deep Sea Research Part II: Topical Studies in Oceanography, 2003, 50(8):1509-1527.
2. Shoji, Y. and Kamiyama, M. Estimation of local site effects by a generalized inversion scheme using observed records of ‘Small-Titan’. Soil Dynamics and Earthquake Engineering, 2002, 22(9): 855-864.
3. Pandey, G.R., Mutsuyoshi, H. and Maki, T. Seismic performance of bond controlled RC columns. Engineering Structures, 2008, 30(9): 2538-2547
4. Liu, J.B. and Lv, Y.D. A direct method for analysis of dynamic soil-structure interaction. Chinese Civil Engineering Journal, 1998, 31(3): 55- 64.
5. Zhao, M. The study on viscoelastic artificial boundary and transmitting artificial boundary. Beijing Polytechnic University, Master Dissertation, 2004.
6. Zhang, B., Li, S.C. and Yang, X.Y., et al. Study on seismic wave motion input with three-dimensional visco-elastic artificial boundary. Rock and Soil Mechanics, 2009, 30(3):774-778.
7. Wang, Z.Y. and Liu, J. B. Study on Wave Motion Input and Artificial Boundary for Problem of Nonlinear Wave Motion in Layered Soil. Chinese Journal of Rock Mechanics and Engineering, 2004, 23(7):1169-1173.
8. Zhang, B. The Seismic Response Analysis of CFST Deck Arch Bridge Considering Structure-Foundation Interaction. Shandong University, Doctoral Dissertation, 2009.
9. Zhou, G.Q. and Liu, X.M. Theory of viscoelasticity. University of Science and Technology of China Press, 1996.

*RaSiM 7(2009): Controlling Seismic Hazard and
Sustainable Development of Deep Mines,
C.A. Tang(ed), Rinton Press, 525-530*

NUMERICAL SIMULATION AND STRESS ANALYSIS OF ROCKBURST IN COAL MINE

ZHEN-HUA LI [1, 2]

1. School of Energy Science & Engineering, Henan Polytechnic University

Jiaozuo, 454000, China

2. School of Resource and Safety Engineering, China University of Mining & Technology

Beijing, 100083, china;

In order to achieve the relation between rockburst and the stress distribution and provide basis for the reasonable protection and control measures of rockburst, numerical simulations were carried out to study the rock stress in rockburst tunnel. The numerical results showed that non-uniform thin-walled stress is the main reason of the frequent rockburst in driving tunnel. When the hard-brittle rock is disturbed, owning to the stress summit close to the surface of tunnel rock, peak stress may exceed the limit rock strength, leading to the occurrence of rockburst.

1 Introduction

Bolstad pointed out that the rockburst research has been carried out more than half a century, but only recently have there been obvious achievements. This achievement is almost entirely due to the numerical simulation, improvement of test means, further understanding of rock behavior and development of new acoustic emission instruments [1]. The numerical simulation method used in analyzing rockburst can be traced back to as early as 1968. Starfield and Fairhurst used the numerical simulation to determine the stiffness of the local mining, analyze the reasonable size of pillars, and to prevent instability destruction (rockburst) in their paper [2]. In our country, the research on numerical simulation of rockburst is focused on the mining and hydropower projects. Lu Jiaming and some others used the finite element method to analyze and forecast rockburst in hydropower chamber [3]. Zhang Mengtao put forward the unified instable theory of the rockburst, and he used finite elements to study the coal mine rockburst based on numerical simulation [4]. Le Xiaoyang used discrete element methods to study rockburst of jointed rock mass, and he compared the result with the result of finite element simulation and actual rockburst. He also found that the result of discrete element was the same with the actual position [5]. Professor Tang Chunan in Northeastern University used RFPA to simulate the gestation and the process of rockburst to achieve accurate results [6].

In order to educe the relation between rockburst and stress distress, and afford some basis to defend and control rockburst, according to the actual geological condition, this paper adopted the FLAC^{3D} engineering analysis software to simulate the stress state of surrounding rocks.

2 Brief Introduction of FLAC^{3D}

According to the actual condition, the thesis adopted FLAC^{3D} finite-difference program developed by the University of Minnesota. FLAC^{3D} algorithm is based on the rapid calculation of Lagrange [7, 8], and it's especially suitable for nonlinear large deformation or instability (such as sliding or separation) issues of rock mechanics, and its grid computing model can deform largely and flow with material. It provides two calculation models to suit a variety of on-site conditions that is large and small deformation. In each calculation step, FLAC^{3D} can calculate the largest imbalance in order to determine the stability of the system [9]. It can also simulate the excavation and support process, as well as the loose of rock and reinforcement effect during the construction process [9].

3 Numerical simulation model design

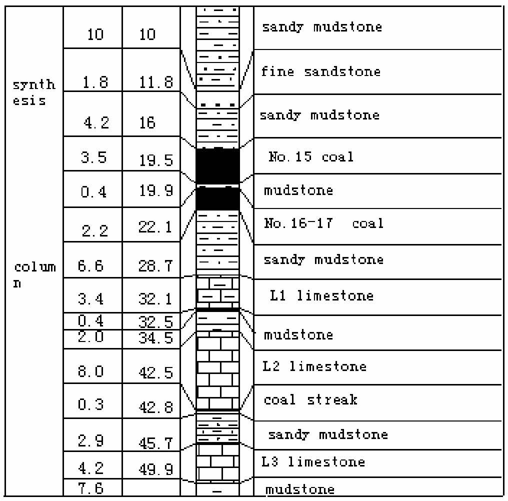

Figure 1 The synthesis column map

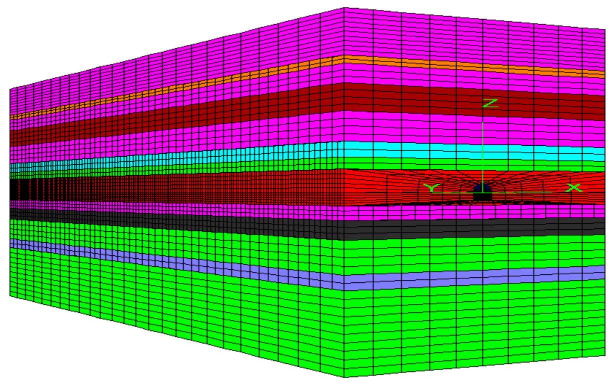

Figure 2 Numerical simulation model

According to the actual engineering geological conditions of the test mine, the numerical simulation model was established. The synthesis column of roadway is shown in figure 1. As the rockburst always occurred in the L1, L2 limestone, so the model select the L2 limestone where roadway is, as well as roof and floor rock, a total of 19 layers of rock, of which 6 layers are the thick and weak layers, and they are far from L2 limestone. Then the 19 layers were generalized based the geology to 13 layers, as in figure 2. The upper of the model was pressured in accordance with the gravity of the overlying rock stress. Four sides were confined by applying confined pressure and the bottom was confined by the vertical stress. The Physico-mechanical parameters of rock are in table 1. The Moore – Coulomb plastic model was adopted to simulate the surrounding rock, and the cable unit was used to simulate prestressed anchor.

Table 1. Physico-mechanical parameters of rock

name	uniaxial compressive strength (MPa)	uniaxial tensile strength (MPa)	cohesion (MPa)	friction angle (°)	elastic modulus (GPa)	poisson ratio	density (kg/m3)
fine sandstone	56.2	*1.03	*4.0	*42	6.1	0.12~0.14	*2660
mudstone	37.8	*0.07	*1.4	*32	5.1	0.14	*2635
coal	18.44	*0.03	1.0	*32	1.986	*0.36	1370
sandy mudstone	40	2.0	3	30	5.7	0.16	2625
L1 limestone	*204	*7.16	*43.41	*47.6	*29.67	0.25	2700
L2 limestone	206.63	4.96	23.78	53.3	34.62	0.25	2700
L3 limestone	*208.80	*5.26	*40.20	*48.5	*40.23	*0.25	2700
L4 limestone	*210.36	*6.23	*41.20	*52.10	*35.98	*0.25	2710

Annotation 1:* represents engineering analogy data

The cross-section size of the numerical model is 60 meters wide and 80 meters high, and 200 meters long along the trend. The roadway is simulated according to the actual size, and its shape is semi-arch, wall is 1.7 meters high, and arch radius is 2.1 meters. The roadway is supported by the resign bolt of endmost anchoring, and the bolt row spacing is 0.7 meters, distance is 0.7 meters. The support technology is the prompt support after tunnelling. During the excavation process, the excavation step of 1.5 meters is the most reasonable and also in accordance with the actual conditions. But as the calculation model include too much units and the restriction of simulation, the calculation process would take too much time. Therefore, the roadway is excavated 20 meters, 50 meters, 80 meters and 100 meters to simulate and study the influence on the distribution of stress state on the surrounding rock and of different length of the roadway.

4 Analysis of simulation result and stress state

4.1 Analysis of simulation result

The numerical simulation was made by excavating step by step. The stress in front of and two side of working face simulated separately by 20 meters, 50 meters, 80 meters, 100 meters, and the vertical Stress distribution nephogram in front of the working space, vertical side Stress distribution isoline in front of the working face, and stress distribution isoline on the section of roadway were educed. According to the results of simulation, we can see that after excavation, stress concentration in front of the working face and on two side of the roadway is one main factor to cause rockburst.

4.1.1 Analysis of stress on the side of roadway

The stress distribution charts on the section of laneway excavation by 20 meters and 80 meters showed: the roadway was in the L2 limestone, because this layer was thick, strong, hard, and coupled with the strong support measure, excavation did not cause damage to the surrounding rock, no plastic zone, and the displacement of the roadway was very small, and the largest displacement was less than 1 centimetre; stress in the surrounding rock of two side increased significantly, and stress near the laneway reached the peak stress; stress concentrated in the top-left section of roadway was obvious and stress gradient was large. The stress on the sidewall of roadway increased as the excavating went on, but not significantly. That was, the length of excavation did not affect surrounding rock stress concentration obviously.

From the above conclusions, we can see that although there was stress in the surrounding rock on the sidewall of roadway, because of the use of strong support method (shotcrete rockbolt mesh), it changed the stress of surrounding rock and with the increase in the length of the excavation, and the stress did not increase. That was the reason why there is nearly no rockburst in the back of excavation. But if the roadway was in the impacting zone of faults, the surrounding rock would be cut, squeezed, and reversed, causing local stress concentration, then the rockburst would occur, so the roadway which had geological structure should be adopted more effective support method.

On the top-left of roadway stress concentrate was obvious and stress gradient was large, and that was one important factor of rockburst, which also matched the field statistics of rockburst, so more research should be focused on stress distribution on the top-left of the working face.

4.1.2 Stress distribution in front of the working face

From the stress distribution isoline or nephogram of working and in front of working, we can draw the following conclusions: there was no plastic region in front of the working face, within the short distance (0 ~ 3 meters) stress increased significantly, no stress decreasing zone, the peak stress formed on the work facing;

within 0 ~ 15 meters distance in front of the working face, stress increased; on the top-left of working face, the stress concentrate was obvious and stress gradient was large,whch was the reason why rockburst occurred frequently on the top-left; From all the stress nephograms we can see as the excavation length increased, stress always concentrated on the top-left, indicating that the increase of roadway excavation length had no obvious affection on stress concentrate after excavation.

4.2 Analysis of rockburst stress state

According to the simulation results, on the sidewall of laneway or in front of the working face, within a short distance (0 ~ 3 meters) there was great stress concentration. Because the stress concentration peak in the surrounding rock was near to the surface of roadway, all the surrounding rock of roadway in the back of working face, there was like a thin leaf between stress peak and the surface of roadway, and on the different parts of roadway the thickness was different, this stress concentration was called non-uniform thin-walled stress concentration. After excavation, in the surrounding rock of sidewall of roadway in front of and in the back of working face, floor and bottom, there would be non-uniform thin-walled stress concentration. On the sidewalls and bottom, the stress concentration became even more evident. Due to the existence of thin-walled stress concentration, the surrounding rock gathered more flexible power, when the rock was disturbed, the flexible power gathered would release in a rock broken way, which was rockburst. But on the bottom of working face, because after the excavation many blasted-rock piled up on the bottom and buried it, even if rockburst occurred on the bottom, we only heard the rockburst sound, which was why the rockburst was always found occurring on the top-left section of roadway. According to the results of the simulation, the thin-walled stress peak increased as the roadway's excavation, but the range was always within 0 ~ 3 meters in front of the working face. Due to the existence of the thin-walled stress, the surrounding rock in front of the working face accumulated a lot of flexibility power; if these power released suddenly that inevitably lead to the geological disaster of dynamic instability, such as burst, loosing, stripping, ejecting and even throwing, which is the rockburst.

Using a circular roadway as an example, the stress distribution of surrounding rock and the formation of non-uniform thin-walled stress in the excavation roadway were analyzed.

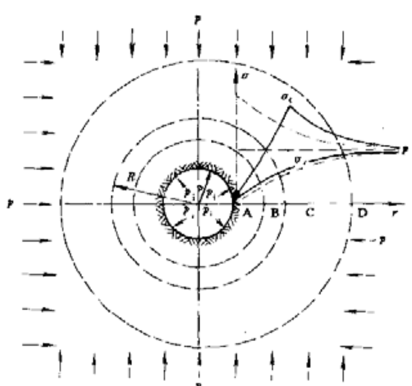

Figure 3 Plastically deforming area and stress distribution of circular tunnel
p—original rock stress; σ_t—tangential stress; σ_r—radial stress; p_i—support resistance; a—the radius of roadway;
R—the radius of plastic zone; A—the fractured zone; B—the plastic zone; C—the flexible zone; D—the original rock stress zone

The rock without mining was usually in a state of elastic deformation before excavation. The original vertical stress of rock *p* was the weight of the overburden rock γH. After excavation the stress would redistribute, that is the surrounding rock stress concentration inside. The stress distribution of plastic deformation and elastic deformation was shown in Figure 3. In plastic circle zone (A), the strength of rock decreased significantly, so the pressure it can afford reduced significantly, and was lower than the original stress γH. The zone where the surrounding rock broken and displaced was called the rupture zone and that was the zone for reducing and unloading stress. The stress of plastic zone outer ring (B) was higher than the original stress. It and the part of stress-increased in elastic zone were loading zone, and also were called the stress increasing zone. The support force was the result of the interaction between support and rock from non-flexible zone.

By using limiting equilibrium theory, under the circumstance of each direction equal pressure ,the calculation formulas of stress in plastic zone, the radius of plastic zone and the periphery displacement of the circular roadway are shown below.

The radial stress is

$$\sigma_r = (p_i + c \bullet ctg\phi)(\frac{r}{a})^{\frac{2\sin\phi}{1\text{-}\sin\phi}} \text{-} c \bullet ctg\phi \qquad (1)$$

The tangential stress is

$$\sigma_i = (p_i + c \bullet ctg\phi)\frac{1+\sin\phi}{1\text{-}\sin\phi}(\frac{r}{a})^{\frac{2\sin\phi}{1\text{-}\sin\phi}} \text{-} c \bullet ctg\phi \qquad (2)$$

The radius of plastic zone is

$$R = a[\frac{(p + c \bullet ctg\phi)(1\text{-}\sin\varphi)}{p_i + c \bullet ctg\phi}]^{\frac{1\text{-}\sin\phi}{2\sin\phi}} \qquad (3)$$

The periphery displacement is

$$u = \frac{a\sin\phi}{2G} \bullet \frac{(p + c \bullet ctg\phi)^{\frac{1}{\sin\phi}}(1\text{-}\sin\varphi)^{\frac{1\text{-}\sin\phi}{2\sin\phi}}}{(p_i + c \bullet ctg\phi)^{\frac{1\text{-}\sin\phi}{2\sin\phi}}} \qquad (4)$$

Where p is the original rock stress; p_i the support resistance; a the radius of circular roadway; r the radius of stress solved; R the radius of plastic zone; φ the internal friction angle of surrounding rock; c the cohesion of surrounding rock; G the shear elastic modulus.

According to Eq. (2) and Eq. (4), the stability and the periphery displacement of the roadway depend largely on the original rock stress p, the internal friction angle φ and cohesion c that reflect the rock strength, the support resistance pi and radius of roadway. Relations between them are as follows:

(1) With the increase of the original rock stress, the periphery displacement of roadway increase exponentially. The index lies on the changes of φ, the smaller φ is, and the greater the index is, the value of the displacement grows rapidly.

(2) With the friction angle φ and cohesion c increase, the radius of plastic zone R increases significantly.

The L2 limestone where the roadway located in is the hard brittle surrounding rock. The curve A in figure 4 is its typical complete stress-strain curve and the curve B is the complete stress-strain curve of rock with lower strength. From the figure, we can see the failure characteristics are different from the elastic-plastic rock which is showed by the curve B. The strength of hard brittle rock is large and its displacement is small. But when the stress exceeds the peak stress, the hard brittle rock will failure instantly with the accumulated flexible power releases suddenly. It can be considered, the roadway is excavated in the hard and brittle rock, just after the excavation, if the original rock stress is lower than the rock strength, the physico-mechanical properties of surrounding rock will not change much, that is, the internal friction angle φ and cohesion c will not decrease significantly. So there will form a smaller radius of the plastic zone, which makes the peak stress remain near the surface of roadway, and form non-uniform thin-wall stress concentration.

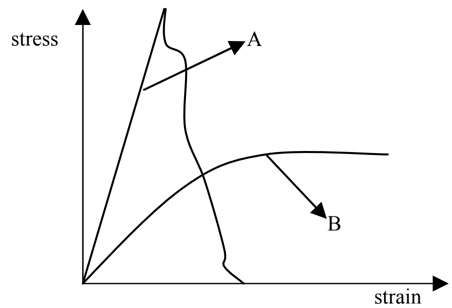

Figure 4 Stress-strain curve of hard brittle rock

5 Conclusions

The existence of non-uniform, thin-walled stress is the important factor of rockburst. The peak stress concentration in surrounding rock is near the roadway surface, as to the hard brittle rock, which allows the peak stress concentration to exceed the ultimate strength of the rock when it is disturbed by rockburst. Therefore, in order to prevent rockburst, it is necessary to take measures to change the stress state in the surrounding rock, that is to change this non-uniform thin-walled stress concentration and make the stress concentration transfer to the deep surrounding rock, to reduce the damage of rockburst or prevent the rockburst.

Acknowledgements

The author wish to acknowledge the collaborative funding support from the Projection of China National "973" Program (2007CB209402).In particular we wish to thank LI Huamin and YAO Jun for their contributions to this research project.

References

1. Muwu, Yun. Tunnel mechanics. Beijing: China railway press, 1983. (in Chinese).
2. Fang, W.T. Development and Prospect of China Coal Industry—the Developmental Trend and Prospects of Mining in Future. The 14th International Conference on Mining, 1990.
3. Zheng, Y.R. Bolt-shotcrete Support Design Guide of Underground Engineering. Beijing: Metallurgical Industry Press, 1988.
4. Zhao, D.Z. Numerical Methods in Engineering Mechanics. Beijing: China Railway Press, 1993.
5. Sun, G.Z. Optimization Design and Application. Beijing: China Communications press, 2000.
6. Wang, R.L. and Jin. X.W. Application of Bolt Support in Villages and Towns Coal Mine.coal, 2000, (6). 35-37.
7. Sheng, Q. and Ren, F. Continuum Medium fast Lagarangian analysis and its Use in Rock Engineering. The 1st Symposium on Rock Mechanics of Dam. Guangzhou: Zhongshan University press, 1993.
8. Zhang, D.R., Tao, L.J. and Li, F.Y. Lagrangian Element Method and its Application Software FLAC. Ground pressure and Strata Control, 1997, 3(4). 224-226.
9. Li, Z.K. and Liang, H.B. The Basic Principle and Using Method Guide of FLAC Program. Beijing: Department of hydraulic engineering, Tsinghua University, 1993.
10. Deng, J.G. and Liu, S.J. Calculation of Elastoplastic Deformation of Wellbore in Soft Mudstone Using Lagrangian Method. Journal of Geomechanics, 1999, 5(1). 33-37.

RaSiM 7(2009): Controlling Seismic Hazard and
Sustainable Development of Deep Mines,
C.A. Tang(ed), Rinton Press, 531-534

THEORETICAL ANALYSIS AND FLAC3D SIMULATIONS ON ROCK CRACKS PROPAGATION CRITERION UNDER BLASTING LOADING

NING LIU , WEI-SHEN ZHU and XIAO-LI XIN

Research Center for Geotechnical and Structural Engineering ,Shandong University

Jinan ,250061, P.R. China

Considering the fracture mechanics, this paper analyzes the stress intensity factor under blasting loading and initial geostress. The rock crack's propagation criterion is introduced and the method of calculating the propagation zone is obtained. In order to prove its feasibility and rationality, one tailrace tunnel is analyzed by dynamical calculation of FLAC3D. The cracks propagation zone is illustrated. The results show the propagation zone is approximately 90~100 times of the cylindrical charge, and are good coincidence with the results from the blasting experiments.

1 Introduction

When explosions happen inside rock, large amount of blasting energy are released, blasting shock waves and stress waves are induced on the surrounding rock. A great number of random distribution cracks appearand break the rock, however, during the excavation of the underground projects, the blasting method is widely used. So with the blasting inside the rock to be excavated, the mechanical parameters of the surrounding rock are inevitably descended or damaged by the appearance and propagation of the cracks. This brings hidden danger to the safe construction of the projects. We can see that the blasting failure is actually the result of crack propagation. Although there are many new blasting techniques, such as the presplitting technique, smooth blasting and so on; for any technique, blasting can make damage of different extents to the rock. Studying the propagation zone of the blasting cracks and establishing crack propagation criterion under blasting load is very important to analyze rock stability and take corresponding safe measurements [1~5].

2 Rock Crack Propagation Criterion under Blasting Load

The crack model was simplified as the following figure, a group tensile cracks was bearing concentrated force *F* and the far compression stress. The force *F* showed the action *T* of the shear force to the initial crack plane made to the tensile cracks and the blasting stress *P*.

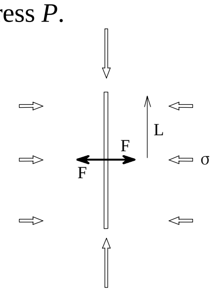

Figure 1 Sketch of crack model

Suppose that τ^* was effective shear stress induced by the combined action of σ_1 and σ_3 on a crack sliding plane, it can be expressed:

$$\tau^* = \tau - \mu\sigma_n = \frac{1}{2}\left\{(\sigma_1-\sigma_3)\sin 2\theta - \mu\left[\sigma_1+\sigma_3+(\sigma_1-\sigma_3)\cos 2\theta\right]\right\} \tag{1}$$

The tensile force f for single crack can be assumed as the horizontal projection of the effective shear stress.

$$f = \tau^* \cos\theta \tag{2}$$

The resultant of the tensile force propagated to the whole crack plane can be equivalent to:

$$T = \frac{1}{\mu}\int_A f dA \tag{3}$$

Where, the above *A* was the area of crack plane.

Substitute Eq.(1) and Eq.(2) to the Eq.(3), we can get

$$T = \frac{1}{\mu}\int_A f dA = \frac{1}{\mu}\tau^* \cos\theta L = \frac{1}{\mu}\cos\theta L\left[(\sigma_1-\sigma_3)\sin\theta\cos\theta - \mu\left(\sigma_1\sin^2\theta + \sigma_3\cos^2\theta\right)\right] \tag{4}$$

The blasting stress *P* can be solved by the maximum blasting stress P_{max} regressed according to figure 2.

$$P_{\max} = \frac{139.97}{Z} + \frac{844.81}{Z^2} + \frac{2154}{Z^3} - 0.8034 \tag{5}$$

Where, $Z = \frac{R}{Q^{1/3}}$ was the ratio distance, *Q* was the hole charge. *R* was the distance between the charge center and the acting plane.

The crack propagation was influenced by stress intensity factor of the crack end. K_{IT} of the cracks induced by the action of the shear stress to the tensile cracks *T* can be expressed [7]:

$$K_{IT} = \frac{T}{\sqrt{\pi L}} - \sigma_3\sqrt{\pi L} \tag{6}$$

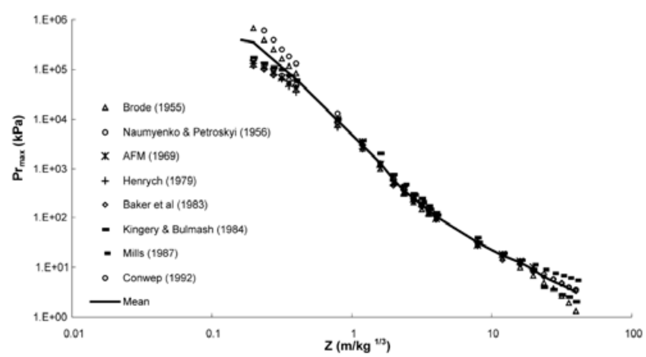

Figure 2 Peak pressure estimation[6]

Where, L is the length of the cracks.

As the stress intensity factor induced by blasting stress P is[8]:

$$K_{IP} = PQ\sqrt{\pi(L+R)} \tag{7}$$

Where, Q is the correction factor of the stress intensity factor.

So we can get the inequality between σ_1 and σ_3 by $K_I = K_{IT} + K_{IP} \geq K_{IC}$. The rock failing criterion under blasting load can be got finally.

$$\sigma_1 \geq \frac{\mu\left(K_{IC} - PQ\sqrt{\pi(L+R)}\right)\sqrt{\pi L}}{L\left(\sin\theta\cos^2\theta - \mu\sin^2\theta\cos\theta\right)} + \sigma_3\frac{\mu\pi + \left(\sin\theta\cos^2\theta + \mu\cos^3\theta\right)}{\left(\sin\theta\cos^2\theta - \mu\sin^2\theta\cos\theta\right)} \tag{8}$$

3 Engineering Application Analysis

Prior to considering the core focus of this paper - the role of designs in supporting development of client understanding - we can comment briefly on the support within the empirical data for the key assumption that clients typically have a poor understanding of the ways in which the technology can be utilise to their advantage, and how this may impact on their business models. A more complete coverage of this issue, and the relevant survey and interview data, is given in [12].

3.1. General Situation of the Project

A tail tunnel lies between the downstream side wall and the water slot of the lower reservoir. The thickness of its overlying rock is 20~270m. From the side wall to the tail pressure regulating well, the axial direction is S50°W. From the tail pressure regulating well to the water slot of the lower reservoir, the axial direction is S20-24°W. The radius of the cavern is 8.5m.The surrounding rock is mixed granite and final invaded dike. The dike contact well, but badly locally with the surrounding rock and with schistosity.

3.2. Calculation Schemes

In order to study the influence the blast made to the reserved rock, simulating analysis on the rock stability under the condition of blasting load was performed. Mohr-Coulomb criterion, that was to say, the elastic-plastic model was adopted and the high elongation calculation mode was chosen. To reflect the influence more exactly, the upper cross section was removed when building the model, This can neglect the influence of the upper cross section excavation to the crack propagation and avoid error to some extent. For the lower cross section, smooth blasting excavation was adopted and the effect of the blast of the surrounding seed cells was neglected. The blasting parameters and the seed cell layout were seen as Figure 3.

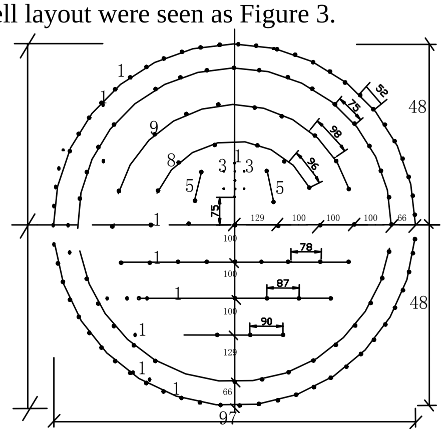

Figure 3 Sketch of seed cells

3.3. Determination of the Parameters

According to the test measurement, the cracks I' fracture toughness of the rock in field was $15\,MN/m^{3/2}$. The angle between the crack and the vertical direction was 45°, the internal friction angle of the crack plane was 45°. The blasting load *P*=150Mpa, the correction factor of the fracture strength factor *Q*=0.2, the distance between the seed cell and the load applied plane *R*=0.05m, then we can get finally

$$\sigma_1 \geq 2.35 + 11.74\sigma_3 \tag{9}$$

3.4. Results analysis

The rock crack propagation zone was got by Eq.(8) and was compared with the plastic zone, then we can find that, the calculating failing zone mainly lied in the bottom and the side walls, the failing zone of the side walls is greater than the plastic zone, but the radius influenced by blast was more or less the same as the plastic zone, and was about 90~100 times of the charge radius, which was agree with the conclusion in reference [9], that is, the blasting crack zone radius of the rock with medium strength is about 70~100 times of the charge radius and the blasting crack zone radius of all the rock tested was equal to or less than 150 times of the charge radius. This can preliminary prove the calculation method on the crack propagation zone under blasting load.

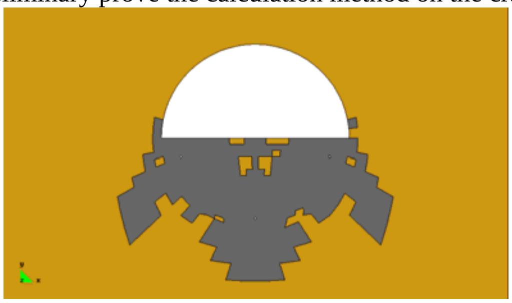

Figure 4 Crack propagation under blasting load

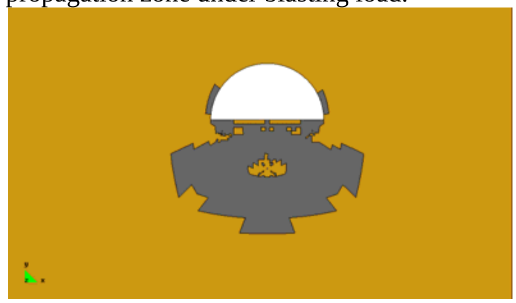

Figure 5 Plastic zones under blasting load

4 Conclusions

(1) Based on the fracture mechanism, the calculating equation of the rock crack zone under blasting load was deduced and the crack propagation criterion was established. By using this criterion in the numerical calculation, the crack propagation zone was finally obtained. The crack propagation inside the rock can be appreciated by visualized images.

(2) Dynamic response of the underground caverns under blasting load was simulated by FLAC3D and proves that it is feasible to use FLAC3D in the underground projects.

(3) An underground tailrace tunnel was calculated by FLAC3D, and it was concluded that the crack propagation zone was about 90~100 times of the charge radius. Compared with other methods, it avoided personal error and reflects the propagation zone more accurately, can make more sense to the projects.

References

1. Dally, J.W., Fourney, W.L. and Holloway, D.C. Influence of Containment of the Bore Hole Pressures on Explosive Induced Fracture. International Journal of Rock Mechanics and Mining Sciences & Geomechanics Abstracts, 1975, 5-12.
2. Stecher, F.P. and Fourney, W.L. Prediction of Crack Motion from Detonation in Brittle Materials. International Journal of Rock Mechanics and Mining Sciences & Geomechanics Abstracts, 1981, 23-33.
3. Xia, X., Li, H.B. and Li J.R. et al. Numerical Simulation of Blast-induced Cracks in Rock. Rock and Soil Mechanics, 2006, 1987-1991.
4. Yang X.L. and Wang, M.S. Mechanism of Rock Crack Growth Under Detonation Gas Loading. Explosion and shockwaves, 2001, 111-116.
5. Li, Q. and Yang, R. Stress Intensity Factor and Fracture Behavior for Crack Propagation Under Blasting Load. Journal of China Coal Society, 2002, 290-293.
6. Hsin, Y.L. and Hong, H. Reliability Analysis of Reinforced Concrete Slabs Under Explosive Loading. Structural Safety, 2001, 157-178.
7. Zhang, Z.C. On the Initiating, Glowing Branching and Sloping of Crack in Rock Blasting. Blasting, 1999, 21-24.
8. Liu, B. and Han, Y.H. Principle Examples and Applications of FLAC. China Communications Press, 2005.
9. Yan, C.B., Xu, G.Y. and Li, X.B. Stability Analysis of Mined-Out Areas Influenced by Blasting Vibration with FLAC3D. Chinese Journal of Rock Mechanics and Engineering, 2005, 24(16). 2894-2899.

RaSiM 7(2009): Controlling Seismic Hazard and
Sustainable Development of Deep Mines,
C.A. Tang(ed), Rinton Press, 535-540

NUMERICAL ANALYSES ON THE STABILITY OF THE UNDERGROUND CAVERNS COMPLEX IN SHUANGJIANGKOU HYDROELECTRIC POWER STATIONS USING FLAC3D

YONG LI, WEI-SHEN ZHU, XIAO-JING LI and QIAN-BING ZHANG

Geotechnical and Structural Engineering Research Center, Shandong University,

Jinan, 250061, P.R. China

For the time being in China, a great number of hydroelectric power stations are under construction. A large number of high mountains and deep canyons exist in these regions. As a result, the construction of hydroelectric projects is confronted with problems induced by high depth, high in situ stress, high hydraulic pressure, long excavation, and so on. The Shuangjiangkou Hydropower station is located on the Dadu River in Sichuan Province, China. The detailed geological conditions are described in this paper. From the in-situ rock stress measurement, the maximum principal stress near the underground cavern complex is up to 38MPa. In the study of the stability of the surrounding rock masses in large underground cavern complex, a 3D numerical simulation was performed using Flac3D. This software can simulate the behavior of 3D structures built of rock or other materials that undergo plastic flow when their yield limits are reached. FISH is a programming language embedded in Flac3D that enables the users to define new variables and functions. Some reasonable numerical results have been achieved using Flac3D. The plastic zones and related principal stresses' vectors after finishing the whole excavations were determined. Most of the plastic zones are distributed in the vicinity of the side walls of the main power house and the surge chamber. Five representative key points at the side wall in the main power house were empirically selected to estimate the stability of the underground caverns complex. The whole displacement variations of the five key points have been gained in the process of excavations. The maximum displacement value is approximately 15cm, and it is concluded that the underground caverns complex is stable in the process of construction. This research obtained the expected effects and provided guidance for the design and construction of the power station.

1 General introduction

China has the No. 1 hydroelectric resources in the world, of which the southwestern region takes up approximately 71%. Unfortunately, the rate of exploitation is only 7.5%. Therefore, aggressive development of the western hydroelectric resources and rapid implementation of the transmission of electricity from the west to the east are two essential components of the Chinese west development strategies and a great number of hydroelectric power stations are under construction. The Shuangjiangkou Hydroelectric Power Station is included in the national development projects. In the preliminary study, it's necessary to study the stability of the underground caverns complex in the whole process of excavations using related numerical software.

A 3D numerical simulation was performed using Flac3D. In the model, the materials can yield and flow, and the grids can deform and move [1]. FISH is a programming language embedded in Flac3D that enables the users to define new variables and functions. The Finite Difference Method (FDM) is the oldest numerical method to obtain approximate solutions to partial differential equation (PDEs) in Engineering, especially in solid mechanics [2]. The basic concept of FDM is to replace the partial derivatives of the objective function (e.g. displacement) by differences defined over certain spatial intervals in the coordinate directions, Δx , Δy , Δz ,which yields a system of algebraic simultaneous equations of the objective functions at a grid (mesh) of nodes over the domain of interest [3]. Solutions of the simultaneous algebraic system equations, incorporating boundary conditions defined at boundary nodes will then produce the required values of the objective function at all nodes, which satisfy both the governing partial differential formulas (PDFs) and specified boundary conditions. The conventional FDM utilized a regular grid of nodes, such as a rectangular grid.

Li et al. studied on the stability of the underground cavern group in Xiluodu Hydroelectric Power Stations using Flac3D [4]. Zhu et al. used Flac3D to carry out some systematic simulation analyses in underground power house of Ertan Project made a prediction analyses for eight similar projects [5]. Zhu et al. studied on the prediction of high wall displacement and stability judging method of surrounding rock for cavern groups considering the deformation moduli of rock masses, buried depths of openings, heights of major houses and lateral pressure coefficient of initial horizontal geostress component [6]. Therefore, the FDM is a very effective tool in preliminarily studying the stability of the underground cavern complex.

2 Project descriptions

The Shuangjiangkou Hydroelectric Power Station is located on the Dadu River in Sichuan Province, China. The slope inclinations are 35°~ 50° at the left bank and 45°~ 60° at the right bank. Below the altitude of 2800m the whole valley looks like a nearly symmetrical V-shaped valley. The mountains stretch along the slope inclinations and reach up to the altitude of 2800m, so the peak must have an effect on the initial in-situ stress field near the underground cavern complex. From the in-situ rock stress measurement, the maximum principal stress near the underground cavern complex is up to 38MPa. The high in-situ stress is absolutely rare in Chinese hydropower stations. There is no zonal cleavage in the dam site. The rock masses are mainly composed of medium or fine-grained granites. The rock masses are in a drastic unloading state towards the exterior directions. Figure 1 shows the location of the Shuangjiangkou Hydroelectric Power Station.

Figure1 Location of Shuangjiangkou Hydroelectric Power Station

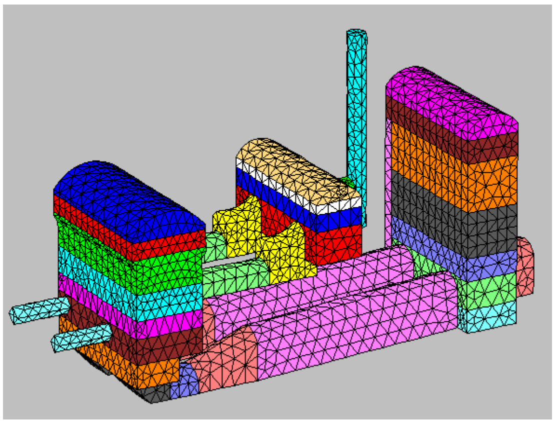

Figure 2 The 3D numerical model of the complex

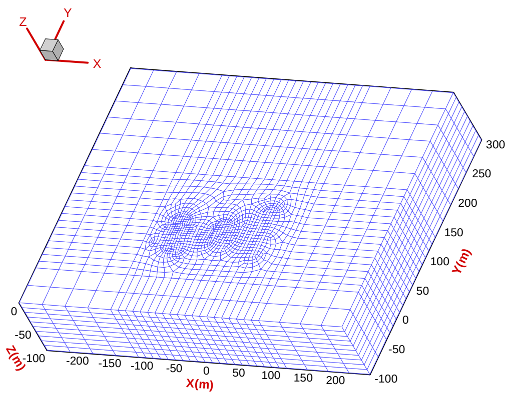

Figure 3 The three dimensions of the numerical model

3 The numerical model description

The numerical simulation of the underground cavern complex is mainly combined with the geomechanical model test of the underground cavern complex which had been finished so that the numerical simulation results can be compared with the experimental results [7].

Figure 2 shows the 3D numerical model of the cavern complex. Figure 3 shows the three dimensions of the cavern complex. In the numerical analysis, the FLAC 3D numerical method was adopted for the underground cavern complex considering the boundary effects, the two generating sets area, including the main power house, the transformer house, the surge chamber, the busbar chamber, et al., as shown in Figure 4 The elements for linings and the surrounding rock masses were the eight-node isoparametric elements. The bolts were modeled using the bolts elements. The whole numerical model has 20754 nodes and 96662 elements. FISH is a programming language embedded within Flac3D that enables us to define new variables and functions.

4 Numerical simulation and results analyses

4.1 The real gravity loads and in-situ stress

The real embedded depth of the cavern complex is approximately 600m. According to the in-situ stress field, the initial horizontal stresses are almost 1.5 times the vertical stresses near the caverns so that the coefficient of horizontal earth pressure was determined to be $K_0 = 1.5$. Table 1 shows the physico-mechanical parameters of the rock mass.

Table 1.The physico-mechanical parameters of the rock mass

Rock mass density	Elastic modulus	Cohesion	Friction angle
26.5 KN/m^3	10.83GPa	2MPa	40.36°
Compressive strength	Tensile strength	Poisson's ratio	
80MPa	4MPa	0.25	

4.2 The excavation subsequences of the cavern complex

Due to some irregular excavating shapes in the in-situ excavations, the whole excavating subsequences have been simplified in the numerical simulation. The whole excavation subsequences can be divided into 20 circles and 102 steps. The excavation footage of every step is 10m. The excavation sequences are I_1, II_1, III_1, I_2, II_2, III_2, I_3, III_3, I_4 and III_4 (see Figure 4).

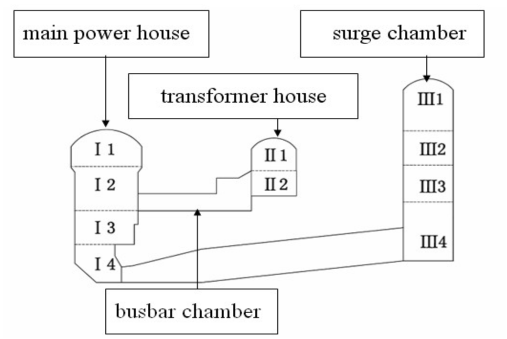

Figure 4 The layout and excavation subsequence

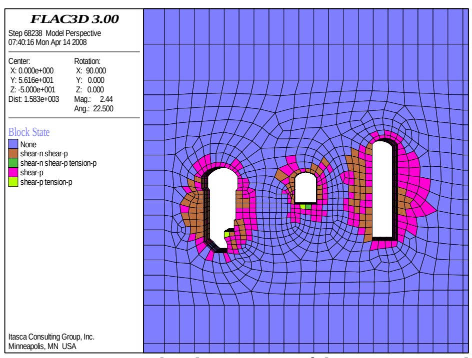

Figure 5 The plastic zones of the caverns complex

4.3 The distribution of the plastic zones

From the numerical simulation results, in the whole process of step-by-step excavations, the unloading effect induced by excavation would be obvious as the excavating sectional area increases gradually. The plastic zones of the main power house, the transformer house and the surge chamber becomes larger and larger in the surrounding rock mass. The compression-shear failures mainly occur in the plastic zones and some splitting failures (so-called tension failure) appear at the some parts of the side walls in the main power house and the surge chamber.

Figure 5 shows the plastic zones of the caverns complex after finishing excavations. A statistical analysis of the developed depths on the plastic zones has been made to estimate the stability of the underground caverns complex as follows:

- The main power house: 2-3m at the arch crown; 6-10m at the upstream side walls; 7-12m at the downstream side walls and 2-3m at the bottom plate.
- The transformer house: 2-3m at the arch crown; 3-6m at the both side walls and 4-6m at the bottom plate.
- The surge chamber: 2-3m at the arch crown; 8-14m at the upstream side walls; 11-15m at the downstream side walls and 4-8m at the bottom plate.

4.4 The stress and displacement behaviours after excavations

The following Figures show the principal stresses and displacement vectors after excavations. σ_1 is the maximum principal stress and σ_3 is the minimum principal stress.

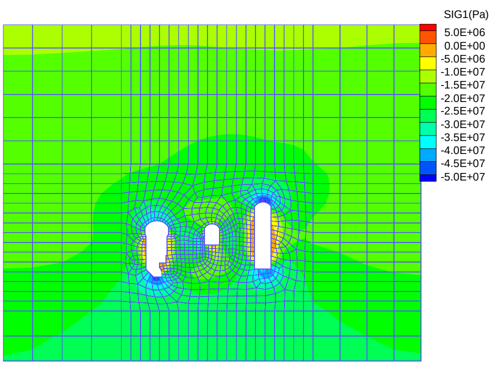

Figure 6 The σ_1 contour after excavations

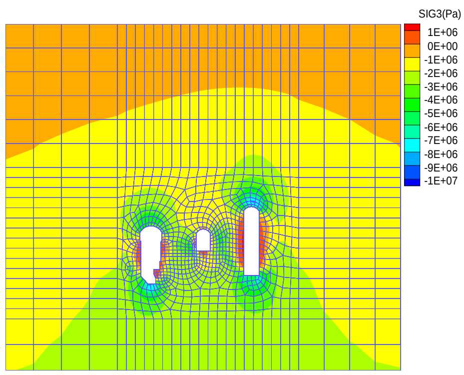

Figure 7 The σ_3 contour after excavations

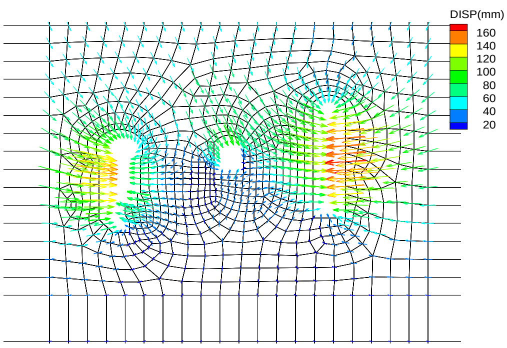

Figure 8 The displacement vectors after excavations

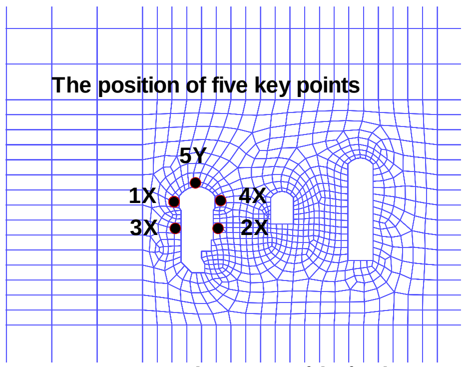

Figure 9 The position of the five key points

4.5 The detailed displacement variations of five key points

Based on the past experiences of studying the stability of the cavern complex, the displacement values of some key points have impact on the stability of the cavern complex. Five typical key points in the surrounding rock mass of the main power house are selected to estimate the stability of the caverns complex. Figure 9 shows the five key points. The following Figures show the displacement variations with the excavation steps of the five key points.

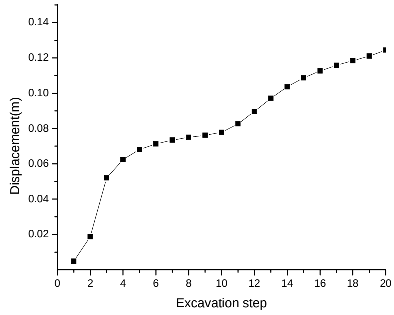

Figure 10 The horizontal displacement variations of point 1X

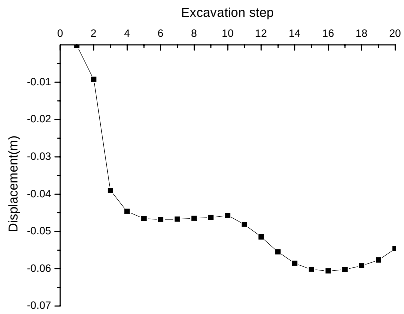

Figure 11 The horizontal displacement variations of point 4X

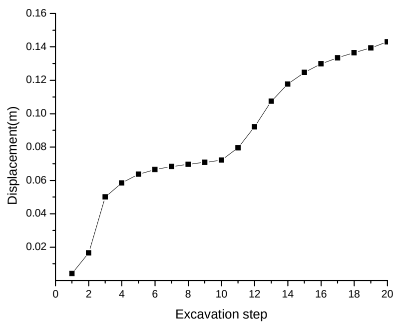

Figure 12 The horizontal displacement variations of point 3X

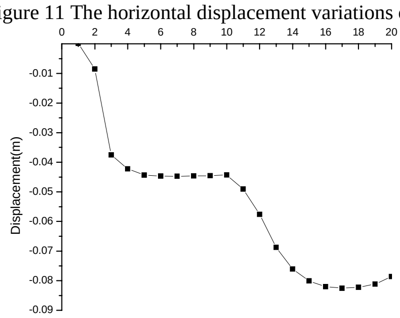

Figure 13 The horizontal displacement variations of point 2X

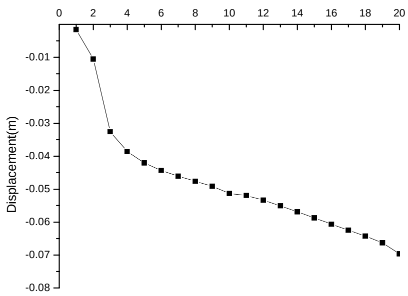

Fig 14 The vertical displacement variations of point 5Y

In the figures above, the displacements of the key points 1X, 2X, 3X and 4X are horizontal, but the displacement of key point 5Y is vertical. For the horizontal displacement, the displacement forward right is positive, conversely negative. For the vertical displacement, the upwards displacement is positive, conversely negative. The maximum displacement value is approximately 15cm appeared at the upstream side wall of the main power house. It can be preliminarily concluded that the caverns complex in the whole process of excavation is totally stable.

5 Conclusions

A numerical simulation has been conducted to initially study the stability of the underground caverns complex in the Shuangjiangkou Hydroelectric Power Station. An FDM method and numerical software Flac3D are selected to study the problem. The related numerical results and conclusions are demonstrated as follows:

(1) The FDM and Flac3D are actually an effective tool in study of the stability of the underground caverns complex of some hydroelectric power stations.

(2) The plastic zones and related principal stresses' vectors after finishing the whole excavations have been determined. The developed depths of the plastic zones of the caverns complex have also been determined, therefore, some reinforcement proposals can be used in the in-situ construction.

(3) Five representative key points at the side wall in the main power house were empirically selected to estimate the stability of the underground caverns complex. The whole displacement variations of the five key points have been gained in the process of excavations. The maximum displacement value is approximately 15cm, and it is concluded that the underground caverns complex is stable in the process of construction.

Acknowledgements

The work was financially supported by the Key Project of Natural Science Foundation of P. R. China (No. 90510019).

References

1. Itasca Consulting Group, Inc. 2001. Fast Lagrangian Analysis of continua in 3-dimensions. FLAC3D version 2.1, user's manual.
2. Jing, L. A review of techniques, advances and outstanding issues in numerical modelling for rock mechanics and rock engineering. International Journal of Rock Mechanics and Mining Sciences, 2003, 40(3). 283-353.
3. Wheel, M.A. A geometrically versatile finite volume formulation for plane elastostatic stress analysis. J Strain Anal., 1996, 31(2), 111-116.
4. Li, Z.K., Dai, R. and Jiang, Y.M. Improvement of the generation of the initial stress field by using Flac3D and application in a huge underground cavern group. Chinese Journal of Rock Mechanics and Engineering, 2002, 21(suppl. 2). 2387-2392.
5. Zhu, W.S., Sun, A.H. and Sui, B. Systematic analysis of underground cavern groups in background for Ertan Project. Chinese Journal of Underground Space and Engineering, 2005, 1(1). 15-18.
6. Zhu, W.S., et al. Study on prediction of high wall displacement and stability judging method of surrounding rock for large cavern groups. Chinese Journal of Rock Mechanics and Engineering, 2007, 26(9). 1729-1736.
7. Zhu, W.S., Li, Y. et al. Model tests and numerical analyses on the stability of a cavern complex. Proceedings of the 42nd US Rock Mechanics Symposium and 2nd U.S.-Canada Mechanics Symposium, San Francisco, June 29-July 2, 2008.

RaSiM 7(2009): Controlling Seismic Hazard and
Sustainable Development of Deep Mines,
C.A. Tang(ed), Rinton Press, 541-548

THREE DIMENSIONAL COMPOSITE ELEMENT METHOD FOR DISCONTINUUM AND ITS APPLICATION

SHENG QIANG and YANG ZHANG

College of Water Conservancy and Hydroelectric Engineering, Hohai University

Nanjing, 210098, P.R. China

SHENG-HONG CHEN

School of Water Resource and Hydropower engineering, Wuhan University

Wuhan, 430072, P.R. China

It is a significant issue to simulate the three dimensional complicated discontinuous rock mass by numerical method in engineering practices. The algorithm developed on the concept of composite element method (CEM) has the capability to consider conveniently discontinuity of various size, orientation, and spacing with discontinuity segments in element. In this way the discontinuities can be simulated explicitly without special elements deployed along the discontinuities. To validate the principle and program, simple examples containing joints of different orientation or number are illustrated. The computation results of the simple examples by CEM are identical with analytic solution. Then the new method is tried to be applied on the excavation of a large-scale underground power station with complicated adjacent rock. The displacement and stress when all excavation is completed are shown, which are in accordance with the general law. Some abnormal displacements reveal that because of large horizontal ground compressive stress, rock burst may occur at two rock wedges which are formed with the wall surface and faults during excavating. Both the simple and the complicated examples show the feasibility and efficiency of the proposed composite element method.

1 Introduction

Discontinuity is the general term of a fault, joint, bedding, etc. in rock masses. The simulation of discontinuities is a crucial problem in the study of the deformation and stability of rock foundations, slopes, and underground caverns. In the past 40 years, many numerical analysis theories and methods have been developed with the aim to calibrate the behavior of discontinuous rock masses. Included are the distinct element method [1], rigid body-spring element method [2], discontinuous deformation analysis method [3], the recently developed block element method [4], manifold method [5], and element–free Galerkin method [6]. The later 3 methods are the most famous and are also more popular because of their special merits.

The methodologies to treat the discontinuities in the finite element analysis can be classified into two categories: the equivalent modeling method which takes the influences of discontinuities into the constitutive relations but does not take into consideration their exact positions; and the explicit modelling method which makes use of special elements [7] to precisely simulate the geological and mechanical properties of the discontinuities. The former is more commonly used to model the joints and fissures of large quantities, while the later is mainly used with larger scale faults and intercalations. For a complicated practical engineering problem, the rational combination of these two methodologies can guarantee an accurate solution.

Recently, an attempt to generalize the composite element into discontinuous rock masses has been achieved [8]. This paper will give further certification to the composite element method algorithm for discontinuous rock mass problem by simulating the excavation of large-scale underground power stations located in complicated rock masses that contain seven faults. The computation results, according with impersonality law, show the effect of the method in large-scale engineering.

2 Principle of Composite Element Method

The finite element mesh should be formed to discrete the structure firstly. The deployment and sizes of the elements in the mesh are dependent on the structure configuration and stress gradient but take no care of the existence of the discontinuity system. Then the algebra and geometry calculation will be conducted using both the messages of the discontinuity system and the finite element mesh, to form the composite element mesh. In such mesh there are definitely some elements containing several discontinuity segments which are defined as composite elements. A composite element may contain several discontinuity segments which delimit the element into some sub-domains named as sub-elements. It should be pointed out that the sub-elements are not necessary to be the standard finite elements. The displacements in each sub-element are interpolated from the nodal displacements assigned to the composite element as:

$$\{\Delta u\}_{rl} = [N]\{\Delta\delta\}_{rl} \quad \text{within the sub-element } rl \tag{1}$$

in which [N] is the shape function of the conventional FEM defined in the whole composite element. However, it should be pointed out that the interpolation expressed in the Eq.(1) is valid only in each of the sub-element respectively.

With the solved nodal displacements, the displacements, the strains as well as the stresses in the each sub-element can be calculated.

In the following content, the subscripts rm (m=1, 2, 3, 4) and j_{rlrm} (l and m=1, 2, 3, 4) will be used to indicate that the quantities are of the rock sub-element and discontinuity segment between rock sub-elements rl and rm respectively. However, for the simplicity the above subscript will be abbreviated as r and j in case of not mistaken will be led to.

After the signal definition, the basic governing equations of a composite element may be deduced as:

$$\begin{cases} ([k]_{r1}+[k]_{j_{r1r2}}+[k]_{j_{r1r4}})\{\Delta\delta\}_{r1}-[k]_{j_{r1r2}}\{\Delta\delta\}_{r2}-[k]_{j_{r1r4}}\{\Delta\delta\}_{r4}=\{\Delta f\}_{r1}+\{\Delta f^{vp}\}_{r1}+\{\Delta f^{vp}\}_{j_{r1r2}}+\{\Delta f^{vp}\}_{j_{r1r4}} \\ -[k]_{j_{r2r1}}\{\Delta\delta\}_{r1}+([k]_{r2}+[k]_{j_{r2r1}}+[k]_{j_{r2r3}})\{\Delta\delta\}_{r2}-[k]_{j_{r2r3}}\{\Delta\delta\}_{r3}=\{\Delta f\}_{r2}+\{\Delta f^{vp}\}_{r2}-\{\Delta f^{vp}\}_{j_{r2r1}}+\{\Delta f^{vp}\}_{j_{r2r3}} \\ -[k]_{j_{r3r2}}\{\Delta\delta\}_{r2}+([k]_{r3}+[k]_{j_{r3r2}}+[k]_{j_{r3r4}})\{\Delta\delta\}_{r3}-[k]_{j_{r3r4}}\{\Delta\delta\}_{r4}=\{\Delta f\}_{r3}+\{\Delta f^{vp}\}_{r3}-\{\Delta f^{vp}\}_{j_{r3r2}}+\{\Delta f^{vp}\}_{j_{r3r4}} \\ -[k]_{j_{r4r1}}\{\Delta\delta\}_{r1}+[k]_{j_{r4r3}}\{\Delta\delta\}_{r3}+([k]_{r4}+[k]_{j_{r4r1}}+[k]_{j_{r4r3}})\{\Delta\delta\}_{r4}=\{\Delta f\}_{r4}+\{\Delta f^{vp}\}_{r4}-\{\Delta f^{vp}\}_{j_{r4r3}}-\{\Delta f^{vp}\}_{j_{r4r1}} \end{cases} \tag{2}$$

in which:

$$\begin{cases} [k]_{rl} = \int_{\Omega_{rl}} [B]_{rl}{}^{T} [D]_{rl} [B]_{rl} \, d\Omega \\ [k]_{j_{rlrm}} = \int_{S_{jrlrl}} [N]^{T} [L]^{T} [D]_{j_{rlrm}} [L][N] dS \qquad rl \neq rm \end{cases} \tag{3}$$

$$\begin{cases} \{\Delta f^{vp}\}_{rl} = \int_{\Omega_{rl}} [B]_{rl}^{T} [D]_{rl} \{\dot{\varepsilon}^{vp}\}_{rl} \, \Delta t d\Omega \\ \{\Delta f^{vp}\}_{j_{rlrm}} = \int_{Sj_{rlrm}} [N]^{T} [L]^{T} [D]_{j_{rlrm}} \{\dot{u}^{vp}\}_{j_{rlrm}} \Delta t dS \qquad rl \neq rm \end{cases} \tag{4}$$

Eqs. (2)-(4) are the basic governing equations of a composite element containing four sub-elements. Generally, if a composite element is composed of m sub-elements, the degrees of freedom of such element will be m times of the conventional finite element.

If the element containing no discontinuity segments, the composite element will be degenerated automatically back to the conventional finite element. In this way the composite elements and the conventional finite elements can be coupled well in one discrete system and there is no essential difficulty in the programming.

When the governing equations of all elements have been formulated, they can be assembled into the governing equation of the whole discrete system (containing both the composite elements and the conventional finite elements) in a rule similar to the conventional finite element method.

Now the main algorithm and program for CEM preprocess has been developed [9]. Complicated jointed rock masses of three-dimension can be treated freely [10].

3 Validation of Composite Element Method

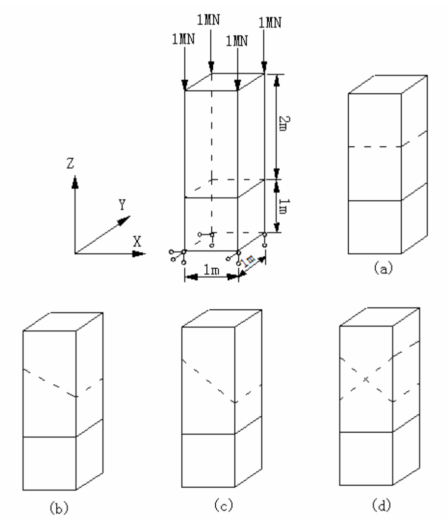

Figure 1 Example of composite element

Figure 1 shows an example which includes two elements. The upper element is composite element and the lower one is finite element. The dimension of the model is 1.0m×1.0m×3.0m (length × width × height). The nodes restraints are also shown in Figure 2. Four concentrate loads, which is 1.0MN separately, on the upper surface of the model. Assume four kinds of joints in the rock model. The rock and joints mechanical parameters are separately shown in Table 1 and Table 2.

Table 3 shows the stress value in rock and on joints comparing with the analytic solution. In the table, σ_z is the vertical stress in rock, σ_t and σ_n are separately the tangential stress and normal stress on joints.

Table 1 Mechanical parameters of rock

Elastic Module E (MPa)	Poisson Ratio μ	Friction Angle ϕ (°)	Cohesive Strength c (MPa)	Tensile Strength σ_T (MPa)
18000	0.17	45	1.0	1.0

Table 2 Mechanical parameters of joints

Case	Dip Angle (°)	Inclination (°)	Normal Stiffness Kn (MN/m^2)	Tangential Stiffness Ks (MN/m^2)	Friction Angle φ(°)	Cohesive Strength c (MPa)	Tensile Strength σ_T (MPa)
(a)	0	0	2000	870	26.5	0.02	0.02
(b)	90	30	2000	870	26.5	0.02	0.02
(c)	90	45	2000	870	26.5	0.02	0.02
(d)J1	90	45	2000	870	26.5	0.02	0.02
(d)J2	270	45	2000	870	26.5	0.02	0.02

According results comparing, the stress value of two methods fit well, which show the validity and robustness of composite element method.

Table 3 Contrast between two methods

Case	Method	σ_z in Rock (MPa)	σ_t on Joints (MPa)	σ_n on Joints (MPa)
(a)	Analysis,	-4.0000	0.0000	-4.0000
	CEM	-4.0000	0.0000	-4.0006
(b)	Analysis	-4.0000	1.7321	-3.0000
	CEM	-4.0000	1.7324	-3.0009
(c)	Analysis	-4.0000	2.0000	-2.0000
	CEM	-4.0000	2.0002	-2.0005
(d) J1	Analysis	-4.0000	2.0000	-2.0000
	CEM	-3.9988	2.0001	-2.0003
(d) J2	Analysis	-4.0000	2.0000	-2.0000
	CEM	-3.9988	2.0001	-2.0003

4 Application to Excavation of Large Underground Engineering

4.1 Computation conditions

PuBugou engineering locates at the middle reaches of DaDuhe river in China. The power station scheme is adopted as an underground plant with the layout as Figure 2, whose maximum cavern dimension is 290.65m×27.3m×66.68m. The caverns are in the mountain with the embedded depth of 220~360m.

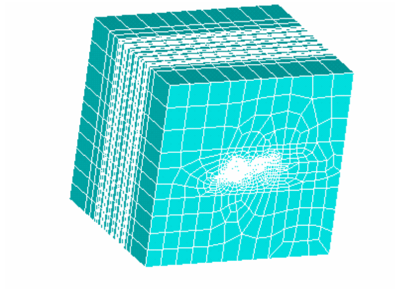

Figure 3 Mesh for calculation

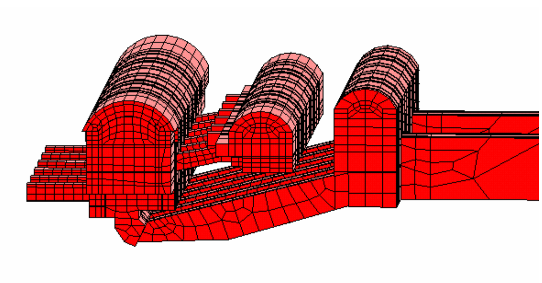

Figure2 Layout of the underground power station

As shown in Figure 3, the model domain is 600m, 494m and 550m along X, Y and Z axes separately. The computation domain includes seven faults: f14, f9, f13, F2, F18, F28 and F29 whose locations and directions can be seen in Figure 4(a)-(g). The geometry parameters of faults are shown in table 5. At first the faults are not considered when generate mesh. Mesh includes 39690 hexahedron elements and 41580 nodes. After the intersecting between joints and rock mass, 8517 composite elements are created.

The character of most rock masses is belong to II, while the character of the fault is belong to V. Table 4 shows the mechanics parameters of various materials.

Table 4 Material mechanics parameters

Material	Unit weight (MN/m^3)	Friction Angle (°)	Cohesion (MPa)	Deformation modulus (MPa)	Poisson's ratio	Tensile Strength (MPa)
Rock II	0.0261	53.5	2.0	18000.0	0.21	2.0
Rock V	0.0261	19.3	0.0	1000.0	0.35	0.8
Concrete	0.0262	60.0	2.0	26000	0.167	2.0

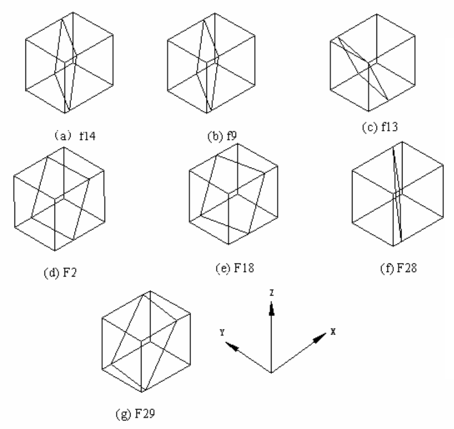

Figure4 Space location of faults

Table 5 Faults geometry parameters

Fault	Strike	Dip Angle	Depth(m)
f14	N70°E	SW76°	0.1
F9	N75°E	NW82°	0.2
F13	N54°E	SE65°	1.5
F2	N40°E	NW70°	0.5
F18	N30°E	NW70°	1.5
F28	N82°E	SE88°	0.5
F29	N50°E	NW55°	1.0

The initial stress formed by inversion shows the maximum principle at the depth about the caverns is compression stress with the numerical value between -30MPa and -20MPa, the direction along the X-axis primarily. The excavation procedure is divided into 8 steps, lining, bolt and anchor is applied on the wall after every excavation step. Therefore the actual computation steps are 16. Bolt is simulated with the equivalent reinforced rock model. Anchor is applied as a couple of concentrated force with the same value but opposite directions.

4.2 Computation results

Computation of three-dimensional elastic composite element method is carried out. Figure 5-6 show separately the displacement vector, vertical stress contour on the center section of generator unit 2.

At two positions, abnormal displacements that are distinct greater than the displacement elsewhere appear. One is located at the intersecting body of main transformer chamber and bus bar gallery, between generator unit 4 and 5 in the cavern axis direction. Another is located at the intersecting body of generator cavern and tailrace tunnel, also between generator unit 4 and 5 in the cavern axis direction. The reason for abnormal displacement is the wedges created by faults and excavation faces. If equivalent finite element method is adopted to simulate the same construction, no wedge should be found. Figure 7 shows the quantity and location of maximum displacement. Figure 8 shows the location of two wedges.

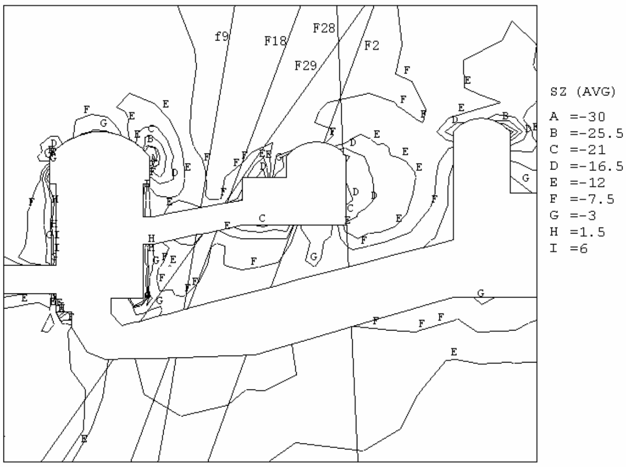

Figure 6 Vertical stress contour on center section of unit 2

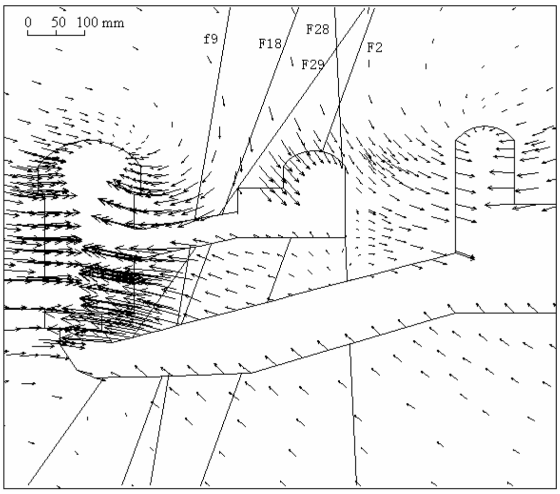

Figure 5 Displacement vector on center section of unit 2

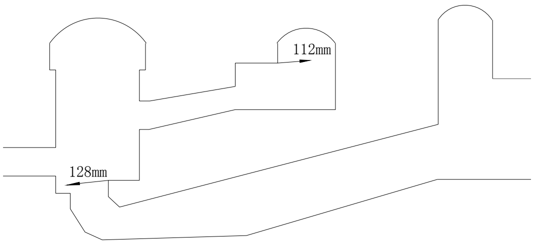

Figure 7 Quantity and location of maximum displacements

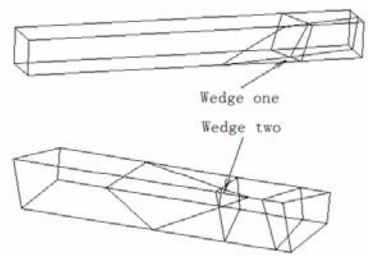

Figure 8 Location of wedges

The deformation of cavern is not symmetry and horizontal displacement is greater than vertical displacement because of the asymmetry initial stress. Stress numerical value and distribution vary with excavation. After all excavation completed, there is rather large horizontal compressive stress with a numerical value between –60MPa and –40MPa at the crest of caverns because the arch crest rock crush after excavation. Another position of large horizontal compressive stress is the arch of tail channel with a numerical value between –40MPa and –30MPa. The horizontal tension stress ranges from 1MPa to 2MPa that exists at the bottom corner of generator cavern, the intersecting point of generator cavern and bus bar gallery, the intersecting point of bus bar gallery and transformer chamber. Large vertical compressive stress ranging from –35MPa to –20MPa is observed at the intersecting point of arch and downstream wall in every cavern.

5 Conclusions

In this paper the theory of the 'composite element method' is presented for discontinuous rock masses. In such an element, some sub-domains of any shape called sub-elements are contained by the intersection of large-scale discontinuities. For each sub-element, there are mapped displacements at the composite element's nodes. The displacements, strains, and stresses within the sub-elements are calculated by the corresponding mapped nodal displacements of the composite element. Meanwhile, the relative displacements, strains, and stresses of the discontinuity segments within the composite element are evaluated by the mapped nodal displacements of the conjoint sub-elements. When no discontinuity segment passes the element, the element will be degenerated to a conventional finite element.

The simple example and the underground cavern excavation studied in this paper show the feasibility and the robustness of the methodology. It is easy to recognize that the application of composite element can simplify the pre-process greatly. The large-scale discontinuities will not be necessarily modeled by the special regular element. The mesh generation work can be concentrated on the other important aspects, such as, the structure configuration, the stress gradient, etc. In practical applications when there are many large-scale faults in the complicated structure, this advantage will become very attractive.

References

1. Cundall, P.A. A Computer Model for Simulating Progressive, Large-Scale Movement in Blocky Rock System. in Proceedings of the Symposium of International Society of Rock Mechanics, (France, Nancy, 1971).
2. Hamajima, R., Kawai, T., Yamashita, K. and Kusabuka, M. Numerical Analysis of Cracked and Jointed Rock Mass. in Proceedings of 5th International Conference on Numerical Methods in Geomechanics, (Japan, 1985).
3. Shi, G.H. Discontinuous Deformation Analysis: A New Numerical Model for the Statics and Dynamics of Deformable Block Structures. Engineering Computations, 1992, 9(2). 157-168.

4. Chen, S.H., Shen, B.K. and Huang, M.H. Stochastic Elastic-Viscoplastic Analysis for Discontinuous Rock Masses. International Journal for Numerical Methods in Engineering, 1994, 37(14). 2429-2444.
5. Shi, G.H. Manifold Method. in Proceedings of the First International Forum on DDA and Simulation of Discontinuous Media, (California, USA, 1996).
6. Belytschko, T., Lu, Y.Y. and Gu, L. Element-free Galerkin Methods. International Journal for Numerical Methods in Engineering, 1994, 37(2). 229-256.
7. Mahtab, M. and Goodman, R.E. Three Dimensional Analysis of Joint Rock Slope. in Proceedings of the 2nd International Congress of ISRM, (Beograd, 1970).
8. Chen, S.H. and Qiang, S. Composite Element Model for Discontinuous Rock Masses. International Journal of Rock Mechanics and Mining Science, 2004, 41(5). 865-870.
9. Qiang, S., Zhang, Y. and Chen, S.H. Research on the Pre-process of Three Dimensional Composite Element Method for Discontinuous Rock. in Proceedings of the sixth European Conference on Numerical Methods in Geotechnical Engineering, (Graz, 2006).
10. Feng, X.M. and Chen, S.H. Composite Element Method for Seepage Characteristics Study of on Rock Masses with Complicated Fracture Network. Chinese Journal of Rock Mechanics and Engineering, 2005, 25(5). 918-924.

RaSiM 7(2009): Controlling Seismic Hazard and
Sustainable Development of Deep Mines,
C.A. Tang(ed), Rinton Press, 549-554

STUDY ON PRESTRESSED CABLE AND ANCHOR PARAMETERS OPTIMIZATION DESIGNS OF DEEP-SEATED ROCK TUNNELS OF COAL MINES BASED ON OBSERVATION AND NUMERICAL SIMULATION

YONG-ZHAN PAN
Qingdao Technological University
Qingdao, 266033, P.R. China
Henan University of Science and Technology
Luoyang, 471003, P.R. China

SHI-BAO LU, YONG-JUN ZHANG, GUANG-MING YU
Qingdao Technological University
Qingdao, 266033, P.R. China

GUO-YAN WANG
Qingdao Technological University
Qingdao, 266033, P.R. China
Liaoning Technical University
Fuxin, 123000, P.R. China

The wall rock endures more strata stress with the increase of extraction in coal mines. The characteristic of tunnels wall rock distortion is distinctly different from others, and rock support and the maintenance of laneways is a difficult task. It is expected that the problem of wall distortion and failure of deep laneways will be more severe in the future. Optimization design of prestressed cable and anchor for a deep-seated rock tunnel a coal mine in Shandong province, China, is presented based on field observation and numerical simulation using UDEC. As a result, the timbering quality was improved visibly following design optimization and wall distortion and collapse were under effective control..

1 Introduction

With the exploitation of coal resources and the increasing depth of mining areas in China, roadway engineering is becoming increasingly complex because of the geological environment. Deformation characteristics of the surrounding roadway rock and upper strata are very different from before with roadway support and maintenance becoming increasingly difficult. In such cases, deformation and failure of the rock wall around deep tunnels will seriously affect normal production and mine safety [1-3].

As for an example, located in north-western city of Jining, Shandong Province, the coal mine has vertical shafts and a designed production capacity of 3,000,000 t/a. The first level is -990m, with the bottom of the deepest tunnel buried at a depth of 1029 meters.

Since the mine was put into operation, a number of chambers and roadways have been damaged. As for the opening great belt lane rock deformations, observation shows that the largest rate of deformation was 20mm/d in the course of driving, and the total deformation around the roadway amounted to 200-500mm. The largest value of the bottom bulge is 1200mm. Although it has been maintained many times, it is still difficult to keep the rock wall steady. The overall characteristics of the roadway are an apparent strata pressure, low strength of the surrounding rock, plastic deformation, and long time rheology.

It is important to study related problems in the deep roadway. These studies can play a guiding role in the stability roadways, and improve mine safety level at the same time.

2 Main measures of tunnel timbering

2.1 Section specification

Section specification is showed in Figure1.

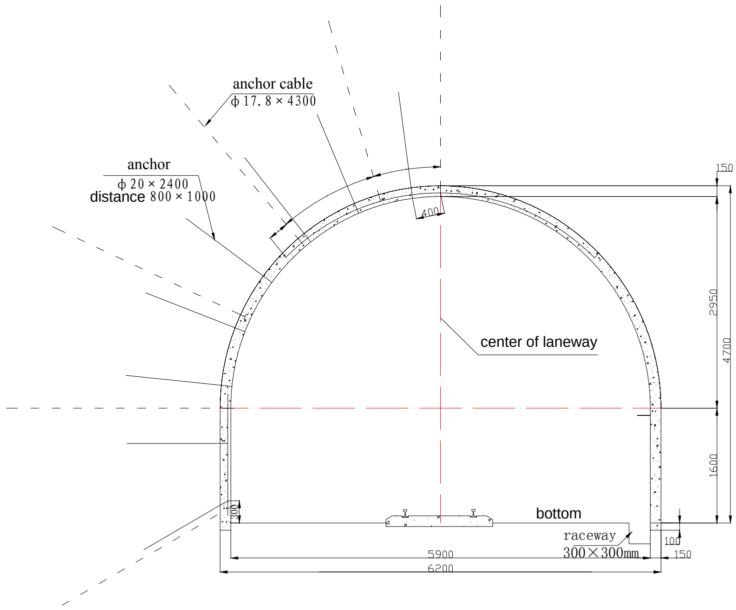

Figure1 Section specification

2. 2 Timbering parameters

Specific timbering parameters of roadway are as follows:

Full-strength bolt is made of reinforcing steel bar ф20 × 2200mm, distance between each otrher is 800 × 1000mm and the number of each row is 16.

Cable is made of tightwire ф17.8 × 4300mm, the distance along the laneway is 1m.

3 Main questions of timbering

3.1 Deformation of the bottom

Deformation of laneway bottom is caused by high earth pressure, which is very serious. The height of laneway fell about 1/2 commonly, some even achieved 2/3. The deformation slows down relatively and tends to stably only after the laneway bottom is processed about 4-5 times. All these slow down the schedule and most laneway is only construct about 50m monthly.

3.2 Convergence deformation of both sides of laneway

According to the observation, the convergence deformation will reach at 300-500mm after roadway is tunneled, section area will be reduced from 16m2 to about 12m2. The result even can be about 8m2 under the influence of dynamic pressure, or the laneway will be destroyed thoroughly.

3.3 Destruction of roof

When the deformation of the laneway reaches certain degree, large-area destruction will appears. The mainly results is crack of concrete on the roof, avulsion of steel support and breaking of anchor cable. All these finally cause the roof to fall. But damage of anchor is seldom discovered.

Damage of semicircle arch laneways focused on arch generally, while rectangular laneways focused on sides. Upper portion of arched is extruded because of horizontal stress. Anchor cable beam is broken and entire timbering is destroyed.

Deformation of laneway around faults is more serious. Damage of anchor focused mainly on two for the top edge of the roof. About 2/5 of the anchor is destroyed because of the strata pressure.

4 Abscission layer observations

In order to find out abscission layer of interior rock layer and the distortion situation of laneway rock wall, the detailed survey is carried on by using the rock drilling detector model YTJ20 shown as Figure2. The working principle of this detector is as follows. Detector with diameter of 25 mm is probed into the drilling; video is displayed on a screen in this process. This video can be edited using computer. Situation of abscission layer in different depth is known in this way.

Figure2 Rock drilling detectors model YTJ20

Abscission layer depth of each observation site is shown in Table.1.

Table.1 Abscission layer depth of each observation site

Laneway	Site	Abscission layer depth of roof (m)
Laneway No.1304	1	3.25
	2	3.11
Laneway No.2305	1	5.03
	2	2.78
	3	4.00

North railway laneway	1	6.82
	2	3.00
	3	8.41
South railway laneway	1	7.23
	2	1.79
	3	1.61
	4	0.79
West railway laneway	1	5.82

Roof abscission layer situation of the observation sites is shown as Figure3. As we can see, abscission layer phenomenon occurs in different depth of roof at this place.

a. 3 0.3m

b. 4 0.5m

c. 5 1.0m

d. 6 1.52m

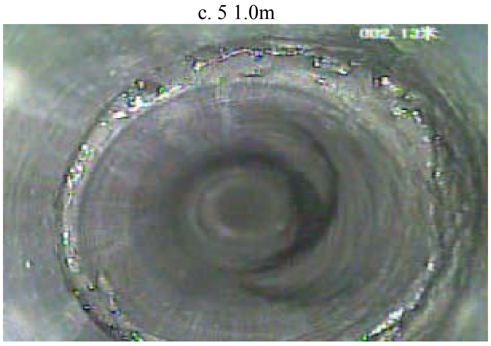

e. 7 2.13m

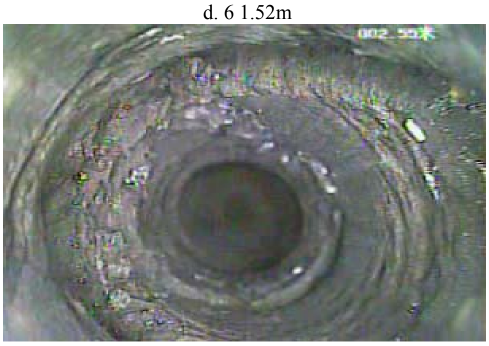

f. 8 2.55m

Figure3 Abscission layer of different depth

5 Numerical simulation of destroys in the deeper portion of laneway

In view of the geology situation, we carried on the preliminary simulation analysis with the software UDEC [4]. Conclusion is as follows:

Distortion is quite obvious in the roof when rock wall is in a good quality.

When rock wall is in bad situation, both the roof and the both sides are destroyed easily. At the same time, the bottom is needed to be reinforced.

The contrast of results of numerical simulation and practice is shown as Figure4 and Figure5.

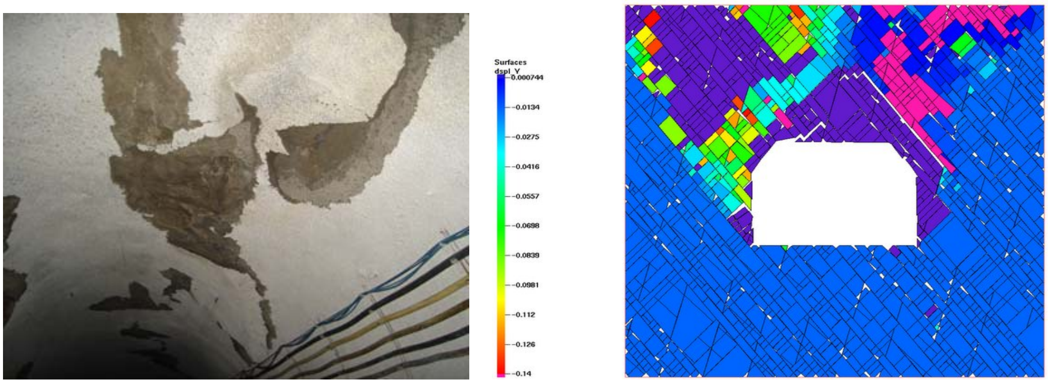

a. Photo on site b. Result of numerical simulation

Figure4 Destroy of laneway in sandstone

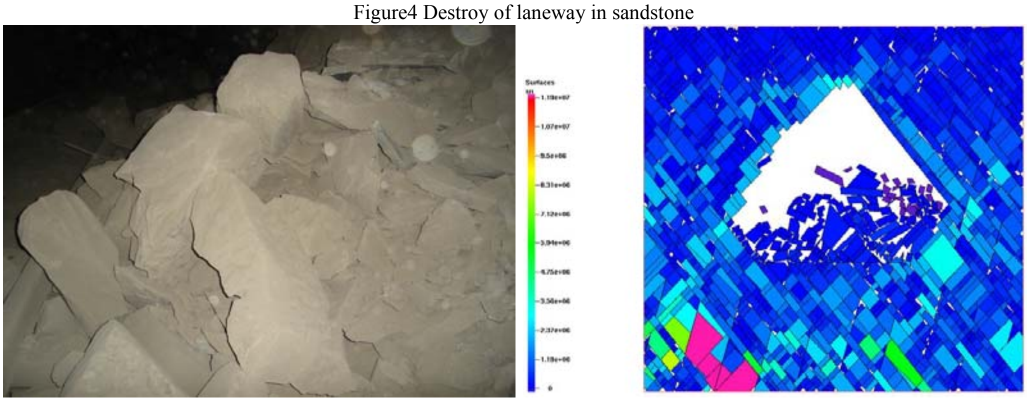

a. Photo on site b. Result of numerical simulation

Figure5 Destroy of laneway in mudstone

6 Optimization result of laneway timbering parameters

Based on all above studies, we optimized the laneway timbering parameters as follows:

As for the results of numerical simulation, the roof is destroyed seriously in this situation. We increased the number of anchor cable of roof and added Tee steel belt further to increase the timbering rigidity. The distance of the anchor cable in roof is changed from 1.2m to 0.8m.

According to the result of abscission layer observation, former length of anchor is in the abscission layer scope and can not restrict the rock wall obviously, so we changed it to 2.6m

The laneway is marked out in good rock wall as far as possible.

Through adopting above measures, the phenomena of tunnel convergence deformation and the cave-in of both sides of the laneway are controlled effectively, the timbering quality is enhanced and safety in production is guaranteed.

7 Conclusions

Along with the increase of coal mine depth, questions of deep laneway timbering are becoming more prominent. This paper studies this problem through abscission layer observations in coal mine laneways and numerical simulation analysis result. After the parameters of anchor and anchor cable union supports are carried on, experience shows that distortion and destruction of the laneway is clearly decreased. Good economic efficiency has obtained with guaranteed safety in coal mine production.

Acknowledgements

The authors thanks for sustain from key Natural Science Fund of China (No:50434020); the National Natural Science Fund of China (No:50874064; 50804026) ; Fund for Young Scholar of Henan University of Science and Technology (No:2006QN029) and Natural Science Fund of Shandong Province.

References

1. Qian, Q.H. and Li, S.C. A Review of Research on Zonal Disintegration Phenomenon in Deep Rock Mass Engineering. Chinese Journal of Rock Mechanics and Engineering, 2008, 27(6). 1278-1284.
2. Lu, S.B., Li, X., Ma, J.Q. and Yue, B. Interpretation of Deform Action Monitoring of Underground Road, Analysis and its Application to No.2 Diggings of Jinchuan Mine. Chinese Journal of Rock Mechanics and Engineering, 2004, V23(3). 488-492.
3. Yang Z.Q., GAO, Q. and Wang, Z.H. Research on prestressed cable parameters optimization designs and its application to Jinchuan Mine No.2. Rock and Soil Mechanics, 2008, V29(5). 1361-1366.
4. Wang, G., Jiang, Y.J. and Li S.C. Crack Expansion Judgment Method for Wall Rock of Underground Caverns and Its Application. Chinese Journal of Underground Space and Engineering, 2008, 4(4). 657-661.

*RaSiM 7(2009): Controlling Seismic Hazard and
Sustainable Development of Deep Mines,
C.A. Tang(ed), Rinton Press, 555-560*

NUMERICAL STUDY OF ACOUSTIC EMISSION IN THE UNLOADING FAILURE PROCESS OF HETEROGENEOUS ROCKS

PENG-ZHI PAN, XIA-TING FENG, and HUI ZHOU

*State Key Laboratory of Geomechanics and Geotechnical Engineering, Institute of Rock and Soil Mechanics,
Chinese Academy of Sciences, Wuhan, 430071, China.*

An elasto-plastic cellular automaton (EPCA) model is used to study the acoustic emission (AE) characteristic in the unloading failure processes of heterogeneous rocks. Different heterogeneity is controlled by homogeneous index, where a low homogeneous index means strong heterogeneity. Initial stresses are firstly applied the rock specimen and then the stress in one direction is released with the stress in the other direction keeping constant. Calculated results indicate that the heterogeneity of rocks has a great influence on the AE modes. For the rock specimen with a very low homogeneous index, AE occurs almost in the whole unloading process, indicating that the tendentiousness of rock burst is weak. However, for the rock specimen with a high homogeneous index, when the stress is released, the AE occurs abruptly, indicating that the rock specimen has a strong tendentiousness of rock burst.

1 Introduction

The study of damage formation in jointed or bulk rock under stress is a subject of widespread interest, with relevance to both artificial applications such as optimization of geothermal recovery, oil recovery, safe design of nuclear waste repositories, rock bursts, and natural processes such as volcanism and seismology [1]. For many reasons, it is important to be able to predict the time, location, and intensity of potential rock fractures. Fracture development in stressed rock has been observed extensively in the laboratory by a number of methods, such as scanning electron microscopy (SEM) [2], optical microscopy (e. g. Cox and Scholz, 1988 [3]) and acoustic emission (AE) (e.g. Lockner et al., 1991 [4]; Lei et al., 2000 [5]). Among these methods, AE technique provides an analysis of the microcracking activity inside the brittle rock volume. It has an important advantage over other techniques in that tests can be performed under confining pressure, which is very important in the simulation of underground conditions.

In the last decade, people all over the world studied the AE characteristic of rocks in order to find the relation between AE and rock failure processes. Li et al. carried out experiments on AE characteristics of full-regime rock failure on stiffness test machines under uniaxial compression conditions [6]. Li et al. studied the characters of AE of marble samples with pre-existed cracks under compression experimentally [7]. Li and Zhou carried out tests and analysis of four kinds of rock's acoustic emission characteristics under uniaxial compression [8]. Qin and Li derived a general expression of the total counts of acoustic emission N relating to the stress intensity factor KI for low-brittle rock, based on the testing principle of acoustic emission and the basic theory of fracture mechanics [9]. Tang presented the basic idea and framework for the numerical simulation of AE in rock failure and a practical computation example was given [10]. Fu and Tang conducted a numerical study on the Kaiser effect in rock failure subjected to uniaxial compression using their self-developed numerical software RFPA [11].

From the literature review, it is clear that most of previous studies on the AE behaviour are confined to the loading failure processes of rocks. The studies of the AE behaviour in the unloading failure processes are seldom found. However, in many cases, rock mass is always in a certain stress state. After the engineering disturbance (e.g. excavation), stress in one or two directions may be removed and the equilibrium state will be changed. Fracture may be occurrence in the stress release process and acoustic emission will be found.

In present work, it is concentrated on numerical study of the AE behaviours in the unloading failure processes of heterogeneous rocks using self-developed numerical tool EPCA [12,13]. The unloading failure process means that the rock specimen is subjected to an initial stresses and then the stress in one direction is released step by step until the failure of rock occurs. Different homogeneous index is considered to study the influence of rock heterogeneity on the AE mode in the failure process.

2 Numerical Tool and Modelling Method

When the EPCA model is used to simulate the failure process of rocks, firstly the rock specimen is discretized into a system composed of cell elements. Then the heterogeneous material model is adopted with homogeneous index m, and the elemental seed parameter s for the heterogeneous mechanical properties of rock, such as Young's modulus, Poisson's ratio, cohesive strength etc. The Weibull's probability density function can be expressed as,

$$p(x)=\begin{cases}\frac{m}{x_0}\left(\frac{x}{x_0}\right)^{m-1}\exp\left[-\left(\frac{x}{x_0}\right)^{m}\right], x\geq 0\\ 0, x<0\end{cases}. \tag{1}$$

where x is the parameter of the element; the scale parameter x_0 is related to the average of element parameter and the parameter, m, defines the shape of the distribution function.

According to initial and boundary conditions, certain loading control method such as constant strain rate or linear combination of stress and strain etc., is adopted to simulate the loading process of rock specimen in order to obtain the complete stress-strain curves of rock failure process. In each loading step, the cell state is updated by the cellular automata updating rule [12] to obtain the displacement field and stress field.

The calculated stresses are substituted into Mohr-Coulomb criterion to check whether or not cell element yield occurs. If the strength criterion is not satisfied, the external force is increased further (in present work, it means that the differential stress increases). Otherwise, the cell element yielded and the corresponding plastic strain produced according to the brittle-plastic constitutive theory (Figure 1a).

As an approximation, it is assumed that the AE counts are proportional to the number of yield cell elements and that the strain energy released by yield cell elements is all in the form of acoustic emissions. By this means, in CA model, since the isoparametric element is chosen as the cell element, according to the state of Gauss point (Figure 1b), each AE event corresponds to the yield Gauss points of a cell element, and the AE energy release of an element is assumed to be the reduction of elastic strain energy during yield. Therefore, the AE counts are accounted by the number of yield Gauss points and the energy releases are calculated from the plastic strain energies of every yield Gauss point. Based on the above assumptions, the cumulative AE counts and cumulative AE energy release can be realistically simulated with EPCA model.

The cell element conforms to loading and unloading law of elasto-plastic theory in EPCA model. Therefore, this model can be conveniently used to simulate the unloading failure process. As shown in Figure 2 错误！未找到引用源。, the point (Gauss point) in a cell element is subjected to an initial stress σ_1, σ_3. If we use the Mohr-Coulomb criterion as the yield criterion, on $\sigma_n-\tau$ coordinate system, at initial state, it is a point on σ_n axes (if $\sigma_1=\sigma_3$). The Mohr circle will become bigger if the stress on σ_3 direction is released step by step with σ_1 remains constant. If the Mohr circle is big enough to touch the Mohr-Coulomb failure surface, the point will be in failure, which means that the point will be in a plastic flow state on residual yield surface.

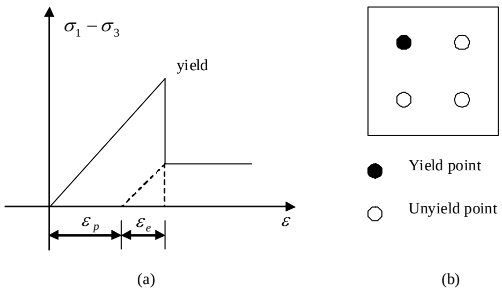

Figure 1 (a) Elasto-brittle-plastic constitutive relation. (b) State of Gauss point.

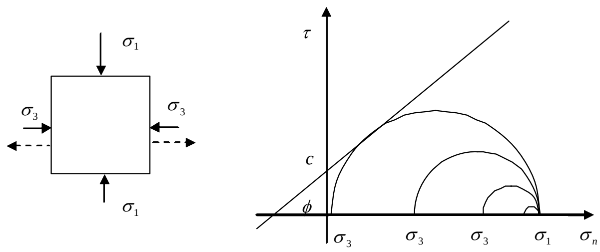

Figure 2 Failure representation of a Gauss point with Mohr-Coulomb criterion

3 Numerical Example

Based on the approach described above, a numerical investigation on the AE characteristic and deformation behavior in the unloading failure process of heterogeneous rock specimen is presented here. The rock specimen is 100mm height and 50mm width. The cell element has a size of 1mm*1mm. Therefore, the specimen contains 5000 cell elements. As the Weibull's distribution is used to the rock parameters assignment, we consider different homogeneous index to study the effect of heterogeneity on AE characteristic and the deformation behavior. Mechanical properties are shown in Table 1. Plane strain problem is assumed. Elasto-plastic loading and unloading and associated plastic flow laws are assumed. Mohr-Coulomb criterion is adopted as the yield criterion.

The specimen is subjected to an initial stresses on axial and radial directions, respectively. The failure process of rock specimen is simulated by unloading the radial stress (or confinement), keeping the axial stress as constant. The unloading rate is 1MP. With the unloading of lateral stress, the differential stress increases.

Table 1 Mechanical parameters of rock specimen

Parameters	Value	Parameters	value
Young's modulus	60GPa	Poisson ratio	0.3
Initial cohesion	15.5MPa	Friction angle	49 degrees
Residual cohesion	1MPa	Residual friction angle	30 degrees
Homogeneous index	1.1, 2.0, 6.0	Random seed	10
CA iterative precision	1e-11	Plastic tolerance	1%
Maximum nonlinear iterative steps	500		

Figure 3 presents the AE characteristic of rock specimens with different homogeneous index in the unloading failure processes. It can be seen that AE modes are great influenced by the heterogeneity. As results, at lower differential stress the rock seems to have no AE occurs. With the decrease of lateral stress, the AE gradually increases for rock specimen with lower homogeneous index. The AE behaves swarm shocks. For rock specimen with higher homogeneous index, AE increases remarkably when the rock draws near breach. The AE behaves main shock. The fact that the AE mode is dependent on the heterogeneity of rocks is great important in the prediction of rock bursts. For rock specimen with very low homogeneous index, acoustic emission occurs almost in the unloading process, which means that the energy stored in the rock specimen is released gradually. In this case, the tendentiousness of rock burst is weak. However, for rock specimen with higher homogeneous index, only a few acoustic emissions are found before the failure of rock specimen, which means that the energy is accumulated in the rock specimen. When the stress is released to a value to lead to the instantaneous failure of rocks, the acoustic emission occurs abruptly, indicating that the rock specimen has strong tendentiousness of rock burst.

The influence of heterogeneity of rocks on the AE modes and rock burst tendentiousness can also be seen from the deformation curves in the unloading failure processes (Figure 4). Comparing with rock specimen with lower homogeneous index, rock specimen with higher homogeneous index has a very big lateral and axial strain in the last unloading step. The axial and lateral strain increments of rock specimen with homogeneous index 6.0 are 4.03e-3 and 6.88e-3, respectively, in the last step. However, for rock specimen with homogeneous index 1.1, the axial and lateral strain increments are 1.16e-4 and 1.85e-4, respectively, in the last step. That is to say, significant elastic energy is released in short time for rock specimen with higher homogeneous index.

It should be noted that, in the lateral unloading process, the axial stress is kept constant. The increasing differential stress leads to the failure of rock specimen. Therefore, it is actually a stress loading control method. Although the elasto-brittle-plastic constitutive relation of each cell element is used, the macro differential stress and strain curve has not a potential of drop down (Figure 4). In the unloading process, the stress of a cell element drops to its residual yield surface when it reaches to peak strength. With the increase of the number of failed cell element, the rock specimen will behave strain harden. When the number of failed cell element increases to a certain value, serious failure in the rock specimen will happen and the calculation will be divergent.

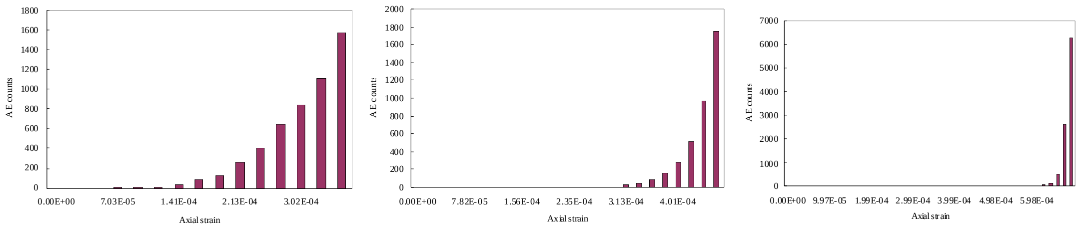

(a) (b) (c)

Figure 3 Axial strain-AE relation of rocks with different homogeneous index. (a) m=1.1; (b) m=2.0 and (c) m=6.0

4 Conclusions

In this study, the numerical rock specimen was subjected on initial stresses on both axial and radial directions. The radial stress (or confinement) is released step by step and axial stress is kept constant to simulate the actual engineering disturbance (e.g. excavation). The AE characteristic of rocks in the unloading processes is investigated numerically by using self-developed numerical tool EPCA.

Results indicated that the heterogeneity of rocks has a great influence on the acoustic emission modes. For rock specimen with very low homogeneous index, acoustic emission occurs almost in the unloading process, which means that the energy is released gradually. In this case, the tendentiousness of rock burst is weak. However, for rock specimen with high homogeneous index, only a few acoustic emissions are found before the failure of the rock specimen, which means that the energy is accumulated in the rock specimen. When the stress is released to a value to lead to the instantaneous failure of rocks, the acoustic emission occurs abruptly, indicating that the rock specimen has strong tendentiousness of rock burst.

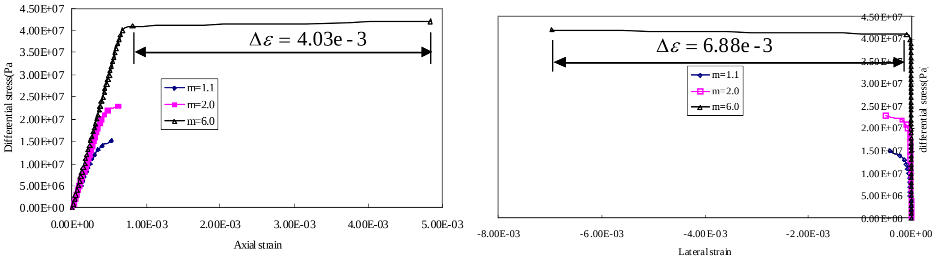

(a) (b)

Figure 4 (a) Differential stress and axial strain relation and (b) differential stress and lateral strain relation.

Acknowledgements

This work was supported financially by the Hi Tech Research and Development Program of China (863 Program) under Grant No. 2006AA06Z117, the National Natural Science Foundation of China (Grant No. 50709036) and Natural Science Foundation of Hubei Province (Grant No. 2008CDB368).

References

1. Lei, X., Masuda, K. and Nishizawa, O., et al. Detailed Analysis of Acoustic Emission Activity during Catastrophic Fracture of Faults in Rock. Journal of Structural Geology, 2004, 26. 247-258.
2. Zhao, Y. Crack Pattern Evolution and A Fractal Damage Constitutive Model for Rock. International Journal of Rock Mechanics and Mining Science, 35. 349-366.
3. Cox, S.J.D. and Scholz, C.H. Rupture Initiation in Shear Fracture of Rocks: An Experimental Study. Journal of Geophysical Research, 1988, 93. 3307-3320.
4. Lockner, D.A., Byerlee, J.D., Kuksenko, V., Ponomarev, A. and Sidorin, A. Quasi-static Fault Growth and Shear Fracture Energy in Granite. Nature, 1991, 350. 39-42.
5. Lei, X.L., Kusunose, K., Rao, M.V.M.S., Nishizawa, O. and Satoh, T. Quasi-static Fault Growth and Cracking in Homogeneous Brittle Rock under Triaxial Compression Using Acoustic Emission Monitoring. Journal of Geophysical Research, 2000, 105. 6127-6139.
6. Li, S.L., Yin, X.G., Wang, Y.J. and Fang, H.Y. Studies on Acoustic Emission Characteristics of Uniaxial Compressive Rock Failure. Chinese Journal of Rock Mechanics and Engineering, 2004, 23(15). 2499-2503.
7. Li, Y.P., Zeng, J., Chen, L.Z. and Wang, Y.H. Acoustic Emission Characters of Pre-cracked Marble under Compression. Underground space, 2004, 24(3). 290-293.
8. Li, J.P. and Zhou, C.B. Experimental Research on Acoustic Emission Characteristics of Rock Mass. Rock and Soil Mechanics, 2004, 25(3). 374-378.
9. Qin, S.Q. and Li, Z.D. On the Relationship between Rock Acoustic Emission Parameters and Fracture

Mechanics Parameters. Journal of Northeast University of Technology, 1991, 12(5). 432-444.
10. Tang, C.A. Numerical Simulation of AE in Rock Failure. Chinese Journal of Rock Mechanics and Engineering, 1997, 16(4). 368-374.
11. Fu, Y.F. and Tang, C.A. Numerical Test on Kaiser Effect in Rock Failure Process. Mechanics in Engineering, 2000, (22). 42-44.
12. Feng, X.T., Pan, P.Z. and Zhou, H. Simulation of the Rock Microfracturing Process under Uniaxial Compression Using an Elasto-plastic Cellular Automaton. Int J Rock Mech Min Sci, 43(7). 1091-1108.
13. Pan, P.Z., Feng, X.T. and Hudson, J.A. Numerical Simulations of Class I and Class II Uniaxial Compression Curves Using an Elasto-plastic Cellular Automaton and A Linear Combination of Stress and Strain As the Control Method. Int J Rock Mech Min Sci, 2006, 43(7). 1109-1117.

RaSiM 7(2009): Controlling Seismic Hazard and Sustainable Development of Deep Mines, C.A. Tang(ed), Rinton Press, 561-568

NUMERICAL SIMULATION OF TRIAXIAL COMPRESSION AND INDUCED ACOUSTIC EMISSION CHARACTERISTICS OF ROCK UNDER DIFFERENT CONFINING PRESSURES

GUO-YING LI, SHU-CAI LI, SHU-CHEN LI and LI-PING LI

Geotechnical and Structural Engineering Research Center, Shandong University

Jinan, 250061, P.R. China

The effect of confining pressures on the mechanical properties and acoustic emission (AE) characteristics of rock are simulated using FLAC3D. In triaxial tests simulation, the homogeneous rock exhibits linear strain-softening behaviour and then ideal plastic behaviour once failure occurs. The numerically simulated results indicate that with the increase of the confining pressures the compressive strength and strain of rock increase, whereas the Young's modulus keeps the same. In addition, using FISH language to compile program, the characteristics of acoustic emission during the triaxial tests of rock are also numerically studied. As the confining pressures increase from null, the cumulative AE events reduce; and the highest AE events increase at first and then decrease. The numerical results agree with the previously numerical results and earlier experimental results.

1 Introduction

Researchers look at mechanical properties of rocks under different confining pressures to study rock failure. Using RFPA (rock failure process analysis) code, Tang, [1] Chen, [2] and Fu [3] simulated the progress of rock failure and associated acoustic emission. The confining pressure effect of rock failure is also researched. D.O. Potyondy and P.A. Cundall [4] studied on the mechanical properties of rock under different confining pressure using PFC (Particle Flow Code). Based on gradient-dependent plasticity, Wang [5] analyzed the inclination angle of shear bands under low confining pressure. In this paper, FLAC3D is used to analyze confining pressure effects of rock. Through compiling FISH functions, the acoustic emission events during the failure process of rock are remembered, and the characteristics of acoustic emission in the triaxial test of rock under different confining pressures are studied.

2 Constitutive Relation and Model

The strain-softening constitutive relation is used in this simulation. The failure criterion used in this model is a composite Mohr-Coulomb criterion with tension cut-off [6]. Prior to the peak strength, the constitutive relation between stress and strain is linearly elastic. Beyond the yield strength, linear strain-softening constitutive relation is selected.

The Mohr-Coulomb failure criterion $f^s = 0$ with:

$$f^s = \sigma_1 - \sigma_3 N_\phi + 2c\sqrt{N_\phi} \qquad (1)$$

The tension failure criterion of the form $f^t = 0$ with:

$$f^t = \sigma_3 - \sigma^t \qquad (2)$$

Where Φ is the friction angle, c, the cohesion, σ^t, the tensile strength.

The specimen geometry is 5 cm long 5 cm wide and 10 cm high. It is divided into 16000 elements and the element size is 2.5 mm. The model under confining pressures is loaded at a constant velocity of $5*10^{-9}$ m/s at two ends of the specimen. The material properties used in the simulation are given in Table 1. The functions of the mobilized cohesion and friction angle can be established by considering laboratory test data, the GSI system as well as back analysis of field measurements [7, 8]. In the present study, linearized functions shown in Table 2 are used.

Five schemes for calculations are adopted in this paper. From scheme 1 to 5, confining pressures are 0, 1.2, 2.4, 3.6 and 4.8 MPa. The confining pressure coefficient is defined as the ratio of the confining pressure and the uniaxial compressive strength. For each scheme, the confining pressure coefficient is 0, 0.055, 0.11, 0.165 and 0.22, respectively.

Table 1 Material properties used in the simulation

Name	Value	Name	Value
Young's modulus(GPa)	30	Shear modulus(GPa)	17.9
Poisson's ratio	0.22	Bulk modulus(GPa)	12.3
Tensile strength(MPa)	0.4	Dilation angle (deg)	5
Density (kg/ m^3)	2500	Gravity acceleration(m/ s^2)	9.8

Table 2 Variation of cohesion and friction angle with plastic strain

Plastic strain	Cohesion (MPa)	Friction angle (deg)
0	3.4	57
0.0003	0.5	49

3 Results and Analysis

3.1 Effect of Confining Pressures on Stress-Strain Curve

Figure1 and 2(a) show the stress-strain curve and AE events-strain curve of rock triaxial test under different confining pressures. The variety of the peak strain and strength with confining pressures are showed in Figure3 and Fig4. The numerical results indicate that higher confining pressure results in higher triaxial strength, higher residual strength as well as higher strain. This reflects that the failure of rock specimen turns from brittle failure at the low confining pressures to ductile failure at the high confining pressures. Thus, confining pressures will enhance the ductility of rock specimen during the failure processes. These numerical results Coincide with the experiment results in paper [1, 9].

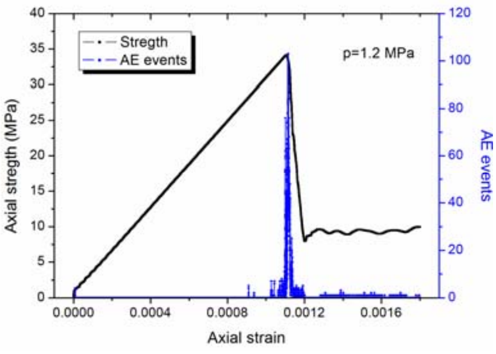

(a)

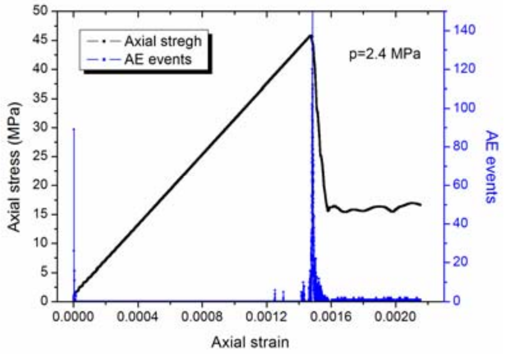

(b)

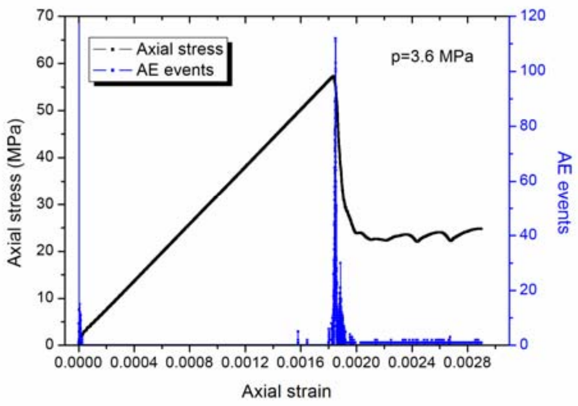

(c)

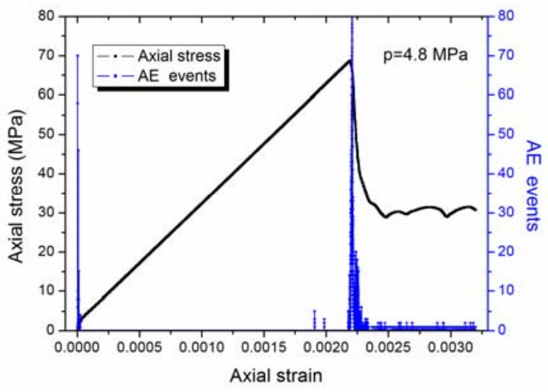

(d)

Figure1. Axial stress-strain curve and AE events-strain curve for different confining pressures.

(a) 1.2 MPa ; (b) 2.4 MPa ; (c)3.6 MPa ; (d)4.8Mpa.

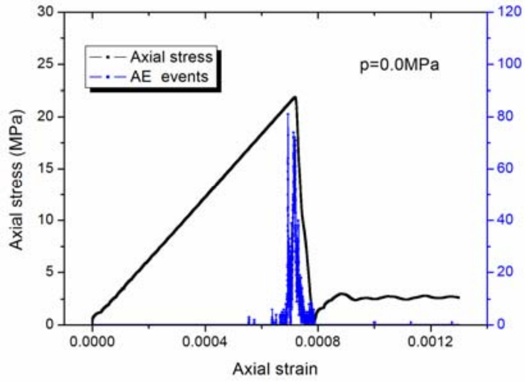

(a)

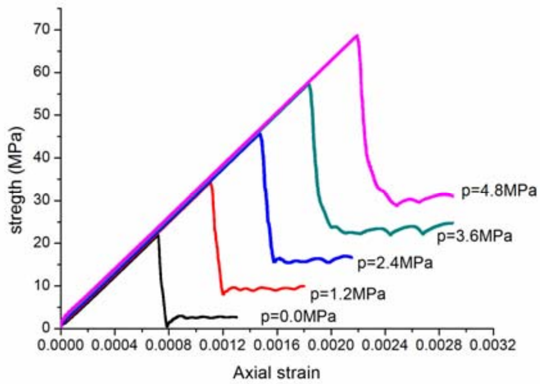

(b)

Figure2. (a) Stress-strain curve and AE events-strain curve for uniaxial test

(b) Axial stress-strain curve for different confining pressures.

3.2 Effect of Confining Pressures on Young's Modulus

As is shown in Figure2 (b), the Young's modulus is not changed. This is mainly because the material properties of the model are homogeneous. The experiment of rock specimens are received the same results [10, 11]. As in these rock specimens there are few imperfections, so the confining press has little effect on the Young's modulus. For the rock specimens with imperfections, the Young's modulus will enhance when improve the confining pressures [9].

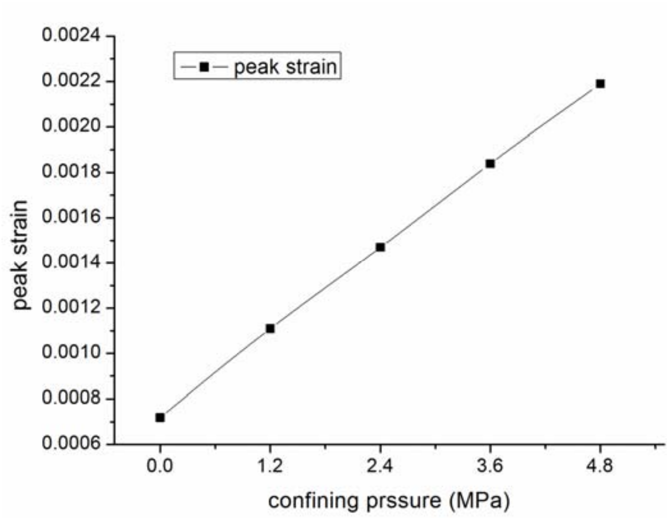

Figure3 .The relationship between peak strain and confining pressure

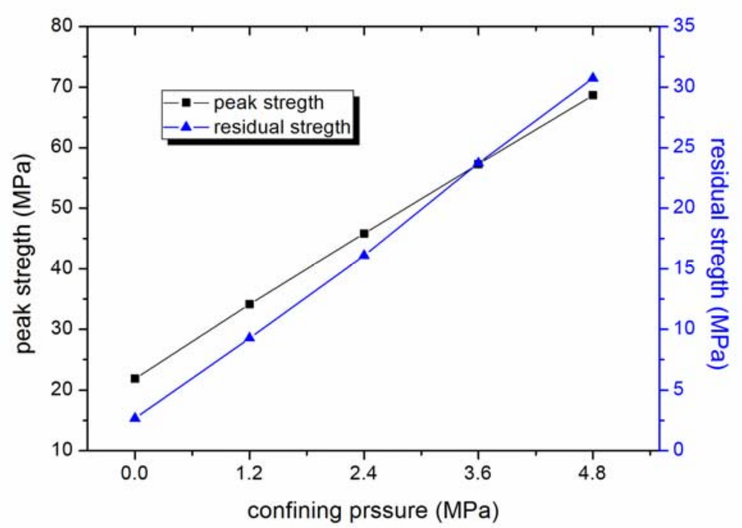

Figure4. The relationship between peak strength residual strength and confining pressure

3.3 Effect of Confining Pressures on Shear Band

Strain localization is defined as the phenomenon of higher plastic strain concentrated in a narrow or limited area during the failure of material. Shear strain localization region often called the shear band [12]. Figure5.and Figure6 show the typical three-dimensional distribution of axial velocity and shear band for rock under confining pressures in 3.6MPa. The shear band distribution of rock for five different schemes is shown in Figure7. It indicates that the inclination angle of shear band decreases with increasing confining pressure. Analysis results are compared with earlier investigations and the agreement is good [13, 14].

3.4 Effect of Confining Pressures on Acoustic Emission (AE) Characteristics

Form Fig 1, It is found that the highest AE events occur in the post-failure stage instead of the maximal stress. This phenomenon agrees with the earlier numerical simulations [1, 15]. Figure8.shows AE events-strain curve for different confining pressures. As the confining pressures improve from null, the highest AE events in the whole tests increase at first; and then, when the confining pressure improve to higher level, the highest AE events decrease. The cumulative AE events also reduce with the confining pressure increases, which can be found in Figure9. This phenomenon can prove the earlier conclusion that confining pressures will enhance the ductility of rock. During the failure process of the material, the total AE events will decrease as the ductility improves.

4 Discussion

The mechanical properties and AE characteristics in triaxial tests are dependent on constitutive relation of rock material and geometry parameters of rock specimen. The conclusion that the Young's modulus keeps the same as the confining pressures increase coincides with the previously experimental measurements. In addition, it should be noted that the present numerical simulation is particularly applicable to the homogeneous rock. The further theoretical investigations and numerical simulations are needed to study the heterogeneous materials.

The presented numerical simulation is applicable for rock specimen under low confining pressure. The maximum confining pressure coefficient is 0.22. As Seeber [16] noticed that if the confining pressure was greater than one-fifth of the axial stress at failure, strain-softening was unlikely to occur.

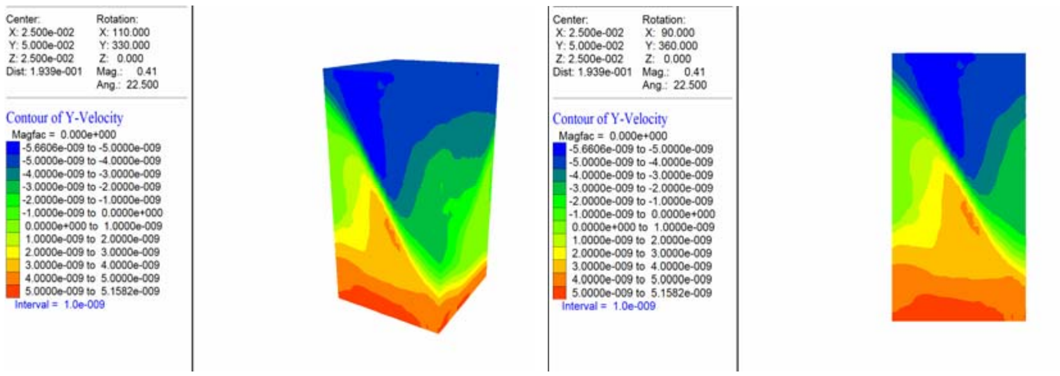

Figure5. Typical three-dimensional distribution of axial velocity for rock under confining pressure in3.6MPa

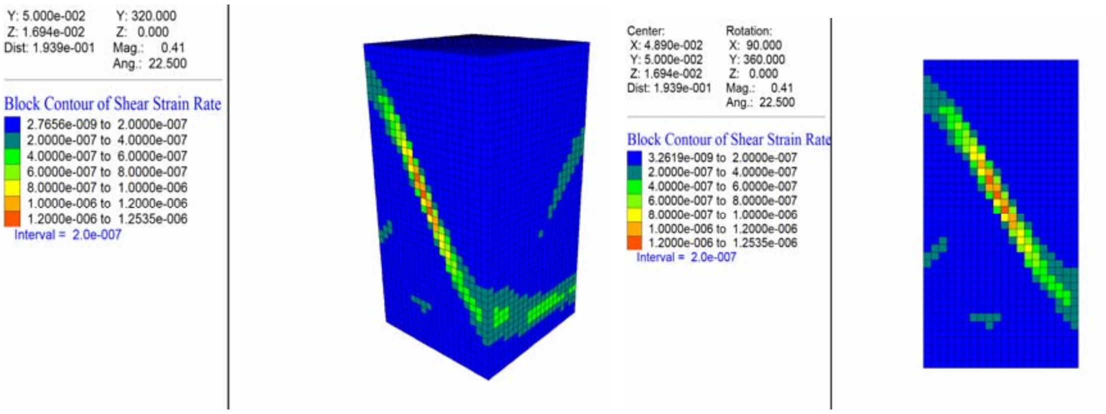

Figure6. Typical three-dimensional distribution of shear band for rockunder confining pressure in3.6Mpa

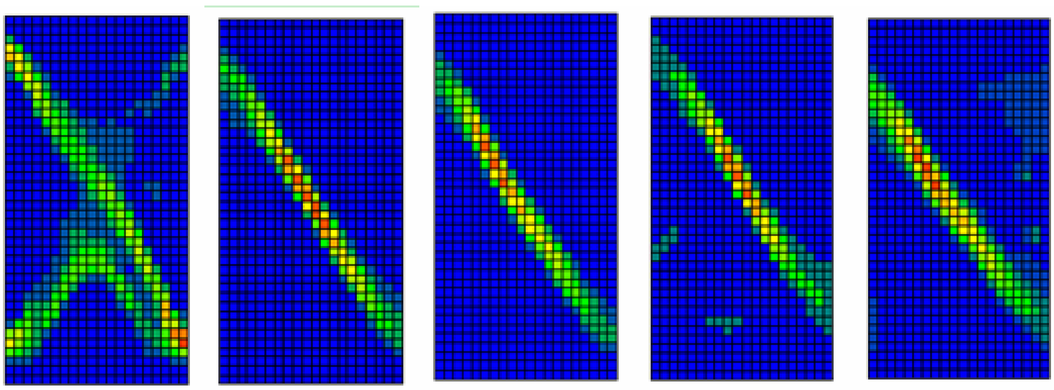

(a) (b) (c) (d) (e)

Fig 7. Shear band distribution of rock under different confining pressures. (a)0 MPa; (b)1.2 MPa; (c)2.4 MPa; (d)3.6 Mpa; (e)4.8Mpa

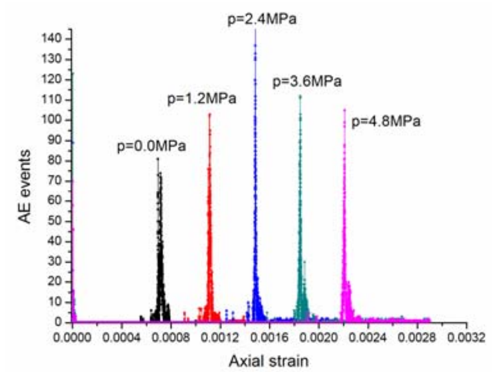

Figure8. AE events -strain curve for different confining pressures.

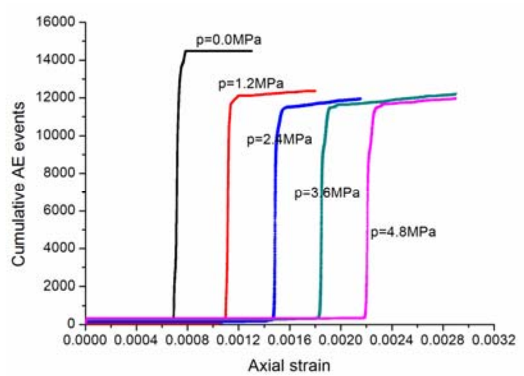

Figure9. Cumulative AE events -strain curve for different confining pressures.

5 Conclusions

The triaxial compression test and induced AE characteristics of rock under different confining pressures are simulated using FLAC3D. Numerical simulations revealed that peak and residual strengths of rock increase with increasing confining pressures. Young's modulus stays constant for homogeneous rock. As confining pressures improve, the ductility of rock specimens will enhance during the fail processes; however, the inclination angle of shear band decreases. As the confining pressure improve, the highest AE events in the tests will increase at first, and then decrease. Higher confining pressure will enhance the ductility of rock and reduce the cumulative AE events during the failure process. This presents numerical results which agree with the previous numerical results and earlier experimental measurements.

Acknowledgments

This work was supported financially by the National Nature Science Foundation of China (Grant nos. 50625927 and 50729904) and the Special Funds for Major State Basic Research Project under Grant no.2007CB209407.

References

1. Tang, C.A., Xu, T., Yang, T.H. and Liang, Z.Z. Numerical Investigation of the Mechanical Behavior of Rock under Confining Pressure and Pore Pressure. International Journal of Rock Mechanics and Mining Sciences, 41(3). 421-422.
2. Chen, Z.H., Fu, Y.F. and Tang, C.A. Confining Pressure Effect on Acoustic Emissions during Rock Failure. Chinese Journal of Rock Mechanics and Engineering, 16(1). 65-70.
3. FU, Y.F. The Numerical Simulation of Effect of Confining Pressures on Failure Process of Rock. Journal of Liaoning Technical University, 19(5). 488-492.
4. Potyondy, D.O. and Cundall, P.A. A Bonded-Particle Model for Rock. Int J Rock Mech Min Sci, 41(8). 1329-1364.
5. Wang, X.B. Numerical Simulation of Failure Processes and Acoustic Emissions of Rock Specimens with Different Strengths. Journal of University of Science and Technology Beijing, 30(8). 837-843.
6. Itasca. FLAC-fast Lagrangian analysis of continua. Version 4. Itasca Consulting Group Inc, 2000.
7. Cai, M., Kaiser. P.K., Tasaka, Y. and Minami, M. Determination of Residual Strength Parameters of Jointed Rock Masses Using the GSI System. International Journal of Rock Mechanics and Mining Sciences, 44 (2). 247-265.
8. Cai, M., Kaiser, P.K., Morioka, H., Minami, M., Maejima, T., Tasaka, Y. and Kurose, H. FLAC/PFC Coupled Numerical Simulation of AE in Large-Scale Underground Excavations. International Journal of Rock Mechanics and Mining Sciences, 44(4). 550-564.
9. Yang, Y.J., Song, Y. and Chen, S.Y. Test Study of Coal's Strength and Deformation Characteristics under Triaxial Compression. Journal of China Coal Society, 31(2). 150-153.
10. You, M.Q. Effect of Confining Pressure on the Young's Modulus of Rock Specimen. Chinese Journal of Rock Mechanics and Engineering, 22(1). 53-60.
11. Wawersik, W.R., and Fairhurst, C. A Study of Brittle Rock Fracture in Laboratory Compression Experiments. International Journal of Rock Mechanics and Mining Sciences, 7(6). 561-575.
12. Wang, X.B. Numerical Simulation of Failure Precursor and Shear Bands for Rock Specimens with Random Material Imperfections. Chinese Journal of Underground Space and Engineering, 3(6). 1047-1050.

13. Liu, H.Y., Kou, S.Q., Lindqvist, P.A. and Tang, C.A. Numerical Studies on the Failure Process and Associated Microseismicity in Rock under Triaxial Compression. Tectonophysics, 2004, 384(1-4). 149-174.
14. Wang, X.B. Analysis on Inclination Angle of Shear Band under Low Confining Pressure Based On Gradient Dependent Plasticity. Chinese Journal of Rock Mechanics and Engineering, 23(1). 31-34.
15. Feng, X.T., Pan, P.Z. and Zhou, H. Simulation of the Rock Microfracturing Process under Uniaxial Compression Using an Elasto-Plastic Cellular Automaton. International Journal of Rock Mechanics and Mining Sciences, 43(7). 1091-1108.
16. Seeber, G. Druckstollcn and Druckschachte. Stuttgart: Enkc, 1999.

RaSiM 7(2009): Controlling Seismic Hazard and
Sustainable Development of Deep Mines,
C.A. Tang(ed), Rinton Press, 569-574

STUDY ON BEHAVIORAL LAWS OF STRATA PRESSURE OF COAL FACE AND ITS CONTROL IN THIN SEAM

BAOFU LI

School of Energy Science and Engineering, Henan Polytechnic University

Jaozuo 454000, Henan, China

QIANG SHAO

School of Energy Science and Engineering, Henan Polytechnic University

Jaozuo 454000, Henan, China

XINXIAN ZHAI

School of Energy Science and Engineering, Henan Polytechnic University

Jaozuo 454000, Henan, China

Abstract: Based on the geological conditions of thin seam with hard roof and soft coal at Caoyao Coal Mine, Yima Coal Group, China, the behavior of strata pressure in coal face was studied with numerical calculation, overall process of first weighting and periodic weighting was reappeared and the related parameters of abutment pressure in front of coal face were obtained. According to the classification of stability and controllability of roof strata, support pattern of coal face in thin seam at Caoyao Mine were proposed. In view of the calculation results, the scheme of feasible matched equipments of coal face in thin seam was accordingly put forward. The conclusions have provided fundamental basis for mechanization mining thin-seam, and have advanced the theory for technology on mining thin seam.

1 Introduction

According to the classification rule of seam thickness in China, seams between 0.8 and 1.3m are classified as thin and seams whose thickness are less than 0.8m are called extremely thin. In terms of recoverable reserves, the reserves of thin seams are widely occupied in Chinese coal mines, 84% of mining areas have thin seams in prospected reserve mining areas. The reserves for thin seams make up 62 billion tons or 17.5% of gross reserves [1]. Due to the narrow mining space and complex geological conditions, mechanized mining in thin seams is comparatively less common. The scale of output in thin seams is far less in contrast to their reserves. Therefore, in order to improve the recovery ratio of coal, prolong mine service life, and obtain high-efficient mining safely, it is important to study the behavioral laws of strata pressure of coal faces in thin seams. Also, the study of an equipment matched plan and technique of mechanization mining are of great importance.

Seam II_1 at the Shanxi Formation of Carbonic-Permian of Shanmian coalfield is extracted at the Caoyao Mine. The average height above sea level on the surface of the shaft field is +700m. Figure1 shows a synthesized histogram of strata of the coal series at the Caoyao Mine. The seam thickness gradually becomes thinner with an increasing overburden. Table 1 shows the distribution characteristics of bore numbers and coal seam thicknesses in the Caoyao shaft field. Output of the mine in 2007 was recorded to 0.23 million tons with a remaining mine service life of 14 years. The thickness of the seam under the +300m level of the mine is

0.8-1.3m. Therefore, mining thin seams with a deeper overburden is an important decision on the economical technology for the Caoyao Mine to improve the recovery ratio of coal and prolong mine service life.

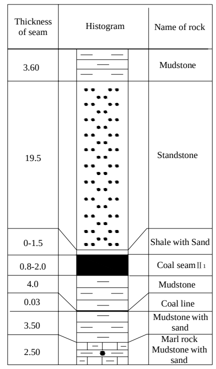

Figure1 Synthesized histogram of strata of coal series at Caoyao Mine

Table 1. Distribution characteristics of bore number and coal seam thickness in Caoyao minefield

Grade on coal seam thickness	Un-minable coal seam	Thin seam 0.8-1.3m	Medium coal seam 1.3-3.5m	Thick coal seam 3.5-8m	Extremely thick coal seam >8m	Total
Bore number	27	15	52	35	4	133
Bore proportion /%	20.3	11.3	39.1	26.3	3.0	100

2 Numerical calculations on law of behaviors of strata pressure of coal face in mining thin seam

2.1 Brief introduction of numerical modeling

Strata movement overlying coal face is a very complex and dynamic processing. In order to understand the mechanics and range of overlying strata movement, damage processing on roof strata deforming should be studied. At present, $RFPA^{2D}$ is numerical calculation software, which can simulate the whole processing on rock crack initiating, expanding until fracturing for simulated rock. Based on the theory of continuum medium mechanics and damage medium mechanics, the software has two functions on stress and failure analyses [2]. So, with RFPA2D, the processing on rock mass rupture and strata movement under mining action can be simulated [3,4,5].

2.2 Numerical calculation model

Mining depth of seamⅡ1 in the simulated model was 550m. One unit width was selected along the strike in the middle of longwall face, and used plane strain model to calculate. Figure2 was mechanics model of numerical calculation. Mechanic parameters of every coal seam and strata were shown in Table 2.

Model top was free boundary and gravity stress was applied according to depth. Left-right boundary of model was simply supported that restrained horizontal displacement. Under boundary of model was clamped. Length and height of model were 300×100m with unit division being 300×100. Mining space of simulation was 2m, and mining thickness was 1m because of unit division. Amendatory Mohr-Coulomb criterion was used as strength criterion of unit failure. Change of vertical stress and abutment pressure with mining of coal face during the first weighting and periodical weighting were calculated from the modeling, respectively.

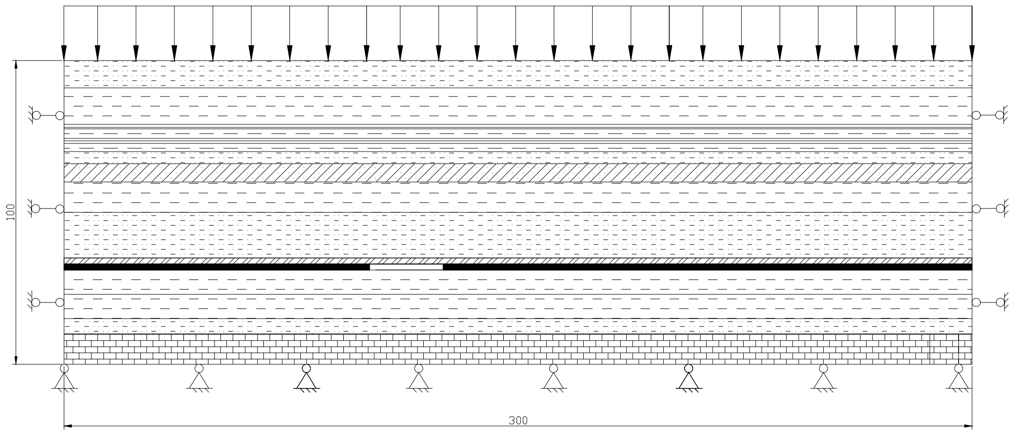

Figure2 Mechanic model of numerical calculation

Table 2. Mechanical parameters of coal seam and strata

Rock strata	thickness of Rock stratum /m	Modulus of elasticity /MPa	compression strength /MPa	Bulk density /10-5N/mm^3
Medium-grained sandstone	9	10000	100	2.7
Sandy mudstone	10	6000	60	2.5
Medium-grained thin sandstone	2.0	8000	80	2.6
Pelitic bauxit	1	6000	45	2.4
Sandy mudstone	8	3000	60	2.4
Medium-grained sandstone	4	8000	90	2.7
Sandy mudstone	6	6000	60	2.4
Sandy mudstone	10	6500	70	2.4
Sandstone	15	6000	80	2.7
Sandy shale	2	1200	10	2.4
II_1 coal seam	1	1500	20	1.4
Sandy mudstone	10	6000	60	2.4
Sandy mudstone	8.0	7000	70	2.4
Medium-grained thin sandstone	5.0	12000	120	2.7
Limestone	8.0	8000	100	2.6

2.3 Numerical calculation results

The model simulated the mining process of coal face. When face mined 6m, immediate roof started to separate and fall. Main roof reached limit collapse interval when face mined 30m, and main roof experienced the first weighting. Front abutment pressure impacted 50-60m during the first weighting of main roof. The maximum stress value was 43.2MPa, and the maximum stress concentration factor *Kmax* was 3.4. The periodical weighting interval of main roof was 18m, which impacted 40-50m due to periodical weighting. The average value *Kmax* for maximum stress concentration factor was 2.8 due to front abutment pressure.

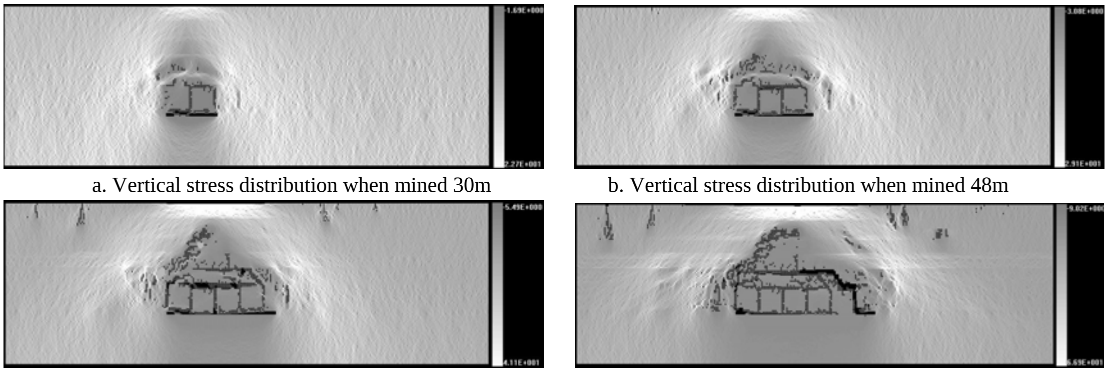

a. Vertical stress distribution when mined 30m b. Vertical stress distribution when mined 48m

c. Vertical stress distribution when mined 66m d. Vertical stress distribution when mined 84m

Figure3 Relation between vertical stress distribution and mining space

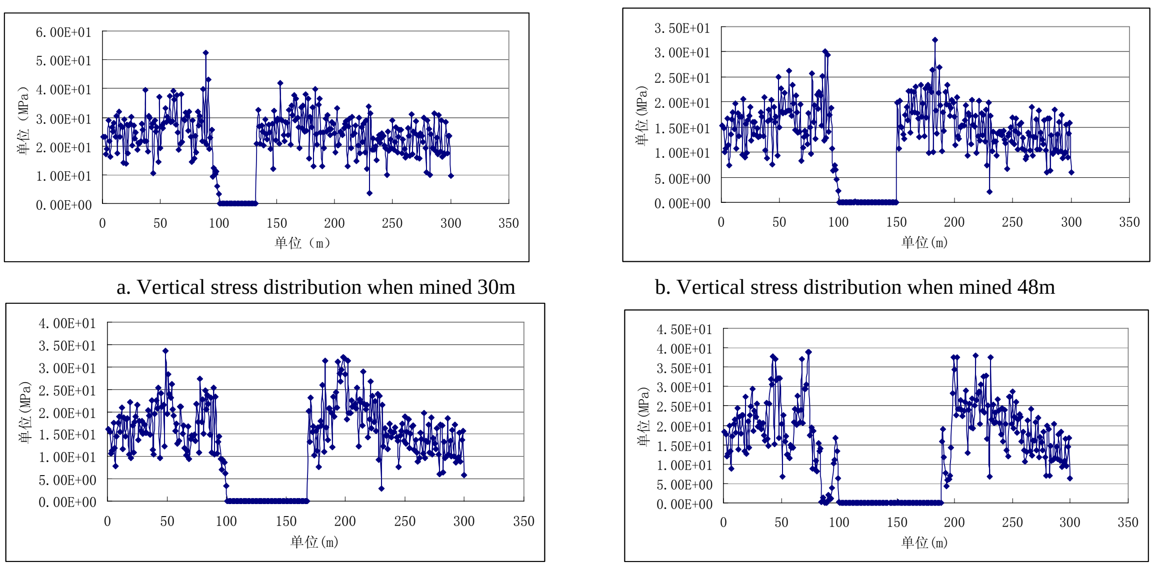

a. Vertical stress distribution when mined 30m b. Vertical stress distribution when mined 48m

c. Vertical stress distribution when mined 66m d. Vertical stress distribution when mined 84m

Figure4 Vertical stress distribution on front and back of coal face during weighting of main roof

3 Classification of stability of surrounding rock in thin seam face and matched equipments scheme

3.1 Classification of stability and control of surrounding rock in coal face

According to Classification method of stability of surrounding rock, the stability of surrounding rock of thin seam face was classified in Caoyao Mine. Coal seam belonged to 2b roof (medium stable). Main roof belonged to Ⅰ roof (Unobvious weighting). Floor belonged to Ⅲa floor (weak).

Based on stability combination of immediate roof, main roof and floor, the surrounding rock of Caoyao Mine was easy to control. Coal face can select light monomer hydraulic support, support shield or light shield to achieve mechanized mining for the thin seam.

3.2 Matched equipments selection in thin seam mining

(1) Matched Equipments requirements in thin seam mining

“Three Machines’ of the fully mechanized face are coal winning machine, scraper conveyor and hydraulic support. Three machines matched are paramount for selecting complete set of fully mechanized equipments. Coal winning machine depends on scraper conveyor to guide. Scraper conveyor moves along using hydraulic support as fulcrum. Hydraulic support moves through scraper conveyor pulling it. Selecting fully mechanized equipments for thin seam are affected by many factors with three machines mutually matching at aspect of transect size, equipment performance and output. This involves implementing optimal combination for different equipments, thus achieving safest and maximum output for thin seam face.

The coal winning machine demands short size and high power due to low mining height. Owing to geological conditions changed greater in thin seam, the machine has more opportunities to cut hard rock than the medium-thick seam. Then the machine requires better capacity of throughing geological structure and rock drilling, and meanwhile, it needs simple structure, high credibility, convenience for maintenance and fixing.

The first requirement for the scraper conveyor is that low height of central sectional groove in thin seam. Secondly, its width increases correspondingly to adapt coal winning machine widen that caused as its height becoming thinner.

Hydraulic support for thin seam of fully mechanized face should have capability of preventing waste rock leaking and adapt change of great height effectively. The support can move fast and having higher automatization degree. It often uses shield support with two pillars in thin seam for fully mechanized face.

(2) Scheme of feasible matched equipments

According to successful example of thin seam mechanization mining in China and combined with surrounding rock of thin seam face in Caoyao Mine, thin seam that of 0.8-1.3m thickness used mechanization mining. The face equipments were MG300-DM coal winning machine, ZZ2200-0.7/1.35 shield support and SGZ630/150 scraper conveyor[6]. The set has been proven successfully in Songzao Coal Group, China. Most output reached 45, 000 ton per month.

4 Conclusions

Based on geological conditions at the Caoyao Mine, the numerical calculation method was used to study the law of behaviors of strata pressure in the thin seam face. The results confirmed basic the law of behaviors of strata pressure and strata movement, including overall process of the first weighting and periodical weighting. The range of the front abutment pressure impacted and the maximum stress concentration factor were obtained.

According to classification of stability and controllability degree of surrounding rock, proper equipments matched plan of thin seam were put forward. Matched equipment capability requirements of thin seam mining were also studied. Based on successful application practices, feasible equipments matched plans for thin-seam mechanization mining were proposed.

Acknowledgment

This project was financially supported by the Natural Science Foundation of Henan Education Bureau (No. 2008B440005). The authors acknowledge financial supports.

Reference

1. Ni, H.P. and Min, H.U. CAO Bide Simple Analysis to Equipment Coordination of Fully Mechanized Thin Coal Seam Face. Coal Mine Machinery, 2007, (4). 83-84.
2. Zhang, H.Q., Zhao, D.S. and Zhao X.D. et al. Visual Study on the Movement Scope of Overlying Strata and the Control of Roof Failure in Stope. Mining Research and Development, 2004, (6). 80-83.

3. Ma, Z.G., Huang, W. and Guo, G.L. et al. Analysis on Failure of Covering Rock in Ehuobulake Mine by Using Mechanics of Systems with Variable Boundaries. Journal of Liaoning Technical University, 2006, (4). 515-517.
4. Sun, X.Y., Xis, Y.C. Contrast Numerical Test of Graben and Horst Influence on Mining Subsidence. Journal of Hunan University of Science & Technology, 2007, (3). 5-8.
5. Tang, C.A., Wang, S.H. and Fu, Y.F. Numerical Test of Rock Failure. Jilin: Jilin University Publishing Company, 2003.
6. Yima Coal Group Co. Ltd. Henan Polytechnic University. Study on Mining Technology with Comprehensive Mechanization in “Three Soft” and Thin Coal Seam in Westward of Yima Coalfield, 2008.

RaSiM 7(2009): Controlling Seismic Hazard and Sustainable Development of Deep Mines, C.A. Tang(ed), Rinton Press, 575-580

EXPERIMENTAL STUDY ON DYNAMIC BEHAVIOR FOR BLASTING EXCAVATION OF LARGER-SPAN SHALLOW TUNNEL

QING-SONG ZHANG, YANG GAO, SHU-CAI LI and ZHEN-HAO XU

Geotechnical & Structural Engineering Research Center of Shandong University

Jinan ,250061, China

In the course of tunnel construction by drilling and blasting method, it is very important to study dynamic behavior induced by blasting. Aimed at investigating the vibration effect by blasting during the excavation of Miaoya diverging tunnel, this paper studies the vibration characteristic of the ground at the larger-span shallow part and the blasting vibration reduction technology for larger-span excavation. According to the regression analysis for the monitored results of blasting-induced vibration, the mathematical model for vertical propagation of blasting-induced vibration has been revised. Some conclusions are drawn on the basis of the analysis of the vibration characteristic of the ground and the tunnel: i.e. i) the dominating vibration frequency at surface mass point is mainly low frequency; ii) the decreasing tendency of dominating vibration frequency at surface mass point is not obvious when distance increases; iii) the high frequency is mostly absorbed by the concrete of the tunnel lining, so that the blasting vibration impacting on the rock becomes weaker; iv) the ground blasting vibration velocity of the excavation region is higher than that of the rock region; and v) the ground blasting vibration velocity at the top of excavation region should be less than that of blasting security control in the larger-span shallow tunnel.

1 Introduction

With the rapid development of the economy, more and more tunnels are designed as twin-arc tunnels or large-span tunnels to connect with the bridge. The damage of ground vibration becomes more serious during the blasting excavation of a large-span tunnel. So far, the research on blasting damage mostly focus on the damage of concrete ling and the stability of rock piles for twin-arc tunnels, in addition to the dynamic analysis of explosive loading of tunnel [1-3]. However, fewer to the ground vibration characteristics for blasting excavation of larger-span shallow tunnel [4]. The earthquake effect of ground for excavation blasting of larger-span tunnels is so complicated, even for the one with less than 30 meters deep and 20 meters net span, the vibration damage for rock cover of an excavated section is more serious [5]. Based on the engineering background of the Miaoya diverging tunnel, the ground vibration characteristics and the controlling technology are studied, the blasting parameter has been optimized, and the safety controlling problem has been resolved.

2 Blasting vibration site monitoring

2.1 Blasting condition and testing scheme

The shallow section of the Miaoya diverging tunnel is the proper place for blast vibration testing. It is about 26 meters wide and 13 meters high, of which the rockcover of entrance is only 3 meters thick. The surrounding rock is mostly composed by tuff with thin shale, with mud randomly. It is very easy for blasting for monocline with 100~300 obliquity. Considering the need of passage in the construction of Zhijinghe super bridge which lies on the face of the tunnel and the blasting vibration damage is so serious, the mid-guiding hole is firstly excavated, the rectangular hole cut blasting with cavity is adopted for the upper half blasting and the parallel hole cut blasting for the other half in order to reduce the blasting damage to the ground and concrete ling.

The blasting vibration testing mostly focuses on the vibration velocity of ground for the excavation blasting, combined with the vibration velocity of concrete ling to get the attenuation of earthquake wave. Although the damage caused by lager-span excavation blasting is reduced by the way of mid-guiding hole excavation, the earthquake effect caused by excavation blasting of other parts is still more serious than that of parallel hole cut blasting. The concrete ling damage is mostly caused by the excavation of parallel hole cut blasting and the blasting parameter can be adjusted by testing the velocity of concrete ling from different place. The blasting face has been taken as the cross centre for the measuring points arrangement in the direction of both parallel and vertical line of tunnel axes, the total measuring points number is 9, arranged at intervals of 3 meters, as showed in figure 1.

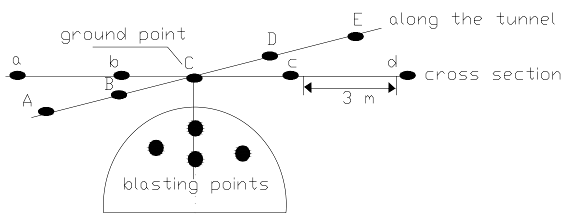

Figure 1 The arrangement of measuring points for ground vibration velocity

Considering the ground measuring points is just under the blasting centre, its vertical velocity is dominant vector for excavation blasting, so the most important information collection focus on the waveform of vertical vibration velocity and three-dimensional velocity should be obtained in order to compare with each other. With the purpose of fully knowing the difference of earthquake effect between different hole cut blasting, information of earthquake wave for three-dimensional vibration velocity of concrete ling should been obtained.

2.2 Testing system and analysis principl

The testing system is composed by IDTS3850 blasting vibration recorder, velocity sensors, PC, printer and so on. Three-dimensional velocity of eight times blasting can be recorded by IDTS3850 blasting vibration recorder which has a sampling rate of 200 Ksps. The waveform and its characteristics parameters can be viewed by the data processing soft. The working principal of testing system is show as figure.2.

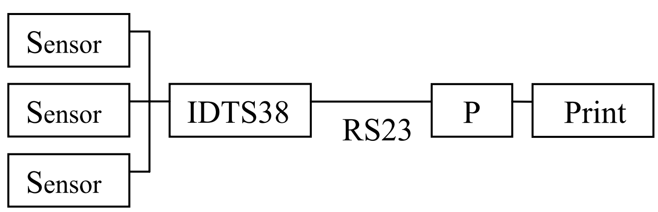

Figure 2 Sketch map of vibration testing system

Before the blasting test, three sensors of velocity have been affixed to the measuring point respectively. the measuring point is vibrated by the earthquake wave which is induced by the blasting of working face when the collecting device for velocity is started, the blasting earthquake wave information is transformed into voltage signal by the sensors and than transformed into data signal by A/D converter, the data signal is recorded into the memorizer which is connected with the computer by its serial device of RS323. When all is ready, the information of blasting earthquake can be analyzed by the data processing soft of EXP3850 Seismograph, such as the analysis on complex vectors, regression analysis on testing data by Sadoy's formula, safety criterion and so on.

3 Analysis of blasting vibration results

Most of the blasting vibration recorders are triggered except for the ones with improper parameters and 45 data groups are obtained. The vibration of concrete ling is tested for twice or three times for that of ground vibration near the entrance, the arrangement line of measuring points for ground vibration is changing with the blasting centre of working face and some measuring points are added along the topography in order to get more precise regression analysis. The regression analysis has been done with the excavation condition in order to adjust the blasting parameters in good time.

3.1 Regression analysis on testing data

So far, the regression analysis has always been done by Sadov's formula in order to make a mathematical model [6-9] to predict the explosive wave propagation with its attenuation behavior, the Sadov's formula is:

$$V = K(Q^{1/3}/R)^{a}. \tag{1}$$

in which, V is the particle vibration velocity(m/s); Q is blasting charge(kg); R is the distance between blasting center with measuring point; K、a are the parameter field factor and attenuation exponent. But the regression analysis is not always accurate because some factors, such as the vertical distance between measuring point and blasting point, he blasting free face, main vibration frequency and so on,is not considered in the Sadoy's formula. Accurate analysis can be obtained by devising the formula and new mathematical model considering the effect the distance between measuring points can be more effective in studying the blasting effect. The devised Sadoy's formula can be described by the following expression:

$$V = K(Q^{1/3}/L)^{a}(Q^{1/3}/H)^{\beta}. \tag{2}$$

in which, L is the horizontal distance between the measuring point and blasting point(m); H is the vertical distance between the measuring point and blasting point(m). The fact has been proved that the devised formula is more precise in the figure 3, in which the regression analysis by Sadoy's formula and devised formula have been contrasted with each other by its correspondence degree of the monitoring value of vibration velocity. Some testing data is show as table 1.

Table 1 Vibration test data of measuring points on the ground

Testing point	Q/ (Kg)	R/ (m)	Vertical velocity V_v/(cm/s)	Tangent velocity V_{HI}/(cm/s)	Radial velocity V_{HL}/(cm/s)
A	18.8	13.2	6.836	0.158	0.324
B	18.8	12.5	7.030	0.386	0.590
C	18.8	10.0	6.836	0.024	0.059
D	18.8	13.6	6.836	0.200	6.835
E	18.8	15.2	3.748	0.314	6.836
a	18.8	12.0	1.978	0.055	0.313
b	18.8	11.2	3.226	0.162	0.381
d	18.8	11.8	3.158	0.235	0.558
e	18.8	13.1	1.500	0.489	0.783

The radial velocity along the blasting centre is difficult to get because the rockcover is so thin, but the error of regression analysis for vertical velocity can be furthest reduced if only vicinal ground points are used. Based on the testing data above and the devised mathematical model, the relation between the ground particle maximal velocity is Vv=95(Q1/3/L)1.285 (Q1/3/H)0.321, and the attenuation of vertical velocity can be obtained for a certain blasting charge calculated by the relation. Contrasted to velocity calculated by theory formula as showed in figure.3, obviously the revised regression is more perfect than that of initial formula.

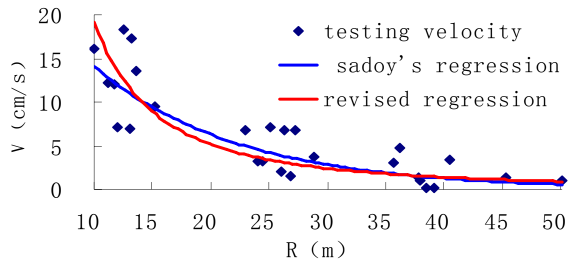

Figure 3 Comparison of theory computed value and monitoring value of vibration velocity

The blasting confinement is improved for the angle between blasting free face and cut hole is lange-angle contrasted to that of holes around cut hole, which leads to the strongest earthquake effect, but there is no linear relation between the blasting charge and its ground earthquake effect. The earthquake effect of other cut mode is weaker than the effect of less charge and other factors. So reducing the blasting charge of cut hole is the most important measure for the ground damage controlling.

3.2 Analysis on ground blasting vibration velocity

For the ground testing points, 37 groups of testing date has been obtained. As showed in Figure.2, the vertical velocity is the biggest for one point. The ground points velocities over the tunnel cross section has a symmetry distribution with the centre point just over blasting point, while the shallow characteristic is reflected by the velocity e along the tunnel axes with a gradual decrease, the tunnel structure of shallow section is changed by the blasting excavation which leads to the propagation varying path and the ground vibration velocity over excavated section is bigger than that of the unexcavated section. The vibration velocity difference for three times testing is showed as figure 4.

In test 1, the ground vibration velocities for excavated section is serious over the ones in criterion because the rockcover is only 3 meters and the maximal section explosive charge is 22.5kg. The concrete crack of rock slope at the entrance and ground soil relax are caused by the serious vibration. In test 2, the maximum section explosive charge of blasting cut hole is reduced to 18.8kg and the safety controlling for ground vibration is proved by the testing result that the maximal velocity is only 7 cm/s. the wavefront of shock wave with a very high pressure firstly arrive at the ground measuring point just over the blasting centre for its shortest distance, and the vibration velocity here suddenly reach a high level, but also have a very quickly attenuation by the damp. In the three times testing, the point B is always the maximal vertical velocity, which is just over the working face. The ground blasting vibration velocity of the excavation region is higher than that of the rock region.

3.3 Analysis on main vibration frequency for blasting earthquake

The earthquake wave of blasting excavation is composed by the wave of different frequency and energy. The structure has been effected by the wavelet at the same time, while the maximal energy of waveform for different frequency appear at different time, so the blasting damage is not deterred by the maximal energy and the safety controlling method with only maximal velocity is not proper. Based on the blasting test experience [10], there are two types of the cases for one safety project with dangerous frequency analysis: one is that the blasting earthquake frequency has a very even and dispersive distribution; the other is the blasting earthquake frequency which causes the project problem has a very narrow distribution which is still wider or near the resonance frequency of the structure itself, and this is also reflected by the frequency of obvious effect. The blasting earthquake wave has propagation characteristics of variety and diversity with different medium, especially for the concrete ling and ground soil of large-span shallow tunnel, their different frequency characteristics must be considered. The distribution of main vibration frequency for measuring points of different distance is showed as figure.5.

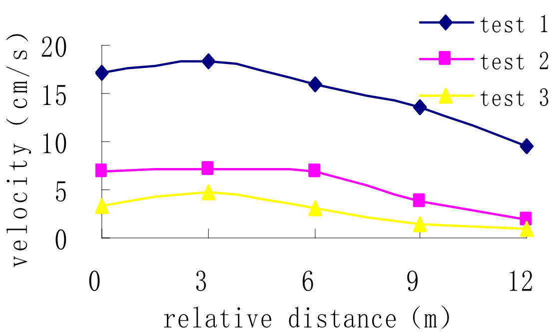

Figure 4 Characteristic curve of ground vibration velocity for larger-span shallow tunnel

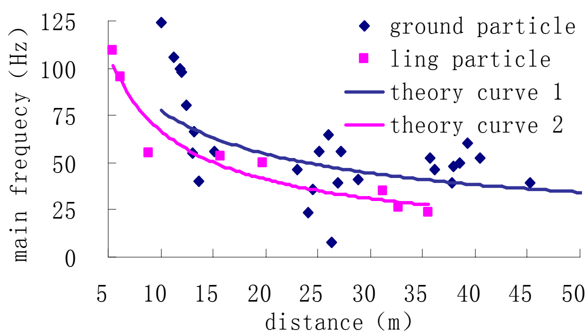

Figure 5 Distribution of main vibration frequency for measuring points of different distance

The blasting earthquake amplitude is gradually damped by the medium, especially for high-frequency vibration damp. Some conclusion can be obtained from figure.5, the high-frequency is not abundant; the low-frequency between 30Hz and 65Hz is the main distribution of vibration frequency, but this narrow distribution value is still higher than that of resonance frequency of concrete ling, so the crack of ling can not be happened. Generally speaking, the attenuation of earthquake vibration with high frequency is obvious by the medium of rock and soil, but litter low frequency can be filtered [11-12]. So the trend of frequency decreases with increasing distance is not obvious for there is certain rockcover on the ground, only opposite to the short distance. So the same reason for the concrete ling, its high frequency of blasting earthquake vibration is mostly filtered because there is a concrete layer about 26 centimetres thin between the surrounding rock and the ling surface. The main frequency of three-dimensional velocity all has a distribution around low value, but the narrow distribution range is different. The vibration frequency decrease with the increasing distance as a whole and this trend is different from that of the ground measuring points.

4 Blasting vibration reduction technology for large-span shallow tunnel

In order to keep the safety of large-span shallow tunnel, the main methods to reduce the blasting vibration are summarized as follows [13]: (1) Shorter excavation width and weaker blasting vibration by excavated mid-guiding hole; (2) Stratum pre-reinforcement of shallow section; (3) Strict controlling for blasting parameters; (4) Proper style on hole cut for vibration reduction; (5) Feedback of blasting effect monitoring; (6) Equipment of weaker blasting damage.

5 Conclusions

(1) The devised mathematical model for forecasting blasting vibration is more accurate than that of the initial Sadoy’s formula, the vertical distance between the measuring point and the blasting point must be considered.

(2) The dominating vibration frequency of the mass point at surface and concrete ling in the tunnel mostly focuses on low frequency at the range of 30Hz to 65Hz, especially at the entrance because the high frequency of concrete ling is mostly absorbed.

(3) The decreasing tendency of dominating vibration frequency at surface mass point is not obvious when the distance increases because some blasting earthquake wave is absorbed by the earth's surface covered with soil of certain thickness, but the vibration frequency of concrete ling decrease with the increasing distance as a whole.

(4) The ground blasting vibration velocity of the excavation region is higher than that of the rock region, so the ground blasting vibration velocity at the top of the excavation region should be less than that of blasting security control in the larger-span shallow tunnel.

(5) According to the blasting criterion, taking the ground and concrete ling as a monitoring goal, the blasting earthquake effect for the larger-span shallow section has been well tested in the excavation of the Miaoya diverging tunnel. Based on the regression analysis of testing data, the blasting parameters have been optimized and some measures have been adopted to reduce the blasting vibration damage, such as shorter excavation width and weaker blasting vibration by excavating mid-guiding holes, stratum pre-reinforcement, strict controlling for blasting parameters, the proper style of hole cut for vibration reduction, feedback of blasting effect monitoring, equipment of weaker blasting damage, etc.

References

1. Zhu, C.Y., Yu, S.C. and Yi, C.P. Analysis on Factors Affecting Stress Distribution in Rock Wall Under Blasting Loads, Rock and Soil Mechanics, 2001, 22. 21-25.
2. Zhang, L. and Lin, C.M. Study about Soil Slope Dynamic Stability Due to Blasting Vibration, Rock and Soil Mechanics, 2005, 26. 1499-1501.
3. Tan, Z.S., Yang, X.L. and Wang, M.S. Effect on Blasting Double Line Tunnel An Existing Tunnel, Chinese Journal of Rock Mechanics and Engineering, 2003. 22. 281-285.
4. Li, L.P., Li S.C. and Zhang, Q.S. ce al. In-situ Testing Study on Shallow-buried Large-span Tunnel, Chinese Journal of Rock Mechanics and Engineering, 2007. 26. 3565-3571.
5. Zhang, J.C., Cao, X.J. and Zhang, S.Y. ce al. Experimental Study on Vibration Effects of Ground Due to Shallow Tunnel Blasting, Chinese Journal of Rock Mechanics and Engineering, 2005, 24. 4158-4163.
6. Li, Y.M. and Ni, Z.F. Ground Vibration Characteristics of Excavation Blasting for Underground Engineering, Chinese Journal of Rock Mechanics and Engineering, 1997, 16. 274-278.
7. Chen, Q., Wang, H.T. and Hu, G.Z. ce al. Monitoring and Controlling Technology for Blasting Vibration Induced by Tunnel Excavation, Rock and Soil Mechanics, 2005, 26. 964-967.
8. Xie, J.M., Xia, Y.Y. and Li, X.P. Study on Blasting Vibration Control of Creep Mass Slope of Longtan Hydropower stating, Chinese Journal of Rock Mechanics and Engineering, 2003, 22. 1929-1930.
9. Yan, Z.X., Wu, D.L. and Wang, Y. ce al: The Study of Blast Vibration Effect and Safety, Rock and Soil Mechanics, 2004, 23. 201-203.
10. Zhao, J.Q., Li, T.C. and Cui, J.H. Seimic Sprectra Characteristics of Tunnel Excavation Balsting, Blasting, 2005, 22. 110-115.
11. Sharma, J. Blasting Induced Vibration Monitoring, The Indian Mining & Engineering Journal, 1998, 37. 36-41.
12. Siskind, E.D. Frequency Analysis and Use of Response Spectra for Blast Vibration Assessments in Mining, Proceedings of the 22nd Annual Conference on Explosives and Blasting Technique (Volume II). New Jersey USA, 1996, February. 176-183.
13. Li, L.P., Li, S.C. and Zhang, Q.S. ce al. Analysis of Dynamic Response on Blasting Excavation of Close-spaced Tunnel. Journal of Highway and Transportation Research and Development, 2008. 25. 100-106.

RaSiM 7(2009): Controlling Seismic Hazard and
Sustainable Development of Deep Mines,
C.A. Tang(ed), Rinton Press, 581-586

NUMERICAL SIMULATION OF FAILURE PROCESS AROUND CIRCULAR OPENINGS IN GRANITE ROCK

QING-LEI YU

Center for Rock Instability and Seismicity Research, Box 138, Northeastern University

Shenyang, 110004, P.R. China

CHUN-AN TANG

Center for Rock Instability and Seismicity Research, Dalian University of Technology

Dalian, 116024, P.R. China

TIAN-HONG YANG

Center for Rock Instability and Seismicity Research, Box 138, Northeastern University

Shenyang, 110004, P.R. China

Digital image processing-based Rock Failure Process Analysis code, abbreviated as RFPA^{2D}-DIP, is introduced to simulate progressive failure of circular openings in granite rock. The proposed method incorporates digital image processing technologies and vector transformation methods. The surface image of rock can be directly imported into the code. First, the actual heterogeneity of rock is extracted from the image by DIP function of RFPA. Second, the image characterized meso-structure is automatically transformed into grid data of finite element method. The mesomaterials, composing of rock components, such as mineral grains and flaws, are classified into different material groups according to their colour characteristic and assigned with their own mechanical properties. In this way, the influence of actual mesostructure can be taken into account during the analysis of mechanical response and failure process. Then an image of granite is taken as an example to demonstrate the proposed method. The progressive failure around circular excavation in granite rock, involving initiation, propagation and coalescence of fractures, is simulated by a factitious increasing of in situ stresses. The proposed code is validated by comparing simulated fracturing pattern with those reported in previous studies. Finally, failure mechanisms are identified for different lateral pressure coefficients. The results show that the heterogeneity of rock can play an important role in the failure behaviours of rock under external loading.

1 Introduction

In mining engineering, different types of collapse due to excavation-induced progressive fracturing are observed around extraction openings [1]. Fracture may manifest itself in various degrees of intensity, ranging from harmless spalling at the excavation perimeter to the explosive violence of rock bursts. Especially in deep mines with high in-situ stress, if induced stress around mine openings exceeds the strength of hard rock mass, the phenomenon of rock burst may occur to damage surrounding mine openings and reinforcement system.

Many scholars have investigated the complex fracturing mechanism by physical model tests. In earlier studies [2,3,4,5], the existence of primary tensile fracture, compressional fracture and secondary or remote fracture around cavities in rock has been demonstrated through physical model tests with circular opening under uniaxial and biaxial loading conditions. However, it must be realized that such experimental approaches, in spite of their great importance, cannot be effectively used to predict future behaviour around underground tunnels and understand fracturing mechanism and evolution process. In more recent developments, micromechanical models have been developed to simulate the instability or loss of integrity of a tunnel or borehole. These models have improved the understanding of the mechanisms and consequences of fracture initiation and propagation [6]. In micromechanical model, the rock microstructures have to be established as the basis of numerical analysis. However, in most of these models, virtual microstructures of rock are generated from statistical tools or random methods numerically due to lacking effective tool to describe heterogeneity of rock. In previous version of RFPA^{2D}, a two-dimensional finite element code that can simulate the fracture and failure process of quasi-brittle materials such as rock, heterogeneity of numerical model is also introduced by defining an element stiffness/strength distribution via the Weibull statistical distribution [7,8]. But it seems that there are few publications available in the relevant literature on the extent and accuracy of the virtual inhomogeneity and microstructure generated from the statistical equivalence to represent the actual inhomogeneity and microstructure of a real rock [9].

By reviewing previous literatures, it is recognized that it is significant to take into account the rock inhomogeneity and microstructure in investigating rock behaviours and analyzing fracturing mechanism. The stability of excavations in rock is also influenced by both rock structure and the stress regime. This has a major motivation in working towards a more comprehensive strategy for investigating the fracture process around underground tunnel or cavities. So in this paper, digital image processing (DIP) technologies are used to extract the microstructures from rock image, which is imported into RFPA code. The aim is to take into account the actual heterogeneity in simulating the fracturing process around circular tunnel in granite.

2 Models of circular opening

2.1 Heterogeneity characterization by DIP

DIP is the term applied to convert an image into a digital form and apply mathematical algorithms to extract information from the image for a certain purpose. Recently, it is widely used in geotechnical engineering, civil engineering and rock engineering. Yue and co-researchers [9] have done lots of work at this. They developed a digital image processing-based finite element method to investigate the effect of microstructure on stress distribution. Digital image of rock, as a resource with a great deal of information, can reflect its microstructure and heterogeneity. With the advent of advanced material characterization techniques and processes, and computational resources, it has become possible to create high-fidelity 2D and 3D material reconstructions that can be accommodated in computational models.

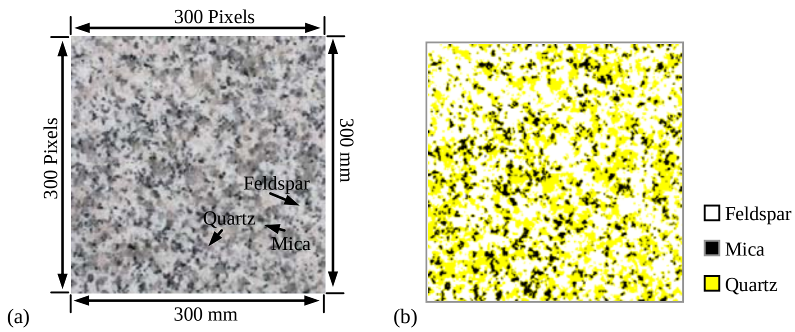

Figure 1 Digital image of granite rock and its processing: (a) an image of granite; (b) image characterized mesostructure

In RFPA-DIP code, the image processed is the colour image and general-purpose DIP technologies (e.g. image smoothing, image segment, edge detection) are employed to extract microstructure from colour image of rock. Figure 1(a) presents a digital image of granite rock obtained by digital camera. Its size is 300×300 pixels and the actual size is 300mm×300mm. Granite usually consists of three minerals: mica, feldspar and quartz. In this image, the dark gray is mica, the light white feldspar and the colour between the two is thought to be quartz mineral, as shown in figure 1(a). The key operation of DIP is to determine the segment threshold. Due to the colour characteristic of the image, the HSI colour space is chose to process the image, HSI standing for hue, saturation and intensity (brightness). According to the *I* variation curve along some scanning ling specified in horizontal axis, two thresholds are determined, T_1 = 100 and T_2 = 170. And then the image segment can be completed by the two thresholds. The result is shown in figure 1(b). By comparing with the original image in figure 1(a), one can observe that the individual minerals have been automatically detected correctly and successfully.

2.2 Numerical model

In RFPA code, at each loading increment, stress equations in elements is solved by FEM, so the image characterized microstructure must be transformed into mesh data. Since a digital image consists of a rectangle array of pixels. A pixel can be considered as a square element of FEM mesh. Its four nodes coordinates can be calculated by the ratio of pixel size to real size and the pixel coordinates of an image [10]. Figure 2(a) shows the transformation from the pixel to mesh data. The process is simple and avoids of complicated and time-consuming mesh-generation steps.

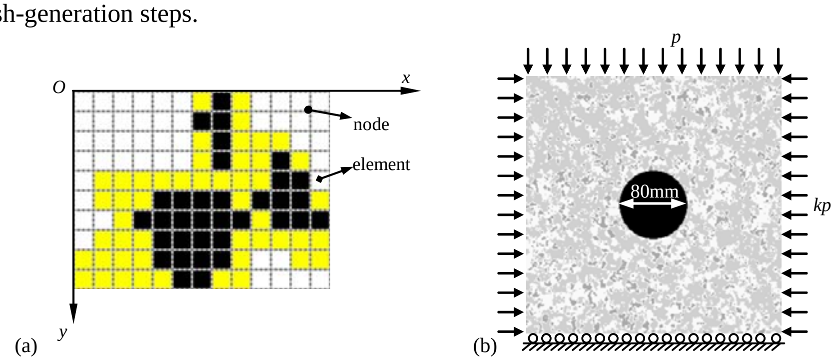

Figure 2 digital image-based numerical model: (a) an example of transformation from the image characterized mesotructure to FEM grid; (b) Numerical model of granite with a circular opening and loading conditions.

The numerical model of granite for simulating progressive failure around circular openings and loading conditions are shown in figure 2(b). Applied boundary stress in the vertical and horizontal directions are denoted as p and kp, respectively, where k is usually called lateral pressure coefficient. The value of k is separately assigned with 0, 0.2, 0.5, 1 and 2 to investigate the influence of variable k on the failure process around a circular opening. The diameter of the circular opening is 80mm, approximately 1/4 of the length of the whole model. According to the method of vector transformation, the model is composed of 300×300 elements. The pressure p in vertical direction is applied step by step to simulate the effect of high in situ stress regime, fixed at 2.5MPa/step, while zero vertical displacement is imposed at the bottom of the model domain. The analyses presented here are performed under plane strain conditions. The mechanical properties of each mineral are listed in Table 1.

Table 1 Mechanical properties of individual minerals

Mineral	Young's modulus/GPa	Uniaxial compressive strength /MPa	Poisson's ratio	Ratio of compressive to tensile
Quartz	96	373	0.08	15
Feldspar	67	172	0.27	12
Mica	40	90	0.25	10

3 Numerical results and discussion

Model results are presented in figure 3(a)-(c), including the AE distribution, maximum shear stress distribution and failure patterns around circular opening. In this simulation, the specimen is under unaxial compression in vertical direction, that is, $k = 0$. In the figure, the notation Step37-6 indicates that this is at the 6th iterative step of the 37th loading step. The AE distribution is shown in figure 3(a), where all the damaged elements are denoted by different colours. Red and white is for tensile and shear damage at current step, respectively, and the black is for being damaged in all preceding step. The maximum shear stress distribution is shown in figure 3(b), where the brightness indicates the magnitude of maximum shear stress. Fracturing process in granite is visually shown in figure 3(c).

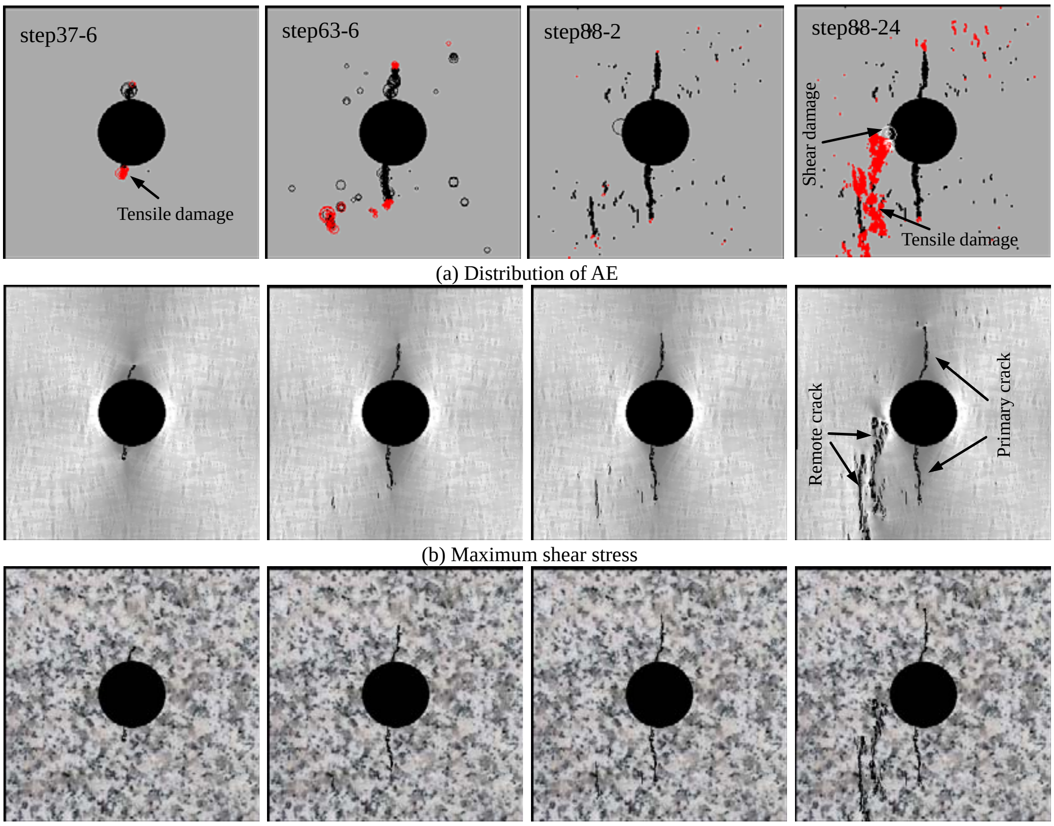

(a) Distribution of AE

(b) Maximum shear stress

(c) Failure process

Figure 3 Failure patterns of granite rock around circular openings under uniaxial compression.

At Step37, notable tensile damage of elements is observed both in the roof and the floor, as shown at Step37-6 in figure 3(a) by red colour. Subsequently, more elements in the roof and floor of the circular opening undergo damage in tensile mode, which eventually leads to the formation of primary crack in the roof and floor (as shown at Step63-6). At Step63, obvious local tensile damage is observed at the lower left of the crack tip in the floor, which is the initiation of remote crack. With external load increasing, primary crack and remote crack both propagate approximately in vertical direction. Another remote crack is also formed at Step88-24, which propagates to the perimeter of circular opening. From the distribution of AE as shown in figure 3(a), it can be inferred that remote crack is mainly caused by tensile damage of many elements and only at final stage, shear modes of damage are observed at the left side of circular opening, denoted by white colour at Step 88-24. The primary crack, remote crack and shear damage zone are presented at Step88-24 in figure 3(b). But in the roof of the circular opening, remote crack is not obviously observed, the reason may be that stress is released during the propagation of primary crack and remote crack and the accumulated energy produced by external load is not enough to drive the initiated crack in the roof to propagate. In this simulation, the fracturing process and final failure patterns correspond closely obtained in physical experiments and other numerical modelling [3]. This correspondence with the physical experiments provides a strong support for the fracture and damage models implemented in RFPA^{2D}-DIP.

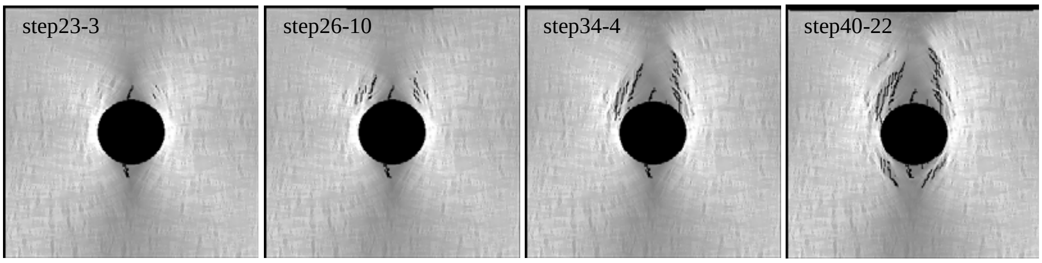

(a) *k* = 0.2

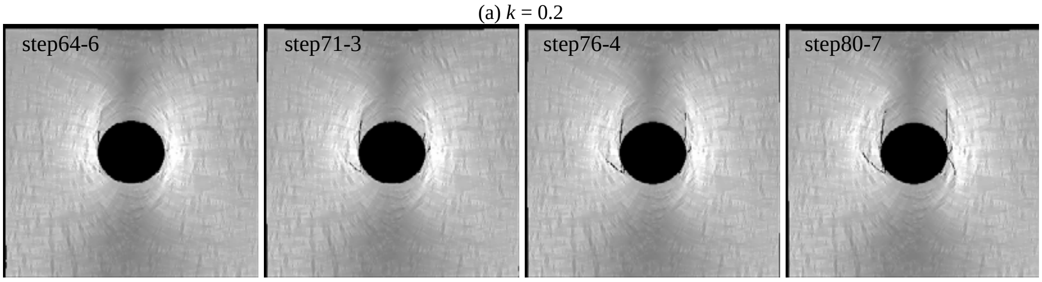

(b) *k* = 0.5

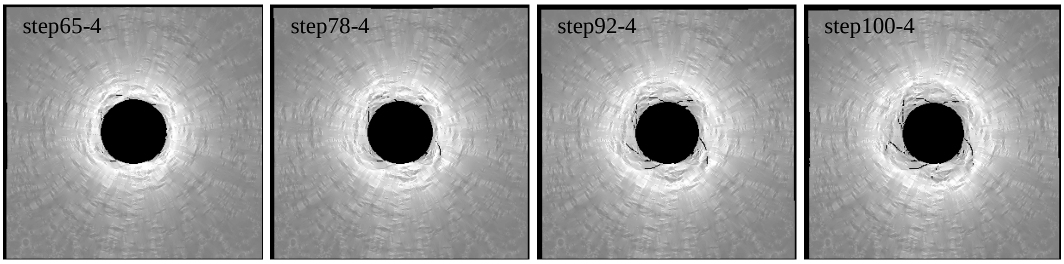

(c) *k* = 1.0

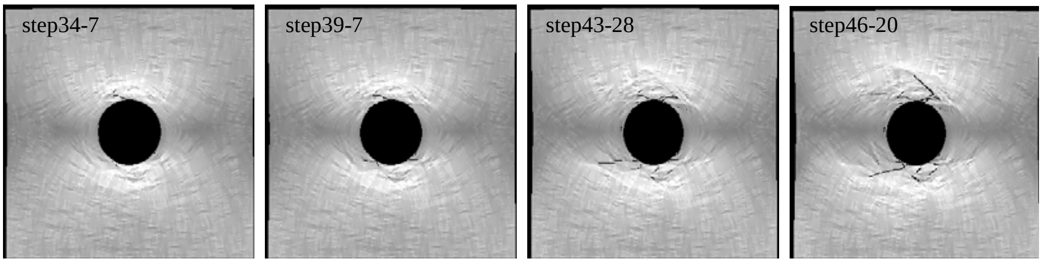

(d) *k* = 2.0

Figure 4 Failure patterns of granite around circular openings for different lateral pressure coefficient. The applied pressure in the vertical direction is fixed at 2.5MPa/step. For each lateral pressure coefficient, the maximum shear stress distributions at four typical steps are given.

In the ensuing, the effects of lateral pressure coefficient *k* on the fracturing process around a circular opening are discussed. A range of magnitude of *k* from 0.2 to 2 was applied to the circular opening model. The results of numerical simulation performed under different lateral pressure coefficient *k* are presented in figure 4. Here, only maximum shear stress distribution at four typical steps is given. When *k* is equal to 0.2, primary crack and four remote cracks are observed both in the roof and floor. Shear damage zone also appears under the loading condition according to the distributions of AE, which are not given here for limited length of paper. The location of starting point for the remote fracture is closer to the perimeter of the circular opening than that under uniaxial compression and the length of primary crack are quite smaller (as shown in figure 4(a)). From the evolution of maximum shear stress during fracturing process as shown in figure 4(a), it is noted that when the primary crack propagates a small distance, the remote cracks at both sides of primary crack initiate and propagate, which restrain the propagation of primary crack during the subsequent loading steps.

According to the elastic theory, when k is larger than 0.3, tensile stress zone around circular opening doesn't exist. So with k increasing, remote crack is not observed and only shear cracks at both sides of the circular opening are produced (k = 0.5). For the case of a hydrostatic stress field (k = 1.0), a uniform boundary stress exists around the opening. However, because of the heterogeneity taken into account in the rock, shear damage occurs at the perimeter of the opening (at Step65-4 in figure 4(c)), and plastic zone is obviously produced. Figure 4(d) presents the results of the case of k equal to 2.0. On the assumption that the rock is a homogeneous medium, the stress distribution in horizontal direction (k = 2.0) are identical with that (k = 0.5) in vertical direction, which means that failure pattern must be the same. But by comparing the numerical results (figure 4(d)) with the results (figure 4(b)), it is found that the fracturing patterns are not the same, because the actual heterogeneity plays an important role during the progressive failure process. The interaction of load with heterogeneity is distinctly different when loading in both directions.

4 Conclusion

This paper has presented a digital image processing-based numerical method for simulating the rock failure process, RFPA^{2D}-DIP. Then the method was applied to simulate the progressive failure process around a circular opening in granite rock under uniaxial and biaxial loading compressions. Based on the results from the simulations, the following conclusions are drawn: (1) For the lateral pressure coefficient less than 0.2, primary tensile crack, remote tensile crack and shear crack develop. When the lateral pressure coefficient exceeds 0.5, primary tensile crack and remote crack cannot be observed, and the shear damage zone or shear cracks are produced. (2) Heterogeneity plays an import role in the fracturing behaviours of rock, and the proposed numerical method can take into account the interaction of load with heterogeneity, which can offer an efficient approach to further investigate the mechanical response and failure mechanism of rock.

Acknowledgements

This work presented in this paper has been supported by the National Natural Science Foundation (Grant No. 10872046, 50874024 and 50674025) of China and National Basic Research Program of China (Grant No.2007CB209405). The authors are grateful for this support.

Reference

1. Diederichs, M.S., Coulson, A., Falmagne, V., Rizkalla, M. and Simser, B. Proceedings of the 5th North American Rock Mechanics Symposium and the 17th Tunnelling Association of Canada Conference, 2002,1325-1332.
2. Hoek, E. Fourth International Conference on Strata Control and Rock Mechanics, 1964, 334-348.
3. Martin, C.D., Read, R.S.and Martino, J.B. Int. J. Rock. Mech. Min. Sci., 1997. 34 (7), 1065-1073.
4. Lajtai, E.Z. Tectonophysics, 1971, 11. 129-156.
5. Gay, N. C. Int. J. Rock. Mech. Min. Sci., 1976, 9. 231-243.
6. Blair, S.C. and Cook, N.G.W. Int. J. Rock. Mech. Min. Sci., 1998, (35). 837-848.
7. Tang, C.A. Int. J. Rock. Mech. Min. Sci., 1997, (34). 249-261.
8. Tang, C.A. Engineering Geology, 1998, (49). 207-214.
9. Yue, Z.Q., Chen, S. and Tham, L.G. Computers and Geotechnics, 2003, 30. 375-397.
10. Yu, Q.L., Tang, C.A. and Tang, S.B. Chinese Journal of Rock Mechanics and Enigeering, 2007, 26. 551-559.

RaSiM 7(2009): Controlling Seismic Hazard and Sustainable Development of Deep Mines, C.A. Tang(ed), Rinton Press, 587-592

STUDY OF MICROSEISM INDUCED BY TECTONIC STRESS AND ITS DAMAGE, PROTECTION OF UNDERGROUND ENGINEERING

GUANG-MING YU

Qingdao Technological University, Qingdao, 266033, P.R. China

YONG-ZHAN PAN

Qingdao Technological University, Qingdao, 266033, P.R. China

Henan University of Science and Technology, Luoyang,471003, P.R. China

GUO-YAN WANG

Qingdao Technological University, Qingdao, 266033, P.R. China

Liaoning Technical University, Fuxin, 123000, P.R. China

WEI-HONG HUANG, XUE-MIN WU

Qingdao Technological University, Qingdao, 266033, P.R. China

With drift movement, plate movement and seafloor spreading happening continuously in the earth’s crust, rock masses in the earth’s crust deform and accumulate large strain energy. Release space is provided for the strain energy - unloading because of excavation of all kinds of underground engineering structures, which can generate many dynamic phenomena such as microseismicity, impact pressure, rock burst and so on. Release of strain energy - unloading induced by underground excavation and the phenomenon of microseismicity is studied and damage characteristics of underground structures are described with an example in this paper. Damage of underground structures is analyzed and protection measures are proposed based on the geodynamic zoning theory, propsed by И.М.Петухов and И.М.Батугина.

1 Introduction

A long-term geologic history shows that drift movement [1], plate movement, and seafloor spreading of the earth's crust occur constantly; which is generalized by the term crustal movement. It seems that the movement is connected to human intervention. In fact, this movement has caused disruption in humans’ lives. On the one hand, disappearance, regeneration and the activity of large or small faulst in the crust are caused by crustal movement, while active faults will cause damage to underground and ground facilities [2, 3]. For example, four collieries in Russia are located on active faults, therefore, the shafts were exposed to twist deformation conditions and were damaged badly and stop production was forced to stop. In another example, a rail accident happened at a nearby railway station in Russia on 30 May 1985 because of fault zone activity [4]. On the other hand, crustal movement produces rock deformation and has accumulated amount of strain energy. Release space is provided for these strain energys and is unloaded because of the excavation of all kinds of underground engineering [5-9]. This has damaged underground engineering pratices and has generated lots of dynamic phenomena such as rock burst, microseism, impact pressure and so on. For example, floor rupture and serious mine seismicity induced by the release of strain energy caused damage of underground openings and ground buildings after underground mining at the Taiji coal mine in the Beipiao mining area. All of the analysis showed that geological stress is an essential force arousing deformation and damage of surrounding rock and support, which provides a necessary condition for classifying attributes of rock mechanics and a precondition for scientific analysis and quantitative calculation of surrounding rock stability. Therefore, in-situ stress fields should be studied sufficiently and evaluated quantitatively when considering the distribution and assumption of ground stress during mining production and underground engineering construction

2 A case study of Geotechnical Engineering damage induced by tectonic stress

Taiji coal mine in Beipiao mining area is a representative model for tectonic stress damage. Ground and underground engineering were damaged by constant mine seimicity which was caused by tectonic stress after mining from 1971.For example, dislocation of southside of rock tunnel at -400m level in west second area (figure 1) and dislocation of shaft well along the fault F6(figure 2). At that time, Taiji coal mine was located in tectonic stress field which was an approximately horizontal compressive stress field with the direction nearly to the east, where the maximum compressive stress is 53500kPa with the direction of N84E because of being extruded by the horizontal regional stress in the direction to the east. The ground and underground engineering was damaged owing to stress equilibrium is destroyed which was induced that release space was provided for tectonic stress because of excavation of underground engineering.

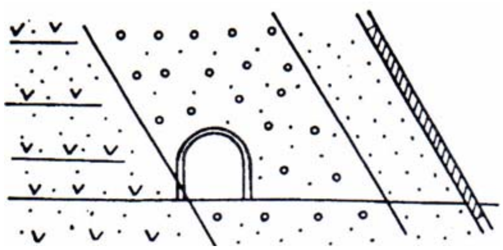

Figure1 Dislocation of the southside of tunnel

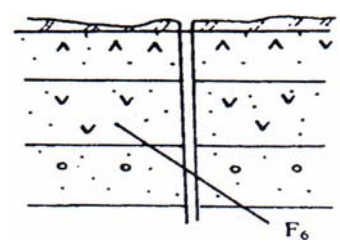

Figure2 Dislocation of shaft along the fault

3 Protection way of tectonic stress----- geodynamic zoning theory[2]

Interaction of faults produced tectonic stress. It is necessary to ascertain the position of fault especially hidden fault and judge activity of fault as well as analyze stress characteristics of fault block rock mass divided by fault for the sake of avoiding active fault zone as possible and taking reinforcement measures in advance.

3.1 Theory basis of geodynamic zoning

Damage and grade of geological structure in the crust were determined according to geodynamic zoning on the theoretical basis of geodynamics, on the premise of interaction of geologic structure block affected by dynamics phenomena and from the whole to part as principles. Based on the results, it provides a foundation for underground engineering protection and mining production according to finding out active geological structure and evaluating stress state as well as predicting temporal and spatial variation of geologic structure block and nearby rock mass stress under underground excavation activity.

3.2 The division of geological structure fault blocks

Generally, formation of contemporary landform and physiognomy is mainly caused by tectonic movement while wind and rain erosion as the secondary factor. So observation and analysis method of landform and physiognomy is used to division of geological fault block considering of all kinds of erosion. It is suitable to observe following principles. Firstly, the highest part should be the least part affected by erosion. Secondly, boundary of fault block is determined according to following symbol, such as Line district of valley or slope bottom, geniculation of valley of continuous distribution, chain lake, tectonic terrace, contour line and so on.

Fault block as the rage of mining area is grade Ⅳ, so grade Ⅴ meets the requirement. The fault blocks at all levels are divided in topographic map according to the scope of corresponding elevation difference. The scope of the minimum elevation difference is determined by next formula.

$$\Delta hmin = 0.1(Hmax - Hmin) \qquad (1)$$

Where *Hmax* represents the maximum absolute elevation, and *Hmin* represents the minimum absolute elevation in topographic map.

Table 1 Range of elevation difference of fault block at different grade

Grade of fault block	I	II	III	Ⅳ	Ⅴ
Topographic Map scale	1:25000000	1:1000000	1：200000 or 1:100000	1:25000	1:20000, 1:10000 or 1:5000
Minimum Elevation Difference(m)	400～500	200～300	100	50	10～25

3.3 Assessment of fault activity in mining area

Several criterions are adopted for assessment potential activity of fault by using of geodynamic zoning, such as mutual dislocation fall of fault block, Shear Stress on the fracture surface, the location of principal axis of stress and data of seismic activity. Firstly it Scores the activity of fault according to every criterion in table 2, then it determines the grade of fault activity according to the total score in table 3.

Table 2 Grade of the fault activity

Types of criterion	Features of fault	scoring criteria
Criterion H	No finding, not parallel to boundary of any fault block	Attention: add 1 in sporadic fault development area
	range＜ Δ hmin	1
	range≥ Δ hmin or parallel to any boundary of the fault block	1
	range≥ Δ hmin	3
Criterion τ	perpendicular to principal axis	0
	acute angle to τ max	1
	consistent with τ max	2
Criterion σ	perpendicular to σ max	Attention: Correction according to form of the fracture surface
	middle (Intermediate)	1
	consistent with σ max	2
Criterion H	Not active for seismic activity	0
	Slight active for seismic activity	1
	active for seismic activity	2

Table 3 Grade of the fault activity

Grade of activity	I	II	III
Σ =H+ τ + σ +S	$\Sigma \geq 7$	$5 \leq \Sigma < 6$	$\Sigma < 5$

3.4 Stress calculation of geologic fault block

Modern geological tectonic framework as calculation model has been constructed according to interaction of fault block and assessment results of fault activity. Based on this calculation model, tectonic stress distribution was calculated in different depth and level by using of finite element program of tectonic stress of fault block (Software of TPS-H) or boundary element program of it(Software of BLOCK)

3.5 Location and protection of geotechnical engineering

It is necessary for reasonably arrangement of geotechnical engineering. For example, avoiding location in high stress area and active fault zone, linear engineering such as tunnel, railway, highway, pipeline an so on should avoid construction in the opposite direction of principal stress according to the results of geodynamic zoning.

4 Application status of geodynamic zoning in our country

Geodynamic zoning theory was introduced to china since 1993, three of significant scientific research projects have been studied and obvious benefit has been obtained.

4.1 Geodynamic zoning in Beipiao mining area[10]

Dynamic phenomena such as coal and gas outburst, mine seismicity, rock burst occurred frequently and the safety of the coal production was menaced seriously in Beipiao mining area, therefore, Dongmei company were cooperated with Geomechanics Research Institute in Former USSR to study on geodynamic zoning in Beipiao mining area. The results showed that a forming discontinuous fault with grade Ⅰ in the direction of N-W through Beipaio mining area named Beipiao fault and others fault had been ascertained exactly. At the same time, activities of the faults were assessed and fault blocks with grade Ⅳ and Ⅴ were divided. Then the tectonic stress region were ascertained with the maximum principal stress in seven level more than 60MP, of which is compression in direction of N25° E.

4.2 Geodynamic zoning in Jilin oilfield

Based on geodynamic zoning in Jilin oilfield, exploitation area in oilfield and active faults in exploration area was determined accurately. Fault block structure of rock mass was found out. Permeability and stress state of oil reservoir was evaluated. The location of mining drilling was arranged reasonably. Well location for increasing yield with cutting seam in exploitation area was appointed

4.3 Study on laws of mining subsidence affected by ground stress of Taiji colliery

Based on geodynamic zoning in Taiji coal mine, the maximum horizontal compression in the direction of E-W was obtained, which was 53500kPa. The features of mining laws affected by horizontal compression was observed, such as enlargement strata movement scope, tremendous movement of the floor of mining area, occurrence of mine seismicity and so on.

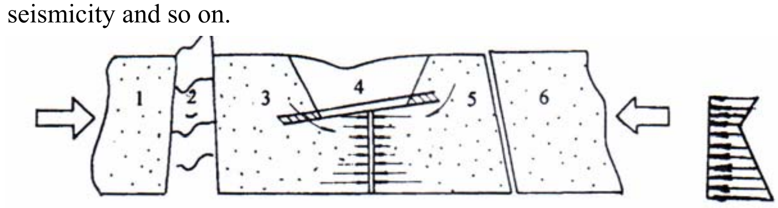

Figure3 Transfer of tectonic stress after mining

Laws of the surface movement affected by ground stress were monitored and calculated, compared with measured data.

5 Application prospect of geodynamic zoning

The basic economic activities made by human in the surface have arrived into Lithosphere about 10-15km, which will destroy the stability of the earth and re-distribute the ground stress to maintain a new balance. So it must have a wide range of application for geodynamic zoning of the ground analysis.

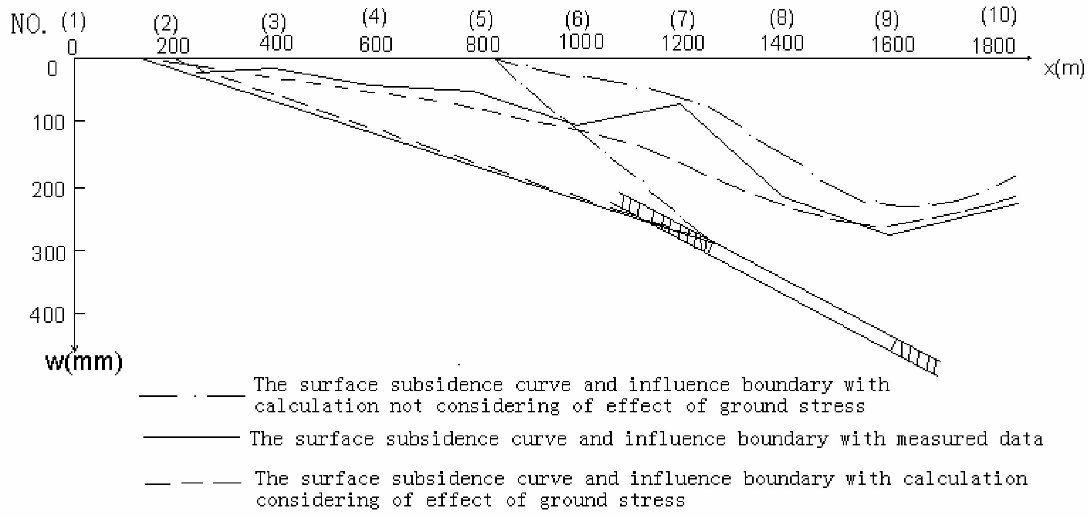

Figure4 Calculation and monitoring result of the surface subsidence

5.1 Application in exploration and development of petroleum and natural gas

According to the results of geodynamic zoning, occurrence location of petroleum and natural gas can be found out and permeability of producing zone can be assessed. At the same time, location of the drillings for increasing output can be arranged rational.

5.2 Application in mining

Based on geodynamic zoning, distribution state of the ground stress in mining area may be accurate evaluated, meanwhile, the location of active fault zone may be determined accurately. Then mineral may be exploited, thus prevents the dynamic phenomena such as rock burst, mine seism, impact pressure, gas Outburst and so on.

5.3 Application in construction of building and structure

Based on geodynamic zoning, the engineering geological conditions in construction area can be evaluated, and the location of active fault zone can be determined. Preventive measures can be taken for protection building and structure.

5.4 Application in forestry and agriculture

Many results may be determined such as the structure of the fault block, formation time and grade of fault, interaction of the fault block and its influence to soil properties. Optimum scheme of land use may be recommend by using of geodynamic zoning

5.5 Application in the other fields

It can analyze the mechanism and consequences of the earthquake and the development of aftershocks. In addition, it has a wide application such as weather forecast, route determination, ecological analysis and control of rock mass etc using geodynamic zoning.

Acknowledgements:

The authors thanks for sustain from key Natural Science Fund of China (No: 50434020); the National Natural Science Fund of China (No: 50874064； 50804026) and Natural Science Fund of Shandong Province.

References

1. An, O. Tectonic Stress Field. Earthquake Publishing House in Beijing, 1992.
2. Song, J.C., Liu, D.Y. and Wang, E.D. etc. Cause and Mechanism of Mine's Fault-Type Earthquake and Its Forecast. Mining Engineering, 2007, 5(3).16-18.
3. Ouyang, Z.H., Yao, G.H. and Xu, M.G. etc. Investigation Into Mining Tremor Mechanism in Puqing Iron Mine. Journal of Wuhan University of Science and Technology (Natural Science Edition), 2008, 31(2). 155-158.
4. И.М.Петухов, И.М.Батугина. Mechanic Computation Methods of Impact Pressure. Moscow, 1991.
5. Ha, Q.L. Loading Rock Mechanics and Unloading Rock Mechanics. Chinese Journal of Geotechnical Engineering, 1998, 20(1). 114.
6. Yu, G.M. Nonlinear Theory and Practical Guidance of Mining Subsidence. Coal Industry Publishing House, 1998.
7. Yu, G.M. and Su, Z.J. The Study of Measuring Method about and Strain in the Vertical Shafts and Surrounding Rocks. Journal of Coal Science &Engineering(China), 1998, (2).
8. Yu, G.M. et al. Experiment of Mining Subsidence and Damage Analysis for Joint Rockmass. Chinese Journal of Mechanics and Engineering, 1998, 17(1). 16-23.
9. Li, Tie., Cai M.F. and Cai, M. A Rockburst Energy Release Model and Energy Release Spectrum for Coalmines in Layered Grounds, 2006, Sup(2). 3679-3686.
10. Duan, K.X. Geodynamic Zoning in Beipiao Mining Area. Journal of China Coal Society, 1995, (4). 1-4.

RaSiM 7(2009): Controlling Seismic Hazard and Sustainable Development of Deep Mines, C.A. Tang(ed), Rinton Press, 593-598

REGRESSION ANALYSIS OF IN-SITU STRESS FIELD IN UNDERGROUND POWERHOUSE AREA OF ONE HYDROPOWER STATION

WEN-DONG YANG, QIANG-YONG ZHANG, XIU-YONG YU, GANG WANG and YUAN LI

Geotechnical and Structural Engineering Research Center, Shandong University,

Jinan, 250061, P.R. China

Based on the measured data of in-situ stress and engineering geological conditions, three-dimensional regression calculating model of the in-situ stress in an underground powerhouse zone is established. It takes into account the actual stratigraphic distribution as well as the fault. The optimal regression coefficient of in-situ stress is obtained through multiple regression method and three-dimensional numerical calculation. The initial in-situ stress in underground powerhouse zone is regressed accurately. The calculated result shows the magnitude and orientation of the principle stress obtained from regression analysis is closed to the measured data. It provides a rational three-dimensional initial in-situ stress field for excavating simulation and analysis of long-term stability of the underground powerhouse. Furthermore, the orientation of maximum principal stress parallels to the powerhouse axes. This result also validates that the design is rational in underground zone of the hydropower station.

1 Introduction

The initial in-situ stress field of rock mass is an important factor of concern in geotechnical engineering design and construction; the reliability and security of which will be influenced by the initial in-situ stress field directly. Therefore, how to reflect the initial in-situ stress accurately is an important task faced in geotechnical project.

Xiao Ming and Liu Zhiming provided regression analysis of initial in-situ stress for thedam region of the Jinping II hydropower station using three-dimensional finite element, and they proposed a three-dimensional stress function fitting method [1]. Xie Hongqiang applied the grey control system theory and finite element method to analyze the initial in-situ stress of the dam region of the Jinping Hydropower Station, and the optimum regression coefficient was derived [2]. Hu Bin discussed possible factors affecting the initial in-situ stress field, and obtained the distribution tendency of initial in-situ stress field of left bank high slope region through multiple regression analysis. A rational three-dimensional initial in-situ stress field for excavating simulation and analysis of long-term stability of the left bank high slope at Longtan hydropower station is provided [3]. Jiang Quan presented a new nonlinear initial in-situ stress back analysis method, which integrates the ground abrasion simulation, elastoplastic calculation and neural network inversion. The method takes the constitution order process into account to some extent by elastoplastic calculation, and it simulates the ground abrasion process by surface excavation [4]. Jia Shanpo proposed a methodology of inversion analysis combining the Nelder-Mead algorithm and finite element method, in which the finite element program is embedded as a module in the Nelder-Mead algorithm. Also, in-situ stress field of the underground powerhouse area of Dagangshan Hydropower Station is inversed [5].

Based on the terrain feature of the underground powerhouse, the effect of the stratigraphic distribution and fault fracture zone is taken into consideration. The initial in-situ stress of rock mass is regressed with three-dimensional finite difference method and regression analysis, so the distribution rule of in-situ stress field in underground powerhouse is obtained.

2 Project Descriptions

The hydropower station locates in the middle reaches of Dadu River, western Sichuan Province. The geological structure in this zone is quite complex and influenced by lots of distributed fault and lower soft rock mass. Thus, the in-situ stress field distributes intricately.

A total of six testing borehole (PD3-1~PD3-6) in underground powerhouse zone distributes on the left bank near the underground powerhouse, and they are made by aperture deforming method. As shown in Figure1.

3 Regression Analysis method of three-dimensional initial in-situ stress

The basic procedure of the three-dimensional initial in-situ stress regression is:

(1) Based on the measured data and engineering geological conditions, three-dimensional geological model is constructed by finite difference program. (2) According to geomechanics analysis, take the principal factor which influences the formation of initial in-situ stress as undetermined factor. The magnitude of stress about the measuring points is calculated with each factor, and multiple regression equation is established between measured data and calculated data of stress value. (3) Optimum relation for coefficient of independent variable in multiple regression equation is obtained by least squares method; thereby the initial in-situ stress in the zone is got [3].

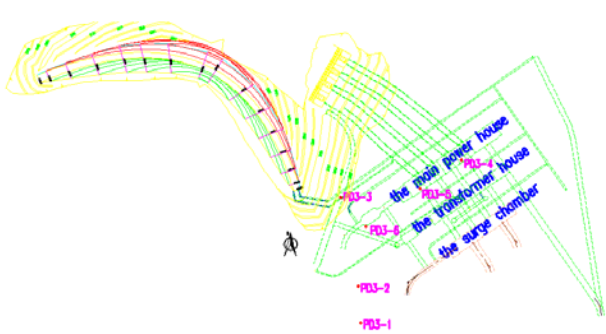

Figure 1 Sketch map of drilling position for measuring points

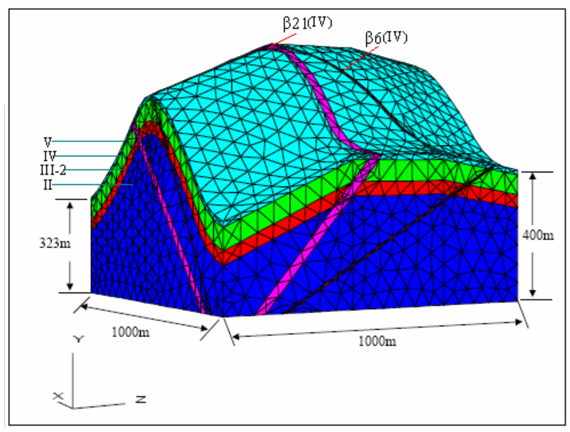

Figure 2 Meshes of numerical calculation

3.1. Calculating principle for regression of three-dimensional initial in-situ stress

According to the multiple regression principle, the regressed in-situ stress value $\widehat{\sigma}_k$ is regarded as dependent variable; consider the calculated stress value σ_k^i corresponding to measuring points as independent variable. σ_k^i is got from the calculation result of gravity field and tectonic stress field. Therefore, the regression equation is as shown:

$$\widehat{\sigma}_k = \sum^{n} L_i \sigma_k^j \tag{1}$$

In the equation, k is the sequence number of measured point; $\widehat{\sigma}_k$ is the regressed value of the k measuring point; L_i is the multiple regression coefficients corresponding to independent variable; $\widehat{\sigma}_k$ is matrix of measured value of 6 stress components; σ_k^i is matrix of calculated value of 6 stress components; n is the number of factors influence the in-situ stress.

The regression calculated value $\hat{\sigma}_k$ can be determined corresponding to each stress σ_k^i. The residual error indicates the eccentricity between measured value σ_k^* and regressed value $\hat{\sigma}_k$, $S_k = \sigma_k^* - \hat{\sigma}_k$. If the number of measured points is m, square sum of residual between total measured value $\sum_{k=1}^{m}\sum_{j=1}^{6}\sigma_{jk}^*$ and regressed value $\sum_{k=1}^{m}\sum_{j=1}^{6}\sigma_{jk}^i$ indicates the eccentricity of all measured data and regression equation.

$$S_r = \sum_{k=1}^{m}\sum_{j=1}^{6} S_{jk}^2 = \sum_{k=1}^{m}\sum_{j=1}^{6}(\sigma_{jk}^* - \sum_{i=1}^{n} L_i\sigma_{jk}^i)^2 \tag{2}$$

In Eq. (2), σ_{jk}^* is the measured value of stress component j in measured point k; σ_{jk}^i is finite difference calculating value of stress component j in measured point k under condition i.

According to the principle of least squares method, the equation which makes S_r be the minimum is shown in Eq. (3).

$$\begin{vmatrix} \sum_{k=1}^{m}\sum_{j=1}^{6}(\sigma_{jk}^1)^2 & \sum_{k=1}^{m}\sum_{j=1}^{6}\sigma_{jk}^1\sigma_{jk}^2 \cdots & \sum_{k=1}^{m}\sum_{j=1}^{6}\sigma_{jk}^1\sigma_{jk}^n \\ symmetry & \sum_{k=1}^{m}\sum_{j=1}^{6}(\sigma_{jk}^2)^2 \cdots & \sum_{k=1}^{m}\sum_{j=1}^{6}\sigma_{jk}^2\sigma_{jk}^n \\ \cdots & symmetry & \sum_{k=1}^{m}\sum_{j=1}^{6}(\sigma_{jk}^n)^2 \end{vmatrix} \begin{vmatrix} L_1 \\ L_2 \\ \vdots \\ L_n \end{vmatrix} = \begin{vmatrix} \sum_{k=1}^{m}\sum_{j=1}^{6}\sigma_{jk}^*\sigma_{jk}^1 \\ \sum_{k=1}^{m}\sum_{j=1}^{6}\sigma_{jk}^*\sigma_{jk}^2 \\ \vdots \\ \sum_{k=1}^{m}\sum_{j=1}^{6}\sigma_{jk}^*\sigma_{jk}^n \end{vmatrix} \tag{3}$$

Undetermined regression coefficients $L = (L_1, L_2, ..., L_n)^T$ is obtained by solving Eq.(3) and the number of it is n. Therefore, the regressed initial in-situ stress of each point is got through the superposition of every calculated value.

$$\sigma_{jp} = \sum_{i=1}^{n} L_i\sigma_{jp}^i \tag{4}$$

3.2. Influence factors of initial in-situ stress

The rock gravity and tectonic stress is regarded as the major influencing factors in regression analysis of in-situ stress.

On the basis of the measured data, the in-situ stress field is regarded as the linear superposition of gravity field and tectonic stress field. The gravity field and tectonic stress field caused by boundary loads is simulated separately, and combined into calculated in-situ stress ultimately.

Take the following 7 factors as basic factors in simulating the rock gravity and tectonic stress, which is also the basic possible factor to do stepwise regression analysis. The 7 factors are shown as follow:

(1) Gravity load; (2) Tectonic stress caused by horizontal compressive load which is parallel to the axes of powerhouse; (3) Tectonic stress caused by horizontal compressive load which is perpendicular to the axes of

powerhouse; (4) Shearing stress in horizontal plane which is along the axes *X*; (5) Shearing stress in horizontal plane which is along the axes *Z*; (6) Vertical shearing stress in vertical plane which is parallel to the axes of powerhouse;(7) Vertical shearing stress in vertical plane which is perpendicular to the axes of powerhouse.

Uniform unit load is applied on the model boundary for different influencing factors; numerical calculation is taken under the independent effect of 7 factors mentioned above respectively.

Based on regressed in-situ stress value of measured points, regression equation for in-situ stress field and all factors is established as follow:

$$\sigma_{total} = L_1\sigma_{C1} + L_2\sigma_{C2} + L_3\sigma_{C3} + L_4\sigma_{C4} + L_5\sigma_{C5} + L_6\sigma_{C6} + L_7\sigma_{C7} + \Delta\sigma \tag{5}$$

In this formula, σ_{total} is in-situ stress; $\sigma_{C1} \sim \sigma_{C7}$ is stress induced by each factor; $\Delta\sigma$ is constant term; $L_1 \sim L_7$ are regression coefficients.

4 Computation module and calculation condition

4.1. Computing range selection and model establishment

In order to simulate the initial in-situ stress of underground powerhouse accurately, large-scale computing field is selected. There are 1000 m in X direction which is perpendicular to axes of underground powerhouse, and 1000 m in Z direction which is parallel to the same axes. In Y direction, there are about 400 m from the earth surface to altitude 700 m.

Three-dimensional numerical calculating meshes are shown in Figure2. The actual topographic feature, rock strata condition are all simulated as well as the large fault β6 and β21 in the computing field.

Normal displacement constraint is applied on bottom boundary and all flanks of the meshed model. Upper boundary is free boundary.

4.2. Parameters

Transversely isotropic model is used, and the mechanics parameter of rock mass is shown in Table 1.

Table 1. Parameters of transversely isotropic model

Material	Young's moduli in the plane of isotropy E（GPa）	Young's moduli in the direction normal to the plane of isotropy E'（GPa）	Poisson's ratio μ	shear modulus for the plane of isotropy G（GPa）	shear modulus for any plane normal to the plane of isotropy G'（GPa）	density ρ（Kg/m^3）
II	24.50	14.00	0.25	9.80	5.60	2.65*10^6
III-2	9.05	6.00	0.30	3.65	2.31	2.62*10^6
IV	2.50	2.00	0.35	0.93	0.74	2.58*10^6
V	0.70	0.70	0.37	0.26	0.26	2.45*10^6

4.3. Analyzed result of measured in-situ stress

Aperture deforming technique is used to measure the in-situ stress of underground powerhouse. In order to apply the measured data (Table 2) to finite difference regression calculating, the measured in-situ stress is transferred to stress component in model coordinate.

Table 2. The results of in-situ stress measurement by aperture deforming technique

Measuring point	Principle stress (MPa)			Azimuth angle (°)			Dip angle (°)		
	σ_1	σ_2	σ_3	β_1	β_2	β_3	α_1	α_2	α_3
PD3-1	22.19	29.37	6.56	15.51	148.38	70.57	9.73	297.00	18.20
PD3-2	20.15	18.15	9.14	13.70	161.00	64.50	7.12	278.6	21.60
PD3-3	18.50	52.84	1.03	10.01	168.34	87.62	4.75	322.8	2.13
PD3-4	13.01	60.95	38.62	10.10	53.03	-51.11	2.43	327.85	-3.88
PD3-5	11.37	44.91	23.46	9.96	91.53	-57.71	2.90	324.43	-20.86
PD3-6	19.28	54.30	0.19	10.70	146.33	84.55	4.58	324.28	5.44

5 Regression result of in-situ stress

Take the measured in-situ stress data as regression target; calculate stress respectively based on seven conditions shown in Eq. (5). Multiple linear regression of Eq. (5) is carried out using least square method. So the regression coefficient are got: $\Delta\sigma$ =4656982.0 L_1=1.460 L_2= 0.180 L_3=0.206 L_4=0.079 L_5=0.143 L_6=0.106 L_7=0.015. Therefore, the regression equation of initial in-situ stress of underground powerhouse is described by Eq. (6).

$$\sigma_{total} = 1.460\sigma_{C1} + 0.18\sigma_{C2} + 0.206\sigma_{C3} + 0.079\sigma_{C4} + 0.143\sigma_{C5} + 0.106\sigma_{C6} + 0.015\sigma_{C7} + 4656982 \quad (6)$$

Multiple correlation coefficient of regression is 0.943 which indicates that the regression formula have good correlation.

Comparison of measured and regressive principal in-situ stresses by aperture deforming technique is shown in Table 3 and Figure3.

Table 3. Comparison of measured and regressive principal in-situ stresses by aperture deforming technique

Measuring point	subentry	σ_1 (MPa)	Azimuth (°)	Dip (°)	σ_2 (MPa)	Azimuth (°)	Dip (°)	σ_3 (MPa)	Azimuth (°)	Dip (°)
PD3-1	Measured value	22.19	29.37	6.56	15.51	148.38	70.57	9.73	297.00	18.20
	Regressed value	17.92	41.92	6.77	12.10	173.70	66.20	8.70	335.23	22.70
PD3-2	Measured value	20.15	18.15	9.14	13.70	161.00	64.50	7.12	278.6	21.60
	Regressed value	18.31	49.82	1.77	11.66	162.93	82.04	8.29	329.94	7.76
PD3-3	Measured value	18.5	52.84	1.03	10.01	168.34	87.62	4.75	322.8	2.13
	Regressed value	16.64	53.52	0.92	9.76	150.51	77.18	3.20	323.74	-12.79
PD3-4	Measured value	13.01	60.95	38.62	10.10	53.03	-51.11	2.43	327.85	-3.88
	Regressed value	12.88	53.05	13.45	11.73	199.58	74.00	3.95	329.00	-8.50
PD3-5	Measured value	11.37	44.91	23.46	9.96	91.53	-57.71	2.90	324.43	-20.86
	Regressed value	15.56	50.79	4.00	12.13	172.64	82.45	5.87	329.65	-6.39
PD3-6	Measured value	19.28	54.30	0.19	10.70	146.33	84.55	4.58	324.28	5.44
	Regressed value	17.75	53.96	2.12	11.40	156.88	78.87	6.07	324.38	-10.92

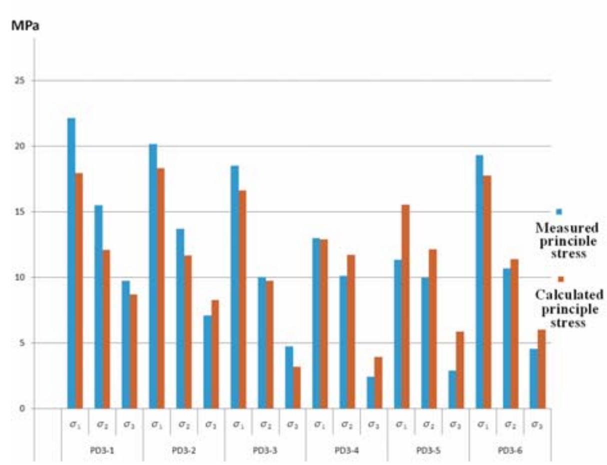

Figure 3 Comparison histogram of measured and calculated principle stress of measuring points

The magnitude and orientation of regressed principle stress are similar to measured data as shown in Table 3 and Figure3.

6 Conclusions

(1) Based on the influence of actual stratigraphic distribution and fault fracture zones, the in-situ stress field is analyzed with multiple regression and three-dimensional numerical calculation. The result indicates that the regressed stress is well fitted to measured data. So, a rational three-dimensional initial in-situ stress field is provided for excavating simulation and analysis of long-term stability of the underground powerhouse at the hydropower station.

(2) The orientation of maximum principle stress is parallel to the axes of powerhouse while the orientation of minimum principle stress is perpendicular to the axes. The result accords with the regulation of underground powerhouse construction, and the designing rationality of this underground powerhouse is validated also.

Acknowledgements

This work was supported by a grant from the National Basic Research Program of China (973 Program) (No. 2009CB724607)， National Natural Science Foundations of China (No. 40772173); Natural Science Foundations of Shandong Province (No.Y2007F52); New Century Excellent Talents in University(NCET-08-0336).The author is deeply appreciated to these supports.

References

1. Xiao, M. and Liu, Z.M. Regression Analysis of 3D Geostress Gield on Jinping Secondary Hydropower Station. Yangtze River, 2000, 31(9). 42-44.
2. Xie, H.Q., Xiao, M.L. and He, J.D. et al. Regression Analysis of Initial Geostress for Dam Region of Jinping Hydropower Station. Journal of Yangtze River Scientif ic Research Institute, 2008, 25(5). 50-54.
3. Hu, B., Feng, X.T. and Huang, X.H. et al. Regression Analysis of Initial Geostress Field for Left Bank High Slope Region at Longtan Hydropower Station. Chinese Journal of Rock Mechanics and Engineering, 2005, 22(11). 4055-4064.
4. Jiang, Q., Feng, X.T. and Chen, J.L. et al. Nonlinear Inversion of 3D Initial Geostress Gield in Jinping II Hydropower Station Region. Rock and Soil Mechanics, 2008, 29(11). 3003-3010.
5. Jia, S.P., Chen, W.Z. and Tan, X.J. et al. Nelder-Mead Algorithm for Inversion Analysis of In-situ Stress Field of Underground Powerhouse Area of Dagangshan Hydropower Station. Rock and Soil Mechanics, 2008, 29(9). 2341-2349.

RaSiM 7(2009): Controlling Seismic Hazard and
Sustainable Development of Deep Mines,
C.A. Tang(ed), Rinton Press, 599-604

NUMERICAL SIMULATION ON EFFECT OF GAS DRAINAGE IN COAL SEAM UNDER HYDRAULIC FRACTURING

TIAN-HONG YANG

School of Resources and Cviling Engineering, Northeastern University

Shenyang, 110004, P.R. China

TAO XU

Center for Material Failure Modeling Research, Dalian University,Dalian, 116622, P.R. China

CHUN-AN TANG

Center for Rock Instability and Seismicity Research, Dalian University of Technology

Dalian, 116024, P.R. China

Methane drainage has become an integral part of modern coal mining operations in low-permeable coal seams, thus some measures such as hydraulic fracturing and stress reducing are used to improve the permeability of coal seams and secure the safety and effectiveness of coal mining activities. In the paper, a coupled gas flow model which incorporated stress, damage and permeability evolution was briefly described and employed to simulate the changes of gas pressure around the boreholes in low-permeable coal seam under hydraulic fracturing, and the seepage mechanism of gas flow was analyzed. Numerical simulations show that the content of gas release was remarkably increased and the gas pressure around the borehole was obviously reduced, which is well agreement with the field findings. The work in the present paper is of great significance to further investigate and understand the mechanism of gas permeability evolution and the mechanism of gas drainage under hydraulic fracturing in both theory and practice.

1 Introduction

Methane drainage has become an integral part of modern coal mining operations in China. When the permeability of the coal seam is lower, thus some measures such as hydraulic fracturing and unloading are taken to improve the permeability of coal seams and secure the safety and effectiveness of coal mining activities. To maintain the safe and effective capture of methane in coal seams requires an understanding of both the permeability evolution of the surrounding rocks and the migration and movement of gas in the coal seam during coal mining, and an establishment of an appropriate mathematical model for coupled gas flow in coal seam during coal mining excavation.

As we know, the stress permeability behaviour of coal or coal measure strata is the key to the effective simulation of methane flow in a coal seam. Extensive research on the stress-permeability relationship and the modelling of methane flow in coal seam has been carried out in past years [1-3]. A more recent study established the post-failure stress-permeability behaviour of coal measure rocks and applied computational fluid dynamics (CFD) to model the resultant flow of methane into mine workings [4-8].

In this paper, according to the coal and rock mass deformation and gas flow theory, a coupled gas flow model incorporated stresses, damages and permeability change was employed to simulate the gas flow before and after hydraulic fracturing in low-permeable coal seam in Dashucun coal mine, Fengfeng Coal Group, Hebei Province for a better understanding of the mechanism of reducing stress to improve permeability and gas drainage.

2 Mathematical Model

In this section we briefly describe the mathematical model of coupled gas flow in coal seam or coal measure strata. More details about the mathematical model can refer to published papers [9, 10].

The fundamental assumption behind the mathematical model in this paper is that the pores and cracks in the coal or rock medium are saturated with free gas and the walls of the pores contain adsorbed gases which are not free. Initially, the section of the rock or coal medium containing the adsorbed and fre gases is in equilibrium with respect to its environment. The total gas content in coal and rock medium can be approximated by an empirical parabolic equation [11, 12]. The gas flow in the pores and cracks which exist in coal or rock medium follows the linear Darcy's law. According to the basic seepage theory of gas flow in porous media, the following equation of the isothermal filtration gas flow in gassy coal and rock can be obtained

$$\alpha_p \cdot \nabla^2 P = \frac{\partial P}{\partial t} \tag{1}$$

where, $\alpha_p = 4\lambda A^{-1} P^{\frac{3}{4}}$, λ is the coefficient of gas filtration in $m^2/(MPa^2 \cdot S)$, A is the empirical coefficient of gas content in $m^3/(m^3 \cdot MPa^{1/2})$ and P is the square of gas pressure p in MPa^2.

For a stress analysis in terms of effective stress, the stress equilibrium equations is expressed according to the effective stress principle

$$\sigma'_{ij,j} + f_i + (\alpha \cdot p \cdot \delta_{ij})_{,j} = 0 \tag{2}$$

where σ'_{ij} is the effective stress tensor,($i, j = 1,2,3$) in MPa. f_i is the body forces per unit volume in MPa, p is the gas pressure, α is a positive constant equal to 1 when individual grains are much more incompressible than the grain skeleton, and δ_{ij} is the Kronecker delta function.

The constitutive equation of deformation fields can be expressed for elastic isotropic materials

$$\sigma'_{ij} = K\delta_{ij}\varepsilon_{ii} + 2G\varepsilon_{ij} \tag{3}$$

where G is shear modulus and K is Lame's constant, ε_{ij} is strain tensor, and ε_{ii} is the volumetric strain.

On the basis of the above the equilibrium, the continuity, and the constitutive equations, the governing equations for mathematical model of coal/rock deformation considering the gas pressure in coal/rock can be represented as

$$(K + G) \cdot u_{j,ji} + Gu_{i,jj} + f_i + (\alpha \cdot p)_{,i} = 0 \tag{4}$$

As for damage induced permeability change, generally speaking, as the stresses increase, the coal and rock permeability decreases significantly in the highly stressed zone which leads to coal compacts during elastic deformation process. However, as the stresses continue to increase beyond the strength of coal and rock, a dramatic and remarkable increase in coal and rock permeability can be expected as a result of the generation of numerous micro fractures on reaching the peak load. Once reaching the peak load, the permeability may gradually drop again should the failed rock be further compacted, or the permeability may increase continuously should the failed rock be further extended. The permeability change equations of coal and rock due to stresses change are incorporated into the mathematical model of the coupled gas flow in the coal seam or coal measure strata due to mining excavations [9, 10].

3 Case Study

In this part the low-permeable coal seam in Dashucun coal mine, Fengfeng Coal Group in Hebei province was targeted to study the gas flow before and after hydraulic fracturing of coal seam to provide some reference and evidence for scientific and reasonable methane management measures.

3.1 Numerical Model

In this paper, a numerical model with a configuration of 5m×3m was set up as shown in Figure 1. Impermeable-boundary conditions of the numerical model were presumed since the boreholes of gas drainage were symmetrically configured. The initial gas pressure in the model was l MPa and the gas pressure of the three boreholes was 0.01 MPa. The mechanical and seepage parameters of the model are listed in the Table 1.

Table 1. Mechanical and seepage parameters for gas drainage

Mechanical and seepage parameters	value
Heterogeneity index, *m*	10
Mean elastic modulus, E_0 / GPa	5
Mean compressive strength, σ_0 / MPa	50
Internal friction angle, ϕ / °	30
Density / (10^3kg/m^3)	2.0
Poisson's ratio, μ	0.25
Gas permeability, λ, m^2/(MPa^2 • d)	0.1
Coefficient of gas content, A	0.05
Coefficient of pore pressure, α	0.01
Initial gas pressure, P, MPa	1
Coefficient of stress coupling	0.05
Time duration per step, Δt /d	0.1
Confining pressure, σ_3, MPa	9

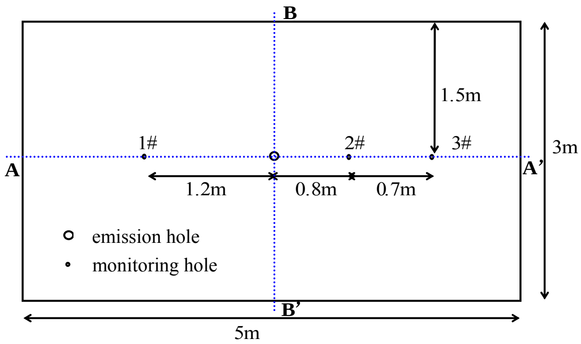

Figure 1 Numerical model

3.2 Modelling Results

3.2.1 Gas drainage before hydraulic fracturing

The evolution distribution of gas pressure around the borehole before hydraulic fracturing with different time, i.e., 0.1d, 1d, 10d and 20d, are respectively presented in Figure 2. It can be seen from the Figure 2 that the gas pressure around the borehole in coal seam decreases from the maximum gas pressure 1.0MPa down to 0.55MPa by a decrease of 45%.

Figure 3 and Figure 4 are respectively the curves of gas pressure along cross-section A-A' and B-B' of intersecting the centre of the boreholes with time before hydraulic fracturing. Numerical simulations show that the gas pressure in the coal seams remarkably decreased at the beginning of gas drainage and the gas pressure obviously slowly decreased after 20 days of gas drainage.

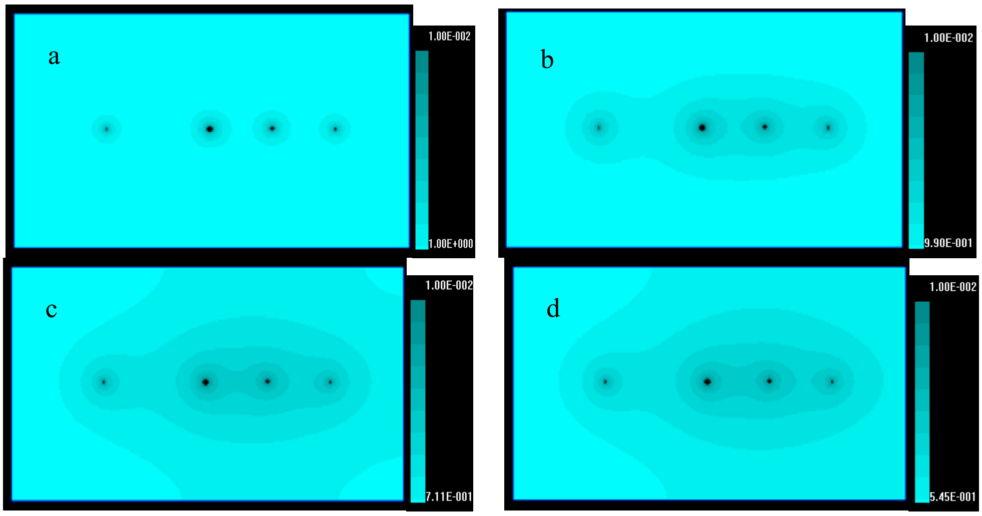

Figure 2 Distribution of gas pressure around the borehole with time before hydraulic fracturing a. 0.1d, b. 1d, c. 10d and d. 20d

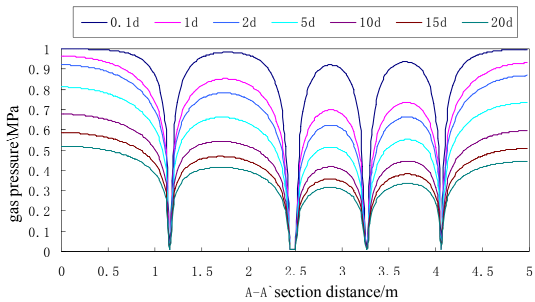

Figure 3   Curves of gas pressure along cross-section A-A' with time before hydraulic fracturing

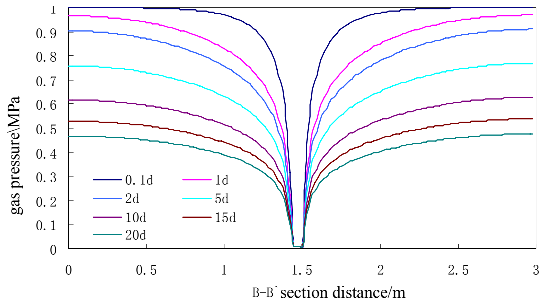

Figure 4   Curves of gas pressure along cross-section B-B' with time before hydraulic fracturing

3.2.2 Gas drainage after hydraulic fracturing

As we know, we employ hydraulic fracturing of borehole in order to form clusters of radial cracks around the borehole and improve the gas permeability of coal seam and thus gain an efficient drainage and capture of gas in coal seam. In the model simulated, the length of radial cracks around the borehole is assumed to be about 0.7 meter based on the in-situ observation in coal mine. The simulated results will semi-quantitatively interpret and analyze the mechanism of gas migration and flow since the model is in planar state in this paper, which is different from the three dimensional states in fields.

Figure 5 presents the evolution distribution of gas pressure around the borehole after hydraulic fracturing with different time (0.1d, 1d, 10d and 20d). It can be seen from the Figure 2 that the gas pressure around the borehole in coal seam decreases from the maximum gas pressure 1.0MPa down to 0.47MPa by a decrease of 53%. It needs to be pointed out that the influencing radius of gas drainage is predominantly controlled by the radial cracks around the borehole.

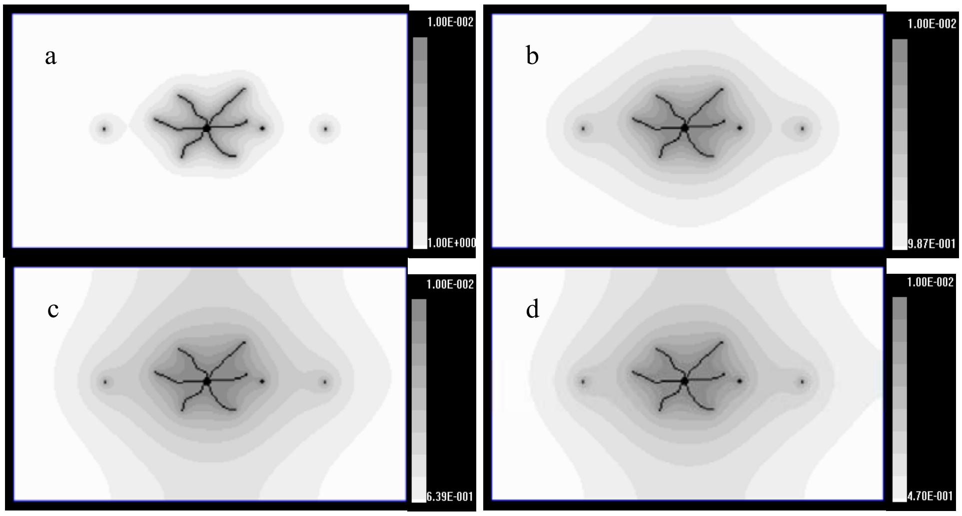

Figure 5 Distribution of gas pressure around the borehole with time after hydraulic fracturing

a. 0.1d, b. 1d, c. 10d and d. 20d

Figure 6 is the comparison curves of gas release before and after hydraulic fracturing. We can obviously see that gas release in the coal seams remarkably increased after hydraulic fracturing around borehole. The curves of gas pressure along cross-section A-A' and B-B' of intersection the borehole centre after hydraulic fracturing are respectively shown in Figure 7 and Figure 8. It can be seen that the gas pressure remarkably decreased after hydraulic fracturing of borehole.

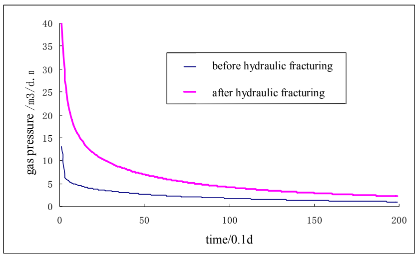

Figure 6 Comparsion curves of gas pressure with time before and after hydraulic fracturing

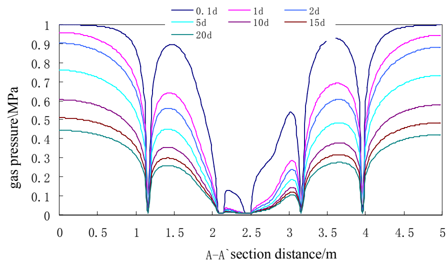

Figure 7 Distribution of gas pressure along cross-section A-A' with time after hydraulic fracturing

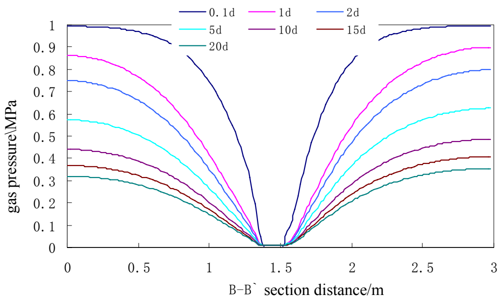

Figure 8 Distribution of gas pressure along cross-section B-B' with time after hydraulic fracturing

4 Conclusions

In the present paper a mathematical model for coupled stress, damage and seepage in coal seam was employed to simulate the dynamic changes of gas permeability and gas seepage law before and after hydraulic fracturing in a low-permeable coal seam in Dashucun coal mine, Fengfeng coal group, and the Hebei province. Numerical simulations show that gas release in the coal seams remarkably increased and the gas pressure is obviously reduced after hydraulic fracturing around boreholes. Numerical results visualized the influencing control radius and decrease effects of gas drainage before and after hydraulic fracturing, qualitatively interpreted the mechanism of improving the effect of gas drainage by hydraulic fracturing. The work in this paper is a great help for a better understanding of the mechanism of reducing stress to improve permeability and gas drainage as well as some theoretical and practical reference for the application of hydraulic fracturing in fields to control and prevent the occurrence of outbursts induced by underground mining.

Acknowledgements

The study presented in this paper is jointly supported by the National Natural Science Foundation of China (No. 2007CB209405, 2005CB221503, 2006CB202201-6, 2006CB202204-2, 50674025, 50504005, 10872046 and 107033).

References

1. Whittles, D. N., Lowndes, I. S., Kingman, S. W., Yates, C. and Jobling, S. Influence of geotechnical factors on gas flow experienced in a UK longwall coal mine panel. International Journal of Rock Mechanics and Mining Sciences, 2006, 43(3). 369-387.
2. Karacan, C. O., Diamond, W. P. and Schatzel, S. J. Numerical analysis of the influence of in-seam horizontal methane drainage boreholes on longwall face emission rates. International Journal of Coal Geology, 2007, 72(1). 15-32.
3. Chen, J. Y., Yan, J. W., Zhang, Y. G. and Zhang, Z. M. Calculating method of actual gas emission rate and application to gas drainage faces. Progress in Mining Science and Safety Technology, 2007, Pts A and B. 1340-1343
4. Brandt, J. Control of gas emissions at high performance longwalls in the German hard coal mining industry. Proceedings of the seventh International Mine Ventilation Congress, Krakow, Poland, 2001, 119-125.
5. Kunz, E. Gas emission problems in straining the workings and control measures. Proceedings of the seventh International Mine Ventilation Congress, Krakow, Poland, 2001, 105-108.
6. Ren, T.X. and Edwards, J.S. Application of CFD techniques to methane prediction and control in coal mines. Proceedings of the 27th International Symposium on Computer Applications in the Minerals Industry, 19-23 April London, UK: The I.M.M, 1998, 733-744.
7. Moloney, K.W., Hargreaves, D.M. and Lowndes, I.S. Assessment concerning the accuracy of computational fluid dynamics (CFD) simulations in underground auxiliary ventilated headings. Proceedings of APCOM XXVI London. London: IMM, 1998, 721-732.
8. Hargreaves, D.M., Moloney, K.W. and Lowndes, I.S. Preliminary computational fluid dynamics (CFD) simulations of methane dispersion in a heading. Proceedings of the second International Symposium on Mine Environmental Engineering, Brunel, UK, 1998.
9. XU, T., Tang, C.A., Song, L., Yang, T.H. and Liang, Z.Z. Computer modeling of coupled gas flow in the failure process of gassy coal-rock. Chinese Journal of Rock Mechanics and Engineering, 2005, 24(10). 1667-1673.
10. XU, T., Tang, C.A, Yang, T.H., Zhu, W.C. and Liu, J. Numerical investigation of coal and gas outbursts in underground collieries. International Journal of Rock Mechanics and Mining Sciences, 2006, 43(6). 905-919.
11. Zhou, S.N. and Lin, B.Q. Theory of gas flow and storage in coal seams. China Coal Industry Publishing House, Beijing, 1998.
12. Yu, Q.X. Prevention and control of methane in coal mines. Press of China University of Mining and Technology, Xuzhou, 1993.

*RaSiM 7(2009): Controlling Seismic Hazard and
Sustainable Development of Deep Mines,
C.A. Tang(ed), Rinton Press, 605-612*

RESEARCH OF MECHANICAL MODEL AND NUMERICAL SIMULATION FOR FLOOR BURST

XUE-FENG XU, LIN-MING DOU, ZONG-LONG MU and XIN-WEI LU

State Key Laboratory of Coal Resource and Mine Safety, China University of Mining & Technology, Xuzhou, Jiangsu 221008, China；

School of Mines, China University of Mining & Technology, Xuzhou, Jiangsu 221008, China

The horizontal stress in the floor of roadway plays an important role in rock burst. According to previous theories, a mechanical model is set up, where the dangerous coefficient of floor burst is initially given, and the distribution laws of horizontal stress rising and vertical stress reducing in the floor are calculated through numerical simulation. Throughout this study, it is concluded that the floor burst is seriously relevant to the following factors, i.e. the elastic modulus of rock, the thickness of soft rock in the floor, the horizontal tectonic stress, and the heave hard roof. As the dangerous coefficient of floor burst is more than or equal to 1, floor burst will happen with the influence of blast firing or roof breaking quickly. The conclusions pave the way of developing theories and taking measures to prevent and control floor burst.

1 Introduction

The rock burst in coal mines is assorted into roof bursts and floor bursts for different positions [1]. At present, the mechanism of roof burst is widely researched [2, 3]. Floor burst often happens during the seam extraction and roadway driving in some coal mines. In these papers [4, 9], the reasons for floor failure and floor burst are researched; however, the reasons for floor burst are very complicated and seriously breakdown-resulted, and there are different reasons for different coal mines. It is very important to find out the mechanism of floor burst. In this paper, the mechanical model of floor burst is set up, and with the method of numerical simulation, the reasons and conditions of floor burst is analyzed. The conclusions achieved provides us theoretical foundation and research ways for further researching of the mechanism of floor burst, and this allows us to take effective measures to prevent and control floor burst.

2 Analysis and mechanical model of floor burst

If the roadway is cut in the natural rock, the stresses distribution around the roadway will change, and the vertical stress will move to the sides of the roadway, and the horizontal stress will move to the roof and floor. According to the theory, the vertical stress can influence stability of the two sides and the horizontal stress can influence stability of the floor [10]. The horizontal stress in the floor of the roadway plays an important role in floor burst, so a mechanical model for researching the influence of horizontal stress on floor failure will be set up in this section.

2.1 Calculation model of stress in the floor

The load on the coal pillar which can be calculated is the weight of overlying strata and the suspended rock above vacant place which move to one side or two sides of the coal pillar [11]. According to the theory, the load in the floor of coal pillar of quadrant roadway is calculated here. Calculation model is shown in figure 1.

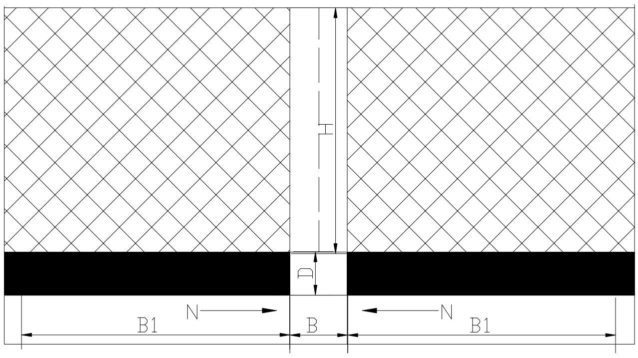

Figure 1 Calculation model of stress in the floor

The load on the coal pillar of single unit is approximately expressed by:

$$P = (B_1 + \frac{B}{2}) \times H\gamma_r + \frac{B_1 D}{2}\gamma_m \tag{1}$$

Where, B_1 is the coal pillar load-carrying range (m); B is the width of roadway (m); D is height of roadway (m); H is depth away from the roof of roadway (m); γ_r is gravimetric density of overlying strata (N/m^3); γ_m is gravimetric density of coal seam (N/m^3).

As the coal seam is cut, mined out space is formatted. Because part of the heave hard roof can't collapse completely, the weight will move to the coal pillar or coal seam which is near to the mined out space, and the vertical stress in the coal pillar or coal seam will increase. The vertical stress is calculated as follows:

$$\sigma_y = K_1 \frac{P}{B_1} \tag{2}$$

Connect equation (1) and (2), vertical stress is given by:

$$\sigma_y = K_1 \frac{(B_1 + \frac{B}{2}) \times H\gamma_r + \frac{B_1 D}{2}\gamma_m}{B_1} \tag{3}$$

Where, K_1 is influence coefficient of hard roof abutment pressure, which influence Possion's ratio (here Possion's ratio isn't considered), if drifting face is the first coal face, K_1 is equal to 1; if there are some other coal faces and the hard roof collapses completely, K_1 is equal to 1; and if there are some other coal faces, and the hard roof can't collapse completely, K_1 is more than 1.

2.2 Calculation of vertical stress

For homogeneous rock, with the gravitation, horizontal stress is given by:

$$\sigma_x = \lambda \sigma_y \tag{4}$$

Where, λ is side pressure coefficient, $\lambda = \frac{\mu}{1-\mu}$, μ is Possion's ratio of rock.

As the horizontal tectonic stress exists, and if Possion's ratio is invariable, horizontal stress is calculated as follows:

$$\sigma_x = K_2 \frac{\mu}{1-\mu} \sigma_y \tag{5}$$

Where, K_2 is influence coefficient of horizontal tectonic stress , if rock is in hydrostatic pressure condition, K_2 is equal to 1; and if there is bigger horizontal tectonic stress through surveying, K_2 is more than 1.

Connect equation (3), (4) and (5), horizontal stress is expressed by:

$$\sigma_x = K_1 K_2 \frac{\mu}{1-\nu} \frac{(B_1 + \frac{B}{2}) \times H\gamma_r + \frac{B_1 D}{2} \gamma_m}{B_1} \tag{6}$$

2.3 Conditions of floor failure

Under the axial direction pressure and gravitation, the floor rock beam reaches yield point, and the minimum axial direction pressure N_{cr} can be given as follows [12]:

$$N_{cr} = \frac{\pi^2 EJ}{B^2} \tag{7}$$

Where, E is floor rock elastic modulus(MPa); J is moment of inertia of quadrant section. If the length of floor rock beam is b; the thickness is h, $J = \frac{bh^3}{12}$, here rock beam is single unit, and the moment of inertia is expressed $J = \frac{h^3}{12}$.

The research conclusions [12] show that the floor failure or floor heaven will happen when the given condition is $N \geq 0.8 N_{cr.}$

The floor rock seam pressure is expressed as follows:

$$N = hk_1 k_2 \frac{\mu}{1-\mu} \frac{(B_1 + \frac{B}{2}) \times H\gamma_r + \frac{B_1 D}{2} \gamma_m}{B_1} \tag{8}$$

And the condition of floor failure is given by:

$$hk_1k_2\frac{\mu}{1-\mu}[(1+\frac{B}{2B_1})\times H\gamma_r+\frac{D}{2}\gamma_m]\geq 0.8\frac{\pi^2Eh^3}{12B^2} \tag{9}$$

After h is eliminated, the condition can be simplificated as follows:

$$k_1k_2\frac{\mu}{1-\mu}[(1+\frac{B}{2B_1})\times H\gamma_r+\frac{D}{2}\gamma_m]\geq 0.8\frac{\pi^2Eh^2}{12B^2} \tag{10}$$

In order to analyze, the dangerous coefficient of floor burst is given as follows:

$$K_{fb}=\frac{k_1k_2\frac{\mu}{1-\mu}[(1+\frac{B}{2B_1})\times H\gamma_r+\frac{D}{2}\gamma_m]}{\frac{\pi^2Eh^2}{15B^2}} \tag{11}$$

Where, the value of $\frac{D}{2}\gamma_m$ is too small to be calculated, and $\frac{B}{2B_1}$ is approximately considered constant.

If $K_{fb}\geqslant 1$, floor failure will happen.

Through the above equation (11), the conclusions show that the depth, the elastic modulus of rock, the thickness of soft rock of floor, the horizontal tectonic stress, the heave hard roof are seriously relevant to the floor burst. If the Possion's ratio is invariable, the dangerous coefficient of floor burst is directly proportional to the depth, the horizontal tectonic stress and the coefficient of hard roof abutment pressure, and inversely proportional to the elastic modulus of rock and the square of the thickness of soft rock of floor.

2.4 The reason of floor bust

If $K_{fb}\geqslant 1$, with the influence of mining activities or shock wave of blast firing or sudden breaking of main roof [13], the floor burst will happen.

3 Numerical simulation

3.1 The model setting up

In Yuejin Coal Mine, during the cutting or driving, floor bursts often happen, and several floor bursts have serious effect on the haulage gateway of 23130 coal face. Based on the geological conditions and the mining conditions of adjacent coal faces, the numerical simulation connecting with the mechanical model is done to analyze the reason of floor bursts.

The geological conditions and the mining conditions are listed as follows: the ground level is +550 m; the depth of the haulage gateway is 875 m; the thickness of coal seam is 8 m, the average dip angle is 11°; the immediate roof is 20-m-thick mudstone; on the immediate roof，there is 20-m-thick mixture composed of mudstone，coal and siltstone, and the main roof is 100-m to 180-m-thick conglomerate; 23030, 23050 and 23090 coal faces are mined out areas，and the higher slice about 4-m-thick coal seam of 23110 is mined out.

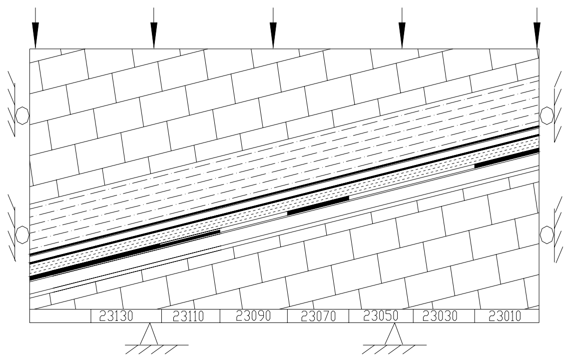

Figure 2 Numerical simulation model

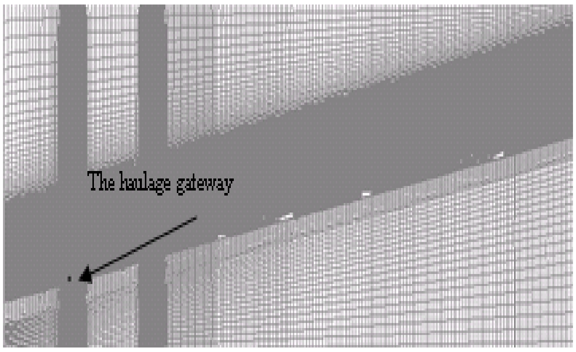

Figure 3 FLAC grid for the model

The return airway of 23130 coal face is excavated along the mined out space, and the haulage gateway is excavated along the roof of intact coal.

In the numerical simulation, FLAC2D software is used. The model length is 1328 m, and the height is 550 m. Other parameters such as the width of each coal face, the dip angle and the depth of coal seam, the mechanical and physical parameters of coal seam and rock come from the data of Yuejin Coal Mine. The numerical simulation model is shown in figure 2, and the FLAC grid for the model is shown in figure 3.

If the researched haulage gateway is not influenced by hard roof abutment pressure, the vertical stress value distributing in the two sides of the floor is 22.40 MPa. In the model, the influence of hard roof abutment pressure is considered, the σ_{yy}-stresses contours and the σ_{xx}-stresses contours around the roadway are shown in figure 4 and 5, and the vertical stress and horizontal stress distribution 2 m away from the floor are shown in figure 6 and figure 7.

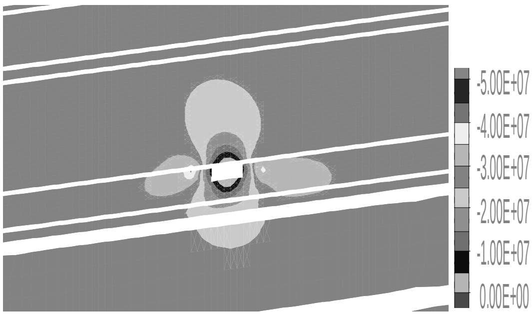

Figure 4 σ_{yy}-stresses contours around the roadway

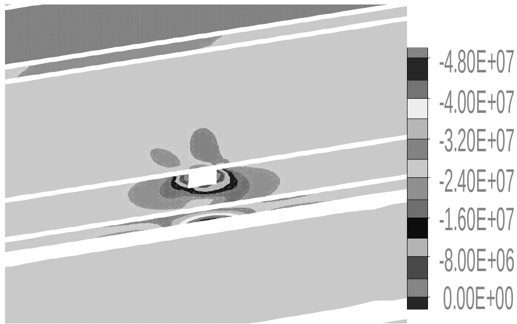

Figure 5 σ_{xx}-stresses contours around the roadway

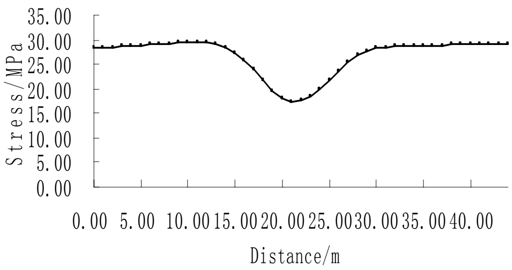

Figure 6 Vertical stress distribution in the floor

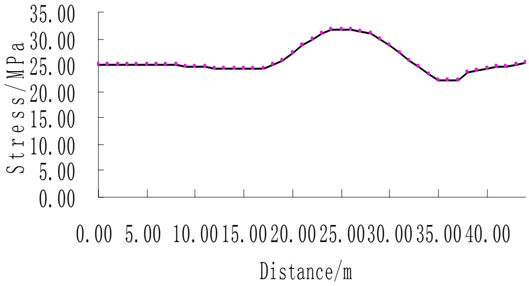

Figure 7 Horizontal stress distribution in the floor

In the figures, distribution laws of horizontal stress rising and vertical stress reducing are found out. The average value of vertical stress is 28 MPa, and the minimum value is 17.36 MPa. The average value of horizontal stress is 24.5 MPa, and the maximum value is 33.70 MPa. The value of horizontal stress concentration coefficient is 1.35.

3.2 The analysis of numerical simulation conclusions

Based on the numerical simulation conclusions, the influence coefficient of hard roof abutment pressure is 1.25; the influence coefficient of horizontal tectonic stress is 1; Possion's ratio is 0.5; $\frac{B}{2B_1}$ is 0.0167; H is 875 m; γ_r is 26000 N/m^3; E is 2.2710^8 Pa; the width of roadway is 4 m. The critical thickness of floor failure is shown as flows:

$$h \le \sqrt{12B^2 \frac{K_1K_2 \frac{\mu}{1-\mu}(1+\frac{B}{2B_1})H\gamma_r}{0.8\pi^2 E}} = 1.76\ \text{m} \tag{12}$$

It can be seen from this equation that when h is less than 1.76 m, the floor failure will happen.

Because there is no coal on the floor of roadway, and the vertical stress reduces and the horizontal stress rises, especially in larger horizontal tectonic stress area, h will exceed the value. Based on the numerical simulation, the thickness ranges from 2 to 3 m is high horizontal stress area, and it is also dangerous area. In Yuejin Coal Mine the haulage gateway is excavated along the roof of coal seam, and if the floor without supporting is soft coal or mixture of coal and soft rock, floor burst will easily happen.

4 Conclusions

(1) In the paper, the mechanical model of floor failure is set up, and the conclusions show that the depth, the elastic modulus of rock, the thickness of soft rock of floor, the horizontal tectonic stress, the heave hard roof and factor of blast firing or sudden breaking of main roof are seriously relevant to floor burst, and the dangerous coefficient of floor burst is given.

(2) The distribution laws of horizontal stress and vertical stress in the floor are found out through numerical simulation, which shows that there are areas of vertical stress rising and horizontal stress reducing, and this will provide favorable conditions for floor bursts.

(3) Based on the mechanical model formula and numerical simulation conditions, the critical thickness of the floor burst in Yuejin Coal Mine is given.

(4) Based on the factors which have an effect on floor burst, some methods such as shearing the hard roof, scalling the floor in deep ares, adding the supporting frame for floor, and enhancing the intensity of floor rock are main methods to prevent and control the floor burst.

Acknowledgements

The authors wish to acknowledge professor Shao fang Liu for her advices for the English paper.

References

1. Qi, Q.X. and Dou L.M. Theory and Technique for Rock Burst. Xuzhou:Publishing House of Chinese University of Mining and Technology, 2008, 10-11.
2. Dou, L.M., Liu, Z.T. and Cao, S.G. et al. Analysis of the Influence on Rock Burst Caused by Hard Roof. Coal Mining Technology, 2003, 28(2). 58-66.
3. Mu, Z.L., Dou, L.M. and Zhang, G.W. et al. Study of Prevention Methods of Rock Burst Disaster Caused by Hard Rock Roof. Journal of China University of Mining & Technology, 2006, 36(6). 737-741.
4. Driad-Lebeau, L., Lahaie, F., Heib, M.A., Josien, J.P., Bigarre, P. and Noirel, J.F. Seismic and Geotechnical Investigations Following A Rockburst in A Complex French Mining District. International Journal of Coal Geology, 2005, 64. 66-78.
5. Niu, B.L., Di, J.Y. and Tang, S.Q. The Mechanism and Control Methods of Rock Burst of Floor Heaven Coal Mining Technology. Coal Mining Technology, 1999, 1. 20-23.
6. Tai, Y.L., Wang, L.G. and Zhang, H.M. The Mechanism and Mathematical Model of the Stress-tensioned Roof and Bottom Plate Rock Burst. Journal of Liaoning Technical University (N atural Science), 1999, 18(5). 553-556.
7. Wang, W.J. and Hou, C.J. Stability Analysis of Coal Pillar and Immediate Bottom of Extraction Opening. Rock and Soil Mechanics, 2003, 24(1). 76-78.
8. Li, H.W., Cheng, J.P. and Guo, J.G. The Research of Mechanism of Floor Heaven in Extraction Opening. Rock Pressure and Roof Manage, 2003, (4). 24-27.
9. Gao, M.Z. Mechanism of Roadway Floor Heave by Bending under Pressure and Its Control. Journal of Anhui University of Science and Techno logy (N atural Science), 2008, 28(1). 20-24.

10. Ni, X.H. Researching and Applying for Geological Stress. Bingjing: Publishing House of Chinese Coal Industry, 2006, 137-160.
11. Qian, M.G. and Shi, P.W. Rock Pressure and Rock Seam Control, Xuzhou: Publishing House of Chinese University of Mining and Technology, 2003, 218-219.
12. Pan, L.Y. Preventing and Controlling Techniques for Deep Coal Mine Rock Burst. Bingjing: Publishing House of Chinese Coal Industry, 1997, 20-22.
13. Gao, M.S., Dou, L.M. and Zhang, N. et al. Strong-soft-strong Mechanical Model for Controlling Roadway Surrounding Rock Subjected to Rock Burst and Its Application. Rock and Soil Mechanics, 2008, 29(2). 359-364.

RaSiM 7(2009): Controlling Seismic Hazard and Sustainable Development of Deep Mines, C.A. Tang(ed), Rinton Press, 613-618

ANALYSIS OF THE EFFECT OF JOINTS ON ROCKMASS STRENGTH

GANG WANG

College of Civil Engineering and Architecture, Shandong University of Science and Technology

Qingdao，266510, P.R. China

YU-JING JIANG

Department of Civil Engineering, Nagasaki University

Nagasaki, 852-8521, Japan

MING-BIN WANG

School of Science, Shandong Jianzhu University

Jinan, 250101, P.R. China

In a rock mass, mechanical deformations will mainly occur as normal and/or shear deformations in the joints with the rock strength being a large extent decided by the mechanical and geometrical behaviour of the joints. The theoretical evaluation of the mechanical properties of fractured rock masses has no satisfactory answer because of the great number of variables involved. Some of these variables, which may influence the rock mass behaviour is poorly documented, are the degree of fracture persistence, joint orientation relative to the loading and joint gap. In this study, some numerical cases are implemented on the effect of joint orientation on the rock intensity. Applying the 2D discrete element code (UDEC), the numerical simulation is carried out to investigate the effect of joints on the rock intensity. The computation results indicate that the orientation and the joints density have great influences on the rock deformation and rock strength.

1 Introduction Guidelines

Under the current increased environmental and regulatory controls, the evaluation of the foundation strength and deformability are significant factors in the construction process of rock engineering; for example, in a nuclear plant. Moreover, the elastic modulus of the rock media determines the foundation deformation and influences earthquake-resistance stability at a large extent. Under the circumstances of hard rock, the static elastic coefficient of rock mass is usually applied to the numerical analysis of foundation stability [1]. Viewed on the microscopic scale, rock material is heterogeneous and contains defects in the form of stiff or soft inhomogeneities, microcracks, and micropores. In a jointed rock mass, mechanical deformations will mainly occur as normal and/or shear deformations in the joints and the rock strength is largely decided by the mechanical and geometrical behaviours of the joints [2-4].

In the continuum approach the rock material, or its parts, are treated as an equivalent homogeneous material whose overall (effective) properties are obtained either experimentally or through the use of analytical or numerical homogenization techniques [3-9]. Experimental characterization of rock is difficult because the samples used in laboratory tests are typically not large enough to provide adequate representation of the heterogeneous nature of rocks (e.g. in case of large grain sizes, large-scale fractures, or macroscopic porosity). The theoretical evaluation of the mechanical strength of fractured rock masses has no satisfactory answer due to the significatnt number of variables involved [6-7]. Some of these variables, the influence of which rock mass behaviour is poorly documented, are the degree of fracture persistence, joint orientation relative to the loading and joint gap. Thus, numerical homogenization techniques are indispensable tools in obtaining effective properties.

Most numerical research has been concentrated on studying the effects of microcracks on the mechanical properties of rocks [4-9]. The static elastic coefficient was found first for a body with a single open or closed crack. In case of a body with many cracks varying in length, it was assumed that their effect on the effective modulus was the same as the effect of many cracks all having the same average length. It was shown that the static elastic coefficient for a cracked body is less than that for a solid body. The fractured rock masses are generally treated as a discontinuous medium. A discontinuous medium is distinguished from a continuous one by the existence of contacts or interfaces between the discrete bodies that comprise the system. A numerical model must represent two types of mechanical behaviour in a discontinuous system: (1) behaviour of the discontinuities; and (2) behaviour of the solid material.

Generally the static elastic coefficient of rock mass is obtained through the flat plate loading tests in the field. In this paper, the 2D discrete element code (UDEC) is selected to simulate the flat plate loading test in the jointed rockmass [8]. A group of numerical experiments, with one joint set and the two intersected joint sets of different gaps and orientations, are established to investigate the effect of joint sets on the elastic coefficient of the rock media. Some significant conclusions are drawn through the analysis of computation results.

2 Discrete element methods

In the distinct element method, a rock mass is represented as an assembly of discrete blocks. Joints are viewed as interfaces between distinct bodies (i.e., the discontinuity is treated as a boundary condition). The contact forces and displacements at the interfaces of a stressed assembly of blocks are found through a series of calculations which trace the movements of the blocks. Movements result from the propagation through the block system of disturbances caused by applied loads or body forces. This is a dynamic process in which the speed of propagation depends on the physical properties of the discrete system. The dynamic behaviour is represented numerically by a timestepping algorithm in which the size of the timestep is limited by the assumption that velocities and accelerations are constant within the timestep.

The calculations performed in the distinct element method alternate between application of a force-displacement law at all contacts and Newton's second law at all blocks. The force-displacement law is used to find contact forces from known (and fixed) displacements. Newton's second law gives the motion of the blocks resulting from the known (and fixed) forces acting on them.

2.1 Equations of Motion

The motion of an individual block is determined by the magnitude and direction of resultant out-of-balance moment and forces acting on it. Consider the one-dimensional motion of a single mass acted on by a varying force. Newton's second law of motion can be written in the form:

$$\frac{d\dot{u}}{dt} = \frac{F^{(t)}}{m} \tag{1}$$

Where $\dot{u}$ = velocity; t =time; and m = mass.

2.2 Conservation of Momentum and Energy

The distinct element method can also be shown to satisfy the conservation laws by using an alternative approach based on the use of Newton's laws of motion. The equations used in UDEC are based on the interaction of bodies by means of springs and the response of the bodies to applied forces.Consider two bodies (denoted by subscripts a and b) in contact for a period, T. By Newton's laws, a common force, F, acts in opposite directions on the two bodies, which accelerate in proportion to the forces. Combining the equations and integrating:

$$m_a \dot{u}_a^{(T)} + m_b \dot{u}_b^{(T)} = m_a \dot{u}_a^{(0)} + m_b \dot{u}_b^{(0)} \tag{2}$$

Eq. (2) indicates that the total momentum at the end of an arbitrary time period is identical to that at the beginning. Suppose a body with initial velocity v_0 is brought to a final velocity of v in a distance S

3 Computation model

To investigate the effect of the joint on the elastic coefficient of the rock media, we performed a series of computation experiments. In response to the flat plate loading test, two groups of computation models are established. One group of experiment models deals with the problems of one joint set, called Model 1 (Figure 1). Another group of tests is designed to show the effect of two interacting joint sets, called Model 2 (Figure 2-3) on the effective elastic moduli. Figure 4 indicates the loading way of the computation model, in which the two joints sets are perpendicular to each other. In order to insure the stability of the numerical results, five increment loading cycles are carried out in the numerical computation. The rock is considered as a Mohr-Coulomb material and the discontinuities in the rockmass are assumed to be Mohr-Coulomb joints. The properties of rock and joint are evaluated by the in-situ experiments, and shown respectively in the Table 1 and 2.

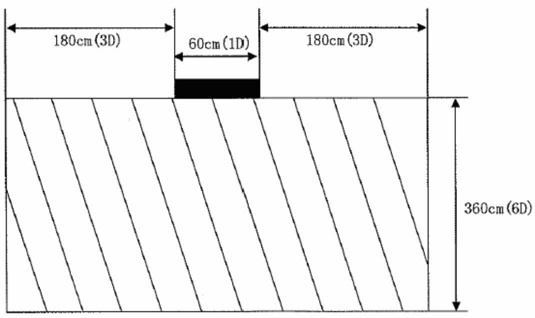

Figure 1 Geometry model for one joint set.

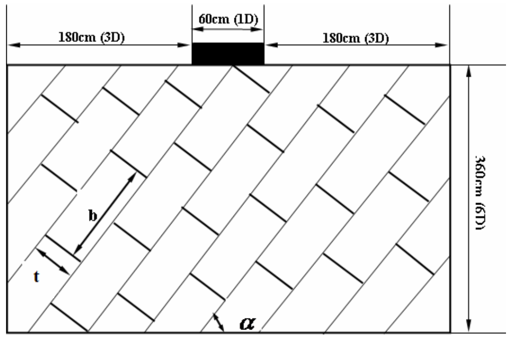

Figure 2 Geometry model for two joint sets

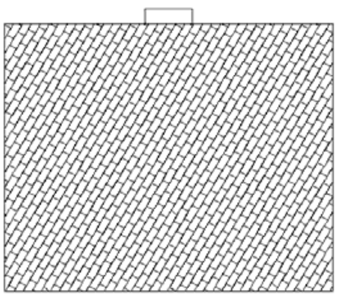

Figure 3 UDEC computation model for two joint sets (t=10, b=20, α=60º)

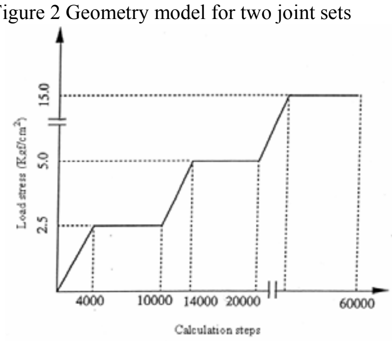

Figure 4 Loading Cycle

Table 1. Physical Parameters of Rock

Density (Kg/m3)	Young's modulus E(MPa)	Poisson's ratio	Cohesive Strength c (MPa)	Internal Friction Angle(°)
2.66×103	7.1×104	0.18	22.3	62

Table 2. Physical Parameters of Joint

Normal Stiffness (MPa)	Shear Stiffness (MPa)	Cohesive Strength c (MPa)	Internal Friction Angle(°)
3.178×104	3.22×103	0.027	35.9

The secant static elastic coefficient can be written as [7]:

$$E_s = \frac{\pi a(1-v^2)}{2}\frac{\Delta p}{\Delta \delta} \tag{3}$$

Where E_s =the static elastic coefficient (secant static elastic coefficient); Δp=increment loading stress (Pa); $\Delta\delta$=increment displacement (m); v=Poisson's ratio; α=the radius of loading plate (m). According the increment displacement and stress from the numerical computations, the static elastic coefficient of all cases is evaluated in the presence of the above empirical formula.

4 Computational results

A series of numerical computations are carried out to simulate the in-situ flat plate loading test. After executed by the simulation program, the static elastic coefficients of the test models are evaluated.

As shown in Figure 5-6, there is a strap of a larger displacement in the plot of displacement vector, which nearly parallel the joint set 1. Based on the increment displacement and stress in the computation results, the secant static elastic coefficient is calculated as shown in the Figure 7-10.

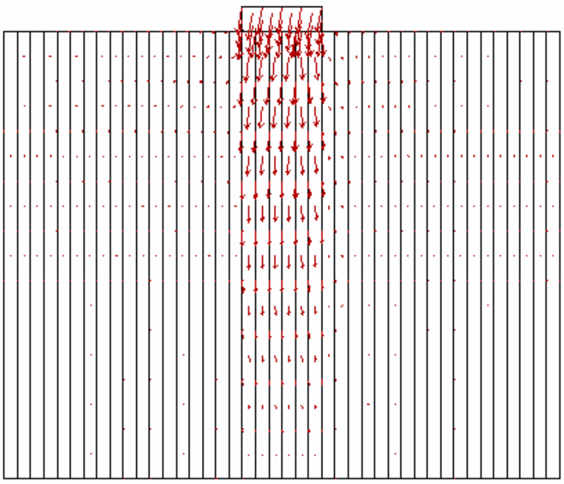

Figure 5 Displacement vector in case of the single joint set

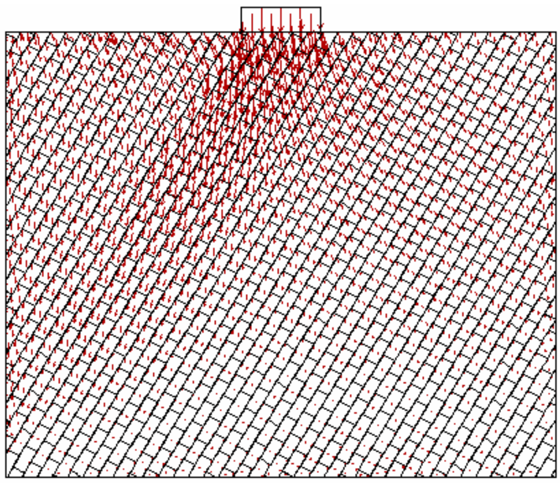

Figure 6 Displacement vector in case of two single joint sets

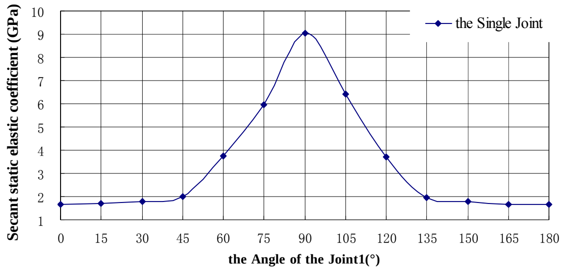

Figure 7 Secant static elastic coefficient variation with the angle of joint1 in case of single joint set

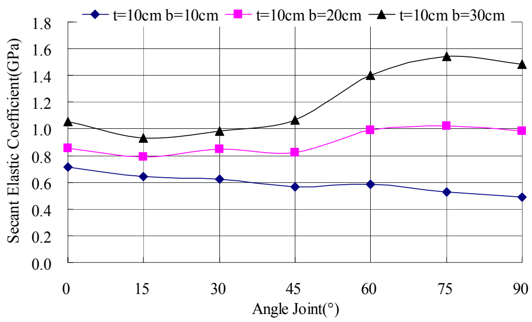

Figure 8 Secant static elastic coefficient variation with the angle of joint1 in case of the two joint sets (t=10cm)

From the Figure 7, it is known that the dip angle have a great effect on the static elastic coefficient of the test model. Comparing these results, the followings are clarified: (1) When the dip angle is 0º and 180º (α=0º and α=180º), the test model has the minimum elastic coefficient. (2) There is peak value of the elastic coefficient on the curves while α=90º. (3) There is a greater increase from α=45 º to 90 º, a less variation between 0º and 45º. (4) The mechanical deformations of the computation model mainly occur as normal and shear deformations in the joints.

In the figure 8, the curves have a complex variation tendency with an approximate shape of saddle, especially under the condition of b=20cm and 30cm, which indicate the joint set 2 has a greater impact on the variation of the elastic coefficient. In case of b=10cm, the case of α=90º has a minimum value and α=0º a maximum value. When b=20cm and 30cm, the cases of α=60º~75º have larger values and the cases of α=30º~45º have less larger values. They indicate that the normal deformations in the joints have main contributions to the vertical displacements of the flat plate model.

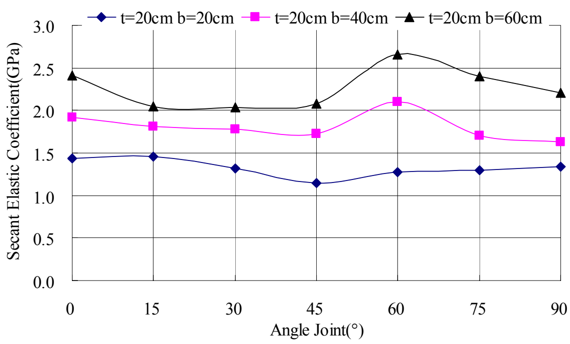

Figure 9 Secant static elastic coefficient variation with the angle of joint1 in case of two joint set (t=20cm)

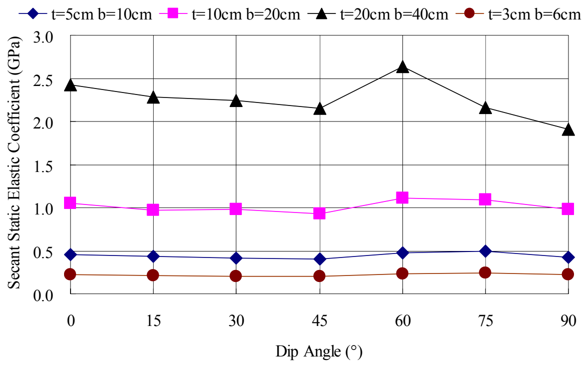

Figure 10 Secant elastic coefficient variation with the dip angle in case of b/t=2

In the figure 9-10, the curves have a more complex shape. The cases of b/t=2 and b/t=3, have the similar shapes, but under the condition of b/t=1, the curve shape is more different from that in the case of single joint set, which show that the joint set 2 of lesser gap has an more significant influence on the variation of the secant static elastic coefficient

5 Conclusions

In this paper a series of numerical computations are described with a number of obtained results. When there is a single joint set in the test model, the curve of the secant static elastic coefficient has the peak value in the case of an angle of 90°.

From the computation results with single joints and double joints, the static elastic coefficients have a large decrease compared to the joint set 2. When the dip angle is 45°~90° in the case of a single joint, the curve has a steep variation; or a mild variation for other cases. When there are two joint sets, the peak value falls between the angle of 50°~70°and the minimum value angle is between 15°~45°.

References

1. Avar, B.B., Hudyma, N. and Karakouzian, M. Porosity Dependence of the Elastic Modulus of Lithophysae-rich Tuff: Numerical and Experimental Investigations. International Journal of Rock Mechanics and Mining Sciences, 2003, (40). 919-928.
2. Jing, L. A Review of Techniques Advances and Outstanding Issues in Numerical Modelling for Rock Mechanics and Rock Engineering. International Journal of Rock Mechanics and Mining Sciences, 2003, (40). 283-353.
3. Walsh J.B. The Effect of Cracks on the Uniaxial Elastic Compression of Rocks. Journal of Geophysics Resource, 1965, (70). 399-411.
4. Budiansky, B. O'Connell RJ. Elastic Moduli of a Cracked Solid. International Journal of Solids Structure, 1976, (12). 81-97.
5. Huang, Y., Hu, K.X. and Chandra, A. A Generalized Self-consistent Method for Microcracked Solids. International Journal of Mechanics Physics Solids, 1994, (42). 1273-1291.
6. Kachanov, M. Elastic Solids with Many Cracks and Related Problems. Advance in Applied Mechanics, 1994, (30). 259-445.
7. Fares, N. Effective Stiffness of Cracked Elastic Solids. Applied Mechanics Reviews, 1992, (45). 336-345.
8. Nemat-Nasser, S. and Hori, M. Micromechanics: Overall Properties of Heterogeneous Materials. Amsterdam. Elsevier, 1993.
9. Kachanov, M. Elastic Solids with Many Cracks: A Simple Method of Analysis. International Journal of Solids Structure, 1987, (23). 23-43.

RaSiM 7(2009): Controlling Seismic Hazard and Sustainable Development of Deep Mines, C.A. Tang(ed), Rinton Press, 619-624

CELLULAR AUTOMATA MODEL TO SIMULATE ROCK THREE POINT BENDING TEST

BAO-QUN WANG[1,2] , MING-TIAN LI[1,2] and QIANG-YONG ZHANG [1]

1. The Research Center of Geotechnical Engineering

Shandong University,

Jinan, P.R.China

2. Shandong Jiaotong University

Department of civil engineering

Jinan , P.R.China

Cellular automata are mathematical models that express self-organization process of the whole system owing to nonlinear interaction among local elements inside the system by constructing simple rules. In this paper a cellular automaton model is presented to simulate rock failure. Force and displacement are taken as the basic state variables. Based on the basic mechanical laws vector updating rules are constructed, which overcomes the shortcomings of arbitrary decision of local rules and scalar variables. Based on this model fracture process of three-point-bend samples was simulated. The influences of pre-existing cracks on the fracture process of three-point-bend samples were studied. The stress-strain curves corresponding to the fracture process were attained.

1 Introduction

Three-points-bending test is using an external load to produce a moment and tensile stress at the edge of the specimen. At present, bending experiments of beam and bending experiments of disk are the popular bending tests. In the determination of fracture toughness of concrete, the three point test is the popular one because of its simple operation. From the test, the $P-\Delta$ curve, $P-CMOD$ curve and load-acoustic emission curve can be obtained. But Chun-an TANG holds that these numerical simulation works still rest on the stage of the brittle materials failure process of concrete, and in the test, concrete and etc brittle materials are looked at as uniform continuum. In this paper, the cellular automata model is put forward and the failure process of three points bend test are simulated by the model. The influence of pre-existing crack to three points bending beam is analyzed and the stress-strain curve and acoustic emission curve correspond to the failure process are obtained.

2 Cellular automata model

Cellular Automata, CA, was proposed by J. von Neuman in the 1950s. It is used to simulate the self-organization phenomena among the cellular of the biological system. And in recent years, CA is regarded as an effective method to analyze the complicated systems. It is a model to express the self-organization process of the whole system owing to nonlinear interaction among local elements inside the system by constructing simple rules. Cellular Automata are composed by cell structures, cell statements, cell neighbours, cell rules and more. It is applied extensively in hydrodynamics, computer sciences, earthquake, etc. Many useful results have been achieved.

2.1 *Cell structure*

The main thought of using cellular automata to solve rock mechanics problems is to discrete rock into cells. To simulate the deformation actually, the joint of the cells is supposed to be beams. By this hypothesis, the cells can be accepted extension, composition and bending deformation. The cell structure can be seen in Figure 1. Each square in the figure is a cell and are joint by beams. Each beam has three degrees of freedom. The deep colout area means central cell of the area.

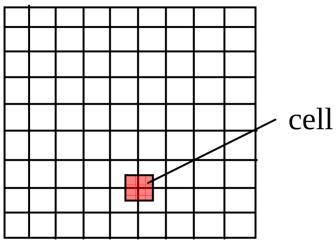

Figure 1 The schematic diagram of cell structure

2.2 *Cell statement*

Cell statement is defined as the following form.

$$\phi_i = \{\{u, v, \varphi\}, \{f_x, f_y, m\}\} \tag{1}$$

Where, u is the displacement and angle of X direction of i, v is the displacement and angle of Y direction of i, φ is the displacement and angle of Z direction of i. f_x is the external force and moment of couple of X direction of i, f_y is the external force and moment of couple of Y direction of i, m is the external force and moment of couple of Z direction of i.

2.3 *Updating rule*

Take any beam, *i* is the studied joint and it is linked with K adjacent joints, j is the j joint of the adjacent joint (in figure 2). The angle of the beam is α_j, which means the angle from X positive direction to bar ij. According to the equilibrium of the joint *i*, the following equations can be obtained,

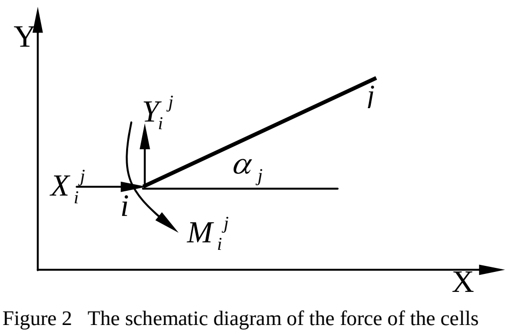

Figure 2 The schematic diagram of the force of the cells

$$\sum_{j=1}^{K} X_i^j + f_x = 0 \tag{2}$$

$$\sum_{j=1}^{K} Y_i^j + f_y = 0 \tag{3}$$

$$\sum_{j=1}^{K} M_i^j + m = 0 \tag{4}$$

Put the relation between force and displacement into equations 2, 3, 4, the updating rules can be formed.

2.4 *Strength criterion*

In this paper, maximum tensile strain criterion is used to judge the initiation of tensile damage and shown as below,

$$\varepsilon_i \geq \varepsilon_{t0} \qquad (5)$$

Where, ε_i is the strain of beam i, ε_{t0} is the strain corresponding to the uniaxial tensile strength of beam ij.

Mohr-coulomb criterion is used to judge the initiation of the shear damage of the material and shown as below,

$$F = \frac{1+\sin\theta}{1-\sin\theta}\sigma_1 - \sigma_3 \geq f_c \qquad (6)$$

Where, θ is internal friction angle, σ_1 and σ_3 is the maximum and minimum principal stress, f_c is the uniaxial compressive strength.

2.5 Damage evolution of the damaged cells

When the cells begin to damage, the deformation and strength of the cells would change. In this paper, the theory of damage mechanics is used to evaluate the deformation and strength of the failure cell. The damage variable is defined as equation 7.

$$D = 1 - \frac{\tilde{E}}{E} \qquad (7)$$

Where, E is elastic modulus of the undamaged microscopic element, $\tilde{E}$ is effective elastic modulus of the damaged microscopic element. Based on the typical test results, the damage evolution equation can be formed.

2.6 The simulation of heterogeneity of rock

Rock is a heterogeneous material. The heterogeneity is one of the most important reasons which cause the nonlinear and complicated failure process of rock. The heterogeneity of the rock can be described with the material strength statistical distribution. Generally, Weibull distribution can fit the material strength. Its shape parameters m can describe the degree of heterogeneity. The distribution is more uniform when m is bigger. The rock heterogeneity is simulated with Weibull distribution which is used to give the valuation of the elastic modulus and strength of the beam between the cells.

3 The simulation and discussion of the failure process of the three-points-bending test

3.1 Mechanical models for three- point- bending test

In this paper, the mortar and concrete sample used by Bažant to study the fracture size effect of concrete are adopted. The sample size is 203.2mm×76.2mm×38mm. The length of the crack at the centre of the beam is $a_0 = 20mm$, the relative deep of the crack is $a_0/d = 0.27$. Mechanics model is shown in Figure 3.

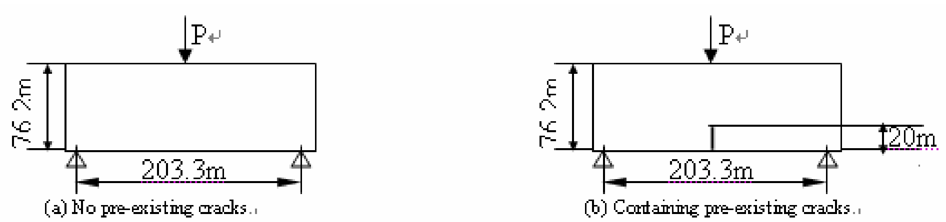

Figure 3 The mechanical models for three-point-bending test

3.2 Numerical simulation

A sample without crack and a sample with pre-exiting crack are generated. The numerical samples are shown in Figure 4. The elastic modulus, uniaxial tensile strength and uniaxial compressive strength are generated with Weibull distribution. The mean value of elastic modulus is 20GPa, the shape parameter is 3.0. The mean value of uniaxial tensile strength is 10MPa, the shape parameter is 3.0. The uniaxial compressive strength is 10 times of the uniaxial tensile strength. Displacement loading is adopted to simulate the process of three-pont-bending test.

（a）　　　　　　　　　　（b）

Figure 4 The numerical samples for the three-point-bending test

The failure process of the sample shown in figure 4(a) is shown in Figure 5 and the corresponding load-loading point displacement is shown in Figure 6.

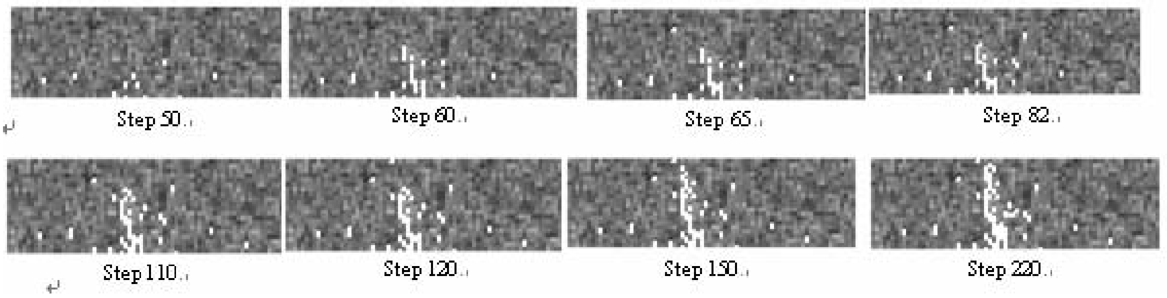

Figure 5 The failure process of the sample shown in figure 4(a)

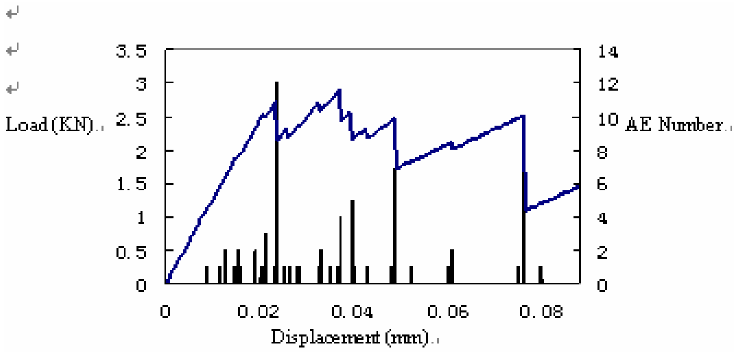

Figure 6 The load-displacement curve of the sample shown in figure 4(b)

As the shape parameter of the test sample shown in figure 4(a) is 3.0, the degree of uniform is poor. So at the beginning of the failure process the failure points distribute discretely. However in the case of the three-points-bending test, the tensile stress is in stress concentration at the middle of the beam. Therefore the crack initiates and propagates in the middle of the beam. Under the influence of rock heterogeneity and stress concentration, the crack of the sample generated, propagated and transfixed.

To compare the sample mentioned above, the sample shown in Figure 4(b) with the pre-existing crack is also simulated. The failure process of the sample is shown in Figure 7 and the corresponding load-loading point displacement is shown in Figure 7.

The sample with pre-existing crack will form main crack propagating from the tip of the pre-existing crack. The crack generation, propagation, and confluence can be seen obviously in the figure of the failure process.

Comparing with the sample which has no crack, the crack initiation and propagation is fixed and it is easy to observe in the test. The pre-existing crack has guiding role to the crack propagation.

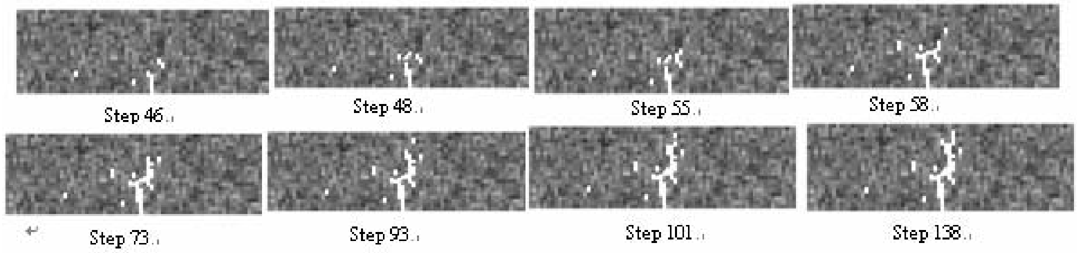

Figure 7 The failure process of the 4(d) three bending sample

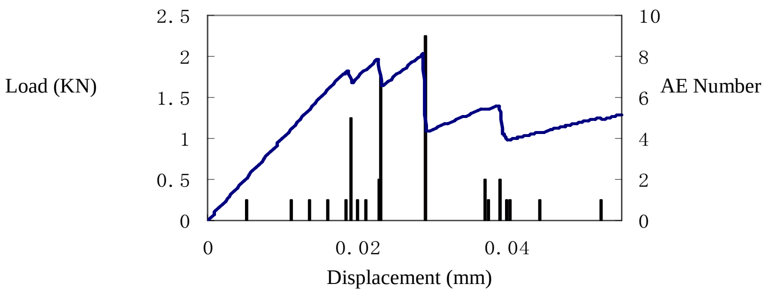

Figure 8 The displacement of load-loading point of bending of the 4(b) sample

In the process of numerical simulation, there is no shear failure. This phenomenon shows that the three points bending is mainly controlled by the tension stress.

The last failure mode of the sample with pre-existing crack for the three-points-bending test is shown in Figure 9. The failure mode which is simulated as shown in figure 7 is the same with the experimental results. It supports that the cellular automata model is practical.

Figure.9 The final failure mode of the specimen

5 Conclusion

(1) The nonlinear nature of rock is considered in cellular automata model and the characteristic of locality is fit for the simulation and treatment of local damage of rock fracture process. Therefore, the cellular automata model simulates the rock failure process, and it has broad application prospects.

(2) The three points bending failure is mainly controlled by tensile stress. The pre-existing crack has a guiding role to the crack extension.

(3) The practical test results show that the cellular automata model is practical.

References

1. Zhou, H., Feng, X.T. and Tan, Y.L. etc. Research on Physical Cellular Automata and Microscopical

Mechanism of Elasticity-Brittleness-Plasticity of Rock. Rock and Soil Mechanics. 23(6). 678－682.

2. Li, M.T., Feng, X.T. and Zhou, H. 2D Vector Cellular Automata Model for Simulating Fracture of Rock under Tensile Condition. Key Engineering Material, 2004, (261-263). 705-710.
3. Zhu, S.B. and Cai Y.E. et al. Modeling Seismicity by 3-D Cellular Automata. Acta Scientiarum Naturalium Universitatis Pekinensis, 42(2). 206-210.
4. Zhou, S.Z., Liu, M.Q. and Liang, B. etc. Engineering Journal of Wuhan University, 39(5) .35-45.

RaSiM 7(2009): Controlling Seismic Hazard and
Sustainable Development of Deep Mines,
C.A. Tang(ed), Rinton Press, 625-632

NUMERICAL ANALYSES ON THE BRITTLE FAILURE OR ROCKBURST OF ROCK MASS INDUCED BY TUNNEL EXCAVATIONS IN VICINITY OF A FAULT

WEN-HUA ZHENG, WEI-SHEN ZHU, MIN YONG, YONG LI and YAN-SHENG RUAN

Geotechnical and Structural Engineering Research Center, Shandong University

Jinan, 250061, P.R. China

The extraordinary distributions of stress and displacement were studied under the conditions of four different factors in vicinity of a fault. Some principles were obtained to predict the occurrences of brittle failures or rockburst. The test designs of orthogonal and uniform methods were adopted in this paper to calculate sixteen engineering schemes using numerical analyses and some regular results were determined. Ultimately, some typical engineering cases were analysed to study the stability of the surrounding rock masses and the possibility of the occurrence of rockburst when the excavations approach a fault.

1 Introduction

Engineering practice proves that failure and instability of rock mass often happen along discontinuities or in the vinicity of it, such as joints and faults, in other words, it has the risk of instability in vicinity of the discontinuities [1].

Some scholars have done many preliminary studies in this aspect: for example, Bieniawski (1976) qualitatively analyzed how the joints' strike and dip influence the tunnel's stability when studying the classification of jointed rock masses. Ren and Zhang studied the tunnel stability in a joints' rock mass under the condition of different tectonic stresses [2]; Zhang and Li discussed on the surrounding rock mass stability of underground caverns influenced by structural plane with different inclination angles[3]. However, due to the condition limitations of the early research, most of the conclusions were qualitative. There are seldom published quantitative results. Therefore, the abnormal stress distribution adjacent to a fault has been studied systematically, and some further research has been done about its influence on the stability of underground engineering projects. This study has great value of engineering application to ensure the safe operation and excavation of underground construction. In addition, according to a number of engineering experiences, it easily leads to rockburst or splitting failure when the excavation of tunnel is near a fault. Therefore, a tentative research will be made in this paper.

The abnormal stress and displacement near faults and influence of faults on tunnel's stress field were selected as the main simulation research targets, and according to systematic numerical simulation test, this paper studies the influences of the primary factors of fault thickness, fault dip, fault deformation modulus and lateral pressure coefficients of initial stresses. Using test design of orthogonal and uniform methods, more than 300 numerical simulations have been done with 10 different conditions, and abnormal stress distribution adjacent to a fault and its influences on stability of tunnel are studied.

2 Numerical model descriptions

There are two kinds of computational domains of surrounding rock mass, 532m × 290m (quasi three-dimensional) and 345m×550m×50m(three-dimensional). Geometric model is built by using of the FEM software ANSYS9.0. The depth of overburden rock mass is approximately 400m. A linear elastic constitutive model is utilized in this numerical simulation test to study the influences of different fault dip, lateral pressure coefficients of initial stress, fault thickness, fault deformation modulus on the stress field. Physico-mechanical parameters of surround rock mass are shown in Table 1.

According to 5 factors and 4 levels of table 2, 16 kinds of numerical simulation test schemes are derived by using test design of orthogonal and uniform methods. More than 300 numerical cases are simulated by using FLAC^{3D}.

Table 1. Physico-mechanical parameters of surrounding rock mass

Type of rock	Deformation modulus (GPa)	Poisson's ratio	Cohesion (MPa)	Friction angle (°)	Tensile strength (MPa)	Bulk Density (KN/m^3)
Surrounding rock near faults	30	0.25	1.2	45	1.5	2600
faults	0.3 1 3 7.5	0.25	0.2	25	0.2	2600

Table 2. Five factors and 4 levels of numerical test

Factor / Level	Dip of fault S1	lateral pressure coefficient S2	fault thickness S3	Young's modulus S4(GPa)	Projection of fault length in the x-axis(m)
1	30°	0.5	1	0.3	30
2	45°	1.0	3	1	40
3	60°	1.5	5	3	45
4	75°	2.5	7	7.5	48

3 Quasi three-dimensional numerical simulation analyses of the calculation results

Several representative results are selected to make a discussion. Figure1 shows the displacement contour of a case. From this figure, apparent dislocations are formed in the contour near the fault. The dominant regions of displacement changes focus on the vicinity of the fault. At the two ends of the fault, the closer to the fault, the greater displacements change. Near the middle part of the fault, the displacements also change obviously.

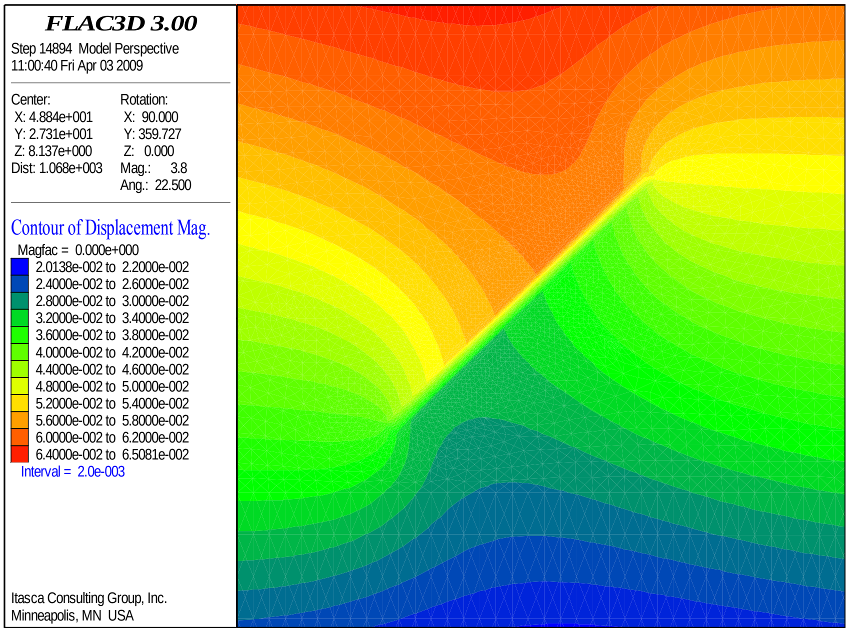

Figure1 Displacement contour near a fault

3.1 The influence of fault thickness on the in-situ stress field

Zhang and Li [4] studied that: the thickness of a fault in different geological conditions is apparently different. The method in this paper is to simulate the fault and its stuffing using the weakened mechanical elements, then the influence of a fault on in-situ stress would be studied. A quasi three-dimensional model is used in this study, and it has approximately 10390 elements and 21028 nodes.

The representative case A: S1=450, S4=0.3GPa, S2=25, S5=45m. The maximum and minimum principal stresses' difference near the end points of the faults with five different thicknesses were compared. As for the upper end of the fault (i.e. point a, x1=0), when the thickness of fault is 5m, the change is about 1.31 times of that while without fault. Within 10m away from the fault, the principal stresses' differences would fluctuate violently, firstly increase, then decline and finally go up again. When the distance is greater than 12m away from the fault, the variation tendency of all cases would go back to the initial values. In vicinity of the fault, the thicker the fault is, the greater the principal stresses' differences would be.

The variation of principal stress difference of each point in section 2 in Figure2 is shown in Figure 4. The variation principles are as following: (1) the peak values often appear closely near the fault; (2) when the fault thickness is 5m, the peak value is 1.31 times of the initial value (without fault); (3) it would decline to the initial value when X=21m, then continue to drop down until X=34m, and finally go back to the initial value when X=80m.

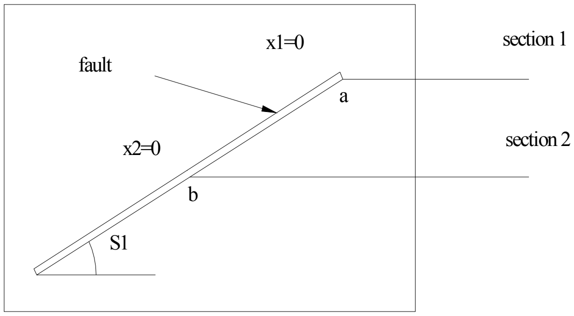

Figure 2 Research area diagram adjacent to a fault

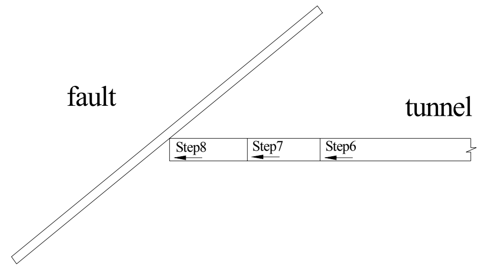

Figure 3 XY planar graph along z axis

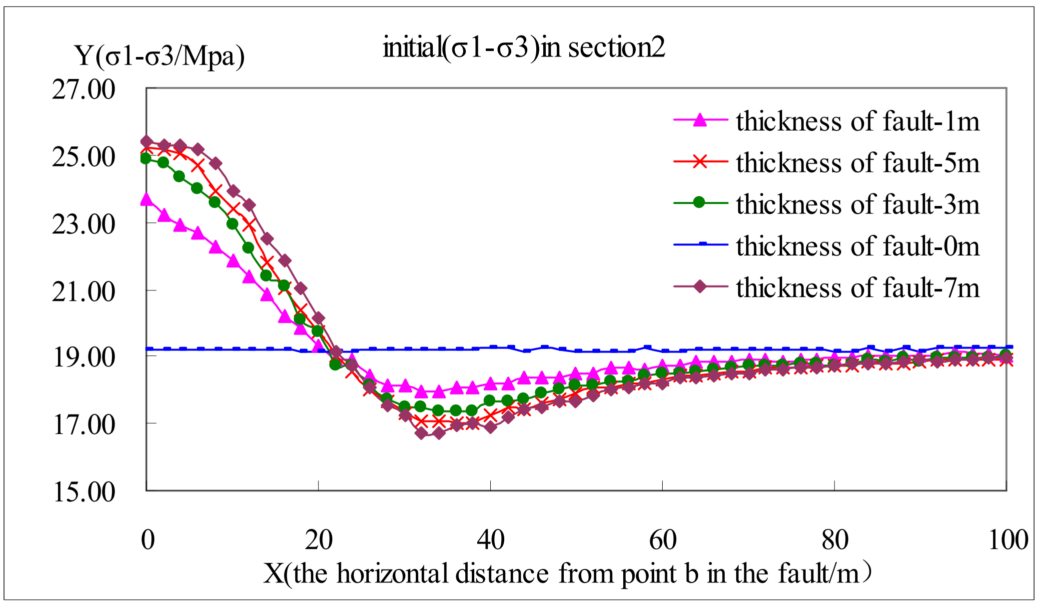

Figure 4 The initial principal stresses' difference of Section 2

3.2 The influence of deformation modulus on the Changes of stress field

The Representative case B: S1=45^0, S3=5m, S2=2.5, S5=48m, the principal stress difference of each point on section 2 of four different deformation moduli is shown in Figure5. The change is below:

The peak values often appear closely near the fault of all cases. When the deformation modulus is 0.3GPa, the peak value would be up to 1.31 times of the initial value. But when X=40m, it would drop to a smaller value and finally go up to the initial value (19.2MPa).

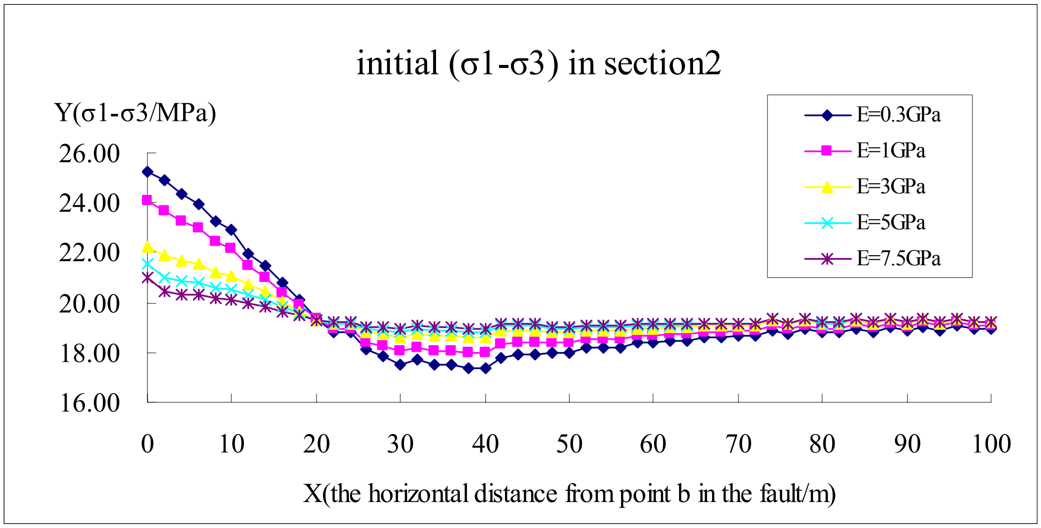

Figure 5 The initial principal stresses' difference of Section 2

3.3 The influence of lateral pressure coefficients of initial stress on the changes of in-situ stress field

According to the measured data all over the world, besides the gravity stress field, most strata of rock masses have horizontal tectonic stress. At the same time, the ratio of the maximum horizontal tectonic stress and the vertical gravity stress K_0 is generally 0.5~5.5. Therefore, the influences of the cases when K_0 is 0.5, 1.0, 1.5 and 2.5 had been studied below.

The representative case C: S1=450, S3=5m, S4=0.3GPa, S5=45m. The principal stress differences of each point on section 2 under the conditions of different lateral pressure coefficients of the in-situ stresses show below:

While K0=0.5, the principal stress difference near the fault is the smallest; when K0=1.0, the difference becomes larger and so is it when K0=1.5; in the case of K0=2.5, the difference is the largest. At the point b: the change with fault is 1.34 times of the initial value. When X2=30m, the maximum change is the smallest and it goes back to the initial value when X2=70m.

3.4 The influence of fault dip on the changes of in-situ stress field

The representative case D: S2=0.5, S3=5m, S4=0.3GPa, S5=40m, the principal stress differences of each point on section 2 under the conditions of four different dips of fault are shown as follows:

When lateral pressure coefficients K0 of in-situ stress in X direction and Z direction are equal to 0.5 and the angle of fault is 300, the shear stress is the smallest; while the dip is 750, the shear stress is the largest. When the fault angle is 300, the curve is undulate most greatly and the peak value reaches at X2=40m. The stresses' differences can be up to 7.77MPa which is 3.7 times of the initial value. Then it drops and goes back to the initial when X2=100m.

4 3D numerical simulation analyses of the calculation results about the tunnel

A true three dimensional numerical simulation model is generated, and the fault is considered to analyze the stability of tunnel surrounding rock mass. There is exactly 345m along X direction, 550m along Y direction and 50m along Z direction for the dimention of comutation model. The thickness and dip angle of the fault is 5m and 45^0 respectively. The tunnel whose diameter is 4m is excavated from the right end of the model approach to the fault, and the whole excavating length of tunnel is 70m. The number of the elements in the model is 194173, and the number of nodes is 43964.

The representative case E: S1=45, S2=0.5, S3=5m, S4=0.3GPa, S5=48m. When the buried depth of the tunnels is 400m, the tunnels are excavated along the dip direction of the fault and approach to it, and the excavation faces have different distances away from the fault, the principal stress differences along the entire tunnel crown and side wall are described as follows.

The principal stress difference has a quite large increase in the arch crown of tunnel near the fault, and then tends to be steady, and the peak value is about 1.2 times of the steady value. But the principal stress difference has a greater mutation when the horizontal distance from the fault is approximately 25m (i.e. right end of the horizontal projection of the fault's upper end).

Now the principal stress difference of several sections with the different distances from the tunnel are selected, and a verified numerical calculations of the stability of the points in these sections according to a rockburst criterion shown in Formula 4.1. Finally, the brittle fracture damage depth distributions of tunnel side walls along X axis are determined, which is shown in Figure 3 and Figure 6.

The fracture damage calculation formula is

$$\sigma_{\max} / R_c \geq 0.3 \qquad (4.1)$$

where, Rc represents the uniaxial strength.

Figure 3 shows the excavating direction (from right to left) and the locations of excavation step 6, 7 and 8. Figure 6 shows the thicknesses and distributions of rockburst incident zones after finishing excavating the steps. It's obvious that the stress concentration appears at right end of the horizontal projection of the fault's upper end (X2=20-25m). When step 6 is excavated, the rockburst incident zones may appear at the working faces and the areas near the side walls. However, when step 8 is excavated, the former rockburst incident zones would not exist.

This calculation scheme above is under the condition of K0=0.5. If K0 is greater than 1.0 or 2.0, the results may be somewhat different. Under some circumstances, the arch crowns of the tunnel would be the rockburst incident zones.

It is concluded that the stress distribution near the tunnel is greatly influenced by the fault. The detailed influences are related to the physical and geometrical parameters of the fault and the in-situ stresses characters. Therefore, the stability assessment analyses should comprehensively consider the impact factors mentioned above.

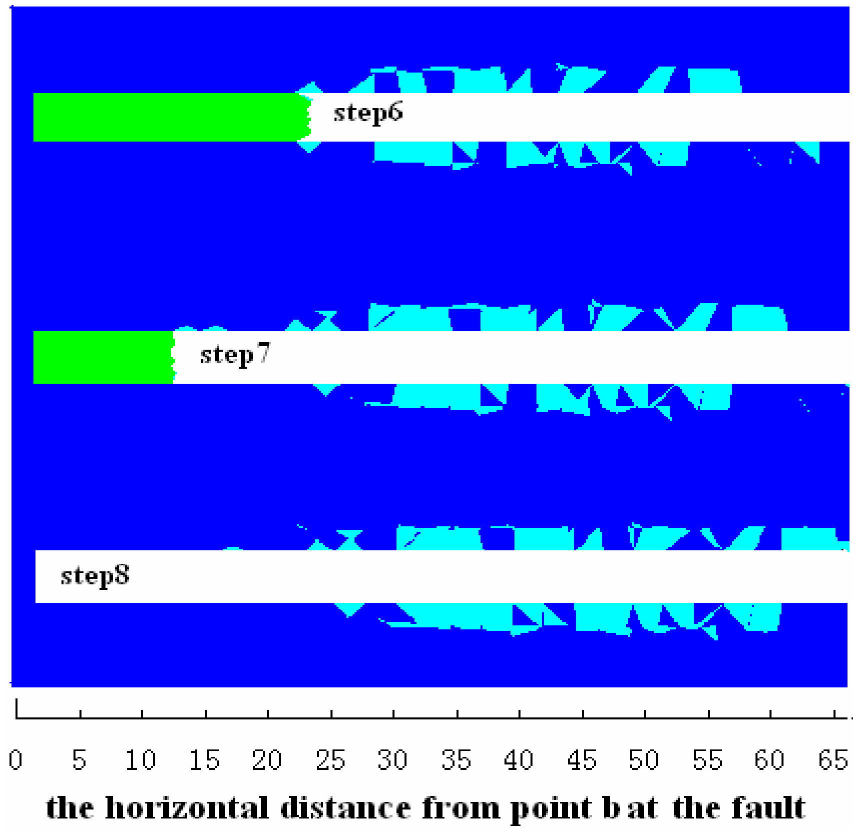

Figure 6 The rockburst incident zones when excavating the tunnel

5 Conclusions and discussions

Multiple factors are considered in this paper, and several conclusions are derived below:

(1) In the quasi 3D calculations, the principal stress difference decreases from the maximum value to the steady state rapidly near the two ends of the fault. This is different from the middle part of the fault. According to different parameters of the fault, in particular for different dip angles, the stress difference may increase or decrease under different conditions, but some sudden increment may occur some distance horizontally away from the fault. Some stress concentrations were obtained below the upper end of the fault, which is a new discovery.

(2) The principal stress difference distribution in certain part in the arch crown and side walls of the tunnel increases suddenly. All of these increase the risk of rockburst or instability.

(3) By using the rockburst failure criterion to analyze, it is shown that the distribution of fracture damage is closely related to the distribution of the principal stress difference and rockburst is also most likely to occur in these areas below the upper end of the fault.

Acknowledgements

This work was financially supported by Natural Science Foundation of P. R. China (No. 90510019, 59939190, and 50579033) and National Research Item of 973 (2002CB412705).

References

1. Jiang, J.G. Stability of joint rock tunnel at different structural stresses. Journal of Southwest Jiaotong University, 1982. (in Chinese)
2. Ren, D.H. and Zhang, P. Different dip structural planes influence cavern’s stability. Journal of China Coal Society, 1988. (in Chinese)
3. Zhang, Z.Q. and LI, N. Influence of weak interbed distribution on stability of underground openings [J]. Chinese Journal of Rock Mechanics and Engineering, 2005. (in Chinese)
4. Zhu, W.S., Ruan, Y.S. and Li, X.J. Abnormal Stress Distribution Adjacent to a Fault and It's Influence on Stability of Tunnel. Chinese Journal of Underground Space and Engineering, 2008. (in Chinese)

RaSiM 7(2009): Controlling Seismic Hazard and
Sustainable Development of Deep Mines,
C.A. Tang(ed), Rinton Press, 633-638

ACTIVE MULTIDIMENSIONAL CONTROL OF RAPID DEFORMATION INSTABILITY OF A COAL ROADWAY IN A DEEP MINE

XIAO-KANG ZHANG, SHENG-RONG XIE and SHOU-BAO ZHANG,

School of Civil and Environment Engineering, University of Science and Technology Beijing

Beijing, 100083, P.R. China

FU-LIAN HE

College of Resources & Safety Engineering, China University of Mining & Technology (Beijing)

Beijing 100083, P.R. China

KAI-QING LI

School of Civil and Environment Engineering, University of Science and Technology Beijing

Beijing, 100083, P.R. China

In this paper, based on the rapid deformation instability characteristics and active control principles of the surrounding rocks at a coal roadway in Xingdong mine, the displacement and stress fields of the surrounding rocks are calculated by using FLAC, and the main factors leading to deforming and failing of the surrounding rocks are analyzed. Moreover, according to new support principles, the combined cable truss support system is studied, which can provide compressive stress support in horizontal and plumb directions, and the responding support parameters are optimized and determined. The field measurement results show that the cable truss support system works reliably to prevent the dangerous deformation and roof caving accident.

1 Introduction

It is well-known that the control of surrounding rocks at coal roadways with large spans and high ground pressure in mines deep as 1000 m have become a key and difficult problem in the international mining engineering field[1, 2, 3]. In the Xingdong coal mine, the mining level has reached the depth of 1200 m, the roadway span was large, both roadway sides were comprised of coal body with many joints and fissures, and the fragmenting area was large. The traditional single bolt and cable support had point contact with the surrounding rock face, so the roadway roof was not under the compound compressive stress state and its strength could not be improved. The rapid deformation of the surrounding rocks at a coal roadway occurred after roadway driving, the convergence between both roadway sides was more than 1 m in one month, and severe roof caving and coal side collapses appeared many times.

The productive geological conditions are complicated and diversified, the basic information including the failure characteristics is not mastered completely, and the interaction mechanism between the surrounding rocks and the supporting structures is not grasped scientifically and adequately, especially to the roadway at the depth of over 1000 m. For the roadway in a coal mine, the deeper the position is, the larger the ground stress and the responding plastic failure are, which makes it more difficult to keep this kind of roadway stable. The traditional supporting method of the single bolt and cable is not able to adapt to the support and control of roadways with high ground stress and large deformation. Based on the deformation instable characteristics of roadways and the active control theory, the technique of active multidimensional control was put forth to solve this problem [5].

2 Theory of Active Multidimensional Control

Based on the active control of high stress roadways in deep coal mines and the multidimensional stress strengthening principle of rock mass and the methods of engineering mechanics and structure design, the active multidimensional control technique was developed. The control principle is shown in figure 1. It is a truss cable system that could provide compressive stress support in horizontal and plumb directions to the roof rocks, so the intensity of roof rocks is enhanced; the roadway control level is improved [4, 6, 7]. Compared with traditional support characteristics, the five advantages of this new technique are as follows:

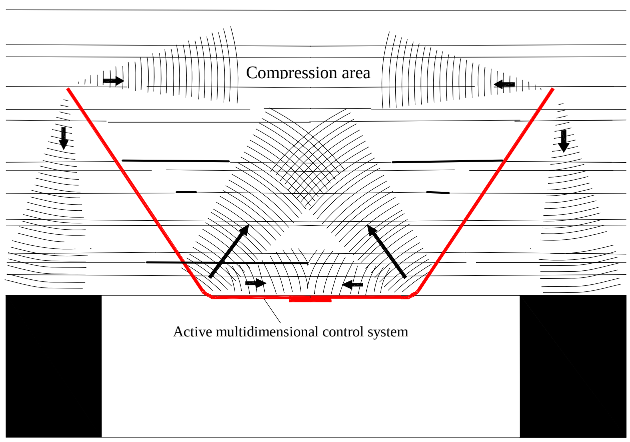

Figure 1 Active multidimensional control system

(1) It can provide compressive stress support in horizontal and plumb directions to the control rocks. If the deformation of roof increases, the support stress will become higher. The new method could reduce the highest tensile stress in the roof rock of roadways' middle areas, and it could make the controlled rock in a multidimensional stress state, so the intensity and ability of anti-deformation of controlled rock are improved [8].

(2) The truss cable has higher anti-shear ability than rock bolt, the truss cable goes through the high shear stress area of the rock beam, and cable, rock beam and rock bolt bear the shear stress together. Then the roof's capability of resisting the shear stress is enhanced.

(3) The cable of new technique has line contact with surrounding rock. The load in the cable is continuous and higher pre-stress could be applied to the cable. Therefore the cable truss control range is larger, so the soft and crushing roof has better stress state.

(4) Anchor points of the new support system are in the three-dimensional compression rock which is over both roadway sides. Those points are not affected by roof separation and deformation, and become the stable base for the new system to provide higher supporting force.

3 Application of Active Multidimensional Control

3.1 Analysis on Existing Problems

In the process of downhill development in the second level in Xingdong mine, the traditional support methods and experiences were referred, and the single bolts and cables were used to support the roadway. Because the depth of the coal seam was over 1000 m, many problems of roadway control happened. Many practical results showed that the roadways which had been droved exist the phenomena of rapid deformation generally, and severe roof caving and coal side collapsing appeared many times. So it will be very difficult and it is a challenging job to drive the downhill development in the second level. The difficulties are as follows.

(1) The position of the roadway is deeper and the ground stress is higher. The rapid deformation of surrounding rocks at a coal roadway occurred after roadway driving, the convergence between both roadway sides was more than 1 m in one month, and severe roof caving and coal side collapsing appeared many times.

(2) Both roadway sides were coal body with many joints and fissures. The additional load caused by the depth increment is transferred to the both roadway sides, so the stress in the roadway sides rises rapidly, which makes the failure area larger in both sides.

(3) In the original support scheme, the cable in the roof is single and plumb, so it could not provide the horizontal stress to the roof, and it also could not produce the horizontal force when the roof is bending to deformation. So the roof could not form a structure at the horizontal direction.

3.2 Scheme of Active Multidimensional Control

Based on the analysis of the existing problems and the theory of active multidimensional control technique, the support schemes of the downhill roadway in the second level were simulated and studied by using software FLAC.

The width of downhill roadway is 5.0m, and the height is 2.8m, the buried depth is about 1000m, the exploration object is 1# coal, and its average thickness is 3.50m. The geological condition shows that the immediate roof is silt-sandy mudstone, its thickness 1.5m; top of it is siltstone, and then is fine sandstone, thickness 3.0m. The direct bottom is fine sandstone, thickness 2.1m.

Figure 2 is the calculation model of downhill surrounding rocks.

The range of the model is width*height=80*60m. The vertical compress stress-24.5MPa was applied on upper boundary. The two side boundaries of the model were fixed level orientation, and bottom boundary was fixed vertical orientation. The constitutive relationship of the surrounding rock is Mohr-Coulomb model.

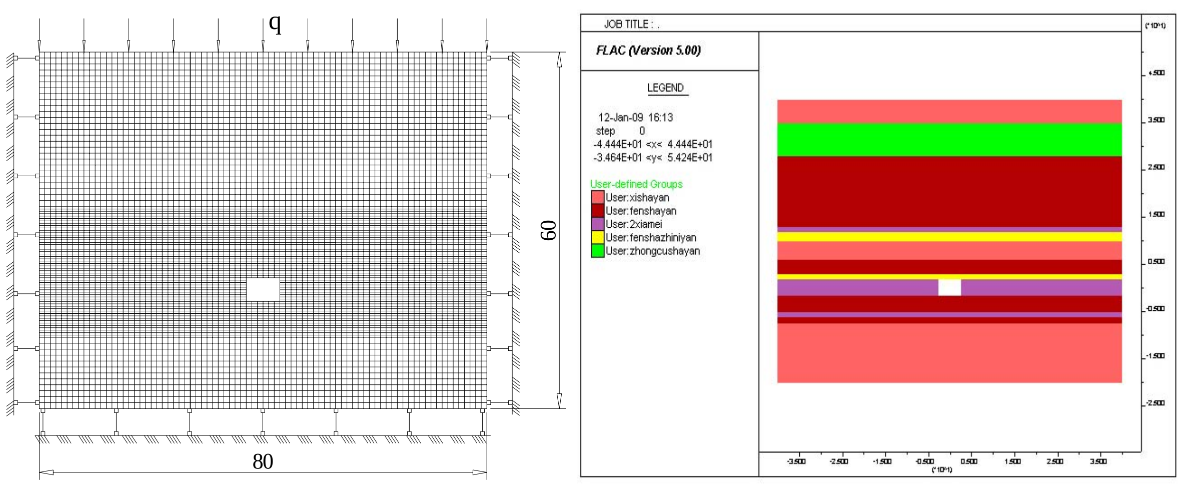

Figure 2 the calculation model of downhill surrounding rock

The simulated schemes with different truss cable parameters are outlined in Table 1. The roadway control effects were analyzed, and the simulated results with different truss cable length are shown in Figure 3. According to the theory of active multidimensional control technique used to the coal roadways with high ground stress in deep mines, compared with the numerical simulated results, the designed scheme adapted to the downhill in the second level in Xingdong mine is shown in Figure 4. The detailed parameters are below: the inclined angle, 70°; the cable length in the cable borehole, 8m; distance between side and cable borehole, 1.3m; distance between every two adjacent truss cables, 0.8m.

Table 1 The Simulated Scheme

Inclined angle of cable	simulated scheme	Length of cable	simulated scheme	distance between side and cable borehole	simulated scheme
40°	1—1	6m	2—1	1.1 m	3—1
50°	1—2	7m	2—2	1.3m	3—2
60°	1—3	8m	2—3	1.5m	3—3
70°	1—4	10m	2—4	1.7m	3—4
80°	1—5				

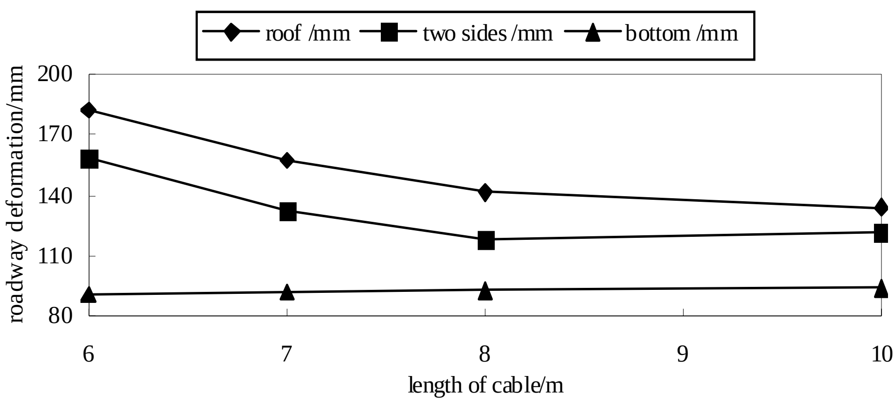

Figure 3 Results when length of cable is different

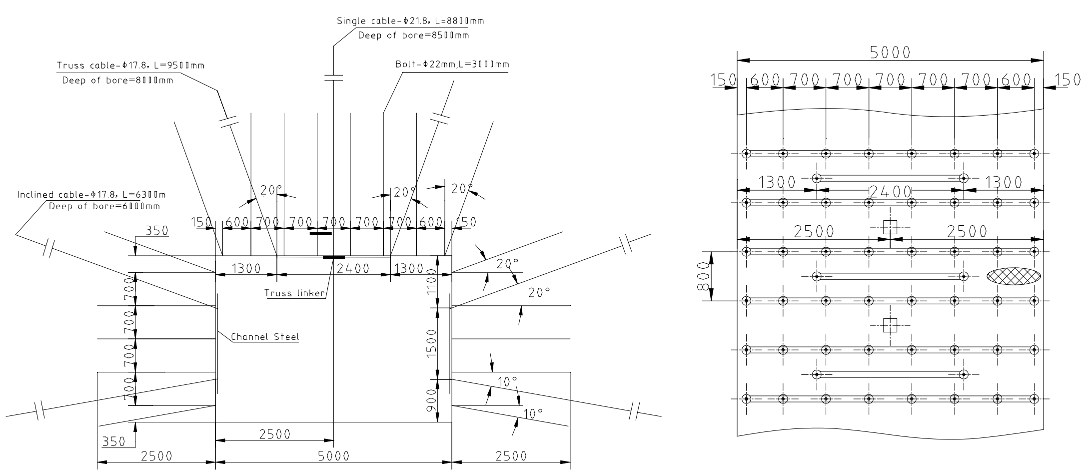

Figure 4 Support scheme to downhill in the second level

Figure 5 is parts of simulated results with the new scheme. The left one is the plasticity indicator figure, and the right one is figure of YY-stress contours.

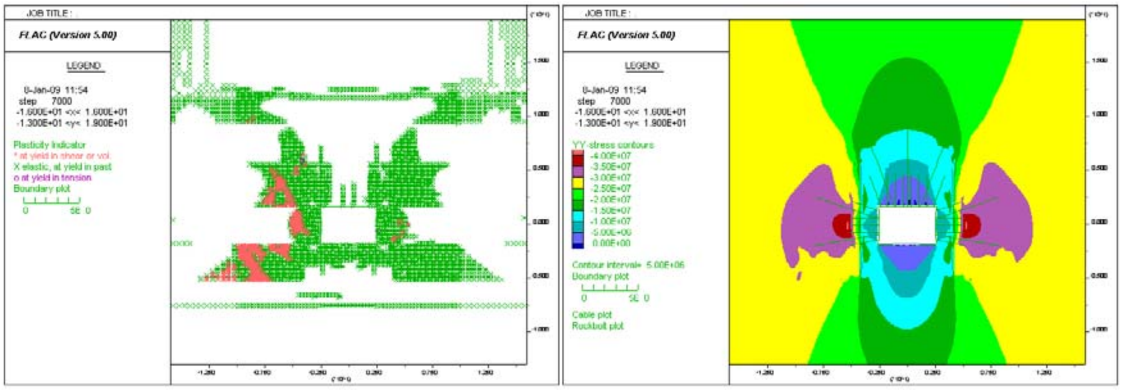

Figure 5 Simulated results with the new scheme

3.3 Measured Results in Situ

The new active multidimensional control scheme was applied in the downhill roadway in the second level, and the roadway displacement was measured and recorded. Figure 6 shows the changing trend of the roadway roof and coal side displacement. During the first month, the measured results show that the maximum roof sagging is 156mm, and convergence between both roadway sides is 205mm. After one month, the deformation rate becomes smaller, and the roadway keeps stable. The engineering practice proves that the new support system worked reliably and prevented the dangerous deformation and roof caving accident.

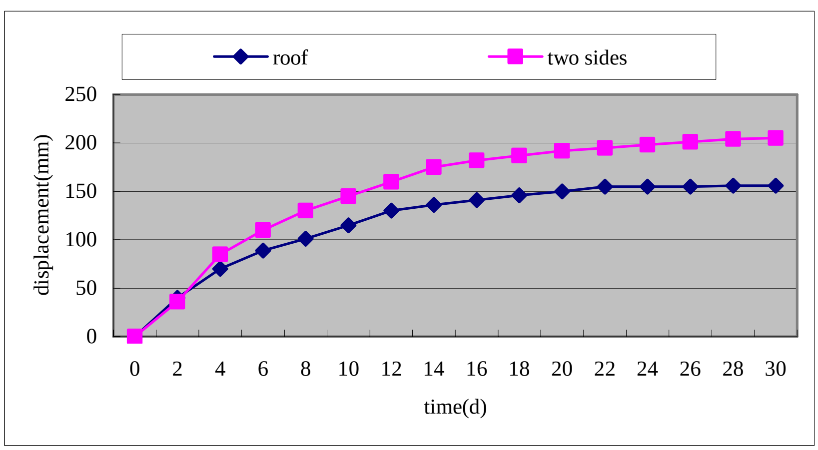

Figure 6 Chart of displacement measured at the downhill roadway

4 Conclusions

The new active multidimensional control technique is a type of control system which can provide compressive stress support in horizontal and plumb directions to the control rocks synchronously. Anchor points of the new support system are in the three-dimensional compression rock which is over both roadway sides. Those points are not affected by roof separation and deformation, and become the stable base for the new system to provide higher supporting force. The new designed active support scheme was formed by analyzing existing problems and using numerical simulation methods adapted to the experimental roadway. The field measurement results showed that the cable truss support system worked reliably and prevented the dangerous deformation and roof caving accident; the final roadway cost fell, and the total benefits rose.

Acknowledgements

The authors wish to acknowledge the Scientific Research Foundation for the Returned Overseas Chinese Scholars under grant No. 2007-1108, and the Teaching and Research Award Fund for Outstanding Young Teachers in Higher Education Institutions of State Education Ministry, People's Republic of China.

References

1. Hou, C.J and Guo, H.L. Orientation of Technical Development of Rock Bolting in In-seam Gateways in China[J]. Journal of China Coal Society, 21(2), 1996. 113-118.
2. Tang, B.Y. and Mitri Hani. Analysis of Roof and Cable Bolt Loads in Gateways. Proceedings in Mining Science and Safety Technology, 2002. 565-571.
3. Zhang, B.S., Kang, L.X. and Yang, S.S. Numerical Simulation on Roof Separation and Deformation of Full Seam Roadway with Stratified Roof and Large Section. Journal of Mining & Safety Engineering, 23(3), 2006. 264- 267.
4. Zhao, H.L., Yao, J.M., He, F.L., et al. Application of Pre-stress Truss Cable in Large Cross Section Coal Roadway. Journal of China Coal Society, 32(10), 2007. 1061-1065.
5. Zhang, S.B., He, F.L. and Xie, S.R. Study on Support Mechanism of Pre-stressed Truss Cable and Its Application. Journal of Coal Science & Engineering, 13(4), 2007. 500-502.
6. Zhang, S.B., He, F.L. and Xie, S.R. Study and Application on Compound Active Pre-stressed Support System. Progress in Safety Science and Technology VII . 2478-2481，(Beijing, 2008).
7. Zhang, Y.G., Xie, K.H., He, F.L., et al. Study on the Bolt-mesh-anchor Surrounding Mechanism of a Roadway in a Soft and Thick Rock Seam. Bulletin of Science and Technology, 21(2), 2005. 157-165.
8. Zhang, Y.G., Xie, K.H., He, F.L., et al. Study on Surrounding Rock Stability of Working Face Supported by Bolt-mesh-anchor in Soft and Thick Coal Seam. Chinese Journal of Rock Mechanics and Engineering, 23(19), 2004. 3298-3304.

RaSiM 7(2009): Controlling Seismic Hazard and
Sustainable Development of Deep Mines,
C.A. Tang(ed), Rinton Press, 639-644

NUMERICAL STUDY OF ROADWAY FAULT IMPACT GROUND PRESSURE TENDENTIOUSNESS OF LAOHUTAI COAL MINE

YAN-BO ZHANG, ZHI-QIANG KANG and FU-PING LI

College of Resources and Environment, Hebei Polytechnic University, Tangshan 063009, P.R. China

HeBei Province Key Laboratory of Mining Development and Safety Technique, Tangshan 063009, P.R. China

Fault impact ground pressure is one sort of dynamic phenomena of fault relatively disturbed and elasticity strain energy rapidly released caused by exploitation. In order to investigate the mechanism of deep roadway fault impact ground pressure, based on the impact ground problem of Laohutai coal mine, numerical study on deep roadway fault impact ground pressure problem were carried out. The effects of the change of fault stress and strain during cut process on roadway in distribution excavation were simulated. The numerical results show that deep rock underground ison the state of nature stress before mining, however the nature stress state is destroyed after excavation, which results in the stress redistribution in roadway. It is possible to cuase the stress concentration of surrounding rock.. The stress at fault increases with the enlargement of excavation range underground. With the concentration of stress, when the coal mine amounts to the limit intensity the elasticity energy accumulated is released by ejection. As a result, fault impact ground pressure is arisen. Finally, forecast and prevention measures on fault impact ground pressure is put forward through the mechanism and characteristic study on Laohutai mine fault impact ground pressure.

1 Introduction

Rock burst is commonly referred to as nonlinear dynamics phenomena that happen in mine alleys and coal rock masses around the mining area. It happens due to the sudden release of deformation energy, and it has the features of abruptness and rapid fieriness which are some of the biggest disasters in a coal mine. When rock burst happens, wall rock releases energy and coal rock is destroyed suddenly which leads to hurricanes, caving sides, bracket breaks, laneway blinding, ground shakes, building damage and personnel casualty. The energy it radiances is 10-5J at the exiguity crack of coal rock. This measure corresponds to -6~5 level on the Richter scale. The first rock burst in the world happened in the south Stanford coalfield of Britain in 1738. Since then it has happened in more than 20 countries including South Africa, Germany, Britain and Russian [1, 2,]. In our country it happened at Fushun Shengli mine in 1933. It happened at 6 mines in 1960, and the number had reached 58 in 1990 and more then 100 in recent years. Most mines in our country are built in 1950s or 1960s. As time goes by, these mines have come to the moment of deep exploitation. This problem has become more and more serious [3].

At present, the most important and valuable sort is according to the fontal physics character of rock burst. It is divided into three sorts, the first is pressure bump rock burst which mainly refers to under the action of elevation stress, coal wedge and rock generate explosive destruction; the second is roof breakdown rock burst which refers to the thick and hard aged roof on the ledge hanging out in large areas, when it reaches to a certain span, breakdown happens. It brings concussive destruction to frontage coal mass. Meanwhile, it creates bow waves which leads to the instantaneous destruction of jamb in limit stress. The third sort is tectonic rock burst which refers to the action of tectonic stress coal rock mass suffering a sudden buckling concussion. Tectonic rock burst is the most important rock burst form recognized by the researchers [4, 5, 6].

Fault rock burst belongs to tectonic rock burst. It also named mine shake which refers to the phenomena of the sudden relative movement of fault that lead to the fierce release of energy due to mining action. The depth is generally 800～1000m and the earthquake magnitude is 3~4 level. The shake time is long, concussion number is large, the frequency is low, stress wave carries large amount of energy and it arises strong surface wave when it reaches ground. Large amount of energy and high level of earthquake magnitude are the main features. The research on fault rock burst, engineering memoir and theory is further than that on experimentation ［7].

2 The mechanism research on fault rock burst

In recently years, many people carry out profound research on the cause and mechanism of fault rock burst from all aspects.

(1) Aspect of stress concentration

Stress concentration of geology tectonic is the main cause of fault rock burst. Mining leads to the stress concentration of fault. When come into fault, it leads to the instant release of stress concentration of super rock stratum, especially the sudden charge of thickness and rake angle of the coal bed, which causes the superposition of tectonic stress. In this condition fault rock burst happens.

(2) Aspect of energy concentration

When there is fault around the working face, the elastic energy resilience accumulated in the coal mass can not be released and it accumulates in the fault. At this time once the support coal or the coal on one side of the fault is mined, the mechanical equilibrium is destroyed. Then the accumulated energy is released causing fault rock burst.

(3) Aspect of mine depth

The direct cause of fault rock burst is the mining of coal bed. The increase in stress caused by mining leads to fault rock burst Engineering excavation decreases the positive stress of fault surface, then the rub resistance in the fault surface decreases causing fault part sudden movement, at last fault rock burst comes into being. Due to the positive stress is caused by the deadweight of rock (neglect of tectonic stress), only when mining depth reaches to a certain degree, fault rock burst can happen.

(4) Aspect of the distance from laneway to fault

The number of fault rock burst in laneway depends on the distance between laneway and fault: fault incidence can be fixed at 30m, the nearer, the higher fault rock burst probability is; the place of fault rock burst is different between hanger and footwall, the probability of hanger is higher.

(5) Others

When do research on mechanism and happen rule, we should regard fault and wall rock as a whole system. For example, fault rock burst can be looked on as a distortion buckling problem of fault zone medium and wall rock under mining induction [8, 9].

3 The characteristics and infl uence factors of Laohutai mine fault rock burst

Laohutai mine field is located in the south of Fushun rural, the middle part of Fushun mine. West strip mine is in the west, Longfeng mine in the east, coal bed outcrop in the south and F1 F8 fault in the north. It measures 4.95km from east to west and 2.5km from south to north. The area is about 10 km2 .

It takes the method of the combination of slope mine and pothole and stage level big alley opening. The first due form level is -225m and it has stoped -225m、-330m、-430m、-580m early or late. Current mining level is between -730m and -830m, stoping sect height is 50m and stoping height mark is -820m. Now the eastern, middle and western parts of the mine are mined at the same time. The method of coal cutting is colligation mechanization and the planed capacity is 3000000t per year.

Tectonic stress field is not only the force of lithosphere tectonic movement and break action, but an important part of area stress condition in the stratum. Under the influence of tectonic stress field, new association forms, meanwhile it takes an important role in the formulation of all kinds of dynamical phenomena. Tectonic stress is the main force factor of rock burst.

Laohutai mine lies in the syncline middle part of Fushun coal field and it,s eastern part has the syncline structure in the east and west direction and western part in south and north direction. It has fourteen big faults. From the aspect of tectonic condition Fushun coal field lies in the intersection of weft sense tectonic zone and Cathaysoid tectonic zone, especially the fault of F1 and F1a which is the main tectonic condition factor in the control area. Large scale rock burst in the diggings is controlled by fault and tectonic characteristics, space position and their relationships. From the aspect of Laohutai mine itself, fourteen large faults and the surrounding anticline structure and sub-first grade break structure are the main causes of rock burst and also the place where rock burst happens frequently.(especially high shake level)

4 Simulate experiment on the fault rock burst of Laohutai mine coal bed laneway

Sudden glide of coal rock mass fault when digging is close to faults is called fault rock burst or mine shake. Theoretical analysis and finite element simulation result indicate that the main influence of mining on fault is to increase shearing strength. So we can simulate the influence of mining on fault rock burst by increasing shearing strength in the lab. Under different pressure, we can carry out research on the concussion glide of fault hanger and footwall along with the increasing shearing strength.

Sudden fault burst happens when the positive stress reaches 30kN and the shearing force reaches 31kN. The movement of hanger and footwall causes big noise, heavy movement of experimental equipment and decrease of shearing force. The fault rock burst happens when the positive stress is 37kN or 48kN. Throughout experiment we find that only when the positive stress reaches to a certain number can fault burst happen. For example, when positive stress is below 16kN, only stable movement occurs not burst. Actually, the positive stress of fault is caused by the deadweight of overburden. This explains why fault rock burst happens only when digging coal bed reaches to a certain degree. Besides, there is possibility of burst once the fault has suffered burst, but shake level is low.

5 Numerical simulation of Laohutai mine coal bed laneway fault rock burst

For the sake of further analysis on the influence of Laohutai mine coal bed laneway fault rock burst, ANSYS finite element numerical mode of fault rock burst is founded. The happen mechanism and rock damage condition are analyzed by numerical modeling so that we can forecast and prevent fault rock burst.

5.1 The three-dimensional model construct of coal bed laneway

Associate with the produce, make three-dimensional finite element calculation mode.

Calculation mode shows the laneway 700m below Laohutai along with a fault in the direction of laneway further details are as follows:

Laneway parameter: cross-section specs: width×height is 4×3m;

Coal bed: coal bed obliquity is almost level; plane thick is 4.0m;

Fault: fault, laneway and coal bed stretch in the same direction. The angle between fault and coal bed is 60°;

Wall rock: predigest model, supposing wall rocks are all argillaceous sandstone.

Boundary conditions adopt the following assumption:

The model size: 50×40×60m；The bottom laneway supports the gravity of the above 700m rocks; The fixation around laneway; Laneway has acting force towards wall rock because of shoring; Rub force exists at fault.

5.2 Calculation model of the rock mechanics parameter

All data summed up, we can gain the mechanics parameter about coal bed and wall rock (table 1):

Table 1. Table of the mechanic parameter

Material	Young"s modulus/MPa	Poisson"s ratio	Density kg/m3	Cohesion force MPa	friction
Coal body	1200	0.26	1300	1.9	33°
Wall rock	3400	0.30	2100	1.25	35°

5.3 The determination of boundary load

1 Overburden rock gravity and wall rock stress: Supposing model can support the gravity of 700m rock

2 Anchoring force: Assuming the anchoring force of anchor arm to roof wall rock is 4 MPa, and force to either side is 4 MPa.

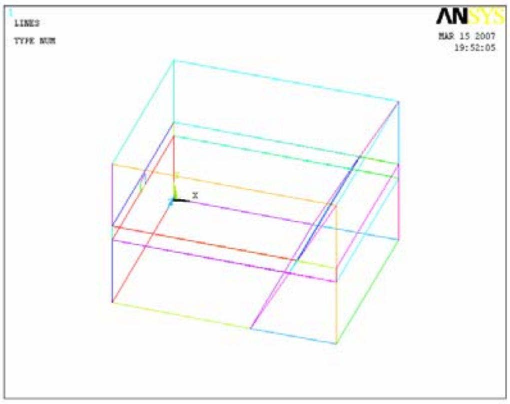

Figure 1 model of unexcavation

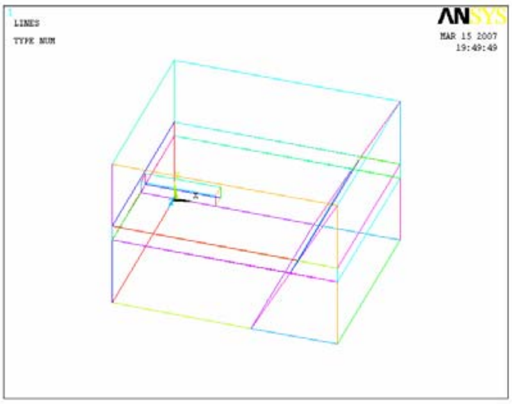

Figure 2 model of the 1st excavating

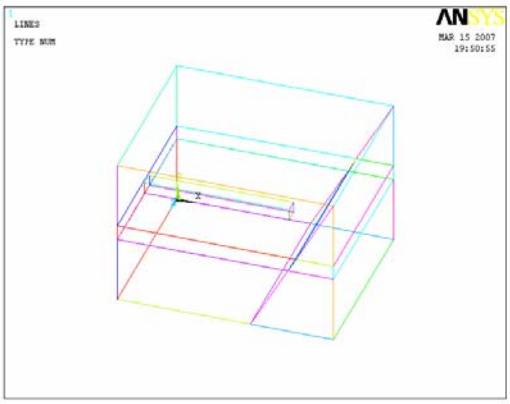

Figure 3 model of the 2nd excavating

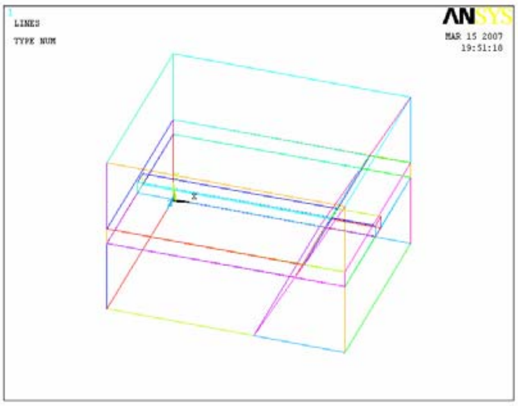

Figure 4 model of the 3rd excavating

3 Rub force: Rub force exists in the fault and the friction is 0.1.

5.4 The three-dimensional finite element simulation of laneway rock burst

The article simulates the influence of fault stress which appears during excavation process and the change of strain, through distributing excavation. The process is divided into three excavations. The model is 60m, simulation analysis is carried out every 20m. The excavation process is as fig1~4 in ANSYS:

5.5 Analyzing the result of laneway rock burst three-dimensional finite element

We can research the happen mechanism of fault rock burst according to the changes of stress and strain in the fault and laneway when the research object plumbs to the direction of fault and passes the fault.

The displacement of laneway and fault and the stress, got from steps of the numerical simulation, are as table 2.

Table 2. Table of stress and distortion

Process	Stress（Pa）	Strain（m）
Before the excavation	0.23×106	0.003
After the first excavation	2.15×106	0.031
After the second excavation	2.69×106	0.033
After the third excavation	3.4×106	0.038

Before the excavation, the rock mass near the fault will have a little strain which is 0.003m as a result of nature action. The distortion is delicacy. After the first excavation, the stress and strain of wall rock on either side of laneway are distributed again and it is stronger near the laneway and fault. By simulation we find that the biggest strain around the laneway is 0.031m.

After the second excavation, the stress near the laneway and fault is stronger than the first time, from 1.25×106MPa to 1.28×106MPa. The biggest strain near the laneway extends to 0.033m.

When the third excavation gets across fault, strong stress gathers around the laneway especially the top which reaches 3.4×106MPa and is a bigger addition than the second time. The biggest strain around the laneway is 0.038m.

The results of the numerical simulation show that before excavation the rock underground is in natural stress but after the excavation the natural stress is destroyed, causing the redistribution and gather of stress. As the mining area extends or moves towards the fault, the stress near the fault is stronger and is gathering. When it reaches to the limit intension, the accumulated elasticity energy is released by way of belch, causing fault rock burst. So laneway excavation forms the prerequisite of fault rock burst.

6 Conclusion

Rock burst has a hysteretic nature, but during the long time of inoculation, there is a change from slow to urgent, which causes rock burst. Inducing factor can expedite the process. In the process of tunnelling, the parameter in the coal rock changes. Analyzing the change and coming up with proper discrimination method provides reference to further defence measures.

Using finite element ANSYS program, this article analyzes the strain and stress distribution when Laohutai mine laneway rock burst happens. The numerical value results show that the stress and movement around the burst are stronger than other place at the same time and other time at the same place. So it is proper to use this analysis for the rock burst forecasting in the process of laneway tunnelling.

We come up with some policies against fault rock burst by calculating the numerical modelling of deep laneway.

(1) As for fault rock burst we can avoid fault movement and prevent rock burst by mining far away from the fault or founding coal wedge.

(2) By taking measures with middle and small faults we can enlarge the angle between the fault surface and working surface, so that we can reduce the uncover area of the fault in the direction of the working surface.

(3) As for the big fault, enlarging the release space of tectonic stress and ingenerating the coal bed to unchain the restriction action of gravity can release tectonic stress in a short time.

Acknowledgements

The authors wish to acknowledge the funding support from HeBei Province Natural Foundation (No E2008000410) and HeBei Province Education Office of China (No 2007454).At the same time, acknowledge the laboratory support from The HeBei Province Key Laboratory of Mining Development and Safety Technique.

References

1. Mroz, Z. and Nawrocki, P. Deformation and stability of an elasto-plastic softening pillar. Rock Mechanics and Rock Engineering , 1989. 69-108.
2. Pan, Y.S. ,Zhang, M.T. and Xu, B.Y. .The analysis of rockburst in coalmine .Journal of Coal Science and Engineering, 1996. 32-38.
3. Pan, Y.S., Li, Z.H. and Zhang, M.T. Distribution, type, mechanism and prevention of rockbrust in China[J]. Chinese Journal of Rock Mechanics and Engineering, 2003, 22(11). 1844-1851.
4. Qi, Q.X., Chen, S.B., Wang, H.X., Mao, D.B. and Wang, Y.X.. Study on the relations among goal bump, rockburst and mining tremor with numerical simulation. Chinese Journal of Rock Mechanics and Engineering, 2003, 22(11). 1852-1858.
5. Wang, C.S. Talking about percussive ground pressure and protective measures. Coal Technology. 2000, 19(2). 25-26.
6. Zhang, C.Q. and Meng, X.K. Reason for producing impact geopressure and preventive measures. Coal Technology. 2005(2). 35-39.
7. Zhou, K.P. Formation Mechanism Analysis on Rock Brust. Coal Technology. 2008(5). 27-31.
8. Pan, Y., Liu, Y. and Gu, S.F. Fold catastrophe model of mining fault rockburst. Chinese Journal of Rock Mechanics and Engineering. 2001,20(1). 43-48
9. Wang Xuebin, Hai Long, Song Weiyuan, Pan Yishan. Fault rockburst is snap-back due to shear strain localization[J]. Chinese Journal of Rock Mechanics and Engineering. 2004, 23(18): 3102-3105

RaSiM 7(2009): Controlling Seismic Hazard and
Sustainable Development of Deep Mines,
C.A. Tang(ed), Rinton Press, 645-650

ANALYSIS OF THE CHARACTERISTICS AND LAWS OF THE SURFACE MOVEMENT WITH MINE SEISMICITY

CHENG-YI CHEN and GUANG-MING YU

Qingdao Technological University, Qingdao, 266033, P.R. China

YONG-ZHAN PAN

Qingdao Technological University, Qingdao, 266033, P.R. China

Henan University of Science and Technology, Luoyang, 471003, P.R. China

RUI-HAO WANG

Qingdao Technological University, Qingdao, 266033, P.R. China

Construction Administer Bureau of Sifang Borough, Qingdao, 266033, P.R. China

GUO-YAN WANG

Qingdao Technological University, Qingdao, 266033, P.R. China

Liaoning Technical University, Fuxin, 123000, P.R. China

A close relationship between the characteristics and laws of mine seismicity with geological fracture exists. Relative displacement on the surface of a fault after mine seismicity can be observed. In order to obtain the characteristics and laws of mine seismicity, observation stations of surface movement are established in the Liaoning mining area. Fault movement observation stations of are established specifically to observe the relative displacement of both sides of faults after mine seismicity. The rules are summarized based on the observation results, which may be useful for mine seismicity identification and disaster prevention.

In order to obtain the characteristics and laws of mine seismicity [1,2], two observation stations of the surface movement i.e.W1 and W2 are established. Along with these station, two observation stations of fault activity i.e. NF1 and WF2 are also set up in the Taiji mining area. One is located on the corresponding surface of the coal seam outcrop in the first mining area, across the faults of F10 and F12 along the highway from Beipiao to Chaoyang. Another is located on the Nantainmen fault outcrop outside of the Beipiao coal field.

1 Survey methods and precision

Levelling observation and distance measurement are included surface observation. Besides, the time and site of ground fracture occurrence are often observed and recorded.

CAISI Ni—007 automatic leveling gradienter and indium steel ruler which is 3 meters are used in levelling measure. This work must abide by the surveying regulations of surface movement and third leveling precision. According to the observation data, the mean square error of height difference every kilometre is ±1.39mm.

The EOT-2000 short-range infrared range finder was used to distance measurement. The mean square error of distance measurement is ±5mm. In fact, square error of distance measurement was 3.6 mm. The instrument is set up at control point to measure directly the distance from control point to observation point. It is required that recording the distance of 3 times, and mutual difference is less than 5mm. The horizontal distance is calculated, not including the cycle error and the instrument additive constant.

Observation times of levelling measurement and distance measurement were shown in table 1.

Table 1. Observation times of surface observation station

	W1	W2	F1
leveling survey	32	8	11
distance measure	10	8	10

2 Observation results [3]

2.1 The observation results of W2 movement observation station

According to the observation data of levelling and distance measurement, the maximum subsidence value and the maximum horizontal movement value were shown in the table 2. Horizontal movement is positive along the uphill direction of inclined coal seam. Otherwise, it is negative.

Table 2. Maximum movement value of w2 observation station

surveying line	Inclined line			Strike line	
Point No.	18	18	30	42	43
The maximum subsidence(mm)	75			93	
The maximum horizontal movement (mm)		+137	-31		57

Movement distribution of other observation points is shown in the figure 1. The movement parameters are uncertain owing to the continual exploitation.

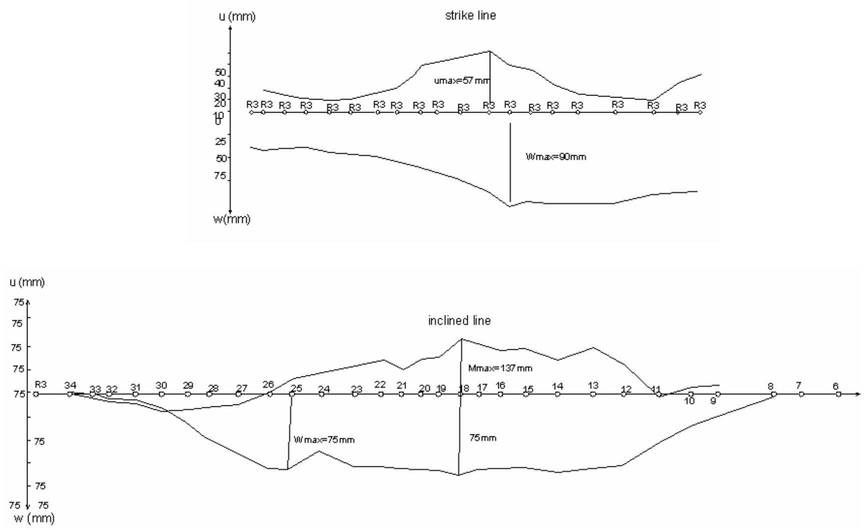

Figure 1 Movement distribution of strike line and inclined line

2.2 The observation results of W1 observation station

Elevation is measured for 32 times. According to the observation results, subsidence value of No.133 is up to 361mm. The maximum subsidence velocity of No.133 is 1.324 mm/day from August 28 to October 4 in1984. Subsidence value of others point can be seen in figure 2.

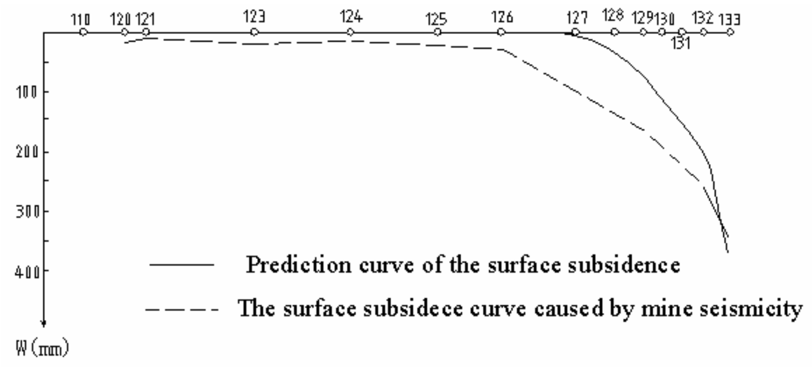

Figure 2 Subsidence curve for inclined line

2.3 The observation results of NF1 observation station

11 times of the levelling measurement were done and the results can be seen in Table 3.

Table 3. Results of leveling

Point No.	II	III	IV	faults	VI	VII	VIII
Subsidence value(mm)	51	51	51		52	52	52

No. Ⅱ, No.Ⅲ and No.Ⅳ locate on the fault footwall, while No.Ⅵ, No.Ⅶ and No.Ⅷ locate on the up wall of it.

2.4 The observation results of WF2 observation station

10 times of distance measurement and 32 times of levelling are done. The maximum tensile value is 23mm and the maximum compression value is 12mm nearby the outcrop of F10 and F12 at May 16 in 1984. The observation results can be seen in table 4.

It can be inferred that outcrop of F12 locates between No. 106 and NO. 107, outcrop of F11 locates between No. 108 and NO. 109, outcrop of F10 located between No. 112 and No. 113.

Table 4. Observation results of leveling in April 1986

Point No.	102	103	105	106	107	108	109	110	112	113	114	115
subsidence（mm）	21	17	7	22	21	21	18	20	20	17	16	17

The surface levelling results can be seen in table 5 when it is confirm that mining seismicity source is in F12 on basis of macroexamination.

Table 5. Subsidence change situation of coal seam floor pre and post mine seismicity

The date of mine seismicity	March 19, 1983	August3， 1983	March27, 1984	May18， 1984	August12，1984
Magnitude（Ms）	1.2	2.5	1.4	1.0	1.4

Point No.	pre	post	pre	post	pre	post	pre	post	pre	post
101	1	5	--2	4	2	6	2	-2	5	2
102	1	4	-2	4	2	7	-2	0	3	2
103	0	4	-1	6	1	7	-2	2	3	3
104	-1	4	-1	5	0	7	-2	2	2	4
105	0	3	-1	5	-11	8	-2	2	2	3
106	0	3	-1	5	2		-2	0	0	0
107	0	3	-1	5	0	7	-2	2	2	2
108	0	3	-2	6	1	5	-1	-1	1	4
109	0	3	-2	5	0	5	-3	-3	0	6
110	-1	2	-1	5	1	6	-4	-6	-1	7

Note: rising is negative and subsidence is positive. All measurements given are in millimeters.

2.5 The investigation results of cracks in the ground

Subsidence basin is formed on the surface after exploitation. There are four cracks near to the border of goaf in the first mining area. The crack width is up to 500mm, and crack spacing is about 10m. The crack angle is 44° .

3 Analysis of the observation results [4]

3.1 Analysis of the observation results for W2 observation station

As is shown in the Figure 1, the subsidence value of observation points on the corresponding surface of old mining area is bigger. The subsidence value of No.25 is up to 75mm which is 15% of the maximum. The scope of surface movement is enlarged due to effect of mine seismicity.

Horizontal movement of observation points on the floor or outcrop of seam is along the uphill direction of inclined coal seam. Horizontal movement of observation points on the roof of seam is along the downhill direction.

3.2 Analysis of the observation results for W1 observation station

Dotted line in Figure3 is prediction range of the surface movement. According to prediction results, the subsidence value of No.126 should be zero. In fact, the range of surface movement has been already enlarged to coal seam floor and the maximum subsidence is up to 30mm from N.126 to No.110 affected by mine seismicity. Based on the investigation results of cracks, the same conclusion can be obtained.

The relationship between the subsidence velocity of No.133 and mine seismicity ($M \geq 1.0$) in Taiji area during observation is shown in Figure4. The subsidence velocity of observation points increased obviously and the maximum velocity was up to 1.324mm/d after mine seismicity happened. The results indicate that the surface movement is affected by mine seismicity.

3.3 Analysis of the observation results for F1 observation station

According to the observation data, we think that there is no relative displacement for both sides of Nantianmen fault because the difference between the subsidence value of fault footwall and hanging wall is 1mm.

3.4 Analysis of the observation results for WF2 observation station

The subsidence value of the observation points in coal seam floor is about 20mm. There was a very small amount of subsidence or uplift phenomenon in coal seam floor when F12 is active pre mine seismicity. The subsidence value of coal seam floor increased obviously after mine seismicity occurred. The subsidence law of coal seam roof is same with floor, not including uplift phenomenon. According to the observation results in May 16, 1984, distance between two points cross- fault is shortened and compression deformation is produced.

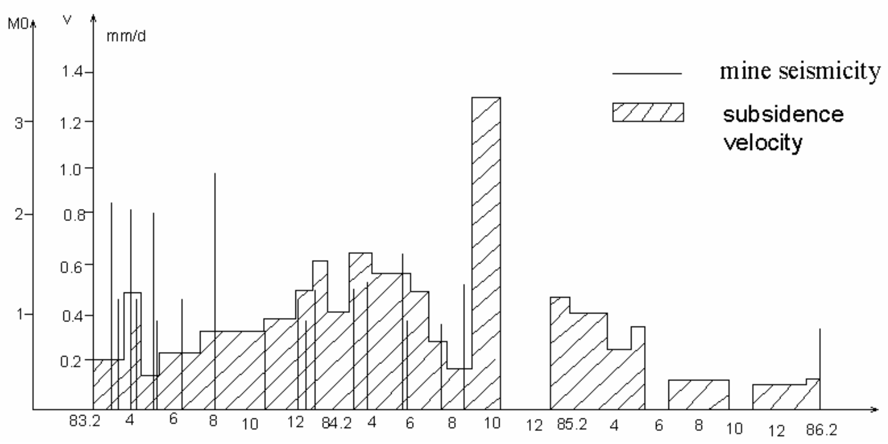

Figure 3 Relationship between the subsidence velocity of No.133 and mine seismicity in Taiji area

Table 6. Shortening amount of distance between two points cross- fault on the surface

No.	106~107	108~109	112~113
Fault name	F_{12}	F_{11}	F_{10}
Shortening amount	12	6	5

4 Conclusions

A connection has not been discovered between the surface movement activity and mine seismicity according to the observation data of W1 observation station due to the influence of mining.

The W2 observation station was set up before mining. The subsidence velocity of No.133 increased after mine seismicity occured. Measured ranges of the subsidence basin which was affected by mining seismicity was bigger than prediction range.

Based on observation data of the NF1 observation station, the relative movement for both sides of fault has not been found. There is not a relationship between the mine seismicity and the Nantianmen fracture.

The results show that there is not a close relationship between mine seismicity and the movement and deformation on the surface.

Acknowledgements

The authors thanks for sustain from key Natural Science Fund of China (No:50434020); the National Natural Science Fund of China (No: 50874064；50804026) and Natural Science Fund of Shandong Province.

References

1. Song, J.C., Liu, D.Y., Wang, E.D., etc. Cause and mechanism of mine′ s fault-type earthquake and its forecast. Mining Engineering, 2007, 5(3). 16-18
2. Jan, D. and Jozef, K. Dynamic events in roof strata-occurrence and prevention. Coal Science & Technology Magazine, 2008, 1. 55-58
3. Beipoao mining bureau. Comprehensive report on Study of The characteristics and laws of mine seismicity in Taiji mining area. 1986,10
4. Beipoao mining bureau. Analysis of the observation results of the surface movement and deformation in Taiji mining area.1986.

*RaSiM 7(2009): Controlling Seismic Hazard and
Sustainable Development of Deep Mines,
C.A. Tang(ed), Rinton Press, 651-656*

A NEW NUMERICAL METHOD FOR MODELING ROCK MASS FAILURE

XIAN-DA FENG, SHU-CHEN LI, LI-PING LI and ZHEN-HAO XU

Geotechnical and Structural Engineering Research Center, Shandong University

Jinan, 250061, P.R.China

In recent years, many failure criteria have been proposed and used to predict the non-linear rock mass failure, among which strain energy density theory is currently widely applied considering a variety of factors. However, analytical solution is hardly suitable for engineering practice due to the complexity of the model and the stringent requirements of the boundary conditions. Therefore, a new numerical method for predicting the rock mass failure is presented in the paper. Based on the strain energy density and the energy dissipation theory, the element failure criterion of the energy is implemented by the FISH of the FLAC3D. The mechanical damage is considered for the elastic module decrease due to the energy dissipation. The non-linear computational analysis process can be implemented by the multi-linear elastic model analysis. Finally, numerical results are provided to demonstrate the utility and robustness of the proposed method.

1 Introduction

Generally speaking, macroscopic failure criteria may be classified into four different types: stress or strain failure criteria; energy type failure criteria; damage failure criteria and empirical failure criteria. Among these failure criteria, the plastic strain energy density failure criterion has been recalled recently to predict failure initiation in various structural elements when subjected to dynamic loads, which was summarized by Jones and Shen(1993) and Jones(1997) [1]. Because of the complexity of this model and the strict boundary conditions, analytical solution is hardly used to predict the failure zones of the rock mass around underground workings. The purpose of the present paper is to develop a numerical method to model the rock mass failure based on the plastic strain energy density and the energy dissipation theory.

2 Strain Energy Density and the Energy Dissipation Theory

2.1. The Strain Energy Density Criterion

One of the most general failure criteria advanced to date is the strain energy density theory [2]. It focuses attention on the fluctuation of the energy from a unit volume of material to the next throughout a medium [2]. The theory is based on the general assumption that progressive material damage can be uniquely related to the rate at which energy is dissipated in a unit volume of material [3]. Since the theory can be applied to any material in general, strain-softening materials are also included [1, 2, 5].

The strain energy density criterion can be described as follows：The strain energy density (dW/dV) can be computed from the stress components σ_{ij} and strain components ε_{ij} by the expression：

$$(dW/dV) = \int_0^{\varepsilon_{ij}} \sigma_{ij} d\varepsilon_{ij} \tag{1}$$

Crack initiation occurs when the strain energy density (dW/dV) reaches a critical value, $(dW/dV)_c$, a quantity that can be obtained as the area under the true stress-strain curve, as shown in Figure 1.

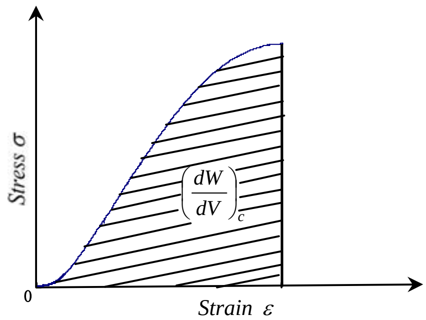

Figure 1 The critical strain energy density.

2.2. The Reduction of the Elastic Modulus Caused by the Energy Dissipation

Referring to Integral Calculus，multi-linear stress-strain curve can be used to approximate the true stress and true strain curve, as illustrated in Figure 2. Stress may increase linearly with strain up to the point of B and the initial elastic modulus is equal to E^1. From then on, there is a permanent degradation of the elastic modulus because of the energy dissipation. The initial elastic modulus E^1 decreases down to the effective elastic modulus E^2。In order to obtain more accurate computed results，the true stress and true strain curve is approximated by means of a multiple reduction of the elastic modulus during the yielding stage BU. Consequently, the non-linear computational result is obtained by the multi-linear elastic model analysis. The macroscopic crack initiates when the stress increases up to the point of ultimate strength U. And then the strain may increase while the stress decreases down to zero at F with the macroscopic crack expanding to macroscopic fracture. During the above process, there is both recoverable elastic deformation and irrecoverable damaged or yielding deformation. The irrecoverable damaged deformation must result in the reduction of the elastic modulus. With the constant energy dissipation, there appears decreased effective elastic modulus such as E^3, E^4 … E*. The calculation accuracy depends on the iteration times of the effective modulus. It will be a close approximation to the true stress-true strain curve if the iteration times are more than enough.

2.3. Strain Softening Constitutive Model of the Energy Dissipation

OUC is a typical step in the multi-linear computation as shown in Figure 2. It can be computed by using the bilinear strain softening constitutive model in Figure 3 [2]. The present model accounts for mechanical damage by decrease in the elastic modulus. For a non-damaged material element, the initial ultimate value of the strain energy density, $(dW/dV)_u$, is equal to the area OUF, Figure 3. The material element at C is damaged with the effective elastic modulus decreasing from E^3 to E^4, Figure 2. The dissipated strain energy density, $(dW/dV)_d$, is equal to the area OUC, while the recoverable strain energy density, $(dW/dV)_r$, is equal to the area OCB, Figure 3. The area BCF represents the additional strain energy density, $(dW/dV)_a$ .In this way，the decreased ultimate strain energy density, $(dW/dV)_u^*$, can be expressed as:

$$(dW/dV)_u^* = (dW/dV)_u - (dW/dV)_d = (dW/dV)_r + (dW/dV)_a \tag{2}$$

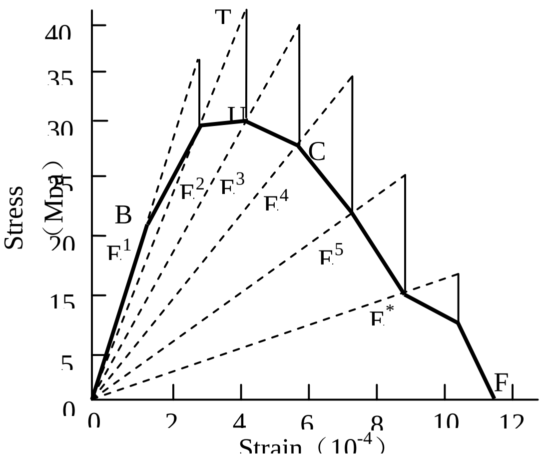

UT：the stiffness loss induced by damage

E* ： effective elastic modulus due to the energy

Figure 2 Effective elastic modulus caused by the energy

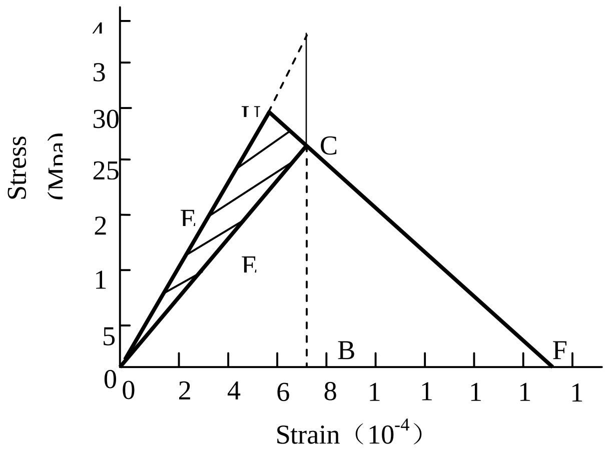

Area OUCB＝Absorbed Strain Energy Density (dW/dV)
Area OCF＝Critical Strain Energy Density $(dW/dV)_u^*$
Area OUC＝Dissipated Strain Energy Density $(dW/dV)_d$
Area OCB ＝ Recoverable Strain Energy Density (dW/dV)

Figure 3 Strain softening constitutive model of the energy dissipation

From Figure 3 the strain energy density as function of the quantities, σ_u, ε_u and ε_f can be obtained：

$$(dW/dV) = 1/2(\sigma\varepsilon + \sigma_u\varepsilon - \sigma\varepsilon_u) \tag{3}$$

$$(dW/dV)_r = 1/2(\sigma\varepsilon) \tag{4}$$

$$(dW/dV)_d = (dW/dV) - (dW/dV)_r = 1/2(\sigma_u\varepsilon - \sigma\varepsilon_u) \tag{5}$$

$$(dW/dV)_u^* = (dW/dV)_u - (dW/dV)_d = 1/2(\sigma_u \varepsilon_f - \sigma_u \varepsilon + \sigma \varepsilon_u) \quad (6)$$

σ_u is ultimate strength; ε_u is ultimate strain; ε_f is fracture strain; E^* is the effective elastic modulus.

3 The Numerical Realization

The above concept in Section 2 is incorporated into Flac3D by the FISH for predicting the failure zones of rock mass. Figure 4 is the flowchart for the numerical realization.

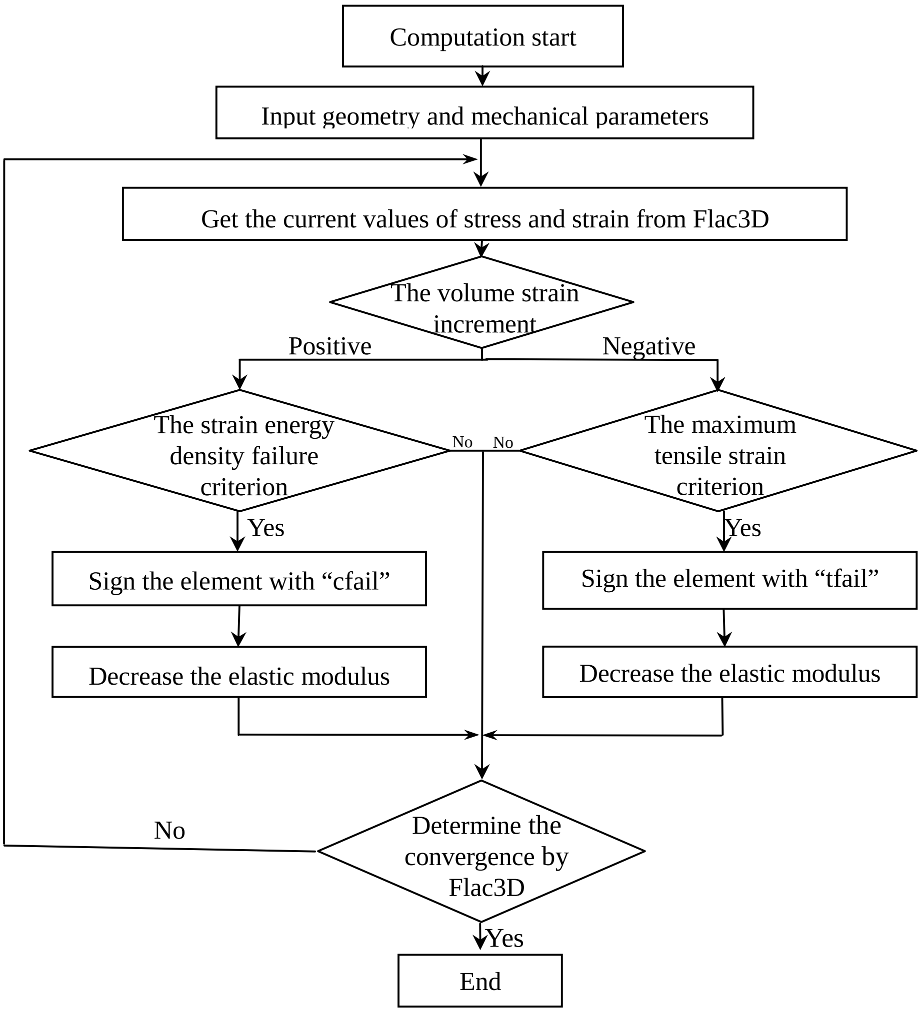

Figure 4 The realization of numerical simulation in FLAC3D

4 Calculation Results

The numerical model has dimensions of 100 m ×100 m × 0.5m. The diameter of the circular opening is 10m. The model is divided into 6,651 elements and has 13,436 nodes, as shown in Figure 5. The mechanical properties of rock masses are specified as: the initial elastic modulus $E = 8.0Gpa$, poisson ratio $\mu = 0.25$, density $\rho = 2500Kg/m^3$, the initial in-situ stress $\sigma_i = 12.5Mpa$, uniaxial compressive strength $\sigma_u = 30Mpa$, the ultimate strain $\varepsilon_{cu} = 2.0\times10^{-4}$, the fracture strain $\varepsilon_{cf} = 3.0\times10^{-4}$, uniaxial tensile strength $\sigma_{tu} = 4Mpa$, internal friction angle $\phi = 30°$ and cohesion strength $c = 6.0Mpa$. In the calculation procedure, the horizontal and vertical press is specified for the model, initially to simulate the in-situ stress. Then the elements in the location of the opening are deleted to simulate the tunnel excavation. Subsequently, the failure patterns of the tunnel are simulated by using strain softening constitutive model of the energy dissipation. The results are shown in Figure 7, in which group "cfail" represents shear failure while group "tfail" shows tensile failure.

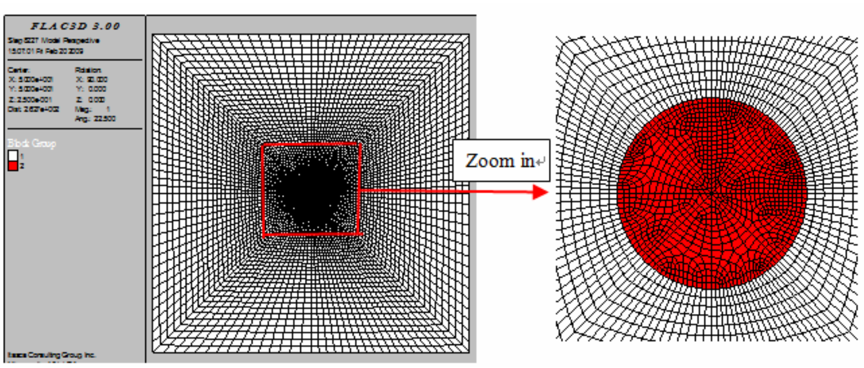

Figure 5 The initial numerical model

It was found that the method can give good prediction of the shape and size of the damage zone in rock mass. Compared with the results by using Mohr-Coulomb model, the shear failure zone increased significantly, as shown in Figure 6 and Figure 7.

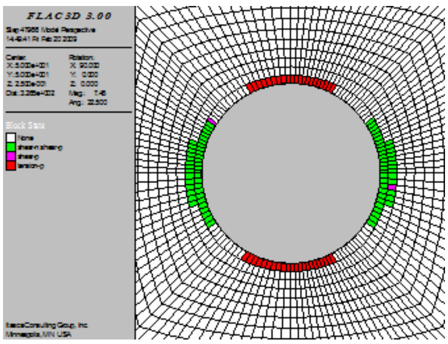

Figure 6 Plastic zones by using M-C model

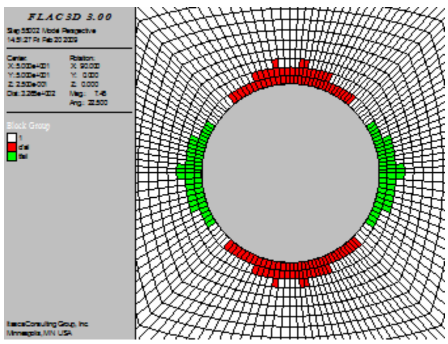

Figure 7 Failure zones by using the new method

5 Conclusions and Future Work

In this paper we present a new method for predicting rock mass failure mainly based on the strain energy density criterion. This method can be used for the failure zones of the rock mass around underground workings.

Specifically, it is implemented by the FISH of Flac3D. The multi-line decrease of the elastic modulus accounts for the energy dissipation induced by mechanical damage.

Indeed，the method in this paper can give a good forecasting for the failure zones of the rock mass around underground workings. However, we believe that it is not sufficient to be able to satisfy the calculation need especially when the rock mass exists in a complex geologic environment that includes high in-situ stresses, high temperatures, and high hydrostatic pressures. Considerable work still remains to be carried out in this area, both in terms of hydro-mechanical coupling, and in more detailed exploration of the proposed method.

Acknowledgements

The authors wish to acknowledge the funding support from the National Basic Research Program of China (973 Program, NO. 2007CB209407), the Natural Science Foundation of P. R. China (NO.50539080 and 50727904) and the Natural Science Foundation of Shandong Province (NO.Y2006F13).

References

1. Li, Q.M. Strain Energy Density Failure Criterion. International Journal of Solids and Structure. 2001, 38. 6997-7013.
2. Carpinteri. Mechanical Damage and Crack Growth in Concrete: Plastic Collapse to Brittle Fracture. Martinus Nijhoff Publishers, Dordrecht. 1986.
3. Sih, G.C. The Strain Energy Density Concept and Criterion, Special Issue in Fracture Mechanics Dedicated to G.R. Irwin, ed. A.K. Rao, J. of Aeronautical Society of India, 1985, 37(1).43-60.
4. Li, S.C. and Zhu, W.S. Damage Constitutive Equations for Energy Dissipation and its Applications to Stability Analysis of Surrounding Rock Mass of Caverns. Chinese Journal of Rock Mechanics and Engineering, 2005, 24(15). 2646-2653(in Chinese).
5. Sih, G.C. Mechanics of Fracture Initiation and Propagation, Kluwer Academic Publishers, Netherlands, 1991.
6. Sun, J.S., Zhu, Q.H. and Lu, W.B. Numerical Simulation of Rock Burst in Circular Tunnels under Unloading Conditions. Journal of China University of Mining & Technology, 2007, 17(4). 0552-0556.
7. J. Nemecek and Z. Bittnar. Experimental Investigation and Numerical Simulation of Post-peak Behavior and Size Effect of Reinforced Concrete Columns. Materials and Structures, 2004, 37. 16l-169.

RaSiM 7(2009): Controlling Seismic Hazard and Sustainable Development of Deep Mines, C.A. Tang(ed), Rinton Press, 657-662

CHARACTERS AND NUMERICAL SIMULATION OF ROCKBURST IN TUNNELS UNDER 2500M DEPTH

QUAN JIANG, XIA-TING FENG and TIAN-BING XIANG

State Key laboratory of Geomechanics and Engineering, Institute of Rock and Soli Mechanics, Chinese Academy of Science

Wuhan, 43007， China

GUO-SHAO SU

Department of Civil and Architecture Engineering, Guangxi University
Nanning, 530004, China

XIANG-BING WAN

East China Investigation and Design Institute, China Hydropower Engineering Consulting Group Co.
Hangzhou, 310014, China

Rockburst is one of the most serious problems in assistant tunnels of the JinPing II hydropower station, the deepest run-through tunnels in China. For reducing the hazard brought by rockburst, some typical rockburst characteristics of assistant tunnels under 2500 m burial depth are summarized in the paper, which reveals that the intrinsic reason for rockburst is the energy release. In order to understand the outburst mechanism, a new energy index, named local energy release rate (LERR), is put forward to simulate the rockburst. By tracking the peak value and valley value of elastic strain energy intensity before and after brittle failure, the evolution of LERR can be gained, which is helpful to easily understand the rockburst from the viewpoint of energy. To test its reliability, the brittle break of Mine-by tunnel in Canada is simulated successfully by LERR. What is more, a typical rockburst in assistant tunnels is analyzed by LERR. All of the simulated results show that LERR can satisfactorily predict the depth of outburst pit and intensity of rockburst, which paves a new way to evaluate the rockburst orientation for deep-buried underground engineering.

1 Introduction

In the excavation of deep-buried underground engineering, a typical problem is sudden dynamic damage of surrounding rock, named rockburst. The characteristics of burst and ejection in rock outburst are a serious threat to the safety of engineers and engineering machinery. In fact, since the first rockburst was observed in a British Stafford coal mine in 1938, the recognition and study of the rockburst phenomenon has been carried out continually. A better understanding of rock outburst was obtained through the experimental work of Cook [1], who provided a theoretical method of rockburst prediction based on the energy opinion that violent damage of rock occurs when an excess of energy becomes available during the post-peak deformation stage [2]. Hagan investigated the failure of pillar foundation at a deep South African gold mine [3]. Tajdus and Majcherczyk analyzed the rockburst hazard at fault zones [4]. Shivakumar summarized spatial distribution characteristics of rockburst at Kolar Gold Mines [5]. Through the study in recent years, there has been a widely accepted concept that strain energy stored in rock mass plays an important role in inducing rockburst. So, Kaiser and Tannnant compiled a handbook to guide rockburst support based on energy release approaches [6]. Also, some numerical methods and experiment predictions of rock outburst are studied by energy analysis [7-11].

Rockburst is one of the most serious problems in assistant tunnels of JinPing II hydropower station, the deepest run-through tunnels in China. The rockburst becomes more frequent in the excavation of assistant tunnels under depths between 2000m to 2500m. For reducing the hazard caused by rockburst, some typical characteristics of rockburst events of tunnels under the 2500 m burial depth are summarized in this paper. To understand the outburst mechanism in assistant tunnels, the rockburst is simulated by numerical methods which adopts an elasto-brittle-plastic model and a new local energy release rate (LERR) index. By tracking the energy density evolvement of numerical elements, the rockburst can be easily understood from a point of view considering the energy. Simulation results of some typical rockbursts show that LERR can predict the depth of outburst pit and intensity of rockburst satisfactorily, which is a new way to evaluate the rockburst orientation of deep buried underground engineering.

2 Rockburst characters of assistant tunnels under depth of 2500 m

2.1 Description of assistant tunnels

JinPing II hydropower station, located at Sichuan province of China, is an important trend hydropower station of Ya-Long River (Figure 1(a). In the project, the supreme challenge is four long hydropower tunnels, the maximum burial depth of which is more than 2500 m. For the purpose of understanding the geology environment of these tunnels and accumulating experience for hydropower tunnels' design, two assistant tunnels, named tunnel A and tunnel B, are excavated firstly. At present, the assistant tunnels have excavated through class II ~ III marble stratum buried more than 2000 and run through in 2008 (Figure 1(b)). In the excavation of assistant tunnels, large scale rockbursts happened frequently. So summarization and study of outburst characters in the assistant tunnels can give a good guideline for excavation and supporting design of hydropower tunnels.

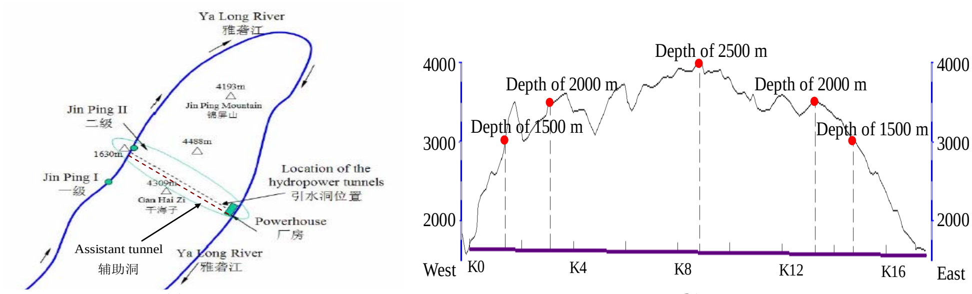

(a) (b)

Figure 1 Jinping II hydropower station (a. position of hydropower tunnels and assistant tunnels, b. longitudinal section of assistant tunnels)

2.2 Rockburst characters of assistant tunnels under 2500 m depth

During the construction of assistant tunnels, many traits about rockburst of Jinping are recognized step by step, which reveals that the release of strain energy is the essential reason. These accumulations provide rare references for measures of preventing rockbursts.

(1) ***Scale characters***. In the process of excavation, there is no obvious sign to indicate the position or scale before appearance of rockburst in assistant tunnels, although carefully investigation of surrounding rock was carried out (Figure 2). During brittle damage process of surrounding rock, schistose spalling with ringing sound often happens firstly. If the thickness of schistose rock is small, the rockburst may develop into superficial spalling with no ejection, which means the release energy is not enough for dynamic activity. In this kind of rockburst pit, the surface is rough and parallels to the surround wall in general. If the thickness of schistose rock is large, the rockburst may develop into deep attack with great dynamic activity. In this kind of rockburst pit, many rupture of rock and parabolic shape of desquamation rock can often be observed.

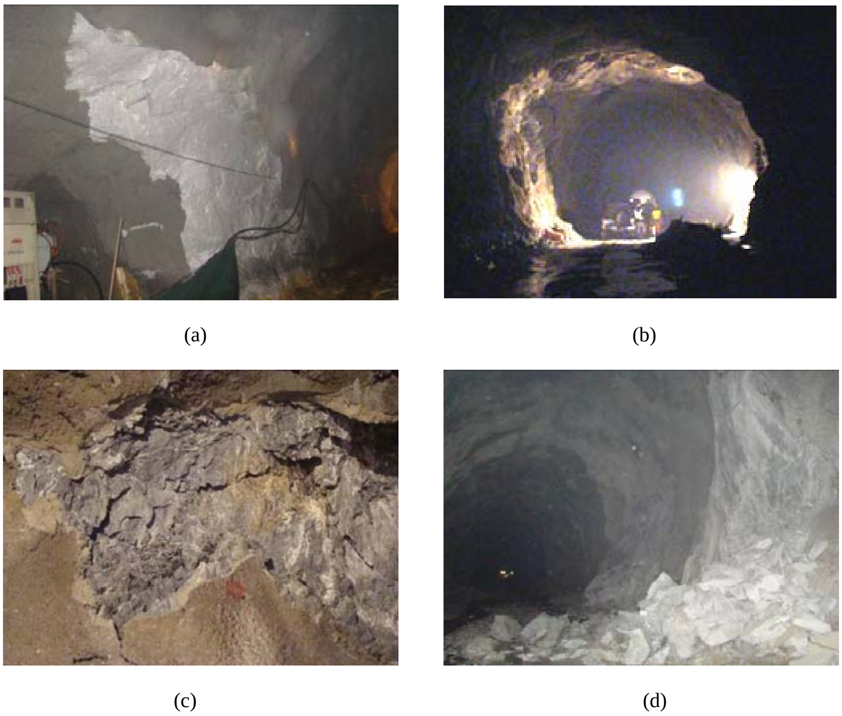

(a) (b)

(c) (d)

Figure 2 Photos of rockburst in assistant tunnels (a. surface spalling, b. deep rockburst pit, c. schistose rupture in pit, d. parabolic shape of desquamation rock)

(2) ***Time characters***. Most rockbursts happened during several hours after excavation. The typical active phase is about 0~20 hours experientially. But the outburst can last for one or two month, even one year. The basic recognition is that the adjustment of stress in surrounding rock can accumulate strain energy again although the foregoing rockburst releases much energy.

(3) ***Space characters***. In the depth more than 2200 m (From BK8 to BK10), about 67.2% of rockbursts happened at right arch and right wall, and about 27.7% of rockbursts happened at left arch and left wall, according to statistics data; only a few rockbursts happened at crown. What is more, the outburst damage often appeared at 6 ~12 m away from excavation face. The position of rockburst in space adapted from the basic orientation relationship of principle stress in tunnel's cross section, which leads to different distribution of elastic strain energy.

(4) ***Rock condition***. Usually, the more fresh, intact and dry the surround rock are, the more possible the rockbursts are, which means that the good rock condition is easy to lead to rockburst. Similarly, the position with complicated geology environment, such as fault, fold, interface of stratum, rockburst is easy to happen. These traits are helpful to predict the rockburst in practice. In fact, this kind of rock condition contributes much to preservation of elastic energy.

3 Analysis index of rockburst

3.1 Index of rockburst assessment

Excavation of underground engineering leads to the change of sudden release of high intensity of energy stored in rock mass. It is still difficult to understand clearly the release and dissipation laws of energy stored in brittle rock mass after peak load under high stress conditions. However, it is generally known that the more release of elastic energy in local rock mass, the greater possibility of brittle failure occurrence and rock failure extent and dynamic energy.In order to quantitatively analyze the intensity of strain-type rockburst, based on the cognition that rockburst is a brittle failure phenomena having intrinsic character of energy release, a new index, Local Energy Release Rate (LERR), is suggested in this paper. The index is an approximate representation of energy release of rock mass per volume for brittle failure and can be considered as a quantitative index of rock bursts risk assessment. The index can be calculated by numerical analysis to trace entire change process of elastic energy intensity in rock masses, using elastic-brittle-plastic mode. The formula can be written as

$$LERR_i = U_{i\max} - U_{i\min} \tag{1}$$

Where, $LERR_i$ is local energy release rate of the i th element. $U_{i\max}$ and $U_{i\min}$ are peak and valley value of elastic strain energy intensity before and after brittle failure occurrence of the i th element respectively. V_i is volume of the i th element.

$$U_{i\max} = [\sigma_1^2 + \sigma_2^2 + \sigma_3^2 - 2\nu(\sigma_1\sigma_2 + \sigma_2\sigma_3 + \sigma_1\sigma_3)]/2E \tag{2}$$

$$U_{i\min} = [\sigma_1'^2 + \sigma_2'^2 + \sigma_3'^2 - 2\nu(\sigma_1'\sigma_2' + \sigma_2'\sigma_3' + \sigma_1'\sigma_3')]/2E \tag{3}$$

Where, σ_1, σ_2, σ_3 are the three principal stresses corresponding to peak strain energy of the element. σ_1', σ_2', σ_3' are the three principal stresses corresponding to the valley strain energy of the element. ν is Poisson's ratio and E is Young's modulus. It can be seen that calculation of the local energy release rate is carried out by tracing dynamic evolutionary process of energy in the elements including concentration, release, transfer and dissipation, which reveals the elastic-brittle-plastic behaviours.

3.2 Verification of LERR in Mine-by tunnel

Atomic Energy of Canada Limited's (AECL) Underground Research Laboratory (URL) excavates the Mine-by tunnel to study brittle damage of deep buried granite tunnel [12, 13]. Because of high geostress, the tunnel appeared obvious 'V' shape brittle damage, which is small scale rockburst (Figure 3). By the numerical simulation with elastic-brittle-plastic model, the LERR is traced. The calculated result shows that the LERR distribution can indicates not only the position of brittle outburst, but also the depth of rockburst pit, which meets the practical rockburst damage very well. So, it shows that LERR is reliable to analyze the rockburst of deep buried underground engineering.

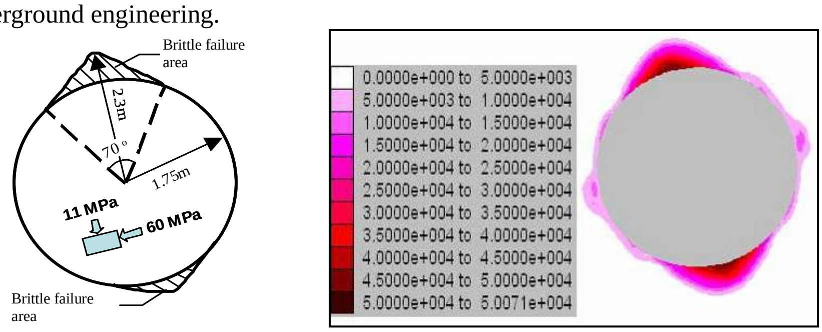

(a) (b)

Figure 3 Contrast between actual rockburst and simulation by LERR in Mine-by tunnel (a. The measured outline of failure zone, b. LERR contour map)

4 Rockburst simulation of Jingping Ⅱ assistant tunnel by LERR

4.1 Introduction of a typical rockburst

When excavating was near to 2500m burial depth, the rockburst intensity became higher and higher. It was hard to record all of rockburst because of great outburst risk. However, several typical rock outbursts were recorded

(Figure 4(a)). A typical scale rockburst happened at the position of BK9+512 on Jan 5th, 2008, where the depth of outburst pit is about 40cm and the volume of desquamation rock is about 2m^3 (Figure 4(b)).

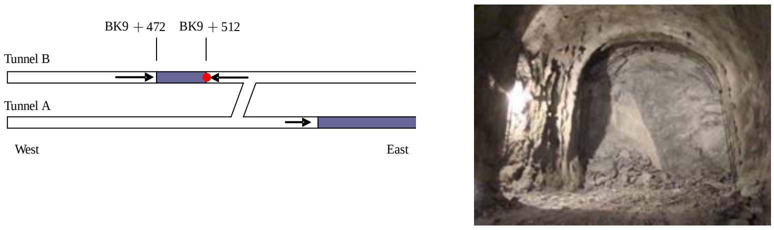

(a) (b)

Figure 4 Observed rockburst in assistant tunnels at BK9+512（a. Position of rockburst, b. photo of rockburst ）

4.2 Initial condition of numerical simulation

To simulate the rockburst at position of BK9+512, a three dimensional model, including tunnel A, tunnel B and cross channel, is built up with 300 × 168.5 × 130 m in length, width and height (Figure 5). In order to simulate the brittle break of rock, an elastic-brittle-plastic model, named rock deterioration model [14], is adopted with the mechanical parameters shown in Table 1.

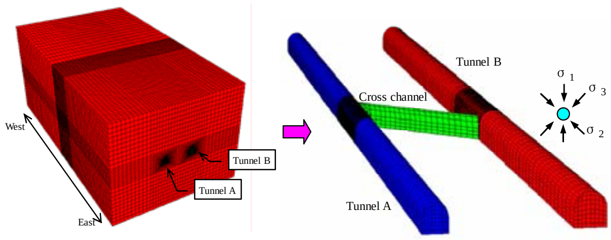

Figure 5 Three dimensional model of assistant tunnels

Table 1 Basic mechanical parameters in numerical simulation

E_o/GPa	E_d/GPa	φ_o/°	φ_d/°	c_o/MPa	c_d/MPa	$\varepsilon_{\varphi}^{p}$ /10^{-3}	ε_{c}^{p} /10^{-3}
23.2	16.2	25	53	25	2	1	2

4.3 Simulation result

From the distribution of LERR at BK9+512 (Figure 6), we can see that the largest energy release appear at the left side of excavation face. The value is about 50~70 kJ. Contrast to calculated result of Mine-by tunnel, the rock in assistant tunnel's excavation face should appear brittle break. Since the LERR at excavation face of BK9+512 is only a little larger than Mine-by tunnel, the rockburst should not appear clear ejection. In fact, the simulating result by LERR at BK9+512 conforms well with the actual rockburst and is harmonious with the simulation of Mine-by tunnel.

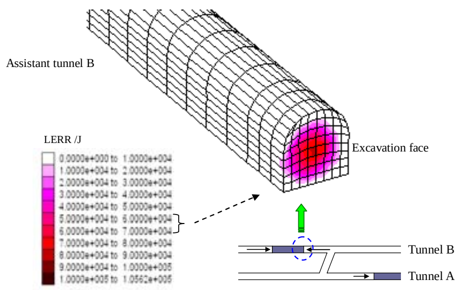

Figure 6 Simulated rockburst of excavation face at K9+512 in assistant tunnel B

5 Conclusions

The concept that strain energy isstored in rock mass plays an important role in inducing rockburst. The basic characteristics of rockburst in the Jinping II assistant tunnels more than 2000 m deep are summarized and the new energy index is used to simulate rock outburst. Based on this study, several specific points of interest are:

(1) The rockburst in Jinping II assistant tunnels had typical laws in scale, space, time and rock condition, which indicates that the energy release is quintessential of rockburst.

(2) Simulation of several rock outburst shows that the energy index of local energy release rates can predict the depth of outburst and intensity of rockburst satisfactorily, which indicates that it is possible to evaluate the rockburst orientation of deep underground engineering.

(3) The value relationship of LERR in three rockburst cases is $LERR_{Mine\text{-}by} < LERR_{BK512}$, which agree swell with the rockburst in scale, although the threshold value of LERR for rockburst needs to be requested still.

Acknowledgements

The work was supported by the National Natural Science Foundation of China under Grant No. 50539090, the National Science and Technology Support Program under Grant No. 2006BAB04A06 and Postdoctor Foundation of China under Grant No. 20080440812. In particular, we wish to thank J. Hou, C.Q. Zhang, S.L. Huang and S.L. Qiu for their contributions to this paper.

References

1. Cook, N.G.W., Hoek, E., Pretorius, J.P.G., et al., Rock mechanics applied to the study of rockbursts. SAIMM, 1966, 66(10). 436-528
2. Linkov, A.M. Rockburst and the instability of rock masses. International Journal of Rock Mechanics and Mining Science & Geomechanics Abstracts, 1996, 33. 727-732.
3. Hagan, T.O. Pillar foundation failure studies at a deep South African gold mine. Proc 2nd International Symposium of Rockbursts and Seismicity in Mines, Minneapolis, 1988. 51-61.
4. Tajdus, A., Majcherczyk, T. and Cala, M. Effect of Fault on rockbursts hazard. Geomechanics, Rakowski, 1996.
5. Shivakumar, K., Rao, M.V.M.S., Srinivasan, C., el al. Multiracial analysis of the spatial distribution of area rockbursts at Kolar Gold Mines. International Journal of Rock Mechanics and Mining Science & Geomechanics Abstracts, 1996, 33(2). 167-172
6. Kaiser, P.K., Tannnant, D.D. and McCreat, D.R. Canadian Rockburst Support Handbook. Geomechanics Research Centre, 1996
7. Wang, J.A. and Park, H.D. Comprehensive prediction of rockburst based on analysis of strain energy in rocks. Tunnelling and Underground Space Technology, 2001, 16(1). 49-57.
8. Mansurov, V.A. Prediction of rockbursts by analysis of induced seismicity data. International Journal of Rock Mechanics and Mining Science, 2001(38). 893-901.
9. Li, Z.H., Dou, L.M., Lu, C.P., et al. Study on fault induced rock bursts. Journal of China University of Mining & Technology, 2008(18). 0321-0326.
10. Hua, A.Z. and You, M.Q. Rock failure due to energy release during unloading and application to underground rock burst control. Tunnelling and Underground space technology, 2001(16). 241-246.
11. Sun, J.S., Zhu, Q.H. and Lu, W.B. Numerical Simulation of Rock Burst in Circular Tunnels Under Unloading Conditions. Journal of China University of Mining & Technology, 2007(17). 0552-0556.
12. Read, R.S. 20 years of excavation response studies at AECL's Underground Research Laboratory. International Journal of Rock Mechanics & Mining Sciences, 2004(41). 1251-1275.
13. Hajiabdolmajid, V., Kaiser, P.K. and Martin, C.D. Modeling brittle failure of rock. International Journal of Rock Mechanics & Mining Sciences, 2002(39). 731-741.
14. Jiang, Q., Feng, X.T. and Chen, G.Q. Study on deterioration model for hard rockmass under high geo-stress. Advance in heterogeneous material Mechanics 2008, China, 2008. 1108-1112.

RaSiM 7(2009): Controlling Seismic Hazard and
Sustainable Development of Deep Mines,
C.A. Tang(ed), Rinton Press, 663-668

NUMERICAL SIMULATION AND ANALYSIS OF THE STABILITY OF SUBLEVEL CAVING WITHOUT FLOOR PILLAR LARGE CROSS-SECTION DRIFT

FU-KUN XIAO

Resources and Environmental Project Institute, Heilongjiang University of Science & Technology

Harbin, 150027, P.R. China

ZHI-HUI GE

Resources and Environmental Project Institute, Heilongjiang University of Science & Technology

Harbin, 150027, P.R. China

The study of the stability of a tunnel when its cross-section is enlarged that meets the demand of a large cross-section for extracting ore, but is also safe for mining, is the subject for this paper. The use of rock failure process analysis code (RFPA^{2D}) simulation is used to analyse the stability of sublevel caving without floor pillars and several large cross-section drifts. The primary stress, displacement and failure zone of these kinds of cross-section of tunnel is calculated. The conclusion is that the tunnel is safe when its cross-section is 6.5m×3.0m and it is 1.5m over the lower wall. This gives some references for the operations of underground mining.

1 Introduction

In the mining process, we can get some useful parameters for the roadway, by engineering simulation analysis, before the start of the main roadway construction. It is also beneficial to improve and maintain the stability of underground engineering, and also to clear the major supporting and reduce support strengthening fee of the roadway. Therefore combining with project features, the numerical simulation to simulate and analyze the stability of geotechnical engineering has important significance on practical study and research [1].

A proposed mining research program, pertaining to the extraction of large cross-sections of ore, was introduced to improve in the practical production of the turning radius of scraper. The large road section was expanded by the scraper to form a large section roadway before the scraper removes large quantities of ore. Literature [2] has been discussed on this method and could improve the recovery rate effectively. The purpose of our calculations is to simulate and analyze the stability of several different section roads by RFPA, a finite element analysis software for geotechnical engineering, and find a reasonable road section which meets the demand of extracting ore safety.

2 Numerical Simulation Calculation Model

The stability of a roadway is very complex and is difficult to analyze by the analytical method. However, the numerical simulation is most widely used to calculate rock mechanics. Comparatively, RFPA^{2D} combines the micromechanics method with the numerical calculation method to study the nonlinear rock mechanical behaviour thorough consideration of heterogeneity characteristics; which is a way to solve the nonlinear continuum mechanics with the continuum mechanics theory. It is an easy and useful tool to analyze and simulate nonlinear mechanics and failure processes of the rock, and is used to analyze the roadway stability in local projects.

Simplified the hanging and foot wall of the ore body as a model shown as figure 1, the average thickness of ore body is 15m and the average angle is 70º, the hanging wall is siliceous about 13m thickness, the footwall is mudstone about 0.3m, and below is amphibolites about 13m thickness. Vertical cross section of the roadway is used as research object for calculating, and model according to the plane problem is made in 30m×33m （180×198=35640 elements） analysis region.

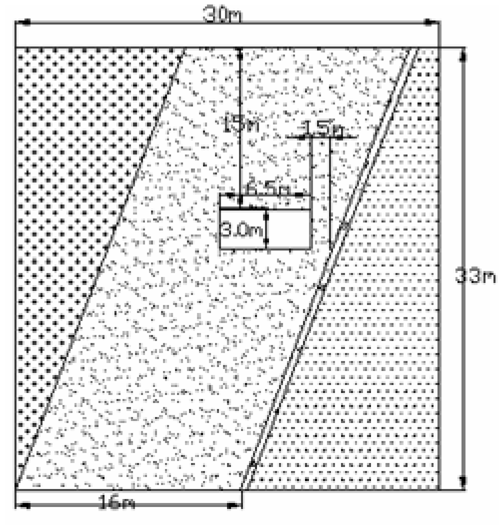

Figure 1 Calculation model

Dead weight of 12m height rock above the roadway is considered. The loose coefficient of overburden from +150 to -220 is 1.6 and the bulk density of complete rock is 2.7t/m^3. So the bulk density of broken overburden is $\gamma = 2.7/1.6 = 1.68\text{t/m}^3$, the height is $H = 150 + 220 = 370\text{m}$.

The gravity stress [3] is:

$$\sigma = \gamma \times H = 6.1\text{Mpa} \qquad (1)$$

Load this part stress uniformly on the rock.

Table 1. The mechanical parameters of model

Strata	Elastic modulus （Map）	Poisson ratio	Compressive strength （Map）	Friction angle(°)	Density kg/m^3	Compressive-tensile strength
Hanging wall	87500	0.304	192.89	46.5	2800	9
Ore body	83400	0.208	167.49	45	3400	9
Footwall mudstone	43900	0.358	123.10	45.5	2800	11
Footwall amphibolites	97000	0.27	110.10	43	2650	10

The upper part fetches 12m height above the roadway (under overburden). There are displacement constraints at the left and right sides, and it can slide freely at vertical direction. The rock is loaded by dead weight and overburden pressure, and mechanical parameters of rock were shown as table 1.

3 Numerical Calculation and Analysis of Results

Using the software RFPA^{2D}(Rock Failure Process Analysis), several methods were taken in this calculation: 1., The road section near the footwall surrounding rock is 4.3m×3.0m; 2. The section which is 1.5 meters away from the footwall is 6.5m×3.0m; 3. The section which is 1.5 meters away from the footwall is 8.0m×3.0m; 4. The section which is 1.5 meters away from the footwall is 9.0m×3.0m；5. The section which is 1.5 meters away from the footwall is 10.0m×3.0m. According the 5 projects analysis, find out a size of safety section and the change law of the roadway stability with roadway section expanding.

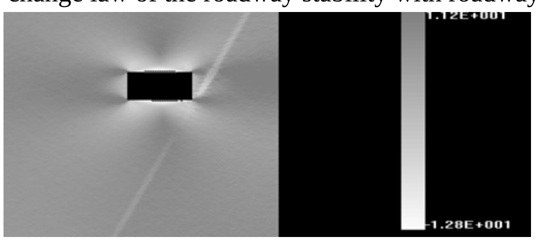

Figure 2 Near footwall, section 4.3m*3.0m
the first principal stress distribution

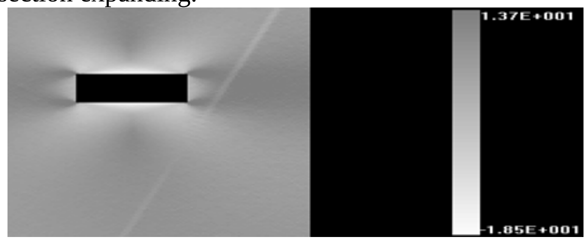

Figure 3 Away 1.5m, section 6.5m*3.0m
the second principal stress distribution

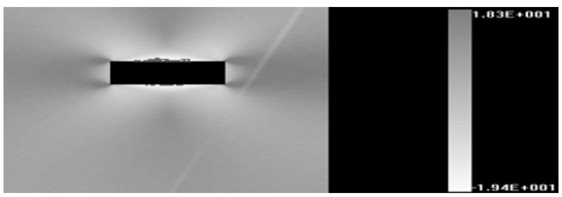

Figure 4 Away 1.5m,, section 8.0m*3.0m
the third principal stress distribution

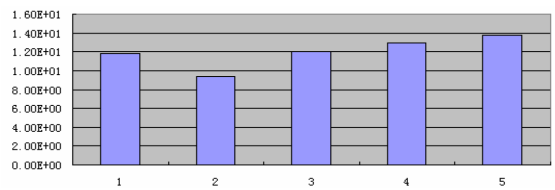

Figure 5 Every scheme compare
with the most displacement

3.1 Stress Analysis

After the roadway is excavated, the stress in surrounding rock releases and adjusts the stable state again, the principal stress distribution map is shown as figure 2~4 (the bigger the lighter). From the results of the stress distribution map, tensile stress appears on top arch and bottom arch after roadway excavation, only the second project's is less than the rock tensile strength 16.7MPa, and what is the main reason for roadway failure. From table 2, stress concentration area appears at the base angle of two sides of roadway. The maximum values are 65.7MPa, 52.2MPa, 66.3MPa, 69.4MPa, 73.7MPa, respectively, and they are less than compressive strength 167MPa. Either tensile stress or compressive stress increases with increasing of the roadway section on the whole.

Table 2. The least main stress in every roadway（Unit Map）

	Left corner	Roof middle	Right corner	Bottom left corner	Floor middle point	Bottom right corner
The first scheme	13.2	17.1	10.4	9.6	16.7	8.3
The second scheme	9.2	14.8	8.6	9.8	12.3	6.5
The third scheme	13.2	17.9	10.3	7.9	17.6	6.8
The fourth scheme	12.1	18.7	9.3	9.2	18.0	6.9
The fifth scheme	13.4	19.2	10.5	13.2	18.6	10.3

3.2 Displacement Analysis

The point where is 12m away from the roof of roadway (boundary reaching of ore rock) takes a little displacement downward per meter. It is easy to found that displacement is increasing with expansion of roadway section from figure 5, only the first scheme displacement caused by the mudstone is more than the second's. The middle point of the roof whose displacement is biggest is easiest to broken from table 3, and which is consistent with the conclusion of failure area and stress area. The second scheme whose displacement is smallest is most safe, which is also consistent with conclusion of failure area and stress area.

Table 3. Every point of roadway displacement (Unit mm)

	Left corner	Roof middle point	Right corner	Bottom left corner	Floor middle point	Bottom right corner
The first scheme	2.23	10.2	2.26	1.06	0.67	1.15
The second scheme	4.20	11.0	4.21	1.93	1.34	1.94
The third scheme	4.21	13.8	4.24	1.96	0.88	2.08
The fourth scheme	5.89	14.5	5.40	1.96	0.79	2.10
The fifth scheme	13.2	30.3	13.9	9.94	5.31	9.79

3.3 Failure Area Analysis

It can be seen from the failure area map (figure 6~9) that the failure area increases obviously with the expansion of roadway section, but the failure dose not appear for 6.5m×3.0m section. But for 8.0×3.0m section failure appears obviously and for 9.0m×3.0m and 10.0m×3.0m section it's more. Because of the design of 4.3m×3.0m section is nearest the footwall, the failure area was appeared by the mudstone affecting. The failure area was almost happened at roof and floor, and the roof is more than the floor. Only in the first scheme, roadway near the mudstone is broken by the effective of footwall mudstone.

Figure 6 Near footwall, section 4.3m×3.0m the first failure area distribution

Figure 7 1.5m away from footwall, section 6.5m×3.0m the first failure area distribution

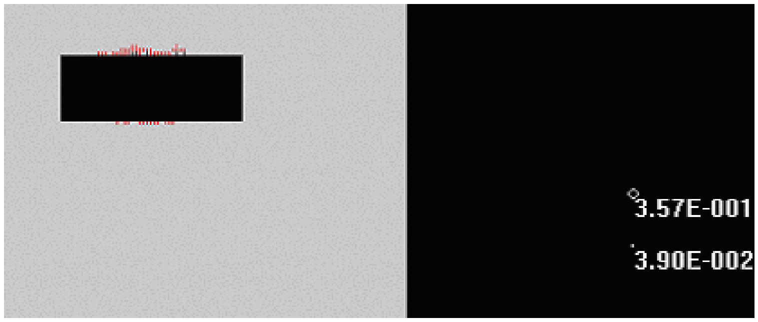

Figure 8 1.5meter away from footwall, section 8.0m×3.0m the third failure area distribution

Figure 9 1.5m away from footwall, section 10.0m×3.0m the fifth failure area distribution

4 Conclusions

The conclusion found by the analysis of the stress, displacement and failure area is as follows:

1. The tension failure often occurs at the roof and is mainly caused by the weight and overburden pressure which causes the roadway to fail. Changes in the roof should be monitored more often during construction to prevent unexpected situations.

2. Comparative analysis under different shape of cross sections shows that the disturbance range of the roof stress increases gradually and roadway stability decreases gradually with the expansion of the roadway section

3. The scheme of 6.5m×3.0m section and 1.5m away to the footwall is safe; for the max stress of the schemes with the bigger section will be bigger than the tensile strength of the rock, and the displacement will be over the allowable range, so it’s not safe.

The rock fracture under the effect of various natural factors is very complex for stress accumulation, transfer and evolution. Only the stability of the whole roadway can be fully evaluated when the effect of the local fault and joints on the roadway are considered.

Acknowledgements

The authors wish to acknowledge the funding support from the Heilongjiang provincial natural science fund (Grant No. E200610) and Heilongjiang Province Office of Education Youth backbone teachers project (Grant No. 1153G035).

References

1. Xiao, F.K., Wang, S.H., and Zhu, W.C. Numerical Analysis of the Partial Unstability of Big Underground Surrounding Rocks. Natural Resources and Environmental Engineering Dept, 2000, 10 (2). 31-34.

2. Xiao, F.K., Sun, H.R., etc. Studies on the Drift Parameters of Strike Subdrifting and Caving without Sill Pillar. Mining Research and Development, 2003, (5). 14-16.
3. Gao, L. Mechanics of Jointed Rock Masses (M). Metallurgical Industry Press, 1979. 34.
4. RFPA'98 User Handbook. Northeast University Rock Breaking Center.
5. Tang, C.A., Fu, F.Y., Zhao, W. Numerical Simulation about Focal Development Pattern. Acta Seismologica Sinica, 1997, 19(4).337-346.

RaSiM 7(2009): Controlling Seismic Hazard and
Sustainable Development of Deep Mines,
C.A. Tang(ed), Rinton Press, 669-672

NUMERICAL SIMULATION OF COAL SEAM BURSTING HAZARD UNDER THE CONDITIONS OF "THREE-HARD"

YONG-WEI PENG

Coal Mining and Design Branch, China Coal Research Institute ,Beijing Mining Technology Department of Tiandi Science&Technology Co.，ltd ,Beijing 100013,P.R.China

QING-XIN QI

China Coal Research Institute, Beijing 100013,P.R.China

YONG REN

Coal Mining and Design Branch, China Coal Research Institute ,Beijing Mining Technology Department of Tiandi Science&Technology Co.，ltd ,Beijing 100013,P.R.China

HONGYAN LI

Coal Mining and Design Branch, China Coal Research Institute ,Beijing Mining Technology Department of Tiandi Science&Technology Co.，ltd ,Beijing 100013,P.R.China

CHUNRUI LI

Coal Mining and Design Branch, China Coal Research Institute ,Beijing Mining Technology Department of Tiandi Science&Technology Co.，ltd ,Beijing 100013,P.R.China

The rockburst mechanism of "three-hard" coal seam was analyzed, and stress variations of coalbed were researched using the numerical simulation method. After the analysis of the mechanics property in simulation and the intensity curve of coal mass, the evaluation method was achieved. The distribution and evolution law of coal seam bursting hazard were studied with this method.

1 Rock burst mechanism under the conditions of "three-hard"

"Three-hard" means that the roof, floor and coal seam are all hard. Production practice and correlation studies indicate that "three-hard" structure is a typical type of structure.

Different occurrence theories for rockburst have been put forward in recently years. The representative theories include strength theory, rigidity theory, bursting liability theory, and instability theory. Each of them has a corresponding calculation formula. Rockburst occurrence needs at least three conditions including the energy condition, strength condition and burst liability.

Under the conditions of “three-hard”, elastic deformation energy is easy to be accumulated when the workface is advanced. Once the hard proof is broken or slipped, a lot of energy will be delivered quickly. Release of the energy may lead to intense vibration and to evoked rockburst.

Most rockburst coalmine in China belongs to this type, such as Xinzhou Coal Mine, Mentougou Coal Mine, Huafeng Coal Mine, and so on.

Due to the complexity, the formula of occurrence conditions is rarely compared to application in practice. Determination bursting hazard zone is important for the coal mine safety in production. But at the present time, the researches are less involved to determine the coal seam bursting hazard. So in this paper, starting with the stress analysis, the coal seam bursting hazard zone under the condition of “three-hard” is researched.

2 Evaluation method of coal seam bursting hazard

According to the index of bursting liability, bursting liability of coal can be tested in laboratory. But bursting liability is just the necessary condition to occur rockburst. The occurrence of rockburst needs the energy condition and intensity condition.

After laboratory test the bursting liability of coal, the bursting liability of coal seam is conformity. But a large number of rockburst examples indicate that bursting hazard at different position in same coal seam is variable.

Ratio of vertical stress/UCS (uniaxial compression strength) is used to evaluate the bursting hazard of coal seam by some researchers. But the rock mass in situ is in complicated forced state. So consideration the stress condition, the index of bursting hazard is put forward to evaluate the bursting hazard of coal seam in this paper,

$$U = (\sigma_1 - \sigma_3) / \sigma_c \tag{1}$$

Where U—index of bursting hazard; σ_1—maximum principal stress; σ_3—minimum principal stress; σ_c—uniaxial compressive strength of intact rock.

Lots of experiments and experience indicates that only U>0.25, the coal (or rock) seam begin to break. When U=1.0, the coal (rock) mass is in limit equilibrium state. So the preliminary criterion was put forward: When U<0.25, the bursting hazard is defined as no bursting hazard, when 1.5>U>0.25, the bursting hazard is defined as weak bursting hazard. When U>1.5, the bursting hazard is defined as strong bursting hazard.

3 Stress variations with mining

For to analysis the stress variation with mining, the three-dimensional numerical simulation model is set up. The embedded depth of coal seam is 700m. Thickness of coal seam is 6m; the length of working face is 200m.

The UCS of overlying strata is 120 MPa. The elements amount of the model are 160272.the main mechanical parameters are shown in Table 1.

Table 1. Main mechanical parameters

Rock stratum	Thickness (m)	Young's modulus (GPa)	Poisson's ratio	Bulk density/ (kN • m-3)	Cohesive strength (MPa)	Internal friction angle
Roof	20	100	0.2	25	30	40
Coal seam	6	4.8	0.4	13.5	7.9	29.12
Floor	8	79.69	0.3	25.1	45	42

The model is shown in Figure 1.The vertical stress distribution when working face is drove for 20m is shown in Figure 2 The maximum principal stress distribution of working face advance 80m is shown in Figure 3 and Figure 4

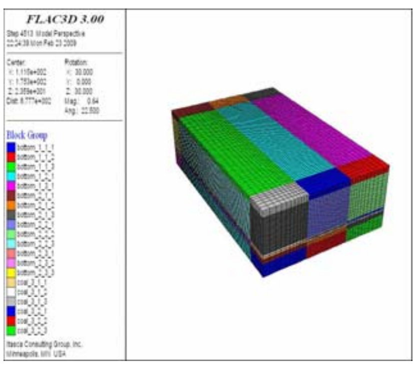

Figure 1 Numerical simulation model

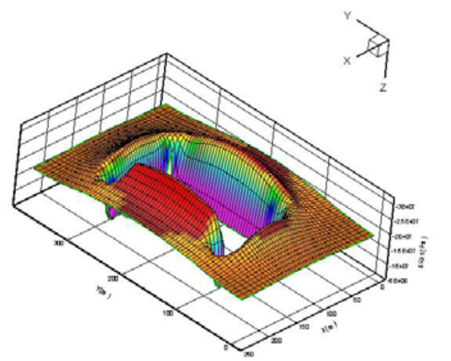

Figure 3 Maximum principal stress distribution 3D of working face advance 80m

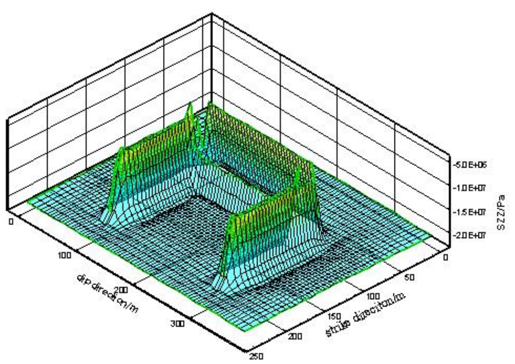

Figure 2 Support pressure distribution of working face advance 20m

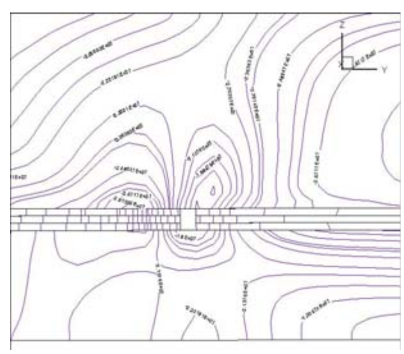

Figure 4 Maximum principal stress distribution contour of working face advance 80m

4 Application of the evaluation method

The principal stress can be extracted to compute index of bursting hazard *U* according to the simulation results. And the region of bursting hazard can be determined. The precaution measures can be taken, according to the region of bursting hazard. For example the working face is drove for 80m, the principal stress are extracted to calculate *U*, and then determine the bursting hazard zone near the tunnel (see Figure 6). Curve 1 is vertical stress/UCS; curve 2 is the results of formula (1).

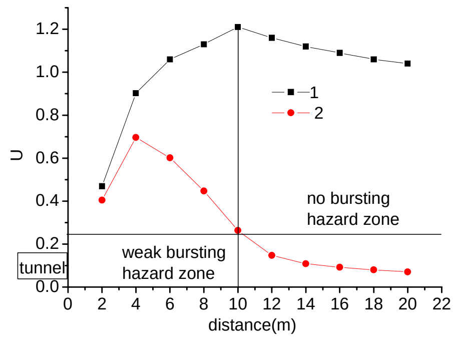

Figure 6 Bursting hazard zone.

5 Conclusions

In this paper, the authors have analyzed the rockburst mechanism of “three-hard” coal seams. Also, the evaluation method of coal seam bursting hazard was put forward. The three-dimensional numerical simulation model is set up to determine the stress variation with mining. According to this method, the bursting hazard zone was determined. For the sake of difficulty to get all the parameter of rock mass, the best way to get principal stress is with actual measurement.

Acknowledgements

The authors wish to acknowledge the collaborative funding support from "Eleventh Fifth” the National Science and Technology support plan key project issues - “Deep mining coal (rock) dynamical disaster multi-parameter identification and solve risk key technology and equipment”. Topic ID: 2006BAK03B06.

References

1. Peng, Y.G., Qi, Q.X., Li, H.Y., et.al. Discussion for Bursting Liability Indexes of Coal. Symposium of High Efficiency Mining and rockburst new technology Xuzhou: China University of Mining and Technology Press, 2008, 128-131.
2. Qi, Q.X. and Dou, L.M. Theory and Technology of Rockburst. China University of Mining and Technology Press, 2008.
3. Jiang, F.X., Wang, C.W., Ye, G.X., et al. Study on Possibility Evaluation Method of Coal Out-burst in Longwall face. Symposium of High Efficiency Mining and rockburst new technology Xuzhou: China University of Mining and Technology Press, 2008, 91-96.
4. Zhang, K.Z. and Xia, J.M. Weight-variable identification model of comprehensive evaluation on burst liability of coal. Chinese journal of rock mechanics and engineering, 2004, 23(20). 3480-3483.

RaSiM 7(2009): Controlling Seismic Hazard and Sustainable Development of Deep Mines, C.A. Tang(ed), Rinton Press, 673-678

STIFFNESS JOINT SLIP INDUCED ROCKBURST AT DEPTH – A CASE STUDY USING DISTINCT ELEMENT METHOD

WEI-JIANG CHU, CHUN-SHENG ZHANG and JIN HOU

East China Investigation and Design institute under CHECC, Hangzhou, China

Hangzhou, 310014, P.R. China

In August 2008, a major stiffness joint was exposed over tens meters behind tunnel face during TBM tunneling on deep Level (1400m below surface) of JP-II Dewater tunnel at Sichuan province, China, which provides a unique opportunity to study the recent joint-slip induced rockburst. Since rockbursts are the results of a violent release of energy from high stress bulb or clutch joint, it is appropriate to check the stress path and significant high stress area when TBM approaching and departing from the stiffness joint to explain the mechanics of joint-slip behaviour and the risk of rockburst occurrence. In this paper, the TBM excavation sequences and joint geometries are examined and simulated through using the 3D distinct element code. The detail of simulation such as in-situ stress, rockmass constitutive model and property is also discussed. The simulated results exhibit significant different area of high stress bulb when tunnel face on hanging of stiffness joint and underlying which give an adequate explanation of where and when the rockburst occurrence.

1 Introduction

The occurrence of rockbursts is one of the most serious hazards associated with deep underground engineering. Some mines and tunnels have been damaged by very large rockbursts and some rockbusts have resulted in threats to underground personnel. This problem became progressively worse as the depth and extent of underground engineering increases. As a result, some research programs were initiated in order to investigate the problem of rockbursts such as CRRP (Canadian Rockburst Research Program), etc. [1]

In general, rockbursts can be defined as a sudden and violent failure of rock where rock fragments are ejected into the excavation. The energy of rockbursts is released as seismic energy radiated in the form of strain waves. There are three kinds of rockbursts in general: strainburst, slip-burst and pillar-burst. [2]

- Stainburst is a self-initiated rockburst that develops due to a disequilibrium between high stresses and the rock strength, i.e. dynamic unstable fracturing. Strainburst usually occurs after blasting, as the blasted face is unable to adjust to the immediately stress increase.
- Slip-burst is defined both by mechanism (stick-slip shear movement on a discontinuity) and the regional nature of driving forces. These bursts are less likely to be triggered by a particular blast. Slip-burst is similar to the mechanics of an earthquake. In most case, mining and tunnelling activity cause slip by the removal of normal stress, although some local intensification of shear stress may also occur.
- Pillar-burst is caused by some combination of fracturing, sliding and buckling that extends deeper into rockmass than a strainbursts and often involves the core or foundation of a pillar. Pillar-bust is often caused by a sudden change in potential energy as the hangingwall and footwall rapidly converge during the failure process.

Seismic events in deep mines of South Africa show slip-burst may release a higher magnitude of potential energy, (up to M_L=3, Finnie, 1999) than normal strainburst. Two types of seismic events can yield relevant information (Ortlepp, 1992) of rockbursts. The first type of failure, here termed Type A (slip-burst), occurs where the stable equilibrium of ancient discontinue has been disrupted due to excavation, causing reactivation along a pre-existing discontinue surface, which often results in a small slip movements, up to 0.4m. This type of slip-burst may be triggered either close to or some distance from the mining face (Richardson and Jordan, 20001). Type B (seismic events of strainburst) occurs in very deep underground engineering, i.e. Witwatersrand gold mines in South Africa, where rockbursts occurs as a result of the high stresses concentrate induce by excavation. The primary difference between the two type of rockbursts is that the failure directly related to a geological discontinue or not. Type B result from the sudden formation and propagation of shear fracture with normal slip displacements (up to 0.1m, Gay and Ortlepp, 1979). The tremors magnitude of strainbursts usually low to medium (up to M_L=1.1, Finnie, 1999). [3]~[4]

Due to the very real difficulties of access and visibility the rockmass that have suffered by slip-burst, very few of useful description of the nature of the damage had been recorded. In this paper we descript a slip-burst which happened in the deep Dewater tunnel of Jingping II hydropower project August 2008, and DEM (Distinct Element Method) was used to gather further understanding of the slip-burst.

2 Method Used in Rockbursts Numerical Modeling

It is unrealistic to expect numerical models to predict the time and location of individual rockburst, due to uncertainties in field data. Models should be used to understand mechanisms and perform comparative simulation that can be used to decide between different excavation strategies and support types. [5] Commonly, there are two broad categories models used in represent rockbursts and their affects: the first may be termed “indirect methods”, in which failure will mot actually modeled; the second is termed “direct methods”, where an attempt is made to model the failure process.

i) Indirect method. Indirect method assumes some quantities which calculate from the result of stress distribution are correlated with seismic events. ERR(Energy Release Rate) and ESS(Excess Shear Stress) are the most common quantities used to asses the rockbursts potential.

   a) ERR. The Chamber of Mines Research Organization (COMRO) of South Africa pioneered the use of boundary element methods and the calculation of ERR (Cook, et al, 1966). Salamon (1984) presented the basic equations for energy storage and release in elastic ground as a result of excavation. Mark Board (1993) extend the origin equation to plastic and discontinue involved situation, so that we can take the energy dissipation due to discontinue slip, plastic deformation of rockmass into consideration. ERR can be used as an index to rank various mining strategies in terms of their potential for producing damaging rockbursts. ERR does not indicate in what location rockbursts might occur.

   b) ESS. Ryder (1988) presented the ESS to study the known discontinue slip induced slip-burst. The same of ERR and ESS is that they all provide risk of rockbursts potential, the different is ERR also provide the most highly stressed regions.

   c) Statistical Event Simulation. The origin form of the statistical event simulation was proposed by Salamon (1993). In this model, statistical parameter derived from underground mapping, such as fracture spacing, length and orientation. These parameters are used to generate statistically simulated. Measured seismic events can used to calibrate statistical model. The approach provides far more information than ERR or ESS.

ii) Direct method. Failure is actually modelled explicitly in the direct method by using PFC (Particle Flow Code). PFC present a solid material by an assembly of many particles that are bonded together with “glue” that can break when strength beyond a given value, discontinue can also be simulated directly. Cundall simulated a strainburst with fragment eject on the left and right side automatically by loading a pillar form upper and bottom. The release of strain energy by bond breakage is more than sufficient to overcome the energy absorption, resulting in a spontaneous ejection of a slab of material at high velocity.

In this paper we used “indirect” method to study slip-burst observed in Dewater tunnel of Jinping Project, analysis work focus on the high stress region of rockmass.

3 Geology and description of Slip-burst on Dewater tunnel

Jinping Second Stage Hydropower Station (JP-II) is located at Yalongjing River in Liangshan Autonomous Region, Sichuan province. The sluice gate is situated at Maomaotan in the west of Jinping Mountain and the plant at Dahuigou in the east. The four hydropower tunnel, each of approximately 16.7 km in length running parallel to each other and crossing the Jinping Mountain, an alpine karst zone, will connect the sluice gate and the plant units. The two transportation tunnels lay parallel to hydropower tunnels which construction works started in November 2003 and breakthrough on 8 August 2008. The dewater tunnel also lay parallel to hydropower tunnels and construct by TBM, the tunnelling work start on May 2008. Figure 1 show the layout of the seven tunnels.

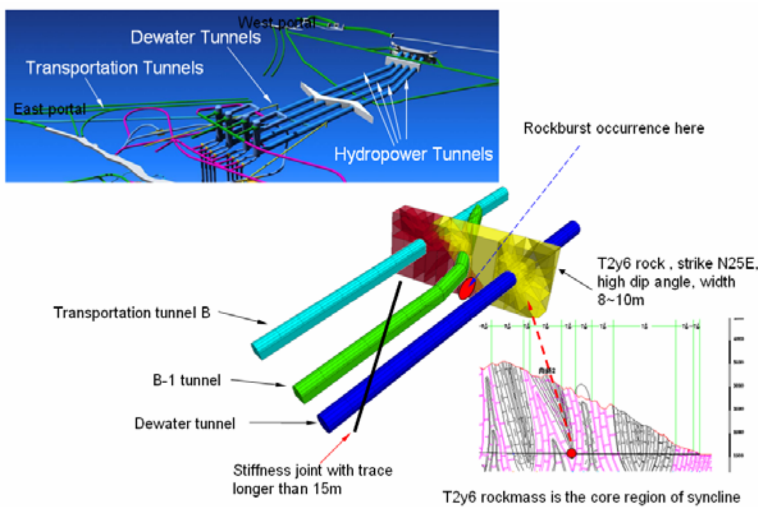

Figure 1 Layout of the Jinping tunnels and the geology of slip-burst region

The Jinping mountain is huge complex fold, the rocks along the tunnels belong to the Triassic period, i.e. they are 205 ~ 250 million years old. The rocks are mainly dipping eastwards in the eastern part and towards west in the western part with strike generally N - S to NNE - SSW. They will therefore, intersect the Jinping tunnel mostly at a right angle. The main rocks are marble, which occupy large parts of group T2 (T2b, T2y, T2z), T2b locate in the middle core of mountain and more brittle than T2y and T2z. Other rocks are schist, meta-sandstone, slate, and mica schist. More than two hundred faults have been encountered during transportation tunnel construction. They are mainly steep dip angle faults, and range in size (thickness) from 1 cm to 5 m, most of them are 0.1 - 0.5 m thick. Joint with strike N – E and N –W are the most common rock structure along the transportation tunnels. Most joint are described as closed, which means that they can be characterized as tight joints. Most huge rockburst observed in transportation tunnels are structure relation, for example, rockburst happened on tunnel face, after tunnel driving, N – E stiffness joint always could be find.

Fig 1 shows the simple geology description of B-1 tunnel. The region locates near the core of second syncline form the East portal and the overburden here is about 1400m. The transportation tunnel B and B-1 tunnel was broken through first, then the TBM began tunnelling the Dewater tunnel. When the TBM tunnelling near the B-1 tunnel the pillar between the two tunnels only 8m so that he risk of pillar-burst is high. In fact the pillar-burst did occurrence, while a violent slip-burst happened near the turning of the B-1 tunnel .

A large closed stiff-joint with middle dip angle was exposed when TBM tunneling through pillar region, During TBM approaching and departing the stiff-joint, spalling become severe and occurrence on each side wall of Dewater tunnel. It's emphasized that spalling always happened on the right spandrel (facing tunnel face) and failure depth limited 30cm if overburden less than 1800m. The spalling failure depth of Dewater tunnel near stiff-joint is about 40~50cm, even severe than high overburden region, show the in-situ stress of this tunnel segment is localized. We cannot tell the which is the most important factor which result in localized in-situ stress, obviously the stiff-joint and tunnel segment located in the core of a syncline have important correlation with in-situ stress, furthermore we can tell the in-situ stress of this tunnel segment is normal faulting regime which mean vertical in-situ stress is the max principle stress ($S_V > S_H > S_h$).

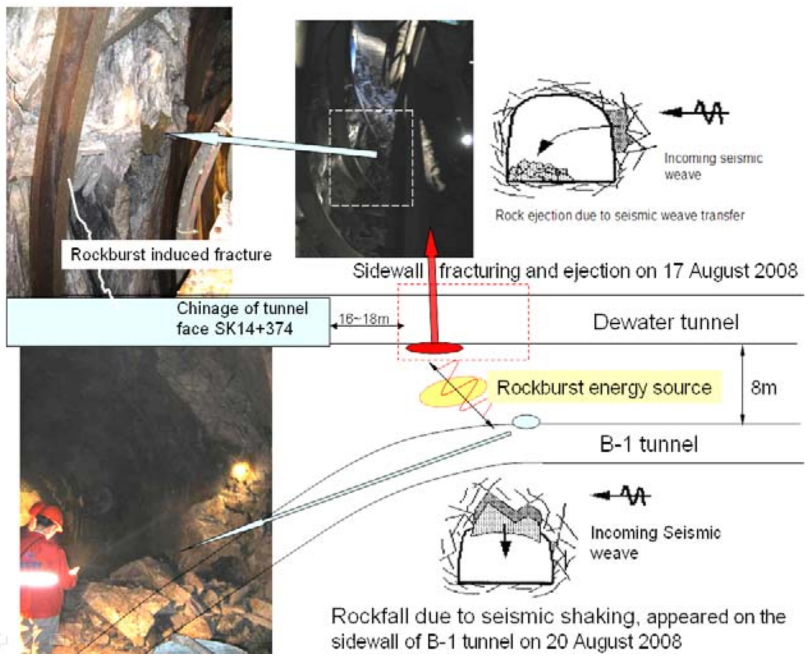

Figure 2 The photo of Rockburst on B-1 tunnel

When TBM tunnelling to chinage 14+374, a severe rockburst was observed on left side wall. Fig 2 is a layout of tunnel face and bockburst location and the photo of romass after rockburst also add to the figure. According to CRRP (Canadian Rockburst Research Program), there are three kinds of rockburst damage mechanism: (1) rock bulking due to fracturing; (2) rock ejection due to seismic energy transfer; (3) rock fall due to seismic shaking. Rock ejection and rock fall were observed on site, Fig 2 also show the site photo of the two kinds damage. Rock ejection happened on the side wall which 16~18m behind tunnel face, rock fall occurrence on B-1 tunnel two day after rockburst happen due to lacking enough support force. The rockburst offer a unique opportunity to study the relationship between stiffness joint and slip-burst, numerical model being used to get more insight and verify some assumption.

4 Numerical Simulation of the Slip-burst

Numerical model based on DEM (Distinct Element Method) being used to understand the rockburst. The main geological structure such as stiffness joint, weak alteration joint 1 and 2, relatively weak marble T_{2y}^{6} are take into consideration in order to identify the major factor that lead to potential rockburst risk best. Fig 3 show the model boundary, size of Dewater tunnel and B-1 tunnel, and main joint strike and dip angle.

A normal faulting regime in-situ stress with estimated lateral coefficient 0.8 being used as model in-situ stress boundary, 0.8 is a rough estimation based on the spalling shape and spalling failure depth due to lacking in-situ stress measurement here.

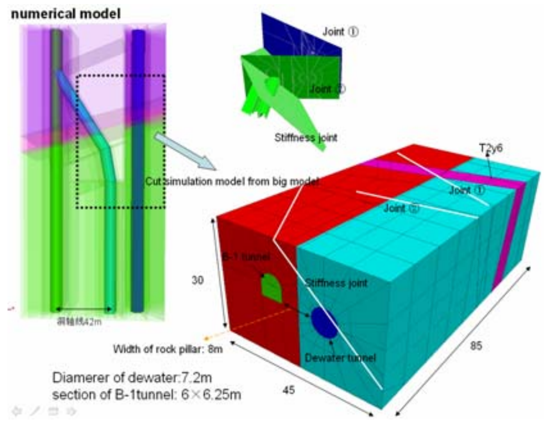

Figure 3 Numerical model for rockburst analysis

Conventional strain softening Mohr-Coulomb constitutive model being used to simulation the excavation response which assuming the value of rockmass cohesion and friction angel continue dropping until residual strength with plastic strain accumulation. The peak strength of rock is obtained with Hoek's GSI experience method.

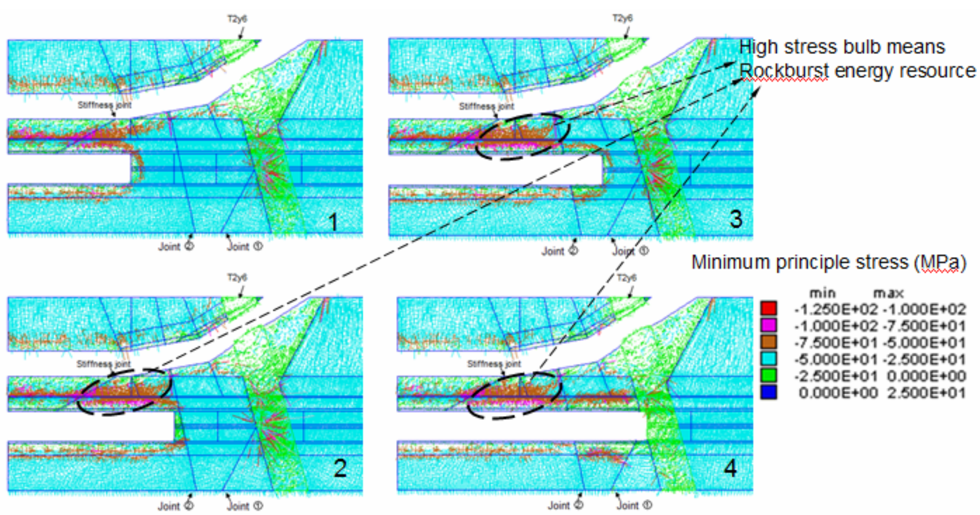

Figure 4 Minimum principle stress of plan view on B-1 tunnel region

TBM heading being simulated by several excavation steps, Fig 4 show the stress distribution in plane view with different tunnel face location. The high stress bulb location exactly corresponding to rockburst occurrence position, which mean numerical model could predict high rockburst potential risk region. Normal faulting regime in-situ stress being using as numerical model boundary condition, the pillar between B-1 tunnel and Dewater tunnel will be stress concentrate by experience conjecture. In face there no pillar burst take place on pillar region while slip-burst occurrence near the turning of pillar, this phenomenon should be explain by numerical model. Fig 5 show different cross-section of model, the minimum principle stress varied a lot between the hanging wall and footwall of stiffness joint.

From Fig 5 we can conclude that even uniform in-situ stress field could result in totally different excavation response due to the existing of stiffness joint and the rockburst on B-1 tunnel is a slip-burst actually.

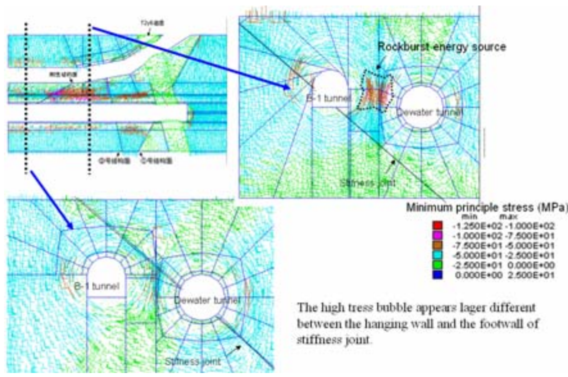

Figure 5 Stress distribution of cross-section view near stiffness joint

5 Conclusion

Based on about 4 years of site observation of the transportation tunnel and 1 year observation of the Dewater tunnel, we have several conclusions:

(1) Most rockburst in the Jinping deep tunnel are structure related, and even alteration joint tip could induce rockburst;

(2) TBM excavation methods damage the surrounding rockmass less than the D&B (Drill and Blasting) method, which can unfavorably initiate rockburst;

(3) DEM can be used to study jointed related rockburst and gain insight on slip-rockburst;

(4) In this paper we discuss a uniform in-situ stress field which the mean existing joints do not affect the in-situ stress distribution, this assumption maybe only be valid on a closed stiffness joint;

(5) Further study should take place on some open or alteration joint change the in-situ field significantly in the joint affection region and result in rockburst on the joint tip.

Acknowledgements

The authors wish to express his thanks to China Postdoctor fund (20080440601), and recognize the contributions made to this work through discussions, by Dr Peter Zhu.

References

1. Canadian rockburst research program 1990-1995, Rockburst Research Handbook, Volume 1: Mining in burst-prone ground. 4-5, 2-6.
2. P. Cundall, M.Board and J.Tinucci. Numerical Modeling Related to Rockburst Research. Proceedings of the International Workshop. (Santiago, 1995): 43-59.
3. R.A. Stewart, W.U. Reimold, E.G. Charlesworth and W.D. Ortleep. The nature of a deformation zone and fault rock related to a recent rockburst at Western Deep Levels Gold Mine, Witwatersrand Basin, South Africa . Tectonophsics, 2001. 173-190
4. W.D. Ortleep. Observation of mining-induced faults in an intact rock mass at depth. International Journal of Rock Mechanics Mining Sciences. 2000. 423-436.
5. Mark Patrick Board, Numerical examination of mining-induced seismicity, PhD thesis, 1994, 1-5.

RaSiM 7(2009): Controlling Seismic Hazard and
Sustainable Development of Deep Mines,
C.A. Tang(ed), Rinton Press, 679-684

MICROSCOPIC SIMULATION OF CALCAREOUS SAND PARTICLE BREAKAGE

JI-ZHU SUN and QIAN GUO

School of Civil Engineering and Architecture; Wuhan University of Technology

Wuhan, 430070, P.R. China;

Abstract： Based on one dimensional compression tests on calcareous sand in laboratory, the cluster element is constructed by the contact-bond model introduced in PFC2D. By using the cluster elements, a numerical model is created. Through the reasonable setting of the micro parameters, the particle breakage characteristics of the natural calcareous sand are simulated in this paper. During the loading process of biaxial numerical tests, the overall variation of particle bonds is recorded and the position of bond breakage and particle rotation are traced, so as to analyze the development of particle breakage and formation of shear band in the numerical sample. The results show that the position of particle rotate is obviously the place where particle breaks. and the breakage approaches the shear band gradually.

1 INTRODUCTION

The calcareous sand is a granular material from halobios evolution, which contains more than 50% CaCO3 and spreads widely in the southern islands of China. Due to some distinct characteristics, such as a high void ratio, particle breakage at a lower stress level, compression, dilatancy and strength; calcareous sand is far different from the general land sand[1]. The study on soil particle breakage investigate sand numerically simulate the particle breakage from macroscopical view [4], before mainly adopted experiments and qualitative analysis [1, 2, 3], and few theories were confined to continual medium mechanics methods, Recent years McDowell etc. simulated particle breakage with discrete element method (DEM) and studied the effect of particle characteristics and breakage rates on macro-mechanical response [5, 6]. However, the micro-mechanics of shear failure process and its relation to the particle breakage was not included.

Jian Zhou and Yu-wei Chi etc. simulated biaxial experiments of sand with the PFC2D, and studied the formation of shear band and its development law from mesoscopical view [7]. However, this study was based on the rigid round disk particles, without developing the particle cluster element of PFC2D. The research shows that particle cluster constructed with PFC2D bond model to simulate the mechanical characteristics of natural sand is more appropriate than the rigid round disk particle element[8].

Based on the compression experimental study of calcareous sand, this paper carries out the microscopic numerical simulation of its shear failure process by introducing the particle flow theory and developing its numerical technique. The macro-mechanics response is connected with its micro-structure of sand so as to have a better understanding or discovery of the particle breakage and its shear band formation as well as evolution of calcareous sand.

2 PFC2D BOND MODEL AND PARTICLE CLUSTER

PFC2D contact-bond model with few microscopic parameters was used to simulate the particle breakage of calcareous sand, this hopes that the quantitative relations between micro-parameters and macro-mechanical behaviours could be studied effectively. A particle cluster was composed of several rigid round disk particles according to the contact-bond model, the particle cluster with different scale or shape could be obtained by changing the scales, numbers or bonding styles of rigid round disk particles. Particle cluster of numerical sample in this paper was composed of 7 iso-radial rigid round disk particles through the contact-bond model, each particle cluster has 12 initial bonds. The shape of cluster is shown in figure 1, the position of initial bonds is presented with the black solid lines.

The breakage process of one particle cluster is diagrammed in figure 2. Before loading no particle breakage occurs and the inner porous area in the cluster is included in the solid area of particle clusters as shown in figure2 (a). The particle breakage occurs when load is increased to some extent after loading and the inner pore as solid area of cluster once is released to turn to be exterior pore as shown in figure.2 (b). The total solid area of sample decreases continuously as the inner pore is released continuously. In this case, it is difficult to determine the variation of porosity accurately, an optional method is to use the area variation A/A0 during loading as a approximation to the variation of porosity in sample[2].

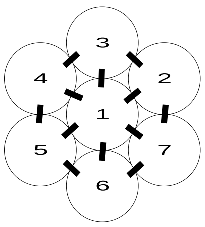

Figure 1. Particle cluster structure

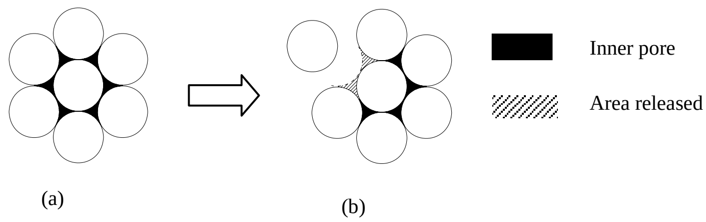

Figure 2. Schematic diagram of particle cluster breakage

3 ANALYSIS OF BI-AXIAL NUMERICAL TESTS

3.1 One-dimensional numerical tests and micro-parameters

When particle clusters were established with contact-bond model, some micro-parameters must be determined: normal bonding strength b_n, tangential bonding strength b_s, normal contact stiffness k_n, tangential contact stiffness k_s, coefficient of particle friction fc and particle density ρ_s. The contact force among particles is affected by contact stiffness k_n and k_s while the bonding intensity of particle cluster is affected by bonding strength b_n and b_s.

One-dimensional compressive numerical tests on particle cluster sample were carried out and different compressive curves were gotten by adjusting micro-parameters. A comparative analysis of one-dimensional compression curves in laboratory tests（reference 9, Figure.4-11）can provide micro-parameters of particle breakage simulation of calcareous sand, as shown in table 1. If not taking into no particle breakage, the normal and tangential bonding strength are both set at 5×1010N in this paper.

Table 1. Calcareous sand micro-parameters in PFC sample

meso-parameters	b_n (N)	b_s (N)	k_n (N/·m)	k_s (N/m)	f_c	ρ_s (kg/m3)
values	50	50	5×106	5×106	0.5	2790

The compressive curve $A/A_0 \sim \log\sigma_y$ in numerical test is shown in figure 3, as well as the varying curve of total bonding number n corresponding with vertical stress σ_y during loading.

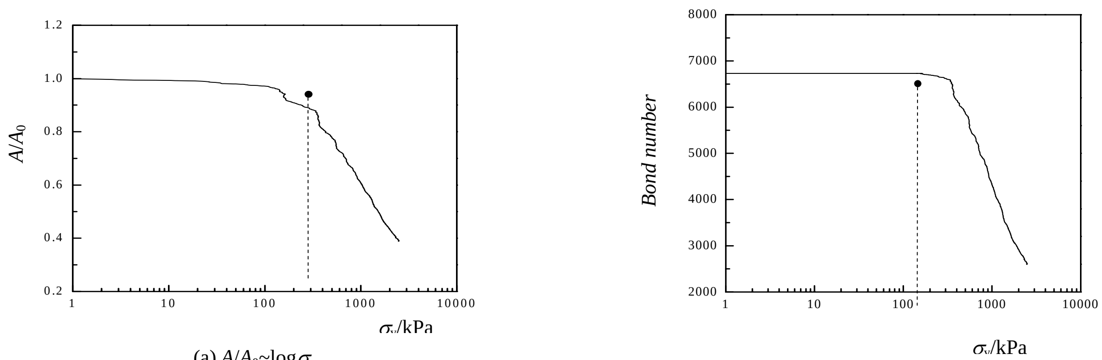

(a) $A/A_0 \sim \log\sigma_y$

(b) $n \sim \log\sigma_y$

Figure 3. One-dimensional compressive numerical tests results

Figure3(b) shows that an evident particle breakage point (shown as black point in figure3(b)) exists in the numerical tests. It corresponds with the yielding stress at about 300kPa on the compressive curve $A/A_0 \sim \log\sigma_y$. figure3(b) also shows that the total bond number of particle cluster remains constant when vertical stress is less than yielding stress. This indicates almost no particle breakage occurs in the sample and deformation of sample is mainly due to pore compaction. While vertical stress exceeds yielding stress, the total bond number of particle cluster decreases linearly as the vertical stress increases. Meanwhile evident particle breakage occurs, it aggravates compressive deformation of the sample.

3.2 Preparation of numerical sample

The preparation of bi-axial sample consists of several steps as the following:

(1) In a two-dimensional space with the length of 30mm and height of 60mm, round particles are generated and the particle sizes vary from 0.1mm to 1.5mm in accordance with normal distribution. The initial porosity is controlled at 0.1, as shown in figure 4(a); (2) The location and size of round particles are recorded with Fish function; (3) The round particles are deleted and particle clusters with the same size as round particles are

generated at the previous location, as shown in figure 4(b); (4) Prescribed isotropic pressure is loaded on sample, as shown in figure 4(c); (5) To wait for loading. There are 2589 particle clusters and 31068 initial bonds in bi-axial sample.

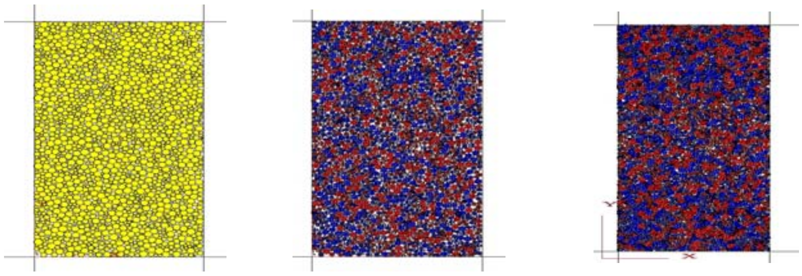

Figure 4. Preparation of bi-axial numerical sample

3.3 Analysis on the numerical tests

(a) Macro-mechanical response

Figure 5 shows the curves of deviatoric stress-axial strain and volumetric strain-axial strain respectively of numerical tests at confining pressure of 200kPa, it generally consist with the test result in reference [10]. Strain softening and slight volume expansion of calcareous sand occur in the later loading as shown in figure 5.

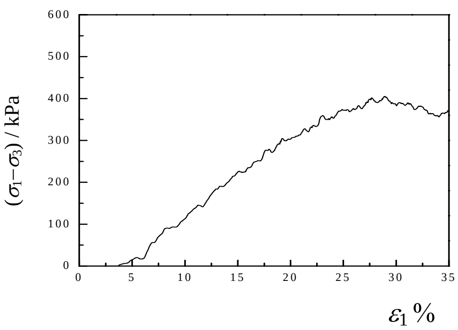

(a) Deviatoric stress and axial strain curve

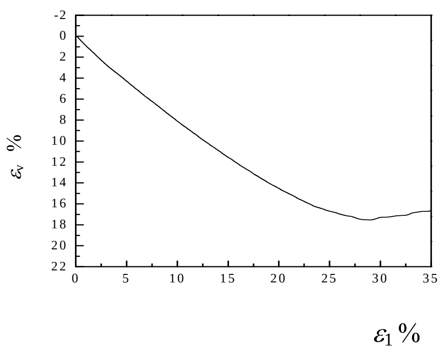

(b) Volume strain and axial strain curve

Figure 5. Macro-mechanical response (200kPa)

(b) Characteristics of particle breakage

Figure 6 shows the change of bonds sum and the corresponding particle breakage rate during loading. 707 bonds are lost during consolidation, corresponding with the breakage rate at 2.28%. When the strain exceeds 10%, the particle breakage begins to accelerate and slows down in the late period as shown in figure 6.

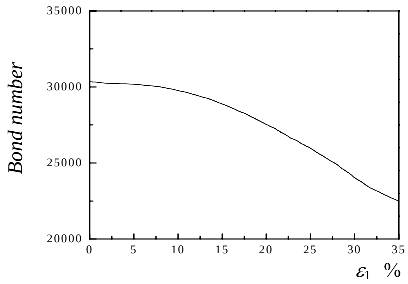

(a) Bonds sum and strain curve

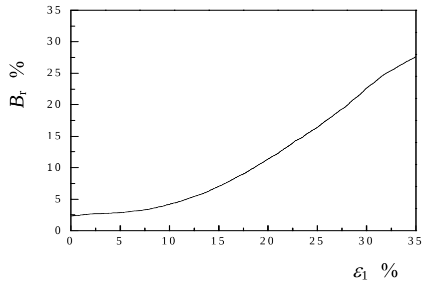

(b) Particle breakage rate and strain curve

Figure 6. Variation rule of bonds sum and particle breakage rate with strain (200kPa)

When the axial strain is 10%, 20% and 30%, bond breakage distribution in the sample is shown in figure 7, in the figure black short line represents the bond breakage caused by tangential contact force among particles exceeding tangential bond strength, while the red ones represents the bond breakage caused by normal contact force exceeding normal bond strength. It can be found from figure 7 that bond breakage occurs mainly in the tangential direction, as the strain grows, the scattered broken bonds gradually converge to some band zones.

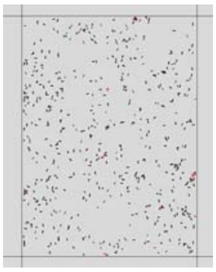

(a) ε_1=10%

(b) ε_2=20%

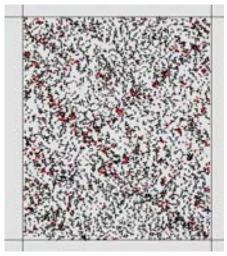

(c) ε_2=30%

Figure 7. Distribution of bond breakage (200kPa)

(c) Characteristics of particle rotation

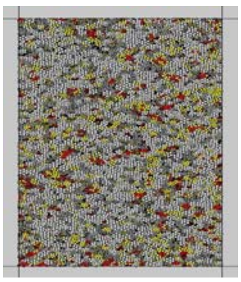

(a) ε_1=10%

(b) ε_2=20%

(c) ε_2=30%

Figure 8. Particle rotation distribution (200kPa)

By monitoring the particle rotation during shear process, the schematic diagrams of particle rotation at different stress levels are shown in Figure 8, in the figure the white zones represents the particles whose rotation amount is from 0° to 10°, the yellow ones from 10° to 20° and the red ones larger than 20°. Comparing figure.7 with figure.8, it figures out that a close relation exist between particle breakage and particle rotation, the position of bond breakage is often the position where larger particle rotation occurs, the zones of bond breakage gradually converges is approaching to the position where shear band forms, and the particle breakage sum grows rapidly as the forming of shear band.

4 Conclusion

Based on the one-dimensional compression tests in the laboratory of calcareous sand and the PFC2D contact-bond model, micro-parameters of the particle cluster are found. Some main conclusions are obtained from basis numerical tests as below: (1) The compressive curves and particle breakage yielding stress are consistent with test results in laboratory. It indicates that numerical tests can preferably reproduce the characteristics of particle breakage under one-dimensional compression. (2) A close relationship exists between particle breakage and particle rotation. The position of bond breakage is often the position where larger particle rotation occurs. In mechanism the particle breakage tends to concentrate towards the shear band. (3) Particle breakage promotes the formation of shear bands, while shear bands accelerate the development of particle breakage. The zones where bond breakage gradually concentrates approaches the positions where shear band forms.

Reference

1. Wang, R., Song, C.J., et al. Engineering Geology of Coral reef at Nansha Island , Beijing: Science press, Beijin, 1997.
2. Wu, J.P., Chu, Y. and Lou, Z.G. Influence of Particle Breakage on Deformation and Strength Properties of Calcareous Sands. Chinese Jounal of Geotechnical Engineering, 1997，19(5). 49-55.
3. Nakata, Y., KatO, Y., Hyodo, M., et al. One-dimensional compression behavior of uniformly graded sand related to single particle breakage strength. Soils and Foundations, 2001, 41(2). 39-51.
4. Daouadji, A., Hicher, P.Y. and Rahma, A. An elastoplastic model for granular materials taking into account grain breakage. European journal of mechanics. A. solids., 2001, 20(6). 113-137.
5. McDowell, G.R. and Harireche, O. Discrete element modeling of yielding and normal compression of sand. Geotechnique, 2002, 52(4). 299-304.
6. Cheng, Y.P., Bolton, M.D. and Nakata, Y. Breakage and plastic deformation of soils simulated using DEM. Geotechnique, 2004, 54(2.). 131-141.
7. Zhou, J., Chi, Y.M., Chi, Y., et al. Simulation of biaxial test by particle flow code. Chinese Journal of Geotechnical Engineering, 2000, 22(6). 701-704.
8. Thomas, P. A. and Bray, J. D. Capturing nonspherical shape of granular media with disk clusters. Journal of Geotechnical and Geoenvironmental Engineering, 1999, 125(3). 169-178.
9. Zhang, J.M. Study on the Fundamental Mechanical Characteristics of Calcareous Sand and the Particle Breakage effects . PHD thesis, Institute of Rock and Soil Mechanics, Chinese Academy of Science, 2004.

RaSiM 7(2009): Controlling Seismic Hazard and
Sustainable Development of Deep Mines,
C.A. Tang(ed), Rinton Press, 685-690

OCCURRING MECHANISM AND NUMERICAL SIMULATION OF TENSION ROCK BURST OF THE ISOLATED COAL PILLAR

LAI-GUI WANG

College of Mechanics and Engineering, Liaoning Technical University

Fuxin 123000, China

NA ZHAO

College of Mechanics and Engineering, Liaoning Technical University

Fuxin 123000, China

In view of the problem that the rock burst of the isolated coal pillar occurs easily and has no practical understanding of the damage theory of the rock burst, the occurring mechanism of tension rock burst of the isolated coal pillar is discussed with finite element software. In which, the fracture and evolution process as a function of the triangle load of the isolated coal pillar is analyzed. The result shows that the coal pillar generates tension fracture on its both sides, the fracture direction is horizontal. After the coal pillar cracks, the stress is released and new stress concentration and the loose region are formed. Tension fracture occurs on both sides of the coal pillar in the horizontal direction. New stress concentration is formed and a loose area is formed after the fracture of the coal pillar on the long-term interaction of roof and floor and geography, the pillar slides in horizontal direction. This can provide the theoretical basis for the prediction and forecast of the rock burst of the isolated coal pillar.

1 Introduction

Rock burst disasters release coal deformation energy in an abrupt, sharp and violent way with a large noise and vibration that can last a few seconds to tens of seconds. Tens of or even hundreds of tons of coal is thrown out in the process of rock burst, causing damage of the supporter, jam of the roadway. The most severe quake in a mine was recorded to be a 5 on the Richter scale. In our country, the coal seams and terrene of most mines have a violent and obvious impact liability with the impact of coal seams at a certain critical depth being fatal. As one of the most important problems of rock mechanics, scholars of various countries have put forth a series of important theories about rock burst from different angles. Such as the strength theory, stiffness theory, energy theory, theory of impact liability, theory of three rules, destabilization theory and so on.

Over the past decade，the disastrous damage of the isolated coal pillar’s high stress rock burst is becoming more and more serious. Examples such as the Xin Wen’s Huafeng coal mine, Wei Shan’s Huang Cheng coal mine, Yan Kuang's Dong Tan coal mine, and Zao Zhuang's Ba Yi coal mine all experienced various degrees of disaster bursts in the isolated coal pillar region under high stress. The problem of isolated coal pillar high stress rock burst is becoming increasingly important with an urgent need for more research. Rock bursts continue to occur and the theory of the destructive process on the high stress rock burst on the isolated coal pillar is important for the prediction, forecasting, and prevention of the high stress rock burst of the isolated coal pillar. The paper primarily researches the isolated coal pillar of cover roof rock, the pillar of coal damaging rules of burst and the evolution inside; providing a theoretical basis for the mechanism of the rock burst of isolated coal pillar.

2 Mechanism of extensional type of rock burst of the isolated coal pillar

Because the intensity of coal body is far less than roof base plate rock's, usually coal body, generally speaking, coal body destructive probability will be great in the same state of stress. Moreover in coal body's roof base plate, the press on coal body is uneven; bearing pressure appears in certain scope of coal seam. And the thickness of coal seam distributes unevenly, in mining thin coal seam process, the possibility of burst increase. There are two important steps in the process of the emergence of compound-type rock burst.

Because of bearing pressure effect, the pressure of horizontal direction is even，coal body are given tension in the horizontal direction around the point of peak value stress of horizontal direction round peak point of application. And tensile intensity of coal body is low, which is the tenth of uniaxial compressive strength, so tensile failure happens round horizontal direction of peak stress point, this is the first process. The next happens in the second process, because long-term geological activity, coal body and peak, there are less friction resistance between base plates, coal body of pulling completely, immediately slide to goaf along up and down board, until all or part of energy is released the system is rebalanced. On the spot burst accident survey from indoor experiment shows that the process of coal body moving after tension fracture is fully proved.

3 Overlying rock of isolated coal pillars supports the pressure

Based on the laboratory test and field monitoring, isolated coal pillar stress at the top center is the largest. Stress distribution is shown in Figure1(a)，In order to simplify the calculation, the supporting pressure of the isolated coal pillars is simplified as a triangle load, as in Figure1 (b). Calculation of the maximum value is based on formula (1)

$$P=\rho gh \qquad (1)$$

In it, P is bearing stress; ρ is the average density of overlying strata; g is acceleration due to gravity, taking 10 m/s2; h as the thickness of overlying strata.

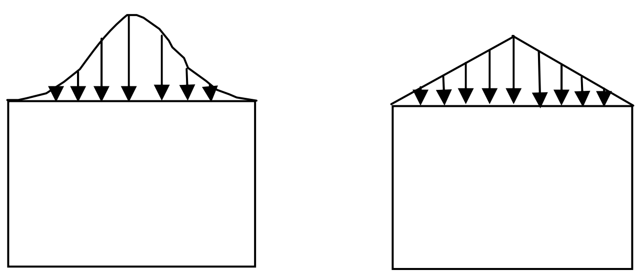

（a）normal pressure distribution （b）triangle pressure distribution

Figure 1 coal pillar pressure distribution

4 brief introduction to the software of the finite element numerical simulation software of tensile fracture

The finite element software of tensile damage of rock uses three node flat triangular elements to get the nodes mean stresses and nodes principal stresses and the directions of the principal stresses, by generating the finite element program, according to tensile fracture criterion and crack criterion to determine whether the nodes are cracked.

The rock tensile strength is comparatively low and generally is 1/10 as Figure 2 shows:

$$\sigma_c=10\sigma_t \qquad (1)$$

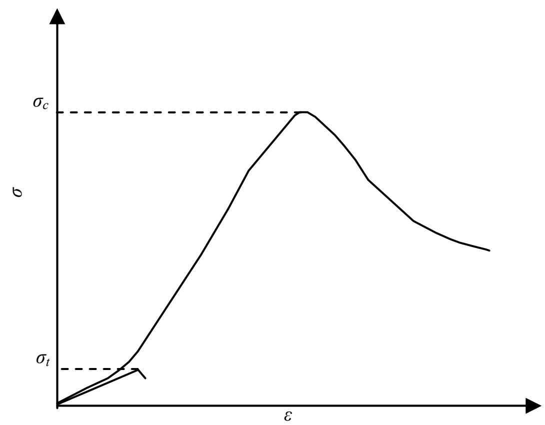

Figure1 stress-strain curve of the rock bearing the pulling and the press

Criterions of rock tension fracture are as follows：

(1) When the maximum tensile stress of node is bigger than the tensile strength ,the node is cracked.

$$\sigma \geqslant [\sigma] \quad (2)$$

In it,σ is the maximum tensile stress of node, $[\sigma]$ is the tensile strength of rock.

(2) When the vector direction of main compressive stress and the direction of maximum tensile stress is vertical, the rock is cracked.

(3) The node bearing the maximum principal tensile stress is cracked first in the stress field under pulling stress.

(4) The rock can still bear the compressive stress after the rock is cracked.

5 Finite element numerical simulation of tensile fracture of isolated coal pillar

5.1 selection of isolated coal pillar mode

Select a single isolated coal pillar whose length is 5m and height is 3m. There is a triangular load on the top and fixed constraint on the bottom.

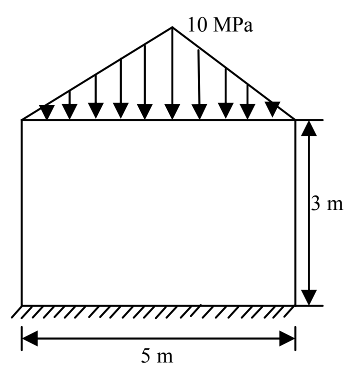

Figure 3 coal pillar model

The mesh is divided as in Figure 4.There are 3348 triangular elements and 1755 nodes. Select of 4 monitoring points to monitor the changing of first principal (tensile) stress in fracturing process as shown in Figure 4.

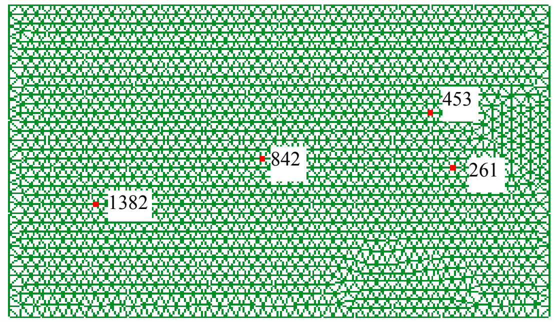

Figure 4 the mesh and the selections of 4 monitoring points

5.2 Process of tensile fracture

Select model as in Figure 3 simulate the tensile fracture process of the coal pillar under the pressure of overlying rock, by using the finite element analysis software of tensile fracture, as in Figure 4. The amplification factor of deformation is 2.

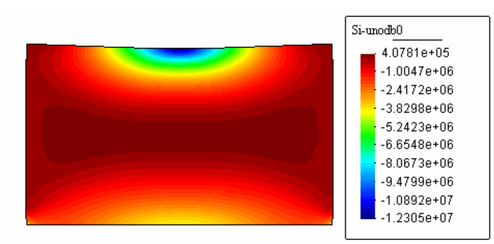

(a) before cracking

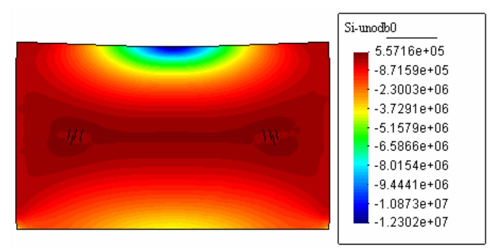

(b)Step 1

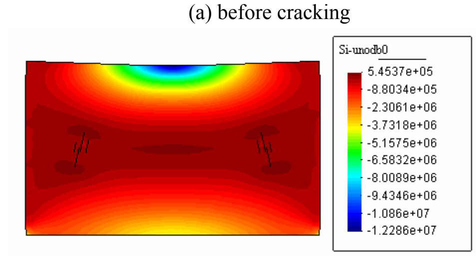

(c)Step 5

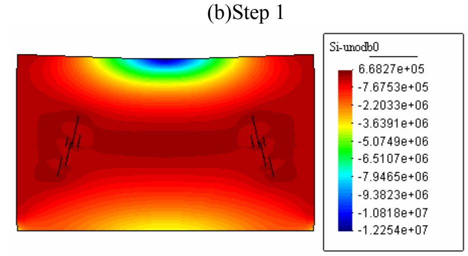

(d)Step 10

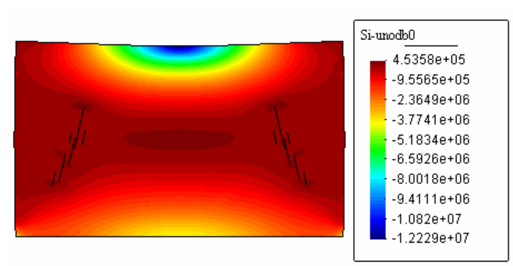

(e)Step 13

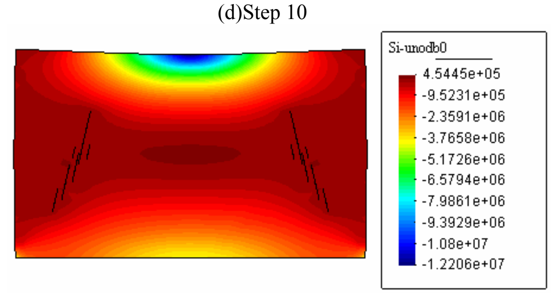

(f)Step 16

Figure 5 the evolution process of fracture of coal pillar

From Figure 5 we can see that it the middle top of the coal pillar is compressed before cracking, but it is in tension in the centre of the coal pillar as in Figure5(a),and because of the influence of constraints on the bottom, tensile fracture occurs in the centre of it first as in Figure5(b),then the crack propagate apart to the top and to the bottom as in Figure5(c)~(d).The stress is released and redistributed to form new stress concentration, then it continues to crack, propagate in the new stress concentration area after cracking. If the step of weighting is small enough and the speed of weighting is great enough, the friction will be diminished. The coal of the both sides of the loose area is thrown out, forming rock burst with larger grades.

Figure5 just verifies the two steps in the process of producing a compound rock burst. Step 1, it is cracked along nearly horizontal in the centre of the coal pillar and the crack propagates, forming loose areas on the both side. Step 2, because long-term interaction between the roof and floor and other geological activities, result in the friction between coal pillar and roof and floor is reduced , the both sides of coal pillar move to the right and left sides of the goaf, until all the accumulated elastic energy is released.

5.3 Change curve of first principal (tensile) stress of monitoring point

Select 4 monitoring points as in Figure 4, monitor the change of first principal (tensile) stress and the change curve is shown as Figure 6.

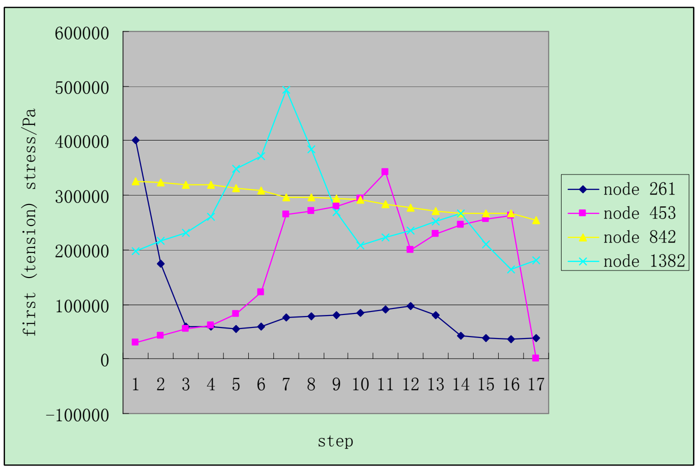

Figure 6 the change curve of first principal (tensile) stress of monitoring point

Figure 6 shows that the stress is released suddenly after the node 261 cracked at step 1, the change of the stress is not obvious after releasing. The stress of node 453 and node 1382 rises first. This is because the other near nodes crack, forming new stress concentration, the stress is released and reduced suddenly, when the node 1382 is cracked at step 7.But the change of the stress of node 842 is not as obvious as node 1382,when the nodes around it are cracked and the stress is released. It shows that the stress is released and redistributed, forming new stress concentration when the node or the neighbouring nodes are cracked. There is an abrupt stress on the cracked node, then the change is not obvious, tending to be steady.

6 Conclusion

By studying the failure mechanism of rock burst of the isolated coal pillar and the numerical simulation of tensile fracture of isolated coal pillar, the conclusions are listed as follows.

(1) There are two main steps in the compound rock burst of the isolated coal pillar: the process of tensile failure in the horizontal direction and the process of the coal moving to the goaf.

(2) The first principal (tensile) stress is redistributed to form a new stress concentration after tensile fracture.

(3) The coal pillar is cracked on the both sides of the center point. When the process of weighting is small enough and the speed of weighting is great enough, the cracked coal moves to both sides of the goaf.

(4) It can provide the theoretical basis to forecast the rock burst of the isolated coal pillar.

Acknowledgements

The authors wish to acknowledge the financial support by the State Key Laboratory of Geohazard Prevention & Geoenvironment Protection Fund (DZJK-0809), National Natural Science Fund (50434020), Science and Technology Fund of Liaoning Province (20022155) and Basic Research of Educational Bureau of Liaoning Province (202182055).

References

1. Zhang, H. Study on the law of the movement and fracture of "isolated island" working face ovenburden.Qingdao: Shandong University of Science and Technology, 2004.
2. Yao, Q.H. Study on appraisal of rock burst hazard in isolated coal pillar. Qingdao: Shandong University of Science and Technology, 2006.
3. Zhu, J.M., Gao, L.X. and Yang, Y.J. Discussed on the reason of deep thick hard roof evoked the rock burst. Coal, 1995, 4(5). 16-19.
4. Li, X.Y., Ma, N.J., Zhong, Y.P., et al. Storage and release regular of elastic energy distribution in tight roof fracturing. Chinese Journal of Rock Mechanics and Engineering, 2007, 26(S1). 2786-2793.
5. Zhang, X.C.，Miao, X.X. and Zhai, M.H. The analysis of the rock burst occurring mechanism in Sanhejian coal mine. Chinese Journal of Rock Mechanics and Engineering, 1998, 17(5). 508-513.
6. Dou L.M. and He, X.Q. The control theory and technology of rock burst. Xuzhou: China University of Mining and Technology Press, 2001.
7. Zhang, M.T. Discussion on the mechanism of coal burst. Journal of Fuxin Mining Institute(Natural Science), 1985, 4(S2). 65-71.
8. Wang,L.G., Pan, Y.S. and zhang,M.T. Reasons of the earthquake caused by underground mining and excavation and the strategy to deal with it. China safety science journal, 1996, 6(3). 40-43.
9. Wang, L.G., Zhao, N., Zhang, L.L.,et al. Numerical simulation of rock fracture process under tension. International Young Scholar Symposium on Rock Mechanics. [S.l.]: [s.n.], 2008. 425-429.
10. Zhao, N., Wang, L.G. and Zhou, Y.F. Finite element numerical simulation of coal roof tension damage in the gob. The Third International Symposium on Modern Mining and Safety Technology. [S.l.]: [s.n.], 2008. 588-592.
11. Wang, L.G., Zhao, N., Zhou, Y.F., et al. Numerical simulation method of rock bearing tension damage. Journal of Liaoning Technical University(Natural Science), 2007, 26(2).198-200.
12. Zhao, N. Study on finite element numerical simulation of rock tension fracture. Fuxin: College of Mechanics and Engineering，Liaoning Technical University, 2008.

RaSiM 7(2009): Controlling Seismic Hazard and Sustainable Development of Deep Mines, C.A. Tang(ed), Rinton Press, 691-694

OCCURRING MECHANISM AND NUMERICAL SIMULATION OF TENSION TYPE OF ROCK BURSTS OF HARD ROOF

NA ZHAO

College of Mechanics and Engineering, Liaoning Technical University

Fuxin 123000, China

LAI-GUI WANG

College of Mechanics and Engineering, Liaoning Technical University

Fuxin 123000, China

The paper analyzes the occurring mechanism of tension rock burst of hard roof and points out that a large area of goaf is formed and a large tensile stress region after a large area of thick hard roof is mined. When the micro-cracks of the internal rock accumulate to a certain extent, it may cause the avalanche type of chain reaction, under the micro-disturbance. The roof rock cracking and formation of the process of separation layer are simulated with finite element software. The result shows that the stress is released and redistributed and a new stress concentration is formed after the roof cracking. Occurring mechanism and numerical simulation of tension rock burst of hard roof can provide theoretical basis for predicting the rock burst of roof bearing tension type.

1 Introduction

Rock burst is one of the most serious natural disasters in coal mines. This disaster releases coal deformation energy in an abrupt, sharp and violent way with a large noise and vibration that lasts from a few seconds to tens of seconds. Rock bursts displace tens or even hundreds of tons of coal, causing damage of the supporter and jam of the roadway. The most severe quake in a mine was recorded to be a 5 on the Richter scale. Complex reasons influence rock bursts, such as serious disasters, and has become an important subject in the research of rock mechanics. In our country, coal seams and terrene of most mines have a violent, obvious impact liability. In fact, the impact of coal seams at a certain critical depth is fatal. As one of the most important problems of rock mechanics, scholars of various countries have put forth a series of important theories about rock burst from different angles, such as: strength theory, stiffness theory, energy theory, theory of impact liability, theory of three rules, destabilization theory and so on.

According to the force conditions of coal and rock mass, mining-induced rock bursts can generally be divided into four categories: coal mining-induced (rock) type of stress rock burst, roof and floor rock burst, caused by tensile stress fault going shear-slip rock burst, and connective-type compound rock burst.

Rock bursts on roofs under tensile stress refers to the sudden roof fracture when mining is carried out to a certain degree; a large area of roof with hard, thick and complete rock hangs in the air. Holders of power of roof rock burst lies in the area where the tensile strength of the roof is greater than the tensile stress. Rock bursts generally occur in the middle part of the goaf, near the edge of the coal pillar, or along the original fracture line where the weak surface continues the expansion of the crack’s instability. A rear roof fracture, or rear for the relatively large gap between the faults, occurs at the location of its occurrence towards the front face. Roof rock burst strength is characterized by: the thickness of the old roof, the integrity, and the quake grade. Rock burst mining-induced earthquakes in the Mentou Mine, Chengzi Mine in Beijing, and some mines in Datong deal with this type of problem. The roof rock burst of 3.9 degrees on the Richter scale, the greatest roof rock burst in the history of the mines, occurred when COAL SEAM 2 was being mined in Mar. 31st, 1987 in the Mentougou Beijing Mine. The quake reached 10 000 m by a high strength rock burst, a great quantity of coal was not only thrown out, but also tens of meters long waterline were found on the roof. This shows that there were cracks leading to water and because the dense thick layer sandstone roof of the Mentougou Mine is generally conductive in water.

2 Occurring mechanism of rock burst of hard roof bearing tensile stress

The main reasons of rock burst of the roof subjected to tensile stress are shown as follows:

(1) Large area of the roof hangs after coal is exploited.

(2) Recycle a lot of coal pillars

(3) The roof is discontinuous when meeting fault;

(4) Strong disturbing factors such as shooting driving even earthquake

The stability of roof is mainly controlled by tensile stress. Generally speaking, the tensile capacity is poor, the rock is compressive, but nor tensile, the tensile strength is only one tenth of the compressive strength. According to the previous researches, the occurrence and evolvement of the micro-crack of rock are all the result of tensile fracture. Every occurrence of tensile fracture is the process of energies releasing when tensile is in instability, leading to microseism. Because the amount of energy released is very small, some only get recorded through special instruments; people will feel the vibration only when it is over certain strength. People often feel this microseism produced by tensile instability when they are in the underground working face. If in some conditions a wide range of tensile stress area occurs in especially thick, hard and intact strata, although it does not reach the tensile strength at that time, and in stable equilibrium, because coal is no uniform, micro-crack occurs in the coal mass in the small area of low tensile strength and tensile stress exceeds tensile strength first. After micro regional crack, original shear stress is borne by coal and rock mass around them which tensile strength is large, tensile stress is relative low, now the state of equilibrium is steady .Because of sustained disturbance and the constant increase of micro-crack, in macroscopic tensile strength of the whole layer is decreased and the stability of equilibrium decrease gradually, then the micro-crack caused by infinitesimal disturbance makes loads transfer, leading to an avalanche-like chain reactions and tensile instability fracture, when in the state of limiting stable equilibrium at last. Roof cracks suddenly generate macro cracks and release elastic energy which the system stored, thus generating rock burst, as in Figure1. There are some common flap top systems of hanging roof, one is hanged-plate which is clamped support around it, another is hanged-plate which clamped support one side and another side hangs, even it is the hanged-plate which is simply supported around it.

Figure 1 the damage form of overlaying roof rock above the goaf

The roof and floor subjected to internal force bear the effect of bending moment; it makes them subjected to pulling stress on one side and compressive stress on the other side. Because of the lower tensile strength of rock, the tensile rock burst could occur when the area bearing tensile stress reaches a certain range. The condition of tensile rock burst occurring is shown as follows:

$$\sigma_m \geqslant \sigma_t \quad (1)$$

Where: σ_m is the equivalent tensile stress of rock; σ_t is the tensile strength of roof.

3 Finite element numerical simulation of tensile fracture of hard roof

3.1 The criterion for rock tensile fracture

The tensile strength of rock is rather low,and is one tenth of compressive strength generally as in Figure4-2.now

$$\sigma_c = 10\sigma_t \quad (2)$$

The criterion for rock tensile fracture as follows:

(1) When the maximum tensile stress of node is bigger than the tensile strength ,the node cracks.

$$\sigma \geqslant [\sigma] \quad (3)$$

In it, σ is the maximum tensile stress of node, $[\sigma]$ is the tensile strength of rock.

(2) When the direction vector of main compressive stress and the direction of maximum tensile stress is vertical, the rock is cracked.

(3) The node bearing the maximum principal tensile stress is cracked first among the stress field under pulling stress.

(4) The rock can Still bear the compressive stress after cracked.

3.2 geometric model

The testing model has sizes of 600m ×560m, the thickness of the overlying rock strata is 500m, the thickness bedrock is 50m, and thickness coal is 10m.

Linear elastic, plane strain model and three-node triangular element are used. There are 7878 elements and 4073 nodes.128 nodes are pre-supposed in abscission layer, interlayer tensile strength of 100kPa and layer tensile strength of 200kPa in layer are set.

3.3 material parameters

Uniform material is set and the parameters of each material are shown as Table 1.

Table 1 material parameters

Region material	Elastic module /Pa	Poisson	Volume weight/（$N \cdot m^{-3}$）
Overlying strata	1.0e9	0.3	2000
Coal layer	0.5e9	0.3	2000
Based rock	1.0e9	0.3	2000

3.4 process of evolution

From the process of evolution of Figure 2 it shows that the cracks occur in the layer and on the top of goaf first, then occur in interlayer and occur in both of them at the same time at last. The overlying strata cave continues to crack at Step 15. The nodes on the top of the nodes, the layer tensile strength of which is larger than 200kPa, cracks at Step 18.They are the boundary points which are not cracked by the set. The nodes the tensile strength of which is smaller than 100 kPa are set as the nodes which could crack in the interlayer. And the interlayer does not crack, so the computing ends.

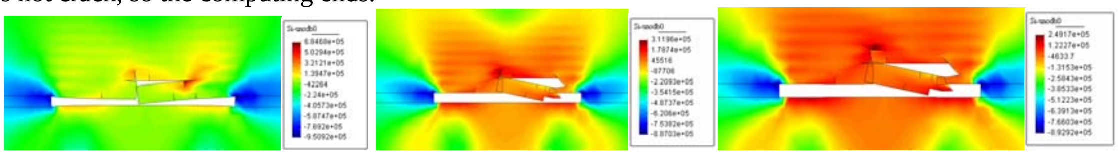

(a)Stpe 10 (b)Step 15 (c)Step 18

Figure 2 nephogram of first main stress

From the evolvement of the first main stress, it shows that the cracks occur in the middle of roof of goaf first, then the stresses are released and redistributed to form new stress concentration after tensile. There are also some problems on the fractured process of roof above, such as the problem on inter-grid, needing the following further research.

4 Conclusion

By studying occurring mechanism and numerical simulation of tension rock burst of hard roofs, the conclusions are listed as follows.

(1) Tensile fracture leads to each micro-crack of roof rock.

(2) Releasing elastic energy in the crack of the roof is an avalanche-like chain reaction, accumulating micro-cracks to a certain degree, caused by the reduction of tensile strength and tiny disturbances.

(3) The stress is released and redistributed to form new stress concentrations after the tensile fracture on the roof.

(4) It can provide the theoretical basis for the forecast of rock bursts.

Acknowledgements

The authors wish to acknowledge the financial support by the State Key Laboratory of Geohazard Prevention & Geoenvironment Protection Fund (DZJK-0809), National Natural Science Fund (50434020), Science and Technology Fund of Liaoning Province (20022155), Basic Research of Educational Bureau of Liaoning Province (202182055) and excellent young fund of Liaoning Technical University(07-105).

References

1. Zhu, J.M., Gao, L.X. and Yang, Y.J. Discussed on the reason of deep thick hard roof evoked the rock burst. Coal, 1995, 4(5). 16-19.
2. Li, X.Y., Ma, N.J., Zhong, Y.P. et al. Storage and release regular of elastic energy distribution in tight roof fracturing.Chinese Journal of Rock Mechanics and Engineering, 2007, 26(S1). 2786-2793.
3. Zhang, X.C., Miao, X.X. and Zhai, M.H. The analysis of the rock burst occurring mechanism in Sanhejian coal mine.Chinese Journal of Rock Mechanics and Engineering, 1998, 17(5). 508-513.
4. Dou, L.M. and He, X.Q. The control theory and technology of rock burst. Xuzhou: China University of Mining and Technology Press, 2001.
5. Zhang, M.T. Discussion on the mechanism of coal burst. Journal of Fuxin Mining Institute(Natural Science), 1985, 4(S2). 65-71.
6. WangLaigui, PanYishan, zhangMengtao. Reasons of the earthquake caused by underground mining and excavation and the strategy to deal with it.China safety science journal,1996,6(3):40-43.

RaSiM 7(2009): Controlling Seismic Hazard and
Sustainable Development of Deep Mines,
C.A. Tang(ed), Rinton Press, 695-698

INFLUENCE OF SPRAYED CONCRETE LAYER THICKNESS ON THE TUNNELING SUPPORTING EFFECT

XIAN-ZHANG GUO

. *Northeastern University*

Shenyang,, 110004. China.

CHUN-AN TANG, ZHENG-ZHAO LIANG and TIAN-HUI MA

School of civil and hydraulic Engineering of Dalian University of Technology Dalian

Dalian,116024,China

In this paper, the failure process of sprayed concrete under tension is numerically studied through the use RFPA3D (Three-Dimension Realistic Failure Process Analysis). The numerical test on the sprayed concrete under biaxial tensile stress is conducted, and then four specimens with different thickness of the sprayed concrete layer are analyzed and compared. The comparisons show that along with the increase of the thickness of the sprayed concrete layer, the load support capacities also increase with a decrease in flexibility. It is indicated that the thickness of the sprayed concrete layer is an important factor influencing the crack distribution and load support capacities of the specimens.

Introduction

Sprayed concrete is a mixture of cement, aggregate and water projected pneumatically sprayed from a nozzle into place to produce a dense homogeneous mass. Concrete can be considered the most cost-effective, versatile building material. The use of sprayed concrete as a support element in tunnels became popular in Europe in the early 1960s [1]. In recent years the use of sprayed concrete has equipped the modern underground construction industry, Water /conservancy and the Hydropower Project in particular, with a fast, cost effective lining system. It plays a positive role in tunnel support, repair and reinforcement. Meanwhile, it was also widely used in the reinforcement of ground buildings and geotechnical slopes.

Experience through previous projects shows that the sprayed concrete layer thickness of the concrete can not satisfy the engineering practices completely. Due to the present situation of sprayed concrete and rock bolt support, the deficiency of sprayed concrete thickness is the key issue pertaining to the engineering quality [2-5].

Some advantages of sprayed concrete are its ease of application, flexibility, control, strength, and savings in formwork. Therefore, there is a need to place more importance on the depth index of the sprayed concrete.

The study of the failure mechanics of sprayed concrete pertains to the qualitative analysis and perceptual level of knowledge. Many scholars analyze the failure phenomenon from field materials; however, the numerical simulation method is still seldom used.

In this paper, using the three-dimension realistic failure process analysis method (RFPA), the crack distribution laws were studied with the different sprayed concrete layer thicknesses. This analysis takes on certain significance for the engineering practices.

2 Model of numerical Simulation

Realistic Failure Process Analysis (RFPA) incorporated into heterogeneity influence for the simulation of crack initiation, propagation and coalescence will help to understand the three-dimensional failure process [6-7]. The code has been developed through consideration of the deformation of a heterogeneous material containing an initial random Weibull distribution of micro-features. The detailed descriptions about the Weibull distribution of material properties and constitutive law of RFPA have been given in [8-10]. The finite element method is employed as the basic stress analysis tool and the Mohr-Coulomb criterion with tension cut-off is utilized as damage threshold. The sprayed concrete consider as the heterogeneous materials and the constitutive model with residual strength after elastic damages and the failed elements are treated with reduced properties[10-12].

3 Model of Sprayed Concrete Structure

The RFPA modelling of the specimen model has been shown in Figure1. To facilitate the research, a part member extracted from sprayed concrete support was analyzed in this paper, shown as Figure2. There are two layer materials constitute the structure, one layer is rock, and the other is sprayed concrete. The load is applied in the double-axial direction with the displacement-controlled loading scheme, for each step, the model is applied with a displacement 0.005mm. Perfect bond between the rock and concrete was assumed, to provide the perfect bond, the link element for the rock was connected between nodes of each adjacent concrete solid element , so the two materials shared the same node.

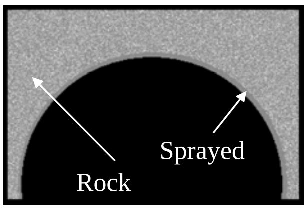

Figure1 Sprayed concrete support model in tunnel.

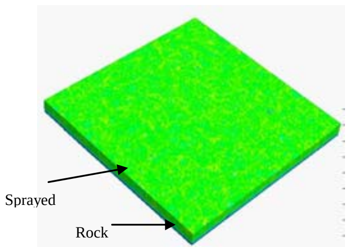

Figure2 numerical simulation model

The material properties for the sprayed concrete : Heterogeneity , Elastic modulus, Compress strength and Poisson ratio are 3 , 25GPa, 80Mpa and 0.18 respectively. The relation among the parameters have been given in [6-12].

Figure3 shows the ultimate failure mode and stress distribution under tensile loading for the specimens with different sprayed concrete layer thickness.

During the initial loading phase of the failure process, the external loading is supported by the concrete and rock. Because of the heterogeneity of the specimen, there are still some elements are damaged in the beginning and then lead to local damage. The first batch cracks of sprayed concrete structure formed with the increasing of the local damage and mutually connected the tensile stress decrease with the crack thoroughly run through the crack specimen. The crack distribution is not well distributed because of the heterogeneity of the materials. No new crack forms yet when the loading reach a certain value, the crack width is increased with the increasing of the external loading.

4 Sprayed concrete specimen failure analysis

4.1. crack distribution

Numerical tests show that the sprayed concrete layer thickness has an important influence on the crack numbers and crack width. The crack number is decreased and the crack width is increased with the increasing of the sprayed concrete thickness, shown as Figure3. Test results indicate that thicker the sprayed concrete provides higher capacity and more brittle and less flexible, then it is easy to appear bed separation leading to the less stability of the tunnel. It is unreasonable for the too thick sprayed concrete layer. The flexibility of the sprayed concrete is decreased with the increasing of the sprayed concrete thickness. Reasonable thickness permits a certain degree of rock deformation, so the internal stress of surrounding rock can be released, the load on the secondary support can be reduced.

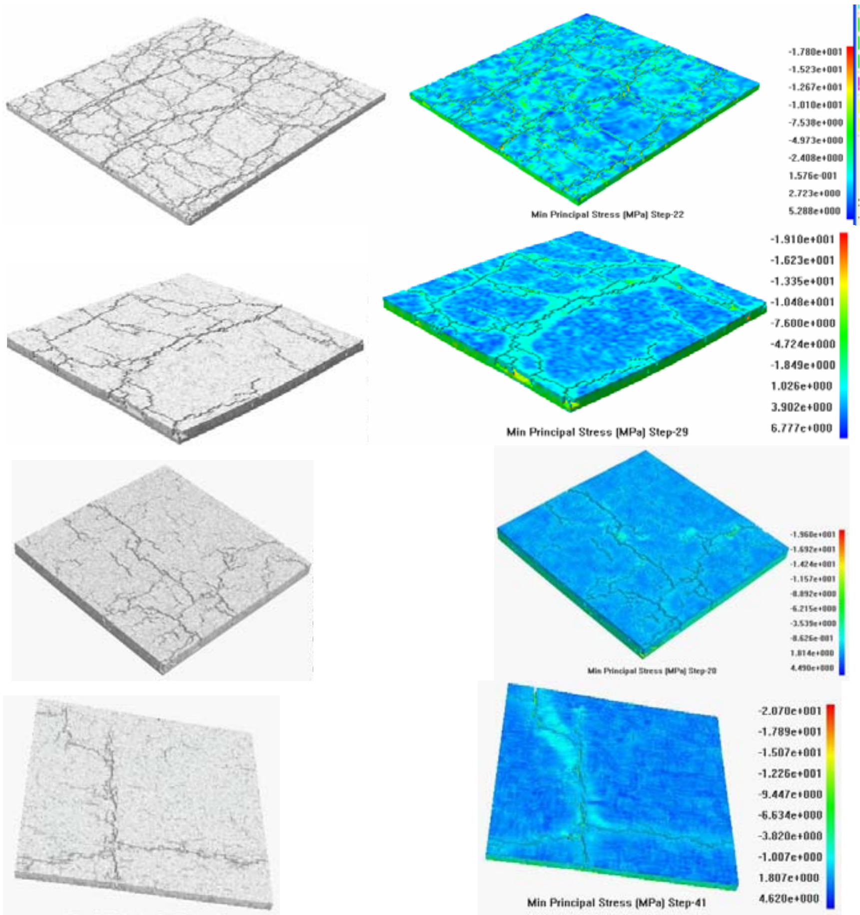

(a) Elastic modulus pictures(numerical test) (b) principle stress distribution field(numerical test)

Figure3 Failure mode of the sprayed concrete model with different layer thickness under biaxial tensile stress(numerical test)

(a) Elastic modulus pictures (b) principle stress distribution fields

4.2. Load-displacement curves

The structure load-displacement curves obtained by the numerical tests for the different sprayed concrete layer thickness are compared in Figure4. There are four specimens that the layers thickness are 60mm, 90mm, 120mm and 150mm respectively. In the figures, 1-1x indicates the sprayed concrete layer thickness is 60mm and the load direction is x axis. 1-2 Y indicates the sprayed concrete layer thickness is 90mm and the load direction is Y axis. 1-4, 1-5 indicate the sprayed concrete layer thickness are 120mm , 150mm,respectively. It can be found that the trend of the load support capacity of the sprayed concrete specimen from the Figure4: the load capacity before local crack occur and the ultimate load capacity are increased with the increasing of the sprayed concrete layer thickness.

5 Conclusions

In this paper, The RFPA^{3D} (realistic failure process analysis) code was used to analyze the support's effect on the tunnel of the sprayed concrete specimens with different layer thickness. It can be found that the load capacity is increased and flexibility is decreased with the increase of the layer thickness of the sprayed concrete from the load-displacement curves. It can be concluded that the thinner the sprayed concrete layer, the more cracks occur. The thicker the sprayed concrete layer, the less cracks occur; but with a greater crack width. Test results indicate that thicker sprayed concrete provides higher capacities and is more brittle and less flexible; then it is easier to observe bed separation leading to the less stability of the tunnel. It is unreasonable for the sprayed concrete layer to be too thick. The flexibility of the sprayed concrete is decreased with the increasing of the sprayed concrete thickness. Adding steel fibres to the spray concrete, and silica-fume, as well as the use of net guniting will be described in subsequent papers.

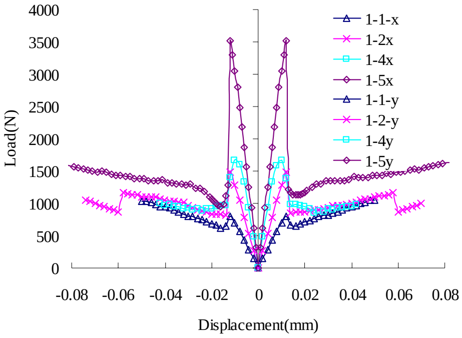

Figure4 Load-displacement curves of model

Acknowledgements

The authors wish to acknowledge the collaborative funding support from the Education Department of Hebei Province (No. 06020546) and Department of Science & Technology of Hebei Province (07215616) and the NSFC (Grant No. 50874024, 50778046and 10672028), The authors are grateful for these supports.

References

1. Technical Committee 9 November 2000, Design of sprayed concrete for underground support. 2000.
2. Wang, J.B. and Yuan, P.Y. Discussion on the Quality Control and Evaluation Method of Shotcrete. Metal Mine, 2001, 295. 9-11.
3. Wu, H.C. Simulation of Shotcrete Support in Tunnel by Means of Curve Structure Element. Rock And soil Mechanics, 1998, 19(1). 38-44.
4. W, Z.Z. and Wang, J.J. Study on Reasonable Composite Lining of Multi-arch Tunnel in Shallow Soft Stratum. Journal of Highway and Transportation Research and Development, 2007, 24(2). 94-98.
5. Sun, H.T., Ding, D.X. and Liu, D.Y. Numerical Analysis of Construction Time for the Tunnel Shotcreting. Chinese Journal of Underground Space and Engineering, 2006, 2(5). 744-748.
6. Liang, Z.Z., Tang, C.A. and Li, H.X. Numerical simulation of the 3D failure process in heterogeneous rocks International Journal of Rock Mechanics & Mining Sciences, 2004, 41. 419
7. Tang, C.A. and Zhu, W.C. Concrete damage and fracture-numerical test. Beijing: Science Press, 2003.
8. Tang, C.A., Tham, L.G., Lee, P.K.K., et al. Numerical tests on micro-macro relationship of rock failure under uniaxial compression. II. Constraint, slenderness and size effects. Int J Rock Mech Min Sci, 2000, 37(4). 570-7.
9. Tang, C.A., Lin, P., Wong, R.H.C., et al. Analysis of crack coalescence in rock-like materials containing three flaws. II. Numerical approach. Int J Rock Mech Min Sci, 2001,38(7). 925-39.
10. Zhu, W.C. and Tang, C.A. Numerical simulation on shear fracture process of concrete using mesoscopic mechanical model. Construction and Building Materials, 2002, 16: 453-463.
11. Zhang, J.X., Liu, J.J., Tang, C.A. et al. Numerical Simulation of Crack Development in Reinforced Concrete Structures under Eccentric Loading. Key Engineering Materials 2005, 297-300. 2654-2659.
12. Zhang, J.X., Tang, C.A., Hui, X.J. Zhu, W.C. and Liang, Z.Z. Numerical Simulation of 3-D Fracture Behaviors on the FRP-Strengthened Concrete Structures. Key Engineering Materials, 2006, 324-525. 423-426.

RaSiM 7(2009): Controlling Seismic Hazard and
Sustainable Development of Deep Mines,
C.A. Tang(ed), Rinton Press, 699-704

EFFECT OF CLAY MINERAL CONTENT ON ROCKBURST BASED ON LABORATORY TEST AND NUMERICAL SIMULATION

XIAO-MING SUN, CHENG CHENG and JIN-LI MIAO

School of Mechanics and Civil Engineering, China University of Mining and Technology, Beijing, 100083, P.R. China

State Key Laboratory for GeoMechanics and Deep Underground Engineering, Beijing, 100083, P.R. China

CHUANG-ZHOU WU

Department of Geotechnical Engineering, Tongji University, Shanghai, 20009, P.R. China

The aim of this paper is to study the effects of clay mineral contents on probability of rock burst from the viewpoint of laboratory test, micro-structural analysis, and numerical simulation. With the sandstone, coal, shale, and limestone specimens from the Jiahe coal mine, the rock burst tests were carried out by a true triaxial rockburst test system developed at China University of Mining and Technology in Beijing, in which one surface can be unloaded suddenly when the sample is loaded on six surfaces at three directions. With the same test procedure for all rock samples, limestone burst occurred while sandstone and shale did not. According to the X-ray diffractions, we find that the clay mineral content in the limestone is 0%, and that the clay mineral content is 20.9% and 44.7% in the sandstone and the shale, respectively. Based on microanalysis, layered and flaky structures of the clay minerals determine that plastic slip may occurs in the specimens so that elastic strain energy is hard to be stored, consequently, the probability of rockburst occurrence is reduced by the existence of clay minerals. We also applied PFC (particle flow codes) to simulate the processes of rock burst occurring on the rock samples with different clay mineral contents. The tests and numerical simulations conclude that the clay mineral contents indeed affect significantly the probability: the higher the contents, the less the rock burst probability.

1 Introduction

Rockburst is a kind of serious hazard. According to the in situ phenomena in field and laboratory tests on rock mechanics, many scholars concluded that various factors affect the occurrence and process of rockburst, and they have tried to predict whether rockburst will happen based on the analysis of these factors.

Kidybinski gave the criterion of rockburst prone utilizing elastic energy index W_{et} [1]. Hou Faliang presented that rockburst may occur because of the overlying rock stratum effect even if there is not horizontal tectonic stress, if only the embedded depth is large enough Also, he gave the formula to calculate the minimum depth (only consider the vertical stress due to self-weight of the overlying rock stratum) for rockburst occurrence based on elastic mechanics [2]. Tan Yi'an studied the in situ rockburst characteristics in the Tianshengqiao Hydropower Station and carried out a series of uniaxial compression tests. He concluded that the rock mass structure (including classification of rock masses, the angle between the major set of joints and the maximum principal stress) has the controlling effects on the occurrence and intensity of the rockburst [3]. Xu Linsheng and Wang Lansheng pointed out that the occurrence of rockburst is not only dependent with the in situ stress condition, but also the rock types and their distribution, rock mass structure, failure break, underground water and other disturbances. They managed to predict the rockburst in the tunnel of Erlang Mountain road utilizing geology suppertime forecasting method [4]. Xie Heping and William G. Pariseau provided that the lowering of the fractal dimension of the microseismic event locations distribution could be used to predict the occurrence and development of rockburst [5]. He Manchao and his colleagues carried out a series of rockburst test on granite utilizing the self-designed true triaxial rockburst process test system and studied the occurrence and process of different types of rockburst due to different initial stresses [6].

Based on a series of rockburst tests on the coal, sandstone, limestone and shale stone from Jiahe coal mine utilizing the rockburst process test system designed by Prof. He Manchao (2004), this paper studies the effect of clay mineral content on the occurrence of rockburst, and this effect is verified by PFC simulation.

2 Laboratory Rockburst Test

2.1 Test System

The true triaxial rockburst process test system includes the principal machine, the hydraulic pressure controlling system and data acquisition system including force and displacement acquisition, acoustic emission acquisition and digital camera recording. During the test, one surface of the specimen can be unloaded immediately from the true triaxial compression condition.

2.2 Test Methods

Stepped loading is applied. The specimen is loaded every 5 minutes with the loading velocity of 0.5Mpa/s. There are two methods for the rockburst tests: (I) The specimen is tri-axially loaded on six surfaces, then unload one surface and increase the vertical load. This method aims at simulating the rockburst due to the stress concentration after excavation; (II) The specimen is tri-axially loaded on six surfaces, then unload one surface and remain the vertical load. This method is used to simulate the rockburst due to stress redistribution and creeping. In this paper, only the second method is applied.

2.3 Specimens

Table1. Physical and Mechanical Properties of the Specimens

Rock Types	Density ρ(g/cm^3)	UCS σ_c(MPa)	Elastic module E(GPa)
Sandstone (-815m level)	2.40	—	—
coal (-850m level)	1.51	12.8	1.4
coal (-910m level)	1.20	11.0	1.1
limestone(-1010m level)	2.65	78.4	36.7
Shale(-1010m level)	2.62	90.2	27.0

The specimens are carried from Jiahe coal mine in Xuzhou, China. They are sandstone from -815m level, coal from -850m level and -910m level, limestone and shale from -1010m level stone. The details see Table 1.

2.4 Test Results

The test results see Table 2. The failure characteristics of the tests on different specimens showed that:

(a) #JHSH I-2 limestone (blocks and sliver ejection)

(b) #JHY I-3 shale (squeezing)

Figure 1 Typical test results of the limestone and shale

(1) Rockburst phenomena including the ejection of blocks and slivers occurs obviously during the test on the three limestone specimens from -1010m level(see Figure1(a));

(2) There are two tests on coal specimens from -850m and -910m level during which bursts occur, though the phenomena including spalling and slight ejection, are weaker than those on limestone specimens. However, only cleavage break rather than burst occur in the test of the other two coal specimens;

(3) No obvious rockburst phenomena occur during the tests on the sandstone specimen from -815m level and the shale specimens from -1010m level. Shear failure occurs during the test on the sandstone, while the 2 shale specimens are crushed and pressed to be squeezing respectively. (see Figure1(b))

Table2 Test Results

No.	Rock Types	Depth(m)	Unloading Times	Unloading stresses state (MPa)			Failure characteristics
				σ_1	σ_2	σ_3	
JHSY I-1	sandstone	-815	1	116.9	59.8	24.3	shear failure
JHM II-1	coal	-850	4	25.8	13.1	4.8	cleavage
JHM I-1	coal	-910	1	22	16.2	10.6	crushed
JHM I-2	coal	-910	1	18.8	15.3	7.6	blocks and sliver spalling
JHM II-1	coal	-910	1	16.8	12.5	6.8	cleavage
JHSH I-1	limestone	-1010	3	116.1	52.0	27.5	blocks and sliver ejection
JHSH I-2	limestone	-1010	1	101.1	60.4	28.9	blocks and sliver ejection
JHSH I-3	limestone	-1010	2	123.1	63.6	30.9	blocks and sliver ejection
JHY I-2	shale	-1010	1	58.6	40.1	17.4	crushed
JHY I-3	shale	-1010	1	46.4	29.1	13.7	squeezing

3 Effect of Clay Mineral Content on the test result

X-ray diffraction analysis for whole rock and clay minerals of the specimens above are carried out. The results see Table 3 and 4.

Table 3 Analytical Results of X-Ray Diffraction for whole rock minerals

specimens	Minerals and contents (%)								
	quartz	feldspar	plagioclase	calcite	dolomite	pyrite	siderite	amorphous minerals	clay minerals
Sandstone (-815m level)	60.2	4.9	6.2	3.4	—	—	4.4	—	20.9
coal (-850m level)	0.4	—	—	1.9	0.3	—	—	90.3	7.1
coal (-910m level)	—	—	—	1.4	—	—	—	97.6	1.0
limestone(-1010m level)	3.7	—	—	96.3	—	—	—	—	—
Shale(-1010m level)	29.5	0.2	2.1	0.7	22.0	0.8	—	—	44.7

According to the analytical results of X-ray diffraction for whole rock minerals (see Table 3), we find the there is no clay mineral in limestone (burst phenomena occur obviously), while the coal (burst occur partially), have the clay minerals with the contents of 7.1% and 1.0% respectively, and the sandstone and shale (no burst occur) have the clay minerals with the contents of 20.9% and 44.7% respectively. We might draw a conclusion from this result that rock burst occurs more easily or obviously during the tests of the rock specimens with less or no clay minerals.

Table 4 Analytical Results of X-Ray Diffraction for clay minerals

specimens	rock types	clay mineral contents(%)						mixed layer ratio ((S)/%)	
		S	I/S	I	K	C	C/S	I/S	C/S
JHYI	sandstone	—	29	4	67	—	—	25	—
JHMI	coal	—	24	—	76	—	—	35	—

JHMIII	coal	—	—	—	100	—	—	—	—
JHSHII	limestone	—	—	—	—	—	—	—	—
JHYI	shale	—	49	6	32	13	—	25	—

The analytical results of X-ray diffraction for clay minerals (see Table 4) shows that the clay minerals in the rock specimens above (if there are clay minerals) are mainly kaolinite and illite/smectite mixed layers. We can see the microstructures of the clay minerals according to the scanning electron microscope (SEM) images (see Figure 2).

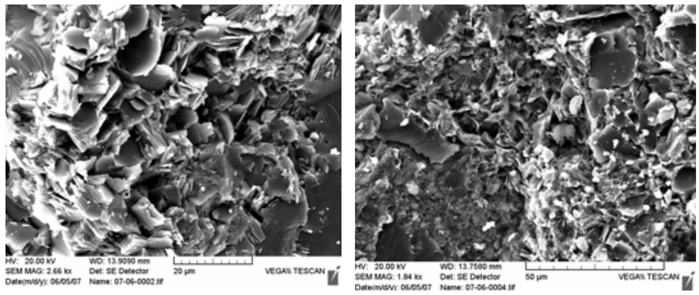

(a) Flaky kaolinite (magnified by 2660 times)　(b) Flaky kaolinite and flaky-flocculent smecitite (magnified by 1840 times)

Figure 2 SEM Images of Clay Minerals in the Sandstone from -815m Level

As we know, crystal clay minerals are mainly silicate with layered structures (see Figure 3), and the basic structural layers consist of tetrahedral and octahedral sheets. Based on the arrangement proportion of the two types of sheets, the layered silicate can be classified as 1:1 layered type and 2:1 layered type. Kaolinite is just a typical 1:1 layered type. Besides, illite/smectite mixed layers is a kind of layered clay mineral [7]. The SEM images show us the flaky and layered kaolinite and the flaky and flocculent smecitite. These layered, flaky and flocculent microstructures determine the low shear strength of the clay minerals, consequently, slip may easily occurs between the layers, and plastic flow may easily occurs in the rock masses.

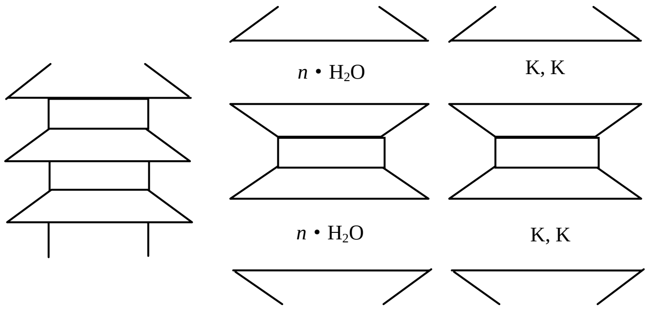

(a) Kaolinite　(b) Montmorillonite　(c) Illite

Figure 3 Structures of clay minerals (according to [8])

Usually, clay minerals have so tiny particles with the particle sizes less than 2 μm that the fracture planes due to static loads are always intergranular instead of transgranular, and the strength mainly maintained by bound water is quite weak. In addition, the accumulation of clay minerals will lead to the decrease of cohesion and internal friction angle of the structural planes and the rock masses beside the planes, therefore, the strength of the structural planes and rock masses is weakened, as well as the integrity of the rock mass is reduced [9].

All these characteristics of clay minerals result in a low elastic module of the rock mass, so the ability of storing elastic strain energy is weakened, meanwhile, energy can be consumed easily because of the low strength and considerable plastic flow. As a result, rockburst phenomena may hardly occur on the rock with larger clay minerals content [9].

Swelling is another characteristic of clay minerals when there is water. Clay minerals have hydrophilic nature owing to the hydration, including the hydration of particle surface and the exchangeable positive ions on the surface of clay minerals. Kaolinite, illite/smectite mixed layers and many other clay minerals will swell easily when they encounter water [10, 11]. Based on this feature, especially for the in situ rock masses with the existence of water, the strength and elastic module are reduced, while plasticity is increased, hence the energy is easy to store while difficult to consume, which lead to the lower probability of rock burst occurrence.

4 PFC2D Analysis

The discontinuum program PFC2D, in which the rock can be represented by a dense packing of non-uniform-sized circular particles that are bonded together at their contact point and whose mechanical behaviour is simulated by the distinct element method, is an efficient tool to analyze the mechanism during the whole process of the rock burst test [12].

In order to analyze the effect of clay mineral content on rockburst, two PFC2D models have been built. The models are both as large as the real specimens. In both models, we use the same particle size (the minimum radius is 8mm, and the particle size ratio is 1.66), and the particle density is 2650kg/m^3. Parallel bond, which acts in parallel with the slip or contact-bond constitutive models and can transmit both force and moment between particles, is utilized and we set the bond modulus as 32GPa.

As we analyzed above, because of the layered and flaky structures of the clay minerals, slip occurs easily between the layers, which lead to a series of characteristics which weaken the probability of rockburst occurrence. Taking this factor into consideration, we set a large enough particle friction coefficient in the first model while a smaller one in the second model. This difference, to some extent, may represent the effect of clay minerals in the rock specimens.

During the numerical tests, the both models experience the similar loading and unloading procedure. At first, biaxial tests with a confinement of 30MPa are carried out on both models, and one of the side walls is deleted before the reach of peak stress. Deleting the wall simulates the unloading on one surface during the test. After the unloading, the vertical stress is remained through a servo control in the simulation.

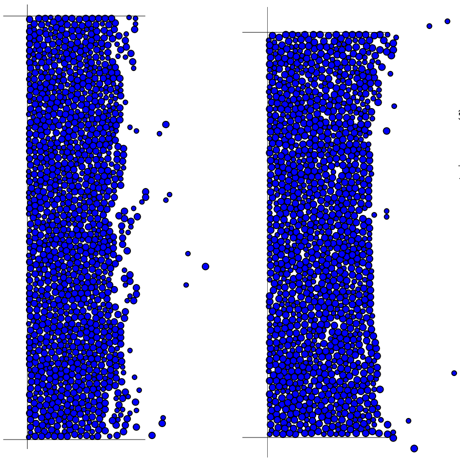

Figure 4 Numerical test results of the two models

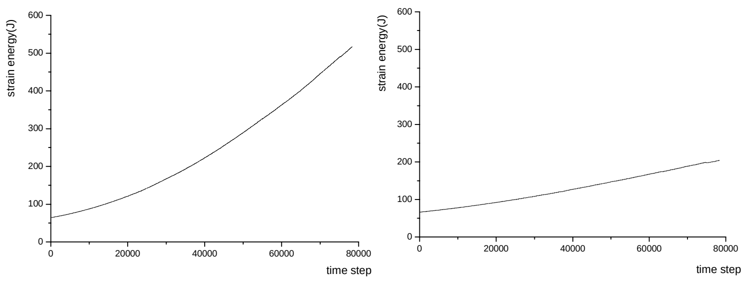

Figure 5 Strain energy-time step curves of the numerical tests before unloading

According to the numerical tests result (see Figure 4), rockburst occurs comprehensively in the first one, many particles burst from the specimen, including the single particles and clustered particles similar to the flakes or blocks of rock fragments. However, in the second model, only very few particles escape from the specimen and the top and bottom of the specimen are pressed to squeeze out.

Figure 5 shows us the strain energy - time step curves of the two tests before unloading. During the same time step, the two models with the same vertical loading velocity and the same confinement stress store different strain energy. The energy of 518J is stored in the first model, which simulate the specimen with less clay minerals, whereas only 204J is stored in the second one. The plastic flow due to the slipping between the particles is the reason of the difference. The numerical test results give an evidence that the energy storing ability of the specimen with less clay minerals is stronger than that of the specimen with more clay minerals, as well the reason is the plastic flow owing to the slipping between the layers as a result of the existence of clay minerals, and that is why only few particles burst from the specimen and the failure type is mainly squeezing out. It is also demonstrated in the numerical tests that the clay minerals in the rock mass limit the probability of the rockburst occurrence.

5 Conclusions

Rockburst tests on specimens of different rock types have been carried out utilizing the true triaxial rockburst process test system. The test results show that rockburst occurs more easily during the tests on the specimens with less clay mineral content, while no rockburst occurred on the specimens with large contents of clay minerals. According to the microanalysis, layered and flaky structures of the clay minerals determine that plastic slip may occur in the specimens so that elastic strain energy is hard to be stored; consequently, the probability of rockburst occurrence is reduced by the existence of clay minerals.

Two PFC2D models with different particle friction coefficients are built to demonstrate the effect of clay mineral content on the rockburst. We find that rockburst occurs on the first model with the smaller friction coefficient, besides, we find that this model stores more strain energy than the other one. This means that elastic strain energy easily can be stored in the specimen with less clay mineral content, and this leads to the high probability of rockburst occurrence.

Both the laboratory test and the numerical simulation show the effect of clay mineral content on the occurrence of rockburst: the higher the clay mineral content, the less the rock burst probability.

Acknowledgements

This work was supported by the National Basic Research Program of China (2006CB202200), the Major Program of National Natural Science Foundation of China (50490270), and Innovative Team Development Project of the Ministry of Education of China (IRT0656).

References

1. Kidybinski, A. Bursting liability indices of coal. J. Rock Mech. Min. Sci. & Geomech. , 1981, 18. 295-304.
2. Hou, F.L., etc. Aplication of Rock Mechanics on the Engineering: Criterion of Rockburst in Round Tunnel and Its Countermeasure. Knowledge Press, 1989, 195-201.
3. Tan, Y.A. Rockbursting Characteristics and Structural Effects on Rock Mass. Science in China (series B) 1992, 35(8). 981-990.
4. Xu L.S. and Wang, L.S. Study on the Laws of Rockburst and its Forecasting in the Tunnel of Erlang Mountain Road. Chinese Journal of Geotechnical Engineering, 1999, 21(5). 569-572.
5. Xie, H.P. and Pariseau, G. Fractal Characteristics and Mechanism of Rocks. Chinese Journal of Rock Mechanics and Engineering, 1993, 12(1). 28-37.
6. He, M.C., Miao, J.L., Li, D.J., etc. Experimental Study on Rockburst Process on Granite Specimen at Great Depth. Chinese Journal of Rock Mechanics and Engineering, 2007, 26(5). 865-876.
7. He, M.C., Yang, X.J. and Sun, X.M. Characteristics of Clay Minerals in Chinese Coal Mines. Science Press, 2006.
8. Zhao, S.D., Liao, H.J., Wang, X.L. Soil Mechanics. High Education Press, 2001.
9. Xu, Z.M., Huang, R.Q., Tang, Z.G., etc. Clay Minerals and Failure of Slopes. Chinese Journal of Rock Mechanics and Engineering, 2005, 24(5). 729-740.
10. Zhao, X.Y. and Zhang, Y.Y. Clay Mineral and Its analysis. Ocean Press, 1990.
11. He, M.C., Jing, H.H. and Sun, X.M. Soft Rock Mechanics. Science Press, 2002.
12. Potyondy, D.O. and Cundall, P.A. A Bonded-particle Model For Rock. International Journal of Rock Mechanics and Minging Sciences, 2004. 41, 1329-1364.

*RaSiM 7(2009): Controlling Seismic Hazard and
Sustainable Development of Deep Mines,
C.A. Tang(ed), Rinton Press, 705-710*

RESEARCH ON THE ENERGY MECHANISM OF COLLIERY ROADWAY ROCK-BURST

HANG LAN

Department of Coal Mining & Designing, Tiandi Science & Technology Co. Ltd,.

Beijing, 100013, P.R. China

QING-XIN QI

China Coal Research Institute.

Beijing, 100013, P.R. China

DE-BING MAO

Department of Coal Mining & Designing, Tiandi Science & Technology Co. Ltd,.

Beijing, 100013, P.R. China

In underground collieries, rock-burst occurs as a result of energy abrupt destabilization, during which elastic strain energy in coal and rock mass after excavating is larger than plastic strain energy due to failure and damage. Current numerical simulations for colliery rock-burst are mostly focused on the degree of stress concentration, not energy the destabilization condition which is the essential nature of rock-burst. Based on energy destabilization, this paper applies finite difference software-FLAC3D to researching roadway rock-burst in colliery. Strain energy of linear elastic model and the ideal elastic-plastic model in FLAC3D are analyzed and related energy discriminate for rock-burst is put forth. If residual elastic strain energy of coal and rock body is positive, rock-burst has the possibility to occur. Strain energy formulas of 2 models are presented and corresponding calculation modules are programmed with FISH-an inner programming language in FLAC3D. With these calculation modules, energy distributions of rock and coal mass surrounding the roadway under different conditions are calculated. Results are shown as follows: elastic strain energy accumulated in coal is larger than that in rock under the same condition of excavating depth and excavating scale. Compared with single coal or rock material models, combined model of coal and rock can accumulate more elastic strain energy in roadway sides, which implies a larger bursting danger in the combined model.

1 Introduction

In underground collieries, rock-burst occurs as a result of abrupt energy destabilization, during which elastic strain energy in coal and rock mass after excavating is larger than plastic strain energy due to failure and damage. Research on the energy mechanism of rock failure and burst [1-8] has been conducted extensively. XIN YUAN-LI presented calculation equations for the energy distribution of elastic beams based primarily on the broken mechanics model of hard roof under equispaced stress and additional stress and analyzed energy accumulation and release rules of hard roof before and after breaking [9]. MEI-FENG CAI analyzed energy distribution rule and rock-burst possibility of surrounding rock according to judgement principles of rock-burst [10]. For numerical simulation research on colliery rock-burst, many papers have focused on the influencing factors of rock-burst [11,12], vertical stress distribution, stress concentration degree [13,14], not on energy essence. This paper applied finite difference software-FLAC3D to research the energy distribution rules of coal and rock mass after excavation and rock-burst discriminate. The following advantages are shown in rock-burst research with FLAC3D: zone strain can be obtained and elastic and plastic strain energy can be programmed with FISH easily.

2 Energy expression of FLAC^{3D}

2.1 Elastic strain energy

Linear elastic model is taken as example. Its stress-strain curve is an inclined straight line. Value of elastic strain energy is equal to the triangle area in shadow, as in Figure 1.

Elastic strain energy under triaxial stress state may be presented according to generalized Hook Law.

$$W_e = \left| (\sigma_1^2 + \sigma_2^2 + \sigma_3^2 - 2\mu(\sigma_1\sigma_2 + \sigma_2\sigma_3 + \sigma_1\sigma_3)) / 2E \right| \tag{1}$$

Where: E is elastic modulus, μ is Poisson ratio, σ_1, σ_2 and σ_3 are respectively maximum, medium and minimum principal stress.

Material parameters and principal stress in Formula (1) may be accessed via FISH. There is no plastic strain energy for linear elastic model.

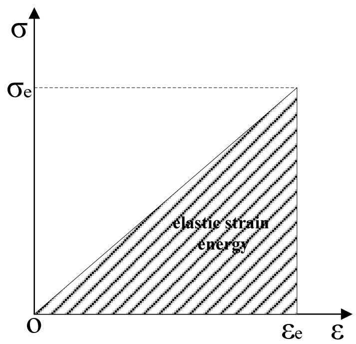

Figure 1 Linear elastic model

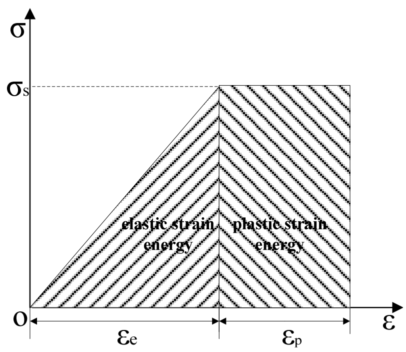

Figure 2 Ideal elastic-plastic model

2.2 Plastic strain energy

Energy will be dissipated for damage and failure after rock reach yield surface. The energy is called as plastic strain energy. Ideal elastic-plastic model in FLAC^{3D} derives from modified Mohr-Coulomb model whose stress-strain curve may be divided into inclined straight line (elastic phrase) and horizontal straight line (ideal plastic phrase), as in Figure 2.

Plastic strain energy is presented as follows.

$$W_p = \left| \sigma_s \varepsilon_p \right| \tag{2}$$

Stress tensor may be divided into stress sphere tensor and deviator tensor. Similar with stress, strain may also be divided into sphere tensor which denotes volumetric deformation and deviator tensor which denotes shape deformation. Thus, Formula (2) may be rewritten as follows.

$$W_p = \left| \sigma_{sm} \varepsilon_{pv} \right| + \left| \sigma_{ss} \varepsilon_{ps} \right| \tag{3}$$

Where: σ_{sm} is mean stress, ε_{pv} is plastic volumetric strain, σ_{ss} is deviator stress and ε_{ps} is plastic shear strain.

$$\sigma_{sm}=I_1/3=(\sigma_1+\sigma_2+\sigma_3)/3 \tag{4}$$

Where: I_1 is stress tensor first invariant.

$$\sigma_{ss}=\sqrt{2J_2/3}=\sqrt{(\sigma_1-\sigma_2)^2+(\sigma_2-\sigma_3)^2+(\sigma_3-\sigma_1)^2}\Big/3 \tag{5}$$

Where: J_2 is stress deviator second invariant.

$$\varepsilon_{pv}=\varepsilon_v-\varepsilon_{ev} \tag{6}$$

$$\varepsilon_{ps}=\varepsilon_s-\varepsilon_{es} \tag{7}$$

Where: ε_{ev} (elastic volumetric strain) and ε_{es} (elastic shearing strain) are calculated with elastic model, ε_v (total volumetric strain) and ε_s (total shearing strain) are calculated with ideal elastic-plastic model whose deformation modulus are the same as linear elastic model.

2.3 Residual elastic strain energy

Rock is a strain softening material whose stress-strain curve may be divided into pre-summit (elastic phrase) and post-summit (strain softening phrase). The difference of elastic strain energy W_e accumulating in pre-summit and plastic strain energy W_p for damage and failure in post-summit is defined as residual elastic strain energy W_r, it may be written as:

$$W_r=W_e-W_p \tag{8}$$

Residual elastic strain energy may change into sound energy, thermal energy and kinetic energy. Among those, both sound energy and kinetic energy are rock-burst's sources. Larger residual elastic strain energy implies more energy for dynamical damage of rock mass. Therefore, following judgement criterion for rock-burst is put forward: if $W_r<0$, rock-burst may occur, conversely, it may not occur.

In FLAC^{3D}, if elastic-plastic model is used, W_e and W_p of every zone are calculated firstly, then Formula (8) is used for residual elastic energy and the possibility of rock-burst may be judged by the distribution of residual elastic strain energy of rock and coal body.

3 Engineering application

Many rock-bursts in collieries occurred in roadway. With energy expressions listed in last chapter, this chapter researched energy distribution of roadway under different conditions.

For comparing distribution of surrounding rock's elastic strain energy of roadways with different lithologies, 3 models are set up (as in Figure 3). (1) roadway is excavated in rock (called as rock model); (2) roadway excavated in coal (called as coal model); (3) coal roadway with rock roof and rock floor (called as combined model). The dimensions, boundary conditions and loading are all the same. Dimension of models are 35m (width) × 10m(length) × 35m(height). Width and height of roadways are all 5m. Bottom boundary and horizontal displacement of 4 walls are fixed. Average loading 10MPa of overlying strata is loaded on top boundary.

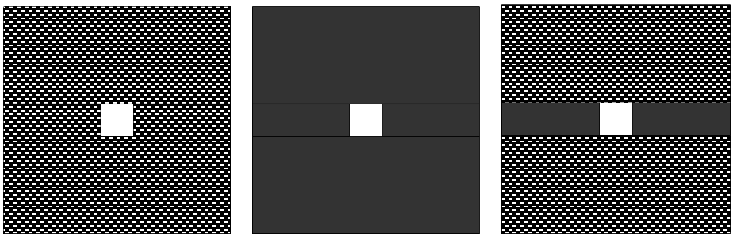

(a) rock model (b) coal model (c) combined model

Figure 3 Numerical simulation model

Figure 4~Figure 6 show distribution of elastic strain energy density of 3 models. Horizontal and vertical axial are respectively width and height of models.From Figure 4 and Figure 5, for single lithology, whatever rock or coal, surrounding rock's maximum elastic strain energy area occur at two sides of roadway, whereas minimum value area occur at roof and floor of roadway. Elastic strain energy value of coal model is far larger than that of rock model under the same excavation depth and excavation scale.

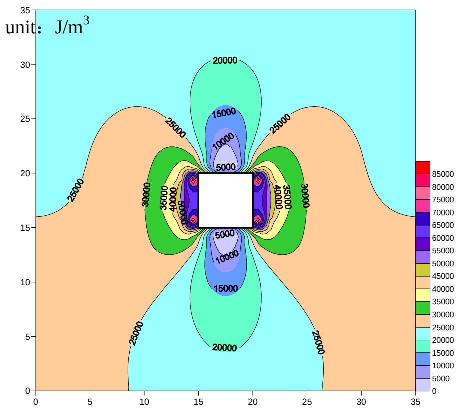

Figure 4 Elastic strain energy distribution of roadway in rock

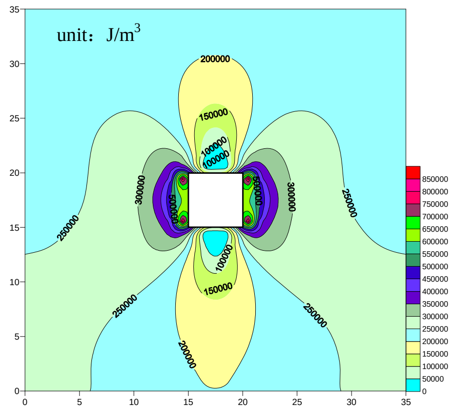

Figure 5 Elastic strain energy distribution of roadway in coal

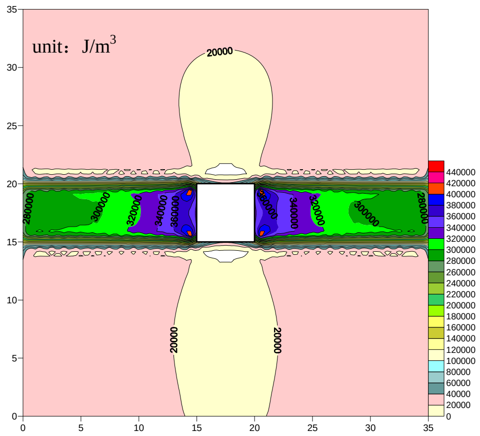

Figure 6 Elastic strain energy distribution of coal roadway surrounding between rock roof and floor

Distribution shape of elastic strain energy density of combined model is very different from those of rock and coal model, as in Figure 6. Elastic strain energy mainly accumulates in coal and adjacent rock. Elastic strain energy in rock is far smaller than that in coal. Rock-burst liability of combined model is larger than rock or coal model, which is accordance with conclusion of literature [15] from experiment.

It's clear that linear elastic model can't be directly used for judging rock-burst because of plastic strain energy's absence. In spite of this, elastic strain energy is more intuitionistic and scientific than stress concentration degree for finding rock-burst dangerous area.

Figure 7~Figure 9 are calculation results from combined model with ideal elastic-plastic model. Figure 7 shows plastic zones distribution of surrounding rock. Figure 8 and Figure 9 respectively shows distribution of plastic strain energy and residual elastic strain energy.

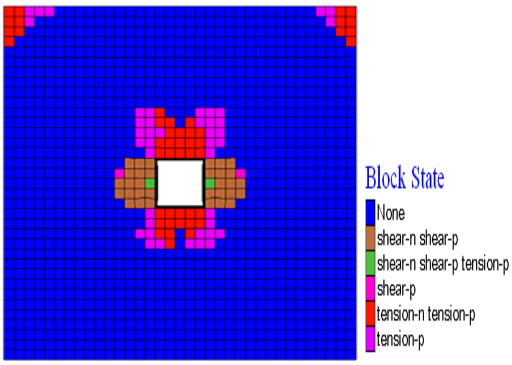

Figure 7 Plastic zones distribution of ideal elastic-plastic model

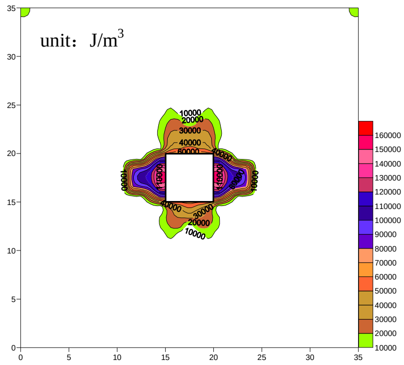

Figure 8 Plastic strain energy distribution of ideal elastic-plastic model

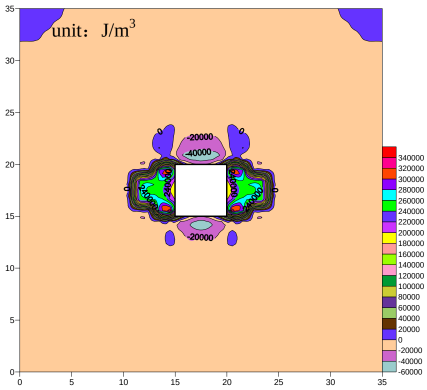

Figure 9 Residual Elastic strain energy distribution of ideal elastic-plastic model ideal elastic-plastic model

From Figure 7, we can find that coal and rock zones near roadway take on shear or tension damage. Plastic zones dissipate plastic strain energy, as in Figure 8. Maximum plastic strain energy areas occur at two sides of roadway.

Figure 9 shows positive residual elastic strain energy area occur at two sides and their adjacent roof and floor, which indicate that damage and failure of surrounding rock do not dissipate all elastic strain energy accumulating in deformation process. Based on formula (8), the residual elastic strain energy will release with kinetic and sound behaviour under some disturbance factor. As a result of this, rock-burst will occur.

4 Conclusions

In this paper, we have researched the energy mechanism of roadway rock-burst in colliery with $FLAC^{3D}$ and obtained the following results.

(1) For single lithology, whether rock or coal, surrounding rock's maximum elastic strain energy area occur at two sides of the roadway, whereas the minimum value area occurs at the roof and floor of the roadway.

(2) Elastic strain energy value of the coal model is far larger than that of the rock model under the same excavation depth and excavation scale.

(3) Ideal elastic-plastic model may be used to calculate residual elastic strain energy of coal and rock mass after excavation. Energy discriminate of rock-burst is: if residual elastic strain energy is positive, rock-burst may occur, conversely, it may not occur.

Acknowledgements

The authors wish to acknowledge the collaborative funding support from the National Major Fundamental Research Program of China (Grant No. 2005CB221504).

References

1. You, M.Q. and Hua, A.Z. Energy Analysis on Failure Process of Rock Specimens. Chinese Journal of Rock Mechanics and Engineering, 2002, 6(21).778-781.
2. Zhao, Z.H., Lu, R. and Zhang, G.Q. Analysis on Energy Transformation for Rock in the Whole Process of Deformation and Fracture. Mining Research & Development, 2006, 5(26). 8-11.
3. Xie, H.P., Peng, R.D. and Ju, Y. Energy Dissipation of Rock Deformation and Fracture. Chinese Journal of Rock Mechanics and Engineering, 2004, 21(23). 3565-3570.
4. Xie, H.P., Ju, Y. and Li, L.Y. Criteria for Strength and Structural Failure of Rocks Based on Energy Dissipation and Energy Release Principles. Chinese Journal of Rock Mechanics and Engineering, 2005, 17(24). 3003-3010.
5. Hua, A.Z. Energy Analysis of Surrounding Rocks in Underground Engineering. Chinese Journal of Rock Mechanics and Engineering, 2003, 7(22). 1054-1059.
6. Zhao, Y.S., Feng, Z.C. and Wan, Z.J. Least Energy Principle of Dynamical Failure of Rock Mass. Chinese Journal of Rock Mechanics and Engineering, 2003, 11(22). 1781-1783.
7. Zhao, Y.S., Feng, Z.C. and Chang, Z.X. The Least Energy Principle of Dynamical Rock Failure. Chinese Journal of Rock Mechanics and Engineering, 2002, (21). 1931-1933.
8. Yin, G.Z., Zhang, D.M., Dai, G.F. and Wan, L. Damage Model of Rock and the Damage Energy Index of Rockburst. Journal of Chongqing University, 2002, 9(25). 75-78.
9. Li, X.Y., Ma, N.J., Zhong, Y.P. and Gao, Q.C. Storage and Release Regular of Elastic Energy Distribution in Tight Roof Fracturing. Chinese Journal of Rock Mechanics and Engineering, 2007, (26). 2786-2793.
10. Cai, M.F., Wang, J.A. and Wang, S.H. Analysis on Energy Distribution and Prediction of Rock Burst During Deep Mining Excavation in Linglong Glod Mine. Chinese Journal of Rock Mechanics and Engineering, 2001, 1(20). 38-42.
11. Li, W. Research and Application of Bumping Prevention and Control Technology in Nantun Mine. Coal Science and Technology, 2008, 4(36). 39-42.
12. Zhang, X.T. and Dou, L.M. Numerical Simulation of the Influence of Hardness and Thickness of Coal Seam on Rock Burst. Journal of Mining & Safety Engineering, 2006, 3(23). 277-280.
13. An, R.D. and Yang, Z.Q. Safety Mining of Coal Pillar in Pressure Bump Deep Area of Zhaogezhuang Mine. Coal Science and Technology, 2008, 11(36). 21-25.
14. Qi, Q.X., Mao, D.B. and Wang, Y.X. Simulation Research on Nonlinear and Discontinuous Characteristic of Rock Burst. New industrialized road to sustainable development of China coal industry. Beijing: Coal Industry Press, 2004.
15. Li, J.Q., Qi, Q.X., Mao, D.B., et al. Discussion on Evaluation Method of Bursting Liability with Composite Model of Coal and Rock. Chinese Journal of Rock Mechanics and Engineering, 2005, sup.1(24). 4805-4810.

RaSiM 7(2009): Controlling Seismic Hazard and
Sustainable Development of Deep Mines,
C.A. Tang(ed), Rinton Press, 711-714

NUMERICAL SIMULATION OF THE ELASTIC-PLASTIC FAILURE PROCESS ON PILLARS

YANG YANG, LI SONG, DA-GUO WANG & QIANG LI

Center for Material Failure Modeling Research, Dalian University

Dalian, 116622, P.R. China

Based on the self-developed Rock Elastic-Plastic Failure Process Analysis code (REPFPA), the failure process of the pillar, from micro crack to macro crack and including unstable failure, is numerically demonstrated. The pillar is assumed to be a non-homogeneous elastic-plastic material. Many numerical tests are carried out, and it is shown that a relationship is developed between the statistical average strength and the ultimate bearing capacity. Macro shear fracture is the main from of cracking resulting from the pillar's elastic-plastic failure.

1 Introduction

In resource exploration, the pillar failure is a very important problem. Establishing pillars maintains mining stability and ensure its safe production. In many cases, the pillar can't be mined completely. So we should consider two factors, the mining stability and the mining rates of ore resources, to ensure the quantity distribution and size of the pillar. Mining rates reaching their maximum under the premise of mining stability is important to improve the economic benefit of mining. Therefore, we have to explore its failure mechanism and failure law.

Rock Failure Process Analysis (RFPA) [1] is developed through the idea of structuralization of program design with the numerical tool, the numerical simulation of the pillar failure process conducted by Professor Tang. Ferrero [2] and others studied the pillar force conditions by numerical simulation. In this paper, the pillar elastic-plastic failure process based on Rock Elastic-Plastic Failure Process Analysis code (REPFPA) [3] is simulated and investigated, which makes relationships between the statistical average strength and the ultimate bearing capacity.

2 Numerical Model

REPFPA is a numerical simulation program and used to study on the elastic-plastic progressive failure process of pillar in the paper. The basic idea had been introduced in the text [3].

The pillar model, including pillar, roof and floor, is plane strain. The pillar has same properties with the rock of roof and floor. With the continuation of mining, the pillar stress increases gradually.

The model size is 3m×3m, the entire domain is divided into 784 8-node isoparametric elements and there are 2505 nodes. The order of Gaussian quadrature is 3 and there are 9 Gaussian points in each element. The displacement "load" is imposed on the structure, the total is 6 mm and the imposition is divided into 15 steps.

The material parameters of the pillar are statistical average values, which are given in Table 1. In the table, E is the Elastic modulus, μ is the Poisson's ratio, t is the thickness, ρ is the density, C is the cohesion, H is the strain hardening parameter, S_c is the compressive strength, S_t is the tensile strength and φ is the internal friction angle.

Table 1. Statistical average values of the eight material parameters

E	μ	ρ	C	H	S_C	S_t	φ
50000.0	0.25	2.5	30.0	30000.0	100.0	20.0	45.0

In order to study the effects of material properties of non-homogeneity, we assume to adopt Weibull distribution law to describe the distribution pattern of material parameters:

$$p(\sigma_i) = c_i m_i (\sigma_i/\sigma_{io})^{m_i - 1} \exp[-(\sigma_i/\sigma_{io})]^{m_i} \tag{1}$$

where c_i stands for material normalized constant, m_i stands for pattern parameter of statistical distribution function, i.e. non-homogeneity coefficient. In the paper, m_2 and m_9 are 5.0, the other m_i (i=1, 3, 4, 5, 6, 7, 8) are 3.5.

3 Numerical Simulation Analysis

3.1. elastic-plastic failure process analysis

With the increasing in load, the number of ruptured elements of the pillar increases gradually.

Table 2 gives the number of ruptured elements and the total number of ruptured elements when the load is imposed.

Table 2. Statistics in rupture element

Load step	1	2	3	4	5	6	7	8	9	10	11	12	13	14	15
Load coefficient	0.7	0.75	0.8	0.85	0.9	0.95	1.0	1.05	1.1	1.15	1.2	1.25	1.3	1.35	1.4
Number of ruptured element	0	2	3	4	11	32	44	77	155	233	200	96	102	101	104
Total number of ruptured element	0	2	5	9	20	52	96	173	328	561	761	857	959	1060	1164

Table 2 gives that the unstable failure of the pillar happens in the tenth step. Figure1 shows the failure patterns. Figure2 shows the stress distribution.

1. Steps 1 to 7 are the random distribution of the rupture element. In this stage, because the load is low, the rupture is not obvious in the early stages of loading, basically with those elements whose strength are weaker and the tensile stress are larger breaking first. This stage corresponds to the stage of steady deformation of the pillar.

2. Steps 8 to 9 is transition stage, in which the rupture element focuses on the tension stress areas, that is, the rupture element focuses on the two triangle areas between the both sides of the pillar (In Figure1). Figure2 shows that they are high stress areas. When further loaded, the more micro rupture is generated in the areas. Because of the effects of the material's non-homogeneity, the distribution of micro rupture of the pillar is uneven, which is centralized to two diagonal lines. It is caused by obvious localization phenomena of deformation and micro rupture. This stage corresponds to the deformation stage of meta-stable of the pillar.

3. The unstable failure of pillar happened in the tenth step. The number of acoustic emission reaches a peak value at this time. It can be found clearly that macro rupture belt is formed in Figure2, and now the load is the ultimate bearing capacity. We research on the relationship between the statistical average strength and the ultimate bearing capacity in next section.

4. Steps 11 to 15 is the stage of unstable failure, at this time the bearing capacity of the pillar is over the ultimate bearing capacity. Although the program can simulate quasi static model and couldn't simulate the mass ejection phenomenon of rock, the appearance of more micro rupture still can be seen as a clearly characteristics of rock burst. Fig1 show that it has appeared on shear failure clearly in the 15th step.

During the deformation and failure process of the pillar, especially before appearing unstable failure in the tenth step, micro-rupture is always generated in the outsides of two wedge areas between roof and floor, because the rock in the area is under three-dimensional stress state, which was proved in field detection and laboratory test of rock samples [4]. Figure2 shows that macro rupture belt is the centralized zone of rupture elements and also high stress area.

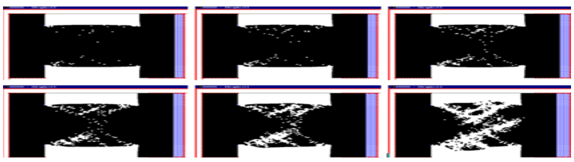

Figure 1 Failure patterns of pillars at step 6, 7, 8, 9, 10, 15

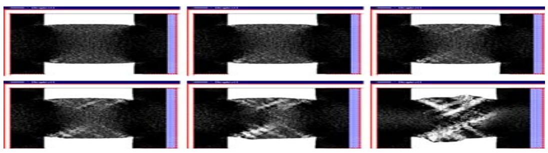

Figure 2 Stress fields in pillars at step 6, 7, 8, 9, 10, 15

3.2. The relationship between the statistical average strength and the ultimate bearing capacity

The previous section shows that the unstable failure of pillar happens in the tenth step, at this time the bearing capacity can be seen as the ultimate bearing capacity. From the results the ultimate bearing capacity is as follows:

$$P_L = 218.39\text{KN/mm} \tag{2}$$

According to the statistical average strength $\sigma_c = 100\text{Mpa}$, we can get:

$$P_L' = 300\text{KN/mm} \tag{3}$$

Because the non-homogeneity of materials is considered, $P_L < P_L^{'}$, the actual bearing capacity of the pillar is much smaller than the theory bearing capacity calculated by the statistical average strength.

3.3. Comparative Study on stress concentration

The previous section shows that there are four “inside right-angle”, which are all sharp angles in the pillar model. In this section, the “inside right-angle” are replaced by “fillet angle” in order to see whether stress concentration affects the pillar failure process.

Table 3 gives the number of ruptured elements and the total number of ruptured elements.

Table 3. Statistics in rupture element

Load step	1	2	3	4	5	6	7	8	9	10	11	12	13	14	15	16
Load coefficient	0.65	0.7	0.75	0.8	0.85	0.9	0.95	1.0	1.05	1.1	1.15	1.2	1.25	1.3	1.35	1.4
Number of ruptured element	0	2	2	4	6	14	28	54	89	147	241	149	141	143	108	57
Total number of ruptured element	0	2	4	8	14	28	56	110	199	364	587	736	877	1020	1128	1185

The conclusions can be got as follows: the four “inside right-angle” has almost no impact on the pillar elastic-plastic failure process. The main reason of the pillar rupture comes from tensile stress and non-homogeneous stress field which is caused by non-homogeneous materials.

4 Summary

The numerical simulation study was conducted on the pillar elastic-plastic failure process with the help of REPFPA. The pillar elastic-plastic failure process can be divided into four stages by the simulation analysis: steady deformation stage, meta-stable deformation stage, unstable failure early stage, and the unstable failure stage. It is shown that there is a relationship between the statistical average strength and the ultimate bearing capacity. The effect of stress concentration was also a point of interest in this paper.

Acknowledgements

The author would like to thank the financial support by the National Natural Science Foundation of P. R. China (Grant No. 50809008).

References

1. Tang, C., Qiao, H. and Xu, X.H. Numerical Simulation on Pillar Failure Process and Acoustic Emission. Journal of China Coal Society, 1999, 24 (3). 266-269.
2. Ferrero, A.M., Giani, G.P. and Kapenis,A. Theoretical and Experimental Study on Geometric Instability of Pillars in Discontinuous Rock. In: Proceeding of 8th Int Con on Rock Mech.Tokyo, Japan, 1995, 555-558.
3. Song, L. and Lin, Y.M. Numerical Simulation on Non-Homogeneous Materials Elastic-Plastic Failure Process. Mechanics and Practice, 2002, 24(4). 30-32.
4. McCreary, R.G., Grant, D. and Falmagne,V. Source Mechanisms Three-Dimensional Boundary-Element Modelling, and Underground Observations at Ansil Mine. Rotterdam: Balkema, 1993. 227-232.

RaSiM 7(2009): Controlling Seismic Hazard and
Sustainable Development of Deep Mines,
C.A. Tang(ed), Rinton Press, 715-720

SEEPAGE-STRESS COUPLING MODEL OF HETEROGENEOUS COAL SEAMS BASED ON DOUBLE-MEDIA MODEL

JIANG-YONG YU and GUI-LAI WANG
College of Mechanics and Engineering, Liaoning Technical University
Fuxin, 123000, P.R. China

CHUN-HUI ZHANG
School of Civil Engineering, Hebei University of Science and Technology
Shijiazhuang, 050018, P.R. China

YANG YANG
Center for Material Failure Modeling Research, Dalian University
Dalian, 116622, P.R. China

To simulate the cleats' effects of coalbed on gas flow, coalbed is considered as double-media composed of rock matrix and cleats. With Weilbull's distribution the heterogeneity of young's modulus and strength of rock matrix are simulated, and the cleats (fractured media) are simulated with Desai thin elements. Based on elastic-plastic mechanical theory, gas flow theory and double-media model the seepage-stress coupling mathematical model of heterogeneous coalbed is presented, and the numerical code is developed. The effect of different distance of single cleat from gas production well on gas flow is studied. Results show that cleats could accelerate gas production. Especially, the recovery of coalbed methane would significantly be improved when gas production just exists in cleat. Some techniques, such as the hydraulic cutting seam, could enhance gas production. This model is suitable for simulating the effect of a heterogeneous coalbed on gas flow, and a new method of simulating gas flow process is provided as a result.

1 Introduction

Methane in coal seams is an important natural energy resource. Methane production technology has been gradually applied in China. The technology not only decreases environmental pollution caused by gas drainage, but also mitigates ignition and the resulting explosion hazard. These factors help provide a guarantee for coal production and energy security in China [1, 2, 3].

Methane production in coal seams is a coupling process of gas flow and solid deformation [4]. During methane production, the effective stress on coal redistributes and the deformation occurs, which causes the pore space and cleats to change. The permeability for coal seams and the gas flow are also influenced. On the other hand, gas pressure in coal seams is influenced by gas flow in porous media. Furthermore, gas flow also affects effective stress on coal. Coupled gas flow and solid deformation in porous media has received considerable attention with a lot of studies being reported [4-9]. Natural coal is a kind of heterogeneous geological material which contains natural weakness at various scales. When coal is subjected to mechanical loading, these preexisting weaknesses can close, open, extend or induce new fractures, which can in turn changes the structure of the coal and alters its fluid flow properties. Accordingly, when methane production is made, the re-distribution of the stress field leads to the initiation and growth of cracks, and potentially creates a highly permeable failure zone. Moreover, natural coal which also contains many types of cleats. The existence of these cleats seriously weakens mechanical properties of coal and influence gas flow. Accordingly, when numerical simulation for methane production both heterogeneity and cleats effects on gas flow and mechanical deformation should be taken into account. However, the mathematical model with the heterogeneity and cleats effect has not been reported. In this paper coal were as double-media composed of rock matrix and cleats. With Weilbull distribution the heterogeneity of young's modulus and strength of rock matrix is simulated, and with Desai thin element the cleats (fractured media) are simulated. Based on elastic-plastic mechanical theory and gas flow theory, the seepage-stress coupling mathematical model of heterogeneous coal based on double-media model is presented, and the numerical code is developed. Different distance's effect of single crack from gas production well on methane production is studied in case study.

2 Mathematical Model

Suppose coal is composed of rock matrix and cleats. Rock matrix is simplified as continuous media simulated by ideal elastic-plastic material. Cleats are simplified as fractured medium model.

2.1 Continuous medium model of rock matrix

1) Free-phase and physical absorbed methane in coal seams exists. According to gas content measurement data, gas content in coal seams can be similarly expressed [1]:

$$W = A\sqrt{p} \tag{1}$$

Where W is gas content, m^3/t, A is coefficient of gas content (ranges from 1 to 4), $m^2/(t\ MPa^{1/2})$; p is gas pressure, MPa.

2) Mathane is viewed as ideal, and its flow is isothermal. Gas's state equation is:

$$\rho = \frac{p}{RT} \tag{2}$$

3) Assuming the effects of gravity is relatively small and can be neglected; the Darcy velocity is given by:

$$q_i = -K_i p_j \tag{3}$$

Where, q_i is Darcy velocity, K_i is gas permeability coefficient, P is gas square pressure, $P = p^2$, p is gas pressure, MPa.

4) Coal is viewed ideal elastic-plastic material, and subjected to Mohr-Coulomb rule.

5) Coal is saturated by methane.

6) The effective stress subjected to modified Taizaghi effective stress theory:

$$\sigma_{ij} = \sigma'_{ij} + \alpha p \delta_{ij} \tag{4}$$

Where, σ_{ij}, σ'_{ij}, α is total stress, effective stress and Biot coefficient, respectively.

7) Coupling equation between gas permeability coefficient and effective stress is given as follows [1, 8]:

$$K = \begin{cases} K_0 e^{-\beta\sigma_3^{'}} & \text{In elastic state} \\ \xi K_0 e^{-\beta\sigma_3^{'}} & \text{In shear failure state} \\ \xi K_0 e^{-\beta\sigma_3^{'}} & \text{In tension failure state} \end{cases} \tag{5}$$

Where K_0 is gas permeability coefficient without stress, ξ, $\xi^{'}$ is modified coefficient of shear and tension failure, respectively ,which obtained by tests.

8) Mechanical properties are assumed locally heterogeneous (including Young's modulus, strength) and are represented by the Weibull distribution [8],

$$\varphi = \frac{m}{s_0}(\frac{s}{s_0})^{m-1}\exp[-(\frac{s}{s_0})^m] \tag{6}$$

Where, s is the element property (strength or elastic modulus) distributed about the mean s_0, the parameter m is a homogeneity index, which may be obtained from the statistical distribution of rock mass parameters [8].

9) Combing (1), (2), (3), under isothermal conditions, the gas flow in porous media is governed by a mass balance equation,

$$\nabla^2 K_i P = S(P)\frac{\partial P}{\partial t} - 2\sqrt{P}\frac{\partial \varepsilon_V}{\partial t} \tag{7}$$

Where, $S(P) = \frac{1}{4}AP^{-3/4}$, ε_V is volumetric strain.

2.2 Fractured element model based on Desai thin element

Cleats are simulated by thin element presented by Desai in 1984[9].

1) The elastic model is adopted, and fractured medium's deformation can be expressed as:

$$\begin{pmatrix} \sigma_s \\ \sigma_n \end{pmatrix} = \begin{bmatrix} D_{ss} & 0 \\ 0 & D_{nn} \end{bmatrix} \begin{pmatrix} \varepsilon_s \\ \varepsilon_n \end{pmatrix} \tag{8}$$

2) Gas flow equation along main fractured direction is given by,

$$q_i = K_{f_i}\frac{\partial P}{\partial s_i} \tag{9}$$

Where, K_{f_i} is gas permeability coefficient along main fractured direction, and is decided by normal pressure,

$$K_{f_i} = K_{f_0} e^{-\beta_1 \sigma_n} \tag{10}$$

Where σ_n is normal pressure, Mpa, K_{f_0} is cleats permeability coefficient without pressure.

3) Gas content in cleats is given by,

$$W_f = A_f\sqrt{p} \tag{11}$$

Where W_f is gas content in cleats, m^3/t, A_f is coefficient of gas content (ranges from 0.1 to 0.3), $m^2/(t\ MPa^{1/2})$.

4) Gas flow equation in cleats is given,

$$\frac{\partial}{\partial x}\left(K_{f_i}\frac{\partial P}{\partial x}\right)+\frac{\partial}{\partial y}\left(K_{f_i}\frac{\partial P}{\partial y}\right)=S_f(P)\frac{\partial P}{\partial t}-2\sqrt{P}\frac{\partial \varepsilon_V}{\partial t} \tag{12}$$

Where $S_f(P)=\frac{1}{4}A_f P^{-3/4}$.

Equation (1) - (12) comprise coupling mathematical model with mechanical heterogeneity and cleats effect. In addition, initial and boundary conditions are specified, and the model can be solved. In this paper, the simulation code is developed based on Coupling Analysis [1].

3 Case Study

As a case, a gas production well in Wang Yingzi Coal Mine, Liaoning province, is studied. The well depth is 173m. Unit weight of overburd is 23 KN/m^3. Self-weight stress is 4 Mpa. Gas pressure is 1.1Mpa. The radius of gas production well is 0.2m. Research region is 40×40m, and fixed boundary and Dirichlet boundary $p = 1.1$ Mpa. Dirichlet boundary of the well is $p = 0.1$ Mpa. Initial condition is $p = 1.1$ Mpa. Then two modes of different distance's effect of single cleat from the well on gas flow are studied. The distance between cleat and gas well of one mode is 13m, and the other is 0(figure 1b).

Other parameters are as follows: Initial permeability coefficient is $23.8m^2/(MPa^2 \times d)$. A is $m^2/(t\times MPa^{1/2})$. Elastic modulus E of coal is 2100 MPa, and homogeneity index m=3. Internal friction angle φ for coal is 30.2°, and homogeneity index m=5. Cohesive strength c for coal is 1.4 MPa, and homogeneity index m=4. Tension strength is 0.1MPa, and homogeneity index m=4. Poisson ratio for coal is 0.3. Modified coefficient for shear failure is 47. Modified permeability coefficient of tensile failure is 109. Cleat is simulated by Desai thin element, and permeability coefficient is 1800 $m^2/(MPa^2 \times d)$, and shear modulus is 0.01MPa, and A_f is $m^2/(t\times MPa^{1/2})$.

Plane strain model is adopted, and 12042 elements are divided. Results can be seen in figure 2~figure 7. Figure 2 and figure 3 is gas pressure distribution in 2880 days for two modes, respectively. It can be seen that cleats remarkably affect gas production. Through comparation of gas pressure distribution for two modes, it can be seen that gas pressure quickly decreases in the later mode because the distance between the cleat and the well is much smaller. So the smaller the cleats' distance from the well is, the easier the gas production is. Accordingly, cleats should be considered in gas production stimulation. Besides, hydraulic cutting technique is effective to improve gas production.

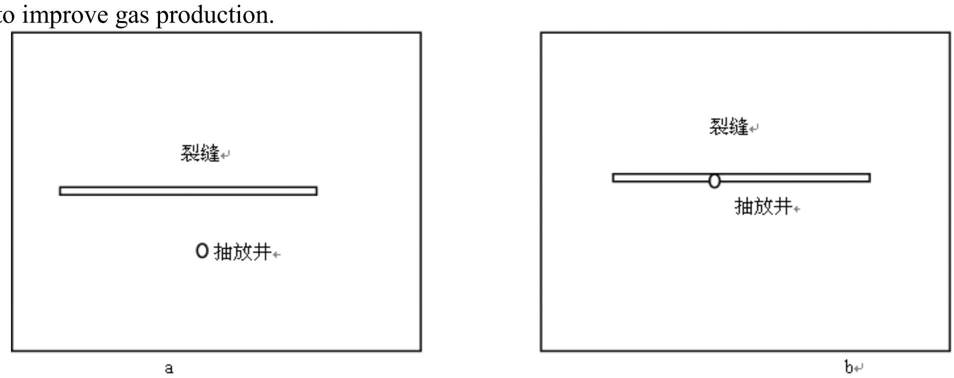

Figure 1 Two case study

In figure4~figure7, the increasing stress at the x and y direction can be seen. In case study, with Weibull distribution randomity of mechanic parameters is simulated, so the increasing stress is different from the results without the randomity of coal. However, general law is similar. It can be inferred that the model in this paer can reflect the effects of coal heterogeneity and cleats on gas production.

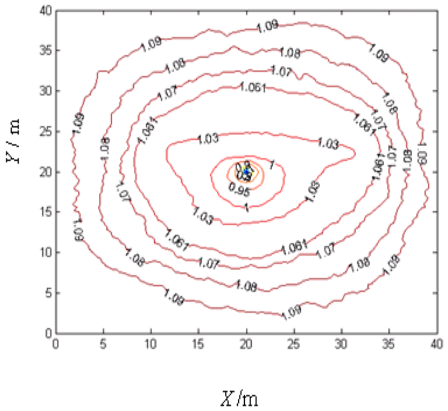

Figure 2 Pressure of gas in 2880 days /MPa

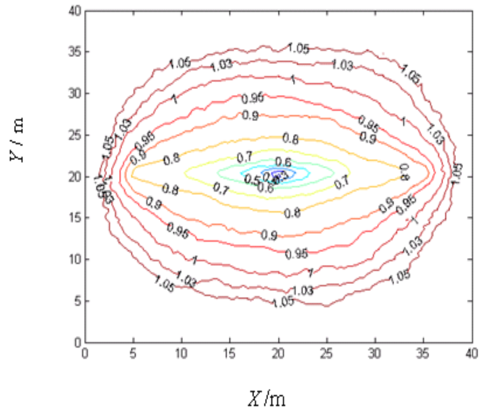

Figure 3 Pressure of gas in 2880 days /MPa

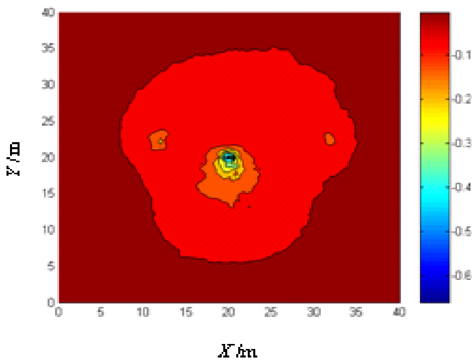

Figure 4 Adding x-stress of coal in 2880 days /MPa

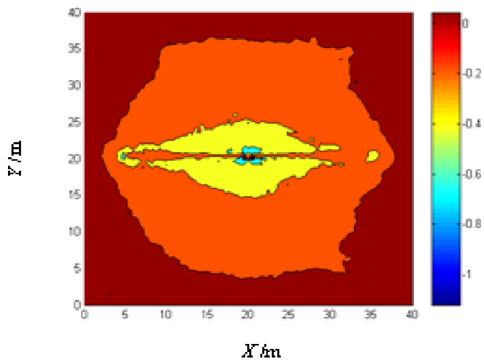

Figure 5 Adding x-stress of coal in 2880 days /MPa

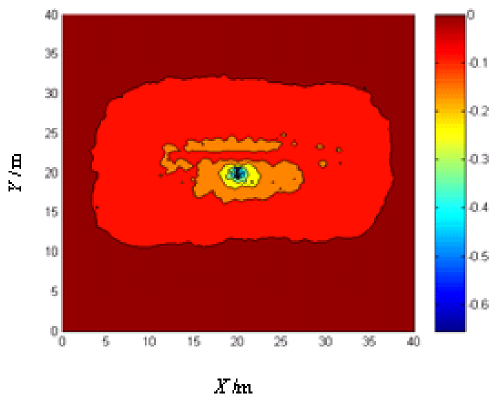

Figure 6 Adding x-stress of coal in 2880 days /MPa

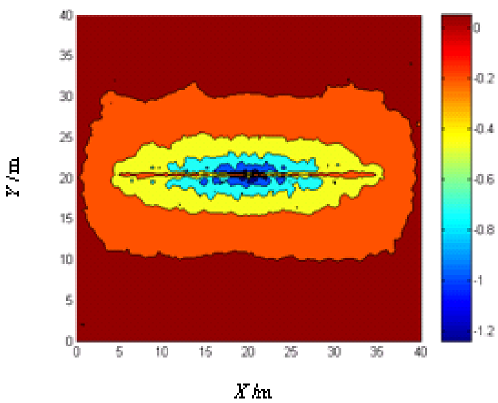

Figure 7 Adding y-stress of coal in 2880 days /MPa

4 Conclusion

As shown in this paper, coal is thought as a double-media composed of rock matrix and cleats. With Weilbull's distribution, the heterogeneity of Young's modulus and strength of the rock matrix is simulated; and with Desai thin element the cleats (fractured media) are simulated. Based on the elastic-plastic mechanical theory and gas flow theory, the seepage-stress coupling mathematical model of heterogeneous coal based on double-media model is presented. Through a case study the following conclusions are achieved as follows:

1) The cleats greatly affect gas production.

2) Some techniques such as hydraulic cutting can remarkably improve gas production.

3) Presented model in this paper can stimulate the effects of heterogeneity of rock matrix and cleats on gas flow and mechanical deformation of coal, and is also an effective model to stimulate gas production.

Acknowledgements

The author would like to thank the financial support by the National Natural Science Foundation of P. R. China (Grant Nos. 50434020, 50804020).

References

1. Zhang, C. and Yu, Y. Consolidation Model of Gas Drainage for Coal and Its Application. Journal of Liaoning Technical University, 2008, 27 (6). 844-846.
2. Yu, Y., Zhang, C. and Wang, L. Mechanism of Improving Mine Gas Drainage by Ultrasonic Disturbance. Journal of Liaoning Technical University, 2008, 27 (6). 805-808.
3. Yuan, L. Key Technique of Safe Mining in Low Permeability and Methane-Rich Seam Group. Chinese Journal of Rock Mechanics and Engineering, 2008, 27 (7). 1370-1379.
4. Otuonye, F. and Sheng, J. A Numerical Simulation of Gas Flow During Coal/Gas Outbursts. Geotech Geol Eng, 1994, 12. 15-34.
5. Valliappan, S. and Zhang, W.H. Numerical Modelling of Methane Gas Migration in Dry Coal Seams. Int J Numer Anal Methods Geomech, 1996, 20. 571-93.
6. Sun, P.D. Numerical Simulations for Coupled Rock Deformation and Gas Leak Flow in Parallel Coal Seams. Geotech Geol Eng, 2004, 22. 1-17.
7. Zhao, Y.S., Hu, Y.Q., Zhao, B.H. and Yang, D. Nonlinear Coupled Mathematical Model for Solid Deformation and Gas Seepage in Fractured Media. Transp Porous Media, 2004, 55. 119-36.
8. Yang, T., Xu, T. and Liu, J. Coupling Model of Stress Damage-Flow and Its Application to the Investigation of Instantaneous Seepage Mechanism for Gas during Unloading in Coal Seam with Depth. Chinese Journal of Rock Mechanics and Engineering, 2005, 24. 2900-05.
9. Desai, C.S. and Zaman, M.M. Thin-layer Element for Interfaces and Joints. International Journal for Numerical and Analytical Methods in Geomechanics, 1984, 8(1). 19-43.

RaSiM 7(2009): Controlling Seismic Hazard and
Sustainable Development of Deep Mines,
C.A. Tang(ed), Rinton Press, 721-726

NUMERICAL APPROACH TO THE INFLUENCE OF THE PROTECTIVE LAYER THICKNESS ON THE MECHANICAL PROPERTIES OF THE REINFORCED CONCRETE BEAM

XIONG CHEN and WEI-HONG LI

Civil and Archit. Eng. College, Dalian University

Dalian, 116622, P.R. China

In this paper, MFPA (Material Failure Process Analysis) is utilized to simulate the failure process of a reinforced concrete member under the condition of four-point bending. The influence of protective layer thickness on the mechanical properties of reinforced concrete beam is the main subject studied. The results indicate that an increase of the protective layer thickness will reduce the sectional effective height of the beam, which decreases the bearing capacity of the member. Therefore, choosing the protective layer thickness properly will yield the preferred properties in the member. In this study, it was found that a reasonable protective layer thickness is within 90 mm. However, it is necessary for the protective layer thickness to be confirmed by relevant specifications and standards on the premise above.

1 Introduction

For sheared reinforced concrete beams, complicated destruction mechanisms and variable influencing factors attract lots of academicians' attentions all around the world. Considering the existing studies, this study of member's shear bearing capacity in oblique sections is comparably sufficient. Basing on the numerous tests and statistics studied, various theories of computation have been presented about the shear bearing capacity in oblique sections; such as the method of limit equilibrium, method of intenerating truss, the nonlinear finite element analysis according to constitutive relations, etc. Failure models set up included arch, truss and combinations of arch and truss. The models showed clearly that in oblique section members' shearing resistance contain: concrete in compressive region, hoops, longitudinal tensile bars (acting as a bolt), aggregate in where the oblique cracks expand (interlocking), etc. For all kinds of components familiar, the concrete specification issued recently assigned the method to the calculation of member's shear bearing capacity in oblique section; building up a complete computation system in regard to the shear design. By contrast, the study of the serviceability limit state majors in whether this state is met with the expansion that the oblique cracks did in width; lacking of enough data as well as clear and a uniform theoretical analysis. The method to calculating the width of oblique cracks has been adopted in the codes in several countries. In concrete specification, the calculation formula of oblique cracks' width hasn't been recorded, while the ultimate width to satisfy the serviceability limit state is ensured by the computation of shear strength indirectly. Though early studies on oblique cracks, and compared with the research in vertical cracks, it was found that there is still some further work to be done.

As the development in PC technology, finite element method and boundary element method have been brought into materials' failure analysis widely, making the computer simulation an effective way to confirm the failure process. In this study, MFPA (Material Failure Process Analysis) is utilized to simulate the failure process of reinforced concrete member under the situation of four-point bending. The cracks' expansion, process of splitting and transformation of member's intensity are studied during the simulation. The influence of protective layer thickness on the mechanical properties of reinforced concrete beam is prior to research, aiming at coming to the ideal combination projects about how to fit reinforcing bars and concrete together and serving for the failure analysis.

2 Matrix of Numerical Simulation

2.1 Abstract of MFPA Numerical Principle

$MFPA^{2D}$ software is a numerical simulation tool which can simulates brittle materials' process when they're in gradual process of failure [1, 2].

It is similar to the progressive failure model informed [3], including two sides, stress analysis and failure analysis. Stress analysis in $MFPA^{2D}$ is based on the finite element method while failure analysis is on the failure criterion to inspect the materials for element failure. The failure elements are dealt with feature degeneration of stiffness (separation) and regeneration of stiffness (contiguity). To simulate the tester's loading, displacement control manner is adopted for the loading. Firstly, calculate the stress according to the displacement increment given; then inspect the models for element failure. If not, add another displacement increment and calculate the stress; if there is, deal the stiffness with degeneration basing on the failure states when the unit is sheared or tensile, and then recalculate the stress using the data dealt. Repeat the process until the material comes to the macroscopic failure. Considering that the tensile strength of brittle materials like glasses is farther less than compressive strength, this paper uses modified Coulomb's law containing stretch and truncation [4] to estimate the failure.

2.2 Calculate the Mathematical Matrix

This paper brings the Four-point bending test of reinforced concrete beam into use to simulate the failure process, studying the mechanical property influenced by the transformation of protective layer thickness. There are four samples and classified into Group A, B, C, D in term of the difference of protective layer's thickness. Samples are created into same numbers of re-bars and same lengths, with different thickness of protective layer. The protective layer thicknesses of different groups are as Table 1.

The protective layer thickness of common reinforced concrete beam is 25mm [5] as our nation states. Because it is the protective layer thickness which is studied to investigate the influence it does to beam's mechanical capacity that the fixed values are not adopted. To attain obvious effects, values are defined in excess of the standards and have great span. This is all about to show the influence clearly the thickness transformation dose on reinforced concrete beam’s mechanical capacities basing on Quantitative Change.

Table 1 Reinforcing bar’s protective layer thicknesses of different specimens

Item	Group A	Group B	Group C	Group D
Cover of reinforcement	30mm	40mm	60mm	90mm

2.3 Compares and Analysis of Failure Forms

According to the modulus of elasticity figures, shear strength figures, maximum principle stress figures and AE figures, it is easy to find that the failure modes of Group A, B, C are the same. So compare the failure modes between Group A and D.

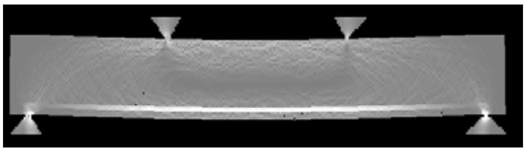

Step 0009-0002

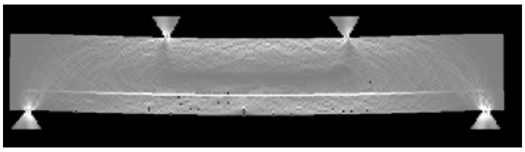

Step 0009-0002

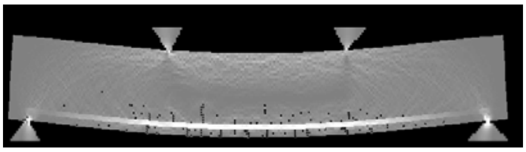

Step 0028-0001

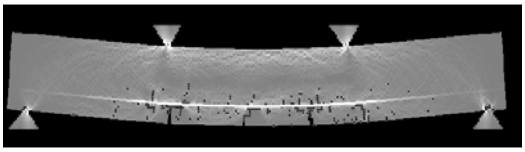

Step 0028-0001

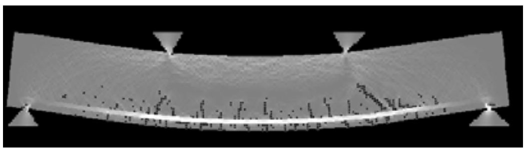

Step 0049-0008

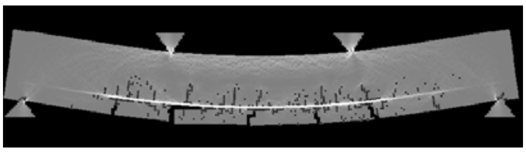

Step 0049-0003

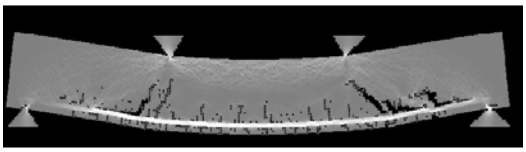

Step 0049-0015

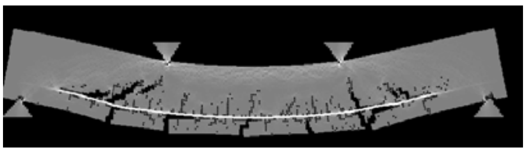

Step 0071-0011

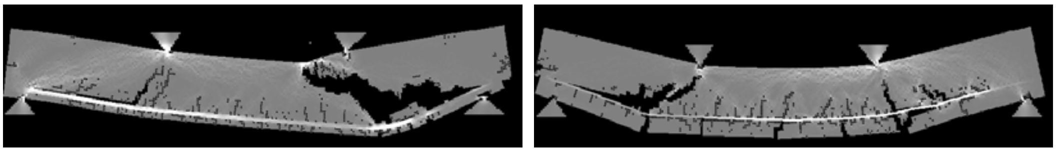

Step 0051-0021 Step 0079-0014

Group A Group D

Figure 1 Distribution of specimens' shear strength of Group A and D

From the figures, it is clear that the shear re-bars bear in Group D is lower than in Group A, which means that the function protective layer has on the beam of Group D is more obvious than the beam of Group A. But cleavage cracks appear in the protective cover of reinforcement which lapses at the same time.

Some of the strain energy releases in the form of elastic wave is named AE (acoustic emission, abbreviated as AE), when the material splits a bit under the load. That is the Acoustic Emission Technique which needs observation and analysis on the elastic waves. Like other materials, concrete would bring AE because of the small cracks load does. The AE figures shall bring great convenience to studies through the MFPA^{2D} software.

Next, the failure process would be analyzed qualitatively from the standpoint of energy through the AE figures between Group A and D.

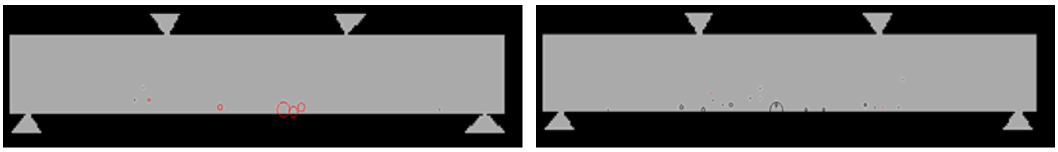

Step 0009-0002 Step 0009-0002

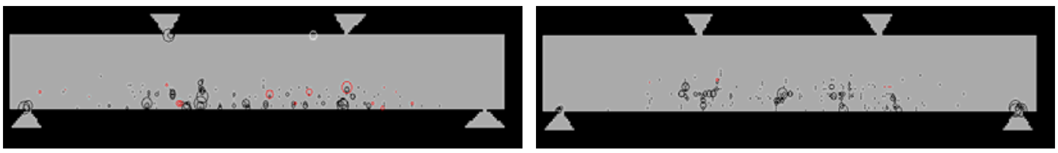

Step 0028-0001 Step 0028-0001

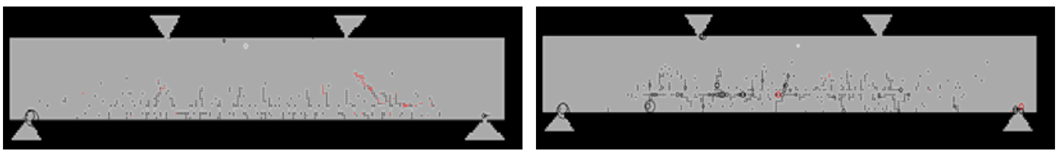

Step 0043-0008 Step 0049-0003

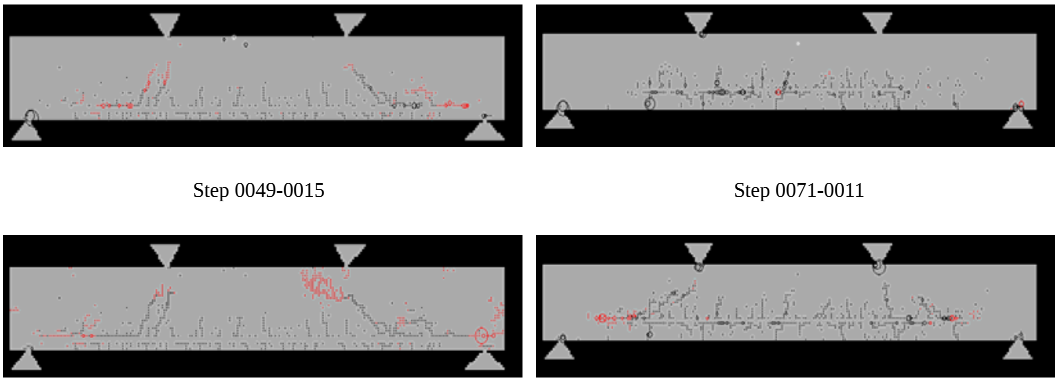

Step 0049-0015 Step 0071-0011

Step 0051-0021 Step 0079-0014

Group A Group D

Figure 2 The comparison of specimens' AE figures of Group A and D

Compared to the modulus of elasticity figures of Group A, at step 0009-0002, there is a little energy release from the beam causing by the small cracks on the edge of tensile region. At step 0028-0001, a set of cracks perpendicular to the edge of the section appear in the flexural-shearing region, in the result of great amount of energy release along the cracks. At step 0043-0008, critical oblique cracks appear with a mass of energy release along it. As the load gains, critical oblique cracks expand upsides and extend along with the released energy under the shearing-compressive surface. At step 0049-0015, critical oblique cracks' expansion slows down and no oblique cracks reappear. Owing to that, a small quantity of energy releases on the edge of oblique cracks, compared with little energy on the rest of the beam. At step 0051-0021, concrete in shearing-compressive region crushes with violent energy release in the place of failure, leading to the whole sample's failure. Compared to the modulus of elasticity figures of Group D, at step 0009-0002, in the protective cover of reinforcement, small cracks with a little energy release appears on the edge of beam's tensile region.

3 Results and discussions from the numerical simulation

By means of MFPA^{2D} software, apart from analyzing the failure modes intuitively from the figures on modulus of elasticity, shear strength, maximum compressive stress, maximum tension stress, AE and distribution of displacement vector, the experimental data can also be dealt with Excel to get the load-step curves of the sample.

From Figure 3, as the gains of protective cover of reinforcement, member's bearing capacity gains faster and faster. But when the protective layer thickness gains to some degree (90mm as the figure shows), the bearing capacity drops quickly. What causes this phenomenon is that the gains of protective cover of reinforcement lead to the decrease of section's effective height as well as beam's bearing capacity. To be up with it, more reinforcements are needed, causing unnecessary waste. From the standpoint of anchoring bond and life requirement, members need thicker protective layers. But only try to increase the thickness of protective layer, beam's sectional effective height would decrease, making the members' bearing capacity declines. So it is necessary to design the protective layer thickness appropriately to make the members deliver excellent value. Through the study, what has been found is that it is reasonable for protective cover of reinforcement to be kept within 90mm generally, however, on the premise of the study the thickness should still be designed and ensured taking the codes.

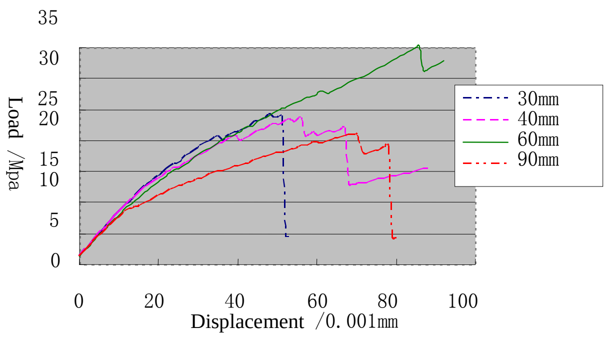

Figure 3 Load-step curves of different simulation specimens

4 Conclusions

The approach to recognize the influence of the protective layer thickness on the mechanical properties of the reinforced concrete beam through MFPA^{2D} numerical simulations was a success. The failure processes, cracks, destabilizations and expansions of the reinforced concrete beam on the condition of different protective layer thicknesses are observed and demonstrated directly.

On the condition of different protective layer thicknesses, the comparisons including modulus of elasticity figures, distribution of shear strength figures, AE figures and load-step curves are studied by the numerical simulation.

From the standpoint of anchoring bond and life requirement, members need thicker protective layers to protect re-bars. On the condition of sectional bearing capacities, it is too thick for protective layers to ensure the bearing capacities to be appropriate and the sectional effective height would decrease, leading to an increase in the number of reinforcement member and unnecessary waste.

According to the studies, it is reasonable for protective cover of reinforcement to be kept within 90mm, on the premise that codes are still an essential need.

References

1. Tang, C.A. Numerical Photoelastic Fringe of Stress Distribution During Failure Process of Material. Mechanics and Practices, 2002, 24(5).47-50.
2. Tang, C.A. Numerical Simulation of Rock Failure and Associated Seismicity. Int. J. Rock Mech. Min. Sci., 1997, 34.249-262.
3. Cui, W.C. Computer Simulation of Composite Materials' Structural Failure Process. Acta Material Composite Sinica, 1996, 13(4).102-111.
4. Brady, B.H.G. and Brown, E.T. Rock Mechanics for Underground Mining. Chapama & Hall, 1993, 106-108.
5. Jiang, L.X. and Lu, W.J. Thickness Control of the Concrete Cover of Steel Bars in Concrete Construction. Industrial Construction, 2005, 1.186-190.

RaSiM 7(2009): Controlling Seismic Hazard and
Sustainable Development of Deep Mines,
C.A. Tang(ed), Rinton Press, 727-730

NUMERICAL ANALYSIS OF THE ELASTOPLASTIC FAILURE PROCESS OF THE SURROUNDING ROCKS OF UNDERGROUND CAVERNS

QIANG LI, LI SONG, DA-GUO WANG and YANG YANG

Center for Material Failure Modeling Research , Dalian University

Dalian, 116622, P.R. China

The elastoplastic failure process of the surrounding rocks of underground cavern is studied in this paper, which is based on the self-developing Rock Elastic-Plastic Failure Process Analysis code (REPFPA). With this numerical tool, numerous numerical tests are carried out, and it is shown that there is a relationship between the shape of cavity and the limit bearing capacity of surrounding rocks. These identifications are crucial for better understanding and interpreting the experimental results and will consequently improve our concepts in the design or analysis of the underground engineering structures.

1 Mathematical Description of Non-homogeneity Model

Wherever it is visible to the naked eye, rock medium displays a quality of uneven distribution and discontinuity. However, such material is still considered a continuous medium in the traditional mechanic analysis of mining and surface projects. This hypothesis is obtained through the statistical average values of all mechanic parameters on a wider scale, when comparing with metal materials [1].

The random distribution of mechanic parameters shows the non-homogeneity of materials. For example, in order to present the distribution of the compressive strength of rocks a histogram is employed where the abscissa is the compressive strength and the ordinate is the number of samples. Fig.1 shows the distribution curve of the compressive strength of rocks in the metallic ore district in Altai. Fig.2 shows the histogram and distribution curve of point load strengths on rocks. It's validated by statistical tests where the curve obeys the Weibull distribution of Normal distribution. Therefore, the study shows that the probability density function and distribution function of uniaxial compressive strength and point load strength are:

$$P_{Is}(x) = 0.009x^{1.9}\exp(-0.003x^{2.9}) \tag{1}$$

$$P_{Sc}(x) = 0.00012x^{1.2}\exp(-0.0006x^{2.1}) \tag{2}$$

$$F_{Is}(x) = 1 - \exp(-0.003x^{2.9}) \tag{3}$$

$$P_{Sc}(x) = 1 - \exp(-0.0006x^{2.1}) \tag{4}$$

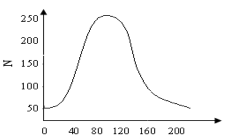

Figure 1 Compressive strength curve in the rock.

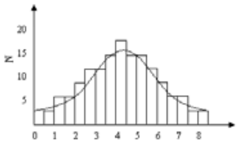

Figure 2 The point load's distribution of Altai metal diggings.

In this paper, statistical method has to be adopted to investigate the fracture of rock considering the non-homogeneity of materials [2].

For the convenience of description, the nine parameters of the surrounding rocks are numbered in Table 1. In terms of the above-mentioned nine parameters, their probability density functions can be uniformly expressed by Weibull distribution [3, 4] as follow:

$$P(\sigma_i) = c_i m_i (\frac{\sigma_i}{\sigma_{i0}})^{m_i - 1} \exp[-(\frac{\sigma_i}{\sigma_{i0}})]^{m_i} \qquad i = 1,2\cdots,9; i \neq 3 \tag{5}$$

where c_i stands for material normalized constant, m_i stands for pattern parameter of statistical distribution function, i.e. non-homogeneity coefficient. In the equation, when *i*=1, it describes the probability density of modulus of elasticity *E*, and here σ_1 stands for *E*; when *i*=7, it describes the limit compressive strength S_c. The other parameters of materials are expressed in the same way. Since the statistical density function of Weibull distribution is not monotone function, its integral function needs to be evaluated.

$$q(\sigma_i) = 1 - c_i \exp[-(\frac{\sigma_i}{\sigma_{i0}})^{m_i}] \qquad i = 1,2\cdots,9; i \neq 3 \tag{6}$$

Table 1. Nine mechanical parameters of the surrounding rock

No.	Parameter	Symbol	No.	Parameter	Symbol
1	Elastic modulus	E	6	Strain hardening parameter	H'
2	Poisson's ratio	μ	7	Compressive strength	Sc
3	Thickness	t	8	Tensile strength	St
4	Density	ρ	9	Internal friction angle	φ
5	Cohesion	C			

2 Numerical Model Setup

This study adopts the elastoplastic stress-strain relationship of the rock. It is based on the bilinear model namely the linear hardening model given in the reference [3, 4, 5], as is shown in Fig.3. The normally consolidated clay, loose sand and some rocks under high ground stress belong to this type [6].

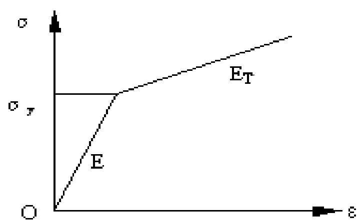

Figure 3 Curve for stress-strain relationship

Under the condition of plane stress, the surrounding rock block is divided by 8-node quadrilateral isoparametric elements. The order of Gaussian numerical integration is 3. Therefore, each element has 9 Gauss points, and there are 9 sub-elements in one element, each of which possesses one Gauss point. The material parameters of specimen are listed in Tab. 2, in which the data are statistical average values. It is supposed that the material parameters obey the Weibull distribution. The morphological parameters of the statistical distribution function (i.e. non-homogeneity coefficient) are all set to be: m_i =2.5(i =1, 2, 3, 4, 5, 6, 7, 8, 9).

Table 2. Statistical average values of the material parameters

E	μ	ρ	C	H´	Sc	St	φ
50000.0	0.25	2.5	30.0	30000.0	100.0	20.0	45.0

For every single sub-element, we adopt the Mohor-Coulumb failure criterion:

$$\sigma_1 - \sigma_3 = 2c\cos\varphi - (\sigma_1 - \sigma_3)\sin\varphi \tag{7}$$

It is used to judge whether the sub-elements are to be failure or not. It can be seen from Fig.1 and Tab.2 that when the stress of Gauss point reaches σ_Y , the material is yield. However, whether the material is to be failure or not depends on the equation (7).

If the sub-element is failure, we will reassign the parameters of material to reduce a certain coefficient which depends on the experimental results. In this case, the reduction coefficient of elastic modulus E and linear hardening parameter H' is 0.9, the reduction coefficient of cohesion and compressive strength is 0.8, and the reduction coefficient of other parameters is 0.0. As this method is being tried recently, and there is a lack of experimental data, so we still have a lot of work to do.

3 Relationship between Limit Bearing Capacity and Shape of Cavity

The size of the surrounding rock block is 320mm×250mm. The surrounding rock block is divided into 792 8-node quadrilateral isoparametric elements and 7128 sub-elements, and there are 2512 nodes. Displacement-controlled load is exerted on the surrounding rock. Boundary displacement is –0.6mm, which can be divided into 30 steps. The load coefficients for each step are: 0.30 for the first step and 0.02 from the second to the thirtieth step. When the load for the thirtieth step is exerted, the actual total displacement is –0.6×0.88mm. For different shape of elliptical cavity in every load step, when the number of ruptured sub-elements reaches maximum, the load is different. When the peak number of rupture elements appears, the material is unstable failure. At the same time, the load is the limit one.

The ratios of long axis and short axis are set to be: a/b = 1.00, 1.25, 1.50, 1.75, 2.00, 2.25, 2.50, 2.75, 3.00 for studying the effects of the shape of elliptical cavity on the surrounding rock's limit bearing capacity.

Fig.4 and Fig.5 present the damage state and stress state of surrounding rock corresponding to the nine ratio values (a/b = 1.00, 1.25, 1.50, 1.75, 2.00, 2.25, 2.50, 2.75). The white color stands for the ruptured elements in Fig.4. In Fig.5, the grayness stands for the relative stress. The lighter the color is, the higher the stress is.

It is shown in Tab.3 that: with the increasing of the ratio values, the ruptured sub-elements in the rock appear later. The process from the first ruptured sub-element to the surrounding rock's unstable damage becomes more centralized. These phenomena are still clear until the ratio a/b =2.75. It's mainly because the shape of cavity changes the stress distribution of the surrounding rock.

Table 3. Limit bearing capacity corresponding to each a/b value

a/b	1.00	1.25	1.50	1.75	2.00	2.25	2.50	2.75	3.00
Limit bearing capacity	11.53	12.63	13.28	13.33	13.75	13.88	14.20	14.38	13.76

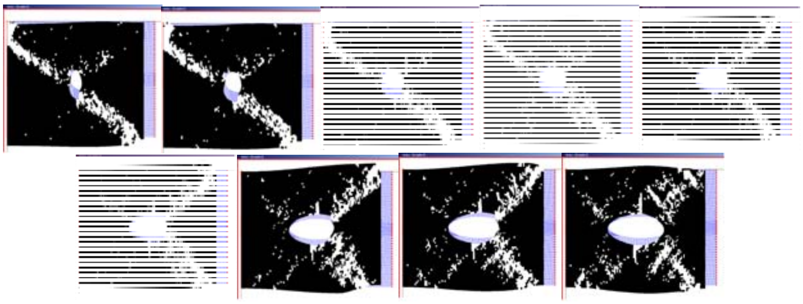

Figure 4 Damage state of surrounding rock in a/b=1.00,1.25,1.50,1.75,2.00,2.25,2.50,2.75,3.00

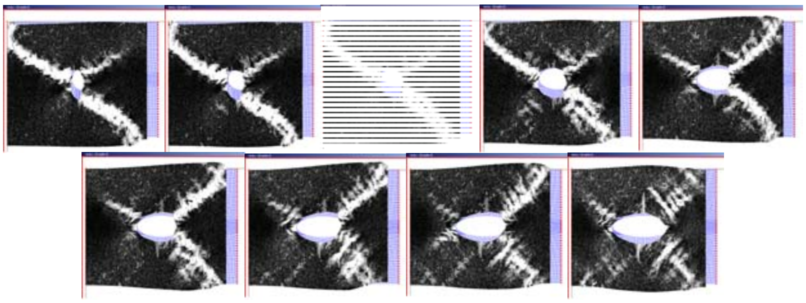

Figure 5 Stress state of surrounding rock in a/b=1.00,1.25,1.50,1.75,2.00,2.25,2.50,2.75,3.00

4 Conclusions

The study on the macro mechanics, especially the limit bearing capacity of engineering rocks, has basic principles but is a difficult subject in the rock mechanics. This paper studies on the relationship between the shape of cavity and the limit bearing capacity of surrounding rocks. Nine *a/b* ratios of elliptical cavity for comparing the limit bearing capacity are taken. These identifications are crucial to understand and interpret the experimental results and will consequently improve concepts in the design or analysis of underground engineering structures.

Acknowledgements

The author would like to thank the financial support by the National Natural Science Foundation of P. R. China (Grant No. 50809008), the Hong Kong Research Council (HKU 7171/06E), the Open Foundation of Hunan Province Key Laboratory of Water & Sediment Science and Water Hazard Prevention (Grant No. 2008SS04), the China Postdoctoral Science Foundation (Grant No. 20060400972) and the Dalian Science and Technology Foundation (Grant No. 2007J23JH027).

References

1. Yin, Y.Q. Constitutive Equation of Rock-Like Material. New Development in Rock Mechanics. Northeastern University Press, 1989.
2. Xie, H.P. Introduction to Fractal Rock Mechanics. Science Press, 1997.
3. Lei, H.N. Principles of Rock Mechanics. Metallurgy Press, 1978.
4. Zhen, Y.R. and Gong, X. N. Principles of Plasticity Mechanics in Rock and Soil. China Building Press, 1989.
5. Li, X.W. Mechanical Properties of Rock. Publishing House of Coal Industry, 1983.
6. Zhang, X.Y. Plastic Theory of Geotechnics. China Communications Press, 1993.

RaSiM 7(2009): Controlling Seismic Hazard and Sustainable Development of Deep Mines, C.A. Tang(ed), Rinton Press, 731-736

STUDY ON THE RESPONSE OF PORTAL WATER INJECTION SHEET PILES UNDER STATIC/SEISMIC LOADS

DAN-DAN WANG, CHUN-HUI ZHANG and QIAN XUE

Polytechnic College, Hebei University of Science and Technology

Shijiazhuang, 050018, P.R. China

LIAN-SHAN SHEN

College of Information Engineering, Dalian University

Dalian, 116622, P.R. China

Portal water injection sheet pile is a new type of space-retaining structure. When static loads are applied, its design and calculation mainly follow the method for double-row piles in pit excavation, and some positive results have been achieved. However, its dynamic characteristics and responses under seismic loads have never been studied before. To further the study on the newly developed portal water injection sheet pile under seismic loads, this paper adopts the nonlinear calculation module of FEM software ANSYS. A model for the interaction between the soil and the sheet piles is set up, and the seismic response analysis for this type of space-retaining structure is performed. The effects of the embedded depth and the distance between the front pile and the back pile on the dynamic characteristics of the portal water injection sheet pile are studied. Results show that both the embedded depth and the pile distance have little effect on the dynamic, and as is different from the situation of static analysis.

1 Introduction

The portal water injection sheet pile (PWISP) is a new type of space-retaining structure developed for the Shengli Oil Company. It was developed based on the combination of the practical needs of hydraulic projects and the technical principle of jet-drilling in the oil industry. It has also been successfully used for disaster prevention and hydraulic projects[1, 2]. It consists of double-row parallel-prefabricated reinforced concrete sheet piles and a connection bent cap on the top of the piles (Figure 1). Its primary technique is to directionally jet and split the stratum with high pressure water. At the same time sheet piles are inserted into the stratum under the control of the directional devices and then the two rows of independent sheet piles are connected together to form a dike, or for other construction purposes, with a series of special methods. In contrast with traditional piles the portal water injection sheet pile has many advantages; such as high pre-fabrication with rapid construction, low cost, and high erosion resistance. With these features taken into consideration, it has broad prospects for engineering applications.

The portal water injection sheet pile under work conditions is mainly subject to static and dynamic loads. For static loads, its design and calculation primarily follows the method for double-row piles in pit excavation, with some positive results [3-5] being achieved. However, its dynamic characteristics and responses under seismic loads have never been studied before. As the portal water injection sheet pile is chiefly used in building engineering and hydraulic engineering, its safety is of extreme importance.

This paper establishes a finite element model for the interaction between the soil particles and the sheet piles, while performing a seismic response analysis for the portal water injection sheet pile adopting the nonlinear calculating module of finite element software ANSYS.

2 Dynamic Nonlinear Interaction Between the Soil and the Sheet Piles

There exist two kinds of nonlinearity between the soil and sheet piles. One is the nonlinearity of the soil material, which has been studied by many researchers [4]. In this paper, the Drucker-Prager model[4] is adopted to consider the influence of this kind of nonlinearity. The other is the nonlinear state caused by the interaction between the soil and the sheet piles. The soil and the reinforced concrete sheet piles widely differ in property. The continuity of the displacement exists only under certain stress level on the interface between the soil and the sheet piles, beyond which slippage and separation are certain to occur. In order to simulate this characteristics, a number of contact elements are used in this paper to reflect the slippage and separation.

2.1 Motion Equation of Interaction System

According to the current dynamic finite element method, the nodal displacement $\{u\}$, velocity $\{\dot{u}\}$, and acceleration $\{\ddot{u}\}$ are regarded as unknown variables, then the governing motion equation for the dynamic response of a system in the finite element formulation can be expressed as:

$$[M]\{\ddot{u}\}+[C]\{\dot{u}\}+[K]\{u\}=\left\{F^{a}\right\}=-[M]\left\{\ddot{u}_{g}\right\} \tag{1}$$

where $[M]$, $[C]$, $[K]$ are the mass matrix, damping matrix and stiffness matrix, respectively, $\left\{F^{a}\right\}$ is the vector of the nodal loads, and $\left\{\ddot{u}_{g}\right\}$ is vector of nodal accelerations.

2.2 Nonlinear Model of Soil

Soil is grainy; and the stress-strain curve of the soil appears nonlinear even at the beginning of loading. Increasing the loads will lead to yielding and soil flowing. Finally the soil collapses. Therefore, the study of the soil nonlinearity includes yield criterion, failure criterion and flow rule[4].

In this paper, Drucker-Prager's yield criterion, which is an approximation to the Mohr-Coulomb criterion [4], is adopted, and can be written as:

$$F=\sigma_{e}-\sigma_{y}=3\beta\sigma_{m}+\left[\frac{1}{2}\{S\}^{T}[M]\{S\}\right]^{0.5}-\frac{6C\cos\varphi}{\sqrt{3}(3-\sin\varphi)}, \tag{2}$$

$$\sigma_{e}=3\beta\sigma_{m}+\left[\frac{1}{2}\{s\}^{T}[M]\{S\}\right]^{0.5}, \tag{3}$$

$$\sigma_{y}=\frac{6C\cos\varphi}{\sqrt{3}(3-\sin\varphi)}\quad, \tag{4}$$

where σ_{e} is the equivalent stress, $\sigma_{m}=(1/3)I_{1}$, I_{1} is the first stress invariant, $\{S\}$ is the deviatoric stress, β is material constant, $[M]$ is the directions transformation matrix of yielding, σ_{y} is the yield parameter of the soil, C is the cohesion of the soil, and φ is the internal friction angle.

The flow rule defines the development of the plastic strain with the yielding. In the Drucker—Prager model, relative flow rule is adopted. As the yield surface is invariant when the soil gradually yields, there is no hardening phase.

2.3 Contact Element

Suppose there is contact between object A and object B, the equation of the entire system can be written as:

$$\begin{bmatrix} K_A & 0 \\ 0 & K_B \end{bmatrix} \begin{Bmatrix} \alpha_A \\ \alpha_B \end{Bmatrix} - \begin{Bmatrix} F_A \\ F_B \end{Bmatrix} = 0 , \tag{5}$$

where K_A, K_B are the contact stiffness of A and B, respectively; α_A, α_B are the contact nodal displacements of A and B, respectively; and F_A, F_B are the nodal forces caused by external loads, respectively.

The objects A and B are linked by two nodal restriction elements. As a result, the nodes with independent conjugated local displacements are defined at the joints, and the internal force work and external force work are equal:

$$A_{i,a} + A_{i,\lambda} = A_{\varepsilon,a} + A_{\varepsilon,\lambda} , \tag{6}$$

$$A_{i,a} = \delta(\{\alpha_2^L\} - \{\alpha_1^L\})^T \{\lambda\} , \tag{7}$$

$$A_{\varepsilon,a} = \delta\{\alpha\}^T \{F\} , \tag{8}$$

$$A_{i,\lambda} = \delta\{\lambda\}^T \{[C]\{a\}\} , \tag{9}$$

$$A_{\varepsilon,\lambda} = \delta\{\lambda\}^T \{a_r\} , \tag{10}$$

Where $A_{i,a}$ is the virtual work of the nodal internal force, $A_{\varepsilon,a}$ is the work of the nodal external force, $A_{i,\lambda}$is the virtual work of the additional nodal internal force caused by external loads, $A_{\varepsilon,\lambda}$is the work of the additional nodal internal force caused by external loads.

The element stiffness matrix of restricting nodes can then be written as follows:

$$\begin{bmatrix} 0 & [c]^T \\ [c] & 0 \end{bmatrix} \begin{Bmatrix} a \\ \lambda \end{Bmatrix} = \begin{Bmatrix} F \\ a_r \end{Bmatrix} , \tag{11}$$

where $[c]$ is the transition matrix from element stiffness matrix to system stiffness matrix, α , α_r are the nodal displacement and initial displacement, respectively, λ , F are the interaction force both nodes and the nodal force caused by external force, respectively.

With the loads increasing, the interaction of the soil with the piles is simulated step by step. At the beginning of the calculation, a contact state(fixation, slippage, stretch, etc) of the contact elements is assumed. Based on assumed state, the matrix of the total stiffness and the vector of equivalent loads are calculated. A group of solutions are obtained by solving the finite element equations, and the assumed contact state is checked. If the contact state does not accord with the assumed contact state, a new contact state is assumed, and the vector of the loads is modified. The iteration proceeds until the results converge.

3 Finite Element Calculation Model of ANASYS

Normally, the portal water injection sheet pile is still in a linear-elastic stage under work conditions when the soil enters into the yielding state. Therefore, the sheet piles are regarded as linear-elastic material, and the soil is regarded as elastic-plastic material simulated by the Drucker-Prager model. Eight-node isoperimetric elements are used to set up the calculation model for the soil and the piles. The size of the soil element is 0.3m×0.3m, and that of the sheet pile element is 0.15m×0.15m.

To accurately simulate the slippage between the sheet piles and the soil, face-face flexibility-rigidity contact elements are applied on the interface between the soil and the piles. The contact elements are automatically generated according to the grid plot and nodes position of the soil and the sheet piles. The finite element model and its size are shown in figure 2.

If the calculation domain is sufficiently large, the influence of the boundary conditions can be neglected. In our analysis, a 60×30m calculation domain is accepted to guarantee the negligible influence from the boundary conditions and the boundary conditions are chosen as follows. Lower boundary: both the x and y displacements are zero. Lateral boundaries: the x displacements are zero. The sheet piles are restricted by the soil, and the strength of the restriction is determined by the magnitudes of the normal and tangent contact stiffness.

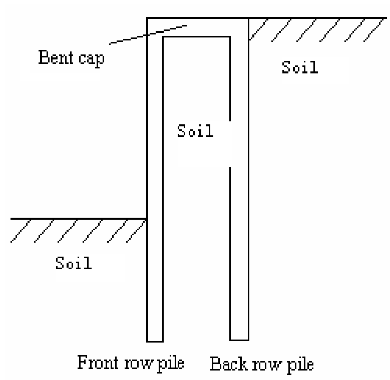

Figure 1 Portal Water Injection Sheet Pile

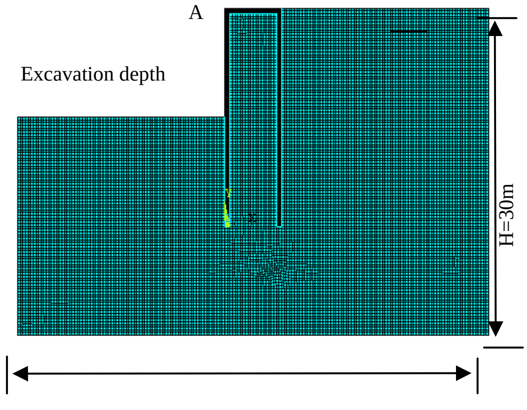

Figure 2 Finite element model

4 Calculation and Analysis

To analyze the static/dynamic characteristics and the effects of the parameters such as the embedded depth on the characteristics, a simplified case is obtained from several practical projects of the Shengli Oil Company. The parameters of the study case are given in table 1. The friction coefficient of contact element is 0.3.

Table 1 Calculation parameters

Soil parameter	Value	Sheet pile parameter	Value
Young's modulus	5×10^4kPa	Young's modulus	6×10^5 kPa
Poisson's ratio	0.4	Poisson's ratio	0.3
Density	1800kg/m^3	Density	2500kg/m^3
Internal friction angle	30°	Length	12m
Cohesion	30 kPa		

4.1 Static Analysis

First, the static responses are calculated when the embedded depth is set to 6m and the distances between the front pile and back pile are 1.5m, 2m, and 3m, respectively. It is found that the distance between the front pile and the back pile has a marked effect on the displacement of the top point A.

Then the distance between the front pile and the back pile is set to be 2m, and the embedded depths are 4m, 5m, and 6m, respectively. It is found that the displacements of the top point A are 5.23cm, 4.4cm, and 4.0cm, respectively. It can be seen that the displacement of the point A markedly decreases with increasing embedment depth.

4.2 Dynamic Analysis

The El-Centro seismic wave is selected as the external seismic loads on the portal water injection sheet pile. The incident wave propagates in the base rock, and the maximum acceleration is 0.374g. The dynamic response of portal water injection sheet pile is then analyzed.

First, the seismic response are calculated when the distance between the front pile and back pile are 1.5m, 2m, and 3m, respectively, while the embedded depth of 6m. The history curves of the additional displacement and acceleration at the top point A are shown in Figure 3, Figure 4 and Figure 5, respectively. It can be seen that the displacement of the point A can reach up to 3.3cm. At the same time, the acceleration is remarkably magnified, too. The amplitude of the acceleration is twice that of the incident wave. Different from the situation under static loads, the change of the distance between front pile and back pile has little effects on dynamic responses.

Then, when the pile distance is 2m, and the embedded depth are 4m, 5m, and 6m, respectively, the history curves of the additional displacement and acceleration of the top point A are shown in Figure 7, 6 and 4, respectively. It can be seen that both additional displacement and acceleration of the top point A slowly increase with decreasing embedded depth.

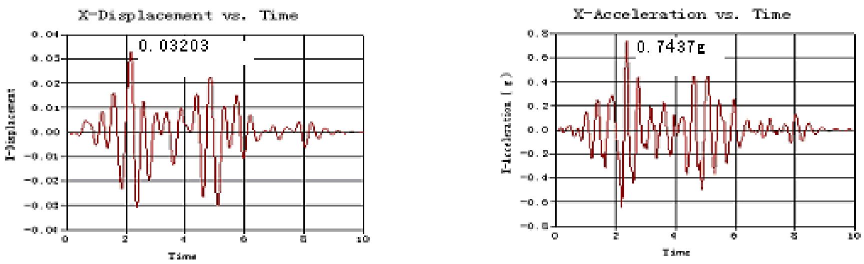

Figure 3 History curve of displacement and acceleration when embedded depth is 6m and the distance is 1.5m

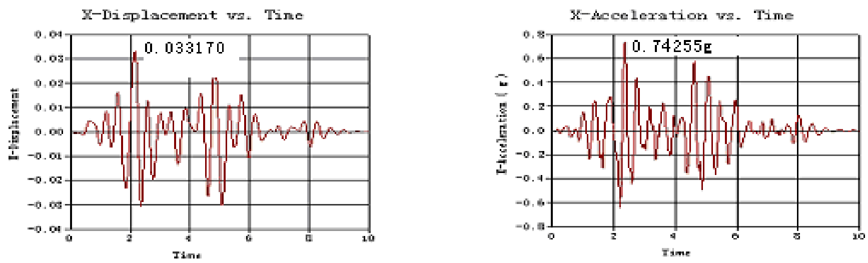

Figure 4 History curve of displacement and acceleration when embedded depth is 6m and the distance is 2m

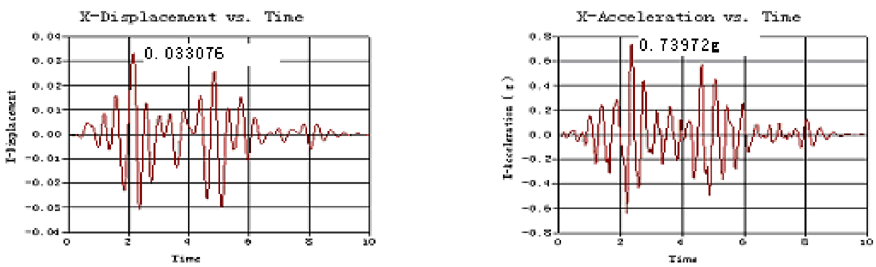

Figure 5 History curve of displacement and acceleration when embedded depth is 6m and the distance is 3m

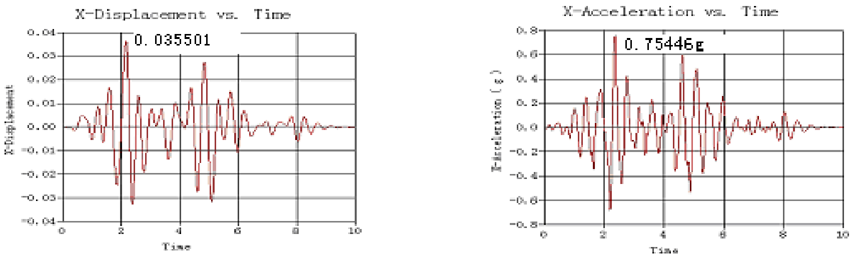

Figure 6 History curve of displacement and acceleration when embedded depth is 5m and the distance is 2m

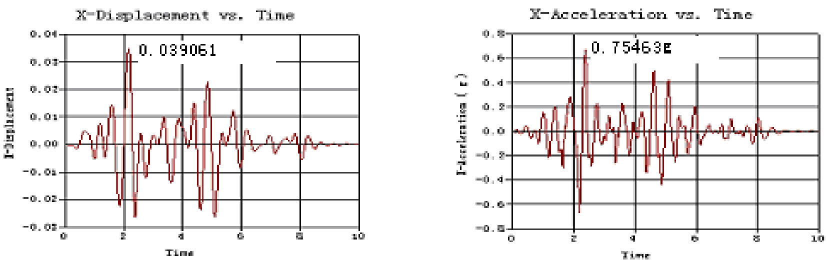

Figure 7 History curve of displacement and acceleration when embedded depth is 4m and the distance is 2m

5 Conclusions

1) The additional displacement at the top A of the sheet pile caused by seismic loads is significant, and reached up to 3.3cm in the study. The amplitude of the acceleration is also remarkably magnified, which can be twice that of the incident wave. However, as is different from the situation of static analysis, the embedded depth and the pile distance have little effect on the dynamic responses.

2) Under seismic loads, with the decrease of the embedded depth of PWISP, the top displacement and acceleration increase. However, the increments are very small, which is differs from the condition of static loading.

References

1. Guo, H.Y., He, F.R., Liu, D.F. and Luo, Y. Techniques and Applications of Water Injection Sheet Plies. In: International Symposium on Safety Science and Technology, (Beijing, 2002).
2. Guo, H.Y., Shun, Q., Liu, L.Y., and Wang, Y.B. Stability Analysis Against Slide of the Portal Water Injection Sheet Pile. Journal of Ocean University of China, 2005, 35(6).1053-1056.
3. Cai, Y.Q., Zhao, Y.Q. and Wu, S.M. FEM Analysis of The Deep Pit Excavation with Retaining Structure of Double Piles in Soft Clay. Journal of Zhejiang University, 1997, 20(4). 65-71.
4. Zheng, Y.R., Shen, Z.J. and Gong, X.N. Plastic Mechanics Principle of Rock and Soil. Chinese Architecture Industry Publishing, 2002.
5. Zhou, C.Y., Liu, Z.Q. and Shang, W. A New Mode for Calculation of Portal Double Row Anti-Sliding Piles. Rock and Soil Mechanics, 2005, 26(3). 441-444.

RaSiM 7(2009): Controlling Seismic Hazard and Sustainable Development of Deep Mines, C.A. Tang(ed), Rinton Press, 737-748

PERSPECTIVES OF COULOMB STRESS TRANSFER APPROACH IN STUDIES OF THE INTERACTION AMONG MINING-INDUCED SEISMIC EVENTS

ORLECKA-SIKORA BEATA

Faculty of Geology Geophysics and Environmental Protection, AGH University of Science and Technology, al. Mickiewicza 30, 30–059 Kraków, Poland

In recent years many studies of temporal and spatial patterns of seismicity induced by mining works provided the evidence for interrelations of seismic events. Seismicity accompanying mining exploitation is controlled by various time–variable natural and anthropogenic factors. In consequence of that the origin of event dependences is complex and difficult to identified. One of the possible causes of interactions among seismic events could be a static stress transfer. Some examples from natural seismicity show that even small stress changes resulting from the coseismic slip can accelerate or prevent future earthquake occurrences. In case of the mining-induced seismicity however, the coseismic stress changes expressed in terms of the Coulomb failure function (CFF) are at least one order smaller than those for earthquakes. Furthermore, they are only a small component of the stress field variations in mines. Despite, the analysis of the Coulomb stress changes caused by mining induced seismic events of energy greater than 10^5J ($M_L \geq 2.0$), which occurred in Rudna Mine in Legnica-Głogów Copper District in Poland suggests that the mining events are capable of producing changes in the state of stress that are sufficient to influence subsequent events. We find that about 70 per-cent of the analyzed seismic events occurred in areas where stress was enhanced due to the occurrence of previous events. For most of the events located inside areas of a calculated negative CFF changes, their modeled rupture zone is partially located inside stress enhanced, providing thus additional evidence for possible triggering at the nucleation point.

Although stress changes alone cannot explain the time evolution of seismicity, they can be incorporated in modeling the future expected seismic activity rate, which is one of the input parameters to the seismic hazard assessment.

1 Introduction

In recent years extensive studies of temporal and spatial patterns of seismicity for different regions and on different scales provided the evidence for interrelations of seismic events. A various techniques has been applied in order to quantify this phenomenon. Analysis of the seismic source size distribution in space and time show that the mining-induced seismicity has the tendency to form nests, swarms and clusters [e.g., 38, 6, 7, 25]. Clear evidence of the interaction of seismicity in a deep South African gold mine was demonstrated by Kijko and Funk [12]. Authors tested the interaction among mining events through the cross-correlation of time changes of activity rates and radiated energy between clusters. The results of analysis suggested that seismicity at given active faces is affected by seismicity at other mining faces and degree of interaction decreases with increase of distance between the faces. Similar conclusions derived Kijko [11] in studying the interevent time of seismicity from one of the deep gold mines in South Africa. He observed a trigger effect indicating internal correlations in the earthquake occurrence process.

Seismicity accompanying mining exploitation is controlled by various time–variable natural and anthropogenic factors. In consequence of that the origin of event dependences is complex and difficult to identified. One of the possible causes of interactions among seismic events could be a static stress transfer. Some examples from natural seismicity show that even small stress changes resulting from the coseismic slip can accelerate or prevent future earthquake occurrences [e.g. 9, 32 and the references therein]. Static stress changes are generally calculated from dislocation models of the seismic source, expressed in terms of the

Coulomb failure function (CFF) [e.g. 14, 13]. The stress changes are calculated on the basis of details of geometry and slip direction of earthquake rupture. Coulomb stress changes can explain the occurrence patterns of both small and strong events, and have been used as a powerful tool for the assessment of future seismic hazard in certain areas.

In case of the mining-induced seismicity the coseismic stress changes are at least one order smaller than those for earthquakes. Furthermore, they are only a small component of the stress field variations in mines and they are not enough to generate another seismic event. Nevertheless, if the rock mass at the location of the next event is already close enough to failure the first tremor can trigger the second one by introducing a positive static stress change to move it into the failure regime. Studies of the sptio-temporal distribution of seismicity recorded in the Creighton Mine in Canada, carried out by Marsan et al. [21], confirmed the existence of a stress diffusion mechanism and its influence on the stronger events occurrence. Analysis of series of seismic events from Polish coal and copper ore mines show that the stress transfer can influence seismicity occurrence in wide range of magnitude. Gibowicz [8] found that the occurrence of mining-induced seismic events is capable of increasing the probability of a second event in magnitude range of 0.7-3.5 resulting in seismic doublets and multiplets. The evidence from shallow tunnels and mines indicates that except for the deformation around underground excavations, unexpected deformations may be observed at areas away from the excavation front. One of the hypothesis which could explain this process is the static stress transfer [35].

The preliminary study of the static stress transfer in mines indicate that strong mining tremors are capable of producing changes in the state of stress of a sufficient magnitude to influence the future seismicity [26]. Authors examined the influence of the cumulative static stress changes due to previous events on the generation of the next ones in Rudna Mine area in Legnica-Głogów Copper District (LGCD) in Poland. They found that more than 50 per-cent of the analyzed seismic events occurred in areas where stress was enhanced due to the occurrence of previous events. For most of the events located inside areas of a calculated negative CFF changes, their modeled rupture zone was partially located inside stress enhanced, providing thus additional evidence for possible triggering at the nucleation point. The statistical test of the null hypothesis stating that there is no influence of CFF changes due to previous events on the subsequent event confirmed that for CFF changes $\geq$ 0.02 bar the static CFF triggering exists and this effect is statistically significant at the 95% confidence level [24, 27].

Although stress changes alone cannot explain the time evolution of seismicity, they can be incorporated in modeling the future expected seismic activity rate, by applying the Dieterich [3] rate- and state-dependent constitutive approach. This approach models seismicity as a sequence of nucleation sources in which the timing of events is determined by distribution of initial conditions over the population of nucleation sources and stressing history. From the rate- and state-dependent friction law an analytic expression for a step increase or decrease in shear stress is derived, which can be applied in studies of temporal behavior of seismicity rate. According to this approach, a sudden Coulomb stress increase causes an increase in seismicity rate, which decays back toward its initial rate with time, while a sudden stress drop causes the seismicity rate to decrease, also recovering toward its reference rate.

In this paper we present the results of modeling the Coulomb stress transfer in Rudna Mine in LGCD, in Poland. We calculate the cumulative static stress changes due to previous events on the generation of the next ones. At each stage of the calculations the future occurrences are correlated with the resulted stress field, each time inverted according to the faulting type of the next event whose triggering is inspected. We quantify the triggering effect by the proportion of events in dataset whose location is consistent with stress increased zones. Next we investigate the effect of Coulomb stress changes on the time behavior of seismicity from Rudna Mine through a stress transfer model which incorporates the rate/state friction. The preliminary results show that this approach is efficient to model the spatial and temporal pattern of seismicity during a sequence of mining-induced seismic events.

2 Method

2.1 Coulomb stress changes modeling

The first step in analysis of faults interaction by modeling the static stress transfer is the calculation of stress field associated with a particular fault. Static displacements, strains and stresses are calculated by solving the elastostatic equation for a dislocation on an extended fault in an elastic, isotropic and homogeneous half–space [e.g. 13]. The second step is the choice of criterion characterizing failure in rocks. Among various criteria the Coulomb failure criterion [10, 31] has been used by a number of authors to study the distribution of aftershocks after a large earthquake and to investigate static stress changes on other faults in the vicinity of a main shock [e.g. 2, 33, 34, 14, 29, 28]. According to Coulomb criterion, failure occurs on a plane when the Coulomb stress σ_f exceeds a specific value:

$$\sigma_f = \tau + \mu' \sigma_n, \tag{1}$$

where τ is the shear stress in the slip direction on the failure plane, σ_n is the normal stress, positive for tension, μ' is the apparent coefficient of friction, which takes into account the effect of the pore fluid pressure. Positive value of CFF moves a fault toward failure, negative value of CFF moves it away from failure.

In next step, the cumulative changes in stress due to the consecutive seismic events in the analyzed time series are calculated. We focus on the influence of seismicity from one month back. The reason of such approach is fact that the mining activity varies in time causing perturbations of stress field around mine excavations whose magnitude also varies in time. The coseismic static stress changes are only a small component of the stress field time-variations in mines and they also fluctuate in time due to mining works.

The possible triggering effect is examined by correlating the particular event location and the stress–enhanced zones.

2.2 Modeling of seismicity evolution in time

According to the rate- and state-dependent seismicity model [3], the seismicity rate, R, is a function of the state variable, γ, at the reference shear stressing rate, $\dot{\tau}_r$:

$$R = \frac{r}{r \cdot \dot{\tau}_r} \tag{2}$$

where r is the background seismicity rate. In the absence of stress changes, the state variable is at the steady state and is equal to:

$$r_0 = \frac{1}{\dot{\tau}_r} \tag{3}$$

and then the seismicity rate is equivalent to the background seismicity rate, $R=r$. The sudden stress step, ΔCFF, causes the change of the state variable to a new value γ_n [3, 4, 36]:

$$r_n = r_{n-1} \exp\left(\frac{-\Delta CEF}{A\sigma}\right) \tag{4}$$

where γ_{n-1} is the value of state variable just before the stress change ΔCFF, A is the constitutive parameter, which in laboratory experiments is found to be 0.005-0.02, σ is the effective normal stress.

Consequently, the rate of seismicity changes to a higher value when a stress increases on a fault or to a lower value when a stress drops. The higher the rate of seismicity at the time of stress increase, the stronger influence of the stress change on the seismicity rate will be observed. The state variable evolves in time according to the formula:

$$r_{n+1} = \left[r_n - \frac{1}{\dot{\tau}_r} \right] \exp\left(\frac{-\Delta CEF}{A\sigma}\right) + \frac{1}{\dot{\tau}_r} \quad (5)$$

where Δt is the time elapsed after the stress perturbation. Thus the changes of seismicity rate due to the stress jump are transient and the duration of the transient is inversely proportional to the stressing rate.

The rate/state transfer approach enables to consider successive stress changes associated with multiple seismic sources and to model their influence on the seismicity rate in time and space.

3 Data used in analysis

The area of our interest is the Rudna Mine, one of three copper ore mines belonging to the Legnica–Głogów Copper District (LGCD), located in the south–west Poland. The seismic network at the Rudna Mine records annually several thousands of mining-induced seismic events with local magnitudes, M_L, ranging from 0.4 up to 4.5, with the completeness level of about 1.2. These events are considered to be directly related to copper ore mining. In the period 1985-2006, on average three rockbursts were triggered annually by tremors, which resulted in over ten accidents and two fatalities [15]. In the LGCD, the seismic activity occurs also directly beneath urbanized and industrialized areas. Underground tremors can cause there strong ground motions affecting natural and built environment. The strongest events have caused peak ground accelerations around 2.0 m/s^2 [16].

For the following analysis, we selected the subset of 153 events with $M_L \geq 2.0$ (seismic energy equal to 1.0×10^5J) that were recorded between 1 July 2005, and 12 December 2006. Figure 1 depicts the spatial distribution of the seismic events incorporated in analysis.

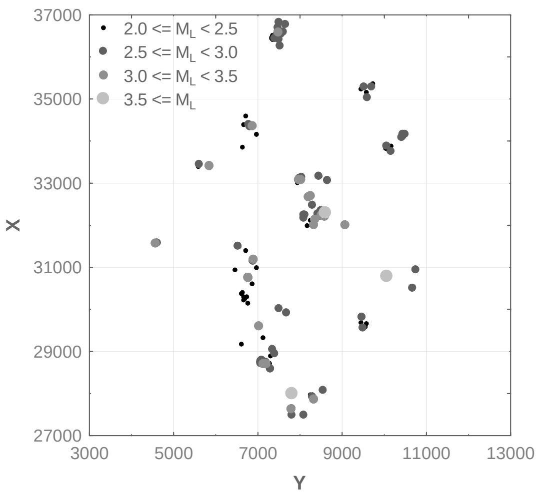

Figure 1 Spatial distribution of the analyzed events with $M_L \geq 2.0$ that occurred in Rudna Mine between 1 July 2005, and 12 December 2006

Source parameters and focal mechanism of analyzed seismic events were calculated at the Institute of Geophysics, Polish Academy of Sciences. Details of applied procedures of moment tensor inversion in time domain and spectral analysis are described by Domański and Gibowicz [5]. To evaluate the source mechanism of selected events, the full moment tensor, a constrained deviatoric solution and a double-couple solution were calculated. The analysis of decomposed moment tensors revealed that the type of process responsible for the mine tremor source nucleation is not uniform. The solutions have dominant shear components (DC), although in some cases the isotropic component (ISO) and the uniaxial compressional or extensional component (CLVD) reaches about 40% or 80% of the overall mechanism, respectively. Fig. 2 presents the histograms of the particular components contributed to the total seismic moment tensor solution of the analyzed seismic events. However, in general, for the analyzed subset of events the full moment tensor solutions are different from the deviatoric solutions and the double-couple solutions, while the two last solutions are very similar to each other. The higher values of CLVD and/or ISO component in the full moment tensor may be partially attributed to the poor focal sphere coverage for the studied area, as it was pointed out by Wiejacz [39]. The deviatoric solutions and the double-couple solutions are more likely to represent mechanism in the source of analyzed events. The solutions of moment tensor without volume change indicate that shearing processes are dominant in the source. Thus, for farther analysis we chose the focal mechanism parameters calculated assuming the double-couple mechanism.

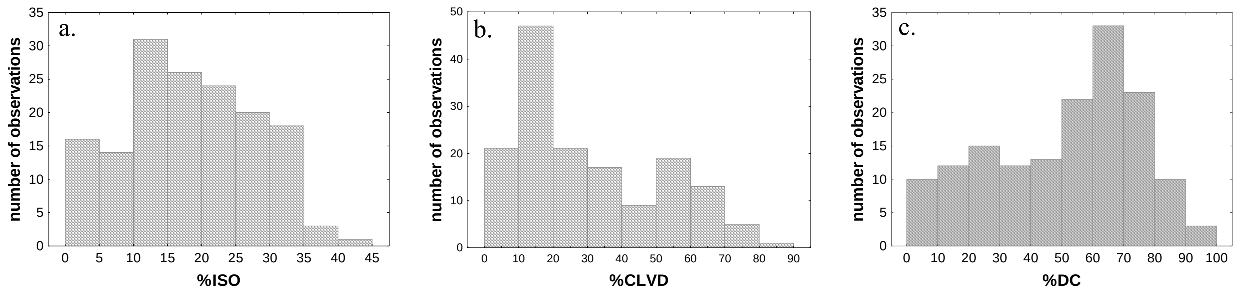

Figure 2 Histograms of a. the isotropic component ISO, b. the linear vector dipole component CLVD and c. the double couple component DC in the total moment tensor solutions of the analyzed seismic events of the Rudna Mine

4 Calculations of stress changes

Stress changes calculations were performed by the use of the software Coulomb 3.0 assuming a seismic event to be a point source [36, 20]. The geomechanical parameters of rocks in the LGCD vary in a wide range, depending on the type of rocks [e.g., 30]. We performed calculations with the shear modulus and the Poisson ratio fixed as 2.2×10^4 MPa and 0.25, respectively. The selected values reflect the averaged geomechanical conditions in LGCD, where the seismogenic zone is composed of limestones, dolomites, anhydrites and sandstones. The apparent coefficient of friction was taken to be equal to 0.8 throughout our calculations. This value is much higher than for Coulomb stress transfer modeling performed for natural earthquakes because rocks in the mining area are characterized by a higher cohesion than is the case in seismic fault zones. However, the previous analysis confirmed that the results of Coulomb stress changes modeling for mining induced seismicity does not depend strongly on the coefficient of friction [27].

Figure 3 presents histogram of the frequency of seismic tremor occurrence as a function of CFF changes (ΔCFF) due to previous occurrences. Negative changes in Coulomb stress denote a decreased likelihood of fault rupture, while positive CFF changes denote an increased likelihood of failure. About 70% of the total considered seismic tremors occurred at locations of positive changes in stress caused by previous events. Most of these events, about 90%, were located inside regions of ΔCFF values larger than 0.1 bar.

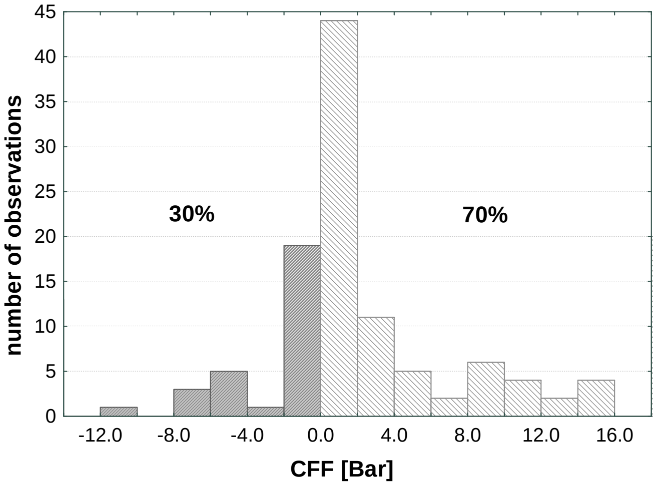

Figure 3 Histogram of frequency of seismic event occurrences in Rudna Mine in the Legnica–Głogów Copper District in the period of 1.07.05-12.12.06 as a function of ΔCFF

5 Estimation of the response of seismic activity to the stress changes

To examine how the stress changes alter the seismic activity in time we choose the set of seismic events that occurred in the seismic zone 32 identified in the Rudna Mine [17, 18]. Fig. 4 presents the extract of seismic activity per week for this seismic zone. The amplification of the seismicity rate is visible just after the occurrence of the two strong shocks, first of local magnitude (M_L) 4.1 that occurred on 2 September 2004 and the second one of M_L 3.7 that occurred on 9 October 2004. One of the possible explanation of this phenomenon could be an influence of the positive coseismic stress changes due to these two strong events on the seismic activity.

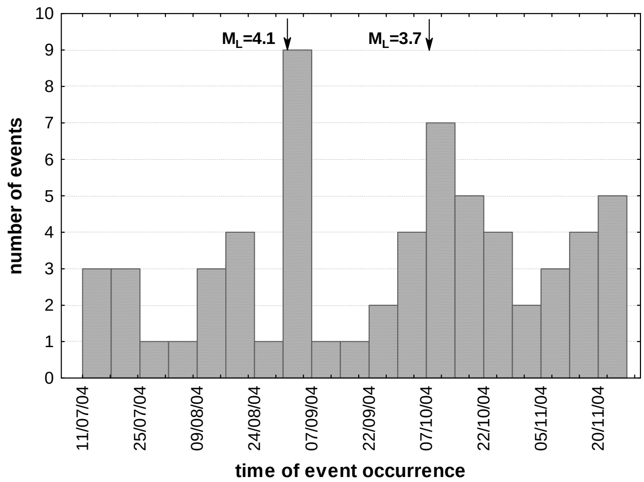

Figure 4 Histogram of the seismic activity of the seismic zone 32 in Rudna Mine in the period of 11.07.04-28.11.04. The black arrows denote the time of occurrence of two strong events of local magnitude 4.1 and 3.7, respectively

To investigate the effect of Coulomb stress changes on the time behavior of seismicity we implement a stress transfer model which incorporates the rate/state friction. The cumulated stress changes associated with the September shock together with the seismic events of $M_L \geq 2.0$ occurred during one month before, computed on a 0.1×0.1 km grid, are shown on Fig. 5. The CFF changes are resolved onto the fault plane corresponding to the stope face. This approach is prescribed by the observations that the seismic events with low energy, often showing implosive components in the source mechanism, occur near to an active mining face and the fault planes tend to be parallel to the nearby face direction [e.g., 40, 23].

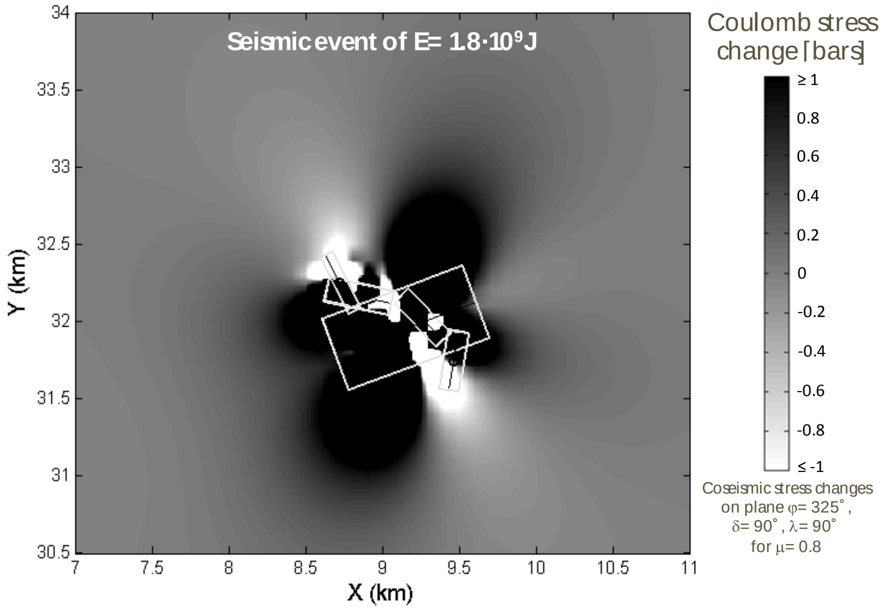

Figure 5 The cumulated stress changes associated with the September shock together with the seismic events of $M_L \geq 2.0$ occurred during one month before, resolved onto the fault plane corresponding to the stope face. Changes are denoted by a gray scale shown in the right part of figure (in bars). The black line is the intersection of target depth with fault plane, the white rectangle is the frame of the fault projected to the surface

To perform these calculations we need to estimate the reference background seismicity rate, stressing rate, the constitutive parameter A and the effective normal stress. The reference background seismicity rate is a crucial parameter in this approach because it controls the intensity of the influence of the stress changes on the seismic activity. We assume a time-independent background seismicity rate and its smoothed value is calculated on the basis of 251 seismic events that have occurred since the last strong event at the completeness of catalogue $M_L = 1.2$. For this purpose we use the two-dimensional nonparametric Gaussian estimation of the probability density function of seismic source location [e.g., 22] with smoothing factor equal 50m that corresponds to the error of event location in the LGCD for epicenter determination [e.g., 19].

The parameter $A{\cdot}\sigma$ has been estimated from seismicity patterns for different earthquake sequences by several authors and ranges between 0.0012 and 0.8 MPa [9]. We performed the calculations for $A{\cdot}\sigma$ =0.05 MPa. The stressing rate, is evaluated from the static stress drop of the September shock divided by the estimated earthquake repeat time, corresponding to the interval between the September shock and the previous strong event, [37]. The static stress drop of the considered tremor is equal to 0.93 MPa and the previous strong seismic event of M_L=3.5 occurred in area of zone 32 on 24.04.2004. The obtained value of the stressing rate, about 0.007 MPa/day, is comparable with value derived from the formula of Dieterich [3]:

$$\dot{\tau}_r = \frac{A \cdot \sigma}{\dot{\tau}_a} \tag{6}$$

where t_a is the time of aftershocks duration and in the case of the September event is about one week.

Fig. 6 shows the comparison between the observed and predicted through the rate/state stress transfer time behavior of seismic activity for the region around the strong tremor within a radius of 2 kilometers.

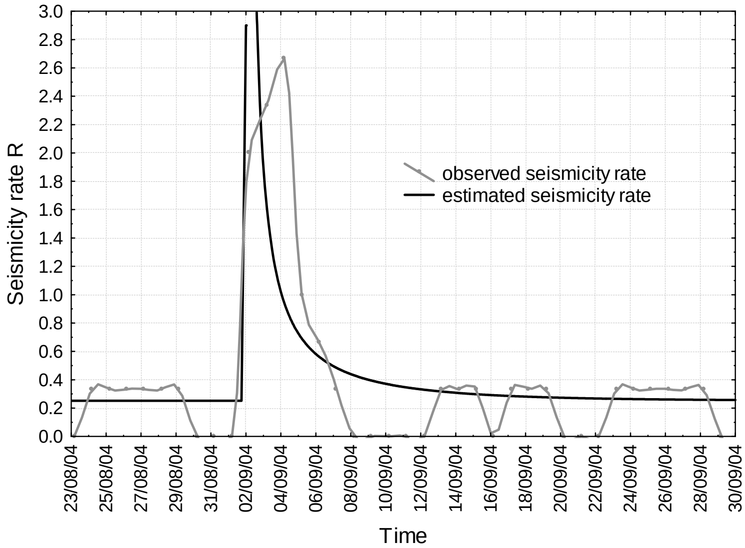

Figure 6 Observed and modeled seismicity rate changes in time for the region around the September tremor of M_L=4.1 within a radius of 2 kilometers. Daily observed seismicity rate, smoothed with a running 3-day window, is gray, the estimated seismicity rate is black. The reference background seismicity rate for this region is 0.25, the Coulombs stress changes are 5.8 MPa, A·σ=0.05 MPa and the stressing rate is 0.007 MPa/day

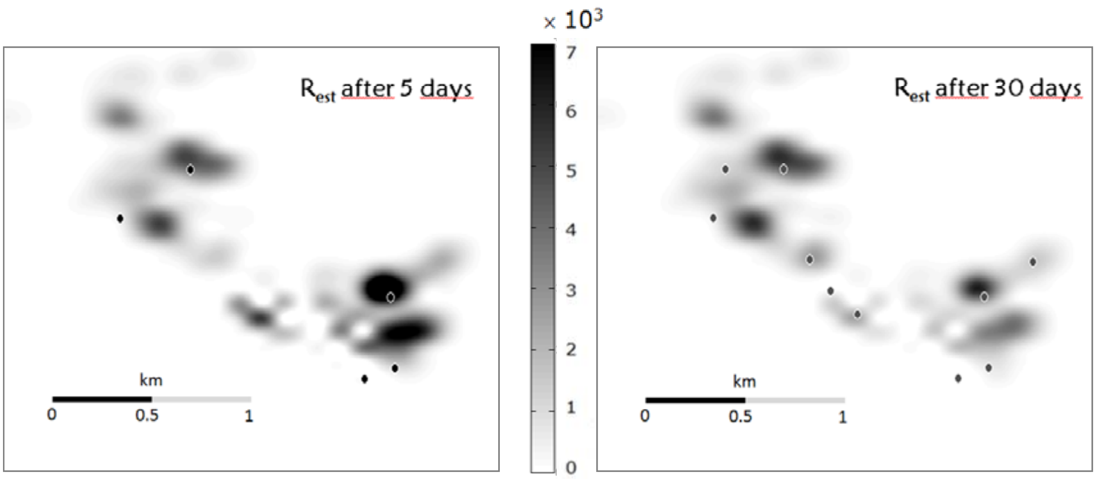

Figure 7 Predicted seismicity rate though the rate/state stress transfer model after the September tremor of M_L=4.1. Black dots display the distribution of seismic events that occurred after the strong event during 5 and 30 days, respectively. The reference background seismicity rate and the Coulomb stress changes vary on the considered region, $A{\cdot}\sigma$=0.05 MPa and the stressing rate is 0.007 MPa/day.

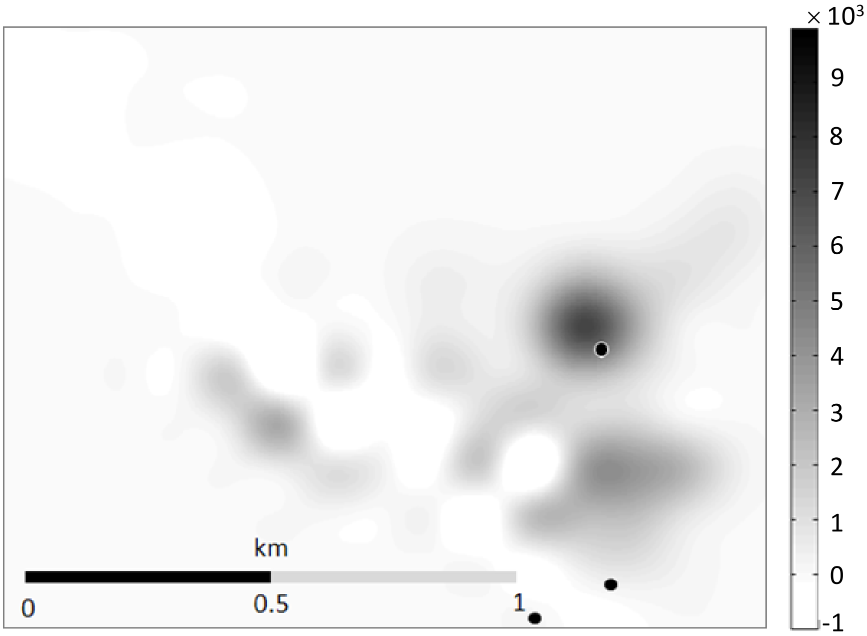

Figure 8 Predicted seismicity rate changes though the rate/state stress transfer model caused by the September tremor of M_L=4.1. Black dots display are the seismic events that occurred after the strong event during 5 days. The reference background seismicity rate and the Coulomb stress changes vary on the considered region, $A{\cdot}\sigma$=0.05 MPa and the stressing rate is 0.007 MPa/day

The modeled evolution of seismicity rate good matches to the observed seismicity rate behavior in time, although the peak of expected rate just after the occurrence of the September shock is much higher than that observed. As shown Catalli et al. [1], this peak of rate is influenced by the selected value of $A{\cdot}\sigma$ and this inconsistency can be the result of the catalog resolution.

We computed the predicted seismicity rate at a fixed time after the occurrence of the September tremor and the results for two periods, 5 and 30 days after strong event, are shown in Fig. 7. The predicted seismicity rate changes after 5 days associated with the September shock, derived by the difference between predicted and background seismicity rate, are presented in Fig. 8. The white dots are the seismic events that occurred after the strong event. Most of events are located in areas characterized by an increase of Coulomb stress and the seismicity rate.

6 Conclusions

In the present work, we have investigated if the perturbations of the stress field due to the coseismic slip of the mining induced seismic events can affect the future seismicity. The analysis was performed in two steps for the seismic tremors of the $M_L \geq 2$ that occurred in the Rudna Mine in the Legnica–Głogów Copper District. In the first step of analysis we have examined the correlation between the static Coulomb stress changes due to the previous seismicity and the location of the successive future seismic events. The calculations of stress changes on the nodal plane of the future seismic event can exhibit poor success rate due to the uncertainties of the focal mechanisms and the ambiguity of the fault plane. Nevertheless, the obtained results are perspective, since it has been shown that most of the events occurred in areas where stress was enhanced due to the occurrence of previous events.

In the next step of our study we applied the Coulomb stress changes and the rate/state friction approach to explain the seismicity rate perturbations in time. The simulations demonstrate that the applied model is efficient to reproduce the spatial and temporal pattern of mining-induced seismicity and confirm that the static stress changes can be the natural cause of the interactions among seismic events.

The results of the preliminary modeling of the stress changes and their influence on the seismicity rate on the mining areas are promising and after detailed investigation this approach could be incorporated in the seismic hazard assessment studies for mines.

Acknowledgements

This work was prepared within the framework of the research project No. PBS-Grecja/10/2007, financed by the Ministry of Science and Higher Education of Poland during the period 2007 to 2009.

References

1. Catalli, F., Cocco, M., Console, R. and Chiaraluce L. Modeling Seismicity Rate Changes during the 1997 Umbria-Marche Sequence (central Italy) through a Rate- and State-Dependent Model, J. Geophys. Res., 113. (2008), DOI: 10.1029/2007/JB005356.
2. Das, S. and Scholz, C.H. Theory of Time-Dependent Rupture in the Earth, J. Geophys. Res., 86, B7. (1981), 6039-6051, DOI: 10.1029/JB086iB07p06039.
3. Dieterich, J. A Constitutive Law for Rate of Earthquake Production and Its Application to Earthquake Clustering, J. Geophys. Res., 99, (1994), 2601-2618.
4. Dieterich, J. Earthquake Nucleation and Its Relationship to Earthquake Clustering, Paper Presented at 1st Workshop, Asia Pac. Econ. Coop. Coop. for Earthquake Simul., Brisbane, Queensland, 2000.
5. Domański, B. and Gibowicz, S.J. Comparison of Source Parameters Estimated in the Frequency and Time Domains for Seismic Events at Rudna Copper Mine, Poland, Acta Geophys. 56, (2008), 324-343, DOI: 10.2478/s11600-008- 0014-1.
6. Dunlop, R. and Gaete, S. Controlling Induced Seismicity at El Teniente Mine: The Sub6 sector case history. in: Gibowicz, S.J. and Lasocki, S. eds. Rockbursts and Seismicity in Mines, A.A. Balkema, Rotterdam, 1997, 233-236.
7. Gibowicz, S.J. An Anatomy of a Seismic Sequence in a Deep Gold Mine, Pure Appl. Geophys. 150, (1997), 393-414, DOI: 10.1007/s000240050084.
8. Gibowicz, S.J. Seismic Doublets and Multiplets at the Polish Coal and Copper Mines, Acta Geophys. 54, (2006), 142-157, DOI 10.2478/s11600-006-0014-y.
9. Harris, R.A. Introduction to Special Session: Stress Triggers, Stress Shadows, and Implications for Seismic Hazard, J. Geophys. Res. 103, B10, (1998), 24347-24358, DOI: 10.1029/98JB01576.
10. Jaeger, J.C. and Cook, N.G.W. Fundamentals of Rock Mechanics, 3rd ed. Chapman and Hall, London, 1979.
11. Kijko, A. Keynote Lecture: Seismic Hazard Assessment in Mines. in: Gibowicz, S.J. and Lasocki, S. eds. Rockbursts and Seismicity in Mines, A.A. Balkema, Rotterdam, 1997, 247-256.
12. Kijko, A. and Funk, C.W. Space-time Interaction Amongst Clusters of Mining Induced Seismicity, Pure Appl. Geophys. 147, (1996), 277-288.
13. King, G.C.P. and Cocco, M. Fault Interaction by Elastic Stress Changes: New clues from earthquake sequences, Adv. Geophys. 44, (2001), 1-38.
14. King, G.C.P., Stein, R.S. and Lin, J. Static Stress Changes and the Triggering of Earthquakes, Bull. Seismol. Soc. Am. 84, (1994), 935-953.
15. Kłeczek, Z. Control of rock-Mass Bursts in Polish Copper Mines LGCD. in: Warsztaty Górnicze 2007 „Zagrożenia naturalne w górnictwie", Ślesin k. Konina, 4-6 czerwca 2007. Bezp. Pr. Ochr. Śr. Gór. 2007 nr 6, 25-27 .

16. Lasocki, S. Probabilistic Analysis of Seismic Hazard Posed by Mining Induced Events. in: Potvin, Y. and Hudyma, M. eds. The Sixth Int. Symp. on Rockbursts and Seismicity in Mines 'Controlling on Seismic Risk' ACG, Perth, 2005, 151-156.
17. Lasocki, S. and Orlecka-Sikora, B. Prediction of Soil Vibrations for Polkowice in 2001 – 2013. Proc. XXV Winter School of Rock Mechanism, Krakow, (2002), 369-384.
18. Lasocki, S. and Orlecka-Sikora, B. Seismic Hazard Assessment under Complex Source Size Distribution of Mining-Induced Seismicity. Tectonophysics, 456, 1-2, (2008), 28-37, DOI: 10.1016/j.tecto.2006.08.013.
19. Leśniak, A. and Pszczoła, G. Combined Mine Tremors Source Location and Error Evaluation in the Lubin Copper Mine (Poland), Tectonophysics 456, 16-27, (2008), DOI: 10.1016/j.tecto.2007.04.012.
20. Lin, J. and Stein, R.S. Stress Triggering in Thrust and Subduction Earthquakes, and Stress Interaction between the Southern San Andreas and nearby thrust and strike-slip faults, J. Geophys. Res. 109, (2004), DOI: 10.1029/2003JB002607.
21. Marsan, D., Bean, Ch.J., Steacy, S. and McCloskey, J. Spatio-Temporal Analysis of Stress Diffusion in Mining-Induced Seismicity System, Geophys. Res. Lett. 26, (1999), 3697-3700, DOI: 10.1029/1999GL010829.
22. Mirek J. and Mirek, K. Nieparametryczna Estymacja Funkcji Gęstości PrawdopodobieńStwa Położenia źródła Sejsmicznego (Nonparametric Estimation of Density Probability Function of Seismic Source Location). Warsztaty Górnicze 2007 z cyklu Zagrożenia naturalne w górnictwie, Ślesin 2007, S.331-337.
23. McGarr, A. Observations Concerning Diverse Mechanisms for Mining-Induced Earthquakes. in: Potvin, Y. and Hudyma, M. eds. The Sixth Int. Symp. on Rockbursts and Seismicity in Mines 'Controlling on Seismic Risk' ACG, Perth, 2005, 107-111.
24. Orlecka-Sikora, B. Ocena Istotności Wpływu Transferu Naprężeń Statycznych Wywołanych Przemieszczeniem Kosejsmicznym Wstrząsów góRniczych na Proces Sejsmogeniczny w Kopalniach. Significance of Static Stress Transfer Caused by Coseismic Slip of Mining-Induced Seismic Events In Seismicity Generation Process in Mines, Geologia, Tom 35, Zeszyt 2/1, (2009), 519-525 .
25. Orlecka-Sikora, B. and Lasocki, S. Clustered Structure of Seismicity from the Legnica–Głogów Copper District, Publs. Inst. Geophys. Pol. Acad. Sc. M-24 (340), (2002), 105-119 .
26. Orlecka-Sikora, B., Papadimitriou, E.E. and Kwiatek, G. A Study of the Interaction Among Mining Induced Seismic Events in the Legnica-Glogow Copper District, Poland, Acta Geophysica, 58, (2), (2009a), doi: 10.2478/s11600-008-0085-z.
27. Orlecka-Sikora, B., Papadimitriou, E.E. and Kwiatek, G., Significance of Static Stress Transfer in Mining-Induced Seismicity Generation Process, the Case Study of Rudna Mine in the Legnica-Głogów Copper District in Poland, IASPEI: International Association of Seismology and Physics of the Earth's Interior, I General Assembly, S4: Induced seismicity, (Cape Town, RPA, 2009).
28. Papadimitriou, E.E. and Sykes, L.R. Evolution of the Stress Field in the Northern Aegean Sea (Greece), Geophys. J. Int. 146, (2001), 747-759, DOI: 10.1046/j.0956-540x.2001.01486.x.
29. Parsons, T., Stein, R.S., Simpson, R.W. and Reasenberg, P.A. Stress Sensitivity of Fault Seismicity: A Comparison between Limited-Offset Oblique and Major Strike-Slip Faults, J. Geophys. Res. 104, (1999), 20183-20202, DOI: 10.1029/ 1999JB900056.
30. Piestrzyński, A. Monograph of KGHM Polska Miedź SA. CBPM „Cuprum", Wrocław , 1996.
31. Scholz, C.H. The Mechanics of Earthquakes and Faulting. Cambridge University Press, Cambridge, 1990.
32. Steacy, S., Gomberg, J. and Cocco, M. Introduction to Special Section: Stress Transfer, Earthquake Triggering and Time-Dependent Seismic Hazard, J. Geophys. Res. 110, (2005), DOI: 10.1029/2005JB003692.
33. Stein, R.S. and Lisowski, M. The 1979 Homestead Valley Earthquake Sequence, California: Control of Aftershocks and Postseismic Deformation, J. Geophys. Res. 88, (1983), 6477-6490, DOI: 10.1029/JB088iB08p06477.
34. Stein, R.S., King, G.L.P. and Lin, J. Change in Failure Stress on the Southern San Andreas Fault System Caused by the 1992 magnitude = 7.4 Landers Earthquake, Science 258, (1992), 1328-1332, DOI: 10.1126/science.258.5086.1328.
35. Stiros, S.C. and Kontogianni, V.A. Coulomb Stress Changes: from Earthquakes to Underground Excavation Failures, Int. J. Rock Mech. Mining Sci. (2008), doi: 10.1016/j.ijrmms.2008.09.013.

36. Toda, S., Stein, R. S., Richards-Dinger, K. and Bozkurt, S. B. Forecasting the Evolution of Seismicity in Southern California: Animations Built on Earthquakes Stress Transfer, J. Geophys. Res., 110, (2005), doi:10.1029/2004JB003415.
37. Toda, S., Stein, R. S., Reasenberg, P. A. and Dieterich, J. H. Stress Transferred by the Mw = 6.5 Kobe, Japan, Shock: Effect on Aftershocks and Future Earthquake Probabilities, J. Geophys. Res., 103, (1998),543– 24,565, doi:10.1029/98JB00765.
38. Trifu, C.-I., Urbancic, T.I. and Young, R.P. Non-similar Frequency-Magnitude Distribution for M < 1 Seismicity, Geophys. Res. Lett. 20, (1993), 427-430, DOI: 10.1029/93GL00426.
39. Wiejacz, P. Investigation of Focal Mechanisms of Mine Tremors by the Moment Tensor Inversion, Ph.D. Thesis, Inst. Geophys. Pol. Acad. Sc., Warsaw, Poland, 1991.
40. Wiejacz, P. and Ługowski, A. Effects of Geological and Mining Structures upon Mechanizm of Seismic Events AT Wujek Coal Mine, Katowice, Poland. in: Gibowicz, S.J. and Lasocki, S. eds. Rockbursts and Seismicity in Mines, A.A. Balkema, Rotterdam, 1997, 27-30.

RaSiM 7(2009): Controlling Seismic Hazard and Sustainable Development of Deep Mines, C.A. Tang(ed), Rinton Press, 749-750

PART II

MANAGING SEISMIC HAZARD

RaSiM 7(2009): Controlling Seismic Hazard and
Sustainable Development of Deep Mines,
C.A. Tang(ed), Rinton Press, 751-756

THE RESEARCH ON DEFORMATION MECHANISM AND HARMONIZATION SUPPORTING TECHNIQUE OF BOLTS AND ANCHORAGE CABLES IN HIGH STRESS ROADWAY OF DEEP MINE

XIAO-XIANG CHEN and PAN-FENG GOU

School of Energy Science and Engineering, Henan Polytechnic University

Jiaozuo, 454000, Henan, China

AN-ZHI YAN

School of Civil Engineering, Henan Polytechnic University

Jiaozuo, 454000, Henan, China

Abstract: Based on the laboratory tests of rock mechanics parameters, the measured results on the spot and numerical simulated results, the deformation mechanism of tailgate in high stress of deep mine was discussed. Furthermore, the thought of harmonization supporting of high pretension, high strength bolts and anchorage cables was proposed. With the aid of the numerical simulation, the supporting parameters of tailgate were optimized. The findings indicated that the tailgate's roof is stave and the deformation of surrounding rock is big. Moreover, it is very important to design bolt and cable's pretension correctly and the harmonization supporting of bolts and anchorage cables is required. In order to increase the elongation ratio of anchorage cables, it is necessary to add the plank under the salvers when stretch-draw the anchorage cables. The obvious controlling effect was obtained when using the harmonization supporting technique of high pretension, high strength bolts and anchorage cables. Finally, the industrial test results showed that the optimal distance and the supporting parameters had good effect to control the deformation of the surrounding rock in high stress roadway of deep mine.

1 Geological Summary

The working face of JI15-12010 is located on the JI2 panel of ShouShan mine, the elevation of the working face is -660m~-680m, and the burial depth is 790m~810m. The major coal seam of the working face is JI15 coal, it is stable, its structure is unitary, the thickness generally is 2.91~4.71m, and the average thickness is 3.50m. This working face is close to the anticlinal axis of BaiShiShan, the fault crevasse is developing , the roof rock is cracked, the integrity of rock mass is bad, the great mass of rock belong to Ⅲ~Ⅳ kind, and partial belong to Ⅱkind. The immediate bottom mostly are mudstone or arenaceous mudstone, the thickness is

0~5.50m, the average thickness is 3.43m, and partial is packsand, the thickness is 0~7.0m, the average thickness is 4.63m. The saturated compressive strength of bottom is averagely 20.7MPa, it belong to the soft bottom.

The working face gas pressure of coal bed is 2.1Mpa, gas density is 17.5m3/t, therefore, the working face may be serious dangerous working face of gas brust after preliminary judgment; Moreover, the mining depth is about 800m, and is close to anticlinal axis of BaiShiShan, so, the working face is located at the high stress region. The designed length of tailgate is 1323m, the shaft and drift excavation was along the roof of coal bed and advanced by breaking false roof, the construction method was blast , the roadway extension is 4m, height is 3.3m, cross section is 13.2m^2, and the supporting mode was combined supporting of high strength bolts and anchorage cables. At present, looking from the stable condition of roadway, the supporting effect is not really ideal, the deformation of surrounding rock was big, the floor heave was serious, the value of floor heave surpassed 1m in serious distortion sector, the existing supporting way was very difficult to satisfy the design requirement, therefore, the rigid supports were used back rearward working face. But the labor intensity of rigid supports are big, investment is high, the tunnelling speed is slow, and it is urgent to seek for a way of quick tunnelling speed and high security.

2 Deformation Mechanism and Supporting Thread

The horizontal distance between main haulageway and upper roadway is 20m, the roof integrality of haulageway is good, but the horizontal distance between tailgate and upper roadway is 10m, the roof integrality of tailgate is bad, the preliminary analysis believed that one of reasons possibly were because that the horizontal distance of tailgate and upper roadway was too near, the stress had superposition on the surrounding rock between tailgate and upper roadway, caused the tailgate to be under the function of high stress for a long time. Afterward, numerical simulation computation had proved this too (separate article will introduce this). Moreover, according to the laboratory test result of rock mechanics parameters, and the observation on the spot, at present, the reason that deformation of roadway was serious may have the following several aspects:

(1)The ground stress itself , particularly the horizontal stress is big where roadway located at, the horizontal stress urged the roof to abscission layer, and the floor heaved.

(2)It intensified the distortion that the lithology of surrounding rock were inconsistent, the deformation is asymmetric. The roof of roadway is laminar shale and sandy mudstone, two sides were coal beds, the deformation of surrounding rock was inevitably big under the high stress function;

(3)The measure of preventing gas brust intensified the weakening of surrounding rock lithology. At present, the measures include boring emissions hole and blast and so on, these measures have remarkable influence on the surrounding rock;

(4)The existing supporting parameters was unreasonable. Although the combined supporting of high strength bolts and anchorage cables were used, but the pretension of bolts was small, the function of high strength bolts cannot display fully, and the bolts and anchorage cables had not achieved harmonization supporting.

According to the existing destruction condition, supporting thread as following was proposed:

(1) The distance between tailgate and upper roadway will be added to 20m, the supporting system of high strength bolts and anchorage cables will be used, and the reasonable anchor form will be chosen;

(2) The high pretension bolts will be used, thus it will cause to realize really active and timely supporting of bolts and anchorage cables, and span from small pretension and high strength to high rigidity and high pretension;

(3) Installing the anchorage cables reasonably, control the surrounding rock cooperate with bolts, the high strength bolts are used on two sides of roadway, the lengthening anchor of resin will be used , surrounding rock will be reinforced by anchorage cables, the four corner will be strengthened by bolts;

(4) The numerical simulation computation will be used to determine the reasonable and effective supporting parameters, and the cross section will be increased;

(5) The construction and monitor technology will be perfected, adjust the supporting parameters promptly according to the deformation state of surrounding rock.

3 Determination of Supporting Parameters

3.1 Plans of Numerical Simulation

According to the geological condition of JI15-12010 working face, altogether 8 supporting plans were proposed, after optimizing, 4 feasible plans were determined, the simulation analysis were carried on these 4 plans by using international popular numerical simulation software UDEC. 4 feasible plans are as follows:

(1) 5 bolts on upper side,4 bolts on nether side, the number of bolts in roof is 6 or 7 , the spacing respectively is 850mm or 750mm;

(2)5 bolts on upper side,4 bolts on nether side, the number of bolts in roof is 7, and 3 anchorage cables were used to strengthen supporting;

(3)5 bolts on upper side,4 bolts on nether side, the number of bolts in roof is 7, and 3 anchorage cables were used to strengthen supporting; 2 anchorage cables were used to strengthen supporting on two sides respectively;

3.2 The influence of bolts spacing on stability of surrounding rock

After contrasting figure 1~ figure 4 , We can got that: with the enlargement of supporting intensity, the supporting effect on roadway is obvious, either deformation of roof or two sides reduce obviously.And from table 1,we can got that,compared with 6 bolts in roof, when 7 bolts in roof ,roof-to-floor convergence quantity reduced 175.2mm, reduced approximately 42.3%, the quantity of floor heave reduced 199.3mm, two sides reduced 207.1mm, obviously, the original plan of 6 bolts in roof can not control big deformation of surrounding rock effectively. According to the principle that “control roof prior to control sides”, roof-to-floor convergence quantity reduced 30.4mm, the quantity of floor heave reduced 32.4mm, two sides reduced 147.7mm after strengthening supporting by using 3 anchorage cables in roof; Considered the surrounding rock are a whole, it can reduce effectively the deformation of roof-floor that control the deformation of two sides, strengthening supporting by using 2 anchorage cables in two sides were used too, the deformation of surrounding rock further reduced after strengthening supporting, Although the reducing scope was small, but considering complex geological condition of this working face, specially the situation of roof are easy to abscission layer, it is very essential that strengthening supporting by using anchorage cables in roof and two sides.

Table 1. Deformation of surrounding rock(mm)

Plans	The number of bolts in roof	Deformation of roof	Floor heave	Deformation of left side	Deformation of right side
1	6	414.3	436	433.1	287.9
2	7	239.1	236.7	309.6	204.3
3	7	208.7	204.3	212.3	154
4	7	179.8	176.2	185.9	142.1

Figure 1~ Figure 4 is the map of supporting and surrounding rock deformation under the circumstances of different supporting parameters.

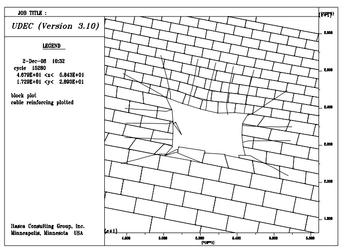

Figure 1.The distortion chart of surrounding rock of 1st project

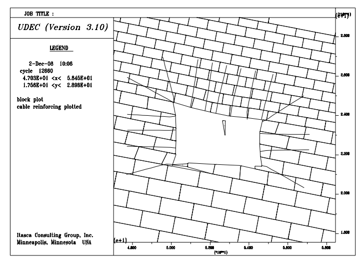

Figure 2. The distortion chart of surrounding rock of 2st project

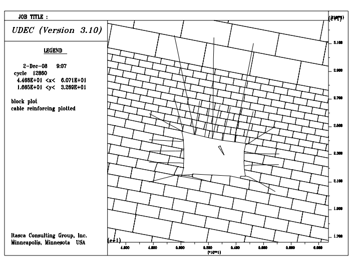

Figure 3. The distortion chart of surrounding rock of 3st project

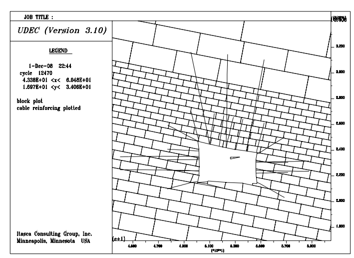

Figure 4. The distortion chart of surrounding rock of 4st project

3.3 The Determination of Supporting Parameters

According to above analysis and optimization, supporting parameters were determined finally:

The number of bolts in roof was 7, 5 bolts on upper side,4 bolts on nether side, the spacing of bolts was 750mm, the distance of row were determined to 800mm. High strength bolts of laevorotatory deformed steel bar were used(high strength and released pressure bolts), they are complete set of products, the specification for φ22×2400mm, matched with the arch tray and high strength nut. The lengthening anchor of resin was used, as the auxiliary supporting, the W steel belts and wire netting were matched , the specification of W steel belts for (wide×thick×high) was (150~200)mm×4.0mm×23mm, the length was 4200mm, has 6 anchor holes on it, the spacing of anchor holes is equal to the bolts', the graticules of 8# galvanized iron wire were used, they jointed with iron wire and the overlapping of neighboring net is 200mm. The anchorage cables in roof was manufactured by 7 portion steel wires of high strength and underrelaxation, and its diameter were 17.8mm, length were 7.2m, effective length were 7.0m, the distance of row were 1600mm. The anchorage cables were connected mutually with 16~20 channel steels.

High strength bolts of laevorotatory deformed steel bar were used in two sides, the specification was φ20×2400mm, the lengthening anchor of resin was used, the W steel belts and wire netting were matched, the specification of W steel belts and wire netting were equal to roof's. The anchorage cables in two sides was manufactured by 7 portion steel wires of high strength and underrelaxation, and its diameter were 17.8mm, length were 6 m, effective length were 5.5m, the distance of row were 3200mm. The anchorage cables were connected mutually with 16~20 channel steels. For increasing elongation ratio of anchorage cables, equipments should be locked, and strengthen the monitor after padding wood pallets that length and wide are appropriate under anchorage cables when constructed anchorage cables of roof .

For guaranteeing the harmonization supporting of bolts and anchorage cables[1],the stress of bolts should be suitable to the design of anchorage cables pretension, in practice process, as a result of bolts pretension is 60~80kN, for synchronized load [2,3],therefore ,the design of anchorage cables pretension is 80~100kN.

4 The Actual Measurement Deformation Analysis of Surrounding Rock

Altogether 10 test points were arranged along the driving direction of roadway, their space were approximately 50m, as space is limited, only two representative spots were taken to analyze.

The test time of 1st test point was 70d cumulatively, hereafter, after January 31, the survey was stopped because that the deformation of surrounding rock in this roadway was stable. From the displacement diagram of surrounding rock of 1st test point (Figure 5),we can got[4]that, the change of cumulative deformation of surrounding rock was quick in initial period that the measuring points were established, but it tended to be stable basically after December 27,the biggest value of deformation was below 170mm, and the convergence speed of roof-to-floor was bigger than two sides', the deformation of surrounding rock experienced 27d approximately from monitoring to stabilization.

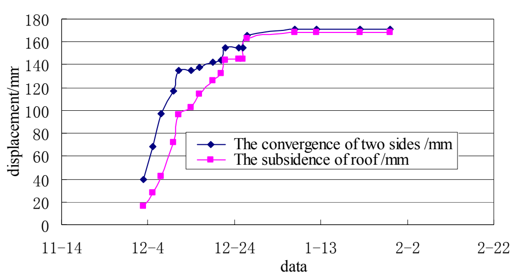

Figure 5. The displacement map of surrounding rock

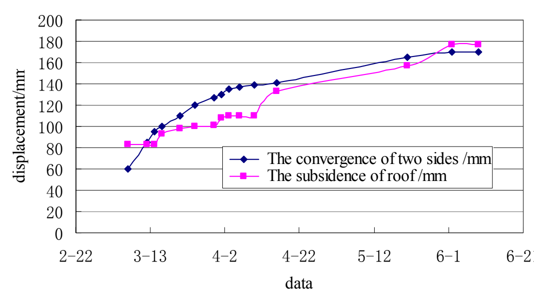

Figure 6.The displacement map of surrounding rock

The test time of 2st test point was 101d cumulatively, and the deformation of surrounding rock was stable basically. From the displacement diagram of surrounding rock of 2st measuring point (Figure 6),we can got that, the change of cumulative deformation of surrounding rock was quick in initial period that the measuring points were established, the biggest value of deformation was about 180mm up to June 21, and the convergence speed of roof-to-floor was smaller than two sides'.

As shown in the above analysis, deformation of surrounding rock tended to stable after test points being established for 25~30d basically, the deformation value of two sides were 160~180mm, roof's were 170~180mm respectively from monitoring to stabilization, controlled effect of this technique project was very obvious, it have satisfied the safety use of roadway.

5 Conclusion

The important reason that roadway deformation was big was that the horizontal distance of the tailgate and upper roadway was improper. This caused the tailgate to be under the function of high stress for a long time. The roadway was close to the anticlinal axis of BaiShiShan, and the horizontal stress was greatest where the roadway was located. The lithological character of surrounding rock is inconsistent, and the existing supporting parameters are unreasonable. The high pretension bolts were used, they caused us to realize the active and timely supporting of bolts and anchorage cables, and span from small pretension and high strength to high rigidity and high pretension, their controlled effect on high stress roadways of deep mines became very obvious. It is very important that design bolts and anchorage cables are of correct pretension. The stress of bolts should be suitable to the design of anchorage cables pretension if want the harmonization supporting of bolts and anchorage cables. In order to increase the elongation ratio of anchorage cables, add the plank under the salver when stretch-draw the anchorage cables. The industrial test results showed that the optimal distance and supporting parameters can control the deformation of surrounding rock in high stress roadways of deep mines.

Acknowledgements

The authors wish to acknowledge the collaborative funding support from the National Natural Science Foundation of China (50874037), Key subject project of Henan province(504906) and Doctor fund of Henan Polytechnic University (648234).

References

1. Tang, L. and Wang, W.P. Coordination between Bolting Support and Surrounding Rock Affected by Ground Pressure. Journal of China Coal Society, 2004, 29(4). 12-16.
2. Kang, H.P., Wang, J.H. and Lin, J. High Pretension Stress and Intensive Bolting System and Its Application in Deep Roadways. Journal of China Coal Society, 2007, 32(12). 1233-1238.
3. Kang, H.P., Jiang, T.M. and Gao, F.Q. Effect of Pretensioned Stress to Rock Bolting. Journal of China Coal Society, 2007, 32(7). 680-685.
4. Wang, Q.S., Li, X.B. and Li, D.Y. Surrounding Rock Deformation Properties and Determination of Support Parameters of Soft Rock Roadway in Deep Mine. Journal of China Coal Society, 2008, 33(4). 364-367.

RaSiM 7(2009): Controlling Seismic Hazard and Sustainable Development of Deep Mines, C.A. Tang(ed), Rinton Press, 757-762

ANALYSIS AND PREVENTION OF ROCKBURST HAZARD AT THE COAL FACE WITH HIGH STRESS AND HARD SANDSTONE

FU-LIAN HE and DONG-PING YIN

College of Resources & Safety Engineering, China University of Mining & Technology (Beijing)

Beijing, 100083, P.R. China

YONG-JUN HE and JING-MING YAO

Civil & Environmental Engineering School, University of Science and Technology Beijing

Beijing, 100083, P.R. China

In this paper, the bump tendency characteristics of coal samples and coal-rock combination samples obtained from panel No. 7251 in the western Yaoqiao coal mine section are measured on the basis of the lab experiments. It is decided that between the roof and coal seam, the bottom has a much higher bump tendency than the coal seam. Rockburst hazard in panel No. 7251 is graded and evaluated, and the key area for preventing rockbursts is ascertained. Moreover, the coal seam infusion technology and its responding parameters of rockburst prevention at the tail entry of panel No. 7251 are formed. The in-situ monitoring results of coal drilling amounts have shown that the rockburst hazard has been successfully eliminated through the use of coal seam infusion, and the safe production at the coal face has been reliably ensured.

1 Introduction

Due to the sudden failure of the underground surrounding rock in coal mines, rockburst is the dynamic and hazardous ground pressure behavior resulting in violent seismicity and the bump of numerous coal and rock blocks [1, 2]. Up to now, China has had more than 60 collieries where rockbursts have happened. As the coal mining depth increases, the rockburst hazard also rises in coal mines [3, 4].

In the Yaoqiao coal mine, main mining of coal seam No. 7 is deep and has bump tendency due to the great number of faults with tectonic stress and relatively large fall. At the fully-mechanized longwall top-coal caving mining faces, the cantilevered hard sandstone roof is long, the periodic weighting is severe, the extent of coal stress concentration is high, and the energy accumulating in the coal body is huge. Therefore, rockburst accidents occur often seriously threatening mine safety and production badly influencing the positive benefits of mining.

In the area where rockbursts happens,, the frequency of loud pop from the coal body reached twice per minute, the discrete top-coal fell, some component parts of the bolt-mesh support system were damaged, the air flow was full of coal dust, and the mining equipment was removed and became askew due to the violent seismicity. The severe roadway deformation and damage resulted from the stress concentration and its sudden release in the panel entries which can cause personal casualty to occur. During rockburst occurence, the roof sagging amounted to 200 ~ 800 mm, the convergence between both roadway sides could be as much as 400 ~ 1000 mm, and the floor heave reached 300 ~ 900 mm.

2 Conditions and Bump Tendency in Face No. 7251

At coal face No. 7251 of western winning district No. 5 in Yaoqiao coal mine, coal seam No. 7 is 3.00 ~ 4.60 m thick, and the dip angle is 9^{o} ~ 13^{o}. The main roof is hard and compact medium-grained sandstone, and its average thickness is 14.81 m. The immediate roof is dark grey sandy mudstone, and its average thickness is 0.44 m. The immediate bottom is grey black mudstone, and its average thickness is 1.29 m. The main bottom is sandy mudstone, and it is 3.24 ~ 3.26 m thick. In the area of panel No. 7251, there are five faults with more than 1 m fall. The mining depth of coal face No.7251 is 595 ~ 640 m, and the face length is about 150 m. The fully-mechanized longwall top-coal caving mining along the strike is adopted. The support-combination of bolt-mesh and I-steel frame is used in the headentry and tailentry.

According to the geological and productive conditions and the demand of rockburst research, the coal and rock cores were got from the surrounding rocks by use of drilling machine TXU−75A and the drilling stems with a diameter of 75 mm. At the lab in China University of Mining & Technology, those cores were processed into the normal coal samples and coal-rock combination samples. As in Figure 1, a sample was loaded at a constant rate of strain increment on the servo-control testing machine, and the responding stress and strain and dynamic breaking time were measured and recorded during the uniaxial compressive testing of a sample. Furthermore, the uniaxial compressive strength and elastic energy index and bump energy index could be calculated, and the bump tendency of coal and rock in face No. 7251 was decided.

The typical complete stress-strain curve of a pure coal sample during compression testing is shown in Figure 2, and the average value of uniaxial compressive strength of coal samples is 10.12 MPa. Generally, coal samples break in the mode of shearing, and the broken coal blocks bounce outside which account for about half a sample.

The typical complete stress-strain curve of a coal-rock combination sample during compression testing is shown in Figure 3. The average value of uniaxial compressive strength of coal-rock combination samples is 17.81 MPa, which means coal-rock samples are stronger than coal samples. The major failure is shearing during the breaking of coal-rock combination samples, and the failure is located in the coal parts of samples. The less the coal content of a sample is, the more violent the breaking is.

The average value of bump tendency parameters of coal samples or coal-rock combination samples is outlined in Table 1. The samples of coal seam No.7 have weak bump tendency, but the combination samples of roof and coal seam No. 7 and bottom have weak-strong bump tendency.

Figure 1 The loading test of a sample.

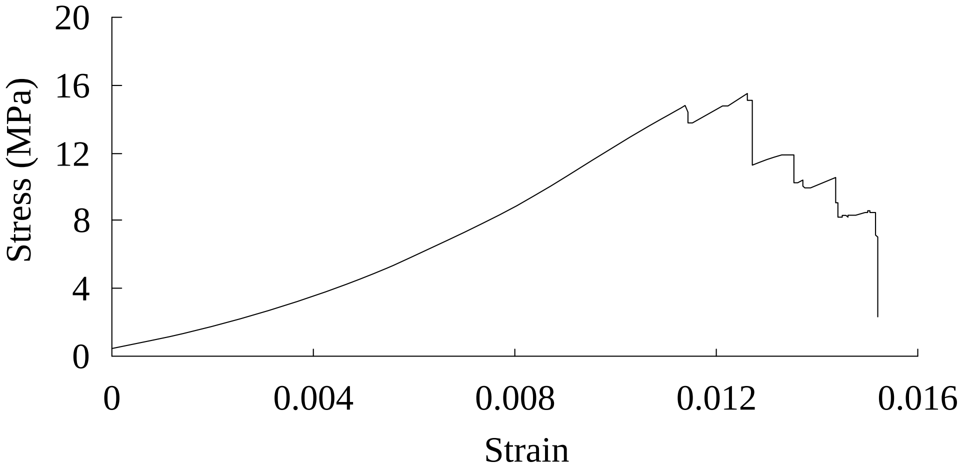

Figure 2 The stress-strain curve of a coal sample.

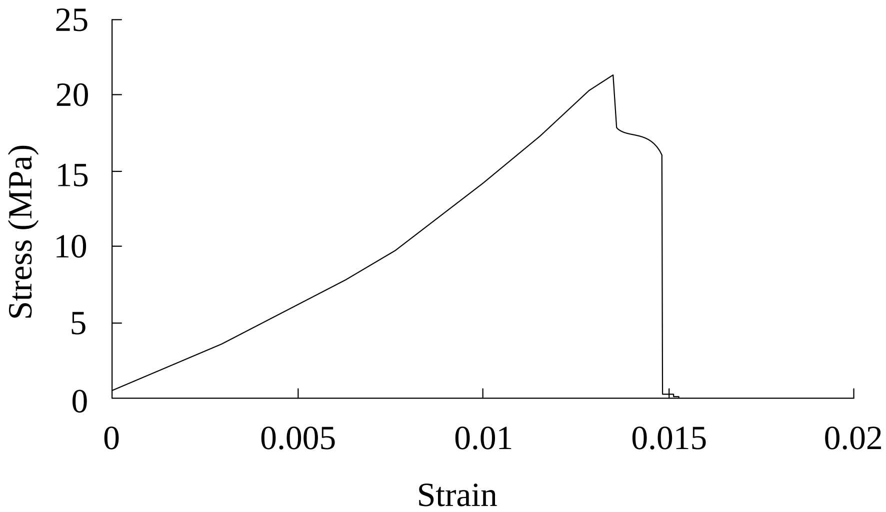

Figure 3 The stress-strain curve of a coal-rock combination sample.

Table 1. The average value of measurement results of bump tendency parameters

Sample type	Dynamic breaking time (ms)	Elastic energy index, U_{ET}	Bump energy index, K_E	Bump tendency
Pure coal		3.73	3.21	Weak
Coal-rock combination	156 ms	4.23	4.81	Weak-strong

3 Rockburst Hazard Prediction

Based on the analysis of the productive and geological conditions and rockburst disasters which have happened in coal mines, the comprehensive index classification method is that the geological and mining factors influencing rockbursts are induced, and that the index value responding to every influence factor is determined, and that the comprehensive index value is solved, and that the rockburst hazard can be predicted finally [5]. In Formula (1), w_i represents the index of a rockburst influence factor, and w_t is the comprehensive index of rockburst hazard situation.

$$w_t = \frac{\sum_{i=1}^{n} w_i}{\sum_{i=1}^{n} w_{imax}} \tag{1}$$

The tailentry of panel No. 7251 is close to the gob area of panel No. 7249, and the headentry of panel No.7251 is adjacent to the coal seam of panel No. 7253. The majority of faults in panel No. 7251 are near the tailentry and parallel to it. Due to the confinement of one fault with large fall, the coal pillar of the tailentry in panel No. 7251 is irregular and almost triangular, and high stress concentration exists in some area of the coal pillar. As a result, the tailentry is the most probable place where rockbursts happen.

The value of w_i and w_t is shown in Table 2. Index w_1 reflects whether rockbursts have happened many times in coal seam No. 7; index w_2 represents the mining depth influence; index w_3 is related to the distance between coal seam No. 7 and hard thick sandstone roof; index w_4 correlates to whether there is the tectonic stress concentration in the mining area; index w_5 depends on the thickness of hard roof strata; index w_6 is decided according to the comprehensive strength of coal body; index w_7 is dependent on the elastic energy index of coal body. w_t is equal to 0.74, which indicates that the rockburst hazard in the tailentry of panel No. 7251 is medium to strong, and the effective monitoring method and prevention measure of rockbursts must be put to use.

Table 2. Rockburst hazard prediction according to geological and mining conditions

Evaluation area	w_1	w_2	w_3	w_4	w_5	w_6	w_7	w_t
Tailentry of panel No. 7251	3	1	3	3	2	0	2	0.74

4 Rockburst Hazard Prevention and Its Effect

The rockburst hazard in the tailentry of panel No. 7251 was monitored by use of the coal drillings method. The monitoring boreholes had a diameter of 42 mm and were drilled in both tailentry sides. During the borehole drilling, the drilling cuttings were weighed once every borehole length of 1.5 m, and whether there were drilling stem sticking and bump behaviours in every borehole was recorded. Those boreholes are 9.0 m long, and they are parallel to coal seam No. 7 and perpendicular to the tailentry sides. The distance between those neighbouring boreholes is 5 ~ 6 m, and the distance between a monitoring borehole and the tailentry floor is about 1.2 m.

By means of coal seam infusion, the surrounding rocks around mine roadways are weakened, their bump tendency decreases, the stress peak zone moves inside along the surrounding coal seam, and the stress concentration extent drops [6, 7]. The rockburst hazard in the tailentry of panel No. 7251 was prevented by use of coal seam infusion with short boreholes. The detailed scheme of coal seam infusion was worked out, and then the preliminary infusion boreholes in both tailentry sides were drilled by use of portable pneumatic drilling

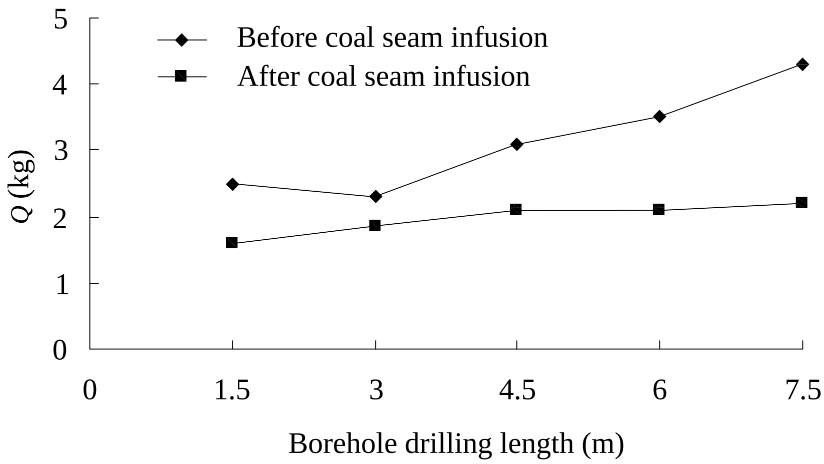

Figure 4 Monitoring results of coal drillings method.

machine TURMAG. The water injection boreholes have a diameter of 42 mm and a length of 10 m, and the distance between the neighbouring boreholes is 8 m. The water injection pressure is 6 MPa. The sealed length of water infusion boreholes is 2m. Hole packers are made of the automatic expansion type of rubber pipes, and their maximum allowable pressure is 25 MPa, and their diameter is 42 + 2 mm.

Based on the monitoring method of coal drillings, the results of coal drillings amount before and after coal seam infusion in the tailentry of panel No. 7251 are shown in Figure 4. Q is coal drillings amount for every borehole length of 1.5m. Before coal seam infusion, Q was larger than the early warning value of coal drillings. Q was especially as large as 4.4 kg, and the dynamic behaviours such as drilling difficulty and stem sticking occurred when the borehole drilling length was 6 ~ 7.5 m, which showed that the rockburst danger was apparent. After coal seam infusion, Q fell to less than 2.5 kg, and the dynamic behaviours such as drilling difficulty did not appear, which indicated that the rockburst hazard was removed.

5 Conclusions

(1) Rockbursts has a negative influence on the safety and production in the Yaoqiao coal mine. The main factors influencing rockburst hazard include the mining depth, faults, the bump tendency of the coal body, hard thick sandstone roof and its weighting, and irregular coal pillars.

(2) The pure coal samples of panel No. 7251 have weak bump tendency, but the samples of coal-rock combination have weak-strong bump tendency.

(3) The comprehensive index of rockburst hazard situation in the tailentry of panel No. 7251 is equal to 0.74, and the rockburst hazard in the tailentry of panel No. 7251 is medium to strong.

(4) The rockburst hazard in the tailentry of panel No. 7251 was prevented through the use of coal seam infusion. The monitoring results of coal drillings method have indicated that the rockburst hazard has been effectively eliminated.

Acknowledgements

Work is supported by the Scientific Research Foundation for the Returned Overseas Chinese Scholars under grant No. 2007-1108, and the Teaching and Research Award Fund for Outstanding Young Teachers in Higher Education Institutions of State Education Ministry, People's Republic of China. The authors sincerely wish to thank the technicians of Yaoqiao coal mine for their contributions to the practice work in this paper.

References

1. Frid, V. Rockburst Hazard Forecast by Electromagnetic Radiation Excited by Rock Fracture. Rock Mechanics and Rock Engineering, 1997, 30(4). 229-236.
2. Li, X.Y. Discussion on Unstability and Damage of Surrounding Rock-Coal Mass. System and Prediction of Rock Burst, 2000, 29(6). 633-636.
3. Liu, X.K. and Xie, J.L. Present Situation of Coal Mine Safety and Discussion of Related Strategy. Coal Technology, 2008, 27(1). 139-141.
4. Pan, Y.S., Li, Z.H. and Zhang, M.T. Distribution, Type, Mechanism and Prevention of Rockbrust in China. Chinese Journal of Rock Mechanics and Engineering, 2003, 22(11). 1844-1851.
5 Dou, L.M. and He, X.Q. Technique of Classification Forecasting Rock Burst in Coal Mines. Journal of China University of Mining & Technology, 2007, 36(6). 717-722.
6. Yao, J.M., He, F.L. et al. Controlling of Rock Burst in Chain Pillars Between Hydraulic Mining Face and Drying Mining Face. Journal of University of Science and Technology Beijing, 2007, 29(3). 247-250, 271.
7. Zhang, M.T., Song, W.Y. and Pan, Y.S. Study on Water Pouring into Coal Seam to Prevent Rock-burst. China Safety Science Journal, 2003, 13(10). 69-72.

RaSiM 7(2009): Controlling Seismic Hazard and
Sustainable Development of Deep Mines,
C.A. Tang(ed), Rinton Press, 763-768

THE ROCKBURST MECHANISM AND PREVENTING TECHNOLOGY OF UNDERGROUND PROJECTS AT HIGH GROUND STRESSES

XIAO-CONG LV, JIN-YU XU and JUN-ZHONG LIU

The Engineering college, Air Force Engineering University

Xi'an, Shaanxi, 710038, P.R. China

With the constant development of economic construction, the exploitation and utilization of the underground spaces are developed into the deep strata, and the geological conditions become more and more complicated. The deep underground projects, located at the special geological environment of high ground stress and brittle rock mass, are apt to rockburst. It is proved that the rockburst is a geological disaster which happens in hard brittle rock mass with lots of energy accumulated. Based on the analysis of stress state of the underground engineering, the possibility of occurrence of rockburst can be estimated by combination with the criterion of tangential stress. For forecasting the occurrence of rockburst accurately, the factors of elastic strain energy and rock brittleness should be considered, and the corresponding criteria are summarized. With the consideration of the accumulative and eruptible characteristics of strain energy and stress distribution in rockmass, the rockburst types and their intensity classification is summarized. Four engineering measures are put forward for preventing and curing the rockburst. The four measures involves stress relieves by blasting, enhances of physical-mechanical properties of rock, improve of the stress conditions of surrounding rock and the reinforcement of rockmass.

1. Introduction

A rockburst is a sudden and violent expulsion of rock from the surrounding rock mass [1]. It is a serious natural disaster and becomes increasingly more likely and dangerous when the depth of extraction increases and geological conditions become more complex [2]. Possible effects of rockbursts include injuries, fatal accidents, damage to equipment, construction and production delays, and higher cost of construction and operation. There is a need for the development of suitable computational methods for the prediction and control of rockbursts. There are basically two types of rockbursts: crush type and shear type. The crush type of rockburst occurs due to the existence of underground openings whereas the shear type occurs due to the presence of faults, dykes, etc. There are various approaches used for the analysis of rockburst [3]. The stress analysis approach is used to predict the extent of failure. In order to predict the occurrence of rockburst, the instability approach is generally used. Instability may be predicted either by computing the Eigen value of the system, or by using a perturbation method. In order to ensure safety in underground excavations and prevent the rock burst, a dynamic simulation model for a cone bolt is proposed based on an experimental study [4]. According to the conditions of geostress, rock structure and performance, conditions of geological structure and hydrological geology, excavation construction factors and so on, the conditions of rockburst formation in underground engineering are elaborated [5].

Based on energy principles, the mechanism and characteristic of rockburst have been discovered and prove that rockburst is a geological disaster which occurs in hard brittle rock mass that has accumulated energy. This paper researches rockburst types and their intensity classification based on correlative scientific production and practical engineering examples. According to the characteristic of rock bodies of deep underground projects at high ground stresses, and the mechanism of rockburst, four engineering technologies have been put forth to prevent and cure rockburst during the constructing period.

2 Analysis of Stress State

To a circular tunnel as an example, the length of the tunnel is much larger than its cross-sectional size, and it can be regarded as in plane strain state, as Figure 1. The stress distribution in rock can be calculated by using the formulas(1)~ (4):

$$\sigma_r(r,\theta)=\frac{\sigma_V}{2}(1+\lambda)\left[1-\frac{a^2}{r^2}\right]-\frac{\sigma_V}{2}(1-\lambda)\left[1+\frac{3a^4}{r^4}-\frac{4a^2}{r^2}\right]\cos 2\theta \quad (1)$$

$$\sigma_\theta(r,\theta)=\frac{\sigma_V}{2}(1+\lambda)\left[1+\frac{a^2}{r^2}\right]+\frac{\sigma_V}{2}(1-\lambda)\left[1+\frac{3a^4}{r^4}\right]\cos 2\theta \quad (2)$$

$$\sigma_l(r,\theta)=\mu(\sigma_r+\sigma_\theta) \quad (3)$$

$$\tau_{r\theta}(r,\theta)=-\frac{\sigma_V}{2}(1-\lambda)\left[1-\frac{3a^4}{r^4}+\frac{2a^2}{r^2}\right]\sin 2\theta \quad (4)$$

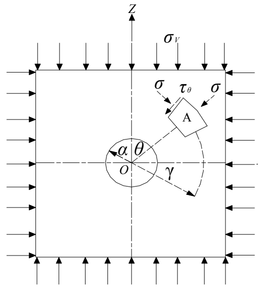

Figure 1 Rockburst Analysis of Stress State

Where σ_V and σ_h are the initial ground-stress; a is the cavity radius; θ is the angle between OA and level direction; σ_r is the radial stress; σ_θ is the tangential stress; $\tau_{r\theta}$ is the shear stress; σ_l is the axial stress ; r is the radial distance from point A to the cavity center; μ is Poisson's ratio; λ is lateral pressure coefficient, $\lambda=\sigma_H/\sigma_V$.

3 Evaluation and Prediction of Rockburst

To confirm the possibility as well as to assess the intensity of rockburst during mining, the present study implemented the contemporary criteria of rockburst in literature[6-9]. In conjunction with analysis on strain energy and stress distribution in rockmass, a comprehensive prediction has been made on rockburst.

Based on the correlative scientific production, practical engineering examples and analysis of stress state in section 2, the possibility of occurrence of rockburst can be estimated by combination with the following criterion of tangential stress. At the same time, for forecasting the occurrence of rockburst, the factors of elastic strain energy and rock brittleness should be considered, and the corresponding criteria are putted forward.

3.1 Criterion of Tangential Stress

This criterion considers both the state of in-situ stress in rockmass as well as the mechanical property of rock. The criterion of tangential stress is expressed by:

$$T_s=\sigma_\theta/\sigma_c \quad (5)$$

where, σ_θ is the tangential stress in rockmass surrounding the openings or stopes (MPa) and σ_c is the uniaxial compressive strength of rock (MPa) . The preliminary study[7] shows that:

(1) T_s<0.3, then no rockburst; (2) T_s =0.3~0.5, then weak rockburst;

(3) T_s =0.5~0.7, then strong rockburst; and (4) T_s >0.7, then violent rockburst.

3.2 Criterion of Elastic Strain Energy

Investigation shows that the occurrence of shock and rockburst could be scaled by the so-called potential energy of elastic strain, PES, i.e. the elastic strain energy in a unit volume of rock masses (as Figure 2). Under uniaxial compression, the elastic strain energy stored in rock specimen prior to the peak strength is given by：

$$\mathrm{PES} = \sigma_c^2/(2E_s) \tag{6}$$

Where, σ_c is the uniaxial compression strength (MPa), E_s is the unloading tangential modulus (MPa).

(1) PES<50 kJ/m^3， then the rockburst hazard is very low;

(2) 50<PES<100 kJ/m^3, then the rockburst hazard is low;

(3) 100<PES<150 kJ/m^3, then the rockburst hazard is moderate;

(4) 150<PES<200 kJ/m^3, then the rockburst hazard is high;

(5) PES>200 kJ/m^3, then the rockburst hazard is very high.

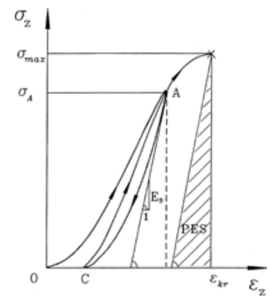

Figure 2 Schematic drawing of calculation of potential elastic strain energy

3.3 Criterion of Rock Brittleness

Rock brittleness is defined by an index of the ratio of uniaxial compressive strength to tensile strength of rock:

$$B = \sigma_c/\sigma_t \tag{7}$$

where, σ_c is the uniaxial compressive strength(MPa), σ_t is the tensile strength of the rock(MPa). Experimental study and in situ investigation show that [7]:

(1) B>40, then no rockburst; (2) B=40~26.7, then weak rockburst;

(3) B=26.7~14.5, then strong rockburst; and (4) B<14.5, then violent rockburst.

4 Classification of Rockburst Types and Intensity

Based on the accumulative and eruptible characteristic of strain energy and stress distribution in rockmass, rockbursts can be mainly classified into three types: blowout-eject type, exfoliate type, wall-collapse type.

Classification of rockburst types and intensity is the foundation for researching the predicting methods and preventing technologies. Synthesizing and analyzing the researches at home and abroad[4,10-12], rockburst intensity can be classified into 3 grades: weak rockburst, strong rockburst and violent rockburst.

Table 1. Classification of rockburst intensity

Rockburst intensity grades	Characters
weak rockburst	There are phenomena of burst-off and spin-off in rock surface, and secluded snapped, tearing sound inside of rock mass. Rockbursts occurr sporadic, and it has less impact on the construction.
strong rockburst	Phenomena of rock burst-off and spin-off are more serious and there is the ejection. It can be heard the clear sound of the burst for a certain duration, and the impact depth is up to 1 m or so. It has a certain influence on the construction.
violent rockburst	Intense burst-off and spin-off. There may be similar sound of fire of scatter-gun Rockbursts with continuity move into the deep rock mass, and the impact depth is up to 2 m or more. It has serious impact on the construction.

5 Engineering Technologies for Preventing and Curing the Rockburst

The supporting of rockburst-prone deep strata is a worldwide conundrum, the ideal supporting measures should have the following characteristics: (l) Supporting structure should have a higher initial stiffness; (2) Supporting structure should have a good load-bearing capacity even in large deformation; (3) Supporting system should have flexible features. At the same time, it should be noted that, due to way design process, there are many uncertain factors such as stent load, failure mechanism, etc., so the strict engineering design methods for rockburst support in rockburst-prone deep strata have not very much practical sense, and it is more important that the supporting concept should be updated.

From the rockburst mechanism, the project site should first try to avoid the high ground stress concentration areas where the rockbursts are prone to occur, and if it is difficult to avoid, the arrangement of tunnel axis should be parallel to the maximum principal stress direction to reduce the stress concentration factor, which can prevent or reduce rockburst intensity level. At present, the rockburst prevention and control measures during the construction can be concluded into the following four categories:

(1) The advance blasting stress relieving method

It is found from the practice and research that the occurrence of rockburst is mainly related to the tangential stress on the tunnel wall. The principle of the stress relieving method is to reduce the tangential stress for preventing and curing rockburst, and its specific approach is that a broken-rock belt was caused inside the surrounding rock mass, which form a low-elastic zone, thereby the stress around the working face and wall reduces and the tangential stress will be transferred into the deeper rock mass.

The advance blasting stress relieving method forms a certain thickness of broken-rock belt by drilling ahead and blasting in the borehole during the construction process. Releasing the stress and excavating are carried out simultaneously. Before the excavation, the original stress has been released, so that the occurrence of rockburst was prevented or weakened.

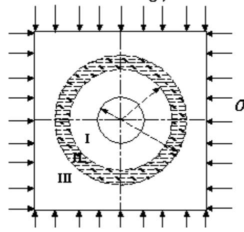

Figure 3 The model of the advance blasting stress relieving method

Acclivitous boreholes are drilled forwards starting at the working face, and an artificial broken-rock belt, which has a certain safe distance *h* from the wall and has a thickness of *δ*, was formed by blasting in the borehole. Because the blasting happens inside of the rock, some cubage- compensatory boreholes(non-charge boreholes) are needed to drill with the exception of the blasting-boreholes, thus the artificial broken-rock belt can be formed. The sketch is shown in the figure 3, where, σ_V and σ_H are the initial horizontal stress and vertical stress respectively. Three regions of *I*, *II* and *III* denote the rock mass within the broken-rock belt, the broken-rock belt and the rock mass outside of the broken-rock belt.

After the advance blasting stress relieving measure, tangential stress changes greatly. The tangential stress reduces within the broken-rock belt, and increases outside of the broken-rock belt, that is to say, the tangential stress of rock within the broken-rock belt was transferred into the deeper rock which locates outside of the broken-rock belt. The purpose of prevention or weakening of rockburst is achieved by reducing the elastic strain energy inside of the rock mass. The transfering degree of tangential stress is relevant to the stress release rate.

(2) Improving physical mechanics properties of rock

The underground project which have occurred rockbursts is mostly located in high ground stress strata where the rock mass table more closely and groundwater is not abundant. Generally, in humid areas with plenty of groundwater, the ground stress in surrounding rock is more easy to release and therefore it is less liable to occur rockburst activities. During the process of underground engineering excavation construction which locates in high ground stress strata, if we often spray cold water on the working surface and the wall, it can reduce the strength of the surface rock. Injecting the high-pressure water into the rock mass by using the advanced drilling, which can be adopted to prevent and cure the rockburst via three effects: First, it can release the strain energy and the maximum tangential stress transfers into the deeper surrounding rock mass; Secondly, high-pressure injection has the role of wedge splitting action, which can soften and reduce the strength of rock; Thirdly, it induces the new tensile cracks and makes the existing cracks to expand further, thus reduces the rock's ability to store strain energy.

(3) Improving the stress conditions of surrounding rock

Drill-blast method should be adopted as far as possible during the construction in rockburst-prone areas. In order to reduce the stress concentration on the surface of surrounding rock, we should take short footage excavation, reduce the amount of dynamite and control the effect of blasting. In weak and strong rockburst areas, using full-face excavation is feasible, which can reduce disturbance to the surrounding rock. In violent rockburst areas, we can use division excavation to reduce the destructive extent of rockburst, and some technologies, such as the advanced drilling method, can be adopted to release the strain energy of rock mass before excavation.

(4) Reinforcement of rock

Generally, the different reinforcement measures matches with different intensity of rockburst, as the table 2.

Table 2 Reinforcement measures

Rockburst intensity grades	Reinforcement measures
weak rockburst	Anchoring bolts: ϕ_1 =22mm, L =1.5~2m, @200cm~250cm, with plum-type layout; spraying concrete or steel fiber concrete with 5~15cm thick on the wall; If it is necessary, the networks of reinforcing steel bar are need to be installed, ϕ_2 =6mm~8mm, @ 20cm × 20cm.
strong rockburst	Shallow-hole, density-anchor, overall networks and spraying concrete; Anchoring bolts: ϕ_1 =22mm, L =2~2.5m, @100cm~200cm, with plum-type layout; spraying concrete or steel fiber concrete with 10~15cm thick on the wall; the standard of networks of reinforcing steel bar is ϕ_2 =6mm~8mm, @ 20cm × 20cm. It is necessary to add additional steel truss support for some serious situation.
violent rockburst	Anchoring bolts: ϕ_1 =22mm, L =2.5~3.5m, @50cm~100cm, with plum-type layout; the standard of

	overall networks of reinforcing steel bar is ϕ_2 =6mm~8mm, @20cm×20cm. Spraying concrete with 5cm thick on the wall for three repeating times. Add additional steel truss support. If it is necessary, working face also should be sprayed 4cm thick concrete to form the close supporting system.
Note: ϕ_1 and L denote the diameter and length of the bolt respectively, ϕ_2 is the diameter of the reinforcing steel bar.	

6 Conclusions

The occurrence and evolution of rockburst have strong, sudden and destructive characteristics, but it still has regularity. The prevention of rockburst is achieved by extracting existing experiences combined with the engineering conditions. During the process of constructive organization, managers must establish the rockburst prevention awareness, decide on the measures for rockburst prevention, adhere to the principles of rockburst prevention, implement the prevention programs, and adopt integrated effective measures with the consideration of the main inducements and possible intensity grade of rockburst. As long as timely prevention and control measures are adopted and the organization is powerful, it is possible to prevent and control rockburst effectively.

References

1. Jaeger, J.C. and Cook, N.G.W. Fundamentals of Rock Mechanics. Chapman & Hall; 1979.
2. Dou, L.M. and He, X.Q. Theory and Technology of Rock Burst Prevention. China University of Mining and Technology Press, 2001.
3. Sharan, S.K. A Finite Element Perturbation Method for the Prediction of Rockburst. Computers and Structures, 2007(85).1304-1309.
4. Pierre, L.S., Hassani, F.P., Radziszewski, P.H. and Ouellet, J. Development of a Dynamic Model for a Cone Bolt. International Journal of Rock Mechanics & Mining Sciences, 2009 (46). 107-114.
5. Xu, L.S. Research of Rockburst Formation Condition in Underground Engineering. Journal of Chongqing Jiao Tong University, 2005, 24(3). 31-34.
6. Qiao, C.S. and Tian, Z.Y. Study of the Possibility of Rockburst in Dong-Gua-Shan Copper Mine. Chinese J. Rock Mech. Eng., 1998, 17. 917-921.
7. Wang, Y.H., Li, W.D. and Li, Q.G. Fuzzy Estimation Method of Rockburst Prediction. Chinese J. Rock Mech. Eng., 1998, 17(5). 493-501.
8. Zhang, J.J. and Fu B.J. Rockburst and Its Criteria and Control. Chinese Journal of Rock Mechanics and Engineering, 2008, 27(10).2034-2042.
9. Wang,J.A. and Park, H.D. Comprehensive Prediction of Rockburst Based on Analysis of Strain Energy in Rocks. Tunnelling and Underground Space Technology, 2001, (16). 49-57.
10. Hou, Y.H., Hu W.D. and Chen, S.G. Advance Blasting Stress Relieving Method and Its Application. Water Resources & Hydropower of Northeast, 2008, 11.17-20.
11. Xu, L.S., Wang, L.S. and Li, T.B. Present Situation of Rockburst Research at Home and Abroad. Journal of Yangtze River Scientific Research Institute, 1999, 16(4).24-27.
12. Driad-Lebeaua, L., Lokmane, N., Semblat, J.F. and Bonnet, G. Local Amplification of Deep Mining Induced Vibrations Part1: Experimental Evidence for Site Effects in a Coal Basin. Soil Dynamics and Earthquake Engineering, 2009, (29).39-50.

RaSiM 7(2009): Controlling Seismic Hazard and Sustainable Development of Deep Mines, C.A. Tang(ed), Rinton Press, 769-776

APPLICATION OF WEIGHTED DISTANCE DISCRIMINANT ANALYSIS METHOD BASED ON ROUGH SET TO ROCKBURST PREDICTION

DAO-HONG QIU, LE-WEN ZHANG and SHU-CAI LI

Geotechnical and Structural Engineering Research Center, Shandong University

Jinan, 250061, P.R. China

WEI CUI

School of Civil Engineering, Shandong University

Jinan, 250061, P.R. China

Rockburst was one of the main engineering geological hazards at deep high terrestrial stress zone and was influenced by many factors. Mahalanobis distance method was a new rockburst prediction method, in which the importance of each factor was thought to be equal. But the importance of each factor was different in fact. Therefore it was necessary to weight each factor. It was presented the rockburst prediction method of weighted Mahalanobis distance method could be developed on the basis of rough set. In this paper, a method of determining weighting coefficient was proposed based on rough set theory. Determining weighting coefficient was translated into estimating significance of attributes among rough set. According to the analysis of main causes of rockburst, the compressive strength, tensile strength, elastic energy index of rock and the maximum tangential stress of the tunnel wall were chosen as the criterion indices. By analyzing the significance of conditional attribute set for decision attribute, the weighing coefficient of each factor was determined by rough set. Finally, the model was applied to predict rockbrust in practical engineering. The results shows that the method is reliable and it can improve the evaluating accuracy of Mahalanobis distance method.

1 Introduction

Rockburst is a familiar geological hazard in deep and long tunnels, was and is considered as a dynamic instability phenomenon of surrounding rock mass of underground space in high geostatic stress and caused by the violent release of strain energy stored in rock mass. Rockburst occurred during excavating underground space in the form of stripe of rock slices or rock fall or throwing of rock fragments, sometimes accompanied by a cracking sound. Many scholars have analyzed the rockburst phenomenon on the area of strength, stiffness, energy, stability, fracture, injury, fractal and mutant, and many prediction methods and empirical correlations have been established[1-3].

The distance discriminant analysis was a classical statistics approach for classifying samples of unknown classes, based on training samples with known classes. Mahalanobis distance method was one of distance discriminant analysis, and it was applied to rockburst prediction. The importance of each factor was equal in this method. Generally, the importance was not the same to all factors, so assigning a weight to each factor was very important. According to the actual situation of Jiangbian hydropower station, four evaluation indices are chosen from the various factors, and the weights of each factor go through rough Set theory. Weighted Mahalanobis distance rockburst prediction model is presented first in this paper according to the theory of the distance discriminant analysis. And the improved Mahalanobis distance method was used in the rockburst prediction of water diversion tunnel of Jiangbian hydropower station and achieved good results, and the method provided a new method for rockburst prediction research.

2 Weighted Mahalanobis Distance Method

2.1 Distance Discriminant Analysis Method

Discriminant analysis is used to determine the category of a sample, and it is a statistical analysis method of strong application and has penetrated into all fields of science. The method extracts the general information from the training samples usually, and constructs a criterion to judge which classifications the new samples belong to. Mahalanobis distance is a common distance discriminant analysis. Here, Mahalanobis distance was introduced as follows.

2.2 Weighted Mahalanobis Distance Method

Supposing a collectivity $G=(X_1,X_2,\ldots,X_m)^T$ with m member indexes, a sample can be expressed as $X=(x_1,x_2,\ldots,x_m)^T$ and the expected value of X_i denoted by u_i ,is $u_i = E(X_i)$,i=1,2,…m. And then the expected value μ of G can be expressed as $\mu = (\mu_1, \mu_2, \cdots, \mu_m)^T$. The covariance matrix of G is $\sum = Cov(G) = E[(G-\mu)(G-\mu)^T]$. The Mahalanobis distance between sample X and collectivity G is defined as $d^2(X,G) = (X-\mu)^T \sum^{-1} (X-\mu)$.

Supposing the weight vector of m indexes is $W = (w_1, w_2, \cdots, w_m)$, to a sample X with m member indexes, the Mahalanobis distance between sample X and collectivity G is defined as $d^2(X,G) = (X-\mu)^T \sum^{-1} (X-\mu)$.

2.3 Distance Discriminant Criterion Between Many Collectivities

Supposing that there are many collectivities: $G_1, G_2, \cdots, G_k \, (k > 2)$, and the sample from G_i(i=1,2, …,k) can be defined as $X_{(t)}^{(i)} = (X_{t1}^{(i)}, X_{t2}^{(i)}, \cdots, X_{tm}^{(i)})^T, (i = 1, 2, \cdots, k; t = 1, 2, \cdots, n_i)$.

Where n_i is the number of training sample from G_i. Then the unbiased estimation of mean vector u_i can be defined as $\overline{X}^{(i)} = \left(\frac{1}{n} \sum_{t=1}^{n_i} x_{t1}^{(i)}, \cdots, \frac{1}{n} \sum_{t=1}^{n_i} x_{tm}^{(i)} \right)^T = (\overline{x_1}^{(i)}, \cdots, \overline{x_m}^{(i)})^T$.

The unbiased estimation S_i of covariance matrix $\sum_i$ of G_i can be defined as $S_i = \frac{1}{n_i - 1}\sum_{t=1}^{n_i}(X_{(t)}^{(i)} - \overline{X}^{(i)})(X_{(t)}^{(i)} - \overline{X}^{(i)})^T$. When $\sum_1 = \sum_2 = \cdots = \sum_k$, the unbiased estimation of $\sum$ can be written as

$$S = \frac{1}{\sum_{q=1}^{k} n_q - k}\sum_{q=1}^{k}(n_q - 1)S_q \cdot \qquad (1)$$

After got the expected value u_i of G_i and the public covariance matrix $\sum$, the distance between sample X and collectivity G can be calculated according to the definition of weighted Mahalanobis distance. Distance discriminant criterion between many collectivities is that: supposing collectivity G_i agrees with $d^2(X, G_l) = \min_{i=1,2,\cdots,k}\{d^2(X, G_i)\}$, then $X \in G_l$ [4,5].

3 Method of Weight Coefficient Calculating Based on RS

The rough sets theory proposed by Professor Z. Pawlak is a mathematical theory dealing with uncertainty and incompleteness of data. Attribute reduction is one of the most important parts, and it can remove the redundancy and incompatibility attributes so that we can obtain the key information and make the decision rule.

3.1 Decision Table

A decision information system is defined as K=(U,R,V,f), where U is a finite set of object, $R = C \cup D$ is a finite set of attribute set, C is the condition attribute set, and D is the decision attribute set. With each attribute $r \in R$, the set of values V is associated. Each attribute has a determinant function f:$U \times A \to V$.

3.2 Rough Sets

The rough sets theory is based on the concept of an upper and a lower approximator of a set. Repository $K = (U, R)$ is given, and for a given subset $X \subseteq U$ and an equivalence relation $R \in K$, the R-lower approximation $\underline{R}X$ of set X in R is defined as $\underline{R}X = \{x \in U \mid [x]_R \subseteq X\}$, and the R-upper approximation $\overline{R}X$ of set X in R is defined as $\overline{R}X = \{x \in U \mid [x]_R \cap X \neq \Phi\}$. $bn_R(X) = \overline{R}X - \underline{R}X$ is defined as R-boundary region of X , and $pos_R(X) = \underline{R}X$ is defined as R-positive region of X , and $neg_R(X) = U - \overline{R}X$ is defined as R-negative region of X.

3.3 Attribute Significance

The attribute significance indicates the importance degree of attribute in information table. The bigger the significance of attribute is the higher its position in the decision information table; otherwise, the lower its position. The dependence between C and D is $k = \gamma_C(D) = \frac{1}{U}\sum_{i=1}^{m}|pos_C(Y_i)|$, $Y_i \in U / D$.

When k=1, D depends on C completely; when 0<k<1, D depends on C partially; when k=0, D is independent with C completely.

The significance of attribute of subset $C' \subseteq C$ to D is $\sigma_{CD}(C_i) = \gamma_C(D) - \gamma_{C-\{C_i\}}(D)$, where

$\gamma_{C-C_i}(D) = \frac{1}{U}\sum_{i=1}^{m}\left|pos_{C-\{C_i\}}(Y_i)\right|$

If $C' = \{a\}$, the significance of attribute of $a \in C$ to D is defined as $\sigma_{CD}(a) = \gamma_C(D) - \gamma_{C-\{a\}}(D)$. The bigger the $\sigma_{CD}(a)$, the higher the position of the attribute a in the decision information table [6,7].

3.4 Weight Coefficient Calculating Based On RS

The calculation process of weighting coefficient as follows:

Step 1. Calculate the dependence $\gamma_C(D)$ of the decision attribute to all conditional attributes.

Step 2. To each evaluation index a , calculate the dependence $\gamma_{C-C_i}(D)$ of the decision attribute to the conditional attributes C-C_i.

Step 3. Calculate the significance $\sigma_{CD}(C_i)$ of each evaluation index C_i

Step 4. Get the weighting coefficient of evaluation index C_i by the formula below.

$$\alpha_i = \frac{\gamma_{C-C_i}(D)}{\sum_{j=1}^{n}\gamma_{C-C_i}(D)} \quad (i=1，2，\ldots，n) \tag{2}$$

4 The Engineering Application

4.1 Engineering Situation

Jiangbian hydropower station lies in southeast of Ganzi Tibetan Autonomous Prefecture in Sichuan Province. It located in the Jiulong River. This power station belongs to be a second-class hydropower project with a total storage capacity of 1.33 million m^3 and installed capacity of 330MW. The water diversion tunnel of Jiangbian hydropower station lies to the left side of Jiulong River, with a length of 8.5Km from intake to surge shaft and a diameter of 8.4m. The buried depth is 100m to 1694m.

The construction of this tunnel have entered the area with the big-buried-depth, and the buried depth is more than 700m and lithology is quartz-biotite schist, remaining 3500m of deep tunnel has not yet been excavated. From the pre-excavation of the situation, it entered the middle rockburst areas when buried depth larger than 550m, and rockburst occurred frequently during the construction. As the influence of rockburst, excavation has been seriously affected. Figure 1 shows the blocks stripped from arch crown and figure 2 shows the cracking and spalling of sidewall because of the high geostress.

Figure 1 Rockfall of arch crown

Figure 2 Cracked surfaces of side wall

4.2 Identification of The Indexes of Criterion

The indexes of criterion should reflect the main factors of rockburst---the properties and stress of surrounding rock. At the same time, they should be obtained easily and can be compared with each other in different cases. In this paper, compressive strength σ_c , tensile strength σ_t , elastic energy index W_{et} and the maximum tangential stress σ_θ are chosen as the indexes of criterion. Compressive rock strength, tensile strength, the elastic energy index can reflect the properties of surrounding rock, and the tangential stress can reflect the virgin geostatic stress condition and the influence of the shape and dimension of the underground space on rockburst.

4.3 Continuous Attribute Discretizing

Rough sets theory only deals with discretization attributes; however the influence factors of rockburst usually are real values. So we should take discretization measure to real attribute values when we calculate the weighting coefficient of evaluation indexs. There are many discretizaion methods such as boo reasoning algorithm, semi-naive algorithm etc. In the geotechnical engineering，through many engineering experiences and research on the single index of rockburst factors, it is discovered that the rockburst level changes with the change of influencing factor, and the change has regularity. So in this paper, real values are discretized according to the gradation of each evaluation index to rockburst level, just as the table 1 shown.

Table 1. Discrete interval of condition attributes

Classified number	compressive strength σ_c /MPa	tensile strength σ_c/σ_t	elastic energy index W_{et}	tangential stress σ_θ/σ_c	Rockburst gradation
1	<80	>40	<2.0	<0.3	No rockburst
2	80~120	40~26.7	2.0~3.5	0.3~0.5	Light rockburst
3	120~180	26.7~14.5	3.5~5.0	0.5~0.7	Medium rockburst
4	>180	<14.5	>5.0	>0.7	Violent rockburst

4.4 Weight Coefficient Calculating Based on RS

To build the decision table, eighteen representative engineering examples are adopted. In the original decision table, row represents the engineering examples and column represents attribute set including the condition attribute set and the decision attribute. Table 2 shows the engineering original data [8]. Then according to table 1, discretize each index. According to the method of RS determining weighting coefficients introduced in this paper, weighting coefficients of all the evaluating indexes can be obtained.

$$W = \{\sigma_c, \sigma_c/\sigma_t, W_{et}, \sigma_\theta/\sigma_c\} = \{0.268, 0.143, 0.143, 0.428\}.$$

Table 2 The engineering original data

No	Project	σ_c /MPa	σ_c/σ_t	W_{et}	σ_θ/σ_c	Rockburst gradation
1	Tianshenqiao Ⅱ hydropower station	88.7	24.0	6.6	0.3	Medium rockburst
2	Ertan hydropower station	220	29.7	7.3	0.41	Light rockburst
3	Longyangxia hydropower station	178	31.2	7.4	0.106	No rockburst
4	Lubuge hydropower station	150	27.8	7.8	0.227	No rockburst
5	Yuzhixi hydropower station	170	14.8	9.0	0.53	Medium rockburst
6	Taopingyi hydropower station	165	17.5	9.0	0.38	Light rockburst
7	Lijiaxia hydropower station	115	23.0	5.7	0.096	No rockburst
8	Pubugou hydropower project	123	24.6	5.0	0.36	Medium rockburst
9	Jinping Ⅱ hydropower project	120	18.5	3.8	0.82	Medium rockburst
10	Laxiwa hydropower project	176	24.1	9.3	0.315	Medium rockburst
11	Norway Sima hydropower station	180	21.7	5.0	0.27	Medium rockburst
12	Norway Heggura road tunnel	175	24.1	5.0	0.37	Medium rockburst
13	Norway Sewage tunnel	180	21.7	5.0	0.42	Medium rockburst
14	Sweden Forsmark nuclear power station	130	21.7	5.0	0.38	Medium rockburst
15	Sweden Vistas tunnel	180	26.7	5.5	0.44	Light rockburst
16	USSR Rasvumchorr mine	180	21.7	5.0	0.317	Medium rockburst
17	Japan kankoshi road tunnel	236	22.1	5.0	0.377	Medium rockburst
18	Italy Raib Zinc sulfate lead mine	140	17.5	5.5	0.774	Violent rockburst

4.5 Weighted Mahalanobis Distance Comprehensive Evaluation

As the samples in table 2 are some typical rockburst data, these eighteen samples are used to build the Mahalanobis distance analysis model. The inputs of the rockburst prediction model are as follow: compressive strength_, ratio of rock compressive strength and tensile strength_, elastic deformation energy index_, ratio of rock tangential stress and uniaxis compressive strength_. The outputs of the rockburst prediction model for the rockburst classification are as follow: no rockburst, light rockburst, medium rockburst and strong rockburst. The rockburst prediction of the water diversion tunnel of Jiangbian hydropower station can be done by using both the trained model above and the weights got from rough set theory.

The indices σ_c , σ_c / σ_t and W_{et} are got from field experiments, σ_θ is determined by using FEM simulation. The evaluation results and the real situation are listed in table 3. Results using fuzzy comprehensive evaluation and artificial neural network are also listed in table 3 for going to compare. The evaluation results are relatively similar with the actual situation, so that the improved Mahalanobis distance method is reliable.

Table 3 Value of evaluating indexes of each tunnel segment

Position	σ_c	σ_c / σ_t	W_{et}	σ_θ / σ_c	Fuzzy	ANN	Weighted Mahalanobis distance method	Practical situation
K4+300	*124*	*18.24*	*2.46*	*0.47*	*Light*	*Light*	*Light*	*Light*
K4+400	*128*	*17.66*	*2.86*	*0.52*	*Medium*	*Medium*	*Medium*	*Medium*
K4+500	*132*	*17.23*	*2.94*	*0.54*	*Medium*	*Medium*	*Medium*	*Medium*
K4+600	*138*	*16.57*	*3.05*	*0.58*	*Medium*	*Medium*	*Medium*	*Medium*

4 Conclusions

(1) A new approach for rockburst prediction, based on a rough set, uses a rockburst prediction model of weighted Mahalanobis distance method. The evaluating result of the method is reliable, and it can improve the evaluating accuracy of non-weighted Mahalanobis distance method.

(2) Put forward a method by adopting RS theory to determine index weighting coefficient, and it translated determining weighting coefficient into estimating significance of attributes among rough set. Through analyzing dependence of rockburst gradation to evaluating index, obtain the significance of each evaluating index, and then calculate the weighting coefficient of each evaluating index in rockburst evaluations model.

(3) The rockburst prediction model of weighted Mahalanobis distance method is obtained through training a large number of practical engineering samples.The prediction accuracy of this method is affected by the representation and accuracy of the training samples. The original sample set selected should be representative; otherwise the evaluating results will change with the change of the sample set.

Acknowledgements

The authors wish to acknowledge the collaborative funding support from the National Basic Research Program of China (NO: 2009CB724607), Chinese National Natural Science Foundation (50539080) and Natural Science Foundation of Shandong Province (Y2007F53).

References

1. Feng, X.T., Webber, S., Ozbay, M.U. et al. An Expert System on Assessing Rockburst Risks for South African Deep Gold Mines. Journal of Coal Science & Engineering, 1996, 2(2). 23-32.
2. Tang, J.P., Pan, Y.S. and Li, Y.J. Numerical Simulation of Deep-Level Rockburst in Fuxin Coalfield. Journal of Coal Science & Engineering, 2005, 11(1). 13-16.
3. Zhou, D.P. and Hong, K.R. The Rockburst Fertures of Taipingyi Tunnel and the Prevention Method. Chinese J, Rock Mech. Eng., 1995, 14(2). 171-178.

4. Zhang, W., Li, X.B. and Gong, F.Q. Stability Classification Model of Mine-Lane Surrounding Rock Based on Distance Discriminant Analysis Method. J. Cent. South Univ. Technol, 2008, 15. 117-120.
5. Gong, F.Q. and Li, X.B. Application of Distance Discriminant Analysis Method to Classification of Engineering Quality of Rock Masses. Chinese Journal of Rock Mechanics and Engineering, 2007, 26(1). 190-193.
6. Lian, C., Yu, L., Jin, H.S. and Yuan, L. The Decision Rules of Rough Set and its Application in Aquaculture. Joumal of Nanchang Institute of Technology, 2006, 25(2).129-132.
7. Pawlak, Z. Rough Sets and Intelligent Data Analysis. Information Science, 2002, 11(147). 1-12.
8. Wang, Y.H., Li, W.D., Lee, P. K.K., et al. Method of Fuzzy Comprehensive Evaluation for Rockburst Prediction. Chinese Journal of Rock Mechanics and Engineering, 1998, 17(5). 493-501.

RaSiM 7(2009): Controlling Seismic Hazard and
Sustainable Development of Deep Mines,
C.A. Tang(ed), Rinton Press, 777-784

APPLICATION OF EXTENSIBLE COMPREHENSIVE EVALUATION TO ROCKBURST PREDICTION IN A RELATIVE SHALLOW CHAMBER

HUAI-FENG SUN, SHU-CAI LI, DAO-HONG QIU, LE-WEN ZHANG and NING ZHANG

Geotechnical and Structural Engineering Research Center, Shandong University

Jinan, 250061, P.R. China

Being a kind of usual geological hazard in deep tunnels and chambers, rockburst greatly threatens the safety of constructors and equipments. It is traditionally thought that rockburst only occurs when buried depth reaches 300m. However, rockburst occurs frequently during initial construction in the main-transformed chamber of a hydropower station where the buried depth is less than 200m. According to the lithology and crustal stress obtained in field experiments, this paper uses extensible comprehensive evaluation to predict rockburst in this relative shallow chamber. After analyzing the reasons of rockburst in the project, it is concluded that rockburst can also occur in relative shallow chamber under some conditions. During the evaluation, lithologic parameters are obtained from field rock mechanical experiments and stress indices are gotten from geostress measurement using hollow inclusion method and FEM simulation. Throughout the comparative analysis and field practical verification, it is proved that the results of the evaluation are reliable and have great guiding role for later construction.

1 Introduction

Many different scholars have put forward many different theories in hopes of cracking the world famous puzzle of rockburst. Generally agreed is that the occurrence of rockburst has a great relationship with buried depth. Studies of rockburst occurred in mines of USSR showed that most of the mining depths are more than 700m. There are a lot of rockburst prediction methods widely used at present like numerical simulation method; artificial neural network model; fuzzy comprehensive assessment method; fractal geometry method; nonlinear grey classification model; nonlinear chaos theory etc [1-5]. We must combine actual situations and known factors during rockburst prediction especially some special geological conditions because of the complexities of geotechnical engineering and the differences of geological conditions. This paper uses extensible comprehensive evaluation to predict rockburst of a chamber whose buried depth is lower than 200m and get the conclusion that rockburst can also occur in relative shallow chamber under some conditions. The main reasons for rockburst in these relative shallow chambers are also analyzed.

2 Extensible Comprehensive Evaluation

Extension theory was proposed in 1983 by Professor Wen Cai of China. It is a law and method to study and solve incompatible problems qualitatively and quantitatively through transformation and calculation by the introduction of matter-element R = (N, C, V) (matter, characteristics, value)[6-9]. Rockburst prediction of this method is based on matter-element theory and extension set theory.

As Extension theory is not the importance in this paper, you can get more information through reference 6 to 9. And its application will be shown during the following process.

3 Engineering Application

3.1 Engineering Situation

Jiangbian hydropower station lies in southeast of Ganzi Tibetan Autonomous Prefecture in Sichuan Province. It is localed on the Jiulong River which is a tributary of the Yalongjiang River. This power station belongs to a second-class hydropower project with a total storage capacity of 1.33 million m^3 and a installed capacity of 330MW. It is mainly formed by head of pivot; water diversion system and underground powerhouse. The underground powerhouse lies to the left of the Yalongjiang River. Yalongjiang River flows to N45ºE with steep terrain which is mainly composed by cliffs and scarp. Structural fractures are poorly developed here, and fault f3 outcropping from ground is the biggest with the occurrence SN~N5°WN/NE∠80°. Chamber groups of the underground powerhouse are composed by the main power house; main-transformed chamber; tailrace etc. The design size of main-transformed chamber is 71.3m×13.6m×23.6m (length×width×height).

Regional is alpine and canyon geomorphology and the powerhouse area is very near to gully. Bedrock is biotite granite of Yanshanian and very hard. Depth of the main-transformed chamber is less than 200m. The first stage has been excavated now. Rockburst occurred frequently during initial construction. Aiming at the situation that rockburst occurred in this relative shallow chamber, we mainly emphasizes analyze lithology and crustal stress. The main-transformed chamber is divided as four parts by length in convenience.

3.2 Choose the Evaluation Indices

Reasonable evaluation indices are decided according to actual situation. Tectonic stress has a great influence in this project because of the fluctuation surface. So that this paper chooses the following factors for the evaluation according to some rockburst criterion and project cases home and abroad. Rock uniaxis compressive strength R_c; Ratios of rock strength stress R_c/σ_1; Elastic deformation energy index W_{et}; Ratio of rock compressive-tensile σ_c/σ_t; Ratio of rock tangential stress and uniaxis compressive strength σ_θ/R_c. All of the single factor rockburst classifications are shown in table 1 using four classification method[7-9].

Table 1 Rockburst classification for single factor

Rockburst Grade	R_c/MPa	R_c/σ_1	W_{et}	σ_c/σ_t	σ_θ/R_c
no rockburst / class 1	<80	>14.5	<2.0	>40	<0.3
weak rockburst / class 2	80 ~ 120	14.5 ~ 5.5	2.0 ~ 3.5	26.7 ~ 40	0.3 ~ 0.5
medium rockburst / class 3	120 ~ 180	5.5 ~ 2.5	3.5 ~ 5.0	14.5 ~ 26.7	0.5 ~ 0.7
strong rockburst /class 4	>180	<2.5	>5.0	<14.5	>0.7

3.3 Dimensionless the Evaluation Indices

In order to be convenient in the calculation, all evaluation indices must be dimensionless. A linear method is used here. The calculation methods are displayed in table 2.

Table 2 Dimensionless calculation method

Efficiency type(type 1)	Cost type(type 2)
$y=\begin{cases}1 & x\ge x_{\max}\\ \dfrac{x-x_{\min}}{x_{\max}-x_{\min}} & x_{\min}<x<x_{\max}\\ 0 & x\le x_{\min}\end{cases}$	$y=\begin{cases}1 & x\le x_{\min}\\ \dfrac{x_{\max}-x}{x_{\max}-x_{\min}} & x_{\min}<x<x_{\max}\\ 0 & x\ge x_{\max}\end{cases}$

Table 3 Extenics classification standards to signal factor

Rockburst Grade	R_c/MPa	R_c/σ_1	W_{et}	σ_c/σ_t	σ_θ/R_c
no rockburst / class 1	0 ~ 0.33	0 ~ 0.275	0 ~ 0.2	0 ~ 0.2	0 ~ 0.3
weak rockburst / class 2	0.33 ~ 0.5	0.275 ~ 0.725	0.2 ~ 0.35	0.2 ~ 0.466	0.3 ~ 0.5
medium rockburst / class 3	0.5 ~ 0.67	0.725 ~ 0.875	0.35 ~ 0.5	0.466 ~ 0.71	0.5 ~ 0.7
strong rockburst /class 4	0.67 ~ 1	0.875 ~ 1	0.5 ~ 1	0.71 ~ 1	0.7 ~ 1

R_c ,W_{et} , σ_θ/R_c belongs to type 1 and R_c/σ_1 , σ_c/σ_t belongs to type 2 for the chosen indices. Table 3 is the extenics classification standards by dimensionlessing the evaluation indices according to the formula.

3.4 Determine the Indices To Be Evaluated

3.4.1 Field Rock Mechanical Experiments

A field rock mechanical experiment lab was built at the construction site in order to forecast rockburst better. We test rock uniaxis compressive strength; Elastic deformation energy index; tensile strength (using brazilian split test) using a type GAW-1000 electro-hydraulic servo rock stiff test machine. Four groups of blocks are collected from the four part of the chamber, and nine specimens are processed from each group. The first three specimens are used in the rock uniaxis compressive strength test, the middle three are used in the elastic deformation energy index test, and the last three are used in the tensile strength test. Results are shown in table4.

Table 4 Measured value of the lithologic parameters

NO	R_c/MPa				W_{et}				σ_t/MPa			
	Measured value			Average value	Measured value			Average value	Measured value			Average value
1	151.14	157.22	160.34	156.23	4.31	4.21	3.89	4.14	8.98	11.61	10.95	10.51
2	148.21	158.4	161.8	156.14	3.57	4.42	4.13	4.04	8.86	12.3	9.74	10.3
3	153.66	155.58	162.77	157.34	4.61	4.11	4.06	4.26	11.18	10.36	10.1	10.55
4	146.31	160.83	159.74	155.63	4.4	4.1	4.1	4.2	10.03	10.48	10.76	10.42

3.4.2 Geostress Measurement Using Hollow Inclusion Method and FEM Simulation

A supplement geostress measurement using hollow inclusion method was done in the main-transformed chamber. The measured value is the secondary stress field because of the excavation. So that a back analysis of initial stress field combing FEM and neural network is adopted [10]. The hollow inclusions used are type KX-81 which are produced by Geomechanics Institute.

A back analysis of initial stress field combing FEM and neural network is adopted according to the results. Figure 1 is the three-dimensional model finite element mesh. Tangential stress of the chamber is calculated as a plane strain problem in this paper and Figure 2 is the finite element mesh. The calculated value of tangential stress is 16.4MPa.

The evaluation indices and its dimensionless values are listed in table 5.

Figure 1 Three-dimensional model finite element mesh

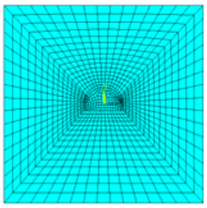

Figure 2 Plane finite element mesh

Table 5 Evaluation indices and it's dimensionless values

NO.	R_c/MPa	R_c/σ_1	W_{et}	σ_c/σ_t	σ_θ/R_c
1	156.23(0.651)	10.30 (0.485)	4.14(0.414)	14.86(0.703)	0.105 (0.105)
2	156.14(0.651)	10.293(0.485)	4.04(0.404)	15.159(0.697)	0.105(0.105)
3	157.34(0.656)	10.372(0.481)	4.26(0.426)	14.918(0.702)	0.104(0.104)
4	155.63(0.648)	10.259(0.487)	4.20(0.420)	14.931(0.701)	0.105(0.105)

3.5 Matter-Element Model for the Rockburst Prediction

The grades no rockburst; weak rockburst; medium rockburst; strong rockburst are recorded as N_{01}; N_{02}; N_{03}; N_{04}, and the evaluation indices R_c, R_c/σ_1, W_{et}, σ_c/σ_t, σ_θ/R_c are recorded as C_1, C_2, C_3, C_4, C_5. The matter-element can be expressed as below

$$R=(N,C,V)=\begin{vmatrix} N & C_1 & V_1 \\ & C_2 & V_2 \\ & C_3 & V_3 \\ & C_4 & V_4 \\ & C_5 & V_5 \end{vmatrix} \tag{1}$$

The classical matter-element can be constructed according to table 3.

$$R_{01}=(N,C,V_{01})=\begin{vmatrix} N_{01} & C_1 & \langle 0.000,0.330\rangle \\ & C_2 & \langle 0.000,0.275\rangle \\ & C_3 & \langle 0.000,0.200\rangle \\ & C_4 & \langle 0.000,0.200\rangle \\ & C_5 & \langle 0.000,0.300\rangle \end{vmatrix} \quad R_{02}=(N,C,V_{02})=\begin{vmatrix} N_{02} & C_1 & \langle 0.330,0.500\rangle \\ & C_2 & \langle 0.275,0.725\rangle \\ & C_3 & \langle 0.200,0.350\rangle \\ & C_4 & \langle 0.200,0.466\rangle \\ & C_5 & \langle 0.300,0.500\rangle \end{vmatrix} \tag{2}$$

$$R_{03}=(N,C,V_{03})=\begin{vmatrix} N_{03} & C_1 & \langle 0.500,0.670\rangle \\ & C_2 & \langle 0.725,0.875\rangle \\ & C_3 & \langle 0.350,0.500\rangle \\ & C_4 & \langle 0.466,0.710\rangle \\ & C_5 & \langle 0.500,0.700\rangle \end{vmatrix} \quad R_{04}=(N,C,V_{04})=\begin{vmatrix} N_{04} & C_1 & \langle 0.670,1.000\rangle \\ & C_2 & \langle 0.875,1.000\rangle \\ & C_3 & \langle 0.500,1.000\rangle \\ & C_4 & \langle 0.710,1.000\rangle \\ & C_5 & \langle 0.700,1.000\rangle \end{vmatrix} \tag{3}$$

And the controlled matter-element is :

$$R_p = (P, C, V_p) = \begin{vmatrix} P & C_1 & \langle 0.000, 1.000\rangle \\ & C_2 & \langle 0.000, 1.000\rangle \\ & C_3 & \langle 0.000, 1.000\rangle \\ & C_4 & \langle 0.000, 1.000\rangle \\ & C_5 & \langle 0.000, 1.000\rangle \end{vmatrix} \tag{4}$$

And the matter-element to be evaluated is displayed according to table 5.

$$R_1 = (P, C, V) = \begin{vmatrix} P & C_1 & \langle 0.651\rangle \\ & C_2 & \langle 0.485\rangle \\ & C_3 & \langle 0.414\rangle \\ & C_4 & \langle 0.703\rangle \\ & C_5 & \langle 0.105\rangle \end{vmatrix} \quad R_2 = (P, C, V) = \begin{vmatrix} P & C_1 & \langle 0.651\rangle \\ & C_2 & \langle 0.485\rangle \\ & C_3 & \langle 0.404\rangle \\ & C_4 & \langle 0.697\rangle \\ & C_5 & \langle 0.105\rangle \end{vmatrix} \tag{5}$$

$$R_3 = (P, C, V) = \begin{vmatrix} P & C_1 & \langle 0.656\rangle \\ & C_2 & \langle 0.481\rangle \\ & C_3 & \langle 0.426\rangle \\ & C_4 & \langle 0.702\rangle \\ & C_5 & \langle 0.104\rangle \end{vmatrix} \quad R_4 = (P, C, V) = \begin{vmatrix} P & C_1 & \langle 0.648\rangle \\ & C_2 & \langle 0.487\rangle \\ & C_3 & \langle 0.420\rangle \\ & C_4 & \langle 0.701\rangle \\ & C_5 & \langle 0.105\rangle \end{vmatrix} \tag{6}$$

3.6 Weights

Different indices have different contribution to the final results, so that we must give different weight to each index. Indices with larger weights have high level of importance. There are a lot of methods getting weights such as AHP; grey relation degree method; neural network method; rough set theory etc. A simple correlation function method is used here in order to confirm the weights.

Let

$$r_{0ji}(v_i, V_{0ji}) = \begin{cases} \dfrac{2(v_i - a_{0ji})}{(b_{0ji} - a_{0ji})} & v_i \le \dfrac{a_{0ji} + b_{0ji}}{2} \\ \dfrac{2(b_{0ji} - v_i)}{b_{0ji} - a_{0ji}} & v_i > \dfrac{a_{0ji} + b_{0ji}}{2} \end{cases} \qquad (i = 1, 2, 3 \cdots n;\ j = 1, 2, 3 \cdots m) \tag{7}$$

And $v_i \in V_{pi}$ (the controlled field and $i = 1, 2, 3 \cdots n$), so that

$$r_{0j\max}(v_i, V_{0j\max}) = \max_{j=1}^{m} \{ r_{0ji}(v_i, V_{0ji}) \} \tag{8}$$

Some index should be given larger weight if data of index i fall into larger category. So

$$r_i = \begin{cases} j_{\max} \times (1 + r_{0j\max i}(v_i, V_{0j\max i})) & if \quad r_{0j\max i}(v_i, V_{0j\max i}) \ge -0.5 \\ j_{\max} \times 0.5 & if \quad r_{0j\max i}(v_i, V_{0j\max i}) < -0.5 \end{cases} \tag{9}$$

Otherwise, some index should be given smaller weight. So that

$$r_i = \begin{cases} (m - j_{\max} + 1) \times (1 + r_{0j\max i}(v_i, V_{0j\max i})) & if \quad r_{0j\max i}(v_i, V_{0j\max i}) \geq -0.5 \\ (m - j_{\max} + 1) \times 0.5 & if \quad r_{0j\max i}(v_i, V_{0j\max i}) < -0.5 \end{cases} \tag{10}$$

$$\text{Weight of } i \text{ is } \alpha_i = r_i \Big/ \sum_{i=1}^{n} r_i \text{ , and } \sum_{i=1}^{n} \alpha_i = 1 \tag{11}$$

Weights to the evaluation indices can be calculated as

$$W = \begin{pmatrix} 0.204278 & 0.215104 & 0.309305 & 0.176741 & 0.094572 \\ 0.207749 & 0.218149 & 0.290882 & 0.187387 & 0.095833 \\ 0.192767 & 0.210668 & 0.327429 & 0.176107 & 0.093028 \\ 0.204841 & 0.211628 & 0.315953 & 0.174971 & 0.092607 \end{pmatrix} \tag{12}$$

3.7 Results of the Extensible Comprehensive Evaluation

According to the formula of Correlation degree and evaluation grade, also consider weights to the evaluation indices, the extensible comprehensive evaluation results are shown in table 6.

Table 6 The extensible comprehensive evaluation results

NO.	$K_1(N_i)$	$K_2(N_i)$	$K_3(N_i)$	$K_4(N_i)$	$Max(K_1(N_i) - K_4(N_i))$	eigenvalue	evaluation result	actual situation
1	-0.3386	-0.0489	0.0004	-0.2849	0.0004	2.9148	Class 3	Weak to medium
2	-0.3486	-0.0787	0.0155	-0.2832	0.0155	2.8898	Class 3	Weak to medium
3	-0.3271	-0.0224	-0.0086	-0.2894	-0.0086	2.9455	Class 3	medium
4	-0.3327	-0.0268	-0.0016	-0.2865	-0.0016	2.9257	Class 3	medium

We can see from the eigenvalue that the evaluation results are class 3 bias class 2. Weak and medium rockburst occurred frequently during initial construction in the main-transformed chamber and the locations are concentrated in side wall and spandrel. Figure 3 shows flake fall-block and obvious blasting pit during a medium rockburst occurred in the right side wall. Fresh rock can be seen in the blasting pit. There are stress release area; stress concentration area and stress normal area from outside to inside for gully terrain. We can analyze from the measured geostress that tectonic stress is relatively large, and the main-transformed chamber is just in the edge of this area. In addition, the surrounding rock is very hard, so that rockburst occurred in this relative shallow chamber. The result using extension comprehensive evaluation is coinciding with the actual situation.

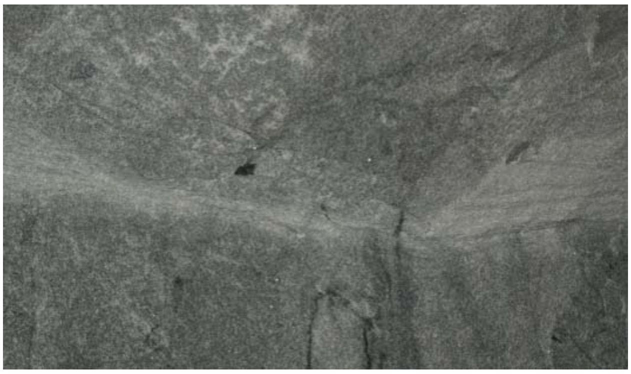

Figure 3 Flake fall-block and obvious blasting pit at the spandrel

4 Conclusions

(1) The evaluation results are generally coinciding to the actual situation, so that extensible comprehensive evaluation is reliable in rockburst prediction.

(2)Generally people think that a relative shallow chamber like this main-transformed chamber is no rockburst, but the evaluation and the actual situation is different. It means that the occurrence and the grade of rockburst in a relatively shallow chamber has little relationship to buried depth. Rockburst can also occur in relative shallow chambers under some conditions.

(3)As the influencing factors are not the same to different chambers, extensible comprehensive evaluation can establish the model by choosing evaluation indices pertinently, especially the field experiment factors.

(4)The prediction method and the results are useful to rockburst prediction of chambers in gully terrain.

Acknowledgements

The authors wish to acknowledge the collaborative funding support from the National Basic Research Program of China (NO: 2009CB724607) and Natural Science Foundation of Shandong Province (Y2007F53).

References

1. Tao, Z.Y. Rockburst and Evaluation Method in High Ground Stress Field. Yangtze River, 1987, (5) 25-32.
2. Wang, Y.H.,Li, W.D., Li, Q.G. etc, Method of Fuzzy Comprehensive Evaluations for Rockburst Prediction. Chinese Journal of Rock Mechanics and Engineering, 1998, 17(5). 493-501.
3. Qian, Q.H., Li, S.C. A Review of Research on Zonal Disintegration Phenomenon in Deep Rock Mass Engineering. Chinese Journal of Rock Mechanics and Engineering, 2008, 27(6). 1278-1284.
4. He, M.C., Miao, J.L., Li, D.J. etc, Experimental Study on Rockburst Processes of Granite Specimen at Great Depth. Chinese Journal of Rock Mechanics and Engineering, 2007, 26(5). 865-876
5. Hoek, E. and Brown, E. T. Underground Evaluation in Rock. Institute of Mining and Metallurgy, 1980.
6. Cai,W. Introduction of Extenics, Systems Engineering-Theory & Practice,1998(1)76-84.

7. Qiu, D.H., Chen, J.P., Zhang, B.H. and Xiao, Y.H. Study on Rockburst Prediction and Prevention in Deep and Over Length Highway Tunnel. Chinese Journal of Underground Space and Engineering, 2006, 2(6). 950-955.
8. Jia, C., Xiao, S.F. and Liu, N. Application of Extenics Theory to Evaluation of Tunnel Rock Quality. Chinese Journal of Rock Mechanics and Engineering, 2003, 22(5). 751-756.
9. Yuan, G.H., Chen, J.P. and Ma, L. Application of Extenics in Evaluating of Engineering Quality of Rock Masses. Chinese Journal of Rock Mechanics and Engineering, 2005, 24(9). 1539-1544.
10. Xu,B., Xie, H.P. and Tu, Y.J. Numerical Simulation of Rockburst Stress State during Excavation of underground Powerhouse of Pubugou Hydropower Station. Chinese Journal of Rock Mechanics and Engineering, 2007, 26(supp.1). 2895-2900.

*RaSiM 7(2009): Controlling Seismic Hazard and
Sustainable Development of Deep Mines,
C.A. Tang(ed), Rinton Press, 785-788*

ROCKBURST ANALYSIS BASED ON DAMAGE CRACK MODEL OF HYPOPLASTICITY

BAO-LIN XIONG and XI-LIANG WANG

Department of Civil Engineering, Shijiazhuang Railway Institute

Shijiazhuang, 050043, P.R. China

CHUN-JIAO LU

Department of Architecture and Art Design, Shijiazhuang Railway Institute

Shijiazhuang, 050043, P.R. China

Hypoplastic constitutive model is developed on the basis of nonlinear tensorial functions and without resorting to concepts of elasto-plasticity theory such as yield surface, plastic potential, flow and hardening rules, and decomposition of deformation into elastic and plastic parts. In this paper, based on the hypoplastic model, damage energy release rate is firstly deduced. By virtue of fracture criterion, damage evolution equation is then determined to analyze the propagating of crack in surrounding rock. Throughout this study, it is made clear that the unstable propagation of cracks is caused by the interaction between cracks and that free surface and then thin layers of rock mass are formed as a result of coalescence of cracks. Finally, formation mechanism of rockburst is concluded and the regularity of rockburst is explained quantitatively.

1 Introduction

Rockburst is the phenomenon of unstable propagation of cracks on excavating underground engineering. Rockbursts are a concern to many scholars because of how destructive they can be.[1,2]. By virtue of fracture mechanics and the elasto-plastic model, formation mechanism of rockburst is discussed.

Hypoplasticity appeared about 30 years ago as an alternative to elasto-plasticity for the description of the irreversible behaviour and has attracted the attention of many Geotechnical scholars [3,4]. The theory is based on nonlinear tensorial functions, and it is developed without recourse to the concepts in elasto-plastic theory such as yield surface, flow rule and the decomposition of the deformation into elastic and plastic parts[5].

This paper probes into the formation mechanism of rockburst based on the damage crack model of hypoplasticity. Initially based on hypoplasticity damage, energy release rate is established. With fracture criterion, the damage evolution equation is ascertained. Finally, the formation mechanism of rockburst is obtained by virtue of the evolution equation.

2 Hypoplasticity

Hypoplasticity is based on hypoelasticity and brought forward over plasticity. This theory thinks stress rate of material $\overset{\circ}{\sigma}$ is determined by the current stress σ and strain rate $\dot{\varepsilon}$ [6].

$$\overset{\circ}{\sigma} = H\left(\sigma, \dot{\varepsilon}\right) \tag{1}$$

Where $\overset{\circ}{\sigma}$ is the objective (Jaumann) stress rate tensor. The Jaumann stress rate is defined as:

$$\overset{\circ}{\sigma} = \dot{\sigma} + \sigma W - W\sigma \tag{2}$$

Where W is the spin tensors. The objective stress rate $\overset{\circ}{\sigma}$ corresponds to the time derivative of $\dot{\sigma}$ only in case of no rotation of principal stress axes.

Kolymbas created basic equation of hypoplasticity in 1991. He uses simple nonlinear tensor function to simulate behavior of nonelastic material.

$$\dot{\sigma} = L(\sigma, \dot{\varepsilon}) + N(\sigma)\|\dot{\varepsilon}\| \tag{3}$$

Where $\|\cdot\|$ is Euclidean norm. Eq. (3) consists of two parts, namely a linear tensorial function $L(\sigma, \dot{\varepsilon})$ in $\dot{\varepsilon}$ and a nonlinear function $N(\sigma)$ in $\dot{\varepsilon}$. As compared with elasto-plasticity theory, hypoplastic constitutive models are incrementally nonlinear. Note that the definition of loading and unloading is relative for the hypoplastic constitutive equation, since the nonlinear part always works for both loading and unloading[7].

3 Damage Crack Model of Hypoplasticity

Consider a spherical cavity which expands quasi-statically and symmetrically in an infinite or finite body starting from an initial radius r_a^0. If the body is finite, it is bounded by an outer sphere concentric with the cavity. In the spherical coordinates r, θ, φ, the symmetric expansion of a cavity is described by the velocity component v_r and the stress components σ_{rr}, $\sigma_{\theta\theta} = \sigma_{\varphi\varphi}$. All these quantities are functions of radius r and time t. The stretching tensor has three nonzero components $\dot{\varepsilon}_{rr} = \dfrac{\partial v_r}{\partial r}$ and $\dot{\varepsilon}_{\theta\theta} = \dot{\varepsilon}_{\varphi\varphi}$. For brevity, we will write $\sigma_r, \sigma_\theta, v$ instead of $\sigma_{rr}, \sigma_{\theta\theta}, v_r$.

Under the assumed symmetry, the process of deformation is governed by a system of three first-order partial differential equations for three unknown functions v, σ_r, σ_θ. The system consists of the equilibrium equation

$$\frac{\partial \sigma_r}{\partial r} + \frac{2}{r}(\sigma_r - \sigma_\theta) = 0 \tag{4}$$

The constitutive equations

$$\frac{\partial \sigma_r}{\partial t} + v\frac{\partial \sigma_r}{\partial r} = H_r\left(\sigma_r, \sigma_\theta, \frac{\partial v}{\partial r}, \frac{v}{r}\right) \tag{5}$$

$$\frac{\partial \sigma_\theta}{\partial t} + v\frac{\partial \sigma_\theta}{\partial r} = H_\theta\left(\sigma_r, \sigma_\theta, \frac{\partial v}{\partial r}, \frac{v}{r}\right) \tag{6}$$

The boundary value problem formulated above is solved numerically by a finite-difference technique.

Differentiating the equilibrium equation (4) with respect to time and using the constitutive equations (5), (6), we obtain the equation

$$\frac{\partial H_r}{\partial r} + \frac{2}{r}(H_r - H_\theta) + \frac{\partial T_r}{\partial r}\left(\frac{v}{r} - \frac{\partial v}{\partial r}\right) = 0 \tag{7}$$

With respect to the velocity $v(r,t)$ as a function of r at a fixed t, this is a second-order ordinary differential equation. Given $\sigma_r(r,t)$, $\sigma_\theta(r,t)$ at a time t, the velocity $v(r,t)$ as a function of radius can be calculated by the integration of this equation with the use of two boundary conditions expressed in terms of velocity and its gradient $\frac{\partial v}{\partial r}$.

To integrate equations (18)-(20), the same implicit scheme is applied as for the spatial integration:

$$\sigma_r^{i+1} = \sigma_r^i + \frac{1}{2}\left(\dot{\sigma}_r^i + \dot{\sigma}_r^{i+1}\right)\Delta t \tag{8}$$

$$\sigma_\theta^{i+1} = \sigma_\theta^i + \frac{1}{2}\left(\dot{\sigma}_\theta^i + \dot{\sigma}_\theta^{i+1}\right)\Delta t \tag{9}$$

Equations(8)-(9) are written for a given material point. The co-ordinates of the material points are updated by the integration of the velocity

$$r^{i+1} = r^i + \frac{1}{2}\left(v^i + v^{i+1}\right) \tag{10}$$

When underground cavern is excavated, secondary stress field is formed by stress intensity or stress relaxation induced by adjusting stress of surrounding rock. The tangent stress σ_θ is increased and the radial stress σ_r is reduced. Under secondary stress field, crack of surrounding rock will develop. The mechanic model is shown in Figure 1.

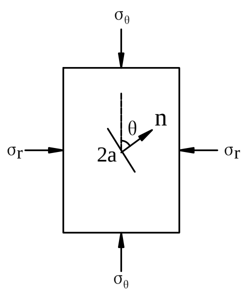

Figure 1 The stress model of crack in surrounding rock mass

The normal stress and effective shear stress in any crack is followed.

$$\sigma_n = \sigma_r \sin^2\theta + \sigma_\theta \cos^2\theta \tag{11}$$

$$\tau = F(\theta)\left[\sigma_\theta - \left(1 + \frac{\mu}{F(\theta)}\right)\sigma_r\right] \tag{12}$$

Where $F(\theta) = \sin\theta\cos\theta - \mu\cos^2\theta$. μ is frictional factor on crack face. In adjusting stress of surrounding rock, with increasing tangent stress σ_θ and reducing radial stress σ_r, frictional slippage of crack will happen when the effective shear stress on crack face τ satisfies $\tau \geq 0$ (that is $\sigma_\theta \geq \left(1 + \frac{\mu}{F(\theta)}\right)\sigma_r$)

$$\sigma_\theta = \frac{\sqrt{3}K_{1c}}{2F(\theta)\sqrt{\pi a}} + \left(1 + \frac{\mu}{F(\theta)}\right)\sigma_r \tag{13}$$

Where K_{1c} is rupture tenacity of rock. Driving force of crack enlarging is shearing force T:

$$T = 2a\tau = 2aF(\theta)\left[\sigma_\theta - \left(1 + \frac{\mu}{F(\theta)}\right)\sigma_r\right] \tag{14}$$

4 Rockburst Analysis

Crack enlarges with increasing of σ_θ and reducing of σ_r and develops parallel to direction of maximum principal stress. The relationship of l over stress field is:

$$K_1 = \frac{2a\tau\cos\theta}{\sqrt{\pi l}} - \sqrt{\pi l}\sigma_r \geq K_{1c} \tag{15}$$

By virtue of analysis of Dyskin and Germanovich [8], factor of stress intensity considering reciprocity of crack and free surface is obtained:

$$K_1 = \frac{2a\tau\cos\theta}{\sqrt{\pi l}} - \sigma_r\sqrt{\pi l} + \frac{3a\tau\cos\theta l^{3/2}}{h^2\sqrt{\pi}} - \frac{3l^2}{2h^2}\sigma_r\sqrt{\pi l} \geq K_{1c} \tag{16}$$

According to dipole asymptotic method and numerical analysis, Dyskin and Germanovich gain the condition that rockburst does not happen in rock.

$$\sigma_r \geq 0.199\frac{a}{h}\sigma_\theta \tag{17}$$

Where h is thickens of slice terrane. When timbering stress of surrounding rock σ_r is satisfied with equation (12), surrounding rock does not burst.

5 Conclusions

Formation mechanism of rockburst is: after excavating underground engineering, adjusting stress of surrounding rock (increasing of the tangent stress and reducing of the radial stress) induces the development of cracks in surrounding rock, and produces rock unstable propagation of cracks and forms brittle fracture of surrounding rock.

When σ_r, σ_θ satisfies $\sigma_r \geq 0.199\frac{a}{h}\sigma_\theta$, surrounding rock does not burst. Timbering criterion of surrounding rock is provided.

References

1. Zhou, R.Z. Regularitv of Rock Bursts and its Analysis Based on Fracture Mechanics. Chinese Journal of Geotechnical Engineering, 1995, 17(6). 111-117.
2. Li, G.P. The Mechanism of Compression-Shear Damage for Rock Mass with its Application to Rockburst. Chinese Journal of Geotechnical Engineering, 1997, 19(6).49-55.
3. Dafalias, Y.F. Bounding Surface Plasticity, I: Mathematical Foundation and Hypoplasticity. Engineering Mechanics, ASCE, 1986, 112(9).966-987.
4. Kolymbas, D. An Outline of Hypoplasticity. Archive of Applied Mechanics, 1991, 61(2). 143-151.
5. Wu, W. and Kolymbas, D. Numerical Testing of the Stability Criterion for Hypoplastic Constitutive Equations. Mechanics of Materials, 1990, 9(4). 245-253.
6. Kolymbas, D. A Novel Constitutive Law for Soils. Second International Conference on Constitutive Laws for Engineering Materials: Theory and Applications, Tucson, (Arizona, 1987).
7. Wu, W., Bauer, E. and Kolymbas, D. Hypoplastic Constitutive Model with Critical State for Granular Materials. Mechanics of Materials, 1996, 23(1).45-69.
8. Dyskin, A.V. and Germanovlch, L.N. Model of Roekbursts Cuused by Craeks Growing Neau Free Surface. Rockbursts and Seismicity in Mines, (Rotterdam, 1993).

*RaSiM 7(2009): Controlling Seismic Hazard and
Sustainable Development of Deep Mines,
C.A. Tang(ed), Rinton Press, 789-796*

RESEARCH ON STABILITY OF SURROUNDING ROCK AND OPTIMAL DESIGN OF SUPPORTING MEASURES OF DEEPLY BURIED LONG TUNNELS

JI-XUN ZHANG, XU-HUA REN, HONG-DAO JIANG and HAI-JUN WANG

College of Water Conservancy and Hydropower Engineering, HohaiUniversity

Nanjing, 210098, P.R. China

High external water pressure and high ground stress are common engineering problems in underground construction in water-rich areas in southwest China. This paper first analyzes the main geological engineering problems of the Jinping II Hydropower Station, followed by the analysis of the excavation methods and the tunnel stability based on the theory of elastic and plastic damage using FEM. An analytical method of the anchorage support and a 3-D nonlinear damage analysis method of the wall rock in the large derivation tunnels are proposed. Random distribution of the mechanical parameters is adopted in the analysis. A local sub-model is introduced to simulate the karst channel and to analyze the influence of external water pressure. The research of the optimal rock support design focuses on tunnel stability and penetrability. Finally, an estimation method for structural reinforcement requirement is suggested and a rock support design proposed.

1 Main Engineering Geological Problems of the Long Deep Buried Tunnel

1.1 Stability of Wall Rock in High Geo-Stress[1]

Wall rock stability is the deformation and damage characteristics of the wall rock after construction, which is related to the construction method of the tunnel. The main influencing factors on the wall rock stability are the geology and engineering practices. The geology factors include formation lithology, geologic structure, ground water, and geo-stress. These factors determine the quality of the geological environment including the wall rock. The engineering factors refer to the shape and size of the tunnel, construction method, and relationship between the tunnel axis and various types of structural planes.

Substantial measured geo-stress data indicates that the level of the geo-stress is mainly related to the depth, geologic structure and lithology. Generally speaking, the accumulation of energy and the geo-stress level of the rock are directly proportional to the depth, hardness, and integrity of the rock. Magmatic rock is formed by magma, so the geo-stress of that rock is high while the difference between the major principal stress and the minor principal stress is also very large. The maximum geo-stress is more than 42MPa in the area where the Jinping II Hydropower Station diversion tunnel is located. While the underground powerhouse of the Laxiwa Hydropower Station (under construction) has a stress of 29.6 MPa. Lastly the underground powerhouse of the

Jinping I Hydropower Station, which belongs to a high geo-stress area, has a maximum geo-stress value of 37.5MPa. The compression stress in some parts of the tunnel in the West Route of South-North Water Transfer Project will be about 50MPa. The possibility of rock burst there is very high because the wall rock stress is redistributed from the high geo-stress condition. Severe rock burst may bring casualties and cause personal injury, thus the complication the construction.

The traditional theory of the supporting structure can not apply to high geo-stress areas. Therefore, it is necessary and urgent to study the theory of combined bearing support structures and main bearing wall rock in the design and construction of high geo-stress areas.

1.2 High External Water Pressure and Water Burst

The initial state of the ground water before tunnel excavation is the natural state of the rock; it is very important to the analysis of seepage control and structure computation. The distribution of the initial seepage field is affected by the lithology, geological structure, ground water dynamic conditions, topography, neo-tectonics and karst.

The topographical conditions are complex. Carbonate rocks are widely distributed and groundwater is active in the area of the Jinping Ⅱ Hydropower Station diversion tunnel. The deeply-buried long tunnel will inevitably encounter engineering problems such as high external water pressure and high geo-stress. In the construction of the trial tunnel (5km-long auxiliary tunnel), water burst happened. The maximum water volume of a single point is 4.91m^3/s, and the stable flow rate is 2-3 m^3/s; the maximum water pressure after plugging is 10.2MPa; the measured maximum major principal stress a depth of 1843m is 42.11MPa (in the long trial tunnel). However, the trial tunnel has not reached its maximum depth, so the external water pressure and the major principal stress are expected to be higher and possibility of water burst is expected to be much higher. There is no such deep-seated tunnel in the world by the action of such a high external water pressure, so it brings a great challenge to design and construct a diversion tunnel.

Until August 2008, the two auxiliary tunnels that were constructed in advance have run-through. According to the data, the maximum water inflow rate on the eastern end was 8.12 m^3/s, the minimum was 5.1 m^3/s, the average was 6.42 m^3/s. On the western end, the respective rates were 1.61 m^3/s, 0.98 m^3/s and 1.3 m^3/s. The average water inflow of the two auxiliary tunnels was 7.72 m^3/s. From the hydro-geological conditions, we can predict that the water inflow rate in the proposed diversion tunnel would be similar to the trial tunnel which had a high water head and large water inflow rate. This can be seen from numerical analysis too. Therefore, the large water inflow and high external water pressure on the lining structure are prominent issues in the construction of the tunnel, possibly with larger stable inflow and instantaneous inflow in single point.

It is generally believed that a tunnel is a high-pressure tunnel when its water head exceeds 10m. It is impossible to hold such a big water head entirely by reinforced concrete lining. During the design of the lining structure in China, there are two methods to deal with the high external water pressure: the theory of permeable lining and the theory of impermeable lining. Considering the flow field analysis in project area, we proposed “ limit emissions measures” which can not only meet the need of project running, but also the need of construction, and is a very effective way to deal with external water.

2 Overview of the Jinping II Hydropower Station Diversion Tunnel

The maximum flow rate of the diversion tunnel is 465 m^3/s, the diameter of the reinforced concrete lining is 11.8m (with the horseshoe-shaped cross-section) and the velocity is 4.11m/s. The diameter of the lock bolt support woth shotcrete is 12.6m (with the horseshoe-shaped cross-section). 80° of the concrete lining at the bottom is covered by the reinforced concrete and has a velocity of 3.77m/s. The full route is very deep, with an average depth of 1500-2000m, the deepest being 2525m. The two auxiliary tunnels are located on the southern side of and parallel to the diversion tunnel, 65m from it. The longitudinal slope of the auxiliary is a "person shape" one, able to drain freely. Its western intake is 1657m high, eastern outlet 1557.896m and highest point 1676.75m (in the middle). The geological profile of the project zone is shown in Figure 1.

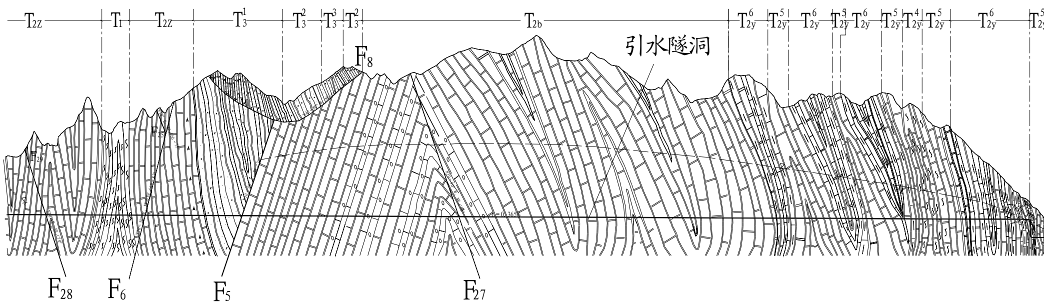

Figure 1 Profile of the diversion tunnel

The region is characterized by the exposed type deep mountain gorge karst area and the major precipitation recharge acceptance. The stratum of karst and non-karst are distributed in a NNE direction while the former is mainly located in the middle part of the Jinping Mountain (later in the east and west side of the mountain).

3 Seepage Analysis

3.1 Karst Features of the Project Zone

The hydro-geological contour of the Jinping region is clear, but the migration of karst groundwater is very complex, especially the groundwater circulation-flow in walley slop zone of Yalongjiang. Below an elevation of 2000m, karst grows weakly using a vertical system. Deep karst have the faults that the directions are NEE and NWW and also the corrosive fissures in the intersection zone. To be specific, the stratigraphic karsts of Yantang in East are solubilisation fissures and the depth of karst development has reached the elevation of Yalong River. The karst at the elevation of the tunnel-line has small and medium-sized solubilisation fissures which seems more severe than what was shown in the longer exploration hole. The degree of the Xidali rock is similar to that of the Yantang under the influence of karst formations. The marble karsts of the central Baishan have medium-sized solubilisation fissures. As it is dominated by the depth of the groundwater cycle (which comes from two main springs), the karsts develop weakly below an elevation of 1730m-1870m. Therefore, we can see that the majority of karsts along the division tunnel (at an elevation of 1600m) are corrosive fissures and a few corrosive holes with little scale. Presently, the features of karst development in auxiliary tunnels are as follows:

①There is a difference between auxiliary tunnel A and B: tunnel B develops more karsts than A. ②Karsts have some rules in the horizontal direction. The small-scale corrosive fissures in T2y5 stratum all developed around Dashuigou, which means that karsts concentrate relatively. During the rainy season, the corrosive tunnels connect with surface runoff from Dashuigou. Yet at a depth of 800m (northwest of Dashuigou), solubilisation fissures and small solubilisation holes are the main karsts (which develop relatively weaker when they are deeper). Karsts develop towards structural plane of steep angles mainly NEE-NWW, NNE-NNW. The main karsts are small vertical karsts tunnels and there are no large-scale typical karsts (such as underground river or hall-style).

3.2 Calculated Analysis Model and Conditions

A three-dimensional calculation model comprehensively takes into account the complex geological conditions and topography of the Jinping II project zone and its developing faults, rumples and joints. The above mentioned factors are also considered in the generalization of a geological mechanical model and calculation of regional landforms of this model [2]. A space 8-node hexahedron solid element is adopted and a sub-model was used in the position of karst tunnels so as to avoid network singularity caused by the excessive difference of unit size on all sides. All the faults and dykes adopt a hexahedral element as their simulation model. The auxiliary tunnels and divisional tunnels are networked respectively for different ranges of grouting circles by the method of refining grids.

Analysis and calculations were made under the following conditions: initial seepage fields, seepage fields without support and seepage fields with support after tunnels were excavated. In the program of tunnel excavation with support, three strategies were proposed for analysis: impervious lining, permeable lining and limited permeable lining (which avoids deterioration of hydrological and hydro-geological conditions in the project zone).

3.3 Seepage Calculation Results

Under the condition that auxiliary tunnels were excavated and grouted and the wall rock of divisional tunnels were grouted with support, the highest groundwater level is ~1870m, the outer water-pressure of the grouting circle is 2.84Mpa and the hydraulic gradient of the inner grouting circle is 28.0 (along the direction of the transverse section of the largest tunnel T2b (cite 4#，8+880)). The groundwater levels of tunnels along the line can be seen in Table 1.

Table 1. Groundwater levels of tunnels along the line

Tunnel length(km)	0.00	3.150	5.556	7.92	8.880	10.238	12.764	15.78
Position head (m)	1642.8	1775.8	1826.7	1868.0	1845.5	1806.4	1752.4	1680.0

4 Wall Rock Stability Analysis of the Jinping II Hydropower Station Diversion Tunnel

4.1 Supporting Design

The design of the supporting diversion tunnel is based on the theory that rock bears loads (the load from loose rock circle, external and inner water pressure, etc). The carrying capacity of the wall rock is fully considered and in order to make the wall rock and the lock bolt support woth shotcrete work as a whole bearing structure, the measures of “lock bolt support woth shotcrete” and “high pressure consolidation grouting” are used during construction. For the diversion tunnel, these measures are propitious to the long-term stabilization of the wall rock while the high external pressure is mainly beard by the reinforced carrying ring of the wall rock. Thin concrete lining can only improve hydraulic conditions and prevent the weathering and washing-out of the wall rock.

4.2 The Computation Model

As studies have shown[3], the difference between deeply-buried rock and common rock lies in their mechanical properties. The traditional constitutive model is ineffective in simulating the damage range and depth of the hard rock in the high geo-stress area. For example, once the traditional elastic-plasticity constitutive model is applied during the wall rock stability analysis, a large yield region will exist in the final result because of the high geo-stress and high elastic modulus. This is not consistent with the actual conditions and is very costly to do. The CWFS constitutive model, proposed by V.Hajiabdolmajid, is adopted in the paper, and a program based on this model is also written and embedded into the flac3d, making the CWFS much more practical.

In order to reflect the heterogeneity of rock, the gridding of the tunnel structure is refined in some local parts. Wibull[4] random distribution is used in the parameter choice with a tension and compression ratio of 1:5 and friction angle Φ of 52º. The homogeneous degree of the elastic modulus is 6.0, the average value is 45000MPa, the homogeneous degree of intensity is 6.0, and the average value is 120MPa.

Several typical tunnel paragraphs are chosen in the calculation, including a 500m-long paragraph around the F5 faultage which is 4435m away from the intake; a 300m tunnel paragraph, which is 8880m away from the intake; and a 500m tunnel paragraph of the third type of wall rock which is 15200m away from the intake. The three local models are employed respectively corresponding to the 3-D numerical calculation of the second type of the wall rock, the third type of the wall rock and the F5 faultage (and the broken rock band around it). In the calculations, the calculation model and supporting structure is different (according to the difference of the requirements to the tunnel paragraphs). The mesh of the models and supporting structure are shown in Figure 2.

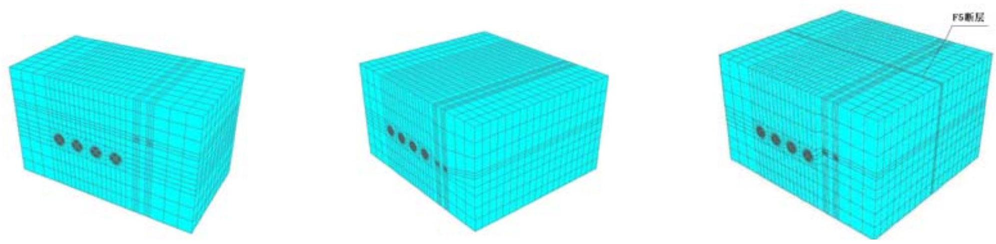

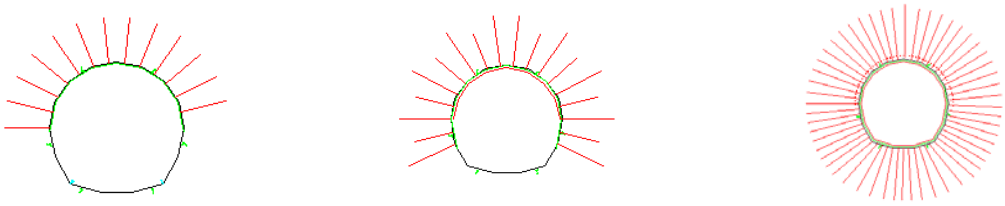

II type wall rock III type wall rock V type wall rock

Figure 2 Calculation model and support structure

4.3 The Solution of the Key Issues

In the calculation of the stability of wall rock and the supporting structure, the current calculation must be based on the previous data of seepage and geo-stress. When the data is cited, interpolation conversion is inevitable (as a result of the different requirements in every step of the calculation and different model and meshing). Therefore, the corresponding procedure is made in accordance with the following ideas: the improved Flac anchor unit [5] is adopted to simulate the reinforcement role of the anchor; and the parameter of the wall rock is enhanced in the grouting area. In order to find out the most reasonable time to do supporting, anchors are laid out in terms of the development of the displacement of wall rock.

4.4 Result Analysis

The results will be illustrated based on the class II adjacent rock. The distribution cloud chart of displacement and stress computed is shown in Figure 3.

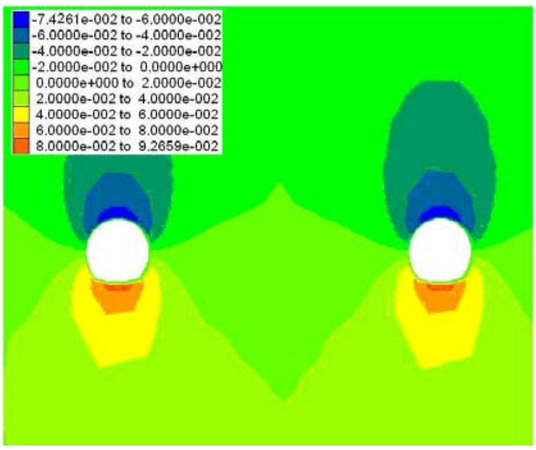

Figure 3 (a) The vertical displacement around the diversion tunnel after lining (m)

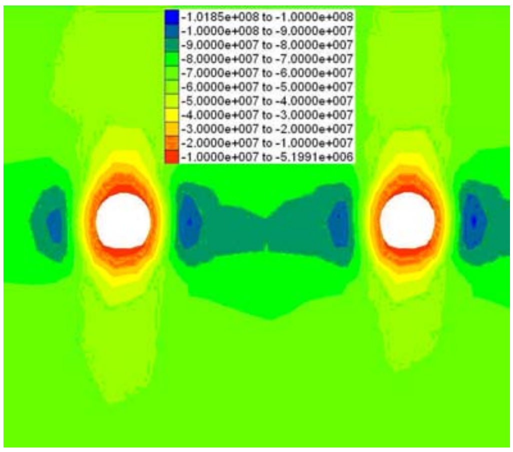

Figure 3 (b) The first principal stress around the diversion tunnel after lining(Pa)

After excavation and prior to lining, the maximum horizontal displacement is 4.98cm and the maximum vertical displacement is 7.45cm. Because the lining of the diversion tunnel begins after the deformation of adjacent rock is complete, the incremental displacement of the lining and rock is not so large. The maximum compressive stress of the vault is 72.5MPa and the maximum compressive stress of the arch feet and the bottom of the side wall is ~101MPa (occurring between the plastic expansion area and non-plastic expansion area; the impact of strength reduction is considered in the rock mass plastic zones). The stress of lining is small and the maximum stress is 1.5MPa. The plastic expansion area around the diversion tunnel ranges from 4.0m-6.0m and after lining, the plastic area ceased expanding.

Considering the groundwater, destruction scope and the depth of the diversion tunnel rock are greater than the case of no groundwater, with the increase scope of about 15% and 10%. The tunnel's tensile stress has reductions: the reduction scope is ~0.2MPa. The compressed stress has increases, the increase scope is ~2.5MPa. All these show that the high groundwater level indeed had a great impact on the stability of the tunnel. Therefore, in the actual construction process, we must take measures to control the range of groundwater outside the scope of the tunnel a certain distance away.

5 Conclusions

（1）The two main geological problems in deep tunnel projects in water-rich regions, high crustal stress and high external water pressure, may cause rock burst and gushing water. These must be studied to prevent negative influences on the stability of the surrounding rocks and support.

（2）Local sub-models are used to simulate karst pipes to find the motion law of ground-water of the karst zone as well as to provide reliable data of seepage for engineering design.

（3）The computational result found through the use of the CWF model to simulate the behavior of deep rock is close to the real situation.

（4）It is stable and safe for the deep and long tunnels of Jinping II to restrict and drain water, to take second high-pressure consolidation grouting after pre-grouting, and to combine surrounding grouted rock and tunnel liner support in order to bear the load and prevent external water pressure. It is also easy to ensure all required steps under the engineering technical levels.

Acknowledgements

Research on the Key Basic Problem of Jinping Project Exploitation and Development on Yalong River (50539090) State Natural Science Foundation committee.

References

1. Zhang, J.X., Ren, X.H., Jiang, H.D. and Wang, H.J. Main Geological Problems in Diversion Tunnel Construction at Jinping Second Class Waterpower Station. Advances in Science and Technology of Water Resources, 2006, (6). 66-70.
2. Ni, S.H. and Xiao, M. Study on Numerical Simulation of Drainage Hole of Seepage Field in Underground Engineering with Implicit Composite Element Method. Rock and Soil Mechanics, 2008, (06).1659-1664.
3. Chen, J.T. and Feng, X.T. Study on Constitutive Model for Hard Rock Under High Geostresses. Rock and Soil Mechanics, 2007, (11).2271-2278.
4. Liu, T.J., Zhu, H.H. and Tang, C.A. Finite Element Analysis on Damage Progress by the Unloading of Surrounding Rock and Stress Field Regulation. Underground Space, 2002, (04). 310-315.

5. Xu, P., Li, Y.P., Ding, X.L., et al, Secondary Development and Application of Visco-elastic Constitutive Model in FLAC(3D) Software. Journal of Yangtze River Scientific Research Institute, 2004, (2).10-13.

RaSiM 7(2009): Controlling Seismic Hazard and
Sustainable Development of Deep Mines,
C.A. Tang(ed), Rinton Press, 797-802

THE DECISION SYSTEM FOR DISASTERS MITIGATION IN DEEP MINE

XIAO-PING ZHANG, SI-JING WANG and GENG-YOU HAN

Institute of Geology and Geophysics，Chinese Academy of Sciences

Key Laboratory of Engineering Geomechanics, Institute of Geology and Geophysics, Chinese Academy of Sciences

Beijing, 100029，P.R. China

MEI LI

School of Earth and Space Sciences, Peking University

Beijing, 100029，P.R. China

Aimed at the requirement of informationization, integration, intellectualization and sharing geomechanics database of deep mine, the decision system for disasters mitigation in deep mine based on 3D geological information systerm, was developed. The frame design of the system was introduced in this article briefly, and the detailed functions were presented. The deep mine's stratum information, shaft, lane, stope, crustal stress, gas distribution, hydrogeology and monitoring information were collected. Furthermore the information was visualized through 3D platform in many different ways. This GIS system not only achieved the data Storage, manage, inquest, analysis, prediction and output graphic automatically, but also supported decision making for deep mine's excavation under the high crustal stress, high gas thickness and high seepage water pressure conditions.

1 Introduction

Currently, deep mining's dynamic disastrous events are becoming more and more frequent with the increase of mining depth and mining intensity, which causes a lot of damage and death. These dynamic disasters mainly include rock burst, gas outburst, gushing water, large deformation of the land, and earthquakes induced by mining. For finer solutions to be found, a comprehensive group involving mining engineers, scientists, and production managers is required, and an effective method involving qualitative and quantitative analysis is needed. So it's very important to offer a platform to provide a basic database for those different research groups. 3D geological information system, which integrates spatial data and attribute data together, is such a platform.

Mines are complex environments, including rock stratum, fault, crustal stress, hydrology as well as shaft, laneway, stope and many more. We can define these complex environments as Complex Giant System(CGS) because it is difficult to find exact solutions[1]. So far, metasynthetic method, combined qualitative analysis and quantitative analysis together, can only make the CGS problems well done [2].

3D geological information system of mines collects data from mine exploration to recovery and closure; including data from geological mapping, boreholes, rockmass characterization, rock engineering properties, orebody geometry delineation, excavation infrastructure layout design, support performance observations, seismicity, disaster events records, expert knowledge and so on. Fortunately, this data can be integrated and analysed properly by this system, and as a result, a real and vivid 3D mine full of information is shown on the computer screen. Only then we have a grasp of the global picture of a mine's performance [3]. The principle of this system is the metasynthetic method, and the system's implement process is show in figure 1.

3D geological information system platform, integrated virtue of both 3D GIS and 3D GMS, not only can express the geometric relation and topological relation of coal beds, lanes, etc., but also can show rock mass model by 3D mesh which offer a useful platform for geomechanics design of underground excavation and dynamic disasters mitigation.

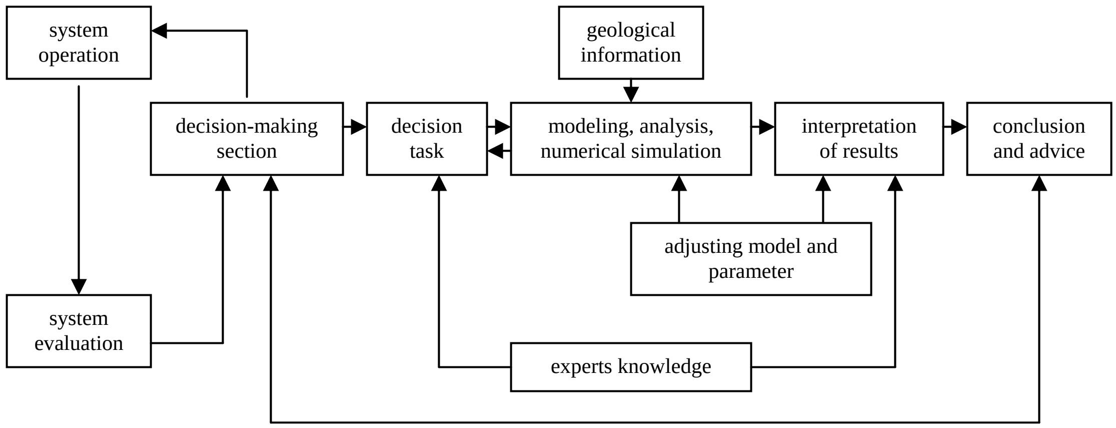

Figure 1 metasynthetic method's implement process

2 System Architecture Design

For the final goal of disaster mitigation, system architecture is designed as figure 2. The system is made up of three main modules: database module, 3D geological information system module and decision making module. Database module offers the basic information data for the system, 3D geological information system module carries out modelling and visualization for database, decision making module offers decision making approach and analysis for the basic information data, export advice for decision-making. The whole system is developed by VC++6.0, OpenGL and SQL Server 2000.

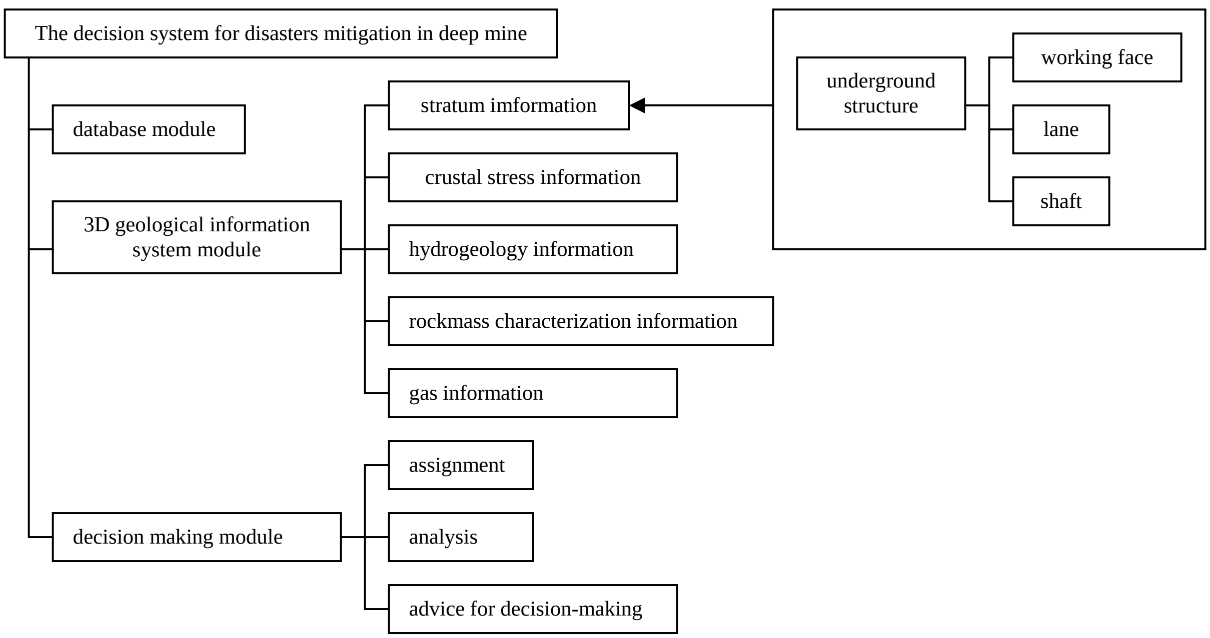

Figure 2 system architecture

Database module, the foundation of the whole system, offers geometry data for 3D geological model construction and offers attribute data such as crustal stress, hydrogeology and gas distribution for decision-making. Considering the actual demand, blended data model is adopted for the database. We storage 2D and 3D diagram in document files, and storage attribute data in database, this two parts make up the final database.

SQL Server 2000 is used to develop geological database, measurement database and deep mine's dynamic disaster information database. Geology database mainly includes information of exploratory lines, boreholes, coal seams, faults, stratum etc., can be input into the database and be managed orderly. Measurement database mainly includes data such as survey traverse and lane, and can calculate, check up and tidy up the survey traverse, estimate forward intersection and run-through and so on. Deep well dynamic disaster information database mainly realize the data input and data management of crustal stress, gas information and hydrology and so on.

3D geological information system module is the basic platform of decision making module, and it was developed by OpenGL and VC++6.0 from the bottom layer[4]. 3D visualisation with topological relation of coal seams, lanes, etc. can be established automatically through the geological information system based on database, rock mass was showed as many hexahedral element. Finally, after these steps, the whole 3D model of deep mine was established. Data and images can be rotated in any direction, magnified to various scales and sliced in arbitrary directions for detailed viewing, analyzing and interpreting.

Decision making module, based on the platform of 3D geological information system, offers functions including rockmass classification, gas distribution analysis, gushing water controlling and crustal stress analyzing, etc. to give advice for decision making.

3 System's Key Technology

3.1 Rock Stratum Modeling

We construct coal seam by the contour map of coal seam floor, but we can't construct rock stratum in the same way for the lack of contour map of stratum in deep mine. So we consider to discrete the space between coal seam to a series of hexahedron(fig 3), each hexahedron accompanied with attributes include lithology information, crustal stress, rockmass classification, hydrogeology information, as distribution information etc.. These attributes can be inquired easily according to it's position, and we can also choose an attribute to show the distribution with different colours[5,6].

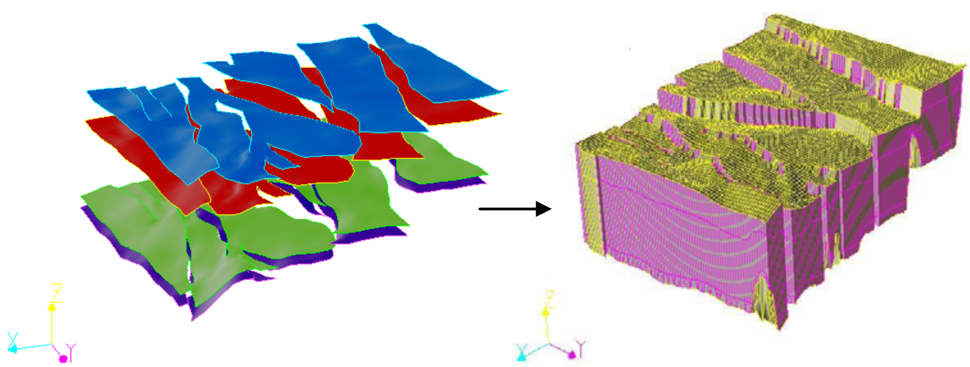

Figure 3 rock stratum between coal seam be discreted into cuboids

3.2 3D Buffer Zone

Buffer zone is the most important part of decision making module, we can pick-up hexahedron they concerned, obtain parameters such as crustal stress, gas, hydrogeology from the hexahedron. These parameters extracted from database offer for users to analysis. In coal mine, tunnel face of laneway, local lane or borehole etc. can be regarded as a buffer zone. A buffer zone produced by points or lines can meet the needs of deep mine's analysis. Figure 4 is a buffer zone around a laneway.

Instructions are input interactive to confirm spatial location which needed to analysis, then form the buffer zone, to analysis disasters in deep mine.

Key algorithm of the buffer zone analysis is how to searching related location in the underground 3D geological information system, then screen out the objects in buffer zone. After these objects being chosen, graph and attributes can be search out to service for analysis.

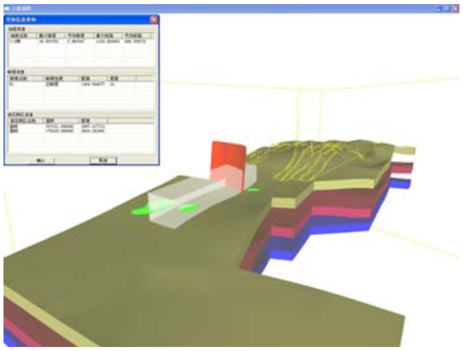

Figure 4 buffer zone around a laneway

3.3 Decision Making Module

In 3D VR system, data is often not structured and stored for interactive data analysis. Recent development in the software company(Datamine, FracSIS, GoCAD, etc.)has removed some of these obstacles and has paved the way for the use of VR in mining[7]. In this system, decision making module is the most important part for problems solving in deep mine.

The decision making flowsheet includes: (1)bringing forward assignments such as design a new laneway, setting stope, working face mining, rushing to deal with an emergency, etc.; (2)choosing analysis module; (3)anacoming the assignment and provide reports for decision making; (4)exporting model data for further numerical simulation in other professional software.

Decision making module mapping relation between data and decision, is a very effective method of analysis. Well chosen model can do good analysis of laneway supporting design, gush out prediction, gas outburst research, rock burst prediction without complicated numerical simulation, and finally qualitative or quantitative result would be offered for decision making. This simple method can be easily grasped by engineer in the field. Core of the analysis model can be the formula, logic comparison or expert judgment. The system offers different analysis methods for the same problem, user can examine the result with different methods.

System exports model data for further numerical simulation in other professional software, and the function always can be prepared for professional researcher to do further research.

3.4 Other Function

Data link , inquiring fuction and other edit functions. Data and images can be rotated in any direction, magnified to various scales and sliced in arbitrary directions for detailed viewing, analysis and interpretation. Figure 5 is the interface of this system.

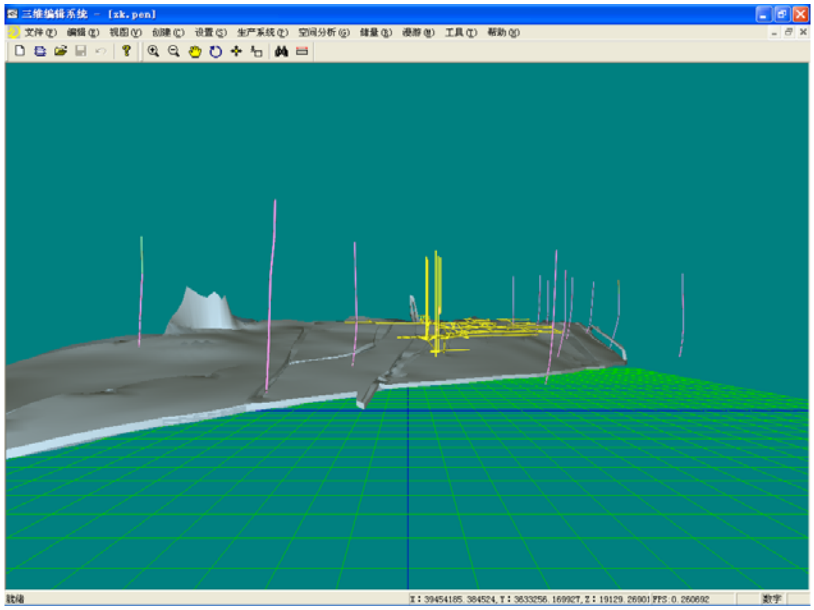

Figure 5 Interface of the system

5 Conclusions and Future Work

This paper introduces the main functions of the decision system for disasters mitigation in deep mines, and it can give some references to developers of similar decision systems. The benefits of this new systems to a mine are significant:

(1) Integration information management

Information includes geological mapping, boreholes, rockmass characterization, rock engineering properties, ore body geometry delineation, excavation and infrastructure layout design, support performance observations, seismicity, disaster events records, expert knowledge, and so on. All of this complex data is integrated together, and is a management success.

(2) 3D visualization of geomechanics data

3D visualization of geomechanics data from database, especially the stratum is discrete between coal seam to a series of hexahedron and show with attributes.

(3) Decision making in a deep mine

In the 3D platform, analysis and calculations can be done to offer helpful information for decision making. Systems can also export model data for further numerical simulation in other professional software, and the function is always be prepared for professional researcher to do further research.

Future work aims at establishing much better mapping relation between data and decision and at making a thorough investigation of rock stratum between coal seams. The application of the Logging technique in deep mines may provide more details of the rock stratum [8].

Acknowledgements

The authors are grateful to Professors Liu Quansheng, Mao Shanjun for kind cooperation in system develop programs. Many thanks are to give to Dr Ye Genxi, Zhang Shiping, LiLi, Qian Haitao for help.

References

1. Liu, D.A., Yang, Z.F. and Ke, T.H. Synthetic Geology Information System and Its Application in the shiplock Slope Engineering of a Hydropower Station. Chinese Jounal of Geotechnical Engineering, 2000, (02). 182-185.
2. Qian, X.S., Yu, J.Y. and Dai, R.W. A New Science Frontier - Opening Complex Giant System and Methodology. Nature Magazine, 1990, 13(1). 3-10.
3. McCormick, B. H., DeFanti, T. A. and Brown (eds.), M. D. Visualization in Scientific Computing. Computer Graphics, 1987, 21(6).
4. Shreiner, D. OpenGL Reference Manual(Third Edition). Addison-Wesley Publishing Company, 1999.
5. Houlding, S.W. 3D Geoscience Modeling - Computer Techniques for Geological Characterization. Springer Verlag, 1994.
6. Li, Q.Q., Yang, B.S., Shi, W.Z., etc. Theory and Methods of Spatial Data Acquisition. Modelling and Visualization. Wuhan University Press, 2003.
7. Kaiser, P.K. Vasak, P. and Suorineni, F.T. New Dimensions in Seismic Data Interpretation with 3-D Virtual Reality Visualization for Burst-prone Mines. The 6th International Symposium on Rockburst and Seismicity in Mines, (Perth, 2005)
8. Ye, G.X., Hatherly, P., etc. Role for Geophysical Logging in Coal Mine Geotechnical Inverstigation. Chinese Journal of Rock Mechanics and Engineering, 2009, 27(5). 33-37.

RaSiM 7(2009): Controlling Seismic Hazard and Sustainable Development of Deep Mines, C.A. Tang(ed), Rinton Press, 803-810

STUDY ON MECHANICAL BEHAVIOR OF HARD ROCK TUNNEL IN HIGH GEO-STRESSES AND OPTIMIZATION OF ROUND LENGTH IN ROCK BURST AREA

ZHI-QIANG ZHANG, XIAO-QUAN SHI and HUA-YUN LI

School of Civil Engineering, Southwest Jiaotong University

Chengdu, 610031, P.R. China

ZHONG-JIN WAN

Sichuan Yaxi Expressway Co., Ltd

Chengdu, 610041, P.R. China

In this paper, three-dimensional finite difference numerical simulation method considering the strain softening effect is conducted to investigate the occurrence of rock burst in the Daxiangling tunnel through the hard rock layer in high geo-stresses. The results show that the deep-lying hard rock tunnel subjected to the high geo-stresses has the mechanical characteristics of stress-strain orthogonality, which is completely different from that subjected to common geo-stresses. So the occurrence location of rock burst usually is perpendicular to the orientation of the maximum geo-stress. Furthermore, it is found that for the Daxiangling expressway tunnel the rational round length in rock burst area should be limited to about 2 m.

1 Introduction

Nowadays with the development of the economy, the need for infrastructures, especially for transportation transfer such as highway and railway in China are continually increasing, which leads to a growing number of long tunnels in engineering [1]. Particular attention is focused on the construction of long, deep-lying tunnels with large sections, because they determine the success of the whole transportation engineering. For the construction of a deep-lying tunnel, increasing attention is focused on these engineering troubles caused by high geo-stresses. The increasing cases demonstrate that the excavation in deep-lying tunnel is subjected to high geo-stresses which differ from the subjected common geo-stresses, especially in the hard rock condition. Failure to recognize the significance of high geo-stresses has led to the occurrence of rock burst in hard rock [2-3]. Thus, the main objective of geotechnical design in deep-lying tunnels through hard rock layer encountered is to predict potential failure of the surrounding rocks including rock bursts subjected to high geo-stresses, and to assess the possibility form that the failure may take.

As the governing engineering from Yaan to Sichang expressway, Daxiangling tunnel is up to 10km long, and more than 50% area are passing through hard rock which consists of liparite and andesite subjected to high geo-stresses according to The Geology Survey Report of Daxiangling tunnel [4]. So the mechanical behaviour of the tunnel is dominated by the level of high geo-stresses. Although the fact that the length of round as shorter as possible is in favour of stability of tunnel has been widely recognized, however, how short the economic length of round should be designed to prevent the occurrence of rock burst is always the puzzled problem. Through taking the secondary stress distribution, energy density and energy release rate as the evaluation criteria of rock stability, the mechanical behaviour of the tunnel running through hard rock layer in high geo-stresses and the prediction of rock burst occurrence are studied by using three dimensional finite difference numerical simulation method considering the strain softening effect. The results show that the deep-lying hard rock tunnel subjected to the high geo-stresses has the mechanical characteristics of stress-strain orthogonality, so it means that the occurrence location of rock burst usually is perpendicular to the orientation of the maximum geo-stress, which is completely different from that in common geo-stresses. Furthermore, taking the tunnel section with the maximum drilling geo-stresses data as investigated subject, the rational length of round is derived through comparing the results of surrounding rock stability corresponding to the different cases from 1m to 15m length of round by using the drilling and blasting method of complete cross-section excavation.

2 Design of Constitutive Model for Hard Rock Tunnel

Although there are quite a few factors leading to rock burst occurrence during tunnel excavation, such as rock property, condition of in-situ stresses, tunnelling method, and length of round, however, among these factors the rock property and the condition of in-situ stress are widely regarded as the two determinant factors [5] causing rock burst, they are called the internal cause and external cause for rock burst respectively. According to the investigation of history cases, it has been proved that only possessing the both causes simultaneously can rock burst occur. Comparing the complete stress-strain curves, as shown in figure 1, it is found that the loading characteristic of hard rock especially post-peak behaviour, is differently from soft rock, after exceeding the limit of rock strength, the post-peak curve drop down rapidly, and seismic energy release in un-stable failure of brittle rock [6]. By analysing the difference of the complete stress-strain curve between hard rock and soft rock, we can draw the conclusion that the two popular plastic constitutive models obeying Mohr-Coulomb and Drucker-Prager criteria can not be used for describing completely the mechanical behaviour of hard rock tunnel, especially in the case of hard rock subjected to high geo-stresses. Thus, the rational constitutive model for hard rock tunnel should be designed to be the elastic-brittle-plastic constitutive model considering the strain softening effect.

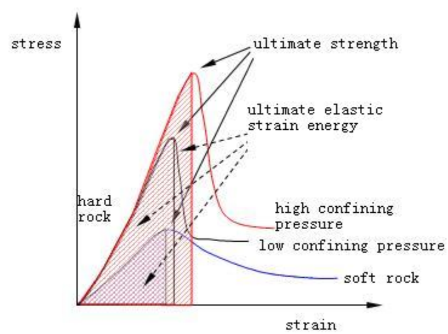

Figure 1 Different complete stress-strain curves of rock

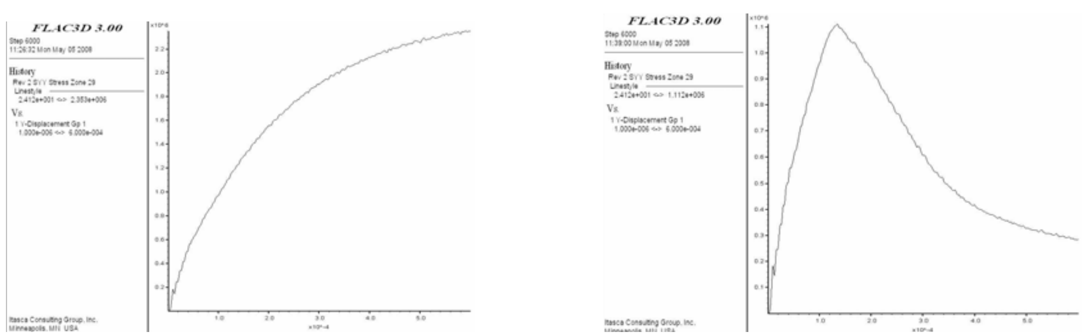

a. Mohr-Coulomb plastic model

b. Strain-softening Mohr-Coulomb model for hard rock tunnel

Figure 2 Design of constitutive model for hard rock tunnel

Based on analysis above, and taking the SZK4 drilling data of rock compression test from The Geology Survey Report of Daxiangling tunnel as investigated subject, a constitutive model considering the strain softening effect for Daxiangling tunnel is obtained by numerical test method, as shown in figure 2b.

3 Stability Analysis of Tunnel Construction

3.1 In-situ geo-stresses

In order to ensure safety of Daxiangling tunnel construction, the in-situ stresses measurement of the three bore-hole (see SZK2, SZK3 and SZK4 in figure 3) along the tunnel axis line by using hydraulic fracturing technique are carried out during construction drawings stage. The quantity value, the orientation of the maximum principal stress and the minimum principal stress of surrounding rock of the tunnel are obtained. Figure 4 gives the change law of three principal stresses of SZK2, SZK3 and SZK4 bore-hole with depth increasing.

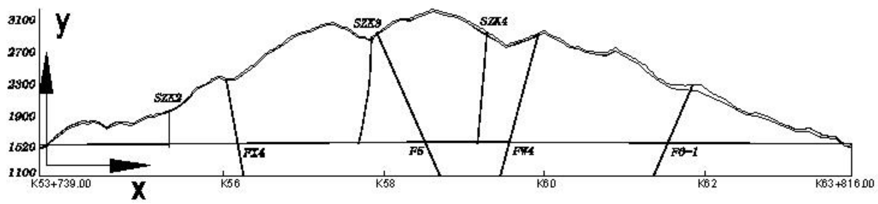

Figure 3 Location of SZK2, SZK3 and SZK4 bore-hole for in-situ stresses measurement of Daxiangling tunnel

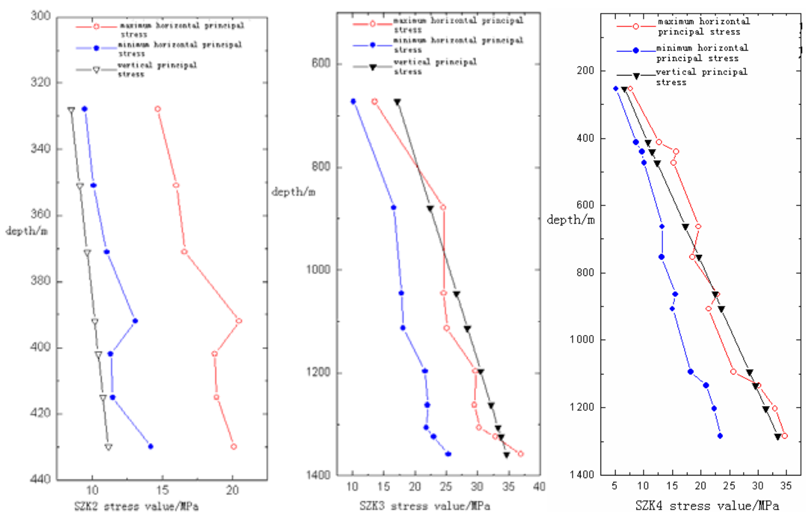

Figure 4 Three principal stresses values along the three bore-hole depth

Table1 lists the three principal stresses of SZK2, SZK3 and SZK4 bore-hole corresponding to the maximum measured depth respectively. Thus, the distribution law of in-situ stress field for Daxiangling tunnel are mainly summarised as the two relational expressions that $\sigma_H > \sigma_h > \sigma_v$ such as SZK2, and $\sigma_v \approx \sigma_H > \sigma_h$ such as SZK3 or SZK4. Herein, σ_H, σ_h and σ_v represent the horizontal maximum principal stress, the horizontal minimum principal stress and the vertical principal stress, respectively.

Table 1. Results of in-situ stresses measurement

Bore-hole	SZK2	SZK3	SZK4
σ_H (MPa)	20	33	35
σ_h(MPa)	14	23	25
σ_v(MPa)	11	35	37
The maximum measured depth	450 m	1340 m	1388 m
σ_C(MPa)	66.8	75.2	120
σ_h / σ_{MAX}	3.34	2.15	3.24

3.2 Choice of case study

According to the definition of high geo-stress[7-8], taking the ratio of the rock compression strength to the maximum principal stress (see table 1) as the evaluation index, it is easy to find that the tunnel area corresponding SZK2, SZK3 and SZK4 bore-hole are subjected to high geo-stress. In order to find out the differences between the deep-lying hard rock tunnel subjected to high geo-stresses and common geo-stresses, in addition to the three high geo-stress cases study above, an assumed case study subjected to one twentieth of SZK4 in-situ stress is selected as the common geo-stress case study called SZK4D in the paper. Table 2 summarizes the four cases study and their corresponding to properties of geo-materials.

Table 2. Properties of geo-materials for 4 cases study

Bore-hole	SZK2	SZK3	SZK4	SZK4D*
γ (g/cm^3)	2.80	2.78	2.67	2.67
σ_C (MPa)	66.87	75.19	120.46	120.46
σ_t(MPa)	5.10	8.50	8.70	8.70
E (GPa)	57.85	53.31	61.22	61.22
μ	0.13	0.14	0.16	0.16
ϕ	47.50	46.70	43.56	43.56
C (MPa)	1.59	2.68	0.88	0.88
Depth of tunnel (m)	450	1340	1388	About 70

3.3 Numerical simulation

Taking SZK4 case study as an example, FLAC^{3D} numerical simulation software [9] is used to establish the three-dimensional finite difference mesh, as shown in figure 5. Considering eliminating size effect, the geometry size is 100×50×100m. The boundary condition of the model is as follows: the base of the model is assumed to be rough, hence it is restrained in all directions. The two sides vertical boundary are confined in x direction, the forth and back vertical boundary are confined in y direction. The top surface is applied stress condition. The in-situ high stress field is simulated by initial stress field and applying boundary condition, as shown in figure 6.

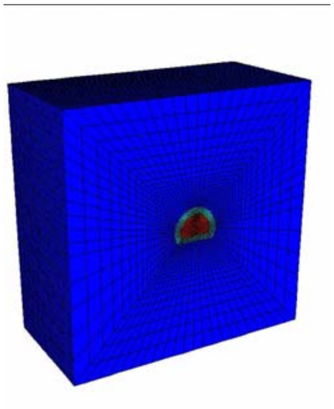

Figure 5 FLAC^{3D} mesh

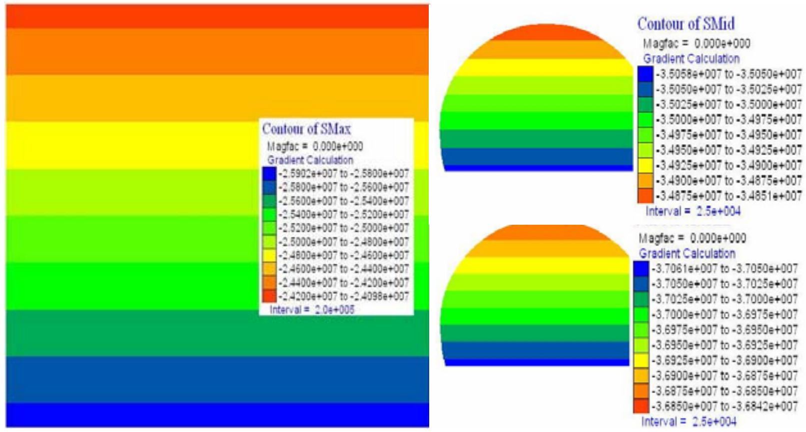

Figure 6 Simulation of the in-situ high stress field for SZK4 case study

3.4 Stability analysis

By calculating three-dimensional strain softening model, the distribution rule of the secondary stress field is obtained after the tunnels are excavated by complete cross-section excavation.

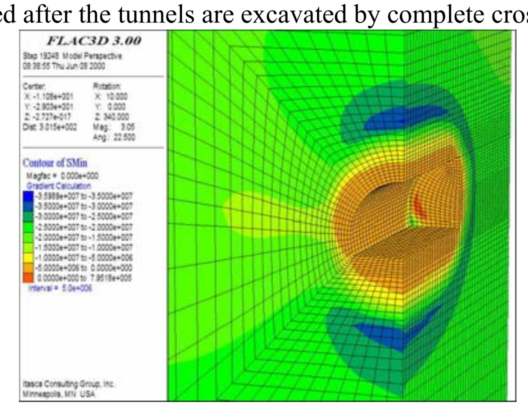

a. SZK2 case study

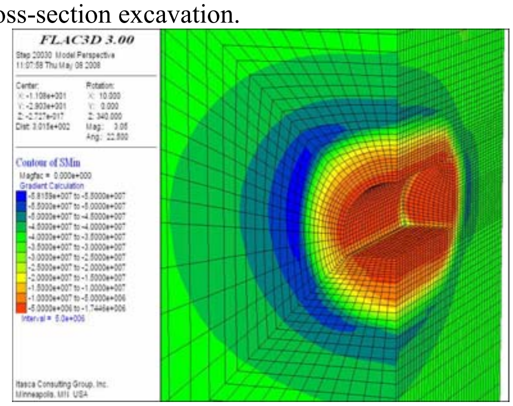

b. SZK3 case study

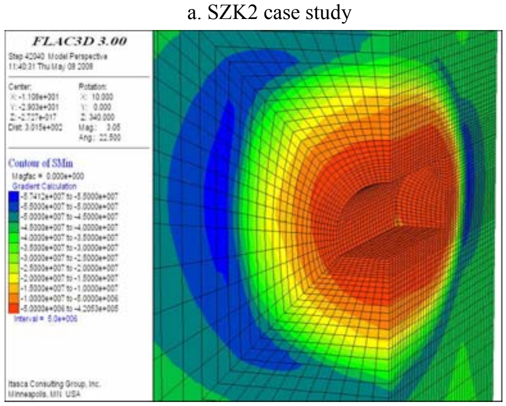

c. SZK4 case study

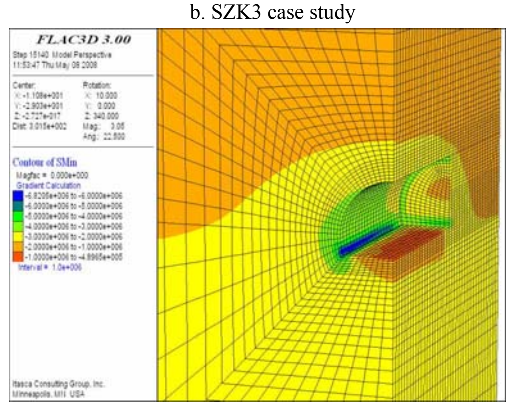

d. SZK4D case study

Figure 7 Distribution contour of the major principal stress σ_θ by complete cross-section excavation

For the case of common geo-stress, the maximum value of the major principal stress σ_θ appears in opening surface (see figure 7d). However, for the case of high geo-stresses, the maximum value of the major principal stress σ_θ appears in internal rock behind plastic zone (see figure 7a~7c), and there are extra stress concentration zone around the maximum σ_θ value. It should be point out that the extra stress concentration zone not only being continually enlarging with in-situ stress increasing, but also the location of the extra stress concentration zone being perpendicular to the direction of the maximum in-situ stress, such as for SZK2 the extra stress concentration zone is located the area of crown. The results show that the deep-lying hard rock tunnel subjected to the high geo-stresses has the mechanical characteristics of stress-strain orthogonality.

3.5 Prediction of rock burst

According to the definition of energy density u (see expression 1), the distribution contour of energy density around tunnel is drawn, as shown in figure 8.

$$u = \frac{1}{2E}(\sigma_1^2 + \sigma_2^2 + \sigma_3^2 - 2\upsilon(\sigma_1\sigma_2 + \sigma_1\sigma_3 + \sigma_2\sigma_3)) \tag{1}$$

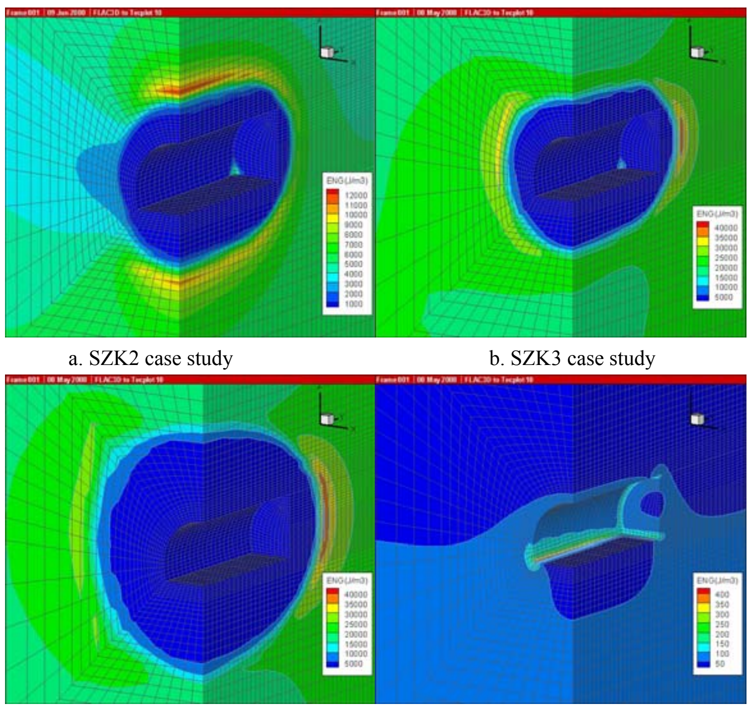

a. SZK2 case study b. SZK3 case study

c. SZK4 case study d. SZK4D case study

Figure 8 Distribution contour of energy density

From figure 8, extracting the maximum value of energy density, the results are listed in the table 3.

Table 3. The maximum energy density for 4 cases study

Case study	SZK2	SZK3	SZK4	SZK4D*
μ_{max}（KJ/m^3）	2.80	2.78	2.67	2.67
Location	In crown	In wall and face	In face and wall	At wall toe

Based on the energy density criterion, it is easily found that SZK3 and SZK4 cases are prone to rock burst occurrence due to their maximum energy density more than the limit value of 40 KJ/m^3. Furthermore, except for the occurrence of rock burst in the face, the occurrence position of rock burst is perpendicular to the orientation of the maximum geo-stress.

4 Optimization of Round Length in Rock Burst area

Considering the most possibility of rock burst occurrence, taking SZK4 case study as investigated subject, the rational length of round is derived by investigating and comparing total energy of elements (whose energy density more than 40 KJ/m^3) and the energy release rate corresponding to the different cases from 1m to 15m length of round.

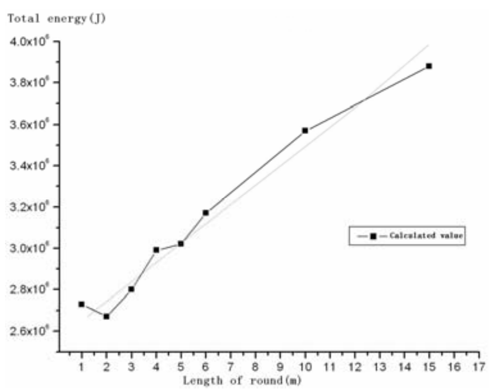

Figure 9 Total stored energy of elements whose energy density more than 40 KJ/m^3 versus length of round

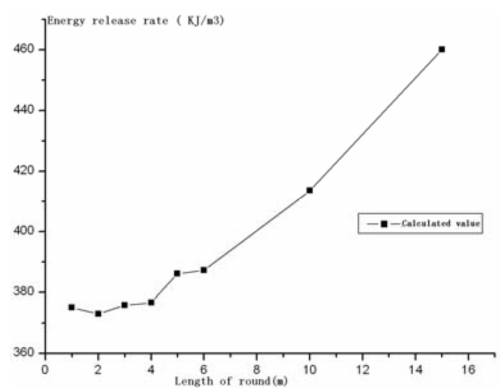

Figure 10 Energy release rate versus length of round

From the overall, it is easily found that total stored energy of elements whose energy density more than 40 KJ/m^3 is generally enhancing with the increase of length of round (see figure 9), that means the more short length of round should be adopted to control or decrease the possibility and range of rock burst occurrence. Fortunately, there is a minimal energy value between 1m and 3m length of round, hence the rational length of round is initially determined to be 2 m. In order to verify the conclusion above, the energy release rate corresponding to the different length of round is calculated, as shown in table 4. The results show that the energy release rate around 2 m length of round is still a minimal value. In addition, it is found that the energy release rate sharply increased while the length of round more than 4m (see figure 10). Hence, in order to the safety of tunnel during excavation, the length of round must be limited below 4m.

Table 4. Calculation results of energy release rate for different length of round

Length of round		1m	2m	3m	4m	5m	6m	10m	15m
Model energy (KJ)	E_I (Energy of initiate conditions)	9.11E+6	9.11E+6	9.11E+6	9.11E+6	9.11E+6	9.11E+6	9.11E+6	9.11E+6
	E_T (Energy of after excavation)	9.20E+6	9.20E+6	9.20E+6	9.19E+6	9.20E+6	9.19E+6	9.20E+6	9.21E+6
	W_G (Gravity acting)	3.50E+4	3.49E+4	3.51E+4	3.50E+4	3.61E+4	3.58E+4	3.84E+4	4.26E+4
	WB (Work done by boundary)	9.72E+5	9.67E+5	9.73E+5	9.72E+5	1.00E+6	9.95E+5	1.06E+6	1.18E+6
Dissipated energy*（KJ）		9.14E+5	9.10E+5	9.16E+5	9.19E+5	9.41E+5	9.45E+5	1.01E+6	1.12E+6
Excavation volume（m^3）		2.44E+3	2.44E+3	2.44E+3	2.44E+3	2.44E+3	2.44E+3	2.44E+3	2.44E+3
Energy release rate (KJ/m^3)		375.07	373.07	375.82	376.78	386.15	387.29	413.53	460.09

Dissipated energy* = $E_I + W_G + W_B - E_T$

Although the optimization of round length determined to be 2m for Daxiangling expressway tunnel, however, the corresponding to the energy release rate is still more than the threshold value 300 KJ/m^3 of rock burst occurrence. Therefore, some measures for controlling rock burst need to be introduced such as drilling hole for stress release in the opening wall and installation of swelled-yielded bolt in the face, etc.

5 Conclusions

In view of the mechanical behaviour of hard rock tunnels subject to high geo-stresses being associated with strain softening characteristics, the rational constitutive model for predicting potential failure of hard rock tunnels including rock burst should be designed to be the constitutive model considering the strain softening effect. A strain softening FLAC constitutive model is established by numerical test methods in this paper.

The research reveals that the deep-lying hard rock tunnel subjected to the high geo-stresses has the mechanical characteristics of stress-strain orthogonality, so it represents the occurrence location of rock burst is usually perpendicular to the orientation of the maximum geo-stress, which is completely different from that in common geo-stresses. In addition, the location of rock burst being situated in the working face is identified.

The optimization of round length in rock burst area should be limited to about 2 m. In order to ensure the safety of the Daxiangling tunnel subjected to the remarkable high geo-stresses, the length of the round should not be beyond 4m during excavation. On this premise of optimization of round length, these effective measures for controlling the occurrence of rock burst should include the measures of drilling distressing holes in the tunnel wall and installing swelled-yielded bolts into the working face.

References

1. Wang, M.S. Discussion On Design And Construction Of Large Tunnel On Passenger Dedicated Line. Journal of Railway Engineering Society, 2005, 85 (1). 10-16.
2. Xu, Z.M.and Huang, R.Q. Progress in Research on Rock Burst Hazard of Long Tunnel with Large Section. Journal of Natural Disaster, 2004, 13 (2). 16-24.
3. Zhang, Z.Q.and Guan, B.S. Basic Analysis of Rock Bursting Occurrence Condition. Journal of the China Railway Society, 1998, 20 (4). 82-85.
4. Sichuan Coal Geological Engineering Design &Research Institute. The Geology Survey Report of Daxiangling Tunnel. Sichuan Coal Geological Engineering Design &Research Institute, 2007.
5. Hou, F.L. and Song, Y.L. The Relations between Rock Burst and the Stresses around the Stope in the Tian-shen-qiao Tunnels. Computer Methods and Advance in Geomechanics, 1991,23(4). 1333-1338.
6. Tang, C. A. Numerical Simulation of Cumulative Damage and Seismic Energy Release during Brittle Rock Failure-Part I: Fundamentals. Int. J. Rock Mech. & Min. Sci., 1998, 35 (2). 113-121.
7. Ministry of Communications, P.R. China. Code for Design of Road Tunnel. China Communications Press, 2004.
8. Ministry of Railway, P.R. China. Code for Design on Tunnel of Railway. China Railway Press, 2005.
9. Itasca Consulting Group Inc. FLAC3D: Fast Lagrangian Analysis of Continua in 3 Dimensions Version 2.0. Minnesota, USA: Itasca Consulting Group Inc., 1993.